Fabian Kiessling
Bernd J. Pichler
Peter Hauff
Editors

Small Animal Imaging

Basics and Practical Guide

Second Edition

Springer

Small Animal Imaging

Fabian Kiessling • Bernd J. Pichler
Peter Hauff
Editors

Small Animal Imaging

Basics and Practical Guide

Second Edition

Springer

Editors
Fabian Kiessling
Universitätsklinikum Aachen
Aachen
Germany

Bernd J. Pichler
Universitätsklinikum Tübingen
Tübingen
Germany

Peter Hauff
Bayer AG, Drug Discovery
Pharmaceuticals
Berlin
Germany

ISBN 978-3-319-42200-8 ISBN 978-3-319-42202-2 (eBook)
DOI 10.1007/978-3-319-42202-2

Library of Congress Control Number: 2016959560

This Springer imprint is published by Springer Nature
The registered company is Springer International Publishing AG
The registered company address is: Gewerbestrasse 11, 6330 Cham, Switzerland

Preface to the Second Edition

This textbook is a practical guide to the use of small animal imaging in preclinical research that will assist in the choice of imaging modality and contrast agent and in study design, experimental setup, and data evaluation. All established imaging modalities are discussed in detail, with the assistance of numerous informative illustrations, and the new edition also includes an extended introduction to emerging technologies such as photoacoustic imaging, hyperpolarized imaging, and novel intravital microscopy techniques.

The second edition includes a variety of other novel features: The section on "Special Applications" has been expanded to include chapters on metabolic imaging, cell tracking, transplant labeling, and imaging of infectious diseases. Additional useful hints are provided on the installation of a small animal unit, study planning, animal handling, and the cost-effective performance of small animal imaging. Furthermore, since many small animal imaging studies fail owing to inadequate contrast agents, a chapter has been added discussing concepts and materials for diagnostic probes in the context of pharmacokinetic demands. Finally, cross-calibration methods and data post-processing are also considered in depth.

While the second edition of this textbook has been updated to encompass emerging new imaging modalities, methods, and applications, the focus remains on practical basics. It will be an invaluable aid for researchers, students, and technicians involved in research into and applications of small animal imaging.

Aachen, Germany — Fabian Kiessling
Tuebingen, Germany — Bernd J. Pichler
Berlin, Germany — Peter Hauff

Preface to the First Edition

During the last decade there have been tremendous advances in molecular biology and many important regulatory pathways of diseases have been identified. Along with these, genomics and proteomics are currently being implemented as important tools in the clinical workflow. On the other hand, there has been significant progress in non-invasive imaging technologies. Nowadays it is possible to scan an entire patient by CT and MRI with high spatial resolution and with exquisite tissue contrast within seconds or minutes. Contrast agents can be applied and their accumulation monitored dynamically to gain functional data about tissue vascularisation, perfusion and permeability. In addition, imaging modalities that are highly sensitive to administered radiolabelled probes like PET and SPECT enable us to elucidate changes in metabolism and proliferation as well as in molecular profiles of tissues with high sensitivity.

Besides these clinically established methods there are novel promising imaging tools and applications which are currently in the stage of development. These include, for example, molecular ultrasound, high field MRI as well as photoacoustic and optical imaging.

Beyond this, imaging modalities have been developed further to such a high degree that they are now able to be applied to very small animals like mice and rats for diagnostic purposes. Current dedicated small animal imaging modalities allow the in vivo assessment of morphological structures or functional, metabolic and molecular processes in mice and rats as in humans.

Utilizing these tools in the preclinical arena can also significantly improve the identification and development of novel diagnostic or therapeutic drugs and facilitate the translation of preclinical findings to the clinics and vice versa. Important surrogate markers and imaging strategies can be developed and tested along with novel therapeutic drugs. Longitudinal data can be obtained from the same animal, which means that the animal can serve as its own control. In this manner the disease progression or the pharmacological effect of a drug can be monitored much more effectively. As a result high statistical power can be achieved with a reduced number of animals, which lowers costs and recognizes ethical considerations on animal protection.

Non-invasive imaging also has the potential to identify therapeutic drugs with limited effectiveness at a very early stage of its development. Therefore it can be used as a preclinical screening tool to boost the clinical drug success rate of currently one in five to, for example, one in three which would significantly lower the development cost for a new drug.

Nevertheless, although there is no doubt about the potentially beneficial role of small animal imaging in preclinical research it has not been broadly established. Many imaging applications have never exceeded the Proof of Principle status and are so time consuming that it is not realistic to use them in preclinical research routinely. This often goes in line with limited data reproducibility. Besides this, in many publications non-invasive imaging acts as an appealing embellishment without having evident impact on its scientific gist. These current obstacles for the implementation of non-invasive small animal imaging are aggravated by failing studies where either a suboptimal imaging modality or contrast was chosen or where failures were made in statistical study planning and animal handling.

Thus, this book aims to be a guide for all who intend to implement small animal imaging in their routine research. It provides concrete hints on how an effective small animal unit can be built up, how the personnel should be trained, where pitfalls in study planning are and which imaging modalities should be used for different purposes. Also, basic problems like the choice of the correct anesthesia and its influence on animal physiology as well as techniques of catheterization for drug administration are considered. Finally this book specifically serves as a guide for the correct and comprehensive quantification and interpretation of imaging data.

We very much hope that this book will be of significant value for our readers in their daily work and we wish every success in the exciting and creative field of preclinical imaging.

Aachen, Germany — Fabian Kiessling
Tuebingen, Germany — Bernd J. Pichler
Berlin, Germany — Peter Hauff

Contents

Part VI Special Applications

Abbreviations

2D	Two-dimension(al)
3D	Three-dimension(al)
μCT	Micro-computed tomography
μMRI	Micro-magnetic resonance imaging
AAALAC	Association for Assessment and Accreditation of Laboratory Animal Care
AC	Air conditioning
ACH	Air changes per hour
ADA	American Disabilities Act
ADME	Adsorption, distribution, metabolization and excretion
ALARA	As low as reasonably achievable
ALS	Amyotrophic lateral sclerosis
AMPH	Amphetamine
AMPT	Alpha-methyl-*para*-tyrosine
AOI	Area of interest
APCs	Antigen presenting cells
APD	Avalanche photodiode
APP	Amyloid precursor protein
ASL	Arterial spin labeling
BAC	Bacterial artificial chromosome
BAL	Bronchoavealoar lavage
BBB	Blood–brain barrier
BCNU	1,3-Bis(2-chloroethyl)-1-nitrosourea
BET	Big endothelin
BGO	Bismuth germinate
BLI	Bioluminescence imaging
BMD	Bone mineral density
BMS	Bulk magnetic susceptibility
BOLD	Blood oxygenation level dependent
BP	Binding potential
BPNP	Bismuth sulfide polymer coating
BSL	Bio safety level
CA	Contrast agents
CAR	Coxsackie and adenovirus receptor
CCAC	Canadian council of animal care
CCD	Charge coupled device
CEA	Carcinoembryonicantigen

CEST	Chemical exchange saturation transfer
CG	Chrysamine G
CM	Contrast media
CMC	Carboxymethylcellulose
CMOS	Complementary metal oxide semiconductor
CNR	Contrast-to-noise ratio
CNS	Central nervous system
COMT	Catechol-O-methyltransferase
COPD	Chronic obstructive pulmonary disease
COV	Coefficient of variation
CR	Congo red
CRF	Corticotropin releasing factor
CSI	Chemical shift imaging
CSS	Cage changing station
CT	Computed tomography
CTDI	CT dose index
CTLS	Cytotoxic T lymphocytes
DCE	Dynamic contrast enhanced
DCIS	Ductal carcinoma in situ
DCT	Discrete cosine transform
DECT	Dual energy CT
DFO	Desferoxamine
DICOM	Digital imaging and communications
DILI	Drug-induced liver injury
DLB	Dementia with Lewy bodies
DLNs	Draining lymph nodes
DMEM	Dulbecco's modified Eagle medium
DNP	Dynamic nuclear polarization
DOI	Depth of interaction
DOT	Diffuse optical tomography
DOTA	1,4,7,10-Tetraazacyclododecane-N,N',N'',N'''-tetraacetic acid
DOTATOC	DOTA-Tyr3-octreotide
DSA	Digital subtraction angiography
DTI	Diffusion tensor imaging
DTPA	Diethylenetriamine-tetraacetic acid
DV	Distribution volume
DVR	Distribution volume ratio
DWI	Diffusion-weighted imaging
DXA	Dual-energy X-ray absorptiometry
EAE	Experimental autoimmune encephalomyelitis
EB-CCD	Electron-bombarded CCD
EBV	Epstein–Barr virus
ECF	Extracellular fluid
ECG	Electrocardiography
EDDA	Ethylendiamin-N,N`diacetic acid
EGF	Epidermal growth factor
EGFR	Epidermal growth factor receptor
EHS	Environmental health and safety

EM	Electromagnetic
EMCL	Extramyocellular lipids
EPSI	Echo planar spectroscopic imaging
ER	Endoplasmatic reticulum
ETS	European convention for the protection of vertebrate animals used for experimental and other scientific purpose
FACS	Fluorescence-activated cell sorting
FAZA	Fluoroazomycin arabinoside
FBP	Filtered back projection
FDG	Fluorodeoxyglucose
FDHT	16beta-18F-fluoro-5alpha-dihydrotestosterone
fDOT	Fluorescence DOT
FES	Fluorine-18 fluoroestradiol
FFD	Free form deformation
FID	Free induction decay
FITC	Fluorescein-isothiocyanate
FLT	18F-3-Deoxy-3-fluorothymidine
FMISO	Fluorine-18 labeled fluoromisonidazole
fMRI	Functional MRI
FMT	Fluorescence-mediated molecular tomography
FMT	l-[3-18F]fluoro-a-methyl tyrosine
FOV	Field-of-view
FSH	Follicle stimulating hormone
FTLD	Frontotemporal lobar degeneration
FWHM	Full-width at half-maximum
Gd-DTPA	Gadolinium-diethylenetriaminepentaacetate
GEM	Genetically engineered mouse
GFP	Green fluorescent protein
GIST	Gastrointestinal stromal tumor
GLUT-1	Glucose transporter 1
GSO	Germanate oxyorthosilicate
GV-SOLAS	Society of laboratory animals
H&E	Hematoxylin and eosin
HFC	High fat/high cholesterol
HK-II	Hexokinase II
hNET	Human norepinephrine transporter
hNIS	Human sodium iodide symporter
HPGe	High purity germanium
HPLC	High-pressure liquid chromatography
HRE	Hypoxia-response element
HSA	Human serum albumin
HSP90	Heat shock protein 90
HSV-tk	Herpes simplex virus thymidine kinase
HTOS	High throughput organic synthesis
HU	Hounsfield Unit
HYNIC	2-Hydrazinonicotinic acid
IACUC	Institutional animal care and use committee
IAPs	Inhibitors of apoptosis proteins

IATA	International air transport association guidelines
ICAM-1	Intercellular adhesion molecule-1
ICCD	Intensified CCD
ICG	Indocyanine Green
ICMIC	In Vivo Cellular and Molecular Imaging Center
ILAR	Institute for Laboratory Animal Research
IMCL	Intramyocellular lipids
IMT	l-[3-123I]iodo-a-methyl tyrosine
ISIS	Image-selected in vivo spectroscopy
IT	Information technology
IVC	Individually ventilated cages
LGSO	Lutetium germanate oxyorthosilicate
LH	Luteinizing hormone
LN	Lymph node
LO	Lead optimization
LPS	Lipopolysaccharide
MAC	Minimum alveolar concentration
MAG3	Mercaptoacetyltriglycine
MAP	Maximum a posteriori
MAR	Micro-autoradiography
MB	Microbubble
MCAo	Middle cerebral artery occlusion
MCP	Microchannel plate
MEMRI	Manganese-enhanced MRI
METH	Methamphetamine
MHC	Major histocompatibility complex
MI	Mechanical index
MLEM	Maximum likelihood expectation maximization
MMP	Matrix metallo proteinase
MRI	Magnetic resonance imaging
MRM	MR microscopy
mRNA	Messenger ribonucleic acid
MRS	Magnetic resonance spectroscopy
MRSI	Magnetic resonance spectroscopic imaging
MSA	Multiple system atrophy
MSCT	Multislice/computed tomography
MTP	Medial tibial plateau
MTT	Mean transit time
NAS	Network attached storage
NCI	National Cancer Institute
NDT	Nondestructive testing
NET	Norepinephrine transporter
NFAT	Nuclear factor of activated T cells
NHL	Non-Hodgkin's lymphoma
NIBIB	National Institute for Biomedical Imaging and Bioengineering
NIH	National institutes of Health
NIR	Near-infrared
NIS	Sodium iodide symporter

NK	Natural killer
NMRS	Nuclear magnetic resonance spectroscopy
NMV	Net magnetization vector
NOTA	1,4,7-Triazacyclononane-1,4,7-triacetic acid
NPC	Neural progenitor cell
NSC	Neural stem cell
NSP	Nucleoside salvage pathway
OAT	Optoacoustic tomography
OCT	Optical coherence tomography
OI	Optical imaging
OPO	Optical parametric oscillator
OPT	Optical projection tomography
OSEM	Ordered subsets expectation maximization
OT	Optical tomography
OVA	Ovalbumin
PAI	Photoacoustic imaging
PAT	Photoacoustic tomography
PBBR	Peripheral benzodiazepine receptor
PBS	Phosphate buffered saline
PD	Proton density
PDGF	Platelet-derived growth factor
PDH	Pyruvate dehydrogenase
PEG	Polyethylene glycol
PEPE	Perfluoropolyether nanoparticle
PET	Positron emission tomography
PFC	Perfluorocarbon
Pgp	P-glycoprotein
PHIP	Para-hydrogen-induced polarization
PKC	Protein kinase C
PLC	Phospholipase C
PMT	Photomultiplier tube
PnAO	Propylenediamine-dioxime
PPE	Porcine pancreatic elastase
PRESS	Point resolved spectroscopy
PS	Phosphatidylserine
PSCA	Prostate stem cell antigen
PSF	Point spread function
PSMA	Prostate-specific membrane antigen
PSPMTs	Position-sensitive PMTs
PTX	Pertussis toxin
PVE	Partial volume effect
QDs	Quantum dots
QM	Quantum mechanics
QWBA	Quantitative whole-body autoradiography
RAID	Redundant drive array
rBV	Relative blood volume
RC	Recovery coefficient
rCBF	Regional cerebral blood flow

REM	Resource equation method
RES	Reticuloendothelial system
RF	Radiowave frequency
RFP	Red fluorescent protein
RGD	Arginine-glycine-aspartate
ROI	Region-of-interest
RSO	Radiation safety offices
RTK	Receptor tyrosine kinase
SA	Serum albumin
SAA	Sugar amino acids
SAI	Small animal imaging
SAIRP	Small-animal imaging research program
SAR	Structure activity relationship
SI	Spectroscopic imaging
siPM	Silicon photomultiplier
SNR	Signal-to-noise ratio
SOP	Standard operating procedures
SPAQ	Sensitive particle acoustic quantification
SPECT	Single photon emission computed tomography
SPIO	Superparamagnetic iron oxide
SPM	Statistical parametric mapping
SR	Synchrotron radiation
SR	Shift reagent
SRTM	Simplified reference tissue model
SSD	Sum of the squared intensity differences
ST	Saturation transfer
STEAM	Stimulated echo acquisition mode
SUV	Standardized uptake value
TAC	Thoracal aortic constriction
TAC	Time activity curve
TCA	Tricarboxylic acid cycle
TCEP	Triscarboxyethylphosphine
TCR	T-cell receptor
TDI	Tissue-Doppler imaging
TE	Echo time
TETA	1,4,8,11-Tetraazacyclotetradecane-1,4,8,11-tetraacetic acid
TK1	Thymidine kinase-1
TKIs	TK inhibitors
TLD	Thermoluminescent dosimeter
TRAIL	Tumor necrosis factor-related apoptosis-inducing ligand
TSTU	Tetramethyluronium tetrafluoroborate
UBM	Ultrasound biomicroscopy
UCA	Ultrasound contrast agents
US	Ultrasound
USPIO	Ultrasmall particles of iron oxide
VAP	Vascular access port

VCAM-1	Vascular cell adhesion molecule-1
VCT	Volumetric CT
VEGF	Vascular endothelial growth factor
VEGFR2	Vascular endothelial growth factor receptor-2
WAG	Waste anesthetic gas

Part I

Role of Small Animal Imaging

Noninvasive Imaging for Supporting Basic Research

1

Pat Zanzonico

Contents

1.1 Introduction

Imaging has long been indispensable in clinical practice. In vivo imaging of small laboratory animals (i.e., mice and rats) is now also firmly established as a critical component of preclinical and translational biomedical research (Beckman et al. 2007; Cherry 2006; Pomper 2001, 2005; Kiessling et al. 2011). Small-animal imaging provides a noninvasive means of assaying biological structure and function in vivo, yielding quantitative, spatially and temporally indexed information on normal and diseased tissues such as tumors. Importantly, because of its noninvasive nature, imaging allows serial (i.e., longitudinal) assay of rodent models of human cancer and cardiovascular, neurological, and other diseases over the entire natural history of the disease process, from inception to progression, and monitoring of the effectiveness of treatment or other interventions. With each animal serving as its own control, not only is biological variability reduced but the number of experimental animals required for a particular study is also minimized. With the ongoing development of genetically engineered (i.e., transgenic and knockout) rodent models of cancer and other diseases, such models are increasingly more realistic in recapitulating the natural history and clinical sequelae of the corresponding human condition, and the ability to track these disease models long term is therefore invaluable. Importantly, in contrast to cell or tissue culture-based experiments, studies

P. Zanzonico, PhD, DABR
Memorial Sloan Kettering Cancer Center,
1275 York Avenue, New York, NY 10021, USA
e-mail: zanzonip@mskcc.org

F. Kiessling et al. (eds.), *Small Animal Imaging*, DOI 10.1007/978-3-319-42202-2_1

in intact animals incorporate all of the interacting physiological factors – neuronal, hormonal, nutritional, immunological, etc. – present in the complex in vivo milieu. Intact whole-animal models also facilitate investigation of systemic aspects of disease such as cancer metastasis, which are difficult or impossible to replicate in ex vivo systems. Further, because many of the same imaging modalities – magnetic resonance imaging (MRI), computed tomography (CT), single-photon emission computed tomography (SPECT), positron emission tomography (PET), and ultrasound (US) – used in the clinic are also used in the laboratory setting, the findings of small-animal imaging are readily translatable to patients.

Prior to the inception of "small-animal imaging," experimental animals were generally imaged using clinical instrumentation (during off-hours, of course), and many useful studies were performed in this way. In many instances, however, the performance of clinical imaging devices is inadequate – most notably, the spatial resolution is prohibitively coarse – for scientifically useful imaging of tumors and organs in mice and rats (Fig. 1.1). The need for better spatial resolution, the development of dedicated small-animal imaging instruments, and of centralized facilities to house these instruments, has also been motivated by a number of practical considerations. First, by incorporating invasive and often clinically impractical corroborative assays (e.g., interstitial probe measurements, histology, immunohistochemistry, etc.) into small-animal imaging studies, new and/or existing clinical imaging paradigms can be clarified, vali-

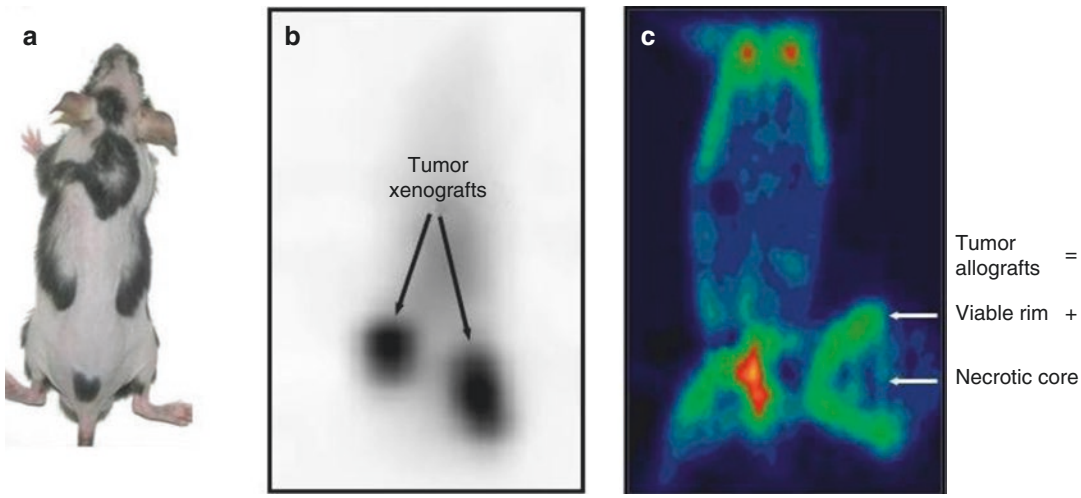

Fig. 1.1 Comparative PET images of tumor-bearing mice acquired with a clinical and a small-animal PET scanner (Zanzonico 2011). (**a**) A photograph (not to scale) showing the orientation of the animals in the PET images. (**b**) A coronal PET image of a mouse with a Lewis Y antigen-expressing HCT15 human colorectal carcinoma xenograft in each of its two hind limbs. The image was acquired at ~2 days postinjection of an yttrium-86 (^{86}Y)-labeled humanized anti-Lewis Y antibody, hu3S193, using a clinical PET scanner, the GE Advance™ (General Electric Medical Systems), with a full-width half-maximum (*FWHM*) spatial resolution of 6 mm and volume resolution of 216 mm^3. (**c**) A coronal PET image with an FSA II murine fibrosarcoma allograft in the right hind limb. The images was acquired at ~1 h postinjection of ^{18}F-FDG using a dedicated rodent PET scanner, the R4 microPET (Concorde Microsystems), with a FWHM spatial resolution of 2.2 mm and volume resolution of 10.6 mm^3. All three tumors were comparable in size (1–1.5 cm in the largest dimension). Although the image acquired on the clinical scanner (**b**) clearly demonstrates high-contrast uptake of the radiotracer by the two tumors, it does not show any heterogeneity of uptake within the tumors. If any such heterogeneity is present, any parameter derived from the measured uptake will reflect some ill-defined value of any such parameter averaged over the entire tumor. In contrast, the image acquired on the small-animal scanner (**c**) distinguishes the differential uptake of FDG between biologically distinct cell subpopulations within the tumor, namely, high uptake in a viable rim and much lower uptake in a largely necrotic core. For any parameters derived from the tracer uptakes in (**c**), therefore, distinct, and more meaningful, parameter values can be derived for the viable rim and for the necrotic core

dated, and/or improved in the laboratory and then translated back to the clinic. Second, biosecurity (i.e., protection from transmission of infectious and other diseases among experimental animals and between animals and humans) of immunodeficient and other genetically engineered animal models requires that such animals remain within a "clean" barrier facility and are not, for example, transported out of such a facility to a clinical imaging area and then back to the facility. Third, in certain institutions and jurisdictions, experimental animals are prohibited by regulation from entry into clinical areas. Fourth, the limited and, at times, unpredictable availability (i.e., at night, overnight, and/or on weekends and holidays) of clinical imaging instrumentation makes it very difficult to plan and perform experiments, especially experiments involving large numbers of animals, multiple imaging sessions, and/or time-sensitive imaging studies.

Imaging-based experimentation in small-animal models is now an established and widely used approach in basic and translational biomedical research and will no doubt remain an important component of such research. Several areas – drug development, treatment monitoring, and novel therapeutic strategies such as adoptive immunotherapy and gene therapy – are particularly productive in the application of small-animal imaging. In drug development, imaging-based assays are particularly amenable to quantitative characterization of pharmacokinetics and pharmacodynamics of new therapeutics and may accelerate the drug discovery process. Transgenic and knockout mouse models of human disease may be used for identification and validation of "drug-able" molecular targets. Clinically translatable imaging paradigms developed and validated in animal models may also provide earlier and more clinically meaningful assays of therapeutic response, enabling clinicians to rapidly distinguish "responders" from "nonresponders" and promptly switch patients from ineffective to potentially more effective therapies, thereby avoiding unnecessary toxicities, expense, and loss of time.

The clinically translatable, noninvasive, and quantitative nature of small-animal imaging makes it an invaluable component of modern biomedical research. And the availability of dedicated small-animal imaging devices and facilities has resulted in wider and more scientifically useful application of imaging in preclinical experimentation.

1.2 Imaging Modalities

Historically, imaging modalities have often been divided into two general categories, structural (or anatomical) and functional (or physiological). Anatomical modalities, depicting primarily morphology with excellent spatial resolution, include x-rays (plain radiography), MRI, CT, and US. Functional modalities, depicting primarily information related to underlying metabolism and biochemistry, include MRSI and functional magnetic resonance imaging (fMRI), (planar) scintigraphy, SPECT, PET, and, now, optical (bioluminescence and fluorescence) imaging. This traditional distinction between anatomical and functional imaging modalities is, however, increasingly arbitrary and inaccurate, as dynamic and/or static MRI, CT, and US imaging may be performed following administration of a blood-flow or molecularly targeted contrast agent and functional images derived. The functional modalities form the basis of the rapidly advancing field of "molecular imaging," defined as the direct or indirect noninvasive monitoring and recording of the spatial and temporal distribution of in vivo molecular, genetic, and/or cellular processes for biochemical, biological, diagnostic, or therapeutic applications (Mankoff 2007). In addition to the foregoing "established" imaging modalities, new modalities, primarily based on optical signaling, are emerging.

1.2.1 Established Modalities

The general relationship between molecular sensitivity and spatial resolution for the various imaging modalities is summarized graphically in Fig. 1.2 (Tichauer et al. 2015) and discussed below. "Reverse translation" of clinical imaging modalities to small-animal research requires substantial improvement in performance (most notably, spatial

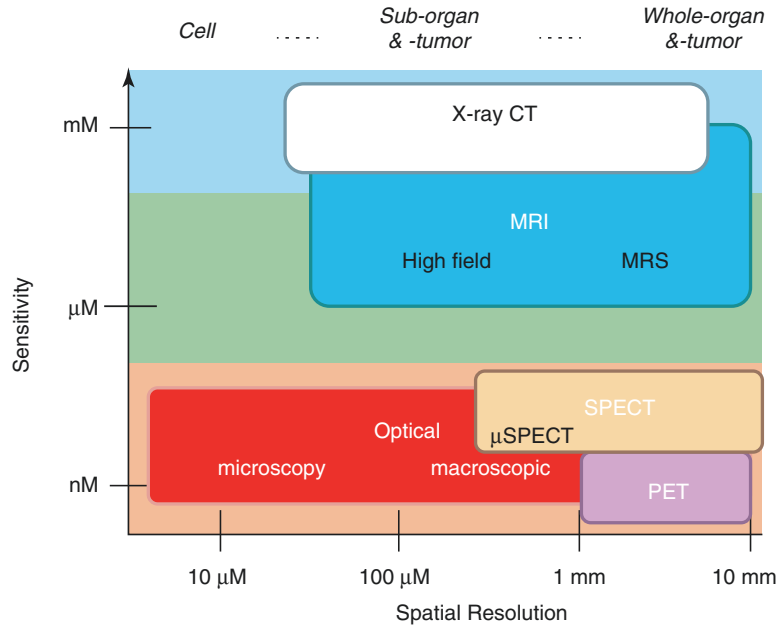

Fig. 1.2 Relationship between molecular sensitivity (i.e., the lowest concentration of an imaging probe/contrast agent that can be accurately detected) and spatial resolution for in vivo imaging modalities (Tichauer et al. 2015)

Table 1.1 Comparative spatial resolution of clinical and preclinical imaging modalities and associated design refinements

	Spatial resolution (mm)		
Modality	Clinical	Preclinical	Clinical-to-preclinical design refinement(s)
MRI	~1 mm	≤100 μm	Higher-field-strength magnets, improved gradient fields and coils
MRSI	~1 cm	~2 mm	"
PET	~5 mm	1–2 mm	Reduced detector-element size, smaller-diameter detector rings
SPECT	~1 cm	0.5–2 mm	Pinhole collimation (and resulting magnification)
CT	1–2 mm	≤100 μm	Higher x-ray flux, smaller focal spot, and higher magnification
US	1–2 mm	≤100 μm	Higher-frequency scan heads

resolution) of the respective modalities and has involved reengineering of many aspects of their imaging hardware, firmware, and software, as discussed below and summarized in Table 1.1 (Beckman et al. 2007; Cherry 2006; Pomper 2001, 2005). The capabilities and limitations of the respective modalities are briefly discussed as well. The reader is referred to the respective modality-specific chapters in references (Bushberg et al. 2012; Cherry et al. 2015) for further details.

Magnetic resonance imaging (MRI) Combining high-strength magnetic fields with non-ionizing radiofrequency (RF) radiation, MRI exploits atomic nuclei with odd numbers of nucleons and thus net magnetic moments (or spins). Briefly, a subject is placed in a uniform, high-field-strength magnetic field, causing a small excess of such nuclei (most commonly hydrogen-1 nuclei in water molecules) to align their nuclear spins with the magnetic field and thereby produce a net magnetization vector parallel to the field (i.e., in the z direction). At that point, there is no net magnetization in the xy plane, that is, perpendicular to the direction z of the magnetic field. A brief RF pulse at the Larmor resonance frequency (typically in the MHz frequency range), determined by the intrinsic gyromagnetic ratio of the nucleus of interest and the strength of the magnetic field, is applied which "flips" the nuclear spins and thus the net magnetization vector from their lower-energy configuration parallel to the mag-

netic field to a higher-energy configuration at some angle other than parallel to the direction *z* of magnetic field; this angle is known as the "flip angle" and depends on the duration and amplitude of the excitation RF pulse. The resulting net magnetization vector can be resolved into components antiparallel and perpendicular to the magnetic field (i.e., along the *z* axis and in the *xy* plane, respectively); one can therefore picture the net magnetization vector as precessing about the *z* direction. Immediately following this excitation pulse, the nuclear spins will begin to revert back to their lower-energy, preexcitation state in a time-dependent manner, emitting RF radiation in the process; the RF energy thus emitted is the imaging signal. The component in the *z* direction (i.e., parallel to the magnetic field) will increase until the magnetization vector has recovered to its maximum value parallel to the applied magnetic field. The time required for the magnetization vector to recover to 0.63 (=1 – 1/*e*) of this maximum value is the T1, or spin–lattice, relaxation time. At the same time, the nuclear spins comprising the component of the magnetization vector in the *xy* plane, originally "in phase" (i.e., rotating synchronously about the z axis), gradually become de-phased, eventually pointing in random directions in the *xy* plane and thus canceling each other out. The time for this free-induction-decay signal (i.e., the *xy* plane signal) to decrease to 0.37 (=1/*e*) of its maximum value is called the T2, or spin–spin, relaxation time. T1 relaxation times are typically in the range of tens of milliseconds and T2 relaxation times in the range of hundreds of milliseconds. The RF excitation pulse sequences can be designed to emphasize the signal from either the *z*-direction or the *xy*-direction magnetization vector, producing either T1-weighted or T2-weighted images, respectively. T1- versus T2-images can differ widely in appearance and thus accentuate different magnetic properties of tissues.

Spatial indexing of the MR signal and thus the creation of images is accomplished with a set of gradient magnets which apply a linearly varying magnetic field across the subject in the *x*, *y*, and *z* directions. These gradient fields are superimposed on the main magnetic field and, together, yield a position-dependent net magnetic field and thus a position-dependent Larmor frequency across the subject. The position dependence of the Larmor frequency thus yields a three-dimensional array of spatially localized MR signals which ultimately comprise the MR image set.

The net magnetic fields in tissue at the microscopic level depend on the local molecular environment as well as the applied magnetic field, yielding the remarkable tissue contrast (including that among soft tissues such as tumors and visceral organs) uniquely characteristic of MRI. Another notable feature of MRI is its excellent spatial resolution (expressed, for example, as the full-width half-maximum (FWHM) of the line or point spread function), typically well under 100 μm in small-animal systems. Magnetic field strengths typically are no greater than 3 tesla (T) in clinical MRI systems, but may exceed 10 T in preclinical systems. Only a very small excess of nuclear spins are actually aligned with the applied magnetic field, depending on the field strength (e.g., 3 per million protons at 1 T). Higher-field strengths yield a greater number of nuclear aligned with the field and thus an improved signal-to-noise ratio (SNR). Resolution can be further improved by utilizing specialized coils which can be placed closer to a structure of interest (e.g., around or on a tumor) than a "whole-body" coil but with a considerably smaller field of view. Of course, MRI systems are expensive (typically over $1 million) and higher-field-strength systems (beyond ~1 T) require superconducting magnets and thus cryogens such as liquid helium as well as magnetically shielded rooms to house the magnet. Loss of the cryogen and thus of superconductivity of such a magnet (a process known as "quenching") is catastrophic. Permanent magnet-based systems do not engender any such risk, but are limited to field strengths no greater than ~1 T.

Administration of paramagnetic materials such as gadolinium-based agents can significantly enhance contrast, and the resulting temporally varying contrast enhancement in combination with dynamic imaging and mathematical modeling can be used to derive various indices of tissue perfusion.

Computed tomography (CT) Computed tomography (CT) is a radiographic imaging modality which yields three-dimensional "maps" of the relative attenuation of x-rays by different tissues. CT images are commonly parameterized in terms of Hounsfield units (HUs), defined as 1,000 $\frac{\mu - \mu_{water}}{\mu_{water}}$, where μ and μ_{water} are the linear attenuation coefficients of the tissue and of water, respectively. On the HU scale, water has a value of 0, air −1,000, and (compact) bone nearly 1,000. The HU values for most soft tissues are in a narrow range of −100 to 100; the differential attenuation among soft tissues is thus so limited that it is difficult to impossible to distinguish different soft tissues (at least without administration of radiographic contrast agents (see below)). In small-animal CT scanners, the x-rays emanate as a cone beam from the x-ray tube focal spot, pass through the subject, and strike an opposed, large-area solid-state radiation detector; the transmission image thus acquired is called a "projection image." (Cone beam geometries are suboptimal for clinical imaging because of the abundant scatter they produce for subjects as large as patients; for mice, however, scatter is far less abundant and far less problematic.) The entire assembly then rotates a small angular increment (of the order of 1–2°) about the longitudinal axis of the subject, and another projection image is acquired. The complete set of transmission images acquired around the subject is mathematically reconstructed to yield a set of contiguous transverse images with excellent spatial resolution (of the order of 100 μm or better); these images can be re-sorted to yield coronal and sagittal images as well.

The x-ray stopping power of a medium such as tissue is determined by its electron density (i.e. the number of electrons per cubic centimeter); this, in turn, is determined by the effective atomic number and the mass density of the medium. As a result, bone (with a relatively high effective atomic number and electron density due to its calcium content), the lung (with a low mass density and electron density due to its air content), and soft tissue can be readily distinguished from one another on CT scans. Different soft tissues, however, are difficult to impossible to resolve, as noted. In clinical CT scanning, therefore, intravenously administered iodinated contrast agents are often used to temporarily increase the electron density of different tissues, with the resulting radiographic enhancement of different tissues related to their differential blood (and therefore contrast agent) content. However, clinical contrast agents are water soluble and thus very rapidly excreted through the kidneys, so that the contrast enhancement is very short lived. Unlike state-of-the-art "spiral" (or "helical") scanners used clinically, in which a complete study can be acquired in a matter of seconds, small-animal CT studies take at least several minutes to acquire the complete set of projection images. As a result, conventional radiographic contrast agents are not suitable for small-animal scanners because of their rapid clearance from blood, and alternatives such as iodinated or metal (e.g., gold)-impregnated nanoparticles or pegylated chylomicron particles have been developed for such devices (Au et al. 2013; Li et al. 2014). These agents persist in the circulation for many minutes to hours and thus are compatible with the long acquisition times for typical small-animal CT scanners.

It should be noted that the radiation doses to experimental animals resulting from radiological studies (i.e., PET and SPECT as well as CT) are considerable, up to ~10 cGy – one to two orders of magnitude higher than those encountered in the corresponding clinical studies. Cumulative absorbed doses from serial imaging of a given animal may thus approach 100 cGy, comparable to single-fraction doses used in external-beam radiation therapy. Investigators should be aware of the magnitude of such doses encountered in small-animal PET, SPECT, and CT studies and potential radiogenic perturbation of their experimental system.

Ultrasound (US) US imaging is based on the generation of high-frequency sound waves by piezoelectric crystals, their propagation through tissue, and their differential reflection versus transmission at interfaces between tissues having different acoustical properties (more specifically,

different acoustic impedances). The reflected sound waves, or echoes, are detected by the same transducer (or "scan head") which produces the sound waves. In order to avoid artifactual echoes created by the air between the surface of the scan head and the animal's skin, any fur must be thoroughly removed to eliminate entrapped air and acoustical gel layered on the animal's skin and into which the scan head is immersed; acoustical gel is, of course, used in clinical US as well. The depth of the echogenic tissue interface is determined by the time interval between the initial generation of the sound wave and the detection of the returning echo. In the conventional imaging mode (i.e., the B, or brightness, mode), US is essentially a two-dimensional (2D) modality, yielding a depthwise image in the plane of the transducer. By translating the transducer while imaging, three-dimensional (3D), or volumetric, images can be created. While clinical systems typically operate in the 3- to 15-MHz frequency range, small-animal US systems operate in the 25- to 75-MHz range, with lower frequencies generally used for rats and the higher frequencies for mice. The spatial resolution of US, which is inversely related to the frequency, is excellent – of the order of 50 μm or better. However, to a considerably greater extent than MRI, CT, PET, and SPECT, US is limited by depth of penetration, ranging from ~3 cm at the higher frequencies to ~1 cm at the lower frequencies in the 25- to 75-MHz range; this is compounded by the fact that the reflected sound waves, which create the US image, must travel through an equal thickness of overlying tissue as the emitted sound waves to return to the scan head. Contrast agents in the form of intravenously injected microbubbles can be used to image the vasculature; the echogenic bubbles remain trapped in the circulation until a higher-power US pulse is used to burst the bubbles. Dynamic imaging performed while the bubbles are injected can yield "maps" of relative perfusion among tissues. Moreover, microbubbles can be affinity-labeled for molecular imaging by surface conjugation of molecularly targeted moieties such as antibodies (e.g., anti-vascular endothelial growth factor receptor (VEGFR) antibody). US is unique in that it is the only real-time imaging modality, capturing images at rates of up to 1,000 frames per second. In addition to contrast (i.e., microbubble)-enhanced dynamic imaging of perfusion, cardiac motion can be imaged (a technique known as "echocardiography") with uniquely high temporal resolution and functional parameters such as the left ventricular ejection fraction derived. US systems are portable and relatively inexpensive and do not require any specialized infrastructure. Potentially confounding biological effects of ionizing radiation are avoided as well. US imaging is often perceived as requiring considerable experience and skill (in terms of positioning and orienting the scan head with respect to the relevant anatomy and real-time recognition of the anatomy).

Radionuclide imaging: single-photon emission computed tomography (SPECT) and positron emission tomography (PET) Radionuclide imaging, including SPECT and PET, utilizes unsealed sources of radioactivity administered, almost always systemically and usually intravenously, in the form of radiotracers (in a clinical setting, also known as radiopharmaceuticals). Diagnostic radionuclide imaging of patients is part of the clinical specialty known as nuclear medicine. Radionuclide imaging in general and SPECT and PET in particular offer a number of important advantages. First, the specific activity (i.e., activity per unit mass) of radiopharmaceuticals and the detection sensitivity of radionuclide-imaging instruments are sufficiently high in that administered activities needed for imaging correspond to non-pharmacologic, non-perturbing mass doses (typically in the sub-nmol range). This is in contrast to CT and MRI, for example, where the mass doses of various contrast agents are far higher – typically in the μmol to mmol range – and thus may perturb the subject under study. (See Fig. 1.1.) Second, radionuclide images are quantitative or at least semiquantitative, meaning that image "intensity" (i.e., counts) reflects the radiotracer-derived activity concentration. For PET, images are routinely absolutely quantitative and may be parameterized, for example, in terms of activity concentration.

For other imaging modalities, the relationship between the contrast agent or other analyte concentrations and image intensities is typically not as direct. Third, a large number and variety of molecularly targeted and/or pathway-targeted radiotracers (such as metabolites and metabolite analogs, neurotransmitters, drugs, receptor-binding ligands, antibodies and other immune constructs, etc.) have been and continue to be developed for increasingly specific characterization of in situ biology. Radionuclide imaging is not without its drawbacks, however. These include relatively coarse spatial resolution (see below), about an order of magnitude poorer than the spatial resolution of CT and MRI. Further, radionuclide imaging is, of course, a radiation-based modality and thus delivers low but non-negligible radiation doses.

The basic paradigm of both SPECT and PET imaging includes acquisition of projection images from multiple angles at 1–3° angular increments around the subject, correction of the acquired data for nonuniform response of the imaging system, and mathematical reconstruction of transverse-section images. The resulting transverse images are essentially contiguous, with no intersection gaps. Therefore, the reconstructed three-dimensional array of volume elements, or voxels, may be rearranged at any angle relative to the longitudinal axis of the subject and thus yield coronal, sagittal, or oblique as well as transverse images. The principal advantage of tomography lies in its improved image contrast and greater quantitative accuracy: by eliminating the count contribution from activities in tissues above and below the section of interest, the target (e.g., tumor)-to-background ratio and the accuracy of image-derived activity concentrations improve. Another important advantage of emission tomography is the ability to visualize the three-dimensional distribution of activity in situ, that is, to ascertain the depths of foci of activity.

Developed in the late 1950s by Hal Anger, the gamma-camera, also known as the scintillation or Anger camera, has long been the predominant imaging device for SPECT and for single-photon (gamma- and x-ray) imaging in general. Gamma-camera scintillation crystals, almost universally, are composed of thallium-doped sodium iodide (NaI(Tl)), with thicknesses of the order of 1 cm; such a crystal stops ~95 % of the 140-kev gamma-rays emitted by technetium-99 m, the most commonly used non-PET radionuclide. In small-animal systems, multiple opposed crystals (e.g., two pairs of opposed crystals) are used, typically square in shape with areas of ~10×10 cm. The gamma-camera collimator, comprised of a lead plate with holes (apertures) through which the radiations must pass to reach the crystal, "directionalizes" the incoming radiation: any radiation traveling at an oblique angle to the axes of the apertures will strike the inter-aperture lead walls (septa) and not reach the crystal, thereby allowing only radiation traveling parallel or nearly parallel to aperture axes to reach the crystal and contribute counts to the resulting image. In clinical systems, so-called parallel-hole collimators, in which the apertures and septa are parallel to one another, are used almost exclusively. For preclinical systems, however, multi-aperture pinhole apertures angled with respect to one another are now used, combining the magnification effect, and improved resolution, of pinhole collimation with the greater sensitivity afforded by multiple apertures as well as multiple detectors; such preclinical systems can achieve a spatial resolution of ~1 mm or better. In such systems, the animal-to-aperture and aperture-to-crystal distances are of the order of 1 cm and 10 cm, respectively, yielding a magnificent factor of ~10. Combined with a crystal, or intrinsic, resolution of ~10 mm or better, a system spatial resolution of ~1 mm ($= \frac{10\,\text{mm}}{10}$) or better is obtained. In small-animal SPECT, administered activities are typically of the order of 10 MBq.

Once the incident radiation passes through the collimator aperture, it strikes and may produce a scintillation (or light "flash") within the crystal. The resulting light signal is distributed among a two-dimensional array of photomultiplier tubes (PMTs) backing the crystal; a PMT is essentially a vacuum tube which converts the

light signal to an electronic signal, which is then amplified by virtue of an ~1,000-V high voltage. The light intensity reaching each PMT varies inversely with the distance between the scintillation and the respective PMT: the farther the PMT is from the scintillation, the less light it receives and the smaller its output pulse. This inverse relationship is the basis of the Anger position logic circuitry for determining the precise position of a scintillation within the crystal. In the older gamma-cameras, the *x* and *y* coordinates were calculated by analog circuitry, that is, using matrices of resistors. In current system, this is done by digitizing the output signal from each PMT and using digital electronics. For SPECT, the gamma-camera assembly actually rotates around the subject to acquire projection images, each typically taking 20–30 s. Because of the total length of time (20–30 min) thus required for such a study, dynamic SPECT imaging remains largely impractical at the current time. Gamma-camera collimators are interchangeable, however, and one may choose to use parallel-hole collimation for either dynamic or static planar imaging (including planar imaging of multiple animals simultaneously). Of course, one sacrifices the resolution-enhancing magnification effect of pinhole collimation, with overall spatial resolution of no better than ~10 mm. With planar imaging, one also sacrifices the visualization of the three-dimensional distribution of activity.

PET is based on the annihilation coincidence detection (ACD) of the two colinear (approximately 180° apart) 511-keV γ-rays resulting from the mutual annihilation of a positron and an electron (Zanzonico 2004, 2012; Zanzonico and Heller 2007). Positrons are emitted by radionuclides having an unstably high proton-to-neutron ratio, typically traveling only a very short distance (~1 mm or less) in tissue or other media before undergoing annihilation. When both photons from an annihilation event interact simultaneously (actually, within ~10 ns) with two detectors connected to a coincidence circuit, the circuit is triggered and a coincidence event generated. In PET, the direction from which an event originated is thus defined electronically, and an important advantage of ACD is that absorptive collimation (as is used in gamma cameras) is not required. As a result, the sensitivity of PET – up to ~10 % for small-animal scanners – is two to three orders of magnitude higher than that of SPECT. Clinical PET scanners typically span a distance of 15–20 cm in the patient's longitudinal direction. Thus, a whole-body PET scan will require data acquisition at six to seven discrete bed positions and subsequent merging, or "knitting," of the discrete images into a whole-body image. In preclinical systems, the longitudinal field of field is typically of the order of 10–20 cm, large enough for a whole mouse to be imaged at a single bed position. In contrast to SPECT, the detector assembly does not rotate (as described below) and projection data completely around the subject are simultaneously acquired. Dynamic PET imaging is therefore practical. The spatial resolution of preclinical PET scanners is typically 1–2 mm and administered activities of ~5 MBq or less are commonly used.

Modern PET scanners generally employ a series of rings of discrete, small-area detectors (i.e., scored block detectors or individual, or pixilated, crystals) encircling the subject. The scintillation detector materials most widely used in PET are: bismuth germanate (BGO, $Bi_4Ge_3O_{12}$), cerium-doped gadolinium oxyorthosilicate (GSO(Ce) or GSO, Gd_2SiO_5:Ce), cerium-doped lutetium oxyorthosilicate (LSO(Ce) or LSO, Lu_2SiO_5:Ce), and cerium-doped lutetium–yttrium oxyorthosilicate (LYSO(Ce) or LYSO, Lu_2YSiO_5:Ce). LSO and LYSO have emerged as the detectors of choice for PET. BGO, GSO, LSO, and LYSO have higher effective atomic numbers and mass densities than NaI(Tl) and thus higher stopping powers for 511-keV annihilation gamma-rays. While the stopping power and resulting detection sensitivity of NaI(Tl) are sufficient for the lower-energy x- and gamma-rays (~70 to ~360 keV) emitted by commonly used single-photon emitters such as technetium-99 m, indium-11 thallium-201, and iodine-131, NaI(Tl) really has inadequate stopping power and therefore sensitivity for 511-keV annihilation gamma-rays.

Optical imaging Despite the very limited penetrability of optical and near-infrared (NIR) light in tissue, specialized technologies have led to widespread and very productive use of light – both bioluminescence and fluorescence – for in vivo imaging of rodents (Contag et al. 1998; Ntziachristos et al. 2005) and, to a much more limited extent to date, of human subjects; for the latter, this has been restricted to fluorescence imaging in an endoscopic or intraoperative setting (Taruttis and Ntziachristos 2012). For optical imaging, animals are placed in a light-tight imaging enclosure and the emitted optical or NIR signal is imaged by a cryo-cooled charge-coupled detector (CCD) (Fig. 1.3). In bioluminescence imaging, cells (e.g., tumor cells) which are to be localized or tracked in vivo must first be genetically transduced ex vivo to express a so-called reporter gene, most commonly, a luciferase gene. After the cells have been implanted, infused, or otherwise administered to the experimental animal, the luciferase substrate (D-luciferin in the case of firefly luciferase) is systemically administered. Wherever the administered substrate encounters the luciferase-expressing cells, the ensuing reaction (such as the D-luciferin-luciferase reaction) emits light, which is detected and localized by the imaging system. The CCD in bioluminescence imaging is maintained at a very low temperature (of the order of −100 °C), thereby ensuring that any electronic output it produces results from light striking the CCD rather than the background "dark current" (which would be prohibitively high at ambient temperatures). In this way, the otherwise undetectably small signal originating in vivo and escaping from the surface of the animal can produce an image. In fluorescence imaging, the cells to be imaged may either be genetically transduced ex vivo to express a fluorescent molecule (or fluorophore) such as green fluorescent protein (GFP) or a fluorophore probe targeting the cells of interest may be systemically administered. In either case, the animal is then externally illuminated with light at an appropriate excitation wavelength (obtained by

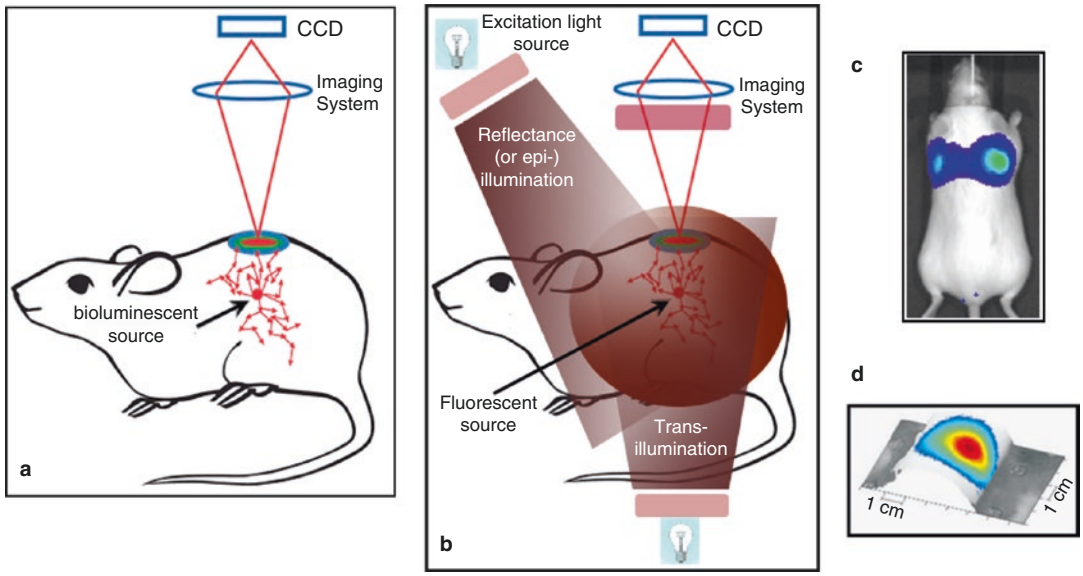

Fig. 1.3 (**a**) Bioluminescence and (**b**) fluorescence optical or NIR in vivo imaging. For fluorescence imaging, the excitation light source may be a white-light source whose emitted light is passed through conventional glass filters to yield a light over a narrow wavelength range centered about the excitation wavelength of the fluorophore being imaged. Alternatively, it may be a laser light source tuned to the appropriate wavelength. In so-called "multispectral" systems, multiple excitation and emission wavelengths and thus multiple fluorophores may be imaged simultaneously. (**c**, **d**) These sample images show a pseudo-color bioluminescence images superimposed on a gray-scale photograph and on a three-dimensional rendering of a mouse, respectively (From reference Zanzonico (2011) with permission)

filtration or with a laser) to energize the fluorophore in situ, and the resulting emitted light (which has a slightly different wavelength than the excitation light) is itself filtered and detected by the CCD; the difference in wavelengths between the excitation and emitted light is known as the Stokes shift. The excitation light may be provided by reflectance (or epi-) illumination of or by transillumination through the animal. Further, by computer processing, the abundant spontaneous fluorescence of the animal's tissues as well as of foodstuffs in the gut must be mathematically separated, or "de-convolved," from the overall fluorescence to yield an image specifically of the fluorophore; this is sometimes known as "spectral unmixing." In practice, the resulting luminescence or fluorescence image is superimposed on a conventional (i.e., white-light) photograph of the animal to provide some orientation as to the anatomic location of the signal(s) in vivo.

Because light emitted at any depth of tissue is scattered and otherwise dispersed as it passes through overlying tissue before emanating from the surface of the animal, the apparent size of the light source is considerably larger than its actual size. Despite the excellent spatial resolution of the photodetectors themselves, the effective resolution of optical and NIR imaging is therefore rather coarse, of the order of several millimeters or greater. Further, for planar optical and NIR imaging, the resulting images are only semiquantitative; attenuation, scatter, and dispersion of the emitted light as it passes through overlying tissue make the measured signal highly depth-dependent. Thus, a focus of cells lying deep within tissue may appear less luminescent or fluorescent than an identical focus of cells at a more shallow depth; if excessively deep, such a focus of cells may be undetectable altogether. NIR radiations, however, have a substantially higher penetrance through tissue than blue to green radiations. Recently, by combining specialized acquisition techniques with sophisticated mathematical modeling of the passage of light through tissue, tomographic bioluminescence and fluorescence images can be reconstructed (Ntziachristos et al. 2005). The resulting three-dimensional images are more quantitative than planar images, with the light intensity thus reconstructed more closely related to the light intensity actually emitted in situ.

1.2.2 Newer Modalities

Cerenkov imaging A new approach to optical imaging is based on the emission of a continuum of visible light associated with the decay of certain radionuclides (actually, with the particles emitted as result of the radionuclide decay) (Beattie et al. 2012; Cerenkov 1934; Dothager et al. 2010; Holland et al. 2011; Li et al. 2010; Liu et al. 2010; Lucignani 2011; Robertson et al. 2009; Ruggiero et al. 2010; Thorek et al. 2012). This phenomenon, now known as the "Cerenkov effect," was first observed in the 1920s and characterized in the 1930s by Pavel Cerenkov (Cerenkov 1934). In 1958, Cerenkov shared the Nobel Prize in Physics with colleagues Ilya Frank and Igor Tamm for the discovery and explanation of the effect which now bears his name. Cerenkov radiation is perhaps familiar to some readers as the bluish "glow" observed in the water pools containing spent, but still radioactive, fuel rods at nuclear reactors. It arises when charged particles such as beta-particles travel through an optically transparent, insulating medium at a speed greater than that of light in that medium. The Cerenkov effect, often analogized to the sonic boom that occurs at the instant a supersonic plane exceeds the speed of sound in air, occurs as the charged particles dissipate their kinetic energy by polarizing the electrons in the insulating medium (most commonly, water) as they travel through the medium. As these polarized electrons then relax (or re-equilibrate), and if the charged particle is traveling faster than light, constructive interference of the light thus emitted occurs, producing the grossly visible Cerenkov radiation.

The application of Cerenkov radiation to in vivo radionuclide imaging is a recent development (Beattie et al. 2012; Dothager et al. 2010; Holland et al. 2011; Li et al. 2010; Liu et al.

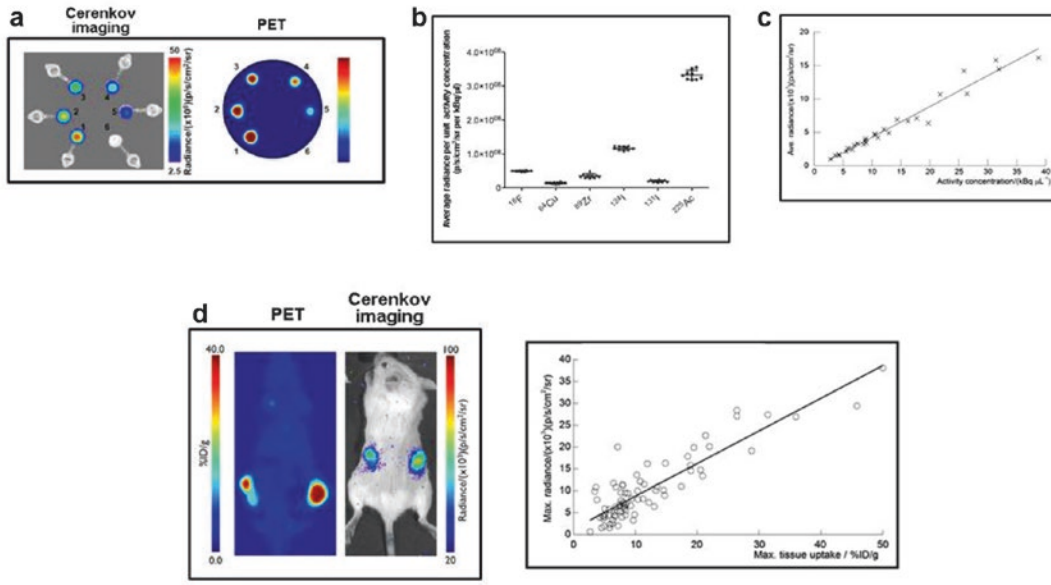

Fig. 1.4 (**a**) Phantom for evaluation of Cerenkov imaging of positron-emitting radionuclides, comprised of a circular arrangement of six 1-ml Eppendorf tubes filled with increasing activity concentrations. *Left panel*: Cerenkov image superimposed on a photograph of the phantom acquired with an Ivis 200 optical imaging system (Caliper Life Sciences). *Right panel*: PET image of the phantom acquired with a Focus 120 microPET scanner (Concorde Microsystems). (**b**) Average radiance per unit activity concentration (in photons (p)/second (s)/cm^2/steradian (sr) per kBq/μl) for different radionuclides as measured using the phantom arrangement and instrumentation described in (**a**). (**c**) Linear correlation ($r = 0.98$) between average radiance (in p/s/cm^2/sr) and activity concentration (in kBq/μl) for ^{89}Zr evaluated again using the phantom arrangement and instrumentation described in (**a**). (**d**) PET image (left panel) and Cerenkov image (right panel) of a ^{89}Zr-anti-PSMA (prostate-specific membrane antigen) antibody (J591) in a mouse with bi-lateral flank LNCaP prostate tumor xenografts at 96 hours post-injection. The Cerenkov image is superimposed on a photograph of the mouse. The two xenografts are clearly visible in both images. (**b**) Linear correlation (r = 0.89) between the Cerenkov image-derived average radiance (in p/s/cm^2/sr) and the PET image-derived maximum tissue uptake (in percent of the injected dose per gram, %ID/g). (Adapted from references Ruggiero et al. (2010), Thorek et al. (2012) with permission)

2010; Lucignani 2011; Robertson et al. 2009; Ruggiero et al. 2010; Thorek et al. 2012). Phantom studies by Ruggiero et al. have demonstrated, using a commercial optical imaging system equipped with a cryo-cooled CCD, measurable emission of Cerenkov radiation associated with a number of clinically relevant radionuclides, including ^{18}F, copper-64 (^{64}Cu), zirconium-89 (^{89}Zr), iodine-124 (^{124}I), iodine-131 (^{131}I), and actinium-225 (^{225}Ac) (Ruggiero et al. 2010) (Fig. 1.4a, b). Importantly, the optical Cerenkov signal is linearly related to activity concentrations (Fig. 1.4c), at least where the effects of attenuation and scatter are minimal. Ruggiero et al. have also produced planar Cerenkov images of the tumor localization of a ^{89}Zr-labeled antibody in prostate-tumor xenografts in mice which compare favorably, both qualitatively and quantitatively, with the ^{89}Zr PET images (Ruggiero et al. 2010) (Fig. 1.4d, e).

Photoacoustic imaging In photoacoustic imaging (Daghighian et al. 1996; Herzog et al. 2012; Gorska-Chrzastek et al. 2004), tissues are illuminated with laser light.[1] In the presence of a fluorescent tracer or fluorescent cells (as described above for conventional fluorescence imaging) or simply due to endogenous tissues fluorescence, some of the delivered energy will be absorbed

[1] When radiofrequency (RF) pulses are used, the technology is termed, "thermoacoustic imaging."

and converted into a small amount of heat, leading to transient thermoelastic expansion of the illuminated tissue and thus ultrasonic (i.e., MHz frequency) emissions. The ultrasonic waves thus emitted are then detected by ultrasonic transducers to form images. Image contrast is provided by the differential fluorophore concentration or endogenous fluorescence and the resulting differential absorption among tissues of the incident excitation light. In contrast to conventional fluorescence imaging, in which scattering in tissue degrades spatial resolution with increasing depth, photoacoustic imaging provides better spatial resolution (of the order of 100 μm) and deeper imaging depth (of the order of 1 cm or greater) because there is considerably less absorption and scattering in tissue of the ultrasonic signal compared to the emitted light signal in fluorescence imaging. When compared with US imaging, in which the contrast is limited because of the similarity in acoustical properties among tissues, photoacoustic imaging provides better tissue contrast. As noted, the optical absorption in biological tissues can be due to endogenous molecules such as hemoglobin or melanin or exogenously administered contrast agents. Since blood exhibits orders of magnitude higher light absorption than other tissues, there is sufficient endogenous contrast provided by oxygenated hemoglobin (HbO_2) and deoxygenated hemoglobin (Hb) for photoacoustic imaging to visualize blood vessels.

Most commonly, photoacoustic scanners use either a tomographic geometry (with an array of up to several hundred US transducers partially surrounding the subject) (Daghighian et al. 1996) or a planar geometry employing a linear transducer array (Kruger et al. 2003; Wang et al. 2004). The tomographic approach offers a large effective aperture for data collection, but suffers from a low frame rate (>10 min per frame), due to the need for hundreds to thousands of laser pulses per frame. The use of a linear array eliminates the need for scanning and thus a two-dimensional frame can be acquired with many fewer laser pulses, providing much higher frame rates. In addition, in the tomographic geometry, the surface of the transducers are of the order of 1 cm from the surface of the subject (up to now, rodents) to accommodate an array of transducers encircling the subject. As a result, the mouse or rat must be immersed in water to provide the necessary acoustical coupling to the transducer; in the multispectral optoacoustic tomography (MSOT) system marketed by iThera Medical, the animal is suspended in a very thin membrane and then immersed in the water, thereby keeping the animal completely dry. Another preclinical photoacoustic imaging system, employing a linear transducer array, is marketed by VisualSonics.

Photoacoustic imaging has been used successfully in preclinical models for tumor perfusion angiogenesis monitoring (Herzog et al. 2012), blood oxygenation mapping, functional brain imaging, and melanoma detection, among other applications. The resulting functional images can be superimposed on high-resolution B-mode anatomic images.

Diffuse optical tomography Diffuse optical tomography (DOT) utilizes NIR light to generate quantitative functional images of tissue with a spatial resolution of 1–5 mm at depths up to several centimeters (Hielscher 2005; Henry et al. 2011). Propagation of NIR light through a medium is dominated by scattering rather than absorption – tissue absorption path lengths are ~10 cm, while scattering path lengths are less than 50 μm – and can be modeled as a diffusion process where photons behave stochastically (in a manner analogous to that of particles in random-walk modeling of diffusion). Quantitative measurements can be obtained by separating light absorption from scattering using spatial- or temporal-modulation techniques. Tissue molecular composition, including the determination of the concentrations of oxy- and deoxyhemoglobin, water, lipid, and exogenous probes, and tissue structure can be determined from absorption and scattering measurements, respectively. Time-modulation systems use picosecond optical pulses and time-gated photon-counting detectors; frequency-modulation systems use an RF-modulated light source, PMTs or fast photodiodes, and RF phase detectors. DOT has been applied to breast cancer diagnostics (4,5), joint imaging (6,7), and blood

oximetry (i.e., activation studies) in human muscle and brain tissue (8,10) as well as to cerebral ischemia and cancer studies in small animals. Commercial instruments are now available that yield tomographic and volumetric image sets. These devices are compact, portable, and relatively inexpensive (~$150 K).

Optical coherence tomography Optical coherence tomography (OCT) is an interferometric technique, typically employing low-coherence NIR light (i.e., light over a broad range of wavelengths), to produce two-dimensional images of tissue surface layers and structure (Huang et al. 1991). The principle of OCT is analogous to that of pulse-echo (i.e., B-mode) ultrasound imaging except OCT uses light instead of acoustic waves to delineate tissue structure by measuring reflectance of light rather than sound waves and thus achieves far better spatial resolution but with less depth penetration. The technique has been described as "an optical biopsy," since OCT can produce near-histologic images (spatial resolution: 1–15 μm) without excision. Due to photon absorption and scattering, its sampled depth is limited to within several millimeters of the tissue surface. The two-dimensional images can be assembled to construct a volumetric image set. In OCT, the axial resolution is proportional to the center wavelength and inversely proportional to the bandwidth of the light source and improves with the index of refraction of the sample. Originally developed for and still most commonly applied to ophthalmology (to obtain detailed images of retinal structure), OCT is being applied for cancer diagnosis and tissue characterization.

Raman spectroscopic imaging When light interacts with matter, most of the light is elastically scattered, retaining its original energy, frequency, and wavelength; this phenomenon is also known as Rayleigh scattering (Fig. 1.5a). However, a small fraction of light is inelastically scattered, with the scattered light having a lower energy and frequency and longer wavelength than the incident light. The process leading to this inelastic scatter is termed the Raman effect (Zavaleta et al. 2011), and the difference in wavelength between the incident and scattered light is called the Raman shift. Because photons with optical energies interact with outer-shell, or valence, atomic electrons, which are responsible for the intramolecular chemical bonds among atoms, materials having different molecular compositions will inelastically scatter light differently. Every molecule therefore has a distinct Raman spectrum (or "signature"), that is, a different Raman shift-dependent intensity of the scattered light; this is the basis of using Raman spectroscopy for noninvasive testing to identify the molecular constituents of various materials (Zavaleta et al. 2011). By illuminating a sample with a highly collimated beam of light and at the same time either translating a scattered-light detector or the sample in two dimensions, spatial indexing of the Raman spectrum can be performed and a Raman-spectrum image created. Though they may appear similar, the Raman effect is distinct from fluorescence in that the former represents a light-scattering phenomenon and the latter light absorption and re-emission. Like fluorescence imaging, Raman spectroscopic imaging has been applied to endogenous (or intrinsic) molecules naturally present in tissue and to exogenously administered materials (as in surface-enhanced Raman scattering (SERS) (see below)).

A drawback of the Raman effect as an analytical tool is that it is a very weak phenomenon, producing only one inelastically scattered photon for every ten million elastically scattered photons. Technical advances, such as the introduction of lasers and of resonance-based enhancements, have greatly expanded the practical applications of the Raman effect. For years now, the Raman effect has been used in a variety of analytical applications and, more recently, in various in vitro cell assays and microscopy. The most commonly used enhancement methods are surface-enhanced Raman scattering (SERS) and coherent anti-stokes Raman scattering (CARS); both SERS and CARS enhance the Raman signal by orders of magnitude. SERS involves adding metal (e.g., gold) nanoparticles which absorb the optical energy and yield an enhanced Raman signal by virtue of the metal surface

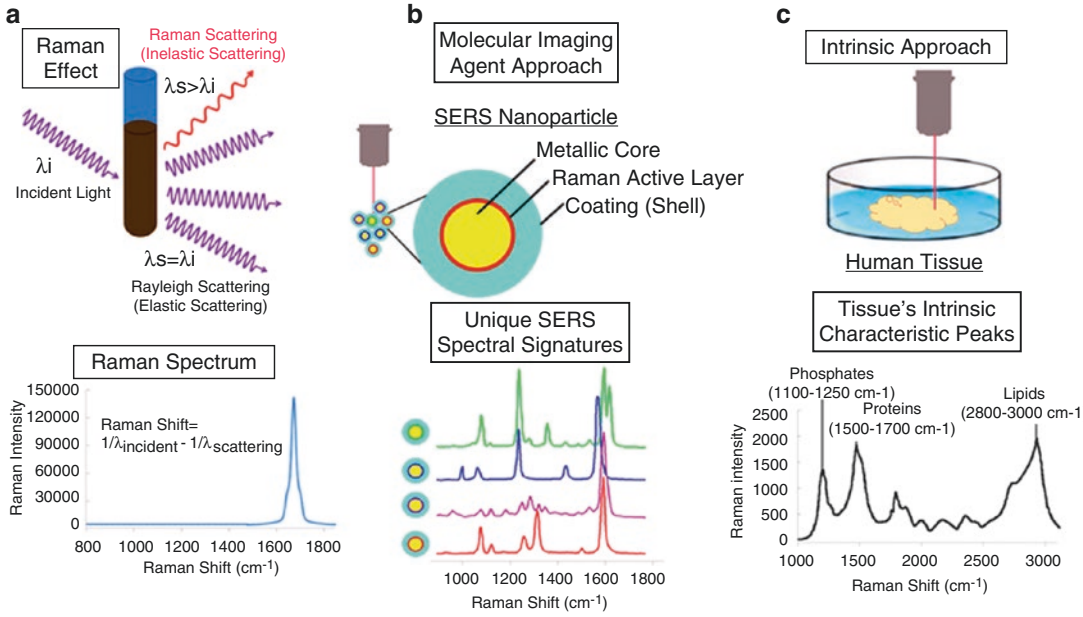

Fig. 1.5 (**a**) Raman effect, showing sample being illuminated with incident photons of wavelength (λi). Most of the incident photons are scattered elastically (Rayleigh scattering) and resulting scattered photons have same wavelength (λs) as the incident photons (i.e., λs=λi). A few photons are inelastically scattered (Raman scattering) at wavelengths longer than incident photons (i.e., λs>λi). The relative proportion of inelastically scattered photons is typically depicted using a Raman spectrum, which is a plot of scattered-photon intensity versus the Raman shift (i.e., the energy difference (expressed as the difference in wave number) between the incident and scattered photons). Multiple different wavelengths of inelastically scattered light can occur and a spectrum plot can therefore include multiple peaks, although a single primary peak, as shown, is also possible. (**b**) Molecular imaging-agent approach showing SERS nanoparticles, which consist of a metallic core, a Raman-active layer adsorbed onto the metal surface, and a shell coating the entire particle. An array of unique spectral signatures can be obtained by modifying the Raman-active layer of the nanoparticle. These unique Raman nanoparticles can serve as molecular-imaging agents for in vitro and in vivo procedures. (**c**) The intrinsic approach, showing a human tissue specimen being illuminated with a laser. The intrinsic Raman spectral signature of tissue can reveal important information about phosphate, protein, and lipid content of cells or tissue of interest (From reference Zavaleta et al. (2011) with permission)

transferring energy to nearby molecules (Fig. 1.5b). The resulting Raman signal provides picomolar sensitivity, which is compatible with tissue tracer concentrations achievable in vivo. Furthermore, labeling SERS nanoparticles with several different molecular ligands can provide simultaneous assay of multiple molecular components. CARS involves illumination with photons of different energies, with one photon energizing a molecule of interest from its ground state to an initial excited state and a second photon energizing the molecule from a "relaxed" state (i.e., at an energy level after releasing energy during the "laser-off" time interval following absorption of the first photon) to a different higher-energy level; this second (or higher) tier of vibrational energy is ~fivefold more intense than the Raman signal after the original pulse (Fig. 1.5c). The CARS technique is often used for high-resolution, three-dimensional microscopy. Its advantages are that there is no need for administered probes (as in SERS) and rapid acquisition of images. Several preclinical studies have utilized the SERS or CARS techniques for in vivo molecular imaging of cell receptors (e.g., RGD-carbon nanotubes that bind to α5β3 integrin-expressing tumors), tumor microvessels, enzyme activity, pH, lipid composition, and myelin composition.

Over the last decade, the biomedical applications of Raman spectroscopic imaging have grown dramatically. Because it is essentially a

surface imaging technique (like most optical imaging techniques), Raman spectroscopic imaging has been applied mainly to examination of the skin and of pathological specimens as well as to small animals. For example, Raman mapping has enabled accurate identification of malignant from benign lesions and normal tissue in the skin, brain, larynx, parathyroids, breast, and urinary bladder. Raman spectroscopic imaging has also been applied endoscopically in the colon.

1.3 Imaging Probes and Contrast Agents

Several different classes of imaging probes and contrast agents are currently employed in small-animal experimentation (Pomper 2005; Serganova and Blasberg 2006; Serganova et al. 2008; Vallabhajosula 2009). These include: (1) "biomarker" or "surrogate"-imaging agents: related to some physiological process (e.g., blood flow) or to some downstream effects of one or more endogenous molecular/genetic processes (e.g., ^{18}F-FDG PET imaging reflecting upregulation of glucose transporters and/or glycolytic metabolic pathways in many tumors); (2) "Direct" imaging of specific molecules: based on binding of radiolabeled ligands (e.g., imaging of the α5β3 integrin, commonly overexpressed in tumor vasculature, with radiolabeled glycosylated RGD (arginine-glycine-aspartate)-containing peptides); (3) Nanoparticles; (4) "Indirect" reporter-gene imaging (Serganova and Blasberg 2006; Serganova et al. 2008; Gambhir and Yagboubi 2010).

Nanoparticles, supramolecular particles with nanoscale dimensions (i.e., dimensions of ~100 nm or less), include quantum dots, superparamagnetic iron oxide nanoparticles (SPIONs), and polymer- or lysosome-based nanoparticles. Perhaps the most attractive feature of nanoparticles for in vivo applications is that they may incorporate various therapeutic as well as diagnostic payloads. Diagnostic payloads include fluorophores (in addition to quantum dots themselves), radionuclides, paramagnetic materials (as in SPIONs), high atomic number elements (such as iodine or gold) for radiographic contrast, or, importantly, combinations of the foregoing image-able materials to produce multimodality tracers. Moreover, multiple copies of such payloads may be incorporated into a single particle, effectively amplifying the image-able signal(s). Further, the surface of nanoparticles may be functionalized (or "decorated") with various affinity labels (such as antibodies) for molecular targeting; multiple copies of such affinity labels may be attached, yielding a multivalent and thus high-affinity targeting construct.

The reporter-gene imaging paradigm (Fig. 1.6), representing a convergence of molecular and cell biology and the imaging sciences, is providing new insights into signal transduction pathways, oncogenesis, endogenous molecular genetic/biological processes, and response to therapy in animal models of human disease. In addition, reporter-gene nuclear imaging is now being applied clinically to the nascent field of adoptive immunotherapy of cancer and will likely find applications in gene therapy as well (Serganova and Blasberg 2005; Serganova et al. 2007).

A general summary of modality-specific imaging probes/contrast agents is presented in Table 1.2.

1.4 Multimodality Imaging

Information derived from multiple modalities is often complementary, for example, localizing the site of an apparently abnormal metabolic process to a pathologic structure such as a tumor. In addition to anatomic localization of "signal" foci, registration and fusion of multimodality images provide a number of important advantages, including intra- as well as inter-modality corroboration of diverse images and more accurate and more certain diagnostic and treatment-monitoring information. Following alignment of the respective images in a common coordinate system (a procedure referred to as *registration*), *fusion* is required for the integrated display of these aligned images. The objectives of image registration and fusion of multimodality images,

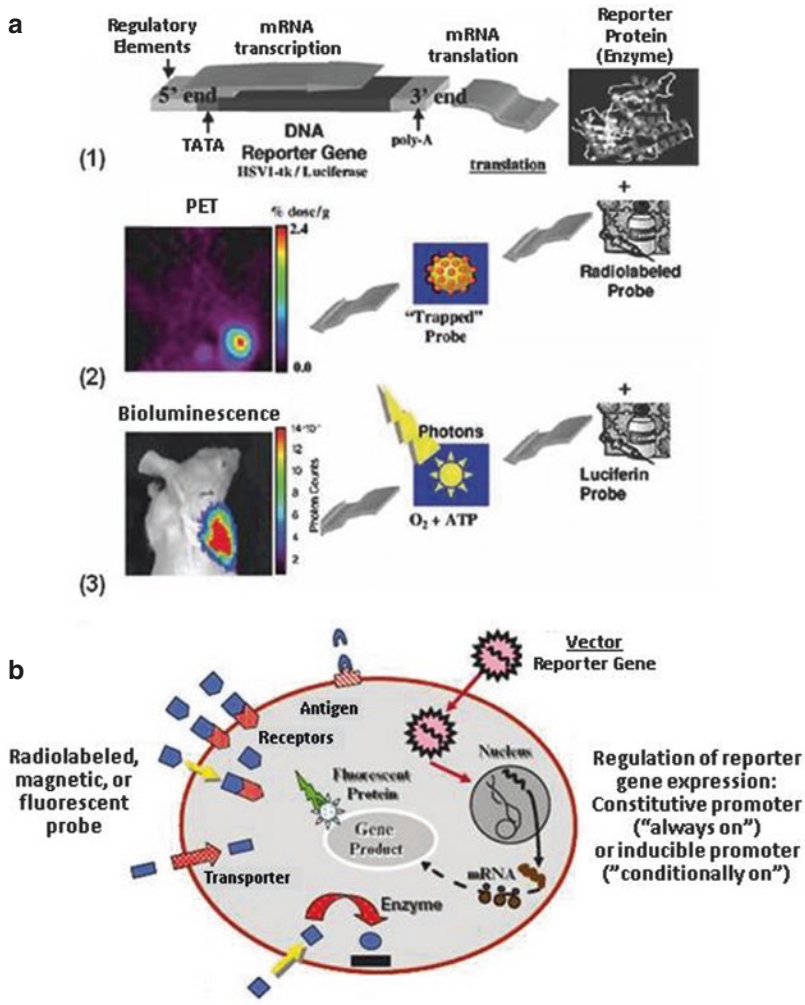

Fig. 1.6 Design of a reporter-gene construct and the indirect reporter imaging paradigm. (**a**) (*1*) The basic structure of a reporter-gene complex is shown, expressing herpes simplex virus 1 thymidine kinase (HSV1-tk) and/or luciferase. (Other reporter genes include the human norepinephrine transporter (hNET) and the human sodium iodide symporter (hNIS).) Control and regulation of gene expression is accomplished through promoter and enhancer regions that are located at the 5′ end ("upstream") of the reporter gene. These promoter/enhancer elements can be "constitutive" and result in continuous gene expression ("always on") or "inducible" ("conditionally on") and sensitive to activation by transcription factors and promoters. Following the initiation of transcription and translation, the gene product accumulates. (*2*) In this case the reporter-gene product is the enzyme HSV1-tk, which phosphorylates certain radiolabeled thymidine analogs; these probes are not phosphorylated by endogenous mammalian tk. The phosphorylated probe does not cross the cell membrane readily, and is effectively "trapped" and accumulates selectively within transduced cells. Probe accumulation thus reflects the level of HSV1-tk enzyme activity and of HSV1-tk reporter-gene expression. (*3*) In this case, luciferase is the reporter-gene product, and expression is detected via its catalytic action on the administered D-luciferin substrate resulting in the production of bioluminescence (see text). (**b**) Different reporter-gene constructs are transfected into target cells by a viral vector. Transcription of the reporter gene to messenger ribonucleic acid (*mRNA*) is initiated by constitutive or inducible promoters, and translation of the mRNA to a protein occurs on the ribosomes. The reporter-gene product can be a cytoplasmic or nuclear enzyme, a transporter in the cell membrane, a receptor at the cell surface or part of cytoplasmic or nuclear complex, an artificial cell-surface antigen, or a fluorescent protein. Often, a complimentary reporter probe (e.g., a radiolabeled, magnetic, or bioluminescent molecule) is administered, and the probe signal is directly related to the level of reporter-gene product, thus reflecting levels of transcription, modulation, and regulation of translation, protein–protein interactions, and/or posttranslational regulation of protein conformation and degradation (From reference Serganova and Blasberg (2006) with permission)

Table 1.2 Probes and contrast agents for small-animal imaging modalities

Modality	Type of probe or contrast agent
MRI[a]	Tl relaxation agents such as gadolinium-diethylenetriaminepentaacetate (Gd-DTPA) T2 relaxation agents such as superparamagnetic iron oxide nanoparticles (SPIONs)
MRSI[a]	Agents (e.g., a drug) containing a natural-abundance magnetic isotope (e.g., fluorine-19) of a non-physiologic element (e.g., fluorine) or an enriched magnetic isotope (e.g., carbon-13) of a physiologic element (e.g., carbon)
PET	Radiotracers labeled with a positron-emitting radionuclide
SPECT	Radiotracers labeled with a single-photon (e.g., x- and gamma-ray)-emitting radionuclide
CT[a]	Molecules or particles containing a high atomic number element (e.g., iodine)[b]
US[a]	Echogenic agents such as microbubbles (Lindner 2004)
Optical: bioluminescence	Substrates such as D-luciferin for enzyme-catalyzed bioluminescent (e.g., luciferase–luciferin) reactions
Optical and NIR: fluorescence[a]	Optical fluorophores such as quantum dots, nanoparticles, fluoroproteins, etc.[c]

[a]MRI, MRSI, CT, US, and optical fluorescence imaging are often performed without administering any probe or contrast agent. For MRI, MRSI, CT, and US, contrast results from intrinsic differences among tissues. For fluorescence imaging, contrast results from administered cells genetically transduced ex vivo to express a reporter fluorophore such as green fluorescent protein (GFP)

[b]Dedicated small-animal CT scanners are commonly *not* spiral scanners and therefore require ~10 min to acquire a study. As a result, water-soluble radiographic contrast agents, which are rapidly cleared from blood through the kidneys, are not suitable for small-animal devices – nearly all of such contrast agents are cleared well before a 10-min scan is completed. Specialized contrast agents which have long residence times in blood, such as polyethylene glycol-coated (i.e., PEGylated) chylomicron remnants impregnated with iodine, must be used instead (Au et al. 2013; Li et al. 2014)

[c]Fluorescent probes may be characterized as "active" or "activatable." Active probes yield a fluorescent signal whenever illuminated by light of an appropriate excitation wavelength; in other words, they are always "on." "Activatable" probes contain multiple fluorophores covalently linked to a molecular backbone and the intact probe is therefore self-quenching. Only in the presence of enzymes which specifically cleave the fluorophore-backbone covalent bonds are the fluorophores dispersed, self-quenching eliminated, and a signal obtained. Depending on the particular covalent bond, fluorescence imaging with activatable probes thus provides a means of detecting and assaying the activities of specific enzymes in situ (Ntziachristos et al. 2005)

therefore, are (a) to appropriately modify the format, size, position, and even shape of one or both image sets to provide a point-to-point correspondence between images and (b) to provide a practical integrated display of the images thus aligned.

In both clinical and laboratory settings, there are two practical approaches to image registration, "software" and "hardware" approaches (Zanzonico 2008; Zanzonico and Nehmeh 2006). In the software approach, images are acquired on separate devices, imported into a common image-processing computer platform, and registered and fused using the appropriate software. In the hardware approach, images are acquired on a single, multimodality device and transparently registered and fused with the device's integrated software. Both approaches are actually dependent on software sufficiently robust to recognize and import diverse image formats. The availability of industry-wide standard formats, such as the ACR-NEMA DICOM standard (i.e., the American College of Radiology (ACR)- National Electrical Manufacturers Association (NEMA) for Digital Imaging and Communications in Medicine (DICOM) standard (Association and ACR-NEMA 1985; Mildenberger et al. 2002)), is therefore critical.

The fusion of multimodality image sets may be as simple as simultaneous display of images in a juxtaposed format. A more common, and more useful, format is an overlay of the registered images, where one image is displayed in one color table and the second image in a different color table. Typically, the intensities of the respective color tables as well as the "mixture" of the two overlaid images can be adjusted. Adjustment (e.g., with a software slider bar) of the mixture allows the operator to interactively vary the overlay so that the designated screen area displays only the first image, only the second

image, or some weighted combination of the two images, each in its respective color table.

Current multimodality, or hybrid, devices include SPECT-CT, PET-CT, SPECT-PET-CT, PET-MRI, SPECT-MRI, and optical-CT scanners (Zanzonico and Nehmeh 2006; Rowland and Cherry 2008; Townsend 2001, 2008; Townsend and Beyer 2002; Townsend et al. 2003; Townsend and Cherry 2001). Such hybrid scanners greatly simplify multimodality image registration and fusion and provide near-perfect registration of images of in vivo function (SPECT, SPECT, or optical) and anatomy (CT or MRI) using a measured, and presumably fixed, rigid transformation between the image sets.

The combination of SPECT or PET with MRI may potentially provide important advantages beyond simply combining functional SPECT or PET information with structural information (as in SPECT- or PET-CT devices). Among multimodality imaging studies, therefore, SPECT- or PET-MRI may ultimately provide the greatest yield of information by combining the quantitative molecular-imaging capabilities of SPECT or PET (including the large number and variety of radiotracers) with the excellent anatomic resolution, marked soft-tissue contrast, and functional imaging capabilities provided by MRI (e.g., perfusion by dynamic contrast-enhanced (DCE) imaging) and MRSI (e.g., quantitation of regional concentrations of metabolites such as lactate, citrate, and choline) (Boss et al. 2010; Pichler et al. 2008; Judenhofer et al. 2008). An important advantage of SPECT- or PET-MRI over other multimodality imaging studies is that the image data can be acquired *simultaneously* because the PET or SPECT and MR imaging signals (i.e., gamma- or x-rays and RF waves, respectively) do not interfere with one another. In contrast, for SPECT- or PET-CT, the respective image data must be acquired *sequentially* because the SPECT or PET and CT signals (i.e., gamma- or x-rays) are similar and largely indistinguishable. However, many technical challenges, related to possible interference between the modalities' hardware, have to be solved when combining SPECT or PET and MRI (Boss et al. 2010; Judenhofer et al. 2008; Judenhofer and Cherry 2013; Ng et al. 2012; Peng et al. 2010; Pichler et al. 2006; Hofmann et al. 2009; Kolb et al. 2012; Sauter et al. 2010).

An important advantage of PET- or SPECT-CT is improved quantitation of radionuclide concentrations in situ afforded by CT-derived attenuation correction of the PET or SPECT images. By appropriate scaling of the attenuation coefficients thus derived from CT x-ray energies (~100 keV) to radiation energies emitted by PET or SPECT radionuclides (e.g., 511 keV in the case of PET nuclides), accurate attenuation correction of the PET or SPECT images can be performed. On the other hand, MR images, of course, do not reflect radiation attenuation and conceivably cannot be used to derive attenuation correction factors. In fact, however, this is not the case: anatomic MR images can be segmented into soft tissue, the lung (air), and bone and appropriate energy-dependent reference values of attenuation coefficients assigned to the respective tissues thus segmented (Pichler et al. 2008; Marshall et al. 2011, 2012). Accurate attenuation correction can thus be performed in PET- and SPECT-MRI as well as PET- and SPECT-CT.

1.5 Illustrative Applications of Small-Animal Imaging

PET-based pharmacodynamic imaging of tumor response to an inhibitor of heat shock protein 90 The development of inhibitors of key oncogenic signaling pathways as targeted therapies of cancer would be expedited by the ability to assess the effect of a drug on its target in vivo. Radionuclide-based molecular imaging, as illustrated by the preclinical PET study shown in Fig. 1.7 (Smith-Jones et al. 2006), is a promising approach to such pharmacodynamic assessment of anticancer drugs. The heat shock protein 90 (HSP90) inhibitor 17-allylaminogeldanamycin (17-AAG) causes the degradation of human epidermal growth factor receptor 2 (HER2), overexpressed on certain aggressive breast cancers, and other oncogenic HSP90 client proteins and has anti-breast cancer activity in preclinical models.

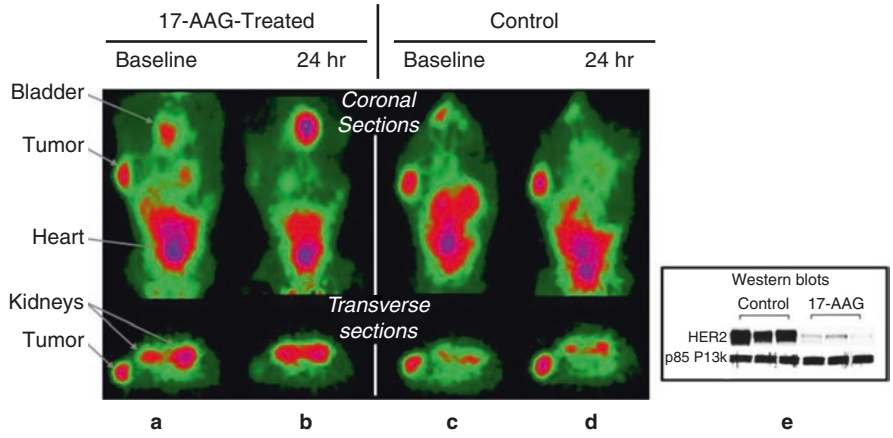

Fig. 1.7 Coronal (*top row with head at bottom*) and transverse (*bottom row with dorsal surface at top*) R4 microPET (Concorde Microsystems) images at 3-h postinjection of the gallium-68-labeled $F(ab')_2$ fragment of Herceptin™ (^{68}Ga-DOTA-$F(ab')_2$ Herceptin) into athymic nude mice with BT474 breast tumor xenografts on the right flanks; DOTA is the metal chelator 1,4,7,10-tetraazacyclododecane-N,N′,N″,N‴-tetraacetate. Herceptin, used in the treatment of some breast cancers, is an antibody directed against the HER2*ν* tyrosine kinase, which is overexpressed in BT474 and other breast tumors. HER2*ν* is a client protein of the heat shock protein 90 (HSP90) chaperone protein. (**a**) One mouse underwent a baseline study followed by treatment with the geldanamycin derivative 17-AAG (an inhibitor of HSP90) followed 24 h later by (**b**) a second scan with ^{68}Ga-DOTA-$F(ab')_2$ Herceptin. The tumor uptake of ^{68}Ga-DOTA-$F(ab')_2$ Herceptin decreased 50 % between the pre- and posttreatment scans. (**c**, **d**) The control (i.e., untreated) mouse also underwent two scans 24 h apart, with no significant change in tumor uptake. (**e**) As corroborated by the Western blots shown, 17-AAG induced degradation of HSP90 and, in turn, HER2*ν*. This study illustrates the application of imaging to characterization of the pharmacodynamics of molecularly targeted anticancer therapy. Hypothetically, for example, breast cancer patients can undergo pre- and post-therapy scans to identify responders (i.e., having scan results analogous to those in (**a**) and (**b**)) and nonresponders (i.e., having scan results analogous to those in (**c**) and (**d**)) to HSP90 inhibitors. Responders would then be effectively treated with such inhibitors, while nonresponders would be switched to alternative treatment (Adapted from reference Smith-Jones et al. (2004) with permission)

Smith-Jones et al. (Smith-Jones et al. 2006) developed a PET-based method for quantitatively imaging the inhibition of HSP90 by 17-AAG, labeling the $F(ab')_2$ fragment of the anti-HER2 antibody Herceptin with the short-lived positron emitter gallium-68 (^{68}Ga). This method was used to noninvasively quantify the time-dependent 17-AAG-induced loss and recovery of HER2 in breast tumor xenografts in mice. The clinically translatable paradigm illustrated in Fig. 1.7 allows noninvasive imaging of the pharmacodynamics of a molecularly targeted drug and should facilitate the rational design and dose and dose-schedule optimization of therapies based on target inhibition. Among other considerations, the study shown in Fig. 1.7 illustrates the important advantage of quantitation provided by radionuclide imaging in general and PET in particular.

Multimodality imaging of progression of bone tumor metastasis A debilitating and painful consequence of advanced prostate and other cancers is the development of bone metastases. At the same time, it has been observed that many cancer cell lines as well as primary human tumors synthesize bombesin, which appears to act in an autocrine fashion to stimulate the growth of the tumor cells it originated from through membrane bombesin receptors. In a preclinical model in mice, Winkelman et al. (Winkelmann et al. 2012) demonstrated that CT combined with SPECT of a bombesin receptor (BB2)-binding radioligand, ^{111}In-DOTA-8-Aoc-BBN(7–14)NH_2, can provide a combined structural and functional map – skeletal anatomy and bombesin receptor status – of metastatic bone lesions, as illustrated in Fig. 1.8. By directly targeting metastatic tumor cells in the bone using a specific (e.g., bombesin)

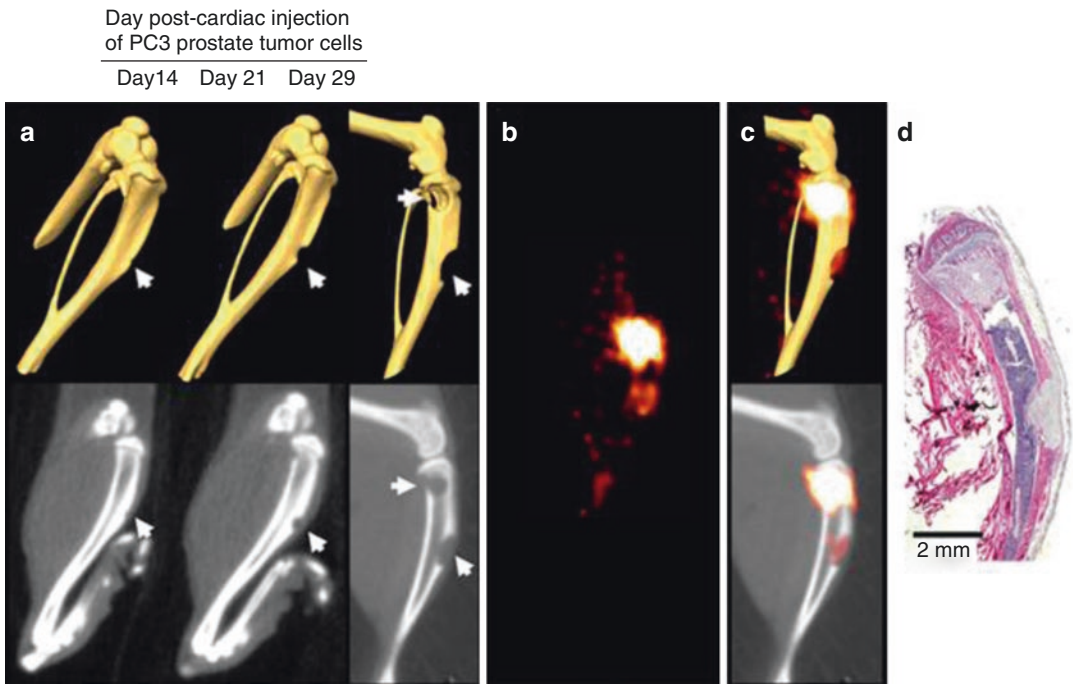

Fig. 1.8 A preclinical SPECT-CT study in a tumor-bearing mouse. (**a**) Progression of two metastases in the tibia (*arrows*) visualized by CT surface renderings (*top row*) and sagittal images (*bottom row*) following intracardiac injection of PC3 prostate-tumor cells. (**b**) Pinhole SPECT image obtained at 1-h postinjection of ^{111}In-DOTA-8-AOC-BBN (7–14) NH2. (**c**) Overlay of anatomic CT images with the SPECT image, showing that the foci of radiotracer uptake correspond to the lytic bone metastases. (**d**) Photomicrograph of the histopathology of the two bone metastases (From reference Winkelmann et al. (2012) with permission)

receptor-binding radioligand, rather than observing by CT the secondary effect of osteolysis, more sensitive and specific early diagnosis of skeletal metastases may be possible.

Reporter gene-based multimodality imaging of tumors Over the years, reporter systems have developed for multimodality gene imaging using bioluminescence, fluorescence, nuclear, and MR imaging techniques. In one such system, a single fusion protein with three functional subunits, FLuc, GFP, and herpes simplex virus 1 thymidine kinase 1 (HSV1 tk), was produced, functionally characterized in vitro, and successfully applied in multimodality in vivo imaging studies in tumor-bearing nude mice (Fig. 1.9) (Doubrovin et al. 2004). HSV1 tk activity is assayed using radioactively labeled thymidine analogs (e.g., ^{124}I- or ^{131}I-2′-fluoro-2′-deoxy-1-β-D-arabinofuranosyl-5-iodo-uracil (FIAU)) for PET and SPECT imaging, respectively; many such nuclear imaging probes have been developed (Gambhir and Yagboubi 2010). Such multimodality reporter-gene constructs provide for the transition from fluorescence microscopy and fluorescence-activated cell sorting (FACS) to in vivo bioluminescence imaging to in vivo nuclear (PET, SPECT, gamma-camera) imaging.

Multimodality imaging of adoptive immunotherapy of cancer Small-animal imaging has been applied to the genetic transfer of antigen receptors for generating tumor-specific T lymphocytes for adoptive immunotherapy of cancer (Brentjens et al. 2003; Sadelain et al. 2003; Gade et al. 2005), and has been invaluable in the translation of this new and promising therapeutic modality to clinical trials. Unlike the physiologic T-cell receptor, chimeric antigen receptors (CARs) encompass immunoglobulin variable regions or

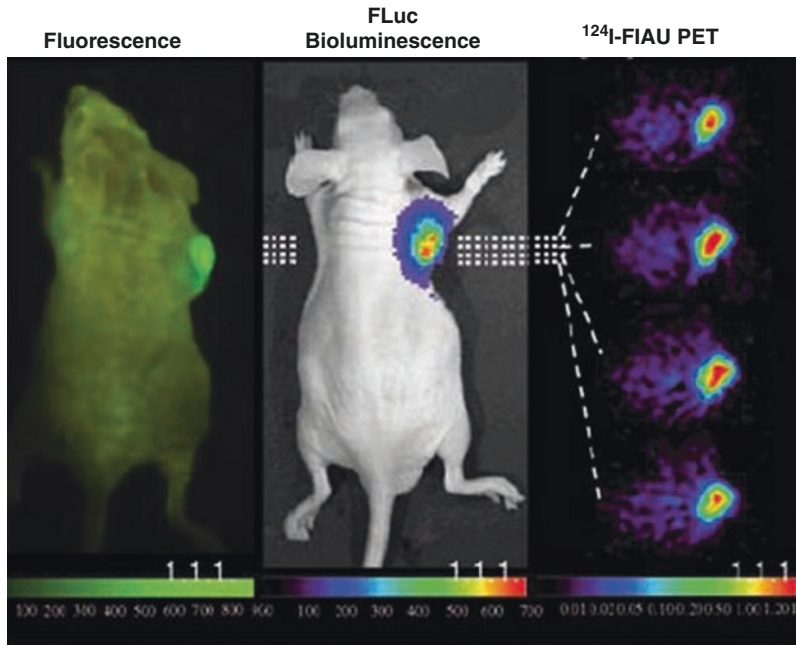

Fig. 1.9 Noninvasive multimodality reporter-gene imaging of a mouse with a subcutaneous xenograft produced from genetically transduced (*right shoulder*) and from wild-type (non-transduced) U87 tumor cells (*left shoulder*). The transduced tumor cells express GFP, FLuc, and HSV1 tk as reporters. Fluorescence image of GFP (*left panel*), bioluminescence imaging of FLuc (*middle panel*), and transaxial PET images of ^{124}I-2′-fluoro-2′-deoxy-1-β-D-arabinofuranosyl-5-iodo-uracil (FIAU) at the levels indicated by the dotted white lines (*right panel*). Note that the negative-control wild-type tumor in the contralateral shoulder is not imaged by any of the modalities (From reference Doubrovin et al. (2004) with permission)

receptor ligands as their antigen recognition moiety, thus permitting T cells to recognize tumor antigens in the absence of human leukocyte antigen expression. CARs encompassing the CD3Z chain as their activating domain induce T-cell proliferation in vitro. The requirements for genetically targeted T cells to function in vivo are less well understood. Animal models have therefore been developed to assess the therapeutic efficacy of human peripheral blood T lymphocytes targeted to prostate-specific membrane antigen (PSMA), an antigen expressed in prostate cancer cells and the neovasculature of various solid tumors. In vivo specificity and antitumor activity have been assessed in mice bearing established prostate adenocarcinomas, using serum prostate-secreted antigen, MRI, CT, and bioluminescence imaging to investigate the response to therapy (Fig. 1.10) (Gade et al. 2005). In three tumor models, orthotopic, subcutaneous, and pulmonary, it was shown that PSMA-targeted T cells effectively eliminate prostate cancer. The eradication of xenogeneic tumors in a murine environment shows that the adoptively transferred T cells do not absolutely require in vivo costimulation to function. Such results provided a compelling rationale for recently initiated Phase-1 clinical trials to assess PSMA-targeted T cells in patients with metastatic prostate cancer.

Simultaneous single-photon scintigraphy and MRI of renal function As noted, an important advantage of SPECT- or PET-MRI over other multimodality imaging studies is that the image data can be acquired simultaneously because the PET or SPECT and MR imaging signals (i.e., gamma- or x-rays and RF waves, respectively) do not interfere with one another. Figure 1.11 presents a proof-of-principle simultaneous dynamic single-photon scintigraphy and DCE MRI study

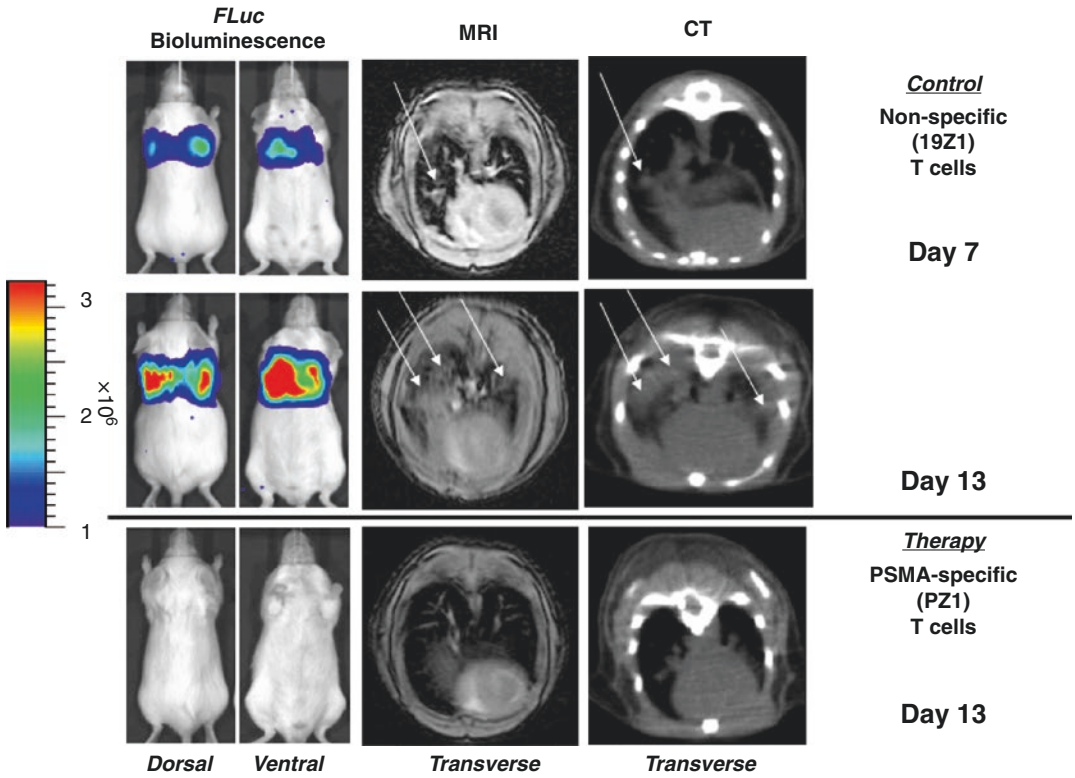

Fig. 1.10 Demonstration, by multimodality (firefly luciferase (*FLuc*) bioluminescence, MR, and CT) imaging, of therapeutic effectiveness of adoptive immunotherapy of cancer. PSMA- and Fluc (as a reporter gene)-transduced RM1 prostate cancer cells were injected intravenously into mice to produce a model of lung metastases and were then treated with systemically administered T cells genetically engineered to express either the PSMA-specific (PZ1) receptor or, as a negative control, the nonspecific (19Z1) receptor. The T cells were administered on the day indicated following infusion of the cancer cells. By all three modalities, the specific, but not the nonspecific, T cells eradicated the lung disease (From reference Gade et al. (2005) with permission)

of renal function (Hamamura et al. 2011). Although the scintigraphic study in this instance is a planar rather than a tomographic study, the principle of truly simultaneous functional imaging studies is clearly demonstrated.

Simultaneous PET and MRI of tumor proliferation and perfusion Figure 1.12 illustrates the capability of dynamic PET and MRI for simultaneous and therefore unambiguous evaluation of multiple functional parameters of tissue. In the study presented in Fig. 1.12 (Judenhofer et al. 2008), dynamic PET imaging of regional tumor proliferation using the partially metabolized thymidine analog ^{18}F-labeled fluoro-thymidine (FLT) and dynamic contrast-enhanced MRI of regional tumor perfusion were performed.

Cerenkov imaging-based lymphography The lymphatic system can be an important indicator of the presence and extent of disease. In oncology, for example, metastatic spread to local lymph nodes (LNs) is a predictor of poor outcome. As a possibly superior alternative to current clinical methods for the visualization of LNs involving regional injection and tracking of ^{99m}Tc-sulfur colloid and dyes, Thorek et al. have investigated Cerenkov lymph node imaging of regionally administered ^{18}F-FDG (Thorek et al. 2012). Using intradermal tail injections of ^{18}F-FDG, Thorek et al. have performed both PET- and Cerenkov imaging-based lymphography in mice, with both modalities demonstrating excellent visualization of lymph nodes (Fig. 1.13). Combined PET/Cerenkov imaging appears to have significant

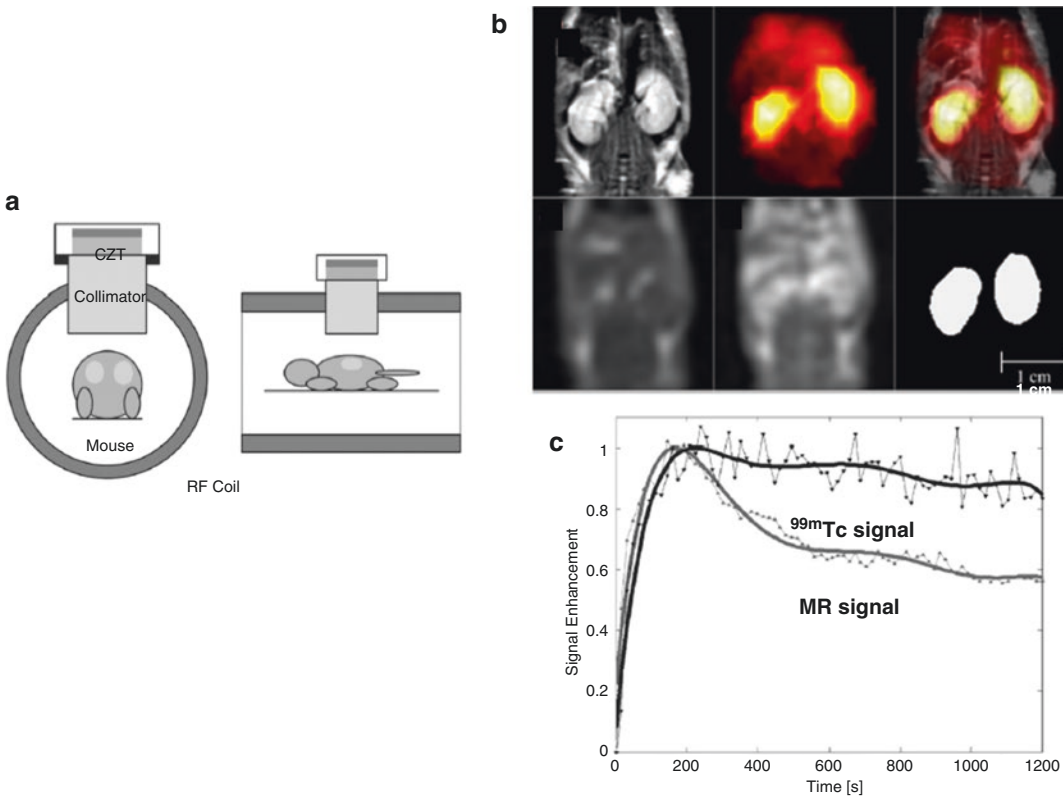

Fig. 1.11 Proof-of-principle single-photon scintigraphy-MR imaging study in a mouse. (**a**) Diagrammatic representation of the system for simultaneous single-photon scintigraphy using a CZT ionization detector and MR imaging. Note that this is not a SPECT (i.e., tomographic) system but rather a planar imaging system. (**b**) Static non-contrast T1-weighted MR image (*upper left panel*). Frame from dynamic ^{99m}Tc-sestamibi study (*upper middle panel*). "Fusion" of T1-weighted MR and ^{99m}Tc-sestamibi images; since the ^{99m}Tc-sestamibi image is a planar image (*upper right panel*), the MR and scintigraphic images are not truly fused. Frame from a dynamic MR study prior to injection of gadopentetate dimeglumine contrast (*lower left panel*). Frame from a dynamic contrast (gadopentetate dimeglumine)-enhanced MR study (*lower middle panel*). Kidney ROIs extracted from the static non-contrast T1-weighted MR image (*lower right panel*). (**c**) Renal signal-versus-time curves following the ^{99m}Tc-sestamibi and gadopentetate dimeglumine injections (Adapted from Hamamura et al. (2011) with permission)

potential as a single-dose, dual-modality tracer for diagnostics (PET/CT) and Cerenkov imaging-guided resection of sentinel lymph nodes.

Photoacoustic imaging of tumor perfusion Herzog et al. (Herzog et al. 2012) have investigated whether multispectral optoacoustic tomography (MSOT) can reveal the heterogeneous distributions of exogenously administered agents and thereby elucidate vascular characteristics of tumors with dimensions of the order of several millimeters. Imaging of subcutaneous tumors in mice was performed by using an experimental MSOT setup that produces transverse images at 10 frames per second with an in-plane resolution of ~150 μm. To study dynamic contrast enhancement, mice with 4 T1 tumors were imaged before and immediately, 20 min, 4 h, and 24 h after systemic injection of indocyanine green (ICG). Dynamic contrast (IGC)-enhanced MSOT successfully demonstrated a heterogeneous distribution of the IGC, presumably reflecting regional tumor perfusion (Fig. 1.14).

Multimodality imaging-guided resection of brain tumors The completeness of the surgical resection is an important factor for the prognosis of brain-tumor patients. In trying to achieve more

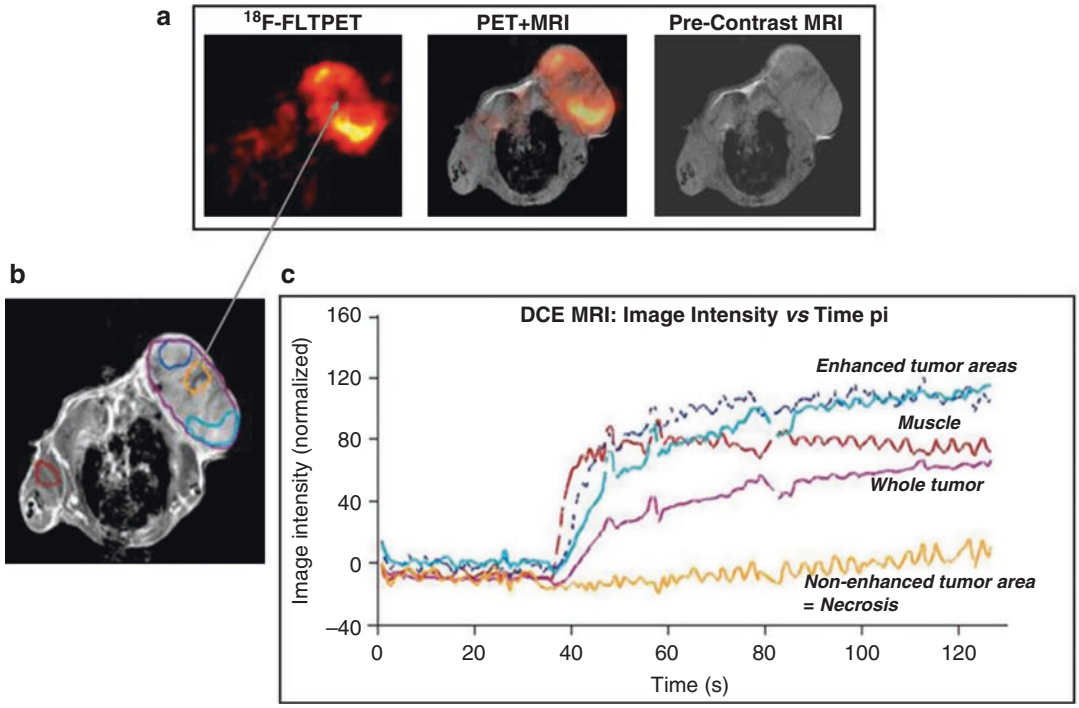

Fig. 1.12 Dynamic PET-MR imaging study of a tumor xenograft. (**a**) ^{18}F-labeled fluoro-thymidine (*FLT*) PET image of a BALB/c mouse with a CT26 colon carcinoma xenograft showing areas of high FLT uptake corresponding to increased cell proliferation (*left panel*). Non-contrast-enhanced T1-weighted MR image, simultaneously acquired and registered with the FLT PET study and showing the gross morphology of the tumor and the underlying normal anatomy (*right panel*). The fused FLT PET and T1-weighted MR images (*middle panel*). (**b**) Contrast (gadopentetate dimeglumine)-enhanced T1-weighted MR image of the same tissue section shown in (**a**), identifying muscle (*red region of interest (ROI)*), whole tumor (purple ROI), enhanced (i.e., perfused and therefore viable) tumor (*light and dark blue ROIs*), and non-enhanced (i.e., non-perfused and therefore necrotic) tumor (*orange ROI*). (**c**) The signal-versus-time postinjection curves for the dynamic contrast-enhanced (*DCE*) MR study, with the color-coded curves for the anatomic ROIs identified in (**b**). Note that the perfused, viable regions of tumor identified by DCE MR imaging (DEC MRI) are, unambiguously, also the most rapidly proliferating regions of the tumor as identified by FLT PET, demonstrating the value of truly simultaneous acquisition of the PET and MR images (Adapted from Judenhofer et al. (2008) with permission)

complete glioma resections, the surgeon encounters several obstacles, including irregular and indistinct tumor margins as well as tumor growth adjacent to or invading crucial neurological structures. A wide variety of techniques have been explored to date in an effort to better visualize tumor margins but have proven entirely satisfactory. Recently, as presented in Figs. 1.15 and 1.16, Kircher et al. have reported a successful proof-of-principle study of a clinically translatable molecular-imaging strategy for more accurately delineating brain-tumor margins using a novel triple-modality MRI-photoacoustic-Raman nanoparticle probe (Kircher et al. 2012).

1.6 Outlook

Imaging-based experimentation in small-animal models is now an established and widely used technology in basic and translational biomedical research and will no doubt remain an important component of such research. With small-animal imaging resources already widely available among academic medical centers, research institutes, and industrial laboratories, its growth is likely to slow, however, compared to that seen over the last two decades. Nonetheless, several areas – drug development, treatment monitoring, and novel therapeutic strategies such as adoptive

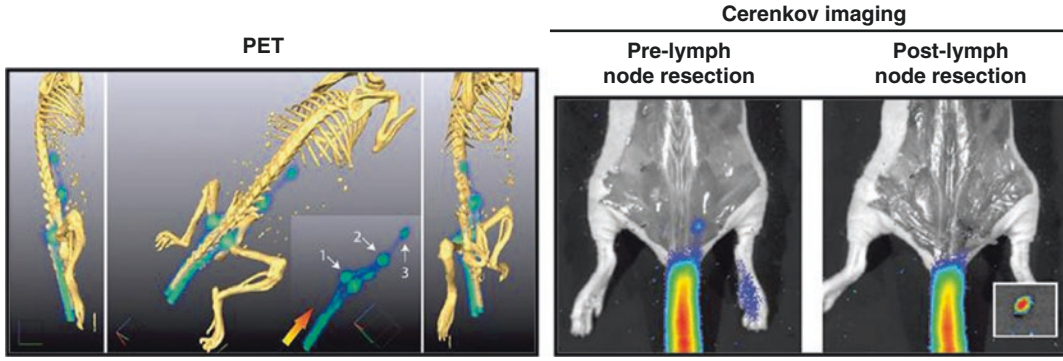

Fig. 1.13 Cerenkov imaging-guided lymph node resection in a normal mouse following intradermal tail injection of ^{18}F-FDG (1.1 MBq). *Left panel:* Volume rendering of fused CT image (*yellow color table*) and PET image (*green color table*) showing lymphatics and lymph nodes in relation to the skeleton. *Right panel:* Cerenkov image superimposed on a photograph of the mouse following removal post-sacrifice of the dorsal skin before (*left image*) and after (*right image*) resection of a luminescent inguinal lymph node. The resected node ex vivo is shown in the inset image (Adapted from Thorek et al. (2012) with permission)

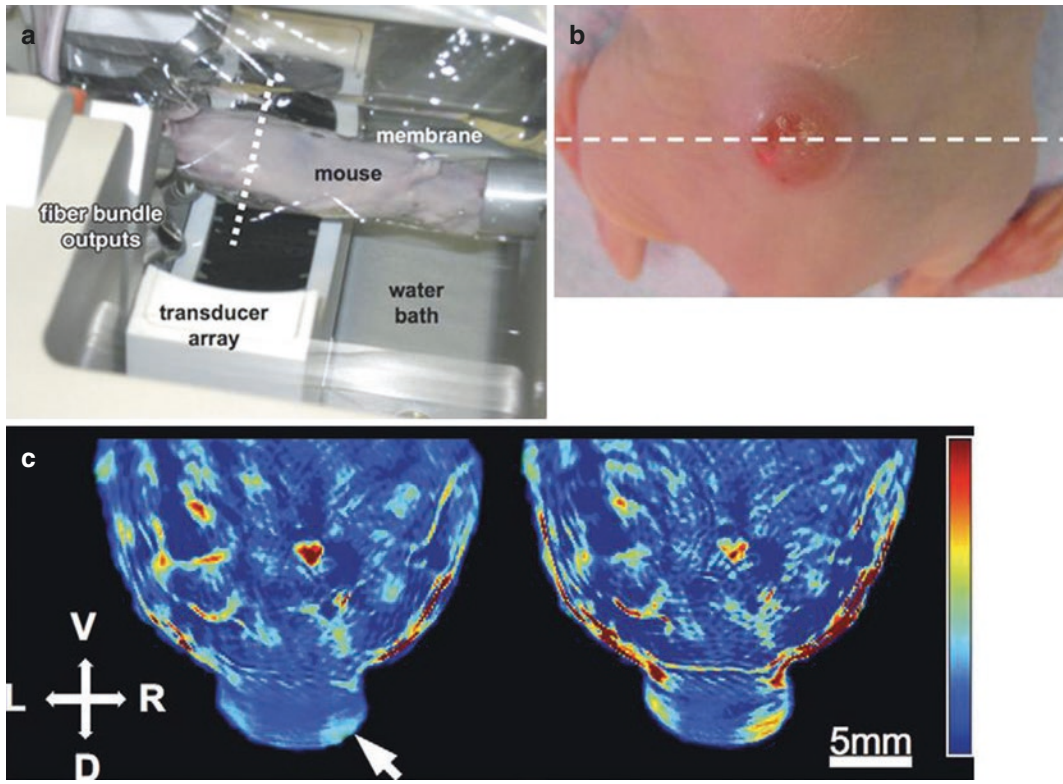

Fig. 1.14 (**a**) Setup for photoacoustic imaging of regional perfusion in a tumor xenograft on the dorsal surface of a nude mouse. Note that the tumor (on the dorsal surface of the animal and therefore not seen) is "immersed" in water. The animal actually remains dry, however, because of the presence of a thin membrane between the animal and the water. (**b**) Photograph of the 4 T1 xenograft on the dorsal surface of the mouse. In (**a**) and (**b**), the *dashed line* indicates the approximate position of the transverse tissue section being imaged. (**c**) Images (acquired at 790 nm) before (*left panel*) and 30 s after (*right panel*) intravenous injection of indocyanine green (*ICG*). (*V* ventral, *D* dorsal, *L* left, *R* right). Note the increase in image contrast in and around the tumor (*arrow*) after injection, identifying the more highly perfused portions of the tumor (Adapted from Herzog et al. (2012) with permission)

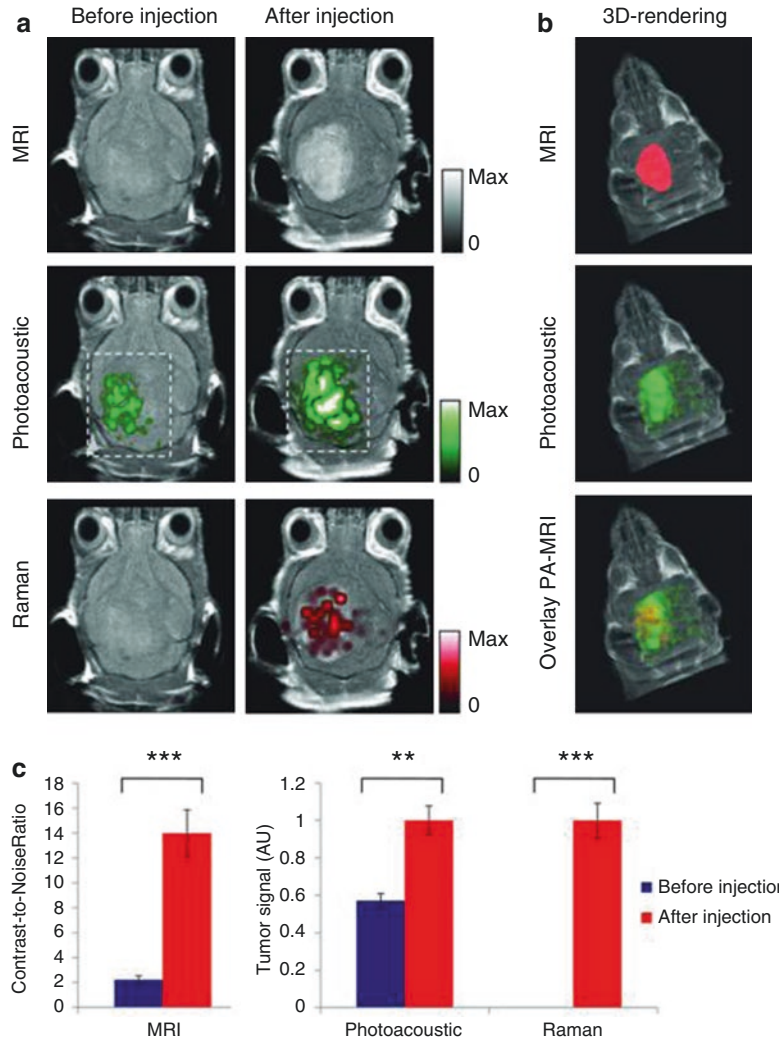

Fig. 1.15 Triple-modality detection with nanoparticle probes of brain tumors in mice. Three weeks after orthotopic implantation with U87MG glioblastoma cells, the brain tumor-bearing mouse was injected intravenously with the nanoparticles, which localized in the tumor due to the EPR (enhanced permeability and retention) effect. Photoacoustic (PA), Raman, and MR images of the brain (skin and skull intact) were acquired before and 2, 3, and 4-h postinjection, respectively. Raman imaging was performed using a commercial Raman microscope (InVia, Renishaw) with a computer-controlled xy-translation stage. (**a**) Axial MR, PA, and Raman images. The postinjection images of all three modalities demonstrated clear tumor visualization. The PA and Raman images were co-registered with the MR image, demonstrating good concordance within the tumor of the nanoparticle distribution among the three modalities. (**b**) Volumetric rendering of MR images with the tumor segmented (*red; top panel*); overlay of the 3D PA image (*green*) over the MR image (*middle panel*); and overlay of the tumor-segmented MR and PA images (*bottom panel*) showing good co-localization of the PA signal within the tumor. (**c**) Quantification of the imaging signals in the tumor shows a significant increase in the MRI, PA, and Raman signals after versus before the nanoparticle injection ("***" indicates $p<0.001$, "**" indicates $p<0.01$). Error bars represent the standard error of the mean, AU, arbitrary units (From Kircher et al. (2012) with permission)

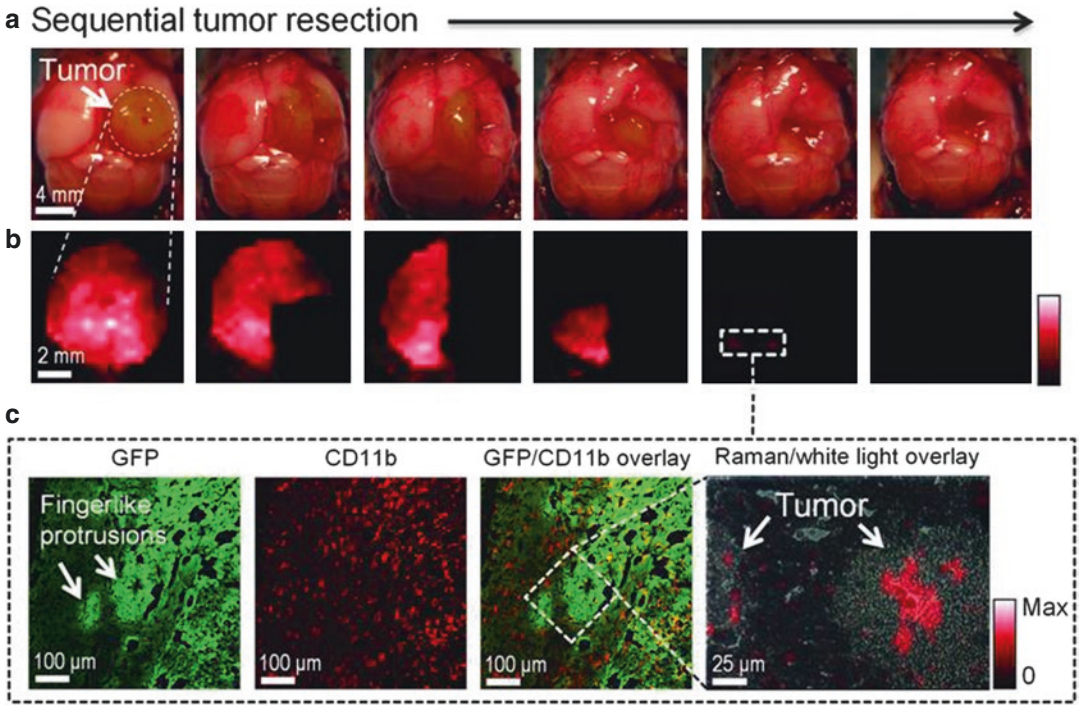

Fig. 1.16 Preclinical model of Raman-guided surgery. (**a**) Following orthotopic implantation with GFP-transduced U87MG glioblastoma cells, the brain tumor-bearing mouse underwent craniotomy under general anesthesia. Quarters of the tumor were then sequentially removed (as illustrated in the photographs). (**b**) Intraoperative Raman imaging was performed after each resection step, until the entire tumor had been removed by visual inspection. After the gross removal of the tumor, several small foci of Raman signal were found in the resection bed (outlined by the *dashed white square*). (**c**) Subsequent immunohistochemical analysis of sections from these foci demonstrated an infiltrative pattern of the tumor in this location, forming finger-like protrusions extending into the surrounding brain tissue. CD11b (*second panel from left*) is a widely used microglial immunohistochemical marker. As shown in the Raman microscopy image (*right panel*), the Raman signal was observed within these protrusions, indicating the selective presence of MPRs in these protrusions. The *white dashed box* not drawn to scale. Raman signal in linear *red color table* (From Kircher et al. (2012) with permission)

immunotherapy and gene therapy – are likely to be particularly productive in the application of small-animal imaging. In drug development, imaging-based assays are particularly amenable to quantitative characterization of pharmacokinetics and pharmacodynamics of new therapeutics and may accelerate the drug discovery process. Transgenic and knockout mouse models of human disease may be used for identification and validation of "drug-able" molecular targets. Clinically translatable imaging paradigms developed and validated in animal models may also provide earlier and more clinically meaningful assays of therapeutic response, enabling clinicians to rapidly distinguish "responders" from "nonresponders" and promptly switch patients from ineffective to potentially more effective therapies, thereby avoiding unnecessary toxicities, expense, and loss of time. Clinically applicable gene imaging techniques will likely be essential if adoptive immunotherapies and gene therapies are to progress. Tumor targeting of immune effector cells and their progeny and delivery and expression of therapeutic genes can likely only be assessed by stable incorporation of a suitable reporter gene into the genomes of effector cells and of therapeutic viral vectors, respectively. Further, in order to maximize the yield of functional information, it is likely that multimodality imaging as well as dynamic imaging (with appropriate kinetic analyses) will become more commonplace.

References

American College of Radiology-National Electrical Manufacturers' Association, ACR-NEMA Digital imaging and communications standard. Washington, DC; 1985.

Au JT, Craig G, Longo V, et al. Gold nanoparticles provide bright long-lasting vascular contrast for CT imaging. AJR Am J Roentgenol. 2013;200:1347–51.

Beattie BJ, Thorek DL, Schmidtlein CR, et al. Quantitative modeling of Cerenkov light production efficiency from medical radionuclides. PLoS One. 2012;7:e31402.

Beckman N, Kneuer R, Gremlich HU. In vivo mouse imaging and spectroscopy in drug discovery. NMR Biomed. 2007;20:154–85.

Boss A, Bisdas S, Kolb A, et al. Hybrid PET/MRI of intracranial masses: initial experiences and comparison to PET/CT. J Nucl Med. 2010;51:1198–205.

Brentjens RJ, Latouche JB, Santos E, et al. Eradication of systemic B-cell tumors by genetically targeted human T lymphocytes co-stimulated by CD80 and interleukin-15. Nat Med. 2003;9:279–86.

Bushberg JTS JA, Leidholdt Jr EM, Boone JM. The essential physics of medical imaging. Philadelphia: Lippincott, Williams & Wilkins; 2012.

Cerenkov PA. Visible emission of clean liquids by action of gamma-radiation. C R Dokl Akad Nauk SSSR. 1934;2:451–454.

Cherry SR. The 2006 Henry N. Wagner Lecture: Of mice and men (and positrons)--advances in PET imaging technology. J Nucl Med. 2006;47:1735–45.

Cherry SR, Badawy RD, Qi J, editors. Essentials of in vivo biomedical imaging. Boca Rato: CRC Press; 2015.

Contag PR, Olomu IN, Stevenson DK, et al. Bioluminescent indicators in living mammals. Nat Med. 1998;4:245–7.

Daghighian F, Humm JL, Macapinlac HA, et al. Pharmacokinetics and dosimetry of iodine-125-IUdR in the treatment of colorectal cancer metastatic to liver. J Nucl Med. 1996;37:29S–32S.

Dothager RS, Goiffon RJ, Jackson E, et al. Cerenkov radiation energy transfer (CRET) imaging: a novel method for optical imaging of PET isotopes in biological systems. PLoS One. 2010;5:e13300.

Doubrovin M, Serganova I, Mayer-Kuckuk P, et al. Multimodality in vivo molecular-genetic imaging. Bioconjug Chem. 2004;15:1376–88.

Gade TP, Hassen W, Santos E, et al. Targeted elimination of prostate cancer by genetically directed human T lymphocytes. Cancer Res. 2005;65:9080–8.

Gambhir SS, Yagboubi SS. Cambridge molecular imaging series. In: Cherry SR, Weber WA, van Bruggen N, editors. Molecular imaging with reporter genes. New York: Cambridge University Press; 2010.

Gorska-Chrzastek M, Grzelak P, Bienkiewicz M, et al. Assessment of clinical usefulness of 131I alpha-methyl-tyrosine and fused SPECT/MRI imaging for diagnostics of recurrent cerebral gliomas. Nucl Med Rev Cent East Eur. 2004;7:135–41.

Hamamura MJ, Roeck WW, Ha S, et al. Simultaneous in vivo dynamic contrast-enhanced magnetic resonance and scintigraphic imaging. Phys Med Biol. 2011;56:N63–9.

Henry DH, Costa L, Goldwasser F, et al. Randomized, double-blind study of denosumab versus zoledronic acid in the treatment of bone metastases in patients with advanced cancer (excluding breast and prostate cancer) or multiple myeloma. J Clin Oncol. 2011;29:1125–32.

Herzog E, Taruttis A, Beziere N, et al. Optical imaging of cancer heterogeneity with multispectral optoacoustic tomography. Radiology. 2012;263:461–8.

Hielscher AH. Optical tomographic imaging of small animals. Curr Opin Biotechnol. 2005;16:79–88.

Hofmann M, Pichler B, Scholkopf B, et al. Towards quantitative PET/MRI: a review of MR-based attenuation correction techniques. Eur J Nucl Med Mol Imaging. 2009;36 Suppl 1:S93–104.

Holland JP, Normand G, Ruggiero A, et al. Intraoperative imaging of positron emission tomographic radiotracers using cerenkov luminescence emissions. Mol Imaging. 2011;10:177–86.

Huang D, Swanson EA, Lin CP, et al. Optical coherence tomography. Science. 1991;254:1178–81.

Judenhofer MS, Cherry SR. Applications for preclinical PET/MRI. Semin Nucl Med. 2013;43:19–29.

Judenhofer MS, Wehrl HF, Newport DF, et al. Simultaneous PET-MRI: a new approach for functional and morphological imaging. Nat Med. 2008;14:459–65.

Kiessling F, Pichler BJ, Hauff P. Small animal imaging. Berlin: Springer; 2011. p. 597.

Kircher MF, de la Zerda A, Jokerst JV, et al. A brain tumor molecular imaging strategy using a new triple-modality MRI-photoacoustic-Raman nanoparticle. Nat Med. 2012;18:829–34.

Kolb A, Wehrl HF, Hofmann M, et al. Technical performance evaluation of a human brain PET/MRI system. Eur Radiol. 2012;22:1776–88.

Kruger RA, Kiser Jr WL, Reinecke DR, et al. Thermoacoustic computed tomography using a conventional linear transducer array. Med Phys. 2003;30:856–60.

Li C, Mitchell GS, Cherry SR. Cerenkov luminescence tomography for small-animal imaging. Opt Lett. 2010;35:1109–11.

Li X, Anton N, Zuber G, et al. Contrast agents for preclinical targeted X-ray imaging. Adv Drug Deliv Rev. 2014;76:116–33.

Liu H, Ren G, Miao Z, et al. Molecular optical imaging with radioactive probes. PLoS One. 2010;5:e9470.

Lucignani G. Cerenkov radioactive optical imaging: a promising new strategy. Eur J Nucl Med Mol Imaging. 2011;38:592–5.

Mankoff DA. A definition of molecular imaging. J Nucl Med. 2007;48:18N–21N.

Marshall HR, Stodilka RZ, Theberge J, et al. A comparison of MR-based attenuation correction in PET versus SPECT. Phys Med Biol. 2011;56:4613–29.

Marshall HR, Prato FS, Deans L, et al. Variable lung density consideration in attenuation correction of whole-body PET/MRI. J Nucl Med. 2012;53:977–84.

Mildenberger P, Eichelberg M, Martin E. Introduction to the DICOM standard. Eur Radiol. 2002;12:920–7.
Ng TS, Bading JR, Park R, et al. Quantitative, simultaneous PET/MRI for intratumoral imaging with an MRI-compatible PET scanner. J Nucl Med. 2012;53: 1102–9.
Ntziachristos V, Ripoll J, Wang LV, et al. Looking and listening to light: the evolution of whole-body photonic imaging. Nat Biotechnol. 2005;23:313–20.
Peng BJ, Walton JH, Cherry SR, et al. Studies of the interactions of an MRI system with the shielding in a combined PET/MRI scanner. Phys Med Biol. 2010;55:265–80.
Pichler BJ, Judenhofer MS, Catana C, et al. Performance test of an LSO-APD detector in a 7-T MRI scanner for simultaneous PET/MRI. J Nucl Med. 2006;47:639–47.
Pichler BJ, Wehrl HF, Kolb A, et al. Positron emission tomography/magnetic resonance imaging: the next generation of multimodality imaging? Semin Nucl Med. 2008;38:199–208.
Pomper MG. Molecular imaging: an overview. Acad Radiol. 2001;8:1141–53.
Pomper MG. Translational molecular imaging for cancer. Cancer Imaging. 2005;5(Spec No A):S16–26.
Robertson R, Germanos MS, Li C, et al. Optical imaging of Cerenkov light generation from positron-emitting radiotracers. Phys Med Biol. 2009;54:N355–65.
Rowland DJ, Cherry SR. Small-animal preclinical nuclear medicine instrumentation and methodology. Semin Nucl Med. 2008;38:209–22.
Ruggiero A, Holland JP, Lewis JS, et al. Cerenkov luminescence imaging of medical isotopes. J Nucl Med. 2010;51:1123–30.
Sadelain M, Riviere I, Brentjens R. Targeting tumours with genetically enhanced T lymphocytes. Nat Rev Cancer. 2003;3:35–45.
Sauter AW, Wehrl HF, Kolb A, et al. Combined PET/MRI: one step further in multimodality imaging. Trends Mol Med. 2010;16:508–15.
Serganova I, Blasberg R. Reporter gene imaging: potential impact on therapy. Nucl Med Biol. 2005;32: 763–80.
Serganova I, Blasberg RG. Multi-modality molecular imaging of tumors. Hematol Oncol Clin North Am. 2006;20:1215–48.
Serganova I, Ponomarev V, Blasberg R. Human reporter genes: potential use in clinical studies. Nucl Med Biol. 2007;34:791–807.
Serganova I, Mayer-Kukuck P, Huang R, et al. Molecular imaging: reporter gene imaging. Handb Exp Pharmacol. 2008;185 Pt 2:167–223.
Smith-Jones PM, Solit DB, Akhurst T, et al. Imaging the pharmacodynamics of HER2 degradation in response to Hsp90 inhibitors. Nat Biotechnol. 2004;22:701–6.
Smith-Jones PM, Solit D, Afroze F, et al. Early tumor response to Hsp90 therapy using HER2 PET: comparison with 18F-FDG PET. J Nucl Med. 2006;47:793–6.
Taruttis A, Ntziachristos V. Translational optical imaging. AJR Am J Roentgenol. 2012;199:263–71.
Thorek DL, Abou DS, Beattie BJ, et al. Positron lymphography: multimodal, high-resolution, dynamic mapping and resection of lymph nodes after intradermal injection of 18F-FDG. J Nucl Med. 2012;53:1438–45.
Tichauer KM, Wang Y, Pogue BW, et al. Quantitative in vivo cell-surface receptor imaging in oncology: kinetic modeling and paired-agent principles from nuclear medicine and optical imaging. Phys Med Biol. 2015;60:R239–69.
Townsend DW. A combined PET/CT scanner: the choices. J Nucl Med. 2001;42:533–4.
Townsend DW. Positron emission tomography/computed tomography. Semin Nucl Med. 2008;38:152–66.
Townsend DW, Beyer T. A combined PET/CT scanner: the path to true image fusion. Br J Radiol. 2002;75: S24–30.
Townsend DW, Cherry SR. Combining anatomy and function: the path to true image fusion. Eur Radiol. 2001;11:1968–74.
Townsend DW, Beyer T, Blodgett TM. PET/CT scanners: a hardware approach to image fusion. Semin Nucl Med. 2003;33:193–204.
Vallabhajosula S. Molecular imaging: radiopharmaceuticals for PET and SPECT. Berlin: Springer; 2009.
Wang Y, Xing D, Zeng Y, et al. Photoacoustic imaging with deconvolution algorithm. Phys Med Biol. 2004;49:3117–24.
Winkelmann CT, Figueroa SD, Sieckman GL, et al. Noninvasive MicroCT imaging characterization and in vivo targeting of BB2 receptor expression of a PC-3 bone metastasis model. Mol Imaging Biol. 2012;14(6): 667–75.
Zanzonico P. Positron emission tomography: a review of basic principles, scanner design and performance, and current systems. Semin Nucl Med. 2004;34:87–111.
Zanzonico P. Multimodality image registration and fusion. In: Dhawan AP, Huang HK, Kim DS, editors. Principles and advanced methods in medical imaging and image analysis. Singapore: World Scientific Publishing Co; 2008. p. 413–35.
Zanzonico P. Small-animal imaging: basics and practical guide. In: Kiessling F, Pichler BJ, editors. Noninvasive imaging for supporting basic research. Heidelberg: Springer; 2011. p. 3–16.
Zanzonico P. Principles of nuclear medicine imaging: planar, SPECT, PET, multi-modality, and autoradiography systems. Radiat Res. 2012;177:349–64.
Zanzonico P, Heller S. Physics, instrumentation, and radiation protection. In: Biersack HJF, Leonard M, editors. Clinical nuclear medicine. Heidelberg: Springer; 2007. p. 1–33.
Zanzonico PB, Nehmeh SA. Introduction to clinical and laboratory (small-animal) image registration and fusion. Conf Proc IEEE Eng Med Biol Soc. 2006;1: 1580–3.
Zavaleta CL, Kircher MF, Gambhir SS. Raman's "effect" on molecular imaging. J Nucl Med. 2011;52: 1839–44.

Non-invasive Imaging in the Pharmaceutical Industry

2

Sally-Ann Emmas, Paul D. Hockings, and John C. Waterton

Contents

S.-A. Emmas (✉)
Personalised Healthcare and Biomarkers, AstraZeneca, Alderley Park, Macclesfield, UK

Alderley Imaging, Cheshire, UK
e-mail: sallyann.emmas@alderleyimaging.com

P.D. Hockings
MedTech West, Chalmers University of Technology, Gothenburg, Sweden

Antaros Medical, BioVenture Hub, Mölndal, Sweden

J.C. Waterton
Biomedical Imaging Institute, Manchester Academic Health Sciences Centre, University of Manchester, Manchester, UK

Alderley Imaging Ltd, Cheshire, UK

2.1 Introduction

The pharmaceutical industry faces an existential threat. Over recent years, the time and costs to get a new drug to market have increased to unsustainable levels whilst productivity is declining. It is critical to both improve efficiency of the drug discovery and development process and to increase success rates, with better predictivity from preclinical to clinical investigation (Kola 2008). Imaging provides unique tools to improve efficiency, predictivity and probability of success.

Imaging uniquely provides non-invasive, localised and quantitative information on focal disease and allows follow-up studies to be carried out within the same animal or human subject. Although animal imaging has been utilised in drug discovery and development since the 1970s, there has been much increased interest over recent years. This has been driven by the ever-expanding roles that imaging can play within drug discovery, by advances in imaging technologies and also by the increased availability and reliability of preclinical scanners for all modalities.

The overall aim for the use of imaging within the pharmaceutical industry is to accelerate drug discovery by improving the speed and quality of decision-making. This can be achieved throughout the drug discovery pipeline, from increasing target confidence, decreasing time taken within the design-make-test cycle, better understanding of preclinical pharmacology and providing toxicology, efficacy and patient segmentation

F. Kiessling et al. (eds.), *Small Animal Imaging*, DOI 10.1007/978-3-319-42202-2_2

biomarkers. Each of these will be explored in more detail, together with examples, throughout this chapter.

The whole range of imaging modalities can be utilised within drug discovery, from optical (bioluminescence and fluorescence), ultrasound, X-ray technologies (radiography, CT and DEXA), magnetic resonance (MRI, MRS) and nuclear medicine (SPECT, PET). Again examples of these will be given throughout this chapter.

Imaging can bring additional ethical benefits in reducing the number of animals (Hultin et al. 2004; McIntyre et al. 2004; Bowyer et al. 2009; Waterton et al. 2000) because the same subject can be followed throughout the study; sample sizes may also be reduced because of better exclusion criteria and more reproducible end points. In addition, refinement of animal experimentation can often be achieved since the sensitivity of imaging end points may allow the use of milder models or even the use of animals that are clinically normal (Tessier et al. 2003; Bowyer et al. 2009).

Many imaging studies within drug discovery are aimed at providing translatable data that will be used within the drug's clinical development, for example, influencing the clinical imaging schedule to look at drug efficacy with an imaging biomarker. Equally, there are examples of where clinical imaging can influence the preclinical imaging approach (Bowyer et al. 2009).

Despite these benefits, it should be recognised that few animals, perhaps only 1–2 % of the total used in pharmaceutical drug discovery projects, ever receive an imaging measurement. Most are assessed using other, equally valid, techniques such as histology, molecular biomarkers or behavioural assessment. The decision to use imaging should be made on a case-by-case basis and will be dependent upon disease area, drug mechanism of action, questions that need to be addressed and the imaging technology within the specific field.

We now briefly describe some examples from our own and other laboratories where imaging has helped decision-making at different points in the drug discovery process.

2.2 Target Confidence

Of all the genes in the human genome, by some estimates, about 10 % offer potential targets for pharmacologic intervention in disease, whilst perhaps only 1 % have been exploited to date (Hopkins and Groom 2002). Imaging can play a valuable role in selecting the target, understanding the relationship between target distribution and activity and measuring focal progression of pathology. It is therefore natural that imaging plays an important role in building target confidence. Formerly, some drug researchers regarded target validation as a task to be carried out when a novel target was identified and then might neglect the quality of the target again until early clinical trials. Today, all companies recognise that it is critical to build target confidence as drug projects progress through the pharmaceutical pipeline in order to reduce the unacceptable levels of attrition seen in late stage clinical trials.

Target validation prior to initiating a chemistry campaign (Example 2.1) In the early phase of drug discovery, with a plethora of novel potential targets, a key issue is speed and agility in exploiting new discoveries in basic biology. There may be no time to develop new tracers or animal models. Target activity can be modulated by, for example, either knocking out or overexpressing the target in mice or using existing small molecules or biologics known to modulate target activity.

Example 2.1: MRI of Lung Oedema in Endothelin Receptor Antagonist Studies

Positive control compounds can be used to test the link between the target and disease modulation. In this example, we investigated the link between inhibition of the endothelin receptor and lung oedema. MRI was selected as the imaging technique of choice because signal from normal lung parenchyma is effectively invisible, thus highlighting areas of oedema in the lung (Beckmann et al. 2001). Lung oedema was induced by injecting big

endothelin-1 (BET) i.v. In vehicle-treated animals, oedema was observed to spread from the vasculature into the lungs whereas in animals pretreated with an endothelin receptor antagonist, oedema formation was effectively blocked (Bell et al. 2007). Chronic obstructive pulmonary disease (COPD) patient symptoms, lung function and quality of life may be improved by reducing extravasation and development of lung oedema. This work shows that blocking endothelin activity impacts lung oedema formation and thus may be a suitable COPD target.

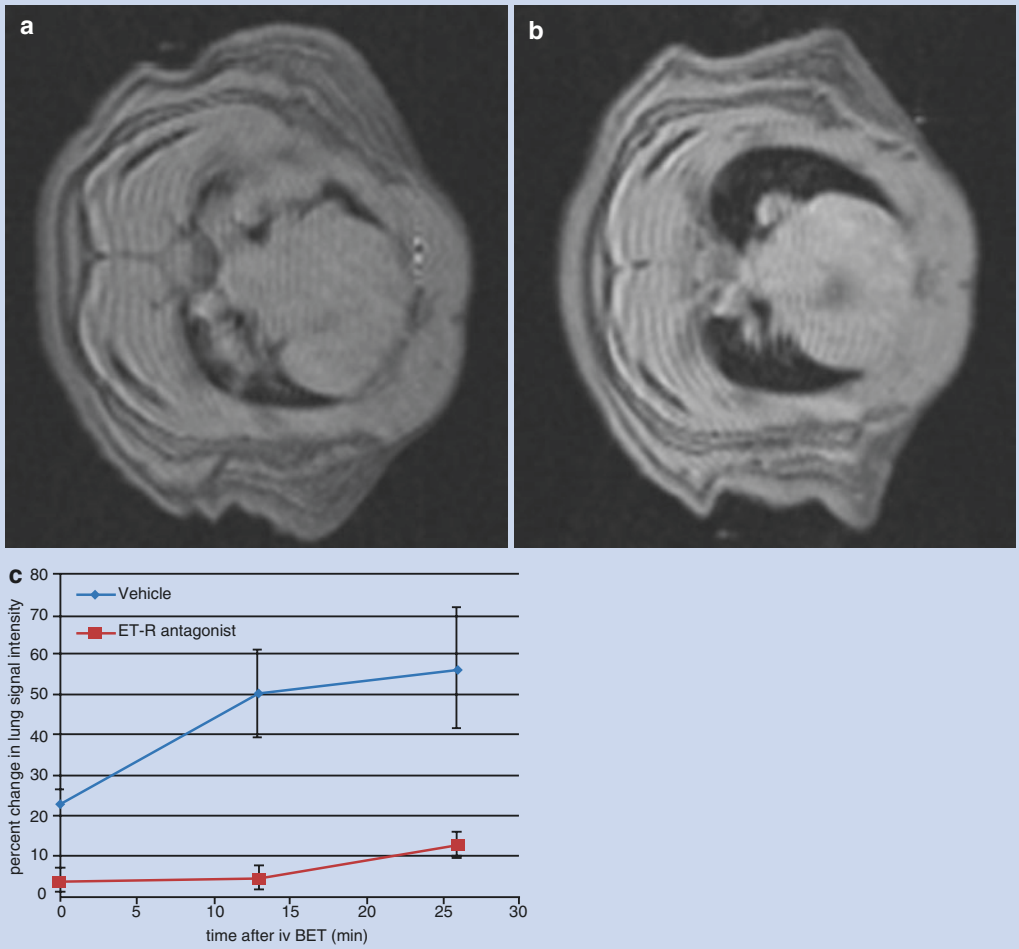

Fig. 2.1 (**a**) MR image through the thorax of a vehicle-treated rat after injection of BET. Note the presence of oedema in the lung. (**b**) Rat pretreated with an endothelin receptor antagonist displays no obvious lung oedema. (**c**) Time course of lung oedema formation after injection of BET

Target confidence in man (Example 2.2) Target validation in man means establishing that target activity is causally related to the symptoms of the disease under investigation. Clearly, one can use the same positive control approach that is used preclinically if clinically approved substances are available. Another approach is to label the drug candidate with a positron-emitting radioisotope to assess target engagement. If, for example, the drug candidate can be shown to engage the target

but the symptoms of the disease are not changed in a meaningful way, then the clinical hypothesis has been de-validated and resources can be deployed in other drug projects.

Example 2.2: PET Receptor Occupancy for Target Validation

PET was used to show that the NPY Y5R antagonist MK-0557 achieved 90 % receptor occupancy, even though there was no clinically meaningful weight loss in obese humans after 1 year of treatment. The PET data gave confidence that the maximal weight loss had been reached for MK-0557 and that this was not a suboptimal dose or brain penetration issue. As a result, this target could be de-validated (Erondu et al. 2006). The same compound produced significant weight loss in a mouse obesity model, so it was hypothesised that the endogenous NPY tone in humans is much lower than that in rodents, highlighting the need for target validation studies in man (Fong 2008).

In conclusion, imaging is a useful tool to build target confidence with the potential to reduce late phase attrition due to lack of efficacy. Importantly, it must be recognised that drug projects can be killed even in a relatively advanced phase if the target is de-validated.

2.3 The Design-Make-Test Cycle

Once the drug developer has selected a credible drug target and has found a starting point in chemical space (assuming the aim is to produce a small-molecule drug), the process of lead optimisation (LO) begins. The structure of the chemical starting point has to be iterated to optimise the in vitro efficacy against target, to optimise pharmacokinetics compatible with oral dosing and to achieve an acceptable toxicological profile. This iterative process is sometimes described as the design-make-test cycle, since the chemists cannot design their next iteration until they have the result of the biological test on the previous iteration. Although the design-make-test cycle sits at the very heart of drug discovery, in vivo studies play a relatively minor part at this stage. Most tests are performed in vitro, since these tend to be inexpensive, rapid and amenable to automation; moreover, it is likely to be unethical to perform an in vivo experiment where an in vitro alternative exists. Rarely, the complexity of the biology makes it impractical to model the disease adequately in vitro, and in vivo models may be required at the later stages of LO (Example 2.3).

Example 2.3: MRI to Support Lead Optimisation for Acute Stroke

An example of in vivo imaging in LO is in focal cerebral ischaemia (stroke) research, where the rat middle cerebral artery occlusion model has been used to choose between compounds with similar in vitro properties. An example is shown below where 13 compounds with good in vitro potency were compared in vivo, using an innovative group-sequential design to reduce animal numbers with no loss in statistical power. In this case, three out of 13 compounds were found inactive in vivo, and ten were found active: one of these ten was eventually progressed into preclinical development.

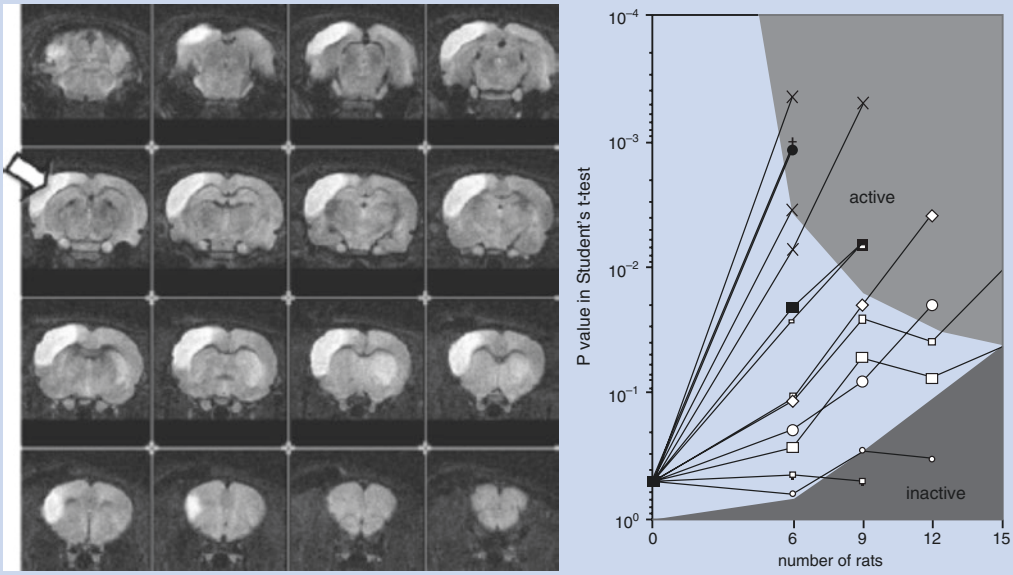

Fig. 2.2 MRI in rat permanent focal cerebral ischaemia model: 16 slices through the brain are shown. The area of infarct (*arrow*) can be easily be segmented to derive the infarct volume in the territory of the middle cerebral artery (Waterton et al. 2000). Inset shows the operation of the group-sequential design: significance testing was performed after 6, 9, 12 and 15 rats were entered for each LO compound, and if the calculated *p* value was very small (*upper grey zone*), a stopping rule was invoked and the compound declared active; conversely, a high *p* value (*lower grey zone*) invoked a second stopping rule and the compound was declared inactive

2.4 Preclinical Pharmacology

Many preclinical models demonstrate aspects of a clinical disease but do not represent the full disease spectrum or time to disease progression. In order to understand drug pharmacological effects, it is important to have good characterisation and validation of the preclinical model and how this relates to the clinical disease state. Typically, model validation studies will be performed using histology and/or other pharmacodynamic end points. Additionally, anatomical, functional and molecular imaging techniques can all play roles in aiding preclinical model characterisation and the changes that ensue following drug administration.

Understanding and being able to quantify changes that result following drug administration in the preclinical setting are obviously of great importance within drug discovery. Such information will be utilised in decisions on the progression of the drug and may be incorporated into the Investigator's Brochure and supporting publications. These imaging techniques and methodologies may be specific only for the preclinical setting due to the type of imaging modality and/or availability/licensing of the contrast agent or may be translatable to the clinical arena.

Below (Examples 2.4 and 2.5) are examples of the use of imaging in preclinical model characterisation and changes following drug administration.

Example 2.4: Hyperpolarised ^{3}He to Monitor Drug Effects in a Murine COPD Model

Hyperpolarised ^{3}He MRI is an emerging respiratory imaging technology with key advantages that it can measure gas distribution and importantly functional end points, which appear to be more sensitive than conventional ^{1}H MRI (Olsson et al. 2009). This imaging methodology can also potentially be translatable to human proof-of-principle studies.

We have used this technology to assess treatment effects of drugs using a lipopolysaccharide (LPS) murine model of lung inflammation to mimic the inflammatory response of COPD. Administration of LPS causes formation of lesions and ventilation defects within the lungs, which can be easily visualised using hyperpolarised ^{3}He. The example shown (courtesy of Lars E. Olsson) compares lung lesion volumes in untreated mice with those exposed to LPS and either treated with vehicle or budesonide. Exposure to LPS induced significant inflammation and large ventilation defects. LPS exposure together with budesonide treatment resulted in a significantly smaller volume of ventilation defects.

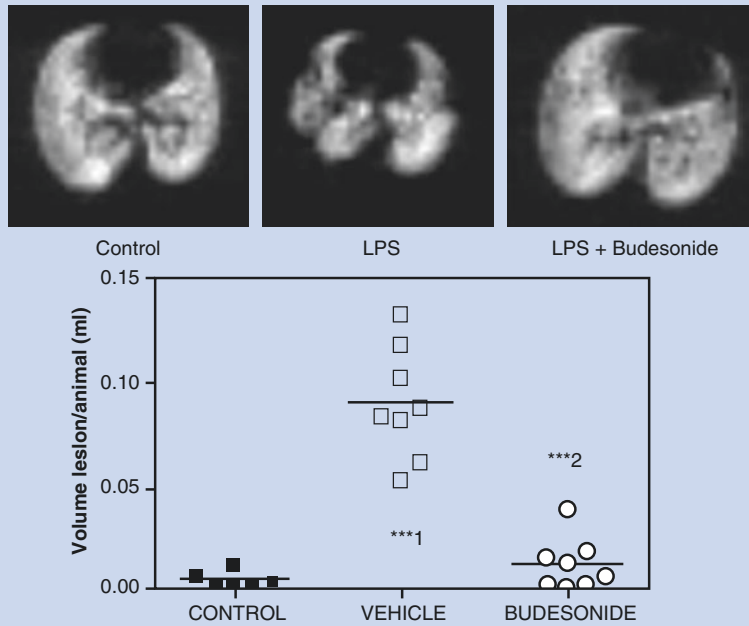

Fig. 2.3 Cross validation of the MRI data was performed using bronchoalveolar lavage (BAL), with inflammatory markers supporting the findings from MRI

Example 2.5: MRI to Evaluate Compound Efficacy in a Guinea Pig Osteoarthritis Model

One of the applications of MRI is to provide high, quantifiable anatomical information. We developed methods to enable high-resolution 3D MRI to characterise cartilage loss in a model of spontaneous knee osteoarthritis in the Dunkin-Hartley guinea pig (Tessier et al. 2003). Using a non-invasive longitudinal technique to monitor disease progression or modification with therapy over time has real cost benefits when dealing with more complex, longer duration disease models.

In this model, we have used MRI to evaluate the effects of doxycycline treatment and compared the results to matrix metalloproteinase (MMP) activity (Bowyer et al. 2009). Guinea pigs (9 months old) were dosed with vehicle or doxycycline (0.6 or 3.0 mg⁄kg⁄day) for 66 days. Fat-suppressed 3D gradient-echo MRI of the left knee was acquired pre- and post-dosing. Change in medial tibial plateau (MTP) cartilage volume (MT.VC) was determined using image analysis. At termination, MTP cartilage was removed from knees and proteolytic MMP activity determined using a fluorescent peptide substrate assay.

Results showed that vehicle-treated animals lost 20.5 % MT.VC. The 0.6 mg⁄kg⁄day doxycycline group lost 8.6 % whilst the 3.0 mg⁄kg⁄day group lost 10.0 %. Endogenous levels of active MMPs were below limits of detection in all samples. However, doxycycline treatment ablated amino phenyl mercuric acid activated MMP-13 and MMP-8 levels and reduced MMP-9 levels by 65 % and MMP-1 levels by 24 %. Doxycycline treatment thus resulted in partial protection from MT.VC loss although it was associated with complete reduction in MMP-13 and MMP-8 and partial reduction in MMP-9 activity. Doxycycline has only limited efficacy in man, and these data suggest that compounds providing better chondroprotection need to be sought.

Imaging may also be employed to evaluate drug distribution (Example 2.6), with drug molecules labelled with a detectable probe and distribution monitored throughout time post injection. This type of approach has been used for many years within the neurology disease area, with drugs typically labelled with ^{11}C and brain uptake and localisation evaluated using PET imaging. With the increased emergence of biological drug compounds, there has been a trend to understand their distribution and areas of accumulation. Due to the long blood half-life of biological compounds, short-lived isotopes such as ^{11}C are not suitable, and therefore, biologics are typically labelled with either a fluorescent tag for optical detection or longer-lived radioisotope such as ^{64}Cu or ^{111}In for PET and SPECT imaging, respectively.

Example 2.6: ^{111}In-DTPA-Pertuzumab Sensitively Detects Trastuzumab-Mediated HER2 Downregulation

Pertuzumab is a HER2 dimerisation inhibitor that binds to an epitope unique from that of trastuzumab. SPECT studies both in vitro and in vivo demonstrated that ^{111}In-DTPA-pertuzumab could sensitively detect HER2 downregulation after 3 days of treatment with trastuzumab and detected a reduction in viable HER2-positive tumour cells after 3 weeks of therapy in MDA-MB-361 human breast cancer xenografts (McLarty et al. 2009).

2.5 Preclinical Toxicology

Safety assessment of candidate drugs involves taking the data from model biological systems (e.g. cell cultures, laboratory animals) and using these results to try to predict toxicity in humans. The continued attrition of late stage compounds due to clinical safety issues indicates that our ability to predict toxicity can be further optimised, and additional tools to provide improved data on which to base predictions would be most welcome. Drug developers need to show that drugs are both efficacious and have acceptable toxicity: whilst in vivo imaging has been used extensively in both preclinical and clinical efficacy studies, it has not as yet

seen widespread use in preclinical toxicology (Hockings 2006).

The ability to image the same animal at multiple time points suggests that imaging is likely to make its greatest contribution in chronic investigational safety studies. There are also clear advantages such as bridging the gap between animals and humans by using the same non-invasive end points and utilising functional safety biomarkers not readily available otherwise, e.g. cardiac function (Cove-Smith 2014) or neurotoxicity (Example 2.7) (Williams 2001; Liachenko 2015).

Example 2.7: T_2-Weighted and Diffusion-Weighted MRI Elucidates Neurotoxicity

L-2-Chloropropionic acid (L-CPA) (not a drug substance but an intermediate) found to be selectively toxic to rat cerebellar granule cells. T_2-weighted and diffusion-weighted MRI measurements were used in rats at 37 h and 48 h post-dosing to characterise the mechanism and evolution of the neurotoxicity. Swelling of the cerebellum was found 37 h post-dosing, and at 48 h post-dosing T2WI and DWI hyperintensities were observed in the cerebellum whether or not necrosis was detected. In addition, the exquisite sensitivity of MRI was demonstrated by the finding of T2WI hyperintensity in the forebrain leading to the discovery in vivo of a new lesion in the habenular nucleus not previously detected in *post-mortem* pathology (Williams et al. 2001).

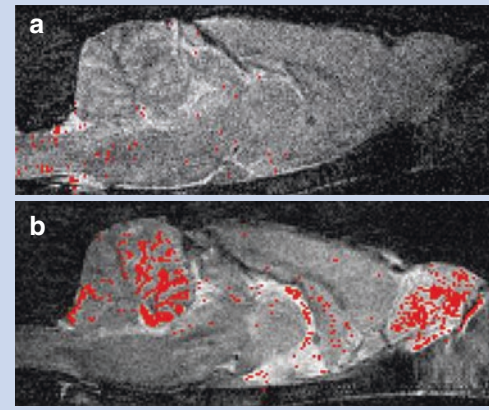

Fig. 2.4 T2-weighted images from (**a**) an untreated rat and (**b**) a treated rat 48 h post-dosing. Red pixels have elevated intensity in both T2W and diffusion-weighted MRI

Despite these examples of safety imaging biomarkers that are ready to use, there are relatively few imaging studies with a safety end point (Examples 2.8 and 2.9). The key blockers for imaging studies tend to be lack of knowledge about in vivo imaging by preclinical toxicologists because of the sparse literature and a lack of time to conduct appropriate validation studies with positive and negative control substances as safety issues arise unexpectedly and then often become critical path activities for drug projects. Other issues can be concerns about confounds from anaesthesia for restraint (not always necessary), logistics and a concern that imaging studies are not usually conducted under (or close to) the exacting regulatory standards of good laboratory practice. However, none of these problems are completely insurmountable.

Example 2.8: Cholestasis

The need for better biomarkers of drug-induced liver injury (DILI) has been identified (Holt and Ju 2006). In particular, drug-induced cholestasis is an area where MR imaging can make a contribution as new clinically approved contrast agents such as gadoxetate (Gd-EOB-DTPA, Bayer Schering) have become available. Gadoxetate is taken up into hepatocytes and subsequently excreted into bile, and hence, cholestasis can be detected by the accumulation of gadoxetate in the liver with resultant enhancement on the MR image.

Ulloa et al. (2013) dosed rats orally with either an investigational chemokine antagonist (CKA) known to inhibit biliary transporter activity in vitro or vehicle. Dynamic contrast-enhanced magnetic resonance imaging (DCE-MRI) was used to assess clearance of gadoxetate by monitoring changes in liver contrast over a 60 min period. The CKA was shown to reduce both the rate of uptake of gadoxetate into the hepatocyte, and biliary efflux. Effects were dose dependent and correlated with effects on plasma chemistry markers of liver dysfunction, in particular bilirubin and bile acids. Gadoxetate DCE MRI may therefore be a suitable biomarker of drug-induced perturbation of hepatic transporters in animal models and ultimately in humans in vivo.

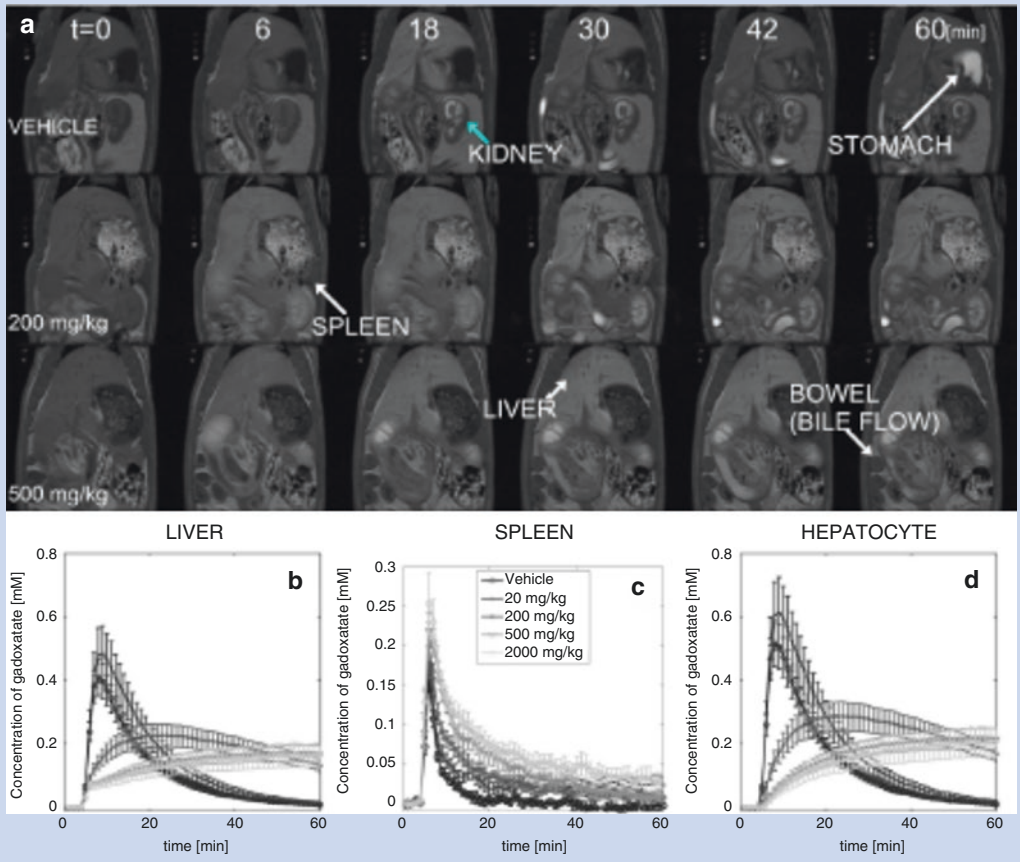

Fig. 2.5 (**a**) Examples of dynamic images at $t=0$, 6, 18, 30, 42 and 60 min after contrast injection, for animals treated with vehicle (top), 200 mg/kg (*middle*) or 500 mg/kg (*bottom*) CKA. Note the enhancement of the small bowel lumen at about 30 min after contrast injection and also the reflux of gadoxetate into the stomach at the end of the acquisition in the vehicle-treated animal. No enhancement was observed in the bowel of the animal treated with 500 mg/kg CKA. (**b**–**d**) Mean concentration of gadoxetate over ROIs covering (**b**) liver, (**c**) spleen and (**d**) hepatocytes. Bars represent SEM

Example 2.9: Gastric Emptying

Gastric emptying is not always studied as part of the safety pharmacology core battery but can be examined if appropriate. The standard assay is to dose a dye such as charcoal and then kill the animal after a fixed period of time and examine intestinal transport. Obviously, this method is limited to examinations at a single time point. Hultin et al. (2004) used functional X-ray of conscious rats after a barium meal to examine the time course of gastric emptying and the effect of various doses of corticotropin releasing factor (CRF). They showed that functional X-ray measurements provided a reproducible and quantifiable method to evaluate gastric motility and emptying.

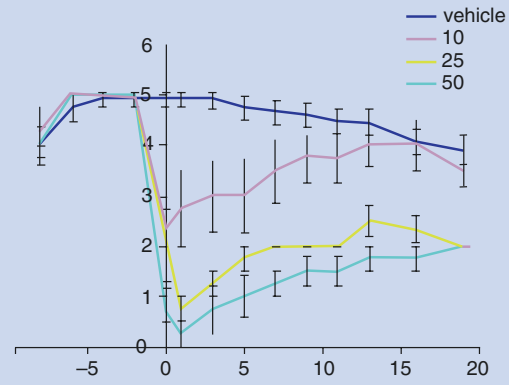

Fig. 2.6 Time course of gastric motility effects after i.v. CRF (mg/kg) in conscious rats

2.6 Biomarkers

In the last few years, the regulatory, academic and drug development communities have developed an increasingly sophisticated understanding of the nature of biomarkers and their use in drug development. A biomarker is now understood very generally (Atkinson et al. 2001), as any "characteristic that is objectively measured and evaluated as an indicator of normal biological processes, pathogenic processes or pharmacologic responses to a therapeutic intervention". Imaging measurements are included within this definition, as are the more familiar molecular biomarkers and even physiologic tests such as electrocardiography or blood pressure. Importantly, from the regulatory perspective, a biomarker is not necessarily seen as a surrogate end point. Thus, a biomarker can still be useful in drug development, even when it is not exhaustively validated to eliminate all possible risk of a false-positive or false-negative outcome. The process of qualification, i.e. understanding the value of a biomarker, involves establishing the relationship between the measured biomarker and the underlying biology, as well as understanding what a biomarker measurement implies for the patient's ultimate clinical outcome. Imaging biomarkers are used in drug development in many diseases, in particular in inflammation, degeneration, ischaemia and neoplasia. In phase 1 and phase 2 trials, imaging biomarkers are used to establish that the drug reaches its target, has some pharmacologic effects on the cell phenotype, causes some local physiologic change such as a change in perfusion or local inflammation and ultimately modifies the structural progression of the disease.

The actual use of imaging biomarkers in phase 1 and phase 2 drug development obviously involves human clinical studies and is therefore outside the scope of this chapter. However, before such an imaging biomarker is used with investigational agents (particularly with first-in-class drugs against targets not previously addressed in man), animal studies using the same imaging biomarker/drug combination are often critical, both in the design of the clinical trial and in interpreting its outcome (Examples 2.10 and 2.11). Ideally, the imaging biomarker has a similar presentation in the animal model and in the human patient. Examples in which imaging biomarkers have been translated between animal and man include cancer (FDG-PET, FLT-PET, DCE MRI, ADC MRI, phosphomonoester MRS), psychiatry (functional MRI, pharmacoMRI), myocardial or cerebrovascular ischaemia (ADC MRI, perfu-

sion), atheroma (ultrasound, CT, MRI and PET measurements of plaque size, composition and inflammation), respiratory diseases (CT and MRI measurements of emphysema, perfusion and ventilation), arthritis (MRI and X-ray measurements of bone lesions, cartilage and synovitis), osteoporosis (bone mineral density measurements) diabetes, obesity, thrombosis, neurodegeneration and many others. Imaging biomarkers are also increasingly used in safety assessment, for example, cardiac ultrasound or MRI (Cove-Smith 2014), to assess and monitor the safety of potentially cardiotoxic anticancer drugs.

Example 2.10: DCE MRI Proof of Principal Biomarker for a Vascular Disrupting Agent

An example of animal imaging to qualify a biomarker for use in human drug development is the use of DCE MRI in the development of ZD6126. DCE MRI was used in this case as a proxy for tumour perfusion. ZD6126 is a vascular destructive agent: it targets immature tumour vasculature causing massive intratumoural infarction. Studies in xenografts in mice and rats in three different laboratories established the dose response, speed of onset and the persistence of the infarction (Bradley et al. 2007; McIntyre et al. 2004; Evelhoch et al. 2004), as well as optimising image analyses at intermediate doses where complete infarction was not achieved. In addition, the relationship between the imaging change and histopathological change was established. These data were then used to design and interpret the phase 1 trials of the compound in man.

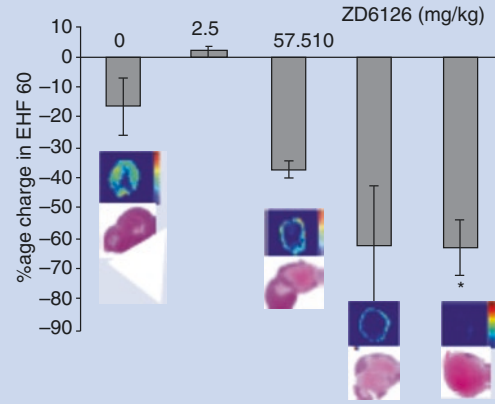

Fig. 2.7 Change in DCE MRI enhancing fraction (EHF_{60}), 24 h after treatment with increasing doses of ZD6126. *Insets* show H&E histopathology and corresponding DCE MRI K^{trans} maps, which can be used to help interpret the changes seen in human tumours (Bradley et al. 2007)

Example 2.11: FDG-PET as a Proof of Mechanism Biomarker for an mTOR Kinase Inhibitor

mTOR is a serine/threonine kinase belonging to the P13K superfamily of kinases, and the P13K-AKTmTOR pathway is involved in glucose uptake and metabolism. Using a human glioma xenograft model (U87-MG), we evaluated whether FDG-PET could be used as a direct mechanistic readout of TOR kinase inhibition. To evaluate this, U87-MG tumour-bearing mice were administered with either a single dose of mTOR kinase inhibitor (AZD8055) or vehicle, 15 min later administered with FDG-PET and imaged 1 h after drug or vehicle dosing. Results showed there was a significant decrease in tumour FDG uptake in the animals treated with AZD8055 compared to vehicle group. Imaging data correlated with histological pharmacodynamic readouts, with marked reductions of both pS6 and pAKT immunostaining with treatment. Therefore, this data provides evidence that FDG uptake is an early sign of metabolic response to mTOR inhibition (Keen et al. 2013).

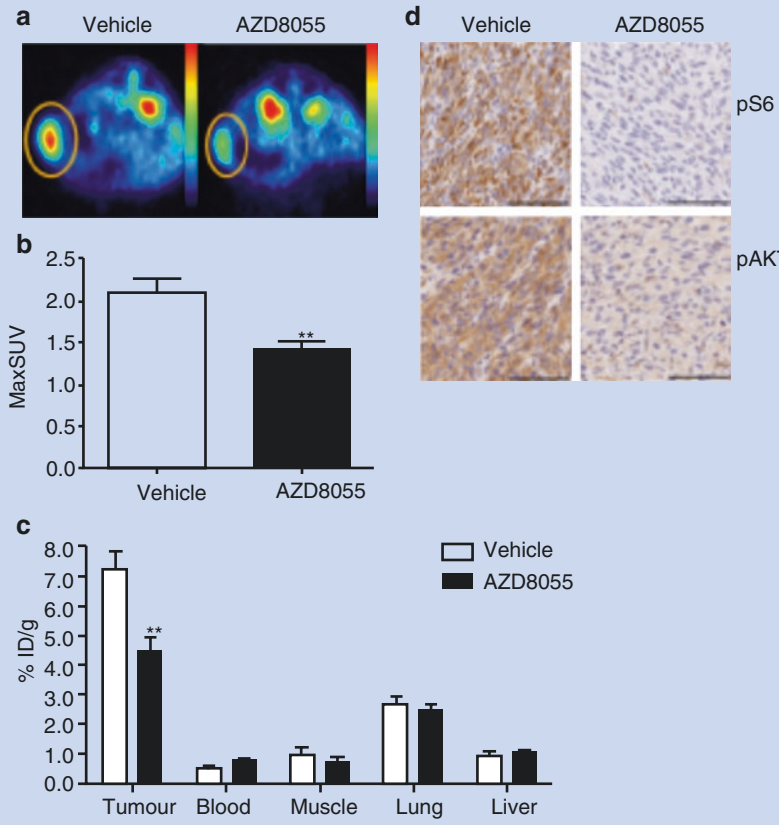

Fig. 2.8 (**a**) Representative axial slice PET images within 1 h of AZD8055 treatment. Tumour is circled. (**b**) MaxSUV uptake in tumour. Data expressed as group mean MaxSUV ± (SEM). $^{**}p<0.01$. (**c**) Ex vivo biodistribution data. Data expressed as group mean %ID/g ± SEM. $^{**}p<0.01$. (**d**) Representative histological micrographs (magnification ×20) of pS6 and pAKT. Scale bar in each image equates to 100 μm. Positive expression of each histological biomarker is shown by the presence of brown staining on the tissue section

What measurements are important using imaging biomarkers in animals? Firstly, we can ask whether the new drug affects the imaging biomarker and the effect size. Using knowledge of the relationship between the animal model and human disease, we can use this information to predict the likely size of the drug effect on the imaging biomarker in a clinical trial, which is of course essential to sample size calculations. We can measure the duration of the effect and the dose response. Importantly, we can verify that the change in the imaging biomarker following drug treatment parallels changes in the underlying histopathology: these measurements are usually much easier to perform in animals than in humans but are essential in qualifying the biomarker. Indeed, the implied clinical hypothesis, that drug-induced change in the imaging biomarker faithfully reflects a desired drug-induced change in the underlying pathology, is often only satisfactorily addressable in an animal study. Finally, we may be able to use our imaging biomarker studies in animals to inform our thinking about whether a given change in the imaging biomarker will predict a specific clinical benefit to the patient or to a specific subset of patients.

Conclusions

As discussed at the beginning of this chapter, the aim for any science or technology used within drug discovery and development is to accelerate the drug discovery process by improving the quality of decision-making. The challenge is to provide data in a timely fashion to impact decision-making. Ex vivo imaging techniques such as histopathology, immunohistochemistry and autoradiography have a role to play, as they have excellent spatial resolution and exquisite molecular sensitivity and specificity. Although in vivo imaging is sometimes more costly and can lack sensitivity and specificity in comparison with the ex vivo modalities, it provides unparalleled translatability and temporal insight into disease progression and response to therapy. In this chapter, we have highlighted the range of drug discovery activities and areas of impact and value that in vivo imaging can have within preclinical drug discovery and development.

References

Atkinson Jr AJ, Colburn WA, DeGruttola VG, DeMets DL, Downing GJ, Hoth DF, Oates JA, Peck CC, Schooley RT, Spilker BA, Woodcock J, Zeger SL. Biomarkers and surrogate endpoints: preferred definitions and conceptual framework. Clin Pharmacol Ther. 2001;69:89–95.

Beckmann N, et al. Pulmonary edema induced by allergen challenge in the rat: non-invasive assessment by magnetic resonance imaging. Magn Reson Med. 2001;45: 88–95.

Bell JP, Chevalier E, Tessier J, Bradley D, Mather ME, Young SS, Bahl AK, Escott KJ, Young A. Use of magnetic resonance imaging (MRI) to track big endothelin-1-induced edema in the rat lung. Am J Respir Crit Care Med. 2007;175:A533.

Bowyer J, Heapy CG, Flannelly JK, Waterton JC, Maciewicz RA. Evaluation of a magnetic resonance biomarker of osteoarthritis disease progression: doxycycline slows tibial cartilage loss in the Dunkin Hartley guinea pig. Int J Exp Pathol. 2009;90: 174–81.

Bradley DP, Tessier JJ, Ashton SE, Waterton JC, Wilson Z, Worthington PL, Ryan AJ. Correlation of MRI biomarkers with tumor necrosis in Hras5 tumor xenograft in athymic rats. Neoplasia. 2007;9:382–91.

Cove-Smith L, Woodhouse N, Hargreaves A, Kirk J, Smith S, Price SA, Galvin M, Betts CJ, Brocklehurst S, Backen A, Radford J, Linton K, Roberts RA, Schmitt M, Dive C, Tugwood JD, Hockings PD, Mellor HR. An integrated characterization of serological, pathological, and functional events in doxorubicin-induced cardiotoxicity. Toxicol Sci. 2014;140:3–15.

Erondu N, et al. Neuropeptide Y5 receptor antagonism does not induce clinically meaningful weight loss in overweight and obese adults. Cell Metab. 2006;4: 260–2.

Evelhoch JL, LoRusso PM, He Z, DelProposto Z, Polin L, Corbett TH, Langmuir P, Wheeler C, Stone A, Leadbetter J, Ryan AJ, Blakey DC, Waterton JC. Magnetic resonance imaging measurements of the response of murine and human tumors to the vascular-targeting agent ZD6126. Clin Cancer Res. 2004;10: 3650–7.

Fong TM. Development of anti-obesity agents: drugs that target neuropeptide and neurotransmitter systems. Expert Opin Investig Drugs. 2008;17:321–5.

Keen HG, Ricketts SA, Maynard J, Logie A, Odedra SAM, Wedge SR, Guichard SM. Examining changes in [^{18}F]FDG and [^{18}F]FLT uptake in U87-MG glioma xenografts as early response biomarkers to treatment with the dual mTOR1/2 inhibitor AZD8055. Mol Imaging Biol. 2014;16:421–30.

Kola I. The state of innovation in drug development. Clin Pharmacol Ther. 2008;83:227–30.

Hockings PD. Magnetic resonance imaging in pharmaceutical safety assessment. In: Vogel HG, Hock FJ, Maas J, Mayer D, editors. Drug discovery and evaluation: safety and pharmacokinetic assays. Heidelberg: Springer; 2006. p. 385–93.

Holt MP, Ju C. Mechanisms of drug-induced liver injury. AAPS J. 2006;8:E48–54.

Hopkins AL, Groom CR. Opinion: the druggable genome. Nat Rev Drug Discov. 2002;1:727–30.

Hultin L, Hyberg G, von Mentzer B, Martinez V. Effects of corticotropin releasing factor and urocortins on gastric emptying and motility in rats assessed by functional X-ray. In: XII European Symposium on Neurogastroenterology and Motility. Cambridge; 2004. p. T150.

Liachenko S, Ramu J, Konak T, Paule MG, Hanig J. Quantitative assessment of MRI T2 response to kainic acid neurotoxicity in rats in vivo. Toxicol Sci. 2015;46:183–91.

McIntyre DJ, Robinson SP, Howe FA, Griffiths JR, Ryan AJ, Blakey DC, Peers IS, Waterton JC. Single dose of the antivascular agent, ZD6126 (N-acetylcolchinol-Ophosphate), reduces perfusion for at least 96 hours in the GH3 prolactinoma rat tumor model. Neoplasia. 2004;6:150–7.

McLarty K, Cornelissen B, Cai Z, Scollard DA, Costantini DL, Done SJ, Reilly RM. Micro-SPECT/CT with 111In-DTPA-Pertuzumab sensitively detects trastuzumab-mediated HER2 downregulation and tumor response in athymic mice bearing MDAMB-361 HUMAN breast cancer xenografts. J Nucl Med. 2009;50:1340–8.

Olsson LE, et al. 1H and hyperpolarized 3He MR imaging of mouse with LPS-induced inflammation. J Magn Reson Imaging. 2009;29:977–81.

Tessier JJ, Bowyer J, Brownrigg NJ, Peers IS, Westwood FR, Waterton JC, Maciewicz RA. Characterisation of the guinea pig model of osteoarthritis by in vivo three-dimensional magnetic resonance imaging. Osteoarthritis Cartilage. 2003;11:845–53.

Ulloa JL, Stahl S, Yates J, Woodhouse N, Kenna JG, Jones HB, Waterton JC, Hockings PD. Assessment of gadoxetate DCE-MRI as a biomarker of hepatobiliary transporter inhibition. NMR Biomed. 2013;26:1258–70.

Waterton JC, Middleton BJ, Pickford R, Allott CP, Checkley D, Keith RA. Reduced animal use in efficacy testing in disease models with use of sequential experimental designs. Dev Anim Vet Sci. 2000;31:737–45.

Williams RE, Prior M, Bachelard HS, Waterton JC, Checkley D, Lock EA. MRI studies of the neurotoxic effects of L-2-chloropropionic acid on rat brain. Magn Reson Imaging. 2001;19:133–42.

Designing a Small Animal Imaging Center

3

David Stout

Contents

D. Stout, PhD
UCLA School of Medicine,
4297 Motor Ave, Culver City, CA 90232, USA
e-mail: davidstoutphd@gmail.com

3.1 Overview

Creation of an animal imaging center is rarely as simple as purchasing a system, placing it in a room somewhere, and turning people loose to use it. There are very few imaging devices that are appropriate to place on a laboratory bench top and use right out of the box without further integration, for example, a microscope. Most systems require training of users and a specialized environment for handling data and animals. Use of animals requires approval of physical spaces, imaging systems, and protocols by the Institutional Animal Care and Use Committee (IACUC), radiation use requires approval from the Radiation Safety Officer (RSO), local institutional veterinary considerations may apply, and usually biosafety approval is required. There may also be other environmental health and safety (EHS) issues to consider, such as magnetic field safety and airflow requirements. The process of comprehensive planning and oversight is now commonplace to house, use, and experiment with animals (Stout et al. 2005; Klaunberg and Davis 2008).

The first step in designing an imaging center is to determine what types of research will be supported, a process that then leads to what imaging modalities and specific imaging systems are required. There are many different imaging modalities and vendors selling various imaging systems, most of which are quite expensive, so careful selection is required to devise the optimal mix of systems (Stout and Zaidi 2009). Imaging

F. Kiessling et al. (eds.), *Small Animal Imaging*, DOI 10.1007/978-3-319-42202-2_3

modalities are now often combined, such as PET/CT, PET/MR, and optical/X-ray, so consideration must be given to whether the combination is useful or limiting with respect to the intended workflow of the center (Fig. 3.1).

The support infrastructure for various imaging systems varies in terms of space, power, air conditioning, and ancillary equipment necessary. For example, a cyclotron and radiochemistry lab or an arrangement for isotope delivery from an outside location is necessary for PET and SPECT systems, magnetic field restrictions are required for high-field MR systems, and a low radiation background location is needed for gamma counters. The use of immune-compromised animals and human xenograft tumors leads to biosafety requirements such as gowning chambers, barrier facilities, and controlled access. Often it is advisable to have a dedicated vivarium to house the animals, which might also include a separate room for surgical or other interventions. Personnel support will depend again on the systems being used and the level of training and support planned for the experiments. The exact engineering and administrative controls required are a function of both the imaging systems and local safety oversight regulations.

Imaging systems capable of examining small animals are a relatively recent development; thus, new systems and methods for imaging are frequently being discovered, created, and brought to market. These new tools, techniques, and protocols may need to be included or exchanged into the center in the future. Either a center employee or a faculty member associated with the center will need to keep informed about developments in imaging systems, methodology, and the changing regulatory environment associated with the field. The lifetime and depreciation schedule of these preclinical systems may be shorter than similar clinical systems.

An example of the changing requirements for imaging is given in Figs. 3.2, 3.3, and 3.4, showing how the imaging center at the Crump Institute at UCLA has evolved over 20 years. At first, a relatively small room to house one or two systems was sufficient (Fig. 3.2). As more systems were added, it became clear that a consolidated location was needed to bring the systems into one area instead of being spread between several buildings (Fig. 3.3). As more systems and support areas were required, eventually a new building was created where the layout could be expanded and optimized, instead of working within the confines of an existing building (Fig. 3.4). A little extra space and planning ahead for possible increases in workflow may save time and money when expansion is needed.

When designing a center, the process can be divided into several categories: vendor-specific site requirements (cooling, power, space), computer infrastructure requirements for archiving and database information, on-site animal use and housing requirements, radiation and biosafety requirements, and human ergonomic planning to make sure people and equipment can easily and safely coexist. Optimal center design often

- Purpose of the imaging facility
- Types of imaging equipment: PET, CT, ultrasound, MRI, optical, etc.
- Ancillary equipment: gamma counter, cryostat, biosafety cabinet, anesthesia
- Ancillary spaces: surgical area, hot lab, supply storage, animal housing, cage cleaning
- Barrier conditions for immune compromised animals (SCID, nude animals)
- Security requirements
- Radiation use and Electromagnetic safety requirements
- Biohazard requirements
- Facilities planning: hoods, air, vacuum, tanks
- Room layouts: space, work path, supply delivery path
- Animal use issues: gowning, access control, waste management, pathogen control
- Vivarium support: cage racks, supplies, cage cleaning, access control
- Anesthesia: vaporizers, induction boxes, waste management
- Mouse handling: prep area, injection techniques
- Mouse imaging chambers: positioning, multimodality, sterility
- Hypothermia prevention: heating systems for before, during and after imaging
- Personnel: locations, break area, training, staffing requirements

Fig. 3.1 Design considerations for a small animal imaging center

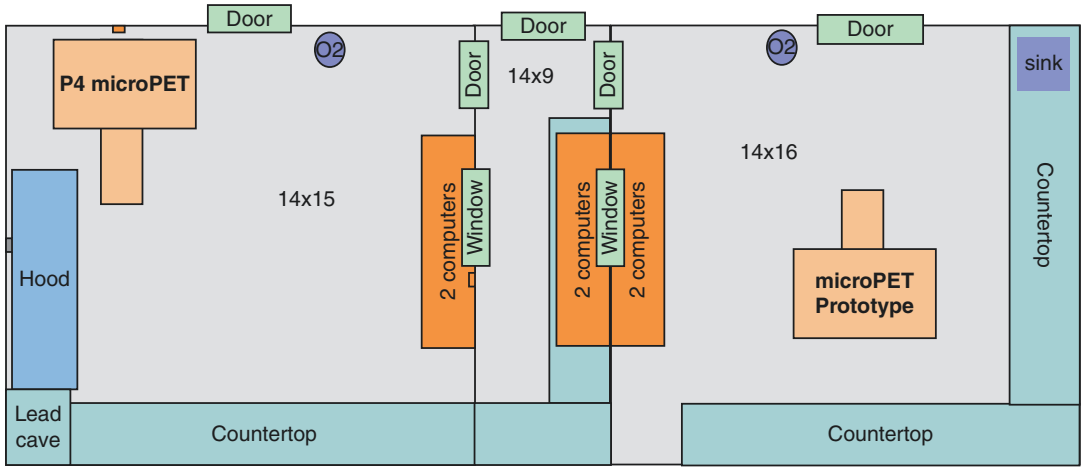

Fig. 3.2 UCLA small animal imaging center from 1990 to 2003, converted from an old fluoroscopy imaging suite. Originally only the left and center rooms were used to house a clinical PET system solely used for animal work. In 1997 it was expanded to include the right side room for the prototype microPET, and then in 2000 the clinical system was exchanged for a commercial microPET system and a biosafety cabinet (hood) added

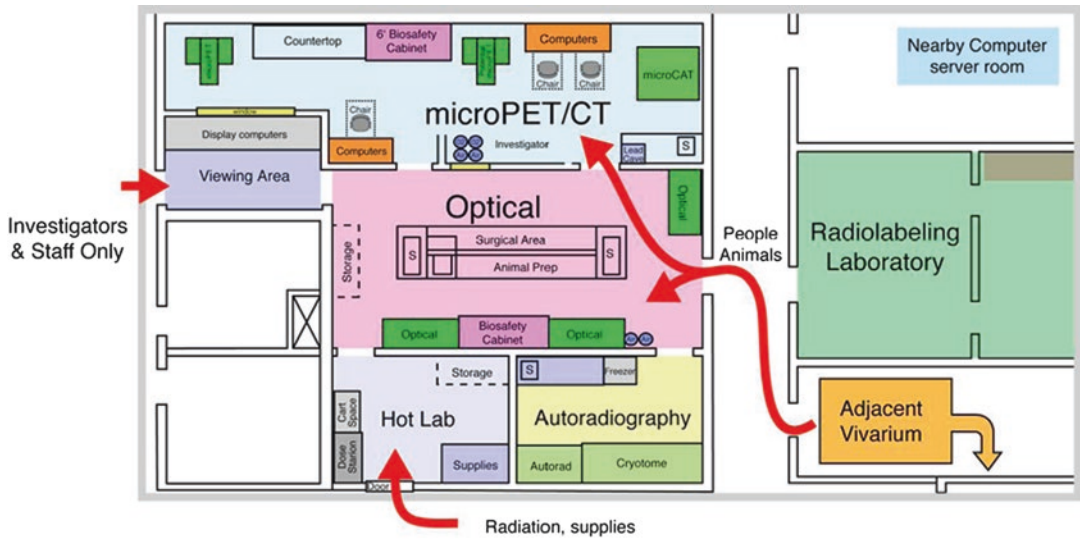

Fig. 3.3 UCLA Crump Imaging center from 2003 to 2009. This location was renovated within an existing building. The computer cluster room and radiolabeling lab were added in 2005 to accommodate expanding support requirements for radiolabeling I-124 and Cu-64 and the need to shift image processing away from the host computers

includes the combined expertise of architects, members of the oversight committees, animal care personnel, and people experienced and familiar with the usage requirements of the imaging systems. Working as a team and getting the center open quickly will reduce the chance of unforeseen obstacles and delays.

3.2 Site Requirements

Equipment manufacturers normally provide site planning guides with equipment specifications and space requirements. Typically there are power and air conditioning requirements that specify dedicated power circuits and appropriate

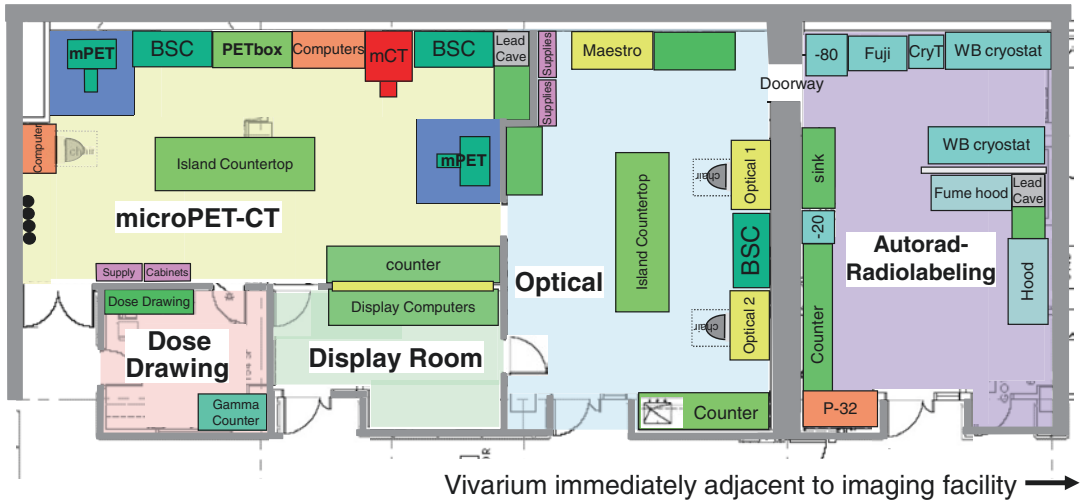

Fig. 3.4 UCLA Crump Imaging center as of 2009. The new location increased space ~50% over the previous design, with the vivarium 10× larger than before. The added space lowers radiation exposure and allows more people to work easily at the same time. A third PET imaging system was added (PETbox), and two spaces remain open in the optical room for future expansion

temperature and humidity ranges. Additional space around the systems is not usually specified but is often necessary for good access during normal use and may be required for servicing and good airflow around the systems. Requirements vary widely based on the systems, from a simple space on a counter to specialized buildings.

Large-scale installations such as cyclotrons and high-field MRI imaging systems require significant space and additional magnetic and radiation shielding requirements. For projects of this scale, manufactures often require specific construction plans and usually work closely with sites to create the appropriate building systems and floor plans. The precise requirements are specific to the system being installed; thus, these types of site plans are highly customized to match the exact requirements for the end user.

Most imaging systems such as PET, CT, SPECT, optical, and autoradiography require a dedicated power circuit, rely on room air circulation for heat removal, and need space either on the floor or counter for use. Except for high-field MR, these systems can be located in almost any room or together in various combinations. Systems using radiation need to have a separate area for holding and dispensing radioactive doses, and consideration is necessary for placement with respect to personnel exposure. It may be required to have dosimetry estimates for both personnel within the center and for any adjacent surrounding areas that may be close enough to have public radiation exposure. Fortunately the amount of radioactivity required for most small animal work is fairly small and represents minimal exposure risks. The physical requirements for imaging systems are often fairly simple to meet; the animal use requirements and biosafety considerations are usually more challenging.

Low-field MR systems have been developed that have well-shielded magnetic fields or fields small enough to not require any special space requirements. Nonetheless, there may be incompatibilities with locating MR systems adjacent to PET, SPECT, or CT systems since the magnetic field can cause artifacts through interacting with detector systems, such as photomultiplier tubes (PMTs). Similarly, MR systems require locations with a stable magnetic field background, to avoid transient changes that will alter MR signals. An example of a poor location for MR systems is near an elevator, which is a large metal mass that moves, thus altering the local magnetic field.

Once purchased and installed, imaging systems need to be evaluated and a determination made whether they are performing as specified. Acceptance testing is an important step that requires personnel to have some training and expertise concerning how the systems should function. This expertise may come from vendor training or experience gained from personnel who trained on similar systems at another site. Proper training is essential; otherwise, the investment of time, money, and resources might not be used properly or appropriately.

3.3 Animal Use Issues

Preclinical imaging work can utilize a variety of animal species, which have different housing and isolation requirements. While mice and rats are now the most frequently used species, there are still many projects that are best conducted with other animal species, including primates, pigs, and dogs. Often the optimal species is based on the availability of a suitable model of human disease, the need to see small structures (resolution and sensitivity limits of systems are what determine what can be measured), and perhaps the importance of behavioral or biochemical measurements.

Design specifications of an imaging center require knowledge of the species intended for use, since there may be restrictions on mixing species in the same physical spaces. There are specific requirements for vivarium and animal use area described by the Association for Assessment and Accreditation of Laboratory Animal Care (AAALAC). Accreditation by this group, although voluntary, is a requirement by various funding agencies. Each institution also has an Institutional Animal Care and Use Committee (IACUC) that oversees all animal work. The types of research will also place demands on design, such as the use of biohazardous materials and carcinogens, different species, and the need to provide support for surgical delivery of biological agents using viral vectors or other kinds of interventions.

Perhaps the best way to meet the animal use constraints is to have a dedicated vivarium associated with the imaging center, where the appropriate physical spaces are provided to enable the intended animal use requirements. The exact requirements depend on the requirements of the institution, planned research, and AAALAC guidelines. There are some procedures such as tumor measurements and drug dosing that may be required frequently and thus are best served within the vivarium rather than in the imaging spaces. The use of immune-compromised animals might require separate housing of animals within dedicated barrier conditions and the use of microisolator cages. Retrofitting or reconfiguring an existing space for proper animal housing may be very difficult, so it is important to determine the needs and requirements in order to create the appropriate vivarium space (Fig. 3.5).

Within the imaging center, the need for proper environmental support is crucial to create accurate and reproducible data (Fueger et al. 2006). This is particularly true for imaging research that involves measuring of in vivo metabolism, where the physiology of the animal can have profound effects upon the results. Equipment vendors vary widely with their environmental support efforts,

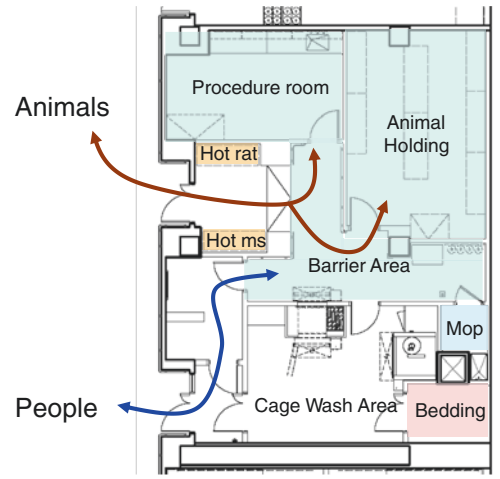

Fig. 3.5 A full vivarium was added to the center in 2009, complete with cash-washing facilities, barrier areas (*in blue*), and separate housing for radioactive animals (hot rat and mouse racks). A procedures room was added with an anesthesia system and ducted biosafety cabinet, suitable for work with biohazardous and carcinogenic materials. Animals enter through a pass-through biosafety cabinet, while people go through the gowning chamber

with some systems providing nothing and others providing heating, anesthesia, and perhaps some positioning mechanism. A great deal of attention is often placed on center layout and equipment specifications; however, the environmental support during imaging procedures is equally important and often far less expensive to properly implement. Good support includes well-designed anesthesia systems to both provide and exhaust anesthetic agents, heating options, barrier containment capabilities, easy to use and clean imaging support devices or chambers, and a good way to reproducibly and optimally position animals within the imaging systems. Various options for imaging chambers are now available to provide barrier containment, gas anesthesia, heating, and positioning (Suckow et al. 2008) (Fig. 3.6).

The housing conditions and husbandry protocols used can have a tremendous impact on images of metabolism. Animals spend the vast majority of time in the vivarium; thus, the conditions within the cages are what determine the metabolism under investigation. Research into housing conditions has demonstrated alterations in tumor size, glucose utilization, blood flow, and many other factors (David et al. 2013a, b; Gordon 2012). The physiology of the animals is altered by caging type (static or ventilated airflow), stocking density (number of animals per cage), nesting materials, diet, presence of shelters, room temperature and humidity, light cycle, and other factors. In particular, the cold stress associated with ventilated cages and singly housed animals can lead to failure of the animal model to adequately replicate human conditions, thus invalidating the research results and potentially resulting in misleading or inaccurate results. The choice of caging type and husbandry practices is often determined by the veterinary support group; thus, it is important to work together to consider how the imaging research will be impacted by the housing conditions.

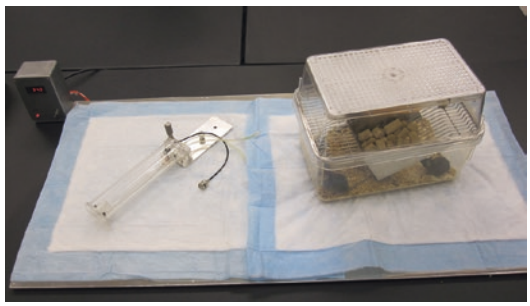

Fig. 3.6 Heating plate used to preheat animals before anesthesia induction. Similar plates are used under all locations where animals are held during and after the imaging process. Also on the plate is an imaging chamber that when connected provides heating, anesthesia delivery, pathogen control and reproducible positioning, and a non-ventilated (static) mouse cage

Any work involving hands-on animal handling ideally has a dedicate location with all the supplies and equipment close at hand. For surgical work, this might include a microscope, heating plate, fiber-optic lighting (incandescent lighting can overheat animals), an anesthetic induction box, and nose cone assembly, along with any other tools or supplies. Waste disposal should also be convenient, such as regular and biohazardous waste containers, sharps containers, or shielded areas for radioactive trash. Frequently used supplies such as absorbent pads, gloves, needles, and syringes need a place ideally suited for easy access, along with cabinets for supply storage.

For imaging, animals usually must be arranged into a reproducible position and provided anesthesia, heating, and some degree of pathogen control. This can be accomplished using imaging chambers together with biosafety cabinets and anesthesia systems to keep the animals within a pathogen-free environment for the entire imaging process (see Fig. 3.7). The chambers can also provide a known reproducible positioning for imaging using multiple imaging systems, enabling separate imaging systems to be used together, for example, acquiring PET/CT images using stand-alone PET and CT systems. The use of imaging chambers has grown with the recognition of physiological support requirements to obtain reproducible results and has become more integrated into the imaging system design (Fig. 3.8). The widespread use of 3D printing technology and computer-aided design (CAD) software has made it easier to design and create chambers, along with fixation devices, customized and disposable chambers.

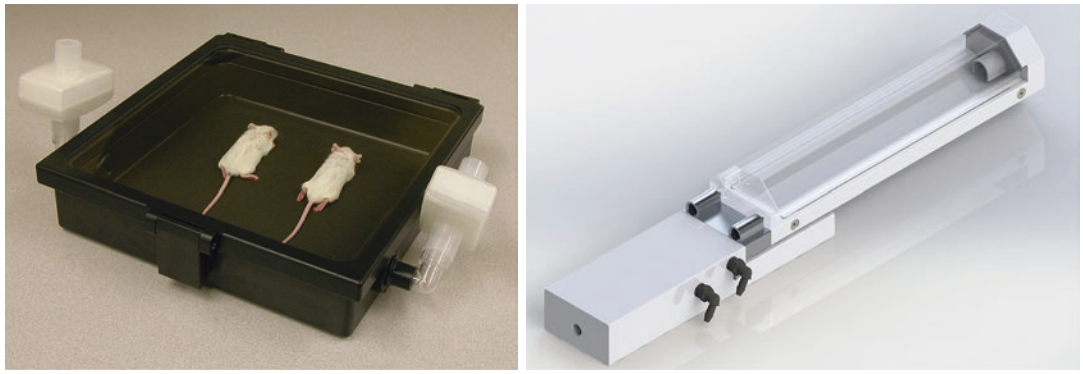

Fig. 3.7 Optical imaging chamber used for bioluminescence and fluorescence systems (*left*), mouse chamber design rending from SolidWorks suitable for 3D printing (*right*)

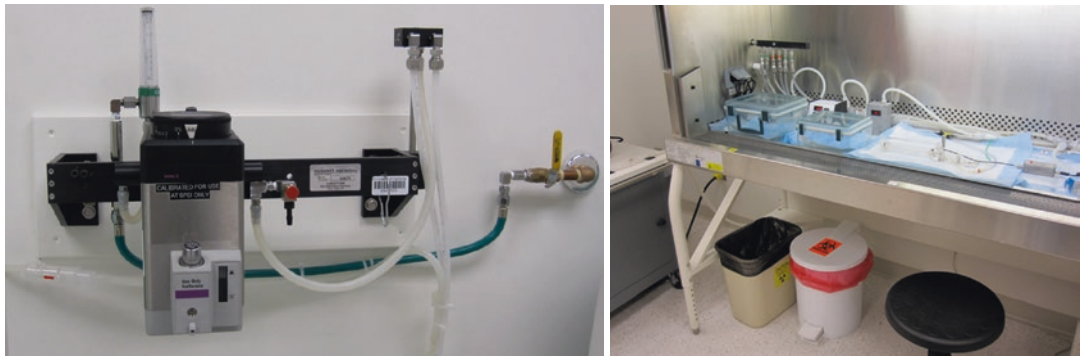

Fig. 3.8 Wall mounted gas anesthesia systems keep the counterspace clear, are easy to use and provide a constant depth of anesthesia (*left image*). This single cost effective system provides anesthetic gas to multiple induction boxes and nose cones in a biosafety cabinet (*right image*), along with microPET and CT systems. A constant pressure system avouds cumbersome flow meters, with the drawback of only providing one concentration of anesthetic at all points of use

3.4 Anesthesia

The use of anesthetic agents to immobilize animals is necessary for most experiments; otherwise, measurement of where and how much signal is present is not possible due to blurring or motion artifacts. The most commonly used anesthetics with preclinical imaging systems are gas inhalants such as isoflurane or sevoflurane, which provide a safe, effective, and constant depth of anesthesia. Injected agents can be used alone or are often in combination with cocktails most suitable for the species being used. There are also an increasing number of options for conscious imaging without anesthesia.

Inhalant anesthetics are the anesthetic of choice for most experiments and are preferred by most investigators and veterinary staff. Induction and recovery of anesthesia is fast, typically a few minutes at most. The depth of anesthesia remains constant, and it can be administered continuously for as long as necessary. Symptoms of overdosing are easy to observe and readily reversed by lowering the amount of anesthetic agent being supplied. Gas anesthetics are not controlled substances in many countries, making procurement and supply storage simple. The combination of ease of use, safety for the animals, and consistency makes gas the ideal anesthetic agent for most preclinical research.

If gas anesthetics are to be employed, then air or oxygen will be needed as a carrier gas. The choice of both carrier gas and anesthetic agent will affect the physiology and resulting image data (Flores et al. 2008). The placement of the supply tanks can be either near the vaporizer or in a specific location ideally suited to delivery and removal of the tanks. Locating the tanks near a door minimizes the need to move bulky and potentially dangerous heavy objects near expensive and sometimes delicate imaging systems. If multiple vaporizers are to be used, a wall-mounted gas manifold, switching valve, and low-pressure alarm are worth considering. For safety reasons, tanks and manifolds must be located away from any electrical panels. Oxygen lines require special installation and soldering to avoid explosions. To save valuable countertop space, vaporizers can be wall mounted, ideally near where animals are used so that access to adjust anesthetic levels is within easy reach.

With gas anesthetics, the waste anesthetic gas (WAG) stream must be addressed to avoid exposure to personnel in the center. A common method for WAG management is the use of F-air charcoal filters; however, these are not a good method for dealing with waste gasses. The WAG must be pulled or pushed through these canisters, which may cause problems. Charcoal quickly forms saturated channels, and it only takes a few minutes until the anesthetic gas starts to leak through the filter and back into the room. Charcoal also only absorbs the gas, later to release it. There is no binding or irreversible trapping of the agent. In a high-use facility, these canisters can add unwanted cost and complexity to the operations and would require frequent changes throughout the day. Destroying the anesthetic agent also presents problems by creating toxic liquids or gasses.

The best option for WAG removal is to either remove gasses using a vacuum system that has a bypass relief opening or dilute and remove the gasses using to room airflow, similar to how noxious gasses are dealt with using a fume hood. Animal use facilities typically require that all room air be completely exhausted to the outside, with no recirculation of any air. One can utilize this exhaust by ducting the anesthetic gasses into the return air duct, where WAG is highly diluted before being released. Either in-house vacuum or a dedicate vacuum pump can also be used to pull waste gasses away from investigators; however, these systems need to be carefully designed to avoid pulling room air into pathogen-free barrier locations or interfering with delivery of the anesthetic gas to the animals. It is important to consider how WAG can be managed and to have environmental health and safety approval of the design before implementation, since the allowable exposure conditions depend on local regulations.

Injected anesthetics have often been used in the past and are still widely used for larger species where safe induction of anesthesia is required before it is safe to use gas anesthesia, as in work with primates. Injected anesthetics are frequently used in a combination of both an immobilizing and dissociative agent, such as ketamine and midazolam. Pentobarbital was often used in the past and went more readily available; however, it typically lasts much longer than imaging experiments require and can easily lead to overdose and death if not correctly administered.

The primary advantage to injected anesthetics is that the equipment required is simple: a needle and syringe along with a bottle of anesthetic agent. The drawback is that these agents are not easily reversed in the event of an overdose nor is it easy to titrate the dose. Stress from poor handling can cause adrenaline to temporarily override the anesthetic effect, leading investigators to sometimes inject a second dose, which can often lead to death by overdose. Animals are constantly metabolizing or excreting the anesthetic agent; thus, unless constantly infused, there is a variable depth of anesthesia, which may have unwanted effects on the data. The recovery times for injected anesthetics are also much longer than inhalant anesthetics. Injectable agents are also drugs of abuse, requiring a prescription, drug logs, and double-lock and key storage, complicating the experimental procedure.

There are some imaging systems capable of imaging live awake animals, using video and post-processing software to remove movement

from the data. Conscious imaging has many advantages, primarily the ability to look at "normal" activity, either behavioral or biochemical. There is some question as to what constitutes normal, since a laboratory environment and handling techniques could induce stress and other unwanted changes in animal metabolism. Acclimatization and good training of personnel handling the animals can make a big difference in creating a stable reproducible environment for conscious experiment. Other reasons to use conscious imaging include the need to measure normal blood pressure, behavior, and heart rates or to avoid other confounding effects of anesthesia on animal physiology.

Regardless of what type of anesthetic agent is used, heating the animals is essential (Suckow et al. 2008). Especially with mice, where the mass is tiny, these animals will quickly become the temperature of the surrounding environment and likely die from hypothermia if not properly warmed. Even mild hypothermia can cause unwanted changes, such as the brown fat activation easily seen with FDG imaging using PET (Baba et al. 2007). Heating ideally starts immediately when the animals enter the imaging center, even before anesthesia induction. All places where animals are kept should be kept warm, including cage storage spaces, induction chambers, surgical areas, injection locations, imaging chambers, and recovery locations.

The choice of anesthetic agent and when to deliver it depends on the specific experiment. In some cases, it might be best to inject imaging agents while animals are conscious, and then wait for uptake and nonspecific clearance before inducing anesthesia and imaging. This conscious injection method allows the use of conscious physiology while preserving the use of anesthesia to keep animals immobile for imaging. There can be complications using this method, such as increased muscle uptake or activation of brain areas due to exposure to light and sound. Anesthetic agents have different effects on physiology, so the best agent to use may depend on what physiological information is under investigation. Other factors, such as circadian rhythm (Collaco et al. 2005), position of the signal within the animal (Virostko et al. 2004), and fasting state (Suckow et al. 2008), can alter the physiology and resulting imaging probe distribution.

3.5 Radiation Use

The use of ionizing radiation requires training, licensing, and application of the radiation safety principle of ALARA: as low as reasonably achievable. X-ray and CT systems produce ionizing radiation; however, the energies are low compared to PET, and the radiation is not present when the source is not turned on. Shielding is fairly simple with only a few millimeters of lead required; thus, these kinds of systems are typically self-shielded and pose little or no exposure risk to nearby personnel when used properly. It is worth pointing out that animals injected with SPECT or PET isotopes placed inside these systems may still create measurable exposure rates, since the energies of these isotopes are higher than the X-ray energies.

SPECT and PET imaging use radioactive isotopes that create ionizing radiation, with half-lives ranging from minutes to days. The principles of time, distance, and shielding apply to using these isotopes, so consideration of all the handling and storage aspects from delivery to final disposal is necessary. Isotopes may be delivered ready for use or may require radiochemistry to prepare the desired radiolabeled compound. If the center is to support radiochemistry, a fume hood and lead shielding may be required within a dedicate room for handling moderate amounts of activity. Metabolically interesting molecules often can contain iodine atoms, and iodine isotopes are readily available for either PET or SPECT imaging. To prevent exposure to personnel and unwanted uptake in the thyroid, usually a special insert chamber with a charcoal filter is required for any radioactive work using iodine. Thyroid scanning is often required when conducting radiochemistry where free iodine might be released.

Once prepared, or if delivered ready to use, radioactive compounds need to be safely stored in a shielded area and dispensed using a dose

calibrator. A lead shielding configuration is often used in combination with an L-shaped shield and lead glass window for dose dispensing. Injections into mice are limited to a small volume, usually less than 250 μl, so very small amounts of liquid are handled. A 1 cc or ½cc tuberculin syringe that has a fixed needle is ideal for this work, since there is very little wasted dead volume compared to a needle with a hub attached to a syringe using a Luer fitting. A dose carrier, either lead or tungsten, can be used to transport the dose to the injection area. Once injected, the syringe can be assayed for residual activity and disposed of in a shielded sharps container. The vial or syringe with the bulk dose can be held until no longer radioactive before defacing and disposal.

The injection site varies depending on the species, probe, and experimental design. Larger animals are often injected into paw or tail vessels; rabbits have easy access via the ear vein; rats and mice can be injected using intraperitoneal tail vein or using surgically implanted catheters. For mice, most often either intraperitoneal or tail vein injections are used. Using a large and heavy shielding cover on the syringe makes injections nearly impossible, so usually the syringe is used quickly with no shielding for injections. An experienced person can inject either ip or iv in only a matter of a few seconds; thus, radiation protection is accomplished using the shortest possible exposure time. Another alternative is to first place a catheter in the blood vessel, reducing the radioactivity handling time to a minimum of just making the tubing connection and injection.

Once injected, the animals are radioactive and need to be kept away from personnel if possible. During imaging, typically shielding is not an option, so the imaging systems ideally should be located away from where people are likely to sit or stand. After imaging, animals can be put back into cages, and the cages kept in a shielded location. Once the experiment is over, the animal, cage, bedding material, and any absorbent padding used for imaging along with any urine or feces should be surveyed for radioactive and disposed of accordingly. For short-lived isotopes, the trash can be held overnight or until surveyed and verified as no longer radioactive before disposal. If longer-lived isotopes are planned for use (>2 h half-life), consideration of where wastes and cages can be stored is necessary.

Storage of radioactive animals and carcasses needs to be considered, as vivarium personnel are often not trained as radioactivity workers nor is it wise to expose other animals or personnel in the vivarium to radioactivity. Fortunately the amount of radioactivity required for imaging and often the short half-life means that there may be very little activity in most animals when they are returned to the vivarium. For most PET experiments, activity levels are low enough that radioactive animals can be stored in a dedicated radioactive cage rack located within the main vivarium room or perhaps in a separate room. One option is to make the investigators responsible for cage care until the isotope has decayed to background. The specific protocol for handling activity and animals depends on the isotope and half-life involved.

The radiation dose to the animals may be of concern, especially with imaging of xenograft tumors. Frequent SPECT or PET imaging and high-resolution CT imaging can lead to substantial radiation exposure (Taschereau and Chatziioannou 2007; Taschereau et al. 2006), which may alter tumor kinetics (Pan et al. 2008). Care should be taken to ensure the radioactivity used is safe and both reasonable for the imaging system characteristics and for the animal. A low-resolution, low-dose CT may be all that is necessary for anatomical localization with PET or SPECT imaging.

3.6 Biosafety

Biosafety concerns play a paramount role in the design of an imaging center. Typically the requirements will dictate what can and cannot be done in a center and also may require certain physical engineering and procedural administrative controls that may constrain how and what experiments are conducted. There may be restrictions about mixing different biosafety

level animals within the vivarium or even within the imaging center, so it is vital that these issues be explored before a plan is created. Requirements vary widely and change with time, so consultation with biosafety personnel is essential.

Biologically interesting events that initiate immune response, cancer progression, or even administration of carcinogenic or biohazardous substances usually require a biocontainment environment. There are four biosafety levels (BSL) used to define the severity of potential problems, ranging from I (no hazard) to IV (severe hazard). In the past, most preclinical work was considered to be of little or no hazard; however, that is no longer true. The need for biosafety protection has grown due to the use of viral agents for genetic manipulations and the widespread use of immune-compromised animals that require protection from environmental pathogens. If one wants to study a communicable disease such as tuberculosis, then there are serious steps required to protect both personnel and the public from inadvertent exposure. The advent of immune-compromised animals capable of sustaining implanted human tumor xenografts has greatly aided our understanding of cancer; however, these tumors represent a risk of exposure to personnel since they may harbor hazardous agents such as viruses or bacteria. For this reason, xenograft work is now considered as BSL II, which requires protection of personnel using gloves and disposable gowns and proper biohazardous trash disposal of anything coming into contact with the animals.

There is an increasing need and interest to study disease processes and communicable airborne agents that require BSL III conditions; however, those represent a much more difficult challenge to study, since any equipment used for this type of work must be sterilized between use. Imaging systems are not designed for this environment or the sterilization process, and maintenance and repair activities by service technicians may be problematic. A better option may be to isolate the animals into sealed chambers and move them out of the BSL III zone for imaging.

3.7 Infrastructure Requirements

Imaging systems require a variety of support systems for efficient use. These range from personnel for operations, training and supply stocking, to counter space, anesthesia systems, and surgical areas to radiochemistry labs, computer networks, database software, archival systems, and websites for scheduling and retrieving data. Often multiple imaging systems are grouped together as a shared resource or core facility that is used by multiple investigators; thus, much of the infrastructure can be shared by the various systems. Lack of comprehensive planning during the design phase can result in budget problems, overtaxed IT support, and other problems with efficient and optimal use of the imaging center.

3.7.1 Personnel

Staffing support will most likely be the greatest budget cost after the center is equipped and operational. There are usually two types of personnel involved with imaging centers: dedicated staff and peripheral support personnel. Dedicated staff are those who work in the center full time as the primary support people for experiments. They typically operate equipment, conduct routine quality control measurements, order and stock supplies, and ensure that everything is ready for any experiments. Peripheral staff are those who may assist part time or who are part of a different group, such as the information technology (IT) computer support, veterinary staff, administrative support, purchasing, and building facilities maintenance people. These people perform vital functions, yet their role may not be very obvious or may not be frequently required. Sometimes these peripheral people may be supported by departmental, institutional, or overhead budgets; other times it may be necessary to include them as part of the budget plan.

The number and type of people working within or as part of the center varies widely with different equipment and between established imaging centers. Some systems lend themselves to easy use by investigators with little or no

oversight, such as optical, microtomes, and autoradiography systems. Other systems such as PET, MR, and ultrasound may operate best with experienced personnel who can ensure the proper use and have the experience and skills necessary to create reproducible and optimal imaging results. Usually there are regulations requiring that only trained personnel can operate devices that use or produce radiation, which is where dedicated staff are useful, especially in a center used by multiple people and projects.

Data analysis may be part of the center support through dedicated personnel, or this function may rest in the hands of the investigators. If not part of the center support, then training about how to work with and quantify image data is needed. A range of support can be found in existing centers. One option is a hands-off low-cost approach, where systems are available for use with very minimal staff support, mainly just keeping everything working and supplies stocked. The other end of the spectrum is a full service center, which may help with the design of the experiment and conducts all the work, analyzes the data, and produces a final set of measurements. Obviously the full service route requires more people and cost, with the benefit of more consistent results. Most common is some sort of middle ground level of support, where dedicated personnel are present to help with experiments, but the investigators are still very involved with acquiring and processing of data. Any of these support levels can work well, though good training and educated users are essential when there is less staffing support.

3.7.2 Computer Infrastructure

The computer infrastructure consisting of wiring, switches, network drives, and perhaps a computer cluster for image processing is literally the backbone upon which the center relies upon for data movement, archiving, and retrieval of information. Creating images and any associated data requires entering information into a software program and database, computational processing either on the host computer associated with the imaging system or on a remote computer, followed by file transfers. Moving files off the host acquisition computer is important since the hard drive on that computer represents a single point of failure should the drive stop working. Shared network drives can be RAID arrays to preserve data integrity should any one drive fail. Automating the file transfer and processing is also well worth the minimal cost to reduce staffing requirements and the potential for human error (Taschereau et al. 2008).

Archiving data first requires making sure all the necessary information has been entered and the appropriate files, images, or records are suitably created and configured, followed by moving the data to a storage location and clearing space on the imaging system computer. There are several data retrieval methods, including using portable hard drives, burning DVDs, USB data sticks, or file transfers through a website interaction. These interactions can be manual (person to person) or automated through the use of an online database (Fig. 3.9).

Data and computer security are serious concerns. It may be advisable to operate using private subnets for the imaging center, to be less exposed to outside hacking attacks and less subject to data traffic flow restrictions from other activities. Virus software and other IT support activities, such as software updates, usually must be restricted to prevent interference with data collection activities. IT services can be scheduled and run at predetermined times when they will not interfere with experiments. Regular disk defragmentation is important and is best done after data has been cleared to archiving and as time permits.

Some imaging devices can both acquire and process data at the same time. This may cause disk access problems if too many processes are attempted at the same time. For this reason, and for system security, it is best not to use the host computer attached to the imaging system for any web browsing or data-intensive activities. A separate computer for database and other uses can be used to minimize any disruptions to the imaging process. Extensive processing required for some imaging modalities may make use of dedicated hardware, computer clusters, or other computers nearby through distributed processing software.

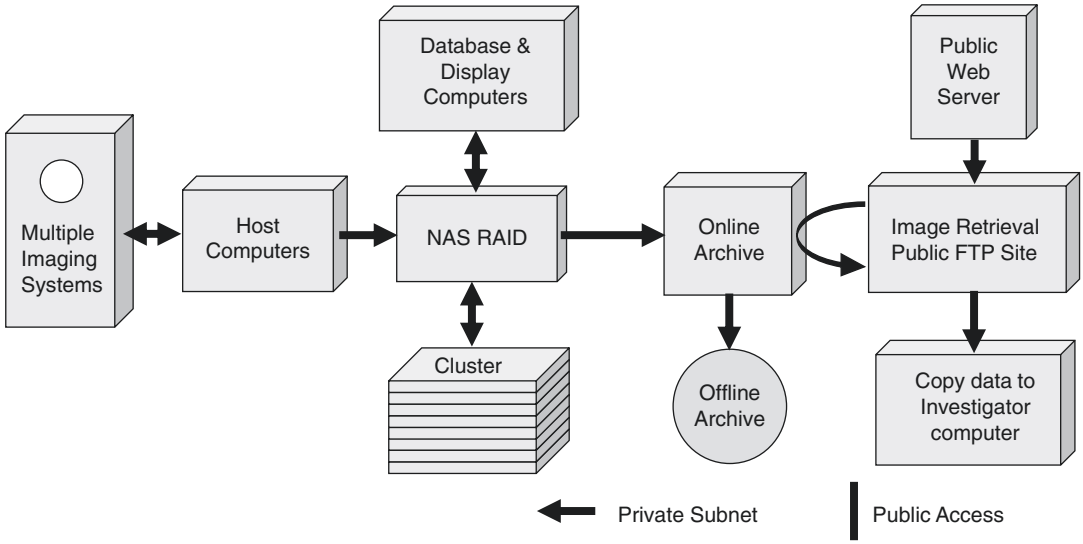

Fig. 3.9 Computer infrastructure layout for a multisystem center using a central network attached storage (NAS) with a redundant drive array (RAID), computer cluster, online archival storage location, and a public access website. The website can only copy data from the secured online archive into a network available folder. Center systems are kept on a private subnet to manage network traffic and for added security

In some cases, the resulting improvement in image resolution is well worth the additional computation cost in order to see small structures or changes (Qi et al. 1998).

3.7.3 Scheduling, Database, and Usage Tracking

The best method for scheduling usage depends on the systems involved and the volume of studies planned for center operations. Some systems such as optical, microtome, surgical areas, and procedures rooms are well suited to using an online calendar for reserving time. Other systems that require staffing or more complex support, such as radiochemistry and cyclotron time, may be best suited to email-based requests followed by scheduling meetings of the personnel involved. Whichever scheduling method is used, the amount of time and resources required needs to be coordinated with supplies, support, and other related activities. The scheduling process is also a good time to ensure there are proper protocols and approvals in place and that any information needed for usage and billing reports is collected.

The online calendar approach enables people to easily see when systems are available for use. For experiments where staffing, isotope, and radiochemistry support or coordination with other imaging systems (PET-CT) are necessary, a schedule where various demands upon the resources are sorted out needs to be created and sent to the people involved. Often this is done on a weekly basis for most imaging centers, so that demands of both clinical and preclinical centers are met, and investigators are given sufficient notice about when they can conduct their experiments. A shared resource where multiple users and perhaps outside contract work are conducted needs to have a way to prioritize projects, based in part on how flexible the various experiments are to moving imaging times or dates (Fig. 3.10).

A well-designed database can make it much easier for investigators to track usage and for the center staff to manage the facility (Truong et al. 2008). Perhaps the most advantageous use of a centralized database is to create unique session identification (ID) numbers to both identify a particular experiment and to track the usage for billing and usage reports. The archival process can be linked to the database by placing all the

Fig. 3.10 Scheduling website (*top left*) and individual equipment access location (*top right*) are useful for scheduling and data retrieval. Search and other functions may also be useful to include (*bottom image*)

information related to a single experiment into a folder named using the session ID number. Any information associated with the experiment can either be entered into the database or added to the folder for archival. Since most grant funding agencies require both archiving of data and public access to at least some of the data, it is often required to have an archival and data tracking system in place. An added benefit is that an online depository of information is much easier to search to find information, compared to having information either only in someone's memory or in a hard-to-find laboratory notebook. As staff, students, and postdocs rotate through labs, sometimes it can be hard for the faculty or lab manager to find older experimental information and to know if something has been tried or worked in the past (Fig. 3.11).

In addition to usage and archival support, a database can be used to track information not otherwise collected by vendor software. While some systems have simple requirements and perhaps software that collects any necessary data, many systems have associated information not directly part of the imaging process. The database might be used to collect information such as metabolite or blood measurements, anesthesia details, physiological monitoring data, or investigation-specific information related to approval licenses, billing information, and usage statistics.

The manager or director of the imaging center will almost certainly be required to know who is using the center and to what extent each investigator is using the facility. There may be regulatory oversight committees that require information reports on biosafety, radiation usage, and animal use. Most likely this person will also write grants, will need to create usage and progress reports, and will be responsible for billing; thus, an easy-to-use comprehensive database is invaluable for center operations.

Along with the computer systems, software will need to be available to investigators to view and analyze the image data. Depending on the vendor, software may be provided that can be freely distributed, or there may be substantial licensing costs. A number of image analysis software programs are also freely available online (OsiriX, AMIDE, ImageJ) that can often read a range of data. Since there is not yet a standardized format for the wide range of preclinical data

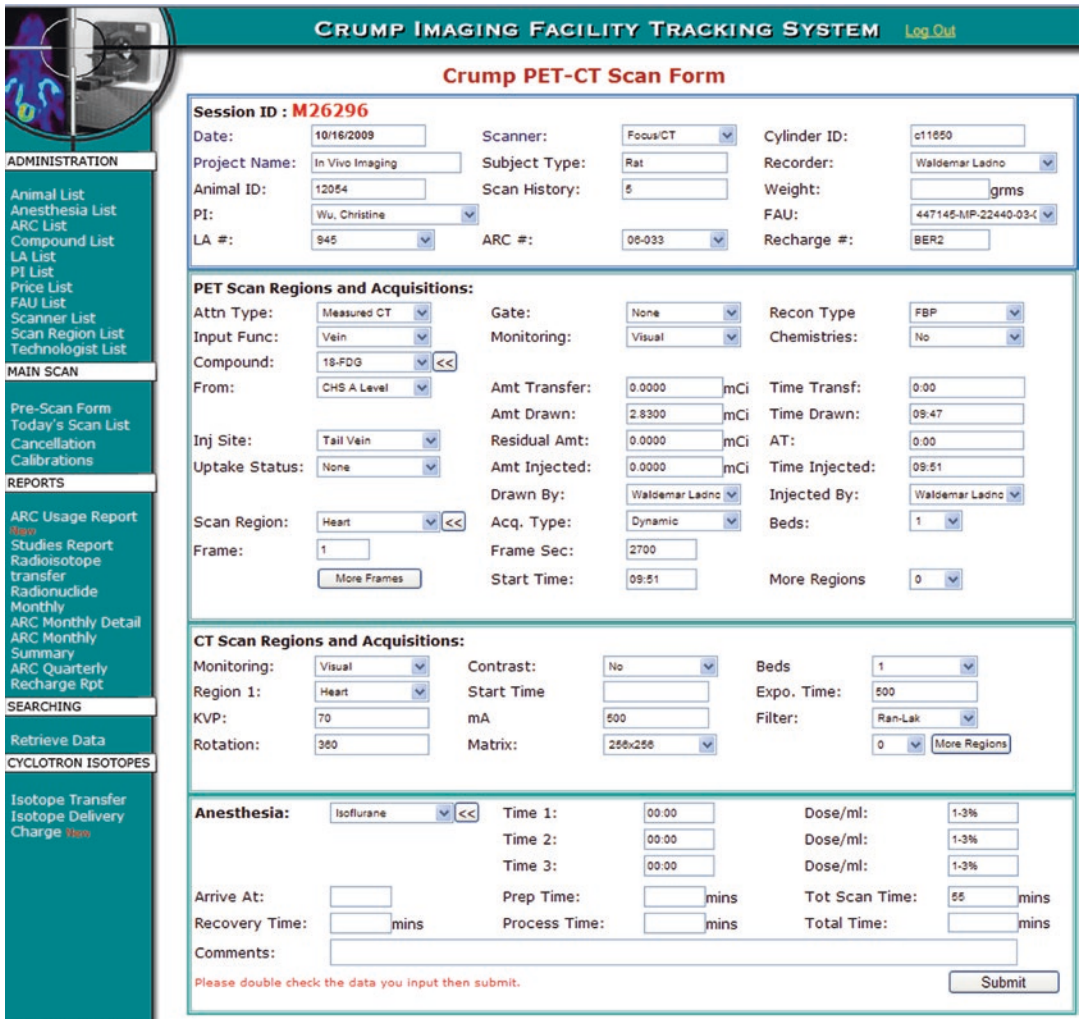

Fig. 3.11 Database software used to generate session identification numbers; track animals, authorizations, and experimental information; and generate billing and usage reports

types, multiple programs may be necessary depending on the imaging system mix within the center. Data analysis may require extensive user training (see below); however, there are tools online that are specifically designed to help with image analysis (Huang et al. 2005).

3.8 Ergonomic Flow

A useful approach to center design is to consider the various types of activities and consider their movement or flow throughout the center: primarily people, animals, radiation, supplies, and data. It is fairly obvious that people move throughout the imaging center, and one would like to minimize the need to move back and forth needlessly. This can be compared to good kitchen design, where a work triangle consisting of a sink, stove, and refrigerator are optimally placed for best use. In an imaging center, you want to have the animal holding, preparation, and imaging areas well laid out. Moving animals frequently can induce stress, so it is worthwhile to consider how animals can be brought into the facility and placed in a holding area to minimize

the need for further movement. Since animals are commonly transported on carts, a location for the cart is needed and a path suitable for easy transport (Fig. 3.12).

Radiation use for PET and SPECT requires a holding area and dose-drawing location and involves the use of lead shielding and somewhat heavy lead dose-carrying holders (pigs). When there are many animals being imaged using short static imaging scans, it may be advantageous to draw multiple doses of radiation at the same time and put them into holders on a cart for transport to the injection location. A path will be needed that is cart friendly, much like that needed for animal entry and exiting from the center.

Supplies require both a suitable path for delivery and storage locations. Some items, such as gas tanks, should be located near doors to avoid having to move heavy bulky items near expensive imaging equipment that might be damaged by inadvertent contact. Other supply items will need to be stored nearby in cabinets or shelving for easy access. Items used frequently need to be easily at hand and trash bins located where needed. The ability to store things openly may be restricted by fire codes and biosafety protocols.

Trash may need to be segregated based on biosafety and radiation safety concerns. Suitable containers need to be located close to where the trash is generated. The right side of Fig. 3.7 shows a biosafety cabinet where animals are anesthetized, injected, placed in imaging chambers, and moved into and out of cages. There are both regular and biohazardous trash cans located under the cabinet in easy reach for the investigator. There is also a shielded location nearby for sharps (not shown). Short-lived isotopes can be put into regular or biohazardous trash and held overnight before disposal. Longer-lived isotopes need to be kept in separately labeled bags and held for suitable decay time. It may be necessary to have the imaging center's janitorial staff educated on what they can and cannot remove or perhaps not allow trash removal at all except by knowledgeable staff after radiation surveys are conducted.

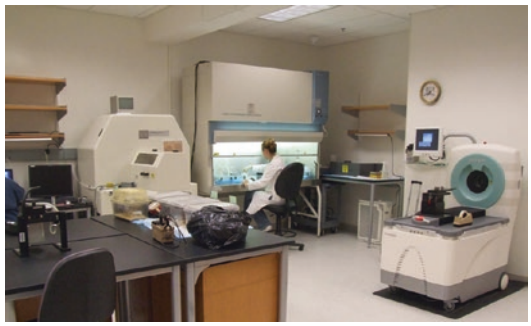

Fig. 3.12 The biosafety cabinet, PET scanner (*right*), and CT system (*left*) are located within easy reach for the investigator. Animals waiting to be injected and imaged are located on a central island on a heating plate. Computers for the imaging systems are located to the left of the CT, where exposure to radiation is lowest

The data flow is quite important and the least visible type of movement critical to imaging center function. A well-defined plan is needed to move data from the imaging systems to any processing locations and to the archival system. Ideally the imaging systems begin each day with empty hard drives. This ensures that space will be available for new data and makes it less like data will be lost due to communication failures when drives nearly full are fragmenting the incoming data. Having empty drives also enables continued data collection if there are network problems requiring hardware replacement.

One additional consideration is the inclusion of a non-animal, non-radiation office area with a window for visibility into the center. This location is where staff are allowed with food and drink, where image verification for archival or analysis can be conducted, and visitors can see operations without interfering with the process or being exposed to radiation. Often times the imaging systems can be fairly loud due to cooling fans, so this room provides a respite from the noise and demands of the imaging work. It is good for moral of both staff and investigators who may spend long hours conducting experiments with little opportunity for break time. This space allows a safe way to let people rest and eat while still remaining close to their animals.

3.9 Training and Education

Imaging systems are becoming an essential tool for biologists and other scientists to evaluate molecular processes in vivo. As these devices

leave the labs where they were developed, these systems are now more automated and less overseen by physicists and programmers; thus, it becomes a challenge to train personnel, service, and operate the systems using staff not familiar with the inner workings of the software and hardware. There are also a wide range of factors where physics meets biology that must be understood, measured, or controlled in order for the research to create useful information. These factors include controlling temperature, anesthesia, positioning, contrast agents, injection methods, data collection, and animal handling conditions. Given that the imaging systems are increasingly tools used by biologists and veterinarians, it is important to recognize that there is a substantial turnover in the people who use these systems, typically staff, students, or postdocs. Education is thus an ongoing requirement, not just a onetime event.

Another area where ongoing education is necessary is in the area of new and improved imaging systems, data analysis techniques, and experimental methods. New imaging systems are still being created and older ones improved through advancements in technology. Careful consideration of these new systems and potential replacement systems is needed given the disruption and cost of adding or changing systems in an operational imaging center. Data analysis tools and optimal methods for conducting research are still very active areas of research; thus, to stay current in the field, someone needs to evaluate and teach these methods to ensure a uniform application within the center.

In theory, all investigators can be taught how to operate imaging systems, and there would be no need for oversight and management of the systems. There is no inherent reason why this cannot be done; however, in practice this method often proves unfeasible for a number of reasons. First is that without common oversight, regulatory compliance becomes exceedingly difficult to monitor, and accidents with radiation or biohazardous materials can more readily occur. It also becomes harder to ensure that established standard operating procedures for data collection and processing are followed. The cost of the equipment and supporting environment usually means that an imaging center is established and used by numerous investigators, which can lead to conflicts and a messy environment when people do not properly clean up after themselves. Inclusion of a manager and/or staff to the center creates the ability to more effectively operate the systems and verify compliance. This leads to two types of education required for operations: training for the staff and education for the users.

3.9.1 Staff Training

In-depth training is necessary for staff operating imaging systems compared to users that may not need to know the inner workings of the devices. Staff need to perform routine calibrations and quality control measurements and may be required to repair or troubleshoot systems when problems crop up. If staff members frequently operate the imaging systems, then they are ideally suited to spotting any problems and ensuring any database and usage information are properly collected. Staff should be knowledgeable about any common or potential errors in image generation and possible solutions. Ideally, the staff members have the knowledge to carry out all aspects of the imaging experiment and thus are available to users who need training or help with their experiments. They may even actively participate in experiments by helping with injections, animal care, and even data analysis.

Ironically, as imaging systems become more automated and less prone to problems, it becomes more difficult to develop the skills and knowledge needed to diagnose and repair these systems. While reliability and ease of use are certainly good things, they mean that there is less opportunity to learn about repair and problems that might be found in images. A good training program with examples of problems therefore becomes essential. Some problems can be intentionally created for teaching purposes, such as no normalization in a PET scan, center of rotation artifacts in SPECT or CT scans, and metal objects in MR and CT images. Other examples of problems may be available from vendors or other sites that have similar equipment. If available,

physicists with expertise in the field are often the best resource for training and troubleshooting help.

Often systems are kept under service contracts for repair; however, the time spent waiting for service may cause the experiment already in process to be lost, as biology and radioactive decay cannot be put on hold. There may have been months of preparation and considerable time and effort put into animals, along with a time course of data collection needed at specific time points. If the problem is simple or readily solved over the phone, staff members may be able to prevent the loss of valuable data, time, and resources.

3.9.2 User Education

In general it is always useful to have very knowledgeable users of imaging equipment who can perform all the necessary steps to acquire and process data. There is however a distinction to be made between what is necessary to know to do the experiment properly and what is beyond necessary and perhaps not relevant to the task at hand. The process of learning the skills required to create the animal models and experimental details being investigated is not trivial; thus, the users are already burdened with a great deal of learning and concern for the experiment at hand and may not be interested in knowing more than what is necessary to acquire image data. A brief overview of the imaging modality and the underlying principles of how signals are generated and measured can be quite useful, whereas a comprehensive explanation of the hardware or software is usually not of much value to the end user.

There are a number of essential things that users must learn and adhere to with any imaging work, primarily related to animal handling and injections of imaging agents. It is imperative that animals be anesthetized, heated, injected, positioned, and handled correctly in order to collect useful data. The precise details are usually specific to the experiment; however, there are certain aspects that are typically the same for all experiments and are suited for creation of a standard operating procedure (SOP) manual. Often the anesthesia, positioning, and heating methods are uniformly applied, as well as injection methodology. Timing, amount, and route of injection may vary, but are typically not widely variable.

Of particular note is the proper training of users to handle animals in a practiced manner. This helps lower the stress to the animals and can be critically important if injected anesthetics are used. Animals highly stressed by poor handling can die or override anesthesia with high adrenaline levels, only to die when injected with additional anesthetics. For this and other reasons related to ease of use, gas anesthesia is highly recommended where experimentally appropriate.

Users of the imaging center often are the people who analyze the data, so there must also be training in the proper techniques to create meaningful information. Image analysis can be simple or complex, depending on the system and level of quantitation desired. Most important is to train people to make appropriate measurements and to do so consistently.

3.10 Security

Preclinical imaging is a euphemism for animal imaging, a name used both to make the title less controversial and to emphasize that the research is aimed at producing scientific discoveries with clinical relevance. Unfortunately some people ignorant of the value of research conducted using animals have become violent and dangerous. This means a restricted access environment is required for the safety and security of both animals and people working with animals. Simply locking the doors is insufficient, as people can come in behind careless people; doors may be left propped open; or the key, password, or access code might fall into the wrong hands. Ideally the animal use areas are restricted to only those people who need to be there, with the use of photo identification badges that are also used as access cards to open doors. This is more secure than the use of passwords or keys and makes it easier to turn

off individual access once a person no longer needs to be in the area. A video surveillance system is essential, in part to ensure people using the center are doing so properly and to ensure safety and accountability in the event of an accident or dispute. There may be times when the biology under investigation requires imaging at certain times not conforming to staffed hours of operation, so a video system enables usage of the facility with at least the option to review what was done if necessary. Access control can be particularly important for biosafety reasons and for high-use centers that may have hundreds of authorized users.

3.11 Budgeting

No description of an imaging center would be complete without a budget plan. The primary costs involved are personnel, service contracts, supplies, and depreciation. Staffing support depends both on the number of people and the level of expertise required. The skills needed for imaging research may come from hiring experienced staff or more likely will be created through trial and error coming from learning on the job. The greatest benefit may come from having good veterinary support, since the health and well being of the animals play a crucial role in all imaging experiments. Service contracts often come with choices for the cost and level or timing of support. Centers with in-house expertise may be happy with minimal support, whereas others may want a fast response or more hands-on help. Supply costs are fairly predictable with time and experience.

The costs of imaging systems are substantial, and replacement expenses are a large budget item best suited to parsing out over time using a depreciation schedule. This is not always possible with certain funding sources, so care is needed in applying any charges toward depreciation. For many institutions, a shared resource instrumentation grant is the best or only option to replacing or acquiring new instruments. This is not ideal, since if the grant is not funded, then the equipment cannot be purchased. A depreciation plan enables equipment purchases to be less dependent on grants and more suitable to expected replacement timing; however, the costs involved may be more than users can afford.

If all the costs associated with the imaging center are factored into any pricing for research, the amount may well be outside of what investigators can afford, especially for modalities requiring extensive support such as PET imaging. Some centers operate on governmental or institutional support and do not charge their users; however, this is rare, and normally some sort of recharge pricing is used to recover some of the costs. The budget may be in part supplied from imaging center grants, core facility budgets on research grants, use of clinical income, or perhaps from contract work with outside companies. With institutional support and due to restrictions on some grants, a subsidized group rate is often needed in addition to nonsubsidized and outside user rates. Many institutions require a detailed budget and sales and service contract in order to charge for services. The creation and maintenance of the documentation and budget items can be taxing and require the help of administrative personnel.

Invariably, someone will be responsible for oversight of the imaging center. This will require a substantial commitment of time and effort toward budget, training, and reporting issues. Grant writing to describe the center and progress reports on usage are ongoing common requirements. Depending on how the data analysis will be handled, there may be a significant need to train and educate people who are new to using the center, either through teaching courses, seminars, or interactive workshops. These important activities are sometimes delegated to junior faculty, who are already challenged with getting their own research plans going and trying to establish tenure. The person in charge of the center will need to have a good understanding of the imaging systems, how to design experiments, budgeting and business skills, and be good at educating new users. Center operations are very similar to running a small business, complete with human resource, marketing, budgeting, production, and sales tracking issues.

3.12 Emergency Planning

The American Disabilities Act (ADA) requires that spaces be wheelchair accessible in the United States, which means wide doors and specific heights and fixtures that must be used. There are also fire safety codes that require rooms over a certain size to have more than one means of egress. These two items can dominate the floor plan determination of an imaging center. The addition of fire sprinklers, eye washes, emergency showers, fire extinguishers, and alarm boxes all have to be made part of any plan. Wide and recessed doorways' secondary doors can take up considerable space where equipment cannot be located. Access may become a critical issue, especially if there are gowning chambers required to enter a space.

Fire and EHS regulations require a hazardous material diamond sign, signifying health, fire, and reactivity labeling covering any materials located within each room. A list of any agents is usually required to be maintained, and limits are often placed on what can be used, depending on the room designation (office, lab, vivarium, etc.). Laboratory space is built to certain standards for fire and safety, which is the type of room most suitable for an animal use imaging center.

Due to both animal use requiring routine disinfection and the use of radiation, all materials used in flooring, wall coverings, and furniture need to be nonabsorbent materials. Cloth or fabric materials are not suitable, especially for chairs, as these can absorb and retain spills or aerosolized agents. Tile floors are also not advised, as the cracks begin to separate and accumulate material as they age. An epoxy or sealed vinyl floor is the best option. Routine cleaning is needed for all surfaces, especially within the biosafety cabinet. Janitorial support may need to be trained in proper cleaning methods, and specific timing may be necessary to avoid disrupting experiments.

In the event of a fire alarm or other declared emergency, a plan must be in place for what to do about animals under anesthesia. Usually personnel are required to evacuate immediately and are not allowed back into the building for minutes to hours. Unfortunately false alarms are all to frequent; however, they must be taken seriously, and leaving people behind is not usually an option. Personnel may want to consider having a plan to take animals out of chambers and anesthesia boxes, quickly putting them into cages. Leaving animals behind under anesthesia may result in their loss if prolonged time is required to clear the problem. The use of oxygen as an anesthetic carrier gas may also be a problem if there is in fact a fire. Disaster planning is also part of the IACUC requirements for all animal housing and use facilities.

3.13 Summary

Defining the types of research to be conducted within a small animal imaging center enables the selection of appropriate equipment and support requirements. Use of animals requires comprehensive planning to house, handle, and image animals in a safe and optimal environment. This includes the appropriate level of biosafety equipment and containment areas, good design for handling and storage of radiation, magnetic field safety, good lighting, power, space, and support equipment for the imaging systems, as well as anesthesia and heating methods. The building, staff, and computer infrastructure can be sized and configured to match the imaging systems, necessary space requirements, and level of support to be provided, given the resources and budget available to the center. A knowledgeable person to oversee operations and to help with training, grants, and budget issues is an important necessity. Data, personnel, and animal security require systems be in place to ensure safety if or when problems might arise.

Careful planning for the center layout, including space set aside for future expansion and planning ahead on how information will be handled and disseminated, will help make the center function well into the future. Automation of routine processes, the use of online databases, and scheduling software will reduce staffing requirements and save costs while at the same time making operations easier and more efficient. A wide

range of expertise is needed to design and build a small animal imaging center; thus, a team of people with various skills is needed to create the center and make sure the functions required are put into place and supported.

References

Baba S, Engles JM, Huso DL, Ishimori T, Wahl RL. Comparison of uptake of multiple clinical radiotracers into brown adipose tissue under cold-stimulated and nonstimulated conditions. J Nucl Med. 2007;48: 1715–23.

Collaco AM, Sima R, Dougherty EJ, Williams BB, Geusz ME. Circadian regulation of a viral gene promoter in live transgenic mice expressing firefly luciferase. Mol Imaging Biol. 2005;7:342–50.

David J, Knowles S, Lamkin D, Stout D. Individually ventilated cages impose cold stress on laboratory mice: a source of systemic experimental variability. JAALAS. 2013a;52:738.

David J, Chatziioannou A, Taschereau R, Wang H, Stout D. The Hidden Cost of Housing Practices: quantifying the metabolic demands of chronic cold-stress of laboratory mice with non-invasive imaging. Comp Med. 2013b;63(5):386–91.

Flores JE, McFarland LM, Vanderbilt A, Ogasawara AK, Williams SP. The effects of anesthetic agent and carrier gas on blood glucose and tissue uptake in mice undergoing dynamic FDG-PET imaging: sevoflurane and isoflurane compared in air and in oxygen. Mol Imaging Biol. 2008;10:192–200.

Fueger BJ, Czernin J, Hildebrandt I, Tran C, Halpern BS, Stout D, Phelps ME, Weber WA. Impact of animal handling on the results of FDG-PET studies in mice. J Nucl Med. 2006;47(6):999–1006.

Gordon CJ. Thermal physiology of laboratory mice: defining thermoneutrality. J Therm Biol. 2012;37:654–85.

Huang SC, Truong D, Wu HM, Chatziioannou AF, Shao W, Wu AM, Phelps ME. An internet-based Kinetic Imaging System (KIS) for microPET. Mol Imaging Biol. 2005;7:330–41.

Klaunberg BA, Davis JA. Considerations for laboratory animal imaging center design and setup. ILAR J. 2008;49(1):4–16.

Pan MH, Huang SC, Liao YP, Schaue D, Wang CC, Stout DB, Barrio JR, McBride WH. FLT-PET imaging of radiation responses in murine tumors. Mol Imaging Biol. 2008;10:325–34.

Qi J, Leahy RM, Cherry SR, Chatziioannou A, Farquhar TH. High-resolution 3D Bayesian image reconstruction using the microPET small-animal scanner. Phys Med Biol. 1998;43:1001–13.

Stout D, Zaidi, H. PET Preclinical Multimodality imaging in vivo. PET Clinics, Elsevier Inc.; 2009.

Stout DB, Chatziioannou A, Lawson T, Silverman R, Phelps ME. Small animal imaging center design: the crump institute at UCLA. Mol Imaging Biol. 2005;1:1–10.

Suckow CE, Kuntner C, Chow PL, Silverman RW, Chatziioannou AF, Stout DB. Multimodality rodent imaging chambers for use under barrier conditions with gas anesthesia. Mol Imaging Biol. 2008;10:1007.

Taschereau R, Chatziioannou AF. Monte Carlo simulations of absorbed dose in a mouse phantom from 18-fluorine compounds. Med Phys. 2007;34(3): 1026–36.

Taschereau R, Chow PL, Chatziioannou AF. Monte Carlo simulations of dose from microCT imaging procedures in a realistic mouse phantom. Med Phys. 2006;33(1):216–24.

Taschereau R, Stout DB, Chatziioannou AF. Preclinical imaging facility data flow integration and automation. New Orleans: Society Nuclear Medicine; 2008.

Truong DC, Chatziioannou AF, Stout DB, Czernin J, Phelps ME, Huang SC. A data portal for molecular imaging. New Orleans: Society Nuclear Medicine; 2008.

Virostko J, Chen Z, Fowler M, Poffenberger G, Powers AC, Jansen ED. Factors influencing quantification of in vivo bioluminescence imaging: application to assessment of pancreatic islet transplants. Mol Imaging. 2004;3(4):333–42.

Noninvasive Small Rodent Imaging: Significance for the 3R Principles

4

Nicolau Beckmann and Birgit Ledermann

Contents

N. Beckmann (✉)
Musculoskeletal Diseases Department,
Novartis Institutes for BioMedical Research,
CH-4056 Basel, Switzerland
e-mail: nicolau.beckmann@novartis.com

B. Ledermann
Global Scientific Operations, Novartis Institutes for BioMedical Research, CH-4056 Basel, Switzerland

4.1 Introduction

Mice and rats are the species most often used in biomedical and pharmaceutical research. Accordingly, the development and use of methods that improve the welfare, i.e., reduce eventual stress, discomfort, and/or pain in small rodents during experimentation and reduce the number of animals is a challenge for achieving scientific, ethical, and economic benefits. At the same time, the quality of the derived data should not be compromised. In the book *The Principles of Humane Experimental Technique* (Russell and Burch 1959), William Russell and Rex Burch introduced in 1959 the 3R concept (replacement, reduction, refinement) in relation to the humane treatment of experimental animals. The authors set the frame in the search for alternatives and changes of experimental procedures that could result in (i) the *replacement* of animals, (ii) a *reduction* in the numbers used, (iii) or a *refinement* of techniques that alleviate potential pain and distress of the animals during the experimental period.

F. Kiessling et al. (eds.), *Small Animal Imaging*, DOI 10.1007/978-3-319-42202-2_4

Replacement often means the use of an inanimate system as an alternative (e.g., a computer model or program, a phantom model). It can also mean the replacement of sentient animals (usually vertebrates) by less sentient animals (usually invertebrates such as flies, worms, and bacteria). It includes as well the use of cell and tissue cultures, whenever possible of human origin (Guillouzo and Guguen-Guillouzo 2008; Spielmann et al. 2008). Recently, microphysiological systems including different cell types in a specific three-dimensional (3D) configuration have been generated to simulate organs with a concrete function. A primary aim of these efforts is the combination of different "organoids" to generate a human on a chip, in order to allow studies of complex physiological organ interactions (Pamies et al. 2014). The advent of human-induced pluripotent stem cells enables the derivation of patient-specific cell lines and thereby provides a range of possibilities for cellular studies aiming at modeling human diseases (Walmsley et al. 2014).

Reduction means an appropriate experimental design and an improved data analysis leading to less animals being used in the experiments without loss of useful information. This may be achieved by reducing the number of variables through good experimental design, by using genetically homogeneous animals (inbred strains), or by ensuring that the conditions of the experiment are rigorously controlled. Furthermore the use of in vitro data might give hints for improving the design of the experiments.

Refinement means a change in some aspects of the experiment leading to a minimization of potential discomfort, distress, and/or pain experienced by the animals. This includes also accommodation and appropriate housing for the respective species as well as training of the animals for the respective procedures and applications. Sufficient accommodation and training have a great impact on the animal stress level. Refinement should result in an overall increase of animal welfare during experimentation and is part of good science. Often, refinement leads to a partial reduction or replacement of animals. Examples include the establishment of humane endpoints for intervention in a study using earlier endpoints derived from noninvasive methods or the use of effective preemptive, peri-, or postoperative analgesic protocols.

Today, the 3R concept has become the generally accepted scientific basis of institutions serving the development of alternatives to animal experiments. Governmental institutions like the European Center for the Validation of Alternative Methods (ECVAM; http://ihcp.jrc.ec.europa.eu/our_labs/eurl-ecvam, Ispra, Italy); the Interagency Center for the Evaluation of Alternative Toxicological Methods (NICEATM/ICCVAM, http://iccvam.niehs.nih.gov/, Research Triangle Park, North Carolina, USA); the UK National Center for the Replacement, Refinement, and Reduction of Animals in Research (NC3Rs, http://www.nc3rs.org.uk, London, UK); or the Zentralstelle zur Erfassung und Bewertung von Ersatz- und Ergänzungsmethoden zum Tierversuch (ZEBET, http://www.bfr.bund.de/cd/1433, Berlin, Germany), as well as charitable trusts or scientific foundations like the Fund for the Replacement of Animals in Medical Experiments (FRAME, http://www.frame.org.uk, UK), the Center for Alternatives to Animal Testing (CAAT, http://caat.jhsph.edu/about/index.html; Johns Hopkins University, Baltimore, USA and University of Konstanz, Germany), or the Swiss 3R Research Foundation (http://www.forschung3r.ch, Münsingen, Switzerland), actively support the development, validation, and acceptance of methods which could replace, refine, or reduce the use of laboratory animals. Of note, the 3R concept has been put forward in Europe in the field of regulatory toxicology and by the EPAA initiative (http://ec.europa.eu/enterprise/epaa/3_3_research.htm). Some of the assays were successfully introduced and replace animal tests in hazard assessments to identify the toxicological properties of chemicals to which humans and the environment are exposed (Basketter et al. 2012). In contrast, it is a more challenging task to replace a given animal test that is used for drug safety and drug regulatory purposes. In addition, the Animal Research: Reporting of In Vivo Experiments (ARRIVE) guidelines have been developed as part of an NC3Rs initiative in order to improve the quality

of research involving animals for the provision of maximum information and minimization of unnecessary experiments (Kilkenny et al. 2010). These guidelines are endorsed by scientific journals, major funding bodies, and learned societies.

Difficulties to substitute animal experiments with in vitro or in silico methods arise when complex regulatory processes, e.g., of the cardiovascular, metabolic, or neuronal systems, are to be analyzed. This is particularly the case when the disease mechanisms are not well understood. Accordingly, at present, animal experimentation remains central to investigate disease-related processes and symptoms. Traditional experiments rely heavily on invasive techniques to monitor changes in blood biochemistry, tissue structure, or function in numerous animal disease models. In some cases, a proportion or all of the animals used during the course of a study are sacrificed for histopathological assessment, with the aim to track the progression or regression of a disease over time or to determine the levels of efficacy or toxicity evident in specific organs or tissues. However, many of these invasive techniques fail to identify crucial steps and details of how a disease develops or how a substance elicits effects.

4.2 The Contributions of Imaging to the 3Rs

Noninvasive imaging techniques provide potential to detect and monitor anatomical, functional, metabolic, or molecular changes within the body of animals with minimal pain, distress, or premature termination. Imaging techniques allow monitoring models of diseases and the response to exogenous substances in a temporal and spatial manner. Therefore, a greater amount of information can be derived from smaller numbers of animals, which in turn, increases the statistical validity of the data by reducing the level of experimental variation (Beckmann 2006; Beckmann and Garrido 2013; Ripoll et al. 2008; Rudin and Weissleder 2003). Noninvasive imaging allows more informative and humane endpoints to be used and, perhaps most importantly, functional details to be studied in the context of a living animal. In the present contribution, the significance of imaging for animal welfare and the 3R concept is discussed and underlined with data from experiments actually applied in the drug development process.

The basic contributions that in vivo imaging can make to the 3Rs are:

4.2.1 Reduction

- With imaging each animal can be used as its own control, allowing paired comparisons, thereby increasing the statistical power of experiments.
- Imaging studies are inherently sequential (only one animal can be scanned at any one time), lending themselves to sequential experimental designs, which use fewer animals to achieve the same statistical power as compared to conventional designs.
- The use of imaging can improve decisions within pharmaceutical research (Beckmann 2006; Beckmann and Garrido 2013; Ripoll et al. 2008; Rudin and Weissleder 2003) and lead, e.g., to an early closure of programs which would otherwise continue to use animals for safety and efficacy testing yet ultimately not deliver a useful medicine.

One typical example is a rat model of prolactinoma. Pituitary hyperplasia is induced by chronic stimulation with estradiol. The variability in pituitary volume before treatment, however, is large, as reflected in a coefficient of variation of 80 %. In order to detect a 50 % volume increase with a statistical significance of $p = 0.05$, group sizes of 35 animals are required. However, monitoring the relative volume increase in each animal by imaging results in a coefficient of variation of 12 % and a sample size of $n = 4$ is sufficient to reach the same level of statistical significance (Rudin et al. 1988).

4.2.2 Refinement

- Imaging allows the measurement of discrete morphological/functional changes which

substitute clinical, often painful signs detectable by visual inspection. This is of specific importance when non-diseased animals are used.
- When diseased, clinically abnormal animals are used, it is often possible to use milder disease models than with conventional structural and functional assessment protocols.
- Noninvasive imaging of animal disease models can provide earlier humane endpoints and rigorous inclusion/exclusion criteria, because of the "online" assessment of the injury progression in long-term disease models.

4.2.3 Replacement

- Imaging biomarkers provide better and earlier decisions in human clinical trials in phase I/II (Beckmann 2006; Beckmann and Garrido 2013). Increased use of imaging biomarkers has the potential to decrease reliance on animal disease model efficacy data and eventually will permit replacement of a proportion of animal experimentation by improved clinical trials (indirect replacement).

In the sections to come, attention is going to be devoted to applications of magnetic resonance imaging (MRI) in the context of experimental lung research and drug development in small rodents to further illustrate the value of imaging in animal welfare.

4.3 Experimental Lung Research in Small Rodents: Nonimaging Techniques

Respiratory diseases such as asthma, chronic obstructive pulmonary disease (COPD), and pulmonary fibrosis involve a complex interaction of many different inflammatory and structural cell types, which release a multitude of inflammatory mediators. Activated eosinophils are considered to play a major role in asthma because they contribute to epithelial cell damage, bronchial hyperresponsiveness, plasma exudation, and edema of the airway mucosa, in addition to smooth muscle hypertrophy and mucus plugging through the release of enzymes and proteins (Hamid et al. 2003; Hogan et al. 2008). COPD is associated with an abnormal inflammatory response of the lungs to noxious particles and gases, encompassing chronic obstructive bronchitis and obstruction of small airways reflecting mucous hypersecretion. Emphysema, a critical component of COPD, comprises an enlargement of air spaces as a result of destruction of the lung parenchyma, leading to the loss of lung elasticity and closure of small airways. Most patients with COPD have all three pathological mechanisms (chronic obstructive bronchitis, emphysema, and mucus plugging) (Barnes, 2002; Barnes et al. 2003). Idiopathic pulmonary fibrosis (IPF) is considered the prototype of lung diseases dominated by fibrosis, which can be induced by a large number of systemic diseases, genetic conditions, and inhalation/exposure to variable materials, including drugs, resulting in scarring and permanent lung remodeling (Gross and Hunninghake 2001; Hunninghake and Schwarz 2007; Leslie 2004). IPF has an unknown cause and is characterized histopathologically by alternating zones of interstitial fibrosis, inflammation, honeycomb changes, and normal lungs (Katzenstein and Myers 1998; Raghu et al. 2011). Although the pathway of remodeling during fibrotic processes is still not completely understood, it is so far known that the lung structure is altered by the loss of alveolar surface area, secondary to alveolar epithelial cell injury, and the loss of lung elasticity, secondary to interstitial inflammation, proliferation/migration of fibroblasts, and deposition of extracellular matrix, primary collagen, and proteoglycans (Verbeken et al. 1994; Westergren-Thorsson et al. 1993). These changes in lung structure lead to a severe impairment of lung function related to a decreased elasticity (Dackor et al. 2011; Ferreira et al. 2011; Manali et al. 2011; Milton et al. 2012; Nava and Rubini 1999).

Small-rodent models have been established in an attempt to mimic and study specific aspects of human respiratory disease and to evaluate new drugs (see Canning 2003; Brusselle et al. 2006;

Lloyd 2007; Martin and Tamaoka 2006; Moore and Hogaboam 2008; Mouratis and Aidinis 2011; Scotton and Chambers 2010 for reviews). The inflammatory status of the lungs in such models is usually inferred from the analysis of bronchoalveolar lavage (BAL) fluid or is determined histologically. The terminal nature of these procedures precludes repeated assessments in the same animal. Pulmonary function tests in rodents are also important for experimental research of various respiratory disorders (Glaab et al. 2007; Hoymann 2007). The techniques used vary from noninvasive barometric plethysmography in unrestrained ("Penh system") or in restrained animals (head-out plethysmography) to invasive methods requiring anesthesia such as orotracheally intubated animals or the use of tracheotomized and ventilated animals (Glaab et al. 2007; Hoymann 2007). The main concern with Penh approaches is that due to the lack of pressure signal, no actual changes in lung resistance and compliance can be determined. An added complication in restrained animals is the fact that they are stressed during measurements. On the other hand, as complications can arise following repeated intubation, invasive methods performed under anesthesia are usually terminal (Glaab et al. 2007; Hoymann 2007). Taking these points together, an ideal examination method should detect and follow the inflammatory response, the site and type of lung damage in living animals, as well as the altered lung function and the time and dose response effect of potential drugs in an animal disease model. Imaging has the potential to fulfill these combined requirements and to provide further knowledge which contributes to the understanding of lung biology in intact animals.

4.4 Imaging in Experimental Lung Research: Basic Considerations for Animal Welfare

An ample variety of techniques including "micro" x-ray computed tomography (micro-CT), positron emission tomography (PET), bioluminescence, fluorescence imaging, MRI, and ultrasound can be used to study various processes such as ventilation, perfusion, pulmonary hypertension, and lung inflammation in small rodents models of pulmonary diseases (Beckmann et al. 2007; Driehuys and Hedlund 2007; Johnson 2007; Schuster et al. 2004; van Echteld and Beckmann 2011). Images from more than one modality can also be fused, allowing structure–function and function–function relationships to be studied on a regional basis. All these techniques offer translational potential from animal to human studies (Schuster et al. 2004; van Echteld and Beckmann 2011).

Every technique has its own merits when imaging the lungs of small rodents, and most of the applications published up to now demonstrate that the approaches are basically complementary. Based on the noninvasive nature of imaging, repetitive measurements are a fundamental asset when adopting it in experimental studies. However, taking the animal welfare into account, some practicalities need to be carefully considered when performing studies in small rodents, which may dictate the choice in favor of a certain technique:

(i) *Dose of radiation* when performing repetitive studies. Accuracy of micro-CT images is determined by the x-ray dose given to the animal. Thus, one concern when using micro-CT is the radiation dose, which despite not being lethal, may be high enough to induce changes in the immune response and other biological pathways, so that experimental outcomes could be affected (Boone et al. 2004). For an ideal scanner, a coefficient of variation (COV) of 1 % in the linear attenuation coefficient can be expected for an image with an isotropic voxel size of 135 μm of a mouse exposed to 0.25 Gy. If the same COV is to be achieved in a 65 μm isotropic voxel, a dose of 5.0 Gy would be necessary;

(ii) *Acquisition conditions* in repeated measurements should interfere minimally with the physiology and the well-being of the animals. This becomes crucial in the context of compound testing in models of lung

diseases. Unexpected results may occur when disregarding the pathophysiological conditions of the animals. For instance, one needs to carefully consider possible interferences between the pathophysiology of the disease models and lung injury complications that might potentially be caused by mechanical ventilation (Nickles et al. 2014), especially if this is applied repeatedly. Indeed, it has been reported that mechanical ventilation of healthy rats can cause an increase of neutrophils in BAL fluid, pulmonary edema, and even hypoxemia that may lead to progressive circulatory failure and death (Walder et al. 2005). Consequently, mechanical ventilation should be avoided whenever possible for the longitudinal investigation of lung disease models with expected inflammatory responses;

(iii) *Respiration and cardiac rates* may vary following a given insult or stimulus. Thus, it needs to be verified whether cardiac and/or respiratory gating may not influence the acquired data. Whenever possible, nongated acquisitions are preferred;

(iv) *The influence of anesthesia* needs to be carefully addressed, especially when performing functional studies. However, repeated anesthesia may be an issue even in anatomical studies, in particular in the context of drug testing. The same holds true in case analgesics or sedatives are used after surgical interventions. Thus, reducing the acquisition times has advantages from the animal welfare perspective.

4.5 Magnetic Resonance Imaging in Experimental Lung Research: Impact on the 3Rs Leads to More Relevant Data

4.5.1 Technical Requirements

The living lung is one of the most challenging organs to image by MRI. Because of the low water density of approximately 20–30 %, the proton density is significantly lower than in other tissues. Moreover, due to the difference in magnetic susceptibilities between lung tissue and the air that comprises about 80 % of the pulmonary volume, local magnetic field inhomogeneities are produced, resulting in very short T_2 and T_2* relaxation times. Using a gradient-echo sequence, mean T_2* values of the order of 500 μs have been measured in vivo at 4.7 T in normal rat and mouse lungs (Beckmann et al. 2001a).

In order to detect a signal from lung parenchyma, especially at high fields, nonstandard techniques need to be used to reduce considerably the *echo time* (TE). Different protocols have been developed to overcome some of the inherent difficulties associated with the detection of parenchymal signal. For rodent imaging, the projection reconstruction method with self-refocused radio-frequency (RF) pulses has been used to achieve TE <300 μs and thus enhance the visibility of lung parenchyma (Gewalt et al. 1993).

A further challenge in lung MRI is that cardiac and respiratory movements can cause marked image artifacts. These problems are more evident in small rodents, because of their higher cardiac and respiratory rates. To address this issue, scan-synchronous artificial ventilation has been developed (Hedlund et al. 2000), in which breathing is restricted to the recovery period after data acquisition, thereby minimizing breathing-related motion artifacts. Breathing rate is kept constant and controlled by initiating a breath after the appropriate number of pulse sequence repetitions. In addition, imaging acquisition is triggered by the electrocardiogram. Although the combination of projection reconstruction methods with synchronous ventilation and cardiac gating enables high resolution images to be obtained from the rat lung (Gewalt et al. 1993), the acquisition time is long, amounting to about 30 to 40 min per image.

From the point of view of animal welfare and for compound testing in vivo in animal models of airways diseases, one needs to carefully consider possible interferences between the pathophysiology of the disease models and lung injury/complications that might potentially be caused by mechanical ventilation (Peng et al. 2005; Walder

et al. 2005). It has been shown that a standard gradient-echo sequence produces sharp proton images from the rat and mouse chest, in which potential artifacts caused by cardiac and respiratory movements are suppressed by image averaging (Beckmann et al. 2001b; Blé et al. 2008), despite the fact that neither respiratory nor cardiac gating is applied. Animals breathe spontaneously during image acquisition. Under the conditions chosen for acquisition (TE of the order of 3 ms), the signal from the lung parenchyma itself is too weak to be detected at 4.7 T. However, the absence of any detectable parenchymal signal in combination with a background devoid of artifacts provides high contrast-to-noise ratio for the detection of fluid signals associated with inflammatory processes in rodent models of airways diseases (Beckmann et al. 2007).

Recently, ultrashort echo time (UTE) MRI based on radial sampling of the k-space has become standard in small animal scanners, allowing the routine acquisition of high-quality images of the lungs in spontaneously breathing rats and mice (Egger et al. 2013, 2014; Takahashi et al. 2010; van Echteld and Beckmann 2011; Zurek et al. 2010, 2012). Movement artifacts are reduced because of the shorter echo times achieved, typically of about 500 μs and 20 μs for two- (2D) and three-dimensional (3D) acquisitions, respectively. Measurement times for 2D and 3D images covering the whole chest of mice or rats are approximately 4 and 10 min, respectively.

4.5.2 Detection and Quantification of the Inflammatory Response: Allergen-Induced Lung Inflammation

A characteristic feature of respiratory diseases such as asthma is edema of the airways due to an increase in the permeability of lung microvessels to plasma proteins. The resulting effect is the leakage of fluid from the microvascular circulation into the surrounding tissue. Assessment of this fluid can be important for diagnostic purposes and for planning and guiding treatment, e.g., with drug candidates.

In rats actively sensitized to ovalbumin (OVA) and challenged with the antigen, an intense, even, edematous signal has been detected in the lungs 24 h after challenge (Fig. 4.1a). By acquiring 20 images displaced from each other by an amount corresponding to a single-slice thickness, the whole thorax of the animal was scanned, and the total volume of the fluid signals was determined (Beckmann et al. 2001b). The volume of fluid signal was dependent on the dose of allergen and reached a maximum between 24 h and 48 h after challenge. Despite the extensive presence of fluid in the lungs, no abnormal behavior of the rats has been noticed. The MRI signal was highly significantly correlated with a variety of inflammatory parameters determined in the BAL fluid recovered from the same animals (Tigani et al. 2002). Of special interest, the strongest correlations were with the eosinophil numbers, eosinophil peroxidase activity (a marker of eosinophil activation), and the total protein content (a marker for plasma extravasation). Importantly, the signal detected by MRI correlated significantly with the perivascular edema assessed by histology (Tigani et al. 2003). After about 100 h following the challenge, the signal had been completely resolved.

4.5.3 Compound Effects Are Detected Earlier Using MRI

Following the validation of the MRI signal against the traditional, terminal techniques, BAL fluid analysis, and histology, it can be used to study the effects of anti-inflammatory compounds in the animal model. In one experimental paradigm, the drugs were given 24 h after the challenge with OVA, a time point when an extensive MRI signal was present in the rat lung. For instance, treatment with the steroid, budesonide, accelerated the rate of resolution of the MRI signal (Fig. 4.1b). A clear trend towards a reduction in the fluid signal was observed as early as 3 h after drug administration, and the effect was statistically significant from 6 to 72 h. The decline in the edematous signal correlated significantly

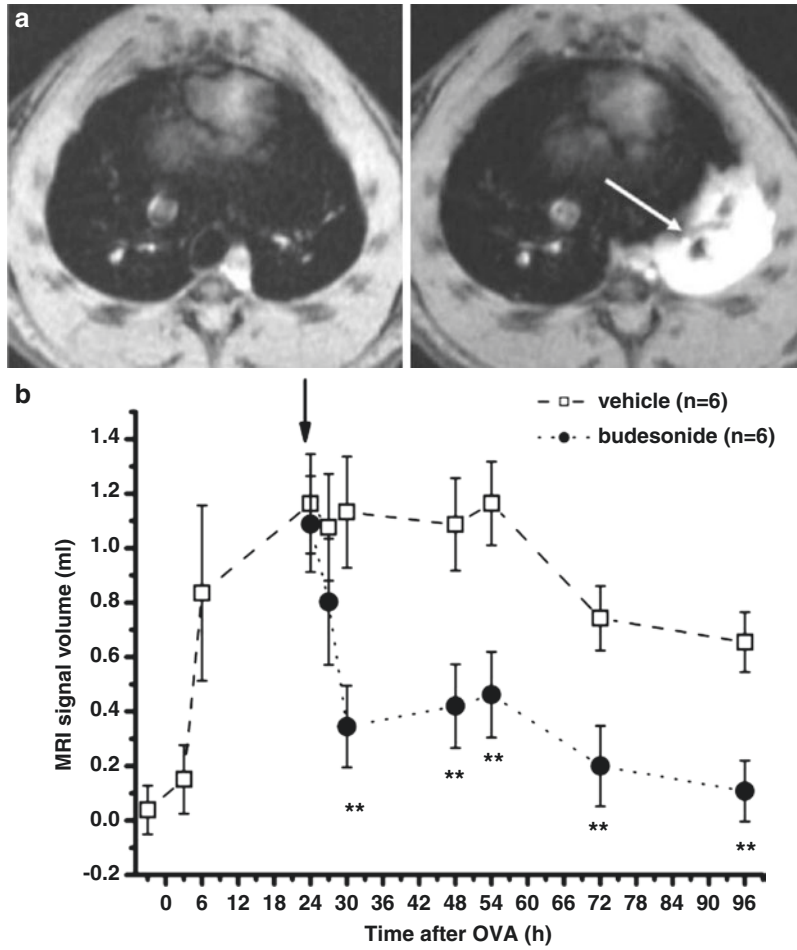

Fig. 4.1 Allergen challenge. (**a**) Axial images through the chest of an actively sensitized BN rat, acquired before (*left*) and 24 h after intratracheal (i.t.) OVA instillation (*right*). Note that the lung parenchyma appears dark; however, following allergen, a prominent MRI fluid signal is seen (*arrow*). This signal is due to edema. The acquisition time for one image was of 1 min. Animal respired spontaneously during image acquisition. (**b**) Volume of fluid signals detected by MRI in the lungs for an OVA dose of 3 mg/kg (i.t.). Administration of the corticosteroid budesonide (1 mg/kg i.t.) 24 h after OVA (*arrow*) leads to an acceleration of the resolution of the MRI signals, suggesting a rapid effect of the compound. This effect is not detectable by conventional BAL fluid analysis. Data are expressed as means ± SEM ($n = 6$ rats per group). For details, see Beckmann et al. (2001b)

with the reduction in perivascular edema quantified by histology (Tigani et al. 2003). This suggests that an effect to suppress perivascular edema underlined the decrease in the MRI signal following treatment with budesonide. By contrast, BAL fluid markers of inflammation were not affected at 6 h after treatment (Tigani et al. 2003). Only at 48 h following steroid administration, an effect was detected in the BAL.

Let us compare from the perspective of animal welfare the imaging approach with the traditional BAL fluid analysis, which necessitates 6 rats per time point. If BAL analysis were to be performed at the same time points as imaging had been carried out, 60 rats would have been necessary in both the compound group and vehicle group, resulting in a total of 120 animals. For the imaging analysis in contrast, only 12 rats were necessary. Moreover, the terminal BAL analysis was not able to detect the rapid effects of the steroid on the established lung inflammation revealed by MRI. Obviously histology could have been performed; however,

besides being time consuming, only information from a very limited region can be obtained. This example demonstrates the clear advantage provided by imaging in reducing considerably the number of animals used in the study while at the same time refining the experiment.

4.5.4 Structural Changes Are Detectable by MRI: Elastase-Induced Emphysema

A second example concerns the use of MRI in a rat model of emphysema (Quintana et al. 2006). For animals treated with porcine pancreatic elastase (PPE), the parenchymal signal intensity was decreased in the first 6 weeks following PPE (Fig. 4.2). Consistent with this, extensive enlargement of the alveoli was observed in alveoli-rich sections of histological slices. A tendency towards recovery of the MRI signal intensity was apparent at week 8, which correlated with a reduction of the emphysematous damage assessed histologically by point morphometry. Related to this reduction in damage could be the fact that following PPE the elastin content initially decreases, but appreciable elastic fiber deposition and granulation of the alveolar airspaces containing fibroblasts, endothelial cells, and a provisional collagen matrix

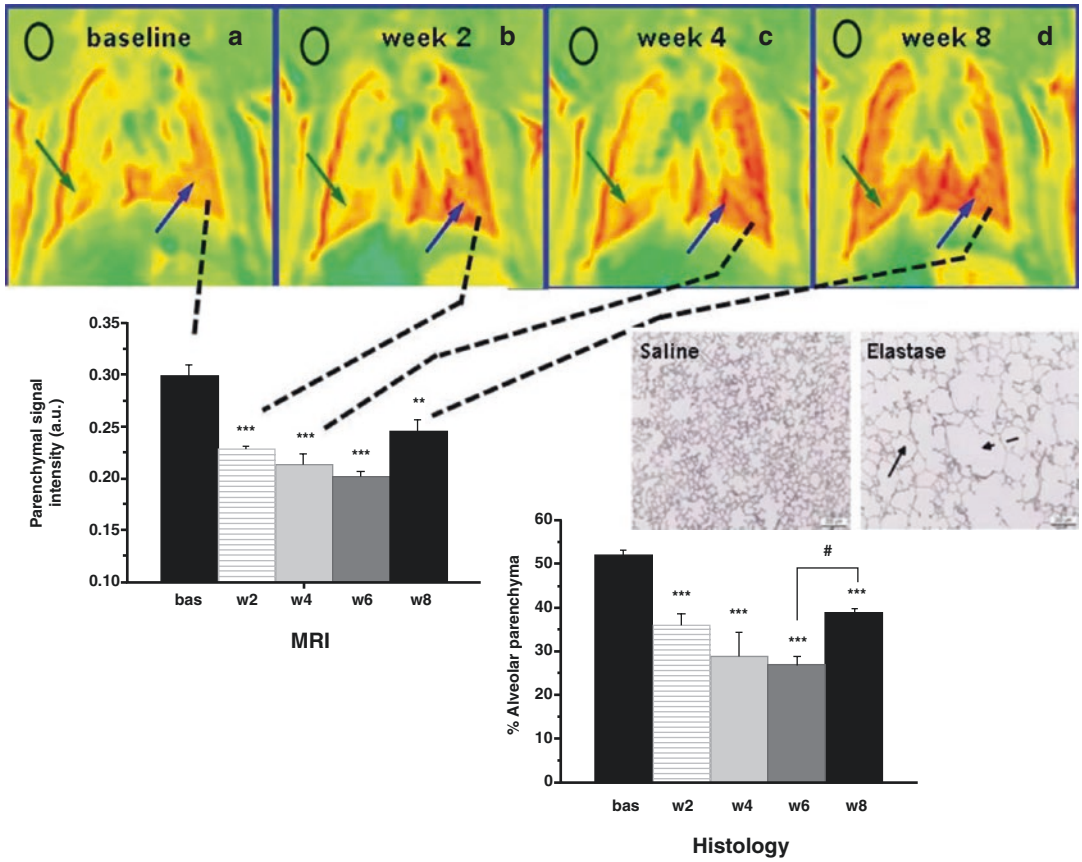

Fig. 4.2 Elastase-induced emphysema. Coronal MRI sections from a rat at baseline and at several time points following i.t. administration of PPE (75 U/100 g body weight). Animal respired spontaneously during image acquisition. Note the decrease in signal intensity from lung parenchyma as denoted by the arrows and the corresponding graph from the mean signal intensity in the lower left side of the lung. Histology from the same anatomical location demonstrated a decrease in the number of alveoli in elastase-treated animals. For details, see Quintana et al. (2006)

are observed weeks after injury. The significant correlation between the MRI signal intensity of lung parenchyma and the percentile alveolar content determined by histology indicates that proton MRI is sensitive to noninvasively detect structural changes of the lung parenchyma related to the development of emphysema in this model (Quintana et al. 2006). However, it is clear that the MRI readouts have to be validated previously against structural changes detected by histopathology.

In this study, 6 rats have been measured using MRI up to week 8 after elastase. With histology, 30 animals were necessary to characterize the temporal effect of elastase at the same time points in which MRI had been performed. Moreover, whereas MRI provided a spatially resolved measure over the lung, histology did only provide a punctual information. Obtaining volumetric information using histology would have been a very difficult task. Finally, histology was time-consuming, whereas MRI provided information readily after image acquisition. This example shows that MRI again clearly contributed to reduce the numbers of animals used in the study and to refine the experiment.

UTE MRI has also been used to track emphysema development in mice lung challenged with elastase (Zurek et al. 2012). Two parameters, namely, signal intensity and T_2, were used to monitor the disease evolution. At week 8, the mean normalized parenchymal signal intensity in elastase-challenged mice was decreased by 28 % with respect to that of control mice. Moreover, T_2 (1.27 ± 0.35 ms vs 0.96 ± 0.18 ms) was found in the emphysema group. The mean signal intensity drop and the reduction of T_2 were prominent at 3 weeks following elastase instillation and stabilized between 3 and 8 weeks. An excellent agreement was found between MRI findings and histological morphometry. In analogy to the rats data discussed before, the present results suggest that proton MRI allows structural changes at alveolar level to be monitored longitudinally in elastase-challenged mice.

4.5.5 Functional Information Can Be Derived Noninvasively

Detection of parenchymal signal enables one to derive ventilation-related information exploring the weakly paramagnetic character of molecular oxygen (Edelman et al. 1996). Indeed, a highly significant negative correlation was found between the parenchymal signal in the rat lung and the partial pressure of oxygen in the blood, for different amounts of oxygen administered (Beckmann et al. 2004). Following this reasoning, an increased parenchymal signal should be consistent with a reduced oxygen level or vice-versa.

Proton MRI has been used to detect the effects of bronchoconstrictor and bronchodilator compounds in spontaneously breathing rats (Beckmann 2006). For instance, a significant increase of the parenchymal signal intensity was observed in the upper airways, from the first minutes following intravenous administration of a compound eliciting bronchoconstriction (Fig. **4.3**). The long lasting signal increase was reversed by application of a bronchodilator agent, consistent with an increase in oxygenation. Airway resistance measures derived invasively in anesthetized, paralyzed, and artificially ventilated rats showed the same time profile as that of the MRI signal. These observations suggest that the MRI signal changes in the upper airways are due to bronchoconstrictor effects. The refinement provided by the method is evident: while the airway resistance assessments were invasive and terminal, MRI has been performed in anesthetized, spontaneously breathing rats. Repeated assessments should also be feasible using MRI, further contributing to reduce the number of animals used in the experiment.

4.5.6 Contributions of MRI for the Refinement of Models of Pulmonary Fibrosis in Small Rodents

The ability of MRI to noninvasively quantify the course of lung injury induced by bleomycin administration to mice (Babin et al. 2012; Egger

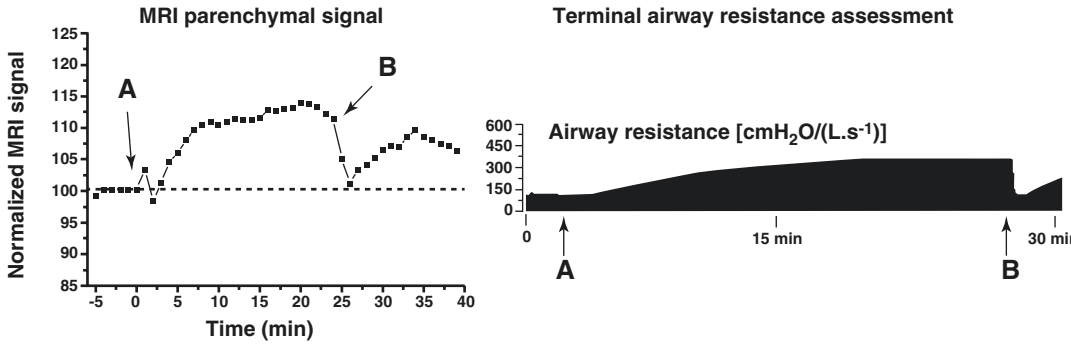

Fig. 4.3 Effects of a bronchoconstrictive (*A*) and a bronchodilating compound (*B*) administered intravenously. For the MRI experiment, the anesthetized rat could respire spontaneously. After positioning the animal in the magnet, images at the same anatomical location were acquired sequentially with a time resolution of 1 min per image. Following the acquisition of baseline images, the bronchoconstrictive agent was injected at time point 0, and the bronchodilator was injected at time point 25 min. The curve on the left shows the signal intensity evaluated in the same region in the upper airways, normalized to the mean signal intensity in the baseline images. The increase of signal after administration of compound *A* signal was consistent with its bronchoconstrictive effects, while the decrease around time 25 min was consistent with the bronchodilating effects of compound *B*. On the right side, the airway resistance measured in another rat is shown, for the same compounds administered. For this terminal experiment, the animal has been tracheotomized and artificially ventilated. Notice the similar profiles of the MRI parenchymal signal and the airways resistance measures. For details, see Beckmann et al. (2007)

et al. 2013) and rats (Babin et al. 2011; Egger et al. 2013; Jacob et al. 2010; Karmouty-Quintana et al. 2007) has been reported earlier. Thus, MRI provides potential to facilitate in vivo pharmacological studies in the model. Repetitive measurements open new avenues in testing compounds as the responses at several time points during the course of treatment can be easily compared. Specifically, studies at the chronic phase, when fibrosis is already established, become amenable.

Initially, we used gradient-echo sequences to detect the long lasting bleomycin-induced injury in the lungs of spontaneously breathing animals (Babin et al. 2011, 2012; Karmouty-Quintana et al. 2007). The sensitivity for detecting lesions elicited by bleomycin increased dramatically by reducing the echo time of the acquisition, i.e., by using UTE rather than gradient-echo sequences (Fig. 4.4). This increase in sensitivity translated into an overall reduction in the measurement times. For gradient-echo acquisitions in mice or rats, measurement times were of about 22 min for 2D images covering the whole chest (Babin et al. 2011, 2012). Measurement times for 2D UTE acquisitions declined to 7.25 min and 4 min in rats and mice, respectively (Egger et al. 2013). For 3D UTE acquisitions achieving an echo time of 20 μs, measurement times were of 11.6 min and 6.9 min for rats and mice, respectively (Egger et al. 2014) (Fig. 4.5).

In addition, by changing the route of bleomycin administration in mice from intranasal to oropharyngeal aspiration, a significant reduction in the bleomycin dose could be achieved while having sustained fibrosis (Egger et al. 2013). One of the first applications of this route can be found in a study dealing with the measurement of mucociliary function in mice by scintigraphy, in which the authors used oropharyngeal aspiration for the instillation of ^{99m}TC-labelled sulfur colloid (Foster et al. 2001). A comparison of intratracheal administration to oropharyngeal aspiration has been performed in a mouse model of silicosis (Lakatos et al. 2006). Mice treated with crystalline silica administered via the oropharyngeal route developed fibrosis with a more homogenous distribution all over the lung and with less variability. Using near-infrared optical imaging, we compared the distribution of a solution containing a fluorescent dye (Cy5.5) following intranasal and oropharyngeal administration (Egger

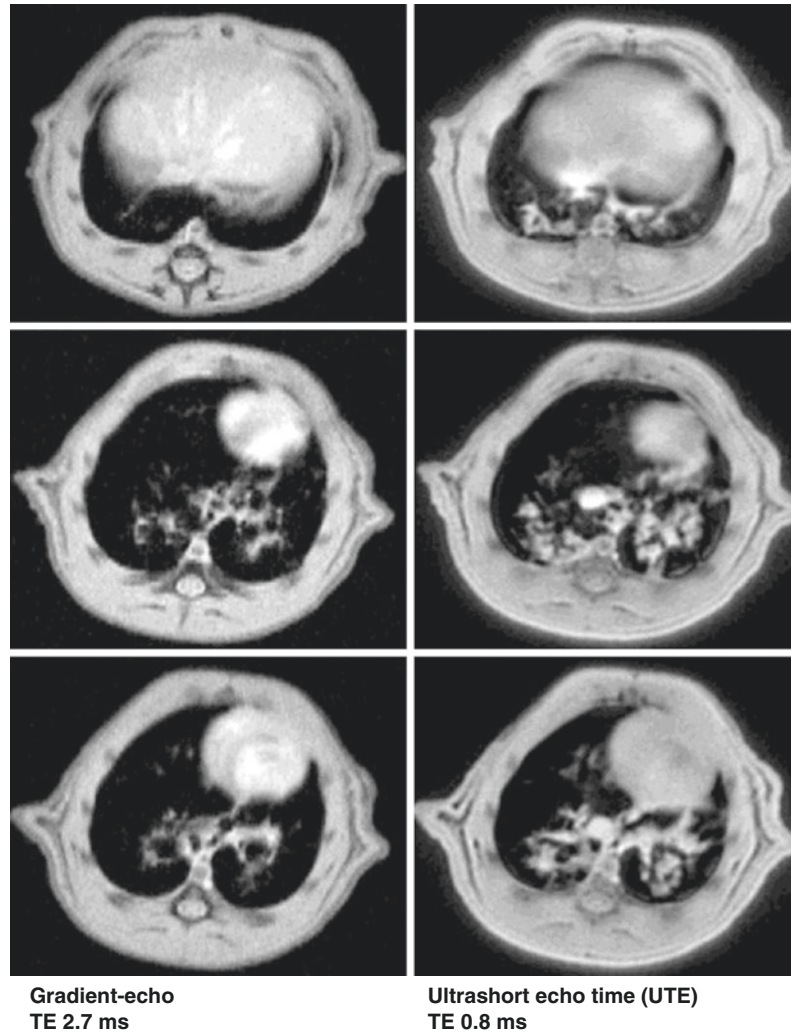

Fig. 4.4 Comparison between 2D gradient-echo and UTE MRI of bleomycin challenge at 4.7 T. Shown are three axial sections through the same rat at approximately the same anatomical location, acquired 15 days after i.t. administration of bleomycin (4 mg/kg). Acquisition times were of 22 min for gradient-echo and 7.25 min for UTE images covering the whole chest. The animal respired spontaneously, and neither cardiac nor respiratory gating was applied during acquisition. It is evident that by reducing the echo time (TE), the sensitivity in detecting bleomycin-induced responses increased significantly

et al. 2013). While a homogenous distribution of the fluorescence signal all over the lung was observed for oropharyngeal aspiration, fluorescence signals appeared mainly in the upper part of the lung and the trachea for intranasal administration.

Changes in lung structure accompanying fibrotic processes lead to a severe impairment of lung function related to a decreased elasticity. Indeed, increased lung elastance and decreased compliance (the reciprocal of elastance) have been reported in small rodent pulmonary fibrosis models (Ask et al. 2008; Card et al. 2007; Ebihara et al. 2000; Manali et al. 2011). Moreover, changes in tidal volume and breathing cycle times have been shown in a mouse fibrosis model (Milton et al. 2012). Egger et al. (2014) reported an increase of MRI-derived total lung volume in bleomycin-challenged small rodents, consistent with increased *postmortem* dry and wet lung weights, hydroxyproline content, as well as collagen amount assessed by histology. In bleomycin-treated rats, MRI acquisitions gated by the respiration showed an increased volume of the lung in the inspiratory and expiratory phases of the respiratory cycle and a temporary decrease of tidal volume. Using a flexiVent® system for the assessment of lung function in tracheotomized and mechanically ventilated animals (terminal procedure), decreased dynamic

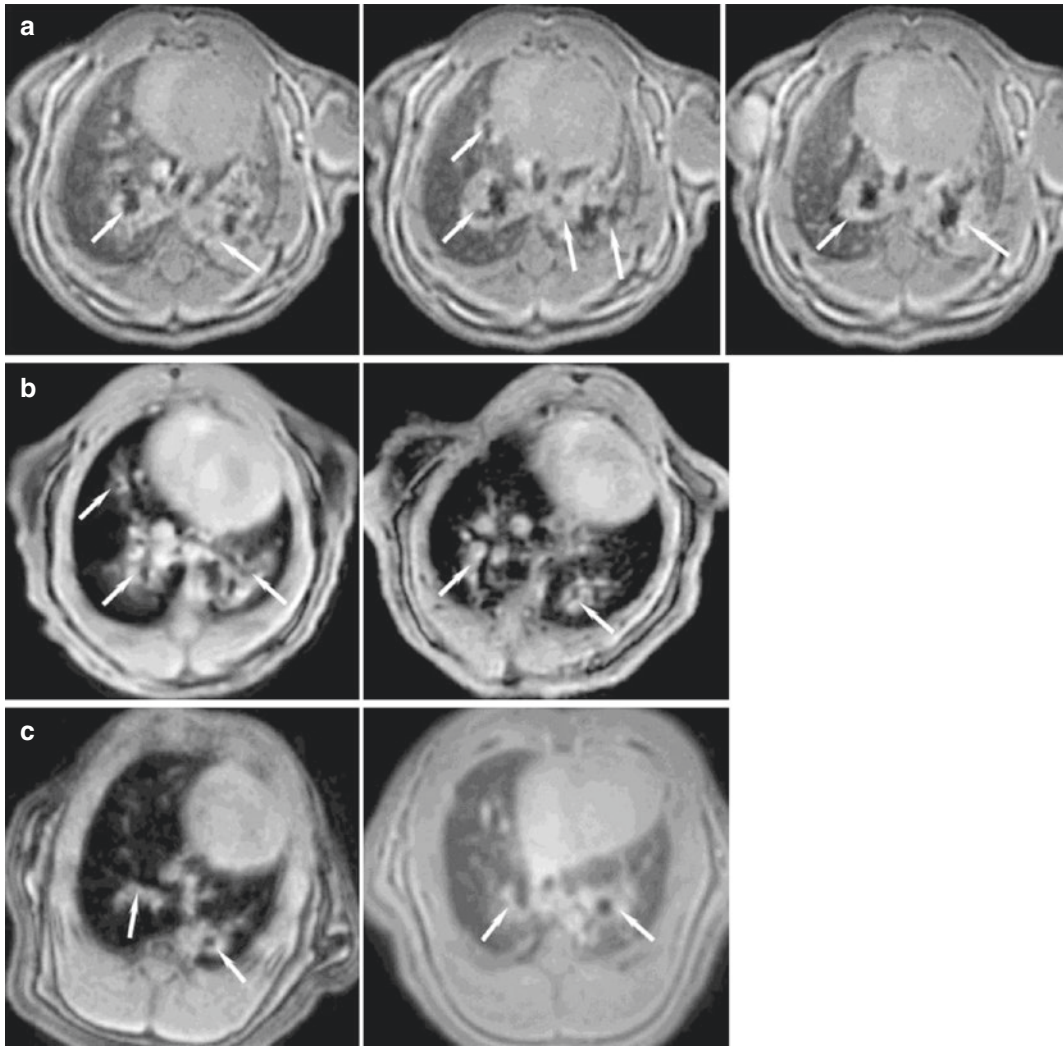

Fig. 4.5 UTE MRI of spontaneously breathing mice or rats following bleomycin challenge. (**a**) Mouse at day 20 after last bleomycin administration, UTE 3D at 7 T (TE 0.02 ms). (**b**) Mice at day 23 after last bleomycin administration, UTE 2D at 4.7 T (TE 0.6 ms). Animals received bleomycin (0.1 mg/kg) by oropharyngeal aspiration, once a day on six consecutive days, resulting in a total dose of 0.6 mg/kg. (**c**) Rats at day 14 after single oropharyngeal aspiration of bleomycin (2 mg/kg), at 7 T. *Left*: UTE 2D (TE 0.8 ms). *Right*: UTE 3D (TE 0.02 ms). Lesions elicited by bleomycin are shown by the *arrows*

lung compliance was found in bleomycin-challenged rats (Egger et al. 2014). Overall speaking, bleomycin-induced increase of MRI-detected lung volume was consistent with tissue deposition during fibrotic processes resulting in decreased lung elasticity, while influences by edema or emphysema could be excluded (Fig. 4.6). In ovalbumin-challenged rats, total lung volume quantified by MRI remained unchanged (Egger et al. 2014).

Also micro-CT has been shown to constitute an important imaging tool to detect pulmonary fibrosis in animal models (Ask et al. 2008; De Langhe et al. 2012; Shofer et al. 2008). Although no major problem may be expected for single acquisitions, radiotoxicity concerns may arise for repeated scanning especially because the lungs are particularly sensitive to cumulative doses of ionizing radiation (Graves et al. 2010; Plathow et al. 2004). Moreover, possible effects of x-rays

on the inflammatory and tissue remodeling processes specific to this disease model cannot be excluded. Velde et al. (2014) have shown an excellent agreement between in vivo MRI, in vivo micro-CT, and standard histological measures of lung fibrosis in mice. UTE MRI appeared particularly useful for detecting early disease, self-gated MRI for improved breathing motion handling.

The efforts summarized in this section indicate that MRI can contribute to the refinement of small rodent models of pulmonary fibrosis: Measurements are performed in spontaneously

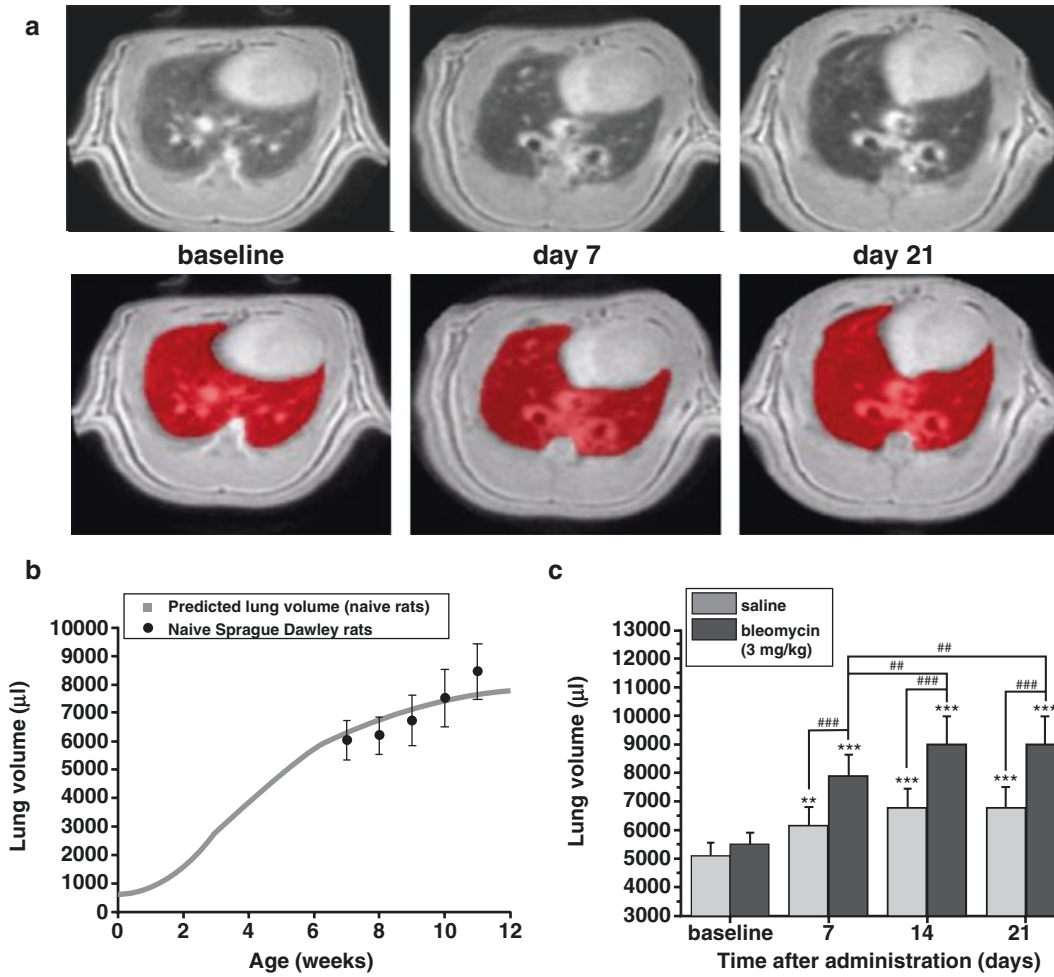

Fig. 4.6 Lung volume quantified by MRI reflects extracellular matrix deposition and altered pulmonary function in bleomycin models of fibrosis. (**a**) Representative images extracted from UTE 3D data sets acquired at 7 T from the same animal before and after bleomycin administration (*top*) and corresponding segmented lung volumes (*bottom*). Mouse at day 20 after last bleomycin administration, UTE 3D at 7 T (TE 0.02 ms). (**b**) Prediction for lung volume of naïve Sprague–Dawley rats (*gray curve*) using the formula of Mirfazaelian and Fisher describing the age-dependent change of the lung weight (Mirfazaelian and Fisher 2007) and a lung density of 0.21 mg/ml (determined from several experiments). MRI-assessed lung volumes for naive rats are shown as means ± SD ($n = 6$ rats). (**c**) Lung volumes (means ± SD, $n = 9$ rats per group) derived from rats challenged with saline or with bleomycin (3 mg/kg) administered via oropharyngeal aspiration. Animals were 7 weeks old at baseline. (**d**) Lung function parameters obtained at day 21 after saline or bleomycin (3 mg/kg) challenge from tracheotomized and artificially ventilated rats by using the flexiVent® system. Values are provided as means ± SD ($n = 9$ rats per group). The levels of significance indicated in the graphs correspond to *t*-test comparisons. See Egger et al. (2014) for details

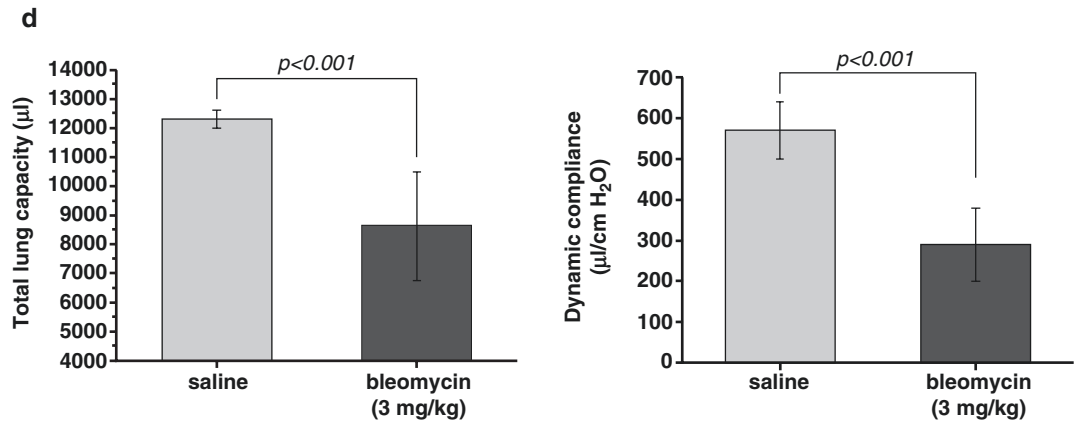

Fig. 4.6 (continued)

breathing animals; improved techniques as UTE enable faster acquisitions and/or impact (reduce) bleomycin dose; functional information related to reduced lung elasticity during fibrosis processes can be derived from lung volume assessments; and direct comparison between MRI and micro-CT indicates that MRI provides an imaging alternative without ionizing radiation for assessing fibrosis in animal models. These characteristics make of MRI an attractive technique for noninvasive assessments of compound effects in these models. Indeed, MRI has been used to evaluate the effects of several compounds and for the in vivo validation of pharmacological targets (Babin et al. 2011, 2012; Egger et al. 2014, 2015). Of note, using MRI, it could be demonstrated that the somatostatin analogue, SOM230, had a therapeutic effect on established lung fibrosis (Egger et al. 2014).

4.6 Final Remarks

The main message of this contribution is that, generally speaking, better science can be achieved when following the 3R principles, for instance, by introducing noninvasive imaging into in vivo experimentation. Using examples from our own experience in adopting MRI in the area of small rodent models of airways diseases, we have shown the win–win situation between animal welfare and the relevance of data obtained from animal studies. We illustrated how noninvasive imaging results in a significant reduction in the number of animals used for experimentation. Depending on the application, a reduction between 80 to 90 % is estimated. Since repeated measurements are feasible, each animal can serve as its own control, thereby reducing the variability of the data. Moreover, as exemplified by the study of anti-inflammatory compounds on established inflammation, imaging provides potential to obtain information not accessible to conventional, *postmortem* assessments. Such an experimental refinement is often the consequence of the fact that imaging provides information of the organ in situ in the intact organism. Thus, data that are more relevant to address therapeutic effects can be obtained using imaging.

Besides therapy testing, in vivo toxicology, encompassing the identification of adverse effects of air pollutants, compounds, or nanoparticles for medical use, will largely profit from imaging (Hockings and Powell 2013; Reid 2006; Wang and Yan 2008). Indeed, noninvasive small rodent imaging is in line with the concept and strategy of toxicity testing in the twenty-first century developed by the US National Academy of Sciences, the US National Academy of Engineering, the Institute of Medicine, and the US National Research Council (http://dels.nas.edu/dels/rpt_briefs/Toxicity_Testing_final.pdf).

Some targeted testing in animals will be needed to sufficiently understand how chemicals are broken down in the body. Combined with imaging techniques, such assays will ensure an adequate toxicological evaluation of chemicals. As an example, it has been shown that the presence and biological effects of carbon nanotubes can be detected in vivo by noninvasive MRI techniques (Al Faraj et al. 2009, 2010, 2011).

Some points need to be kept in mind, however, when adopting imaging in animal studies:

Validation against established methods Before imaging is able to make a contribution to address a given question, the readouts need to be carefully validated against standard, often terminal measures. During this phase, the value of imaging is unknown. However, well-validated readouts are likely going to be more relevant and thus better suited to have also an impact on animal welfare.

Anesthesia and its interaction with readouts Anesthesia can become a limiting factor of small animal imaging: it may not only influence the results of functional acquisitions but also interfere with drug studies. Although healthy small rodents easily recover from gas anesthesia, this may represent an additional burden when the animals have been subjected to, e.g., a chemical stimulus to elicit a pathology and are in addition treated with drugs. It is recommended to carefully conceive the studies in order to achieve a balance between the gain in information and the number of times an animal is anesthetized. Also, the minimum interval between sequential imaging sessions needs to be considered. As a pragmatic way, acquisition times under 30 min and a minimum interval of 3 h between sequential anesthesias are recommended. Also, gas anesthesia is preferable, since it is easier to control and recovery time is of a few minutes only.

Imaging acquisition guided by physiological requirements It is important to adapt the imaging acquisitions to the biology of the species and not vice-versa. In the case of lung studies, for instance, it is recommended to perform acquisitions on spontaneously breathing animals, as artificial ventilation may induce lung injury.

Overall speaking, it is our experience that imaging can make substantial contributions to the 3R concept. As imaging systems are largely available in hospitals for diagnostic purposes, there is potential to address translational aspects from the animal models to the human situation and vice versa. In this sense, a more humane treatment of experimental animals and more relevant animal studies become feasible. It remains the responsibility of the investigator to conceive the experiments in a way that their nature and performance are continuously refined to ensure that the 3R concept is respected in every biomedical activity addressed using imaging.

References

Al Faraj A, Cieslar K, Lacroix G, Gaillard S, Canet-Soulas E, Crémillieux Y. In vivo imaging of carbon nanotube biodistribution using magnetic resonance imaging. Nano Lett. 2009;9:1023–7.

Al Faraj A, Bessaad A, Cieslar K, Lacroix G, Canet-Soulas E, Crémillieux Y. Long-term follow-up of lung biodistribution and effect of instilled SWCNTs using multiscale imaging techniques. Nanotechnology. 2010;21(17):175103.

Al Faraj A, Fauvelle F, Luciani N, Lacroix G, Levy M, Crémillieux Y, Canet-Soulas E. In vivo biodistribution and biological impact of injected carbon nanotubes using magnetic resonance techniques. Int J Nanomedicine. 2011;6:351–61.

Ask K, Labiris R, Farkas L, Moeller A, Froese A, Farncombe T, McClelland GB, Inman M, Gauldie J, Kolb MR. Comparison between conventional and "clinical" assessment of experimental lung fibrosis. J Transl Med. 2008;6:16.

Babin AL, Cannet C, Gérard C, Wyss D, Page CP, Beckmann N. Noninvasive assessment of bleomycin-induced lung injury and the effects of short-term glucocorticosteroid treatment in rats using MRI. J Magn Reson Imaging. 2011;33:603–14.

Babin AL, Cannet C, Gérard C, Saint-Mezard P, Page CP, Sparrer H, Matsuguchi T, Beckmann N. Bleomycin-induced lung injury in mice investigated by MRI: model assessment for target analysis. Magn Reson Med. 2012;67:499–509.

Barnes PJ. New treatments for COPD. Nat Rev Drug Discov. 2002;1:437–46.

Barnes PJ, Shapiro SD, Pauwels RA. Chronic obstructive pulmonary disease: molecular and cellular mechanisms. Eur Respir J. 2003;22:672–88.

Basketter DA, Clewell H, Kimber I, Rossi A, et al. A roadmap for the development of alternative (non-animal) methods for systemic toxicity testing- T4 report. ALTEX. 2012;29:3–91.

Beckmann N. In vivo MR techniques in drug discovery and development. New York: Taylor & Francis; 2006.

Beckmann N, Garrido L. New applications of NMR in drug discovery and development. Cambridge, UK: Royal Society of Chemistry; 2013.

Beckmann N, Tigani B, Mazzoni L, Fozard JR. MRI of lung parenchyma in rats and mice using a gradient-echo sequence. NMR Biomed. 2001a;14:297–306.

Beckmann N, Tigani B, Ekatodramis D, Borer R, Mazzoni L, Fozard JR. Pulmonary edema induced by allergen challenge in the rat: noninvasive assessment by magnetic resonance imaging. Magn Reson Med. 2001b;45:88–95.

Beckmann N, Cannet C, Zurbruegg S, Rudin M, Tigani B. Proton MRI of lung parenchyma reflects allergen-induced airway remodeling and endotoxin-aroused hyporesponsiveness: a step toward ventilation studies in spontaneously breathing rats. Magn Reson Med. 2004;52:258–68.

Beckmann N, Cannet C, Karmouty-Quintana H, Tigani B, Zurbruegg S, Blé FX, Crémillieux Y, Trifilieff A. Lung MRI for experimental drug research. Eur J Radiol. 2007;64:381–96.

Blé FX, Cannet C, Zurbruegg S, Karmouty-Quintana H, Bergmann R, Frossard N, Trifilieff A, Beckmann N. Allergen-induced lung inflammation in actively sensitized mice assessed with MR imaging. Radiology. 2008;248:834–43.

Boone JM, Velazquez O, Cherry SR. Small-animal X-ray dose from micro-CT. Mol Imaging. 2004;3:149–58.

Brusselle GG, Bracke KR, Maes T, D'hulst AI, Moerloose KB, Joos GF, Pauwels RA. Murine models of COPD. Pulm Pharmacol Ther. 2006;19:155–65.

Canning BJ. Modeling asthma and COPD in animals: a pointless exercise? Curr Opin Pharmacol. 2003;3:244–50.

Card JW, Voltz JW, Carey MA, Bradbury JA, Degraff LM, Lih FB, Bonner JC, Morgan DL, Flake GP, Zeldin DC. Cyclooxygenase-2 deficiency exacerbates bleomycin-induced lung dysfunction but not fibrosis. Am J Respir Cell Mol Biol. 2007;37:300–8.

Dackor RT, Cheng J, Voltz JW, Card JW, et al. Prostaglandin E2 protects murine lungs from bleomycin-induced pulmonary fibrosis and lung dysfunction. Am J Physiol Lung Cell Mol Physiol. 2011;301:L645–55.

De Langhe E, Vande Velde G, Hostens J, Himmelreich U, Nemery B, Luyten FP, Vanoirbeek J, Lories RJ. Quantification of lung fibrosis and emphysema in mice using automated micro-computed tomography. PLoS One. 2012;7(8):e43123.

Driehuys B, Hedlund LW. Imaging techniques for small animal models of pulmonary disease: MR microscopy. Toxicol Pathol. 2007;35:49–58.

Ebihara T, Venkatesan N, Tanaka R, Ludwig MS. Changes in extracellular matrix and tissue viscoelasticity in bleomycin-induced lung fibrosis. Temporal aspects. Am J Respir Crit Care Med. 2000;162:1569–76.

Edelman RR, Hatabu H, Tadamura E, Li W, Prasad PV. Noninvasive assessment of regional ventilation in the human lung using oxygen-enhanced magnetic resonance imaging. Nat Med. 1996;2:1236–9.

Egger C, Cannet C, Gérard C, Jarman E, Jarai G, et al. Administration of bleomycin via the oropharyngeal aspiration route leads to sustained lung fibrosis in mice and rats as quantified by UTE-MRI and histology. PLoS One. 2013;8(5):e63432.

Egger C, Gérard C, Vidotto N, Accart N, Cannet C, et al. Lung volume quantified noninvasively by MRI reflects extracellular-matrix deposition and altered pulmonary function in small rodent bleomycin models of fibrosis. Am J Physiol Lung Cell Mol Physiol. 2014;306:L1064–L1077.

Egger C, Cannet C, Gérard C, Dunbar A, Tigani B, Beckmann N (2015) Hyaluronidase modulates bleomycin-induced lung injury detected non-invasively in small rodents by radial proton MRI. J Magn Reson Imaging. 2015;41:755–64. doi:10.1002/jmri.24612.

Ferreira JC, Benseñor FE, Rocha MJ, Salge JM, et al. A sigmoidal fit for pressure-volume curves of idiopathic pulmonary fibrosis patients on mechanical ventilation: clinical implications. Clinics (Sao Paulo). 2011;66:1157–63.

Foster WM, Walters DM, Longphre M, Macri K, Miller LM. Methodology for the measurement of mucociliary function in the mouse by scintigraphy. J Appl Physiol. 2001;90:1111–7.

Gewalt SL, Glover GH, Hedlund LW, Cofer GP, MacFall JR, Johnson GA. MR microscopy of the rat lung using projection reconstruction. Magn Reson Med. 1993;29:99–106.

Glaab T, Taube C, Braun A, Mitzner W. Invasive and non-invasive methods for studying pulmonary function in mice. Respir Res. 2007;8:63.

Graves PR, Siddiqui F, Anscher MS, Movsas B. Radiation pulmonary toxicity: from mechanisms to management. Semin Radiat Oncol. 2010;20:201–7.

Gross TJ, Hunninghake GW. Idiopathic pulmonary fibrosis. N Engl J Med. 2001;345:517–25.

Guillouzo A, Guguen-Guillouzo C. Evolving concepts in liver tissue modeling and implications for in vitro toxicology. Expert Opin Drug Metab Toxicol. 2008;4:1279–94.

Hamid Q, Tulic' MK, Liu MC, Moqbel R. Inflammatory cells in asthma: mechanisms and implications for therapy. J Allergy Clin Immunol. 2003;111(Suppl):S5–12.

Hedlund LW, Cofer GP, Owen SJ, Johnson GA. MR-compatible ventilator for small animals: computer-controlled ventilation for proton and noble gas imaging. Magn Reson Imaging. 2000;18:753–9.

Hockings PD, Powell H. In vivo MRI/S for the safety evaluation of pharmaceuticals. In: Garrido L, Beckmann N, editors. New applications of NMR in drug discovery and development. Cambridge, UK: Royal Society of Chemistry Publishing; 2013. p. 361–75.

Hogan SP, Rosenberg HF, Moqbel R, Phipps S, Foster PS, Lacy P, Kay AB, Rothenberg ME. Eosinophils: biological properties and role in health and disease. Clin Exp Allergy. 2008;38:709–50.

Hoymann HG. Invasive and noninvasive lung function measurements in rodents. J Pharmacol Toxicol Methods. 2007;55:16–26.

Hunninghake GW, Schwarz MI. Does current knowledge explain the pathogenesis of idiopathic pulmonary fibrosis? A perspective. Proc Am Thorac Soc. 2007;4:449–52.

Jacob RE, Amidan BG, Soelberg J, Minard KR. In vivo MRI of altered proton signal intensity and T2 relaxation in a bleomycin model of pulmonary inflammation and fibrosis. J Magn Reson Imaging. 2010;31:1091–9.

Johnson KA. Imaging techniques for small animal imaging models of pulmonary disease: micro-CT. Toxicol Pathol. 2007;35:59–64.

Karmouty-Quintana H, Cannet C, Zurbruegg S, Blé FX, Fozard JR, Page CP, Beckmann N. Bleomycin-induced lung injury assessed noninvasively and in spontaneously breathing rats by proton MRI. J Magn Reson Imaging. 2007;26:941–9.

Katzenstein AL, Myers JL. Idiopathic pulmonary fibrosis: clinical relevance of pathologic classification. Am J Respir Crit Care Med. 1998;157:1301–15.

Kilkenny C, Browne WJ, Cuthill IC, Emerson M, Altman DG. The ARRIVE Guidelines for Reporting Animal Research. PLoS Biol. 2010;8:e1000412.

Lakatos HF, Burgess HA, Thatcher TH, Redonnet MR, Hernady E, et al. Oropharyngeal aspiration of a silica suspension produces a superior model of silicosis in the mouse when compared to intratracheal instillation. Exp Lung Res. 2006;32:181–99.

Leslie KO. Pathology of interstitial lung disease. Clin Chest Med. 2004;25:657–703. vi.

Lloyd CM. Building better mouse models of asthma. Curr Allergy Asthma Rep. 2007;7:231–6.

Manali ED, Moschos C, Triantafillidou C, Kotanidou A, et al. Static and dynamic mechanics of the murine lung after intratracheal bleomycin. BMC Pulm Med. 2011;11:33.

Martin JG, Tamaoka M. Rat models of asthma and chronic obstructive lung disease. Pulm Pharmacol Ther. 2006;19:377–85.

Milton PL, Dickinson H, Jenkin G, Lim R. Assessment of respiratory physiology of C57BL/6 mice following bleomycin administration using barometric plethysmography. Respiration. 2012;83:253–66.

Mirfazaelian A, Fisher JW. Organ growth functions in maturing male Sprague–Dawley rats based on a collective database. J Toxicol Environ Health A. 2007;70:1052–63.

Moore BB, Hogaboam CM. Murine models of pulmonary fibrosis. Am J Physiol Lung Cell Mol Physiol. 2008;294:L152–60.

Mouratis MA, Aidinis V. Modeling pulmonary fibrosis with bleomycin. Curr Opin Pulm Med. 2011;17:355–61.

Nava S, Rubini F. Lung and chest wall mechanics in ventilated patients with end stage idiopathic pulmonary fibrosis. Thorax. 1999;54:390–5.

Nickles HT, Sumkauskaite M, Wang X, Wegner I, Puderbach M, Kuebler WM. Mechanical ventilation causes airway distension with proinflammatory sequelae in mice. Am J Physiol Lung Cell Metab. 2014;307:L27–37.

Pamies D, Hartung T, Hogberg HT. Biological and medical applications of a brain-on-a-chip. Exp Biol Med. (Maywood) 2014;239:1096–107.

Peng X, Abdulnour RE, Sammani S, Ma SF, Han EJ, Hasan EJ, Tuder R, Garcia JG, Hassoun PM. Inducible nitric oxide synthase contributes to ventilator-induced lung injury. Am J Respir Crit Care Med. 2005;172:470–9.

Plathow C, Li M, Gong P, Zieher H, Kiessling F, et al. Computed tomography monitoring of radiation induced lung fibrosis in mice. Invest Radiol. 2004;39:600–9.

Quintana HK, Cannet C, Zurbruegg S, Blé FX, Fozard JR, Page CP, Beckmann N. Proton MRI as a noninvasive tool to assess elastase-induced lung damage in spontaneously breathing rats. Magn Reson Med. 2006;56:1242–50.

Raghu G, Collard HR, Egan JJ, Martinez FJ, et al. ATS/ERS/JRS/ALAT Committee on Idiopathic Pulmonary Fibrosis. An official ATS/ERS/JRS/ALAT statement: idiopathic pulmonary fibrosis: evidence-based guidelines for diagnosis and management. Am J Respir Crit Care Med. 2011;183:788–824.

Reid D. MRI in pharmaceutical safety assessment. In: Beckmann N, editor. In vivo MR techniques in drug discovery and development. New York: Taylor & Francis; 2006. p. 537–54.

Ripoll J, Ntziachristos V, Cannet C, Babin AL, Kneuer R, Gremlich HU, Beckmann N. Investigating pharmacology in vivo using magnetic resonance and optical imaging. Drugs R D. 2008;9:277–306.

Rudin M, Weissleder R. Molecular imaging in drug discovery and development. Nat Rev Drug Discov. 2003;2:123–31.

Rudin M, Briner U, Doepfner W. Quantitative magnetic resonance imaging of estradiol-induced pituitary hyperplasia in rats. Magn Reson Med. 1988;7:285–91.

Russell WMS, Burch RL. The principles of humane experimental technique. London: Methuen; 1959.

Schuster DP, Kovacs A, Garbow J, Piwnica-Worms D. Recent advances in imaging the lungs of intact small animals. Am J Respir Cell Mol Biol. 2004;30:129–38.

Scotton CJ, Chambers RC. Bleomycin revisited: towards a more representative model of IPF? Am J Physiol Lung Cell Mol Physiol. 2010;299:L439–41.

Shofer S, Badea C, Qi Y, Potts E, Foster WM, Johnson GA. A micro-CT analysis of murine lung recruitment in bleomycin-induced lung injury. J Appl Physiol. 2008;105:669–77.

Spielmann H, Grune B, Liebsch M, Seiler A, Vogel R. Successful validation of in vitro methods in toxicology by ZEBET, the National Centre for Alternatives in

Germany at the BfR (Federal Institute for Risk Assessment). Exp Toxicol Pathol. 2008;60:225–33.

Takahashi M, Togao O, Obara M, van Cauteren M, Ohno Y, et al. Ultra-short echo time (UTE) MR imaging of the lung: comparison between normal and emphysematous lungs in mutant mice. J Magn Reson Imaging. 2010;32:326–33.

Tigani B, Schaeublin E, Sugar R, Jackson AD, Fozard JR, Beckmann N. Pulmonary inflammation monitored noninvasively by MRI in freely breathing rats. Biochem Biophys Res Commun. 2002;292:216–21.

Tigani B, Cannet C, Zurbrugg S, Schaeublin E, Mazzoni L, Fozard JR, Beckmann N. Resolution of the oedema associated with allergic pulmonary inflammation in rats assessed noninvasively by magnetic resonance imaging. Br J Pharmacol. 2003;140:239–46.

van Echteld CJ, Beckmann N. A view on imaging in drug research and development for respiratory diseases. J Pharmacol Exp Ther. 2011;337:335–49.

Velde GV, De Langhe E, Poelmans J, Dresselaers T, Lories RJ, Himmelreich U. Magnetic resonance imaging for noninvasive assessment of lung fibrosis onset and progression: cross-validation and comparison of different magnetic resonance imaging protocols with micro-computed tomography and histology in the bleomycin-induced mouse model. Invest Radiol. 2014;49(11):691–8. doi:10.1097/RLI.0000000000000071.

Verbeken EK, Cauberghs M, Lauweryns JM, Van de Woestijne KP. Structure and function in fibrosing alveolitis. J Appl Physiol (1985). 1994;76:731–42.

Walder B, Fontao E, Totsch M, Morel DR. Time and tidal volume-dependent ventilator-induced lung injury in healthy rats. Eur J Anaesthesiol. 2005;10:785–94.

Walmsley GG, Hyun J, McArdle A, Senarath-Yapa K, Hu MS, Chung MT, Wong VW, Longaker MT, Wan DC. Induced Pluripotent Stem Cells in Regenerative Medicine and Disease Modeling. Curr Stem Cell Res Ther. 2014;9:73–81.

Wang YX, Yan SX. Biomedical imaging in the safety evaluation of new drugs. Lab Anim. 2008;42:433–41.

Westergren-Thorsson G, Hernnäs J, Särnstrand B, Oldberg A, Heinegård D, Malmström A. Altered expression of small proteoglycans, collagen, and transforming growth factor-beta 1 in developing bleomycin-induced pulmonary fibrosis in rats. J Clin Invest. 1993;92:632–7.

Zurek M, Bessaad A, Cieslar K, Crémillieux Y. Validation of simple and robust protocols for high-resolution lung proton MRI in mice. Magn Reson Med. 2010;64:401–7.

Zurek M, Boyer L, Caramelle P, Boczkowski J, Crémillieux Y. Longitudinal and noninvasive assessment of emphysema evolution in a murine model using proton MRI. Magn Reson Med. 2012;68:898–904.

Part II

Study Planning and Animal Preparation

Institutional Preconditions for Small Animal Imaging

5

René H. Tolba

Contents

5.1 Background

Research with laboratory animal models, in particular genetically modified rodents like mice and rats, are increasingly recognised as powerful discovery tools in medical research. One major limitation in the use of experimental animals is often the need to sacrifice the animals to perform blood, tissue or molecular analysis. This is a major obstacle to observe the biological process under investigation in vivo. Functional, molecular as well as morphologic quantitative imaging techniques are an important tool for providing data about biochemical, genetic or pharmacological processes in vivo and repetitively in the same animal. Therefore, the same animals are used as intra-individual controls; this will reduce the standard deviation and will further reduce the number of animals needed per study. This is in line with the 3 R principles: *replacement of animal experiments*, *reduction of animal experiments and refinement of experiments* first described in 1959 by W.M.S. Russell and R.L. Burch (The Principles of Humane Experimental Technique):

- Laboratory animal facility and laboratory animal housing
- Housing systems (micro-isolator, IVC, isolator)
- Laws and regulations
- Institutional preconditions (diets, water and hypoxia, etc.)
- OCCUPATIONAL HEALTH AND SAFETY OF PERSONNEL
- Animal Transport

R.H. Tolba
Institute for Laboratory Animal Science,
RWTH Aachen University, Aachen, Germany
e-mail: rtolba@ukaachen.de

F. Kiessling et al. (eds.), *Small Animal Imaging*, DOI 10.1007/978-3-319-42202-2_5

5.1.1 Laboratory Animal Facility

The *Guide for the Care and Use of Laboratory Animals* published in 1996 by the Institute for Laboratory Animal Research (ILAR) states: "A well-planned, well-designed, well-constructed, and properly maintained facility is an important element of good animal care and use, and it facilitates efficient, economical, and safe operation".

There are several factors influencing the design and size of the laboratory animal facility. The determining criteria are given by the institutional research topics, the number and species of animals to be housed as well as the location of the facility (e.g. on campus, in an existing building or off campus).

The animal facility has to be designed and constructed in accordance with all applicable state and local building codes. In addition moreover there are several international, national and local laws regarding biosafety, hazardous substances, controlled substances, occupational health and animal welfare as well as laws governing the use of genetically modified organisms which is important to know and to implement. Knowledge of these rules and regulations are essential already at the design phase of the future facility. The planning phase of the facility is allocated with approximately 10 % of the building costs, but responsible for approximately 80 % of the running costs of the facility. The flexibility of the building for future aspects of biomedical research should also be accounted for. Therefore, the facility design is a crucial step in creating an optimal and economic facility.

5.2 Functional Areas of the Facility

The size and the location (central vs. de-central or multisite) will determine whether areas for separate service functions are needed or necessary. Sufficient space is required to ensure:

- Separation of animal species or accommodating of individual projects
- Import, quarantine and export animals
- Provide space for animal housing

In some very small facilities, directly to or nearby an experimental laboratory or imaging unit, some functional areas listed below could be unnecessary or included in the central animal facility:

- Space for administration, supervision and direction of the facility
- Staff quarters, showers, sinks, lockers and toilets
- Highly specialised laboratories (e.g. microsurgical operation theatres)
- Individual areas for premedication and preparation, surgery, intensive care, wake-up rooms, necropsy, behaviour testing, etc.
- Hazardous areas for special biological, chemical or radioactive agents
- Receiving and storage areas for food diets, bedding and cage equipment
- Washing area for cage equipment
- An autoclave for equipment and a disinfection chamber or pass-through box
- Area for holding soiled and unclean equipment and waste disposal
- Area for storing waste prior to incineration or removal (if necessary)

5.3 Operative Framework According to Accepted Standards

- Guide for the Care and Use of Laboratory Animals (8th Edition NRC 2011)
- EU Directive 2010/63 on the protection of animals used for scientific purposes
- AAALAC standards for accreditation
- National legislation and references (e.g. AVMA Panel on Euthanasia, etc.)

5.3.1 Temperature and Humidity Control

Air conditioning (AC) is a prerequisite for regulating environmental parameters for laboratory animal facilities. Temperature and humidity control is necessary to ensure laboratory animal well-being as well as to prevent variations due to changing climatic conditions. In general the AC

systems should be able to provide the following conditions throughout the year for rodents within the range of approximately 20–23° (69.8–73.4 F).

The relative humidity should be controllable within the range of 30–70 % throughout the year with a mean of 50–60 %. According to the geographical location of the facility, it is sometimes necessary to define a wider range (energy saving and technical options).

5.3.2 Ventilation and Room Pressurisation

Ventilation of the animal rooms and the rest of the facility is necessary to ensure a balance of air quality (remove CO_2 and NH^3, provide fresh air and O_2), animal comfort and energy efficiency to provide cage environments that optimise animal welfare and research efficiency.

The AC systems should provide a healthy and comfortable environment for researches and facility personnel. According to the number of animals, personnel and equipment used in the room 15–18 air changes per hour (ACH) are needed.

Ventilation with at least ten ACH is defined as minimum by AAALAC.

Pressurisation of the rooms with +50 Pascal for the prevention of contamination of the single animal rooms is often used as a safety measure. The animal room is then in positive pressure in relation to the inner floor (passage corridor) and the inner floor again in +50 Pascal overpressure to the exterior floor. This will ensure a pressure gradient (+150 Pascal overall) from the animal rooms to the inner corridor to the exterior and provide maximum protection against airborne contamination.

Heating, ventilating and air conditioning systems should be designed so that normal operation can be continued with a standby system. In brief, a 100 % redundancy is needed. The normal systems should run with 80 % (Security reserve additional capacity for weather extremes, etc.) and the second system has to back up the entire first system. The animal facility and human occupancy should be ventilated with a separated system.

5.3.3 Power and Lighting

The electrical system should provide appropriate lighting and sufficient number of power outlets with a matching power supply.

Lighting: dual light sources should be installed in all animal rooms. Both light sources are needed during working of animal technicians only. For the well-being of the animals, only one light source is needed.

The light intensity in the room should be 300–450 lx (measured 1 m above the floor). The light intensity in the animal cage is, depending on the cage material, much lower (ca. 60 lx). This will ensure that no negative effects, even for albinotic animals, are triggered by the lightning.

A time-controlled lighting system should be used to ensure a regular diurnal time/night cycle.

In general an emergency (standby power) system is needed for critical system components. For other systems a power backup emergency system (15 s start time) is needed. Ultrasonic light-dimming devices should be avoided, because they might create odious noises.

5.3.4 Noise Control + Vibration

The facility must be provided with noise-free or maximally noise-reduced environment. Noise control is a very important – *and still* underestimated – factor in the design and the construction of an animal facility. This starts with the selection of the material for walls and ceilings as well as the installation of plants and machinery (e.g. covered or vibration isolated like on a submarine!). No ultrasonic sources, e.g. for alarm systems! Rodents are able to hear in the ultrasonic range.

5.3.5 Animal Husbandry

The caging system is an important factor in the social and physical well-being of laboratory animals. The housing system has to provide adequate space according to species, the

size and number of animals as well as for the needs of the experiments. We must meet the needs of the laboratory animals regarding maintenance of body temperature, urination, defecation (in combination with bedding material) and reproduction:

- Provide easy and safe access to food and water from young to adult animals and provide adequate ventilation on cage level. Nowadays, cages are constructed from durable, sturdy materials such as polycarbonate, polysulphone, polyphenylsulphone or etherimed. Three principle cage designs are available, namely, open cages (US: static), filter top cages (micro-isolators) or as individually ventilated cages (Figs. 5.1, 5.2, 5.3 and 5.4).
- *Laws and Regulations*
  In order to meet all laws concerning an animal facility, the management should contact as early as possible the local authorities and discuss specific items directly. According to our experience, this is the easiest and safest

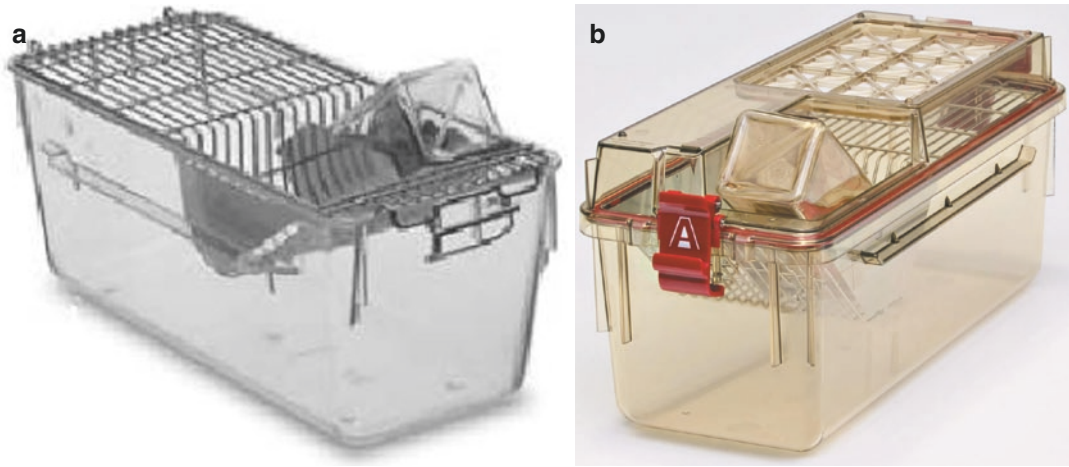

Fig. 5.1 (**a**) Euro-type 1 super long, Makrolon plastic, open cage, Tecniplast, Italy. (**b**) Euro-type 1 super long, polysulphone plastic, filter top, Allentown, USA

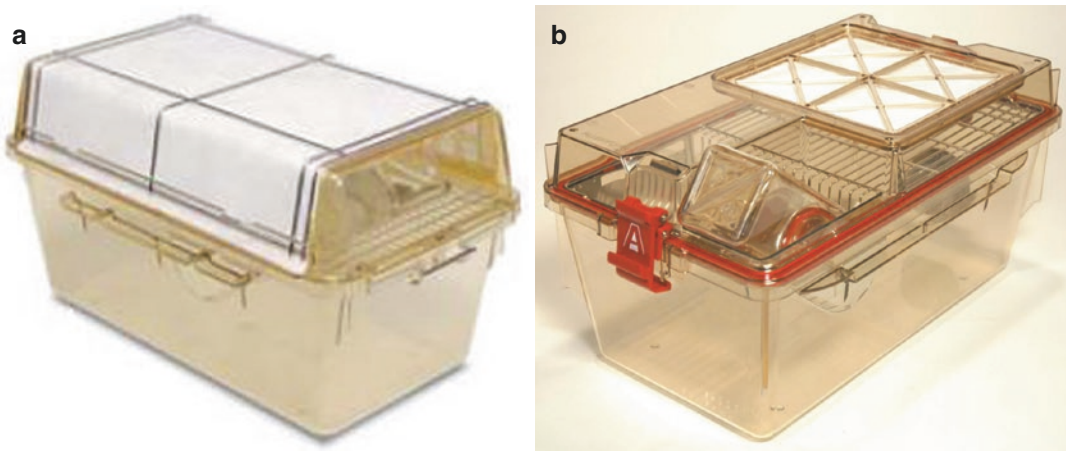

Fig. 5.2 (**a**) Euro-type 2 long cage, polysulfone plastic, filter top cage, Tecniplast, Italy. (**b**) Euro-type 2 long cage, polysulfone plastic, filter top cage, Allentown, USA

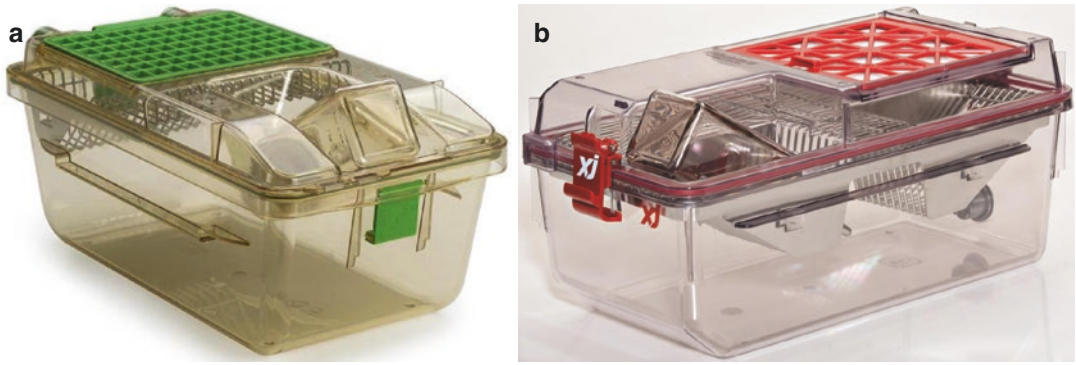

Fig. 5.3 (**a**) Green line cage, polysulfone plastic, individually ventilated cage, Tecniplast, Italy. (**b**) Allentown XJ cage, polysulfone plastic, individually ventilated cage, Allentown, USA

way to prevent costly mistakes and foster good communications and understanding between the parties. A brief description of some laws and regulations can be found in the references (e.g. laws regarding genetically modified organism, Animal Protection Act, Occupational Health and Safety Regulations, etc.).

5.3.6 Institutional Requirements (Diets, Water, etc.)

Many experimental purposes require using preconditioned animals especially for imaging. In most instances, protocol approval by the Institutional Animal Care and Use Committee (IACUC) or the responsible authorities before the start of the experimental procedure is required. This is particularly needed if the animal is restricted in the use of food or water or any other environmental deprivation like low oxygen tension, etc. Within this is intended.

5.3.7 Occupational Health and Safety of Personnel

Philip b. Crosby (born 1926), one of the pioneers in quality management, stated: "Quality begins with people not with things".

The selection of appropriate staff for the laboratory animal facility is the key component in the management of an animal facility. The other critical factor is the initial in-house training of staff at all levels. Within this training the "occupational health and safety programme" has to be trained to all personnel to become familiar. This is a continuous effort with annual refresher courses. Only through continuous training efforts the facility will be able to ensure a programme that is a life and does not only exist in written form. The programme has to establish and maintain, for example, chemical, biological, physical safety, safety equipment and "safe work practices" as well as "personal protective equipment". The programme should be reviewed periodically and adjusted to the facility and programme needs.

5.3.8 Animal Transport

The transport of laboratory animals from one place in the facility to another is very important and must be undertaken with care. Consideration for the transport of animals is according to factors like the mode of transport, the species (always only one species in one transport box), the transport container or cage, the animal density in the box, food and water during transport, protection from contamination from outside, protection of the environment if the animals are infectious as well as transport injuries and transport stress. Especially when being used for imaging purposes, the transport stress can have a major influence on the quality of the imaging

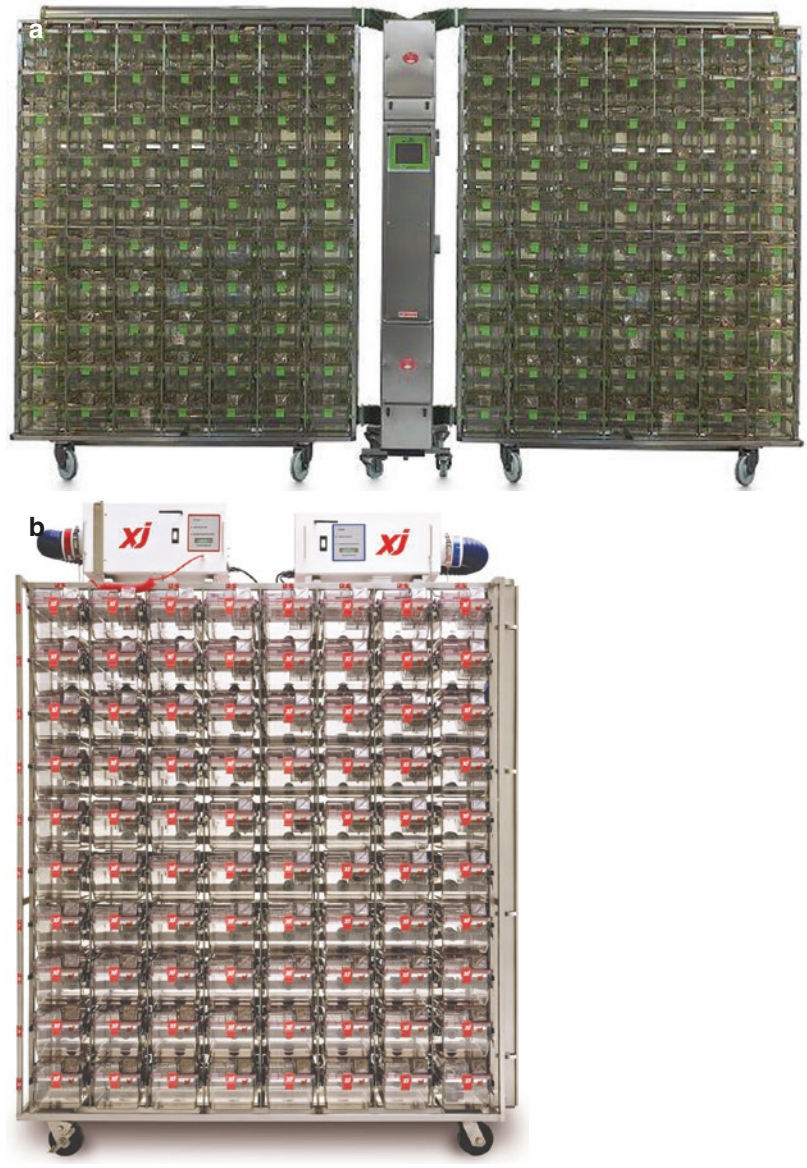

Fig. 5.4 (**a**) Individually ventilated cages, green line, polysulfone plastic, racks and ventilation unit, Tecniplast, Italy. (**b**) Individually ventilated cages, Allentown XJ system, polysulfone plastic, racks and ventilation unit, Allentown, USA

process or the quality of the data measured (e.g. transport stress, higher blood pressure and higher microcirculation!).

The mode of transport of animals depends also on the distance (in house, shipping to other locations) as well as seasonal and climatic conditions. To minimise the stress for the animals, special commercially available HEPA-filtered transport containers should be used with a special food (e.g. jelly food) to provide enough food and water during the transport period. Before starting the experiment or imaging, the animals should acclimatise at least 5–7 days to the new surroundings. Most countries have implemented special laws regarding the transport of living animals (the USA, Canada, European Community, etc.). For air transport the International Air Transport Association guidelines (IATA, www.iata.org) are

mandatory. Some countries, e.g. Great Britain, still require quarantine of animals after shipping from other countries before handing them over to the recipient.

5.4 Classifications of Rodents (Based on Microbiological Status)

Axenic (*germ-free*) – Animals completely free of all microorganisms.
- Bred, reared and maintained under sterile conditions (e.g. isolator).

Gnotobiotic – Animals with a defined microbial flora.
- Germ-free animals deliberately administered certain varieties of harmless bacteria to aid in digestion.
- Bred, reared and maintained under sterile conditions (e.g. isolator).

Specific pathogen-free (*SPF*) – Animals which are free of disease-causing microbes or pathogens.
- Founder animals of an SPF colony are caesarean derived.
- Bred, born, reared and maintained in environments which prevent exposure to or transmission of pathogens (e.g. barrier or individually ventilated cages, IVC).

Conventional – Animals with an undetermined microbiological status.
- Raised and maintained under standard conditions.

5.4.1 General Considerations for an Animal Facility

It is desirable to operate a central animal facility with several units (barriers) for different animals' species and different hygiene levels. The other options are several *smaller* units close to the laboratories (satellite facilities, multisite, de-centralised).

The animal facility has a core breeding unit (repository) in a *specific pathogen-free* (*SPF*) status. Specific pathogen-free is a term used for laboratory animals that are free of particular pathogens that are tested every 3 months according to specific recommendations (recommendations for the health monitoring of rodent and rabbit colonies in breeding and experimental units, FELASA Working Group on Health Monitoring of Rodent and Rabbit, Colonies: FELASA working group on revision of guidelines for health monitoring of rodents and rabbits, M Mähler (Convenor), Berard et al. (2014)).

It has to be always accompanied by a list of the tested and absent or found pathogens.

The health monitoring is assured through sentinel mice or investigating direct samples.

Analogous to the "canary in the coal mine", sentinel rodents monitor the pathogen status of investigators' or breeding rodents. A specific number of animals or cages are monitored by sentinel animals. It can be a section/area in a room or a rack that is monitored with two sentinel animals. Every time a rodent cage is changed (usually weekly), about a tablespoon of soiled bedding from that cage is transferred to the sentinel cage. In this way, sentinels are exposed to whatever pathogens may be present in the urine, faeces, fur, saliva, dander, etc. from 100 % of the cages on the rack. Because of this, investigator personnel are *not allowed to* handle or move sentinels or sentinel cages.

At the end of the monitoring period (usually one quarter or 12 weeks), the sentinels are sampled and tested for a specific list of infectious agents. Sentinels may be tested more or less frequently for selected pathogens or prior to shipping or experimental needs. Only when no pathogens on the list are found (*NO* positive results) the animals are specific pathogen-free.

To assure this hygienic level, in general no researcher has access to the core breeding unit. This minimises the risk of infection for this unit. Animals to this core are only transferred via embryo transfer. Embryo transfer refers to a step in the process whereby several embryos from donors (the transferred line) are placed into the uterus of a foster mouse with the intent to establish a pregnancy. By using this technique, it is possible to transfer a line with a minimal risk of bacterial or viral contamination to the barrier unit.

From the core breeding unit, the animals are then transferred according to the researcher's need to an experimental barrier, where several personnel have access to the animals. It is possible to have several units according to different hygienic levels or experimental needs. It is also possible to build one unit outside of the barrier. It is sometimes essential to transport animals within the building or between campus buildings in order to facilitate research. To ensure the integrity and well-being of the animals being transported into the imaging facility, a system has to be set up that will facilitate the research while minimising the risk of spreading a contaminant. Once the animals have left the barrier, they never go back to this unit. Following imaging, radiation, e.g. the animals are returned to a different unit or quarantine room.

Employing this one-way policy will minimise the risk of infections for animals in other units.

5.5 Housing of Animals

Animals can be housed in open caging, plastic "shoe box" cages from macrolone, polysulfone or etherimide plastic with stainless steel wire-bar lid. Additional items also include bedding, water bottle, food and cage card holder (See Figs. 5.1–5.4).

Open caging is the easiest way to house rodents, but there is a greater risk of contaminating the animals as well as causing allergies to the personnel. Currently the micro-isolator technique is a widely used system. In addition, there is a plastic top that holds a permeable filter. It is also possible to use individually ventilated cages (IVC) in general or for special procedures where the whole cage rack (and the cages in the rack) is separately ventilated with HEPA-filtered air and no connection with the outer space of the room. Each single cage is separately ventilated and maintained with a small overpressure to protect the animals inside. The inside of the cage, filter top, wire lid, water bottle, bedding and food is considered "clean", that is, free of particles which may contain disease-causing pathogens. The outside surfaces of the cage and top are potentially contaminated or "dirty". A transfer of animals is never performed "open" in the room.

For this purpose, the closed IVC cage is transferred to a cage changing station (CSS), a mobile microbiology safety cabinet. In this laminar air flow-protected environment, the IVC cage can be opened and animals can be transferred into the new, clean cage without contact to possible contaminated air or persons in the room.

After the experimental procedure or the imaging process, animals can be transferred into an IVC rack near the imaging facility or a special designated room in the facility. When there is a known risk of infection, a higher biosafety level (e.g. BSL-2), it is also possible to have these cages in a permanent negative pressure to ensure biosafety.

Bibliography

"Replacement of animal experiments, Reduction of animal experiments and Refinement of experiments" first described in 1959 by W.M.S. Russell and R.L. Burch (The Principles of Humane Experimental Technique).

Animal Welfare Act – 9 CFR Chapter 1, Subchapter A, Animal Welfare, USA.

Berard M, Feinstein R, Gallagher A, Illgen-Wilcke B, Pritchett-Corning K, Raspa M. Recommendations for the health monitoring of rodent and rabbit colonies in breeding and experimental units, FELASA Working Group on Health Monitoring of Rodent and Rabbit, Colonies: FELASA working group on revision of guidelines for health monitoring of rodents and rabbits: M Mähler (Convenor). Lab Anim. 2014;48(3):178–92.

Biosafety in microbiological and biomedical laboratories. 5th ed. HHS Publication No. (CDC). 2009. p. 21–1112.

Council Directive on the Approximation of Laws, Regulations and Administrative Provisions of the Member States Regarding the Protection of Animals Used for Experimental and Other Scientific Purposes. European Union (Directive 86/609/EEC). 1986.

CPCSEA Guidelines for Laboratory Animal Facility. Indian J Pharmacol. 2003;35:257–74. Special.

DIRECTIVE. 2010/63/EU OF THE EUROPEAN PARLIAMENT AND OF THE COUNCIL of 22 September 2010 on the protection of animals used for scientific purposes. European Commission. 2010.

Guide for the Care and Use of Agricultural Animals in Agricultural Research and Teaching, Federation of Animal Science Societies. First Revised Edition; 1999.

Guide for the Care and Use of Laboratory Animals. 8th ed. National Research Council, National Academy of Sciences; 2011.

Guide to the Care and Use of Experimental Animals, Canadian Council on Animal Care. Vol. 1, 1993.

GV-Solas gelbes Heft Tiergerechte Haltung: Labormäuse. http://www.gv-solas.de/auss/hal/maushaltung.pdf.

GV-SOLAS Gelbes HEFT Nr. 1: Planung, Struktur von Versuchstierbereichen tierexperimentell tätiger Institutionen. Hilken G, Haemisch A, Kluge R, Tolba R. 5. Auflage in Bearbeitung. www.gv-solas.de.

Occupational Health and Safety in the Care and Use of Research Animals. National Research Council, National Academy of Sciences; 1997.

Planning and designing research animal facilities. Hessler JR, Lehner NDM, editors. American College of Laboratory Animal Medicine Series, AP.

Statistical Considerations for Animal Imaging Studies

6

Hannes-Friedrich Ulbrich

Contents

H.-F. Ulbrich
Research and Clinical Sciences Statistics,
Bayer Pharma AG, Müllerstr. 178,
13353 Berlin, Germany
e-mail: hannes-friedrich.ulbrich@bayer.com

> If an experiment is well designed, it is relatively easy to get help with the statistical analysis; but if it is incorrectly designed, it may be impossible to extract any useful information from it. Festing (2000a, p. 191)

With or without help, designing an experiment is a challenging task for the experimenter. Based on some examples, crucial steps for designing animal imaging studies will be explained, accompanied by some hints for efficient study conduct and data evaluation.

Statistics provides such techniques and procedures; therefore, it can be seen as an essential component of empirical research, in biology as a whole as well as in animal imaging.

6.1 Design of Experiments in Animal Imaging

In order to separate the signal from the background noise, an experiment can be conducted. An experiment is understood as a procedure for collecting scientific data on the response to (effect of) an intervention. In this chapter, the terms experiment and study will be used synonymously describing controlled experi-

F. Kiessling et al. (eds.), *Small Animal Imaging*, DOI 10.1007/978-3-319-42202-2_6

Terminology

- Experiment – procedure for collecting scientific data on the response to (effect of) an intervention
- Experimental unit – the smallest unit to which an intervention can be assigned to independently of any other
- Intervention – the entire description of what an experimental unit is assigned to
- Observational unit – the smallest unit on which a response will be determined
- α – the (nominal) significance level
- $(1-\beta)$ – the (nominal) power
- Δ – the (relevant) difference of interest
- σ – standard deviation (square root of the variance)

ments as opposed to observational studies. Since observational studies (also named surveys) investigate mostly responses on preexisting "conditions," they are a kind of scientific investigation less likely to be performed as animal imaging study.

Experiments must be planned carefully and the planning process should be completed before the experiment begins. This planning should also include the statistical methods intended for assessing the results. Changes after the start of the experiment are indeed sometimes necessary; they shall be kept to an absolute minimum. Changes after the experiment has begun are usually very complex to implement and have statistical as well as credibility consequences to be considered carefully when changing the experimental plan. Therefore, along with the clear objective of the study, essentials of the experimental design shall be fixed in advance in a research plan or study protocol. The study plan shall be accessible for and understood by everybody (lab technician as well as researcher) involved in conducting the experiment.

Designing the experiment is one of the most important tasks during the planning phase. As stated by Festing (2002a, p. 191), "if an experiment is well designed, it is relatively easy to get help with the statistical analysis; but if it is incorrectly designed, it may be impossible to extract any useful information from it."

An experimental design is the manner in which the experimental units – most likely the individual animals in an animal imaging study – are arranged in accordance with the different interventions and the effects that are considered to influence the experiment. The principles of good experimental design are universal and have been known for more than 50 years (Cox 1958). Applying them to animal experiments and animal imaging experiments, in particular, requires some additional thoughts.

6.2 Comparing Interventions

Example 1: "treatment" vs. "control" Arguably, the simplest design is to work with two groups – "treatment" and (vehicle) "control" as the interventions – measuring the response (e.g., diameter of a lesion) of each group member once; the difference between the average group responses shall be the effect of interest. There will always be variability between the responses of the members of each group. Taking this variability into account, the difference between the groups can be used to determine whether the disparity between groups is a real one. If this difference is not completely obvious, statistical analysis (e.g., Student's *t*-test) has to be employed. The objective of that experiment shall be to show the superiority of the treatment over vehicle control.

Even in that simple case, the following conditions must be clearly established before the experiment gets started:

1. How certain has the result to be (rather confirmation or exploration, delivering test results or estimations)?
2. What are the different interventions of interest?
3. What will be measured – once or repeatedly – to assess the results of the experiment (identification of experimental units, measurement schedule, to be measured items)?

4. What results are to be expected under the different interventions (determination of experimental variation, their different sources, how to limit it or allow for it in a fair manner)?
5. How can the experiment be organized and conducted that most information is obtainable from the resources used?
6. How large will the experiment be (the "right" number of experimental units – neither too much nor too few – taking scientific and ethical considerations into account)?
7. How will the results be analyzed, again to gain as much information as possible?

If based on profound prior information, e.g., in a later stage of development, an experiment is planned to confirm that "treatment" is really superior to "control," then null hypothesis, alternative hypothesis, as well as the (biological) relevant difference Δ between the populations' average responses are known beforehand. The researcher is familiar with the amount of biological (among animals) and measurement variability for each group. So, let us assume that this total variability σ is equal for each group. The groups in the experiment are expected to be samples from the respective populations. The test statistic (e.g., Student's *t*-test) to be used for deciding the relevant question has been fixed.

It is now the researcher's obligation to decide on both the significance level (the nominal α-level) and the power (1-β) for the intended test statistic. The significance level α indicates the likelihood that the two groups will be found to be different, although there is no difference between the respective populations. Therefore, the significance level has to be sufficiently low (common values are 5 or 1 %, meaning that if there were 100 experiments done with samples from populations without any difference, five or one, respectively, of these experiments would show a significant result – just by chance alone).

Statistical power (1-β) states how large the likelihood has to be that we correctly reject the null hypothesis (in favor of the alternative one is aiming for) with the intended significance level α (as above) if the distance between the underlying populations is equal to the (biological) relevant difference Δ. The power has to be set by the researcher. A power of let say 80 % tells us that eight of ten experiments done with samples from populations different by the (biological) relevant difference will let us reject the null hypotheses at the preset significance level α. (Two out of ten potential experiments will fail to show a significant result.)

For confirmatory experiments α and (1-β) are clearly the measures for how certain the results have to be. With a chosen test statistic and the decisions made how large α, (1-β), Δ, and σ shall be, the size of this experiment (sample size) can be determined (see below).

As long as Δ and σ are not yet known (e.g., in earlier stages of development), experiments are rather of exploratory than confirmatory nature. Exploratory analysis is an approach to analyzing data for the purpose of suggesting (new) hypotheses about the causes of observed phenomena, assessing assumptions on which statistical data modeling and evaluation will be based as well as providing a better basis for further data collection through experiments. An exploratory approach, therefore, should collect evidence for more specific hypotheses to be followed during further research and development.

Example 2: two different treatments Let us imagine a slight change, instead of testing "treatment" against (vehicle) "control," one might be interested in comparing two absolutely new substances called *A* and *B* for the purpose of getting information on whether the one or the other is more promising for further development. Since this will be the first experiment with interventions applying *A* and *B*, nothing is known in advance on whether *A* is better than *B* or vice versa, nothing on the variability σ let alone a difference Δ considered to be relevant.

Rather than comparing *A* and *B* by using a statistical test, an estimate of the difference μ between *A* and *B* should be derived along with an appropriate (1-α) confidence interval, (1-α) conventionally being 95 or 99 %.

Beyond comparing different substances, the interventions of interest in an experiment comparing *A* with *B* might also be:

- Low dose of substance X (*A*) – high dose of substance X (*B*)
- Once per day application (*A*) – twice per day application (*B*) of the same substance X and dose
- Once per day application of a full dose (*A*) – twice per day application (*B*) of half the full dose of the same substance X

If, for example, contrast media (CM) were used and an interaction between CM and substance X (drug–contrast medium interaction as a special case of drug–drug interaction) could not be excluded, then the interventions *A* and *B* might actually become:

- Low dose of X under CM (*A*) – high dose of X under CM (*B*)

Whatever the results of the latter comparison, conclusions drawn from such an experiment are valid only for the combination of X and CM as applied; whether the observed differences between *A* and *B* are the same as would have been between low and high dose of X alone is beyond the results of this particular experiment.

While comparing devices and/or specific adjustments of the same technical device (e.g., different scanning modes), interventions *A* and *B* translate to two different device adjustments.

Example 3: more than two treatments Let us again change the above experiment a little and extend it by some more substances of interest, making it a comparison of four interventions called (by substances used) *A*, *B*, *C*, and *D*. Here, a lot of different questions might be of interest, e.g.:

- Are there any differences at all between the interventions *A* to *D*?
- Are there any pairwise differences – between *A* and *B*, or *A* and *C*, or *A* and *D*, or *B* and *C*, or *B* and *D*, or *C* and *D*?
- Are there any differences between a particular (reference) intervention, say, *D* and any of the others?

In each case a different number of questions is to be addressed – one, six, or three, respectively – by the otherwise same experimental setting.

In each of the abovementioned examples, it is assumed that an animal within the experiment belongs to exactly one particular intervention group and that an animal's response to the intervention is measured once. The measurements are independent of each other; each animal serves as both experimental and observational unit.

Neither this independence nor the unity of experimental and observational unit has always to be the case.

Example 4: intraindividual differences, more observational than experimental units The following three experiments explore the effect of one and only one intervention by measuring each animal twice in either of the following manners:

(4a) Before and after the intervention – the animal is measured at two distinct time points.
(4b) Both an area of interest (say, tumor) and an appropriately chosen reference area (tumor-free) – the animal is measured twice at the same time point, but on two different locations.
(4c) Both an area of interest (say, tumor) and an appropriately chosen reference area (tumor-free) – as in 4b but the animal being completely scanned, area of interest and reference area measured by defining them as part of one and the same picture or sequence.

The different animals in the experiment are still independent of each other; the two measurements taken from the same animal are not. Each animal is an experimental unit, each animal's measurement time (*4a*) or location (*4b*, *4c*) an observational unit (regardless of how many variables are actually to be measured, how many values therefore to be taken).

These experiments are one-group experiments where the experimenter is interested in whether the intraindividual differences are merely in favor of the intervention.

6.3 Measuring the Desired Effect: Definition of Endpoints

Comparison of interventions "better," "worse," or even "different" does not have any meaning without the reference to a (biologically) meaningful endpoint, a quantity measured, a property or characteristic determined, or a value derived from a combination of the former. Measurable quantities might be the length, width, height, or body temperature of an animal; the animal's sex can be determined; and the tumor volume can be derived from its length, width, and depth. For mammals, only sex seems to be well defined, all others need further specification.

Example 5: Endpoint specification Let us consider Beagle dogs to be the experimental animal; the following endpoints determined for each animal might be of interest in the experiment:

- Length: from the tip of the nose to base of the tail, i.e., excluding the tail and (hind) legs
- Width: hip width – as distinguished from the shoulder width or maximum overall width
- Height: height of the withers
- Body temperature: taken in the ear – as opposed to taken in the mouth or the anus

Since not directly measurable, some quantities might be derived:

- Tumor volume: calculated as
  $(\pi/6) \cdot length \cdot width \cdot height$
  assuming the shape of an ellipsoid – rather than assuming a rectangular prism
  $length \cdot width \cdot height$
- Tumor volume (if the height/depth was not easily measurable): calculated as
  $(\pi/6) \cdot length \cdot width^2$
  assuming the shape of an ellipsoid and height to be equal to width of the tumor
- Lesion area: circumscribing the lesion at a monitor, the value then be given by the machine

Since different measurement devices (carpenter's rule vs. Vernier caliper; different CT scanner modes) as well as different measurement points (ear or anus body temperature) and different biological conditions (calmness or stress; different moments of the day) affect the values obtained, consistent endpoint definition includes the specification of the measurement devices and their parameters, measurement areas, and time points of reading, among others.

Defining an endpoint less precisely than possible does make an experiment less conclusive by adding to the noise or generating bias (see below).

For each endpoint, one has to know its type:

- Nominal – values are clearly distinct categories without any internal order, e.g., colors like black, red, and green or gender
- Ordinal – values are distinct categories that can be (completely) ordered from low to high, e.g., quality of a signal: very poor, poor, moderate, good, very good
- Cardinal – counts, i.e., nonnegative integer numbers, e.g., number of liver lesions
- Interval scaled – continuous measurable quantities for which the precision of the measurement is an important issue, e.g., height (measured in mm or inch or any other unit of length)

The type of the endpoint is an important parameter for deciding on an appropriate statistical evaluation strategy: starting with an adequate data description (e.g., rates, proportions, medians and interquartile ranges, means, and standard deviations), useful graphs (e.g., pie charts, bar charts or histograms, box plots), appropriate tests of significance (e.g., χ^2-tests for contingency tables, *t*-tests, or ANOVA for Gaussian distributed data), and regression models (like logistic regression or multivariate linear regression).

The answer to the question whether interval-scaled variables can be fairly well described by a Gaussian ("normal") distribution has a deep impact on the abovementioned decision as well. The body length of adult animals of either sex (but not for both sexes together!) is a good example where a Gaussian distribution can be assumed. For others: if there is no published consensus on the matter, deciding if the data can be described by a particular distribution can be a problem. Transforming the data (e.g., by a log transformation, see Keene 1995) might be an option.

The answer to the question is also important for sample size estimation.

6.4 Sources of Variability

Variability of all biological phenomena is a major cause of the complexity of biological experiments. Animals are different even within the range of the same species.

Avoiding as much variability as possible is certainly a good way to increase the signal-to-noise ratio.

Genetically, monozygotic littermates are more similar to each other than dizygotic, which are more similar than the offspring of two different dams. Animals of the same strain but different breeders might be more different than animals of the same breeder. Animals of different ages – especially juveniles – are likely to be more diverse than ones of the same age. Since the body weight of male as well as female juveniles is highly correlated with age, it can be concluded that juveniles of the same sex and weight are more similar to each other than juveniles of either different sex or weight.

Differences in the animals' *environment* before and during the experiment might make them more or less similar. Different feeding schemes or diets during upbringing, different cages in multianimal caging conditions, and different locations of cages within stables (leading to different microclimate conditions: light, temperature, draft, frequency of human contact) are likely to cause additional variability among animals.

Any *measurement procedure* itself carries more or less variability. This variability might be caused by the device, device parameters differently set, the experimenter's ability to handle the device, her or his ability to handle the animals, or the experimenter's reading. In animal imaging studies, anesthetization of the animal, the animal's position toward a scanner, and chosen reference areas for background signal measurement are important sources of (undesired) variability.

If each specific variability is fairly spread over all animals and measurement occasions during the experiment, it simply adds up to the overall noise impairing the signal-to-noise ratio. Otherwise, variability might be related to bias.

6.5 Avoiding Bias

Example 6: Assessment bias Consider an experiment comparing a traditional treatment scheme (intervention *A*) with a new one (*B*) developed and proposed by the experimenter himself/herself. The number of clearly visible lesions (within a specific organ) was chosen as primary endpoint; the less the number of lesions, the better the treatment scheme. The experimenter's decision whether to consider a lesion as clearly visible might subconsciously be associated with the interest to show the superiority of the new scheme; the decision might no longer be inherently fair for both interventions. The change in results (number of lesions recorded) caused by the subjective element to assessing observations leads to bias – this particular bias is called assessment bias.

Any systematic difference between intervention groups apart from the intervention itself might cause the experiment's results to be biased, e.g.:

- Heavier animals allocated to a particular intervention group – allocation bias
- Different devices (or device modes) used for measuring different groups
- Different animal housing conditions (climate, light, multicaging conditions) for different groups

- Different observers (e.g., lab technicians of different expertise) for different groups – observer bias
- Different times of the day for measuring different groups

Being aware of the potential bias while designing the experiment helps avoiding it.

In animal imaging studies, assessment bias might be important. Arguably, the best idea to prevent assessment bias is to keep the observer "blind" toward the intervention group an animal belongs to. This might be accomplished by:

- Different individuals as facilitator (handling and treating the animals) and observer (taking the measurements)
- Identification of the animals by a haphazard numbering scheme not known to the observer
- Letting the observer see the animals for inspection in random order

6.6 Blocking

There is another important way to increase by design the signal-to-noise ratio of an experiment: blocking. By blocking, one splits the animals into homogeneous subsets in such a way that variation within each subset is considerably lower than variation between subsets.

Example 7: Blocking by sex While designing an animal experiment, it is always recommended to think about potentially different responses by animals of different sex. Such differences might be caused by the body size or hormone configuration or some other trait different between the sexes. Splitting the experiment virtually into two otherwise completely identical – one based on the females, the other based on the males – would make the experiment one with block design.

Complete blocking means splitting the experiment in such a way that within each block all the interventions take place, while one and the same animal number ratio between the interventions is maintained.

Example 8: Complete blocking by sex and weight and breeder Let us consider an experiment where the experimenter wants to get more information on the new intervention *A* as compared to the well-known intervention *B* by planning one and a half as much animals for *A* as for *B*, a three to two animal number ratio between interventions is needed. For scientific reasons, the experiment has to be a large one, based on more animals than one breeder can supply by a certain date. It is assumed that the interventions themselves might affect heavier animals less than lighter ones, supposedly females will react (slightly) differently from males.

Since one and a half as many animals are planned for *A* as compared to *B*, the smallest possible block size is five animals. Therefore, each block has to have a size of a multiple of five. Blocking then might look like Table 6.1.

6.7 Dropouts

An animal not adhering to its appointed intervention any longer is called a dropout. Leaving the experiment prematurely might happen for quite different reasons, e.g.:

- Death (without or with – in multianimal caging – cannibalism)
- Escape
- Infection
- Premature stop of intervention for animal welfare reasons (e.g., an observed tumor volume of *2000* mm^3 or above, like in Hanfelt 1997, p 298)
- Early sacrifices (e.g., every other animal after half experiment time for histological examination)

Early sacrifices can and shall be planned in full – including the consequences for sample size and evaluation. Escaping an unlocked cage hopefully never happens; nevertheless, it is the only one of the above examples that might be considered as completely independent of the intervention. Loosing animals that way is a waste of resources, anyway.

Table 6.1 Complete blocking by weight and sex and breeder

Block 1	5 heaviest *female* animals of *breeder 1*
...	
Block n_1	5 lightest female animals of breeder 1
Block (n_1+1)	5 heaviest *male* animals of breeder 1
...	
Block (n_1+n_2)	5 lightest male animals of breeder 1
Block (n_1+n_2+1)	5 heaviest *female* animals of *breeder 2*
...	

All other examples given must be thought of as potentially intervention related and, therefore, likely to generate bias, i.e., causing an unjust change in observed effect(s). Having to take out animals for welfare reasons has to be considered like any other premature termination while designing the experiment. Besides recording the dropout time (and reason), any measurement to be taken (e.g., body weight and histological examination) has to be decided on during the design phase.

Example 9: Design with dropout Intervention *A* shall be the placebo in a xenograft experiment to compare different doses of a novel substance (say, interventions *B*, *C*, *D*, and *E* being increasing doses) for inhibition of tumor growth by limiting angiogenesis. Substances will be applied on day 0, and animals will be checked daily for body weight and tumor length and width by an experienced lab technician; every seventh day up to day 28, the animals have to undergo an imaging procedure for measuring angiogenesis and tumor volume. Midterm, on day 14, after the imaging procedure, one third of the animals shall be sacrificed for histological examination. All others are to be histologically examined after day 28.

It is expected for certain that animals of the placebo group have to be taken out earlier because of unbearable tumor load, *2000 mm*^{3} being set as the limit. Nobody knows when this will happen to the first animal or whether this will affect any animal of the interventions *B* to *E*.

The study protocol has to make clear how the tumor volume is to be determined from length and width (as taken daily by the lab technician), who is responsible for the calculations and the timely decision, and whether to stop the experiment for that particular animal. It has to be decided who takes this responsibility for the days when the main lab technician will not be available because of weekends, holidays, or sick leave.

Furthermore, it has to be defined what happens to an animal reaching the tumor burden limit on a day without scheduled imaging procedure (say, on day 6) – to be imaged or not before leaving is here a decent question. And what about the histological examination?

It is extremely important to have the animals foreseen for midterm sacrifices identified before the experiment actually begins. Although it might sound appealing to some, sacrificing on day 14 merely animals with already larger tumor volumes (and therefore more likely to be excluded the following days) would generate bias – most probably of a quite remarkable amount. This has to be avoided.

6.8 Regression, Repeated Measures, Experimental Units, and Other Topics

Example 9 (Continued): Another Look Intervention *A* more precisely defined as vehicle control might be considered as a treatment with a dose of 0 units of the new substance. Such an experiment can be planned not only for comparing the different doses to the control but also for establishing a dose–response relationship by fitting a regression model. The type of the regression (linear or nonlinear, e.g., logistic) suitable depends on a lot of additional knowledge or assumptions like the type of the response variable and monotonicity of responses – to name a few.

Example 9 (continued) – Yet another look As stated in the study protocol, each animal has to be repeatedly examined – daily (starting on day 0) for body weight and tumor volume and weekly by the expensive (device availability and cost of use) and animal stressing (anesthesia) imaging procedure. Let us suppose the tumor volume deter-

Check Box: Designing an Experiment in Animal Imaging

First and foremost, a clear objective must be defined. The following is a (nonexhaustive) list of intertwined questions to be considered in designing an animal imaging experiment:

- Shall the experiment be designed in collaboration between experimenter and (bio) statistician in plenty of time before the experiment starts?
- What is the main (biological) effect of interest? Are there any secondary effects to be considered as well?
- Is the experiment part of either exploratory or confirmatory research?
- What tentative design supports the main question (randomized group comparison, intraindividual comparison, more advanced or specialized designs, etc.)?
- How is the experimental unit defined (e.g., species, strain, knockout, immune deficient, sex, etc.)?
- What quantities shall describe the desired effect(s) – the primary (and further) endpoint(s)?
- What are the measurable quantities and how do they relate (e.g., by judging them using a score or by using a particular mathematical formula) to the quantities describing the effect?
- Measurement schedule (and observational unit) – what measurements are to be carried out, when, how often, by how many observers?
- Will the observers be "blind" regarding the intervention each particular experimental unit undergoes?
- What are the major sources of to-be-expected variability (animals, measurement devices, observers, environment, etc.)?
- What measures can and will be taken to limit any of these variabilities (single strain, unisex, single observer, etc.)? What's not feasible?
- How are the different interventions defined? What are the relations between them (e.g., doses equidistant on logarithmic scale)?
- How is it assured that the environment conditions (i.e., all conditions besides the intervention itself) are kept equal for each experimental unit during the whole experiment?
- How are the data to be collected, kept, and checked for plausibility?
- How shall the endpoint(s) be summarized within each intervention?
- How can the overall effect be expressed in comparative terms between interventions (signal)?
- What, if any, is the minimum magnitude of the signal one is interested in?
- Assigning the experimental units – is there any blocking factor (necessary)?
- What, if any, is the likely drop-out rate; might it be intervention specific?
- How many experimental units (animals) are needed – overall, per intervention – taking into account the to-be-expected drop-out rate and pattern?
- How will the animals be randomized (allocated) to the different interventions?
- What kind of graphical technique (scatter plot, box plot, etc.) will be used to support:
  - Checking the raw data
  - Presenting the (main) results
- What kind of statistical procedures will eventually be used for data evaluation?
- Checking the assumption(s) for the chosen statistical evaluation strategy – will it be done at all, how, and to what consequences?

Wanting the results to be published, the following topics (likely to be requested by the editors) might also be of interest from the beginning:

- How to describe the used statistical methods (especially if uncommon methods were to be used)? What references are needed?
- How to describe design changes – if there were any unavoidable – and checking procedures related to the chosen statistical evaluation strategy?

mined by the imaging procedure is the experiment's primary endpoint. Then one gets up to five measurements (on day 0, 7, 14, 21, 28) per animal. Although this approach increases the number of measurement values remarkably for each intervention group, it does not increase the number of experimental units; values taken of the same animal cannot be considered independent of each other (as values of different animal are). The use of a significance test based on the assumption of independent experimental units (like *t*-tests, U-tests, or classical ANOVA) would be inappropriate here. The observational unit here would be each animal's daily check, whereupon values on the primary endpoint (volume determined by imaging) are only to be taken at some of them.

The proper identification of the experimental unit is a crucial issue for the validity of both the chosen design and the related statistical evaluation strategy.

Rodents are highly social animals. Therefore, (moderate) multianimal caging might be considered for preventing the animals from isolation (and the stress caused by crowding) for a long-term experiment. Since multianimal caging influences the single animal's stress level and body weight, animals within the same cage can rarely be considered as independent to each other. The cage becomes the experimental unit – with consequences on sample sizes, drop-out patterns, and statistical evaluation strategy.

The normal biological diurnal rhythms of an animal's biochemistry and physiology alter its responses depending on the time of day that treatments are applied, samples are taken, or an anesthesia is administered before imaging.

Example 10: Time of the day as a potential for bias Imagine an experiment on tumor vascularization where always starting at seven in the morning all animals of intervention *A* will be imaged, followed by *B*, *C*, *D*, and finally *E*. All the animals of intervention *E* are imaged late in the afternoon. Whatever the interactions of the circadian rhythm and the interventions are, such a design does not level them out fairly. It is, therefore, recommended to think about alternatives such as a random order of animals. On the other hand, if a sequence that is too complicated to be handled correctly makes the whole process error-prone, one should rather apply a less complicated order.

Example 11: A warning Occasionally, experiments are conducted under multianimal caging conditions without single animal identification. If there were only one observational unit (measurement time point) per animal, the experiment could still be well designed taking advantage from the unity of observational and experimental unit.

A similar experiment where animals are to be measured on more than one occasion would be questionable by design, since intraindividual changes over time (see example *4a*) are not determinable. The cage would be the observational unit and, therefore, the experimental unit as well, a scenario likely to be less efficient with regard to the number of animals to be included.

6.9 Measurement Schedules

Animals have a circadian rhythm, and humans as creatures have it as well. Beyond that, as social beings, most humans are used to living according to a hebdomadal rhythm. This has to be considered as an additional challenge for the design of experiments lasting several days or even weeks. Daily examination means including weekends and holidays.

Example 12: Tumor doubling time and weekend measurements Imagine an experiment with (non-shrinking) tumors and tumor doubling time (the time it takes the tumor from observation start to grow to twice its volume) as primary endpoint. Precision of time measurement shall be 1 day. It is quite a natural choice to evaluate tumor doubling times by a time-to-event analysis. Not determining the tumor volume on weekends would mean that Monday's reading finds tumors that already had doubled their volume either by Saturday, Sunday, or Monday. Since it is not possible to decide, which tumors had doubled by

Saturday, Sunday, or Monday, respectively, the actual time measurement precision is three (!) days (instead of the intended one).

For any time-to-event analysis, time measurement precision is of particular importance. Sometimes a biweekly measurement (e.g., on Monday evenings and Friday mornings for measures not influenced by any circadian rhythm) might be sufficient and the best choice – having only one observer (lab technician) involved.

6.10 Animal Allocation and Randomization

> Designing an experiment is like gambling with the devil: only a random strategy can defeat all his betting systems. RA Fisher (quoted in Box et al. 2005)

Randomized experimentation is not haphazard. Randomized allocation of animals (or, more generally, experimental units) to the different interventions should be based on random digits generated by a (pseudo-)random number generator. Random digits can be found in Machin et al. (2009, p. 300). In simpler cases tossing a fair die or (for a two-intervention experiment with equal group size) a coin can be used. More complex cases can be addressed by using software, although there seems to be no randomization software covering all possible designs. SAS® proc PLAN might be a good start; for a list of available randomization software, see Bland (2014).

Without a true random process as independent basis, animal allocation is prone to bias. Except for random deviances, randomization balances groups with respect to all factors other than intervention. Differences between the responses are, therefore, due to the different interventions. Complete randomization would be a valid option, but with the risk of ending up with only roughly the intended number of animals per group. Blocked randomization is a better choice since it balances the animals within each block as intended. Blocked randomization is a natural complement for blocked designs (see above), covering also in the simplest case: a whole experiment understood as one block.

6.11 Sample Size Estimation

> The goal of estimating sample size in the planning of experiments is not specifically to reduce the number of animals used in the experiment. Rather, it is to estimate the minimum number of animals required to accomplish the research goals (i.e., to reliably determine whether an important effect exists). Khamis (1997, p. 55)

Sample size – in case of an animal imaging experiment, the number of animals needed for the experiment – has to be decided on before the experiment starts.

Two main strategies for determining sample size have been described (Festing and Altman 2002): one often labeled *resource equation method* (REM) and the other *power analysis* method.

For determining the sample size by the power analysis method, one has to have chosen a design and the primary endpoint. Depending on the design, the intended ratios between the sample sizes for each group have to be set. One has to know the relevant difference Δ considered to be what Khamis calls the "important effect" and the to-be-expected variability σ. Both the intended significance level α and power $(1-\beta)$ must be fixed. The sample size necessary for the experiment can then be estimated by using either tabulated values (like in Machin et al. 2009), published sample size formulas (like in Horn and Vollandt 1999), or specialized software like SAS® proc POWER or nQuery Advisor®.

Example 12: Sample size for a one-sided t-test Let us consider a two-group comparison for a Gaussian distributed endpoint by assuming the same variability within both groups. Both groups shall have the same number of animals (sample size ratio = 1). The comparison could then be conducted by using Student's *t*-test. Suppose intervention *A* would give a mean response of 12 units and one were interested if intervention *B* could increase the response up to 20 units, for both interventions a (within-group) variability (standard deviation) of $\sigma = 8$ units can be realistically assumed based on prior

Table 6.2 Sample size for a one-sided *t*-test

	A	*B*	Effect Δ	Standard deviation σ	Effect size δ	Significance level α	Power $(1-\beta)$	*n* per group
As described	12	20	8	8	1	0.05	80	14
Increased power	12	20	8	8	1	0.05	90	18
Lower significance level	12	20	8	8	1	0.01	80	22
Smaller effect Δ	12	16	4	8	0.5	0.05	80	51
Larger variability	12	20	8	16	0.5	0.05	80	51

knowledge. Then the effect of interest Δ would become $\Delta = \mu_B - \mu_A = 20 - 12 = 8$ units, an effect of the same size as the standard deviation $\sigma = 8$ units (commonly expressed as an effect size of $\delta = 1$). Asking for a nominal power $(1-\beta)$ of 80 % and a nominal significance level α of 5 % for groups of the same size would give a minimum of 14 animals per group, i.e., 28 animals overall. Some alterations of the request can be found in Table 6.2.

As one can see, increasing power, lowering significance level, an increased variability, or a smaller effect of interest requires larger sample sizes.

If dropout has to be assumed for the experiment, the sample size has to be increased by the reciprocal of the anticipated drop-out rate.

It might be most common to have all groups of the same size (all sample size ratios being one), but for many-to-one comparisons (two or more different interventions all compared to one control), a larger number of animals for the control group might be advisable (Horn and Vollandt 1999, p. 36).

Compared with the power analysis, the REM is simple but quite crude. The REM depends on the law of diminishing returns and is based on the suggestion of Mead (1988, p. 587). One has to know the number of different interventions (*T*), the number of blocks (*B*), and a third number *E* recommended by Mead to be between 10 and 20 representing the variability. The number of animals needed should be calculated by $N = (T-1) + (B-1) + E + 1$. Dividing *N* by the number of interventions might give a noninteger number to be allocated to each group. These noninteger should be rounded up.

Before applying this approach, it might be useful to consider that REM-based sample size estimations remain the same regardless of any changes in:

- Desired significance level
- Intended power of the experiment
- Variability
- Desired important effect to be shown

Therefore, it might be worthwhile to compare REM-based sample size estimations with power analysis ones even in cases when the latter can be based only on very weak assumptions on relevant difference Δ or expected variability σ.

Sample sizes determined have to be checked for compliance with any legal and animal welfare regulations (e.g., Australian Government 2008), available facilities, and costs before actually starting the experiment. "The number of animals used in an experiment should be the minimum sufficient to answer the question posed" (NC3RS 2013).

6.12 Study Design and Research Plan

Whatever the decisions on the particular design issues are, all of them shall be addressed in the research plan (study protocol).

Many of the aforementioned issues might be difficult to decide on. It is always a good start to check the literature for similar experiments and the design used, effect and variability estimates, as well as any hints about the difficulties of using that design.

Depending on the particular scientific question, there are some recommendations worthwhile to consider on how to deal with factors that might have influence but one is not interested in:

- Leave out factors by keeping them constant, if possible, e.g., a male-only experiment, based on the same number of animals, is likely to show an effect more clearly – if there is one – than a mixed male–female experiment.
- If one cannot leave a factor out, block for it, if the factor is measurable before the experiment starts.
- Randomize the experiment, randomize in blocks, and describe exactly in advance how animals will be randomized.
- Decide on an adequate sample size, i.e., taking into account the experiment's objective, resources needed, and lab animal welfare.

In principle, a well-designed experiment has to be repeatable under exactly the same (as well as modified) conditions. The conditions are set in the research plan. Every experiment is to more or lesser extent prone to both error (e.g., application of the wrong substance) and unforeseeable incidents (e.g., animals catching or already bearing an infection).

Design as complex as necessary, as simple as possible.

Depending on experience and prior knowledge as well as the complexity of the intended experiment, developing the appropriate design takes considerable time.

The more complex the design (and therefore the experiment), the more consulting a biostatistician *during* design phase is recommended.

6.13 Practical Considerations for Conduct and Evaluation of Experiments in Animal Imaging

6.13.1 Data Structure

Setting up the experiment logistics shall include the development of an appropriate data structure. Valuable criteria for appropriateness, besides the self-evident correctness, are convenience for data input and usefulness for statistical evaluation.

Each record (row in a data table) has to be unequivocally identified (by animal number, time point of measurement, etc.).

Convenience for data input during study conduct inhibits the error rate. Codes instead of lengthier text entries support transparency of data handling. Entering the data in the same sequence as the measurements are to be taken prevents from assignment mistakes; eventually the unequivocally identified records can be reordered by any sorting procedure.

Since it is always possible that a measurement cannot be taken (because of measurement device failure or early drop-out), codes have to be foreseen for "missing" values. (A period [.] is usually a better choice than a particular number like 0 or −9 because it cannot be confused with a valid value while generating means or the like.)

Usually there is more than one possibility to structure data of a particular experiment correctly. Transforming data from one into another structure is possible but laborious. Depending on the statistical evaluation strategy and the statistics software intended for use, there are more as well as less favorable among all available data structures.

For both data clarity and smooth transfer into statistics software, it is strongly recommended to keep the raw data (measured data and record identification) separate from any evaluation such as means, counts, or graphs. Using a spreadsheet program, this can simply be accomplished by reserving one sheet for the raw data alone; graphs and means (and virtual copies of the raw data) can then be compiled in any other sheet by referencing to the raw data sheet.

6.13.2 Document the Unexpected

While conducting an experiment, it is always possible to encounter a situation not foreseen in the planning phase: allocation errors might occur; animals might react strangely, get eczema, or move because of premature recovery from anesthesia. It is recommended to document these events immediately, since they might occur again and become a remarkable (interesting although unwanted) result of the experiment.

6.13.3 Changes in Study Design

If the number of unexpected occurrences increases, one might be inclined to change the study design. In general that is not recommended. During the experiment there is no time for either sound analysis of reasons for the unexpected or solid redesign. Changes must be documented in both the study plan and the report. Taking the efforts of the design stage into account, it is clear that changes must be the exception, not the rule, because they are complex to implement, have statistical consequences requiring careful consideration, and may have an impact on the credibility of results, as it is difficult to prove that a change has not been made to favor the results hoped for by researchers (see assessment bias).

Almost certainly it is better to conduct the well-designed experiment as planned to get as consistent as possible information including about what went wrong than to end up with a lot of information generated under no repeatable conditions.

6.14 Statistical Evaluation of Animal Imaging Experiments

Results of an experiment should be assessed by an appropriate statistical analysis reflecting the purpose of the experiment, even if in some cases the results of the experiment appear to be so clear-cut that they seem obvious (in either or the other direction).

Evaluating the animal imaging experiment should be quite easy if the experiment was well planned, the data adequately recorded, and the experiment went fully according to that plan without any unexpected irregularities.

Any analysis shall begin with examining the raw data (as well as the data derived by a formula) for consistency, easily and most efficiently performed by using graphical methods.

6.15 Outliers

Looking at the data, one might find some data points outside the range of prior expectation and, therefore, be tempted to declare them "outlier." Simply excluding them is a high-handed step; it reduces the number of valid values and is likely to change the effect (by generating bias) in an unjust manner.

Therefore, any exceptional looking value should be declared "outlier" if and only if there were independent evidence that the information is incorrect (e.g., because of measurement device failure or concomitant animal condition like an infection). These exceptional looking values shall be documented including the reason for declaring them "outlier"; if it is clear that the reason is independent of the interventions, these values should be excluded from the analysis.

6.16 Hints on Evaluating the Data

Evaluating the experiment and describing its results shall consist of:

- Description and presentation of the raw data, i.e., the data as measured or obtained, and the derived data as well, depending on the amount of data and the type of each endpoint in either single case or aggregated way (e.g., by the number of values, minimum, maximum, mean, standard deviation, median, or mode)
- Estimation of the effect(s) and its variability, presented by the estimates and confidence intervals
- Calculation of the planned test statistics and related *p*-values
- Formulation of the statistical models built, reporting the units of the models, and therefore, the coefficients are based on
- The measures of model checking
- Interpretation of the statistical results from the experimenter's perspective to answer the main as well as other scientific questions the experiment was actually designed for

The extent to which each of the topics applies depends on both the design of the experiment and the intended audience for the report. It is rarely possible to omit the first and last of the above topics.

Graphing the data whenever you can is a good advice. Graphs or, more specifically, charts are one of the primary means of exploration and communication in the practice of science.

Charts have advantages for communicating experimental and statistical findings. They make it easy to observe magnitude and direction of differences or trends, to assess the importance of effects, or to check for deviances from the assumptions made. The first addressee of the charts shall be the experimenter or the experimental team itself.

To develop appropriate charts, one needs to take into account the type and number of endpoint(s) to be displayed. Whether the chart's objective is composition (univariate) or comparison of values across groups is another crucial point for selecting a graph. It is recommended to sketch the graphs needed for evaluation by hand and to check them beforehand for completeness and consistency. Completeness covers topics such as titles and axis labels including units, legends, and the information how many data points contribute to the chart; consistency includes whether different charts use the same axis scale or whether a unique color scheme is applied across graphs.

Finding a software capable of producing the chosen graphs and charts might be a challenge.

Translating statistical findings into biological meaning is the first step of reporting results.

Tables, graphs, and the narrative shall support each other. *The Chicago Guide to Writing about Multivariate Analysis* by Miller (2013, the outstandingly extended version of Miller 2004) gives a lot of advice on how to organize data and findings for presentation.

While interpreting statistical significance, one should again be aware of the strong relationship between α-level, power (1-β), sample size, variability σ, and the effect Δ considered relevant. Biological (or substantial) relevance and statistical significance are no synonyms; the latter should undoubtedly support to establish the former.

Convincing others of the importance of the experiment's findings should be based on one's own confidence that a replication of the experiment would allow for the same conclusions, although the magnitudes will be slightly different. This confidence is to largest extent based on the experiment's design.

And therefore, in other words:

> Experiments using laboratory animals should be well designed, efficiently executed, correctly analyzed, clearly presented, and correctly interpreted if they are to be ethically acceptable. Festing and Altman (2002)

Reference and Further Reading

There are at least half a dozen good textbooks available on experimental design in general (e.g., Atkinson et al. 2007), some of them being updated by new editions every couple of years (e.g., Montgomery 2012). Many of them take their illustrative examples from a particular field of science (from animal science to industrial quality control). Since there is no textbook (yet) directly dedicated to the design of experiments in animal imaging studies, Chow and Liu (1999), Festing (2002b), Festing et al. (2002), or Festing and Nevalainen (2014) might be a good choice.

References

Atkinson A, Donev A, Tobias R. Optimum experimental designs, with SAS. Oxford: Oxford University Press; 2007. ISBN 978-0-19-929660-6.

Australian Government. Guidelines to promote the well-being of animals used for scientific purposes – The assessment and alleviation of pain and distress in research animals. 2008. http://www.nhmrc.gov.au/_files_nhmrc/publications/attachments/ea18.pdf. Accessed 07 Oct 2014.

Bland M. Directory of randomisation software and services – Randomisation programs. 2014. http://www-users.york.ac.uk/~mb55/guide/randsery.htm. Last updated 15 Sept 2014, accessed 07 Oct 2014.

Box GEP, Hunter JS, Hunter WG. Statistics for experimenters. 2nd ed. New York: Wiley; 2005. ISBN 978-0-471-71813-0.

Chow S-C, Liu J-P. Design and analysis of animal studies in pharmaceutical development. London: Chapman & Hall; 1999. ISBN 978-0-8247-0130-7.

Cox DR. Planning experiments. New York: Wiley; 1958 (Reprint 1992). ISBN 978-0-471-57429-3.

Festing MFW (ed.). Experimental design and statistics in biomedical research (Special Issue). ILAR J. 2002b; 43(4):191–258.

Festing MFW. Introduction. The design and statistical analysis of animal experiments. ILAR J. 2002a;43:191–3.

Festing MFW, Altman DG. Guidelines for the design and statistical analysis of experiments using laboratory animals. ILAR J. 2002;43:244–58.

Festing MFW, Nevalainen T (ed.). Experimental design and statistics (Special Issue). ILAR J. 2014;5(3):379–530.

Festing MFW, Overend P, Gaines Das R, Cortina Borja M, Berdoy M. The design of animal experiments: Reducing the use of animals in research through better experimental design. London: Royal Society of Medicine; 2002. ISBN 978-1-85315-513-0.

Hanfelt JJ. Statistical approaches to experimental design and data analysis of in vivo studies. Breast Cancer Res Treat. 1997;46:279–302.

Horn M, Vollandt R. A survey of sample size formulas for pairwise and many-one multiple comparisons in the parametric, nonparametric and binomial case. Biom J. 1999;42:27–44.

Keene ON. The log transformation is special. Stat Med. 1995;14:811–9.

Khamis HJ. Statistics and the issue of animal numbers in research. Contemp Top Lab Anim Sci. 1997;36:54–9.

Machin D, Campbell M, Tan SB, Tan SH. Sample size tables for clinical studies. 3rd ed. Chichester: Wiley-Blackwell; 2009. ISBN 978-1-4051-4650-0.

Mead R. The design of experiments: Statistical principles for practical application. Cambridge: Cambridge University Press; 1988. ISBN 978-0-521-28762-3.

Miller JE. The Chicago guide to writing about numbers. Chicago: Chicago University Press; 2004. ISBN 978-0-22652-631-7.

Miller JE. The Chicago guide to writing about multivariate analysis. 2nd ed. Chicago: Chicago University Press; 2013. ISBN 978-0-22652-787-1.

Montgomery DC. Design and analysis of experiments. 8th ed. Hoboken: Wiley; 2012. ISBN 978-1-118-09793-9.

NC3RS – National Centre for the Replacement, Refinement and Reduction of Animals in Research. Responsibility in the use of animals in bioscience research. 2013. http://www.nerc.ac.uk/about/policy/policies/animals-in-research.pdf. Accessed 07 Oct 2014.

Anesthesia and Analgesia in Laboratory Animals

7

Marc Hein, Anna B. Roehl, and René H. Tolba

Contents

7.1 Introduction

The anatomic structures and neurophysiologic mechanisms leading to the perception of pain are similar in humans and nonhuman animals.

Therefore, it is reasonable to assume that if a procedure is painful to humans, is damaging or potentially damaging to tissues, or induces escape and emotional responses in an animal, it must be considered to be painful to that animal.

The "COUNCIL DIRECTIVE of 24 November 1986 on the approximation of laws, regulations and administrative provisions of the Member States regarding the protection of animals used for experimental and other scientific purposes (86/609/EEC)" was the first European-wide regulation to address this issue.

In Article 8 it states:

1. "All experiments shall be carried out under general or local anaesthesia.
2. Anaesthesia should be used in the case of serious injuries which may cause severe pain.
3. If anaesthesia is not possible, analgesics or other appropriate methods should be used in order to ensure as far as possible that pain, suffering, distress or harm are limited and that in any event the animal is not subject to severe pain, distress or suffering.
4. Provided such action is compatible with the object of the experiment, an anaesthetized animal, which suffers considerable pain once anaesthesia has worn off, shall be treated in

M. Hein • A.B. Roehl • R.H. Tolba
RWTH Aachen University, Aachen, Germany
e-mail: rtolba@ukaachen.de

F. Kiessling et al. (eds.), *Small Animal Imaging*, DOI 10.1007/978-3-319-42202-2_7

good time with pain-relieving means or, if this is not possible, shall be immediately killed by a humane method."

Therefore, not only according to international standards it is good scientific practice to use appropriate anesthesia and analgesics, it is also a moral imperative.

7.2 Anesthesia

Definition
Anesthesia is a pharmacologically induced reversible state of amnesia, analgesia, loss of consciousness, loss of skeletal muscle reflexes, and decreased stress response.

Legal Basis in the European Union (EU) and the United States of America (USA)
Directive 2010/63/EU of the European Parliament and of the Council
of 22 September 2010
on the Protection of Animals Used for Scientific Purposes
Article 14
Anesthesia

1. Member states shall ensure that, unless it is inappropriate, procedures are carried out under general or local anesthesia and that analgesia or another appropriate method is used to ensure that pain, suffering, and distress are kept to a minimum.

   Procedures that involve serious injuries that may cause severe pain shall not be carried out without anesthesia.
2. When deciding on the appropriateness of using anesthesia, the following shall be taken into account:
   (a) Whether anesthesia is judged to be more traumatic to the animal than the procedure itself
   (b) Whether anesthesia is incompatible with the purpose of the procedure.
3. Member states shall ensure that animals are not given any drug to stop or restrict their showing pain without an adequate level of anesthesia or analgesia.

   In these cases, a scientific justification shall be provided, accompanied by the details of the anesthetic or analgesic regimen.
4. An animal, which may suffer pain once anesthesia has worn off, shall be treated with preemptive and postoperative analgesics or other appropriate pain-relieving methods provided that it is compatible with the purpose of the procedure.
5. As soon as the purpose of the procedure has been achieved, appropriate action shall be taken to minimize the suffering of the animal.

7.2.1 United States of America

USDA Animal Welfare Act Regulations §2.31(d)(1)(iv)(A) and (ix) "Procedures that may cause more than momentary or slight pain or distress to the animals will be performed with appropriate sedatives, analgesics, or anesthetics, unless withholding such agents is justified for scientific reasons, in writing, by the principal investigator and will continue for only the necessary period of time…Activities that involve surgery include appropriate provision for pre-operative and post-operative care of the animals in accordance with established veterinary medical and nursing practices."

PHS Policy IV.C.1.a-b "Procedures with animals will avoid or minimize discomfort, distress, and pain to the animals, consistent with sound research design. Procedures that may cause more than momentary or slight pain or distress to the animals will be performed with appropriate sedation, analgesia, or anesthesia, unless the procedure is justified for scientific reasons in writing by the investigator."

Guide for the Care and Use of Laboratory Animals, p. 64 "An integral component of veterinary medical care is prevention or alleviation of pain associated with procedural and surgical protocols…Pain is a stressor and, if not relieved, can lead to unacceptable levels of stress and distress in animals. The proper use of anesthetics and analgesics in research animals is an ethical and scientific imperative…

In general, unless the contrary is known or established, it should be assumed that procedures that cause pain in humans also cause pain in animals."

7.2.2 General Considerations

Anesthesia in laboratory animals is depending on:

- Species
- Body weight
- Application route of the anesthetic drugs (i.p., i.m., s.c., etc.)
- Physical examination with or without surgical procedure
- Duration of the procedure (short term vs. long term)
- Survival experiment vs. final experiment
- Pain exposure
- Compatibility of the anesthetic drugs with the experimental goal
- Personal and technical equipment available

Starvation or deprivation of food and water is not recommended routinely in laboratory animals below 2 kg of body weight. Small laboratory animals like rodents develop easily a hypoglycemia or a metabolic acidosis. A hypoglycemia slows down the metabolism of anesthetic drugs and prolongs recovery after anesthesia (Ref. 3 S. 143).

If the experimental setting is depending on an empty gastric and bowel lumen, full absorbable diets are recommended. In a special field of research, where a mild hypoglycemia is needed, food deprivation can be performed with close surveillance for 8–12 h before induction of anesthesia.

7.2.2.1 Hypothermia

Small laboratory animals develop very easy hypothermia. Hypothermia is defined as body temperature below 35 °C (95 °F). Reasons are reduced muscle activity, low temperature in the laboratory, alcoholic disinfection, anesthetic side effects (inhibition/interaction with the central nervous thermoregulation system), and peripheral vasodilatation.

Hypothermia is killer no. 1 in small laboratory animals.

Animals will develop hypoventilation and hypercapnia, followed by a metabolic acidosis, lowering of blood pressure, bradycardia, shock, etc.

Preventive measures:

- Check the temperature of the animal.
- Usage of warming pads.
- Usage of prewarmed fluids.
- Keep the anesthesia as long as needed and as short as possible.

Keeping the animal warm is much better and easy in contrast to warm it up after the procedure.

7.3 Anesthetic Methods

7.3.1 Surgical Anesthesia

Any anesthesia administered of permitting performance of an operative procedure, as differentiated from diagnostic and therapeutic anesthesia, should provide loss of sensation and an adequate muscle relaxation. This requires Stadium III2 according to Guedel in humans, which is difficult to adapt to small animals. Alternatively, responses to different stimuli could be used to judge anesthetic depth. With increased anesthetic depth, stimuli with increasing intensity (noise, pain, intubation) are needed to provoke responses, which were attenuated at different levels (Fig. 7.1). In the majority of cases, the absence of limb movement after tail pressure should provide a sufficient anesthetic level for most procedures. The loss of hemodynamic responses (increase of blood pressure or heart rate) or apnea in spontaneous breathing animals might indicate a level, which is too deep. On the other hand, the return of righting reflex will indicate a good recovery of anesthesia.

7.3.2 Pharmacological Anesthesia

Any anesthesia administered for diagnostic or therapeutic procedures should be accompanied with loss of consciousness and skeletal muscle reflexes. This requires Stadium III1 according to Guedel and does not allow a surgical procedure.

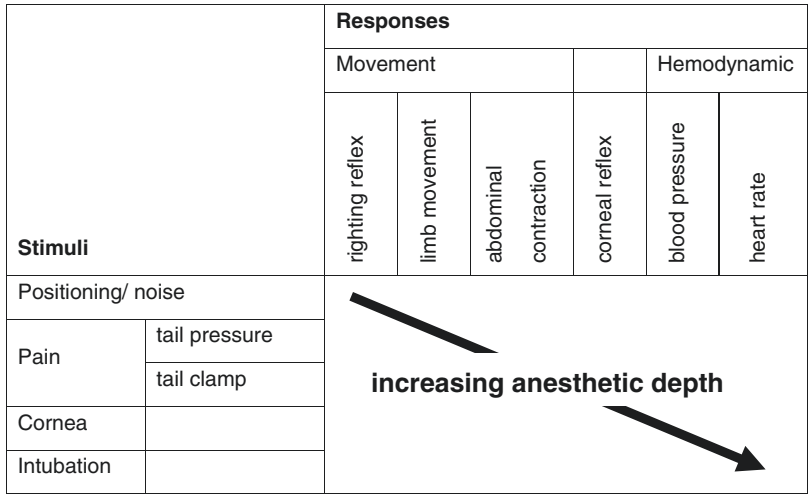

Fig. 7.1 Matrix of relevant stimuli and responses to judge anesthetic depth. Stimuli are in approximately increasing order of noxiousness and responses in increasing difficulty of suppression

Nevertheless, in most cases, this is the anesthetic approach of choice in imaging laboratory animals.

7.3.2.1 Mode of Administration

Drugs given to induce or maintain general anesthesia are either given as:

Gases or vapors (inhalational anesthetics)
Injection anesthetics

It is possible to combine these two forms, with an injection given to induce anesthesia and a gas used to maintain it (or vice versa), although it is possible to deliver anesthesia solely by inhalation or injection.

Volatile Anesthetics in Rodent Anesthesia

Volatile anesthetics provide main advantages for rodent anesthesia compared to intravenous or intraperitoneal applications of hypnotic drugs. Induction and emergence from anesthesia and delivered concentration can easily be controlled, resulting in low cardiopulmonary complications and mortality, especially if only limited monitoring of the animal is available (Hacker et al. 2005). Volatile anesthetics (VA) are lipophilic halogenated ethers which are liquid at room temperature and thus require special vaporizers for safe application in spontaneous breathing or mechanical ventilated animals. VA differs in their hypnotic potency, which correlates linear with their fat solubility (Meyer-Overton hypothesis). This correlation is described by the minimum alveolar concentration (MAC) that is needed to prevent movement in 50 % of the subjects in response to a painful (surgical) stimulus (Table 7.1). The MAC value is different between species and strains and dependent of age and gender. Even the interindividual variability ranges between 4 and 10 % and should be specified in case of doubt if different drugs are compared at equipotent anesthetic levels. Furthermore, body temperature and duration of anesthesia and repetitive application will influence the MAC (Stratmann et al. 2009). The end-expiratory gas concentration, which corresponds to the alveolar and thus blood partial pressure, can be taken as a measure for brain partial pressure under steady-state conditions. VA concentrations can be measured by infrared absorption spectroscopy with analyzers in the main or side stream of the respiratory circuit. Thus, the target drug dosage can be controlled during anesthesia and easily adjusted if needed. The loss of consciousness normally occurs at 0.5 MAC and can be judged by the loss of the righting reflex. For mono-anesthesia with VA, twofold higher values are needed if 95 % of

Table 7.1 Properties of commonly used volatile anesthetics in rodents

	Halothane	Isoflurane	Sevoflurane	Desflurane
$\lambda_{blood\text{-}gas}$	2.5	1.43	0.7	0.4
$\lambda_{brain\text{-}blood}$	1.9	1.6	1.7	1.3
$\lambda_{fat\text{-}blood}$	51	45	47.5	27.2
Metabolism [%]	10–20	0.2	2	0.02
MAC [%]	1.1–1.2	1.2–2.4	1.9–3.7	5.7
LORR [%]	0.6–0.7	0.6–1	1.1–1.4	3.7
LD_{50}/ED_{50}	2.2	4.3	-	2.5
Apneic index	2.3	3.1	2.5	1.6
Induction [VOL%]		5	6–8	
Maintenance [VOL%]		1.5–2.5	3–4	
Recovery (1.6 MAC, 2 h)				
RORR [min]	25	10	6.2	4.4
ROMC [min]	56	36	15	9.8

λ partition coefficients, *MAC* minimum alveolar concentration, *LORR* loss of righting reflex, LD_{50}/ED_{50} ratio of median lethal and effect dosage, *RORR* return of righting reflex, *ROMC* return of muscle coordination (Komatsu et al. 1997; Petrenko et al. 2007; Pancaro et al. 2005; Kissin et al. 1983; Eger and Johnson 1987)

the animals should not respond to painful stimuli or righting. The combination with other anesthetics like opioids, barbiturates, ketamine, midazolam, or α-agonists might reduce the MAC values by 50–90 % and should be very carefully adjusted.

The uptake of VA depends on differences in partial pressure between lung and blood and solubility and cardiac output. The blood/gas partition coefficient (λ_{BG}) or "blood solubility" correlates inversely with the induction rate (Table 7.1). The high cardiac output related to body weight of rodents accelerates the uptake compared with large animals or humans. Induction and emergence are additionally influenced by the fat/blood (λ_{FB}) and brain/blood (λ_{BB}) partition coefficients and continuous duration of application. High values delay especially the recovery from anesthesia (Table 7.1).

VA demonstrates additional analgesic and muscle relaxant properties with different characteristics. All VA depress the pulmonary and cardiovascular function in a dose-dependent manner, with qualitative and quantitative differences. Respiratory depth (tidal volume) is commonly reduced and partially compensated by an increase in respiratory frequency (RF). At higher concentrations (>1.5 MAC), RF decreases and the response to carbon dioxide tension is suppressed, as a consequence of the inhibition of brain stem neurons. This leads to a reduction of minute volume resulting in hypercapnia. The respiratory depression can partly be antagonized by surgical stimulation. Respiratory complications include apnea at higher concentrations (>1.6–3.1-fold of MAC, or "apneic index") and during induction, coughing, salivation, and broncho- or laryngospasm (Table 7.1).

In general, concentrations of VA for relevant cardiovascular depression are about 50 % higher than for respiratory depression. Thus, surveillance of respiration in spontaneous breathing animals could avoid cardiovascular complications. No increase of heart rate to a noxious stimulus appears first at 2.1–2.9 MAC. This characteristic explains the good safety margins of VA as judged by the ratio of median lethal to the effective dosage (LD_{50}/ED_{50}, Table 7.1). Despite this, the drugs differ in their negative inotropic and vasodilatory potency. All of them lead to a dose-dependent reduction of myocardial contractility, which reaches a significant level above 1.3–1.5 MAC (Preckel et al. 2002; Heerdt et al. 1998; Hettrick et al. 1996). No differences between the drugs exist, if concentrations are adjusted to with the corresponding MAC values (Kanaya et al. 1998). Vasodilatation increases up to 0.9 MAC while maintaining atrioventricular coupling and cardiac output.

All substances increase brain perfusion, which could lead to an increase of intracranial pressure. VA are triggers of malignant hyperthermia, but to our knowledge only described for special inbred strains in rodents. At least VA provides organ-protective properties. They are able to increase tolerance to ischemia and reduce reperfusion injury if applied before (preconditioning) or at time of reperfusion (postconditioning). This phenomenon is described in the heart, brain, kidney, liver, and lung (Weber et al. 2005; Matchett et al. 2009; Schmidt et al. 2007; Reutershan et al. 2006).

Halothane

Halothane is a core medicine in the WHO's "Essential Drug List" but is superseded by newer inhalational anesthetic agents for human use. It provides good hypnotic but minor analgetic and muscle relaxant properties. It is the only drug sensibilizing the heart for catecholamines and may induce complex ventricular extrasystoles. Due to its high solubility, induction and emergence from anesthesia is slow. Halothane shows the highest metabolism rate (ca. 30 %) and thus the highest toxicity, and might induce hepatitis.

Isoflurane

Isoflurane is the most commonly used VA in veterinarian and human anesthesia. It is characterized by a good hypnotic, analgesic, and relaxant action. It is the drug with the highest safety margin. Induction and emergence from anesthesia are faster compared to halothane. In mice an opisthotonus could occur during the on- and offset of anesthesia. Isoflurane induces bronchodilatation, but increases pulmonary vascular resistance. The high apneic index demonstrates the low depression of the respiratory function.

Sevoflurane

Sevoflurane is a sweet-smelling VA, which is frequently used for induction in pediatric anesthesia. The analgesic and muscle relaxant component of the drug is less compared to isoflurane. No hepatic toxicity was found. Fluorides from metabolism and compound A, which develops in dry and warm carbon dioxide absorbents, are able to induce renal injury. Vasodilation is less expressed than during isoflurane application (Conzen et al. 1992). Respiratory depression is less pronounced compared with isoflurane, although the apneic index is lower (Groeben et al. 2004). The incidence of breath holding during induction correlates with the applied concentration (Pancaro et al. 2005).

Desflurane

Desflurane has the lowest hypnotic potency and thus the highest MAC value. Therefore, desflurane has the most rapid onset and offset of the VA, which is nearly regardless of duration and concentration. Thus it is an ideal agent for repeated use, especially in functional brain imaging. Despite its low toxicity, it induces the highest respiratory depression, with breath holding during induction, broncho- and laryngospasm, coughing, and salivation. Reduction of myocardial contractility and vasodilation is higher than during isoflurane or sevoflurane anesthesia (Hettrick et al. 1996).

Anesthetic Management

In rodent anesthesia, isoflurane or sevoflurane, which is higher in price, should be preferred related to its low respiratory and cardiovascular depression. Halothane should not be used anymore due to its high toxicity and low safety margins. Less experience exists with desflurane in rodents, which is the most expensive drug among the VA. The short recovery from anesthesia, as documented by return of righting reflex and recovery of muscle coordination (Table 7.1), marks the only advantage. Comparable recovery times could be observed after sevoflurane application.

For induction anesthesia, chambers with tubing connectors on opposite ends of the box are recommended, which could be connected to an anesthesia machine. Direct application of the liquid agent should be avoided. Chambers should not be larger than needed. The time, which is needed to reach 95 % of the concentration set on the vaporizer, could be calculated as follows:

$$T_{95}\left[\text{min}\right] = 3 \cdot \text{box volume}\left[\text{l}\right] / \text{gas flow}\left[\text{l} / \text{min}\right]$$

A fast onset of inhalational anesthesia can be obtained with a fresh gas flow of 5 l/min (100 % oxygen) with an inspiratory concentration of 5 % isoflurane or 6–8 % sevoflurane. For maintenance, concentrations should be reduced to 1.5–2.5 % for isoflurane and 3–4 % for sevoflurane in spontaneous breathing or mechanical ventilated rodents. Actively scavenged chambers (charcoal) and coaxial mask with connection to scavenging systems should be used to reduce waste gas and thus exposure of the operator.

Airway Management

Most studies are performed in spontaneous breathing rodents. This setting requires face masks with a tight seal and minimal dead space to impede rebreathing and thus hypercapnia. Ideally, coaxial masks are used to scavenge waste gas. Procedures needing a depth anesthesia or including thoracotomy require an intubation of the animal and controlled mechanical ventilation. Oral intubations as well as tracheotomy are feasible procedures. The use of transillumination (indirect light from the neck), intubation guides, and an intubation speculum in an upright position (60°) of the animal provides good conditions. Standard intravenous cannulas with 20–14 gauge sizes can be used. Blind intubation should be avoided, because already a marginal mucosal edema might produce a relevant obstruction of the upper airway. Repeated traumatic attempts will increase salivation, which further complicates the procedure.

Different rodent anesthesia machines are available. The simplest design contains a flowmeter for oxygen and air, a vaporizer, a breathing circuit, a mask, and a scavenging system. It could be expanded with an oxygen flush valve and a pressure control unit. Parallel connection of additional breathing circuits enables the simultaneous use in several animals. For controlled ventilation, special ventilators for small animals as well as human ventilators may be used. Long breathing tubes with a low compliance should be avoided especially if a volume-controlled modus is used. Tidal volume (V_t) and respiratory frequency (RF) for rats and mice could be calculated as follows:

$$V_t\left[\text{ml}\right] = 6.2 \cdot \text{bodyweight}\left[\text{kg}\right]^{1.01}$$

$$\text{RF}\left[1/\text{min}\right] = 53.5\,\text{bodyweight}\left[\text{kg}\right]^{-0.26}$$

A pressure-controlled ventilation with a maximum pressure of 10–15 mbar and an end-expiratory pressure of 5 mbar will avoid mechanical lung injury. Surveillance of the animal includes inspection of respiratory excursion, capnometry, and pulse oximetry.

7.4 Anesthetics

Ketamine (Ketavet®) is an *N*-methyl-D-aspartate (NMDA) antagonist and induces a dissociative anesthesia. It elevates the sympathicus tonus and the muscle tonus. It is not recommended to use the substance alone (psychedelic during wake-up phase, no surgical tolerance in visceral surgery alone). It should be used in combination with other anesthetic drugs (sedatives, neuroleptics, hypnotics, etc.).

	Mouse	Rat	Hamster	Guinea pig
Ketamine + xylazine	80–100 mg/kg (K) 5–10 mg/kg (X) i.p.	60–90 mg/kg (K) 5–10 mg/kg (X) i.p. Duration: 30–45 min	80–100 mg/kg (K) 5–10 mg/kg (X) i.p.	40 mg/kg (K) 5 mg/kg (X) i.p. Duration: 60 min
Ketamine + medetomidine	75 mg/kg (K) 1.0 mg/kg (M) i.p.	75 mg/kg (K) 0.5 mg/kg (M) i.p oder s.c.	80–100 mg/kg (K) 0.25 mg/kg (M) i.p.	40 mg/kg i.p. or i.m. 0.5 mg/kg (M) i.p. Duration: 40 min
Sedation	44 mg/kg s.c.	50–100 mg/kg i.p.	40–80 mg/kg i.p.	22–44 mg/kg i.m.

Ketamine application is possible to nearly every route (i.v., s.c., i.p., i.m., oral, rectal).

Pentobarbital (Release ad us. vet; Nembutal®) and thiopental are barbiturates and used either intraperitoneally or intravenously. The therapeutic window is very narrow, and even in the therapeutic range, side effects like respiratory problems and respiratory and/or cardiac arrest can occur.

	Mouse	Rat	Hamster	Guinea pig
Pentobarbital	30–70 mg/kg i.p.	30–55 mg/kg i.p.	40–90 mg/kg i.p.	15–40 mg/kg i.p. Duration: 90 min
Thiopental	25–50 mg/kg i.p.	20–40 mg/kg i.p.	20–40 mg/kg i.p.	15–20 mg/kg i.v. 15–20 mg/kg i.p.

7.5 Analgetics

Definition

"Pain" is derived from the Latin "poena" and has been defined by the Committee on Taxonomy for the International Association for the Study of Pain (http://www.iasp-pain.org/) as "an unpleasant sensory and emotional experience associated with actual or potential tissue damage."

According to international recommendations, it is a good scientific practice that "all procedures that may cause more than momentary or slight pain or distress to the animals will be performed with appropriate sedatives, analgesics, or anesthetics," e.g., according to the US Regulations and Guidelines Regarding Recognition and Alleviation of Pain in Laboratory Animals.

Carprofen (Rimadyl®) is a nonsteroidal antiphlogistic drug with analgetic and antipyretic potency in combination with anti-inflammatory properties. For postoperative pain management, the drug should be given during surgery, because the drug is released with some delay.

	Mouse	Rat	Hamster	Guinea pig
Carprofen	4–5 mg/kg s.c. Duration: 24 h	4–5 mg/kg s.c. Duration: 24 h	4–5 mg/kg s.c. Duration: 24 h	4–5 mg/kg s.c. Duration: 24 h

Meloxicam (Metacam® 5 mg/ml ad us. vet) is also a nonsteroidal antiphlogistic drug. It is used for the peri- and postoperative pain management and rheumatoid diseases.

	Mouse	Rat	Hamster	Guinea pig
Meloxicam	10 mg/kg p.o., s.c. (1–2 mg/kg s.c.) Application: 1×/day	0.2–1 mg/kg p.o., s.c. (1–2 mg/kg s.c) Application: 1×/day	0.2 mg/kg p.o., s.c. first day Application: 1×/day 0.1 mg/kg p.o., s.c. from second day Application: 1×/day	0.5 mg/kg p.o., s.c.

Fentanyl (Fentanyl-Janssen®, Fentanyl-Curamed®) is a short-term opioid-analgetic drug 100 times stronger than morphine. In combination with a hypnotic drug, it is possible to reduce the fentanyl dosage by ca. 50 %.

	Mouse	Rat	Hamster	Guinea pig
Fentanyl	0.025–0.6 mg/kg s.c.	0.01–1.0 mg/kg s.c. 2.0–4.0 g/day p.o.	k.A.	n.a.

Buprenorphine (Temgesic) is a semisynthetic opiate with partial agonist actions at the mu opioid receptor and antagonist actions at other opioid receptors.

Buprenorphine is a thebaine derivative with analgesia approximately 25–40 times as potent as morphine.

	Mouse	Rat	Hamster	Guinea pig
Buprenorphine	0.05–0.1 mg/kg s.c., i.p. Duration: 8–12 h 1.1 mM in DMSO topic	0.01–0.05 mg/kg s.c., i.p. Duration: 6–12 h 0.4 mg/kg p.o.	0.05–0.1 mg/kg s.c., i.p. Duration: 8–12 h Dosage interval: 3×/day s.c.	0.05 mg/kg s.c. Duration: 6–12 h

High first-pass effect; dosage is ten times higher given orally.

Local Anesthetics Infiltration of wounds, intercostal spaces, etc. would provide long-term analgesia with minimal systemic side effects. Bupivacaine and ropivacaine are ideal drugs for this purpose. Beyond a cumulative dosage of 5 mg/kg bupivacaine, systemic side effects should be considered, whereas no side effects could be observed after s.c. application of 25 mg/kg ropivacaine in rats (Danielsson et al. 1997).

7.6 Sedation

Medetomidine (Domitor®), the active form is medetomidine hydrochloride, is a specific α_2-adrenergic agonist. Noradrenaline release is reduced and this resulted in sedation and anxiolyses. It can be given by intramuscular injection (IM), subcutaneous injection (SC), or intravenous injection (IV). It is not recommended for diabetics; it is contraindicated in patients with cardiac disease. Following administration, marked peripheral vasoconstriction and bradycardia are noted. Dosage of induction agents (i.e., propofol) can be drastically reduced, as may the volumes of anesthetic gases (i.e., halothane, isoflurane, sevoflurane) used to maintain general anesthesia.

Combination with ketamine is very common.

	Mouse	Rat	Hamster	Guinea pig
Medetomidine	30–100 µg/kg s.c.	30–100 µg/kg s.c.	n.a.	n.a.

The effects of medetomidine can be reversed using atipamezole (Antisedan®) 1.0 µg/kg s.c., i.p., or i.v.

Xylazine (Rompun®) is an agonist at the α_2-adrenergic receptor. It is ten times less selective than medetomidine. As with other α_2-agonists, adverse effects include bradycardia, conduction disturbances, and myocardial depression. The effects of xylazine can be reversed using yohimbine (Yobine) or atipamezole (Antisedan). In laboratory animal anesthesia, xylazine is often used in combination with ketamine.

	Mouse	Rat	Hamster	Guinea pig
Xylazine	5–10 mg/kg i.m., i.p., s.c.	5–10 mg/kg i.m., i.p., s.c.	n.a.	5 mg/kg i.m., i.p.
Xylazine + ketamine	See ketamine	See ketamine	See ketamine	See ketamine

n.a. not available

Midazolam (Dormicum®) is a benzodiazepine, which provides dose-dependent sedation, hypnosis, and muscle relaxation without analgesia. It is commonly used for premedication (1–2 mg/kg i.m.). If it is combined with ketamine (5–10 mg/kg i.m.), the dosage should be reduced to

0.5–1 mg/kg i.m. Its action could be antagonized with flumazenil.

Modified according to:

Duke University and Medical Center: Guidelines for Rodent Analgesia

Guidelines for the Assessment and Management of Pain in Rodents and Rabbits, July 2006

Guidelines for Anesthesia and Analgesia in Rodents and Rabbits, April 2009

University of South Florida: Guidelines on Anesthesia and Analgesia in Laboratory Animals

University of Pennsylvania: IACUC Guideline Rodent Anesthesia & Analgesia Formulary, Mai 2008

CliniPharm Wirkstoffprofile, Stand 09.12.09

GV-SOLAS, Ausschuss für Anästhesie und Analgesie: Schmerztherapie bei Versuchstieren

http://www.gv-solas.de/index.php?id=33

http://www.iasp-pain.org/trms-p.html

References

Anaesthesia and Analgesia in Laboratory Animals

Conzen PF, Vollmar B, Habazettl H, Frink EJ, Peter K, Messmer K. Systemic and regional hemodynamics of isoflurane and sevoflurane in rats. Anesth Analg. 1992;74:79–88.

Danielsson BR, Danielson MK, Boo EL, Arvidsson T, Halldin MM. Toxicity of bupivacaine and ropivacaine in relation to free plasma concentrations in pregnant rats: a comparative study. Pharmacol Toxicol. 1997;81:90–6.

Eger 2nd EI, Johnson BH. Rates of awakening from anesthesia with I-653, halothane, isoflurane, and sevoflurane: a test of the effect of anesthetic concentration and duration in rats. Anesth Analg. 1987;66:977–82.

Groeben H, Meier S, Tankersley CG, Mitzner W, Brown RH. Influence of volatile anaesthetics on hypercapnoeic ventilatory responses in mice with blunted respiratory drive. Br J Anaesth. 2004;92:697–703.

Hacker SO, White CE, Black IH. A comparison of target-controlled infusion versus volatile inhalant anesthesia for heart rate, respiratory rate, and recovery time in a rat model. Contemp Top Lab Anim Sci /Am Assoc Lab Anim Sci. 2005;44:7–12.

Heerdt PM, Gandhi CD, Dickstein ML. Disparity of isoflurane effects on left and right ventricular afterload and hydraulic power generation in swine. Anesth Analg. 1998;87:511–21.

Hettrick DA, Pagel PS, Warltier DC. Desflurane, sevoflurane, and isoflurane impair canine left ventricular-arterial coupling and mechanical efficiency. Anesthesiology. 1996;85:403–13.

Kanaya N, Kawana S, Tsuchida H, Miyamoto A, Ohshika H, Namik A. Comparative myocardial depression of sevoflurane, isoflurane, and halothane in cultured neonatal rat ventricular myocytes. Anesth Analg. 1998;87:1041–7.

Kissin I, Morgan PL, Smith LR. Comparison of isoflurane and halothane safety margins in rats. Anesthesiology. 1983;58:556–61.

Komatsu H, Nogaya J, Kuratani N, Ueki M, Yokono S, Ogli K. Psychomotor performance during initial stage of exposure to halothane, enflurane, isoflurane and sevoflurane in mice. Clin Exp Pharmacol Physiol. 1997;24:706–9.

Matchett GA, Allard MW, Martin RD, Zhang JH. Neuroprotective effect of volatile anesthetic agents: molecular mechanisms. Neurol Res. 2009;31:128–34.

Pancaro C, Giovannoni S, Toscano A, Peduto VA. Apnea during induction of anesthesia with sevoflurane is related to its mode of administration. Can J Anaesth. 2005;52:591–4.

Petrenko AB, Tsujita M, Kohno T, Sakimura K, Baba H. Mutation of alpha1G T-type calcium channels in mice does not change anesthetic requirements for loss of the righting reflex and minimum alveolar concentration but delays the onset of anesthetic induction. Anesthesiology. 2007;106:1177–85.

Preckel B, Ebel D, Mullenheim J, Frassdorf J, Thamer V, Schlack W. The direct myocardial effects of xenon in the dog heart in vivo. Anesth Analg. 2002;94:545–51.

Reutershan J, Chang D, Hayes JK, Ley K. Protective effects of isoflurane pretreatment in endotoxin-induced lung injury. Anesthesiology. 2006;104:511–7.

Schmidt R, Tritschler E, Hoetzel A, Loop T, Humar M, Halverscheid L, Geiger KK, Pannen BHJ. Heme oxygenase-1 induction by the clinically used anesthetic isoflurane protects rat livers from ischemia/reperfusion injury. Ann Surg. 2007;245:931–42.

Stratmann G, Sall JW, Eger 2nd EI, Laster MJ, Bell JS, May LDV, Eilers H, Krause M, Heusen F, Gonzalez HE. Increasing the duration of isoflurane anesthesia decreases the minimum alveolar anesthetic concentration in 7-day-old but not in 60-day-old rats. Anesth Analg. 2009;109:801–6.

Weber NC, Preckel B, Schlack W. The effect of anaesthetics on the myocardium–new insights into myocardial protection. Eur J Anaesthesiol. 2005;22:647–57.

Anaesthetics

A reference source for the recognition & alleviation of pain & distress in animals.

Animal Welfare Information Center, United States Department of Agriculture.

National Agricultural Library 2003: http://www.nal.usda.gov/awic/pubs/awic200003.htm.

Drug Administration

8

Peter Hauff and Klaus Nebendahl†

Contents

†Author was deceased at the time of publication

PD Dr. P. Hauff (✉)
Bayer AG, Drug Discovery, Pharmaceuticals,
Müllerstr 178, Berlin 13353, Germany
e-mail: peter.hauff@bayer.com

†K. Nebendahl

8.1 General

For biomedical research purposes, the most commonly used laboratory animals are mice, followed by rats. All over the world, the percentage usually varies around 80–90 % of the total number of animals used (Tierschutzbericht 2011). For this reason this chapter goes in detail only on these two species.

Drugs and other test substances such as chemical elements, compounds, antibodies, cells, etc., can be administered to small laboratory animals through a variety of routes. Numerous routes of administration have been well documented in the literature. As every route has both advantages and disadvantages and as, for instance, the absorption, bioavailability and metabolism of the substance are factors which should be considered carefully, a knowledge of available methods and techniques of administration and of the disposition and fate of the administrated substance will aid the scientist to choose the most suitable route for his/her purpose. Therefore, the exact details of any administration must be checked prior to any experiment.

A complete review of all methods used for administration would go far beyond the scope of this chapter. For a full discussion of all administration routes available, the reader is referred to the periodical literature. Only some administration routes, techniques and guidelines for sites of administration, preparation of sites, injection techniques and safe injection volumes will be

F. Kiessling et al. (eds.), *Small Animal Imaging*, DOI 10.1007/978-3-319-42202-2_8

described here. As a number of questions often arise concerning the suitability of solutions for injection and unfortunately precise answers are often not forthcoming (Waynforth and Flecknell 1992a, b), some remarks are made in respect to volume and rate of injection, absorption of the administrated substance, bioavailability and distribution of substances in the body as well as factors that may modify the dosage or site of substance injection.

An introduction to this topic would be incomplete without a reference to humane treatment of mice and rats which are the most frequently used animals in experimental studies. The German "Animal Welfare Act" (Tiersch 2013) claimed that pain, suffering and harm may be inflicted on animals only in so far as unavoidable to attain the purpose of the experiment and, where unavoidable, they shall be limited to the absolute minimum. The "European convention for the protection of vertebrate animals used for experimental and other scientific purpose" (ETS 123 1986) stated that persons carrying out procedures shall have had appropriate education and training in handling and restraining experimental animals, should have the foundation for responsible use of the animals and should attain a scientifically high standard, in order to protect the animals used in procedures which may possibly cause pain, suffering or distress and to ensure that, where unavoidable, they shall be kept to a minimum.

First and foremost of moral reasons and not because of legal reasons, it must be kept in mind that nearly every administration can be performed relatively painless, if attention is given to the proper restraint of the animal and adequate technical skill is employed.

8.2 Principles of Administration

8.2.1 Handling and Restraining

Nearly every animal can be trained to accept handling and restraining and can become familiar with the attending persons. Though time consuming, it is essential to minimise distress. For this reason all procedures should be carried out by persons well known to the animal. Sedation or general anaesthesia is generally only required if the technique involved is more than a pinprick or the administered substances have side effects like causing pain.

8.2.2 Site of Administration

Numerous sites have been described in the literature to administer substances to small laboratory animals, but some of these sites are unacceptable nowadays, for example, footpad injection of Freund's complete adjuvant.

8.2.3 Preparation of the Site

Sometimes the area must be clipped or cleaned with warm water. Afterwards, the skin should be swabbed with disinfectants or alcohol. To prevent pain it is sometimes necessary to apply local analgesics to the site before administration.

8.2.4 Safety and Solubility of Substances

All parenteral administration must be done using an aseptic technique, and the substances or injection solutions must be sterile and free from pyrogenous material. In order to administer an accurate dosage and to avoid causing tissue damage due to the toxicity of the substance, the volume and the way of administration have to be considered. If the substance has to be diluted, the selected thinning agent must be safe. Physiological saline (0.9 % sodium chloride) or other physiological solvents like phosphate-buffered saline (PBS) or various culture media are suitable vehicles. Although distilled water can be used sometimes, saline should be preferred because water *ad injectionem* injected subcutaneously causes pain and injected intravenously produces haemolysis.

For reasons of solubility or rate of absorption, some substances require a more complex solvent to render them suitable for administration.

Many solvents, for example, water, water with 0.85 % sodium chloride, 60 % polyethylene glycol, 10 % Tween 80 and 0.5 % methylcellulose, have been found suitable in most instances and do not greatly affect the activity of interest of the substances to be investigated due to their own inherent properties (Woodard 1965). All of these vehicles can be administered by any of the injection routes available, but the concentrations mentioned are the maximum practicable, and in many cases it is possible and indeed desirable that lower concentrations should be used (Waynforth and Flecknell 1992a, b). When administrating drugs, the solvent should ideally be the same as the one in which the drug is normally formulated.

Lipid-soluble substances can only be dissolved in oil, but their absorption is delayed when administered. As oil cannot be injected intravenously, lipophilic substances should be injected in a 15 % oil–water emulsion. Oil-based adjuvants or oil–water emulsions injected intraperitoneally may cause acute peritonitis. Therefore, they should only be administered by this mode when all other routes have proved ineffective.

Substances can be injected in the form of a suspension. Since suspended particles have the tendency to sediment, these particles should be evenly distributed before the suspension is injected intravenously. If injected intravenously it should be noted that the particles will be filtered out in the capillary beds of the extremities and the lung, modifying the distribution of the injected material and sometimes causing pulmonary distress to the animal (Waynforth and Flecknell 1992a, b).

8.2.5 Concentration of Substances

The concentration can vary over a fairly wide range without greatly influencing the results of the experiments. Lower concentrations are clearly desirable (Waynforth and Flecknell 1992a, b). Factors limiting the use of aqueous solutions for parenteral administration are probably related to their osmotic pressure. Low concentrations can be corrected by the addition of sodium chloride but ought not to be so high as to materially exceed the osmotic pressure of 0.15-M sodium chloride (Woodard 1965). Highly concentrated solutions can be administered intravenously provided the rate of injection is kept slow and precaution is taken to avoid getting the solution outside the vein (Shimizu 2004).

8.2.6 pH of the Injected Solution

Because extremes in pH cause local tissue damages, solutions should be neutral (pH 7.0–7.3) ideally. But rodents, like humans, tolerate injections of solutions within a fairly wide range of pH. For all routes of administration, a working range is in the range of pH 4.5–8.0 (Woodard 1965). The widest tolerance to pH is shown by the intravenous route because of the buffering capacity of the blood and of the very quick dilution through the side-on flow of venous blood, followed by the intramuscular and then the subcutaneous route. Nevertheless, especially when low or high pH solutions are intravenously injected, the rate of injection must be kept slow, and the administration should be done extremely cautious to avoid solutions getting outside the vein.

8.2.7 Volume and Frequency of Administration

Though volume and frequency of administration are mainly determined by the requirements of the experiment, the animal should not be strained or stressed. The volume of substances given is limited by their toxicity and by the size of the animal and should be as small as possible. Likewise the frequency of administration should be restricted to a minimum, to avoid unnecessary stress. Volume and rate of injection have to be considered, particularly if solutions are given intravenously, because haemodynamic changes and pulmonary oedema may occur and very rapid injections can produce cardiovascular failure and be lethal. Some recommendations regarding the

maximum injection volumes of the Society of Laboratory Animals (GV-SOLAS, August 2010) are listed in the chapter Appendix of this book.

8.2.8 Rate of Absorption/ Distribution of Administered Substances

The rate of absorption is influenced by the blood flow to the site of administration, the nature of the substances and the manner and concentration in which they are presented (Wolfensohn and Lloyd 1994). It influences the time course of substance effect and is an important factor in determining substance dosage (Waynforth and Flecknell 1992a, b). Only in a few cases is it possible to inject substances at the place where they should be effective. Normally, they must be absorbed from the site of administration into the blood. Therefore, the size of the absorbing surface, the blood flow to the site of administration and the solubility of the substance in the tissue fluids are important factors which determine the rate of absorption. While endogenous compounds normally pass through biological membranes by special transport mechanisms, the penetration of xenobiotics follows physical principles, such as passive diffusion according to the concentration gradient (Frimmer and Lämmler 1977). Lipid solubility, physicochemical properties, degree of ionisation and molecular size of substances are important factors in respect to the rate of absorption. Substances which are highly soluble in body fluids will be absorbed quickly. Substances which are ionised and are not lipid soluble will only be absorbed if a specific carrier exists (Wolfensohn and Lloyd 1994). As absorption of administered substances mostly happens by diffusion down a concentration gradient, the absorption of substances is dependent on the dosage.

8.3 Enteral Administration

Enteral administration involves the introduction of substances into the gastrointestinal tract via the mouth or through the anus using a suppository. The latter method is not very practical when working with small laboratory animals (Baumans et al. 1993). The advantage of enteral administration is the fact that it is possible to give comparatively large amounts of non-sterile substances or solutions. For oral preparations, a pH value as low as 3 can be tolerated for a solution of fairly high buffer capacity (Woodard 1965). On the other hand, alkaline solutions are very poorly tolerated by the mouth.

In principle, gastrointestinal absorption takes place over the whole length of the digestive tract. Absorption of most orally given substances occurs by diffusion of their non-ionised forms, since the mucosal lining of the gastrointestinal tract is almost impermeable for ionised molecules. Consequently, absorption of substances will be enhanced in the acid stomach or in the nearly neutral intestine depending on the ionic character of the compound. The far larger surface area of the intestinal villi, however, makes intestinal absorption dominant in most cases (Claassen 1994a).

Buccal or sublingual administration would avoid the destructive effects that may be encountered in the stomach following oral administration (Woodard 1965). Consequently, this route is sometimes required in animal experimentation. The absorption rate of substances has not been investigated to any considerable extent and is probably insignificant in small rodents. It is known that the mucosa of the mouth cavity can only absorb hydrophobic, non-ionised substances.

For substances given orally, the stomach is a significant site of absorption for many acidic or neutral compounds, whereas only the weakest bases are absorbed to any appreciable extent at normal gastric pH values (Baggot 1977). All other substances are absorbed only at a very small rate.

Using the oral administration route, it should be known that substances can be destroyed by the gastric juice, that the food content of the stomach influences both the rate and order of gastric emptying and that the rate of substance absorption is markedly influenced by its residence time in the stomach and is directly related to the rate at which substances are passed from the stomach into the intestine (Levine 1970).

Because of its extensive surface area and rich blood supply, the upper small intestine of rodents is the major site of absorption for all substances

after oral administration. Absorption in the intestine is dependent on (1) the physicochemical state of the substances, (2) the non-absorptive physiological function and state of the intestine, (3) the metabolic activity and function of the absorbing cells and (4) the structure of the absorbing surface (Levine 1970). Through the efflux of intestinal juice, pancreas juice and bile, the intestinal content becomes nearly neutral. This will reduce the degree of ionisation and the absorption rate of substances will increase. Lipid-soluble substances of the digestive content are rapidly absorbed, whereas, dependent on size, the absorption of solids is moderate.

Using the oral administration routes, it has to be kept in mind that enzymes of the microflora of the digestive tract can metabolise substances. Under physiological conditions, microorganisms are only to be found in the large intestine, and normally such enzymatic metabolism applies only to those substances which are not yet absorbed in the upper tract. Therefore, oral administration can have the disadvantage that enzymes of microorganisms can alter substances before they are absorbed in the bowel. If the metabolites are not biologically active, the administration of these substances may be without any effect. On the other hand, some insoluble substances become soluble as the result of enzyme activity during their passage through the stomach and the small intestine, and hence their absorption then becomes possible in the large intestine.

Excluding those absorbed in the mouth and rectum, all substances given and absorbed through the gastrointestinal tract are transported by the portal vein to the liver. Some substances can be metabolised there to a large extent, before reaching the systemic circulation and/or the site of action. This phenomenon is called "first-pass effect" (Löscher et al. 2006) and has to be considered in selecting routes of administration.

8.3.1 Oral Administration (per os)

The simplest method to administer substances is by mixing them with food or drinking water. However, this method is neither very accurate nor it is practicable with substances which are unpalatable, insoluble or chemically unstable in drinking water or when they irritate the mucosa of the gastrointestinal tract.

Giving substances with food or drinking water is an easy method of administration. For example, training of the animal is not necessary because no handling or restraining is required. Furthermore, as the animal is not disturbed, the administration takes place without any stress, and eating, drinking or digestion happens under normal physiological conditions. Thereby, it is secured that only the substances are effective.

Mixing substances into meal food must be done carefully, and decomposition must be prevented otherwise the animal might refuse to eat the substances or incalculable substance doses will be taken up. As decomposition of the food is only prevented by feeding pellets, this feeding method is recommended. But to prepare an accurate mixture and to pelletise the meal food, some technical equipment is necessary. In most cases, it is best to involve a foodstuff company to produce an exact mixture pressed in pellets.

The daily food and water intake of the animal must be known before starting so that the amount of substances to be mixed with food or drinking water can be calculated (Table 8.1).

Other factors may also come in play. If – for instance – the circadian rhythm influences the

Table 8.1 Estimated average food[a] intake of mice and rats

	Growing		Adult		Pregnant		Lactating	
	Mouse	Rat	Mouse	Rat	Mouse	Rat	Mouse	Rat
g/day	3–5	8–25	5–7	25–30	6–8	25–35	7–15	35–65

Source: Ritskes-Hoitinger and Chaewalibog (2003)
ME content: 8–12 MJ/kg diet. *ME* metabolisable energy
[a]Food intake can vary dependent on strain, body weight, activity, condition of holding (temperature and humidity) and other factors

effect of a substance, the feeding behaviour of the animal should be known. Mice and rats are not nibblers but spontaneous meal eaters. As they are nocturnally active animals, they ingest most of their food during the dark period (Ritskes-Hoitinger 2004). For instance, rats eat only small parts of their food during the day and consume 80 % of their daily food intake at night taking 5–8 meals in this time (Claassen 1994b).

Fasting is often used, as an empty stomach is considered prerequisite for bioavailability and drug absorption. An empty stomach is as well often required when applying substances per gavage because it is sometimes considered that the content of the stomach could dilute the test substances or even interact with it. But fasting causes severe changes in physiological and biochemical processes of the animal, which become more severe with longer duration of food withdraw (Claassen 1994c), and leads to increased locomotory and grooming behaviour (Vermeulen et al. 1997). In consideration of these facts, it must be known how long the animal must or can be starved without any harm to its welfare. For instance, Jeffrey et al. (1987) observed variable amounts of food in the stomachs of male rats following an overnight fast and noted that the diet type and diet regimen can result in variable quantities of food being retained in the stomach. Schlingmann et al. (1997) found that the stomach of rats fasting 6, 12 and 18 h was almost empty and that only food deprivation for 6 h did not cause any *distress*. As food deprivation will result in a decreased need for water, this feeding schedule leads to a gradual increase of the haematocrit value, with a corresponding decrease in plasma volume. A decrease of the plasma and interstitial volume may result in a significant decrease of substance distribution volume. Various investigators reported, for example, that after overnight food restriction, the glutathione content per gram liver diminished by 45–57 % in mice and that fasting effects may vary to a great extent between strains and individuals. Therefore, Claassen (1994c) advanced the view that the use of fasting animals in experiments seems only be permitted when the feeding condition functions as a factor in the experimental design.

Oral administration by diet or drinking water is not suitable when the exact amount of substance intake is required. Because food and water wastage happens at all time, it is, for instance, impossible to determine the exact amount of diet or water intake of rodents. Therefore, neither the precise food or water intake nor the correct intake of substances with food or water is normally feasible. The only way this can be done is by keeping the animals in metabolic cages and recording the wastage.

The feeding or drinking intake is influenced by conditions of housing and especially by the environment too. Normally, the temperature in rooms for laboratory animals is well controlled by air conditioning. It should be noted that high temperatures will decrease the intake of food and increase the consumption of water. For instance, the water intake of rats at 22 °C is about 20 % higher than the food intake, while at 30 °C water intake is more than double (Weihe 1987). For this reason the temperature and humidity has to be recorded during the experiment.

The substances in food or drinking water can cause the animal to refuse to eat or drink, and the animal may lose weight or becomes dehydrated. To stimulate the consumption of rodents, the substances can be administered in fat dripping, and if it does not interfere with the experiment, sucrose cubes or a 10 % glucose solution can be given. If the substances increase the metabolic rate, overeating must be prevented to avoid an overdose. For these reasons, the animal and its food and water intake must be observed carefully.

Another disadvantage is that, for observing or measuring food or water intake, the animal must be individually housed. Numerous reports about mice and rats refer that this condition provoke ad libitum-fed rodents to eat more than group-housed animal and that this housing condition may cause stress to animals and will reduce the success of oral administration (Claassen 1994b).

8.3.2 Intragastric Administration by Gavage

This route of administration is carried out using a special steel needle. This bulb-tipped gastric gavage needle helps to prevent damaging the

oesophagus or stomach and from passing through the glottal opening into the trachea. The diameter of the bulb and the length of the needle will depend on the size of the animal to be gavaged.

Before starting administration, the feeding needle is checked to be of suitable length, i.e. reaching from the mouth to the caudal end of the breastbone (outside of the animal) and this should be noted on the tube (Fig. 8.1).

The chosen needle and the appropriate syringe filled with the desired amount of solution are linked together, and the needle can be moistened with water or oil to make it slippery. For administration, the conscious animal must be restrained very firmly by gripping a fold of skin from the scruff of the neck down the back so that the head of the animal is kept immobile. Firm restrain with complete immobilisation of the head of the animal is essential for the following procedure. Its position is vertical with the head tipped slightly forward. No mouth gag is necessary. To force the jaw open, pressure can be applied to the mandible. The ball tip is inserted behind the incisors into the back of the mouth. Using the needle as a lever, the head of the animal can be tipped back. As soon as a straight line is formed, the needle is passed gently through the mouth and pharynx into the oesophagus (Shimizu 2004). The animal usually swallows as the feeding needle approached the pharynx; these swallowing movements can help so that the probe slips through the oesophageal opening. If any obstruction is felt, no force must be exerted and another try must be made to find the oesophagus opening. As it is important to prevent the tube from entering the trachea, the animal must be well observed. For example, the needle can usually be seen passing down the oesophagus on the left side of the neck (Wolfersohn and Lloyd 1994). Being in the trachea, the animal will cough, and it is possible to feel the tube touching the cartilage rings of the trachea (Baumans et al. 1993). Once in the oesophagus, the tube is gently pushed down into the stomach. The passage may be obstructed at the sphincter to the entrance of the stomach. Manipulation of the syringe to produce a gentle thrusting movement combined with a gentle backward and forward movement will often overcome this difficulty.

Once the needle is in place, the solution is administered slowly. If any obstruction is felt, if the animal coughs, chokes or begins to struggle vigorously or if the injected solution is seen coming out through the mouth or nose, these may indicate that the needle entered the respiratory tract and the injection is being made erroneously into the lunge. Any of these signs would necessitate immediate stop of the administration and withdrawal of the needle. The animal must be observed very carefully. If there is any sign of lung damage, the animal should be euthanised humanely. Once it has been ascertained that the needle is in the right position, the solution can be given fairly rapidly. As soon as the administration is finished, the tube must be withdrawn. Administering a corrosive solution, the needle must be flushed with saline before pulling back to make sure that the mucosa of the upper gastric tract will not be irritated or even damaged (Fig. 8.2).

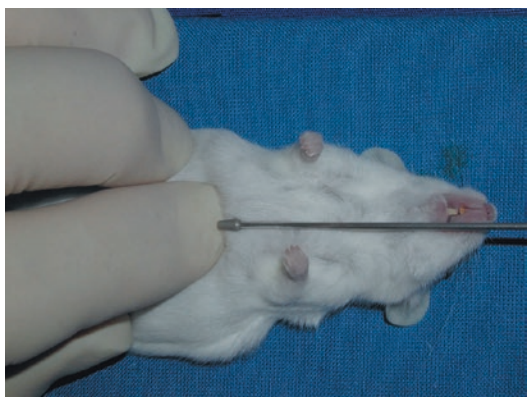

Fig. 8.1 Measuring the suitable length of a probe for intragastric administration in mice, i.e. reaching from the mouth to the end of the breastbone

Fig. 8.2 Radiograph of gavage in a rat with a straight, blunt-ended stainless steel needle. The stomach is filled with X-ray contrast medium

Using this technique there could be a certain risk of introducing trauma or a fatal accident as mentioned before. For this reason, only well-trained, skilled personnel should carry out intragastric administration. First training should be done with dead animals. When training with anaesthetised animals, it is important to choose an anaesthetic that allows the animals to retain its swallowing reflex (e.g. ketamine/xylazine).

However, intragastric administration by gavage can be performed very rapidly. A very well-trained person can feed as many as 120 well-trained animals per hour as example (Ferrill and Hill 1943). When properly performed, accidental tracheal infusion is rare (Kraus 1980).

Knowledge of small rodent's drinking or feeding habits will help to determine whether or not a substance is given on a full stomach or an empty one. When fed ad libitum, animals will never have an empty stomach at any time of the day. The stomach of a mouse or rat is maximal packed at the end of the dark period, and a minimum of content is found at the end of the light period. Therefore, if no overnight food restriction is done, the animals should receive only a very small volume. Otherwise, the animals have to be starved prior to the administration of larger volumes.

By this method substances can be administered directly into the stomach with accurate dosages and reliable timing. When a liquid volume is administered by gavage, a substantial amount of the dose passes rapidly through the stomach to the small intestine. This occurs both in fasted and in fed animals (Claassen 1994d) and results in the substances being absorbed very rapidly. For example, within one minute after quinine solution administration to the fasting animal, 30 % (mice) and 24 % (rat) of the dose are transferred to the small intestine (Watanabe et al. 1977). Absorption is much faster than that with dietary administration, leading to a peak and not a slow and prolonged gradient in the blood.

Using a special feeding needle for capsules and filling the substances into commercially available gelatine miniature capsule, this technique can also be used for intragastric administration of solid materials (Lax et al. 1983, Waynforth and Flecknell 1992a).

8.4 Parenteral Administration

Application of substances other than via the gastrointestinal tract to the body is called parenteral administration. Methods of parenteral administration without penetrating the skin are topical applications and inhalation. Other methods are implantation of catheters and subcutaneous or intraperitoneal implantation of pellets, osmotic pumps or vascular access ports (VAPs). But the most common parenteral routes are injection of substances, solutions or suspensions into the mouse or rat subcutaneous, intraperitoneal or intravenous. Small amounts of solutions or suspensions are injected, and large volumes are infused.

The rate of absorption is dependent on the route of administration. The most rapid absorption is achieved by intravenous injection. The large surface area of the abdominal cavity and its abundant blood supply also facilitate rapid absorption after intraperitoneal injection. But the absorption from this route is usually one-half to one-fourth as rapid as it is from the intravenous route (Woodard 1965). Some injected fluids cause tissue irritation. Therefore, they should only be used after being diluted with solutions (e.g. sodium chloride solution) and should, if possible, be given directly into the blood stream where the solution becomes quickly diluted.

Animals must be properly handled and restrained in order that injection procedures can be carried out without endangering either the animal or the operator. Various proper restraining techniques and many commercially available mechanical restraining devices have been described in literature. But it is outside the scope of this chapter to discuss in detail this issue. The reader is pointed out to the special literature about restrain. The duration and extent of handling or restraining will depend, among other factors, on the application method chosen and the requirements of the experiment.

Over the years many different routes and methods of injection techniques have been used and documented. Some of these recommended techniques are the same as for venous blood collection or bleeding procedures. Although injec-

tions should normally be given without anaesthesia, this is not a general rule. For instance, if the person carrying out the injection is not well trained, or if the substances are irritating, it is better to anaesthetise the rat or mouse with a short-acting narcotic.

When using injection or infusion techniques, several points deserve special attention. These methods require strict asepsis. Sharp and sterile needles of a size appropriate to the size of the animal and, in particular for intravenous injection, by the size of the selected vessel must be used. The required needle gauge depends on the viscosity and volume as well as the speed of injection of a fluid. To assure short injection and restrain time, larger diameter needles are necessary for injection of large volumes or viscous fluids. On the other hand, using too thin needles, there is the risk that the needle may snap from the syringe. But as a thin needle causes less pain and prevents the fluid from flowing back, the smallest needle should be always selected. The injection of cold fluids is painful (Baumans et al. 1993), so the fluid must be brought at least to room temperature or better still up to body temperature before used. Substances administered into the blood circulation must be soluble in suitable solvents, and, because of the risk of embolism, air bubbles in the fluid have to be avoided.

As the physiological principles of fluid administration cannot be discussed here in depth, only some recommendations are given with respect to administration volume and needle sizes.

8.4.1 Topical Application

The skin is a convenient site for the administration of drugs. The absorption of substances through the skin is an area of research that has been extensively studied for a number of years. Dermal absorption represents a pathway for substances to enter the body, particularly in cases of occupational and environmental exposure.

Numerous factors can affect the extent of percutaneous absorption of a substance. These include the physicochemical properties of the substance, the attributes of the vehicle and the permeability of the skin (Franklin et al. 1989; Wester and Maibach 1986). Important factors affecting dermal absorption are the water and lipid solubility properties of the substances used for topical application. The outermost layer of the skin is essentially a lipid barrier, whereas the viable epidermis, which lies below the stratum corneum, is basically of an aqueous environment (Guy and Hadgraft 1991). Thus, the ability of a substance to be absorbed through skin and enter the systemic circulation is determined by its ability to partition into both lipid and water phases.

The most usual sites are the skin covering the back or the abdomen. When not using hairless or nude animal, the hair must be removed. This can be done either with a depilatory or with an electric clipper or wet shaver. As depilatories are chemical substances, they could interfere with the study. Their use should therefore be considered carefully. After clipping the hair, the hairless area should be cleaned of any fat and grease and other debris. If possible the animal should be prepared several days in advance so as not to affect the experiment. Shaving should be done at least 1 day ahead because of microinjuries. The substances should be dissolved in a volatile solvent or mixed in a suitable cream before application and then applied with a dropper or smeared onto the skin with a swab. Some precautions are usually necessary to prevent the animal from licking or scratching the application sites (Woodard 1965).

As active hair growth or the age of the skin will influence absorption of topically applied substances, the state of the hair cycle should be taken into consideration (Waynforth and Flecknell 1992a).

8.4.2 Inhalation

The inhalation route, necessary for some drugs or vaccines, is the nearest akin to an intravenous injection because of the relatively large lung alveolar surface presented for absorption by a membrane that is separated from the blood by one or two cell layers. Consequently, absorption

of gases or aerosols that reach the alveoli is virtually complete. The greatest problem in using this method is the generation of a suitable aerosol of the test substances (Shimizu 2004) and to accurately determine its dosage (Waynforth and Flecknell 1992a).

8.5 Administration by Injection

8.5.1 Intradermal Injection (i.d.)

The intradermal (intracutaneous) injection is not recommended in general and should be restricted to cases of absolute necessity (CCAC 2002). It is a tricky procedure in any species, but especially difficult in the mouse because the skin is very thin (Suckow 2001). The usual sites and the preparation of the skin are the same as for topical applications. Before starting the injection, the site must be clean and swabbed with an antiseptic.

Local or general anaesthesia is generally required for accurate intradermal injection techniques and for humane considerations (Pekow and Baumans 2003). Only very small quantities of solutions – per injection site 0.02–0.05 mL – can be deposited intradermal. For injection, a special short-bevelled hypodermic needle or an ordinary 27-G needle is held bevel down almost parallel to the skin and is pierced only within 1 mm or 2 mm into the skin of mice or rats, respectively. Resistance should be felt both as the needle advance and as the fluid is injected.

A successful intradermal injection of even a small quantity of fluid results in a hard bleb at the injection site, while no bleb is formed when the injection is done by mistake subcutaneously (Fig. 8.3).

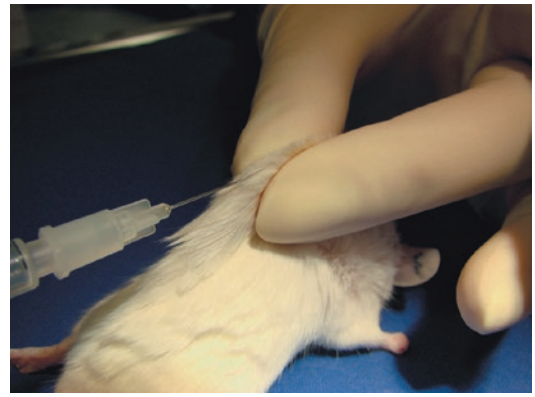

Fig. 8.3 Intradermal injection in a mouse

8.5.2 Intramuscular Injection (i.m.)

This route usually results in more rapid absorption than from the subcutaneous route (Woodard 1965). Absorption usually takes 45–60 min for most fluids. Repository forms are available which remain for days and weeks (Moreland 1965).

Intramuscular injections are usually avoided in the mouse because of its small muscle mass, and as muscle masses of the rat are not very large, the number of practical injection sites and the volume that can safely be given by the intramuscular routes are restricted.

Intramuscular injections are frequently painful, due to the distension of muscle fibres which occurs, and therefore good technique and restraint are required (Wolfensohn and Lloyd 1994). An overview of recommended injection volumes and suggested hypodermic needle sizes are given for mice in Table 8.2 and for rats in Table 8.3. The respective recommendations from the GV-SOLAS can be found in the chapter Appendix of this book.

The intramuscular route should only be used if a less painful alternative is impossible, or if it is clinically required (Working Party Report 2001). If necessary, the injection may be given into the quadriceps muscle of the mice. In rats, the quadriceps feels like a small peanut on the front of the thigh and can be immobilised with the thumb and forefinger of one hand while injecting with the other (Wolfensohn and Lloyd 1994). The muscles of the posterior thigh area of mice and rats should be avoided because the sciatic nerve runs along the back of the femur. Irritant substances that are inadvertently injected in close proximity to this nerve may result in lameness or in the animal's self-mutilation of the affected limb. Intramuscular injections for rats can also be given into the gluteus muscles of the hind leg.

Table 8.2 Recommended administration volumes and suggested needle sizes for mice

	s.c.		i.m.		i.p.		i.v.	
	mL/kg	Gauge	mL/kg	Gauge	mL/kg	Gauge	mL/kg	Gauge
Wolfensohn and Lloyd (1994)	0.5[a]	25 G		27 G	2–3	27 G		25–28 G
Diel et al. (2001)	5		0.1[b]		10		5	
Pekow and Baumans (2003)[c]	0.25	25 G	0.05[b]	27 G	0.5	25 G	0.3[d]	26 G
Bihun and Bauck (2004)	2–3	21–26 G	0.03[b]	23–26 G	10	21–26 G	0.5–3[d]	23–26 G
Shimizu (2004)	2–3	<25 G	0.05	25–27 G	2–3	<23 G	0.2	<25 G
Weiss et al. (2009)[e]	0.5		0.03		1.5		0.15	

[a]2–4 sites
[b]Per site
[c]Weight of the animal: 25 g
[d]Slow (1–3 min)
[e]Weight of the animal: 30 g

Table 8.3 Recommended administration volumes and suggested needle sizes for rats

	s.c.		i.m.		i.p.		i.v.	
	mL/kg	Gauge	mL/kg	Gauge	mL/kg	Gauge	mL/kg	Gauge
Waynforth and Flecknell (1992a, b)	Up to 5	21–25 G	0.2		Up to 10		2[a]	23–25 G
Wolfensohn and Lloyd (1994)	1–2[b]	25 G	0.1	25 G	5–10	23–25 G	1	25–27 G
Diel et al. (2001)	5		0.1[c]		10		5	
Pekow and Baumans (2003)[d]	1	25 G	0.1[c]	25 G	2	25 G	4[a]	25 G
Bihun and Bauck (2004)	5–10	21–26 G	0.2–0.3[c]	22–26 G	10	22–26 G	0.5–3[a]	22–26 G
Weiss et al. (2009)[e]	2[c]		0.25[c]		5		1.25[a]	

[a]Slow (1–3 min)
[b]2–4 Sites
[c]Per site
[d]Weight of the animal: 200 g
[e]Weight of the animal: 250 g

During the injection procedure, the animal must be anaesthetised or manually restrained by another person. Penetration by the needle of only few mm is sufficient for a deep intramuscular injection and avoids the risk of damaging the periost of the femur. The tip of the needle should always be directed away from the femur. Care is taken to visualise the depth at which the needle is placed, ideally centering the tip near the middle of the muscle group. The use of a short needle gives better control (Pekow and Baumans 2003). Sometimes an intramuscular injection will fail, even though the needle is felt to be in the muscle mass, because it actually lies in one of the fascial planes (Waynforth and Flecknell 1992a). Prior to injection of the fluid, aspiration by pulling back lightly on the plunger of the syringe must be done to rule out accidental injection into a blood vessel. After injection, the site should be massaged to disperse the dose because of the difficulties described; the intramuscular administration should only be used if there is no alternative and should only be performed by well-trained persons (Wolfensohn and Lloyd 1994) (Fig. 8.4).

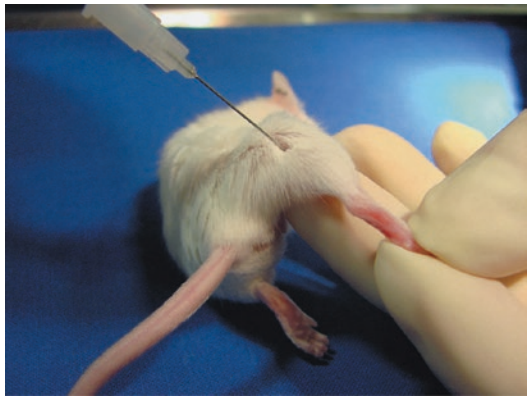

Fig. 8.4 Intramuscular injection into the area of the gluteal muscles of the hind leg in a mouse using a 26-G needle

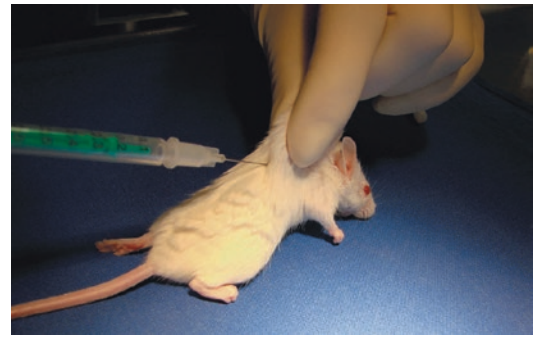

Fig. 8.5 Subcutaneous injection in a mouse at the base of a fold of loose skin (area at the back) using a 26-G needle

8.5.3 Subcutaneous Injection (s.c.)

In comparison with other routes of administration, the subcutaneous injection has several advantages. The subcutaneous area is well supplied with capillaries, but their number may differ at various sites of injection, and this may lead to differences in the rate of substance absorption. Nevertheless, as this method of administration will produce a substance depot, subcutaneous injection is the best option when a relative long period of substance absorption from a repository injection site is desired. This technique is painful if the pH or osmolarity is wrong, or if the material is irritant or cytotoxic. Tissue necrosis can occur (Working Party Report 2001). Substances or solutions which have such adverse characteristics should be diluted with suitable fluids before being subcutaneously administered. On the other hand, oil suspensions can be given subcutaneously. An increased rate of absorption can be achieved by the additional use of hyaluronidase injected at the same site (Woodard 1965).

Subcutaneous injection is the preferred method for the administration of substances into small laboratory animals. This is due to the simplicity of the injection technique, greater choice of injection sites and the possibility to deposit large volumes. Normally, the scapular region is the preferred site for a single subcutaneous injection. Other recommended sites are the back or the ventral abdomen. As subcutaneous injections of compatible solutions are rarely painful (Wolfensohn and Lloyd 1994), a conscious animal can usually be used.

Recommended injection volumes and suggested hypodermic needle sizes for aqueous solutions are given for mice in Table 8.2 and for rats in Table 8.3 or in the chapter Appendix. Viscous solutions or suspensions require a needle of 2–4 wire gauge numbers smaller.

For subcutaneous injection, a fold of loose skin is lifted between the thumb and the forefinger, and at the base of the fold, the needle, attached to the syringe, is passed in an anterior direction through the skin parallel to the body of the animal, to avoid penetrating deeper tissues. Ideally, the whole of the needle shaft should lie subcutaneously as this prevents leakage of the injected fluid. When in position, the tip of the needle should be moved up and down to reveal its whereabouts and also to ascertain that the needle is truly subcutaneous. If the tip cannot be discerned, then the needle could be in an intraperitoneal or intramuscular position and must be slightly withdrawn to lie subcutaneously. Before injecting the substance, aspiration has to be done to ensure that the needle has not entered a blood vessel or has moved out of the skin again (Fig. 8.5).

8.5.4 Intraperitoneal Injection (i.p.)

Also the Joint Working Group of Refinement (Working Party Report 2001) stated that this

route should not be used routinely (except for administration of certain anaesthetics); this application procedure is one of the most frequently used parenteral routes of administration in small laboratory animals. But this technique is not recommended for pregnant animals since the needle can puncture the gravid uterus. The large surface area of the abdominal cavity and its abundant blood supply facilitate rapid absorption. Absorption from this rote is usually one-half to one-quart as rapid as that from the intravenous route (Woodard 1965). However, for long-term studies, repeated injections may lead to tissue reaction and adhesions. As relative large volumes can be given intraperitoneal, potentially irritant substances can be generously diluted. When using this method, it has to be kept in mind that substances given intraperitoneal are first absorbed into the portal circulation. Biotransformation of the injected substances may take place in the liver before they reach the general circulation, so that their bioavailability is quite different from that of an intravenous injection.

Intraperitoneal injections are generally undertaken without anaesthesia. Recommended injection volumes and suggested hypodermic needle sizes are given for mice in Table 8.2 and for rats in Table 8.3 or in the chapter Appendix.

The abdomen can be divided into four quadrants by the midline and a line perpendicular to it passing through the umbilicus. The upper two quadrants are a hazardous area to inject because the liver, stomach and spleen are situated here. For this reason, the intraperitoneal injection should be placed into one of the lower quadrants of the abdomen. To avoid injection onto the caecum at the right, the injection into mice should be done into the caudal left abdominal quadrant (Suckow 2001), and while using rats, the application should be done into the right quadrant to avoid punctuation of vital organs (Fig. 8.6).

Mice and small rats can be properly restrained and injected by one person. When injecting larger rats, it is advisable to have an assistant. The hindquarter and tail are restrained by the assistant, and the operator extends one of the animal's hind legs and carries out the injection (Waynforth and Flecknell 1992a).

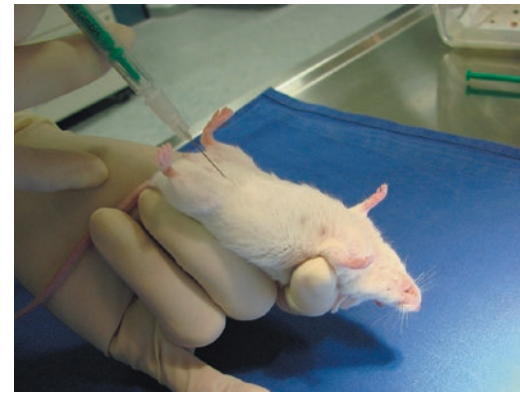

Fig. 8.6 Intraperitoneal injection into the lower left quadrant of a mouse using a 26-G needle

At the start of the administration, some investigators tilt the animal so the head is lower than the abdomen in an attempt to slide the viscera cranially and away from the needle. However, the viscera are quite immobile because of the slight vacuum in the abdomen, and this manipulation is of questionable value (Fallon 1996).

Because of the risk that the injection is made between the skin and the abdomen muscles or the risk of accidental penetration into the viscera, the short needle should enter the skin neither parallel nor vertical but rather at an angle of 10–20°. With a quick, firm motion, the tip of the needle is inserted through the skin subcutaneously. To avoid leakage from the puncture point, the needle is run through subcutaneous tissue in a cranial direction for 2–3 mm, and then a final short thrust is made through the abdominal wall, holding the needle nearly vertical (Shimizu 2004). It is necessary to insert only the tip of the needle into the peritoneal cavity; otherwise, the intestine can be punctured (Waynforth and Flecknell 1992a). Prior to administration of the compound, aspiration must be done. If any kind of fluid – urine, intestinal content or blood – is pulled back into the syringe, the needle is probably in one of the abdominal organs and should be repositioned. This may have no serious consequences for the animal but may be associated with slow and erratic absorption of the compound. This is a particular problem in the case of anaesthetics as the animal will not respond as expected to the drug.

Redosing under these circumstances is tricky as the initial dose will eventually be absorbed and, combined with the second dose, may prove fatal (Suckow 2001).

As there are only few references to incorrect intraperitoneal injections, it is often assumed that an intraperitoneal injection always delivers the substances to the peritoneal cavity. But a lack of references to the possible occurrence of injection errors makes it likely that it is not always realised that such errors may be a source of experimental variation. Nevertheless, a significant part of the injections are actually made intragastrically, intraintestinally, subcutaneously, retroperitoneally or intracystically (Claassen 1994e). The frequency of erroneous injections by skilled investigators has been reported by Lewis et al. (1966), who stated that in nearly 20 % of the animals, parts of the material were not injected into the peritoneal cavity. But even the well-controlled use of a standardised injection technique can only reduce the number of erroneous injections to 5.5 % (Schneider and Schneider 1970). Sometimes it is possible to recognise the error, for instance, when the injection is made into the intestine, fluid will be seen often issuing from the rectum immediately after the injection (Waynforth and Flecknell 1992a, b), or the animal will defecate.

If an injected fluid needs to be quickly diluted in the blood, then the intravenous instead of the intraperitoneal route should be given preference, thus also avoiding the risk of peritonitis.

8.5.5 Intravenous Injections (i.v.)

Intravenous administration offers various advantages over other routes of injection. For example, it gives control over the rate of introduction into the general circulation, rapid response, etc., and it provides the most complete availability of substances with minimal delay. By controlling the administration rate, constant plasma concentrations can be obtained at the required level. Unexpected side effects during administration can be halted by stopping the injection. Compounds that are poorly absorbed by the digestive tract or are unacceptably painful when given intramuscularly or subcutaneously may be administered intravenously when given carefully into the vein without leaks into the surrounding tissues.

Several general points on intravenous injection or infusion deserve special attention. Except in terminal experiments, reasonable aseptic techniques with sterile equipment must be employed, particularly when animals are being used in long-term studies and frequent injections are required. The syringe plus needle must first be filled with the solution for injection so that no air bubbles are administered. When using large veins, it should be easy to aspirate blood if the needle lies correctly, but it is not always possible to do so with small veins. After injecting a small amount of the solution into a small vein, the injected fluid should be washed away by the blood in the vessel. If this does not happen, the position of the needle is questionable. As soon as a bleb should arise, the position of the needle is certainly not in the vein but in the surrounding tissue. A fresh attempt must be made, or the needle should be moved in the surrounding tissue in such a way that it then enters the vein. When finishing the intravenous injection, a swab always has to be pressed on to the injection site while pulling out the needle to prevent backflow of administered fluid and/or blood.

Once the vessel has to be used several times, the first injection should be made as distal as possible in relation to the heart, and subsequent administrations should be placed progressively more proximal. This proceeding is necessary because multiple puncture of the same vein and frequent injections of substances can damage and/or block the vein and the distal part of the vessel can no longer be used for subsequent administrations.

While selecting the site of injection, consequences of a possible intravascular thrombosis or a possible extravascular administration of substances, have to be considered.

Mice and rats have no readily accessible veins of sufficient size for venipuncture. Therefore, many methods for vascular access have been described in the literature for mice (Salem et al.

1963; Suckow 2001; Shimizu 2004), for rats (Kraus 1980; Petty 1982; Cocchetto and Bjornsson 1983; Waynforth and Flecknell 1992a; Nebendahl 2000) and for mice and rats (Moreland 1965; Pekow and Baumans 2003). Percutaneous injections are made with conscious animals into the lateral tail vein, lateral marginal vein (v. saphena) or dorsal metatarsal vein and with anaesthetised animals into the sublingual vein or penile vein. Some techniques are difficult to be performed; therefore, many methods have been developed to make this task easier, including the use of a wide range of hypodermic needle sizes, improving visibility of the injection site by magnification, transillumination, shaving, surgical incision and the application of heat, tourniquets and chemicals for vasodilatation. After making a skin incision and surgical exposition, administrations can be made into the external jugular vein or femoral vein. Both routes require the use of anaesthesia.

Different restraint devices and other equipment have been recommended to immobilise the mouse or rat and thus facilitate injection. Anaesthetising the animal is considered helpful, but may be contraindicated for some experiments. Use of these methods or equipment cannot guarantee a successful injection. For instance, the vein can be deflected by the needle; an inserted needle can dislodge or perforate the vein whenever the syringe is manipulated or when the restrained animal flinches (Nachtman et al. 1988).

As some routes require special technical expertise and skill, they are not advisable for persons who rarely use them. Such persons should confine themselves to methods they can perform or are easy to learn. To avoid pain and shock, injection must always be given slowly, especially when administering large volumes.

8.5.5.1 Lateral Tail Vein

The most common sites for intravenous injection in mice or rats are the lateral tail veins. These vessels are readily visualised but are quite small in diameter, and injection into them requires considerable practice and skill. From the tip to the root of the tail, the lateral vein lies immediately beneath the skin, but the vein narrows from the root to the tip. Because of the very small diameter at the tip of the tail, the vessels are not visualised at the tail top even in albino animals. Therefore, the whole length of the vein cannot be used for this administration technique. Videm (1980) presented a simple and relatively rapid method using the lateral vein of a rat at the root of the tail where the skin, after being shaved, is thin and smooth and where the vessels are superficial and accessible for intravenous injection.

As anaesthesia causes decrease in blood pressure, it is normally not used. So in conscious animal, the use of a restraint device is necessary for lateral tail vein injection because the tail is sensitive. Several types of clear plastic restraint devices which allow tail access are commercially available for small laboratory animals (Waynforth and Flecknell 1992a; Fallon 1996; Pekow and Baumans 2003).

Since the tail is a major thermoregulatory organ with a large surface available for heat loss, an enhanced blood flow in the dilated veins and hence a successful venipuncture can be ensured by warming prior to injection. Warming the whole animal by placing the animal into a thermostatically warmed “hot box” (Conybeare et al. 1988), warming the tail under a heating lamp (Shimizu 2004) or holding the tail in warm water for 1–2 min (Barrow 1968; Fallon 1996) can induce tail veins dilation. When placing animals in a warmed box, the chamber temperature should not exceed 37 °C, and the animal must be observed constantly for signs of distress (Working Party Report 2001). Another method to obtain a good venous filling is constriction. Several methods are described using finger pressure (Barrow 1968) and/or a tourniquet (Videm 1980; Petty 1982; Waynforth and Flecknell 1992a). The pressure or the tourniquet must be released just before the injection is made.

For injection, the tail should be bent down with one hand, while the vein is punctured at the angle of the bend with the needle and syringe held in the other hand. The vessel must be entered at a very small angle almost parallel to the vein. The tip of the needle is then advanced only few millimetres. Aspiration of

blood to confirm correct needle placement can be done with rats, but is not productive in mice (Pekow and Baumans 2003). Starting the injection, no resistance will be felt as the fluid is administered and the vein will appear to "blench out" (Suckow 2001). Failure of insertion is identified by swelling of the tail or blanching of the skin. For slow intravenous injections, a butterfly needle (needles with attached flexible tubing) should be used, because as soon as the needle has been seated in the vessel and taped in place, the flexible tubing permits the animal some freedom from complete restraint and the tip of the needle cannot be pulled out or penetrate through the vessel during the injection period.

The injection is carried out using a 23–25-G needle or better a 27-G butterfly set (Fig. 8.7).

8.5.5.2 Lateral Marginal Vein (Large Saphenous Vein) of Rats

In the opinion of Grice (1963), injection into this vein or saphenous vein of a rat provides the method of choice. The animal may be anaesthetised or placed in a restrainer, leaving one hindlimb free. The posterior and lateral surface of the thigh and leg of the hindlimb are shaved. The rat is held firmly by an assistant placing the right hand over the hips of the animal, with the free limb positioned between the first and second fingers and applying sufficient pressure to cause this vein to become quite prominent without the use of any form of tourniquet. The left hand of the assistant holds the foot firmly (Pearce 1957).

Pearce (1957) recommended a 26- or 27-G hypodermic needle for injection (Fig. 8.8).

8.5.5.3 Dorsal Metatarsal Vein (Small Saphenous Vein)

Everett and Sawyer (1956) first described this injection technique for rats. The vein is found on the dorsal surface of the foot. The skin over the lateral plantar surface is shaved and swabbed with antiseptic. The operator holds the foot by the toes during the procedure, and an assistant aids by holding the knee in such a manner that sudden flexion and withdrawal of the foot are prevented. A 26-gauge hypodermic needle kept almost horizontal to the surface and directed towards the ankle is inserted through the skin and into the vein at a point where it just starts to travel up the foot after first crossing the foot and supplying the toes with blood.

Everett and Sawyer (1956) recommended a 26-G hypodermic needle for injection (Fig. 8.9).

8.5.5.4 Penis Vein (Penile Vein)

The advantage of this method is in its applicability to animals – for instance, mice – having no easily accessible site to intravenous injection (Salem et al. 1963). Petty (1982) maintained that the dorsal penis vein injection is much simpler, more rapid, more reproducible and easier

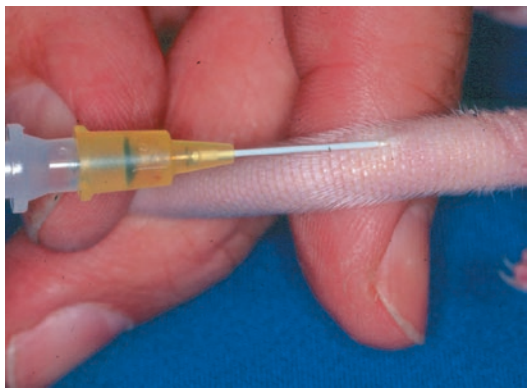

Fig. 8.7 Lateral tail vein injection in a rat using a 24-G "over-the-needle" catheter

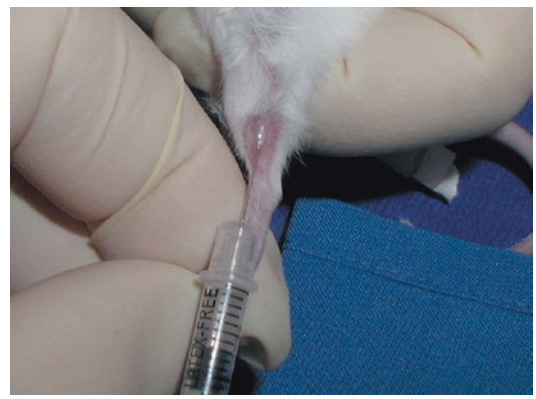

Fig. 8.8 Insertion of a 29-G needle into the lateral marginal vein of a mouse

Fig. 8.9 Dorsal metatarsal vein injection in a rat using a 26-G needle

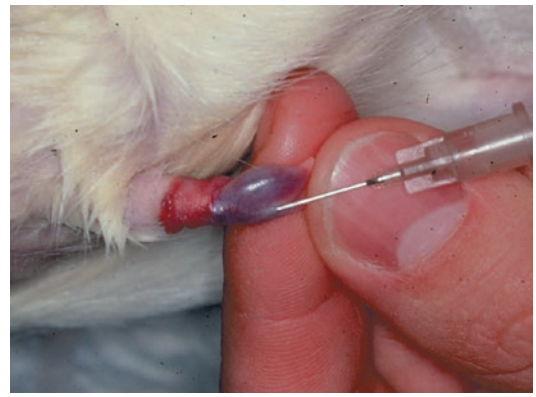

Fig. 8.10 Dorsal penis vein injection in a rat using a 26-G needle

to accomplish than tail vein injection and the technique can be learned easily. But Waynforth and Flecknell (1992a) stated that this route should only be used under special circumstances, because of the consequences of damage to the vein.

Nightingale and Mouravieff (1973) investigated whether the penile vein is part of the portal or general circulation. Based on these experiments, they concluded that injection into this vein leads to the general circulation and that a first-pass effect on metabolism is not to be expected.

The anaesthetised animal is placed on its back on the table. The glans penis is exposed by sliding the prepuce downwards while pressing at the base of the penis. It is held at the very tip with the thumb and the forefinger. If it is not placed under too much tension, the penile vein is easily seen as a distinct central vein. Once the vein is pierced, aspiration of blood is virtually impossible, therefore only a very small volume has to be injected first to see if it flows freely. After the injection, the injection site is pressed with a swab for a few seconds, and the gland is encouraged to retract to prevent further bleeding (Waynforth and Flecknell 1992a).

For rats from weaning age and older, Waynforth and Flecknell (1992a) recommended a 24-G hypodermic needle and a 30-G for smaller animals, and Salem et al. (1963) a 26–30-G needle for mice (Fig. 8.10).

8.5.5.5 Sublingual Vein (Tongue Vein)

As the entire procedure, namely, anaesthesia, suture and injection, can be done in less than 5 min, Petty (1982) recommended the sublingual vein for rats, which is frequently overlooked as an injection site. As the injection technique is described in detail for rats by Petty (1982), Waynforth and Flecknell (1992a) or Diehl et al. (2001) and for adult mice by Waynforth and Parkin (1969), the reader is referred to these articles. Also, this technique is easy to perform, and any differences in the eating or drinking habits of the animals were noted after injection; the necessity of repeated anaesthesia limited frequent injections by this method.

Waynforth and Flecknell (1992a) recommended for rats and mice a 25- or 30-G and Diel et al. (2001) for rats a 23–25-G hypodermic needle for injection (Fig. 8.11).

Without special experience, access to the jugular vein or the femoral vein is only possible after surgical exposition of these vessels. As injections via a needle or infusions via a catheter require a similar preparation, more details in respect to these injection techniques are given later.

8.5.5.6 Intravenous Injection or Infusion by Catheter

Chronic venous cannulation, implantation of indwelling vascular catheters or vascular access ports (VAPs) in small laboratory animals are an accepted and extremely useful experimental

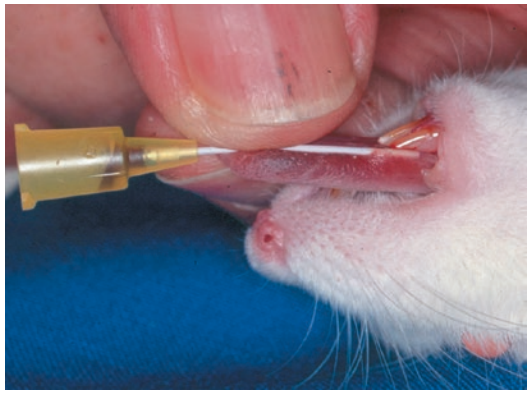

Fig. 8.11 Sublingual vein injection in a rat using a 24-G "over-the-needle" catheter

technique for repeated injections or permanent infusions, since they reduce the stress of multiple injection associated with, for example, restraint and discomfort due to repeated needle pricks into vessels. Short-term catheterisation of a few days is relatively easy to accomplish, for instance, using an over-the-needle catheter; however, complications increased with the amount of time required for the catheter to be maintained and are related to the side of placement.

A number of authors have described techniques for chronic catheterisation of different blood vessels of mice or rats (Desjardins 1986; Joint Working Group on Refinement 1993). Each technique has its own individuality, and the investigator must adapt to meet the needs of the experimental design (Petty 1982). The procedures described differ also in the various protection devices employed to prevent the animal from manipulating the catheter through pushing, pulling away or biting, in the methods of maintaining proper catheter placement and of exteriorizing the catheter, in the use of different surgical techniques and in the methods used to maintain the patency of the catheter.

The procedures used to fit animals with an indwelling vascular catheter fall into two general categories:

1. Direct access is accomplished by attaching a syringe or a piece of tubing to the exteriorised distal end of the catheter just before injection or infusion. This requires some form of handling or restraint of the animal. The duration and extent of these manipulations will of course depend on the method chosen for implantation, on the type of catheter, on the requirement of the study and in particular on the experience of the operator.
2. Remote access involves tethering the animal, usually by a protecting device, as the catheter is extended beyond the animal's home cage. This method permits access to the vascular system of otherwise undisturbed, freely moving animals housed singly.

As advances in the polymer industry have led to the production of many synthetic materials with acceptable biocompatibility, catheters for nearly every vessel of small laboratory animals are available nowadays. Also various methods have been used to minimise the incidence of thrombotic occlusion of the intravascular catheter or to remove existing thrombotic obstructions to prolong the patent lifetime of catheters; standardised instructions for routine catheter care have not been created till now.

To prevent clotting in the catheter, it should be flushed with heparinised saline or another anticoagulant after placement and between infusions or injections, if not daily, at least twice a week, and the dead space in the cannula is then replaced by a carefully calculated amount of fresh anticoagulant. A concentration of 10–1,000 IU heparin per millilitre saline is recommended (Joint Working Group on Refinement 1993). If the catheter still becomes blocked, it may be possible to dissolve the thrombotic occlusion by filling the catheter with a solution of urokinase or streptokinase (Hurtubise et al. 1980). Cannulas without heparin form small clots at the tip that, if dislodged, can cause pulmonary, renal or heart infarcts.

Percutaneous Insertion of the Catheter

Percutaneous methods involve the implantation of the catheter into a blood vessel by piercing the vessel with a needle and pushing the catheter through the needle into the vessel.

In a non-surgical approach, catheters are inserted into a vessel of an animal. For instance,

Little et al. (1962) and Rhodes and Patterson (1979) inserted the needle through the intact skin into the tail vein of a rat and Marini and Garlick (2006) in the same vessel of a mouse. When blood flowed freely, the catheter was guided through the trough of the needle into the vein. Nachtman et al. (1988) or Waynforth and Flecknell (1992a) used a commercially available over-the-needle catheter, comprising a short cannula fitted over the needle which is only a few mm longer than the cannula. This unit has two distinct advantages over hypodermic needles. It provides a visual check that the vein has been entered as blood fills the needle, and once the cannula is established in a vessel, any movement by the animal or the operator does not lead to penetration or laceration of the vessel wall as easily as a hypodermic needle because its cannula is pliable and blunt. After positioning the tip of the needle and cannula into the vein, the needle is withdrawn while holding the cannula firmly in place. Once the cannula has been filled with blood, the needle can be withdrawn completely.

Practical Hint

Another easy and cost-effective way of catheterisation of the lateral tail vein of mice is used in non-invasive imaging experiments with MRI and CT frequently. A tail vein is catheterised using a 30-G needle connected to a 10-cm PE 10 polyethylene catheter (Portex) filled with 0.9 % NaCl. Successful puncture of the mouse tail vein is controlled by blood reflux into the catheter and by the injection of 20-µL 0.9 % NaCl. Ten centimetres of this catheter contains a volume of 10-µL. Then, the needle is fixed on the mouse tail with superglue. The distal end of the catheter can be connected with a PE 50 polyethylene catheter (Portex) containing the contrast agent and a 1-mL tuberculin syringe. After each examination, the needle can be removed from the tail vein.

Surgical Implantation of the Catheter

Numerous methods are available for implantation of catheters in different veins and/or arteries of small laboratories rodents (Petty 1982). Cocchetto and Bjornsson (1983) reviewed many articles on arterial and venous implantations and gave methodological notes as well as procedural comments. Detailed procedures of preparing catheter equipment and inserting the catheter have been described, for instance, by Weeks and Davis (1964) and Harms and Ojeda (1974), who gave details about an easy-to-prepare cannula and a simple procedure for cannulation.

Frequently used vessels for chronic catheterisation are the tail vein, extern and intern right jugular vein, femoral vein and artery or the left carotid artery and the aorta. Surgical techniques for the permanent catheterisation of the jugular vein of rats (Remie et al. 1990) or of mice (Bardelmeijer et al. 2002), of the tail vein (Born and Moller 1974), of the jugular vein, femoral and carotid artery (Yoburn et al. 1984) and of the carotid artery, dorsal aorta, jugular and tail vein (Waynforth and Flecknell 1992b) are comprehensively described in the mentioned reports. The reader is pointed to these articles.

As it is not easy to get a tube into a surgically exposed, small vessel of a small rodent, a lien vessel cannulator is sometimes needed. There are various techniques to fix the extravascular or intravascular portion of a catheter with the vessel and the surrounding tissue or within the lumen of the blood vessel. Details can be found in the article by Cocchetto and Bjornsson (1983). The intravascular catheters are commonly exteriorised by subcutaneous tunnelling from the vascular incision site to the back of the neck or between the shoulder blades (Cocchetto and Bjornsson 1983), and sometimes also to the root of the tail (Jones and Hynd 1981).

The various procedures for protecting the catheter differ in the protective device used to prevent the animal from manipulating the free end of the catheter and/or the connection to the infusion pump. Many authors have addressed the problem of the protection of the catheter from kinking and chewing by the animal or described techniques for proper catheter placement. Other writers have directed their attention towards minimal restraint or towards methods of compensation for rotational movement of the animal in the cage (References see Nebendahl 2000). If catheters are implanted for continuous infusion over long periods and the use of a portable pump is not

practical, the tube must be connected with an infusion pump. Therefore, it is necessary to take special precautions to prevent twisting and kinking of the delivery tubing through movements of the animal. The freedom of the animal must be inhibited as little as possible by the protective device and must allow the animal to move in an unrestricted manner within its cage. If the implanted tube is to be used for multiple injections, the free end of the tube must also be protected from biting or pulling out. For this purpose, the same protective device as for long-term infusion can be used. But if the catheter is exteriorised in the neck area and only a short piece is outside the body, it is not necessary to protect the catheter, if the animal is housed singly.

Animals are not only stressed by the surgical procedure but also by the fact that they have to wear a protecting device and are housed singly or are limited in their movement (Birkhahn et al. 1976; O'Neill and Kaufman 1990). In general, the animals require a period of several days to recover from the procedures for the implantation of chronic catheters. For instance, during the first four postoperative days, the normal weight gain is disturbed and even weight loss can occur (Popovic and Popovic 1960).

As a general rule, infusion of about 1 % of the blood volume per hour will not affect fluid disposition. Infusion of larger volumes should be based on preliminary studies designed to determine whether the cellular and ionic components of blood are maintained in a normal range (Desjardins 1986). For example, Steiger et al. (1972) developing a long-term, unrestrained intravenously fed rat model infused 30–60 mL/day of a specially formulated solution into rats weighing 140–250 g for weeks. However, at low flow rates less than 0.5 mL/h, catheter occlusion by thrombosis may be observed (Cox and Beazley 1975).

As it is well established that an exteriorised vascular catheter is a source for the introduction of infection into the body, it is particularly important to avoid this as an infected animal will be useless for experimentation apart from the welfare aspects in the suffering it may cause. Therefore, it is essential to look for further methods for parenteral administration which does not have the known liability of exteriorised vascular catheter to become infected.

8.5.6 Other Methods for Parenteral Administration

8.5.6.1 Pellets

The delivery of substances at a slow, steady rate over a period specified can be supplied by using controlled – drug delivery releasing pellets. The pellets – available via www.innovrsrch.com – release the active product in the animal effectively and continuously. They are intended for simple subcutaneous implantation (Shimizu 2004).

8.5.6.2 Osmotic Minipumps

Implantable osmotic minipumps are commercially available and are designed to deliver as a continuous infusion of precise volumes for a long period of up to 6 weeks without the need for external connection or frequent animal handling. This small device has been used very successfully in small laboratory animals, and numerous reports about the use of osmotic minipumps can be ordered from the bibliography of the manufacturer (www.alzet.com).

The minipump system is composed of three concentric layers – the substance reservoir, the osmotic sleeve and the rate-controlling, semipermeable membrane. An additional component, called the "flow moderator" is a 21-G stainless steel tube with a plastic end cap. For more details and the principles of operation, see the technical information manual of the manufacturer (Fig. 8.12).

Meanwhile, twelve different pumps are available for rats and mice varying in size from 1.5 × 0.6 cm to 5.1 × 1.4 cm, with a fixed volume delivery rate between 0.11 and 10.0 µL/h, a nominal duration from 1 day to 6 weeks and a reservoir volume from 100 µL to 2 mL (Fig. 8.13).

Because of the mechanism by which the pumps operate, their delivery profile is independent of the chemical and physical properties of the agent dispensed. Successful delivery of an

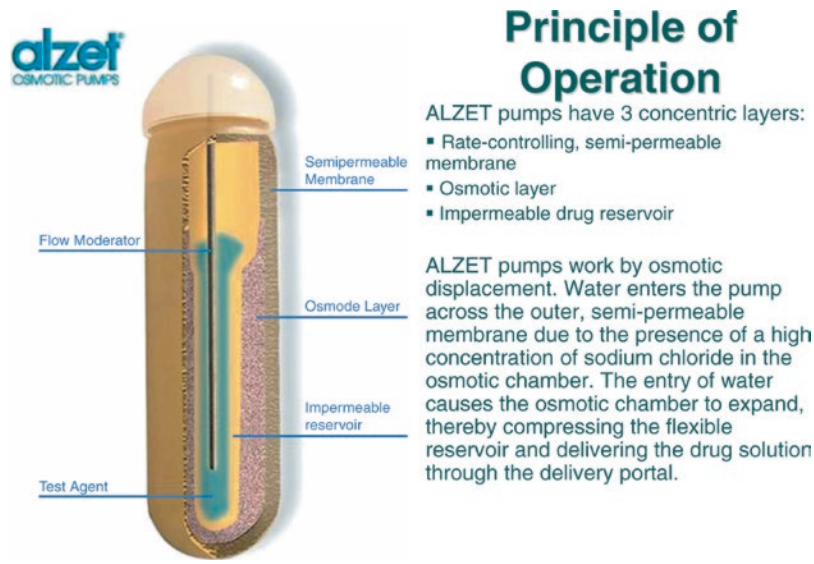

Fig. 8.12 Principles of operation of an ALZET® osmotic pump (Source: www.alzet.com with permission from ALZET®)

enormous range of compounds has been reported in the literature (http://www.alzet.com/products/guide_to_use/pump_selection.html). The average pumping rate should be calibrated, and correct performance should be checked before implantation. The minimal animal sizes for subcutaneous or intraperitoneal implantation of pumps are 10 g for mice and 20 g for rats. Implantation is a surgical procedure and should be done using aseptic technique. In addition, all pump models are easily attached to a catheter, such that a pump, implanted either subcutaneously or intraperitoneally, is used to infuse into a vessel, organ or tissue. Full instruction for the correct use of the minipumps can be found in the Alzet® technical information manual.

The compelling advantages of these minipumps are that they can be placed in situ without further need for infusion equipment and that a large number of animals can be treated effectively with a uniform infusion rate. However, infusion is limited to specific volumes for restricted time periods (Desjardins 1986). The disadvantage can perhaps be solved by implanting a new pump.

8.5.6.3 Vascular Access Port (VAP)

A VAP is a subcutaneously implanted miniaturised device which allows long-term vascular access without the mentioned disadvantages of exteriorised vascular cannula. They are commercially available for mice and rats. A VAP permits continuous access to the venous or arterial system for compound administration. Using strict aseptic technique, the cannula of the VAP is inserted into a vein or artery (femoral artery or vein, jugular vein and carotid artery are common sites, but the portal vein (Gervaz et al. 2000) and other vessels are used too) and secured in place. The other end of the cannula is attached to the port that is secured in a subcutaneous location, most often over the shoulders. The surgical technique for implantation is described in detail by Waynforth and Flecknell (1992b). When the surgical incisions are closed, the entire system, VAP and cannula, is internal. When the animal is to be used, it is either restrained manually or in a suitable restraint apparatus. To access the port for injection, the skin over it must be shaved and disinfected. A needle is inserted through the skin and the diaphragm into the reservoir of the VAP, stopping when it hits the hard reservoir base. Administration of fluids can then be made. Special Huber point needles may be used to prolong the life of the port (Desjardins 1986; Suckow 2001) (Fig. 8.14).

8.5.6.4 Oroendotracheal Intubation

With an expanding use of small laboratory animals in research involving surgery of increasing

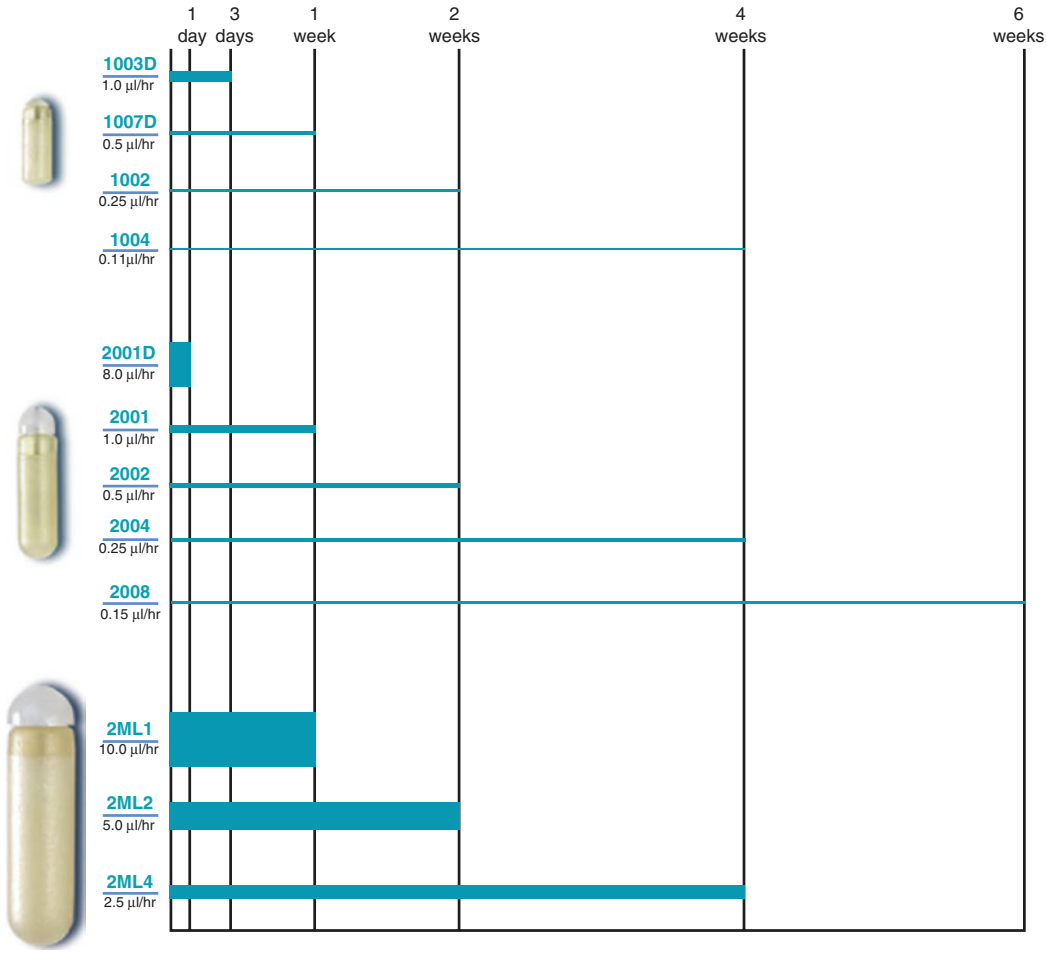

Fig. 8.13 Available ALZET® osmotic pump models (Source: www.alzet.com with permission from ALZET®)

complexity, there is an increasing need for the improvement of anaesthetic techniques for these animals. A free airway is useful in reducing mortality during and after operations. Inhalation anaesthetics provide excellent control over induction and maintenance of anaesthesia but are difficult to use because of the mode of delivery and miniaturising the standard anaesthetic protocol. Numerous reports using a mask (Dudley et al. 1975; Levy et al. 1980; Norris and Miles 1982; Szczesny et al. 2003) or a self-inflating bag mask (Schumacher et al. 2003) for administration of volatile anaesthetics in spontaneously breathing small laboratory animal have been published. However, there is the problem of adequately fitting masks, lack of control of ventilation, waste of anaesthetic gases and hazardous pollution of the operating room.

However, intubation procedure for small laboratory animals requires special miniaturised equipment and skill to perform safely oroendotracheal intubation. Numerous acceptable techniques for this application procedure of rats including blind intubation are reported. More information about many of these methods with rats can be found by Nebendahl (2000), Heard (2004) or Henke and Erhardt (2004).

Also, the majority of animal research is based on mouse models, but there are only few reports about endotracheal intubation of mice. All these reports stressed that direct visualisation of the glottis is indispensable. For example, Costa

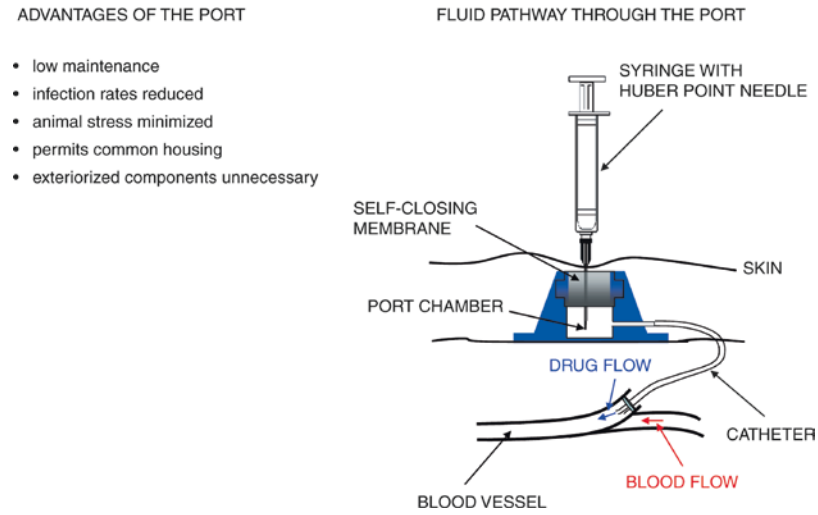

Fig. 8.14 Vascular access port. Fluid pathway through the port and advantages of a port

et al. (1986) developed a fibre-optic laryngoscope for transoral tracheal intubation technique of mice, and Brown et al. (1999) described a simple constructed metal blade used as a laryngoscope to facilitate oropharyngeal exposure and transillumination of the neck to facilitate visualising of the trachea. Vergari et al. (2003) used to facilitate the intubation tube entering the trachea a small bore, straight fibre-optic arthroscope and Spoelsta et al. (2007) a purpose-made laryngoscope and a self-built plastic support. Hamacher et al. (2008) described in detail a microscopic wire guide-based orotracheal mouse intubation.

For starting intubation of small laboratory animals, an endotracheal cannula of suitable size must be selected. For instance, Proctor and Fernando (1973) used for the intubation of rats a 16-G nylon intravenous cannula. Flecknell (1996) recommended the use of a 12- or 16-G arterial cannula and Remie et al. (1990) a modified 14–18-G Hemolock arterial stick and Costa et al. (1986) a 16-G Teflon tubing for rats. Some authors recommend modification of the introductory end of the tube to facilitate penetration of the tracheal lumen or to prevent unintentional intubation of a bronchus and the Luer fitting to provide connection to an anaesthetic circulation (Proctor and Fernando 1973; Flecknell 1996).

Prior to intubation, the animal is anaesthetised to a sufficient depth to abolish the cough and swallowing reflex. For premedication, sedatives and tranquilisers together with injectable anaesthetics are administered, or a face mask/nose cone connected to the anaesthesia machine or a transparent induction chamber, which should have both an inlet for delivery a fresh gas and an outlet for effective removal of waste anaesthetic gases (Otto 2004), can be used. Atropine administration (0.04 mg/kg) is useful in reducing mucus secretion and helps to prevent tube blockage (Flecknell 1996). Laryngospasm may be prevented or be alleviated by spraying a local anaesthetic solution on the cannula or on the vocal cords before intubation. A careful examination of the pharynx and larynx must be carried out, and if the laryngeal region is covered with mucus, the area must be cleared with cotton-tipped applicator to allow visualisation. Techniques of intubation are described in detail for rats by Flecknell (1996), Heard (2004) and Henke and Erhardt (2004).

In the following, an intubation method for mice under direct vision using adopted Seldinger vessel cannulation technique is described in detail. The anaesthetised mouse is positioned in dorsal recumbence on a slant board. An elastic band is then affixed to the upper incisors and fastened to the board, to extend the head and neck.

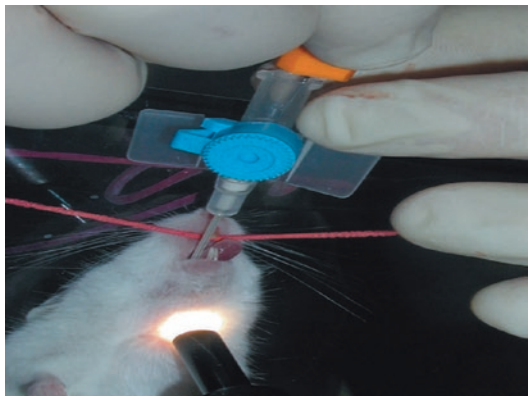

Fig. 8.15 Insertion of an endotracheal tube (over-the-needle catheter) into the trachea of a mouse using the Seldinger technique

The end of a flexible fibre-optic rod of a powerful light source is positioned so that it contacts the surface of the skin in front of the neck near the pharyngoepiglottic region. The light penetrating tissue will illuminate the larynx and the focal cords can be located. The tongue pulled gently forward and to one side. A slight pressure exerted on the ventral surface of the neck may further facilitate visualisation of the glottis. Now a tube – Costa et al. (1986) recommend a 19-G cannula for mice and a 16-G cannula for rats and Spoelsta et al. (2007) a 24-G intravenous catheter – must be brought via the pharynx alongside the epiglottis, through the laryngeal opening into the trachea (Fig. 8.15).

After connecting the tube to the ventilator, the animal must be ventilated, and chest movement and air exchange must be checked for correct cannula placement. If the tube becomes plugged with mucus secretion during ventilation and causes respiratory difficulties, the cannula must be exchanged with a new one.

8.5.6.5 Intratracheal/Intrabronchial Administration

Some experimental protocols require that substances be given intratracheal or intrabronchial; for these studies, intubation techniques can be used too (Lany et al. 1980; Costa et al. 1989; Smith 1991). The administered volume for a rat (bodyweight: 200 g) should be not larger than 0.04 mL.

References

Baggot JD. In: Meyer Jones I, Booth NH and McDonald LE (eds.). Veterinary Pharmacology and Therapeutics. 5th edn. Ames: Iowa State University Press. 1977; p. 43–78.

Bardelmeijer HA, et al. Cannulation of the jugular vein in mice: a method for serial withdraw of blood samples. Lab Anim. 2002;37:181–7.

Barrow RH. Modified intravenous injection technique in the rat. Lab Anim Care. 1968;18:570–1.

Baumans V, et al. Experimental procedures. In: van Zutphen LFM, Baumans V, Beynen AC, editors. Principles of laboratory animal science. Amsterdam: Elsevier; 1993. p. 299–318.

Bihun C, Bauck L. Basic anatomy, physiology, husbandry, and clinical techniques. In: Quesenberry KE, Carpenter JW, editors. Ferrets, rabbits, and rodents: clinical medicine and surgery. Philadelphia: W.B. Saunders; 2004. p. 286–315.

Birkhahn RH, et al. The stress response in the rat from harnessing for chronic intravenous infusion. J Surg Res. 1976;21:185–90.

Born CT, Moller ML. A simple procedure for long-term intravenous infusion in rats. Lab Anim Sci. 1974;24:355–8.

Brown RH, et al. A method of endotracheal intubation and pulmonary functional assessment for repeated studies in mice. J Appl Physiol. 1999;87:2362–5.

CCAC (Canadian Council on Animal Care). Guidelines on acceptable immunological procedures. Ottawa: CCAC; 2002. http://www.ccac.ca/gui_pol/policies.

Claassen V, editor. Oral drug administration. In: Neglected factors in pharmacology and neuroscience research. Amsterdam: Elsevier; 1994a. p. 59–115.

Claassen V, editor. Food and water intake. In: Neglected factors in pharmacology and neuroscience research. Amsterdam: Elsevier; 1994b. p. 267–86.

Claassen V, editor. Fasting. In: Neglected factors in pharmacology and neuroscience research. Amsterdam: Elsevier; 1994c. p. 290–320.

Claassen V, editor. Food restriction. In: Neglected factors in pharmacology and neuroscience research. Amsterdam: Elsevier; 1994d. p. 321–42.

Claassen V, editor. Intraperitoneal drug administration. In: Neglected factors in pharmacology and neuroscience research. Amsterdam: Elsevier; 1994e. p. 46–56.

Cocchetto DM, Bjornsson TD. Methods for vascular access and collection of body fluids from the laboratory rat. J Pharm Sci. 1983;72:465–92.

Costa DL, et al. Transoral trachea intubation of rodents using a fiberoptic laryngoscope. Lab Anim Sci. 1986;36:256–61.

Conybeare G, et al. A improved simple technique for the collection of blood samples from rat and mice. Lab Anim. 1988;22:177–82.

Cox CE, Beazley RM. Chronic venous catheterization: a technique for implanting and maintaining venous catheters in rats. J Surg Res. 1975;18:607–10.

Desjardins C. Indwelling vascular cannulas for remote blood sampling, infusion, and long-term instrumentation of small laboratory animals. In: Gay WJ, Heavner JE, editors. Methods of animal experimentation, vol VII, part A. Orlando: Academic; 1986. p. 143–94.

Diel K-H, et al. A good practice guide to the administration of substances and removal of blood, including routes and volumes. J Appl Toxicol. 2001;21:15–23.

Dudley W, et al. An apparatus for anesthetizing small laboratory animals. Lab Anim Sci. 1975;25:481–2.

ETS 123. European convention for the protection of vertebrate animals used for experimental and other scientific purpose. Strasbourgh: Council of Europe; 1986.

Everett JW, Sawyer CH. The small saphenous vein as a route for intravenous injection in the white rat. Nature. 1956;178:268–9.

Fallon MT. Rats and mice. In: Label-Laird K, Swindle MM, Flecknell P, editors. Handbook of rodent and rabbit medicine. Oxford: Pergamon; 1996. p. 1–38.

Flecknell P, editor. Anaesthesia. In: Laboratory animal anaesthesia, 2 edn. London: Academic; 1996. p. 15–73/159–237

Ferrill HC, Hill C. A simplified method for feeding rats. J Lab Clin Med. 1943;28:1624–5.

Franklin CA, et al. Use of percutaneous absorption data in risk assessment. J Am Coll Toxicol. 1989;8:815–27.

Frimmer M, Lämmler G. In: Frimmer M and Lämmler G (eds.). Pharmakologie und Toxikologie. 2nd edn. Stuttgart: Schattauer Verlag. 1977; p. 9–31.

Gervaz P, et al. Permanent access to the portal vein in rats: an experimental model. Eur Surg Res. 2000;32: 203–6.

GV–SOLAS. Recommended maximum injection volumes in lab animals of the Society for Laboratory Animal Science (GV-SOLAS), Aug 2010. http://www.gv-solas.de/auss/tie/Injektionsvol_August_2010.pdf.

Grice HC. Methods for obtaining blood and for intravenous injections in laboratory animals. Lab Anim Care. 1963;14:483–93.

Guy RH, Hadgraft J. Principles of skin permeability relevant to chemical exposure. In: Hobson DW, editor. Dermal and ocular toxicology. Fundamentals and Methods. Boca Raton: CRC Press; 1991. p. 221–46.

Hamacher J, et al. Microscopic wire guide-based orotracheal mouse intubation: description, evaluation and comparison with transillumination. Lab Anim. 2008;42:222–30.

Harms PG, Ojeda SR. A rapid and simple procedure for chronic cannulation of the rat jugular vein. J Appl Physiol. 1974;36:391–2.

Heard DJ. Anestesia, analgesia, and sedation of small mammals. In: Quesenberry KE, Carpenter JW, editors. Ferrets, rabbits, and rodents: clinical medicine and surgery. Philadelphia: W.B. Saunders; 2004. p. 356–69.

Henke J, Erhardt W. Nager. In: Henke J et al., editors. Anästhesie & Analgesie beim Klein und Heimtier. Stuttgart: Schattauer; 2004. p. 642–63.

Hurtubise MR, et al. Restoring patency of occluded central venous catheters. Arch Surg. 1980;115:212–3.

Jeffrey P, et al. Does the rat have an empty stomach after an overnight fast? Lab Anim. 1987;21:330–4.

Joint Working Group on Refinement. Removal of blood from laboratory mammals and birds. Lab Anim. 1993;27:1–22.

Jones PA, Hynd JW. Continuous long-term intravenous infusion in the unrestrained rat - a novel technique. Lab Anim. 1981;15:29–33.

Kraus AL. Research methodology. In: Baker HJ et al., editors. The laboratory rat, Research applications, vol. 2. New York: Academic; 1980. p. 19–23.

Lany J, et al. A simple method for exact intratracheal installation in small laboratory rodents. Cancer Lett. 1980;10:91–4.

Lax ER, et al. A simple method for oral administration of drugs in solid form to fully conscious rats. Lab Anim. 1983;17:50–4.

Levine RR. Factors affecting gastrointestinal absorption of drugs. Am J Dig Dis. 1970;15:171–88.

Levy DE, et al. A mask for delivery of inhalation gases to small laboratory animals. Lab Anim Sci. 1980;30:868–70.

Lewis R, et al. Error of intraperitoneal injections in rats. Lab Anim Care. 1966;16:505–9.

Little JR, et al. Determination of lymphocyte turnover by continuous infusion of H ^{3}-Thymidine. Blood. 1962; 19:236–42.

Löscher W, et al. Allgemeine Pharmakologie. In: Löscher W, Ungemach FR, Kroker R, editors. Pharmakotherapie bei Haus- und Nutztieren. 7th ed. Berlin: Parey; 2006. p. 4–7.

Marini JC, Garlick PJ. Non-surgical alternatives to invasive procedures in mice. Lab Anim. 2006;40: 275–81.

Moreland AF. Collection and withdraw of body fluids and infusion techniques. In: Gay WJ, editor. Methods of animal experimentation, vol. 1. New York: Academic; 1965. p. 1–42.

Nachtman RG, et al. Commercial over-the-needle catheters for intravenous injections and blood sampling in rats. Lab Anim Sci. 1988;38:629–30.

Nebendahl K. Routes of administration. In: Krinke GJ, editor. The laboratory rat. San Diego: Academic; 2000. p. 463–83.

Nightingale CH, Mouravieff M. Reliable and simple method of intravenous injection into the rat. J Pharm Sci. 1973;62:860–1.

Norris ML, Miles P. An improved, portable machine designed to induce and maintain surgical anaesthesia in small laboratory animals. Lab Anim. 1982;16:227–30.

O'Neill PJ, Kaufman LN. Effects of indwelling arterial catheters or physical restraint on food consumption and growth patterns of rats: advantages of non-invasive blood pressure measurement techniques. Lab Anim Sci. 1990;40:641–3.

Otto K. Anesthesia, analgesia and euthanasia. In: Hedrich H, editor. The laboratory mouse. San Diego: Elsevier; 2004. p. 555–69.

Pearce KA. A route for intravenous injection in the albino rat. Nature. 1957;178:709.
Pekow CA, Baumans V. Common nonsurgical techniques and procedures. In: Hau J, van Hoosier GL, editors. Handbook of laboratory animal science, vol. II. 2nd ed. Boca Raton: CRC; 2003. p. 351–90.
Petty C. Blood. In: Petty C, editor. Research techniques in the rat. Springfield: Charles C. Thomas; 1982. p. 66–107.
Popovic V, Popovic P. Permanent cannulation of aorta and vena cave in rats and squirrels. J Appl Physiol. 1960;15:727–8.
Proctor E, Fernando AR. Oro-endotracheal Intubation in the rat. Br J Anaesth. 1973;45:139–42.
Remie R, et al. Anaesthesia of the laboratory rat. In: van Dongen JJ et al., editors. Manual of microsurgery on the rat. Amsterdam: Elsevier; 1990. p. 159–69.
Rhodes ML, Patterson CE. Chronic intravenous infusion in the rat: a nonsurgical approach. Lab Anim Sci. 1979;29:82–4.
Ritskes-Hoitinger M, Chaewalibog A. Nutrition requirements, design, and feeding schedule in animal experimentation. In: Hau J, van Hoosier GL, editors. Handbook of laboratory animal science, vol. II. 2nd ed. Boca Raton: CRC; 2003. p. 351–90.
Ritskes-Hoitinger M. Nutrition of laboratory mice. In: Hedrich H, editor. The laboratory mouse. London: Elsevier Academic; 2004. p. 463–79.
Salem H, et al. Mico-method for intravenous injection and blood sampling. J Pharm Sci. 1963;52:794–5.
Schlingmann F, et al. Food deprivation: how long and how. In: O'Donoghue PN, editor Harmonization of laboratory animal husbandry. Proceedings of the Sixth FELASA Symposium. London: Royal Society of Medicine Press; 1997. p. 89–92.
Schneider G, Schneider G. Zur Technik der intraperitoneal Injektion bei Ratten. Z Versuchstierk. 1970;12: 16–9.
Schumacher J, et al. A miniature self-inflating bag-mask ventilator for rats. Lab Anim. 2003;37:360–2.
Shimizu S. Routes of administration. In: Hedrich H, editor. The laboratory mouse. San Diego: Elsevier; 2004. p. 527–42.
Smith G. A simple non-surgical method of intrabronchial installation for the establishment of respiratory infections in the rat. Lab Anim. 1991;25:46–9.
Spoelsta EN, et al. A novel and simple method for endotracheal intubation of mice. Lab Anim. 2007;41: 128–35.
Steiger E, et al. A technique for long-term intravenous feeding in unrestrained rats. Arch Surg. 1972;104: 330–2.
Suckow MA. Experimental methodology. In: Suckow MA et al., editors. The laboratory mouse. Boca Raton: CRC; 2001. p. 113–34.
Szczesny G, et al. Long-term anaesthesia using inhalatory isoflurane in different strains of mice – the haemodynamic effects. Lab Anim. 2003;38:64–8.
Tiersch G. Animal Welfare Act. Tierschutzgesetz vom 04.Juli 2013 (BGBL Jahrgang 2013 Teil I Nr. 36; 2182–2196). 2013.
Tierschutzbericht der Bundesregierung. Drucksache 17/6826, ISSN 0722–8333. 2011.
Vergari A, et al. Video-assisted orotracheal intubation in mice. Lab Anim. 2003;37:204–6.
Vermeulen JK, et al. Food deprivation: common sense or nonsense? Anim Technol. 1997;48:45.
Videm S. A method for blood sampling and intravenous injections in rats. Z Versuchstierk. 1980;22:101–4.
Waynforth HB, Parkin R. Sublingual vein injection in rodents. Lab Anim. 1969;3:35–7.
Waynforth HB, Flecknell PA. Administration of substances. In: Waynforth HB, Flecknell PA, editors. Experimental and surgical technique in the rat. 2nd ed. London: Academic; 1992a. p. 1–67.
Waynforth HB, Flecknell PA. Specific surgical operations. In: Waynforth HB, Flecknell PA, editors. Experimental and surgical technique in the rat. 2nd ed. London: Academic; 1992b. p. 203–310.
Watanabe J, et al. Gastric emptying rate constants after oral administration of drug solutions to mice, rats and rabbits. Chem Pharm Bull (Tokyo). 1977;25:2147–55.
Weeks JR, Davis JD. Chronic intravenous cannulas for rats. J Appl Physiol. 1964;19:540–1.
Weihe WH. The laboratory rat. In: Poole TB, editor. The UFAW handbook on the care & management of laboratory animals. 6th ed. Essex: Longman; 1987. p. 309–30.
Weiss J, et al. Verabreichung (Applikation) von Substanzen und Probeentnahme. In: Weiss J, Becker K, Bernsmann K, Dietrich H, Nebendahl K, editors. Tierpflege in Forschung und Klinik. Stuttgart: Enke; 2009. p. 362–70.
Wester RC, Maibach HI. Dermatopharmacokinetics: a dead membrane or a complex multifunctional viable process. In: Bridges JW, Chasseaud LF, editors. Progress in drug metabolism, vol. 9. London: Taylor & Francis; 1986. p. 95–109.
Wolfensohn S and Lloyd M. In: Wolfensohn S and Lloyd M (eds.). Handbook of Laboratory Animal Management and Welfare. Oxford: Oxford University Press. 1994; p. 143–173.
Working Party Report. Refining procedures for the administration of substances. Lab Anim. 2001;35:1–41.
Woodard G. Principles of drug administration. In: Gay WJ, editor. Methods of animal experimentation, vol. 1. New York: Academic; 1965. p. 343–59.
Yoburn BC, Morales R, Inturrisi CE. Chronic vascular catheterization in the rat: comparison of three techniques. Physiol Behav. 1984;33:89–94.

Part III

Imaging Modalities and Probes

How to Choose the Right Imaging Modality

9

Fabian Kiessling, Bernd Pichler, and Peter Hauff

Contents

For non-invasive imaging of small animals, a variety of different modalities are available, about which a detailed introduction will be given in the following chapters. All imaging modalities have strengths and limitations, and a non-invasive imaging study will be most effective if the imaging modality is chosen according to its ability to reveal in the best way the in vivo parameter of interest, however, under consideration of costs and measurement time per animal (Fig. 9.1 and Table 9.1). Certainly, one frequent demand is the determination of the size of a single lesion, for example, of a subcutaneous tumour or lymph node. Previously size determination was mostly done using a calliper. Calliper measurements, however, only provide two dimensions, are user dependent and afflicted with large measurement errors for polymorphic or heterogeneous lesions, where a differentiation between necrosis and viable tissue is mandatory. In addition, reproducibility of the data is limited.

For lesion size determination, ultrasound, CT and MRI can be considered to be the most suitable imaging modalities. Ultrasound is most cost and time effective, and measurements can be performed in the laboratory environment. However, ultrasound is user dependent unless an automated scan method is applied, which is implemented in recent high-frequency ultrasound devices (Foster et al. 2002). Unfortunately, it is difficult to perform automated whole-body ultrasound scans. Manual ultrasound scans, however, are marked by a lower reproducibility and reliability, which

F. Kiessling (✉)
Experimental Molecular Imaging, University Clinics, RWTH-Aachen University, Aachen, Germany
e-mail: fkiessling@ukaachen.de

B. Pichler
Laboratory for Preclinical Imaging and Imaging Technology of the Werner Siemens-Foundation, Department of Radiology, University of Tuebingen, Tuebingen, Germany

PD Dr. P. Hauff
Bayer AG, Drug Discovery, Pharmaceuticals, Müllerstr 178, Berlin 13353, Germany
e-mail: peter.hauff@bayer.com

F. Kiessling et al. (eds.), *Small Animal Imaging*, DOI 10.1007/978-3-319-42202-2_9

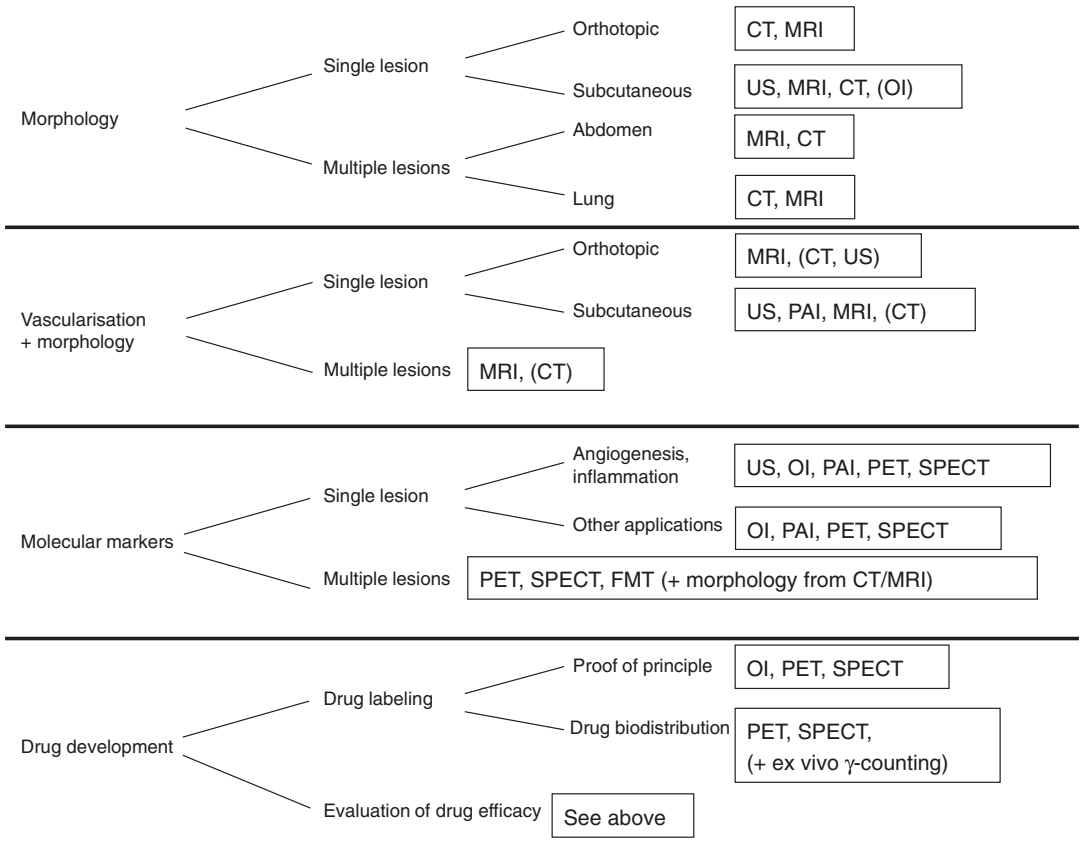

Fig. 9.1 Sketch illustrating major indications for small animal imaging and the recommended imaging modality. The order of the imaging modalities represents their priority for the particular imaging indication. Please note that this recommendation has been composed based on the author's experiences and focuses on broad and high-throughput implementation of small animal imaging. *OI* optical imaging, *FMT* fluorescence molecular tomography, *VCT* volumetric CT, *PAI* photoacoustic imaging

limits the suitability of ultrasound for whole mouse and whole rat imaging and for screening for multiple lesions.

Scanning with CT and MRI has the advantage that an entire animal can be investigated easily and that in scanners with a large gantry opening, more than one animal can be examined at the same time (Bock et al. 2003). However, when using CT, the X-ray dose deposited at the animal has to be considered. It can easily exceed 250 mGy for a whole-body mouse scan and significantly accumulate in repetitive scans (Bartling et al. 2007). In this case a relevant influence on the biological system and pathological condition in specific disease models cannot be excluded anymore. Nevertheless, when scanning with considerably low resolution (>150 µm voxel side length), a higher throughput can be achieved with CT (less than 1 min measurement time/mouse for some dedicated µCT scanners) as compared with MRI (usually 5–20 min for a morphology-based scan protocol).

On the other hand, it is an advantage of MRI that sequences with different weightings can be combined that enables to depict tissue oedema or necrotic areas easily. The excellent soft tissue contrast can also be important to localise and delineate lesion of interest. This particularly holds true for pathologies that are not below the skin such as pancreatic or prostate tumours (Hamzah et al. 2008; Kiessling et al. 2004). In CT and ultrasound, contrast material may be applied to enhance the contrast but carries the risk of inducing undesired side effects on the

Table 9.1 This table gives an overview on approximated scan times for a mouse/rat using different imaging devices and for different applications

Typical measurement times per animal		
MRI	Morphologic scan	10–30 min
	+ Vascularisation[a]/spectroscopy	+20 min
	Molecular imaging (including relaxometry)	30 min and more
µCT[b]	Morphologic scan	20 s–1 h (depending on spatial resolution and scanner type)
	+ Vascularisation[a]	+1–15 min
US (PAI)	Morphologic scan (+ Doppler)	1–5 min
	Contrast-enhanced scan[a]	~.5–15 min
	Molecular imaging	~5–15 min
OI/FMT[b]	All applications[a]	Few seconds to minutes
PET/SPECT	All applications[a]	10–30 min

Please note that the scan times can highly vary depending on the scanner type as well as on the required image resolution and contrast to noise ratio. This particularly holds true for µCT and high-field MRI. Our data refer to standard applications with a moderate image resolution

OI optical imaging, *FMT* fluorescence molecular tomography

[a]5–10 additional minutes are required for contrast agent injection/animal catheterization

[b]Consider that long image reconstruction times may occur

animal. Especially for CT, dedicated contrast agents are required ensuring a long blood retention rate. For mouse CT imaging, the injected volume of contrast agent can easily reach 300–400 µl which is critical with respect to the "animal use and care guidelines". In addition, such high injected volumes can cause pathophysiological effects and influence the biodistribution of drugs and other diagnostic agents. Furthermore, contrast agent administration is time consuming and cost intensive.

The size of the lesion also has to be considered. Relevant measurement errors may derive from partial volume effects, and thus small lesions should be imaged with high spatial resolution. This, however, would demand for higher X-ray exposure in CT. As a consequence, for size determination of small orthotopic lesions outside the lung, MRI using dedicated small animal scanners is the method of choice.

Another imaging approach is optical imaging (bioluminescence and fluorescence). Optical imaging technologies are mostly easier to use, less expensive and can be placed on each laboratory bench. Although, optical technologies are not suited for morphological and less suited for functional imaging due to their low spatial resolution, great advantages are seen in their in vivo use for cellular and molecular imaging in preclinical research. This becomes possible due to the availability of different optical probes such as targeted probes, probes activated due to enzymatic reactions (activatable probes) or probes that can be produced by cells themselves in the form of bioluminescent enzymes or fluorescent proteins (e.g. GFP, HcRed). In oncology research optical imaging may also be applied to estimate tumour size (Choy et al. 2003; Hoffman 2005). However, it is important to note that the transfection of cells with fluorescent proteins can alter their biological properties and that the fluorescence will only be present in viable parts of tumours. In addition, one has to consider that two-dimensional optical imaging is surface weighted and that the lesion size may be under- or overestimated depending on the distance of the tumour from the skin surface.

Phenotyping of transgenic animals is another field of broad interest. In this context, it is often necessary to scan a high number of animals and to characterise several organs simultaneously including the skeleton and the vessels. MRI and µCT may both be used. If skeletal abnormalities or calcifications are expected, µCT may be preferential, while abnormalities in abdominal organs often are better seen in MRI. For the determination of body

fat – an important biomarker for animal models of diabetes – specialised commercial systems are available that either base on NMR (Nixon et al. 2010) or X-rays (Stiller et al. 2007). However, if the phenotype causes a change at the functional or molecular level, optical imaging, PET or SPECT might be advantageous.

Clinical studies showed that a pathologic process often is not described sufficiently by morphological information and that lesion size can have limited impact on the patient's prognosis for many diseases. In addition, the evaluation of novel therapeutic drugs in the clinics can be facilitated significantly if the preclinical and clinical imaging protocols are adjusted to each other.

Therefore, besides the assessment of tumour size, there is increasing demand for a more sophisticated imaging beyond morphology.

In this regard, MRI offers a wide range of applications to supplement the morphological information. Some of them can be applied without the need to inject contrast agents and thus can easily be integrated in the scan protocols with only moderate additional measurement time requirement. Information about metabolism can be obtained by MR spectroscopy; vessel morphology and tissue perfusion can be assessed by time of flight angiography and arterial spin labelling (ASL) techniques. Diffusion-weighted imaging provides an important measure of cell density (Semmler et al. 2007).

For a detailed vascular characterisation of tissues, however, contrast material has to be administered. Dynamic contrast-enhanced (DCE) MRI can provide valuable information about relative blood volume, vascular perfusion and permeability and can be combined with relaxometric measurements of the relative blood volume and with sophisticated imaging techniques like "vessel size imaging" providing a measure of the mean microvascular diameter in the tissue (Troprès et al. 2001). However, when intending to use these techniques in animal experiments, one should consider that approximately 5–10 min is additionally required for animal preparation (particularly for catheterisation) and that depending on the scan protocol, the measurement time will increase by 10 to >30 min. Thus, at least 30-min examination time should be scheduled per animal. Another important point is that these contrast-enhanced examinations more frequently fail due to dislocation of the catheter or motion of the animal. Thus, when planning a study that includes the analysis of tissue vascularisation by contrast-enhanced scans, the number of animals should be chosen higher as for a purely morphology-based examination.

For vascular characterisation also ultrasound offers some interesting options (Kiessling et al. 2009). Without the need of contrast agent administration, Doppler techniques can be used to visualise vessels by their flow and thus to assess the relative blood volume in the tissue. It can also be used to estimate blood flow velocities and determine cardiac data (echocardiography). However, it has to be considered that the sensitivity of Doppler for blood flow depends on the pulse frequency and with devices operating between 3 and 40 MHz, slow blood flow in microvessels may not be detected sufficiently. Microbubbles can be administered as contrast agent and sensitive Doppler- and B-mode scan techniques are available to assess microvascular characteristics (Kiessling et al. 2009). An extended explanation of the ultrasound techniques for the determination of relative blood volume, blood velocity and perfusion is given in Chaps. 14.1 and 14.2. Vessel permeability cannot be determined since microbubbles do not leave the vascular bed.

Microbubbles can also be coated with specific ligands to act as molecular probes (Kiessling et al. 2009; Kaufmann and Lindner 2007). While it is certainly a limitation that only intravascular targets can be addressed, the high sensitivity of ultrasound for these microbubbles and the option of scanning with exquisite spatial resolution make ultrasound highly attractive for research on angiogenesis and inflammation. In this regard, it might be of interest to know that in mice and rats, the method also works reliably in the brain without the need to open the skull (Reinhardt et al. 2005). In conclusion, ultrasound is highly suited for functional and molecular vascular imaging of superficially localised tissues like skeletal muscle, subcutaneous tumours and the brain. Cardiac functional imaging is another field where

ultrasound can compete with the other imaging modalities. In the abdomen, however, identification of the lesion can be difficult, and the optimal access way may often be occupied by bowel gas, which gives advantage to other imaging modalities. Here, to the author's experience, DCE MRI and DCE CT may be chosen for functional and PET, SPECT or optical imaging for molecular imaging demands.

Ultrasound imaging may be combined with photoacoustic imaging, which enables the assessment of microvascular morphology and tissue oxygenation even without the need for contrast agent injection (please find more details in Chap.16.5). In addition, for photoacoustic imaging contrast materials can be kept considerably small, and perfusion measurements, vessel permeability assessment and extravascular molecular imaging become possible. In addition, it opens perspectives for reporter gene imaging.

Molecular imaging is increasingly applied in clinical studies, and some applications are already implemented in clinical routine disease diagnosis concepts. It is clearly expected that molecular imaging will gain further importance in preclinical and clinical drug development, in the evaluation of drug efficacy and in therapy response monitoring.

PET and SPECT may be preferred for testing drug biodistribution and for assessing target binding kinetics because these modalities have the highest sensitivity for contrast agents. In addition, as compared with signalling molecules of other modalities like dyes or nanoparticles, the conjugation of a radioisotope less affects the properties of a biomolecule, and the probes can be kept considerably small. The possibility of absolute quantification and the option of a relatively easy clinical translation are further advantages of nuclear imaging methods. However, the need for radioactive tracers raises special demands on animal handling, staff education, laboratory safety and expensive infrastructure. Particularly, for studies with large animal numbers, the total amount of handled radioactivity can become significant.

Thus, for initial experiments on the binding of many new drugs, optical methods may be preferred since optical imaging is cheap, and the probes are easy to handle. Nevertheless, it should be kept in mind that two-dimensional optical imaging is not quantitative and surface weighted and that even in optical molecular tomography, quantification is difficult. In addition, for small molecules like glucose, amino acids and nucleic acids, coupling of a dye will most probably change its pharmacokinetics or inhibit its uptake by cellular transporters. The same holds true for RNA chains that better should be radiolabeled if it is the aim to study its natural biodistribution.

The situation is different if it is not the aim to accurately assess the pharmacokinetic and the accumulation of a biomolecule and of a therapeutic substance but to monitor its effect on tissue metabolism, cellular proliferation, angiogenesis and apoptosis or on the general molecular tissue profile with targeted probes. Then, the targeted probes just have to reliably indicate tissue function or metabolism and must not be close in its binding characteristics and biodistribution to the natural ligand.

In this context, it can be reasonable to supplement data about lesion size with molecular analyses, e.g. by using [^{18}F]FDG-PET to quantify glucose metabolism or [^{18}F]FLT-PET to assess cell proliferation. Using these tools therapy response and the development of therapy resistance can often be detected earlier and more specifically as compared with lesion size determination alone, which cannot distinguish between viable and necrotic tissue. Alternatively, one may intend to develop novel-specific probes to more directly and more effectively monitor therapy response by a decrease in target density or by the change of the molecular marker profile. These types of agents would be called companion diagnostics and are important candidates in the emerging field of precision or personalised medicine. A huge advantage of nuclear imaging, using specific radiolabeled tracers which allow absolute quantification, is its option to perform pharmacokinetic modelling and calculate rate constants for the individual tissue compartments.

If it is the intension to solely investigate the molecular regulation on preclinical level, one is considerably free in the choice in the imaging

modality. In this context the strengths and limitations of the available imaging modalities are summarised in Fig. 9.1. However, if it is intended to develop non-invasive imaging procedures for monitoring and personalising the use of novel therapeutic drugs in later clinical studies, the imaging modality should be chosen depending on the clinical need. Here PET may be superior in most cases that go along with whole-body imaging. Optical imaging and optoacoustic imaging may be used if intraoperative imaging is intended or if endoscopic imaging (like bronchoscopy, gastroscopy or coloscopy) will be applied. Molecular ultrasound may also gain clinical importance for imaging that goes along with interventions like needle biopsy of breast and prostate lesions, for therapy response control via the quantification of intravascular target molecules (e.g. up- or down-regulation) or between whole-body staging intervals and for cardiovascular analysis.

Some readers may wonder that in regard to molecular imaging, MRI was not mentioned so far although some exciting studies were published using targeted paramagnetic liposomes and USPIO (Kiessling et al. 2007). However, these studies report more on successful proof of principle studies than on the use of MRI to answer a complex biological question. Before the latter can be achieved, some significant improvements are required that are not easy to achieve. Firstly, the sensitivity of MRI to contrast agents is several magnitudes lower than that of optical, ultrasound and nuclear imaging methods. Thus, targeted diagnostic probes have to be administered in high dosages, which carry the risk of inducing undesired biological effects on the target tissue. Furthermore, large signalling molecules have to be coupled to the ligand in order to make it detectable. This makes the optimisation of the pharmacokinetic properties of the compounds difficult. Thus, a significant percentage of the targeted probes may accumulate unspecifically in the interstitial space or in necrotic tissue or is removed from the blood by the reticuloendothelial system (Kiessling et al. 2014). These limitations may be overcome in the future, and there might be high potential for more recent molecular MRI techniques like CEST and PARACEST (Modo and Bulte 2007) or MRI with hyperpolarised probes.

Considering all these different demands on preclinical imaging, it becomes clear that an all-around imaging modality is not available and that for a complex scientific question, the different imaging modalities have to be combined. As a consequence, the manufacturers offer tools for retrospective fusion of CT and MRI data with PET, SPECT and optical imaging data. Even some dual-modality imaging devices (e.g. μSPECT-CT and μPET-CT) were commercialised for small animal imaging recently, and PET inserts for small animal MRI scanners were constructed at different places (Judenhofer et al. 2008). In this regard, there is an intense debate in the scientific community if these dual-modality scanners really improve imaging efficacy. Certainly, for some demands it is highly attractive to have the option of assessing different information simultaneously. Particularly, the combination of MRI with PET, SPECT and optical imaging would enable an ideal combination of functional and targeted imaging. Very often, high-resolution morphological images from CT or MRI are required to accurately quantify the molecular information from PET, SPECT or optical imaging by providing landmarks for defining the region of interests or correcting partial volume effects. In addition, the implementation of dual-modality devices saves laboratory space and thus can reduce costs. On the other hand, it can hamper high-throughput imaging significantly when only having a dual-modality scanner instead of two separated devices since, for example, one long SPECT scan can consume the measurement time required for several routine μCT scans.

Finally, not only the right imaging hardware have to be selected to reveal the maximum of information for a specific study, advanced image analysis tools, experienced users and established workflows are equally important.

References

Bartling SH, Stiller W, Semmler W, Kiessling F. Small animal computed tomography imaging. Curr Med Imaging Rev. 2007;3:45–9.

Bock NA, Konyer NB, Henkelman RM. Multiple-mouse MRI. Magn Reson Med. 2003;49(1):158–67.

Choy G, Choyke P, Libutti SK. Current advances in molecular imaging: non-invasive in vivo bioluminescent and fluorescent optical imaging in cancer research. Mol Imaging. 2003;2:303–12.

Foster FS, Zhang MY, Zhou YQ, et al. A new ultrasound instrument for in vivo microimaging of mice. Ultrasound Med Biol. 2002;28:1165–72.

Hamzah J, Jugold M, Kiessling F, Rigby P, Manzur M, Marti HH, Rabie T, Kaden S, Gröne H-J, Hämmerling GJ, Arnold B, Ganss R. Vascular normalization in RGS5-deficient tumours promotes immune destruction. Nature. 2008;453:410–4.

Hoffman RM. The multiple uses of fluorescent proteins to visualise cancer in vivo. Nat Rev Cancer. 2005;5:796–806.

Judenhofer MS, Wehrl HF, Newport DF, Catana C, Siegel SB, Becker M, Thielscher A, Kneilling M, Lichy MP, Eichner M, Klingel K, Reischl G, Widmaier S, Rocken M, Nutt RE, Machulla HJ, Uludag K, Cherry SR, Claussen CD, Pichler BJ. Simultaneous PET-MRI: a new approach for functional and morphological imaging. Nat Med. 2008;14:459–65.

Kaufmann BA, Lindner JR. Molecular imaging with targeted contrast ultrasound. Curr Opin Biotechnol. 2007;18:11–6.

Kiessling F, Huber PE, Grobholz R, Heilmann M, Meding J, Lichy MP, Fink C, Krix M, Peschke P, Schlemmer HP. Dynamic MR-tomography and proton MR spectroscopy of prostate cancers in rats treated by radiotherapy. Invest Radiol. 2004;39:34–44.

Kiessling F, Jugold M, Woenne EC, Brix G. Non-invasive assessment of vessel morphology and function in tumours by magnetic resonance imaging. Eur Radiol. 2007;17:2136–48.

Kiessling F, Huppert M, Palmowski M. Functional and molecular ultrasound imaging: concepts and contrast agents. Curr Med Chem. 2009;16:627–42.

Kiessling F, Mertens ME, Grimm J, Lammers T. Nanoparticles for imaging: top or flop? Radiology. 2014;273:10–28.

Modo MJ, Bulte JMW. Molecular and cellular MR imaging. Boca Raton: CRC Press; 2007.

Nixon JP, Zhang M, Wang C, Kuskowski MA, Novak CM, Levine JA, Billington CJ, Kotz CM. Evaluation of a quantitative magnetic resonance imaging system for whole body composition analysis in rodents. Obesity. 2010;18(8):1652–9.

Reinhardt M, Hauff P, Linker RA, Briel A, Gold R, Rieckmann P, Becker G, Toyka KV, Maurer M, Schirner M. Ultrasound derived imaging and quantification of cell adhesion molecules in experimental autoimmune encephalomyelitis (EAE) by Sensitive Particle Acoustic Quantification (SPAQ). Neuroimage. 2005;27:267–78.

Reiser MF, Semmler W, Hricak H. Magnetic Resonance Tomography (1st Ed). Springer-Verlag, 2007; ISBN 10: 354029354X / ISBN 13: 9783540293545

Stiller W, Kobayashi M, Kazuhiko K, Stampfl U, Richter G, Wolfhard S, Kiessling F. Initial experience with a novel low-dose micro-CT system. Röfo. 2007;179:669–75.

Troprès I, Grimault S, Vaeth A, et al. Vessel size imaging. Magn Reson Med. 2001;45:397–408.

How to Identify Suitable Molecular Imaging Biomarkers

10

Norman Koglin, Andre Mueller, Andrew W. Stephens, and Ludger M. Dinkelborg

Contents

10.1 Introduction

The generation and development of successful imaging agents remains a challenging endeavour. There is still a high demand for new probes to address unmet medical needs to tackle life-threatening diseases in the neurological, oncological and cardiovascular space. The primary focus of diagnostic and biomarker development is on earlier detection of pathological changes, better characterisation of disease and/or the development of probes that allow for optimal patient selection and monitoring of therapy. A biomarker can be generally defined as a characteristic that is objectively measured and evaluated as an indicator of normal biological processes, pathogenic processes or biological responses to a therapeutic intervention (Biomarkers Definitions Working Groups 2001). Biomarkers can be derived from the following major categories (Waterton and Pylkkanen 2012):

- Biofluids (blood, urine, cerebrospinal fluid [CSF], etc.) yielding molecular (e.g. DNA, protein, metabolite) or cellular measures
- Solid tissue samples yielding, for example, molecular, cellular or histopathologic measures
- Physiologic measurements such as lung function and blood pressure
- Imaging measures

In the clinical setting, the information derived from (several) biomarker(s) is com-

N. Koglin (✉) • A. Mueller • A.W. Stephens
L.M. Dinkelborg
Piramal Imaging GmbH, Berlin, Germany
e-mail: norman.koglin@piramal.com

F. Kiessling et al. (eds.), *Small Animal Imaging*, DOI 10.1007/978-3-319-42202-2_10

bined with the results from other clinical investigations to establish the diagnosis and to characterise the disease (i.e. staging and prognosis). In addition, biomarkers can be used for the prediction and/or monitoring of the clinical response of a disease to a therapeutic intervention.

Medical imaging provides the ability to detect and localise changes that are important to determine whether a disease is present or a therapy is effective, by depicting alterations in anatomic, physiologic, biochemical or molecular processes (Smith et al. 2003). Imaging has the unique benefit that it can localise and interrogate the exact disease focus such as plaque deposition, an infarct or tumour—unlike biofluids and physiologic measurements, which tend to integrate information from the entire body. Moreover, and unlike solid tissue samples, imaging biomarkers are usually applied by intravenous injection and can be assessed non-invasively, allowing further repetitive follow-up. In general, imaging biomarkers can be distinguished in morphological and molecular biomarker. The following sections will focus on molecular imaging biomarkers.

The high detection sensitivity of radiopharmaceuticals, in particular when labelled with positron-emitting radioisotopes, makes them uniquely suitable as imaging biomarkers. Of note, the tracer principle allows the investigation of biological or pathological processes without disturbing them. Radiolabelling, combined with advanced detector technologies, allows for highly sensitive detection, quantification and three-dimensional visualisation. Such technological advances together with disease-specific probes make it possible to visualise pathological changes at the cellular or molecular level, before structural changes of organs or tissues can be observed.

To select an appropriate target and direct the development of new radiolabelled molecules, it is important to investigate and understand the addressed biomedical question in detail. This chapter will focus on the identification and selection of suitable molecular imaging biomarkers. Examples will be shown and discussed, as well as general prerequisites that should be taken into account when generating and developing such agents.

10.2 Medical Need

Significant advances in the molecular understanding of many diseases, their diagnoses and treatments have been achieved in recent decades. This is also reflected by an increased overall life expectancy of the population, especially in industrialised countries. Nevertheless, several diseases continue to place a high burden on individuals and society: neurodegenerative, oncological and cardiovascular diseases in particular are still associated with high morbidity and mortality, representing high unmet medical needs. Increasing elucidation of the underlying molecular mechanisms and pathways implicated in several of these diseases has helped to identify promising new drug targets. While targeting individual pathways or single mutations can be highly efficacious in specific disease subsets, it does require stratification of patients and/or early prediction of response to therapy to ensure that a treatment is given only to those patients who are likely to benefit from this specific intervention. This also avoids unnecessary toxic effects related to treatment in patients who do not respond to the intervention.

The promise of new imaging biomarkers, especially using molecular imaging approaches, lies in the earlier detection and better characterisation of such diseases as well as facilitating therapy selection and monitoring. As the development of a new imaging biomarker can be laborious and expensive, the relevance of the biomedical question to be addressed should be informed first by a recent literature search and/or insights from physicians talking about their experiences from routine practice. Depending on the purpose of the biomarker and its intended use, demonstration of clinical utility should be addressed early in development to ensure the new imaging biomarker gets integrated into the diagnostic workup, with immediate benefits for patients in clinical practice and health-economic advantages.

10.3 General Prerequisites for Imaging Biomarker Selection

The selection of a relevant biomedical question and an associated target for imaging can only be achieved through intense multidisciplinary collaboration. Certain general prerequisites must be considered from the outset, and various functions—biology, chemistry, radiochemistry, clinic, etc.—should be involved from the start. Because biomarkers can play a role in diverse aspects from biomedical research to daily clinical utility, the potential applications of the biomarker should be identified as early as possible. Development and validation can then follow a fit-for-purpose strategy. Agents intended for preclinical/clinical visualisation of target engagement of a drug can be developed very differently than those intended as companion diagnostics or for incorporation into standard diagnostic regimens.

In identifying the most appropriate target, it must be taken into account that an imaging target should show sufficient altered expression, accessibility or occupancy under a pathological condition. Contrary to therapeutic targets, where the drug needs to block a (signalling) pathway or enzyme activity to achieve a therapeutic effect, imaging targets need not necessarily have a primary role in the disease. A secondary marker can also be appropriate, if its presence is directly linked with the disease.

In general, the ideal target should show a sufficient number of accessible binding sites and/or an amplification mechanism. In addition, a suitable retention mechanism and clearance from non-targeted areas is needed to generate sufficient image contrast. Signal detection of even small quantities from a target-bound ligand can be readily achieved with modern clinical scanners, but can be compromised by a high background from healthy tissue, yielding low contrast or poor image quality and requiring further optimisation (Frangioni 2009).

Traditionally, imaging biomarkers were primarily designed for targeting cellular receptors or transporters. They were either tightly bound and often internalised or transported into the cell and trapped inside by metabolic transformation, while unbound ligand was cleared from the target organ. More recently, a class of new imaging biomarkers has become available that binds to misfolded protein aggregates such as amyloid-beta (Aβ) deposits in the brain. This new paradigm required different lead optimisation, as well as new types of analysis and quantitation.

Today a broad range of tracing molecules is available for targeting structures of interest—from small molecules (<500 Da) to peptides (~2000 Da), antibodies or larger proteins (≥150 kDa). In addition, various strategies have been developed to optimise certain parameters of these molecules, such as to increase their metabolic stability or fine-tune binding properties and clearance patterns. Different demands on the choice of radioisotope and half-life are determined by the pharmacokinetic characteristics or molecular structure. For example, binding molecules that have a slow clearance from blood and healthy tissues, e.g. antibodies, require a radioisotope with a longer half-life, allowing sufficient time to obtain adequate image contrast. On the other hand, small molecules and peptides usually show faster clearance and can be labelled with short-lived radioisotopes having a half-life ranging from several minutes to few hours. The nature and size of the radioisotope vary from covalent-bound radioisotopes to radiometal-based isotopes that require chelates for labelling of the targeting moiety. This also influences the radiolabelling strategy and needs to be considered carefully in the design and development of a radiotracer.

Extracellular targets, such as receptors or transporters localised on cell membranes, can usually be directly accessed through ligands supplied via the blood. Ligands that address intracellular targets must first penetrate the cell membrane. An additional consideration for targets within the brain is that they need to have the ability to cross the blood–brain barrier. This places special demands on the tracer design such as sufficient lipophilicity to allow for cell membrane penetration if the uptake is not transporter mediated.

The concept of binding potential (BP) has been developed especially for CNS binding-based

radiotracers. The BP provides a measurement of the in vivo radiotracer–target interaction and comprises the total biological target density (B_{max}) and the binding affinity, represented as the radiotracer dissociation constant (K_d). Collective expertise in the field suggests that a BP, or ratio of B_{max} to K_d, of ≥5 is suitable for quantitative comparisons with positron emission tomography (PET) imaging, especially in clinical research settings (Patel and Gibson 2008). Operationally, successful receptor-based imaging agents have a low nanomolar affinity for their target.

When the targeted radiotracer is yet to be developed, the dissociation constant will not be known; however, the B_{max} value can be used to estimate the ideal K_d. If the B_{max} is unknown, it can be measured using autoradiography or estimated through semiquantitative immunochemical methods (Wang et al. 2013).

For radiotracers that compete with endogenous ligands in vivo, the effective target density available for radiotracer binding ($B_{available}$) is B_{max} scaled to the fraction of targets unoccupied by the native ligand. The percentage change in expression or occupancy of the biological target is also crucial and must exceed the margins of error for the technique (Van de Bittner et al. 2014).

In addition, the receptors present on the cell surface may exhibit different conformational states, preferring the binding of ligands that are either agonists or antagonists. Different proportions of these receptor states may exist. Traditionally, the focus was on the development of agonists that would allow for receptor internalisation upon binding and receptor activation. More recently, it has been shown that in some situations the antagonist-preferring state of the receptor may dominate. Indeed, an increased targeting can be achieved with radiolabelled antagonists (e.g. for somatostatin and gastrin-releasing peptide [GRP] receptors) even without internalisation as a cellular trapping mechanism (Ginj et al. 2006, Mansi et al. 2011).

Physiological variations in the endogenous ligand concentration may confound the measurement of the receptor density in vivo. In addition, many transmembrane receptors utilise homo- or heteropolymerisation and internalisation as their regulatory mechanism. In such situations, the number of binding sites may also vary.

Another aspect to consider when transporters or enzymes are being investigated as an imaging target is whether substrate or inhibitor molecules are used. If a substrate is being developed, then one transporter/enzyme molecule can carry/convert more than one ligand, and the B_{max} can indeed be higher than the number of actual target sites. In addition, the binding constant for substrates is usually not in the nanomolar range, as in case of receptor ligands or inhibitors. The binding constant for substrates is determined by the physiological concentration of the natural substrate and the fact that the ligand must be easily released once the conformational change of the transporter or enzyme takes place and the ligand is localised inside the cell or becomes converted. If an efficient cellular uptake and intracellular trapping mechanism for the radiotracer exists, then clearly the number of substrate-based ligands may far exceed the number of target sites, representing a signal amplification mechanism. However, if rapid clearance of a ligand occurs, this can limit the cellular uptake so that in fact no amplification takes place.

10.4 Preclinical Research Aspects

The most pragmatic approach in target selection for an imaging biomarker is to build on the existence of a high-affinity small-molecule ligand library with established structure–affinity relationships, as is typically the case for ligands that are derived from drug development efforts with validated targets. Alternatively, already known ligand–target relationships and their role in the pathophysiology of a disease can be used to label an already described marker. Appropriate in vitro assays and animal models of the disease are available in such a situation to further investigate the binding and imaging capabilities of novel derivatives and radioligands. However, it should be noted that good drug candidates are not necessarily readily converted into good imaging agents. Generally, pharmacokinetic parameters require further optimisation.

For highly novel targets without known ligands, it needs to be assessed whether binding to such targets can be assayed ('assayability') and whether ligands can be designed and structure–activity relationship studies can be performed ('druggability'). A robust in vitro model to study the binding of ligands to the target is crucial. Due to the time- and cost-intensive nature of de novo ligand discovery, such investigations are ideally reserved for targets that clearly meet the fundamental requirements: high target density, with a large percentage change in density or occupancy that correlates strongly with the disease or biomedical question to be addressed.

After the discovery and selection of a first lead compound, the optimisation of binding properties or other parameters is usually the next step in preclinical models. This preclinical phase is a multistep process, involving many iterations. Most approaches fail on moving from the in vitro to the in vivo setting; very few compounds show promising targeting and pharmacokinetic properties and can be further advanced to clinical development.

10.5 Preclinical Research Examples

The following section contains preclinical research examples and highlights different aspects of how small-animal imaging can either facilitate the longitudinal characterisation of disease models such as in neurodegenerative diseases (Sect. 10.5.1), can support receptor-based imaging approaches in prostate cancer (Sect. 10.5.2) or can provide important pharmacokinetic parameters to support the preclinical characterisation and selection of suitable transporter substrates in a tumour model (Sect. 10.5.3).

10.5.1 Preclinical Amyloid PET

The clinical need and the development of imaging biomarkers for the detection of Aβ plaques are described in more detail in Sect. 10.6.1. Along with the clinical development and the routine clinical application of such agents, considerable research effort is spent on the characterisation and application of suitable disease models to extend research in Alzheimer's disease (AD). Goals include broadening the knowledge and molecular understanding of the disease, as well as exploring preventive and therapeutic interventions. The ability to visualise and quantify longitudinal changes of Aβ plaque load during the life of an individual animal can play a crucial role in such a setting. Small-animal PET studies of longitudinal design with suitable imaging agents allow the rate of Aβ accumulation to be measured, so that interventions for attenuating plaque formation can be tested. However, there are some controversies in the literature with regard to the fitness of amyloid imaging in different AD mouse models. Comparisons between recent small-animal amyloid PET studies are difficult, due to the diversity of mouse models, radiotracers, imaging protocols and quantification strategies (Virdee et al. 2012).

To characterise common transgenic AD mouse models in more detail, a longitudinal small-animal PET study was described recently using the same PET tracer in several AD mouse strains, applying standardised methods and correlating PET findings with histological analysis (Brendel et al. 2015a). The results are summarised in Fig. 10.1. The inserted upper images represent group-averaged sagittal PET slices, normalised to the cerebellum and overlaid on a magnetic resonance imaging (MRI) mouse atlas. Dots indicate corresponding assessments of $SUVR_{CTX/CBL}$ in individual mice. Dashed lines express the estimated time-dependent progression in PS2APP (red), G384A (green) and APP/PS1dE9 (purple) mice. Longitudinal progression in APPswe mice is indicated by a continuous blue line. The inserted lower images depict representative ex vivo autoradiography results. Wild-type (WT) level expresses the mean standard uptake value ratio of cortex to cerebellum ($SUVR_{CTX/CBL}$) of pooled WT mice.

Partial-volume effect correction (PVEC) can be applied and would lead to an increase of the estimated slopes in the longitudinal analyses. Plaque load at the end of the study was further

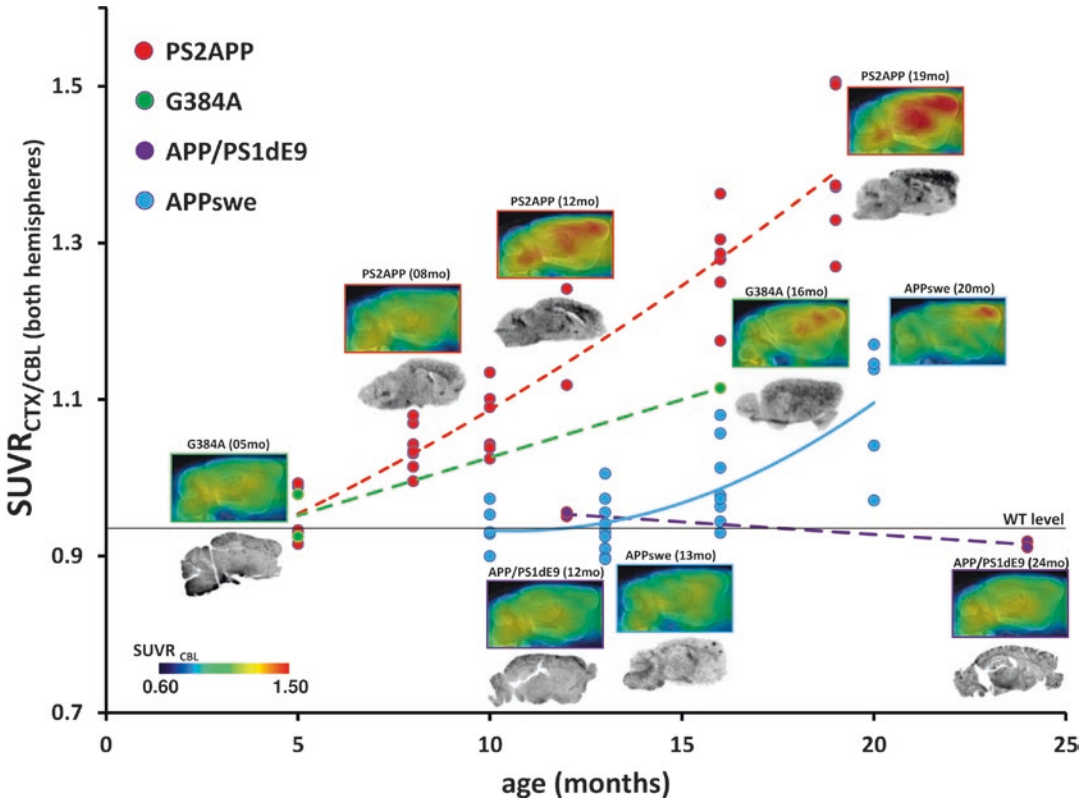

Fig. 10.1 Multimodal analysis of four AD mouse strains investigated in a cross-sectional amyloid PET study (Taken from Brendel et al. 2015a)

analysed by autoradiography and histochemistry and was found to correlate well with the imaging data. Application of PVEC was also found to be useful when the amyloid burden is underestimated by PET.

Subsequent to the characterisation of these animal AD models, the same research group further investigated one experimental therapeutic intervention (gamma-secretase modulation) in one transgenic AD model (Brendel et al. 2015b). For the first time, a large-scale, serial preclinical amyloid PET study was conducted in such a setting. Multimodal data analysis included biochemical and histopathological findings, in addition to the serial, non-invasive amyloid PET investigations. PET imaging accommodated the large interindividual differences in initial plaque load and kinetics, thus affording sensitive detection of treatment effects. Prediction of treatment response was facilitated by individual amyloid PET measurements of baseline amyloid level. The modalities applied to study plaque load should not be considered mutually exclusive, but rather supply complementary information that adds further value to any single modality alone.

Another research group investigated the dynamics of amyloid plaque deposition and related physiological effects such as regional cerebral blood flow (rCBF) in animal models of AD by means of a multi-tracer and multimodality imaging approach (Maier et al. 2014). Using a multiparametric PET and MRI approach, it was demonstrated that Aβ deposition is accompanied by a decline of rCBF in the presence of cerebral Aβ angiopathy (CAA). The loss of perfusion correlated with the growth of Aβ plaque burden but was not related to the number of CAA-induced microhaemorrhages. In a mouse model of parenchymal beta-amyloidosis and negligible CAA, rCBF remained unchanged. It can be concluded

that vascular amyloidosis is the major contributing factor to the observed loss of perfusion. With this study, the feasibility and cross-correlation were demonstrated for the gold standard for rCBF quantification, ^{15}O-H_2O-PET, with arterial spin labelling MRI examination in the mouse brain.

In conclusion, these three examples from studying mouse models of a neurodegenerative disease highlight how small-animal imaging approaches can provide new insights in disease models to support research with excellent translation capabilities to the clinical setting.

10.5.2 Prostate Cancer Imaging

The development of new agents for prostate cancer imaging remains an active area of research with the goal of improving the accurate detection and staging of primary prostate cancer and improving restaging in the recurrent setting. Considerable achievements were made recently with regard to receptor-based imaging to overcome the limitations of currently employed agents or methods lacking high sensitivity and specificity (Jadvar 2015). Of note, several radiolabelled small molecules have been developed that bind to prostate cancer-specific targets, such as the prostate-specific membrane antigen (PSMA) or the gastrin-releasing peptide receptor (GRPr) (Lütje et al. 2015; Mansi et al. 2013). While those derivatives have entered the clinical stage and are being further investigated and characterised, none has yet been fully validated and approved for routine clinical use.

The following example illustrates the investigation of two new agents targeting GRPr in prostate cancer. Both agents are peptides with optimised GRPr-binding sequence derived from the natural bombesin peptide. They are both antagonists and have a very similar binding sequence. The only difference in the binding sequence is a methyl group at a glycine residue in the ^{18}F-bombesin derivative. Both bind to the GRPr with nanomolar affinity: the non-radioactive ^{19}F-bombesin analogue binds with an IC_{50} of 0.94 nM (K_i = 0.13 nM) to the human GRPr receptor. The IC_{50} of the non-radiolabelled DOTA-RM2 was found to be 7.7–9.3 nM (K_d = 2.5–3.1 nM) for the human GRPr.

Both tracers selectively bind to the GRPr and not to other bombesin receptor subtypes such as NMBr or BBR3. However, different radiolabelling approaches were used to attach the radiolabel: direct ^{18}F-labelling or ^{68}Ga-labelling via DOTA chelator (Honer et al. 2011; Becaud et al. 2009; Höhne et al. 2008; Mansi et al. 2011). Accordingly, the part of the molecule where the radiolabel is introduced showed differences, as did the linker connecting it with the binding sequence (Fig. 10.2a).

Both agents were found suitable for clinical translation based on the tumour-targeting potential observed in animal models. In vivo, the ^{18}F-bombesin analogue shows specific and effective targeting of GRPr in two prostate cancer xenografts (PC-3, LNCaP). Uptake in the androgen-independent PC-3 xenograft was 4–6 % ID/g at 1 h postinjection (p.i.), and the uptake in the androgen-dependent LNCaP xenograft was 2–3 % ID/g at 1 h p.i. Low uptake in nontarget organs resulted in high tumour-to-tissue (T/T) ratios at 1 h p.i. favourable for PET imaging (e.g. T/blood = 19, T/muscle = 50).

The other derivative, ^{68}Ga-RM2, also shows specific and effective targeting of GRPr in the two prostate cancer xenografts (PC-3 and LNCap). In the PC-3 xenograft, an uptake of 14 % ID/g at 1 h p.i. was determined. For the LNCaP xenograft, a tumour uptake of 6 % ID/g at 1 h p.i. was found. Low uptake in nontarget organs resulted in high T/T ratios at 1 h p.i., favourable for PET imaging (e.g. T/blood = 25, T/muscle = 130).

However, it was also noted in rodent biodistribution that the structural differences resulted in altered pharmacokinetic properties: the ^{18}F-derivative showed a mixed hepatobiliary (70 %) and renal (10 %) clearance, whereas the ^{68}Ga-derivative was characterised by a predominant renal clearance (>80 %) (Fig. 10.2b).

Successful targeting of primary tumours in prostate cancer patients was confirmed with both agents; however, the pharmacokinetic pattern in mice was also observed in patients as shown in Fig. 10.2b (Sah et al. 2015; Kähkönen et al. 2013).

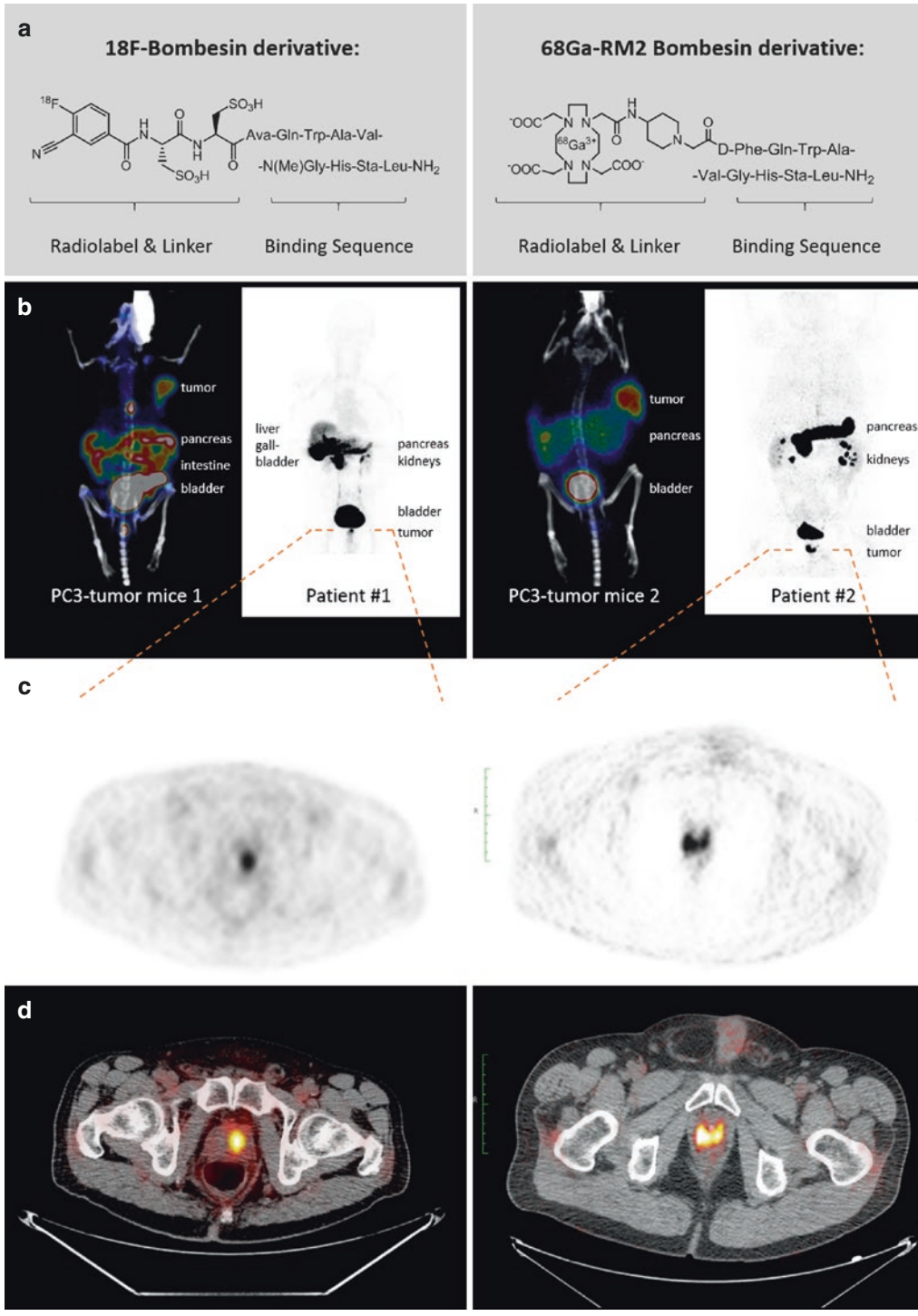

Fig. 10.2 Comparison of ^{18}F- and ^{68}Ga-labelled bombesin derivatives. (**a**) The chemical structures for both compounds are shown on top. (**b**) The whole body images show tracer biodistribution and tumour uptake in the PC-3 tumour mouse model (*left*) and in a prostate cancer patient (*right*) for each compound. (**c**) Axial PET image and (**d**) axial PET/CT image through the prostate showing tumour uptake for both compounds in patients (^{18}F-derivative *left* and ^{68}Ga-derivative *right*)

Meanwhile it was decided to continue with the investigation of the ^{68}Ga-derivative. The observed 2–3 times higher tumour uptake ^{68}Ga-RM2 in mice might have led to a higher tumour detection rate in humans. Although no direct head-to-head comparison in the same patients was performed, the ^{68}Ga-derivative correctly detected tumours in 10/11 subjects in a first-in-man study, whereas the ^{18}F-derivative failed to detect tumours in 2/5 subjects with biopsy-confirmed primary prostate cancer. Interestingly, although the ^{18}F-bombesin analogue showed a higher affinity to the human GRPr in vitro, the combination of better pharmacokinetic properties and tumour targeting of the ^{68}Ga-derivative could eventually lead to more sensitive lesion detection, as lesions with a lower receptor density might also be detected. In addition, the low abdominal background signal of the ^{68}Ga-derivative could enable better detection of potential lymph node metastases, such as in the para-aortic area.

10.5.3 Tumour Metabolism Imaging

Subcutaneous syngeneic or xenograft tumour models in rodents can be still considered the mainstay of oncological research testing the efficacy of new drugs. However, subcutaneous tumour models derived from well-established cell lines can be misleading, as they might have developed artificial features during cultivation and propagation in cell culture. To circumvent such potential artefacts, patient-derived tumours are increasingly studied after implantation and propagation in mice. Usually a reduction of tumour growth is measured when a treatment is efficacious. However, imaging approaches are also employed to study treatment effects during the preclinical development of new drugs. This is especially preferred for spontaneous or orthotopic tumour models where the lesions might not be accessible for calliper measurements, and an early read-out is desired after start of treatment. In addition, such orthotopic or spontaneous tumour models might better mimic the disease and the environment that is usually present for a given tumour.

Various aspects of tumour biology can be visualised in preclinical tumour models with the prospect of clinical translation. The investigation of specific adaptations of the tumour metabolism beyond glycolysis has recently gained special attention, as it offers new opportunities for both detection and treatment of tumours (Hensley et al. 2013). For example, new compounds are currently being investigated targeting glutaminase as one of the key enzymes in the glutaminolytic pathway or mutated versions of the enzyme isocitrate dehydrogenase (Gross et al. 2014; Turkalp et al. 2014). The visualisation of specific tumour targets or deranged metabolic pathways other than glycolysis may offer potential advantages for better detection and characterisation of tumours in situations where ^{18}F-2-fluoro-2-deoxyglucose (FDG) has limitations. This is especially the case in situations where a high physiological background is observed, such as in the brain or in the liver (Shreve et al. 1999). This is of increasing importance as the development of new targeted therapies is getting increasingly expensive and new drugs are usually tailored to a specific disease (subset) requiring patient stratification and specific monitoring of therapy. This demands the use of biomarkers at various stages—i.e. for disease characterisation, drug selection or therapy monitoring. PET tracers, with their unique properties, can play an important role in this setting. New PET agents being developed should be also profiled in this setting.

The following example highlights how small-animal imaging can support the characterisation of PET agents of one distinct class of compounds and assist selection of the most appropriate candidate for the clinical stage. Previously it was shown that ^{18}F-labelled glutamate derivatives can be efficiently taken up through the amino acid exchanger system x_C^- which represents the entry to a deranged pathway in tumour metabolism involved in chemoresistance and detoxification of aberrant reactive oxygen species (Koglin et al. 2011). This approach can be used for tumour visualisation in various preclinical models with low background from healthy tissues and was successfully translated to the clinical setting (Baek et al. 2012).

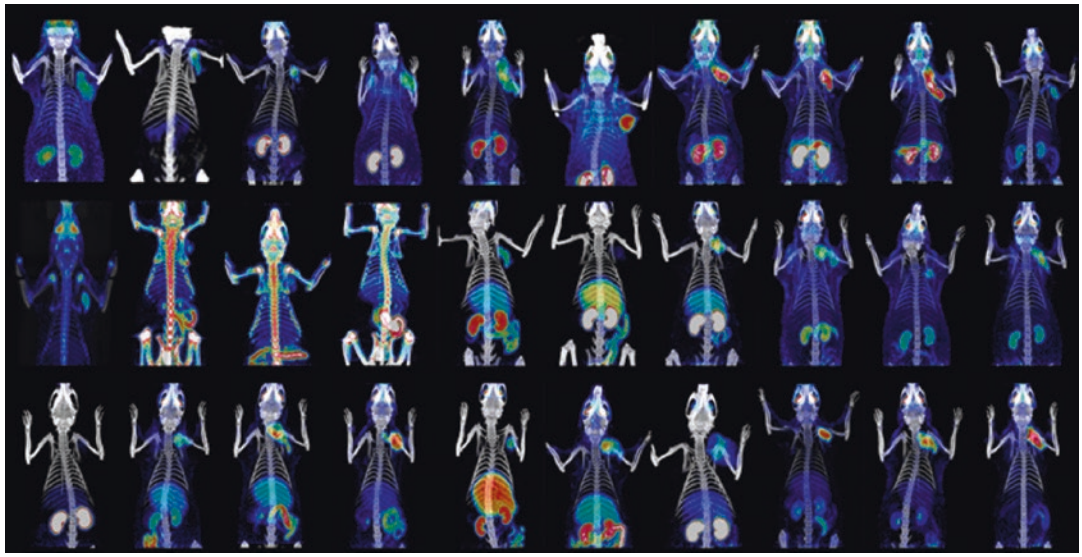

Fig. 10.3 Comparison of biodistribution and tumour-targeting potential of various ^{18}F-labelled glutamate derivatives in H460 tumour-bearing rats. Tumour cells were implanted on the right shoulder of each animal. Despite showing comparable biological activity in in vitro assays, differences in the tumour-targeting potential, distribution, excretion as well as different metabolic stability can be easily observed

This type of transporter substrates has been studied in detail (Mueller A et al. unpublished data, Piramal Imaging, data on file). Similar derivatives with slight structural modifications have been synthesised, retaining the dicarboxylic amino acid backbone as a structural motif to facilitate recognition by the transporter. Biological activity of these derivatives was first examined in cell uptake studies using adherent cells. However, it became clear that many derivatives exhibit similar behaviour in this assay, making further differentiation and selection of the most potent candidate impossible. Figure 10.3 illustrates how small-animal imaging was employed to characterise the 30 candidates in the same tumour model. Such an approach allows important distribution and retention parameters to be assessed simultaneously over time—informing selection of the most promising candidate without the more laborious classical biodistribution analysis, which would place a higher demand on the number of animals in the study group. Surprisingly, slight structural modifications that were indistinguishable by in vitro assays led to different pharmacokinetic and tumour-targeting properties in vivo.

10.6 Clinical Development Aspects

Progression to the clinical stage should follow as soon as a suitable imaging candidate has been identified. The administered mass doses of radiopharmaceuticals are generally low enough to lack pharmacologic activity and to produce relatively large safety margins. First-in-man evaluation of diagnostic radiopharmaceuticals may start under the microdosing concept (injection of <100 μg mass dose). The mass doses injected by radiotracers are usually severalfold, or even several orders of magnitude, lower than the no observed adverse effect level (NOAEL) doses tested in preclinical toxicology and safety studies with the non-radioactive derivative (US Department of Health and Human Services et al. 2012; www.ema.europa.eu/docs/en_GB/document_library/Scientific_guideline/2009/09/WC500002720.pdf). This allows the first clinical investigation of a new tracer molecule with a limited and defined non-clinical pharmacology, toxicology and safety package. Such first-in-man imaging studies yield critical

information about the general viability of this new approach and may even help to establish a clinical proof of concept. Depending on the clinical question addressed, it is important to clarify whether these studies are intended to prove or disprove that the imaging agent is suitable in binding with high signal to noise allowing localisation by imaging or that the target is a useful biomarker. Often, these questions cannot be addressed independently, making exploratory clinical development difficult. Despite such difficulties with this approach, promising diagnostic radiopharmaceuticals can be more rapidly identified and selected before entering full development. This is different from clinical studies for classical drug development, where phase I studies mainly investigate dosage and safety parameters.

During clinical development, the imaging biomarker must demonstrate that it is sufficiently robust, reliable and well characterised to allow its use as a routine clinical tool and to support decision-making. The qualification and technical validation of imaging biomarkers are dependent on their intended use and should fit the purpose: it typically includes the standardisation of acquisition and analysis, imaging–pathology correlation, cross-sectional clinical–biomarker correlations and correlation with outcome (Waterton and Pylkkanen 2012).

Over the past decade, it has become clear that regulatory approval of a new imaging agent requires clear demonstration of its clinical efficacy and utility, together with a validated method for interpreting images—specifically, how imaging results provide clinically useful information (Gorovets et al. 2013). This is different from the imaging agents that previously received marketing authorisation and has significant ramifications for the design of clinical studies. There is an increasing demand for explicit proof of the medical benefit of a diagnostic agent in terms of improved survival or quality of life. This is a paradigm shift that requires health-economic aspects to be factored into early clinical study design, so that the impact of the biomarker on patient management and clinical decision-making is already established once the agent receives approval and no further major studies are required to demonstrate this.

The potential of using imaging methods in drug development clinical trials has yet to be fully exploited. Unlike biomarkers derived from biospecimens, imaging biomarkers can involve more complex methods for data acquisition and offer various options for image processing. All these factors may increase data variability. Efforts to reduce measurement variability between centres and to increase the reproducibility of quantitative variables, such as standard uptake value, are reflected in accreditation programmes for PET sites run by imaging societies (e.g. European Association of Nuclear Medicine, Society of Nuclear Medicine and Molecular Imaging), national health institutes (e.g. US National Institutes for Health) or agencies (e.g. US Food and Drug Agency). Given the short half-life of radiopharmaceuticals, the logistics of developing a distribution network to supply them for global therapeutic clinical trials present an ongoing obstacle. Study sites with a primary focus on therapeutic clinical trial expertise may not have ready access to the radiotracer or to the associated imaging expertise required to use it; a risk management approach for imaging biomarker-driven clinical trials in oncology was proposed recently to mitigate these risk factors (Liu et al. 2015).

10.6.1 Example for Clinical Development of Aβ Imaging Agents

Alzheimer's disease is a devastating disease, ultimately leading to death. There is a great need to develop agents that impact directly on the mechanistic causes of the disease. Despite huge efforts in the past, no breakthrough has yet been achieved to significantly delay or halt progression of the disease. Several late-stage drug candidates have failed to show compelling evidence of efficacy. This can be attributed to both intrinsic and extrinsic factors. 'Intrinsic' refers to the properties of the drug itself: potency and toxicity. 'Extrinsic' relates to clinical design issues: inclusion of patients with

too advanced disease or without confirmed AD pathology. The current late-stage development drug candidates for AD are antibodies or small molecules directed against either Aβ itself or against the formation or accumulation of the pathological amyloid peptide. While there continues to be controversy surrounding the exact role of Aβ plaques in AD, it is clear that such plaques are a *conditio sine qua non* of AD and any therapy directed against them requires a biomarker to measure their existence.

In the past, mainly neuropsychological tests were used to clinically diagnose AD (McKhann et al. 1984). However, clinical tests take time and can lack accuracy, particularly at an early stage of the disease; nor can they sufficiently rule out AD as the underlying aetiology of cognitive decline (Albert et al. 2011). Autopsy was the only method to definitively diagnose AD, and it was repeatedly shown that 20–30 % of clinically diagnosed AD subjects do not have Aβ plaques (Beach et al. 2012). Other investigated biomarkers that are associated with AD are based on either morphological imaging (e.g. MRI), functional imaging such as glucose metabolism (FDG-PET) or analysis of Aβ-peptides in biofluids such as CSF. Although MRI can detect brain atrophy and shrinkage of the whole brain or particular regions of the brain affected by AD and FDG-PET can reveal areas of hypometabolism that can be attributed to AD, both imaging methods are visualising rather downstream effects that are often associated with AD but are unspecific, and the aetiology of the disease cannot be measured or visualised. The invasive procedure that is needed to obtain CSF can be associated with patient complaints and side effects (Duits et al. 2015). In addition, the results obtained from CSF measurements may differ depending on the modalities of lumbar puncture, storage and analysis methods and still require efforts for standardisation (Schoonenboom et al. 2005).

Given the limitations of the clinical diagnosis and other available biomarkers investigated in AD, significant efforts have been made in the past decade to identify new imaging biomarkers for visualisation of Aβ plaques in the brain. After identification of promising compounds, a requirement from regulatory authorities for approval was that the new imaging agents had to demonstrate diagnostic efficacy by comparison of the results from the scan assessment with histopathology. To achieve this, end-of-life patients were scanned during life with the agents under investigation. After death, an autopsy was performed to prove that the signal of the PET imaging agent did indeed correspond to the relevant pathology. Three new PET imaging agents with proven binding to Aβ plaques have been developed and achieved regulatory approval: Amyvid™, Neuraceq™ and Vizamyl™ (http://www.ema.europa.eu/docs/en_GB/document_library/EPAR_-_Product_Information/human/002422/WC500137635.pdf; http://www.ema.europa.eu/docs/en_GB/document_library/EPAR_-_Product_Information/human/002553/WC500162592.pdf; http://www.ema.europa.eu/docs/en_GB/document_library/EPAR_-_Product_Information/human/002557/WC500172950.pdf). They are indicated, as an adjunct to other diagnostic evaluations, in subjects with cognitive decline who are being evaluated for AD and other causes of cognitive decline. A negative PET scan evaluation indicates the absence of Aβ plaques, so that AD can be ruled out. A positive Aβ PET scan indicates the presence of plaques at pathological levels. However, a positive scan alone does not establish the diagnosis of AD or any other cognitive disorder, because Aβ plaques may also be present in patients with other types of neurologic conditions as well as elderly people with normal cognition.

Aβ PET imaging represents a perfect example of how AD drug development can be enabled. The need to include patients at early disease stage, and the increasing role of biomarkers, is also reflected in a recently published draft guidance document by the FDA to support the development of drugs in AD (http://www.fda.gov/downloads/drugs/guidancecomplianceregulatoryinformation/guidances/ucm338287.pdf). Never before have multiple drug companies unified the use of a PET imaging technique to establish global multicentre therapeutic trials. Several large phase II and III drug trials are underway requiring Aβ PET as an inclusion criterion or as treatment monitoring

tool. Activities are ongoing to improve quantification and standardisation across radiotracers. The use of reliable biomarkers is the key to the successful development of this class of therapeutic agents and points the way to future agents.

10.7 Summary and Conclusions

Molecular imaging biomarkers offer great opportunities to address unmet medical needs in various diseases and to enable drug development. Improved understanding of diseases at the molecular level led to advances in target discovery and validation as well as ligand discovery, optimisation and labelling. Small-animal imaging can support biomarker discovery and validation at various stages, for example, by the longitudinal characterisation of disease models. In addition, comparison of ligand pharmacokinetics, the selection of the most suitable agent or drug development approaches can be supported by preclinical imaging. Clinical development of new imaging agents ultimately culminates in the regulatory approval for routine clinical use in a given indication. Broader access will also stimulate more research and enables drug development. The routine use and implementation of new imaging agents in diagnostic regimens will be of benefit for the patients and society to lower the burden of disease.

References

Albert MS, DeKosky ST, Dickson D, Dubois B, Feldman HH, Fox NC, et al. The diagnosis of mild cognitive impairment due to Alzheimer's disease: recommendations from the National Institute on Aging–Alzheimer's Association workgroups on diagnostic guidelines for Alzheimer's disease. Alzheimers Dement. 2011;7:270–9.

Baek S, Choi CM, Ahn SH, Lee JW, Gong G, Ryu JS, et al. Exploratory clinical trial of (4S)-4-(3-[18F] fluoropropyl)-L-glutamate for imaging xC- transporter using positron emission tomography in patients with non-small cell lung or breast cancer. Clin Cancer Res. 2012;18:5427–37.

Beach TG, Monsell SE, Phillips LE, Kukull W. Accuracy of the clinical diagnosis of Alzheimer disease at National Institute on Aging Alzheimer Disease Centers, 2005–2010. J Neuropathol Exp Neurol. 2012;71:266–73.

Becaud J, Mu L, Karramkam M, Schubiger PA, Ametamey SM, Graham K, Stellfeld T, Lehmann L, Borkowski S, Berndorff D, Dinkelborg L, Srinivasan A, Smits R, Koksch B. Direct one-step 18F-labeling of peptides via nucleophilic aromatic substitution. Bioconjug Chem. 2009;20(12):2254–61.

Biomarkers Definitions Working Groups. Biomarkers and surrogate endpoints: preferred definitions and conceptual framework. Clin Pharmacol Ther. 2001;69:89–95.

Brendel M, Jaworska A, Griessinger E, Rötzer C, Burgold S, Gildehaus FJ, et al. Cross-sectional comparison of small animal [18F]-florbetaben amyloid-PET between transgenic AD mouse models. PLoS One. 2015a;10:e0116678.

Brendel M, Jaworska A, Herms J, Trambauer J, Rötzer C, Gildehaus FJ, et al. Amyloid-PET predicts inhibition of *de novo* plaque formation upon chronic γ-secretase modulator treatment. Mol Psychiatry. 2015b;20:1179–87.

Duits FH, Martinez-Lage P, Paquet C, Engelborghs S, Lleó A, Hausner L, et al. Performance and complications of lumbar puncture in memory clinics: Results of the multicenter lumbar puncture feasibility study. Alzheimers Dement 2015. pii: S1552–5260(15)02702-8. doi:10.1016/j.jalz.2015.08.003.

Eli Lilly Nederland BV. Amyvid 800 MBq/mL solution for injection (florbetapir 18 F). Summary of product characteristics (last updated 22/09/2015): http://www.ema.europa.eu/docs/en_GB/document_library/EPAR_-_Product_Information/human/002422/WC500137635.pdf.

Frangioni JV. The problem is background, not signal. Mol Imaging. 2009;8:303–4.

GE Healthcare Ltd. Vizamyl 400 MBq/mL solution for injection (flutemetamol 18 F). Summary of product characteristics (last updated 10/11/2015): http://www.ema.europa.eu/docs/en_GB/document_library/EPAR_-_Product_Information/human/002557/WC500172950.pdf.

Ginj M, Zhang H, Waser B, Cescato R, Wild D, Wang X, et al. Radiolabeled somatostatin receptor antagonists are preferable to agonists for in vivo peptide receptor targeting of tumors. Proc Natl Acad Sci U S A. 2006;103:16436–41.

Gorovets A, Marzella L, Rieves D, Yang L. Efficacy considerations for US Food and Drug Administration approval of diagnostic radiopharmaceuticals. J Nucl Med. 2013;54:1479–84.

Gross MI, Demo SD, Dennison JB, Chen L, Chernov-Rogan T, Goyal B, Janes JR, Laidig GJ, Lewis ER, Li J, Mackinnon AL, Parlati F, Rodriguez ML, Shwonek PJ, Sjogren EB, Stanton TF, Wang T, Yang J, Zhao F, Bennett MK. Antitumor activity of the glutaminase inhibitor CB-839 in triple-negative breast cancer. Mol Cancer Ther. 2014;13(4):890–901.

Hensley CT, Wasti AT, DeBerardinis RJ. Glutamine and cancer: cell biology, physiology, and clinical opportunities. J Clin Invest. 2013;123(9):3678–84.

Höhne A, Mu L, Honer M, Schubiger PA, Ametamey SM, Graham K, Stellfeld T, Borkowski S, Berndorff D,

Klar U, Voigtmann U, Cyr JE, Friebe M, Dinkelborg L, Srinivasan A. Synthesis, 18F-labeling, and in vitro and in vivo studies of bombesin peptides modified with silicon-based building blocks. Bioconjug Chem. 2008;19(9):1871–9.

Honer M, Mu L, Stellfeld T, Graham K, Martic M, Fischer CR, Lehmann L, Schubiger PA, Ametamey SM, Dinkelborg L, Srinivasan A. Borkowski S 18F-labeled bombesin analog for specific and effective targeting of prostate tumors expressing gastrin-releasing peptide receptors. J Nucl Med. 2011;52(2):270–8.

ICH guideline M3(R2) on non-clinical safety studies for the conduct of human clinical trials and marketing authorisation for pharmaceuticals. Step 5. 2009. EMA/CPMP/ICH/286/1995. www.ema.europa.eu/docs/en_GB/document_library/Scientific_guideline/2009/09/WC500002720.pdf Accessed 18 Jan 2016.

Jadvar H. Positron emission tomography in prostate cancer: summary of systematic reviews and meta-analysis. Tomography. 2015;1(1):18–22.

Kähkönen E, Jambor I, Kemppainen J, Lehtiö K, Grönroos TJ, Kuisma A, Luoto P, Sipilä HJ, Tolvanen T, Alanen K, Silén J, Kallajoki M, Roivainen A, Schäfer N, Schibli R, Dragic M, Johayem A, Valencia R, Borkowski S, Minn H. In vivo imaging of prostate cancer using [68Ga]-labeled bombesin analog BAY86-7548. Clin Cancer Res. 2013;19(19):5434–43.

Koglin N, Mueller A, Berndt M, Schmitt-Willich H, Toschi L, Stephens AW, et al. Specific PET imaging of xC- transporter activity using a ^{18}F-labeled glutamate derivative reveals a dominant pathway in tumor metabolism. Clin Cancer Res. 2011;17:6000–11.

Liu Y, deSouza NM, Shankar LK, Kauczor H-U, Trattnig S, Collette S, et al. A risk management approach for imaging biomarker-driven clinical trials in oncology. Lancet Oncol. 2015;16:e622–8.

Lütje S, Heskamp S, Cornelissen AS, Poeppel TD, van den Broek SA, Rosenbaum-Krumme S, Bockisch A, Gotthardt M, Rijpkema M, Boerman OC. PSMA Ligands for radionuclide imaging and therapy of prostate cancer: clinical status. Theranostics. 2015;5(12):1388–401.

Maier FC, Wehrl HF, Schmid AM, Mannheim JG, Wiehr S, Lerdkrai C, et al. Longitudinal PET-MRI reveals β-amyloid deposition and rCBF dynamics and connects vascular amyloidosis to quantitative loss of perfusion. Nat Med. 2014;20:1485–92.

Mansi R, Wang X, Forrer F, Waser B, Cescato R, Graham K, et al. Development of a potent DOTA-conjugated bombesin antagonist for targeting GRPr-positive tumours. Eur J Nucl Med Mol Imaging. 2011;38:97–107.

Mansi R, Fleischmann A, Maecke HR, Reubi JC. Targeting GRPR in urological cancers – from basic research to clinical application. Nat Rev Urol. 2013;10:235–44.

McKhann G, Drachman D, Folstein M, Katzman R, Price D, Stadlan EM. Clinical diagnosis of Alzheimer's disease: report of the NINDCS-ADRDA Work Group under the auspices of Department of Health and Human Services Task Force on Alzheimer's disease. Neurology. 1984;34:939–44.

Patel S, Gibson R. In vivo site-directed radiotracers: a mini-review. Nucl Med Biol. 2008;35:805–15.

Piramal Imaging Ltd. Neuraceq 300 MBq/ml solution for injection (florbetaben 18 F). Summary of product characteristics (last updated 12/10/2015): http://www.ema.europa.eu/docs/en_GB/document_library/EPAR_-_Product_Information/human/002553/WC500162592.pdf.

Sah BR, Burger IA, Schibli R, Friebe M, Dinkelborg L, Graham K, Borkowski S, Bacher-Stier C, Valencia R, Srinivasan A, Hany TF, Mu L, Wild PJ, Schaefer NG. Dosimetry and first clinical evaluation of the new 18F-radiolabeled bombesin analogue BAY 864367 in patients with prostate cancer. J Nucl Med. 2015;56(3):372–8.

Schoonenboom NS, Mulder C, Vanderstichele H, Van Elk EJ, Kok A, Van Kamp GJ, et al. Effects of processing and storage conditions on amyloid beta (1–42) and tau concentrations in cerebrospinal fluid: implications for use in clinical practice. Clin Chem. 2005;51:189–95.

Shreve PD, Anzai Y, Wahl RL. Pitfalls in oncologic diagnosis with FDG PET imaging: physiologic and benign variants. Radiographics. 1999;19(1):61–77.

Smith JJ, Sorensen AG, Thrall JH. Biomarkers in imaging: realizing radiology's future. Radiology. 2003;227:633–8.

Turkalp Z, Karamchandani J, Das S. IDH mutation in glioma: new insights and promises for the future. JAMA Neurol. 2014;71(10):1319–25.

US Department of Health and Human Services Food and Drug Administration, Center for Drug Evaluation and Research (CDER). Guidance for industry. Alzheimer's disease: developing drugs for the treatment of early stage disease. 2013. http://www.fda.gov/downloads/drugs/guidancecomplianceregulatoryinformation/guidances/ucm338287.pdf. Accessed 18 Dec 2015.

US Department of Health and Human Services, Food and Drug Administration, Center for Drug Evaluation and Research (CDER). Investigational New Drug Applications for Positron Emission Tomography (PET) Drugs. 2012. www.fda.gov/downloads/drugs/…/ucm291573.pdf. Accessed 18 Jan 2016.

Van de Bittner GC, Ricq EL, Hooker JM. A philosophy for CNS radiotracer design. Acc Chem Res. 2014;47:3127–34.

Virdee K, Cumming P, Caprioli D, Jupp B, Rominger A, et al. Applications of positron emission tomography in animal models of neurological and neuropsychiatric disorders. Neurosci Biobehav Rev. 2012;36:1188–216.

Wang Y, Zhang Y-L, Hennig K, Gale JP, Hong Y, Cha A, et al. Class I HDAC imaging using [(3)H]CI-994 autoradiography. Epigenetics. 2013;8:756–64.

Waterton JC, Pylkkanen L. Qualification of imaging biomarkers for oncology drug development. Eur J Cancer. 2012;48:409–15.

Concepts in Diagnostic Probe Design

11

Igor Jacobs, Gustav J. Strijkers, Henk M. Keizer, Henk M. Janssen, Hisataka Kobayashi, and Klaas Nicolay

Contents

Abbreviations

ADME	Absorption, distribution, metabolism, and excretion
BBB	Blood–brain barrier
CEST	Chemical exchange saturation transfer
CNR	Contrast-to-noise ratio
CT	Computed tomography
DCE-MRI	Dynamic contrast-enhanced magnetic resonance imaging
DO3A	1,4,7-tris(carboxymethylaza) cyclododecane-10-azaacetylamide
DOTA	1,4,7,10-tetraazacyclododecane tetraacetic acid
DTPA	Diethylenetriaminepentaacetic acid
EPR effect	Enhanced permeability and retention effect
G	Generation
HER2	Human epidermal growth factor receptor 2

I. Jacobs • K. Nicolay (✉)
Biomedical NMR, Department of Biomedical Engineering, Eindhoven University of Technology, High Tech Campus 11, office 1.247, Eindhoven 5656, AE, The Netherlands
e-mail: k.nicolay@tue.nl

G.J. Strijkers
Biomedical NMR, Department of Biomedical Engineering, Eindhoven University of Technology, High Tech Campus 11, office 1.247, Eindhoven 5656, AE, The Netherlands

Biomedical Engineering and Physics, Academic Medical Center (AMC), Amsterdam, The Netherlands

H.M. Keizer • H.M. Janssen
SyMO-Chem BV, Eindhoven, The Netherlands

H. Kobayashi
Molecular Imaging Program, Center for Cancer Research, National Cancer Institute, National Institutes of Health, Bethesda, MD, USA

F. Kiessling et al. (eds.), *Small Animal Imaging*, DOI 10.1007/978-3-319-42202-2_11

MRI	Magnetic resonance imaging
OI	Optical imaging
PAMAM dendrimers	Poly(amidoamine) dendrimers
PEG	Poly(ethylene glycol)
PEO	Poly(ethylene oxide)
PET	Positron emission tomography
PPI dendrimers	Poly(propylene imine) dendrimers
QD	Quantum dot
RES	Reticuloendothelial system
SNR	Signal-to-noise ratio
SPECT	Single-photon emission computed tomography
US	Ultrasound

11.1 Introduction

Magnetic resonance imaging (MRI), computed tomography (CT), ultrasound (US) and certain specialised optical imaging (OI) techniques can produce valuable medical images on the basis of endogenous contrast mechanisms. The nature and scope of such intrinsic contrast-generating properties is largely determined by the physical principles of the imaging technique and the way in which the imaging signal is generated and detected. However, many clinical imaging protocols involving MRI, CT, US and OI make use of contrast agents to enhance the specificity and/or the sensitivity of disease detection. Contrast agents are essential for nuclear imaging with positron emission tomography (PET) and single-photon emission computed tomography (SPECT), since these techniques rely exclusively on the measurement of the spatial distribution of gamma (γ) rays generated by radioactive decay of injected tracer compounds. Without these tracers, no (PET or SPECT) signal is generated, which also explains why nuclear imaging necessitates the use of an additional imaging device to provide anatomical and, therefore, x-ray attenuation information. In most cases, CT is used for that purpose. Most optical imaging in biomedical research also requires the injection of exogenous contrast material to generate usable signal.

The molecular properties of contrast materials are dictated by two main factors, i.e. the imaging method for which they are going to be used and the biomedical application, which they should address. Each imaging method has its own characteristics in terms of how signal is generated and detected, and this has major consequences for the optimal design of the contrast material. On the other hand, the molecular properties of the contrast agent, including its size, shape, chemical composition and charge, have a major influence on their in vivo pharmacokinetic and pharmacodynamic properties. For these reasons, the optimisation of contrast material design should involve an integrated approach in which all above factors are considered in a balanced manner, so as to arrive at a design that is most suitable for a (range of) specific application(s). Design criteria must include the use of materials that are safe and affordable if the agent is ultimately to be used in humans.

This chapter will provide an overview of the prime design criteria for diagnostic contrast materials. In view of the overwhelming breadth of contrast-enhanced (bio)medical imaging, we have decided to focus the overview on MRI contrast agents and, more specifically, on a particular class of MRI contrast agents, i.e. dendrimers. Dendrimers have been extensively studied, and they represent a unique class of materials in that they can be synthetised in a very broad range of sizes while keeping the chemical composition essentially the same. By tuning the size and other molecular characteristics, the dendritic agents can either be designed to act as low-molecular-weight contrast materials or behave like high-molecular-weight nanoparticles. The specific focus on dendrimers aims to provide a basic understanding of the relation between molecular properties and in vivo behaviour, which offers important handles for design optimisation. Many findings with dendrimers have broad implications and can be generalised to other contrast agents, not just for MRI but also for the other imaging methods. When appropriate, we will make a side step and describe hallmarks of contrast materials for other imaging modalities as well. James and Gambhir (2012) have provided

an excellent in-depth overview of recent advances in the design of contrast materials and the strengths and limitations of the different biomedical imaging modalities. For more specific reviews of the state of the art in the design of contrast materials for biomedical imaging, see Geraldes and Laurent (2009), Mulder et al. (2013) and Nicolay et al. (2013) for MRI; Li et al. (2014) for CT; Licha and Resch-Genger (2011) and Khemthongcharoen et al. (2014) for OI; Huang et al. (2015) for PET; Gnanasegaran and Ballinger (2014) for SPECT; and Kiessling et al. (2014), Wen et al. (2014) and van Rooij et al. (2015) for US.

11.2 Desired In Vivo Behaviour of Diagnostic Contrast Materials

Ideally, shortly after injection, diagnostic imaging probes would very specifically distribute to the target of the imaging study, e.g. sites of disease activity, and otherwise be excreted reaching low levels in the background. This would create the best opportunities for sensitive as well as specific detection of the location and severity of the disease process. Following the imaging study, the probe should preferably be eliminated rapidly from the entire organism including the target. Clearance ideally occurs via the kidneys into the urine as this represents the fastest elimination pathway. It goes without saying that the contrast material should be biocompatible, should be stable for the entire duration of the imaging study and should not cause any adverse effects.

In reality, the above ideal situation does not hold. In fact, the optimal design of contrast materials for diagnostic biomedical imaging depends on many parameters, in a very complex fashion, and usually represents a compromise between mutually conflicting factors. Unfortunately, most of these factors can only be dealt with in an empirical (partly trial and error, and therefore time consuming) fashion, as there is currently a lack of quantifiable criteria that can rationally and time efficiently steer the process of contrast agent development. This paragraph is intended to provide some feeling for the parameters that play a dominant role in determining the efficacy of a contrast agent for a certain diagnostic task. For further reference, the reader is referred to specialised literature. As examples, Geraldes and Laurent provide a comprehensive classification of MRI contrast agents (Geraldes and Laurent 2009), while Chen and Chen (2010), Choi and Frangioni (2010), Rosenblum et al. (2010), Kobayashi et al. (2011) and Wu et al. (2015) present an in-depth description of the design criteria for guiding the development of probes for (molecular) imaging. James and Gambhir (2012) also portray the dominant probe design considerations.

First and foremost, the probe should be capable of generating sufficiently strong signal (or signal change) on the diagnostic images, as acquired with the modality of choice. This criterion is typically expressed as the signal-to-noise ratio (SNR) and/or contrast-to-noise ratio (CNR), depending on the imaging modality, which is achieved upon probe injection. The concentrations of the probe, which are needed to produce a sufficiently high SNR or CNR, differ strongly among the different imaging modalities. This is caused by the very different intrinsic sensitivities of each modality. PET imaging can detect picomolar concentrations of an agent, while MRI usually needs on the order of micromolar concentrations. PET is therefore considered a tracer technique, while MRI definitely is not. The multiple orders of magnitude difference in intrinsic sensitivity among modalities implies that biocompatibility and stability of contrast material is much less of an issue in the case of PET than with MRI since the doses of the agent will be dramatically lower. However, PET is associated with exposure to ionising radiation, in particular when combined with CT, as is common practice since PET lacks anatomical information. In contrast, MRI does not involve the use of ionising radiation. For these reasons, the optimal choice of imaging probe and imaging technology is typically a balance between several pros and cons. Obviously, not only the above factors but also the information sought after by the imaging study

plays a key role in guiding the choice of probe and imaging modality.

The above issue of detecting sensitivity is also strongly influenced by the question whether sufficient quantities of contrast material can reach the intended target site. As contrast agents are most often injected intravenously, they will first be distributed in the vascular space. What ideally happens next is largely dependent on the goal of the imaging study. Most imaging-based tumour diagnoses require that the contrast agent leaks from the vascular compartment into the extravascular, intratumoural space. This implies that the probe should (i) be sufficiently small to cross the tumour vascular endothelium, (ii) circulate in the blood sufficiently long to allow suitably high intratumoural levels to be reached for generating a significant imaging signal and (iii) persist in the tumour compartment sufficiently long while being essentially completely cleared from the circulation, in order to achieve an as high as possible tumour-to-background ratio on the images. These factors are governed by the biodistribution of the imaging agent over time and are often collectively considered under the absorption, distribution, metabolism and excretion (ADME) concept, which is a leading theme in pharmacology. ADME describes the disposition of a foreign compound within a living organism, and, as such, knowledge of the ADME properties of a contrast material may provide strong leads for optimising its molecular properties for the desired application. As will be shown further on, ADME information typically aids to define rules of thumb for guiding contrast agent design rather than providing quantitative handles for predictable, fully rational design optimisation.

Most of the insights in in vivo contrast agent properties have been collected by extensive studies in small animals, particularly mice. However, contrast agent behaviour is different in humans. Distribution volumes are obviously much bigger in humans, while the rates of physiological processes are usually much slower. Nevertheless, the extensive small animal studies have yielded a wealth of information on many aspects of contrast agent behaviour and as such offer an essential starting point for the translation of novel contrast agent concepts from the preclinical to the clinical setting. The most relevant factors governing diagnostic probe design will be highlighted next.

11.3 Basic Design of Dendrimers for Diagnostic Imaging and Therapy

As stated above, the focus of this chapter is on dendrimer-based contrast materials. Dendrimers have been very extensively studied, and this has led to a reasonably coherent set of design criteria. This paragraph describes the molecular architecture of dendrimers and features general aspects of their usefulness in diagnostic imaging, with an emphasis on MRI, as well as therapeutic applications. More specific qualities are presented in upcoming sections. For papers on the basics of dendrimer design and biomedical uses, see Bosman et al. (1999), Boas and Heegaard (2004), Barrett et al. (2009), Bumb et al. (2010), Menjoge et al. (2010), Mintzer and Grinstaff (2011) and Longmire et al. (2011, 2014).

Dendrimers are a class of macromolecules that are characterised by branching polymerisation, which results in a three-dimensional structure (Fig. 11.1). The term “dendrimer” is inspired by the Greek words “dendron”, which means “tree”, and “meros” meaning “part” and refers to the basal structure of dendrimers: a central core from which numerous polymerised branches extend out to the molecule’s periphery. The structure of dendrimers consists of three main elements: the core, interior and shell. The core has major effects on the three-dimensional shape of the dendrimer, i.e. spherical, ellipsoidal or cylindrical. The architecture and composition of the interior part affects the host–guest properties. The surface can be further polymerised or modified with an enormous diversity of functional peripheral groups. The stepwise addition of polymeric elements from the core outwards creates monodisperse molecules that differ only in size with each successive layer, which are referred to as a “generation” (i.e. G1, G2 and G3) (Fig. 11.1). This remarkable flexibility in the molecular

structure, composition and size of dendrimers explains the enormous interest they have generated for use as carriers for imaging and therapeutic agents. A very important attribute of dendrimers is their multivalency, with the number of surface end groups exponentially growing with each generation. Dendrimers for imaging are most often prepared by chemical conjugation of imaging labels to the end groups. Paramagnetic dendrimers, suited for ^{1}H-MRI, are synthesised by coupling DOTA or DTPA moieties to the end groups, followed by incorporation of Gd^{3+} ions (Fig. 11.1). Chelation of the paramagnetic Gd ion via high-stability complex formation with, for example, DOTA or DTPA is needed, since free Gd^{3+} ions are highly toxic (Aime et al. 1998; Sherry et al. 2009). The application of Gd-labelled dendrimers as MRI contrast agents is primarily based on shortening of the T_1 relaxation time, one of the prime MRI contrast parameters. The presence of the paramagnetic agent can either be detected with the use of T_1-weighted MRI (causing a higher signal intensity as compared to the pre-contrast scan) or more quantitatively assessed with T_1 parameter mapping. In the latter case, multiple MR images are acquired with different degrees of T_1 weighting, followed by pixel-wise fitting of the data to estimate the T_1 relaxation time. The degree of T_1 shortening can be used to estimate the local contrast agent concentration. This conversion of T_1 change to contrast agent concentration requires knowledge of the molar

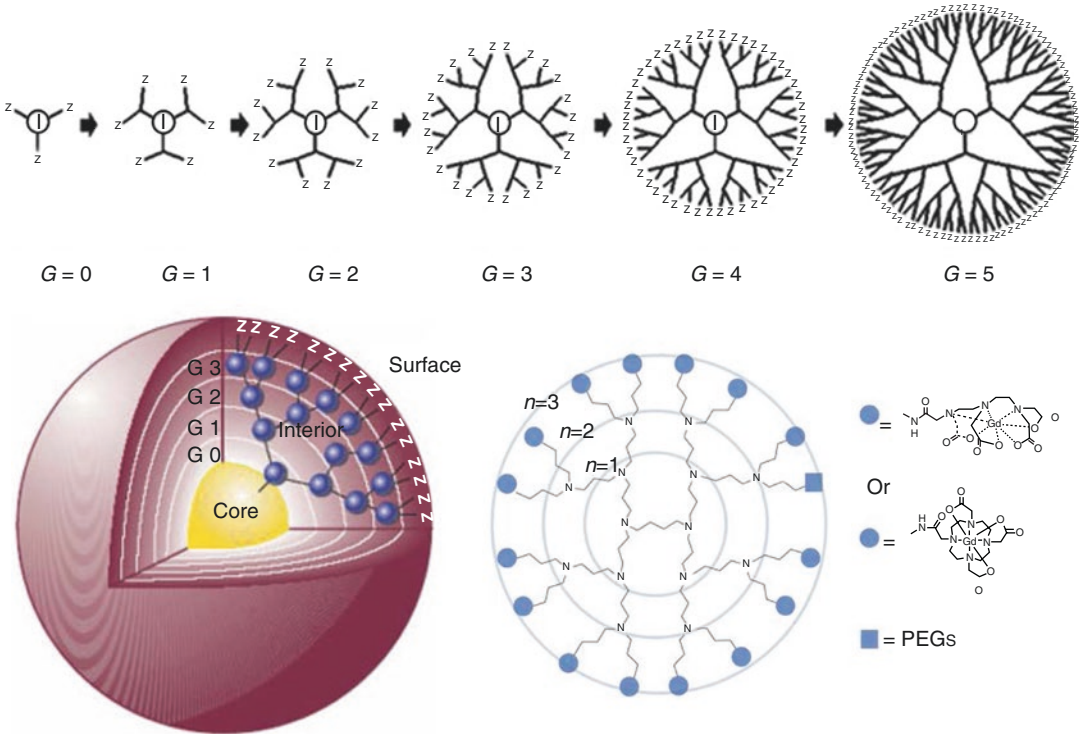

Fig. 11.1 Architecture of dendrimers. (*Top*) Schematic structures of different generation dendrimers, starting with the basic core element (= G0, here with 3 functional groups) and branching further out towards the generation 5 material (= G5). For each generation, two new branches are added to each existing arm doubling the number of functional end groups. (*Bottom*, *left*) Build-up in three dimensions of a dendrimer, starting from the inner core and increasingly extending the dimensions and the number of surface functionalities with every next generation. (*Bottom*, *right*) Schematic example of a paramagnetic Gd-DTPA- or Gd-DO3A-conjugated G3 PPI dendrimer for contrast-enhanced MRI. The Gd-containing units are conjugated to the distal ends of the dendrimer. A variety of conjugation methods and a range of conjugated moieties (e.g. PEGs) can be chosen. The structures shown are schematic example pictures only. For details on employed dendritic molecular structures, see the specific literature references

relaxivity, r_1, in units of $mM^{-1}s^{-1}$, which can be obtained by measuring the T_1s of a contrast agent dilution series in aqueous buffer (Strijkers et al. 2007). Gd-DTPA, Gd-DOTA and related low-molecular-weight Gd chelates have very similar r_1s in the order of 1–4 $mM^{-1}s^{-1}$, depending on the magnetic field strength (for further details, see Sect. 11.4) (Nicolay et al. 2013; Aime et al. 1998). Dendrimers tend to have higher relaxivities than simple Gd chelates.

The multivalent nature of dendrimers (Fig. 11.1) is also widely exploited to synthesise dendrimers with multiple appending ligands (for achieving high-affinity binding to specific molecular targets). The options are essentially endless. Furthermore, dendrimers are suitable as drug carrier devices, as a wide range of therapeutic agents, including DNA and RNA, can be incorporated in the molecule's interior (Barrett et al. 2009; Baker 2000; Kannan et al. 2014). Several dendrimer formulations of therapeutic agents are in clinical trials (Kannan et al. 2014). A docetaxel–dendrimer conjugate is in a phase 1 clinical trial for advanced or metastatic cancer. The dendrimer's molecular architecture also readily allows for combinations of imaging and therapy (Kannan et al. 2014) in theragnostic (or theranostic) applications, in which diagnostic imaging converges with therapeutics (Loudos et al. 2011). The focus in the rest of the chapter will be on the use of dendrimers as contrast agents for diagnostic imaging.

11.4 The Effects of Contrast Agent Size

The ability to control the molecular structure of dendrimers generates quite unique flexibility to tune their size while minimally affecting the overall chemical composition. This aspect continues to be one of the main assets of the use of dendrimers for diagnostic imaging, as contrast agent size is a major factor controlling its behaviour in vivo and hence its usefulness in diagnostic imaging. Below we will highlight some of the main manifestations of dendrimer size effects in diagnostic MRI. There are many eloquent reviews on this topic (Menjoge et al. 2010; Longmire et al. 2008, 2011, 2014; Kobayashi et al. 2010a).

A very illustrative example of the consequences of the variation of the size of paramagnetic Gd-DTPA-labelled dendrimers for contrast-enhanced MRI is shown in Fig. 11.2. Langereis et al. (2006) report the preparation of G0, G1, G3 and G5 poly(propylene imine) (PPI) dendrimers and their use for in vivo whole-body contrast-enhanced MRI in mice. The dendrimer contrast materials, which had molecular weights ranging from 0.7 to 51.2 kDa for the G0 and G5 dendrimers, respectively, were compared to Gd-DTPA (0.6 kDa) as the non-dendrimer control. The number of Gd ions per molecule ranged from 1 for Gd-DTPA and the G0 dendrimer to 4, 16 and 64 for the G1, G3 and G5 dendrimers, respectively. First, the materials were characterised by ionic relaxivity measurements at a field strength of 1.5 tesla (Table 11.1). Measurements were done in mouse plasma to mimic the conditions in the blood compartment. Interestingly, on a per Gd ion basis, the ionic r_1 relaxivities increased strongly from circa 4 $mM^{-1}s^{-1}$ for Gd-DTPA to about 19 $mM^{-1}s^{-1}$ for the G5 material. The ionic r_2 relaxivities, which describe the contrast agent-induced shortening of the T_2 relaxation time (like T_1 a fundamentally important MRI contrast parameter) (Strijkers et al. 2007), were shown to increase in similar proportions with increasing molecular weight. The r_2 increased, however, even more significantly, reaching values of about 25 $mM^{-1}s^{-1}$ for the G5 agent, where this value is on a per Gd ion basis. These pronounced increases in r_1 and r_2 with dendrimer generation can be explained on the basis of their higher molecular weights. The larger molecular size causes the correlation times characterising the rotational mobility of the molecules to increase in proportion. This enhances the efficacy of the T_1-shortening magnetic interactions, which reaches an optimum when the time scale of the dendrimers' molecular tumbling is similar to the resonance frequency of the MRI scanner, i.e. around the Larmor frequency. It turns out that in many macromolecular systems, including higher-generation dendrimers, the molecular mobility quite

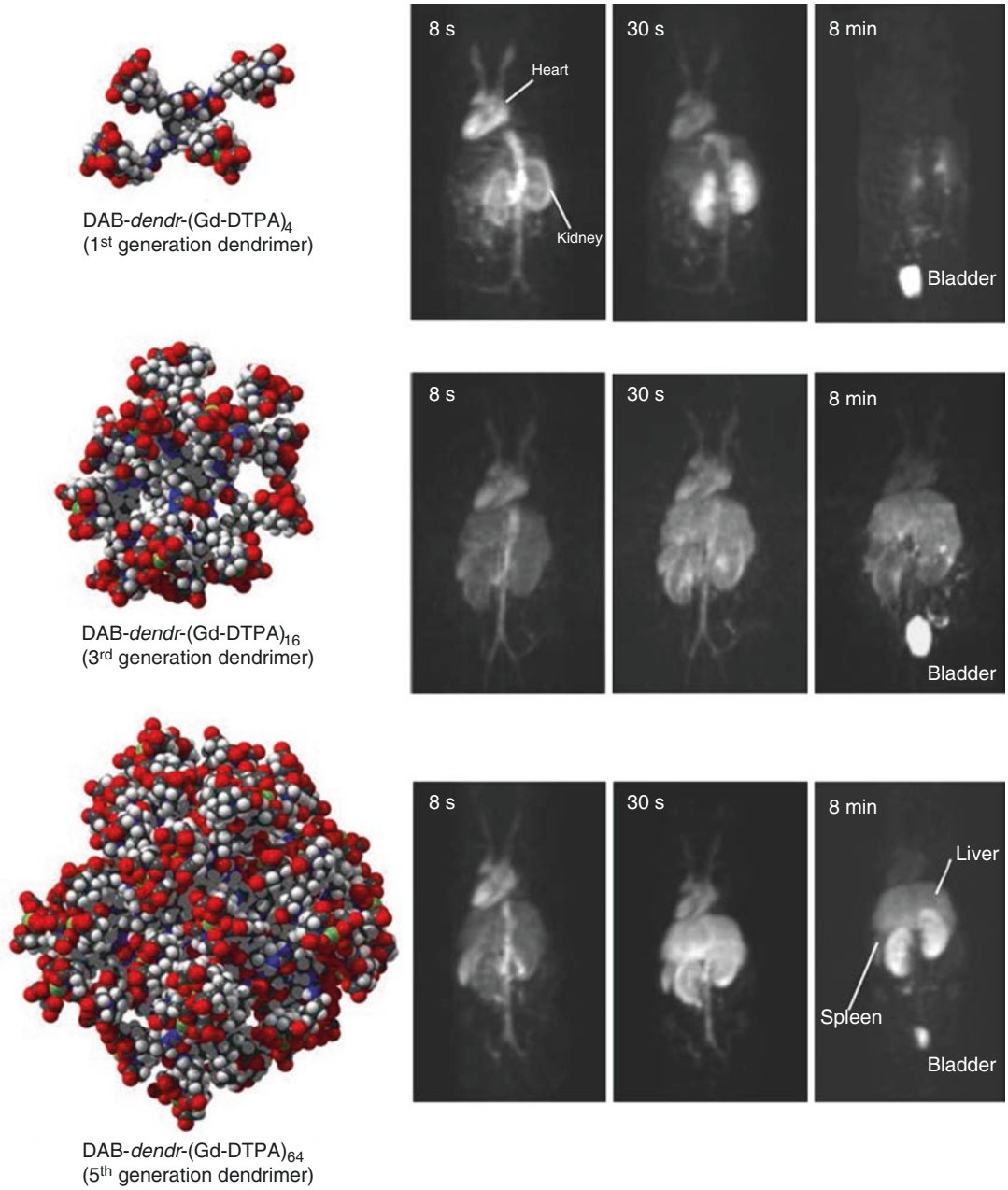

Fig. 11.2 Whole-body contrast-enhanced MRI of mice at 1.5 tesla. Maximum intensity projections of digitally subtracted contrast-enhanced whole-body MR images show good visualisation of the cardiovascular system and the renal parenchyma directly after paramagnetic agent injection (8 s). In time, the lower-generation PPI dendrimer appears to accumulate in the kidney, whereas the higher generations do so in the liver and spleen. Eight minutes after administration of MRI contrast agent, the higher-generation PPI dendrimers accumulate in the renal collecting system of the kidney and to some extent in the bladder (Modified with permission from Langereis et al. 2006)

closely matches the Larmor frequency corresponding to a magnetic field strength around 1 tesla. This explains why graphs depicting the ionic relaxivity r_1 as a function of magnetic field display a characteristic (macromolecular) peak around this field strength (Nicolay et al. 2013;

Table 11.1 Longitudinal (r_1) and transverse (r_2) relaxivities of Gd-DTPA, the reference Gd-DTPA complex (G0) and different generations of Gd-DTPA-terminated PPI dendrimers (G1, G3 and G5) in mouse plasma at 1.5 T and 20 °C

	Ionic r_1[a] ($mM^{-1}s^{-1}$)	Ionic r_2[a] ($mM^{-1}s^{-1}$)	No. of Gd ions	Mol. r_1[b] ($mM^{-1}s^{-1}$)	Mol. r_2[b] ($mM^{-1}s^{-1}$)	MW[c] (kDa)
Gd-DTPA	4.2 ± 0.1	4.5 ± 0.3	1	4.2	4.5	0.6
G0	8.1 ± 0.3	8.6 ± 0.2	1	8.1	8.6	0.7
G1	11.4 ± 0.4	12.0 ± 0.5	4	45.6	48.0	3.1
G3	15.2 ± 0.2	17.9 ± 0.8	16	243	286	12.7
G5	19.3 ± 0.4	25.0 ± 0.6	64	1,235	1,600	51.2

For details, see Langereis et al. (2006)

[a]The ionic relaxivity is defined as the relaxivity per Gd^{3+} ion

[b]The maximum molecular relaxivity (mol. $r_{1,2}$) is defined as the ionic relaxivity (ionic $r_{1,2}$) multiplied by the theoretical number of Gd^{3+} moieties attached to a single dendrimer

[c]Theoretical molecular weight (kDa)

Aime et al. 1998; Strijkers et al. 2007). Longmire et al. (2014) have reported r_1 and r_2 relaxivity profiles of G6 PAMAM dendrimers as a function of magnetic field strength. The authors indeed observed the characteristic peak in the r_1 profile around 1 tesla, followed by a drastic reduction at higher magnetic fields. The maximal r_1 values at the optimal field strength as reported by Longmire et al. (2014) are similar to those found by Langereis and coworkers (Langereis et al. 2006). A very important study by Ogawa et al. (2010) reported that the architecture of paramagnetic Gd-loaded dendrimers has a major effect for their T_1-shortening efficacy. Similarly sized lysine-grafted dendrimers, in which the Gd chelates are partly buried in the dendrimer interior, had lower r_1 values than those observed in traditional poly(amidoamine) (PAMAM) dendrimers. The Gd chelates are localised on the dendrimer surface in the latter case, enabling the unhindered interaction between bulk water protons and the paramagnetic centres (Ogawa et al. 2010) that is a prerequisite for maximising the ionic r_1 (Strijkers et al. 2009). Such differences in molecular arrangement of the Gd chelates in the lysine-grafted versus more regular PAMAM dendrimers also explain the different responses of the ionic r_1 relaxivities to an increase in temperature. At higher temperatures, lysine-grafted paramagnetic dendrimers have higher r_1 values, which are attributed to the enhanced accessibility of water protons to the internal Gd chelates. Temperature elevations rather cause a drop in r_1 for PAMAM dendrimers with similar size due to a decrease in the rotational correlation time (Ogawa et al. 2010).

As indicated above, the macromolecular advantage of higher relaxivity r_1 is lessened at high field strengths, which are most often used for small animal MRI (i.e. at magnetic fields of 7 tesla and beyond); the difference between paramagnetic Gd-labelled low- and high-molecular-weight agents is smaller. The above pattern of the MR relaxation dispersion profile, as the r_1 field dependence phenomenon is also called, explains the recent interest in the use of relatively low-field MRI scanners for small animal contrast-enhanced MRI.

Figure 11.2 demonstrates that the dendrimer-induced signal enhancement on T_1-weighted MRI scans of mice differs strongly among different PPI dendrimer generations (Langereis et al. 2006). Low-molecular-weight compounds, such as the G1 material, initially enhance the blood pool followed by a rapid signal increase in the kidneys and sometime later the bladder. This is due to the fact that this agent is cleared via the renal clearance pathway leading to elimination from the organism via the urine. The higher-generation dendrimers have very different distribution profiles, in which the liver (as well as the spleen) shows strongly increased signal, while the kidney and bladder are enhanced considerably less and with a significant time delay as compared to the G1 agent. Similar pronounced effects of dendrimer size on dynamic whole-body MRI scans in small animals have been frequently reported (Longmire et al. 2011, 2014; Kobayashi

et al. 2003; Kobayashi and Brechbiel 2005; de Lussanet et al. 2005).

Much of the above results on the size dependence of dendrimer behaviour can be understood in terms of the size dependence of blood clearance via the kidneys. Choi and Frangioni (2010; Choi et al. 2007) have done a series of seminal studies with the use of quantum dots (QDs), brightly fluorescent nanomaterials that can be prepared in a wide range of sizes. They noted that QDs with hydrodynamic diameters <5.5 nm were rapidly and efficiently excreted from the body via the urine. Larger-sized particles persist for much longer and are mainly eliminated by the reticuloendothelial system (RES) predominantly involving the liver and spleen, as is known to generally hold for nanomaterials that escape renal clearance (Choi and Frangioni 2010). It goes without saying that clinical translation of RES eliminated agents can only occur in case that their constituents are completely nontoxic and are eliminated from the body in a reasonably short period of time.

In analogy to the QD studies, several groups have extensively evaluated the biodistribution of dendrimers by quantitatively measuring dendrimer content in various tissues and organs at several time points after intravenous injection. Thus, Gillies et al. (2005) have measured the biodistribution of dendrimers, with molecular weights ranging from circa 20,000 to 160,000, in mice. The authors used poly(ethylene oxide) (PEO)-coated ^{125}I-radiolabelled dendrimers and reported that these had circulation half-lives between 8 and 50 h for the lowest- and highest-molecular-weight materials, respectively. However, clearance from other organs, such as the liver, can take substantially longer. The next section will provide more details on the consequences of specific changes in the surface properties of dendrimers on their biodistribution behaviour.

Maeda and collaborators (2010, 2013) have made vital contributions to the understanding of the effects of molecular size as well as composition on the in vivo biodistribution and in particular the tumour homing of macromolecular agents for imaging and therapy. Tumour penetration of different materials is to a large extent governed by what Maeda called the enhanced permeability and retention (EPR) effect. The EPR phenomenon describes the extravasation of materials from the blood compartment into the extravascular, interstitial space of the tumour and the prolonged retention of macromolecular materials in the tumour interstitial space as compared to the situation in normal tissues. The EPR phenomenon, which among others is caused by the incomplete endothelial lining of tumour blood vessels, is widely exploited for tumour diagnosis as well as for the delivery of therapeutic agents.

The pronounced difference in MRI enhancement pattern among different generation dendrimers, as depicted in Fig. 11.2, is widely exploited for the characterisation of diseased tissues and in particular for tumour diagnostics. De Lussanet et al. used differently sized PPI dendrimers for tumour characterisation (de Lussanet et al. 2005) and employed tracer kinetic modelling of dynamic MRI enhancement data. Low-molecular-weight dendrimers were found to primarily report on microcirculatory blood flow characteristics, whereas the use of high-molecular-weight agents provided handles for quantifying vascular permeability and vascular volume.

Recently, Jacobs et al. (2015) reported a conceptually novel design of dendrimer-enhanced MRI scanning for improved tumour characterisation. Instead of assessing MRI signal dynamics upon injection of different dendrimer generations in different animals, Jacobs and collaborators performed sequential injections of three differently sized contrast agents and monitored MRI responses to each of these within single animals. Subsequently, the MRI data were subjected to tracer kinetic modelling by jointly analysing the signal dynamics for all three consecutive injections in one go. All three dynamic response curves were sampled over a time span of less than 45 min. Therefore, it could be assumed that tumour physiology, including tumour microcapillary perfusion, was identical throughout the duration of the session. This allowed for significant reductions in the uncertainty of modelling estimates of vascular permeability and blood

volume fraction as compared to the traditional approach. Figure 11.3 shows typical examples of dynamic contrast-enhanced MRI (DCE-MRI) curves from a single pixel in the MR images upon injection of Gd-containing G5 and G2 dendrimers as well as Gd-DOTA, the control low-molecular-weight clinical Gd chelate. For details, see the legend in Fig. 11.3. The above multi-agent approach can potentially be used for the detailed evaluation of anti-vascular tumour therapies. For these studies of Jacobs et al., PPI-based G2 and G5 materials were prepared with hexa-ethylene glycol-spaced Gd-DO3A end groups, as opposed to using materials with the Gd chelate directly attached to the dendrimer's exterior groups.

One of the merging clinical applications of dendrimer-enhanced MRI is in lymphatic imaging, which was also shown to benefit from a judicious choice of dendrimer size. Despite the vital role of the lymphatic system in health and disease, there is a lack of effective tools for high-spatial resolution lymphatic imaging. An example of the utility of paramagnetic dendrimers for this sort of application can be found in Longmire et al. (2014). In this case, the contrast material was injected interstitially, and serial MRI scans were made over time to monitor the agent's accumulation in the lymphatics. Kaminskas and Porter (2011) have presented evidence that lymphatic imaging is in general improved with dendrimer generation and that the dendrimer's molecular composition strongly affects the rate of drainage and retention profiles. Opina et al. (2014) have employed a Gd-loaded G5 PAMAM dendrimer preparation and have shown that this material is very effective for use in lymphatic imaging. However, the authors noted that the material is only very slowly cleared from the body and that this may obstruct its eventual clinical translation for lymphatic visualisation.

11.5 The Effects of Surface Characteristics

The effects of modifications of the surface properties of dendrimers on their in vivo characteristics and utility as contrast agents have been extensively studied. The consequences of surface modifications can to a large extent be ascribed to alterations in the interactions between dendrimers and blood constituents. It is important to stress that many of the findings reported below do not exclusively apply to dendrimers but are equally valid for a wide range of other nanoparticles, including liposomes, micelles and microemulsions that are also extensively studied for their diagnostic and therapeutic usefulness (Mulder et al. 2006, 2009; Hak et al. 2009; Langereis et al. 2013, 2014).

The best-studied surface modification of dendrimers is PEGylation, i.e. the covalent chemical coupling of poly(ethylene glycol) (PEG) chains to the distal ends of dendrimer side groups. PEG modification could enhance the utility of dendrimers for two reasons. First, it is known to reduce dendrimer toxicity, in particular dampening the haemolytic properties of certain dendrimer materials, particularly those that have primary amine end groups (Malik et al. 2000; Tack et al. 2006; Gajbhiye et al. 2007). Secondly, it causes the dendrimers to escape from RES recognition resulting in reduced plasma clearance and prolonged circulation half-life (Kobayashi et al. 2001a, b). Elimination of nanoparticles like dendrimers from the circulation by the RES is initiated by serum opsonins that attach to the surface of the agents. This is followed by phagocytosis by macrophages and sequestration of the foreign materials in the liver and spleen. PEGylation in a way camouflages the nanoparticles, thereby preventing adhesion of opsonins so that the nanomaterials remain in circulation and temporarily evade the RES. This is usually referred to as the stealth effect of PEGylation. PEG chains achieve the reduced opsonisation by a combination of steric and hydration effects. The lengths of PEG chains can essentially be varied at will, and the effects that such variations have on dendrimer properties have been widely studied (Kojima et al. 2011).

Figure 11.4a serves to illustrate the prominent effects of PEG conjugation on the blood clearance kinetics of a G4 PAMAM dendrimer material (Kobayashi et al. 2001b). Coupling of one or two 20,000 Da PEG chains causes a strong prolongation of the blood residence times.

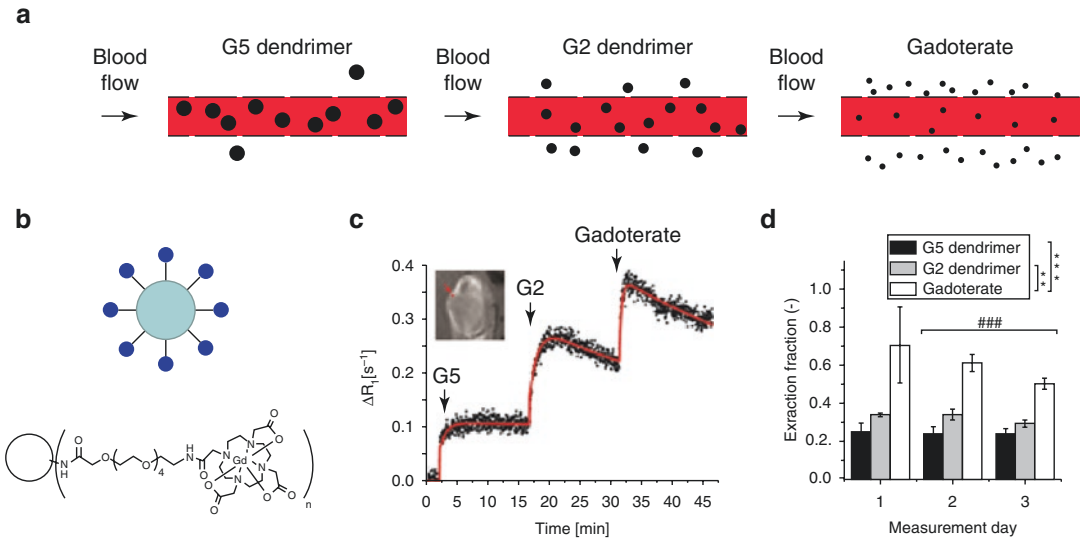

Fig. 11.3 Dynamic contrast-enhanced MRI of mouse tumours with the use of differently sized Gd-based contrast agents. (a) Schematic representation of the effect of contrast agent size on its leakage from the vascular compartment into the extravascular, extracellular space. In this study, G5 dendrimers, G2 dendrimers and the low-molecular-weight clinically approved gadoterate were compared in terms of contrast enhancement patterns. (b) Dendrimer schematic illustrating the conjugation of multiple Gd-DO3A moieties. (c) Typical changes in longitudinal relaxation rate, R_1 (i.e. $1/T_1$), over time following the sequential injection of the three contrast materials. Data points were taken from a single pixel in the tumour periphery, as depicted on the T_2-weighted image (see inset). Note that the different materials, as expected, cause distinctly different enhancement profiles. The G5 dendrimer is only very slowly cleared from the circulation, explaining the absence of significant reduction in R_1 change following the abrupt increase upon injection. (d) Extraction fractions for the different materials as deduced from mathematical modelling of the dynamic MRI data. Three consecutive measurements ($n=5$) were done at 2-day intervals. The data show the reproducibility of the measurements and modelling findings for each of the materials by itself and that the extraction fractions are significantly lower for each of the dendrimers compared to gadoterate. Extraction fractions tended to be lower for the G5 than the G2 dendrimer; however, this did not reach significance. Statistical tests: $^{###}P<0.001$ between measurement day 2 and measurement day 3. $^{**}P<0.01$, $^{***}P<0.001$ between the different contrast agents. For further details, see text. MRI measurements were made at a field strength of 7 tesla (Reproduced with permission from Jacobs et al. 2015)

Likewise, the PEGylation has a remarkable effect on the biodistribution of the material over the main organs (Fig. 11.4b). Whole-body T_1-weighted MRI scans of mice injected with non-PEGylated or two-chain PEGylated dendrimers (Fig. 11.4c, d, respectively) are in line with the biodistribution data: PEGylation causes the blood signal to be brighter for a longer time while showing a similar enhancement of the kidneys and a slightly increased disposition in other organs such as the liver and spleen.

Kojima et al. (2011) have systematically investigated the effects of PEGylation of dendrimers on their MRI relaxivity properties. Generation 4 and 5 PAMAM dendrimers bearing Gd chelates were conjugated with two different PEG chains (i.e. 2 or 5 kDa). Conjugation of the 2 kDa PEG chains barely affected the r_1 relaxivity, while 5 kDa PEG chains caused a reduction in r_1 (and also r_2). The highest r_1 was measured for shorter PEG, higher-generation conjugates. These effects can most likely be explained by a combination of two counteracting factors. PEGylation may interfere with the access of water protons to the paramagnetic Gd^{3+} ions, reducing relaxivity. For the larger dendrimers, this is partly compensated for by the reduced molecular mobility that leads to higher r_1. As indicated earlier, the positive effect on r_1 of reduced mobility holds at clinical field strength up to circa 1.5 tesla and gradually vanishes towards the higher field strengths typical for most small animal MRI instruments.

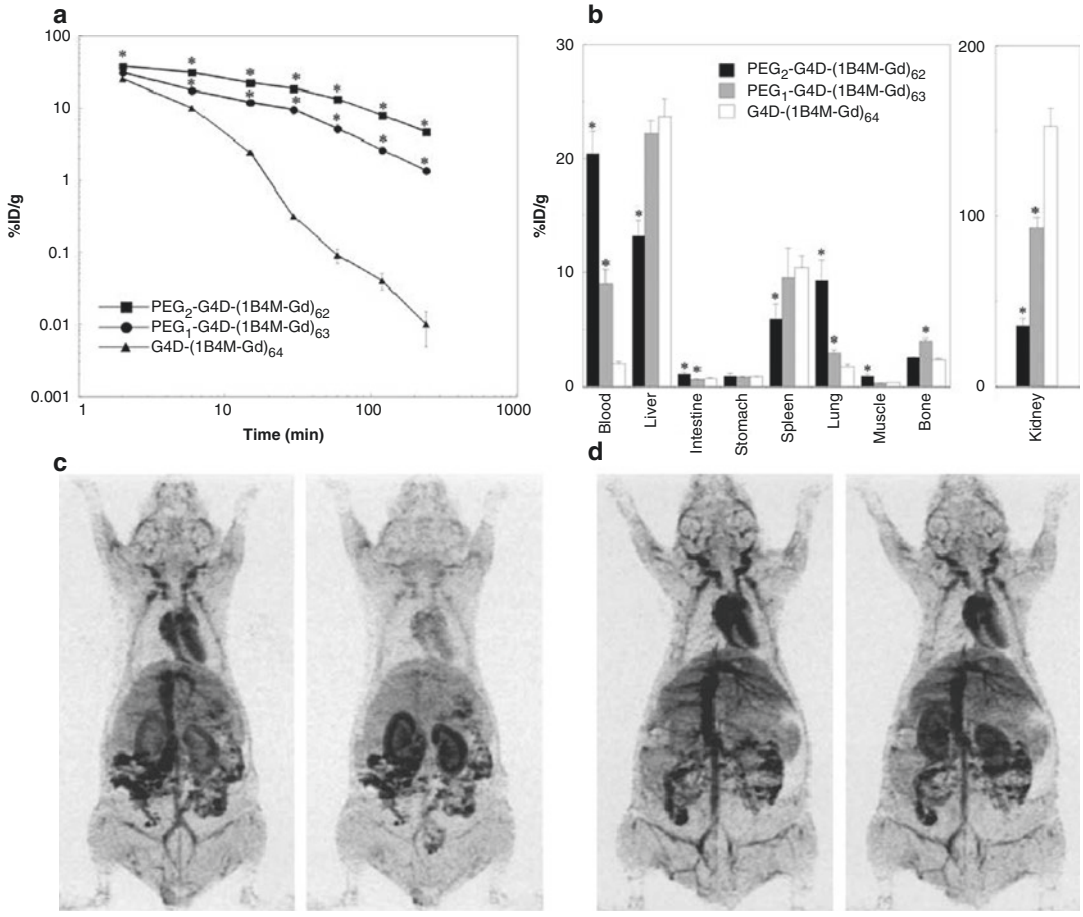

Fig. 11.4 The effect of PEGylation on dendrimer biodistribution properties. (a) Blood clearance of ^{153}Gd-labelled G4 PAMAM dendrimers, either conjugated with no, one or two 20 kDa PEG chains, in normal nude mice. The data are expressed as the mean percentages of the injected dose per gram of blood ± SD ($n = 4$ per time point). PEGylation leads to prolonged blood circulation due to the fact that the material becomes more hydrophilic. (b) The distribution of the same three materials was determined at 15 min after injection. The data are expressed as the mean percentages of the injected dose per gram of material ± SD ($n = 5$ per time point). The dendrimer with two PEG chains remained in the blood significantly longer and accumulated significantly less in the liver and kidney than the other two materials. Overall, the positive effects of PEG conjugation on the dendrimer contrast materials were found to have prolonged retention in the circulation, increased excretion and decreased organ accumulation. (c, d) Typical examples of whole-body 3D MRI of mice injected with 0.033 mmol Gd/kg of dendrimer without (c) and dendrimer with two PEG chains (d). The images, which are negative displays with higher intensity darker than lower intensity, were obtained at 2 min (*left*) and 10 min (*right*) post-injection and are shown as maximum intensity projections. Darker blood and brighter kidneys were noted on both early and delayed images with the PEGylated versus the non-PEGylated material (Reproduced with permission from Kobayashi et al. 2001b)

It is important to note that not only the surface properties of dendrimers dictate their in vivo fate in terms of clearance pathways and biodistribution and thereby their utility for contrast-enhanced MRI. The chemical nature of the dendritic core also has major consequences. As an example, Kobayashi et al. (2001a) showed that G4 PPI dendrimers rapidly accumulate in the liver, whereas G4 PAMAM dendrimers act as vascular contrast material since they have much longer blood retention. It should be noted that the G4 PAMAM material is higher in molecular weight (and thus in size) than the G4 PPI material. The distal end groups of the two classes of

dendritic materials were conjugated with chelating moieties to allow complexation of Gd^{3+} ions for MRI detection. The authors argued that the very different behaviour of the different dendrimer contrast materials is due to the overall more hydrophobic nature of the liver-seeking dendrimers.

It is worth noting that PEGylation of dendrimers causes increased solubilisation of a broad range of therapeutic agents in their core and also the PEG layers themselves afford drug-loading capacity (Gajbhiye et al. 2007). PEGylated dendrimers form stable complexes with plasmid DNA and achieve improved gene transfection compared to non-PEGylated dendrimers.

Zhang et al. (2014) have extensively studied the effects of conjugation of various functional groups to the surface of G5 PAMAM dendrimers, including the attachment of acetyl and succinamic acid groups, on the encapsulation and release of the anticancer drug doxorubicin. The nature of the functional group was shown to strongly affect these properties and thus represents an important handle for optimising the properties of dendrimers as drug delivery system.

11.6 The Effects of Shape and Flexibility

The shape of molecules in general is an important determinant of their functionality per se as well as their in vivo behaviour, and this similarly applies to dendrimers (Longmire et al. 2011). Indeed conjugation of two long, linear PEG chains to G4 PAMAM dendrimers led to the formation of an asymmetric elongated nanoparticle that underwent relatively rapid renal clearance. By contrast, when the same generation dendrimer was fully decorated with short PEG tails, no renal clearance was observed despite the similar physical size. Large-scale systematic studies into the shape phenomenon unfortunately are lacking as yet.

Gillies et al. (2005) have provided evidence that dendrimers with higher internal flexibility are excreted faster into the urine, as compared to materials with decreased flexibility and otherwise comparable properties. The authors prepared different generation PEO-conjugated dendrimers with the number of PEO arms ranging from two to eight. Comparison of the renal clearances for the four-arm versus eight-arm polymers indicated that the more branched polymers were excreted more slowly into the urine, a result attributed to their decreased flexibility.

As noted in Sect. 11.4, the translational and rotational mobility of a dendrimer-based MRI contrast agent as a whole affects its relaxivity properties, especially at lower magnetic field strength. However, also the local internal dynamics of a contrast agent can have profound effects on its relaxivities r_1 and r_2. One manifestation of this phenomenon is the aforementioned influence of temperature changes on r_1. This partly has to do with the temperature dependence of water proton accessibility to the paramagnetic centres and partly with temperature-induced changes in local segmental rotational correlation times. Systematic studies that are backed up by measurements of the internal molecular dynamics of dendrimer contrast agents by independent techniques are currently scarce. Consequently, in-depth exploitation of these phenomena, let alone using them for directed molecular design, is lacking as well.

11.7 The Effects of Charge

The charge of dendrimers and of nanoparticles in general can significantly alter their in vivo characteristics. In the setting of drug delivery, for example, cationic nanoparticles typically deliver their therapeutic cargo more efficiently. This is partly related to the improved ability of cationic drug delivery systems for cellular internalisation and subcellular routing as compared to anionic and neutral delivery systems (e.g. see Asati et al. (2010)).

However, cationic dendrimers are known to be more cytotoxic (among others causing haemolysis and changes in red blood cell morphology) than anionic species, which generally are well tolerated in particular when equipped with PEG or other polymeric moieties (Malik et al. 2000). These effects are also dependent on dendrimer generation. For these reasons, anionic dendrimers

are usually preferred for diagnostic imaging applications.

Jaszberenyi et al. (2007) have studied a number of different PAMAM and hyper-branched dendrimers that had either been conjugated with negatively charged Gd-DOTA or neutral Gd-DO3A chelates for MRI detection. Surprisingly, at field strengths below 1.5 tesla, the Gd-DOTA-conjugated material had twice as high r_1 as the Gd-DO3A-conjugated counterpart. The authors attributed this remarkable difference to differences in the internal dynamics of the two materials. The Gd-DOTA agent has a higher rigidity, possibly due to electrostatic repulsive forces between the negatively charged end groups, which also increase the effective hydrodynamic size of the macromolecule. Interestingly, these authors found that the attachment of PEG chains has little effect on the r_1.

The above observations demonstrate that subtle alterations in the molecular composition and architecture may have major consequences for the efficacy of dendrimers as MRI contrast agents, which usually are hard to predict. It should be noted, however, that some of these relaxivity modulations might be pronounced at relatively low magnetic fields but without practical consequences at the higher fields that are typically used in preclinical MRI.

11.8 Passive Versus Active Targeting

An impressive body of research is devoted to improving the specificity of diagnostic imaging read-outs by using ligand-conjugated contrast materials. In the setting of cancer diagnostics, the idea is to equip the contrast agent with a ligand (e.g. a peptide, synthetic ligand or monoclonal antibody) that allows enhanced sequestration of the contrast agent at those sites where the target of the ligand is abundantly present. In the case of cancer imaging, the target could, for example, be a cell surface receptor (either overexpressed on tumour cells or on endothelial cells lining tumour blood vessels) and an extracellular matrix component (such as fibrin), or one could report on the presence of a disease-specific enzyme (such as a member of the matrix metalloproteinase isoenzyme family). Obviously, ligand attachment can be expected to alter the shape, the size and the global and local motional dynamics of contrast materials.

The added value of ligand conjugation of dendrimers for diagnostic imaging has mainly been explored with the use of receptor-targeted compounds. Examples include the HER2, transferrin and folate receptors (for review, see Agarwal et al. (2008)). In most cases, these materials were also equipped with fluorescent moieties for optical detection. Increasingly, however, the utility of target-specific MRI with paramagnetic ligand-conjugated dendrimers is being explored (for overview, see Kobayashi et al. 2011; Godin et al. 2011; Cheng et al. 2011). Also combinations of dendrimers with superparamagnetic iron oxide nanoparticles for targeted tumour MRI are studied (e.g. see Yang et al. 2015). For the sake of clarity, the present description will be restricted to the use of targeted paramagnetic Gd-based systems.

Han et al. (2011) have conjugated a seven-amino acid peptide ligand for recognition of the human transferrin receptor to PEGylated G5 PAMAM dendrimers that were also equipped with Gd-DTPA for in vivo tumour imaging with MRI. The peptide had been identified with the use of the phage display technique. In a very complete study, the authors extensively characterised the dendrimer contrast material in vitro and used it for in vivo MRI detection of tumours growing subcutaneously in mice. Both targeted and nontargeted versions of the paramagnetic G5 dendrimers had relatively high r_1 relaxivities at 4.7 tesla (i.e. 10.7 $mM^{-1}s^{-1}$ versus 4.8 $mM^{-1}s^{-1}$ for the single Gd-DTPA molecule), the field strength at which the authors did all MRI scanning in their study. This r_1 relaxivity per Gd^{3+} ion corresponded to a value of 984.4 $mM^{-1}s^{-1}$ for the entire G5 dendrimer molecule as a whole. The paramagnetic dendrimers showed negligible haemolytic toxicity up to high concentrations. Tumour cells readily internalised the transferrin-targeted dendrimers, as

deduced from fluorescence microscopy analysis of isolated cells. Very little uptake occurred for the nontargeted material. Whole-animal fluorescence imaging studies in tumour-bearing mice showed that both targeted and nontargeted dendrimers mainly distributed towards the liver, kidney and spleen, in agreement with biodistribution studies alluded to above. Tumour enhancement was most prominent for the targeted material. Interestingly, the level of tumour homing was very low in the case of C6 glioma growing in the mouse brain, both for targeted and nontargeted agents. The promising results of the qualitative fluorescence studies led the authors to embark on in vivo MRI studies of both tumour models and both types of agents. Examples of MRI scans of subcutaneous xenografts in the mouse hindleg are depicted in Fig. 11.5. The authors employed T_1-weighted MRI for detecting the presence of paramagnetic material. The latter leads to a local T_1 shortening, which causes a signal intensity increase on the MR images. This so-called positive contrast change was strongest with the targeted dendrimer and amounted to 187 % compared to pre-contrast signal values at 24 h after contrast injection (Fig. 11.5b). Maximal signal changes for Gd-DTPA and nontargeted dendrimers (Fig. 11.5a, b) were much smaller and occurred earlier (i.e. 121 and 130 % at 30 min after injection) and totally disappeared within hours. The entire time course of MRI signal changes with all three agents is depicted in Fig. 11.5b. Similar to the above fluorescence findings, negligible MRI signal changes on T_1-weighted scans were noted in case of the C6 glioma with any of the dendrimer types (Han et al. 2011). The reason for the low level of contrast enhancement in case of the brain tumour is unclear but is possibly related to the presence of the blood–brain barrier (BBB) limiting extravasation of the nanoparticulate dendrimers. Brain tumour detection with contrast-enhanced imaging may thus require more elaborate materials that are capable of crossing the (intact) blood–brain barrier.

Chen et al. (2012) have conjugated cyclic RGD tripeptide and Gd-DTPA to generation 3 dendrimers for DCE-MRI of tumour angiogenesis and for monitoring the early responses to anti-angiogenic therapy with bevacizumab. The DCE-MRI data measured at 30 min post-contrast injection provided evidence for specific targeting and allowed detection of the response to therapy in terms of reduced MRI contrast enhancement.

Target-specific MRI is very challenging because of the low intrinsic sensitivity of the technique and the fact that many interesting tissue biomarkers occur in relatively low levels. Detection of molecular disease markers with MRI will therefore never become routine, especially when it comes to detecting sparse markers. Nuclear imaging techniques have a better chance of clinical translation in this setting, since these only need tracer levels of probes. As an example, Sato et al. (2001) have used dendrimers that were loaded with anti-sense oligo-DNA and that were labelled with ^{111}In as a nuclear imaging tracer, for tumour imaging with scintigraphy and for monitoring of gene delivery. Ligand-conjugated dendrimers are also being explored for enhancing the specificity of the delivery of therapeutic cargo to disease sites, in particular tumours (Kesharwani and Iyer 2015; Prabhu et al. 2015).

11.9 Biocompatibility and Safety

The in vitro and in vivo toxicity of dendrimers has been extensively studied (for comprehensive reviews, see Cheng et al. (2011); Jain et al. (2010)). The main issue here is the presence of many primary amine end groups in the most widely employed PAMAM and PPI type of dendrimer materials (see Fig. 11.1), leading to a high density of cationic surface charges for these molecules. This design feature constrains direct in vivo use, since it causes these dendrimers to be toxic. This toxicity is primarily attributed to interactions between the positive charges at the dendrimer's exterior and negatively charged biological membranes in vivo (Jain et al. 2010). Such interactions may lead to membrane disruption, via pore formation, and explains the toxic effects that dendrimers exert on cells in the blood as well as the general cytotoxicity. In order to eliminate or at least minimise this toxicity, two

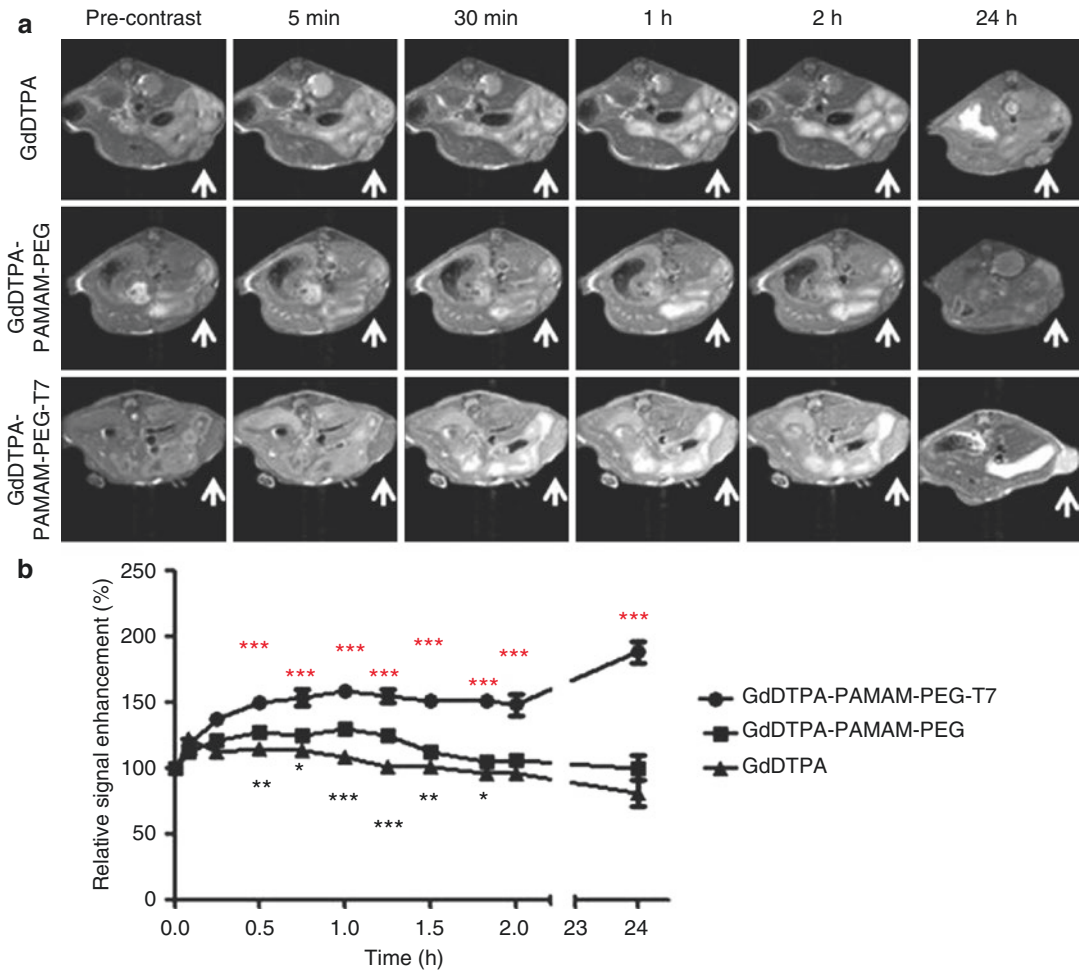

Fig. 11.5 Tumour-associated transferrin-specific MRI with ligand-conjugated paramagnetic dendrimers. MR was done on mice with subcutaneous Bel-7402 xenografts. (**a**) T_1-weighted MR images of nude mice were measured at various time points after the intravenous injection of Gd-DTPA (top row), Gd-DTPA-PAMAM-PEG (second row; representing nontargeted contrast material) and Gd-DTPA-PAMAM-PEG-T7 (bottom row; this is the transferrin-targeted dendrimer preparation). Scans were made using a 4.7 T small animal MR instrument. Images were acquired pre-injection, 5 and 30 min, as well as 1, 2 and 24 h post-injection. The white arrow indicates the location of the xenograft. (**b**) Quantitative analysis of MR images. The average MR signal intensity was measured for each tumour, and the relative signal intensity was then calculated as the ratio of the signal intensity at the different time points in the post-contrast images compared to the pre-contrast image, indicated in percentage. Statistical tests: $*P<0.05$, $**P<0.01$ and $***P<0.001$. The *red asterisks* indicate Gd-DTPA-PAMAM-PEG-T7 versus the other groups. *Black asterisks* represent Gd-DTPA versus Gd-DTPA-PAMAM-PEG (Reproduced with permission from Han et al. 2011)

main strategies are being employed. The first approach is to synthesise dendrimers that are fully biocompatible, consisting of a biodegradable core and with branching units that consist of molecular units that are also biocompatible (e.g. intermediates of metabolic pathways). The second, most widely used approach is to mask the positive charges on the dendrimers' exterior by surface engineering, e.g. by amidation of the amine end groups. A prime example of this masking approach is PEGylation (see Sect. 11.5), which aids to conceal the positive charges on cationic dendrimers, thereby reducing their interactions with negatively charged membranes. This

surface engineering much improves the biological inertness and thereby the biocompatibility of the material.

Biodegradability of contrast agents is yet a completely different issue, as it would necessitate the use of materials that can be taken apart by enzymatic reactions or under the influence of harsh conditions (such as low pH) in some tissue compartments. An appreciable level of biodegradability seems advantageous at first sight, as it may help to more rapidly eliminate materials that might otherwise reside in the organism for a prolonged period of time. However, materials that are highly biodegradable may fall apart in many small pieces, each of which could have very different biodistribution, as well as safety and biocompatibility profiles. For these reasons, it is attractive that the elimination of foreign materials from the body, including contrast materials for diagnostic imaging, occurs relatively rapid and in intact form. This notion explains that relatively fast renal clearance, leaving little time for material processing, is the preferred elimination route. It is evident that this criterion may not always be fulfilled as it sets very restrictive boundary conditions, in terms of size, surface architecture and other molecular characteristics of dendrimer-based contrast materials that may be at variance with their intended use.

11.10 Probes for Multimodality Imaging

Routinely, dendrimer contrast agents for MRI are labelled with Gd chelates, as detailed above. However, a very interesting alternative is to equip the dendritic structures with fluorine atoms instead, to allow for ^{19}F-MRI (Yu 2013). ^{19}F is the second most sensitive nonradioactive nucleus for MRI, the ^{1}H nucleus being first. In addition, because there is no endogenous source of signal, ^{19}F-MRI can be used as a hotspot imaging modality (Chen et al. 2010), which greatly simplifies image interpretation. Higher-generation dendrimers can readily be equipped with many chemically equivalent ^{19}F-atoms to enhance the detection sensitivity, which continues to be a major challenge for MRI. One of the prime virtues of ^{19}F-MRI is that it directly detects the fluorinated contrast materials. In case of using Gd-based contrast agents for ^{1}H-MRI, the contrast materials are indirectly detected via their effect on the magnetic properties of nearby water protons. This may have major consequences for image interpretation and complicate the quantitative analysis of contrast changes in ^{1}H-MRI images in terms of contrast agent concentrations, as we have previously shown upon cell internalisation of Gd-containing paramagnetic liposomes (Kok et al. 2009). ^{19}F-MRI does not suffer from this effect, again because of its direct probe detection properties (Kok et al. 2011).

Criscione et al. have explored the utility of fluorinated PAMAM dendrimers, which exhibit spontaneous self-assembly into nanoscopic and microscopic particulates (Criscione et al. 2009). The nanostructures disassemble at low pH, creating options for controlled release of encapsulated agents. Huang et al. have similarly prepared fluorinated dendrimers for use with ^{19}F-MRI, except that they co-conjugated Gd-DOTA chelates (Huang et al. 2010). This approach will improve the time efficiency of ^{19}F-MRI, as images can be obtained at shorter repetition times due to the intramolecular T_1-shortening effect of Gd on nearby ^{19}F-nuclei. Jiang et al. (2009) have proposed a dendrimer-like low-molecular-weight fluorinated contrast agent for ^{19}F-MRI, which is also rapidly excreted. The molecule produces a relatively strong signal from 27 magnetically equivalent fluorine atoms and was shown to allow for whole-body ^{19}F-MRI of time-dependent changes in its biodistribution. Finally, G1, G3 and G5 dendrimers with hydrophobic CF_3-labels buried at the interface between the PPI dendritic core and the PEG corona have been introduced recently (de Kort et al. 2014). These materials are water soluble (and non-aggregating) such that they could be employed for probing hydrogels with the use of NMR diffusometry. The suitability of these novel nanoprobe systems for ^{19}F-MRI remains to be established.

Many different dendrimer-based probes for imaging with non-MRI methods have been prepared over the years. Kobayashi and coworkers have explored the utility of radioactive labelling

of dendrimers for nuclear imaging (Kobayashi et al. 1999, 2000). The main virtue of nuclear imaging techniques is that they afford very high detection sensitivities, enabling the use of tracer quantities of contrast materials. PAMAM dendrimers incorporated with nuclear labels, such as ^{111}In, allowed for quantitative whole-body scintigraphy studies of their biodistribution, including their tumour-homing capabilities (Kobayashi et al. 1999, 2000). Liu and others (2013) have employed dendrimer-stabilised gold nanoparticles for targeted tumour imaging with CT imaging. Tumour homing was enhanced by conjugation of ligands for binding to the folate receptor, which is overexpressed on a variety of tumour types. In line with findings for other nanomaterials, the liver and spleen took up the majority of the gold nanoparticles. Importantly, the delivery of folate receptor-targeted CT contrast material at the tumour site was two times higher than that of nontargeted nanoparticles. Equipping dendrimers with labels for detection by optical techniques provides many opportunities for in vivo and ex vivo microscopy analysis of their biodistribution and tumour delivery properties in diagnostic and/or therapeutic studies. As an example, Kobayashi et al. (2007) have conjugated G6 PAMAM dendrimers with five different optical labels and used these sophisticated materials for multicolour lymph node imaging in tumour-bearing mice. Specific detection of individual dendrimers is possible by spectrally selective excitation of the different optical probes (see also Kaminskas and Porter 2011).

Multimodality imaging is an approach whereby two or more imaging modalities are used in a complimentary fashion to compensate for the limitations of each imaging method while exploiting their individual strengths. A well-established example of multimodal imaging of this sort is the combination of PET and CT imaging, where PET delivers contrast-enhanced functional and molecular imaging data and CT provides the anatomical information that is essential for the interpretation of the PET scans. A potentially valuable approach towards contrast-enhanced diagnostic imaging is enabled by the use of contrast materials that can be detected by two or more different imaging modalities (James and Gambhir 2012). Dendrimers are ideally suited for this type of multimodality imaging, since the large number of end groups at the periphery of higher-generation dendrimers allows for controlled sequential conjugation of several different imaging labels. As an example, G6 dendrimer for dual-modality MRI–fluorescence imaging was conjugated with Gd-DTPA and the Cy5.5 fluorophore (Kobayashi et al. 2011; Talanov et al. 2006) and was shown to afford effective sentinel lymph node imaging in mice (Fig. 11.6). The most relevant attribute of such dual-labelled dendrimers for MRI and optical detection is that they are ideally suited for cross modality validation. In this case, MRI is employed for in vivo analysis of the spatial distribution of contrast enhancement patterns (e.g. in three dimensions in a tumour mass). The spatial resolution of MRI, however, is too low to precisely pinpoint the location of the contrast material at the (sub)cellular level. Following sacrifice and tumour slicing, fluorescence microscopy detection of the optical label in the dual-labelled dendrimer can be employed to determine its spatial distribution at the (sub)cellular level as well as its co-localisation with vital cellular markers (e.g. an endothelial cell surface marker in case of vascular targeted contrast material).

In recent years the added value of dual-modality MRI–CT imaging for tumour diagnostics has been actively explored with the use of dendrimer-assisted formation of nanoparticles for dual-mode MRI–CT scanning. The MRI–CT combination is of interest since it joins the high soft tissue contrast and flexible image orientation abilities of MRI with the high spatial and density resolution and relatively low cost of CT. Shi and coworkers have demonstrated that this dendrimer-enhanced MRI–CT approach provides effective tools for tumour detection in animal models (Wang et al. 2012; Chen et al. 2013, 2015; Li et al. 2013, 2014; Wen et al. 2013; Cai et al. 2015).

A particularly powerful multimodal combination is afforded by hybrid PET–MRI (Wehrl et al. 2015). This combination differs fundamentally from the ones mentioned above, in the sense that

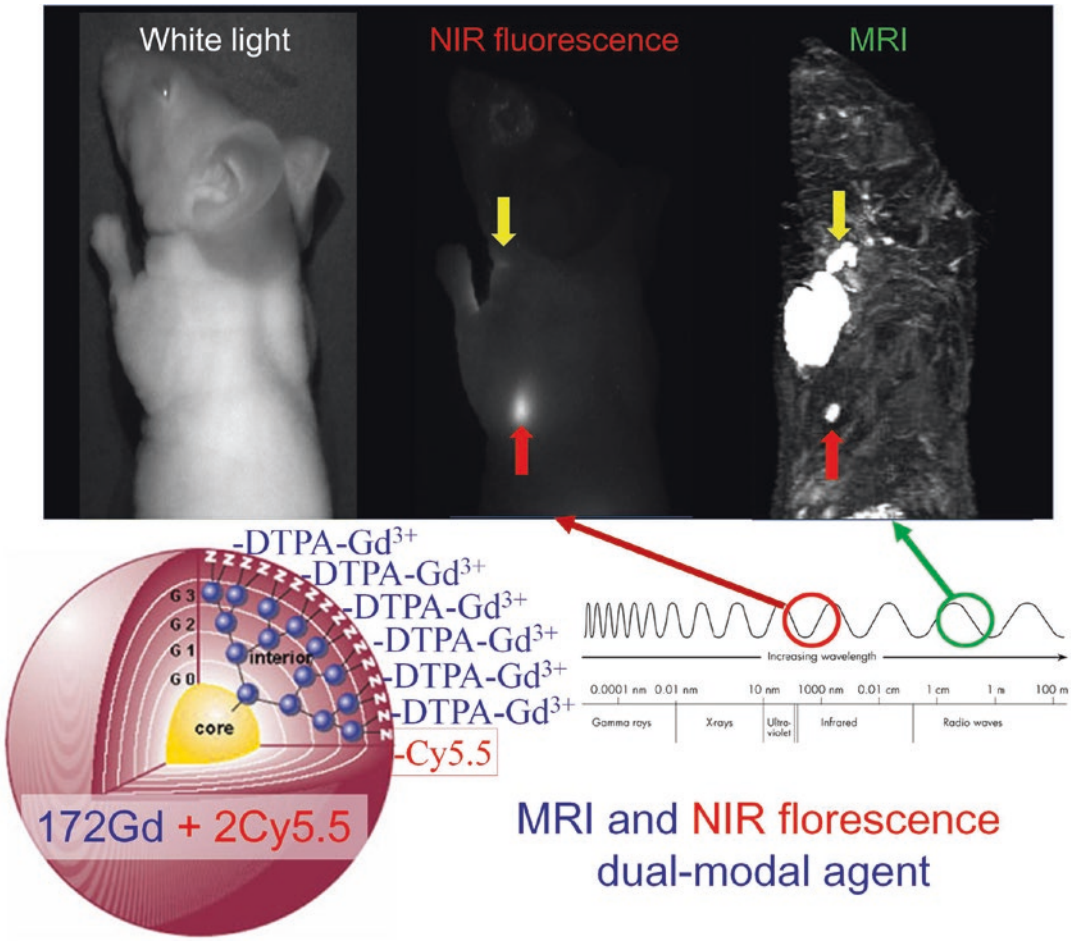

Fig. 11.6 Dual-modality MRI and near-infrared (NIR) optical sentinel lymph node imaging of breast cancer in a mouse. As indicated schematically, G6 PAMAM dendrimer-based dual-labelled contrast material of approximately 10 nm in diameter, containing on average 172 Gd^{3+} ions and 2 Cy5.5 fluorophores, was employed. Both MRI and NIR optical images define neck (*yellow arrow*) and axillary lymph nodes (*red arrow*) as sentinel lymph node in this mouse model of breast cancer (Reproduced with permission from Kobayashi et al. 2011)

in this case image acquisition of the two modalities is done at the same time. To that end, the two scan devices are fully integrated, making use of MRI-compatible PET detectors. Hybrid PET–MRI instruments are available both for small animal and human scanning. It should be noted, however, that there are no pressing reasons why PET and MRI scans should always be done simultaneously to nevertheless benefit from their combination. Back-to-back MRI and PET scans, followed by multimodal image registration, can likewise be of great value. The combination of PET with MRI is almost ideally synergistic. PET has a very high detection sensitivity and specificity, and new PET tracers can relatively easily be translated to the clinic, since one needs only tracer amounts of material. MRI does not make use of ionising radiation (while CT that is now mostly used in combination with PET does) and produces images with a remarkable range of different soft tissue contrast options. With respect to contrast agents for hybrid PET–MRI, two options come to mind. As a first step, one could inject a cocktail of a PET and an MRI contrast agent. Single agents for hybrid PET–MRI scanning are presently mainly based on (super)paramagnetic

nanoparticles for MRI detection that are radiolabelled with ^{64}Cu or ^{18}F for PET detection (de Rosales 2014). When using these dual-modality contrast agents, one could imagine that PET provides whole-body analysis of contrast agent distribution and local concentration measurements, guiding the MRI scanning towards locations at which a high-resolution local analysis is carried out (exploiting all capabilities of MRI, including contrast agent detection). The added value of hybrid PET–MRI per se is being actively explored and will be defined in the years to come. The development of hybrid PET–MRI contrast materials is also still in its infancy. To the best of our knowledge, hybrid PET–MRI with dendrimer contrast materials has not been reported until now. In view of the orders of magnitude differences in sensitivity between PET and MRI, combined with the present limited medical need for assessing diagnostic agents with multiple imaging methods in vivo, the added value of hybrid PET–MRI probes is questionable. The same applies to the CT–MRI combination. Hybrid MRI–optical imaging agents have proven utility for in vivo–ex vivo validation purposes, as explained above.

11.11 Smart Imaging Probes

An interesting domain of contrast agent development concerns the design of so-called smart imaging probes. Although loosely defined, the annotation smart refers to the fact that these agents are designed to report on changes or spatial differences in physiological environment. Examples include the use of contrast materials that respond differently depending on the local pH; see, for example, the PPI dendrimer-based CEST agents that are able to probe the pH of the solution (Pikkemaat et al. 2007). A special class of smart agents is represented by activatable probes that allow one to control the magnitude of the imaging signal and minimise the background signal in relation to the presence of the biological activator that represents a special class of smart agents. Here, the activator can, for example, be a specific enzyme, in the presence of which imaging signal is generated and in the absence of which no signal occurs. This approach leads to higher target-to-background ratios than would be measured in case of conventional imaging agents that are “always on”. Smart agents are widely explored for optical detection and are particularly based on fluorescence quenching–dequenching schemes (Kobayashi et al. 2010b). To the best of our knowledge, no smart probes that are based on dendrimers have been described as yet. The flexible nature of dendrimer design, which offers many options for anchoring a broad range of compounds to the surface, provides many opportunities for exploring the added value of dendrimer-based responsive materials for diagnostic imaging. In view of the low intrinsic sensitivity of MRI and the principles of the detection of MRI contrast agents, smart probes for use with MRI are not expected to come to routine imaging application.

Conclusions

The design of powerful contrast agents is of vital importance for enhancing the specificity and sensitivity of diagnostic medical imaging. In general, the optimal molecular structure of a contrast agent will depend on a multitude of factors, including the imaging modality and application(s) for which it is intended, its biocompatibility and stability and safety profile. In recent years, a multitude of novel contrast agents has been designed and experimentally tested for all major imaging modalities. Many of these have shown to be useful for in vivo imaging of small animals in the context of biomedical research into novel diagnostic procedures, disease mechanisms and therapy development. The translation of novel contrast materials from the preclinical to the clinical setting obviously is a complex process. In recent years, very few contrast agents have made it from the preclinical to the clinical setting. Exploratory human studies are relatively easy to conduct for nuclear imaging agents, as these require relatively small amounts of contrast materials. Therefore, safety issues are less pressing with PET than with MRI, for

example, as the lower sensitivity of the latter technique requires the use of substantial contrast agent quantities. It is improbable that a single imaging test will answer all clinical questions related to a certain diagnostic problem. Therefore, it may be expected that multimodality imaging agents are going to be widely explored in the near future and have a significant impact on the future of personalised medicine (Iagaru and Gambhir 2013). These developments will continue to require in-depth translational studies of contrast materials in a multidisciplinary setting, joining expertise ranging from chemistry to medical technology assessment.

Acknowledgements The work in the authors' laboratory related to the topic of the chapter was financially supported by the BSIK project entitled Molecular Imaging of Ischemic Heart Disease (project number BSIK03033), the European Union Network of Excellence Diagnostic Molecular Imaging (DIMI, LSHB-CT-2005-512146), the Netherlands Technology Foundation STW (VIDI grant GJS; grant number 07952), the Center for Translational Molecular Medicine (CTMM) projects VOLTA and PARISk and the Netherlands Heart Foundation programme grant (grant number 2006 T106) and was partly performed in the framework of the European Cooperation in Science and Technology (COST) Actions D38 "Metal-Based Systems for Molecular Imaging Applications" and TD1004 "Theragnostics Imaging and Therapy: An Action to Develop Novel Nanosized Systems for Imaging-Guided Drug Delivery". The Intramural Research Program of the National Institutes of Health, National Cancer Institute, Centre for Cancer Research, supported H. K.

References

Agarwal A, Saraf S, Asthana A, Gupta U, Gajbhiye V, Jain NK. Ligand based dendritic systems for tumor targeting. Int J Pharm. 2008;350(1–2):3–13. doi:10.1016/j.ijpharm.2007.09.024.

Aime S, Botta M, Fasano M, Terreno E. Lanthanide(III) chelates for NMR biomedical applications. Chem Soc Rev. 1998;27(1):19–29. doi:10.1039/A827019z.

Asati A, Santra S, Kaittanis C, Perez JM. Surface-charge-dependent cell localization and cytotoxicity of cerium oxide nanoparticles. ACS Nano. 2010;4(9):5321–31. doi:10.1021/nn100816s.

Baker JR, Jr. Dendrimer-based nanoparticles for cancer therapy. Hematology Am Soc Hematol Educ Program. 2009:708–19. doi:10.1182/asheducation-2009.1.708.

Barrett T, Ravizzini G, Choyke PL, Kobayashi H. Dendrimers in medical nanotechnology. IEEE Eng Med Biol Mag. 2009;28(1):12–22. doi:10.1109/MEMB.2008.931012.

Boas U, Heegaard PM. Dendrimers in drug research. Chem Soc Rev. 2004;33(1):43–63. doi:10.1039/b309043b.

Bosman AW, Janssen HM, Meijer EW. About dendrimers: structure, physical properties, and applications. Chem Rev. 1999;99(7):1665–88.

Bumb A, Brechbiel MW, Choyke P. Macromolecular and dendrimer-based magnetic resonance contrast agents. Acta Radiol. 2010;51(7):751–67. doi:10.3109/02841851.2010.491091.

Cai H, Li K, Li J, Wen S, Chen Q, Shen M, et al. Dendrimer-assisted formation of Fe3O4/Au nanocomposite particles for targeted dual mode CT/MR imaging of tumors. Small. 2015;11(35):4584–93. doi:10.1002/smll.201500856.

Chen K, Chen X. Design and development of molecular imaging probes. Curr Top Med Chem. 2010;10(12):1227–36.

Chen J, Lanza GM, Wickline SA. Quantitative magnetic resonance fluorine imaging: today and tomorrow. Wiley Interdiscip Rev Nanomed Nanobiotechnol. 2010;2(4):431–40. doi:10.1002/wnan.87.

Chen WT, Shih TT, Chen RC, Tu SY, Hsieh WY, Yang PC. Integrin alphavbeta3-targeted dynamic contrast-enhanced magnetic resonance imaging using a gadolinium-loaded polyethylene gycol-dendrimer-cyclic RGD conjugate to evaluate tumor angiogenesis and to assess early antiangiogenic treatment response in a mouse xenograft tumor model. Mol Imaging. 2012;11(4):286–300.

Chen Q, Li K, Wen S, Liu H, Peng C, Cai H, et al. Targeted CT/MR dual mode imaging of tumors using multifunctional dendrimer-entrapped gold nanoparticles. Biomaterials. 2013;34(21):5200–9. doi:10.1016/j.biomaterials.2013.03.009.

Chen Q, Wang H, Liu H, Wen S, Peng C, Shen M, et al. Multifunctional dendrimer-entrapped gold nanoparticles modified with RGD peptide for targeted computed tomography/magnetic resonance dual-modal imaging of tumors. Anal Chem. 2015;87(7):3949–56. doi:10.1021/acs.analchem.5b00135.

Cheng Y, Zhao L, Li Y, Xu T. Design of biocompatible dendrimers for cancer diagnosis and therapy: current status and future perspectives. Chem Soc Rev. 2011;40(5):2673–703. doi:10.1039/c0cs00097c.

Choi HS, Frangioni JV. Nanoparticles for biomedical imaging: fundamentals of clinical translation. Mol Imaging. 2010;9(6):291–310.

Choi HS, Liu W, Misra P, Tanaka E, Zimmer JP, Itty Ipe B, et al. Renal clearance of quantum dots. Nat Biotechnol. 2007;25(10):1165–70. doi:10.1038/nbt1340.

Criscione JM, Le BL, Stern E, Brennan M, Rahner C, Papademetris X, et al. Self-assembly of pH-responsive fluorinated dendrimer-based particulates for drug delivery and noninvasive imaging. Biomaterials.

2009;30(23–24):3946–55. doi:10.1016/j.biomaterials.2009.04.014.

de Kort DW, van Duynhoven JP, Hoeben FJ, Janssen HM, Van As H. NMR nanoparticle diffusometry in hydrogels: enhancing sensitivity and selectivity. Anal Chem. 2014;86(18):9229–35. doi:10.1021/ac502211q.

de Lussanet QG, Langereis S, Beets-Tan RG, van Genderen MH, Griffioen AW, van Engelshoven JM, et al. Dynamic contrast-enhanced MR imaging kinetic parameters and molecular weight of dendritic contrast agents in tumor angiogenesis in mice. Radiology. 2005;235(1):65–72. doi:10.1148/radiol.2351040411.

de Rosales RT. Potential clinical applications of bimodal PET-MRI or SPECT-MRI agents. J Labelled Comp Radiopharm. 2014;57(4):298–303. doi:10.1002/jlcr.3154.

Gajbhiye V, Kumar PV, Tekade RK, Jain NK. Pharmaceutical and biomedical potential of PEGylated dendrimers. Curr Pharm Design. 2007;13(4):415–29. doi:10.2174/138161207780162999.

Geraldes CFGC, Laurent S. Classification and basic properties of contrast agents for magnetic resonance imaging. Contrast Media Mol Imaging. 2009;4(1):1–23. doi:10.1002/cmmi.265.

Gillies ER, Dy E, Frechet JM, Szoka FC. Biological evaluation of polyester dendrimer: poly(ethylene oxide) "bow-tie" hybrids with tunable molecular weight and architecture. Mol Pharm. 2005;2(2):129–38. doi:10.1021/mp049886u.

Gnanasegaran G, Ballinger JR. Molecular imaging agents for SPECT (and SPECT/CT). Eur J Nucl Med Mol Imaging. 2014;41 Suppl 1:S26–35. doi:10.1007/s00259-013-2643-0.

Godin B, Tasciotti E, Liu X, Serda RE, Ferrari M. Multistage nanovectors: from concept to novel imaging contrast agents and therapeutics. Acc Chem Res. 2011;44(10):979–89. doi:10.1021/ar200077p.

Hak S, Sanders HM, Agrawal P, Langereis S, Grull H, Keizer HM, et al. A high relaxivity Gd(III)DOTA-DSPE-based liposomal contrast agent for magnetic resonance imaging. Eur J Pharm Biopharm. 2009;72(2):397–404. doi:10.1016/j.ejpb.2008.09.017.

Han LA, Li JF, Huang SX, Huang RQ, Liu SH, Hu X, et al. Peptide-conjugated polyamidoamine dendrimer as a nanoscale tumor-targeted T1 magnetic resonance imaging contrast agent. Biomaterials. 2011;32(11):2989–98. doi:10.1016/j.biomaterials.2011.01.005.

Huang R, Wang M, Zhu Y, Conti PS, Chen K. Development of PET probes for cancer imaging. Curr Top Med Chem. 2015;15(8):795–819.

Huang Z, Sengar RS, Nigam A, Abadjian MC, Potter DM, Grotjahn DB, et al. A fluorinated dendrimer-based nanotechnology platform: new contrast agents for high field imaging. Invest Radiol. 2010;45(10):641–54. doi:10.1097/RLI.0b013e3181ee6e06.

Iagaru A, Gambhir SS. Imaging tumor angiogenesis: the road to clinical utility. AJR Am J Roentgenol. 2013;201(2):W183–91. doi:10.2214/AJR.12.8568.

Jacobs I, Strijkers GJ, Keizer HM, Janssen HM, Nicolay K, Schabel MC. A novel approach to tracer-kinetic modeling for (macromolecular) dynamic contrast-enhanced MRI. Magn Reson Med. 2015;75(3):1142–53. doi:10.1002/mrm.25704.

Jain K, Kesharwani P, Gupta U, Jain NK. Dendrimer toxicity: Let's meet the challenge. Int J Pharm. 2010;394(1–2):122–42. doi:10.1016/j.ijpharm.2010.04.027.

James ML, Gambhir SS. A molecular imaging primer: modalities, imaging agents, and applications. Physiol Rev. 2012;92(2):897–965. doi:10.1152/physrev.00049.2010.

Jaszberenyi Z, Moriggi L, Schmidt P, Weidensteiner C, Kneuer R, Merbach AE, et al. Physicochemical and MRI characterization of Gd3+ -loaded polyamidoamine and hyperbranched dendrimers. J Biol Inorg Chem. 2007;12(3):406–20. doi:10.1007/s00775-006-0197-3.

Jiang ZX, Liu X, Jeong EK, Yu YB. Symmetry-guided design and fluorous synthesis of a stable and rapidly excreted imaging tracer for (19)F MRI. Angew Chem Int Ed Engl. 2009;48(26):4755–8. doi:10.1002/anie.200901005.

Kaminskas LM, Porter CJ. Targeting the lymphatics using dendritic polymers (dendrimers). Adv Drug Deliv Rev. 2011;63(10–11):890–900. doi:10.1016/j.addr.2011.05.016.

Kannan RM, Nance E, Kannan S, Tomalia DA. Emerging concepts in dendrimer-based nanomedicine: from design principles to clinical applications. J Intern Med. 2014;276(6):579–617. doi:10.1111/joim.12280.

Kesharwani P, Iyer AK. Recent advances in dendrimer-based nanovectors for tumor-targeted drug and gene delivery. Drug Discov Today. 2015;20(5):536–47. doi:10.1016/j.drudis.2014.12.012.

Khemthongcharoen N, Jolivot R, Rattanavarin S, Piyawattanametha W. Advances in imaging probes and optical microendoscopic imaging techniques for early in vivo cancer assessment. Adv Drug Deliv Rev. 2014;74:53–74. doi:10.1016/j.addr.2013.09.012.

Kiessling F, Fokong S, Bzyl J, Lederle W, Palmowski M, Lammers T. Recent advances in molecular, multimodal and theranostic ultrasound imaging. Adv Drug Deliv Rev. 2014;72:15–27. doi:10.1016/j.addr.2013.11.013.

Kobayashi H, Brechbiel MW. Nano-sized MRI contrast agents with dendrimer cores. Adv Drug Deliv Rev. 2005;57(15):2271–86. doi:10.1016/j.addr.2005.09.016.

Kobayashi H, Wu C, Kim MK, Paik CH, Carrasquillo JA, Brechbiel MW. Evaluation of the in vivo biodistribution of indium-111 and yttrium-88 labeled dendrimer-1B4M-DTPA and its conjugation with anti-Tac monoclonal antibody. Bioconjug Chem. 1999;10(1):103–11. doi:10.1021/bc980091d.

Kobayashi H, Sato N, Saga T, Nakamoto Y, Ishimori T, Toyama S, et al. Monoclonal antibody-dendrimer conjugates enable radiolabeling of antibody with markedly

high specific activity with minimal loss of immunoreactivity. Eur J Nucl Med. 2000;27(9):1334–9.
Kobayashi H, Kawamoto S, Saga T, Sato N, Hiraga A, Ishimori T, et al. Positive effects of polyethylene glycol conjugation to generation-4 polyamidoamine dendrimers as macromolecular MR contrast agents. Magn Reson Med. 2001a;46(4):781–8.
Kobayashi H, Kawamoto S, Saga T, Sato N, Hiraga A, Ishimori T, et al. Novel liver macromolecular MR contrast agent with a polypropylenimine diaminobutyl dendrimer core: comparison to the vascular MR contrast agent with the polyamidoamine dendrimer core. Magn Reson Med. 2001b;46(4):795–802.
Kobayashi H, Kawamoto S, Jo SK, Bryant Jr HL, Brechbiel MW, Star RA. Macromolecular MRI contrast agents with small dendrimers: pharmacokinetic differences between sizes and cores. Bioconjug Chem. 2003;14(2):388–94. doi:10.1021/bc025633c.
Kobayashi H, Koyama Y, Barrett T, Hama Y, Regino CA, Shin IS, et al. Multimodal nanoprobes for radionuclide and five-color near-infrared optical lymphatic imaging. ACS Nano. 2007;1(4):258–64. doi:10.1021/nn700062z.
Kobayashi H, Longmire MR, Ogawa M, Choyke PL, Kawamoto S. Multiplexed imaging in cancer diagnosis: applications and future advances. Lancet Oncol. 2010a;11(6):589–95. doi:10.1016/S1470-2045(10)70009-7.
Kobayashi H, Ogawa M, Alford R, Choyke PL, Urano Y. New strategies for fluorescent probe design in medical diagnostic imaging. Chem Rev. 2010b;110(5):2620–40. doi:10.1021/cr900263j.
Kobayashi H, Longmire MR, Ogawa M, Choyke PL. Rational chemical design of the next generation of molecular imaging probes based on physics and biology: mixing modalities, colors and signals. Chem Soc Rev. 2011;40(9):4626–48. doi:10.1039/c1cs15077d.
Kojima C, Turkbey B, Ogawa M, Bernardo M, Regino CA, Bryant Jr LH, et al. Dendrimer-based MRI contrast agents: the effects of PEGylation on relaxivity and pharmacokinetics. Nanomedicine. 2011;7(6):1001–8. doi:10.1016/j.nano.2011.03.007.
Kok MB, Hak S, Mulder WJ, van der Schaft DW, Strijkers GJ, Nicolay K. Cellular compartmentalization of internalized paramagnetic liposomes strongly influences both T1 and T2 relaxivity. Magn Reson Med. 2009;61(5):1022–32. doi:10.1002/mrm.21910.
Kok MB, de Vries A, Abdurrachim D, Prompers JJ, Grull H, Nicolay K, et al. Quantitative (1)H MRI, (19)F MRI, and (19)F MRS of cell-internalized perfluorocarbon paramagnetic nanoparticles. Contrast Media Mol Imaging. 2011;6(1):19–27. doi:10.1002/cmmi.398.
Langereis S, de Lussanet QG, van Genderen MH, Meijer EW, Beets-Tan RG, Griffioen AW, et al. Evaluation of Gd(III)DTPA-terminated poly(propylene imine) dendrimers as contrast agents for MR imaging. NMR Biomed. 2006;19(1):133–41. doi:10.1002/nbm.1015.
Langereis S, Geelen T, Grull H, Strijkers GJ, Nicolay K. Paramagnetic liposomes for molecular MRI and MRI-guided drug delivery. NMR Biomed. 2013;26(7):728–44. doi:10.1002/nbm.2971.
Langereis S, Hijnen N, Strijkers G, Nicolay K, Grull H. Multifunctional liposomes for MRI and image-guided drug delivery. Ther Deliv. 2014;5(1):21–4. doi:10.4155/tde.13.128.
Li K, Wen S, Larson AC, Shen M, Zhang Z, Chen Q, et al. Multifunctional dendrimer-based nanoparticles for in vivo MR/CT dual-modal molecular imaging of breast cancer. Int J Nanomedicine. 2013;8:2589–600. doi:10.2147/IJN.S46177.
Li X, Anton N, Zuber G, Vandamme T. Contrast agents for preclinical targeted X-ray imaging. Adv Drug Deliv Rev. 2014;76:116–33. doi:10.1016/j.addr.2014.07.013.
Licha K, Resch-Genger U. Probes for optical imaging: new developments. Drug Discov Today Technol. 2011;8(2–4):e87–94. doi:10.1016/j.ddtec.2011.11.003.
Liu H, Xu Y, Wen S, Chen Q, Zheng L, Shen M, et al. Targeted tumor computed tomography imaging using low-generation dendrimer-stabilized gold nanoparticles. Chemistry. 2013;19(20):6409–16. doi:10.1002/chem.201204612.
Liu H, Wang H, Xu Y, Shen M, Zhao J, Zhang G, et al. Synthesis of PEGylated low generation dendrimer-entrapped gold nanoparticles for CT imaging applications. Nanoscale. 2014;6(9):4521–6. doi:10.1039/c3nr06694k.
Longmire M, Choyke PL, Kobayashi H. Dendrimer-based contrast agents for molecular imaging. Curr Top Med Chem. 2008;8(14):1180–6.
Longmire MR, Ogawa M, Choyke PL, Kobayashi H. Biologically optimized nanosized molecules and particles: more than just size. Bioconjug Chem. 2011;22(6):993–1000. doi:10.1021/bc200111p.
Longmire MR, Ogawa M, Choyke PL, Kobayashi H. Dendrimers as high relaxivity MR contrast agents. Wiley Interdiscip Rev Nanomed Nanobiotechnol. 2014;6(2):155–62. doi:10.1002/wnan.1250.
Loudos G, Kagadis GC, Psimadas D. Current status and future perspectives of in vivo small animal imaging using radiolabeled nanoparticles. Eur J Radiol. 2011;78(2):287–95. doi:10.1016/j.ejrad.2010.06.025.
Maeda H. Tumor-selective delivery of macromolecular drugs via the EPR effect: background and future prospects. Bioconjug Chem. 2010;21(5):797–802. doi:10.1021/bc100070g.
Maeda H, Nakamura H, Fang J. The EPR effect for macromolecular drug delivery to solid tumors: Improvement of tumor uptake, lowering of systemic toxicity, and distinct tumor imaging in vivo. Adv Drug Deliv Rev. 2013;65(1):71–9. doi:10.1016/j.addr.2012.10.002.
Malik N, Wiwattanapatapee R, Klopsch R, Lorenz K, Frey H, Weener JW, et al. Dendrimers: relationship between structure and biocompatibility in vitro, and

preliminary studies on the biodistribution of 125I-labelled polyamidoamine dendrimers in vivo. J Control Release. 2000;65(1–2):133–48.

Menjoge AR, Kannan RM, Tomalia DA. Dendrimer-based drug and imaging conjugates: design considerations for nanomedical applications. Drug Discov Today. 2010;15(5–6):171–85. doi:10.1016/j.drudis.2010.01.009.

Mintzer MA, Grinstaff MW. Biomedical applications of dendrimers: a tutorial. Chem Soc Rev. 2011;40(1):173–90. doi:10.1039/b901839p.

Mulder WJ, Strijkers GJ, van Tilborg GA, Griffioen AW, Nicolay K. Lipid-based nanoparticles for contrast-enhanced MRI and molecular imaging. NMR Biomed. 2006;19(1):142–64. doi:10.1002/nbm.1011.

Mulder WJ, Strijkers GJ, van Tilborg GA, Cormode DP, Fayad ZA, Nicolay K. Nanoparticulate assemblies of amphiphiles and diagnostically active materials for multimodality imaging. Acc Chem Res. 2009;42(7):904–14. doi:10.1021/ar800223c.

Mulder WJ, McMahon MT, Nicolay K. The evolution of MRI probes: from the initial development to state-of-the-art applications. NMR Biomed. 2013;26(7):725–7. doi:10.1002/nbm.2976.

Nicolay K, Strijkers G, Grüll H. Gd-containing nanoparticles as MRI contrast agents. In: The chemistry of contrast agents in medical magnetic resonance imaging. Hoboken: John Wiley & Sons, Ltd; 2013. p. 449–87.

Ogawa M, Regino CA, Marcelino B, Williams M, Kosaka N, Bryant Jr LH, et al. New nanosized biocompatible MR contrast agents based on lysine-dendri-graft macromolecules. Bioconjug Chem. 2010;21(5):955–60. doi:10.1021/bc9005442.

Opina AC, Wong KJ, Griffiths GL, Turkbey BI, Bernardo M, Nakajima T, et al. Preparation and long-term biodistribution studies of a PAMAM dendrimer G5-Gd-BnDOTA conjugate for lymphatic imaging. Nanomedicine (Lond). 2015;10(9):1423–37. doi:10.2217/nnm.14.113.

Pikkemaat JA, Wegh RT, Lamerichs R, van de Molengraaf RA, Langereis S, Burdinski D, et al. Dendritic PARACEST contrast agents for magnetic resonance imaging. Contrast Media Mol Imaging. 2007;2(5):229–39. doi:10.1002/cmmi.149.

Prabhu RH, Patravale VB, Joshi MD. Polymeric nanoparticles for targeted treatment in oncology: current insights. Int J Nanomedicine. 2015;10:1001–18. doi:10.2147/IJN.S56932.

Rosenblum LT, Kosaka N, Mitsunaga M, Choyke PL, Kobayashi H. In vivo molecular imaging using nanomaterials: general in vivo characteristics of nano-sized reagents and applications for cancer diagnosis (Review). Mol Membr Biol. 2010;27(7):274–85. doi:10.3109/09687688.2010.481640.

Sato N, Kobayashi H, Saga T, Nakamoto Y, Ishimori T, Togashi K, et al. Tumor targeting and imaging of intraperitoneal tumors by use of antisense oligo-DNA complexed with dendrimers and/or avidin in mice. Clin Cancer Res. 2001;7(11):3606–12.

Sherry AD, Caravan P, Lenkinski RE. Primer on gadolinium chemistry. J Magn Reson Imaging. 2009;30(6):1240–8. doi:10.1002/jmri.21966.

Strijkers GJ, Mulder WJ, van Tilborg GA, Nicolay K. MRI contrast agents: current status and future perspectives. Anticancer Agents Med Chem. 2007;7(3):291–305.

Strijkers GJ, Hak S, Kok MB, Springer Jr CS, Nicolay K. Three-compartment T1 relaxation model for intracellular paramagnetic contrast agents. Magn Reson Med. 2009;61(5):1049–58. doi:10.1002/mrm.21919.

Tack F, Bakker A, Maes S, Dekeyser N, Bruining M, Elissen-Roman C, et al. Modified poly(propylene imine) dendrimers as effective transfection agents for catalytic DNA enzymes (DNAzymes). J Drug Target. 2006;14(2):69–86. doi:10.1080/10611860600635665.

Talanov VS, Regino CAS, Kobayashi H, Bernardo M, Choyke PL, Brechbiel MW. Dendrimer-based nanoprobe for dual modality magnetic resonance and fluorescence imaging. Nano Lett. 2006;6(7):1459–63. doi:10.1021/nl060765q.

van Rooij T, Daeichin V, Skachkov I, de Jong N, Kooiman K. Targeted ultrasound contrast agents for ultrasound molecular imaging and therapy. Int J Hyperthermia. 2015;31(2):90–106. doi:10.3109/02656736.2014.997809.

Wang H, Zheng L, Guo R, Peng C, Shen M, Shi X, et al. Dendrimer-entrapped gold nanoparticles as potential CT contrast agents for blood pool imaging. Nanoscale Res Lett. 2012;7:190. doi:10.1186/1556-276X-7-190.

Wehrl HF, Sauter AW, Divine MR, Pichler BJ. Combined PET/MR: a technology becomes mature. J Nucl Med. 2015;56(2):165–8. doi:10.2967/jnumed.114.150318.

Wen S, Li K, Cai H, Chen Q, Shen M, Huang Y, et al. Multifunctional dendrimer-entrapped gold nanoparticles for dual mode CT/MR imaging applications. Biomaterials. 2013;34(5):1570–80. doi:10.1016/j.biomaterials.2012.11.010.

Wen Q, Wan S, Liu Z, Xu S, Wang H, Yang B. Ultrasound contrast agents and ultrasound molecular imaging. J Nanosci Nanotechnol. 2014;14(1):190–209.

Wu LP, Ficker M, Christensen JB, Trohopoulos PN, Moghimi SM. Dendrimers in medicine: therapeutic concepts and pharmaceutical challenges. Bioconjug Chem. 2015;26(7):1198–211. doi:10.1021/acs.bioconjchem.5b00031.

Yang J, Luo Y, Xu Y, Li J, Zhang Z, Wang H, et al. Conjugation of iron oxide nanoparticles with RGD-modified dendrimers for targeted tumor MR imaging. ACS Appl Mater Interfaces. 2015;7(9):5420–8. doi:10.1021/am508983n.

Yu YB. Fluorinated dendrimers as imaging agents for F-19 MRI. Wiley Interdiscip Rev Nanomed Nanobiotechnol. 2013;5(6):646–61. doi:10.1002/wnan.1239.

Zhang MG, Guo R, Keri M, Banyai I, Zheng Y, Cao M, et al. Impact of dendrimer surface functional groups on the release of doxorubicin from dendrimer carriers. J Phys Chem B. 2014;118(6):1696–706. doi:10.1021/jp411669k.

X-Ray and X-Ray-CT

12

Robert Brauweiler, Klaus Engelke,
Martin Hupfer, Willi A. Kalender,
Marek Karolczak, and Hubertus Pietsch

Contents

R. Brauweiler • K. Engelke • M. Hupfer
W.A. Kalender • M. Karolczak
Institute of Medical Physics,
University Erlangen-Nuernberg, Henkestrasse 91,
Erlangen 91052, Germany

H. Pietsch (✉)
MR & CT Contrast Media Research,
Global Drug Discovery, Bayer Pharma AG,
Müllerstrasse 178, Berlin 13353, Germany
e-mail: hubertus.pietsch@bayer.com

12.1 X-Ray and X-Ray-CT: Methods and Devices

Robert Brauweiler, Klaus Engelke,
Martin Hupfer, Willi A. Kalender, and
Marek Karolczak

Since their discovery in 1895, x-rays have been widely used for imaging humans. Recently they have also gained on importance in small-animal imaging (SAI). Most techniques known from clinical medicine, including single- and dual-energy x-ray imaging, have been successfully ported to SAI and are the subject of this chapter. As trivial as it is, simple x-ray examinations may bring diagnostically valuable information in a variety of applications. Unenhanced radiography reveals skeletal anatomy, contrast-enhanced imaging allows improved visualization of the vasculature and strongly vascularized areas, and dedicated methods such as bone densitometry deliver quantitative information. In analogy to clinical x-ray imaging, we will separately describe standard two-dimensional (2D) projection imaging and the more advanced three-dimensional (3D) computed tomography (CT) imaging techniques. Also in analogy to clinical applications, CT is considered to be of significantly higher importance as it provides more information and possibilities than conventional 2D approaches. It will therefore be covered in much more detail.

F. Kiessling et al. (eds.), *Small Animal Imaging*, DOI 10.1007/978-3-319-42202-2_12

The x-ray instrumentation used for small-animal examinations does not differ, in principle, from that known from clinical medicine. The main difference lies in the required higher resolution levels, which implies the use of special components: x-ray tubes with very small focal spots, so-called micro-focus tubes, and image detectors with small detector elements in order to produce sharp images. Respective micro-focus tubes offer spot sizes down to a few micrometers (μm) but can only provide very limited power values. Typical focal spot sizes are 5–50 μm, and the typical power values are of the same order of magnitude with 5–50 watts (W). Nowadays x-ray imaging is done almost exclusively using digital image capture; respective detectors with small pixel sizes and large matrices record the x-ray intensity and convert the detected intensity directly into an electric signal. In clinical radiology, pixel sizes of typically 150–300 μm are in use; for SAI, pixel sizes of 50–100 μm are preferred due to the relatively small size of mice and rats. It is technologically feasible to provide the necessary detectors of typically 5 by 5 cm^2 covering the entire animal in one projection. Typical pixel sizes of about 50 μm and matrix sizes of 1000 by 1000, i.e., a "1 k × 1k" matrix, result in an active sensor area of 5 by 5 cm^2. Respective detector technology has become available during the past decade. Further developments presently aim at higher frame rates, i.e., to capture more images per second; further reduction of the pixel size is not a topic due to technical and cost reasons. Furthermore, spatial resolution in in vivo imaging may be limited by artifacts due to animal movement, breathing, and heart motion so that very high resolution of typically 50 μm or less is only a topic for ex vivo imaging.

Whenever significantly higher resolution is desired in spite of this, the necessary smaller effective pixel sizes can be provided by magnification techniques. In practice this means that the object is placed close to the source and the smallest focal spot size is selected. In this way resolution values of a few micrometers can be reached although pixel sizes are 50 μm or more. The magnification approach can be used in equal fashion for 2D and 3D high-resolution imaging. In general, the x-ray components for 2D projection and for 3D CT imaging are very similar in most respects and often identical.

The purpose of this chapter is to give an overview on technical and methodological aspects and developments of x-ray imaging for SAI and to provide general recommendations regarding the responsible use of x-rays. Readers interested in more details, in particular with respect to the physics and technology involved, are referred to standard textbooks on imaging, e.g., Kalender (2011) as an introduction and overview on CT. Further materials on micro-computed tomography (micro-CT, μCT) imaging can, for example, be found in Holdsworth and Thornton (2002), Paulus et al. (2000), Ritman (2004), Badea et al. (2006), Bartling et al. (2007), Del Guerra et al. (2008), and Engelke et al. (2008).

12.1.1 2D X-Ray Projection Imaging

12.1.1.1 Radiography

In many anatomical studies, valuable information can be obtained from simple 2D projection images as known from classical radiography. They suffer in quality with respect to contrast and general visibility from overlying structures which overshadow organs or structures of interest. But they do provide high-resolution and low-noise images at acceptably low radiation dose. Also, imaging is performed very fast since a single x-ray pulse is sufficient. Figure 12.1 shows examples of SAI projection images. Unenhanced 2D radiographs are typically used for imaging the skeleton since the soft tissue contrast is very limited.

12.1.1.2 Angiography

To enhance contrast of vessels and of strongly vascularized areas, x-ray contrast media are applied by intravenous or intra-arterial injection. In most cases, the iodinated x-ray contrast media used in clinical radiology are applied. However, alternative x-ray tracers are of great topical interest; the results of respective development efforts are pri-

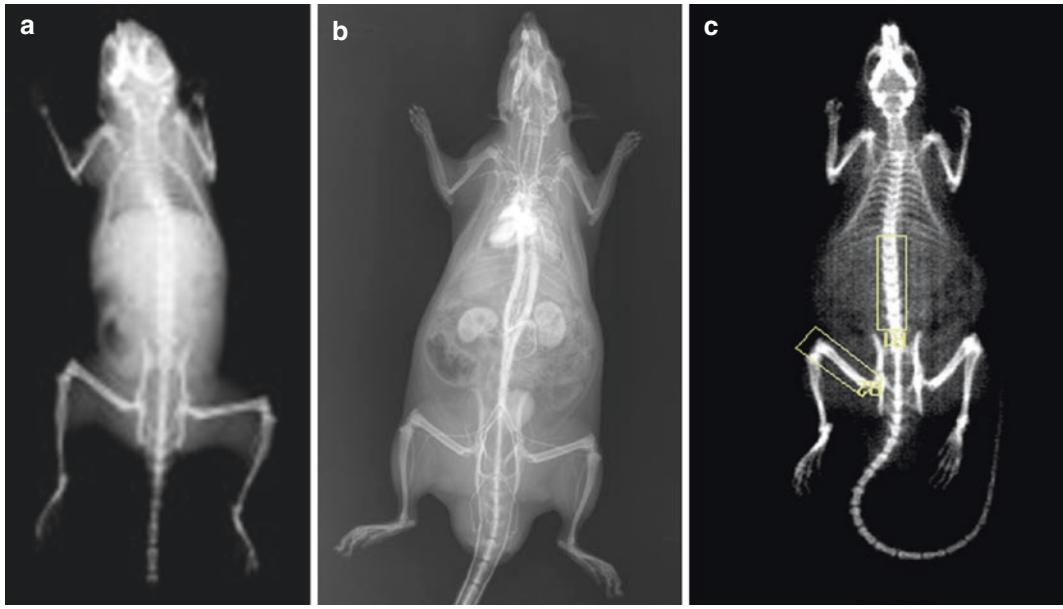

Fig. 12.1 2D x-ray projection imaging. Examples of (**a**) radiography, (**b**) angiography, and (**c**) bone densitometry of a rat

marily tested and evaluated in small-animal studies (see Chap. 12.2). The main area of application is direct angiography, the examination of vascular structures (Fig. 12.1b) (Ehling et al. 2014); subtracting pre- and postinjection images after contrast medium administration yields the typical digital subtraction angiography (DSA) images, which are established in clinical radiology (Almajdub et al. 2008; Badea et al. 2008). Vascular studies may also reveal functional information to some degree when series of images are taken to assess contrast medium kinetics indicating perfusion or other tissue or lesion characteristics.

Although simple in concept, angiographic studies are challenging when applied to SAI. The application is not trivial due to the small size of the animal. The rapid contrast flow in small animals, due to their high heart rates (e.g., up to 600 beats per minute for mice), is significantly higher than in humans and demands fast imaging capabilities, in particular high detector frame rates. This in turn requires high x-ray photon flux and the respective high x-ray power in order to acquire the necessary data in acceptably short time. High power, however, is in conflict with the desired small focus size, so the two have to be matched.

12.1.1.3 Bone Densitometry

In addition to imaging skeletal structures by standard radiography, there often is an interest to determine bone mineral density (BMD) values quantitatively. For this purpose, the same techniques are employed as in clinical medicine; for 2D projection measurements, dual-energy x-ray absorptiometry (DXA) (Kastl et al. 2002; Libouban et al. 2002; Soon et al. 2006; Nazarian et al. 2009) is most commonly used. During the examination two measurements with x-ray beams of different energies, i.e., different high-voltage settings and filtration, are obtained. In most cases this is done by scanning the complete body or excised bones with a fan beam instead of a cone beam. Since soft tissues and bones exhibit different absorption behavior at the two energy levels, they can be differentiated from each other (more details on this technique are offered in Sect. 12.1.4). With proper calibration and subtraction of soft tissue, skeletal structures can be isolated and BMD can be determined.

Standard clinical bone densitometers with special software are commonly used today for bone mineral density and body composition measurements of small animals. The investigation of

mice is not recommended because partial volume artifacts caused by the limited spatial resolution of these scanners results in high accuracy errors. An example is shown in Fig. 12.1c. Some devices allow both in vivo and ex vivo measurements and whole-body or selected region-of-interest examinations within a few minutes.

12.1.2 3D X-Ray CT Imaging Principles (Micro-CT)

Micro-CT (μCT) has been promoted for various applications for about three decades by now. The focus was originally on very high-resolution imaging. Technical applications were most important initially and are often referred to as "nondestructive testing" (NDT); they also bear relevance for research in medicine as indicated by the image of a stent in Fig. 12.2d. Medical micro-CT applications initially focused on preclinical research such as the in vitro evaluation of biopsies or small specimens. In vivo imaging of small animals became feasible in the last decade due to the advent of new detector technology and is growing in importance. Small animals can in principle be examined on typical in vitro scanners with the animal rotating. Vice versa, specimens can be examined on in vivo scanners. It appears both logical and instructive nevertheless to clearly distinguish these two scanner types and to describe them separately as follows below.

Flat-detector CT scanners recently introduced in clinical medicine which offer larger fields of measurement are sometimes also used for SAI applications (Bartling et al. 2007). However, they typically only offer spatial resolution of about 200–300 μm which is only marginally superior as compared to clinical CT. Their use is likely to diminish since dedicated SAI micro-CT scanners have become more widely available. Therefore, they are not considered further in the discussions below. We will here use the arbitrary, but accepted definition that the term micro-CT is applicable only if spatial resolution of 100 μm or better can be achieved (Kalender 2011; Bartling et al. 2007).

12.1.2.1 In Vitro Micro-CT Imaging

The aim of most in vitro applications is to investigate high-contrast object structures at very high spatial resolution, typically at 5–50 μm. For this purpose x-ray sources with very small focus sizes of also 5–50 μm are used. A typical scanner design is shown in Fig. 12.2a. The magnification can be easily varied by translating the sample between x-ray source and detector. The sample to be scanned is rotated by 360° during the scan. Depending on the resolution requirements, scan times of typically 10–300 min may result.

Even higher spatial resolutions of below 1 μm can be achieved by the use of synchrotron radiation (SR) sources, which offer high-intensity monochromatic radiation in parallel-ray geometry. As a consequence the spatial resolution is determined by the x-ray detector, and therefore SR micro-CT set-ups are typically equipped with detectors specifically developed for these applications. They are not commercially available. SR micro-CT is the tool of choice for specific research questions but is not of practical importance for typical SAI.

Since micro-focus x-ray tubes are limited by very low power levels, long scan times result. This is inconvenient but not very problematic for biopsy and specimen work although, for example, soft tissue samples may suffer deformations during long scan times, in particular if not embedded properly. Of course, for biopsy and specimen imaging the radiation dose received by the sample is not a matter of concern.

One typical application of micro-CT in preclinical research is the 3D quantification of trabecular bone structure of rats and mice, which nowadays is an integrated part of the development of bone-protective agents used against osteoporosis. Human bone biopsies (e.g., Fig. 12.2c) are also routinely investigated with micro-CT. With the exception of metal objects with high-Z materials, these scanners are also used for the inspection of technical objects such as the vessel stent (Fig. 12.2d). Such examinations serve to control and to optimize the manufacturing process of the respective materials and for quality control.

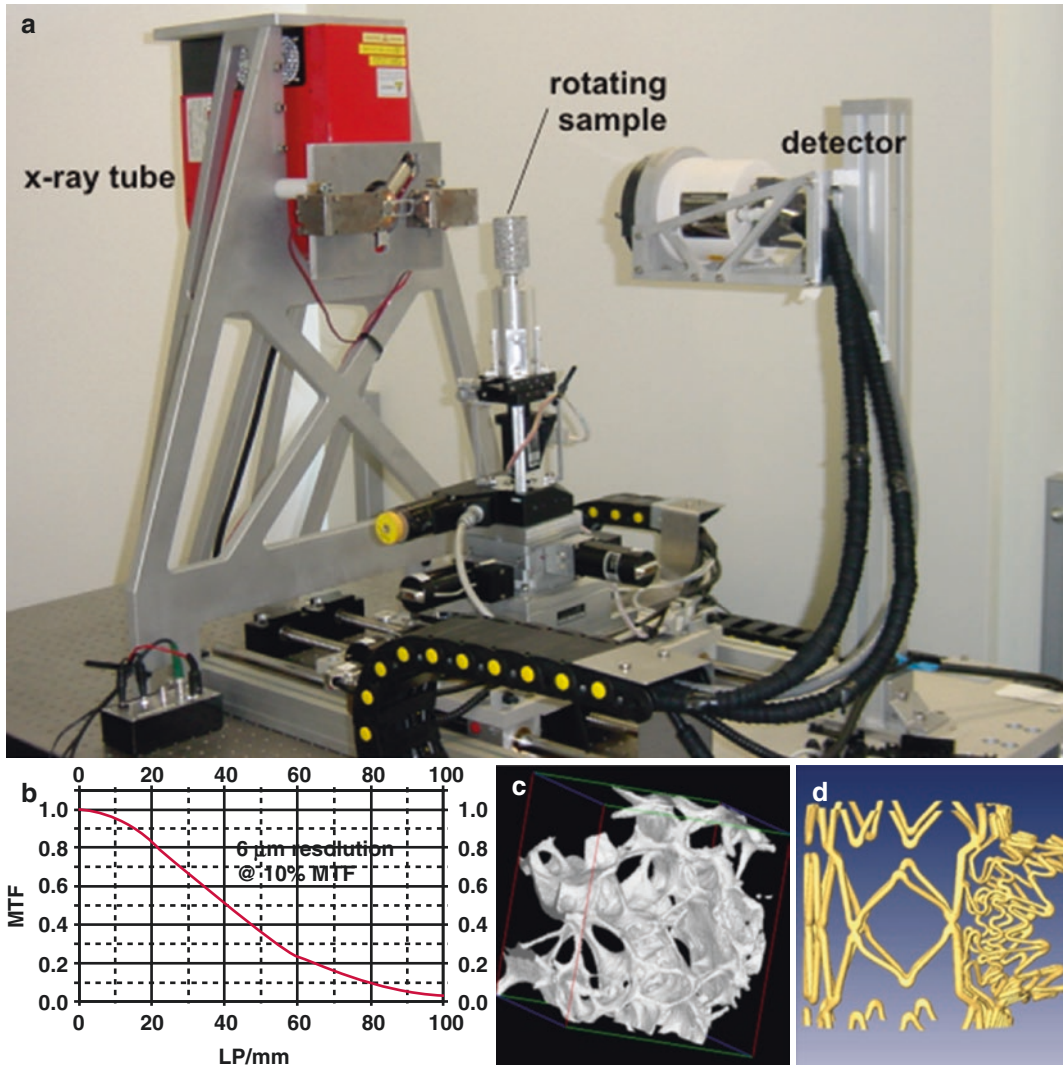

Fig. 12.2 3D µCT imaging in vitro. (**a**) Typical experimental scanner setup for very high resolution. (**b**) Measured modulation transfer function demonstrating resolution down to 6 µm. (**c**) 3D display of a bone biopsy sample. (**d**) 3D display of a bifurcating vascular stent imaged for controlling production quality

12.1.2.2 In Vivo Micro-CT Imaging

In vivo imaging of small animals poses several demands which are different from the in vitro imaging task. They are very similar in most respects to those relevant for clinical imaging: speed is of high importance, and dose has to be kept "as low as reasonably achievable," i.e., the ALARA principle is valid for SAI in the same way as it is for clinical imaging. This is not common practice and general knowledge in the field yet. Anecdotal reports, mostly "private communication," stated that animals suffered acute radiation damage; precise dose values for the CT protocols in use were generally not available, however. This situation has to be improved. Therefore aspects of quality control and dose assessment will be stressed below.

Some features that distinguish in vivo from in vitro imaging with micro-CT are summarized in Table 12.1. Again, x-ray sources with a focus size

smaller than used in clinical imaging are demanded; however, typically 50–200 µm are accepted to allow for higher power levels. It is understood that area detectors – as opposed to a single linear array – are the component of choice to use a full cone beam and to thereby make efficient use of the available x-ray power. Modern SAI scanners allow for scan times of a few seconds up to a few minutes whereas scan times of typically 20–30 min were the standard for many years.

Table 12.1 Some typical features characterizing and distinguishing in vitro and in vivo micro-CT

	In vitro scanning	In vivo scanning
Focal spot size	1–50 µm	50–200 µm
X-ray power	1–50 W	10–300 W
Spatial resolution	5–100 µm	50–200 µm
Scan times	10–300 min	0.1–30 min
Field of measurement	1–100 mm	30–100 mm
Dose	Not important	ALARA

A practical demand in SAI is that the animal remains stationary and that it can be supplied with anesthetizing gas, electrodes, etc., during the course of the examination. Therefore it is mandatory that the gantry rotates and the animal remains stationary at rest on the bed. Scanners vary in size significantly; desktop scanners can be accommodated relatively easily in an animal laboratory environment. In addition to the micro-CT scanner itself, technical facilities to monitor, to prepare, and to support the animal are necessary; this may include cardiac and respiratory monitors, warming pads, and anesthetizing gas. A respective scanner and a scan preparation scene are shown in Fig. 12.3.

Some typical imaging results are shown in Fig. 12.3c–e, all derived from a single scan after contrast medium injection. Image planes can be placed arbitrarily in the scanned volume for all CT examinations; here a sagittal (Fig. 12.3c) and a coronal view (Fig. 12.3d) were chosen to give

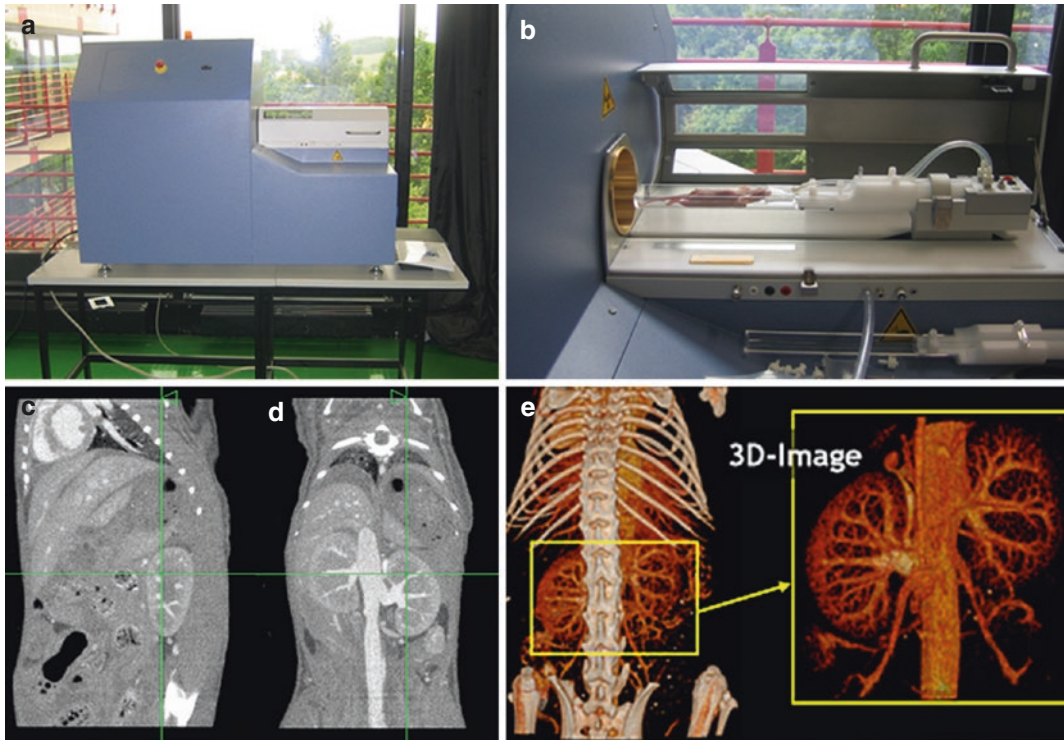

Fig. 12.3 Micro-CT in vivo imaging. (**a**, **b**) Typical desktop micro-CT scanner for small-animal imaging (Courtesy of F. Kießling, Aachen). (**c**–**e**) Scan of a mouse after contrast medium injection showing sagittal and coronal views (**c**, **d**) and rendering the kidney vasculature in very fine detail (**e**) (Courtesy of P. Hauff, Berlin)

an overview of the complete anatomy. Using appropriate software for post-processing, which is available for most scanners today, details can be rendered in a quasi isolated fashion (e.g., Fig. 12.3e).

12.1.3 Quality Control and Dose Considerations

It is understood that animal experiments have to be justified ethically in every respect. All precautions have to be taken that the animal is not submitted to an undue burden. The consequence of these considerations is that control of image quality and dose has to be ensured. To a certain degree, SAI has to adhere to the same principles that are valid for clinical imaging.

12.1.3.1 Image Quality

Image quality and dose are measured during acceptance testing when a new scanner is installed and should be tested at regular intervals thereafter or whenever problems arise. The phantoms necessary for measurements are mostly cylinders. With typical diameters of 20 and 32 mm, they mimic well the attenuation presented by mice and lean rats. They also correspond to the 20 and 32 cm diameters of phantoms used for clinical CT mimicking the typical attenuation for head and body scans. A list of the most important image quality parameters to be checked is given in Table 12.2. The necessary phantom types are listed there as well; examples are shown in Fig. 12.4.

The accuracy and stability of CT values are important to allow for follow-up studies and for comparability to other studies. Water cylinders are commonly used to check these two parameters. They also allow determining image noise and image homogeneity at the same time; this is important to monitor scanner performance over time and to check dose efficiency.

Spatial resolution can be assessed in two ways: by objective quantitative measurement such as a point response function and modulation

Table 12.2 Important image quality parameters and typical phantoms for their assessment

Parameter	Phantom
CT values	Water or water-equivalent plastic
Noise	Water or water-equivalent plastic
Homogeneity	Water or water-equivalent plastic
Spatial resolution	Wire, typ. 10 µm diameter tungsten in air
Spatial resolution	Bar pattern
Contrast resolution	Low-contrast patterns
Calibration	Materials at defined concentration, e.g., Ca or I
Dose	Cylinder with bore hole

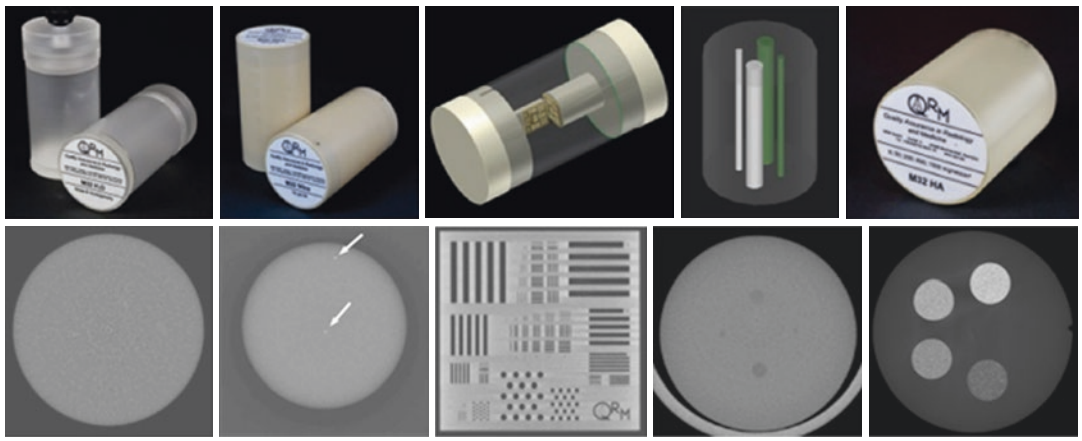

Fig. 12.4 Quality assurance phantoms (see list in Table 12.2) shown by photos (*top row*) and by CT images (*bottom row*). From left to right: water phantom, wire resolution phantom, bar resolution phantom, low-contrast resolution phantom, hydroxyapatite calibration phantom (Courtesy of QRM GmbH, Möhrendorf, Germany)

transfer function calculation or by visual inspection of regular patterns. The first is necessary for acceptance testing and reliable longitudinal control; the latter is more intuitive and allows a direct comparison to the imaging task at hand such as an assessment of trabecular bone structures.

The capability of discerning low-contrast structures such as typical soft tissue details, often referred to as low-contrast resolution, can be tested with respective patterns in a low-contrast phantom. If reliable quantitative measurements of bone density or other tissue parameters are desired, calibration phantoms containing samples of the respective material at defined concentrations are necessary. For bone density measurements, for example, phantoms with different concentration of hydroxyapatite are in use.

12.1.3.2 Dose Assessment

The x-ray dose to the animal under examination depends on many variables. It is hard to determine experimentally with high accuracy in small animals, but the order of magnitude should be known. Measurement concepts similar to those used in clinical CT involve a simple ionization chamber measurement in a phantom of a diameter similar to the animal in question. The chamber, typically 10 cm long, averages dose over its complete length and does not give a direct measure of the dose to the mouse or to single organs. It is possible to estimate these values by using the concept of the CT dose index (CTDI), which is commonly used in clinical CT (Kalender 2011) and can be used for micro-CT in a similar way (Hupfer et al. 2012a). The alternative is using small thermoluminescent dosimeters (TLD) which provide direct point measurements and can even be used in cavities of the animal or a specimen. TLD measurements are a very cumbersome and error-prone procedure, however. Calculations provide a practical and more elegant alternative.

The calculation of 3D dose distributions is possible for micro-CT in a manner analogous to methods used in general radiology and in radiation therapy treatment planning. For this purpose, so-called Monte Carlo methods are used: based on the CT image set which reflects the x-ray attenuation of the animal or object in question, the path of thousands of photons through the animal is simulated for each single projection, and the deposition of energy due to each photon interaction with tissue is recorded and assigned exactly to the volume element where this occurred. The method can take arbitrary scanner geometries and scan protocols into account, which makes it very flexible; results are very reliable, can be achieved more easily than by measurements, and can be carried out retrospectively for any image data set (Deak et al. 2008). An example is shown in Fig. 12.5. Here the 3D dose distribution was calculated for a whole-body scan of a mouse carried out with three 360° rotations at 50 kV and a total collimation of 40 mm. Dose values ranged between 8 and 32 mGy in this case as indicated by the color scale for soft and bone tissue, respectively. The dose distributions resemble the original CT images as structures which absorb more energy show up as high-contrast structures in the CT images and in the dose images in a similar manner. For a 360° scan, the dose distribution is rather homogeneous over the complete volume; for projection radiography, dose is always very high at the entrance and low at the exit point.

12.1.3.3 Dose Optimization

Optimization of dose simply means that a given task should be achieved at the minimum dose necessary, i.e., the ALARA principle has to be applied. It does not mean that dose reduction is the sole purpose, definitely not to levels where image quality, in particular the visibility of soft tissue structures, is impaired. In addition to the general optimization principle which aims at avoiding or limiting damage to the animal, there are also practical considerations to be taken into account. The need and demand for repeated studies on one and the same animal over an extended time span, e.g., to measure tumor volume growth rates, make it a necessity to limit dose and to ensure that no radiation effects interfere with the study objectives.

It is not generally known which dose levels are critical and which are not. The “low-dose range” for humans is mostly specified up to

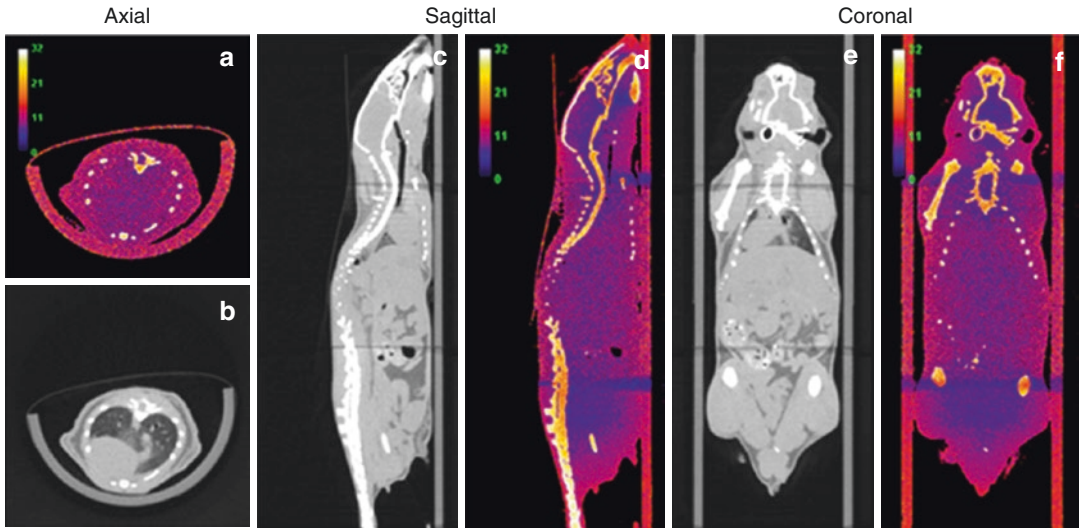

Fig. 12.5 3D dose distributions can be calculated accurately using Monte Carlo methods. Transverse (**a**, **b**), sagittal (**c**, **d**) and coronal views (**e**, **f**) of the CT and the dose values are shown, respectively. Dose to the mouse is relatively homogeneous and was kept well below 50 mSv in this examination

200 mSv and is defined as the range where no detrimental effects associated with radiation have been observed (UNSCEAR 2000; Kalender 2011). It appears reasonable to try and limit dose in SAI to this low-dose range whenever possible.

In order to be able to do so, dose values associated with all scan protocols available to the user have to be known. The respective data should be specified by the manufacturer; they are directly related to the tube voltage, the tube current, and the scan time. This allows for a first orientation. Whenever parameters are changed, e.g., by doubling the scan time at otherwise unchanged parameters, the dose will also double. While this may appear trivial, it is not trivial to decide on the level of image quality needed and the implication of this decision on dose.

The two most important image quality features, spatial resolution and image noise, are linked to dose by the following two basic relations:

1. Noise variance changes inversely proportional to the dose *D*.

$$\sigma^2 \propto \frac{1}{D}$$

2. Noise variance changes inversely proportional to the 4th power of the spatial resolution element *d*.

$$\sigma^2 \propto \frac{1}{d^4}$$

The basic message of formula 1 is that low image noise which is desirable in many cases is associated with high dose and vice versa. Dose optimization here means to accept that noise level where diagnosis is still possible, but not to aim for "brilliant, nearly noise-free" images as this would entail unnecessarily high dose. In any case, the noise level will only change slowly with changes in dose; an increase in dose by a factor of 4, for example, will result in a reduction of noise by a factor of 2 only. The effect is demonstrated in Fig. 12.6a–c using a low-contrast phantom comparing low-, medium-, and high-dose acquisition.

The basic message of formula 2 is that noise levels can be influenced much more efficiently by the choice of the resolution level in the images. This depends both on the acquisition and on the image reconstruction parameters. The user can influence it most easily by choosing "smooth," "standard," or "sharp" reconstructions after the scan; the choice will depend on the task. When

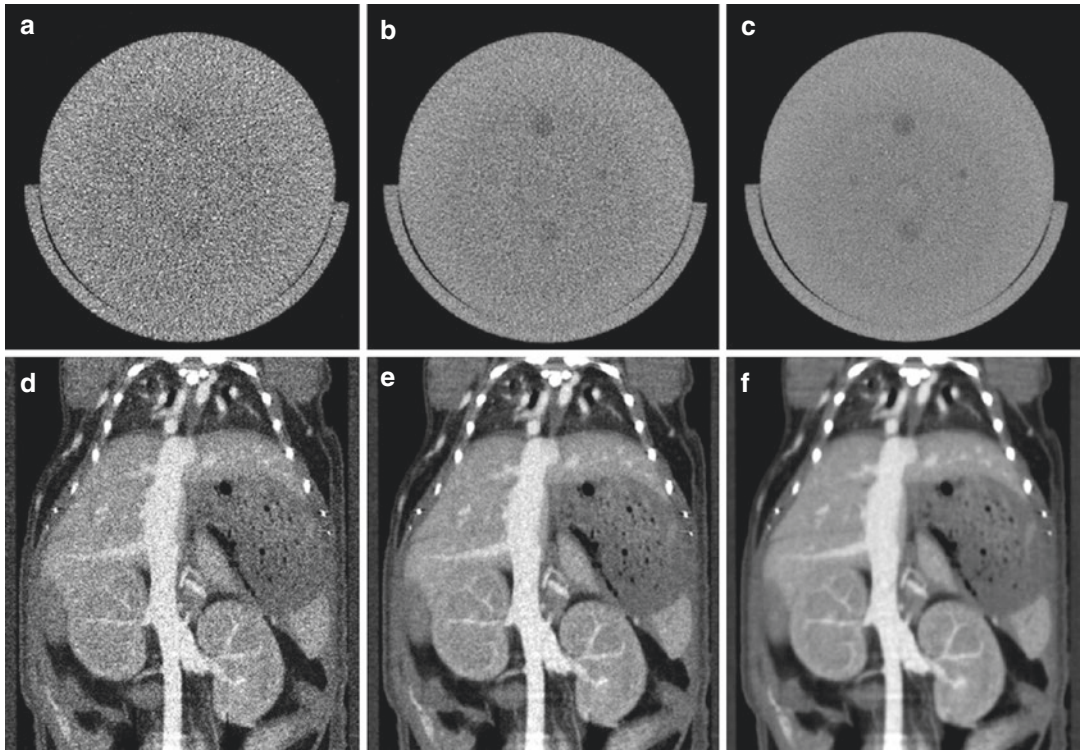

Fig. 12.6 Noise is a function of the dose and of the level of spatial resolution. (**a**–**c**) Noise is reduced when increasing dose as demonstrated by scanning a low-contrast phantom with 18, 55, and 185 mAs at 40 kV. (**d**–**f**) Noise is decreased more efficiently when reconstructing images with softer kernels, however at the expense of reduced spatial resolution

imaging high-contrast structures such as bone or contrast-filled vessels, the signal is high and high resolution is desired. A sharp reconstruction is indicated and the high noise can be tolerated since the contrast is high. When imaging low-contrast structures such as abdominal organs or other soft tissues, the signal is low. To provide an adequate contrast-to-noise ratio for diagnosis, noise has to be kept low. Smoothed images with reduced spatial resolution are appropriate in such cases and preferred to increasing dose. The effect is demonstrated in Fig. 12.6d–f using the data of a single scan reconstructed with sharp, standard, and smooth reconstruction.

There are further possibilities to limit or to reduce dose which, again, are similar to the general radiation protection principles applied in clinical radiology. Most basic is the recommendation to employ x-rays only when there is a clear indication. Repetition of examinations should be limited to the necessary minimum. The examination range should be limited to the field of interest; this simply means, for example, that whole-body examinations should be avoided when only a single organ is of interest. A more difficult topic is the choice of the "optimal" energy as it will depend on the equipment at hand but also on the goal, i.e., the question if soft tissue (density differences), skeletal structures (calcium), or vessels (iodine or other contrast materials) are to be imaged (Kalender et al. 2009). Tube voltages from 40 to 80 kV are indicated as opposed to the tube voltages of 80 to 120 kV used in clinical radiology (Hupfer et al. 2012b).

12.1.4 Advanced Micro-CT Techniques

There are quite a number of CT applications that go beyond the routine tasks of 3D imaging of the anatomy with or without contrast media. The

range of "advanced" applications is wide and not well defined. We will here focus on three topical examples but hope that many more applications will evolve and gain in importance.

12.1.4.1 Dynamic Micro-CT

Static imaging with micro-CT does not always deliver sufficient diagnostic results. Dynamic imaging may be conducted for singular, for example, contrast agent first pass studies, or repeated periodic and nonperiodic events. In the latter case, acquisition can be synchronized with physiological signals, for example, breathing or ECG signals. Tomographic images can then be reconstructed for selected phases of the physiological cycle. In any case temporal resolution of the scanner needs to be high enough to differentiate between phases of a given function.

Although the principle may sound simple, it is a challenge in SAI due to the fact that animal physiology differs from that of humans. Table 12.3 summarizes some of the basic dynamic properties, the breathing and heart rates for humans, rats, and mice. Small animals breathe significantly faster than humans; also their blood circulation and typical heart rates are higher. Both facts mean that in order to acquire "still" images of an animal without motion artifacts, the acquisition system must be able to record views (projections) in time intervals of only a few milliseconds. This is not possible in micro-CT at present.

However, remarkable capabilities for fast and repeated scanning have become available recently. The area detectors which almost all modern micro-CT scanners are equipped with have relatively low frame rates. A high-end scanner equipped with an acquisition system delivering 25 frames (projections) per second can resolve at best 40 ms time intervals of a dynamic cycle. This might be just sufficient to conduct breath synchronization, but is not sufficient for cardiac imaging. Nevertheless, dynamic imaging of contrast medium passage, i.e., the recording of concentration-time curves, is well possible. The assessment of tissue or organ perfusion is one of the goals. Typically temporal resolution of a few seconds would be necessary to conduct such examinations based on the observation of the first pass of a contrast agent in the vascular system. Using a model test setup, it can be shown that temporal resolution is sufficient (Fig. 12.7). In this case, the perfusion model (Fig. 12.7a) was scanned with a dual-source micro-CT of the type shown in Fig. 12.3a with 4 s rotation time and 1.4 s effective scan time per image. Apparently it can match the temporal resolution of fast clinical CT as shown by the arterial concentration curves (Fig. 12.7b). As a result, comparatively cheap clinical contrast agents can be used for micro-CT, allowing for new applications such as tumor angiogenesis imaging (Fig. 12.8).

Table 12.3 Dynamic parameters for humans and small animals

	Human	Rat	Mouse
Breathing rate	12–20 min^{-1}	80–150 min^{-1}	80–150 min^{-1}
Heart rate	60–80 min^{-1}	300–500 min^{-1}	300–800 min^{-1}
Circulation time	6 s	1 s	1 s

12.1.4.2 Dual-Energy CT

In the concept of dual-energy CT (DECT) imaging, the object under investigation is scanned with two different energy spectra, typically by using two different voltage settings and filtration. DECT exploits the dependence of the x-ray attenuation properties of matter on energy; different materials, for example, water (soft tissue) and calcium (bones), exhibit different relationships between x-ray energy and attenuation (Fig. 12.9a). Based on this, images resulting from the two scans can be combined in order to extract additional information about the object composition (Alvarez and Macovski 1976; Kalender et al. 1986). The two scans can either be conducted simultaneously if the scanner is equipped with two tube-detector systems or sequentially one after another with the tube voltage altered between scans. In the near future, new detector technology based on direct-converting photon-counting sensors may allow for dual- or even multiple-energy imaging with only one tube-detector system and one tube voltage. It can furthermore provide the same image quality at

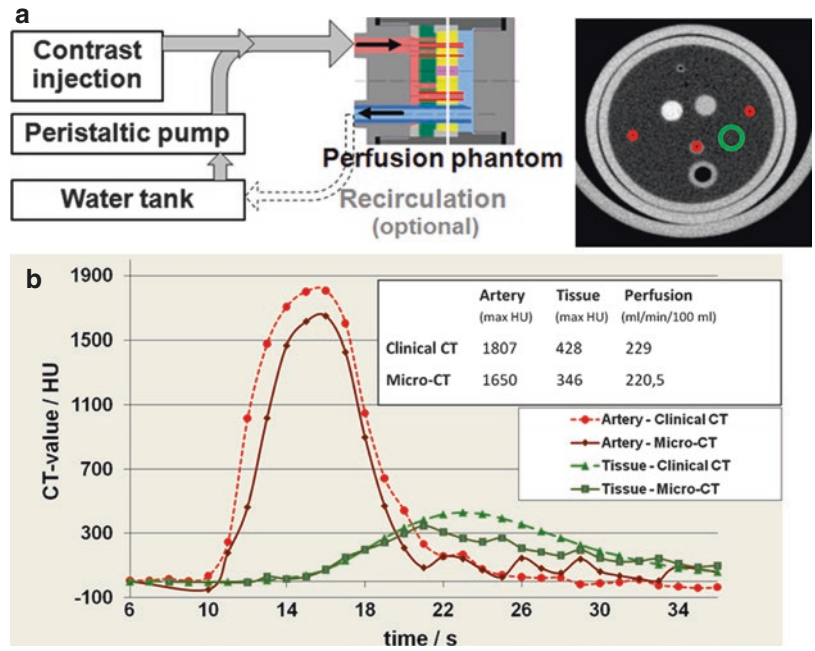

Fig. 12.7 Dynamic micro-CT using fast dual-source micro-CT. A perfusion model (**a**) was used to show that micro-CT can provide information on contrast medium kinetics similar to clinical CT (**b**)

reduced radiation dose due to its higher dose efficiency of almost 100 % (Kalender et al. 2012).

Dual-energy CT is already established in clinical radiology (Flohr et al. 2006; Johnson et al. 2007; Schlomka et al. 2008); micro-CT applications are also under development. Both improved visualization and differentiation of different tissues, such as bone and materials (Fig. 12.9b–d), and possibilities for selective quantification, such as bone mineral independent of the soft tissue and fat marrow components, are of high interest.

12.1.4.3 Image Post-processing and Rendering

The task of "reading" the images and documenting the findings plays an important role and should not be underestimated with respect to the necessary expertise and time required. Quantitative evaluation often necessitates automated evaluation procedures to ensure objective and reproducible results. For example, the quantification of bone mineral density requires the transformation of the measured CT values into BMD values. This can be solved using a calibration phantom simultaneously scanned with the sample or by a calibration performed before or after the sample scan. In addition a segmentation step is required to select the desired analysis volume of interest, for example, the vertebrae or the knee. In order to minimize the effects of noise and partial volume artifacts, 3D segmentation algorithms with local adaptive thresholds should be preferred to global threshold-based segmentation approaches that are often applied slice by slice. Figure 12.10 shows an example of advanced 3D segmentation in which the same algorithm was used for the thin trabeculae in the metaphysis and the thicker ones in the epiphysis.

Visualization in appropriate or, simply, in an adequate and convincing manner is often worth the effort. Different visualization or rendering techniques such as 3D shaded surface displays, maximum intensity projections, volume rendering, and virtual endoscopy are routinely used in clinical radiology and should be considered for SAI using micro-CT. A short introduction to such techniques can be found, for example, in (Kalender 2011). Figure 12.11 shows screenshots of a respective example.

12.1.5 Conclusions and Recommendations

Small-animal imaging using x-rays bears many similarities to imaging humans with respect to the technology and scan approaches but also with respect to the general philosophy. Scanning shall and must not mean an unnecessary burden for the animals.

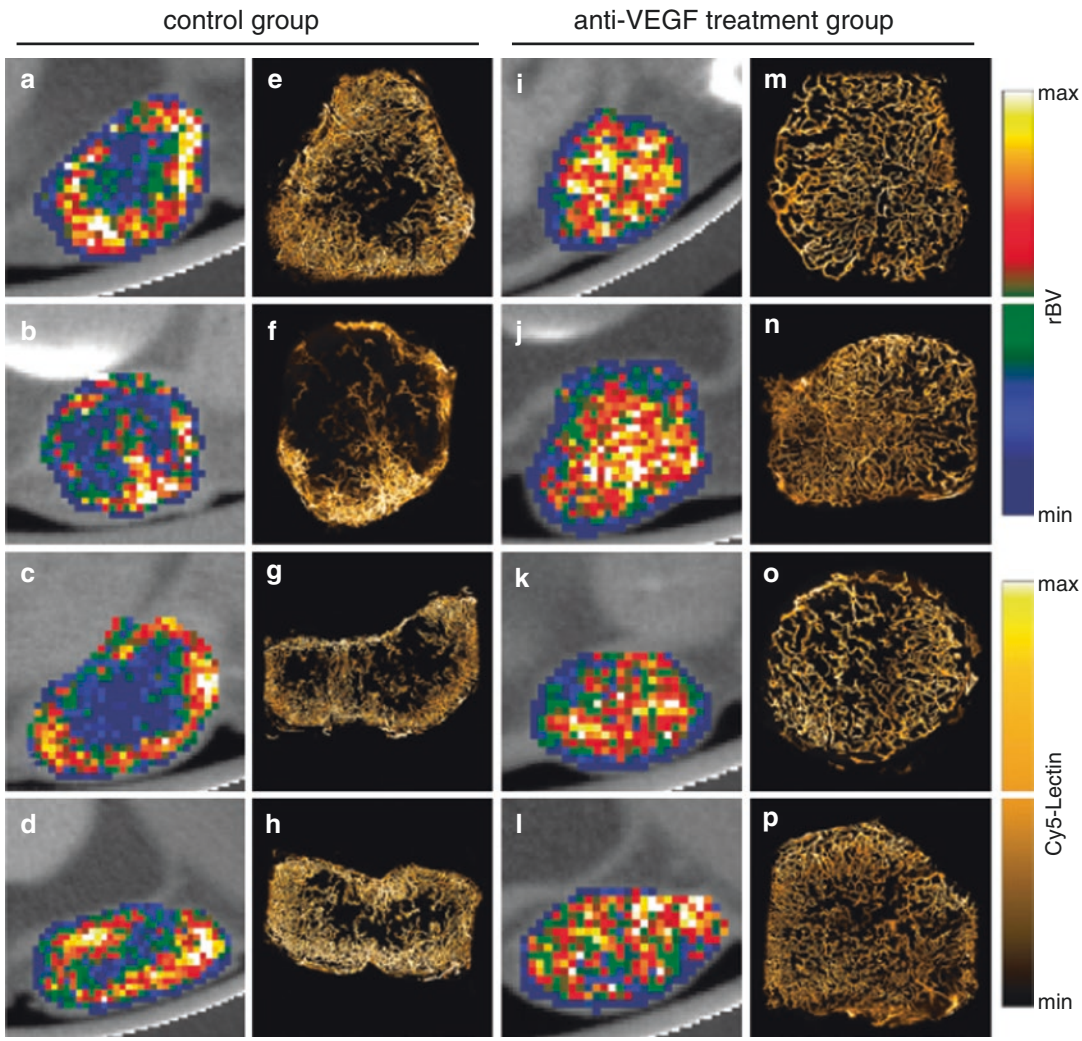

Fig. 12.8 Comparison of physiological relative blood volume maps obtained with in vivo dynamic contrast-enhanced micro-CT with structural vessel maps obtained with ex vivo fluorescence ultramicroscopy for 4 representative tumors of the control (*left panel*) and treatment (*right panel*) groups, respectively. Tumors of the control group revealed fundamentally different spatial relative blood volume patterns (**a**–**d**) than did the tumors of the treatment group (**i**–**l**). Micro-CT maps showed excellent agreement with the corresponding tumor vascular architecture (**e**–**h**, **m**–**p**). (Reprinted with permission from Poeschinger et al. 2014)

Dose values are known! To try and limit levels of organ dose values to below 100 mGy per examination appears to be a possible consensus (Ford et al. 2003; Boone et al. 2004; Kalender 2011). Unless there is good reason, we therefore should not expect or demand spatial resolution much below 100 µm for SAI in view of scan times, noise, and dose. Accordingly the most recent scanner designs are optimized to provide short scan times of about one or only a few minutes at resolution levels just below 100 µm with exposure levels in the range of 10–50 mGy or even below. Depending on the desired low-contrast resolution and the resulting signal-to-noise levels, different settings may be required; higher dose levels have to be accepted in that case.

Advanced techniques, similar to the special applications available in clinical CT, are partly available today and will become more elaborate. Future developments will aim at higher speed, at higher dose efficiency, and, possibly most important, at supporting multimodality imaging.

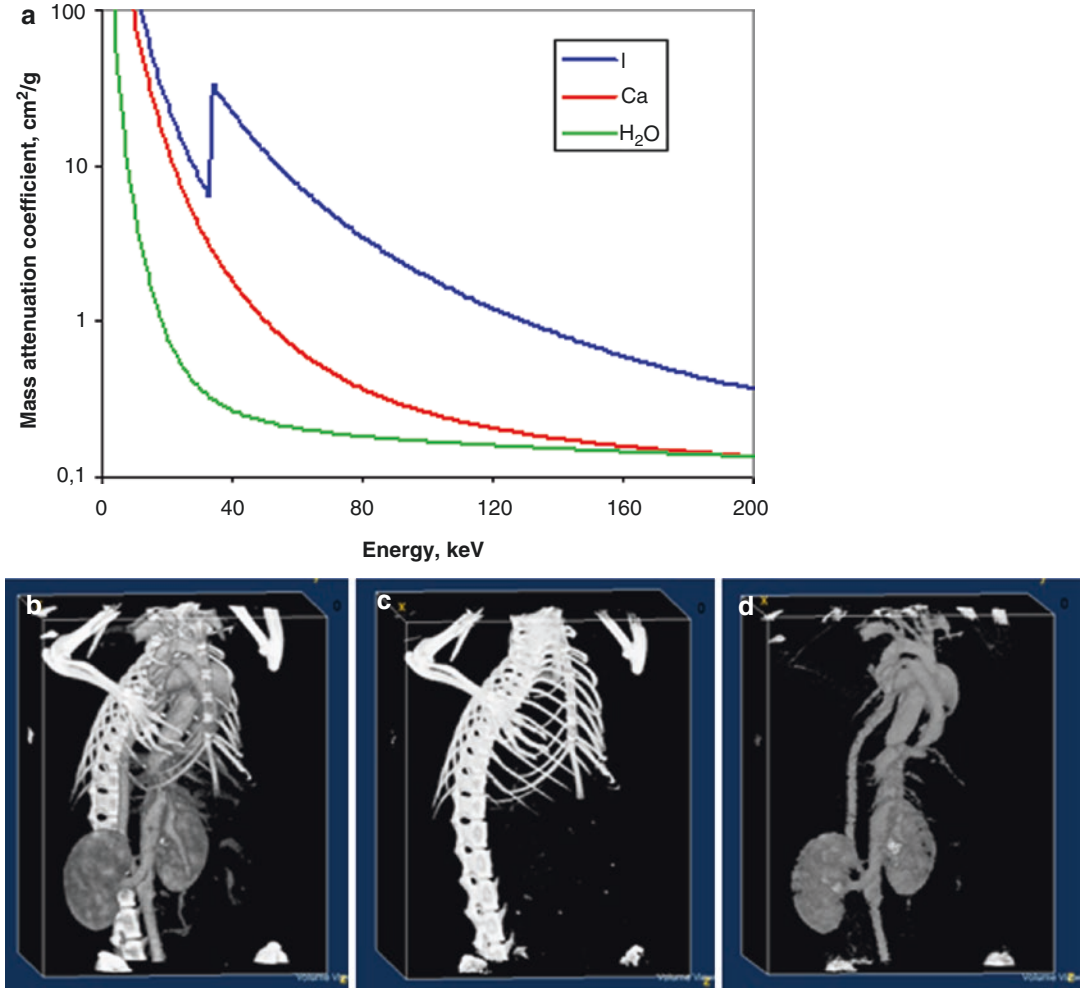

Fig. 12.9 Dual-energy micro-CT. The differences in the energy dependence of different materials (**a**) are exploited by scanning the animal at two different energies. This allows viewing high-atomic-number materials such as calcium and iodine only (**b**) and even to separate these into calcium (**c**) and iodine images (**d**)

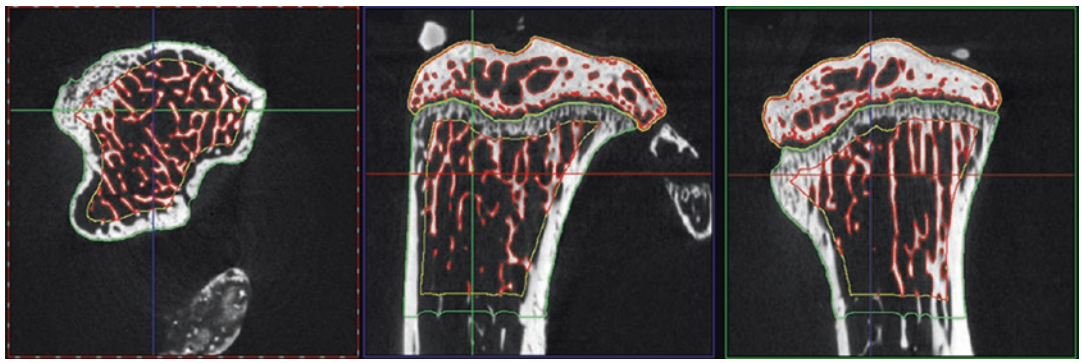

Fig. 12.10 Example for a fully automated analysis of trabecular bone structures of a rat femur scanned by micro-CT (Lu 2011)

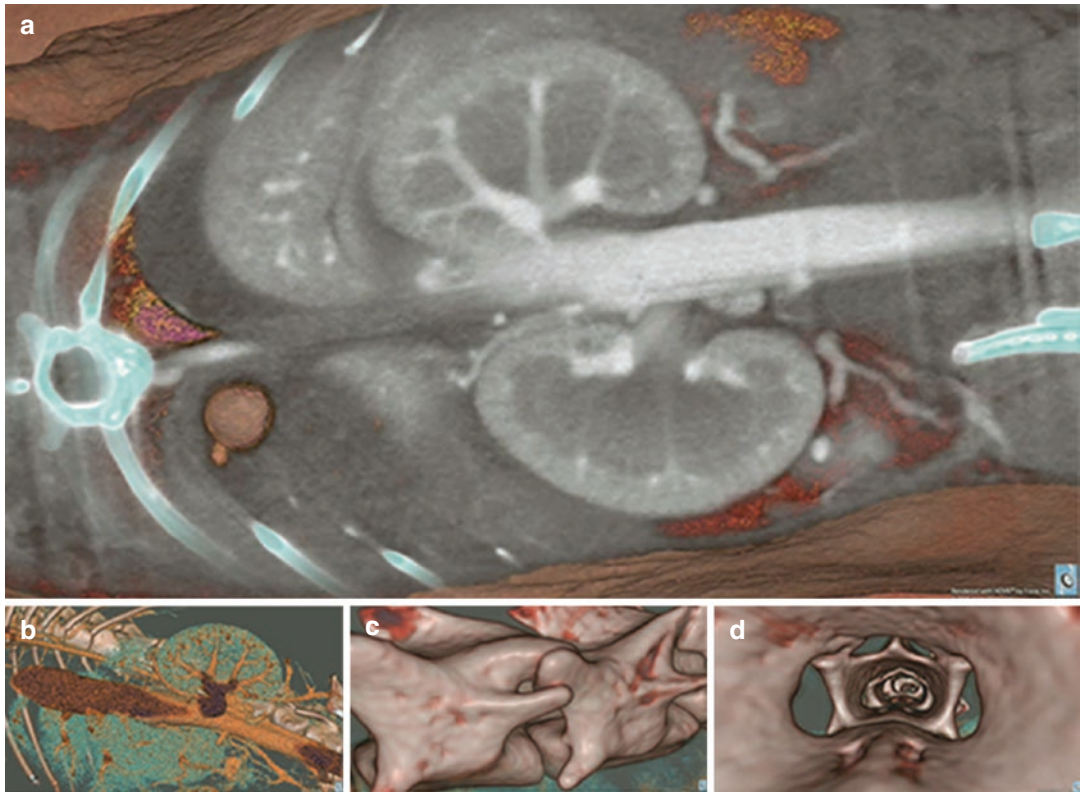

Fig. 12.11 3D data sets can be viewed in arbitrary perspectives and display schemes. (**a**, **b**) Overviews in volume rendering technique. (**c**) Shaded surface display of the spine. (**d**) Virtual flight through the spinal canal

Combination scanning with CT and positron emission tomography or CT and fluorescence imaging are primary examples for this trend.

12.2 CT Contrast Agents

Hubertus Pietsch

12.2.1 Introduction

The contrast in x-ray images is typically produced by attenuation of the x-rays in the examined tissues or samples. Without contrast, only skeletal structures of sacrificed or live animals can be visualized in detail. The transit and accumulation of contrast media (CM) in different organs (enhancement) improve the differentiation of morphological structures, particularly between normal and pathological tissue.

Contrast enhancement for computed tomography (CT) imaging is primarily achieved in practice by the use of water-soluble contrast agents that distribute exclusively in the extracellular fluid (ECF) space. A major problem with these agents, however, is their short duration of contrast enhancement, which has been partially solved by the use of a bolus or continuous bolus infusions in conjunction with rapid-sequence scanning techniques and significant efforts to create agents for opacification of specific organs, such as the liver and spleen.

The CM used for x-ray or micro-CT (μCT) imaging differ in their patterns of biodistribution after intravenous injection. The most suitable classification system for CM is to distinguish between *extracellular fluid CM* (ECF-CM), *vascular space CM* (blood pool enhancement), and *hepatocellular or tissue-specific CM* (Table 12.4).

Table 12.4 Classification of x-ray contrast media for small-animal CT imaging

Iodinated extracellular fluid CM (urographic water-soluble CM)	Vascular space CM (blood pool agent)	Hepatocellular CM (tissue-specific CM)	Gastrointestinal CM
Monomeric nonionic CM	*Macromolecular CM*	*Iodine-containing lipid*	*Iodinated CM*
Iopromide	Dysprosium-DTPA-dextran CM	Iopromide liposomes	Diatrizoate (ionic CM)
Iohexol		Iodixanol liposomes	Iopromide-370 (nonionic CM)
Iopamidol	*Oil emulsions of ethiodol and iodine*	Cholesteryl ioponate	
Ioversol		Polyiodinated triglyceride emulsion (ITG-LE)	*Barium sulfate*
		Fenestra DC	
Iopentol	*Iodine-containing micelles*		
Iomeprol	MPEG-iodolysine micelles		
Iobitridol		*Dysprosium EOB DTPA*	
Ioxilan	*Nanoparticles*		
	Bismuth sulfide polymer coating (BPNP)		
Dimeric nonionic CM	Gold nanoparticles		
Iotrolan			
Iodixanol	*Liposomal encapsulation of iodinated CM*		
	Polyethylene glycol-coated (PEG) iopromide liposomes		
	PEG iohexol liposomes		
	Lipid mixture with iodixanol		
	Polyiodinated triglyceride emulsion (ITG-LE)		
	Fenestra VC		

Furthermore, with oral administration of contrast agents such as iodine or barium, the gastrointestinal tract can be visualized (*gastrointestinal CM*).

12.2.2 X-Ray Contrast Media for Small-Animal Imaging

12.2.2.1 Iodinated Extracellular CM

Iodinated extracellular CM are either negatively charged ionic molecules (e.g., diatrizoate) or nonionic molecules (e.g., iopromide, iomeprol, and iodixanol). In this review, we will only discuss nonionic iodinated contrast agents (low-osmolar CM), which were introduced more than 20 years ago and have become standard contrast agents in clinical CT.

Nonionic CM can be divided into two classes with regard to their chemical structures: nonionic monomers and nonionic dimers. All of these agents are based on a benzene ring with three iodine atoms attached (2,4,6-triiodobenzoic acid). The monomers contain one tri-iodinated benzene ring, while the dimers contain two tri-iodinated benzene rings. The benzene ring of nonionic CM lacks an ionizable carboxyl group and is made soluble by including several hydrophilic groups as side chains. Furthermore, the carboxyl group is reacted with an amine to make the molecules electrically neutral in solution. Both monomeric and dimeric nonionic compounds are low-osmolar CM. The nonionic monomers have an osmolality that is almost twice that of plasma, and the ratio between the number of iodine atoms and the number of

particles in the solution is 3:1. The nonionic dimers are iso-osmolar with plasma (300 mOsm/kg) and are present in a 6:1 ratio.

Comparison of Properties Among Nonionic Contrast Media

Nonionic CM differ from one another with regard to important physicochemical properties, including water solubility, viscosity, osmolality, and electrical charge.

The *water solubility* of these contrast agents must be very good as highly concentrated CM solutions are used; for example, up to 800 mL is a typical dose of iopamidol or iopromide administered in adults, the equivalent of approximately 240 g of iodine (Rau et al. 1997; Rosovsky et al. 1996). As with sugars or peptides, the solubility of nonionic CM is mediated by hydrolytic groups (–OH, –CONH–).

Viscosity is a measure of the flow properties of solutions depending on temperature and is measured as millipascals per second. It increases with both higher CM concentrations and falling temperature. The viscosities of the various CM are different at the same iodine concentration and temperature.

The viscosity of a contrast medium is of considerable practical importance. When thin-bore needles, cannulae, and catheters are used, high-viscosity preparations can only be administered with considerable effort. Rapid administration of large volumes, as is necessary in μCT, and injection through thin-bore cannulae and catheters are greatly facilitated by the use of low-viscosity CM such as iopromide. When prewarmed to body temperature, the viscosity of CM further decreases (Krause 1994; Hughes and Bisset 1991).

The osmotic pressure of a solution is determined by the concentration of dissolved particles. Normally, osmotic pressure is calculated in the unit *osmolality*, which describes the concentration of solute (osmoles) per kg of water (mOsm/kg H_2O). The osmolality of CM depends mainly on the concentration and only slightly on the temperature, and different CM can display greatly divergent osmolalities at the same concentration.

Greater tolerability of low-osmolality agents has been demonstrated in many animal experiments and several clinical studies. The low osmolality causes less pain at the injection site and reduced heat sensation during power injection (Kim et al. 1990). Furthermore, hemodynamic and cardiovascular changes such as vasodilatation, bradycardia, and pulmonary hypertension are greatly reduced. At comparable iodine concentrations, the nonionic monomers (low-osmolar CM) have in vitro a lower viscosity but a higher osmolality compared with nonionic dimeric CM (iso-osmolar CM) (Fig. 12.12). A rise of the iodine concentration of CM solution increases exponentially its viscosity (Jost et al. 2010).

12.2.2.2 Vascular Space CM: Blood Pool Imaging Agents

For μCT, a concentration of intravascular CM that enables the enhancement of 50–60 Hounsfield units (HU) over a period of at least 15 min would be desirable to allow efficient blood pool imaging, which would be especially useful for imaging of cardiovascular diseases (e.g., stenosis, ischemia, atherosclerosis, capillary permeability, and neovascularity).

Three points seem to be necessary for a blood pool contrast agent:

1. The size of the CM molecules must be larger than the capillary fenestrations.
2. Phagocytosis by the RES should be avoided as long as possible.
3. A radiopaque moiety must be structurally incorporated within the particle.

There are two different methods used to ensure the prolonged circulation of imaging agents in an effort to make them suitable for blood (vascular) imaging. The first uses in vivo labeling of blood cells or plasma components with diagnostic labels, while the second uses synthetic *macromolecules*, *colloidal solutions,* and/or *liposomes* carrying diagnostic labels.

Macromolecules include proteins (e.g., bovine serum albumin), synthetic polypeptides (e.g., dextran), or polyamino acids (e.g., poly L-lysine).

By the middle of the 1900s, however, methods for modifying liposome surfaces were introduced, resulting in *liposomes* that could avoid the

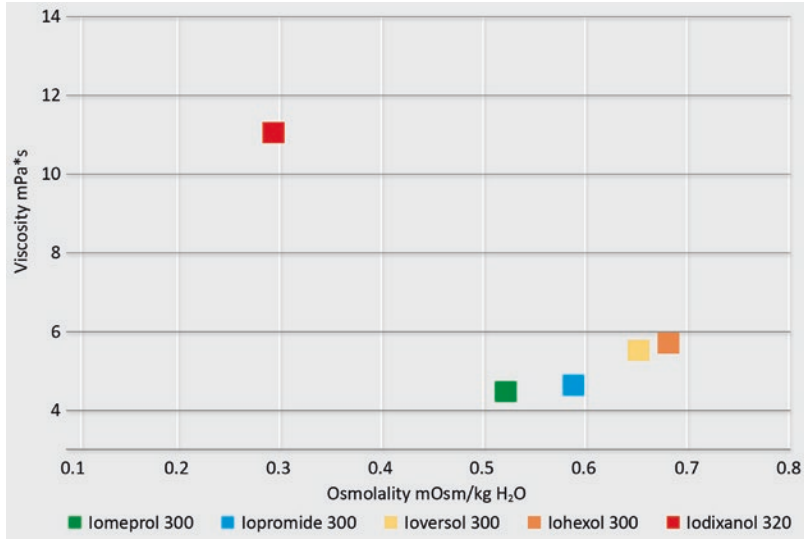

Fig. 12.12 Osmolality and viscosity of nonionic monomeric CA (iomeprol, iopromide, ioversol, iohexol) and nonionic dimeric CA (iodixanol) as formulated for injections into humans or animals

RES for prolonged periods of time (Allen 1994; Senior 1987). The half-life of conventional liposomes in the blood stream after intravenous application can be increased as follows:

1. A reduction in liposome size to below 100 nm
2. An increase in cholesterol content in the capsule
3. The use of saturated (gel-state) phospholipids
4. The use of uncharged lipids
5. The use of higher liposome doses

Alternatively, the surfaces of liposomes can be altered by the inclusion of glycolipids (e.g., monosialoganglioside GM) or polymers (typically polyethylene glycol (PEG)). This alteration results in a sterically stabilized liposome with a more hydrophilic surface that is less able to bind plasma opsonins, resulting in decreased RES uptake and a prolonged circulation half-life (Allen 1994).

Surface-modified liposomes are able to avoid the mononuclear phagocytic system (MPS), thus allowing targeting to non-MPS organs. Furthermore, the inclusion of lipid derivates of PEG in the liposome membrane has been shown to very potently increase the liposomal circulation times of iohexol, liposomes, and iopromide (Koa et al. 2003; Sachse et al. 1997).

For μCT imaging, a new family of CM has been developed. The Fenestra family is comprised of iodinated lipids that provide contrast enhancement integrated into a novel oil-in-water lipid emulsion.

Fenestra VC, a 20 % (wt/ol) oil-in-water lipid emulsion formulation containing an iodinated triglyceride (glyceryl-2-oleoyl-1,3-di-7-(3-amino-2,4,6-triiodophenyl)-hepanoate) (ITG-DHOG), provides prolonged vascular contrast for the visualization of cardiac, abdominal, tumor, and peripheral vasculature.

It is hepatotropic and is taken up by hepatocytes via an energy-dependent and ApoE receptor-mediated pathway. The surface of the vehicle is modified by the addition of methoxy-polyethylene glycol 1-2-distearyl phosphatidyl-ethanolamine, which enables long-lasting blood pool contrast enhancement. The formulation is iso-osmolar with plasma and has a particle size of 150 nm and an iodine concentration of 50 mg/mL (Choukèr et al. 2008).

12.2.2.3 Hepatocellular CM

A number of approaches have been investigated in an effort to identify radiopaque imaging agents that selectively accumulate in the liver and spleen. These include, among others, radiopaque liposomes, polyiodinated triglyceride, and metal

complexes of EOB DTPA such as the dysprosium complex.

In the 1990s, various preparation methods for liposomes carrying CT radiopaque molecules were available, which allowed iodine encapsulation with efficiencies up to 50 % and corresponding encapsulated iodine-to-lipid ratios (mg/mg) between 0.4 and 4.7. Liposomes with narrow size ranges and maximum particle sizes well below 5 m can be produced with these methods. When injected intravenously, these particles are rapidly taken up by macrophages localized in the liver, spleen, and bone marrow. In various animal experiments, liver opacification with density increases at or above 50 ΔHU has been demonstrated, allowing the delineation of small focal lesions (Seltzer et al. 1988).

An *iodinated triglyceride emulsion* (IT-LE) packed into the lipophilic core of a synthetic chylomicron remnant has been described by Bakan. This emulsion can be used to image the liver parenchyma as it is internalized by the hepatocytes, whereas liver tumor cells have less functional lipoprotein receptors and, therefore, show little enhancement.

Fenestra LC contrast medium contains the emulsion described by Bakan and provides extended hepatobiliary contrast enhancement, which is useful for the visualization of abdominal anatomy and function. It is comprised of iodinated lipids that provide contrast enhancement and a novel oil–water lipid emulsion that serves as a hepatocyte-selective delivery system. This formulation in a synthetic oil-in-water lipid emulsion particle resembles a chylomicron remnant, which helps in selective localization of the lipids to various sites within the body.

Fenestra LC, properly termed 1,3-bis-[7-(3-amino-2,4,6-triiodophenyl)-heptanoyl]-2-oleoyl glycerol (DHOG), is a commercially available hepatocyte-selective iodinated contrast medium for preclinical use only. Its structure and particle size of 90–180 nm are similar to endogenous chylomicron remnants (75–400 nm), allowing for fast receptor-mediated uptake in the liver. DHOG is supplied as an opaque solution at a concentration of 50 mg I/mL. Furthermore, it is iso-osmotic with plasma at 300–350 mOsm/kg and has a viscosity of 3–4 cP at 37 °C (Choukèr et al. 2008).

12.2.3 Pharmacokinetic Properties of CM for X-Ray or µCT

The CM used for x-ray and CT imaging differ in their pharmacokinetic behaviors and patterns of distribution following intravenous injection.

12.2.3.1 Iodinated Extracellular CM

High water solubility, low distribution coefficients between butanol and buffer, and low binding to plasma proteins (<5 %) are all properties of nonionic ECF-CM that contribute to their pharmacokinetic behavior, enabling them to be rapidly cleared from the blood within minutes following intravenous injection. The first pass of the CM with the highest vascular contrast is only retained for approximately 3 min. Following intravenous administration, nonionic CM are rapidly distributed between the vascular and interstitial spaces with a distribution half-life of about 25 min. They are then cleared from the blood with an elimination half-life of about 20 min. in rats and excreted without tubular reabsorption or secretion, mainly via glomerular filtration.

In patients with normal renal function, the extrarenal elimination of ECF-CM is minimal (<2 %). These agents are not metabolized after intravenous injection (Krause 1994).

The pharmacokinetic behavior of nonionic CM after intravenous injection in small animals is comparable to that seen in human patients.

After intravenous injection of ^{125}I-labeled iopromide (60 mg I/kg body weight) in rats, 82 % of the dose is excreted via the kidneys within 3 h, and the elimination half-life in the blood and urine is about 20 min. In rats, about 90 % of the dose is recovered from the urine and 10 % from the feces, regardless of the dose administered (Mützel et al. 1983).

Hydrophilicity prevents ECF-CM from crossing cell membranes. After oral or intraduodenal administration of ^{125}I-labeled iopromide to rats, less than 2 % of the dose is absorbed (Mützel et al. 1983).

12.2.3.2 Vascular Space CM: Blood Pool Imaging Agents

CM that remain in the vasculature with adequate enhancement for at least 15 min are called blood pool contrast agents.

A number of different approaches have been taken to produce longer-lasting blood pool contrast agents for CT. Some important examples include:

- Water-soluble *macromolecular agents such as dysprosium-DTPA-dextran*, which have shown blood pool contrast enhancement for up to 45 min in rabbits (Vera and Mattrey 2002)
- *Iodinated oil emulsions of ethiodol*, which remain intravascular for 20 min after injection in phantom studies of excised canine hearts and in rabbits (Cassel et al. 1982)
- Iodine-substituted *poly*-l-*lysine* micelles (*MPEGiodolysine*), which cause noticeable enhancement in the blood, liver, and spleen for more than 3 h following intravenous injection into rats (Torchilin et al. 1999)
- *Nanoparticles*, which can act as blood pool CT-CM (e.g., *nanosized bismuth sulfide with a polymer coating (BPNP)* and *gold nanoparticles*)

Rabin et al. (2006) described a *polymer-coated* Bi_2S_3 with excellent stability at high concentrations (0.25 M Bi^{3+}) and high x-ray absorption at fivefold greater than iodine. After intravenous administration of 250 I, BPNPs are distributed with a half-life of 140 ± 15 min in mice. Delayed imaging at 12–24 h after injection shows that the BPNPs are distributed to organs containing phagocytic cells (e.g., the liver, spleen, and lymph nodes). For example, in one study, the liver signal intensity increased from −22 ± 77 to 740 ± 210 HU at 24 h (Rabin et al. 2006). This enhancement likely reflects the uptake of BPNPs into Kupffer cells and hepatocytes.

Animal studies have demonstrated that *gold nanoparticles* (250 gold atoms per molecule) are useful as x-ray contrast agents. Gold provides about 2.7 times greater contrast per unit weight than iodine, and its greater absorption of x-rays in comparison with iodine enables good contrast at lower x-ray doses.

Gold nanoparticles (1.9 nm in diameter) have been injected intravenously into mice at a concentration of 270 mg Au/cm^3 and a volume of 0.01 mL/g. In this experiment, the blood gold concentration decreased in a biphasic manner with a 50 % drop between 2 and 10 min, followed by a slower decrease by another 50 % between 15 min and 1.4 h. The highest tissue gold concentration 15 min after injection was in the kidney (10.60 ± 0.2 % of the injected dose per gram of measured tissue). Whole-body gold clearance was 77.5 ± 0.4 % of the total injected after 5 h, and retention in the liver and spleen was minimal with elimination via the kidneys (Fig. 12.13).

Given that CT *liposomes* with extended circulation times may be useful as blood pool (vascular) imaging agents, some groups have evaluated the imaging properties of various surface-modified, contrast-carrying liposomes (Sachse et al. 1997; Schmiedl et al. 1999).

In a study by Sachse et al., conventional and surface-modified liposomes containing the nonionic monomeric CM iopromide were tested as potential blood pool agents. In a biodistribution study using rats, no significant differences in blood concentration were found 1 h after injection between two different *PEG coating agents* (DSPE-PEG2000- or CHHS-PEG2000) and unmodified conventional liposomes at a dose of 250 mg total I/kg body weight (approximately 500 mg total lipid/kg). At 4 h after injection, however, the DSPE-PEG liposomes displayed a significantly higher blood level compared to the other liposome formulations, amounting to approximately 28 % of the dose (1.1 mgI/g wet weight) compared to 16 % for the unmodified liposomes (Fig. 12.14).

The new pool-selective emulsion (ITG-PEG) CM, including Fenestra VC, differ from the previous approaches in that their mean particle size is less than 150 nm in diameter. Furthermore, they remain in the blood for several hours after injection and are cleared within 24 h.

Ford et al. and Graham et al. investigated the pharmacokinetic behavior of *Fenestra VC* (concentration 50 mg I/mL) in mice. After a single injected dose of 0.5 mg I/g body weight, the peak enhancement in the right ventricle and vena cava occurred at 0.25 h, providing an

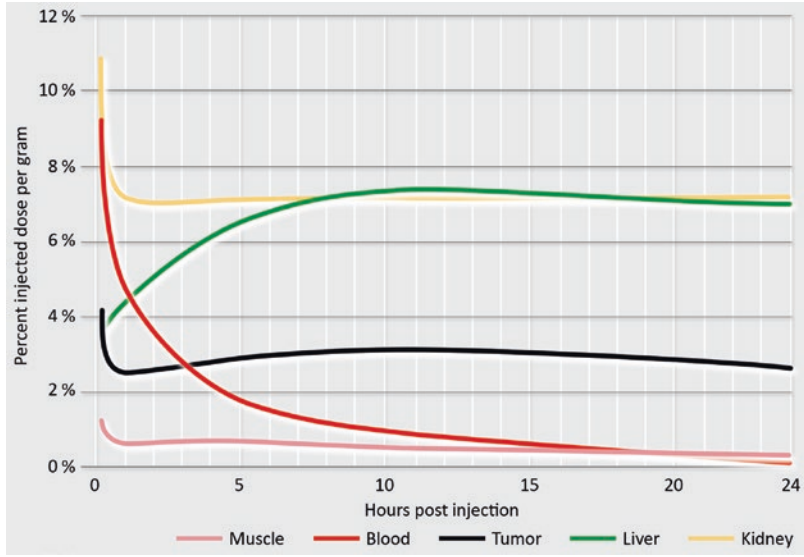

Fig. 12.13 Pharmacokinetic data for the biodistribution of gold in mice following intravenous injection of 0.2 mL gold nanoparticles (percent injected dose per gram in the blood, kidneys, liver, muscle, and tumor over a 24 h period) (Hainfeld et al. 2006)

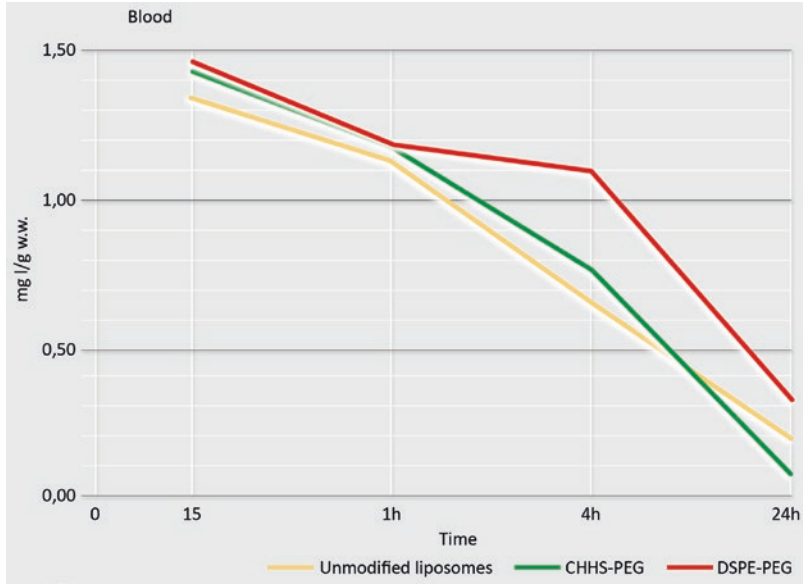

Fig. 12.14 Biodistribution of unmodified and modified iopromide liposomes in the blood of rats at a dose of 250 mg total I/kg body weight. Data are the mean values from four animals (Sachse et al. 1997)

enhancement of 340 HU over the baseline values. This vascular enhancement persisted for 2–4 h after injection before returning to near baseline values by 24 h after injection. The half-life in blood was approximately 8 h. When the PEG moieties were eliminated from these particles, the formulation was eliminated by the hepatobiliary system. Subsequent enhancement occurred in the liver (290 HU over baseline) and spleen (410 HU over baseline) at 24 h after injection (Ford et al. 2006). Fenestra requires 48 h to be cleared; however, some researchers have observed spleen enhancement weeks after a single injection (Fig. 12.15).

12.2.3.3 Hepatocellular CM

In this section, we will only describe liposomes and an iodinated triglyceride emulsion as they have been most successful as hepatocyte-selective CM for CT.

After intravenous injection, *liposomes* are mainly taken up by the phagocytic cells of the RES, which is comprised of circulating blood macrophages and localized macrophages in the

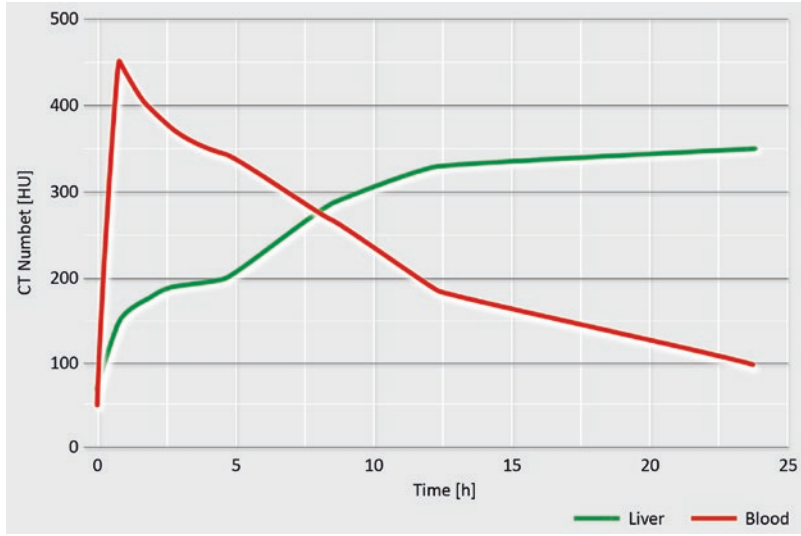

Fig. 12.15 Fenestra VC is cleared from the blood into the liver parenchyma with equal enhancement of the blood and liver after injection at a dose of 0.015 mL/g body weight (0.75 mg I/g body weight) in mice (Graham et al. 2008)

liver (Kupffer cells), spleen, and bone marrow. This biodistribution pattern can be used for passive targeting of the liver and spleen as they are the main sites of liposome uptake (Poste 1983).

Liposome uptake can be increased by the incorporation of negatively charged lipids (e.g., phosphatidic acid, phosphatidyl glycerol, and phosphatidyl serine), the effects of which are more pronounced for smaller liposomes (Senior 1987).

The incorporation of cholesterol into the liposome membrane results in increased plasma stability, prolonged blood circulation, and decreased intracellular degradation.

The organ distribution of liposomes is a function of liposome dose, which is reflected by reduced liver uptake at higher doses and seems to be due to saturation of the endocytotic uptake mechanism into Kupffer cells (Senior 1987).

In one study, iopromide-carrying liposomes with a diameter of approximately 0.5 m and an encapsulation efficiency ranging from 30 to 40 % showed dose-dependent pharmacokinetics in rats after an intravenous injection. The terminal half-life in blood increased from 0.8 h for a 250 mg I/kg dose to 2.9 h for a 1,000 mg I/kg dose. The elimination of iodine occurred mainly via renal clearance and was complete within 7 days. Liver enhancement was observed at a dose of 200 mg I/kg, which is equivalent to the clinically relevant value of 30 HU (Krause et al. 1993).

After intravenous injection of *Fenestra LC, an iodinated triglyceride emulsion,* it distributes to the vasculature of the liver and passes through the endothelial fenestrations into the space of Disse. There it binds to the apoE receptor on hepatocytes and is subsequently internalized into these cells and excreted via the biliary system.

In one study, a dose of 1 g I/kg body weight was injected intravenously into mice. The liver showed steadily increasing enhancement with a peak enhancement of 300 % at 300 min postinjection compared to the baseline value. At 48 h post injection, the enhancement was still at 50 %. The contrast agent then underwent primary elimination via biliary excretion (Fig. 12.16) (Henning et al. 2008).

12.2.4 Indications for CM Used for X-Ray and μCT Imaging

There are numerous applications for x-ray CM in small-animal CT (Table 12.5), including the characterization of structures, vessels (e.g., tumor vascularization), tumors, and soft tissue morphology and function. Nonionic, extracellular, water-soluble agents are generally applied in CT, primarily due to their relative safety and availability. A major problem with these agents, however, is their short duration of contrast

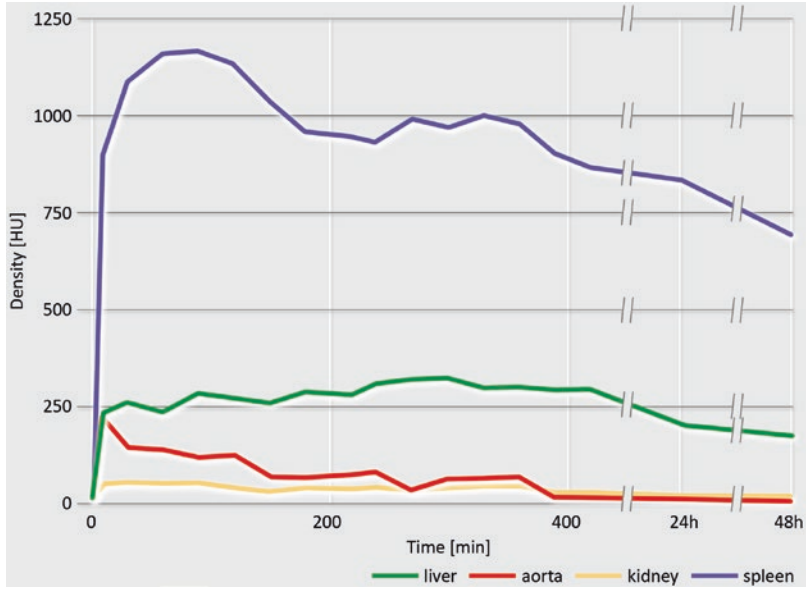

Fig. 12.16 Organ densities of the liver, aorta, spleen, and kidney parenchyma in Hounsfield units measured before and at various points after intravenous injection of Fenestra LC at a dose of 1 g I/kg body weight in mice (Henning et al. 2008)

Table 12.5 Overview of the applications of contrast media in CT after intravenous administration in small animals

Contrast medium	Application
Extracellular fluid CM	Head imaging for stroke assessment (perfusion CT, CT angiography)
	Heart imaging
	Abdomen imaging (kidney, urinary tract)
	Liver imaging (tumor detection)
	Angiography (alternative to catheter angiography)
Vascular space CM (blood pool CM)	Tumor imaging
	Early detection of tumors by angiogenesis
	Cardiovascular imaging
	Myocardial infarction
	Imaging of structural and functional abnormities, including thrombi and atherosclerotic lesions
Hepatocellular or tissue-specific CM	Liver imaging
	Detection of focal liver lesions
	Tumor characterization
	Hepatic parenchyma imaging

enhancement. This problem has been partially solved by using bolus injections or bolus infusions of CM in conjunction with rapid-sequence scanning techniques. In addition, many agents have been generated for specific opacification of the blood pool, liver, and spleen. Blood pool imaging can aid in the detection of structural and functional abnormalities such as those caused by thrombi or atherosclerotic lesions. Furthermore, it would be of particular interest to evaluate the current state of blood flow and investigate irregularities caused by pathological changes.

The combined use of μCT and hepatocellular CM allows for detailed noninvasive imaging of hepatic tumors, the hepatic parenchyma, and other liver lesions that in the past would have required euthanization of the animal or placement of the tumor in a flank location or someplace other than the liver.

References

X-Ray and X-Ray-CT

Almajdub M, Magnier L, Juillard L, Janier M. Kidney volume quantification using contrast-enhanced in vivo X-ray micro-CT in mice. Contrast Media Mol Imaging. 2008;3(3):120–6.

Alvarez RE, Macovski A. Energy-selective reconstructions in x-ray computerized tomography. Phys Med Biol. 1976;21(5):733–44.

Badea CT, Hedlund LW, Lin MD, Boslego Mackel JF, Johnson GA. Tumor imaging in small animals with a combined micro-CT/micro-DSA system using iodinated conventional and blood pool contrast agents. Contrast Media Mol Imaging. 2006;1(4): 153–64.

Badea CT, Drangova M, Holdsworth DW, Johnson GA. In vivo small-animal imaging using micro-CT and digital subtraction angiography. Phys Med Biol. 2008; 53(19):R19–50.

Bartling SH, Stiller W, Semmler W, Kiessling F. Small animal computed tomography imaging. Curr Med Imaging Rev. 2007;3:45–59.

Boone J, Velazquez O, Cherry SR. Small-animal X-ray dose from micro-CT. Mol Imaging. 2004;3(3): 149–58.

Deak P, van Straten M, Shrimpton PC, Zankl M, Kalender WA. Validation of a Monte Carlo tool for patient-specific dose simulations in multi-slice computed tomography. Eur Radiol. 2008;18:759–72.

Del Guerra A, Belcari N, Llacer GL, Marcatili S, Moehrs S, Panetta D. Advanced radiation measurements techniques in diagnostic radiology and molecular imaging. Radiat Prot Dosim. 2008;131(1):136–42.

Ehling J, Theek B, Gremse F, Baetke S, Moeckel D, Maynard J, Ricketts S, Gruell H, Neeman M, Knuechel R, Lederle W, Kiessling F, Lammers T. Micro-CT imaging of tumor angiogenesis: quantitative measures describing micromorphology and vascularization. Am J Pathol. 2014;184(2):94–108.

Engelke K, Prevrhal S, Genant HK. Macro and micro imaging of bone architecture. In: Bilezikian J, Raisz L, Martin TJ, editors. Principles of bone biology, 3rd ed. vol. II:1905–1942. Academic Press; 2008.

Flohr T, McCollough CH, Bruder H, et al. First performance evaluation of a dual-source CT (DSCT) system. Eur Radiol. 2006;16:256–68.

Ford NL, Thornton MM, Holdsworth DW. Fundamental image quality limits for microcomputed tomography in small animals. Med Phys. 2003;30(11):2869–77.

Holdsworth DW, Thornton MM. Micro-CT in small animal and specimen imaging. Trends Biotechnol. 2002;20(8):S34–9.

Hupfer M, Kolditz D, Nowak T, Eisa F, Brauweiler R, Kalender WA. Dosimetry concepts for scanner quality assurance and tissue dose assessment in micro-CT. Med Phys. 2012a;39(2):658–70.

Hupfer M, Nowak T, Brauweiler R, Eisa F, Kalender WA. Spectral optimization for micro-CT. Med Phys. 2012b;39(6):3229–39.

Johnson TRC, Krauß B, Sedlmair M, et al. Material differentiation by dual energy CT: initial experience. Eur Radiol. 2007;17:1510–7.

Jost G, Pietsch H, Lengsfeld P, Hütter J, Sieber MA. The impact of the viscosity and osmolality of iodine contrast agents on renal elimination. Invest Radiol. 2010;45(5):255–61.

Kalender WA, Perman WH, Vetter JR, Klotz E. Evaluation of a prototype dual-energy computed tomographic apparatus. I. Phantom studies. Med Phys. 1986;13(3): 334–9.

Kalender WA, Deak P, Kellermeier M, Van Straten M, Vollmar S. Application- and patient size-dependent optimization of x-ray spectra for CT. Med Phys. 2009;36(3):993–1007.

Kalender WA. Computed tomography. Fundamentals, system technology, image quality, applications. 3rd ed. Erlangen: Publicis; 2011.

Kalender WA, Beister M, Boone JM, Kolditz D, Vollmar SV, Weigel MCC. High-resolution spiral CT of the breast at very low dose: concept and feasibility considerations. Eur Radiol. 2012;22(1):1–8.

Kastl S, Sommer T, Klein W, Hohenberger W, Engelke K. Accuracy and precision of bone mineral density and bone mineral content in excised rat humeri using fan beam dual-energy X-ray absorptiometry. Bone. 2002;30(1):243–6.

Libouban H, Simon Y, Silve C, et al. Comparison of pencil-, fan-, and cone-beam dual X-ray absorptiometers for evaluation of bone mineral content in excised rat bone. J Clin Densitom. 2002;5(4):355–61.

Lu J. Advanced methods for the quantification of trabecular bone structure and density in micro computed tomography. ed. Institute of Medizin. Physik der FAU Erlangen-Nürnberg vol. 20, Shaker Verlag, Aachen 2011.

Nazarian A, Cory E, Muller R, Snyder BD. Shortcomings of DXA to assess changes in bone tissue density and microstructure induced by metabolic bone diseases in rat models. Osteoporos Int. 2009;20(1):123–32.

Paulus MJ, Gleason SS, Kennel SJ, Hunsicker PR, Johnson DK. High resolution X-ray computed tomography: an emerging tool for small animal cancer research. Neoplasia. 2000;2(1–2):62–70.

Poeschinger T, Renner A, Eisa F, Dobosz M, Strobel S, Weber TG, Brauweiler R, Kalender WA, Scheuer W. Dynamic contrast-enhanced micro computed tomography correlates with 3-dimensional fluorescence ultramicroscopy in antiangiogenic therapy of breast cancer xenografts. Invest Radiol. 2014;49(7): 445–56.

Ritman EL. Micro-computed tomography - current status and development. Annu Rev Biomed Eng. 2004;6: 185–208.

Schlomka JP, Roessl E, Dorscheid R, et al. Experimental feasibility of multi-energy photon-counting K-edge imaging in preclinical computed tomography. Phys Med Biol. 2008;53(15):4031–47.

Soon G, Quintin A, Scalfo F, et al. PIXImus bone densitometer and associated technical measurement issues of skeletal growth in the young rat. Calcif Tissue Int. 2006;78(3):186–92.

UNSCEAR. Annex D: medical radiation exposures. New York: United Nations Publications; 2000.

CT Contrast Agents

Allen TM. The use of glycolipids and hydrophilic polymers in avoiding rapid uptake of liposomes by mononuclear phagocyte system. Adv Drug Deliv Rev. 1994;13:285–309.

Bakan DA, Doerr-Stevens JK, Weichert JP, et al. Imaging efficacy of a hepatocyte-selective polyiodinated triglyceride for contrast-enhanced computed tomography. Am J Ther. 2001;8:359–65.

Cassel DM, Young SW, Brody WR, et al. Radiographic blood pool contrast agents for vascular and tumor imaging with projection radiography and computed tomography. J Comput Assist Tomogr. 1982;6(1):141–6.

Choukèr A, Lizak M, Schimel D, et al. Comparison of Fenestra VC contrast-enhanced computed tomography imaging with gadopentetate dimeglumine and Ferucarbotran magnetic resonance imaging for the in vivo evaluation of murine liver damage after ischemia and reperfusion. Invest Radiol. 2008;43:77–91.

Ford NL, Graham KC, Groom AC, et al. Time-course characterization of the computed tomography contrast enhancement of an iodinated blood-pool contrast agent in mice using a volumetric flat-panel equipped computed tomography scanner. Invest Radiol. 2006;41(4):384–90.

Graham KC, Ford NL, MacKenzie LT, et al. Noninvasive quantification of tumor volume in preclinical liver metastasis models using contrast-enhanced X-ray computed tomography. Invest Radiol. 2008;43:92–9.

Hainfeld JF, Slatkin DN, Focella TM, et al. Gold nanoparticles: a new X-ray contrast agent. Br J Radiol. 2006;79:248–53.

Henning T, Weber AW, Bauer JS, et al. Imaging characteristics of DHOG, a hepatobiliary contrast agent for preclinical microCT in mice. Acta Radiol. 2008;15:342–9.

Hughes PM, Bisset R. Non-ionic contrast media: a comparison of iodine delivery rates during manual injection angiography. Br J Radiol. 1991;64(761):417–9.

Kim SH, Park JH, Kim YI, et al. Experimental tissue damage after subcutaneous injection of water soluble contrast media. Invest Radiol. 1990;25:678–85.

Koa C-Y, Hoffman EA, Beck KC, et al. Long-residence-time nano-scale liposomal iohexol for X-ray-based blood pool imaging. Acta Radiol. 2003;10:475–83.

Krause W, Leike J, Sachse A, et al. Characterization of iopromide liposomes. Invest Radiol. 1993;28(11):1028–32.

Krause W. Preclinical characterization of iopromide. Invest Radiol. 1994;29(1):S21–32.

Mützel W, Speck U, Weinmann H-J. Pharmacokinetics of iopromide in rat and dog. In: Taenzer V, Zeitler E, editors. Contrast media in urography, angiography and computed tomography. Stuttgart: Thieme; 1983. p. 85–90.

Poste G. Liposome targeting in vivo: problems and opportunities. Biol Cell. 1983;47:19–38.

Rabin O, Perez JM, Grimm J, et al. An X-ray computed tomography imaging agent based on long-circulating bismuth sulphide nanoparticles. Nat Mater. 2006;5(2):118–22.

Rau T, Mathey D, Schofer J. High-dose tolerance of iodinated x-ray contrast media. New developments in x-ray and MR angiography symposium CIRSE, 9.9.96, Funchal, Madeira. Cardiovasc Intervent Radiol. 1997;20:8–9.

Rosovsky M, Rusinek H, Berenstein A, et al. High-dose administration of non-ionic contrast media: a retrospective review. Radiology. 1996;200:119–22.

Sachse A, Leike JU, Schneider T, et al. Biodistribution and computed tomography blood-pool imaging properties of polyethylene glycol-coated iopromide-carrying. Invest Radiol. 1997;32(1):44–50.

Schmiedl UP, Krause W, Leike J, et al. CT blood pool enhancement in primates with iopromide-carrying liposomes containing soy phosphatidyl glycerol. Acad Radiol. 1999;6:164–9.

Seltzer SE, Gregoriadis G, Dick R. Evaluation of the dehydration-rehydration method for production of contrast-carrying liposomes. Invest Radiol. 1988;23(2):131–8.

Senior JH. Fate and behaviour of liposomes in vivo: a review of controlling factors. Crit Rev Ther Drug Carrier Syst. 1987;3:123–93.

Torchilin VP, Frank-Kamenetsky MD, Wolf GL. CT visualization of blood pool in rats by using long-circulating, iodine-containing micelles. Acad Radiol. 1999;6:61–5.

Vera DR, Mattrey RF. A molecular CT blood pool contrast agent. Acad Radiol. 2002;9:784–92.

MRI

13

Aileen Schroeter, Markus Rudin, Eliana Gianolio[$], Alessandra Viale[$], Daniela Delli Castelli[$], Silvio Aime, Jan-Bernd Hövener, Jessica A.M. Bastiaansen, Arnaud Comment, Stephan Düwel, Jan H. Ardenkjaer-Larsen, and Markus Becker

Contents

[$]Author contributed equally with all other contributors.

A. Schroeter (✉) • M. Rudin
Institute of Biomedical Engineering, University and ETH Zürich, Zürich, Switzerland
e-mail: schroeter@biomed.ee.ethz.ch

E. Gianolio • A. Viale • D. Delli Castelli • S. Aime (✉)
Department of Molecular Biotechnology and Health Sciences, University of Torino, Torino, Italy
e-mail: silvio.aime@unito.it

J.-B. Hövener (✉)
Department of Radiology, Medical Physics, Medical Center – University of Freiburg, Faculty of Medicine, University of Freiburg, Breisacher Straße 60a, 79106 Freiburg, Germany

German Consortium for Cancer Research (DKTK), Partner Site Freiburg, Im Neuenheimer Feld 280, 69120 Heidelberg, Germany
e-mail: jan.hoEvener@uniklinik-freiburg.de

J.A.M. Bastiaansen
Department of Radiology, University Hospital Lausanne (CHUV) and University of Lausanne (UNIL), Center for Biomedical Imaging (CIBM), Lausanne, Switzerland

A. Comment
Institute of Physics of Biological Systems, Ecole Polytechnique Fédérale de Lausanne, Lausanne, Switzerland

S. Düwel
Department of Nuclear Medicine, Department of Chemistry, Institute of Medical Engineering, Technical University of Munich, GE Global Research, Munich, Germany

J.H. Ardenkjaer-Larsen
Department of Electrical Engineering, Technical University of Denmark, Kongens Lyngby, Denmark

GE Healthcare, Broendby, Denmark

M. Becker
Bruker BioSpin MRI GmbH, Ettlingen, Germany
e-mail: markus.becker@bruker-biospin.de

F. Kiessling et al. (eds.), *Small Animal Imaging*, DOI 10.1007/978-3-319-42202-2_13

13.1 Basics of Magnetic Resonance Imaging (MRI)

Aileen Schroeter and Markus Rudin

Principles of nuclear magnetic resonance spectroscopy (NMR) (Ernst et al. 1987; Slichter 1990) and of magnetic resonance imaging (MRI) (Haacke et al. 1999; Bradley and Bydder 1997) have been the subject of several monographs to which the reader is referred. In the subsequent sections, we give a short summary on some important aspects of MRI: slice selection, image formation, some basic imaging sequences, as well as some contrast modules relevant for contrast-enhanced imaging.

13.1.1 Interaction of a Nuclear Magnetic Moment with a Static Magnetic Field

Nuclei with an odd number of protons and/or neutrons have a nonzero nuclear angular momentum $\hbar \cdot \vec{I}$, which is a vector quantity composed of the spin angular moments of the individual nucleons (protons and neutrons), and $\hbar$ the Planck constant $h/2\pi$. The associated magnetic dipole moment $\vec{\mu}$ then becomes

$$\vec{\mu} = \gamma \cdot \hbar \cdot \hat{I}_z \tag{13.1}$$

with γ being the gyromagnetic ratio, which is a nucleus-specific value (e.g., for protons $\gamma/2\pi$=42.577 MHz/Tesla). In a static magnetic field $\vec{B}_0$, the energy of the magnetic moment becomes

$$E = -\vec{\mu} \cdot \vec{B}_0 = -\gamma \cdot \hbar \cdot \hat{I}_z \cdot B_0 \tag{13.2}$$

In (Eq. 13.2) we assumed the external field to be applied along the z-axis, i.e., $\vec{B}_0 = (0, 0, B_0)$. Based on the laws of quantum mechanics, only discrete values for the spin angular momentum $I = \frac{1}{2}, 1, \frac{3}{2}, \ldots$ and hence only discrete energy states of the spin system are possible. The eigenvalues of $\hat{I}_z$ are $-I \le m_I \le I$, which in the simplest case of a nucleus with a spin $I = \frac{1}{2}$ such as the proton can take only the two values $m_I = \pm\frac{1}{2}$ corresponding to the two energy states (Fig. 13.1)

$$E_{\pm 1/2} = \mp\frac{1}{2} \cdot \gamma \cdot \hbar \cdot B_0 \tag{13.3}$$

The energy difference between the individual energy states depends linearly on the amplitude of the magnetic field. Transitions between energy states occur by absorbance or emission of an energy quantum $\hbar\omega_0$, the frequency of which has to fulfill the resonance condition

$$\omega_0 = E_{+1/2} - E_{-1/2} = \gamma \cdot B_0 \tag{13.4}$$

When considering macroscopic samples, ensembles of nuclear spins are being investigated. They distribute among the individual energy levels according to Boltzmann's law. The relative population difference between two adjacent states (polarization P) becomes

$$P = \left(p_{m_I+1} - p_{m_I}\right) / \left(p_{m_I+1} + p_{m_I}\right) = \tanh\left(-\frac{\gamma \cdot \hbar \cdot B_0}{2 \cdot k \cdot T}\right) \tag{13.5}$$

k being the Boltzmann constant and T the absolute temperature. As the energies involved in the magnetic Zeeman interaction are significantly smaller than the thermal energy $k \cdot T$ at body temperature, the population difference between energy states is small. For protons at magnetic field strengths of 7 Tesla, the difference is approximately 30 ppm, i.e., only 30 out of one million nuclear spins contribute to the signal. The low quantum energy of magnetic interactions is the principal reason of the low sensitivity of MR techniques.

13.1.2 Classical Description of NMR: Bloch Equations and Relaxation

In thermal equilibrium, the macroscopic magnetization vector $\vec{M} = 1/V \cdot \sum_V \vec{\mu}$ resulting from the ensemble of nuclear magnets will align parallel to the magnetic field. Generation of a non-equilibrium condition, e.g., by rapidly changing the direction of the field, will induce a torque $\vec{M} \times \vec{B}_0$, which causes $\vec{M}$ to change as a function of time due to the conservation of the angular moment,

$$d\vec{M} / dt = \gamma \cdot \vec{M}(t) \times \vec{B}_0 \tag{13.6}$$

For $\vec{B}_0 = (0, 0, B_0)$, the solution of (Eq. 13.6) describes the precession of the magnetization vector $\vec{M}$ around the z-coordinate axis with the precession frequency $\omega_0 = \gamma \cdot B_0$, the so-called Larmor frequency (Fig. 13.1). The time-dependent transverse magnetization $M_{xy}(t) = M_{xy}(0) \cdot \exp(-i \cdot \omega_0 \cdot t)$ will induce an oscillatory voltage in a pickup coil, the MR signal.

Equation 13.6 describes the undamped precession of the magnetization vector around the magnetic field. Yet, any physical system will return to its equilibrium state $\vec{M}_0$ given sufficient time. This is phenomenologically accounted for by introducing relaxation terms, the longitudinal $R_1 = 1/T_1$ and the transverse relaxation rate $R_2 = 1/T_2$. The rate R_1 characterizes the return of the system to the equilibrium state $\vec{M}_{eq} = (0, 0, M_0)$, while R_2 describes the loss of phase coherence due to stochastic variations in the local magnetic field. They will be discussed in more detail later in this chapter. The Bloch equations describing the behavior of the magnetization in a static magnetic field read

$$d\vec{M} / dt = \gamma \cdot (\vec{M} \times \vec{B}_0) - \underline{\underline{R}} \cdot (\vec{M}(t) - \vec{M}_{eq}) \tag{13.7}$$

with the relaxation matrix $\underline{\underline{R}}$ consisting of the diagonal elements (R_2, R_2, R_1). For $\vec{B}_0$ pointing along the z-axis, the equation for transverse and longitudinal component of magnetization vector becomes

$$d\vec{M}_{xy} / dt = \gamma \cdot (\vec{M} \times \vec{B}_0)_{xy} - R_2 \cdot (M_{xy} - M_{xy,eq}) \tag{13.7a}$$

$$d\vec{M}_z / dt = \gamma \cdot (\vec{M} \times \vec{B}_0)_z - R_1 \cdot (M_z - M_{z,eq}),$$

with the solution (Fig. 13.3).

$$M_{xy}(t) = M_{xy}(0) \cdot \exp(-i \cdot \omega \cdot t) \cdot \exp(-R_2 \cdot t) \tag{13.8}$$

$$M_z(t) = M_0 \cdot \{1 - [(M_z(0) / M_0) - 1]\} \cdot \exp(-R_1 \cdot t)$$

where $M_i(0)$ describes the magnetization components at $t = 0$ and M_0 the equilibrium magnetization pointing along z. In (Eq. 13.8) we used the frequency ω to account for the fact that the effective field experienced by the nuclear spin may deviate from B_0 due to local effects by the tissue susceptibility (see below) or by effects of the local chemical environment (chemical shift). For biological tissue, relaxation times are typically of the order of $T_1 = 1$ s and $T_2 = 50$ to 100 ms, depending on the tissue type and the magnetic field strength.

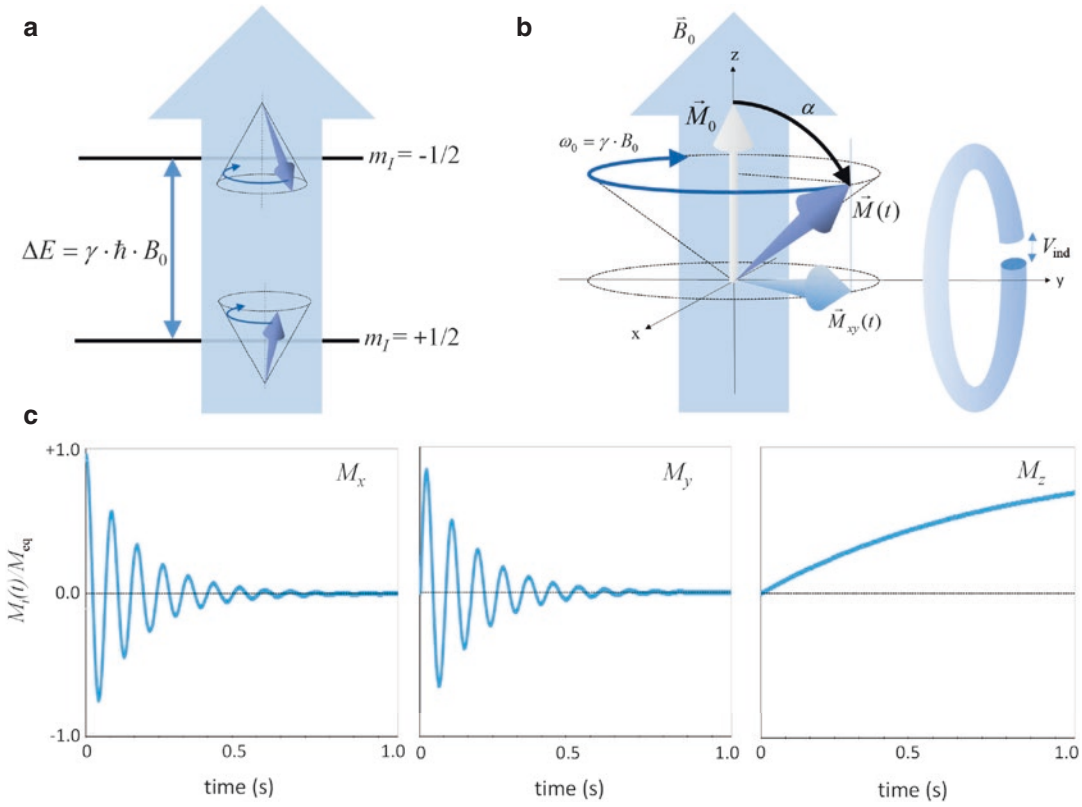

Fig. 13.1 Basics of nuclear magnetic resonance (NMR): (**a**) Spin $I = 1/2$ system in external magnetic field along z-axis. The only two possible states are characterized by the eigenvalues of $\hat{I}_z$ operator, $m_I = +½$ (parallel) and $m_I = -½$ (antiparallel to the main magnetic field). The energy difference between the two states is $\Delta E = \hbar \cdot \omega_0 = \gamma \cdot \hbar \cdot B_0$. (**b**) Generation of a nonequilibrium state by rapidly changing the magnetic field direction (radio-frequency pulse along the x-axis, nutation angle is α). The resulting magnetization $\vec{M}_z(t)$ precesses around the static magnetic field $\vec{B}_0$ with the Larmor frequency ω_0. The rotating transverse component $\vec{M}_{xy}(t)$ induces a voltage V_{ind} in a pickup coil, the NMR signal. (**c**) Time dependence of the transverse and longitudinal magnetization components assuming the static magnetic field along the z-axis and an initial state with only transverse magnetization. Values used for the computation were offset frequency $\Delta\omega_0 = 60$ s^{-1}, $R_1 = 1$ s^{-1}, and $R_2 = 5$ s^{-1}

13.1.3 The MR Experiment

In order to induce transitions between the energy eigenstates of an ensemble of magnetic nuclei in a static magnetic field or in classical terms to generate nonequilibrium magnetization, a time-dependent electromagnetic field with components perpendicular to $\vec{B}_0$ has to be applied. We assume the field to be oriented along the x-axis; hence

$$\vec{B}_1(t) = 2 \cdot B_{1.} \cos(\omega \cdot t) \cdot \vec{e}_x \qquad (13.9)$$

The total magnetic field to which the sample is exposed is then the vector sum of $\vec{B}_0$ and $\vec{B}_1(t)$.

The linearly polarized field $\vec{B}_1(t)$ is commonly decomposed into two counter-rotating circularly polarized fields. It can be shown that only the component rotating in parallel to the Larmor precession will lead to resonance, while the effect of the counter-rotating component can be neglected (Bloch and Siegert 1940). This is accounted for by describing MR experiments in a coordinate frame that rotates with the Larmor frequency around the z-axis (*rotating frame* concept (Ernst et al. 1987)); hence in (Eq. 13.8), the frequency ω has to be replaced by $\omega - \omega_0$ as in the rotating frame only the frequency offset with regard to the basic frequency $\omega_0 = \gamma \cdot B_0$ is considered. There are also practical implications of the decomposition of $\vec{B}_1(t)$ in two counter-rotating fields: using a so-called quadrature excitation coil that generates a circularly polarized RF field yields a B_1-field that is $\sqrt{2}$ times larger compared to that generated by a conventional linearly polarized coil.

In modern *Fourier transform* (FT) MR experiments, the signal is detected in the time domain following excitation by a short electromagnetic pulse, and the spectral information is obtained by Fourier transformation of the observed free induction decay (FID) (Ernst et al. 1987; Ernst 1966). Hence, $B_1(t)$ is only switched on in the time interval $0 \le t \le \tau$, τ being the pulse duration, which has to be chosen such that the frequency spectrum of the pulse covers the desired spectral range. The angle by which the magnetization is rotated from its equilibrium orientation is given by

$$\alpha = \gamma \cdot B_1 \cdot \tau \tag{13.10}$$

Following a pulse around the x-axis with a nutation angle α, the initial magnetization is of the form $\vec{M}(0) = M_0 \cdot (0, \sin\alpha, \cos\alpha)$ and evolves according to (Eq. 13.8).

13.1.4 Measurement of Relaxation Rates

Relaxation rates are governed by the interaction of nuclear spins with their environment and are therefore an important source of contrast in MRI. Up to now we have discussed two relaxation rates, R_1 and R_2. As discussed, transverse relaxation arises from loss of phase coherence due to fluctuations in the magnetic interaction of nearby nuclear spins, which leads to fluctuations in the resonance frequencies. Yet, dephasing may also occur due to static magnetic field inhomogeneities ΔB_0 of the order of parts per million that arise from technical imperfections of magnets and more importantly due to local differences in the magnetic susceptibility $\Delta\chi$ of biological tissue

$$\Delta B_0 = \mu_0 \cdot \Delta\chi \cdot B_0 \tag{13.11}$$

μ_0 being the magnetic constant. This additional term is accounted for by introducing an additional transversal relaxation rate R_2*, which can be approximately defined as

$$R_2^* \approx R_2 + \gamma \cdot \Delta B_0 \tag{13.12}$$

and which governs the dephasing of the magnetization vectors of a spin ensemble.

Measurement of the Transverse Relaxation Rate R_2 The inhomogeneities of the B_0 field are static, and, hence, the destructive interference imposed can be accounted for using an elegant method proposed by Hahn (Hahn 1950). The spin system is excited by a 90° radio-frequency pulse around the x-axis. Following the pulse the individual magnetization vectors experience only the static magnetic field and precess around the z-axis at their individual angular frequency $\omega_i = \gamma \cdot (B_0 + \Delta B_{0i})$ and therefore get out of phase. At a time $T_E/2$ following the initial excitation, a 180° pulse is applied, e.g.,

around the *y*-axis. Following this pulse, the vectors precess again around the static field at their respective ω_i. At $t = T_E$ (i.e., $T_E/2$ following the 180° pulse), the individual magnetization vector will be in phase again co-aligned along the *y*-axis forming a so-called spin echo (Fig. 13.2). Compared to the FID, the echo amplitude is reduced according to

$$M_{xy}\left(T_E\right) = M_{xy}\left(0\right)\cdot\exp\left(-R_2\cdot T_E\right) \tag{13.13}$$

caused by loss in signal coherence due to stochastic processes (e.g., microscopic motion) leading to fluctuation in the local magnetic fields that cannot be accounted for. In order to get accurate values for R_2, measurements have to be carried out at multiple T_E values (multi-echo experiment).

Measurement of the Longitudinal Relaxation Rate R_1 For measurement of R_1, the longitudinal component of the magnetization has to be translated into detectable transverse magnetization. This requires the generation of a nonequilibrium state $M_z\left(0\right) \neq M_0$, and after a delay, the longitudinal magnetization $M_z(t)$ is probed by applying a 90° RF pulse. The signal is then given by

$$M_z\left(t\right) = M_0\cdot\left\{1+\left(M_z\left(0\right)/M_0-1\right)\cdot\exp\left(-R_1\cdot t\right)\right\} \tag{13.14}$$

For so-called inversion recovery experiments, $M_z\left(0\right) = -M_0$ (Fig. 13.2), and for *saturation recovery* $M_z\left(0\right) = 0$.

A modification of the latter sequence is the steady-state saturation experiment, in which a sequence of 90° pulses is repeated at an interval $T_R < 1/R_1$. For calculation of R_1 the experiment has to be repeated at various delays T_R. Under steady-state condition, the signal is given by

$$M_{xy}\left(0\right) = M_{z,\text{steady-state}}\left(T_R\right)\cdot\sin\alpha = M_0\cdot\sin\alpha\cdot\frac{1-\exp\left(-R_1\cdot T_R\right)}{1-\cos\alpha\cdot\exp\left(-R_1\cdot T_R\right)} \tag{13.15}$$

and becomes maximal at the so-called Ernst angle

$$\cos\alpha_{\text{opt}} = \exp\left(-R_1\cdot T_R\right) \tag{13.16}$$

Reduction of the T_R with simultaneous optimization of the pulse angle to maximize signal intensity is the basic principle of fast low angle shot (FLASH) MR imaging (see below).

Fig. 13.2 Measurement of relaxation rates. (**a**) Hahn spin-echo experiment. After excitation by a $(90°)_x$ pulse, the nuclear magnetization is aligned along the *y*-axis and precesses around the static magnetic field (*z*-axis). Due to magnetic field inhomogeneities, the individual spin packets become dephased leading to a signal decay (*FID*) characterized by the rate R_2*. After $T_E/2$ a refocusing pulse is applied $(180°)_y$ and the individual magnetization vectors are flipped around the *y*-axis. After the pulse the precession around static magnetic field continues leading to the formation of an echo signal (constructive interference). The amplitude of the spin echo is reduced by a factor $\exp(-R_2T_E)$ as compared to the amplitude of the initial FID. (**b**) Inversion recovery experiment. At $t=0$ the magnetization is inverted by application of 180° pulse. After the inversion delay T_I a 90° readout pulse generates observable transverse magnetization with the amplitude of the signal being determined by (Eq. 13.14) for $M(0)=-M_0$. Zero signal intensity is observed at $T_I=\ln 2/R_1$

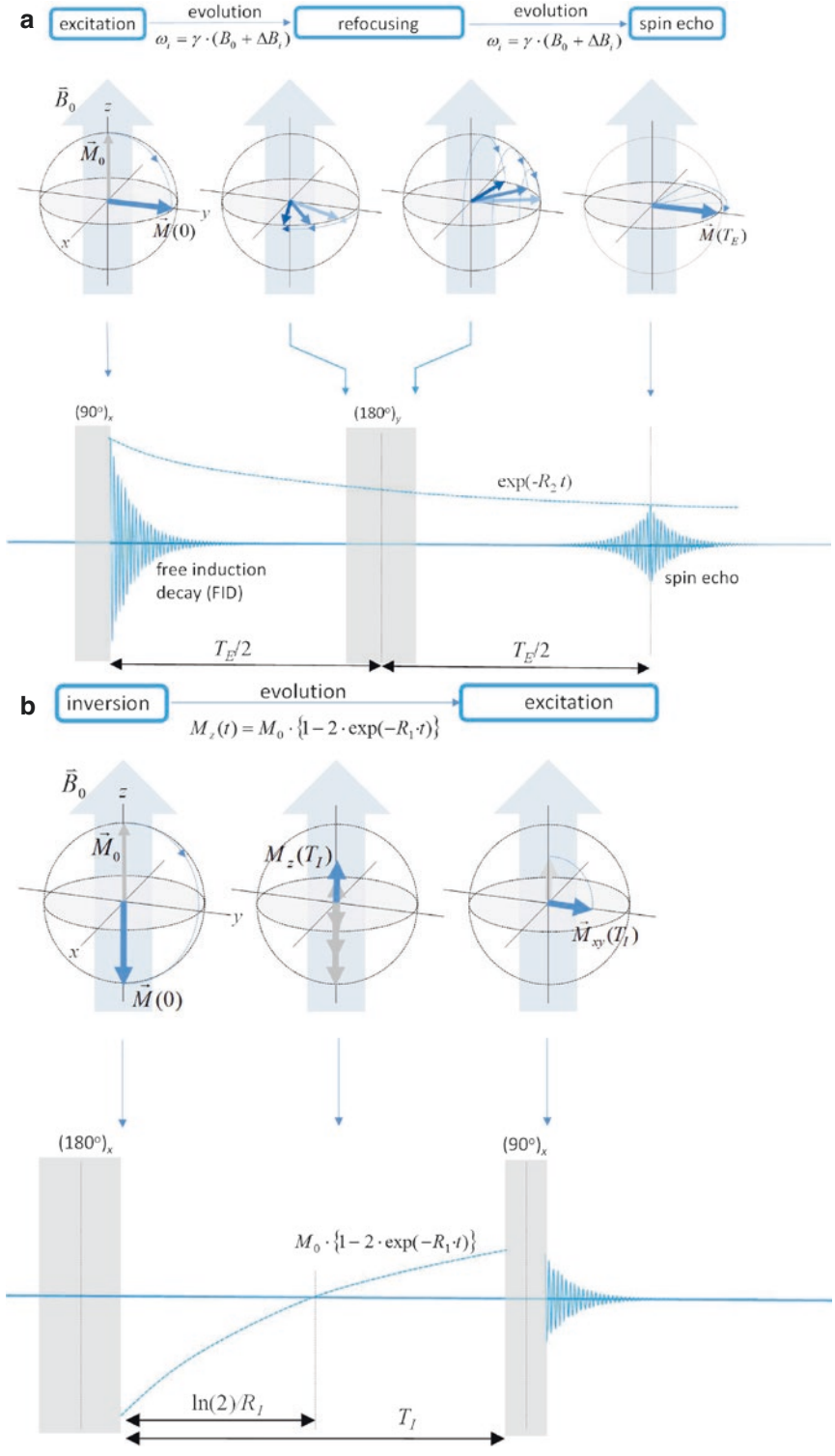
a
excitation
evolution
$\omega_i = \gamma \cdot (B_0 + \Delta B_i)$
refocusing
evolution
$\omega_i = \gamma \cdot (B_0 + \Delta B_i)$
spin echo
$\vec{B}_0$
z
$\vec{M}_0$
y
x
$\vec{M}(0)$
$\vec{M}(T_E)$
$(90°)_x$
$(180°)_y$
$\exp(-R_2 t)$
free induction
decay (FID)
spin echo
$T_E/2$
$T_E/2$
b
inversion
evolution
$M_z(t) = M_0 \cdot \{1 - 2 \cdot \exp(-R_1 \cdot t)\}$
excitation
$\vec{B}_0$
z
$\vec{M}_0$
$M_z(T_I)$
y
x
$\vec{M}_{xy}(T_I)$
$\vec{M}(0)$
$(180°)_x$
$(90°)_x$
$M_0 \cdot \{1 - 2 \cdot \exp(-R_1 \cdot t)\}$
$\ln(2)/R_1$
T_I

13.1.5 Principles of Magnetic Resonance Imaging (MRI)

13.1.5.1 Spatial Encoding

MRI procedures are based on the use of magnetic field gradients that render the resonance field and, hence, the corresponding Larmor frequency dependent on the position of the resonant nucleus (Lauterbur 1973). Consider a one-dimensional case. Application of a magnetic field gradient G_x along the x-axis renders the resonance frequency dependent on the location (Fig. 13.3), which for a time-invariant gradient G_x becomes

$$\omega(x) = \omega_0 - \gamma \cdot G_x \cdot x \tag{13.17}$$

It is obvious that by recording a sufficient number of projections with varying orientations of the magnetic field gradient G, the three-dimensional distribution of spins can be reconstructed. This projection reconstruction approach is analogous to x-ray CT and has originally been proposed by Lauterbur (1973).

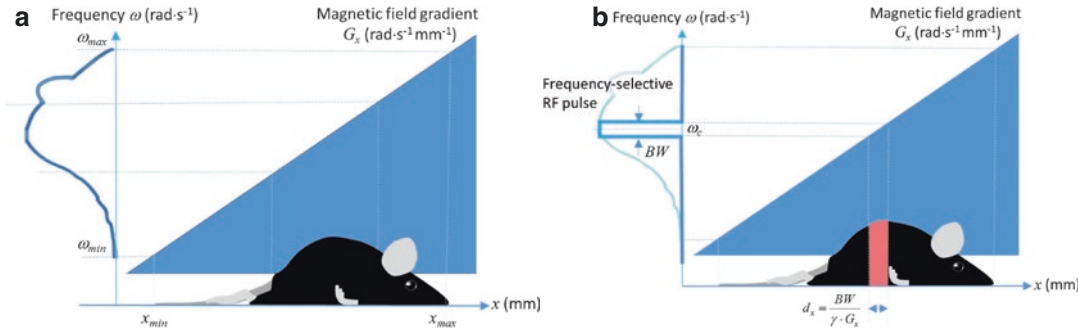

Fig. 13.3 Spatial encoding and slice-selective excitation. (**a**) Frequency encoding is achieved by applying a magnetic field gradient G_x (shown for the x-direction). As a result, the resonance frequency becomes dependent on the location according to (Eq. 13.17), and the frequency spectrum excited corresponds to a projection of the sample along the gradient direction as long as the RF pulse is of sufficient bandwidth BW. The steepness of the gradient determines the spectra dispersion. (**b**) By combining the effect of the magnetic field gradient with a band-limited pulse of a center frequency ω_c and a bandwidth BW, a slab is excited of thickness $d_x = \mathrm{BW}/\gamma \cdot G_x$ (indicated in pink). The slab thickness can be varied by changing either the gradient strength or the pulse bandwidth. Note that frequency values are in rad·s^{-1} according to $\omega = 2\pi \cdot \nu$

Modern MRI sequences operate in Fourier space (Ernst et al. 1987). In FT MRI the imaging data set is collected as a 2D (or 3D) array in time domain. The transverse magnetization is encoded during two time intervals t_1 and t_2, during which it evolves under the influence of the respective magnetic field gradients G_1 and G_2

$$M_{xy}(t_1, t_2; x, y) = M_0 \cdot \exp\left\{-i \cdot \gamma \cdot y \cdot \int_0^{t_1} G_1(t') \cdot dt'\right\} \cdot \exp\left\{-i \cdot \gamma \cdot x \cdot \int_0^{t_2} G_2(t') \cdot dt'\right\} \tag{13.18}$$

The signal is sampled during the t_2-domain collecting N_2 data points, while the signal evolution during t_1 leads to a signal phase at $t_2 = 0$ that is given by the first exponential term in (Eq. 13.18). In order to sample the N_1 data lines required for image reconstruction, this procedure has to be repeated while incrementing the product $G_1 \cdot t_1$ during subsequent excitations (today, the time t_1 is kept constant and the gradient amplitude is being increased). It is important that for both dimensions, the Nyquist sampling theorem has to be obeyed, i.e., the sampling rate has to be chosen such that the maximum frequencies can be accurately mapped. In MRI the respective gradients

are called phase encode (G_1) and readout gradient (G_2), and we will use these terms for the rest of the chapter. The image (in frequency domain) is then obtained by a 2D-FT of the time domain data set,

$$I(x,\ y) = I(\omega_1,\ \omega_2) = F_2\left\{M_{xy}(t_1, t_2)\right\} \qquad (13.19)$$

The principal proton-carrying constituents of biological tissue are water and lipid molecules of adipose tissue. The resonance frequency of a nuclear spin is determined by the externally applied magnetic field (Eq. 13.4) and its local chemical environment, which is determined by the electron configuration. Similar to hydrogen nuclei electrons possess a spin momentum, which is approximately 650 times larger than that of the proton. Also the motion of the charged electron imposes additional local fields in the vicinity of the nucleus. These contributions are comprised in the so-called chemical shift term, which is described as a second rank tensor in order to account for the local anisotropy. Yet, in biological tissue typically only the value of its trace σ is of relevance. The chemical shift is measured to a reference frequency (ω_0), in imaging typically the frequency of the protons of bulk tissue water. Hence the expression for the resonance frequency (Eq. 13.4) for a nuclear spin j has to be modified to

$$\omega_j = \gamma \cdot (1 - \sigma_j) \cdot B_0 = \omega_0 - \gamma \cdot \sigma_j \cdot B_0 \qquad (13.20)$$

This has implications with regard to spatial encoding. (Eq. 13.17) has to be modified to

$$\omega(x) = \omega_0 - \gamma \cdot \sigma_j \cdot B_0 - \gamma \cdot G_x \cdot x \qquad (13.21)$$

This frequency cannot be discriminated from

$$\omega(x') = \omega_0 - \gamma \cdot G_x \cdot x' \qquad (13.22)$$

Hence, signals originating from nuclei j appear displaced with regard to those of water by an amount

$$x' - x = \frac{\sigma_j \cdot B_0}{G_x} \qquad (13.23)$$

which is the reason for the so-called chemical shift artifact. These can be avoided by either selective excitation of the water or the lipid resonance or by selective suppression of either of the two. Similar to lipids the various metabolite signals are shifted with regard to the water resonance. Yet, this is not a problem as metabolite concentrations are in the millimolar range as compared to 80 M water protons.

13.1.5.2 *K*-Space

A very convenient way to analyze MRI experiments is the so-called *K*-space concept (Ljunggren 1983). Consider a spin density distribution, which defines the observable transverse magnetization $M_{xy}(x)$. Let us again consider a one-dimensional case. For an arbitrary time-variant gradient $G_x(t)$, the signal after demodulation with the Larmor frequency (rotating frame description) is given by

$$s(t) = \int_{x_{\min}}^{x_{\max}} M_{xy}(x) \cdot \exp\left\{-i \cdot \gamma \cdot x \cdot \int_0^t G_x(t') \cdot dt'\right\} \cdot dx \qquad (13.24)$$

By introducing a time-dependent spatial frequency $k_x(t)$ according to

$$k_x(t) = \frac{\gamma}{2\pi} \int_0^t G_x(t') \cdot dt' \qquad (13.25)$$

Equation 13.24 can be reformulated as

$$s(k_x) = \int_{x_{\min}}^{x_{\max}} M_{xy}(x) \cdot \exp\{-i \cdot 2\pi \cdot k_x \cdot x\} \cdot dx \qquad (13.26)$$

Equation 13.26 corresponds to a Fourier integral, i.e., the signal $s(k_x)$ is the FT of the transverse magnetization $M_{xy}(x)$, which by itself is proportional to the spin density of the sample. Hence, the spin density is Fourier encoded along x by the applied gradient G_x. Correspondingly, $M_{xy}(x)$ can be obtained by the inverse FT of the *K*-space signal $s(k_x)$

$$M_{xy}(x) = \int_{k_{x\min}}^{k_{x,\max}} s(k_x) \cdot \exp\{+i \cdot 2\pi \cdot k_x \cdot x\} \cdot dk_x \qquad (13.26a)$$

It is straightforward to expand this concept to two or three dimensions,

$$M_{xy}(x,\ y,\ z) = \iiint s(k_x,\ k_y,\ k_z) \cdot \exp\left\{+i \cdot 2\pi \cdot \left(k_x \cdot x + k_y \cdot y + k_z \cdot z\right)\right\} \cdot dk_x \cdot dk_y \cdot dk_z \qquad (13.27)$$

A prerequisite for accurate reconstruction of the original spin density distribution is the complete coverage of *K*-space considering the Nyquist sampling theorem for $j=x, y$. The distance between adjacent *K*-space samples should fulfill the condition

$$\Delta k_j \leq \frac{1}{2 \cdot \gamma \cdot G_j \cdot j} \qquad (13.28)$$

Nevertheless, there is considerable freedom regarding trajectories for *K*-space sampling (Fig. 13.4). A limitation of MRI data acquisition is its sequential nature, i.e., many pulse sequences (see below) require sequential acquisition of individual *K*-space lines, which is of course time-consuming. *K*-space can be undersampled, if independent information is obtained, e.g., by using multiple receiver coils. Such parallel acquisition techniques (Sodickson and Manning 1997; Pruessmann et al. 1999; Griswold et al. 2002) are today standard in clinical MRI, but less common in animal imaging as acceleration leads to a reduction in the signal-to-noise ratio (SNR). Alternatively, methods use the sparsity of the MRI signal (either in image or *K*-space) for *K*-space undersampling and hence acceleration (sparse sampling, compressed sensing; (Lustig et al. 2007)).

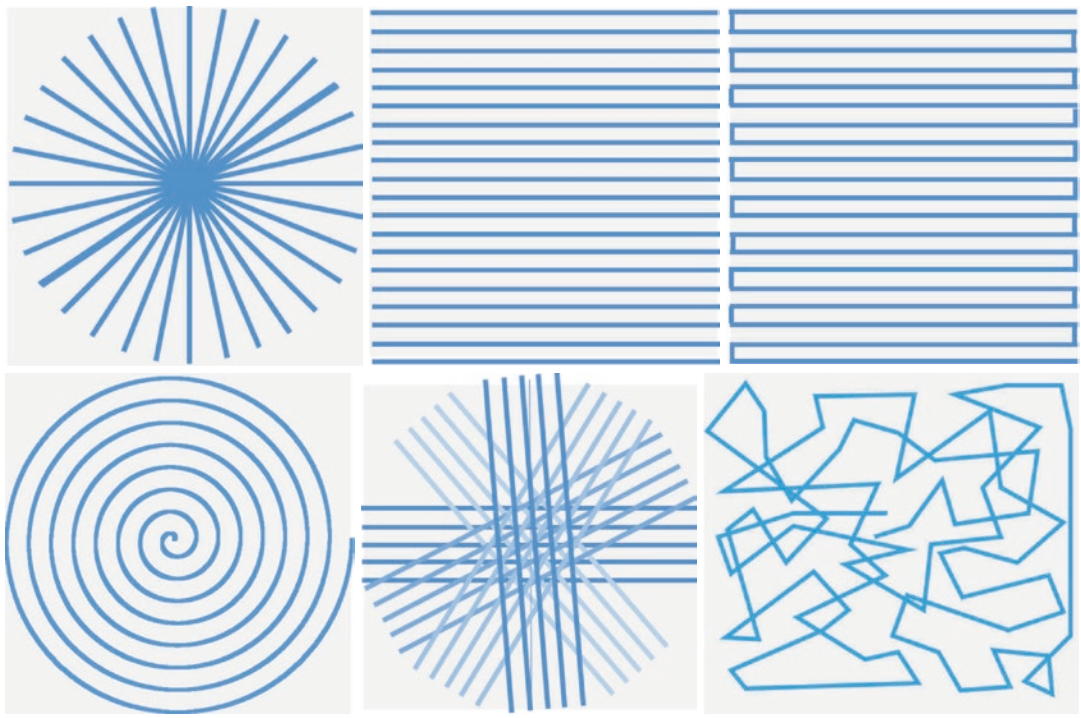

Fig. 13.4 Examples of *K*-space trajectories. They include from *top left* to *bottom right* radial sampling, sequential linear sampling, single pulse-echo planar imaging trajectory, spiral sampling, PROPELLER (periodically rotated overlapping parallel lines with enhanced reconstruction), and completely random sampling

13.1.5.3 Slice Selection

Combining the application of a magnetic field gradient G_x with frequency-selective excitation leads to the excitation of a slice with a width that is determined by the bandwidth $\Delta\omega$ of the RF pulse. The resonance condition is fulfilled only for nuclear spins within a slab *i* defined by

$$x_i \pm \Delta x / 2 = \frac{\omega_i - \omega_0 \pm \Delta\omega / 2}{\gamma \cdot G_x} \qquad (13.29)$$

The frequency offset $\omega_i - \omega_0$ determines the position of the slice center. Ideally, the pulse profile corresponds to a rectangular frequency profile with zero amplitude outside and full amplitude within this range. In the time domain, such a profile corresponds to a sinc-pulse of infinite duration. In practice, pulses are of limited duration, which leads to deviation from the rectangular profile. Various pulse profiles have been suggested to approximate the ideal frequency response including truncated sinc-pulses such as sinc3 or sinc5, Hermite pulses, adiabatic pulses, or Shinnar–Le Roux (SLR) selective pulses (Pauly et al. 1991). An important criterion in pulse optimization is the performance for nuclear spins that resonate at a different frequency compared to ω_0 (off-resonance effects).

Due to the finite bandwidth of the pulse and, hence, the finite slice thickness, individual spin packets across the slice will precess at different Larmor frequencies (due to the slice selection gradient) and hence will be dephased at the end of the pulse. To avoid signal loss this dephasing has to be compensated by a reversal of the slice selection gradient (gradient echo). Compensation of dephasing requires $G_{sl} \cdot \tau / 2 = G'_{sl} \cdot t_c$, with τ being the pulse duration, G'_{sl} the amplitude of the compensation gradient and t_c the duration of the compensation gradient.

13.1.6 Some Basic Image Acquisition Modules

Image acquisition requires full coverage of the 2D or 3D *K*-space, and numerous trajectories can be designed to achieve this objective (Fig. 13.5). To illustrate the principle, we will discuss some simple sequences, which appear as basic elements of more complex pulse sequences, in some detail.

(a) *Spin-echo experiment* (Fig. 13.5a): A standard image acquisition module relies on the spin-echo experiment (see above) and yields R_2 contrast. A 2D pulse sequence is shown in Fig. 13.5 together with the respective *K*-space diagram. Transverse magnetization is generated by a slice-selective 90° pulse. The frequency and phase encoding occurs during the evolution period $T_E/2$ by application of gradient pulses in the readout and phase-encoding direction. The spin-echo signal is recorded following a slice-selective refocusing pulse while applying a readout gradient. After a repetition delay T_R, the next excitation pulse is applied. For each sequential acquisition, the phase-encoding gradient is incremented.

The advantage of the spin-echo acquisition is the compensation for effects due to static magnetic field inhomogeneity, while the major drawback of conventional spin-echo is the long image acquisition time. Each line in *K*-space has to be recorded sequentially with a sufficiently long recovery delay in-between individual acquisitions to allow for R_1 relaxation and, hence, improved signal-to-noise ratio. In order to shorten acquisition times, several fast spin-echo techniques have been developed such as rapid acquisition with relaxation enhancement (RARE (Hennig et al. 1986)). In the RARE experiment, an echo-train consisting of *N* echoes with different values for the phase-encoding gradient for the individual echoes of the train is recorded. The time for data acquisition is thereby reduced by a factor *N*, *N* typically ranging from 4 to 128. For driven equilibrium a 90° pulse is applied at the time point of the second echo formation to restore longitudinal magnetization and thus shortening the recovery period.

(b) *Gradient echo* (Fig. 13.5b): Alternative fast MRI data acquisition methods are based on signal refocusing due to reversal of the readout gradient. A typical example of this class of methods is fast low angle shot (FLASH) pulse sequence (Frahm et al. 1986). Transverse magnetization is generated by application of an α-pulse. As the repetition delay T_R is chosen such that $T_R << T_1$, the optimal pulse angle has to be $\alpha_{opt} << 90°$; e.g., for $T_R = 10$ ms and $T_1 = 1$ s we obtain $\alpha_{opt} = 8.1°$.

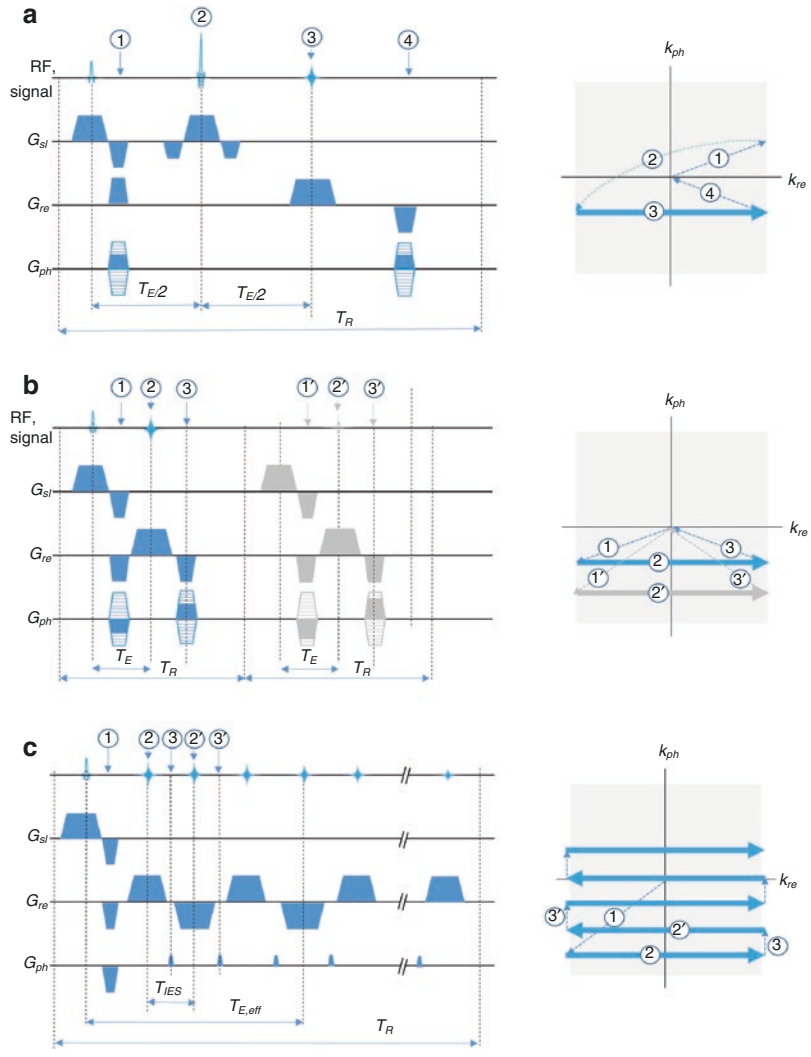

Fig. 13.5 Pulse sequences and *K*-space diagrams for basic MRI acquisition modules. (**a**) Spin echo, (**b**) gradient echo, (**c**) echo planar imaging. Abbreviation indicates slice-selective gradient (G_{sl}), readout (frequency encoding) gradient (G_{re}), phase-encoding gradient (G_{ph}); repetition delay (T_R), echo delay (T_E), inter-echo spacing (T_{IES}), effective echo delay ($T_{E,eff}$), and the respective *K*-space coordinates for the readout (k_{re}) and phase-encoding direction (m_{ph}). Numbers link trajectory in *K*-space diagram to pulse sequence timing diagram

Images recorded using gradient echo sequences are both R_1– and R_2*-weighted and allow for rapid data acquisition. As static magnetic field inhomogeneities are not refocused, differences in magnetic susceptibility between adjacent structures will cause artifacts such as signal loss due to loss of coherence within a voxel or image distortion due to geometrical misregistration caused by frequency shifts, which become prominent for long T_E values (strong R_2* weighting). Variants of the basic gradient echo experiment are, e.g., Snapshot FLASH (Haase 1990) and fast imaging with steady precession (FISP (Bruder et al. 1988)).

The total image acquisition time can be significantly shortened by generating multiple gradient echoes using a single excitation pulse with incrementing the phase encoding for the subsequent echoes. In echo planar imaging (EPI (Mansfield 1984), Fig. 13.5c), this is achieved by inserting a short gradient pulse (gradient blip) along the phase-encoding direction. EPI was the first rapid imaging technique introduced as early as 1976 and has become the standard readout module for functional MRI. Images can be collected in less than 100 ms.

13.1.7 Contrast in MRI

The signal in MRI depends on the total number of magnetic nuclei in a voxel (spin density ρ), which determines the maximal achievable magnetization, and on all processes that modulate this magnetization such as the RF pulse angle generating detectable nonequilibrium magnetization, all biophysical processes leading to loss of phase coherence of the transverse magnetization components (R_2, R_2*, microscopic motion such as diffusion and microcirculation, coherence transfer), exchange of magnetization due to proton transfer (chemical exchange), as well as the processes that drive the system back to the equilibrium state. All these processes are influenced by the environment of the nuclear spin under investigation and hence characteristics for a type of tissue. It is beyond the scope of this chapter to review the various mechanisms involved in detail, and the reader is referred to the appropriate references (e.g. Haacke et al. 1999). Instead we discuss some basic aspects of the various parameters affecting the signal intensity and hence contrast in MR images.

Longitudinal and Transverse Relaxation We have already introduced longitudinal and transverse relaxation, R_1 and R_2, which are inherently different processes: R_1 characterizes the return of the system to the equilibrium state $\vec{M}_{\text{eq}} = (0, 0, M_0)$ and involves exchange of energy with the environment, the lattice, hence the term spin–lattice interaction. R_2 describes the loss of phase coherence due to fluctuations in the local environment, which modulate the (dipolar) interaction of the nuclear magnets and hence their individual resonance frequencies. Hence, "transverse relaxation" is strictly speaking not a relaxation process. There are several theoretical approaches describing relaxation: the phenomenological approach of the Bloch equations (Bloch 1946; Bloch et al. 1946), a model considering the transition probabilities of the spin system under investigation and its environment (Slichter 1978), semiclassical relaxation theory describing the spin system using quantum mechanics and the environment in classical manner (Redfield 1965), and finally a full quantum mechanical description (Wangsness and Bloch 1953; Bloch 1957).

We briefly outline some concepts of the approach based on perturbation theory (Carrington and McLachlan 1969). Apart from the external magnetic field B_0, the nuclear spin of interest experiences additional local magnetic fields $B'(t)$ due to the interaction with neighboring spins as well as moving electrical charges

$$\vec{B}_{\text{loc}}(t) = \vec{B}_0 + \vec{B}'(t) \tag{13.30}$$

We assume $B'(t) << B_0$, so that these additional terms can be treated as a perturbation of the Zeeman interaction (Eq. 13.2). We limit our discussion to the spin system $I = 1/2$. When

expressing the perturbation term in Eq. (13.30) in the eigenbasis of (Eq. 13.2) (states $m_I = \pm 1/2$), the elements linking the two states, i.e., involving transitions between states $m_I = +1/2$ and $m_I = -1/2$, lead to R_1 relaxation, while the lifetime of the states and the fluctuation of the energy difference between the states lead to R_2 relaxation. Changes in $B'(t)$ occur over a large frequency range and are described by a so-called spectral density function $J(\omega)$, which is related to the *autocorrelation function* $G(\tau)$ via a Fourier transform. If we assume the autocorrelation function to be characterized by an exponential decay, i.e., $G(0)\cdot\exp(i\cdot\omega\cdot\tau_c)$ with the correlation time τ_c, we obtain a Lorentzian function for the spectral density

$$J(\omega) = \frac{2\cdot\tau_c}{1+\omega^2\cdot\tau_c^2}\,\overline{f^*(t)\cdot f(t)} \tag{13.31}$$

with $\overline{f^*(t)\cdot f(t)}$ describing the temporal average of the fluctuations $f(t)$, the asterisk indicating the complex conjugate. As already stated R_1 relaxation involves nuclear spin transitions, i.e., the elements of the perturbation term linking the two states $m_I = \pm 1/2$, and hence depends on the spectral density of the perturbation $-\gamma\cdot\hbar\cdot B'(t)$ around the resonance frequency ω_0, while R_2 is governed by the fluctuation of the energy states of the spin system, which occurs close to zero frequency. Combining this information results in (Carrington and McLachlan 1969)

$$R_1 = \frac{\gamma^2}{2}\cdot\left(\overline{B'^2_x + B'^2_y}\right)\cdot\frac{2\cdot\tau_c}{1+\omega_0^2\cdot\tau_c^2}$$

$$R_2 = \frac{\gamma^2}{2}\cdot\left\{2\cdot\tau_c\cdot\overline{B'^2_z} + \frac{1}{2}\cdot\left(\overline{B'^2_x + B'^2_y}\right)\cdot\frac{2\cdot\tau_c}{1+\omega_0^2\cdot\tau_c^2}\right\} \tag{13.32}$$

R_1 $(=1/T_1)$ depends both on the resonance frequency (it increases with ω_0) and the correlation time and reaches a minimum for $\tau_c = \omega_0^{-1}$, while T_2 decreases with increasing correlation time (Fig. 13.6).

Quantitative estimation of relaxation rates requires knowledge of the local fluctuation in the magnetic field $B'(t)$ and of correlation time τ_c, which is inherently difficult to obtain in particular for living tissue. Interactions to be considered include magnetic dipole interactions, chemical shift anisotropy, nuclear spin–rotational coupling, interactions with quadrupolar nuclei ($I \geq 1$), or the interaction with the magnetic moments of unpaired electrons. The last contribution is of relevance with regard to MRI contrast agents.

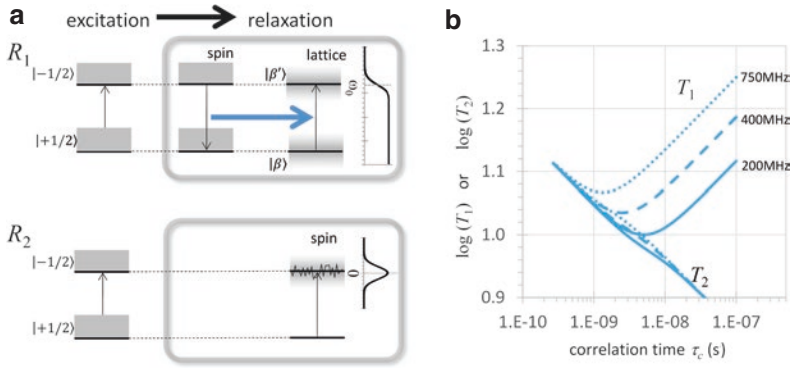

Fig. 13.6 Longitudinal and transverse relaxation. (**a**) Cartoon of R_1 and R_2 relaxation in a spin $I = 1/2$ system. While R_1 involves energy dissipation between the spin system of interest and its environment (lattice), R_2 is governed by fluctuations in the resonance frequency due to stochastic molecular motion and due to the finite lifetime of the excited state. The spectral density functions $J(\omega)$ are indicated for R_1 and R_2 relaxation. (**b**) T_1 and T_2 as a function of the correlation time for 200, 400, and 750 MHz normalized to minimum value for T_1 at 200 MHz. Notice that T_1 increases with increasing resonance frequency

Relaxation Due to Static Susceptibility Differences (R_2*) R_2* has been discussed previously (Eqs. 13.11 and 13.12) and is the principal contribution determining contrast in gradient echo MR images.

Microscopic Motion: Diffusion and Perfusion Motion of a nuclear spin in an inhomogeneous magnetic field leads to changes in the resonance frequency and correspondingly to signal loss due to dephasing. This is accounted for by introducing a diffusion term in (Eq. 13.7), yielding the modified Bloch–Torrey equation

$$d\vec{M} / dt = \gamma \cdot \left(\vec{M} \times \vec{B}_0\right) - \underline{\underline{R}} \cdot \left(\vec{M}(t) - \vec{M}_{eq}\right) + \nabla\left(\underline{\underline{D}} \cdot \nabla M\right) \tag{13.33}$$

where $\underline{\underline{D}}$ is a second rank tensor accounting for the anisotropic diffusion. The last term in (Eq. 13.35) represents the divergence of the vector field analogous to Fick's second law. Diffusion sensitivity can be enhanced by applying a magnetic field gradient G. Solving (Eq. 13.33) yields an additional term that depends on the degree of magnetic field inhomogeneity (~amplitude of the diffusion-sensitizing gradient), the diffusion coefficients, and the diffusion time. Assuming an isotropic medium in which diffusion behaves according to the Einstein equation (i.e., the mean displacement is proportional to the square root of the product diffusion coefficient times the diffusion time) and can be described by a Gaussian, the signal attenuation imposed can be written as

$$\vec{M}(t;D) = \vec{M}(t) \cdot \exp(-b \cdot D) \tag{13.34}$$

where $\vec{M}(t)$ accounts for relaxation terms and D stands for the apparent diffusion coefficient (ADC), as a tissue voxel comprises multiple compartments with different values for diffusion coefficients. The factor b comprises parameters specific to the measurement sequence such as magnetic field gradient amplitude(s) and timing aspects including gradient duration and separation (Bihan 1991; Stejskal and Tanner 1965). Measurements using at least two different b-values allow determining the diffusion coefficient D. For non-Gaussian behavior, (Eq. 13.34) is not valid.

The classical diffusion MR sequence as first described by Stejskal and Tanner (1965) is a basic spin-echo sequence with a pair of diffusion-sensitizing gradients of amplitude G and duration δ applied prior and after the refocusing pulse. The time between the two pulses shall be Δ. Let us consider just the effects of this gradient pulse pair. The first pulse will lead to an additional phase shift for a diffusing spin according to

$$\phi_1 = \gamma \cdot \delta \cdot G \cdot x_1 \tag{13.35}$$

where x_1 is the position of the spin at the beginning of the first pulse. During the second gradient pulse, the spin will acquire an analogous phase shift ϕ_2. The refocusing pulse in the pulse sequence reverts the phase shift ϕ_1; hence, the total phase shift acquired as a result of this gradient pair is given by $\phi_2 - \phi_1$. For nonmoving spins this difference will vanish. For diffusing spins, the gradient pair will lead to a signal attenuation that can be described as

$$b(G, \delta, \Delta) \cdot ADC = \int \rho(x_1) \cdot \int P(x_1, x_2, \Delta) \cdot \exp\left(-i \cdot \gamma \cdot \delta \cdot G \cdot (x_2 - x_1)\right) \cdot dx_2 \cdot dx_1 \tag{13.36}$$

where $\rho(x_1)$ describes the spin density and $P(x_1, x_1, \Delta)$ the diffusion propagator (the likelihood of finding a spin originally located at x_1 at a location x_2 after the diffusion time Δ), while the exponential term is the frequency term describing the phase evolution. The integration accounts for all possible displacements throughout the sample. The integral corresponds to a Fourier integral and can be solved in a straightforward manner if the diffusion propagator is assumed to be Gaussian. Under these conditions the attenuation term becomes (Stejskal and Tanner 1965)

$$b(G, \delta, \Delta) = (\gamma \cdot \delta \cdot G)^2 \cdot \left(\Delta - \frac{\delta}{3}\right) \tag{13.37}$$

By measuring the attenuation for different *b*-values, the *ADC* can be determined.

Anisotropic Diffusion Assuming a water diffusion coefficient in gray matter of $D=0.8\cdot10^{-3}$ mm^2s^{-1}, water molecules diffuse approximately 4 µm assuming a diffusion time of 10 ms. This compares with cell dimensions in tissue; hence, the water molecule will inherently encounter impenetrable tissue barriers (lipid membranes) on its path. As a result, diffusion will be hindered in an anisotropic manner depending on the microstructure of the tissue. Assessing this anisotropy provides an attractive tool for tissue characterization, in particular in highly oriented tissues such as white matter in the brain (Moseley et al. 1990) or cardiac and skeletal myofibers (Stoeck et al. 2016; Heemskerk et al. 2005).

For anisotropic diffusion, the diffusion term in (Eq. 13.33) is described by a tensor $\underline{\underline{D}}$, which is characterized by its three principal values D_1, D_2, D_3 and three Eulerian angles ϕ, θ, ψ defining the tensor orientation in three-dimensional space (Fig. 13.7a). This implies that at least six independent measurements are required to determine $\underline{\underline{D}}$. For practical purposes, some relationships are commonly used. The trace of the diffusion tensor is invariant and corresponds to the value for the isotropic diffusion, hence

$$D = \mathrm{tr}\left(\underline{\underline{D}}\right) = \frac{1}{3}\cdot\left(D_1 + D_2 + D_3\right) \tag{13.38}$$

The degree of anisotropy is captured in the expression for the fractional anisotropy FA, which takes values in the range $0 \le \mathrm{FA} \le 1$ and is given by

$$\mathrm{FA} = \sqrt{\frac{3}{2}}\cdot\sqrt{\frac{\left(D_1 - D\right)^2 + \left(D_2 - D\right)^2 + \left(D_3 - D\right)^2}{D_1^2 + D_2^2 + D_3^2}} \tag{13.39}$$

In oriented tissue, commonly the relationship $D_1 >> D_2 \approx D_3$ holds. Under these conditions, one uses the terms radial $D_\perp$ and axial diffusivity $D_\parallel$, which are defined as

$$D_\perp = \frac{1}{2}\cdot\left(D_2 + D_3\right) \tag{13.40a}$$

$$D_\parallel = D_1 \tag{13.40b}$$

For oriented biological structures such as nerve or muscle fibers, the largest principal value Q_1 ($D_\parallel$) is pointing along the long axis of the structure, while the smaller values Q_2, Q_3 (or $D_\perp$) point perpendicular to it. Hence, the direction $\vec{e}_1$ indicates the direction of the fiber. This is exploited by fiber tracing algorithms, which aim at reconstructing fiber orientations within tissue (DTI tractography). This has found most widespread application in the reconstruction of white matter structures in the brain (Fig. 13.7b, c).

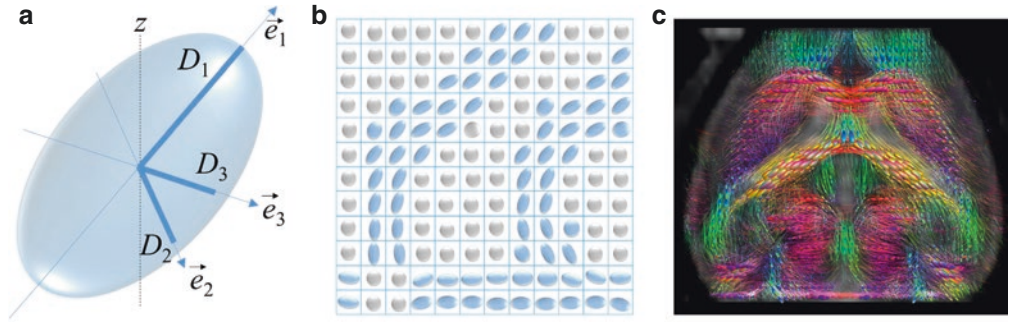

Fig. 13.7 Diffusion tensor imaging and tractography. (**a**) A case of oriented tissue water diffusion is described by a second rank diffusion tensor with the principal values D_1, D_2, D_3 and three orientations of the principal components $\vec{e}_1$, $\vec{e}_2$, and $\vec{e}_3$ (or the Eulerian angles ϕ, θ, ψ). The orientation of the main magnetic field is indicated by z. (**b**) Plotting the diffusion tensor in each voxel yields information on oriented tissue structures (fiber tractography). (**c**) Reconstruction of white matter structures in mouse brain using fiber tractography (Image: courtesy Dr. Valerio Zerbi, ETH Zürich, Dr. Joanes Grandjean, UZH/ETH Zürich)

An issue in tractography is crossing fibers as indicated in the bottom left corner of Fig. 13.7b. The form of the diffusion tensor does not allow the unambiguous reconstruction of fiber tracts. This problem can be addressed using high angular resolution diffusion imaging (HARDI (Tuch et al. 2002)), which used gradient encoding with a high number of different orientations and also explores the vicinity of a voxel. HARDI and related methods have become the standard DTI approach for mapping structural connectivity in the brain.

Intravoxel Incoherent Diffusion (IVIM) Apart from Brownian motion of water molecules in a voxel, pseudorandom motion may also occur due to blood flow in the microvasculature. Hence, (Eq. 13.34) must be extended according to

$$\vec{M}\left(t;\, D, f\right) = \vec{M}\left(t\right) \cdot \left\{ f \cdot \exp\left(-b \cdot D_f\right) + \left(1 - f\right) \cdot \exp\left(-b \cdot D\right) \right\} \tag{13.41}$$

with f being the volume fraction of the microcirculation compartment and D_f the apparent diffusion coefficient attributed to this compartment. Measurements at multiple b-values allow determining the relevant parameters, i.e., the microvascular flow fraction f and the tissue diffusion coefficient D (Le Bihan et al. 1988; Le Bihan 2011). The plot $\ln(M(t;\, D,\, f)$ versus b reveals multi-exponential (bi-exponential) behavior with prominent flow contribution for small b-values and pure diffusion dominating for intermediate values, while for high b-values, effects of restricted diffusion become more prominent.

Contrast Due to Chemical Exchange/ Magnetization Transfer The MR signal of a magnetic nucleus in a compound i may be influenced by exchange processes that cause transfer of magnetization, e.g., as by chemical reaction that involves transfer of the nucleus under investigation to another molecular entity j, by binding of the molecule i to a macromolecular structure leading to line broadening due to incomplete motional narrowing and hence residual dipolar interactions or due to spin diffusion. Exchange reactions are described by kinetic equations relating the concentrations c of the reaction partners,

$$d\vec{c} \,/\, dt = \underline{\underline{K}} \cdot \vec{c}\left(t\right) \tag{13.42}$$

with $\underline{\underline{K}}$ being the kinetic matrix capturing the reaction scheme. In order to describe magnetization transfer, we have to replace the concentrations c by the longitudinal components of the magnetization vector and to add the kinetic term to the Bloch equations (Eq. 13.7a).

$$d\left(M_z\right) / dt = \underline{\underline{K}} \cdot \left(M_z\right) - \left(\underline{\underline{\delta_{ij} \cdot R_{1i}}}\right) \cdot \left\{ \left(M_z\right) - \left(M_{z,\,\mathrm{eq}}\right) \right\} \tag{13.43}$$

The bracket (M_z) stands for a vector comprising the longitudinal magnetization of all partners involved in the exchange process. As additional information for solving (Eq. 13.43), we use the principle of micro-reversibility, which states that at equilibrium $k_{ij} \cdot M_{zi} = k_{ji} \cdot M_{zj}$ (Eq. 13.43) can be solved using, e.g., a transformation to the eigenbasis.

Saturation transfer is a special case of the more general magnetization transfer experiment. In this case the kinetic scheme is simplified by selectively saturating the signal of a specific resonance (Forsen and Hoffmann 1963). We will illustrate this for a two-site exchange process $i \leftrightarrow j$. Assume that the resonance of j is selectively saturated. Then the relaxation matrix and the kinetic matrix reduce to a single element each, R_{1i} and k_{ij}. This leads to a simple differential equation

$$dM_{z,\,i} \,/\, dt = -k_{ij} \cdot M_{zi} - R_{1i} \left\{ M_{zi} - M_{zi,\,\mathrm{eq}} \right\} \tag{13.44}$$

with the solution

$$M_{zi}\left(t\right) = M_{zi,\mathrm{eq}} \cdot \left\{ \frac{R_{1i}}{R_{1i} + k_{ij}} + \frac{k_{ij}}{R_{1i} + k_{ij}} \cdot \exp\left(-\left(R_{1i} + k_{ij}\right) \cdot t\right) \right\}. \tag{13.45}$$

Equation 13.45 describes a single exponential decay of the magnetization of *i* as a function of the duration of the saturation pulse. The equation reveals that in the presence of exchange processes, the relaxation rate R_{1i} has to be replaced by an apparent relaxation rate $R_{1i,\,\mathrm{app}}$, which in the case of saturation transfer describing a two-site exchange becomes $R_{1i,\mathrm{app}} = R_{1i} + k_{ij}$. For very long pulses a steady-state condition is reached according to

$$M_{zi,\,\mathrm{steady-state}} = M_{zi,\,\mathrm{eq}} \cdot \frac{R_{1i}}{R_{1i} + k_{ij}}. \qquad (13.46)$$

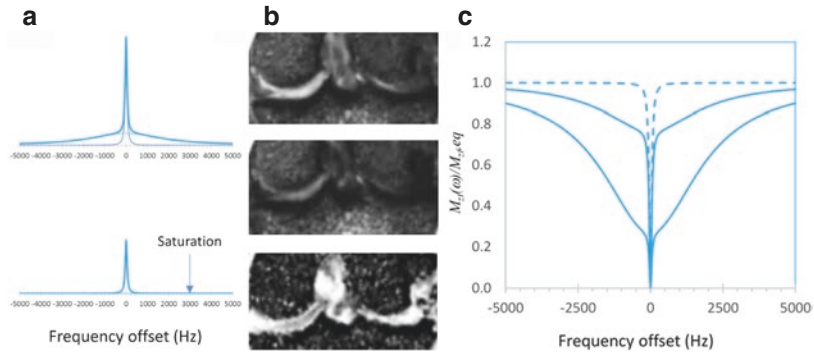

Fig. 13.8 Magnetization transfer contrast. (**a**) Principles of MT contrast: The MR signal comprises the contributions of free and macromolecule-bound water. The latter is not visible due to large line width caused by dipolar couplings. Upon off-resonance saturation, the broad signal is suppressed and the signal due to bulk water reduced as a result of the exchange process. (**b**) Magnetization (saturation) transfer experiment in the goat knee. Image recorded in the absence of off-resonance saturation (*top*), with off-resonance saturation (*middle*) and difference image, indicating significant MT in articular cartilage, which is rich of macromolecules (proteoglycans). (**c**) Z-spectra describing off-resonance magnetization transfer. For all traces $M_{zf}(\omega)/M_{zf,\mathrm{eq}}$ the values T_{1f}=2 s, T_{2f}=100 ms, T_{1b}=1 s, T_{1b}=100 μs, and $\gamma \cdot B_1$=239 Hz have been used. (**a**) In the absence of magnetization exchange and (**b**) with magnetization exchange via cross-relaxation and k_{fb}=1 s^{-1}, k_{bf}=10 s^{-1}, and (**c**) k_{fb}=1 s^{-1}, k_{bf}=1 s^{-1}

In addition to chemical exchange, magnetization transfer can occur by means of magnetic cross-relaxation, i.e., transfer of magnetization from one species to another via dipole–dipole interactions. The cross-relaxation between mobile and restricted molecules (e.g., free and bound water) has been widely studied in vivo as it offers an attractive new contrast mechanism in MRI (Fig. 13.8).

Biological tissue is composed of mobile and immobile molecules. Mobile components such as water have relatively long T_2 relaxation times (50–200 ms) giving rise to narrow resonances (20–40 Hz), while the bound fraction of water has a long correlation time and hence a short T_2 (10–100 μs) giving rise to broad signals (5–50 kHz), which are too broad to be detected under in vivo conditions (Fig. 13.8a). Note that in this case both the free pool *f* and the bound pool *b* have the same resonance frequency. Hence, in order to study proton exchange between the two pools, on-resonance saturation cannot be applied (Wolff and Balaban 1989). However, in the case of homogeneously broadened resonances, the broad component can be saturated by off-resonance irradiation, which under steady-state conditions leads to a signal reduction that depends on the frequency offset $\Delta\omega$, the intensity of the saturating B_1 field, the rate constants of the exchange reaction, and the relaxation rates of the compounds involved,

$$\frac{M_{zf}(\omega)}{M_{zf,\,\mathrm{eq}}} = \left\{ R_{1f} \cdot \left[\left(R_{1b} + k_{bf} \right) + \frac{\gamma^2 B_1^2 T_{2b}}{1 + \Delta\omega_b^2 T_{2b}^2} \right] + R_{1b} k_{fb} \right\} / D \qquad (13.47)$$

with

$$D = \left[R_{1f} + k_{fb} + \frac{\gamma^2 B_1^2 T_{2f}}{1 + \Delta\omega_f^2 T_{2f}^2} \right] \cdot \left[R_{1b} + k_{bf} + \frac{\gamma^2 B_1^2 T_{2b}}{1 + \Delta\omega_b^2 T_{2b}^2} \right] - k_{fb} k_{bf}$$

Plotting $M_{zf}(\omega)$ as a function of the frequency offset yields the so-called z-spectra (Fig. 13.7). In the presence of additional exchange partners, e.g., amide groups, the z-spectrum will exert an additional peak at the respective resonance frequency. Chemical exchange saturation transfer (CEST) has raised considerable interest as contrast mechanism to probe specific molecular interaction. Molecules of interest are both endogenous biomolecules such amino acids, sugars, proteins, and synthetic biomolecules designed by chemical and genetic engineering (Bar-Shir et al. 2015; McMahom and Chan 2014).

Phase Contrast and Susceptibility Mapping The MRI signal is a complex signal consisting of a real component $\Re$ (absorption) and an imaginary component $\Im$ (dispersion) or when expressed in polar coordinates of a magnitude ($\sqrt{\Re^2 + \Im^2}$) and a phase ($\tan\phi = \Im / \Re$). In the vast majority of MRI application, images are represented as magnitude images. More recently it has been realized that the signal phase contains interesting information regarding inclusions that have a different magnetic susceptibility than the adjacent tissue. This has been exploited, e.g., in the imaging of blood vessels or microhemorrhages, which contain relatively high amounts of paramagnetic iron, or for mapping myelinated structures. The MR phase shift ϕ accrued in a gradient echo experiments depends linearly on the field offset ΔB_0 and the echo time T_E,

$$\phi = \gamma \cdot \Delta B_0 \cdot T_E \tag{13.48}$$

ΔB_0 depends on the susceptibility difference between structures and their orientation with respect to the static magnetic field. The field perturbation induced by an inclusion of different magnetic susceptibility can be described as a dipole field,

$$\Delta \vec{B}_0(\vec{r}) = \frac{\mu_0}{4\pi} \cdot \left(\frac{3 \cdot (\vec{r} - \vec{r}_d) \cdot (\vec{M}_\chi(\vec{r}) \cdot (\vec{r} - \vec{r}_d) - |\vec{r} - \vec{r}_d|^2 \cdot \vec{M}_\chi(\vec{r})}{|\vec{r} - \vec{r}_d|^5} \right) \tag{13.49}$$

with

$$\vec{M}_\chi(\vec{r}) = \chi(\vec{r}) \cdot \frac{\vec{B}_0}{\mu_0 \cdot (1 + \chi(\vec{r}))} \approx \frac{\chi(\vec{r}) \cdot \vec{B}_0}{\mu_0 \cdot}$$

In (Eq. 13.49) $\vec{r}$ indicates the location at which the dipole field $\Delta\vec{B}_0(\vec{r})$ is calculated, and $\vec{M}_\chi(\vec{r})$ the local magnetization induced by a point dipole source at $\vec{r}_d$. This simple model allows estimating phase shift for specific geometries (Haacke et al. 2004; Schäfer et al. 2009; Hsieh et al. 2015). Phase information can be exploited by generating pure phase images or by combining phase information with magnitude information yielding so-called susceptibility weighted images (SWI (Haacke et al. 2004)), which enable detecting regions with altered susceptibility with high sensitivity, in particular when moving to high magnetic field strength. An aspect to be considered is phase wrapping: phase shifts of 2π cannot be discriminated. Hence, phase maps have to be unwrapped in order to avoid phase jumps.

The inherent nature of dipole fields leads to a blurring of images, i.e., local magnetic field changes due to an inclusion extend well beyond its physical dimension. This is accounted for by susceptibility maps, which involves solving the inverse problem, i.e., deducing the localization and spatial extent of a structure of different magnetic susceptibility based on its perturbation of the magnetic field (Haacke et al. 2015).

Generating Contrast in MR Images The values for the contrast parameters discussed previously vary across tissues and thus constitute the source of contrast in MR images. Depending on the question, emphasis of a specific parameter or a combination of parameters is envisaged, which can be achieved by tailoring the MRI data acquisition. Imaging pulse sequences are typically composed of a contrast and a readout module (Fig. 13.9). In many cases the two building blocks cannot be separated, e.g., in a multi-spin-echo sequence for measuring R_2 or in a multigradient echo sequence for measuring R_2*. Figure 13.9 shows some exemplary contrast modules for measuring R_1 (a), the apparent diffusion coefficient (b), and exchange rates by saturation transfer (c). Today, the readout modules are typically rapid acquisition protocols such as fast gradient echo methods (Snapshot FLASH, FISP, EPI).

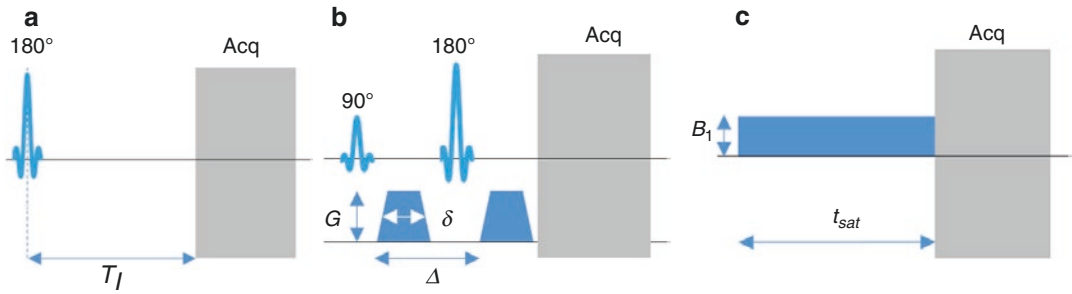

Fig. 13.9 Some contrast modules used in MRI. (**a**) Inversion recovery experiment involving a slice-selective inversion pulse preceding data acquisition by an inversion delay T_I. (**b**) The basic Stejskal–Tanner sequence for measuring diffusion properties involves a gradient pair incorporated into a spin-echo sequence. G indicates the gradient amplitude, δ the pulse duration, and Δ the delay between the two gradient pulses. (**c**) Saturation transfer experiment for measuring chemical exchange properties. Data acquisition is preceded by a frequency-selective RF pulse of amplitude B_1 and duration t_{sat}

MRI Fingerprinting The various contrast mechanisms are the basis for the excellent soft tissue contrast in MRI. By choosing an appropriate pulse sequence, contrast may be optimized for a specific condition, e.g., to differentiate infarcted tissue from the healthy brain. Yet, contrast-to-noise ratio depends on the specific sequence parameters and on the imaging hardware rendering comparison across centers difficult. As MRI parameters are characteristic for tissues, it has been proposed already in the early days of MRI to acquire MR parameter maps, which would constitute a quantitative tissue characteristic. As described above the classical MRI sequence combines a contrast module with a readout module yielding an image displaying a specific contrast, i.e., quantitative information is typically obtained only for a single parameter at a time. Yet, knowledge of a single parameter value is hardly sufficient to describe a complex biological structure/condition; instead a set of parameters should be assessed, i.e., a tissue "fingerprint." Using classical measurement strategies, different MR parameters would have to be measured in a sequential manner, which may be prohibitive due to time limits. Recently, Ma et al. (2013) proposed a radically different approach, which they dubbed "MR fingerprinting" (Fig. 13.10).

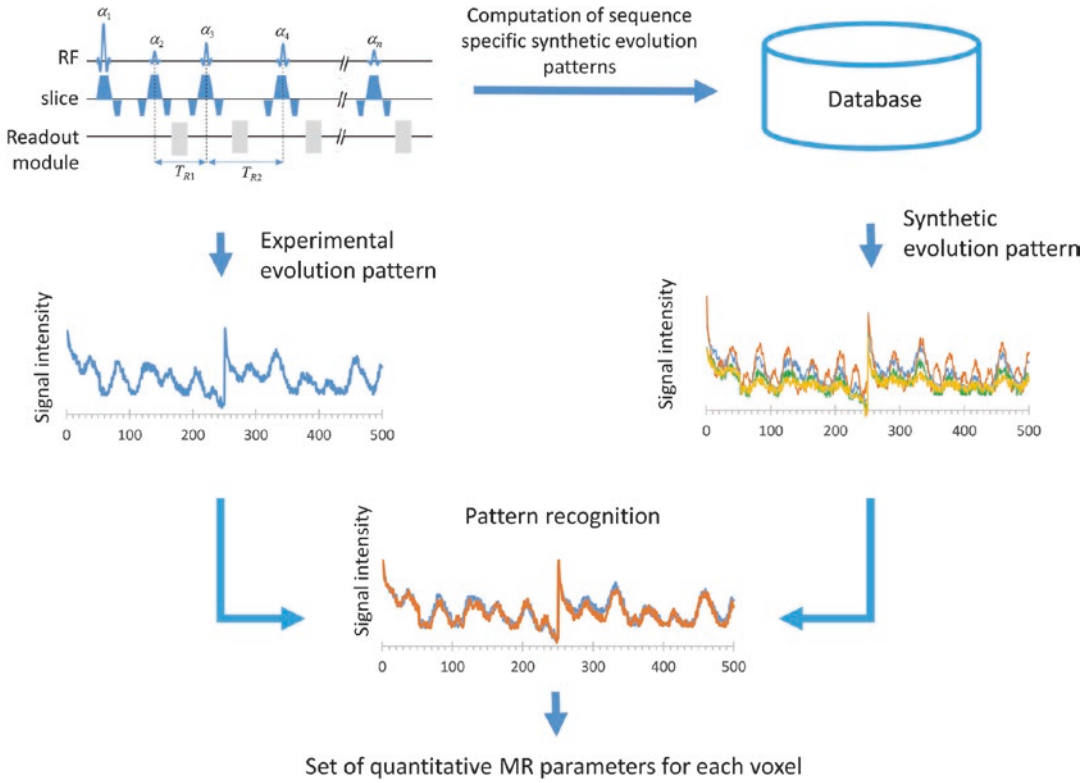

Fig. 13.10 Concept of MR fingerprinting. Data are acquired using a pseudorandomized MR pulse sequence yielding an experimental signal evolution pattern $S(i)$ for each voxel, i. indicating the number of data points acquired. Using a multidimensional space of MRI parameters, synthetic signal evolution traces are calculated for the specific sequence for each combination of parameters $S(i; p_{1j}, p_{2j}, \ldots, p_{Nj})$. Pattern recognition algorithms are used to compare experimental and synthetic spectra. The optimal match then yields a set of MR parameters for each voxel

The basic idea is to use a pseudorandomized acquisition by designing a pulse sequence with varying parameters such as flip angles and phases of radio-frequency pulses, repetition time, echo time, and *K*-space sampling patterns. As a result, each tissue type characterized by a unique set of parameters such as proton density, relaxation times, and diffusion coefficient elicits a unique signal evolution pattern or fingerprint. These patterns are then compared with synthetic patterns computed for a large set of parameter values for the specific pulse sequence and stored in a database. Computed and experimental signal courses are compared using pattern recognition algorithms, and the optimal match yields the desired set of quantitative MR parameter for each voxel. The total acquisition time is comparable to the acquisition time of a conventional MRI scan.

13.1.8 Sensitivity/Sensitivity Enhancement

The principle problem in small animal MRI as compared to clinical MRI is the reduced sensitivity, i.e., a reduction in the signal-to-noise ratio (SNR) per unit time, which is given by

$$\frac{\mathrm{SNR}}{t} \propto F^{1/2} \cdot \frac{\gamma \cdot B_0 \cdot (B_1 / I)}{\sqrt{4 \cdot k \cdot (R_S \cdot T_s + R_C \cdot T_C)}} \cdot M_T \cdot V_{\mathrm{voxel}} \cdot \sqrt{\frac{N_{\mathrm{re}}}{\mathrm{BW}}} \cdot \sqrt{N_{\mathrm{ph}}} \cdot \sqrt{N_A} \cdot \frac{1}{t} \qquad (13.50)$$

with F being a scanner-specific factor, the term (B_1/I) accounting for the coil efficiency (the B_1 field produced per unit current), M_T the total magnetization, and V_{voxel} the voxel volume. N_{re} and N_{ph} stand for the number of readout (frequency encoding) and phase-encoding steps, while N_A represents the number of averages. The noise term consists of two major terms: the noise generated by the sample and the noise due to the receiver coil. Both contributions are represented by thermal noise terms characterized by an apparent resistance R_S and R_C, respectively, and by a corresponding temperature T_S and T_C. If we compare now a human with a mouse head, the voxel volume for the latter is reduced by a factor of typically 1000 (voxel dimensions are 1 mm^3 for humans and (100 μm)^3 for mice). If we furthermore assume that the volume contributing to sample noise is reduced by the same amount and that all other parameters are kept identical, we would expect a reduction SNR/t by a factor of 30. Several strategies may be pursuit to account for this loss in sensitivity, either by increasing the signal per unit volume, by decreasing the noise, or a combination of both.

Increasing the static magnetic field strength B_0 will increase the sensitivity by a factor of B_0^x, wi th $x \geq 1$ (Haacke et al. 1999). Hence, animal imagers operate at higher magnetic field strength (4.7–21 Tesla) than clinical scanners (1.5–7 Tesla). The highest gain in sensitivity is obtained by using optimally adapted RF transmitter/receivers, i.e., by maximizing the ratio B_1/I. The dimension of the MRI receiver should ensure optimal probe filling with the inductivity in close proximity to the sample. M_T can be increased by increasing the polarization of the sample, e.g., by increasing the static field or by using polarization enhancing strategies such as dynamic nuclear polarization (Overhauser 1953; Ardenkjaer-Larsen et al. 2003a). Finally the signal can be increased by averaging; however, due to the statistical nature of the noise process, *SNR* would only improve according to the square root of the number of acquisition, which will inevitably lead to very long imaging times.

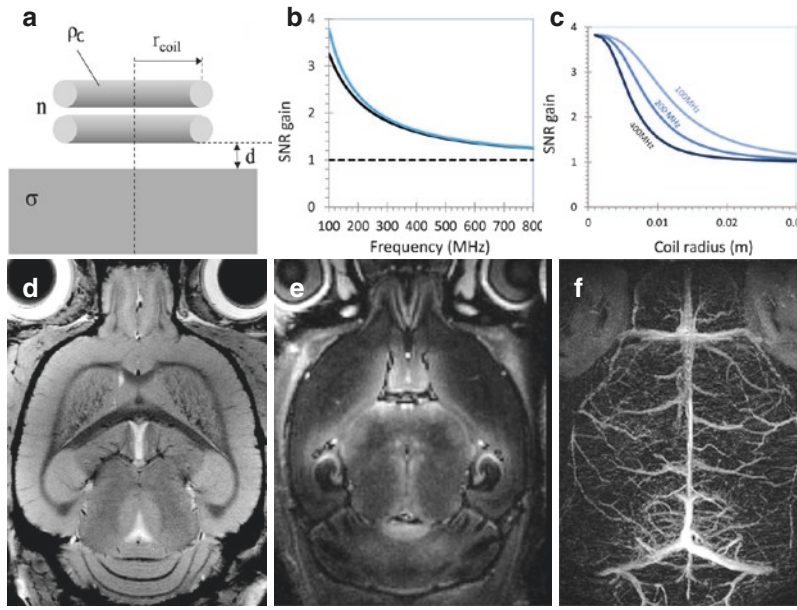

Fig. 13.11 High-resolution MRI of mouse brain using cryogenic RF transmitter/receiver surface coil. (**a**) Surface coil of radius r_{coil}, n turns, and made of a material with resistivity ρ_C. The coil is placed at a distance d from a semi-infinite lossy sample characterized by the electrical conductivity σ. (**b**) SNR gain of low temperature detection for a circular surface coil of radius 10 mm as a function of the resonance frequency and for several operating temperatures: room temperature reference (*dashed line*), 25 K (*black solid line*), at 0 K (*blue line*). (**c**) SNR gain as a function of coil radius for three resonance frequencies. (**d**) Horizontal cross section through mouse brain recorded using a spin-echo pulse sequence. Voxel dimensions are 50×50×150 μm^3, acquisition time was 10 min. (**e**) Manganese-enhanced T1-weighted horizontal cross section through mouse brain at the same resolution recording using a gradient echo sequence. Image acquisition time was 3 min. Note excellent demarcation of dentate gyri. (**f**) 3D high-resolution contrast-enhanced angiogram of mouse brain cortical vasculature obtained as difference image pre- minus post-contrast agent (Endorem) administration. Voxel dimensions are (60 μm)^3; data acquisition time was 30 min. All images were recorded on Bruker Biospec 94/30 MRI system equipped with a quadrature transmit/receive cryogenic coil (Bruker Biospin GmbH, Ettlingen, Germany)

Alternatively, the SNR can be improved by reducing the noise contributions. This is achieved by optimizing the filling factor, i.e., by keeping the volume of the sample that contributes to noise minimal. Alternatively, the electronic noise by cooling of the detector coil may lead to substantial increases in SNR ((Ratering et al. 2008; Baltes et al. 2009); Fig. 13.11). While sample noise is dominating in human MRI and hence reducing electronic noise has a negligible effect on overall SNR, sample and electronic noise contributions become comparable for sample volumes of the order of a few milliliters. In this case, the reduction of detection coil/electronics temperature becomes attractive. It becomes obvious that the SNR gain is higher at lower resonance frequencies and also increases with decreasing coil radius, i.e., reduced sample volume and hence sample noise contribution.

13.1.9 Conclusion

Today MRI has become an indispensable tool for radiologic imaging but also for applications in basic biomedical research. Its major strength is its versatility and the fact the MR signal depends on a multitude of independent parameters that are determined by the biophysical properties of tissue. Hence, MRI sequences can be tuned to provide excellent soft tissue contrast yielding excellent anatomical definition or physiological information. Yet, this multiparametric signal dependence is also a disadvantage as it renders the extraction of quantitative information difficult. Even if tissue parameters could be measured quantitatively, it is in general difficult to translate this kowledge into biomedically relevant information such as quantitative measures of physiological parameters or local concentrations of specific compounds/metabolites. The principal limitation of MRI, however, is its inherently low sensitivity due to the low quantum energy involved in the resonance process. This will limit its use for molecular imaging applications. Nevertheless, novel imaging strategies/agents employing the various MRI contrast mechanisms are being developed at a rapid pace trying to overcome this limitation, rendering MRI an attractive tool also for cellular and molecular imaging.

13.2 MR Contrast Agents

Eliana Gianolio, Alessandra Viale, Daniela Delli Castelli, Silvio Aime

13.2.1 Introduction

The superb spatial resolution and the outstanding capacity of differentiating soft tissues have determined the widespread success of magnetic resonance imaging (MRI) in clinical diagnosis (Rinck 2003). The contrast in an MR image is the result of a complex interplay of numerous factors, including the relative T_1 and T_2 relaxation times, proton density of the imaged tissues, and instrumental parameters. The MR image contrast can be further enhanced by the administration of suitable MRI contrast agents (CAs).

Unlike contrast agents used in x-ray computed tomography and in nuclear medicine, the currently used MRI contrast agents are not directly visualized in the image. Only their effects are observed as the contrast is affected by the variation that the CA causes on water proton relaxation times and consequently on the intensity of the NMR signal (Brücher and Sherry 2001). Generally, the purpose of a CA is to reduce T_1 or T_2 in order to obtain a hyper- or ipo-intense signal in short times and a better signal-to-noise ratio with the acquisition of a higher number of measurements. CAs that predominantly reduce T_1 are called *positive*, whereas those that mainly affect T_2 are called *negative*. The search for positive MRI contrast agents was oriented toward paramagnetic metal complexes because unpaired electrons display remarkable ability to reduce T_1 and T_2 of their solutions (Engelstadt and Wolf 1988; Rinck 1993), whereas iron oxide particles are most used negative agents.

Another class of contrast agents is represented by CEST agents. They act through the transfer of saturated magnetization to the "bulk" water signal. Such a saturation transfer leads to a decrease of the MR signal intensity, and therefore these species too act as negative agents.

In recent years much attention has been devoted to chemicals that are sensitive enough to be directly visualized in MR images. For instance, ^{19}F-containing systems have been proposed. The required local concentration is of course much higher than that used in the case of paramagnetic agents. Nevertheless it has been shown that carriers bearing with a large number of fluorine containing molecules may yield ^{19}F-MR images. One advantage deals with the possibility of exploiting different chemical shifts of the F-19 resonances thus allowing the detection of more than one agent in the same image. Another emerging class of frequency-encoded agents is represented by ^{13}C-hyperpolarized molecules. These molecules display a high sensitivity that allows their direct visualization in a MR image; moreover it has been possible to acquire images of the hyperpolarized products of their metabolism (metabolic imaging). The introduction of these hyperpolarized systems opened a new horizon in the study of abnormalities of cellular metabolism and, if successfully translated to clinics, represents a real breakthrough in the field of medical imaging (Fig. 13.12).

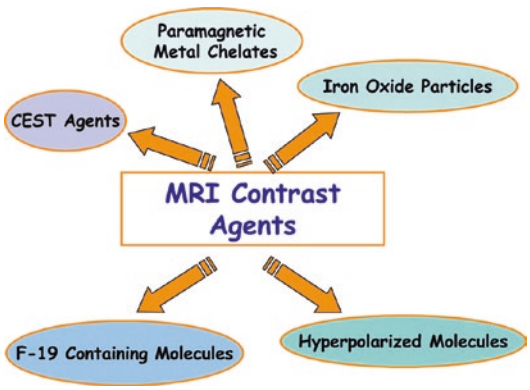

Fig. 13.12 Classes of MRI contrast agents

13.2.2 T_1-Paramagnetic Mn- and Gd-Based Relaxation Agents

Paramagnetic substances are under intense scrutiny as MRI contrast agents since the early days of NMR tomography. Although stable organic radicals, NO and O_2, were also considered, it was immediately clear that paramagnetic metal complexes are the candidates of choice for this application.

On this basis, the metal ions more suitable for this application have been identified among those ones having the higher number of unpaired electrons, namely, Mn(II) and Fe(III) (five unpaired electrons) in the transition metal series and Gd(III) (seven unpaired electrons) among the lanthanides.

Currently, several Gd-based and one Mn-based agents are available for clinical applications. Their use has led to remarkable improvements in medical diagnosis in terms of higher specificity, better tissue characterization, reduction of image artifacts, and functional informations. Besides acting as catalyst for the relaxation of water protons, a paramagnetic MRI contrast agent has to possess several additional properties in order to guarantee the safety issues required for "in vivo" applications at the administered doses, namely, high thermodynamic (and possibly kinetic) stability, good solubility, and low osmolality (Brücher and Sherry 2001; Tweedle 1989).

The first CA approved for clinical use was Gd-DTPA (Magnevist®, Schering AG, Germany) that, in more than 10 years of clinical experimentation, has been administered to many millions of patients. Other Gd(III)-based CAs similar to Magnevist® became soon available: Gd-DOTA (Dotarem®, Guerbet SA, France), Gd-DTPA-BMA (Omniscan®, GE Health, USA), and Gd-HPDO3A (ProHance®, Bracco Imaging, Italy) (Weinmann et al. 2000). These CAs have very similar pharmacokinetic properties because they distribute in the extracellular fluid and are eliminated via glomerular filtration. In neurological diseases, they are particularly useful to delineate lesions as a result

of the disruption of the blood–brain barrier. Two derivatives of Gd-DTPA have been successively introduced, Gd-EOB-DTPA (Schmitt-Willich et al. 1999) (Eovist®, Schering AG, Germany) and Gd-BOPTA (Uggeri et al. 1995) (MultiHance®, Bracco Imaging, Italy). They are characterized by an increased lipophilicity due to the introduction of an aromatic substituent on the carbon backbone of the DTPA ligand. This modification significantly alters the pharmacokinetics and the biodistribution of these CAs as compared to the parent Gd-DTPA making them particularly suitable as hepatospecific agents (Fig. 13.13).

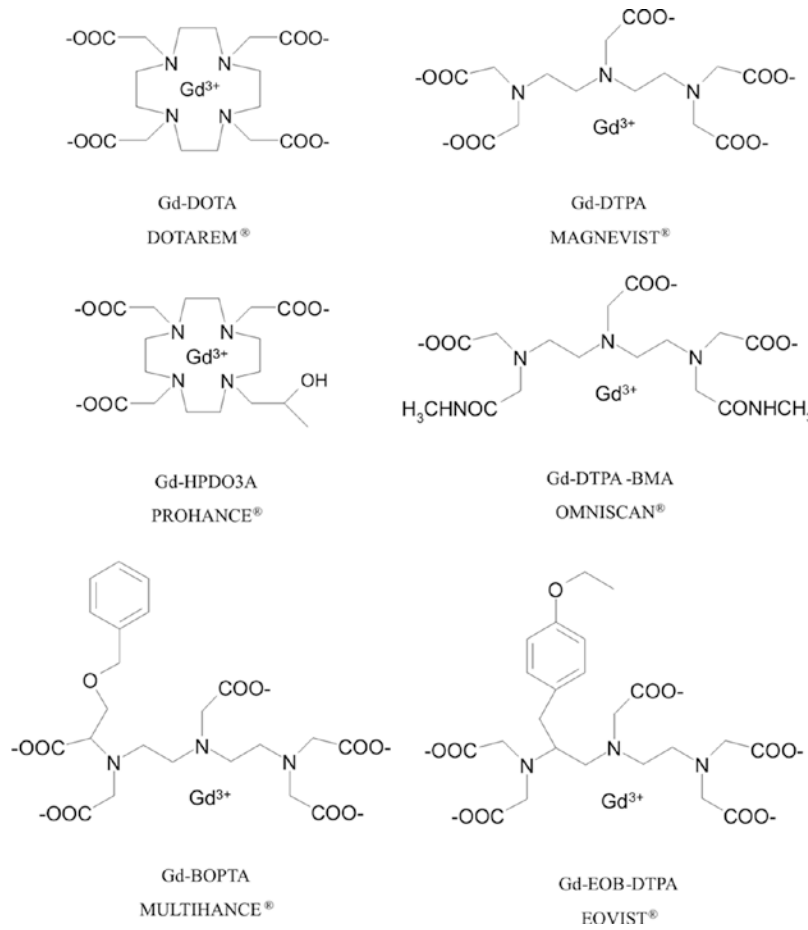

Fig. 13.13 Structures of the Gd(III)-based MRI contrast agents currently used in the clinical practice

Paramagnetic chelates of Mn(II) (five unpaired electrons) have also been considered. The main drawback appears to be related to the stability of these complexes. Mn(II) is an essential metal; therefore evolution has selected biological structures able to sequester Mn(II) ions with high efficiency. Combined with the fact that Mn(II) forms highly labile coordination complexes, it has been difficult to design Mn(II) chelates that maintain their integrity when administered to living organisms. Actually, MnDPDP has entered the clinical practice and is recommended as a hepatotropic agent (Rummeny and Marchal 1997). It is the only agent that does its job by releasing metal ions to endogenous macromolecules. The huge proton relaxation enhancement brought about by the resulting Mn(II) protein adducts is responsible for the MRI visualization of hepatocytes also at low administered doses of MnDPDP (Fig. 13.14).

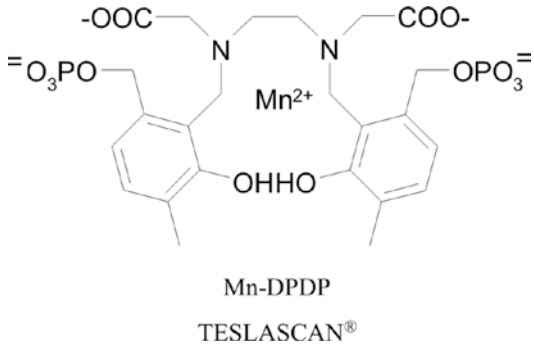

Fig. 13.14 Structure of the Mn(II)-based MRI contrast agent used in the clinical practice

13.2.2.1 Theory of Paramagnetic Relaxation

The efficiency of a relaxation agent is commonly evaluated in vitro by the measure of its relaxivity (r_1), that, for commercial CAs as Magnevist, Dotarem, ProHance, and Omniscan, is around 3.4–3.5 mM^{-1} s^{-1} (at 20 MHz and 39 °C). It represents the relaxation enhancement of water protons in the presence of the paramagnetic complex at 1 mM concentration. The observed longitudinal relaxation rate (R_1^{obs}) of the water protons in an aqueous solution containing the paramagnetic complex is the sum of three contributions (Eq. 13.51) (Banci et al. 1991): (i) the diamagnetic one (R_1^{o}), whose value corresponds to proton relaxation rate measured in the presence of a diamagnetic (La, Lu, Y) complex of the same ligand; (ii) the paramagnetic one, relative to the exchange of water molecules from the inner coordination sphere of the metal ion with bulk water (R_{1p}^{is}); and (iii) the paramagnetic one relative to the contribution of water molecules that diffuse in the outer coordination sphere of the paramagnetic center (R_{1p}^{os}). Sometimes also a fourth paramagnetic contribution is taken in account, that is, due to the presence of mobile protons or water molecules (normally bound to the chelate through hydrogen bonds) in the second coordination sphere of the metal ion (Botta 2000).

$$R_1^{obs} = R_1^{o} + R_{1p}^{is} + R_{1p}^{os} \tag{13.51}$$

The inner-sphere contribution is directly proportional to the molar concentration of the paramagnetic complex [C], to the number of water molecules coordinated to the paramagnetic center, q, and inversely proportional to the sum of the mean residence lifetime, τ_m, of the coordinated water protons and their relaxation time, T_{1M} (Eq. 13.52).

$$R_{1p}^{is} = \frac{q[C]}{55.5\left(T_{1M} + t_m\right)} \tag{13.52}$$

The latter parameter is directly proportional to the sixth power of the distance between the metal center and the coordinated water protons (r) and depends from the molecular reorientational time, τ_R, of the chelate, from the electronic relaxation times, T_{iE} ($i = 1, 2$), of the unpaired electrons of the metal (which depend on the applied magnetic field strength) and from the applied magnetic field strength itself (Eqs. 13.53 and 13.54).

$$\frac{1}{T_{1M}} = \frac{2}{15}\left(\frac{\mu_o}{4\pi}\right)^2 \frac{\gamma_I^2 g_e^2 \mu_B^2 S\left(S+1\right)}{r_H^6}\left(\frac{7\tau_c}{1+\omega_S^2\tau_c^2} + \frac{3\tau_c}{1+\omega_I^2\tau_c^2}\right) \tag{13.53}$$

$$\tau_c^{-1} = \tau_R^{-1} + \tau_m^{-1} + T_{iE}^{-1} \tag{13.54}$$

The outer sphere contribution depends on T_{iE}, on the distance of maximum approach between the solvent and the paramagnetic solute, on the relative diffusion coefficients, and again on the magnetic field strength. The dependence of R_{1p}^{is} and R_{1p}^{os} on magnetic field is very important because the analysis of the magnetic field dependence allows the determination of the principal parameters characterizing the relaxivity of a Gd(III) chelate. This information can be obtained through an NMR instrument in which the magnetic field is changed (field cycling relaxometer)

to obtain the measure of r_1 over a wide range of frequencies (typically 0.01–50 MHz). At the frequencies most commonly used in commercial tomographs (20–63 MHz), τ_R of the chelate is the primary determinant of the observed relaxivity. A quantitative analysis of r_1 dependence on the different structural and dynamic parameters shows that, for systems with long τ_R (e.g., protein-bound complex), the maximum attainable r_1 values can be achieved through the optimization of τ_M and T_{1e} (Banci et al. 1991).

All the available commercial CAs are monohydrated ($q=1$) systems with a molecular weight of ca. 600–800 Da and rotational correlation times (τ_R) around 60–80 ps. For most of the polyaminocarboxylate complexes, the exchange lifetime τ_M is typically found to be in the range of few hundreds of ns and $T_{1e} \approx 1$ ns at 0.5 T, and thus the inner-sphere relaxivity, r_{1p}^{IS}, assumes a value of ca. 2.5–3.5 $mM^{-1}\,s^{-1}$, at 25 °C. Therefore, as it was early recognized, it is evident that at 0.5 T the overall correlation time is largely dominated by the rotational correlation time, whereas the contribution of both the exchange lifetime and the electronic relaxation plays an almost negligible role.

An important structural parameter that influences the *inner-sphere* relaxivity is the hydration number q. This represents a scaling factor in the equation that defines inner-sphere relaxivity, and then a higher number of coordinated water molecules ($q>1$) provide a clear advantage in terms of efficiency. The use of hepta- or hexadentate ligands would in principle result in Gd(III) complexes with two and three coordinated water molecules, respectively, but the decrease of the denticity of the ligands is likely to be accompanied by a decrease of their thermodynamic stability and an increase of their toxicity. Furthermore, systems with $q=2$ may suffer a "quenching" effect upon interacting with endogenous anions or with proteins, as donor atoms from lactate or Asp or Glu residues may replace the coordinated water molecules (Aime et al. 1998).

13.2.2.2 Blood Pool Agents

Several systems have been studied over the last two decades for the design of macromolecular Gd(III) complexes as MRI blood pool contrast agents. These paramagnetic macromolecules do not diffuse across healthy vasculature and remain intravascular thus reporting on the anatomy of the vessel bed. In addition to higher vascular retention time, macromolecular systems are often endowed with sensibly higher relaxivities (at 0.5–1.5 T), thanks to the elongation of reorientational correlation times of slowly tumbling systems.

The most straightforward method to increase the plasma circulation time and promote vascular confinement of a contrast agent is to covalently bind it to biomacromolecules such as proteins, polysaccharides, and dextrans.

An alternative to covalent binding has been pursued by exploiting the non-covalent reversible interaction between low molecular weight hydrophobic Gd(III) complexes and proteins.

Human serum albumin (HSA) has been by far the most investigated protein for binding of Gd(III) chelates. Besides the attainment of high relaxivities, a high binding affinity to HSA enables the Gd(III) chelate with a long intravascular retention time which is the property required for a good blood pool agent for MR angiography. In blood, HSA has a concentration of about 0.6 mM, and its main physiological role deals with the transport of a huge number of substrates (Carter and Ho 1994).

In Table 13.1 a list of Gd(III) complexes and the relevant parameters of their binding interaction to HSA are reported.

Although the theory of the paramagnetic relaxation foresees relaxivities up to 100–120 $mM^{-1}s^{-1}$ (at 20 MHz) for complexes bound to macromolecular systems, the data listed in Table 13.1 show r_1^b values significantly lower than the predicted ones. The primary reason for the quenching of the relaxation enhancement is often associated to the occurrence of a long exchange lifetime, τ_M, of the coordinated water molecule (Aime et al. 1999).

Table 13.1 Affinity constant and relaxivity of the adducts of some Gd(III) complexes with HSA, calculated at 0.47 T and 298 K. The coordinated water exchange life time of free complexes is also reported

Metal complex	$n \times K_A$ (M^{-1})	$R_1{}^b$ ($mM^{-1}s^{-1}$) 20 MHz	$\tau_M{}^{298}$ (ns)	Reference
[Gd-BOPTA (H_2O)]$^{2-}$ 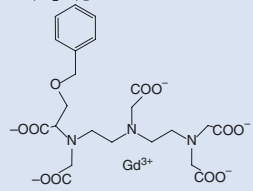	4.0×10^2	33.0	280	Aime et al. (2001)
[Gd-DOTA(BOM)$_3$(H_2O)]$^-$ 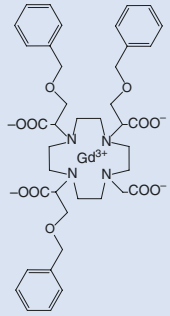	2.0×10^4	44.0	80	Aime et al. (1996)
MS-325 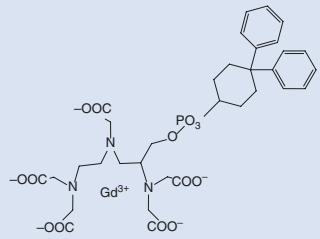	9.0×10^4	37.2	250	Lauffer et al. (1998) Aime (1999)
B22956 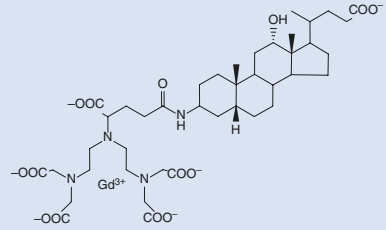	2.6×10^4	27.6	250	Aime (1999)
B25716 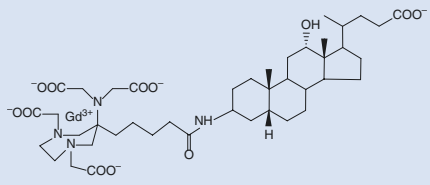	2.0×10^4	29.0	195	Gianolio et al. (2014)

Table 13.1 (continued)

Metal complex	$n \times K_A$ (M^{-1})	$R_1{}^b$ ($mM^{-1}s^{-1}$) 20 MHz	$\tau_M{}^{298}$ (ns)	Reference
S-RRR Gd-4 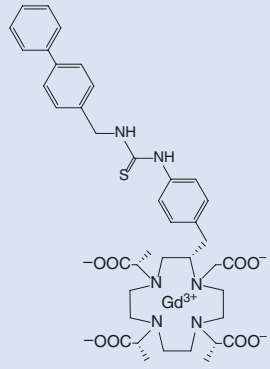	2.1×10^5	46.8	70	Botta *Inorg. Chem.* 2013
S-SSS Gd-4 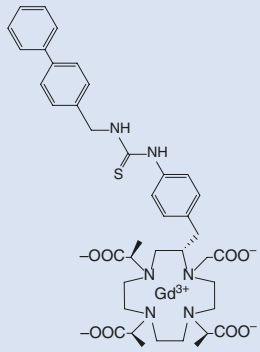	1.5×10^4	37.6	8	Botta *Inorg. Chem.* 2013
Gd-AAZTA-C17 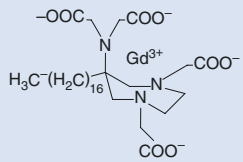	2.4×10^4	84	90	Gianolio et al. (2007)
Gd(4b) 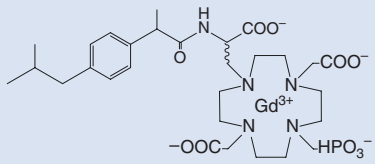	1.25×10^4	19	2.4	Boros et al. (2014)

Nevertheless, it has been recently demonstrated (Avedano et al. 2013) that "simply" optimizing water exchange rate and molecular tumbling does not guarantee that highest relaxivities will be attained.

Upon considering two isomeric Gd^{3+} chelates with very similar electronic relaxation properties but very different dissociative water exchange kinetics, a direct side by side comparison of the effect of varying water exchange kinetics on relaxivity has been possible.

The results described By Avedano et al. showed that the relaxivity of the chelate with "optimal" dissociative water exchange kinetics is actually lower than that of its isomeric chelate with "suboptimal" dissociative water exchange. Analysis of the relaxometric data revealed that the origin of this unexpected result lies in a difference in hydration state (q/r_{GdH}^6) between the two isomers. These results demonstrate that, far from being a matter of little importance, the hydration state (number and position of water molecules in the inner coordination sphere) can have a very profound effect on relaxivity.

Caravan and coworkers (Zhang et al. 2005) tackled the problem of the residual of a Gd(III) complex bound to HSA by designing a system containing two anchoring sites to the protein. Interestingly, the observed relaxivity for such adduct, though quite high (60 $mM^{-1}s^{-1}$), is still significantly lower than that foreseen by the paramagnetic relaxation theory.

More recently, Boros et al. (Boros et al. 2014) reported the characterization and the albumin binding properties of two Gd complexes derived from the single amino acid chelator DOTAlaP functionalized with ibuprofen. While one of the two complexes contains no inner-sphere water, the other derivative resulted to be a mixture of ca. 15 % $q=1$ and 85 % $q=0$. In the presence of HSA, the system with $q=1$ displayed a very short mean water residency time ($\tau_M{}^{310}=2.4$ ns) and enhanced relaxivity at intermediate and high fields. Magnetic resonance imaging in mice showed that Gd(4b) was able to provide 38 % better vessel to muscle contrast compared to the clinically used HSA binding agent (MS-325).

In this context it is worth of mention a derivative of Gd-AAZTA containing a long aliphatic chain (Gd-AAZTAC17) (Gianolio et al. 2007). The complex showed to have the outstanding properties of the parent complex, namely, (i) two inner-sphere water molecules in fast exchange with the bulk, (ii) high thermodynamic stability in aqueous solution, and (iii) a nearly complete inertness toward the interaction with bidentate endogenous anions. Already at sub-millimolar concentrations (cmc 0.1 mM), the presence of the hydrophobic chain induces the formation of micelles, with a relaxivity (per Gd(III) ion) of 30 $mM^{-1}s^{-1}$ at 20 MHz and 298 K. At concentration lower than cmc, Gd-AAZTA-C17 displays a high affinity binding to human serum albumin (HSA) with $K_a=2.4\times10^4$ M^{-1}, yielding a macromolecular adduct endowed with the higher relaxivity value (84 $mM^{-1}s^{-1}$) up to now reported for HSA-bound Gd complexes.

While 1–1.5 T remain the dominant field strengths for clinical MRI, also 3 T and 7 T scanners begin to be installed for human diagnostic procedures. The primary benefit of high field is the increased signal-to-noise ratio, which enables greater spatial resolution and reduced acquisition time. In addition, the inherent T_1 of tissue increases with increasing magnetic field.

Recently, a new magnetic resonance albumin binding contrast agent (B25716) has been reported (Gianolio et al. 2014), and its in vivo preclinical behavior in oncological applications, in comparison with the well-known analogue B22956, is discussed. Being based on an AAZTA gadolinium coordination cage, B25716 displays, as expected, superior relaxivity in water. The binding affinity toward albumin is similar for B22956 and B25716. The unexpected result is that the interaction with HSA leads to the loss of one of the two inner-sphere water molecules of the Gd-AAZTA moiety, thus causing a marked decrease of the expected relaxation enhancement. However, such a drawback is in part mitigated by an important contribution to the overall relaxivity arising from water molecules in the second coordination sphere of the paramagnetic ion. Moreover, the r_1 peak typical of macromolecular contrast agents is shifted

toward high fields with respect to that observed in B22956, leading to considerably higher relaxivity of the new compound in physiological environments at clinically relevant magnetic fields (3 T and 7 T). The superior sensitivity of B25716 has been confirmed through a preclinical magnetic resonance experimental assessment on a murine cancer model. The tumor signal intensity enhancement observed in the MR images for B25716 turned out to be significantly higher than that observed for B22956 (Fig. 13.15). B25716 also shows an improved persistence time, both in blood and in the tumor lesions, so extending the available time window for the magnetic resonance image acquisition after the administration of the contrast agent.

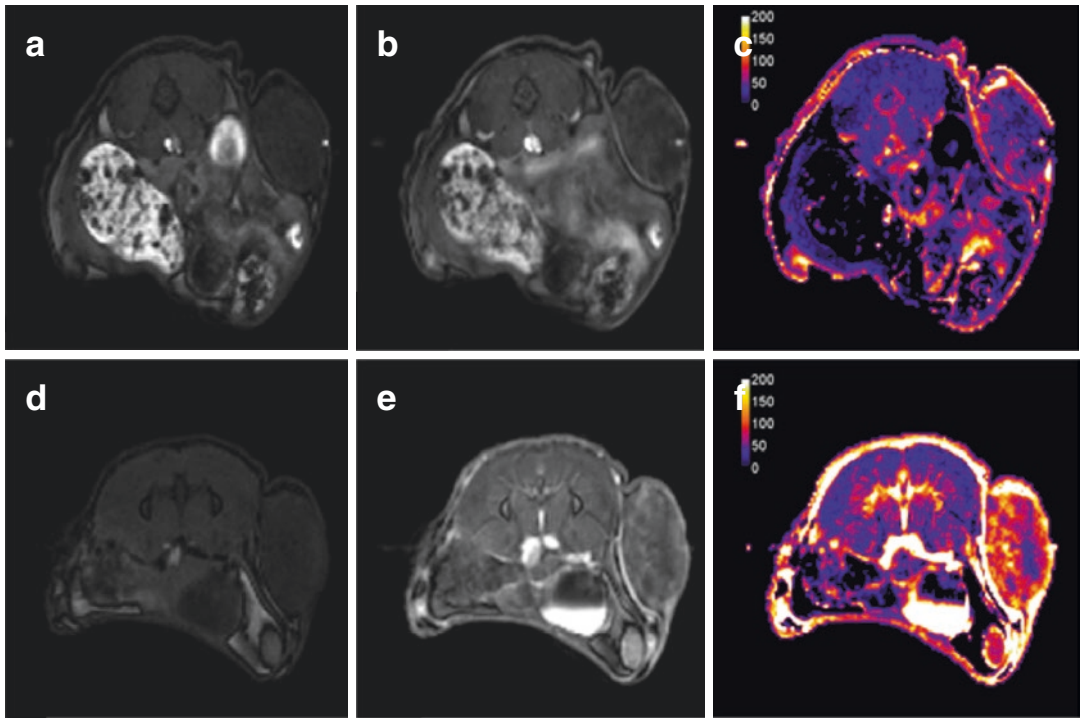

Fig. 13.15 MRI images obtained after the injection of B22956 (*upper row*) and B25716 (*lower row*). Images refer to the same animal imaged two days apart. Panels (**a, d**) pre-contrast images. Panel (**b, e**) post-contrast images obtained averaging the acquisitions measured during the first 10 min after the contrast agent injection. Panel (**c, f**) parametric images showing the signal enhancement obtained from post- and pre-contrast images. The enhancement measured in vivo after B25716 injection was approximately twice that obtained with B22956 (Reprinted from Ref. (Gianolio et al. 2014) with permission from Springer International Publishing AG)

As recalled above, the blood pool agents based on the non-covalent interaction between a Gd complex and HSA yield high relaxivities at magnetic field strengths of 0.5÷1.5 T. At higher field there is a sudden decrease in relaxivity. On the contrary, small molecule agents with very short correlation times, such as Gd(DTPA) (Magnevist®), display a modest relaxivity decrease with increasing field strength but exhibit relatively low relaxivity due to their rapid tumbling. The interplay of water exchange and rotational correlation time for Gd-based T_1 agents at fields ranging from 0.47 to 9.4 T was investigated by Caravan et al. (2009) showing that optimal ranges are the following: $5 < \tau_M < 25$ ns and $0.5 < \tau_R < 2$ ns.

Several examples have been reported in which the control and optimization of τ_R has been tackled through the rigid attachment of the corresponding Gd complexes to a molecular construct of appropriate size (Fig. 13.16).

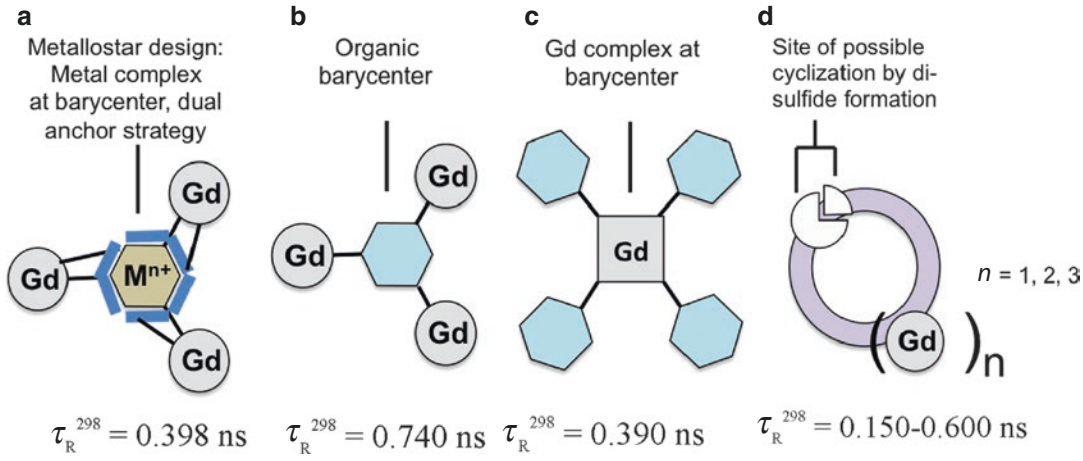

Fig. 13.16 Schematic representation of Gd-containing systems with τ_R between 0.15 and 1 ns by following different approaches: (**a**) Matallostar design with a metal complex at the barycenter; (**b**) Organic barycenter; (**c**) Gd-complex at the barycenter; (**d**) site of possible cyclization by disulfide formation

A multisite attachment strategy was employed by Desreux and coworkers (Paris et al. 2006) for the design of metallostars, where a metallic barycenter is used as a point of attachment for multiple Gd(DTTA)-type complexes (Fig. 13.16, approach a). As the clusterization of multiple copies of the Gd complex increases, the overall size, the elongation of τ_R combined with the increase of the Gd complex payload, allows to obtain high relaxivity. Meade and colleagues employed click chemistry to attach multiple Gd complexes to rigid, all-organic barycenters (Fig. 13.16, approach b) (Mastarone et al. 2011; Song et al. 2008). Alternatively, Parker and coworkers showed that the rigid Gd complex can itself be placed at the barycenter of a molecule of variable size (Fig. 13.16, approach c) (Fulton et al. 2006) obtaining very high relaxivity.

In the system recently proposed by Caravan and coworkers (Boros et al. 2012), the complex is linked to the peptide backbone via the short methylene linkage of the alanine side chain. Gadolinium coordination of the amide carbonyl, which is also used for coupling to the polypeptide, provides the second point of attachment and results in a rigid incorporation of the complex into the polypeptide (Fig. 13.16, approach d). This design restricts internal motion and enables control over τ_R.

13.2.2.3 Gd-Based Probes for Molecular Imaging

Molecular imaging (Weissleder and Mahmood 2001) deals with in vivo characterization and measurement of biological processes at the cellular and molecular level. With molecular imaging, early diagnosis of disease will become possible as the detection of altered biochemical process largely anticipates the anatomical changes that are at the basis of current diagnostic modalities.

MRI-Gd(III)-based agents are much less sensitive than radionuclear and optical imaging probes. Therefore, MR molecular imaging invariantly involves the need of accumulating a high number of contrast-enhancing units at the site of interest.

This is the case of ferritin that, once deprived of its iron content, can be loaded with Gd complexes or

with Mn^{2+}aquo ions. In the former case each ferritin unit attains a relaxivity of ca. 800 mM^{-1} s^{-1} (as it contains 8–10 Gd-HPDO3A complexes) (Aime et al. 2002a, b, c), whereas in the latter one, the r_1 value is almost an order of magnitude higher (because each ferritin can host in its inner aqueous cavity up to 400 Mn^{2+} ions) (Kalman et al. 2010). Ferritin loaded with a paramagnetic payload is well uptaken by hepatocytes that, either in vitro or in vivo, result quickly labeled by these probes and well detected in the corresponding MR images (Geninatti-Crich et al. 2012). Another example of naturally occurring carriers that has been shown to efficiently label cells is represented by LDL (low-density lipoproteins) particles. This system consists of a high molecular weight protein that wraps around the lipidic core. It has been found that up to 400 Gd complexes can be loaded on each LDL particle provided that the metal chelates are functionalized with a long aliphatic chain inserted well inside into the lipidic core (Geninatti-Crich et al. 2007; Briley-Saebo et al. 2009). Gd-labeled LDL particles are internalized into tumor cells that display an upregulation of LDL transporters committed to deliver the required amounts of cholesterol needed for the fabrication of the cellular membranes in the daughter cells.

The basis for the design of a Gd-containing imaging probe is first dictated from the concentration and localization (vascular, extracellular matrix, on the cellular membrane, intracellular) of the target molecule (Aime et al. 2002a). Of course, the most accessible targets are those present on the surface of endothelial vessels. In principle they can be visualized by a number of macromolecular conjugates containing many Gd(III) complexes endowed with the proper vector recognizing the given target. A nice example of targeting an endothelial site has been reported some years ago by Sipkins et al. (1998) in the targeting of a specific angiogenesis marker, the endothelial integrin $\alpha_v\beta_3$, whose presence has been shown to correlate with tumor grade. After that seminal paper many systems based on the RGD targeting peptide have been proposed for the visualization of both tumor cells and endothelial cells in neo-formed vessels. It has been shown that when the targeting peptide is conjugated to the surface of micelles or liposomes, the latter ones allow a clear visualization of the tumor cells characterized by the overexpression of the integrin receptors. Strijkers et al. (2010) showed a good ability to visualize the angiogenic endothelium in tumor-bearing mice. MRI indicated that the RGD liposomes are localized to a large extent in the tumor rim after being injected intravenously. Nonspecific liposomes, coupled with the scrambled RAD peptide (RAD liposomes), also targeted the tumor, but showed a diffuse distribution pattern. The different mechanisms of accumulation were established by fluorescence microscopy, which revealed that RGD liposomes were exclusively associated with tumor blood vessels, whereas RAD liposomes were mainly localized in the extravascular compartment. In a related paper, the same authors, using optical techniques and MRI, described a dual-targeting system consisting of paramagnetic liposomes conjugated to both RGD-peptides, for integrin targeting, and anginex-peptide, for galectin-1 targeting (Fig. 13.17). They demonstrated that the dual-targeting approach produces synergistic targeting effects, yielding a marked increase in the uptake of the nanoparticles as compared to single ligand targeting. Moreover, they found that these nanoparticles exhibit a strong anti-angiogenic activity, since both RGD and anginex act as inhibitors, upon binding to their receptors, which creates a great opportunity for their use in combined imaging and therapy of angiogenesis (Kluza et al. 2010).

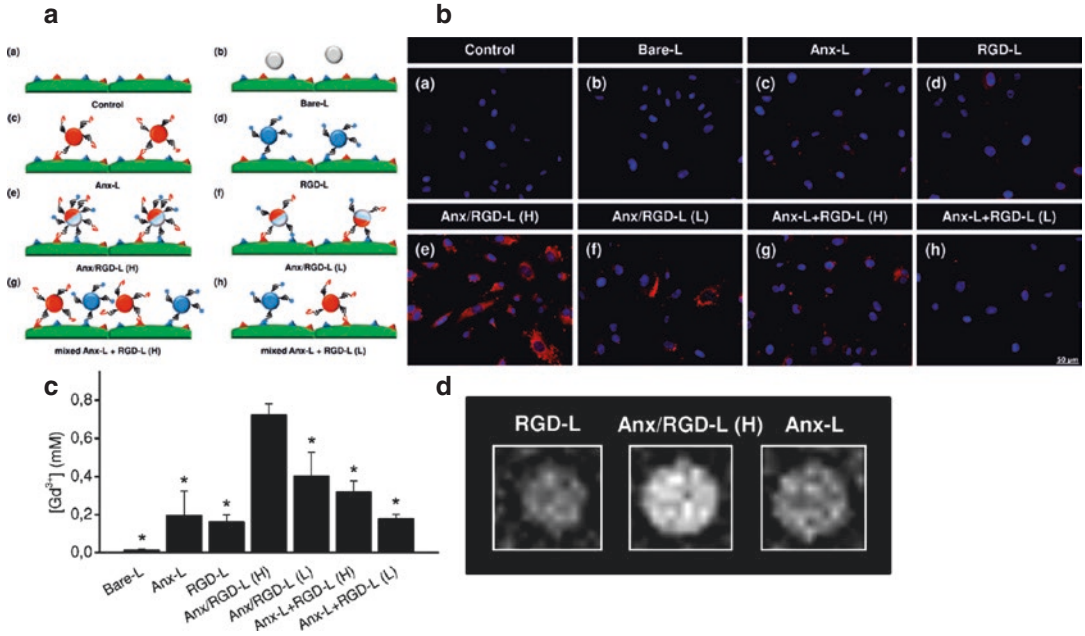

Fig. 13.17 (**a**) Schematic representation of the experimental setup. Efficacy of the cellular uptake has been investigated for the following conditions: *(a)* culture medium (*control*), *(b)* nontargeted liposomes (*bare-L*), *(c)* Anx-conjugated liposomes (*Anx-L*), *(d)* RGD-conjugated liposomes (*RGD-L*), *(e)* Anx and RGD dual-conjugated liposomes containing high concentration of peptides [*Anx/RGD-L (H)*], *(f)* Anx and RGD dual-conjugated liposomes containing low concentration of peptides *[Anx/RGD-L (L)*], *(g)* mixture of Anx-L and RGD-L containing high concentration of peptides [mixed *Anx-L + RGD-L (H)*], and *(h)* mixture of Anx-L and RGD-L containing low concentration of peptides [mixed *Anx-L + RGD-L (L)*]; (**b**) fluorescence microscopy images of HUVEC incubated under different conditions (see legend to **a**). Cell nuclei were stained with DAPI (*blue fluorescence*) and red fluorescence originates from the rhodamine-labeled contrast agent. (**c**) Uptake levels of the liposomal contrast agent achieved with the different targeting strategies; (**d**) representative T_1-weighted images of cell pellets after incubation with RGD-L, Anx/RGD-L (H), and Anx-L (Adapted with permission from Ref. (Kluza et al. 2010). 2010 Copyright American Chemical Society)

The same $\alpha_v\beta_3$ target has been addressed by means of several other nanosized diagnostic systems, such as multifunctional nanosheets (Hu et al. 2014), silica nanoparticles (Hua et al. 2014), differently engineered polymeric Gd complexes (Goswami et al. 2013), or natural carriers such LDL (Chen et al. 2010) or ferritin (Kitagawa et al. 2012) conjugated to RGD peptide.

The large size of these constructs limits their delivery to targets on the endothelial walls. To target receptors in solid tissues, other routes have to be followed. Bhujwalla and coworkers (Artemov et al. 2003) have developed and applied a two-component Gd-based avidin–biotin system for the visualization of HER-2/scan receptors. The latter is a member of the epidermal growth factor family, and it is amplified in multiple cancers. Their approach consisted of addressing the extracellular domain of the receptors by means of a biotinylated mAb. After clearance of the unbound mAb, Gd-labeled avidin is administered and binds, with high affinity, to the biotinylated mAb. The expression level of the receptor was estimated at 7×10^5 receptors/cell, and the average number of Gd-DTPA units per avidin molecule was 12.5. The method has been successfully applied in an experimental mouse model of breast carcinoma.

As far as the cell internalization of Gd-chelates is concerned, several routes have been explored, namely, pinocytosis, phagocytosis, receptors and receptor-mediated endocytosis, etc. (Aime et al. 2002a).

13.2.2.4 Gd Complexes as Responsive Agents

The term "responsive" refers to diagnostic agents whose contrasting properties are sensitive to a given physicochemical variable that characterizes the microenvironment in which the probe distributes. Typical parameters of primary diagnostic relevance include pH, temperature, pO_2, enzymatic activity, redox potential, and concentration of specific ions and low-weight metabolites.

Unfortunately, their clinical use is still uncertain mainly because an accurate measurement of one of the abovementioned parameters with a given relaxing probe requires a precise knowledge of the local concentration of the contrast medium in the region of interest. Only if the actual concentration is known, the observed change in the relaxation rate of water protons can be safely attributed to a change of the parameter to be measured.

pH Sensitive

The design of a Gd(III)-based complex whose relaxivity is pH dependent requires that at least one of the structural or dynamic parameters determining its relaxivity is made pH dependent. In most of the examples so far reported, the pH dependence of the relaxivity reflects changes in the hydration of the metal complex.

For instance, it was found that the relaxivity of a series of macrocyclic Gd(III) complexes bearing β-arylsulfonamide groups is markedly pH dependent on passing from about 8 $s^{-1}mM^{-1}$ at pH<4 to ca. 2.2 $s^{-1}mM^{-1}$ at pH>8 (Lowe et al. 2001). It has been demonstrated that the observed decrease (about fourfold) of r_1 is the result of a switch in the number of water molecules coordinated to the Gd(III) ion from 2 (at low pH values) to 0 (at basic pHs). This corresponds to a change in the coordination ability of the β-arylsulfonamide arm that binds the metal ion only when it is in the deprotonated form. Despite the good pH responsiveness of this probe, its practical use is limited by the need to know its local concentration in order to unambiguously assign the observed variations in MR signal intensity to changes in relaxivity and not to changes in the local concentration of the paramagnetic agent.

In principle, one may recover the concentration data by introducing in the pH-responsive system a concentration reporting moiety consisting, for instance, of a highly sensitive NMR heteronucleus (e.g., ^{19}F, ^{31}P, ^{13}C). Following this approach, a system was reported (Gianolio et al. 2009) in which the Gd(III) and ^{19}F-containing moieties are "hosted" by the same carrier, which is a poly-β-cyclodextrin substrate consisting of 8–10 β-CD units. The binding of the Gd complex and the ^{19}F-containing reporter to the poly-β-CD substrate has been ensured by the functionalization of both molecules with an adamantane moiety that is known to strongly bind the β-CD cavity (Fig. 13.18a). The pH responsiveness is provided by a Gd(III)-chelate whose coordination cage, analogously to the parent system reported by Lowe et al., contains a β-arylsulfonamide group whose protonation–deprotonation step takes place at pH=6.7. A change in hydration of the paramagnetic center occurs resulting in a dramatic effect on the observed relaxivity of the complex.

Another approach consisted in the setup of a dual MRI/SPECT pH-responsive agent where the SPECT-active moiety acts as a reporter of the concentration thus allowing the transformation of the observed ^1H-relaxation rates into relaxivities to recover the information relative to the pH determination (Gianolio et al. 2011). In the dual system, the MRI moiety and the SPECT moiety are represented by two chelates differing only in the coordinated lanthanide(III) ion being Gd(III) for the former and Ho(III) for the latter (Fig. 13.18b). As recalled above (Lowe et al. 2001), the relaxivity of Gd(III)-L is strongly pH dependent, while Ho(III)-L displays very low relaxivity enhancement at any pH values, as expected because the magnetic properties of Ho(III) ion make it a shift reagent rather than a relaxation agent. Ho(III)-L was prepared using a commercial $HoCl_3$ salt whose natural abundance is 100 % ^{165}Ho (SPECT inactive). ^{165}Ho, when exposed to a neutron flux, is transformed into ^{166}Ho which is unstable ($t_{1/2}$=26.6 h) and emits γ-radiation which may be exploited for the determination of the probes concentration via gamma camera. Ho(III)-L and Gd(III)-L are expected to share the same biodistribution when administered in vivo, and hence the mixture of Gd(III)-L and Ho(III)-L can be used as a dual MRI/SPECT probe.

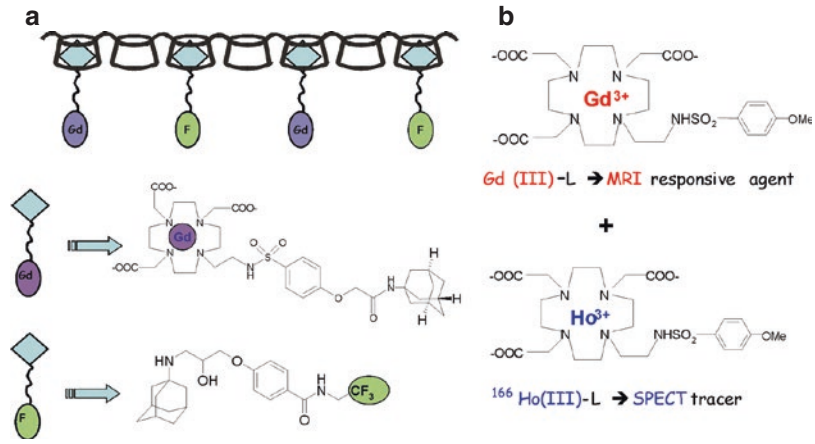

Fig. 13.18 Schematic representation of the pH-responsive systems described in (**a**) reference Gianolio et al. 2009 and (**b**) Gianolio et al. 2011

An analogous approach was reported by Caravan and coworkers (Frullano et al. 2010) who showed that the task to have a concentration-independent pH-responsive probe can be successfully tackled by using a dual MRI/PET agent consisting of a Gd-containing moiety, whose relaxivity is pH dependent, and a ^{18}F-containing moiety that acts as PET reporter of the concentration of the agent. The two moieties are covalently linked through a proper spacer. In practice one may envisage the use of a mixture made of a very small amount of the radioactive species and a large amount of the stable ^{19}F-containing isotopomer.

In some cases the pH dependence of the relaxivity is associated with changes in the structure of the second hydration shell. Two such systems have been reported by Sherry's group. The first case dealt with a macrocyclic tetramide derivative of DOTA (Gd-DOTA-4AmP) that possesses an unusual r_1 vs. pH dependence (Zhang et al. 1999). The relaxivity of this complex increases from pH 4 to pH 6, decreases up to pH 8.5, remains constant up to pH 10.5, and then increases again. The authors suggested that this behavior is related to the formation/disruption of the hydrogen bond network between the pendant phosphonate groups and the water bound to the Gd(III) ion. The deprotonation of phosphonate occurring at pH > 4 promotes the formation of the hydrogen bond network that slows down the exchange of the metal-bound water protons. On the contrary, the behavior observed at pH > 10.5 was accounted for in terms of a shortening of τ_M catalyzed by OH^- ions. It has been demonstrated that this complex can be successfully used "in vivo" for mapping renal and systemic pH (Raghunand et al. 2003). More recently, the same Gd complex was used to measure pH in a rat brain glioma model in vivo (Martinez et al. 2011). The method was based on a single infusion of a cocktail of contrast agents (CAs). The cocktail contained Gd-DOTA-4AmP and Dy-DOTP, whose effects on relaxation are sensitive and insensitive to pH, respectively. The Gd-CA dominated the spin–lattice relaxivity (R_1), whereas the Dy-CA dominated the spin–spin relaxivity (R_2^*). The ΔR_2^* effects were used to determine the pixel-wise concentration of [Dy] which, in turn, was used to calculate a value for [Gd] concentration. This value was used to convert R_1 values to the molar relaxivity and, hence, pH maps (Fig. 13.19).

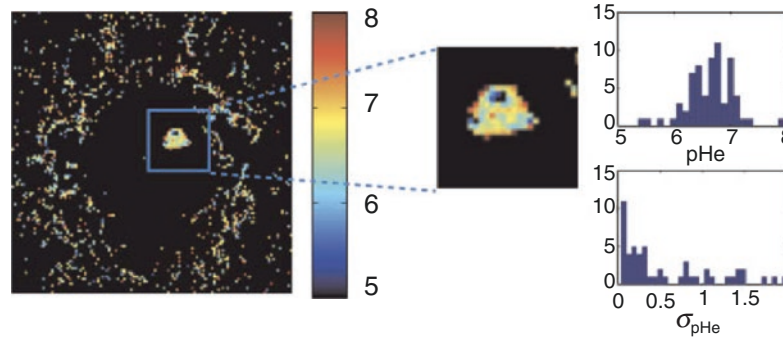

Fig. 13.19 pH maps of a rat brain glioma. The graphs on the right represent histograms of pH values and of pH uncertainty (Adapted from Ref. (Martinez et al. 2011) with permission from John Wiley & Sons Inc)

Agents Sensitive to the Redox Potential

A diagnostic MRI probe sensitive to the in vivo redox potential would be very useful for detecting regions with a reduced oxygen partial pressure (P_{O2}), in several pathologies including strokes and tumors. The current status of the research focused on redox- and hypoxia-sensitive T_1 contrast agents has been recently reviewed (Do et al. 2014; Tsitovich et al. 2014).

The principle of reversible or nonreversible binding of low molecular weight Gd complexes to larger macromolecules in order to obtain high relaxivity adducts has been exploited in the design of redox-responsive agents that bind reversibly to human serum albumin (HSA) in a redox-sensitive fashion. A series of Gd(III)-DOTA mono(amide) derivatives with free thiol groups that can form a covalent S-S bond with the cysteine-34 residue of HSA have been synthesized (Raghunand et al. 2006; Jagadish et al. 2012; Raghunand et al. 2010). When bound to albumin, the longitudinal relaxivity of Gd(III) complexes is higher than in the unbound form due to the increased rotational correlation time of the complex. The thiol/disulfide ratio depends on the extracellular redox state, and in reducing microenvironments, the albumin-bound Gd(III) complexes are cleaved from HSA by reduction of the disulfide bond. The utility of one of these complexes as an MRI reporter of tumor redox status was demonstrated in in vivo experiments with mice bearing Mia-PaCa-2 or NCI-N87 tumor xenografts.

Other thiol-targeting complexes which modulate their relaxivity values by the hydration state (number of inner-sphere waters) of the Gd^{3+} ion were reported (Carrera et al. 2007; Digilio et al. 2009, 2010; Menchise et al. 2011). These probes are DO3A derivatives bearing a 2-pyridyldithio functionality, which gives spontaneous reaction with –SH groups present on small molecules such as glutathione or on proteins. Exofacial protein thiols (EPTs) are a pool of –SH groups attached to proteins that are expressed on the surface of various cells. As these thiol groups are located on the extracellular surface, it has been proposed that they may act as sensors of the cell's redox state. The thiol groups may present as free –SH or in the oxidized S-S form depending on the extracellular redox state; given that the probes are able to selectively bind to free –SH groups, the uptake efficiency may be taken as reporter of the extracellular redox microenvironment. It has been demonstrated that the complexes are internalized and accumulate inside cells upon formation of a disulfide bridge and the amount of Gd^{3+} inside the cells can be modulated by the redox state of the exterior thiol groups.

An alternative approach considers the use of complexes of redox-active metal ions, in which the oxidation states have different magnetic properties, to create MRI agents that directly sense redox changes. A system based on the Mn(II)/Mn(III) redox switch was first reported by Aime et al. (2000) for a manganese–porphyrin complex incorporated into β-cyclodextrin (CD) host by means of supramolecular interactions. The formation of the supramolecular adduct allowed to enhance the difference in relaxivity between Mn(II)- and Mn(III)-porphyrin, at the clinical fields, being ca. 3 times higher in the case of

Mn(II)-porphyrin/poly-β-CD adduct. The poly-β-CD adduct of Mn(II)-porphyrin was shown to be oxidized completely to Mn(III)-porphyrin in the presence of 40 Torr pO_2, while the extent of oxidation and the observed relaxivity were shown to be roughly proportional to the pO_2 at oxygen levels less than 40 Torr.

Another redox-activated manganese-based agent was reported recently (Loving et al. 2013). The ligand (HBET) is capable of stabilizing both the 2+ and the 3+ oxidation states of manganese. At 4.7 T, Mn(II)-HBET showed a 3.3-fold higher relaxivity than its Mn(III) counterpart due to the fact that the former has one inner-sphere water molecule, whereas the second has none (Fig. 13.20). Cyclic voltammetry of Mn(II)-HBET yielded a half-cell reduction potential of 0.356V which is accessible to biologically relevant reducing agents like glutathione (GSH) or oxidizing ones like H_2O_2.

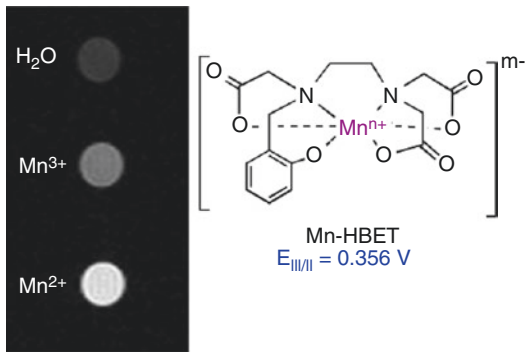

Fig. 13.20 Structure of Mn(II)/(III)-HBET, half-cell reduction potential and T_1-weighted MR image recorded at 4.7 T of tubes containing pure water, 0.5 mM Mn(III)-HBET, and 0.5 mM Mn(II)-HBET in pH 7.4 TRIS buffer (Adapted with permission from Ref. (Loving et al. 2013). 2013 Copyright American Chemical Society)

Enzyme Responsive

MRI offers the possibility to report about events that occur along the life of a given cell in response to a specific biological activity. The possibility to monitor gene expression, for example, noninvasively, in real time and at a high-resolution level, makes the use of MR-based probes an interesting challenge. The probe has to be designed in order to change its MRI properties upon the occurrence of the event that one aims at visualizing (Hingorani et al. 2014; Bogdanov et al. 2002).

One of the most popular gene reporter is lacZ gene, which encodes for the expression of β-galactosidase enzyme. The first attempt to tackle the issue of the MRI visualization of β-Gal gene expression was carried out by Meade and coworkers (Moats et al. 1997) by reporting that the relaxivity of a galactopyranose-substituted tetraazamacrocycle coordinated to a Gd(III) ion can be specifically "switched on" by removing the sugar with β-galactosidase. Since Meade's seminal work, MRI detection of β-Gal expression has been under intense scrutiny with the aim of exploring amplification routes that would allow its improved implementation in in vivo studies.

Recently, a new Gd(III)-based probe which resulted to be a good β-galactosidase substrate in B16F10 melanoma either in vitro or in vivo has been reported (Arena et al. 2011). The designed probe consists of a Gd-DOTA monoamide chelate bearing a tyrosine –OH functionality protected by a galactose moiety (Gd-DOTAtyr-gal). Upon cleavage of the galactose moiety (step activated by the action of β-galactosidase), the tyrosine group, in the Gd-DOTAtyr product, becomes available for the tyrosinase-activated melanin polymerization. The formation of the paramagnetic melanin-like macromolecule can be assessed by MRI because the relaxivity of Gd(III) complexes increases, in the field range 0.5–1.5 T, if they are part of macromolecular systems. The ability of Gd-DOTAtyr-gal to visualize stably expressing LacZ melanoma tumors in vivo, upon its direct intratumoral injection, was also demonstrated.

A related approach relies upon enzymatic removal of a structural moiety that prevents binding of a pro-RIME Gd(III) complex to HSA (RIME = receptor-induced magnetization enhancement). As shown above, binding of Gd(III) complex to HSA slows down the molecular rotation of the Gd(III) complex resulting in an additional increase in the relaxivity. On the basis of this concept, a Gd(III)-based contrast

agent for in vivo visualization of β-galactosidase in tumor was reported (Chang et al. 2007). The difference in T1 relaxivity in the absence and presence of β-galactosidase was adequate for robust in vivo imaging of β-galactosidase activity in the tumor tissues. More recently (Chen et al. 2012b), the same authors described an analogous system responsive to β-glucuronidase, which is a key lysosomal enzyme and is often overexpressed in necrotic tumor masses. The contrast agent (Gd[DOTA-FPβGu]) consists of a Gd(III) complex bound to a β-glucuronidase-specific substrate (β-D-glucopyranuronic acid). Enzymatic removal of β-glucuronic acid followed by nucleophile attack from HSA leads to the formation of the stable high molecular weight and high relaxivity biomacromolecule ([Gd(DOTA-FP)]-HSA) (Fig. 13.21a). In vitro MR imaging signal intensity of β-glucuronidase-overexpressing cell line is 15 % higher than that of a cell line expressing moderate levels of β-glucuronidase. Furthermore, in vivo evaluation of [Gd(DOTA-FPβGu)] for imaging β-glucuronidase in an animal tumor model was very encouraging, as, 30 min after the injection, a 2.5-fold increase in signal enhancement was measured in tumor overexpressing the enzyme over that with low expression level (Fig. 13.21b).

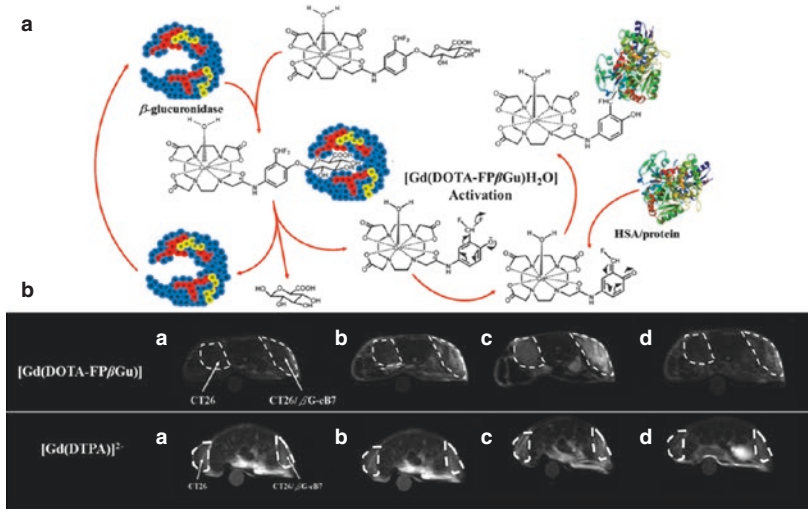

Fig. 13.21 (**a**) Schematic representation of β-glucuronidase induced transformation of pro-RIME [Gd(DOTA-FPβGu)] into ([Gd(DOTA-FP)]-HSA); (**b**) representative T_1-weighted (TR/TE 100/13 ms) MR images of mice bearing CT26 and CT26/mβG-eB7 xenografts after injection of contrast agents ([Gd(DOTA-FPβGu)] compared to [Gd(DTPA)]) (*A*) pre-contrast images or at (*B*) 5 min, (*C*) 10 min, and (*D*) 90 min, after intravenous injection of 0.1 mmol/kg contrast agents (Adapted with permission from (Chen et al. 2012a, b). 2012 Copyright American Chemical Society)

A related system was recently reported (Napolitano et al. 2013) which aims at the identification and quantification of the expression and activity of the glutamate decarboxylase (GAD) enzyme, as well as at the evaluation of GAD-positive neurons either in vitro or in vivo. The design of the agent (Fig. 13.22) is in line with the mechanism of activation of the β-Gal contrast agent early developed by Meade and colleagues (Moats et al. 1997), i.e., through the cleavage of the coordinated glutamate moieties by the GAD enzyme, an increased hydration at the Gd(III) center results in an enhanced relaxivity. Moreover, the cleavage of the glutamic moiety or moieties yields a complex with a residual positive charge that further enhances the observed relaxivity through the electrostatic interactions with negatively charged biomacromolecules. This study is

the first proof of principle to discriminate between engrafted stem cells and GABAergic neurons due to the selective activation of the incorporated contrast agent in vivo, using MRI (Aswendt et al. 2012). The change in T1 relaxation rate was analyzed quantitatively for the in vitro and in vivo experiments, yielding ≥200 ms difference in T1 in vitro and ≥100 ms in vivo.

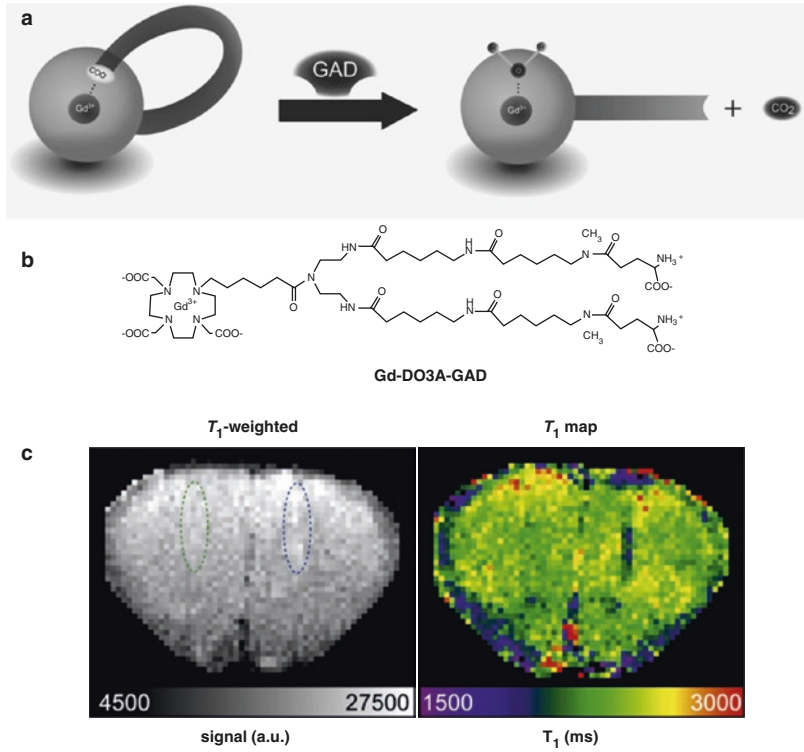

Fig. 13.22 (**a**) Schematic representation of the mechanism of action of the Gd-DO3A-GAD-responsive agent whose structure is depicted in (**b**). (**c**) *Left*: representative T_1-weighted image at 0.5 h after implantation of labeled differentiated cells (*right striatum*) and labeled undifferentiated cells (*left striatum*). *Right*: corresponding T_1 map revealing distinct lower relaxation rate for the differentiated cell graft (Adapted with permission from refs (Napolitano et al. 2013) (2013 Copyright American Chemical Society) and (Aswendt et al. 2012) (2012 copyright Elsevier B.V.))

13.2.3 T_2 Susceptibility Agents

13.2.3.1 Iron Oxide Particles

These materials consist of superparamagnetic iron oxides that are made of ferric (Fe3+) and ferrous (Fe2+) ions (Muller et al. 2005). Their peculiar magnetic behavior is associated with the occurrence of domains in their microcrystalline structure that alter markedly the characteristic properties of ferrimagnetism and ferromagnetism such as spontaneous magnetization, residual magnetization, and magnetic hysteresis. These particles (that per se are a kind of ferrite and, therefore, ferrimagnetic) are magnetically transformed into a paramagnetic substance. Inside each domain the magnetic moments of the various ions sum up to yield large magnetic moments, in principle analogous to a single paramagnetic ion but of much larger strength, for which they are called superparamagnetic.

The distortion of the magnetic field caused by the superparamagnetic core induces large changes in magnetic susceptibility which, in turn, leads to hypo-intensities in T_2- or T_2*-weighted images. Thus the areas containing the particles display fast transverse relaxation rates and low signal intensity ("negative contrast"). Due to the large

magnetic susceptibility of an iron oxide particle, the signal void is much larger than the particle size, enhancing detectability at the expenses of resolution. These particles have been used to track "in vivo" different cell types (Cunningham et al. 2005), including T lymphocytes (Kircher et al. 2003), macrophages (Engberink et al. 2007), and stem cells (Frangioni and Hajjar 2004).

Iron oxide particles for MRI applications are classified into two classes, namely, superparamagnetic iron oxide (SPIO) and ultrasmall superparamagnetic iron oxide (USPIO) on the basis of the overall size of the protective cover on the surface of the magnetic particle (Corot et al. 2006). In fact in both types of particles, the iron oxide colloid particles are encapsulated by organic materials such as dextran and carboxydextran to improve their compatibility with the biological systems (Fig. 13.23). The difference in the overall size of the particles causes marked changes in two important properties as far as their use as MRI contrast agents is concerned:

(i) Upon intravenous administration their blood pool lifetime is strongly affected by their dimensions. USPIOs have longer half-life in the blood vessels than SPIO because their smaller size (<50 nm) makes their uptake more difficult from macrophages. On the contrary, SPIOs (with diameters of the order of 100–200 nm) are very rapidly removed from the circulation by the reticuloendothelial system (RES). For instance, 70–80 % of injected AMI-25 particles (size 57–250 nm) are taken up by the liver, 6 % by the spleen, and a small amount by the bone marrow (Schumann-Giamperi 1993). USPIO remains in blood for longer time and more readily accumulate in the lymph nodes and bone marrow.

(ii) In terms of relaxation enhancement properties, the larger magnetic susceptibility of SPIO yields to larger R_2/R_1 relaxation rates and higher T_2-shortening effects than those brought about by the smaller USPIO particles.

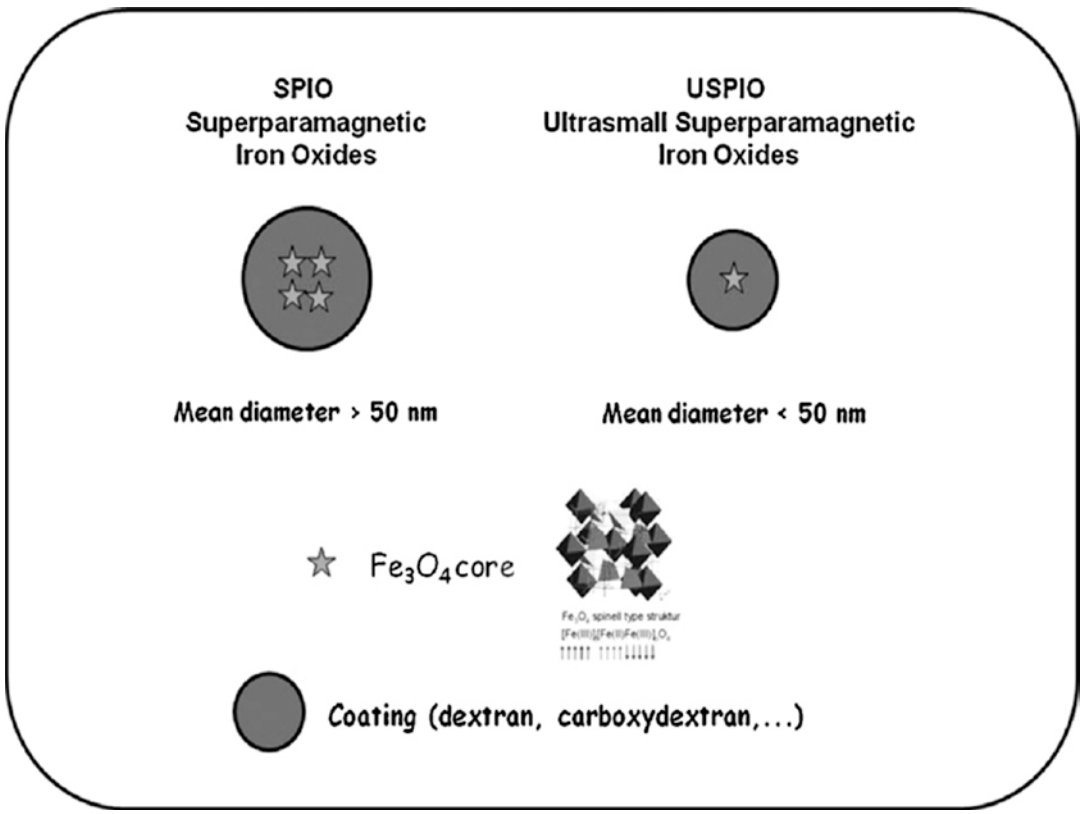

Fig. 13.23 Schematic view of the composition of superparamagnetic iron oxide particles

SPIOs and USPIOs (and also MPIOs, the micron-sized iron oxide particles) are under intense scrutiny as tools for cellular labeling for tracking cells' migration, in particular into the nervous system. SPIOs appear to work better than USPIOs in labeling experiments first of all because the phagocytic uptake increases with the particle size. Cells incubated with SPIOs result in an increase of R_2 upon increasing the local cellular concentration. Typically, R_2 of monocytes labeled with SPIO at the concentration of 1.0 mg Fe/mL is 13.1 s^{-1}. This has led to a detection limit of 58 labeled monocytes per voxel volume of 0.05 μL (Engberink et al. 2007).

Although SPIOs are more suitable for in vitro cellular labeling, USPIOs are frequently preferred for in vivo studies, thanks to their longer blood pool half lifetime. Thus, in vivo labeling by USPIO has been pursued in several diseased states, namely, stroke (Saleh et al. 2004) and multiple sclerosis (Dousset et al. 2006). In humans, the lifetime of blood pool is more than 34 h, whereas the $t_{1/2}$ of SPIO appears to be shorter than 6 min and such a half lifetime markedly limits their possibility to label endogenous monocytes in circulation.

13.2.3.2 Paramagnetic Particles

In the late 1980s, it was reported that paramagnetic low molecular weight Dy(III) complexes can act as T_2-susceptibility agents in MRI images when they are unequally distributed in vessels and in the surrounding tissues (Rosen et al. 1991). The effect can be further enhanced when the paramagnetic complexes are entrapped in vesicles such as liposomes (Fossheim et al. 1997). The observed behavior is well accounted for in terms of the field gradients created by the compartment containing the paramagnetic ions that induce the spin dephasing of the water protons diffusing in the outer region of the compartment. It is straightforward to note that any nanosized system containing paramagnetic metal ions would act as a T_2-susceptibility agent. In this context, paramagnetic liposomes have a high potential owing to the high payload of paramagnetic complexes that can be either entrapped in their inner cavities or, upon suitable functionalization with lipophilic substituents, be incorporated in their membrane bilayer (Terreno et al. 2007a).

The use of paramagnetic liposomes has been demonstrated advantageous for developing highly sensitive T_2-susceptibility agents as possible alternative to the well-established class of iron oxide nanoparticles. The compartmentalization effect, which is proportional to the magnetic field strength, is clearly illustrated in Fig. 13.24.

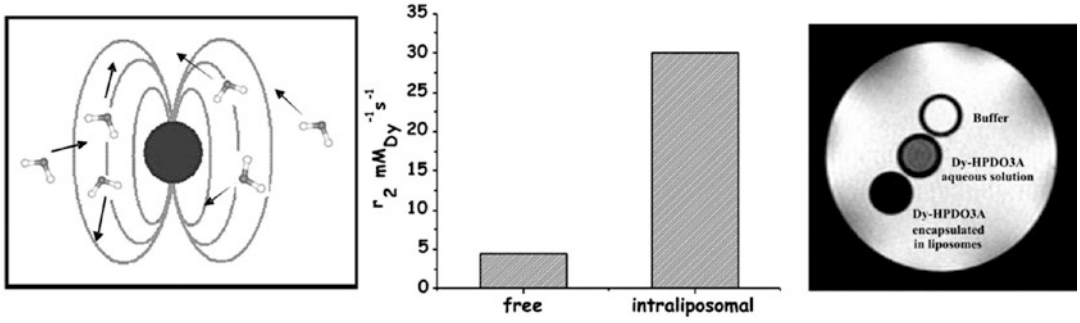

Fig. 13.24 *Left*: schematic view of the interactions between the local magnetic fields generated by a paramagnetic nanoparticle and the water molecules diffusing around it. *Middle*: effect of the liposome encapsulation of a paramagnetic complex (Dy-HPDO3A) on the transverse relaxation rate at 7 T and 312 K. *Right*: in vitro RARE $T_{2\text{weighted}}$ MR image obtained at 7 T and 312 K

The sensitivity of such systems is dependent on the intrinsic paramagnetism (described by the effective magnetic moment, μ_{eff}) of the Ln ion (Dy(III) is the most effective one) and on the overall concentration of the paramagnetic center compartmentalized in the vesicle. Hence, the incorporation of amphiphilic Dy(III) complexes in the liposome bilayer, in addition to the encapsulation of huge amounts of a hydrophilic Dy(III) agent in the aqueous cavity, yields to a marked sensitivity enhancement that makes these systems interesting agents for high-field applications.

Another class of liposome-based T_2-susceptibility agents is represented by magnetoliposomes, in which iron oxide particles are encapsulated in liposomes (Bulte and De Cuyper 2003). Upon their interaction with externally applied magnetic fields, these systems have been exploited in novel magnetic targeting experiments (Babincova et al. 2000), as well as drug delivery carriers (Babincova et al. 2004), and in hyperthermia therapeutic (Ito et al. 2005). As far as their applications in MR molecular imaging is concerned, magnetoliposomes have been successfully used as blood pool agents (Martina et al. 2005), for targeting bone marrow (Bulte et al. 1999) and solid tumors (Fortin-Ripoche et al. 2006).

Another class of very promising paramagnetic nanoparticles to be used as T_2-susceptibility MRI contrast agents is represented by lanthanide oxide particles. Peters and coworkers (Norek et al. 2008) reported the characterization of Dy_2O_3 dextran-coated particles endowed with very high transverse relaxivities. They found that the relaxivity is dependent on the particle radius being the optimal value around 70 nm. Under those conditions the r_2 value is about 190 s-1 mM-1 at 7 T and 25 °C, which is comparable with the relaxivity of, for example, PEGylated magnetoliposomes ($r_2 = 240\ s^{-1}\ mM^{-1}$) or protein-coated magnetoferritin ($r_2 = 218\ s^{-1}\ mM^{-1}$) at $B = 1.5$ T.[35]

The efficiency is even higher at higher magnetic fields, as the proton relaxivity r_2 in the presence of Dy_2O_3 nanoparticles is increasing with B^2, in contrast to superparamagnetic entities, which, due to their constant magnetic moment, produce no r_2 enhancement at $B > 1.5$ T.

13.2.4 CEST Agents

The novel landscape of molecular imaging prompted the search for new paradigms in the design of MR imaging reporters. A general insight deals with the exploitation of the resonance frequency, the key parameter of the NMR phenomenon.

A convenient way to generate a "frequency-encoding" contrast is to exploit the well-known (either in NMR or in MRI fields) magnetization/saturation transfer (ST) phenomena (Henkelman et al. 2001). The basic rationale is to deal with a system containing at least one set of protons whose exchange with the bulk, k_{ex}, is slow on the NMR/MRI timescale, i.e., k_{ex} has to be smaller than the difference in the resonance frequency between the two exchanging pools ($k_{ex} < \Delta\omega$). Upon irradiation of the mobile protons by using a proper radio-frequency field (of intensity B_2), saturated magnetization is transferred, via chemical exchange, to the bulk water resonance, which will decrease the MRI signal in the image voxels containing the agent. The resulting contrast is usually called CEST (chemical exchange saturation transfer) contrast, and the same acronym is also used for defining the class of chemicals that are able to generate it. The basic CEST experiment is sketched in Fig. 13.25.

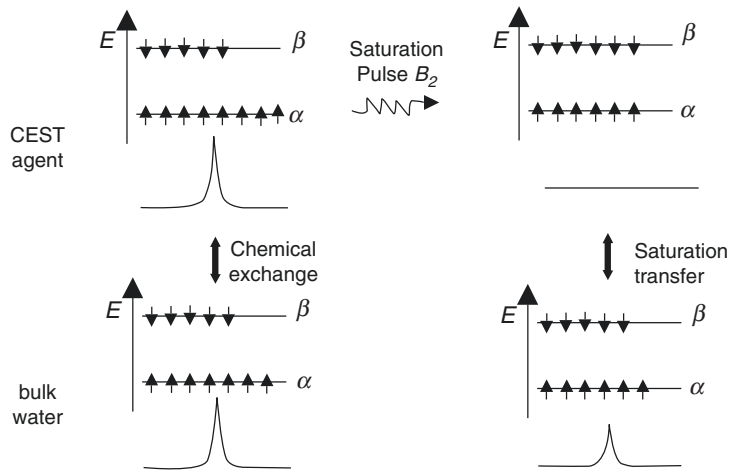

Fig. 13.25 Schematic picture illustrating the saturation transfer process mediated by chemical exchange. The application of the saturation field B_2 at the resonance frequency of the spins of the CEST agent equals their populations. The chemical exchange perturbs the Boltzmann equilibrium of the bulk water protons due to the transfer of an excess of CEST spins from the high energy level. The CEST contrast arises from the consequent decrease in the spin population difference between α and β states

With respect to the conventional MRI agents, CEST probes allow the design of MRI protocols in which the contrast can be generated "at will" only if the proper frequency corresponding to the exchangeable protons of the CEST agent is saturated. As a consequence, the pre-contrast image can be recorded almost simultaneously to the post-contrast ones as their acquisition simply differs from the on/off switch of the irradiation field. Even more important, this new approach offers the intriguing possibility of visualizing more than one agent in the same region, thus opening new exciting perspectives for the MRI applications in the biomedical field.

In addition to that, CEST agents were very soon identified as candidates for designing concentration-independent responsive probes. In fact, the presence of two magnetically non-equivalent "CEST-active" proton sites whose ST efficiency is differently dependent on the physico-chemical variable of interest allows the exploitation of a ratiometric approach that makes the MRI response independent of the concentration of the imaging probe (Ward et al. 2000). The most critical issue for the translocation of CEST agents to "in vivo" applications is represented by their low sensitivity. Theoretically, the *ST* effect is dependent upon several parameters, among which particularly relevant are k_{ex} and the number of mobile protons per molecule. The simulated curves reported in Fig. 13.26a, calculated by using the theoretical model recently described by Woessner et al. (2005a), show dependence of *ST* % on k_{ex} at different B_1 field intensities. For a given set of parameters ($\Delta\omega$, T_1, and T_2 for the exchanging proton sites, concentration of mobile protons, magnetic field strength, irradiation time), the increase of k_{ex} leads to a *ST* enhancement up to a specific k_{ex} value, after which, the efficiency of the saturation transfer drops off. Such a decrease cannot be ascribed to the approaching of the coalescence condition, because, being $\Delta\omega$ the same for all simulations, it occurs at different k_{ex} values. Rather, it is the result of the reduced number of mobile spins effectively saturated by the B_1 field owing to the broadening of their resonance associated to the increase of k_{ex}. The simulated profiles indicate that k_{ex} cannot be increased at will and, furthermore, that high B_1 intensity is required for maximizing the ST effect. It is important to recall here that the use of too high B_1 values for an in vivo MR scans is limited, for safety purposes, by the SAR (specific absorption rate) value. For this reason, the design of highly sensitive CEST agents has been pursued trying to

develop molecules bearing mobile protons that realize the best compromise between the exchange rate and the B_1 intensity needed to efficiently saturate their NMR signal. This way of proceeding led to the development of two families of CEST agents, namely, DiaCEST and ParaCEST, where the prefixes Dia and Para identify diamagnetic or paramagnetic systems, respectively. In particular, the use of paramagnetic agents has extended the range of exchange rate that can be exploited before coalescence takes place, thus allowing for higher saturation transfer efficiencies; the drawback of this approach is represented by the high power needed for a complete saturation of the spins that in some cases is beyond the limits posed by SAR threshold.

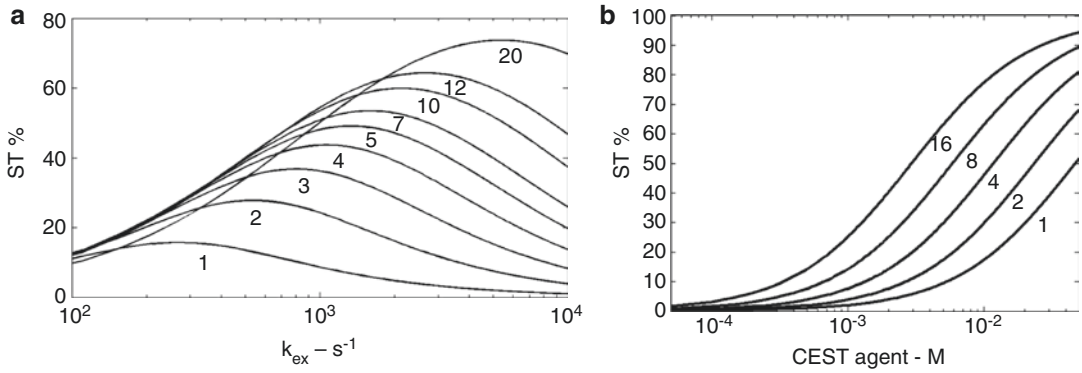

Fig. 13.26 (**a**) Simulated k_{ex} dependence of *ST %* at different B_1 field intensity. (The data were calculated at 7 T, $\Delta\omega = 50$ ppm, concentration of mobile protons 50 mM, irradiation time 4 s.) (**b**) Simulated dependence of *ST %* on the concentration of saturated mobile protons. (The data were calculated at 7 T, $\Delta\omega = 50$ ppm, k_{ex} 3300 s^{-1}, B_1 11.75 μT, irradiation time 4 s)

Figure 13.26b reports a theoretical curve describing the dependence of the ST effect on the concentration of the irradiated protons. By considering a ST detection threshold of about 10 %, the required concentration of mobile protons is in the order of few mM, and, therefore, the corresponding minimum concentration of CEST agent is dependent upon the number of irradiated mobile protons. Consequently, the most promising route to improve the sensitivity of CEST agents is to increase the number of mobile protons per single molecule. A step further on this line of thinking has been represented by the family of LipoCEST agents that exploited the very large pool of mobile water protons belonging to the intraliposomal cavity. In the following paragraphs a description of the main peculiarities of these three families of CEST agents, together with some representative examples, will be provided. It is worth mentioning that contrary to what happens for other types of contrast agents described in this chapter, even some endogenous molecules can be exploited to generate a CEST contrast. However, this topic is beyond the purpose of this chapter and it will not be discussed.

13.2.4.1 DiaCEST

The first paper proposing saturation transfer mediated by chemical exchange as a way to generate MRI contrast is dated 2000, when Balaban and coworkers proposed the use of small-sized diamagnetic molecules (Ward and Balaban 2000). Actually, the detection limit for these CEST agents (which typically contain less than 10 protons/molecule), like amino acids, heterocyclic compounds, sugars, etc., is in the mM range (Ward et al. 2000; Aime et al. 2002a). A significant sensitivity improvement was achieved by investigating the ST properties of macromolecular agents (polyamino acids, dendrimers, RNA-like polymers) (Goffeney et al. 2001). Such systems contain thousands of mobile protons and,

consequently, their detection limit is the μM range. With the aim of designing safe and clinically translatable CEST probes, Longo et al. proposed the use of diamagnetic molecules possessing mobile pools that were already approved for clinical use (Longo et al. 2011). In particular, they reported the CEST properties of iopamidol, a molecule containing two pools of mobile protons that was selected being a diagnostic agent for CT used since 1981. In addition, iopamidol has been proven to be a good pH-responsive agent, allowing for the in vivo pH measurements in the kidneys (Longo et al. 2013). Other authors followed the same approach. The feasibility of using iopromide as an extracellular pH sensor was successfully tested either on phantoms or in vivo on mouse model of MDA-MB-231 mammary carcinoma. A very interesting DiaCEST agent proposed in 2013 by Golay and coworkers is glucose, with the aim to find a MRI alternative to the conventional FDG-PET protocol to assess glucose consumption and glycolysis rate (Nasrallah et al. 2013). The authors showed that this technique, named glucoCEST, is sensitive to glucose accumulation in colorectal tumor models. Furthermore, the protocol allowed the distinction between tumors with different metabolic characteristics and pathophysiology.

13.2.4.2 ParaCEST

As said above, a good CA for CEST applications has to possess mobile protons whose exchange rate with water (*kex*) is as high as possible before their broadening makes the RF irradiation ineffective. Roughly, this condition occurs when *kex* approaches the separation (in Hz) between the chemical shift values, $\Delta\omega$, of the two exchanging sites ($kex \approx \Delta\omega$). Therefore, larger $\Delta\omega$ values enable the exploitation of higher *kex* values, thus resulting in an enhanced CEST effect.

In 2001 Zhang et al. (2001) showed that a particularly useful source of highly shifted exchangeable protons can be provided by the slowly exchanging water protons bound to a paramagnetic Eu(III)-chelate. Since then, a huge number of paramagnetic complexes have been designed for CEST studies, and this class of molecules has been dubbed ParaCEST agents. Besides metal-coordinated water protons, alternative sources of highly shifted exchangeable protons have been proposed.

The first example proposing the use of amide protons of the ligand in a ParaCEST agent for the detection of a CEST contrast was reported in 2002 (Aime et al. 2002b). This approach might offer a better control of the basic requisites of a CEST-CA as, in principle, one may design the molecular structure of the complex in order to pursue optimal values for the chemical shifts and exchange rates of the amide protons.

Among the different Ln(III) ions investigated, the Yb(III) complex was the most efficient agent when the amide protons were saturated (k^{CEST} 180 s^{-1}, $\Delta\omega$ offset = –16 ppm), with an observed effect of 52 %, at pH 7.4, in a 25 mM solution of the agent (7 T, B_2 intensity 25 μT). Other important findings from this work were (i) the observation that the $\Delta\omega$ offsets for the same proton site are strongly dependent on the magnetic property of the Ln(III) ion, (ii) the demonstration of the remarkable pH dependence of the CEST contrast upon irradiation of the amide protons, and (iii) the exploitation of the two different proton pools for detecting pH in a concentration-independent ST response mode. The CEST sensitivity displayed by [Ln-DOTAMGly] complexes is dependent on the irradiated proton site: for amide protons a CEST effect of 5 % requires a millimolar complex concentration of the metal complex, whereas for the metal-coordinated water protons the threshold lowers down to 0.5–1 mM (Terreno et al. 2004).

Woods et al. demonstrated that also OH groups can be exploited in a CEST experiment with a ParaCEST probe, at least under certain experimental conditions (Woods et al. 2006). Figure 13.27 reports the Z-spectrum of a 36 mM solution of $[Eu\text{-}CNPHC]^{3+}$ (see the figure inset) acquired in d_3-acetonitrile containing small amount of water (25 °C, 23 °C, B_2 intensity 2 μT).

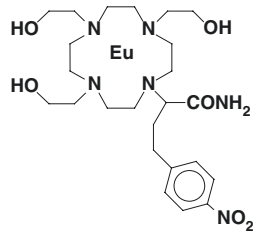

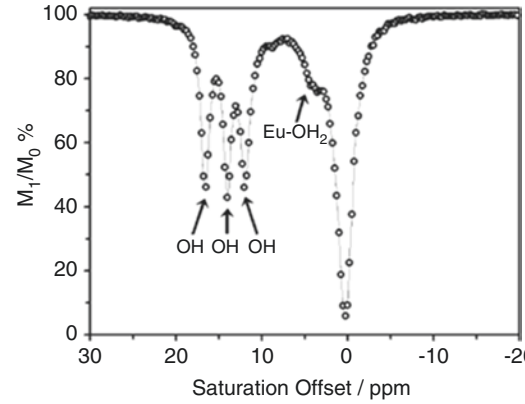

Fig. 13.27 Z-spectrum (*right*) of a 35 mM solution of $[Eu\text{-}CNPHC]^{3+}$ (*left*) (6.3 T, 25 °C) (Adapted with permission from (Woods et al. 2006). 2006 Copyright American Chemical Society)

The three distinct CEST peaks corresponding to the three nonequivalent coordinating OH groups can be easily detected along with a fourth peak attributable to the metal-bound water protons.

The possibility of using coordinated OH protons as a source of CEST contrast led the way to the use of Ln-HPDO3A (HPDO3A: 10-(2-hydroxypropyl)-1,4,7,10-tetraazacyclododecane-1,4,7-triacetic acid) complexes as ParaCEST agents (Fig. 13.28). The Gd(III) complex of HPDO3A ligand is a clinically approved MRI contrast agent marketed as ProHance™. Thus, Ln(III)HPDO3A complexes are supposed to have thermodynamic and kinetic stabilities, in vivo distribution, and excretion properties very similar to those shown by ProHance™. Unfortunately, the Gd complex itself cannot be used as CEST agent because, among the lanthanide ions, Gd(III) shows the lowest ability as shift reagent because of the symmetric distribution of the seven unpaired electrons in the *f* orbitals. Moreover, as detailed in the previous paragraphs, Gd-based complexes are T_1 agents, and short T_1 of the bulk water is detrimental for the CEST efficiency. Concerning the choice of the lanthanide, it has been reported that Yb(III) is

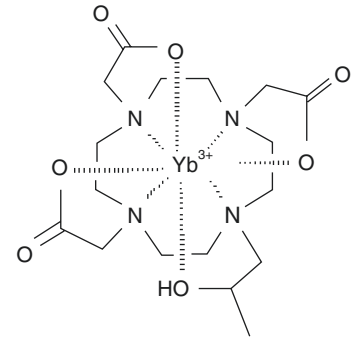

Fig. 13.28 Yb(III)HPDO3A structure

the most efficient ion due to the best compromise between shifting ability and T_2 shortening (Delli Castelli et al. 2011). Figure 13.29 reported the proof of concept on the ability of this CEST agent to report about pH. A phantom containing 14 capillaries filled up with solutions of Yb(III)HPDO3A either at different pH values or at different concentrations was subjected to a MRI investigation. By acquiring the Z-spectrum, it was possible either to determine the temperature of the sample from the chemical shift of the –OH groups or measuring the pH according to the proper ratiometric calibration.

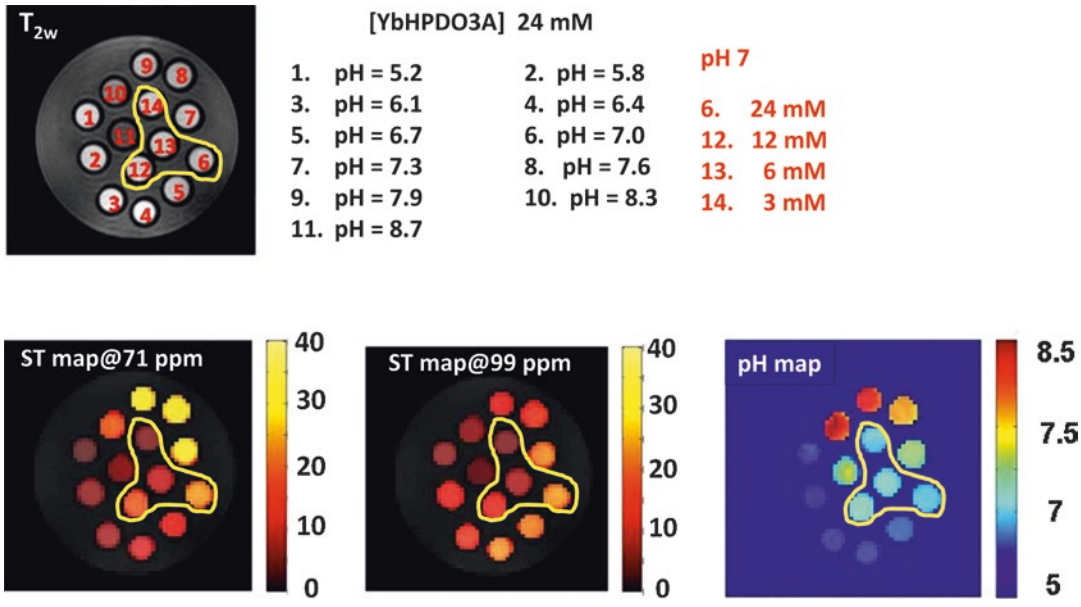

Fig. 13.29 MR images of a phantom containing 14 capillaries containing Yb(III)HPDO3A either at different pH or concentrations. (**a**) T_{2w} image, tubes from one to eleven contains a 20 mM solution of YbHPDO3A at increasing pH values (5.2; 5.8; 6.1; 6.4; 6.7; 7.0; 7.3; 7.6; 7.9; 8.3; 8.8), while tube twelve contains Yb(III)HPDO3A 10 mM at pH 7.0, tube thirteen contains Yb(III)HPDO3A 5 mM at pH 7.0, tube fourteen contains Yb(III)HPDO3A 3 mM at pH 7.0. (**b**) CEST map acquired on the same phantom after irradiating the frequency corresponding to 71 ppm; (**c**) CEST map acquired on the same phantom after irradiating the frequency corresponding to 99 ppm; (**d**) ratiometric map image. The experiment has been performed at 20 °C

The same authors in 2014 reported the successful use of this probe in vivo in a preclinical model of melanoma as extracellular pH reporter (Delli Castelli et al. 2014). A significant sensitivity enhancement for ParaCEST agents could be attained by designing polymeric systems containing a high number of ParaCEST units. A couple of examples have been presented so far, involving the linkage of ParaCEST agents, similar to those discussed in this section, to macromolecules like dendrimers (Pikkemaat et al. 2007), or to nanosized systems like perfluorocarbon nanoparticles (Winter et al. 2006).

An alternative approach to lanthanide complexes as ParaCEST agents has been proposed by Morrow and coworkers based on the use of transition metal ions complexes. Certain transition metal ions including Fe(II), Co(II), or Ni(II) have paramagnetic properties that are generally well suited for their application as ParaCEST agents. These complexes may produce relatively narrow and highly shifted proton signals. Amide-appended macrocyclic complexes with the abovementioned metal ions were recently shown to act as ParaCEST agents at physiological pH and temperature. Studies of transition metal ion-based ParaCEST agents in biological media to date are scarce, and their in vivo potential has still to be investigated (Olatunde et al. 2014).

13.2.4.3 LipoCEST

Nanovesicles able to entrap solvent in their cavity, like liposomes, represent an ideal system for developing highly sensitive CEST agents. In fact, the number of water protons inside the liposome cavity is several order of magnitude larger (10^6–10^9 depending on the size of the vesicle) than molecular systems. In addition, liposome membranes are water permeable, and the exchange rate of the intraliposomal water protons (i.e., the k_{ex} of the CEST pool) can be properly modulated by changing the lipid composition. The exchange rate of the water protons is not very fast (10^2–

10^3 s^{-1}), and, therefore, high ST efficiency can be attained without using high intensity B_2 fields. To act as CEST agent, the resonance frequency of the intraliposomal water protons must be different to the bulk water protons in which the liposomes are suspended, and this task was successfully accomplished by encapsulating a paramagnetic shift reagent (SR) in the liposome cavity (Aime et al. 2005).

Paramagnetic lanthanide(III) complexes are recognized as the best class of shift reagents, especially those having a highly symmetric macrocyclic structure, like [LnDOTMA], [LnDOTA], or [LnHPDO3A] (Fig. 13.30), where one fast-exchanging water molecule is axially coordinated to the metal center, thus maximizing the induced paramagnetic shift that is dominated by the dipolar contribution.

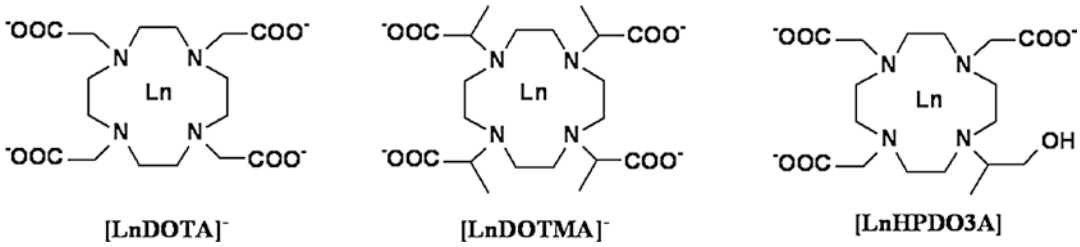

Fig. 13.30 Macrocyclic Ln(III)-based complexes typically used as shift reagents for liposome-based CEST agents

Tm(III) and Dy(III) are the most used Ln(III) ions in virtue of their high values (of opposite sign) of the dipolar constant, C_D, that directly affects the dipolar contribution.. The liposome encapsulation of high amount (*ca*. 200 mM) of the SRs induces paramagnetic shift offset of about ± 4 ppm. The sensitivity of these nanosystems, dubbed LipoCEST, is very high: sub-nanomolar amounts of vesicles are sufficient to generate a ST of *ca*. 10 % in vitro. Next, it was recognized that the development of LipoCEST agents with highly shifted intraliposomal water protons could be very beneficial for improving the potential of such systems.

Two approaches have been adopted to achieve this task: (i) to exploit the contribution to the chemical shift of the intraliposomal water arising from bulk magnetic susceptibility (BMS) effects and/or (ii) to increase the concentration of paramagnetic centers encapsulated in the liposome cavity. The former route requires the compartmentalization of the paramagnetic agent in not spherical vesicles, whereas traditional liposomes adopt a spherical shape (Fig. 13.31a).

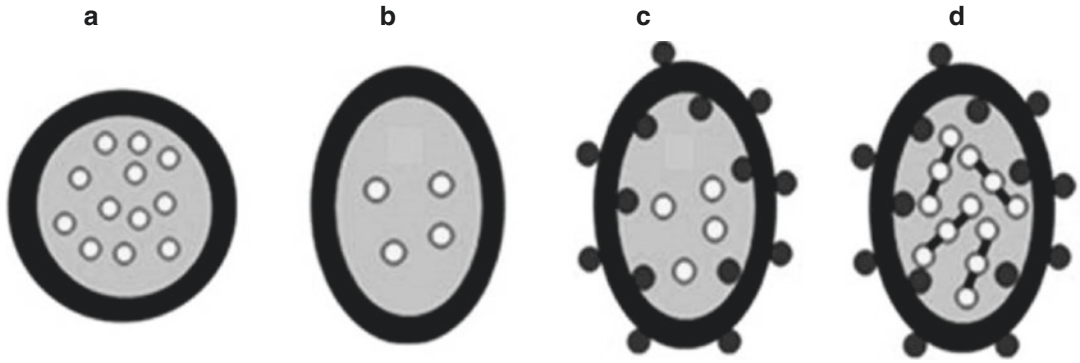

Fig. 13.31 (**a**) Spherical LipoCEST; (**b**) not-spherical LipoCEST; (**c**) not-spherical LipoCEST with amphyphilic shift reagent in the membrane; (**d**) not-spherical LipoCEST with amphyphilic shift reagent in the membrane and trinuclear shift reagent in the acquous phase

Liposomes are flexible objects and, due to the water permeability of their membrane, they are sensitive to osmotic forces. When suspended in a hyperosmotic medium, liposomes react by shrinking themselves, leaking water, and changing shape. Hence, a liposome encapsulating an ipotonic solution of a SR (better a neutral one as [LnHPDO3A]) is dialyzed against an isotonic buffer (step necessary for the separation of the not encapsulated SR) to yield a system that will no longer be spherical (Fig. 13.31b). As a consequence, the BMS contribution will be operative and the $\Delta_{intralipo}$ value will increase. In addition, the osmotic shrinkage concentrates the SR in the liposome aqueous core, thus enhancing the extent of the dipolar contribution either. A nice demonstration of this effect was obtained by encapsulating a Gd(III) complex ([GdHPDO3A]), for which the dipolar contribution is null (C_D for Gd is zero). The observation of the signal of the intraliposomal water protons at *ca*. 7 ppm from the bulk and the detection of a CEST effect upon saturation highlighted the validity of this approach (Aime et al. 2007). When the BMS contribution is added to the dipolar one (for instance, encapsulating [TmHPDO3A]), a further increase in the $\Delta_{intralipo}$ values can be obtained (Terreno et al. 2007b).

A significant increase in the shift of the intraliposomal water resonance has been achieved by incorporating molecules in the amphiphilic paramagnetic complexes to the liposome's membrane. The incorporation of an amphiphilic SR in a nonspherical LipoCEST (Fig. 13.31c) has two main advantages: (i) it increases the overall amount of paramagnetic centers in the liposome cavity (at least for the portion pointing inward) with the consequent increase of both dipolar and BMS contributions, and (ii) it strongly affects the magnetic anisotropy of the liposome membrane, thus allowing the switch from the parallel to the perpendicular alignment of the vesicles within the static magnetic field of the NMR/MRI spectrometer. Since the orientation of the vesicles can modulate the sign and the magnitude of the paramagnetic shift, the $\Delta_{intralipo}$ values for these systems are strongly dependent on the magnetic properties of the incorporated SR (Delli Castelli et al. 2008).

The amount of paramagnetic centers encapsulated in the aqueous core of a liposome can be further increased by using neutral polynuclear hydrophilic SRs (Fig. 13.31d) (Terreno et al. 2008b) In fact, as the maximum concentration allowed is limited by osmotic rules, neutral multimers should increase the overall payload of paramagnets inside the vesicle.

By using all the above strategies, it is now possible to prepare liposome-based CEST agents with $\Delta_{intralipo}$ values in the interval ± 60 ppm. This result is relevant for the sensitivity issue, even if for osmotically shrunken liposomes the advantage of saturating far from the bulk water resonance is partly counterbalanced by the decreased number of intraliposomal water protons that can be saturated due to the osmotic shrinkage. However, the current range of available $\Delta_{intralipo}$ values makes these nanosystems promising candidates for the multiple detection of CEST agents, as it has been already reported as proof of concept on an ex vivo model (Terreno et al. 2008c).

13.2.4.4 ErythroCEST

Red blood cells are known to be naturally oriented in the presence of an external magnetic field owing to their biconcave shape. Ferrauto et al. show that, analogously to shrunken LipoCEST, the water molecules in the cytoplasm of red blood cells can be exploited as source of exchangeable protons provided that their chemical shift is properly shifted by the intracellular entrapment of a paramagnetic shift reagent. The sensitivity of this system is the highest displayed so far among CEST agents (less than 1 pM of cells), and the natural origin of this system makes it suitable for in vivo applications (Ferrauto et al. 2014).

13.2.5 Hyperpolarized Molecules

Since the early days of NMR, hyperpolarization is considered the most appropriate way to tackle the sensitivity issue.

The energy difference between the nuclear spin states involved in the NMR transitions is very low, and therefore these states are almost identically populated. The NMR signal intensity is proportional to polarization (P), which depends upon the difference in the spin level population according to Eq. 13.55:

$$P = \frac{|N_+ - N_-|}{N_+ + N_-} = \tanh\left(\frac{\gamma \cdot \hbar \cdot B_0}{2 \cdot k_B \cdot T}\right) \quad (13.55)$$

where N_+ and N_- represent the numbers of spins in the two different orientations with respect to the applied magnetic field B_0, γ is the gyromagnetic ratio of the nucleus, k_B is the Boltzmann constant, and T the absolute temperature. Thus NMR and MRI result to be rather insensitive techniques in respect with other analytical and imaging methodologies. However, it has been shown that a nonequilibrium state, characterized by a larger difference in the spin levels populations (hyperpolarized state), can be achieved, thus providing a route of raising the sensitivity of the NMR experiment. Hyperpolarized molecules yield very strong signal enhancements and make possible the observation of low γ heteronuclei, which usually are not detectable due to their low natural abundance and gyromagnetic ratios. Since they do not show any background signal in the corresponding images, it is possible to obtain very clear images where only the regions reached by the agent are visible on a black background. This has been exploited in many MRI experiments, ranging from vascular to perfusion studies, up to new and promising applications in molecular and metabolic imaging.

Hyperpolarized agents generate the contrast in a different way with respect to standard MRI contrast agents. In fact, while the latter act on the relaxation of water protons causing a positive (T_1-CA) or a negative (T_2-CA) effect on the water signal intensity, hyperpolarized molecules are themselves source of the NMR signal. In this case signal intensity and SNR linearly depend upon their concentration and polarization level.

The main drawback of hyperpolarization is its short lifetime. In fact, relaxation processes reequilibrate the spin populations on the T_1 timeframe, destroying hyperpolarization. As a consequence, the type of molecules that can be used as hyperpolarized probes is limited to small molecules containing at least one long-relaxing nucleus (usually ^{13}C) possibly isolated from dipolarly coupled proton nuclei. Furthermore, images of hyperpolarized substances must be acquired very quickly after administration, by using either single-shot experiments or pulse sequences consisting of small flip angles, in order to preserve magnetization. A number of fast imaging pulse sequences have been implemented (mainly echo planar imaging (EPI), echo planar spectroscopic imaging (EPSI), and spiral CSI), allowing to obtain high-resolution images in times as low as 1 s: this allows to detect the formation of metabolic products in real time after administration of the hyperpolarized compound. Further points to keep in mind when dealing with hyperpolarized contrast agents are the need for wider gradient amplitudes (due to the lower gyromagnetic ratio of ^{13}C with respect to ^{1}H) and for wider spectral widths (due to the larger ^{13}C chemical shift dispersion). Details about pulse sequences for metabolic imaging have been recently reviewed (Brindle et al. 2011). Further optimizations of sequences are still being carried out by several groups in order to achieve even higher resolution in the short times dictated by hyperpolarization (Lau et al. 2011; Reed et al. 2012).

13.2.5.1 Hyperpolarization Techniques

According to Eq. 13.51, hyperpolarization can be obtained by simply maintaining the sample at very high magnetic field and ultralow temperature for a time sufficient to force the system into a nonequilibrium state in which the spin populations are consistently altered (Fig. 13.32). This has been sometimes called the "brute force" approach. Due to very long relaxation times in the ultralow temperature range, "relaxation switches" are necessary to decrease the polarization time.

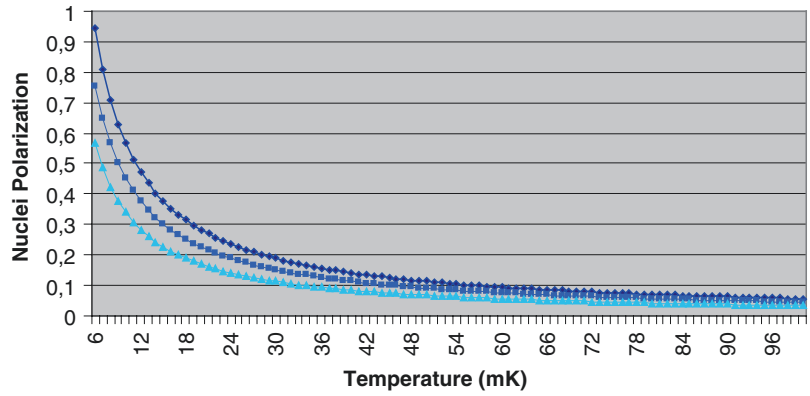

Fig. 13.32 Temperature dependence of polarization at 20 T (*deep blue*), 16 T (*blue*), and 12 T (*cyan*)

In spite of the potential general applicability of the method, this approach is not easily applicable due to difficulties in reaching very high magnetic field strengths and very low temperature conditions. Furthermore, the relaxation switches, if not completely removed or inactivated after the completion of the polarization process, may cause relaxation and polarization loss.

For these reasons, other hyperpolarization techniques have been developed, namely, spin-exchange optical pumping (SEOP) of noble gases, para-hydrogen-induced polarization (PHIP), and dynamic nuclear polarization (DNP).

Hyperpolarization of He-3 and Xe-129 by Optical Pumping and Spin Exchange (SEOP)

When a noble gas (He-3 or Xe-129) is mixed with a vapor of an alkali metal or of metastable atoms (usually ^{3}He atoms) and the mixture is irradiated with circularly polarized light from lasers at suitable frequency, the angular momentum of the laser light is adsorbed by the alkali or metastable atoms, which result to be polarized. Then, interatomic collisions allow polarization to be transferred to the noble gas atoms via a "spin-exchange" process (Fig. 13.33) (Albert et al. 1994; Moller et al. 2002; Altes and Salerno 2004).

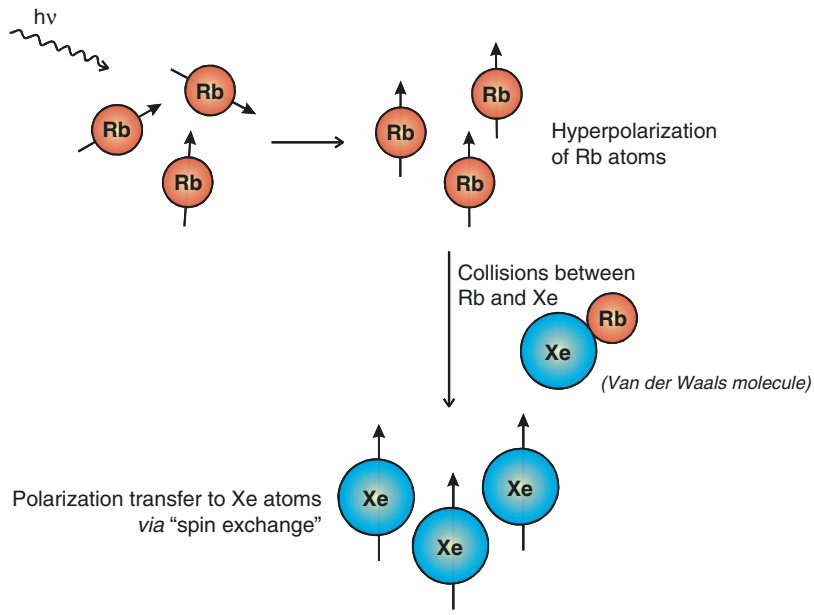

Fig. 13.33 Schematic representation of the laser-induced hyperpolarization of noble gases

Hyperpolarized noble gases have found applications in MRI of the lungs and in a limited number of perfusion studies (Liu et al. 2014). Xe-129 solubility and lipophilic properties have been exploited for functional MRI, and its binding to hemoglobin has been used to measure blood oxygenation (Swanson et al. 1997; Wolber et al. 2000).

Some methods for intravenous injection of both Xe and He have been developed: Xe can be dissolved in some biocompatible carriers (Wolber et al. 1999), while ^{3}He has been loaded in microbubbles suitably functionalized with peptides (Callot et al. 2001). Nevertheless, applications of dissolved noble gases are rare mainly due to difficulties in the dissolution process, and research in this field is still ongoing (Acosta et al. 2012).

Finally, HP-xenon-based biosensors which trap Xe atoms in molecular cages functionalized with suitable vectors have been proposed in order to target specific biomolecules. In one of the first developed systems, Xe has been encapsulated in a cryptophane cage, bound to a biotin unit for protein recognition (Spence et al. 2001). As the cage-encapsulated Xe is in exchange with free Xe and the two corresponding NMR signals are well shifted, an interesting development has been introduced to enhance the sensitivity of the sensor. In fact, by irradiating the Xe resonance in the targeted cage, saturated magnetization is transferred to the signal of free Xe which is exchanging with it, in a way similar to what occurs for CEST agents. Therefore this class of agents has been named Hyper-CEST (Schroder et al. 2006). A number of different Xe biosensors have been designed in the past years: among these, a particularly interesting one is a sensor composed of many cryptophane-A molecular cages assembled on an M13 bacteriophage, which can be detected at a concentration as low as 230 fm, representing the current lowest limit for NMR/MRI-based contrast agents (Stevens et al. 2013). Biosensors that produce measurable changes in Xe-129 chemical shift based upon the activity of oligonucleotides, proteins, enzymes, or cells have also been reported (Taratula and Dmochowski 2010; Boutin et al. 2011).

Dynamic Nuclear Polarization (DNP)

Dynamic nuclear polarization (DNP) is a method which consists in irradiating electrons to promote the transfer of thermal polarization (which is much higher for electrons due to their high g value) to nuclei in solids via "flip-flop" transitions (Comment et al. 2007a). Nuclei are polarized by two different mechanisms, which can operate separately or in parallel depending on the conditions: (i) the solid effect causes nuclei to be polarized in a single step by means of a two-quantum transition and (ii) thermal mixing, on the contrary, is a two-step process where the first step is a single-quantum transition. Thermal mixing is generally the experimentally dominant mechanism when the width of the ESR line is comparable to or larger than the NMR frequency and the concentration of electron spins is high (Comment et al. 2007a).

In practice, the material to be polarized is dissolved in a glass-forming solvent, doped with a stable radical species, and placed into the magnetic field. The solution is frozen and irradiated. At the end of the polarization process, the sample is raised above the liquid helium level and is rapidly dissolved in hot water, still inside the magnetic field. It is then quickly transferred for the MRI acquisition. It has been demonstrated that by using this dissolution method, a good level of polarization is maintained for the time necessary for the acquisition of the MR image (Ardenkjaer-Larsen et al. 2003b).

In principle every nucleus in every molecule can be hyperpolarized by DNP. Examples include DNP hyperpolarization of ^{15}N in urea (Ardenkjaer-Larsen et al. 2003b), carbazole (Hu et al. 2000), amino acids (Hall et al. 1997), and choline (Gabellieri et al. 2008) and of ^{89}Y

in Y(III) chelates (Merritt et al. 2007a). Among these, choline appears very promising since its ^{15}N nucleus is characterized by a particularly long T_1 (285 s at 11.7 T and 298 K), and this allowed to follow its fate in vitro in the presence of purified human choline kinase, which promotes its conversion to phosphocholine, opening the way to metabolic imaging of ^{15}N-choline (Gabellieri et al. 2008). Nevertheless, no in vivo applications have been reported up to now. In fact, at the moment only ^{13}C has been used for in vivo MRI experiments. This is due to the higher gyromagnetic ratio of ^{13}C with respect to other low-relaxing nuclei such as ^{15}N, which increases its sensitivity, and to the availability of dedicated RF coils tuned at the ^{13}C frequency.

Many examples of ^{13}C-containing substrates hyperpolarized by DNP have been reported. The most challenging application of these hyperpolarized ^{13}C tracers is their use in molecular/metabolic imaging, which exploits the high signal intensity for visualizing the products of metabolism few seconds after administration of the agent.

The first studies of metabolic pathways by ^{13}C-hyperpolarized substances have been performed by using hyperpolarized [1-^{13}C]pyruvate. Pyruvate is a key molecule in major metabolic and catabolic pathways in the mammalian cells, as it is converted to alanine, lactate, or carbonate to a different extent depending on the status of the cells. The first reported application of hyperpolarized [1-^{13}C]pyruvate is the visualization in vivo of a rat sarcoma (Golman et al. 2006a): the maps of distribution of pyruvate, alanine, and lactate after pyruvate injection showed that the tumor can be localized by the highest NMR ^{13}C signal from lactate produced few seconds after injection. The various tumor histologic grades could also be differentiated on the basis of lactate levels (Albers et al. 2008). ^{13}C-hyperpolarized pyruvate CSI has been first applied to the study of transgenic adenocarcinoma of mouse prostate (TRAMP), which is a model of prostate cancer that well mimics the human tumor with regard to both histopathology and disease progression (Chen et al. 2007a; Lupo et al. 2010). A number of studies have also shown that the method can be applied to monitor the tumor response to treatment, as the lactate/pyruvate ratio decreases upon both radiotherapy and chemotherapeutic treatments, in both prostate and other organ cancers (Day et al. 2007a; Witney et al. 2009; Senadheera et al. 2010; Park et al. 2011; Day et al. 2011; Lodi et al. 2013). In dogs, whose prostate size and anatomy are similar to those of human prostate, the lactate/pyruvate ratio (even if lower than what is found in murine models) has been shown to be high enough to allow the spatial location of the tumor, giving confidence that the protocol may actually be extended to clinical applications upon optimizing the coil geometry and data acquisition parameters (Nelson et al. 2008). In fact, the clinical phase of trial is currently ongoing in order to develop a method for monitoring the therapeutic treatment of prostate cancer and possibly for choosing the best therapy for each single subject (Nelson et al. 2013a) (Fig. 13.34).

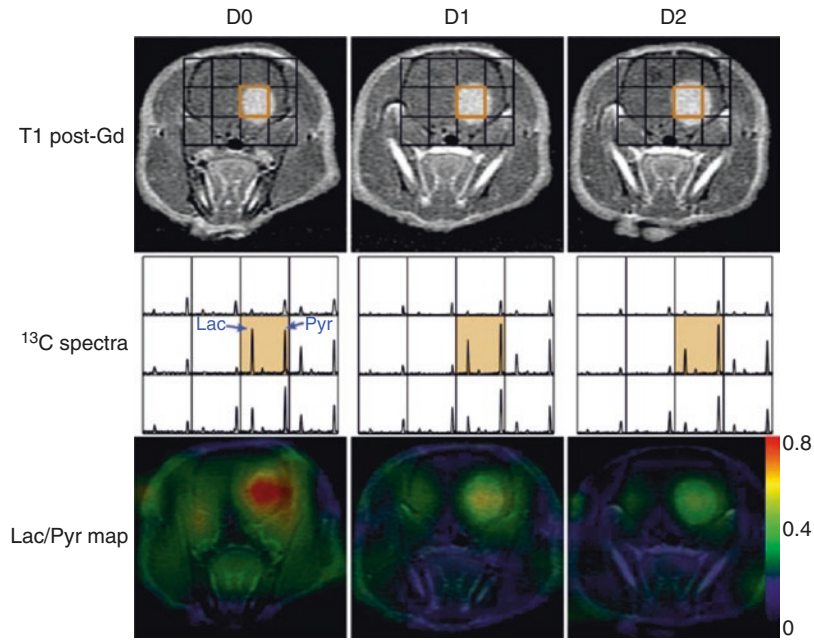

Fig. 13.34 A rat with intracranial implantation of human glioblastoma cells treated with temozolomide. *D0*, pretreatment; *D1*, 1 day after the initiation of treatment; *D2*, scan. The lactate peak decreased shortly after the treatment, resulting in a drastic drop in Lac/Pyr (Reprinted from Ref. (Park et al. 2011) with permission from John Wiley & Sons Inc)

The methodology has also been successfully applied to other types of tumors, such as lymphomas, breast cancer (Harris et al. 2009), renal metastatic cells (Keshari et al. 2013), and liver and brain tumors, toward the translation to the clinics. Among these, brain and liver tumors are the most difficult to be characterized by the classical MRI methods and/or other imaging techniques. In brain, the PET determination of fluorodeoxyglucose (FDG) is not useful for the diagnosis of brain tumors due to the high FDG uptake levels of normal gray matter. Liver tumors are also difficult to be characterized by the classical MRI imaging modalities due to their intrinsic heterogeneous structure. Therefore, there is great interest in finding useful biomarkers which can be followed by a high-resolution technique.

A study carried out on rats with human glioblastoma xenografts (U-87 and U-251, which differ for main histopathologic features) showed that both pyruvate and lactate signals are higher in the tumor tissues than in normal brain and other tissues for both the tumor types, allowing for diagnosis and localization of the tumoral masses, and a strong correlation has been found between the lactate level and the tumor-proliferating activity. These findings clearly support the view of using hyperpolarized [1-^{13}C] pyruvate for the characterization of tumor tissues in the brain (Park et al. 2010).

The Morris hepatoma 7777, a fast growing hepatocellular carcinoma model, has been recently studied by hyperpolarized [1-^{13}C]pyruvate MRI. This tumor is characterized by higher alanine transaminase (ALT) levels rather than by higher LDH levels as usually found in other types of tumor. CSI showed in this case that tumors present a net increase in the alanine/total carbon ratio with respect to normal livers, while the increase in the lactate/pyruvate ratio is not so different with respect to normal tissues (Yen et al. 2010; Darpolora et al. 2011). Higher alanine levels after injection of hyperpolarized 1-^{13}C-pyruvate have also been found in a transgenic liver cancer model of both human hepatocellular and hepatoblastoma tumors. Very interestingly, in this case alanine production

through ALT enzyme was much increased in pre-tumor tissues, being the regions with the highest levels those areas where tumor nodules would eventually develop, but not in established tumor tissues, where on the contrary the flux to lactate, mediated by LDH, was predominant. This suggests that alanine may be used as an early biomarker for liver tumor diagnosis (Hu et al. 2011a).

Besides hyperpolarized pyruvate, other DNP hyperpolarized molecules have been tested for molecular/metabolic imaging: examples include [1-^{13}C]lactate for a complementary investigation of LDH activity (Chen et al. 2008a; Mayer et al. 2012a; Vengatesh et al. 2012; Kennedy et al. 2012), ^{13}C-aminoacids for visualizing amino acid metabolic pathways (Gallagher et al. 2008a; Gallagher et al. 2011b; Chen et al. 2011; Hu et al. 2011b), [1,4-$^{13}C_2$]fumarate for detection of necrotic regions (Zandt et al. 2009, Witney et al. 2010; Clatworthy et al. 2012; Bohndiek et al. 2012), ^{13}C-bicarbonate for tissue pH evaluation (Gallagher et al. 2008b; Gallagher et al. 2011a), [2-^{13}C]pyruvate for visualization of the Krebs cycle (Schroeder et al. 2009a, b; Marjanska et al. 2010; Schroeder et al. 2012; Hu et al. 2012), [1,2-$^{13}C_2$]-pyruvate for simultaneous investigation of cardiac pyruvate dehydrogenase flux, Krebs cycle metabolism and pH (Chen et al. 2012a), ethyl-[1-^{13}C]-pyruvate for imaging brain metabolism (Hurd et al. 2010), [1-^{13}C]-ketoisocaproate for imaging of branched-chain amino acid metabolism in tumors (Karlsson et al. 2010), mixtures of labeled substrates for simultaneous assessment of multiple enzymatic activities (Wilson et al. 2010; von Morze et al. 2012b), ^{13}C ascorbic and dehydroascorbic acid for visualizing the redox status (Keshari et al. 2011a; Bohndiek et al. 2011), ^{13}C-urea for perfusion studies (von Morze et al. 2011, 2012a), and $^{13}C_6$-glucose to be visualized by MRI as an alternative to FDG-PET (Allouche-Arnon et al. 2013).

Hyperpolarized molecules are currently being investigated not only for the diagnosis and monitoring of tumors but also for the study of different pathologies in organs such as the heart, liver, and kidneys.

Cardiac metabolism, both in isolated rat hearts and in vivo, has been assessed by hyperpolarized MRI after injection of [1-^{13}C]-pyruvate. For example, it has been demonstrated that it can show the glycolytic switch characteristic of myocardial ischemia by the increase in the lactate level. Still more informative, the pyruvate transformation into bicarbonate promoted by pyruvate dehydrogenase (PDH) can be monitored: the bicarbonate level in the myocardium is lower or absent in the ischemic or postischemic area due to a diminished activity of PDH. Metabolic alteration is also evident by following the flux of [2-^{13}C]-pyruvate to [1-^{13}C]citrate and [5-^{13}C]glutamate. Information derived from hyperpolarized MRI of the heart may be of paramount importance in monitoring cardiomyopathies and myocardial activity restoration after an ischemic damage, a heart failure, and/or an intervention (Schroeder et al. 2011; Malloy et al. 2011).

Liver metabolism after ethanol assumption has also been investigated by the use of hyperpolarized [1-^{13}C]pyruvate, showing increased lactate production due to increased NADH from ethanol metabolism (Josan et al. 2012).

Hyperpolarized MRI of [1-^{13}C]pyruvate has been shown to be applicable to the diagnosis of diabetic renal damages, as an appreciable increase in the lactate/pyruvate ratio measured in diabetic rats' kidneys compared with the control ones, whereas the bicarbonate/pyruvate ratio was unchanged (Laustsen et al. 2013). Conversely, pyruvate metabolism has been found to be not informative about renal acute pathologies such as tubular necrosis (ATN) and glomerulonephritis (GN). In these cases, MRSI of hyperpolarized [1,4-$^{13}C_2$]fumarate has allowed the detection of early tubular necrosis and its distinction from glomerular inflammation in murine models, thanks to the increased production of [1,4-$^{13}C_2$] malate (mediated by the fumarase enzyme) observed in the former case and not in the latter. The malate/fumarate ratio has been found to correlate with the histologic grade of necrosis in the first hours after induction (Clatworthy et al. 2012) (Fig. 13.35).

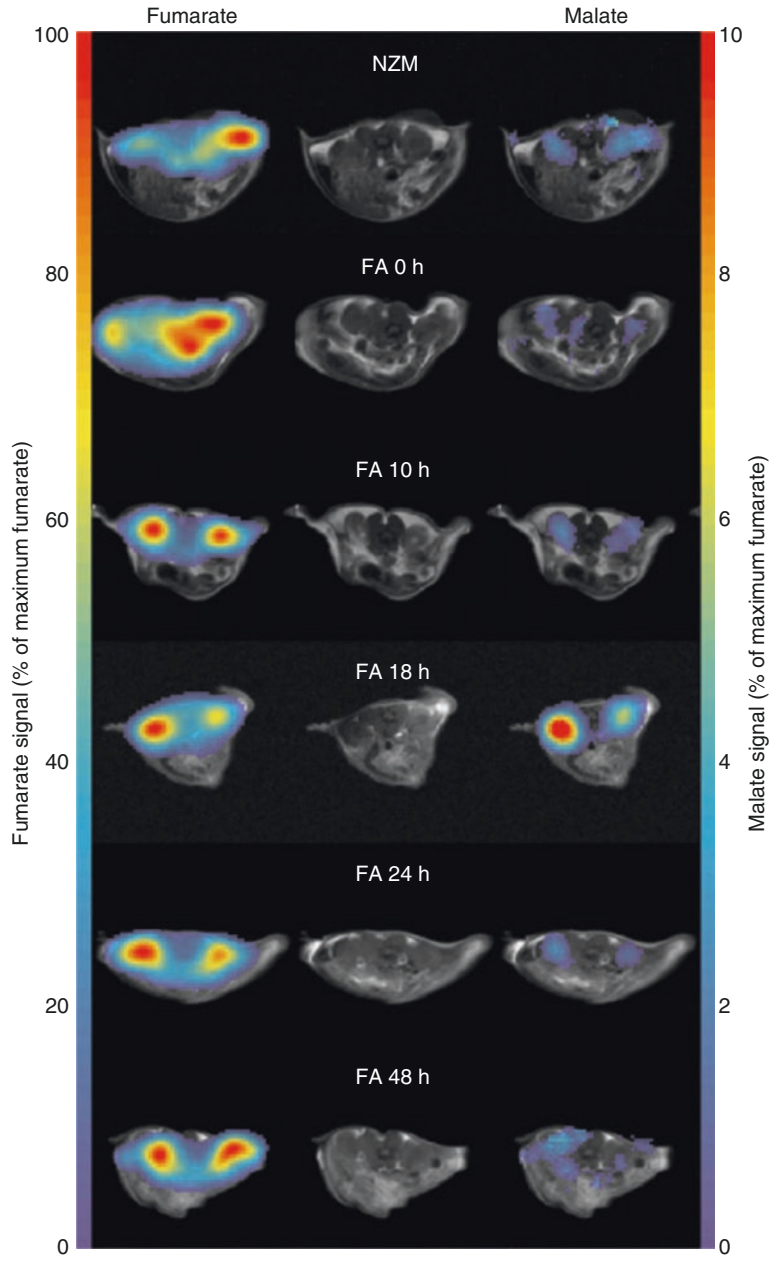

Fig. 13.35 Distribution of normalized [1,4-$^{13}C_2$] fumarate and [1,4-$^{13}C_2$] malate signals following fumarate injection in an NZM2410 mouse and at 0, 10, 18, 24, and 48 h after induction of ATN in mice. Each chemical shift image has been normalized separately to its maximum signal intensity (Reprinted from Ref. (Clatworthy et al. 2012), with permission from the National Academy of Science USA)

Para-Hydrogen-Induced Polarization (PHIP)

The hydrogen molecule entered in the field of hyperpolarization because the change in the relative populations of its nuclear spin states is easy to fulfill, without the need for complex hyperpolarization devices. In fact, nuclear spins in the H_2 molecule can be either aligned or opposed: three degenerate levels correspond to the nuclear isomer named ortho-hydrogen

(oH_2, $S=1$, 75 % natural abundance), while only one nuclear state corresponds to the nuclear isomer named para-hydrogen (pH_2, $S=0$, 25 % abundance). The para-hydrogen state has lower energy, and it is therefore possible to enrich hydrogen in the para form by maintaining the H_2 gas at low temperature. A paramagnetic catalyst is required for the enrichment because the ortho–para transition is otherwise forbidden by symmetry rules. The hydrogen hyperpolarization process thus simply consists in maintaining the hydrogen gas at low temperature in the presence of charcoal or iron oxide or other paramagnetic substances, and the pH_2 enrichment degree depends on the temperature, being about 50 % at 73 K and almost 100 % at 4 K.

The spin order of the para-hydrogen molecule can be transferred to other molecules by chemical reaction. In hydrogenation reactions carried out with H_2 enriched in the para form, the product molecules present NMR spectra which are characterized by strongly enhanced absorption/emission signals which, in theory, may be up to 10^5 times higher than those observed when normal hydrogen is used. This phenomenon has been called para-hydrogen-induced polarization (PHIP) (Bargon and Natterer 1997; Duckett and Wood 2008). Such polarization can then be transferred from H atoms to neighboring heteronuclei in the hydrogenated products via scalar couplings or nuclear Overhauser effect (nOe) (Barkemeyer et al. 1995; Aime et al. 2003a, b).

For MRI applications two operations must be carried out after the para-hydrogenation has taken place: (1) the antiphase pattern of the heteronucleus signal obtained after polarization transfer must be converted into an in-phase signal in order to allow the image acquisition (this can be achieved by a field cycling procedure (Johannesson et al. 2004a) or the application of a suitable pulse sequence (Goldman et al. 2005a)); (2) the catalyst used for para-hydrogenation and (if present) the organic solvent must be removed before injection. The catalyst (usually cationic Rh(I) complexes) may be removed by cation exchange and the solvent by spray distillation. The fulfillment of these operations requires time that is at the expenses of the attainable signal intensity, as polarization decay occurs on the T_1 timescale. An alternative method for the attainment of pure aqueous solutions of hyperpolarized molecules consists of carrying out the para-hydrogenation reaction in an organic solvent not miscible with water and then quickly extracting the hyperpolarized water-soluble molecule by phase transfer (Aime et al. 2008).

The first examples of MRI of PHIP hyperpolarized ^{13}C agents dealt with molecules of limited biocompatibility (Golman et al. 2001a, 2005a, b; Ishii et al. 2007; Johansson et al. 2004a; Magnusson et al. 2007).

Only more recently, it has been shown that hyperpolarized succinate can be obtained by para-hydrogenation of fumarate (Chekmenev et al. 2008a), and it has been used to perform in vivo CSI (Bhattacharya et al. 2009). This is the first example of a biocompatible agent hyperpolarized by PHIP.

Then, hyperpolarized [1,4-$^{13}C_2$]diethylsuccinate (obtained by para-hydrogenation of [1,4-$^{13}C_2$]diethylfumarate) has been reported to visualize the TCA cycle metabolism in vivo (Zacharias et al. 2012a) (Fig. 13.36).

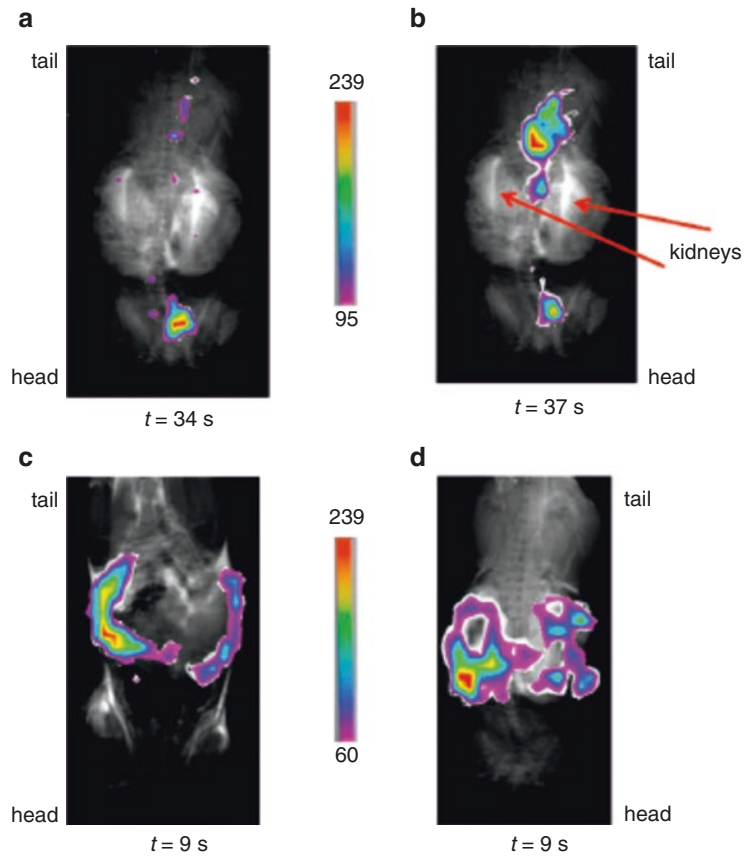

Fig. 13.36 ^{13}C imaging in vivo of a rat after injection of hyperpolarized [1,4-$^{13}C_2$] diethylsuccinate. Images A–D are overlays of ^{13}C FISP images (60° flip angle) in false color taken of different injections of hyperpolarized diethyl succinate over the proton image of the mouse with the same 6 cm FOV, central slice placement, and slice thickness (Reprinted with permission from Ref. (Zacharias et al. 2012a). 2012 Copyright American Chemical Society)

Another interesting study deals with the use of 2,2,3,3-tetrafluoropropyl-^{13}C-propionate-$d_{2,3,3}$ (TFPP), hyperpolarized by para-hydrogenation of its unsaturated precursor 2,2,3,3-tetrafluor opropyl-^{13}C-acrilate-$d_{2,3,3}$ for the detection of atheromatous plaques in vivo, by exploiting the ability of TFPP to bind to lipid bilayers. When TFPP was hyperpolarized and administered in vivo to atheromatous mice in a pilot study, increased binding was observed on the endocardial surface of the intact heart in fat mice compared with normally fed controls (Bhattacharya et al. 2011a).

Finally, hyperpolarized [1-^{13}C]phospholactate (obtained by para-hydrogenation of [1-^{13}C]phosphoenolpyruvate) has been suggested as a potential contrast agent as after injection it undergoes dephosphorylation by phosphorylase enzyme, thus yielding hyperpolarized [1-^{13}C]lactate (Shchepin et al. 2014a, b).

As it is based on the addition of a para-hydrogen molecule to an unsaturated substrate, the PHIP method appears to be strongly limited in terms of the number of candidate molecules. Nevertheless, it has been recently shown that a good signal enhancement can be detected for the ^{15}N resonances of N-containing substrates reversibly coordinated to an Ir complex that has been added of a para-hydrogen molecule (Adams et al. 2009a; Gloggler et al. 2011). The observed behavior opens interesting perspectives to polarization via para-H_2, as it shows that enhanced NMR signals can be obtained without hydrogenation of the substrate as previously assumed.

As it is based on the addition of a para-hydrogen molecule to an unsaturated substrate, the PHIP method appears to be strongly limited in terms of the number of candidate molecules. Nevertheless, it has been recently shown that a good signal enhancement can be detected for the

^{15}N resonances of N-containing substrates reversibly coordinated to an Ir complex that has been added of a para-hydrogen molecule (Adams et al. 2009a). The observed behavior opens interesting perspectives to polarization via para-H2, as it shows that enhanced NMR signals can be obtained without hydrogenation of the substrate as previously assumed.

13.2.6 Conclusions

The field of MRI-CA is still continuing to grow and new ideas further widen their range of applications. The limited sensitivity of MRI probes is the major limitation for a widespread diffusion of MRI in molecular imaging studies. Therefore much work is currently focused on the task of accumulating a sufficient number of contrast units at the targeting sites. This task is pursued mainly through (i) exploitation of cellular uptake pathways that use the cell itself as a container for the accumulation of the imaging payload or (ii) the setup of nano (or even micro)-sized particles containing a huge amount of the imaging reporting units. The latter approach has opened new horizons that conjugate imaging science and nanotechnology. An important feedback from this merging is, for instance, the development of new protocols of imaging-guided therapy that may find great interest in the domain of personalized medicine.

13.3 In Vivo Magnetic Resonance Imaging and Spectroscopy with Hyperpolarized Agents

Jan-Bernd Hövener, Jessica A.M. Bastiaansen, Arnaud Comment, Stephan Düwel, Jan H. Ardenkjaer-Larsen

13.3.1 Introduction

Magnetic resonance (MR) is a powerful, noninvasive tool that provides anatomical, functional, and chemical information of biological systems. MR is the basis of nuclear MR spectroscopy (NMR), in vivo spectroscopy (MRS), in vivo imaging (MRI), and in vivo spectroscopic imaging (MRSI). Anatomical and functional MRI has already been widely implemented for human and preclinical applications. MRS, on the other hand, is hardly used for routine in vivo examinations. At the same time, the information provided by MRS is unique and allows for early diagnosis or monitoring the response of pathologies to therapy. The routine application of MRS has been severely hampered by the overall low sensitivity of MR.

All atoms that possess a nuclear magnetic moment, such as hydrogen (^{1}H), phosphorus (^{31}P), and carbon (^{13}C), are detectable in MR experiments. The nuclear magnetic moment of a given nuclear species is characterized by its nuclear spin that has a restricted number of energy eigenstates in an external magnetic field, two for a spin-½ particle like ^{1}H or ^{13}C (denoted + and −). The general state of spins is described by a superposition of these eigenstates. At thermal equilibrium, the population of the associated energy levels, $n(+)$ and $n(-)$, follows the Boltzmann distribution and is referred to as thermal polarization P_{therm}. P_{therm} depends on the thermal energy $E_t = k_B T$, where k_B is the Boltzmann constant and T the temperature, as well as the magnetic energy $E_m = \pm \hbar\gamma B_0/2$, where γ is the gyromagnetic ratio of the nuclei, $\hbar$ is Planck's constant, and B_0 is the magnetic field. Considering a spin−½ nucleus, P_{therm} can be described by

$$P_{\text{therm}} = \frac{n(+)-n(-)}{n(+)+n(-)} = \tanh\left(\frac{E_m}{E_t}\right) = \tanh\left(\frac{\hbar\gamma B_0}{2k_B T}\right)_{T \gg 0} \approx \left(\frac{\hbar\gamma B_0}{2k_B T}\right) \tag{13.56}$$

At room temperature and in a magnetic field of several Tesla (T), the magnetic energy of the nuclear spins is $\approx 10^{-26}$ J and thus much smaller than the thermal energy of $\approx 10^{-21}$ J. Consequently, both energy states are nearly equally populated (Fig. 13.37), resulting in a weak net alignment of the magnetic moments with respect to the magnetic field. Only this fraction P_{therm} is detected in

MR experiments. For ^{1}H, for example, P_{therm} is no more than 0.2 ppb in the Earth's magnetic field and 10 ppm at 3 T, illustrating MR's low sensitivity. Yet the high concentration of water in vivo (~40 M) provides sufficient signal to enable high-resolution MRI. The concentration of most relevant metabolites is typically much lower, in the μM to mM range. As a result, conventional MRS in humans requires relatively large detection volumes of the order of cubic centimeters, and long scan times in the order of minutes to obtain a sufficient signal-to-noise ratio (SNR). Clinical and preclinical applications of MRS include the detection of brain metabolites (Xu et al. 2008; Bachert et al. 1992; Pfeuffer et al. 1999) or the measurement of energetically relevant metabolites, pH, and reaction fluxes (Bachert et al. 1992; McRobbie et al. 2006; Schlemmer et al. 2005) like phosphoryl exchange kinetics in skeletal muscle (Nabuurs et al. 2010) with ^{31}P-MRS. ^{13}C-MRS allows to investigate in vivo enzymatic fluxes (Duarte and Gruetter 2013), but requires isotopic enrichment because the natural abundance of ^{13}C is low (1.1 %).

13.3.2 Hyperpolarization

Despite these limitations, the preclinical application of MRS to study molecular and metabolic processes is an active field and gaining interest. It is currently the only technique that allows to study separate biochemical processes simultaneously in vivo (Bastiaansen et al. 2016).

To exploit the potential of MRS further, however, a substantial SNR gain is necessary. The hyperpolarization (HP) of nuclear spins has successfully demonstrated a signal enhancement of several orders of magnitude (Bowers and Weitekamp 1987; Ardenkjaer-Larsen et al. 2003a, b, c; Shchepin et al. 2014c) and enabled novel research avenues, such as the real-time measurement of metabolic processes with unprecedented resolution (Golman et al. 2006b).

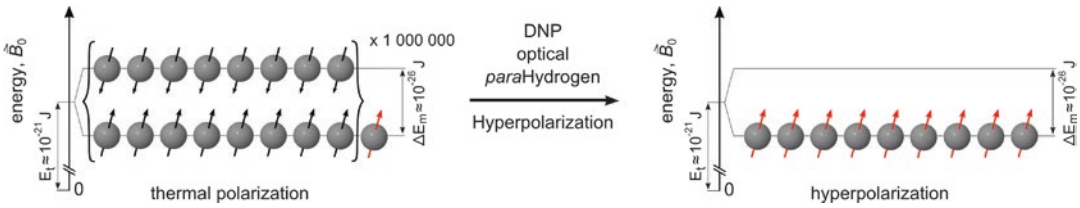

Fig. 13.37 Schematic view of a thermally polarized (*left*) and hyperpolarized (*right*) ensemble of nuclear spin–½ particles like ^{13}C in a magnetic field, where the energy levels are populated following the Boltzmann distribution (Eq. 13.56). Only the population difference between both levels is effectively detected by MR (indicated in *red*)

The goal of HP is to create a nuclear spin polarization which is significantly greater than P_{therm} (Fig. 13.37). This goal is achieved by using one of the following methods: brute force, using a very low temperature and a strong magnetic field (Johnson et al. 1973; Hirsch et al. 2015), spin-exchange optical pumping for noble gases (Happer 1972), *para*-hydrogen (pH_2) (Bowers and Weitekamp 1986; Chekmenev et al. 2008b; Goldman and Johannesson 2005b), or dynamic nuclear polarization (DNP) (Abragam and Goldman 1978) followed by dissolution (Ardenkjaer-Larsen et al. 2003c; Comment 2013).

Although it provides strong signal enhancement, one must bear in mind that HP is inherently transient because it represents a state that is strongly out of equilibrium. The hyperpolarized agent is prepared externally in a polarizer and must be rapidly injected before the nuclear polarization relaxes to thermal equilibrium.

Despite these challenges, hyperpolarized MRS and MRI have provided novel insights into biochemical processes. Clinical trials investigating (cancer and cardiac) metabolism have already been completed (Kurhanewicz et al. 2011; Nelson et al. 2013a; Cunningham et al.

2016). As HP techniques continue to draw attention from the research community, this chapter intends to provide an overview as well as a practical guide for the HP experiment, from HP generation to application, detection, and interpretation (Fig. 13.38). For more details, the reader is referred to several review articles and other book chapters (Witte and Schröder 2013; Comment and Merritt 2014; Keshari and Wilson 2014; Ardenkjaer-Larsen et al. 2010, 2011a, b; Hurd et al. 2012; Bowers 2007; Sriram et al. 2007; Canet et al. 2006; Duckett and Mewis 2012).

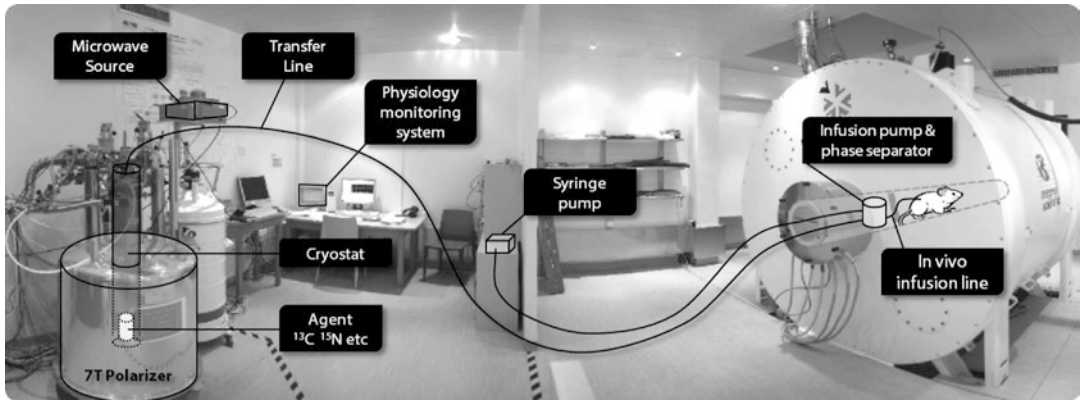

Fig. 13.38 Experimental setting for an in vivo HP experiment using dissolution DNP: an agent is hyperpolarized in a polarizer and rapidly transferred to an injection pump located inside the MRI scanner. The injection pump is triggered after the end of the hyperpolarized agent transfer. The agent is then automatically administered to the animal via a catheter

13.3.3 Hyperpolarization Methodologies

In general, biomedical HP experiments require a suitable agent and a polarizer. In addition, a MRI system in close proximity is mandatory, because, once generated, HP decays exponentially as defined by the longitudinal relaxation time T_1 that is typically of the order of a few tens of seconds. Thus, the agents have to be hyperpolarized on-site for immediate use. The concept of $p\mathrm{H_2}$-based HP and dissolution DNP is presented in the following.

13.3.3.1 Hyperpolarization Using Para-Hydrogen

Para-hydrogen ($p\mathrm{H_2}$) was discovered in the early days of quantum mechanics, where it served as a model system to demonstrate newly discovered quantum effects (Farkas 1930; Hund 1927; Bonhoeffer and Harteck 1929). It is a spin isomer of dihydrogen gas ($\mathrm{H_2}$), which consists of two hydrogen atoms, each with a nuclear spin of ½. There are four configurations of the spins with respect to a magnetic field, one that is antisymmetric with respect to interchanging both spins, $p\mathrm{H_2}$, and three configurations that are symmetric, *ortho*-hydrogen ($o\mathrm{H_2}$) (Fig. 13.39). All four states are approximately equally populated at room temperature, 25 % $p\mathrm{H_2}$ and $3 \cdot 25\,\%$ $o\mathrm{H_2}$. At low temperatures, the equilibrium is shifted toward $p\mathrm{H_2}$, but the conversion from $o\mathrm{H_2}$ to $p\mathrm{H_2}$ is relatively slow and can exceed days. The conversion rate is highly accelerated by exposing the cold gas to a catalyst, namely a paramagnetic collison partner, such as ferric hydroxide oxide (Fe(OH)O). Highly enriched $p\mathrm{H_2}$ is being produced in large quantities by a continuous flow of $\mathrm{H_2}$ through a catalyst bed at ≈ 25 K (Tam and Fajardo 1999; Feng et al. 2012a; Hövener et al. 2013a; Gamliel et al. 2010). When stored in an appropriate vessel in the absence of the catalyst, the conversion back to thermal equilibrium is sufficiently slow to maintain enriched $p\mathrm{H_2}$ at room temperature for several days (Hövener et al. 2013a; Wagner 2014), producing a "spin order reservoir" readily available for the HP of other molecules.

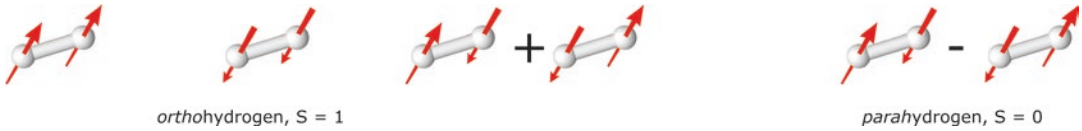

Fig. 13.39 Schematic view of four spin configurations of dihydrogen gas. Note that a normalization factor ($2^{-½}$) was omitted for the combined spin states (Figure reproduced with permission from NMR in Biomedicine)

pH$_2$ alone has a combined spin 0 and does not yield MR signal. It is, however, a pure spin state that can be modified to enhance MR signal. The effect of pH$_2$ on MR signal was first described in the 1980s, where pH$_2$ was added to a precursor molecule by catalytic addition to an unsaturated bond (Fig. 13.40a), known as *pH_2 and synthesis allows dramatically enhanced nuclear alignment* (PASADENA) (Bowers and Weitekamp 1986, 1987), *adiabatic longitudinal transport after dissociation engenders net alignment* (ALTADENA) (Pravica and Weitekamp 1988), or *pH_2-induced polarization* (PHIP) (Eisenschmid et al. 1987; Hommeltoft et al. 1986). In the following decade, the phenomenon was applied in NMR and chemistry mostly to enhance ^{1}H-signal that has a relatively short T_1 of a few seconds (Bowers 2007; Canet et al. 2006; Duckett and Mewis 2012; Natterer and Bargon 1997; Duckett 1999). The efficient transfer of HP to longer-lived ^{13}C-nuclei by applying a specific pulse sequence (Goldman and Johannesson 2005b; Haake et al. 1996; Goldman et al. 2006; Kadlecek et al. 2010; Cai et al. 2013; Bär et al. 2012) or field cycling (Johannesson et al. 2004b) was key to enable first in vivo applications (Golman et al. 2001a, b; Goldman et al. 2005b; Hövener et al. 2009b; Olsson et al. 2006).

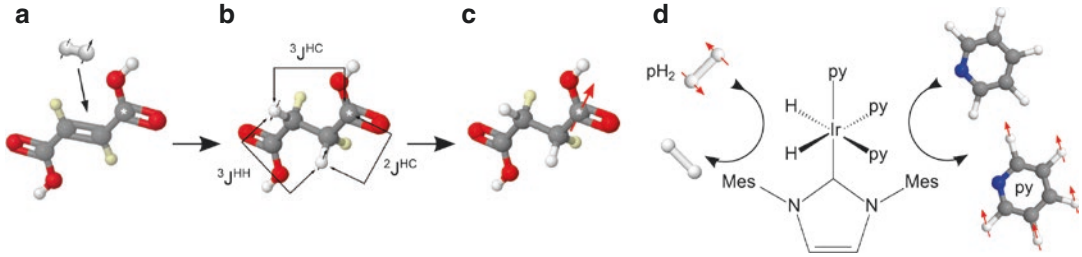

Fig. 13.40 Schematic view of HP by catalytic addition (**a**–**c**) and reversible exchange (**d**) of pH$_2$. After the addition of pH$_2$ to an unsaturated precursor (**a**), a pulse sequence in conjunction with the J-couplings (**b**) is used to create hyperpolarized ^{13}C. In SABRE (**d**), HP is transferred from pH$_2$ to an agent in a low magnetic field via a temporary J-coupling network formed by a catalyst. Note that after the exchange, H$_2$ may carry observable polarization as well

A method for HP without covalent addition of pH$_2$ to a precursor was described in 2008 (Adams et al. 2009b, c) (Fig. 13.40d). S*ignal amplification by reversible exchange* (SABRE) is a promising technique in particular with respect to high X-nuclei HP that was reported recently (Barskiy et al. 2016; Theis et al. 2014, 2015). Its in vivo application, however, has yet to be explored. An interesting feature of SABRE is that it allows the continuous renewal of the hyperpolarized state in solution (Hövener et al. 2013b, 2014a; Rovedo et al. 2016).

Currently, several pH$_2$-generators, pH$_2$-polarizers, as well as biologically relevant agents have been described that were polarized to more than 10 % in some cases (e.g., Refs. Shchepin et al. 2014c; Chekmenev et al. 2008b; Goldman and Johannesson 2005b; Hövener et al. 2009a; Tam and Fajardo 1999; Feng et al. 2012a; Hövener et al. 2013a; Gamliel et al. 2010; Hövener et al. 2009a, b; Waddell et al. 2011; Kadlecek et al. 2011; Invento; Lickert et al. 2013; Mewis et al. 2014; Borowiak et al. 2013; Hövener et al. 2014b; Shchepin et al. 2014c; Chekmenev et al. 2008b;

Hövener et al. 2013b, 2014b; Chekmenev et al. 2008c; Bhattacharya et al. 2011b; Lego et al. 2014; Roth et al. 2010; Reineri et al. 2008, 2010; Shchepin et al. 2012; Golman et al. 2003a; Trantzschel et al. 2012; Zacharias et al. 2012b; Reineri et al. 2015). This section focuses on the ^{13}C-HP of biomolecules in aqueous solution using PHIP.

The pH$_2$-HP Experiment

The essential requirements for the pH$_2$-HP experiment are pH$_2$, a hydrogenation catalyst with a suitable precursor, and a polarizer, i.e. a setup to carry out the hydrogenation and spin order transfer (Table 13.2, Fig. 13.41):

(a) Ultrapure H$_2$ gas is commercially available or may be produced on demand by chemical reaction (Gamliel et al. 2010) or hydrolysis. The simplest way to enrich pH$_2$ is a flow of H$_2$ gas through a copper tube immersed in liquid nitrogen, filled with a conversion catalyst, such as Fe(OH)O, yielding a *para*-enrichment of $\approx$50 %. Alternatively, a cryostat may be used to produce close to 100 % pH$_2$ (Tam and Fajardo 1999; Feng et al. 2012a; Hövener et al. 2013a). Typically, pH$_2$ is stored in aluminum cylinders that provide a lifetime exceeding days (Hövener et al. 2013a; Wagner 2014).

As H$_2$ forms an explosive mix with air at a concentration of 4–74 vol.% (Beeson and Woods 2003), it poses a safety hazard that must be carefully addressed in accordance with applicable regulations. To this end, a dedicated setup for clinical use was proposed (Fig. 13.41, left) (Hövener et al. 2013a). Further risk reduction can be achieved by on-demand production of H$_2$ by hydrolysis or chemical reaction (Gamliel et al. 2010).

(b) The hydrogenation catalyst is prepared fresh in aqueous solution from 1,4-bis[(phenyl-3-propanesulfonate) phosphine] butane disodium salt (e.g., Sigma-Aldrich 717347, MDL MFCD15144866) and bis(norbornadiene) rhodium (I) tetrafluoroborate (CAS 36620-11-8, e.g., STREM, USA) to yield 2 mM concentration as described in Hövener et al. (2009b).

The SABRE catalyst and the preparation of an aqueous solution were described in Truong et al. (2014) and Cowley et al. (2011). As the biological effect of either catalyst is not yet fully investigated (Freundlich et al. 2006), catalyst and agent should be separated before injection. Heterogeneous catalysts that are solid supported or allow removal by filtration were investigated but have not yet let to sufficient polarization levels for in vivo application (Koptyug et al. 2007, 2010; Kovtunov et al. 2008, 2009; Shi et al. 2014; Glöggler et al. 2015). Extracting the agent by phase separation is also feasible (Reineri et al. 2011).

Several ^{13}C- and deuterium-labeled precursors are commercially available, such as [1-^{13}C, 2,3-^{2}H$_2$] fumarate (CAS 1018681-16-7, MDL MFCD28137808, e.g., Sigma-Aldrich, USA, or Cambridge Isotopes Laboratories, USA), and the synthesis of others was described (Shchepin et al. 2014c; Reineri et al. 2008, 2010; Shchepin et al. 2012; Reineri et al. 2015; Roth et al. 2010).

(c) While a standardized pH$_2$-polarizer does not exist, the basic features and experimental steps are similar for all described implementations (Coffey et al. 2016; Hövener et al. 2009a, b; Waddell et al. 2011; Kadlecek et al. 2011; Invento) (Table 13.2, Fig. 13.41, right). After the preparation of pH$_2$ and the catalyst solution, the HP is a two-step process that takes a few seconds:
   1. Addition of pH$_2$ to the unsaturated precursor by means of hydrogenation
   2. Spin order transfer with a radio-frequency (RF) pulse sequence or field cycling

To yield a high polarization, pH$_2$ must be rapidly added to the precursor to preserve the spin order. This homogeneous catalytic hydrogenation is carried out in a reactor at an elevated temperature, e.g., 60° C, and pressure, e.g., ten bar, located inside a low-field NMR unit (Hövener et al. 2009a, b; Borowiak et al. 2013; Agraz et al. 2013) that is capable of ^{1}H-decoupling and spin order transfer. Several spin order transfer pulse sequences were described and compared (Goldman and Johannesson 2005b; Kadlecek et al. 2010; Cai et al. 2013; Bär et al. 2012; Norton 2010), as well as routines and equipment assuring a high polarization gain (Hövener et al. 2009a; Borowiak et al. 2013; Agraz et al. 2013).

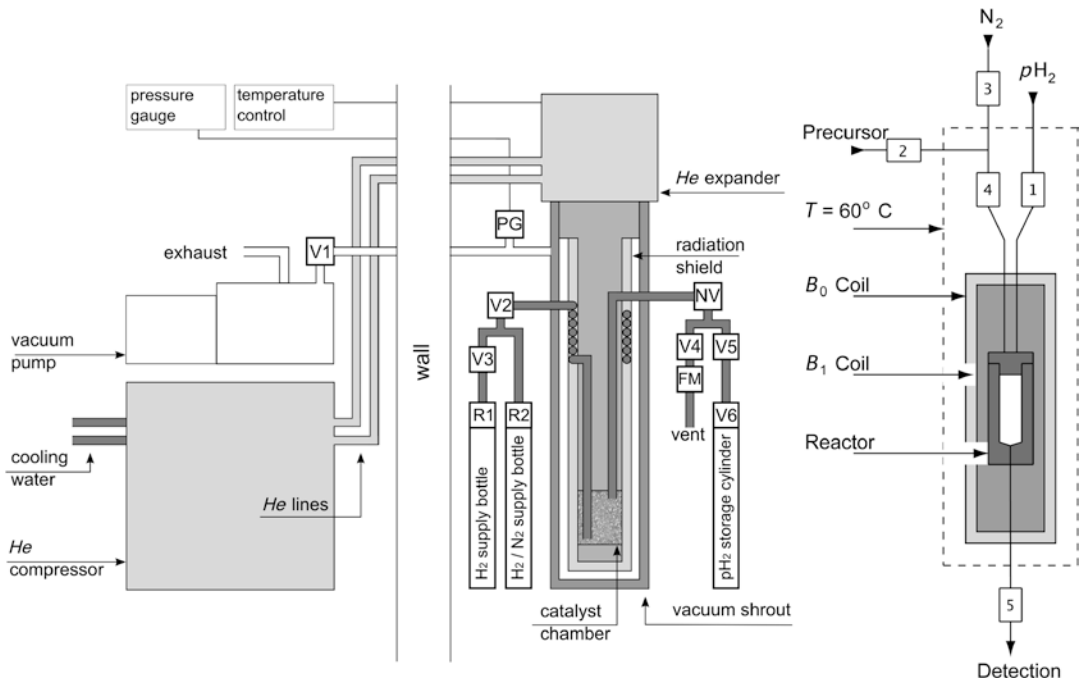

Fig. 13.41 Schematic view of a pH_2-generator (*left*) and pH_2-polarizer (*right*). The H_2-containing components of the generator are mounted on the outside wall of a building (Hövener et al. 2013a). The polarizer contains a reaction chamber for the catalytic addition of pH_2 to an unsaturated precursor within a low-field NMR unit (Hövener et al. 2009b) (Parts of this figure reproduced with permission from NMR in Biomedicine). Abbreviations: numbers and *V* valves, *R* regulator, *NV* needle valve, *PG* pressure gauge, *T* temperature, *FM* flow meter, *He* Helium

Table 13.2 Workflow example of a pH_2-HP experiment

Generate pH_2 When: e.g. > 5 h b.d. Duration: 4 hrs	• Flush lines with N_2, H_2, start cool down (≈3-4 h) • At 22K: purge receiver bottle, fill with pH_2 (<1h) • Perform QA: quantify enrichment e.g. by NMR
Prepare Chemistry When: 2 h b.d. Duration: 30 min	• Prepare hydrogenation catalyst (20 min) • Adjust pH • Add precursor
Start Polarizer When: 2 h b.d. Duration: 30 min	• Warm up low-field NMR (2 h) • System adjustments: Low-field ^{1}H-NMR to adjust frequency, flip angle
Automated HP When: Minutes b.d. Duration: Minutes	• Warm precursor solution (min) • Mix pH_2 and precursor in reactor (s) • Hyperpolarization by SOT sequence (<1 s) • Eject agent (no s) and transfer to MRI

b.d **Before detection of hyperpolarized agent** *QA* **quality assurance,** *SOT* **spin order transfer**

13.3.3.2 Dissolution DNP

HP by DNP relies on the magnetic moment of the unpaired electron spin as a source of spin order to polarize atomic nuclei. In contrast to nuclear spins, the magnetic moment of electron spins is much stronger and yields a high thermal polarization already at, e.g., 2 K and 3 T. DNP describes a process where thermal polarization is transferred from electrons to nuclei at cryogenic temperatures in a strong magnetic field using microwave irradiation (Abragam and Goldman 1978). Once the nuclei are polarized, the sample is dissolved rapidly (during the dissolution process), using a heated, pressurized solvent such as water.

Based on the original dissolution DNP apparatus proposed by Ardenkjær-Larsen et al. (Ardenkjær-Larsen et al. 2003a, b, c), two types of commercially available polarizers were designed, the "HyperSense" for preclinical use and the "SpinLab" for sterile use (Oxford Instruments and General Electric). Some practical considerations for operating these setups are given below.

Table 13.3 Exemplary workflow of the DNP-HP experiment

Agent Preparation When: 3h - several months b.d. Duration: 1-4 hours	• mix radical and agent
Polarizer Preparation When: 45min - 2h b.d. Duration: 5 min	• start cooldown of polarizer • load sample into polarizer
Solid-state Polarization When: 40min - 2h b.d. Duration: 30min - 2h	• adjust microwave frequency • start microwave irradiation • monitor polarization level
Dissolution Preparation When: 5 min b.d. Duration: 5 min	• insert dissolution agent into polarizer • pressurize and heat dissolution agent
Dissolution and Injection Duration: 2-10 s	• perform dissolution (and filter radical) • transfer agent into desired collection flask • draw substance from collection flask and inject
Polarizer Cleaning When: 5 min a.d. Duration: 5 min	• rinse dissolution path several times with water/ethanol/acetone/helium gas/air

b.d. **before detection of hyperpolarized agent,** *a.d.* **after detection**

The DNP-HP Experiment

HyperSense General Considerations on Setup and Components

The HyperSense (HS) DNP polarizer is composed of a 3.35 T NMR, which allows to irradiate a frozen sample between 1.2 and 1.5 K with microwave irradiation of ca 94 GHz and up to 100mW power. It consumes liquid helium and liquid nitrogen for cooling as well as gaseous helium or air for the dissolution procedure. Helium and nitrogen have to be refilled regularly, according to usage. The required lab space amounts to 1.0 m × 1.7 m at a height of less than 3 m. The vacuum pumps need an additional space of approximately 40 cm × 80 cm, preferably as close as possible to the polarizer, in a separate room to reduce noise and heat load. For operation, single- and triple-phase power is needed.

Operating Steps

The HS-DNP process may be summarized in seven basic operating steps. As an example, the values for ^{13}C pyruvate HP are given in parentheses.

1. Hardware preparation: Turn on HS spectrometer electronics, and initiate the cooldown of

the variable temperature insert which will receive the sample.
2. Sample preparation: Mix the HP agent with a glassing and a relaxation moiety, and insert into the sample cup (30 μL of 14 M ^{13}C-pyruvic acid, doped with 1 mM Dotarem (Guerbet, Villepinte, France) and 15 mM trityl radical OX063 (Oxford Instruments, Abingdon, UK). As pyruvate acts as a glassing moiety, no extra substance is required).
3. Sample insertion: The cup holding the sample is inserted into the polarizer.
4. Microwave frequency calibration: The frequency is gradually increased over a user-defined range to identify the frequency which results in the highest polarization.
5. Sample polarization: Start radiating the microwave into the sample at the calibrated frequency (≈45 min). If desired, monitor polarization level at predefined regular time intervals using low-flip angle excitations.
6. Dissolution: The dissolution agent is heated up and flushed into the sample cup under high pressure, transporting the dissolution to be collected in a container near the MR scanner or NMR spectrometer (5 mL of 80 mM TRIS buffer and 80 mM NaOH).
7. Cleaning and hardware shutdown: Flush tubes several times with water and ethanol/acetone. Set HS to idle.

The sample preparation and microwave frequency calibration can be performed beforehand to save time. Sample solutions such as pyruvate can be prepared in larger quantities and frozen at −20°C for several months. Unless the HS hardware or polarizing agent or radical in the sample preparation is modified, the microwave frequency for a specific sample should remain constant.

Optimization Parameters

- Sample cup size: small (up to 100 μL) and big (up to 600 μL) of concentrated sample.
- Buildup rate, maximum polarization level, and T_1 depend on several parameters including the concentrations of the HP agent, the glassing agent, the radical and the relaxation agent and have to be optimized for each HP agent individually.

SpinLab

The SpinLab (Fig. 13.42) (Ardenkjaer-Larsen et al. 2011c) was developed to achieve high polarization of multiple samples without consumption of liquid cryogens. The system uses a superconducting magnet at 5 T in a cryostat with a sorption (charcoal) pump to maintain a temperature below 0.9 K in the sample space. The sorption pump needs to be regenerated overnight and runs on a 12/12 h cycle. The polarizer has a cryocooler and a compressor to provide the primary cooling.

The sample and dissolution medium is contained in a sealed fluid path (Fig. 13.42). This allows assembly in a clean room without exposure of the sample to the uncontrolled environment of the polarizer lab space. For animal and phantom experiments, the fluid path is prepared in the polarizer lab space. The sample is loaded into the sample vial that contains a maximum of 2 mL. The sample vial is glued with a UV curing glue to the outer tubing. The outer tubing is a thin-walled tube with another tube running inside. The inner tube connects to a syringe through a valve. A maximum of 60 mL of dissolution medium is contained in the syringe that is heated to 130 °C and ejected by a 250 psi (17 bar) pressure when dissolution is commanded. The syringe can be filled with less dissolution medium to dissolve the sample in a minimum of about 5 mL. The dissolution medium is directed to the vial through the inner tube and returns through the lumen between the inner and outer tube.

The sample is introduced into the cryostat through an airlock insertion system that isolates the internal cryogenic environment from the atmosphere. The insertion system controls the position of the sample inside the cryostat via motorized rollers that grip and drive the outer tube of the fluid path through the dynamic seal. The polarizer is designed to simultaneously handle up to four fluid paths by having four air locks and heater modules. After positioning the sample(s) in the cryostat at the polarization position, the sample is irradiated with microwaves

(MW) at ca 140 GHz. The output of the MW source is ca 60 mW, but only a few mW reaches the sample, which is adequate to obtain maximum polarization and polarization buildup rate. All samples are positioned within the same NMR coil in the polarization chamber. The polarization of each sample is therefore determined by lifting one sample at a time out of the NMR coil before measurement and then subtracting measurements to derive individual signals. Once the sample is polarized, a dissolution process is initiated to transfer the sample from the cryo vial to the receiver. Dissolution typically takes 5–10 s depending on solvent volume. The polarizer is controlled by a graphical user interface and touch screen that guides the operator through the steps of loading samples, starting polarization, and dissolving the sample.

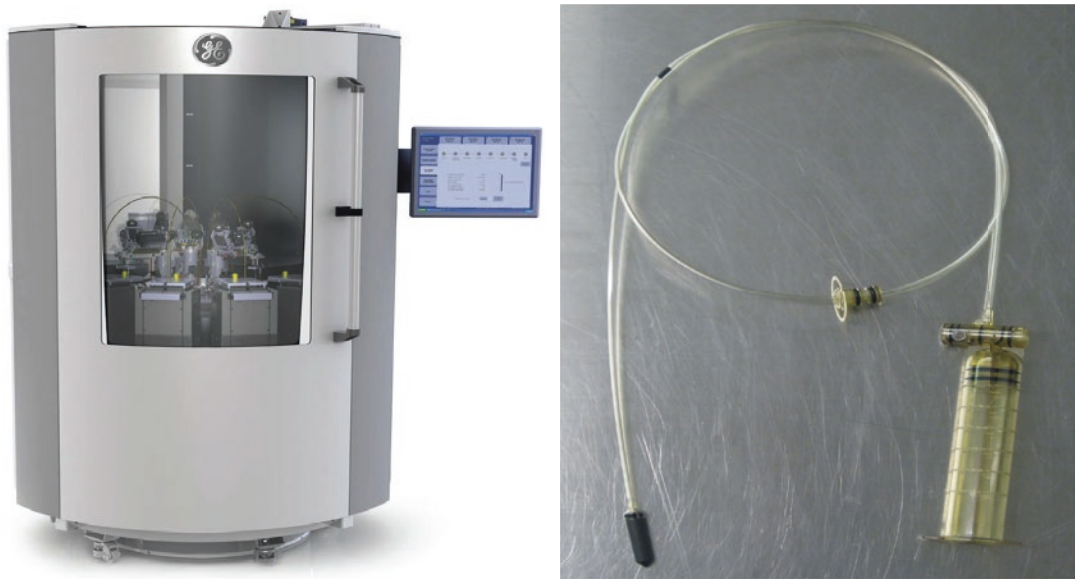

Fig. 13.42 SpinLab polarizer (*left*) and fluid path (*right*). The polarizer consists of a 5 T superconducting magnet and cryostat. The cryostat has a sorption pump that can drive the temperature of a helium bath to <0.9 K. The sample is irradiated with microwaves at 140 GHz. The polarizer has four channels that allow individual loading of the fluid path to the right. The fluid path consists of a sample vial that can accommodate up to 2 mL of sample, glued to the long tubing. A dynamic seal allows the tubing to be pushed into the cryostat. The dissolution syringe contains the solvent for dissolution and is heated to 130 °C. The transfer tube allows the user to collect the hyperpolarized solution in a container of choice

Other DNP Implementations

The operation scheme of the other types of polarizer that have been implemented is similar to the one described above. Details specific to these alternative systems are described below:

- Most alternative designs are based on the use of a room temperature bore superconducting magnet (Comment et al. 2008; Batel et al. 2012; Lumata et al. 2014). This feature simplifies the implementation and the maintenance of the apparatus since the variable temperature insert is replaced by a cryostat that runs independently from the helium bath used to cool the superconducting magnet.
- The system developed by Comment et al. features a microwave insert with circular geometry (Comment et al. 2007b): this simplification

in the microwave design adds an additional step to the dissolution process (step #6 above consists in two substeps, 6a and 6b) since it requires the removal of the waveguide (6a) prior to the insertion of the dissolution insert (6b).

- Similar to the SpinLab design, other systems have been designed with multi-sample capability for rapid consecutive in vivo hyperpolarized MR experiments (Batel et al. 2012; Hu et al. 2013).
- In order to obtain even larger polarization levels, several implementations increase the static magnetic field from 3T (HyperSense) over 5 T (Ardenkjaer-Larsen et al. 2011b; Jannin et al. 2008; Jóhannesson et al. 2009) to 7 T (Cheng et al. 2013a) and/or lower the sample temperature from 1.2–1.4 K to 1 K (Cheng et al. 2013a) or below (Ardenkjaer-Larsen et al. 2011b).

13.3.4 Hyperpolarization Agents

Once the desired polarization level is reached, the hyperpolarized state starts decaying with T_1 toward its thermal equilibrium. To minimize polarization losses, a rapid transfer of the hyperpolarized agent from the polarizer to the target is required. In current DNP-HP animal systems, the time between the start of the dissolution process and the beginning of the in vivo injection can be as short as 2 s, incurring negligible polarization losses. However, in clinical settings the solution requires filtration and safety checks before injection, with considerable signal loss.

Several approaches exist to increase the T_1 of the hyperpolarized nucleus. These include exploiting long-lived states (Pileio and Levitt 2009; Emondts et al. 2014; Feng et al. 2012b; Vasos et al. 2009), the use of nuclei with inherently long T_1 such as lithium (Van Heeswijk et al. 2009) and silicon (Cassidy et al. 2013; Kinrade and Swaddle 1986; Dementyev et al. 2008), or continuous HP (Hövener et al. 2013b, 2014a). To date, the by far most frequently used method is ^{13}C-labeling of a carbonyl position and deuteration of adjacent hydrogen sites (Hövener 2008; Allouche-Arnon et al. 2011; Rodrigues et al. 2014).

The group of ^{13}C-positions with long T_1 in metabolically interesting agents has a chemical shift typically larger than 150 ppm. In contrast, nuclei used for thermally polarized ^{13}C MRS require a shorter relaxation time to allow for signal recovery after excitation for repetitive acquisitions. These groups have a typical chemical shift of 15–100 ppm and contain carbons close to hydroxyl groups, such as glucose (60–100 ppm) as well as CH, CH_2, and CH_3 groups (45–60 ppm, 25–45 ppm, and <25 ppm, respectively).

Today, a multitude of HP agents is available (Keshari and Wilson 2014; Bär et al. 2012). In order to provide a concise overview, we attempt to classify the agents according to their function as metabolic, functional, and inert.

13.3.4.1 Metabolic Agents

Hyperpolarized MR allows the study of real-time metabolism in vivo, by detecting the hyperpolarized label flow along a cascade of enzymatic reactions in a metabolic pathway.

Compared to thermally polarized ^{13}C MRS, the enhanced SNR provided by HP enables a dramatically improved time resolution on the order of 1 s. The most revealing HP agents are among the major fuel sources for tissues and organs, including the carbohydrates pyruvate (Golman et al. 2006b, c; Kohler et al. 2007), lactate (Bastiaansen et al. 2014; Chen et al. 2008b; Mayer et al. 2012b), and glucose (Rodrigues et al. 2014), as well as fatty acids like acetate (Jensen et al. 2009; Bastiaansen et al. 2013), butyrate (Bastiaansen et al. 2015; Ball et al. 2014), and octanoate (Yoshihara et al. 2015). Each agent probes different metabolic pathways (Fig. 13.43) and pool sizes and may exhibit different cellular uptake. Other entry points to the tricarboxylic acid (TCA) cycle include (diethyl) succinate (Chekmenev et al. 2008b; Zacharias et al. 2012b) or fumarate (Gallagher et al. 2009).

13.3.4.2 Inert Agents

Inert agents describe molecules which do not interact specifically with a target structure. Such agents include iodine-rich molecules for x-ray angiography as well as gadolinium complex agents for MRI. One of the first in vivo examples of ^{13}C HP was angiography (Golman et al. 2001a, b). Later, hyperpolarized ^{13}C agents were used for perfusion imaging with urea (Golman et al. 2003b), tert butanol (Grant et al. 2011), and others (Johansson et al. 2004b), as well as hyperpolarized water (Lingwood et al. 2012; McCarney et al. 2007). Hyperpolarized lithium, also inert, was evaluated as a sensor of the presence of contrast agents at nanomolar concentrations (Van Heeswijk et al. 2009).

13.3.4.3 Functional Agents

Functional or targeted agents describe molecules that bind to a specific target, e.g., a pathology. Typically, these agents consist of a functional part for targeting and a hyperpolarized part that provides the signal. Similar concepts have been applied in molecular imaging, e.g., using antibodies and optical detection methods. However, the time required for targeting is typically much longer than the duration of the hyperpolarized signal. Consequently, the application of hyperpolarized functional agents is focused on fast-binding targets (e.g., vascular applications, plaque) (Bhattacharya et al. 2011b) and long-lived HP agents like Si-nanoparticles (Cassidy et al. 2013) or specifically constructed agents (Nonaka et al. 2013). An interesting approach is to separate the binding from HP like in HyperCEST (Schröder et al. 2006).

13.3.4.4 Physiological Agents

Physiological agents have been used to monitor parameters such as pH or redox state. It was demonstrated that ^{13}C HP enables to measure the tissue pH in vivo, derived from the ratio of the formed carbon dioxide $^{13}CO_2$ to the infused hyperpolarized bicarbonate $H^{13}CO_3^-$ (Gallagher et al. 2008c; Scholz et al. 2015). This relationship is governed by the Henderson–Hasselbalch equation (Eq. 13.57),

$$\mathrm{pH} = \mathrm{pK_a} + \log_{10} \frac{\left[\mathrm{HCO_3^-}\right]}{\left[\mathrm{CO_2}\right]} \tag{13.57}$$

where the acid dissociation constant of CO_2, pK_a, was assumed to be 6.15 for in vivo cardiac pH measurements (Schroeder et al. 2009b). By using this relationship one has to assume that both compounds are in similar compartments and in vivo relaxation times have to be taken into account. Other sensitive probes to measure in vivo pH are hyperpolarized ^{89}Y complexes. The ^{89}Y nucleus has an extremely long T_1 and displays chemical shift dependence on pH (Jindal et al. 2010).

Hyperpolarized ^{13}C-dehydroascorbate was used as a sensor for endogenous redox state, using its conversion into [1-^{13}C] ascorbic acid (Keshari et al. 2011b).

13.3.5 The In Vivo Experiment

Prior to the application of the HP in vivo, the polarizer, animal, and MRI systems have to be prepared (Tables 13.3 and 13.4). The formulation of the HP agent should not affect the physiology of the animal, especially when metabolic processes are investigated:

- The pH should be in the physiological range, e.g., from 6.5 to 8.2, by use of a buffer solution.
- The temperature should be between room temperature and 37 °C.
- The solution should be close to isotonic, which can be achieved by the addition of salts for dilute samples or dilution of the agent until the maximum tolerated injection volume is reached.

In many preclinical studies in rodents with pyruvate, the concentration of pyruvate is 80 mM, and sodium chloride is added to isotonicity. A much higher concentration can be generated for large sample volumes. In clinical or large animal studies, the formulation is diluted to be slightly hypertonic.

Table 13.4 Workflow example of an in vivo HP experiment

Polarizer Preparation	• method specific, see Tables 13.1 and 13.2
Animal Preparation When: 1 h b.i. Duration: 30 min	• anesthesia • catheter surgery
MRI Preparation When: 30 min b.i. Duration: 30 min	• animal placement • scanner adjustments • anatomy reference scans
HP Experiment	• retrieve and transfer hyperpolarized sample • inject sample (order may vary) • start imaging (order may vary)

b.i. **before injection**

13.3.5.1 Animal Handling

Animal models used for HP MR experiments are typically mice and rats, less frequent pigs or larger animals. In vivo animal handling must conform to governmental and institutional guidelines and typically involves similar animal preparations as in, for example, conventional ^{13}C MRS experiments in vivo, where ^{13}C-labeled agents are infused for prolonged times. To ensure the well-being of the animal and to obtain representative and reliable data, maintaining a healthy physiology is necessary. On the animal preparation side, this includes the capability to monitor and follow-up on several physiological parameters throughout the experiments, plus the ability to inject agents and take blood samples, and, if desired, the means to extract tissue samples (for ex vivo tissue analysis of endogenous metabolite pool sizes and labeling patterns).

Physiological parameters to be monitored are the respiration rate, heart rate, and the temperature. Monitoring the heart rate is accomplished using ECG pads or the insertion of a blood pressure sensor via a catheter placed in one of the arteries. Respiration rates are typically measured using airpads and pressure sensors, while the temperature is measured by a rectal sensor.

Blood samples can be taken via an arterial catheter, and the same line can be used to measure the blood pressure to monitor the heart rate. Blood samples are needed to measure the plasma levels of lactate and glucose, which are helpful physiological indicators, and samples can be transferred to blood gas analyzers to measure the pH and oxygenation levels. Plasma samples can also be stored to quantify the final ^{13}C enrichments of the metabolites.

13.3.5.2 Preparation of MRI System

In addition to a standard human or small-bore MRI system, appropriate channels for ^{13}C or ^{2}H decoupling as well as dedicated RF coils are needed for HP experiments. The preparation of the MRI system for these experiments includes the standard adjustments for routine ^{1}H imaging as well as the adjustment of the ^{13}C (or other) channel, like shimming and calibration of transmitter and receiver gains. A narrow spectral line width, which depends on the homogeneity of the magnetic field, is essential for spectroscopic experiments. A small line width improves the SNR and detection limit but also the separation of multiple metabolite resonances. The ^{13}C resonances of most metabolically relevant compounds are clustered in the spectral region between 170 and 180 ppm. To ensure a narrow line width,

several shimming methods are available, including manual shimming according to the line shape, automated, and iterative variation of the shim currents, and more complex methods such as FASTESTMAP (Gruetter and Tkáč 2000). It is crucial to verify the field homogeneity prior to each HP experiment by acquiring a ^{1}H spectrum of the region of interest before starting the experiment.

The ^{13}C and ^{1}H channels can be adjusted by permanently placing a spherical glass bubble filled with a ^{13}C-labeled reference solution, such as uniformly labeled ^{13}C-formic acid or glucose, on the RF coil. Note that the resonances of the reference should not overlap with the hyperpolarized resonances.

Dual ^{1}H and ^{13}C probes enable the acquisition of standard ^{1}H MR images for anatomical reference and correct animal positioning, as well as ^{1}H decoupling during ^{13}C acquisition (Adriany and Gruetter 1997; Evelhoch et al. 1984). Surface coils placed adjacent to the region of interest help to improve the sensitivity. Experiments involving deuterated agents may require an additional coil for ^{2}H decoupling, although the ^{13}C-^{2}H splittings are reduced by the ratio of the gyromagnetic ratios of ^{2}H/^{1}H. Adiabatic RF pulses help to improve the inhomogeneous excitation profile of surface coils.

13.3.5.3 Hyperpolarized Agent Administration

Typically, the hyperpolarized sample is either transferred manually from the polarizer to the infusion line or automatically through tubing (Cheng et al. 2013b). An infusion pump located next to the animal inside the imaging magnet may be used to inject the solution. This pump can also be designed to act as a phase separator to remove the gases and enables a clean agent injection within 2 s of dissolution (for dissolution DNP) (Cheng et al. 2013a).

It was observed that strong polarization losses occur during the transfer of succinate depending on pH (Hövener 2008), as well as in glutamine and urea (Chiavazza et al. 2013). This effect is alleviated by exposing the sample to a low magnetic field during the transfer or by buffering the solution at high field (Shchepin et al. 2014c; Coffey et al. 2014) and shortening the transfer time.

Once the sample has undergone quality checks or adjustments when necessary, it can be infused into the animal via a catheter, typically inserted in the jugular, femoral, or tail vein. The tail vein is commonly used for longitudinal studies, for example, in studies of disease progression, where the subject needs to recover after the HP experiment. However, the maximum infusion rate in the tail vein is less than that in the jugular or femoral vein.

A Good Practice Guide to the administration of substances was published by Diehl et al. (2001) (Table 13.5). Injection rates should be evaluated on the basis of cardiac output and injection volume compared to total blood volume. For a reference on physiological values for different species, see (Davies and Morris 1993). The combination of the volume and rate should be inversely correlated so that larger volumes are given at lower injection rates. When administering multiple doses to an animal, consider the total dose volume administered and refer to values given for repeated intravenous infusion in the paper by Diehl et al. (2001).

Table 13.5 Maximum volumes and rates for injection of a bolus in animal models

Mouse rapid bolus i.v.		Rat rapid bolus i.v.		Dog rapid bolus i.v.	
Max vol. (mL/kg)	Max rate (mL/s)	Max vol. (mL/kg)	Max rate (mL/s)	Max vol. (mL/kg)	Max. rate
5	0.05	5	0.05	2.5	Dose given over 1 min

Adapted from Diehl et al. (2001)

The physiological effect of a rapid bolus on the heart and lung is buffered when it is administered in a peripheral vein or artery. Thereby the bolus is mixed with and diluted in blood, and the peak concentration reaching these key organs is reduced. For central venous administrations, it is recommended to confirm the tolerance of the procedure by control administrations of saline/osmotic solutions before administering the hyperpolarized formulation. Conducting pilot studies is recommended when applying a new technique. Consider experiments with saline volume controls when changing anesthetic regime, species, injection site, or rate. Also consider including osmotic/pH control in animals when changing the formulation.

If injection rates and/or volumes in excess of the recommended are desired, refer to institutional guidelines and discuss with the veterinarian. This is sometimes the situation for HP agents due to the fast signal decay. The following tables can be considered as maximum doses and injection rates in well-monitored healthy animals under stable anesthesia for pyruvate (Table 13.6). For other circumstances, e.g., in animals with compromised health (e.g., stroke and infarction models), it is strongly recommended to refer to the Good Practice Guide and use careful dose escalation if higher doses and/or injection rates are required to ensure adequate imaging data.

Table 13.6 Recommended maximum injection doses and rates for dogs, rats, and mice based on literature of well-established protocols

Dog:					
Pyruvate conc.	Osmolarity (mOsm/kg)	pH	Dose vol. (mL/kg)	Injection rate (mL/s)	Injection site
500 mM	~1000	6–8	2.9	5	Cephalic vein
500 mM	~1000	6–8	2.9	5	Jugular vein
500 mM	~1000	6–8	2.0	5	Left atrium
250 mM	~500	6.5–8	5.7	5	Cephalic vein
150 mM	~300	7–7.4	7.0	7	Cephalic vein
Rat:					
Pyruvate conc.	Osmolarity (mOsm/kg)	pH	Dose vol. (mL/kg)	Injection rate (mL/s)	Injection site
80 mM	~250	8.1 ± 0.1	10	0.17	Tail vein
Mouse:					
Pyruvate conc.	Osmolarity (mOsm/kg)	pH	Dose vol. (mL/kg)	Injection rate (mL/s)	Injection site
80 mM	~250		~0.3 mL/animal	0.025	Jugular vein

13.3.6 Data Acquisition

The information gained from metabolic studies using a hyperpolarized agent is reflected in its spatial localization, its resonance frequency, and its time course. The metabolism changes the structure of the hyperpolarized agent and thus its resonance frequency or chemical shift (CS), typically by a few ppm. Dedicated detection schemes follow the fate of these nuclei along their metabolic pathway.

The hyperpolarized MR signal exhibits some peculiarities, which are absent in thermal MR measurements. Despite an initially strong HP, the overall signal of the injected agent and its metabolic products in vivo is weak because of dilution and small metabolite pool sizes. Furthermore, the signal intensity changes over time because of T_1 relaxation.

These properties require fast, CS-resolved detection schemes, which make efficient use of the limited hyperpolarized signal. Typically, a trade-off between either temporal, molecular (CS), or spatial (imaging) resolution has to be made, depending on the signal available and the goal of the study. Given sufficient signal,

the data can be displayed as metabolic maps (spectroscopic imaging, MRSI).

Some of these effects are mitigated by using echoes or spectrally selective pulses which excite the injected agent less than the metabolic products (Scholz et al. 2015; Larson et al. 2008b; Koellisch et al. 2015). The highest spectroscopic sensitivity is typically obtained by unlocalized or slice-selective (adiabatic) excitations with an RF coil adjacent to the region of interest. Provided that sufficient signal is available, spatial encoding allows to obtain images of metabolic or enzyme activity, e.g., FID CSI (Golman et al. 2006b), EPSI (Cunningham et al. 2007; Chen et al. 2007b), spiral CSI (Mayer et al. 2006), IDEAL spiral CSI (Wiesinger et al. 2012), spin echo (Cunningham et al. 2007; Josan et al. 2011), and multi-echo SSFP (Leupold et al. 2009). This approach was used, e.g., to identify tumor regions of increased pyruvate to lactate turnover in rats (Golman et al. 2006c) and men (Nelson et al. 2013a).

Whereas MR sequences for HP are a lively field of research (Durst et al. 2015; Nelson et al. 2013c), thus far, only relatively simple spectroscopy sequences like CSI (Fig. 13.43) are available as a product.

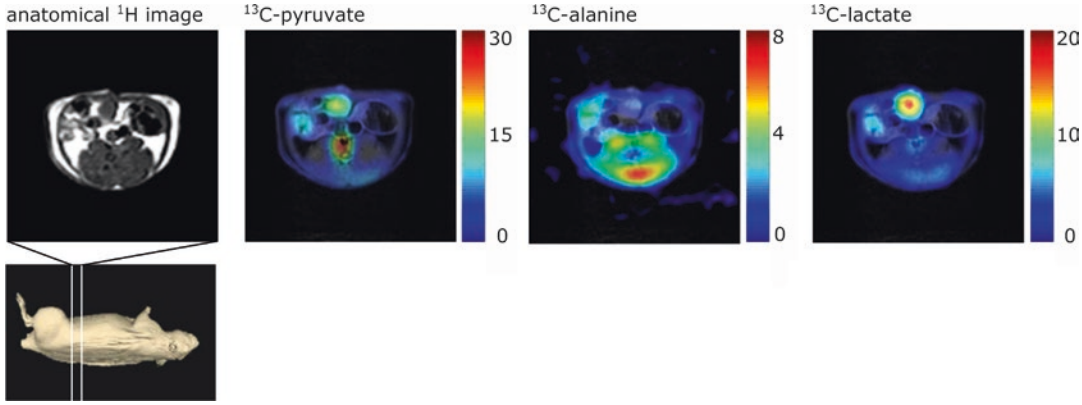

Fig. 13.43 Example of metabolic imaging with hyperpolarized ^{13}C-pyruvate of a tumor-bearing rat. The location of the image slab in the rat and the corresponding transversal ^{1}H-MRI is illustrated. The ^{13}C-NMR signal distribution obtained simultaneously from pyruvate, lactate, and alanine was calculated, and the color images representing the intensity of each metabolite are projected on the anatomical ^{1}H image. Alanine is most prominent in the skeletal muscle around the spinal cord, while the P22 tumor tissue is indicated by the highest signal for lactate. Note the different scales (Figure reproduced with permission from Cancer Research (Golman et al. 2006c))

13.3.7 Data Analysis and Interpretation

Spectra obtained during HP experiments are analyzed by determining the area of each resonance. The most commonly used software is the Bayesian analysis (Bretthorst 1990) and jMRUI (Naressi et al. 2001). Commonly used methods to analyze data are to determine relative metabolite ratios and to apply metabolic models to obtain kinetic information about the reaction pathways measured (Fig. 13.44).

For the estimation of kinetic rate constants, mathematical modeling is typically performed (Bastiaansen et al. 2013; Harrison et al. 2012; Zierhut et al. 2010; Day et al. 2007b; Witney et al. 2011). It is not always required, since it was shown that the ratio of observed metabolites scales linearly with the kinetic rate constants estimated using mathematical modeling approaches (Bastiaansen et al. 2013). In specific cases, it is possible to derive a mathematical framework which calculates the kinetic rate constants directly based on the ratio of observed metabolites, and their longitudinal relaxation time, obliterating the need for using complex mathematical modeling (Khegai et al. 2014).

Changes in pool size can influence observations of the kinetic rate constants (Bastiaansen et al. 2014; Day et al. 2007b; Merritt et al. 2007c). Therefore correct data interpretation regarding metabolic flux changes and information about the endogenous concentration of metabolites is necessary. Pool size changes can be affected by a change in diet, or disease, and have been observed in several studies using hyperpolarized agents. Tissue metabolite extractions for the interpretation of metabolic fluxes are typically being employed in conventional ^{13}C NMR and similarly can be used with HP techniques to retrieve pool size information.

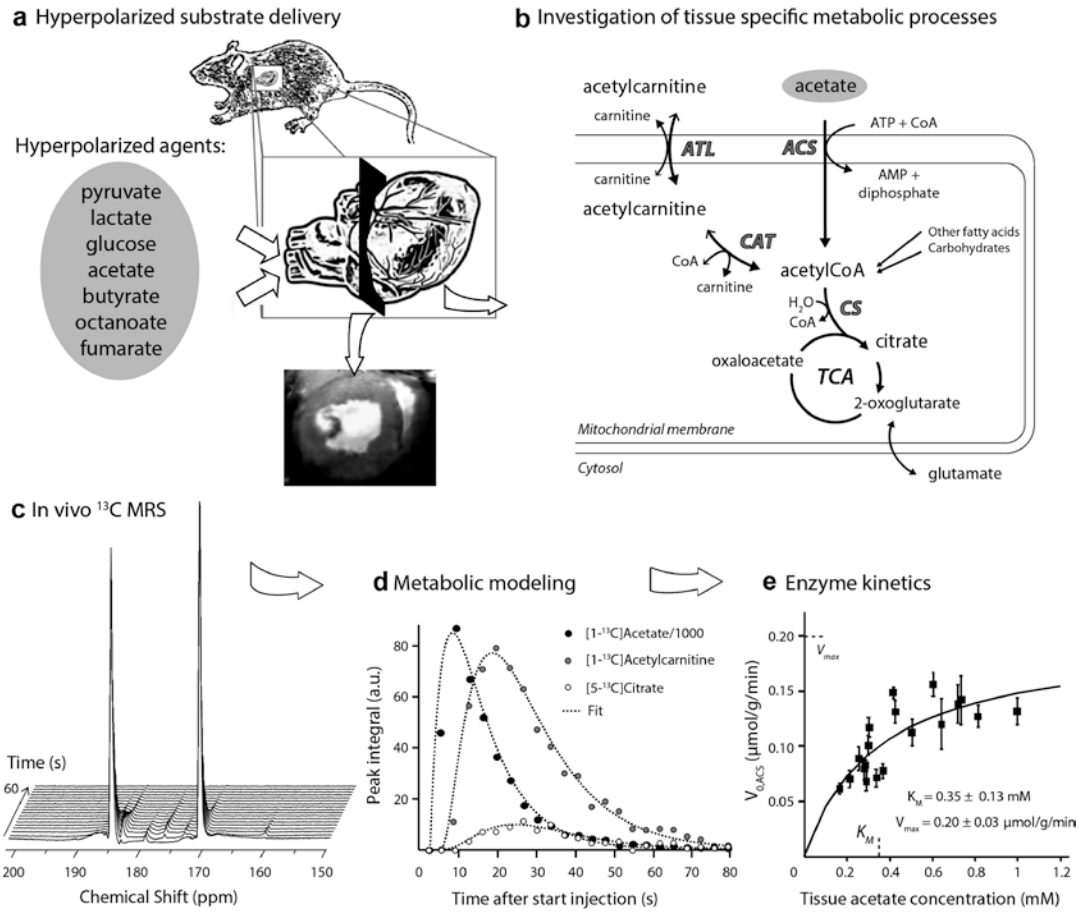

Fig. 13.44 Example of real-time measurement of enzymatic fluxes. Hyperpolarized agents are injected to target metabolism in specific tissue (**a**). In this example the intracellular metabolism of acetate was followed in vivo (**b**). Spectral data acquisition of hyperpolarized acetate metabolism reveals the formation of acetylcarnitine in real time (**c**). Data is analyzed by quantifying the spectral areas and using metabolic modeling (**d**). This results in the estimation of kinetic rate constants. Together with the information regarding acetate uptake and accumulation in the tissue, Michaelis–Menten parameters V_{max} and K_m could be determined (**e**) (Adapted from (Bastiaansen et al. 2013, 2015))

13.4 MR Spectroscopy

Markus Becker

13.4.1 Introduction

Spectroscopy can be a very useful tool in a variety of purposes; unfortunately, we are still waiting for the final breakthrough in clinical applications. Therefore, nuclear magnetic resonance spectroscopy (NMRS) is mainly used in preclinical research facilities. This chapter tries to explain where spectroscopy is a helpful and strong tool and to give guidance for successful work.

13.4.1.1 The New Contrast

To get the best result out of a spectrum, NMRS should be considered as an additional contrast besides standard MR imaging examinations like T_1, T_2, and proton density (PD) measurements. For a successful recording and analysis of a spectrum, the imaging information is needed not only just for the placement of the voxel but also to get the best spectroscopy result, after collecting and analyzing all anatomic information. For diagnostic purposes or for monitoring of treatments, the only need is to define the area of interest, for example, necrotic regions of a tumor.

13.4.2 Applications

For a beginner in the field of NMRS, it is difficult to choose the right examination protocol for a specific application or research project, because there are various methods and sequences available which have different pros and cons depending mainly on the tissue type. In general, the sequences can be separated in localized, nonlocalized, and imaging comparable techniques (spectroscopic imaging).

Localized:

- Point resolved spectroscopy (PRESS)
- Stimulated echo acquisition mode (STEAM)
- Image-selected in vivo spectroscopy (ISIS)

Nonlocalized:

- Free induction decay (FID)

Spectroscopic imaging (SI):

- Chemical shift imaging (CSI-FID)
- Hybrid chemical shift imaging (CSI-PRESS, CSI-STEAM)
- Echo planar spectroscopic imaging (EPSI)

Table 13.7 can be used as a starting point to assume quality and difficulty to achieve useful results.

Table 13.7 Selection of measurement methods; quality and difficulty

Tissue/body part	^{1}H single voxel quality/difficulty	^{1}HS I quality/difficulty	XN MR quality/difficulty
Brain	PRESS good/easy	PRESS CSI good/easy	^{31}Pgood/easy
	STEAM good/easy	STEAMC SIf air/easy	^{13}Cf air/difficult
		EPSI good/difficult	^{23}Naf air/difficult
Muscle	PRESS good/easy	PRESSC SIf air/easy	^{31}Pgood/easy
	STEAM good/easy	STEAMC SIf air/easy	^{13}Cf air/difficult
Liver	PRESS good/easy		^{31}P good/fair
	STEAM good/easy		
Tumor, subcutaneous	PRESS good/difficult		^{31}Pgood/easy
	STEAM good/fair		^{13}Cgood/easy

13.4.2.1 What to Expect from Spectroscopy?

The examiner has to choose what kind of substance he wants to monitor. Is it a native signal or an exogenously applied chemical, like a drug or marker? What is the expected concentration and what is the chemical shift? For the different body parts, the following section will discuss few examples on how to set up an examination protocol.

13.4.2.2 Brain and Liver

The main examination pathway for brain and liver models is shown in Fig. 13.45. This diagram leads to the preferred examination method.

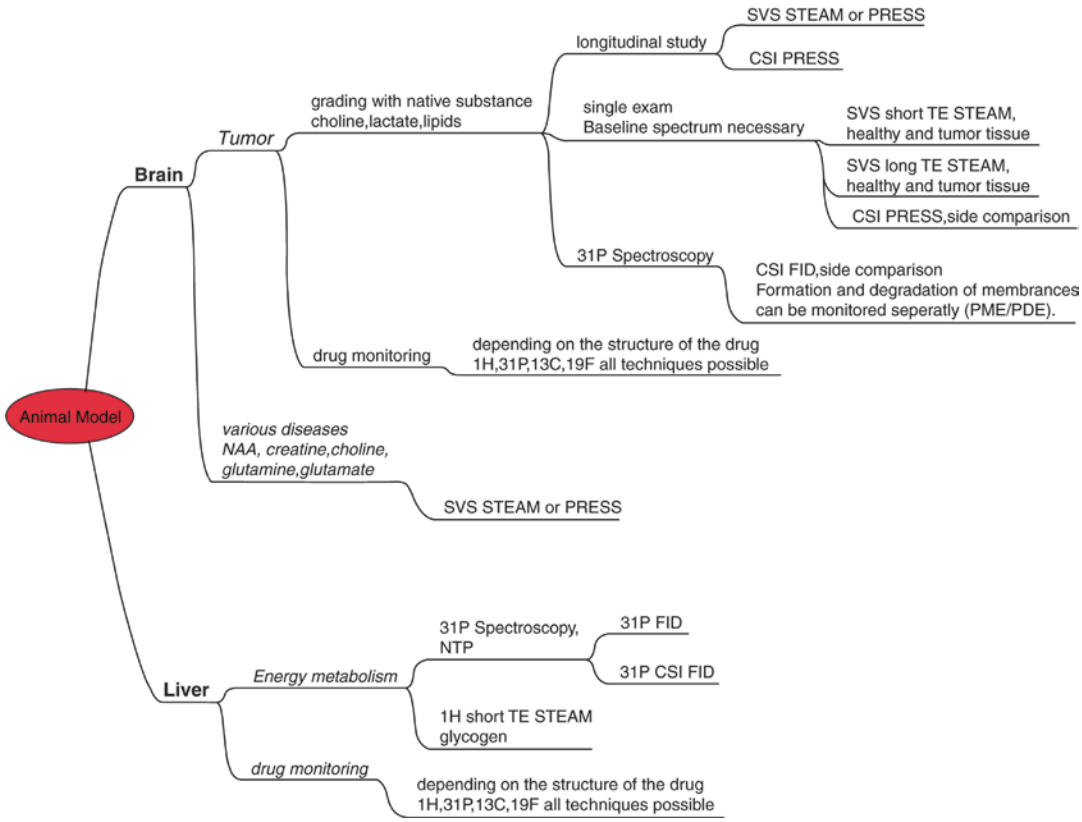

Fig. 13.45 Pathway from animal model to preferred examination method for the brain and liver

Brain

Examination of the brain is the easiest task for spectroscopy. Since the overall magnetic field homogeneity is good, automatic shimming routines are available enabling proper shimming (Fig. 13.46).

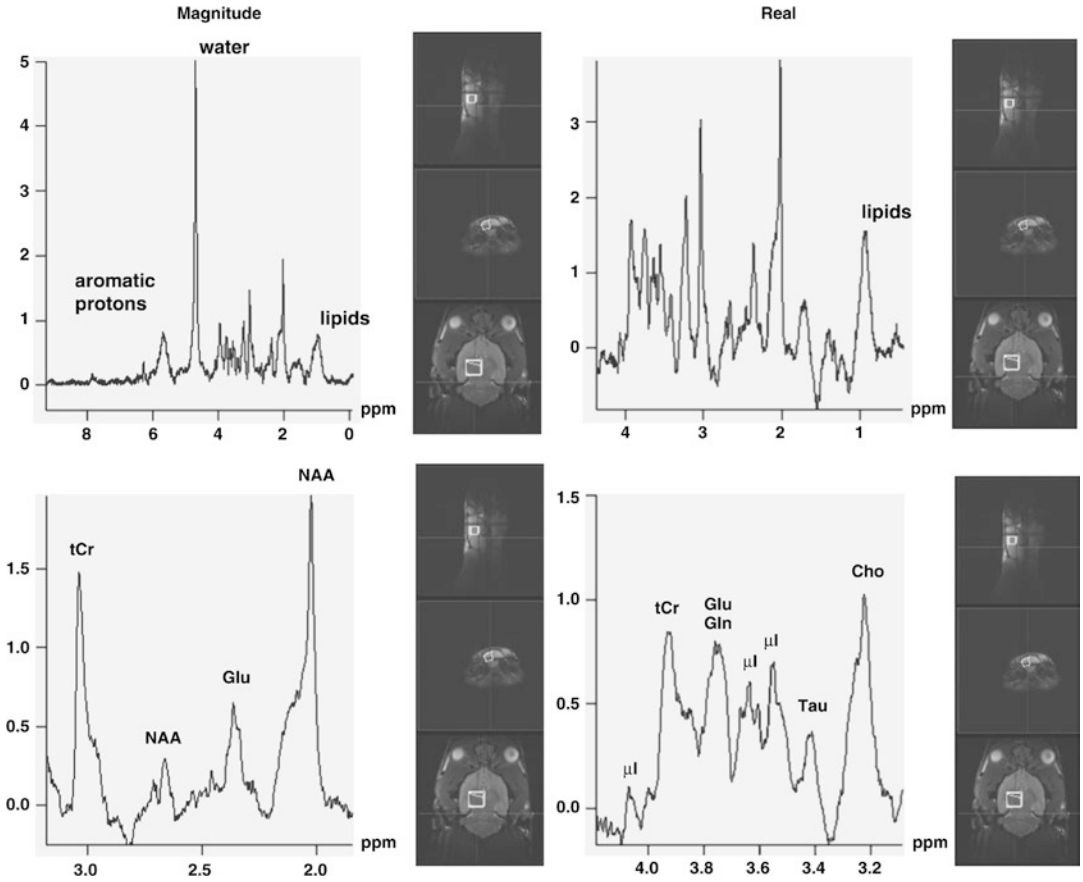

Fig. 13.46 Rat brain spectrum (PRESS) from a healthy tissue. *Up left*: full spectrum. Other quadrants: spectrum magnified. Following signals can be identified: creatine and phosphocreatine (tCr), *N*-acetylaspartate (NAA), glutamine (Glu), glucose (Glc), myo-inositol (μI), choline (Cho), taurine (Tau)

In a brain tumor model NMRS allows to monitor the membrane metabolism of the tumor cells by detection of the choline signal. The concentration of the choline is approximately 2 mM and the chemical shift is 3.24 ppm. Absolute quantification of the choline is possible, but complicated (Dong et al. 2006). For tumor staging and longitudinal studies, it is in most cases sufficient to quantify choline by calculating the quotient I(choline)/I(creatine). The creatine concentration is almost independent of the activity of the tumor cells with one exception: high tumor grades develop a necrosis where the dead cells accumulate lipids. These necrotic areas should be identified by imaging methods prior to the spectroscopic experiments. The other possibility to identify the different active areas of the tumor is chemical shift imaging (CSI) with a metabolic map. However, CSI is very time-consuming and the spatial resolution is poor. As an example, a CSI from a mouse brain is shown in Fig. 13.47.

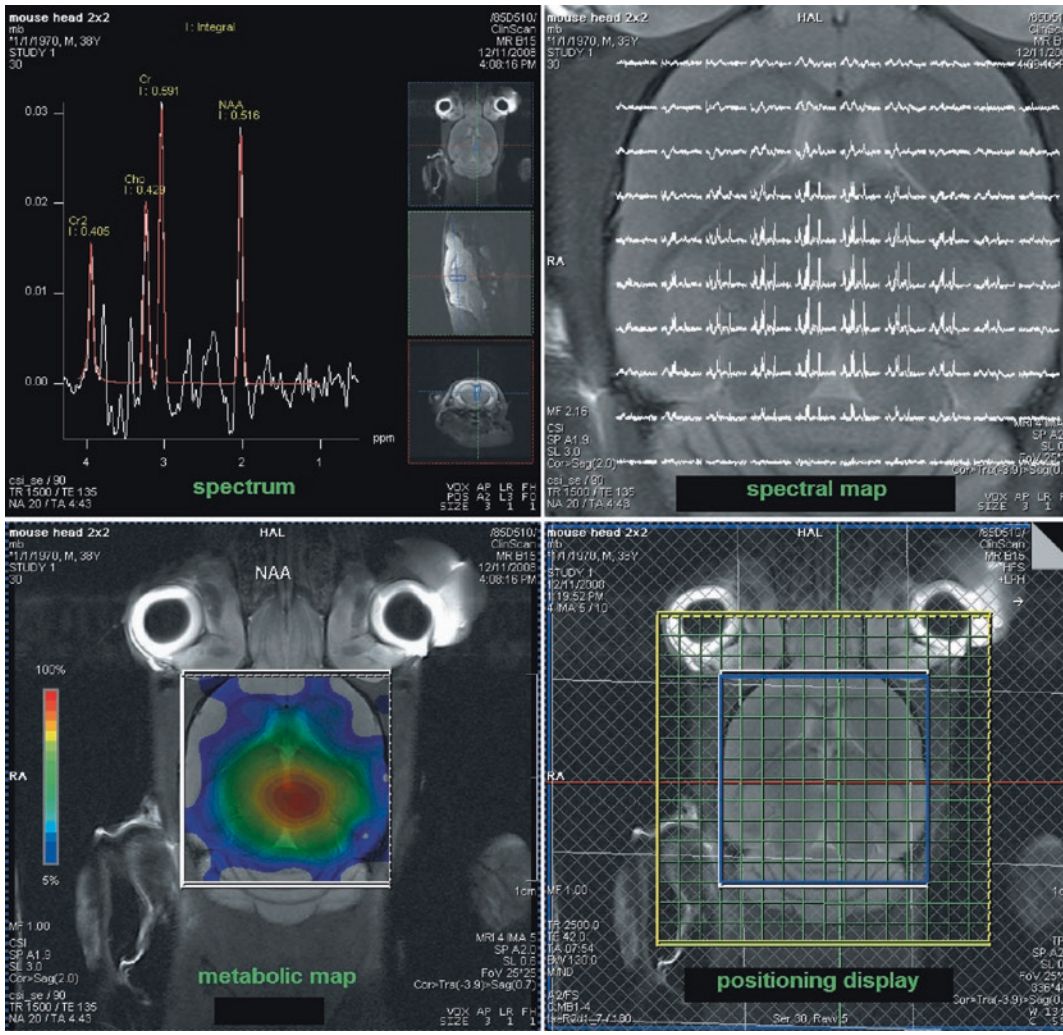

Fig. 13.47 Mouse brain CSI-PRESS from a healthy animal with metabolic (*lower left*) and spectral map (*upper right*). The metabolic map is calculated from the fitted NAA signal (*upper left*). The map has a centric symmetry, because of the combination of the imperfect pulse shape and interpolation (zero filling)

Liver

Liver spectroscopy has not been performed frequently due to problems in reproducibility and quality of the spectra. A major problem is respiration and, in some areas, heart motion. Additionally, the high quantity of iron in the liver makes shimming difficult and the resulting signals are broad. Respiratory gating combined with cardiac triggering is necessary to avoid motion artifacts.

The aim of a liver spectroscopy is to study metabolism such as glycogen storage diseases and drug metabolism (Bollard et al. 2000). ^{31}P, ^{13}C, ^{1}H, and ^{19}F are therefore the most interesting nuclei where ^{31}P is used to study the energy metabolism, ^{13}C and ^{19}F are assessed for monitoring drug metabolism, and ^{1}H for the development of metastasis (Fig. 13.48).

13.4.2.3 Muscle and Subcutaneous Tumor

The main examination pathway for muscle and subcutaneous tumors is shown in Fig. 13.49, leading to the preferred examination method.

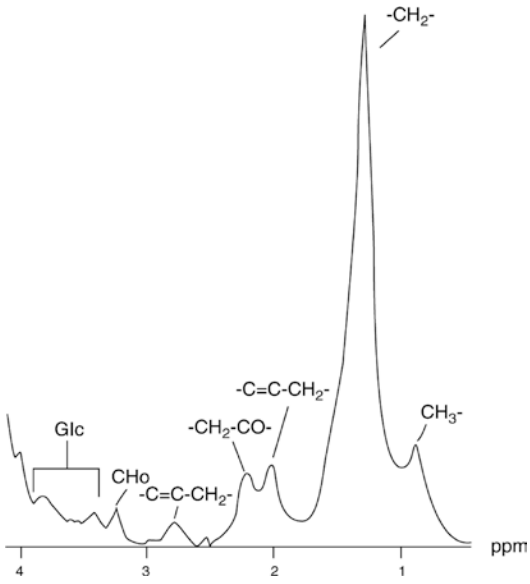

Fig. 13.48 ^{1}H spectrum of a mouse liver (STEAM). Mainly signals of triglycerides are visible. The multiplet of glucose (*Glc*) cannot be resolved

Muscle

Muscle spectroscopy is important for studies focusing on mitochondrial diseases, enzymatic deficiencies, and energy metabolism. ^{31}P spectroscopy is the most useful nucleus for muscle examinations, because it allows to measure α, β, γ−NTP (nucleoside-5′-triphosphate[1]), phosphocreatine creatine, and free phosphate. The chemical shift of the phosphate provides the pH of the muscle, calculated with the following formula (Barker et al. 1999; Petroff et al. 1985):

$$\mathrm{pH} = \mathrm{pK} + \log\frac{\delta_{H_2PO_4^-} - \delta_p}{\delta_p - \delta_{HPO_4^{2-}}} = 6.803 + \log\frac{5.73 - \delta_p}{\delta_p - 3.22}.$$

Additionally, it is possible to calculate the manganese (Mg^{2+}) concentration by the shift from the NTP signals (Barker et al. 1999; Bottomley and Hardy 1989).

[1]It is not possible to separate the signals of adenosine from all other nucleobases; therefore NTP is the general term.

With ^{1}H spectroscopy, triglycerides can be identified and separated in the triglycerides in intra- and extramyocellular lipids (IMCL, EMCL) (Neumann-Haefelin et al. 2003). It has been suggested that IMCL plays an important role in the development of type 2 diabetes, while EMCL level is relatively constant (Pan et al. 1997; Renema et al. 2003) (Fig. 13.50).

Subcutaneous Tumor

With an implanted tumor model, NMRS allows to study tumor growth and treatment effects. Subcutaneous tumors are easy to access and are therefore ideal for X-nuclei spectroscopy. The membrane and energy metabolism can be monitored with 31P NMRS, 13C-labeled drugs, and even with spectroscopy, it is possible to examine treatment response (Fig. 13.51).

With ^{31}P spectroscopy, it is possible to monitor the energy and membrane metabolism of the tumor simultaneously. A highly active tumor produces PE and PC to build up membranes. During successful treatment, the amount of metabolites of the membrane degradation increases (GPC, GPE) (Podo 1999). For quantification of the signals of a subcutaneous implanted tumor, an external reference can be attached easily. Nevertheless, absolute quantification is difficult (Street et al. 1997).

13.4.3 MR Sequences and Spectrum Processing

The number of different sequences or methods is very large. The usage of the expressions "method" and "sequence" is vendor specific, but did not diverge in substance. A sequence is the chronology of radio-frequency (rf) pulses, gradients, and delays and receives events during the measurement. The most important sequences are PRESS, STEAM, FID, CSI, EPSI, and ISIS. A complete

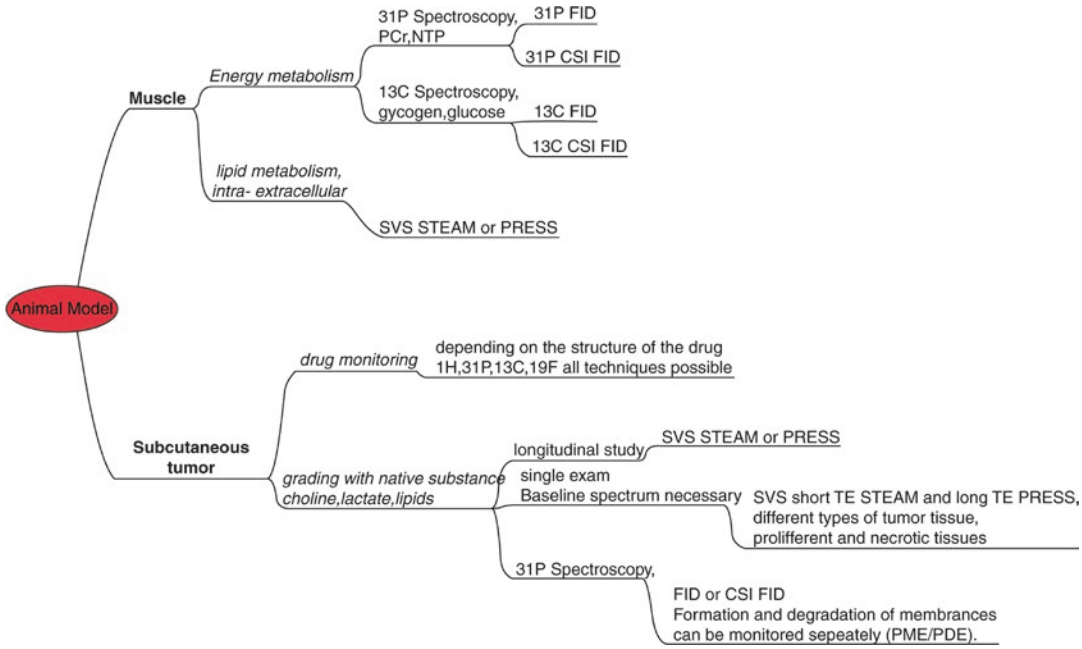

Fig. 13.49 Pathway leading to a preferred examination method for nuclear magnetic resonance spectroscopy of muscles and subcutaneous tumors

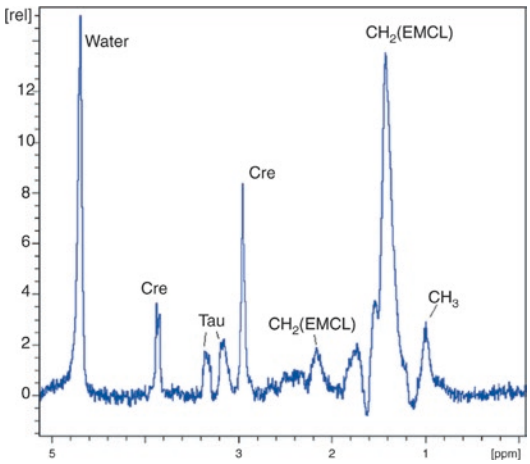

Fig. 13.50 ^{1}H spectrum of a rat thigh (PRESS). In this case only signals of the extramyocellular lipids are detected (EMCL). In ^{1}H spectra, it is possible to separate creatine from phosphocreatine (3.85 and 3.9 ppm)

list can be found at de Graaf (1998), *In Vivo* NMR Spectroscopy.

13.4.3.1 PRESS

This single voxel sequence is based on three spatially localized pulses, one 90° excitation and two 180° refocusing pulses. PRESS is the technique with the highest S/N, but has some limitations. The minimum echo time is bigger than with STEAM; therefore the number of detectable metabolites is limited. The 180° pulse has a great demand on the power amplifier to minimize the chemical shift artifact which increases linearly with field strength. In general, when going to higher field strength, more amplifier power is needed. To optimize the shape of the voxel, it is necessary to use saturation regions, called outer volume suppression. This technique is available from all vendors, the measurement is easy, and the results are good in at least 70 % of the examinations.

13.4.3.2 STEAM

Three 90° spatially localized pulses are used to generate a stimulated echo. The advantages to PRESS are a smaller minimum echo time, less chemical shift artifacts, and unnecessary outer volume suppression. The main drawback is the reduced S/N which is only 50 % of the PRESS sequence. For a very precise definition of a voxel, the STEAM sequence is more appropriate;

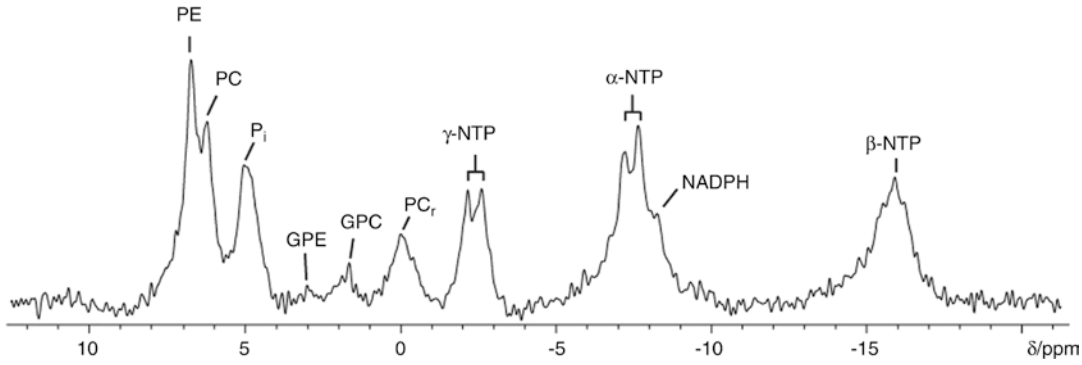

Fig. 13.51 ^{31}P NMR spectrum of a subcutaneous implanted human breast cancer (^{1}H decoupled, FID). Signals are *O*-phosphoryl ethanolamine (*PE*), *O*-phosphoryl choline (*PC*), phosphate (P_i), 1-glyceryl phosphoryl ethanolamine (*GPE*), 1-glyceryl phosphoryl choline (*GPC*), phosphocreatine (*PCr*), nucleosid-5 -triphosphate (α-,β-,γ-NTP), nicotinamide adenine dinucleotide phosphate (NADPH)

however, for a high S/N, the PRESS method is superior.

13.4.3.3 ISIS

A combination of eight experiments with three 180° slice-selective pulses and one 90° pulse is leading to one localized spectra. This sequence is one of the oldest techniques to get localized spectra (Ordidge et al. 1986). For proton spectroscopy, ISIS is replaced by PRESS and STEAM, but for X-nuclei it is still useful and the first choice for localization. The 180° pulse has a great demand on the power amplifier, and the pulse is therefore very long, resulting in a small excitation bandwidth. Only a small part of the X-nucleus chemical shift scale can be measured localized.

13.4.3.4 CSI

CSI is a combination of spectroscopy and imaging to achieve localized spectra in a whole slice. CSI can be used in two or three dimensions. It is possible to calculate images from various signals to get metabolic information of the examined tissue. In proton CSI the sequence is a combination of a large voxel, prepared with PRESS or STEAM with phase-encoding gradients to divide this large volume into smaller voxels. In each voxel a full spectrum is measured. An advantage of this technique is that one gets a large number of localized spectra obtained (in a short time). This is very helpful for comparisons between healthy and diseased regions within one subject. The disadvantage is that the voxels are not well defined, due to the point spread function. The point spread function describes how a strong signal in one voxel is also visible in the neighbored voxels (de Graaf 1998).

13.4.3.5 EPSI

EPSI is derived from an EPI sequence where the *k*-space is filled with an EPI readout. The advantage of EPSI is the high S/N and the option to measure a small voxel size. The main drawback is the processing of the spectra. The vendors do not support the processing of the native EPSI data, so in most cases the user needs some special home-built software to view and analyze the spectra.

13.4.3.6 FID

The FID or pulse-acquire sequence is mainly used for X-nucleus spectroscopy. For ^{1}H spectroscopy, it is only used when the water concentration is low, because of the insufficient water suppression in most of the applications. FID is the technique with the highest S/N, but with no localization. The localization of the signal can be done with the choice of the coil. A surface coil has a limited sensitive volume, which can be used to acquire spectra of a specific organ, e.g., liver, muscle, and subcutaneous tumor.

13.4.4 Processing

The type of processing of the spectrum is not as important as one may think. However, the most important thing is that processing is always done in the same way, so that you can rely on it and compare data from different subjects of imaging sessions. The processing steps affect the signal intensities and the resulting area calculation.

The processing steps can be divided in two parts, the time and frequency domain.

13.4.4.1 Time Domain Processing

(a) Deleting/adding of time domain points
Sometimes the first complex data points of the X-nucleus FID are corrupted from insufficient hardware, resulting in broad background signals and phase distortions.

Unfortunately, the first time domain point is responsible for the intensity of the whole spectrum, so by deleting points, the S/N is going down. To minimize this effect, linear prediction can be used to restore the missing points.

(b) Zero filling and linear prediction
Zero filling is just adding points with the intensity zero to the FID. After the Fourier transformation (FFT), the spectrum is higher resolved, similar to an interpolation in images. Because zero filling is not the real measured FID, the number of added zero points is limited. In practice, measured points can be doubled or quadrupled the number of measured points, e.g., 1024 recorded complex data points can be filled up to 4096 points without affecting the spectrum too much.

However, a better way than zero filling is linear prediction. With linear prediction, points can be added to the FID, simulating measured data.

(c) Filter functions
After zero filling an intensity jump is often observed between the measured FID and the added points. In the spectrum this appears as ringing artifacts at the foot of the signals, comparable to Gibbs ringing in imaging. To smooth these artifacts, the FID is multiplied with a filter function. The basic filter function is the exponential function; Gaussian and Hanning filters influence the resulting resolution and S/N more precisely.

(d) Eddy current compensation
Localized spectra are often affected by eddy currents, because of the necessary gradients, especially at small voxel sizes. The water signal can be used to correct these distortions.

(e) Frequency correction
The B_0 field of the magnet is changing during time, resulting in a mild shift of the signals during the recording of the spectrum with more than one acquisition. The resulting spectrum has therefore broader signals than necessary. By correction of this magnet shift, the summarized spectrum has signals with a smaller half width. Again, different schemes to compensate this effect are implemented from the vendors (Fig. 13.52).

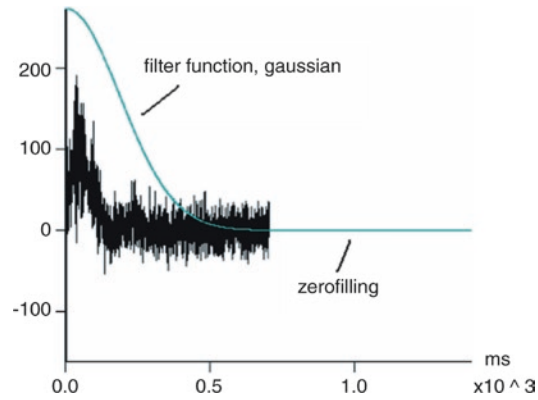

Fig. 13.52 Time domain processing. Free induction decay with filter function (*blue*) and zero filling

13.4.4.2 Frequency Domain Processing

(a) Phase correction
After FFT one gains a complex spectrum with signals having a 90° phase shift between the real and imaginary part of the spectrum. By multiplying the spectrum with a constant complex phase factor, the phase of the signal is changed to display the peak in absorption mode. The absorption mode means that all signals are on one side of the baseline. If there is more than one signal, there is often a phase

difference between the signals which can be corrected by multiplying the spectrum with a linear complex phase factor. If it is not feasible to get all signals to the absorption mode, a quadratic phase correction can be applied.

(b) Baseline correction
The baseline of the spectrum is in most cases not straight because of large signals in the neighborhood of the target signal, macromolecules with broad resonances, signals from the housing of the coil, and the support material where the animal is placed on. A baseline correction is done by fitting a spline curve to the spectrum and subtracting the curve from it.

(c) Curve fitting
To analyze the spectrum, it is necessary to calculate the signal intensities and the area under the signal. The area under the signal reflects the number of NMR-detectable molecules in the measured volume. For calculation of the area, time, and frequency domain, fitting routines are available. Time domain algorithms are more precise and phase- and baseline correction independent. There are freeware fitting processing software packages available.

Frequency domain fitting routines are not very reliable, but in most cases sufficient for a quick analysis of the spectrum, e.g., for tumor staging. The variations of the native signal intensities between individual animals are much greater than the fitting error. For detecting and quantifying the signal of a drug, a time domain fit is recommended (Fig. 13.53).

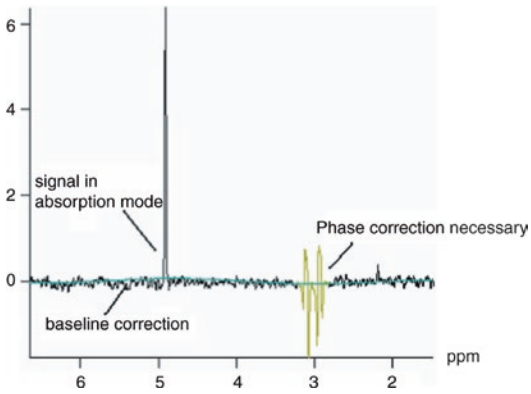

Fig. 13.53 Frequency domain processing. Spectrum with phase and baseline correction (*blue*)

13.4.5 MR Coils

13.4.5.1 Transmit Coil

In general, it is possible to use the same coils for ^{1}H spectroscopy as for imaging; however, it is recommended to use a coil with a homogeneous B_1 field for transmit of the RF pulse. This leads to a more precise definition of the flip angles than with a surface transmit coil. The drawback is the higher power demand and the higher RF deposit in the animal so that the animal can heat up. This is especially important for X-nucleus application with ^{1}H decoupling. Circular polarized coils are advantageous over linear polarized because of their lower power consumption and bigger homogeneous B_1 volume.

13.4.5.2 Receive Coil

To receive the signal, it is important that the coil picks up the signal with minimum signal loss. A multichannel receive coil offers the highest possible S/N. The signal of each element is combined to a summarized and phase-corrected spectrum.

X-nucleus coils are usually not designed as multichannel coils, only as linear or circular polarized coils. They are mainly combined transmit/receive coils. Again, circular polarized[2] coils are preferred over linear coils due to higher S/N by factor of 1.41.

13.4.6 Examination

In vivo examinations start with high-resolution imaging to define the region for spectroscopy as good as possible. Therefore, it might be necessary to measure images with T_1, T_2 contrast and contrast media.[3] After defining the region of interest, the voxel or slice is placed in this area. The voxel definition is not very accurate because of the chemical shift artifact in single

[2] Circular polarized coils are often named as quadrature coils.

[3] After all these steps it is possible to measure. The final processed spectrum is usable in most of the cases and gives the missing information about the tissue composition. Washout of contrast media in animals is much faster than in humans resulting in no interference with a following spectroscopy exam.

voxel spectroscopy and the point spread function in CSI.

After placement of the voxel, the frequency and amplifier adjustment has to be performed, following by shimming and water suppression (only ^{1}H). The adjustments are either automatically done or require user interaction, depending on the system. It is often necessary to control the quality of the adjustments, especially the shim and the water suppression (Fig. 13.54).

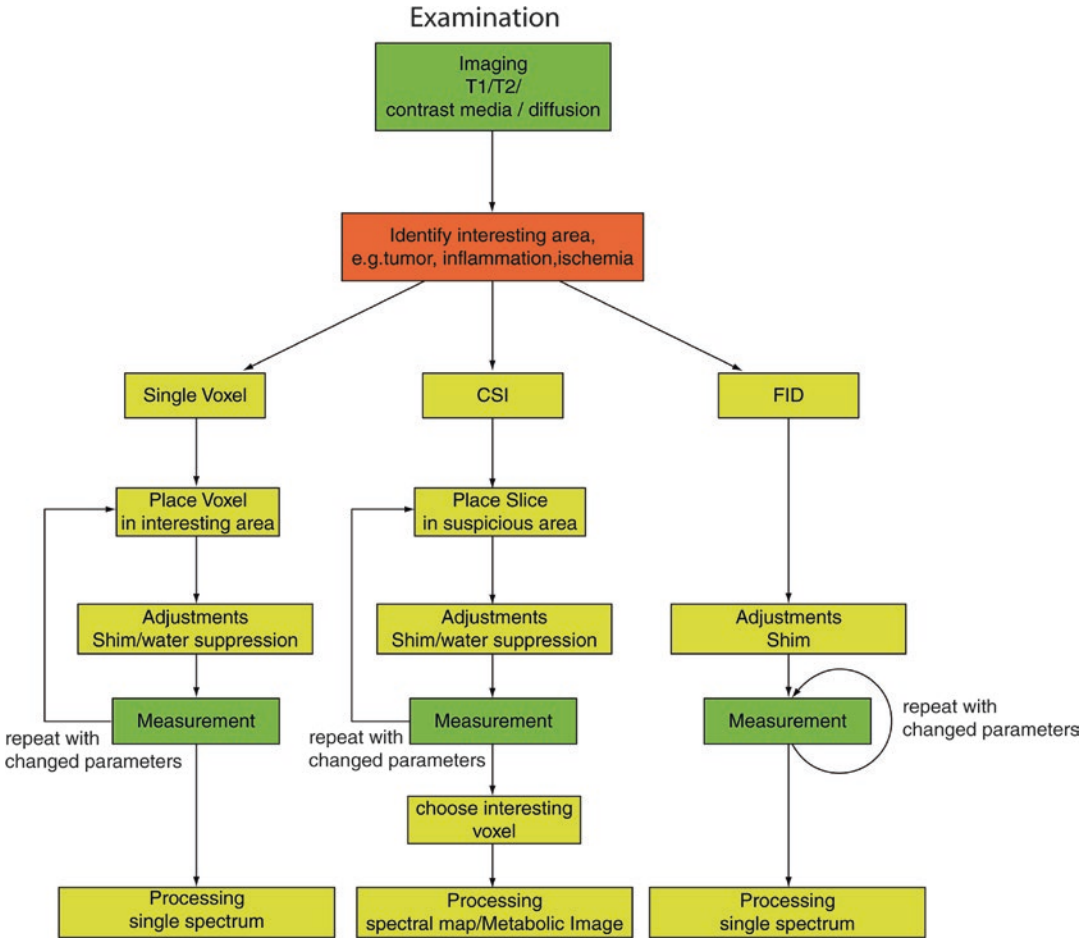

Fig. 13.54 Flowchart of a spectroscopic examination. After imaging and placing the voxel or slice in the interesting area, frequent measurements with different parameters can be done

References

Basics of Magnetic Resonance Imaging (MRI)

Ardenkjaer-Larsen JH, Fridlund B, Gram A, Hansson G, Hansson L, Lerche MH, Servin R, Thaning M, Golman K. Increase in signal-to-noise ratio of > 10,000 times in liquid-state NMR. Proc Natl Acad Sci U S A. 2003a;100:10158–63.

Baltes C, Radzwill N, Bosshard SC, Marek D, Rudin M. Micro MR imaging of the mouse brain at 9.4T using a cryogenic RF probe. NMR Biomed. 2009;22:834–42.

Bar-Shir A, Bulte JWM, Gilad AA. Molecular engineering of nonmetallic biosensors for CEST MRI. ACS Chem Biol. 2015;10:1160–70.

Bihan L. Molecular diffusion nuclear magnetic resonance imaging. Magn Reson Q. 1991;7:1–30.

Bloch F. Nuclear induction. Phys Rev. 1946;70:460–74.

Bloch F. Generalized theory of relaxation. Phys Rev. 1957;105:1206–22.

Bloch F, Siegert AJF. Magnetic resonance for nonrotating fields. Phys Rev. 1940;57:522.
Bloch F, Hansen WW, Packard M. The nuclear induction experiment. Phys Rev. 1946;70:474–85.
Bradley WG, Bydder GM. Advanced MR imaging techniques. London: Martin Dunitz Ltd; 1997.
Bruder H, Fischer H, Graumann R, Deimling M. A new steady-state imaging sequence for simultaneous acquisition of two MR images with clearly different contrast. Magn Reson Med. 1988;7:35–42.
Carrington A, McLachlan AD. Introduction to magnetic resonance. New York: Harper & Row; 1969.
Ernst RR. Sensitivity enhancement in magnetic resonance. Adv Magn Reson. 1966;2:1–135.
Ernst RR, Bodenhausen G, Wokaun A. Principles of nuclear magnetic resonance in one and two dimensions. New York: Clarendon Press (Oxford); 1987. p. 108 ff–54 ff.
Forsen S, Hoffmann RA. Study of moderately rapid chemical exchange reactions by means of nuclear magnetic double resonance. J Chem Phys. 1963;39:2892–901.
Frahm J, Haase A, Matthaei D. Rapid NMR imaging of dynamic processes using the FLASH technique. Magn Reson Med. 1986;3:321–7.
Griswold MA, Jakob PM, Heidemann RM, Nittka M, Jellus V, Wang J, Kiefer B, Haase A. Generalized autocalibrating partially parallel acquisitions (GRAPPA). Magn Reson Med. 2002;47:1202–10.
Haacke EM, Brown RW, Thompson MR, Venkatesan R. Magnetic resonance imaging: physical principles and sequence design. New York: John Wiley & Sons; 1999.
Haacke EM, Xu Y, Cheng YC, Reichenbach JR. Susceptibility weighted imaging (SWI). Magn Reson Med. 2004;52:612–8.
Haacke EM, Liu S, Buch S, Zheng W, Wu D, Ye Y. Quantitative susceptibility mapping: current status and future directions. Magn Reson Imaging. 2015;33:1–25.
Haase A. Snapshot FLASH MRI. Applications to T1, T2 and chemical shift imaging. Magn Reson Med. 1990;13:77–89.
Hahn E. Spin echoes. Phys Rev. 1950;80:580–94.
Heemskerk AM, Strijkers GJ, Vilanova A, Drost MR, Nicolay K. Determination of mouse skeletal muscle architecture using three-dimensional diffusion tensor imaging. Magn Reson Med. 2005;53:1333–40.
Hennig J, Nauerth A, Friedburg H. RARE imaging: a fast imaging method for clinical MR. Magn Reson Med. 1986;3:823–33.
Hsieh CY, Cheng YC, Neelavalli J, Haacke EM, Stafford RJ. An improved method for susceptibility and radius quantification of cylindrical objects from MRI. Magn Reson Imaging. 2015;33:420–36.
Lauterbur PC. Image formation by induced local interactions: examples employing magnetic resonance. Nature. 1973;243:190–1.
Le Bihan D. Diffusion, confusion and functional MRI. Neuroimage. 2011;62:1131–6.
Le Bihan D, Breton E, Lallemand D, Aubin ML, Vignaud J, Laval-Jeantet M. Separation of diffusion and perfusion in intravoxel incoherent motion MR imaging. Radiology. 1988;168:497–505.
Ljunggren S. A simple graphical representation of Fourier-based imaging methods. J Magn Reson. 1983;54:338–43.
Lustig M, Donoho D, Pauly JM. Sparse MRI: the application of compressed sensing for rapid MR imaging. Magn Reson Med. 2007;58:1182–95.
Ma D, Gulani V, Seiberlich N, Liu K, Sunshine JL, Duerk JL, Griswold MA. Magnetic resonance fingerprinting. Nature. 2013;495:187–9.
Mansfield P. Echo planar imaging by NMR. Br Med Bull. 1984;40:1987–90.
McMahom MT, Chan KWY. Developing MR probes for molecular imaging. Adv Cancer Res. 2014;124:297–327.
Moseley ME, Cohen Y, Kucharczyk J, Mintorovitch J, Asgari HS, Wendland MF, Tsuruda J, Norman D. Diffusion-weighted MR imaging of anisotropic water diffusion in cat central nervous system. Radiology. 1990;176:439–45.
Overhauser AW. Polarization of nuclei in metals. Phys Rev. 1953;92:411–5.
Pauly JM, Le Roux P, Nishimura D, Macovski A. Parameter relations for the Shinnar-Le Roux selective excitation pulse design algorithm. IEEE Trans Med Imaging. 1991;10:53–65.
Pruessmann KP, Weiger M, Scheidegger MB, Boesiger P. SENSE: sensitivity encoding for fast MRI. Magn Reson Med. 1999;42:952–62.
Ratering D, Baltes C, Massner J, Marek D, Rudin M. Performance of a 200 MHz cryogenic RF probe designed for MRI and MRS of the murine brain. Magn Reson Med. 2008;69:1440–4.
Redfield AG. The theory of relaxation processes. Adv Magn Reson. 1965;1:1–32.
Schäfer A, Wharton S, Gowland P, Bowtell R. Using magnetic field simulation to study susceptibility-related phase contrast in gradient echo MRI. Neuroimage. 2009;48:126–37.
Slichter CP. Principles of magnetic resonance. Berlin: Springer Verlag; 1978. p. 150.
Slichter CP. Principles of magnetic resonance. 3rd ed. New York: Springer Verlag; 1990.
Sodickson DK, Manning WJ. Simultaneous acquisition of spatial harmonics (SMASH): fast imaging with radiofrequency coil arrays. Magn Reson Med. 1997;38:591–603.
Stejskal EO, Tanner JE. Spin diffusion measurements: spin echoes in the presence of a time-dependent field gradient. J Chem Phys. 1965;42:288–92.
Stoeck CT, von Deuster C, Genet M, Atkinson D, Kozerke S. Second-order motion-compensated spin echo diffusion tensor imaging of the human heart. Magn Reson Med. 2016;75:1669–76. doi:10.1002/mrm.25784. [Epub ahead of print].
Tuch DS, Reese TG, Wiegell MR, Makris N, Belliveau JW, Wedeen VJ. High angular resolution diffusion imaging reveals intravoxel white matter fiber heterogeneity. Magn Reson Med. 2002;48:577–82.

Wangsness RK, Bloch F. The dynamical theory of nuclear induction. Phys Rev. 1953;89:728–39.
Wolff SD, Balaban RS. Magnetization transfer contrast (MTC) and tissue water proton relaxation in vivo. Magn Reson Med. 1989;10:135–44.

MR Contrast Agents

Acosta RA, Blümler P, Münnemann K, Spiess H-W. Progr Nucl Magn Reson Spectrosc. 2012;66:40–69.
Adams RW, Aguilar JA, Atkinson KD, Cowley MJ, Elliott PIP, Duckett SB, Green GGR, Khazal IG, López-Serrano J, Williamson DC. Science. 2009a;323:1708–11.
Aime S, Botta M, Fasano M, Geninatti Crich S, Terreno E. J Biol Inorg Chem. 1996;1:312–9.
Aime S, Botta M, Fasano M, Terreno E. Chem Soc Rev. 1998;27:19–29.
Aime S, Chiaussa M, Digilio G, Gianolio E, Terreno E. J Biol Inorg Chem. 1999;4:766–74.
Aime S, Botta M, Gianolio E, Terreno E. Angew Chem Int Ed. 2000;39:747–50.
Aime S, Fasano M, Terreno E, Botta M. In: Merbach AE, Tóth E, editors. The chemistry of contrast agents in medical magnetic resonance imaging. Chichester: Wiley; 2001.
Aime S, Barge A, Delli Castelli D, Fedeli F, Mortillaro A, Nielsen FU, Terreno E. Magn Res Med. 2002a;47:639–48.
Aime S, Cabella C, Colombatto S, Geninatti Crich S, Gianolio E, Maggioni F. J Magn Reson Imag. 2002b;16:394–406.
Aime S, Frullano L, Geninatti Crich S. Angew Chem. 2002c;41:1017–9.
Aime S, Delli Castelli D, Terreno E. Angew Chem Int Ed. 2003a;42:4527.
Aime S, Gobetto R, Reineri F. J Chem Phys. 2003b;119:8890–7.
Aime S, Delli Castelli D, Terreno E. Angew Chem Int Ed. 2005;44:5513–5.
Aime S, Delli Castelli D, Lawson D, Terreno E. J Am Chem Soc. 2007;129:2430–1.
Aime S, Dastrù W, Giovenzana GB, Gobetto R, Reineri F, Santelia D, Viale A. J Am Chem Soc. 2008;130:15047–53.
Albers MJ, Bok R, Chen AP, Cunningham CH, Zierhut ML, Zhang VY, Kohler SJ, Tropp J, Hurd R, Yen Y-F, Nelson SJ, Vigneron DB, Kurhanewicz J. Cancer Res. 2008;68:8607–15.
Albert MS, Cates GD, Driehuys B, Happer W, Saam B, Springer Jr CS, et al. Nature. 1994;370:199–201.
Allouche-Arnon H, Wade T, Friesen Waldner L, Miller VN, Gomori JM, Katz-Brull R, McKenzie C. Contrast Media Mol Imag. 2013;8:72–82.
Altes TA, Salerno M. J Thorac Imaging. 2004;19:250–8.
Ardenkjaer-Larsen JH, Fridlund B, Gram A, Hansson G, Hansson L, Lerche MH, Servin R, Thaning M, Golman K. Proc Natl Acad Sci U S A. 2003b;100:10158–63.
Arena F, Singh JB, Gianolio E, Stefanìa R, Aime S. Bioconjug Chem. 2011;22:2625–35.
Artemov D, Mori N, Ravi R, Bhujwalla ZM. Cancer Res. 2003;63:2723–7.
Aswendt M, Gianolio E, Pariani G, Napolitano R, Fedeli F, Himmelreich U, Aime S, Hoehn M. Neuroimage. 2012;62:1685–93.
Avedano S, Botta M, Haigh JS, Longo DL, Woods M. Inorg Chem. 2013;52:8436–50.
Babincova M, Altanerova V, Lambert M, Altaner C, Machova E, Sramka M, Babinec P. Z Naturforsch. 2000;55c:278–81.
Babincova M, Leszczynska D, Sourivong P, Babinec P, Leszczynski J. Med Hypotheses. 2004;62:375–7.
Banci L, Bestini I, Luchinat C. Nuclear and electronic relaxation. Weinheim: VCH; 1991.
Bargon J, Natterer J. Progr Nucl Magn Reson Spect. 1997;31:293–315.
Barkemeyer J, Haake M, Bargon J. J Am Chem Soc. 1995;117:2927–8.
Bhattacharya P et al. Abstract n. 461, 50th experimental nuclear magnetic resonance conference, Pacific Grove, California, 29 Mar – 3 Apr 2009.
Bhattacharya P, Chekmenev E, Reynolds WF, Wagner S, Zacharias N, Chan HR, Büngerd R, Ross BD. NMR Biomed. 2011a;24:1023–8.
Bogdanov A, Matuszewski L, Bremer C, Petrovski A, Weissleder R. Molec Imag. 2002;1:16–23.
Bohndiek SE, Kettunen MI, Hu D, Kennedy WC, Boren J, Gallagher FA, Brindle KM. J Am Chem Soc. 2011;133:11795–801.
Bohndiek SE, Kettunen MI, Hu D-E, Brindle KM. Cancer Res. 2012;72:854–64.
Boros E, Polasek M, Zhang Z, Caravan P. J Am Chem Soc. 2012;134:19858–68.
Boros E, Karimi S, Kenton N, Helm L, Caravan P. Inorg Chem. 2014;53:6985–94.
Botta M. Second coordination sphere water molecules and relaxivity of gadolinium(III) complexes: Implications for MRI contrast agents. Eur J Inorg Chem. 2000;(3):399–407.
Boutin C, Stopin A, Lenda F, Brotin T, Dutasta J-P, Jamin N, Sanson A, Boulard Y, Leteurtre F, Huber G, Bogaert-Buchmann A, Tassali N, Desvaux H, Carrière M, Berthault P. Bioorg Med Chem. 2011;19:4135–43.
Briley-Saebo KC, Geninatti-Crich S, Cormode DP, Barazza A, Mulder WJM, Chen W, Giovenzana GB, Fisher EA, Aime S, Fayad ZA. J Phys Chem B. 2009;113:6283–9.
Brindle KM, Bohndiek SE, Gallagher FA, Kettunen MI. Magn Reson Med. 2011;66:505–19.
Brücher E, Sherry AD. Stability and toxicity of contrast agents. In: Merbach AE, Tóth E, editors. The chemistry of contrast agents in medical magnetic resonance imaging. Chichester: Wiley; 2001.
Bulte JW, De Cuyper M. Methods Enzymol. 2003;373:175–98.
Bulte JW, De Cuyper M, Despres D, Franck JA. J Magn Reson Imaging. 1999;9:329–35.

Callot V, Canet E, Brochot J, Viallon M, Humblot H, Briguet A, Tournier H, Cremillieux Y. Magn Res Med. 2001;46:535–40.
Caravan P, Farrar CT, Frullano L, Uppal R. Contrast Media Mol Imaging. 2009;4:89–100.
Carrera C, Digilio G, Baroni S, Burgio D, Consoli S, Fedeli F, Longo D, Mortillaro A, Aime S. Dalton Trans. 2007;43:4980–7.
Carter D, Ho JX. Adv Prot Chem. 1994;45:153–203.
Chang YT, Cheng CM, Su YZ, Lee WT, Hsu JS, Hsu GC, Cheng TL, Wang YM. Bioconjug Chem. 2007;18:1716–27.
Chekmenev EY, Hovener J, Norton VA, Harris K, Batchelder LS, Bhattacharya P, Ross BD, Weitekamp DP. J Am Chem Soc. 2008a;130:4212–3.
Chen AP, Albers MJ, Cunningham CH, Kohler SJ, Yen Y-F, Hurd RE, Tropp J, Bok R, Pauly JM, Nelson SJ, Kurhanewicz J, Vigneron DB. Magn Res Med. 2007a;58:1099–106.
Chen AP, Kurhanewicz J, Bok R, Xu D, Joun D, Zhang V, Nelson SJ, Hurd RE, Vigneron DB. Magn Res Imag. 2008a;26:721–6.
Chen W, Jarzyna PA, van Tilborg GAF, Nguyen VA, Cormode DP, Klink A, Griffioen AW, Randolph GJ, Fisher EA, Mulder WJM, Fayad ZA. FASEB J. 2010;24:1689–99.
Chen AP, Hurd RE, Gu Y, Wilson DM, Cunningham CH. NMR Biomed. 2011;24:514–20.
Chen AP, Hurd RE, Schroeder MA, Lau AZ, Gu Y, Lam WW, Barry J, Tropp J, Cunningham CH. NMR Biomed. 2012a;25:305–11.
Chen SH, Kuo YT, Singh G, Cheng TL, Su YZ, Wang TP, Chiu YY, Lai JJ, Chang CC, Jaw TS, Tzou SC, Liu GC, Wang YM. Inorg Chem. 2012b;51:12426–35.
Clatworthy MR, Kettunen MI, Hu D-E, Mathews RJ, Witney TH, Kennedy BWC, Bohndiek SE, Gallagher FA, Jarvis LB, Smith KGC, Brindle KM. Proc Natnl Am Soc. 2012;109:13374–9.
Comment A, van den Brandt B, Uffmann K, Kurdzesau F, Jannin S, Konter JA, Hautle P, Wenckebach WT, Gruetter R, Van der Klink JJ. Conc Magn Reson Part B. 2007a;31B:255–69.
Corot C, Robert P, Idee JM, Port M. Adv Drug Deliv Rev. 2006;58:1471–504.
Cunningham CH, Arai T, Yang PC, McConnell MV, Pauly JM, Conolly SM. Magn Reson Med. 2005;53:999–1005.
Darpolora MM, Yen Y-F, Chua M-S, Xing L, Clarke-Katzenberg RH, Shi W, Mayer M, Josan S, Hurd RE, Pfefferbaum A, Senadheera L, So S, Hofmanna LV, Glazer GM, Spielman DM. NMR Biomed. 2011;24:506–13.
Day SE, Kettunen MI, Gallagher FA, Hu D-E, Lerche M, Wolber J, Golman K, Ardenkjaer-Larsen JH, Brindle KM. Nat Med. 2007a;13:1382–7.
Day SE, Kettunen MI, Krishna Cherukuri M, Mitchell JB, Lizak MJ, Morris HD, Matsumoto S, Koretsky AP, Brindle KM. Magn Reson Med. 2011;65:557–63.
Delli Castelli D, Terreno E, Carrera C, Giovenzana GB, Mazzon R, Rollet S, Visigalli M, Aime S. Inorg Chem. 2008;47:2928–30.
Delli Castelli D, Terreno E, Aime S. Angew Chem Int Ed. 2011;50:1798–800.
Delli Castelli D, Ferrauto G, Cutrin JC, Terreno E, Aime S. Magn Reson Med. 2014;71:326–32.
Delli Castelli D, Terreno E, Longo D, Aime S. Nmr in biomedicine 2013;26:839–49.
Digilio G, Catanzaro V, Fedeli F, Gianolio E, Menchise V, Napolitano R, Gringeri C, Aime S. Chem Commun. 2009;28:893–5.
Digilio G, Menchise V, Gianolio E, Catanzaro V, Carrera C, Napolitano R, Fedeli F, Aime S. J Med Chem. 2010;53:4877–90.
Do QN, Ratnakar JS, Kovacs Z, Sherry AD. Chem Med Chem. 2014;9:1116.
Dousset V, Brochet B, Deloire MSA, Lagoarde L, Barroso B, Caille JM, Petri KG. Am J Neuroradiol. 2006;27:1000–5.
Duckett SB, Wood NJ. Coord Chem Rev. 2008;252:2278–91.
Engberink RDO, van der Pol SMA, Döpp ED, de Vries HE, Blezer ELA. Radiology. 2007;243:467–74.
Engelstadt BL, Wolf GL. Contrast Agents. In: Stark DD, Bradley WG Jr, editors. Magnetic resonance imaging, the V.C. St. Louis: Mosby Company; 1988.
Ferrauto G, Delli Castelli D, Di Gregorio E, Langereis S, Burdinski D, Grull H, Terreno E, Aime S. J Am Chem Soc. 2014;136:638–41.
Fortin-Ripoche JP, Martina MS, Gazeau F, Menager C, Wilhelm C, Bacri JC, Lesieur S, Clement O. Radiology. 2006;239:415.
Fossheim SL, Kellar KE, Fahlvik AH, Klaveness J. Magn Reson Imag. 1997;15:193–202.
Frangioni JV, Hajjar RJ. Circulation. 2004;110: 3378–83.
Frullano L, Catana C, Benner T, Sherry AD, Caravan P. Angew Chem Int Ed. 2010;49:2382–4.
Fulton DA, Elemento EM, Aime S, Chaabane L, Botta M, Parker D. Chem Commun. 2006;14:1064–6.
Gabellieri C, Reynolds S, Lavie A, Payne GS, Leach MO, Eykyn TR. J Am Chem Soc. 2008;130:4598–9.
Gallagher FA, Kettunen MI, Day SE, Hu D-E, Ardenkjær-Larsen JH, Zandt R, Jensen PR, Karlsson M, Golman K, Lerche MH, Brindle KM. Nature. 2008a;453:940–3.
Gallagher FA, Kettunen MI, Day SE, Lerche M, Brindle KM. Magn Reson Med. 2008b;60:253–7.
Gallagher FA, Kettunen MI, Brindle KM. NMR Biomed. 2011a;24:1006–15.
Gallagher FA, Kettunen MI, Day SE, Hu D, Karlsson M, Gisselsson A, Lerche MH, Brindle KM. Magn Reson Med. 2011b;66:18–23.
Geninatti Crich S, Lanzardo S, Alberti D, Belfiore S, Ciampa A, Giovenzana GB, Lovazzano C, Pagliarin R, Aime S. Neoplasia. 2007;9:1046–56.
Geninatti-Crich S, Cutrin JC, Lanzardo S, Conti L, Kalman FK, Szabo I, Lago NR, Iolascon A, Aime S. Contrast media Molecul Imag. 2012;7:281–8.
Gianolio E, Giovenzana GB, Longo D, Longo I, Menegotto I, Aime S. Chem Eur J. 2007;13:5785–97.
Gianolio E, Napolitano R, Fedeli F, Arena F, Aime S. Chem Commun. 2009;28:6044–6.
Gianolio E, Maciocco L, Imperio D, Giovenzana GB, Simonelli F, Abbas K, Bisi G, Aime S. Chem Commun. 2011;47:1539–41.

Gianolio E, Cabella C, Colombo Serra S, Valbusa G, Arena F, Maiocchi A, Miragoli L, Tedoldi F, Uggeri F, Visigalli M, Bardini P, Aime S. J Biol Inorg Chem. 2014;19:715–26.
Gloggler S, Muller R, Colell J, Emondts M, Dabrowski M, Blumicha B, Appelt S. Phys Chem Chem Phys. 2011;13:13759–64.
Goffeney N, Bulte JWM, Duyn J, Bryant Jr LH, van Zijl PCM. J Am Chem Soc. 2001;123:8628–9.
Goldman M, Johannesson H. C R Phys. 2005a;6:575–81.
Goldman M, Johannesson H, Axelsson O, Karlsson M. Magn Reson Imaging. 2005b;23:153–7.
Golman K, Axelsson O, Johannesson H, Månsson S, Olofsson C, Petersson JS. Magn Reson Med. 2001a;46:1–5.
Golman K, Zandt R, Lerche M, Perhson R, Ardenkjaer-Larsen H. Cancer Res. 2006a;66:10855–60.
Goswami LN, Quanyu Cai LM, Sarma SJ, Jalisatgi SS, Hawthorne MF. Inorg Chem. 2013;52:1701–9.
Hall DA, Maus DC, Gerfen GJ, Inati SJ, Becerra LR, Dahlquist FW, Griffin RG. Science. 1997;276:930–2.
Harris T, Eliyahu G, Frydman L, Degani H. Proc Natnl Am Soc. 2009;106:18131–6.
Henkelman RM, Stanisz GJ, Graham SJ. NMR Biomed. 2001;14:57–64.
Hingorani DV, Yoo B, Bernstein AS, Pagel MD. Chem Eur J. 2014;20:9840–50.
Hu JZ, Solum MS, Wind RA, Nilsson BL, Peterson MA, Pugmire RJ, Grant DM. J Phys Chem A. 2000;104:4413–20.
Hu S, Balakrishnan A, Bok RA, Anderton B, Larson PEZ, Nelson SJ, Kurhanewicz J, Vigneron DB, Goga A. Cell Metab. 2011a;14:131–42.
Hu S, Zhu M, Yoshihara HAI, Wilson DM, Keshari KR, Shin P, Reed G, von Morze C, Bok R, Larson PEZ, Kurhanewicz J, Vigneron DB. Magn Reson Imaging. 2011b;29:1035–40.
Hu S, Yoshihara HAI, Bok R, Zhou J, Zhu M, Kurhanewicz J, Vigneron DB. Magn Reson Imaging. 2012;30:1367–72.
Hu H, Li D, Liu SL, Wang MZ, Moats R, Conti PS, Li ZB. Biomaterials. 2014;35:8649–58.
Hua LAH, Du J, Wei J, Wang L, Yang H, Wu D, Shi H, Li F, Yang S. Biomaterials. 2014;35:5381–92.
Hurd RE, Yen Y-F, Mayer D, Chen A, Wilson D, Kohler S, Bok R, Vigneron D, Kurhanewicz J, Tropp J, Spielman D, Pferfferbaum A. Magn Reson Med. 2010;63:1137–43.
Ishii M, Emami K, Kadlecek S, Petersson JS, Golman K, Vahdat V, Yu J, Cadman RV, MacDuffie-Woodburn J, Stephen M, et al. Magn Reson Med. 2007;57:459–63.
Ito A, Shinkai M, Honda H, Kobayashi T. J Biosci Bioeng. 2005;100:1–11.
Jagadish B, Guntle GP, Zhao D, Gokhale V, Ozumerzifon TJ, Ahad AM, Mash EA, Raghunand N. J Med Chem. 2012;55:10378–86.
Johannesson H, Axelsson O, Karlsson M. C R Phys. 2004a;5:315–24.
Johansson E, Mansson S, Wirestam R, Svensson J, Petersson JS, Golman K, Stahlberg F. Magn Reson Med. 2004a;51:464–72.
Josan S, Spielman D, Yen Y-F, Hurd R, Pfefferbaum A, Mayer D. NMR Biomed. 2012;25:993–9.
Kalman FK, Krisztian F, Geninatti-Crich S, Aime S. Angew Chem Int Ed. 2010;49:612–5.
Karlsson M, Jensen PR, Zandt R, Gisselsson A, Hansson G, Duus J, Meier S, Lerche MH. Int J Cancer. 2010;127:729–36.
Kennedy BW, Kettunen MI, Hu D-E, Brindle KM. J Am Chem Soc. 2012;134:4969–77.
Keshari KR, Kurhanewicz J, Bok R, Larson PEZ, Vigneron DB, Wilson DM. Proc Ntnl Am Soc. 2011a;108:18606–11.
Keshari KR, Sriram R, Koelsch BL, Van Criekinge M, Wilson DM, Kurhanewicz J, Wang ZJ. Cancer Res. 2013;73:529–38.
Kircher MF, Allport JR, Graves EE, Love V, Josephson L, Lichtman AH, Weissleder R. Cancer Res. 2003;63:6838–46.
Kitagawa T, Kosuge H, Uchida M, Dua MM, Iida Y, Dalman RL, Douglas T, McConnell MV. Mol Imaging Biol. 2012;14:315–24.
Kluza E, van der Schaft DWJ, Hautvast PAI, Mulder WJM, Mayo KH, Griffioen AW, Strijkers GJ, Nicolay K. Nano Lett. 2010;10:52–8.
Larson PEZ, Kerr AB, Chen AP, Lustig MS, Zierhut ML, Hu S, Cunningham CH, Pauly JM, Kurhanewicz J, Vigneron DB. J Magn Reson. 2008a;194:121–7.
Lau AZ, Chen AP, Hurd RE, Cunningham CH. NMR Biomed. 2011;24:988–96.
Lauffer R, Parmelee D, Dunham S, et al. Radiology. 1998;207:529–38.
Laustsen C, Ostergaard JA, Lauritzen MH, Nørregaard R, Bowen S, Søgaard LV, Flyvbjerg A, Pedersen M, Ardenkjær-Larsen JH. Diabetes Metab Res Rev. 2013;29:125–9.
Levin YS, Mayer D, Yen Y-F, Hurd RE, Spielman DM. Magn Reson Med. 2007;58:245–52.
Liu Z, Araki T, Okajima Y, Albert M, Hatabu H. Eur J Radiol. 2014;83:1282–91.
Lodi A, Woods SM, Ronen SM. NMR Biomed. 2013;26:299–306.
Longo DL, Dastrù W, Digilio G, Keupp J, Langereis S, Lanzardo S, Prestigio S, Steinbach O, Terreno E, Uggeri F, Aime S. Magn Reson Med. 2011;65:202–11.
Longo DL, Busato A, Lanzardo S, Antico F, Aime S. Magn Reson Med. 2013;70:859–64.
Loving GS, Mukherjee S, Caravan P. J Am Chem Soc. 2013;135:4620–3.
Lowe MP, Parker D, Reany O, et al. J Am Chem Soc. 2001;123:7601–9.
Lupo JM, Chen AP, Zierhuta ML, Bok R, Cunningham CH, Kurhanewicz J, Vigneron DB, Nelson SJ. Magn Reson Imaging. 2010;28:153–62.
Magnusson P, Johansson E, Månsson S, Petersson JS, Chai C-M, Hansson G, Axelsson O, Golman K. Magn Reson Med. 2007;57:1140–7.
Malloy CR, Merritt ME, Sherry AD. NMR Biomed. 2011;24:973–9.
Mansson S, Johansson E, Magnusson P, Chai C-M, Hansson G, Petersson JS, Stahlberg F, Golman K. Eur Radiol. 2006;16:57–67.

Marjanska M, Iltis I, Shestov AA, Deelchand DK, Nelson C, Ugurbil K, Henry P-G. J Magn Reson. 2010;206:210–8.
Martina MS, Fortin JP, Menager C, Clement O, Barratt G, Grabielle-Madelmont C, Gazeau F, Cabuil V, Lesieur S. J Am Chem Soc. 2005;127:10676–85.
Martinez GV, Zhang X, Garcia-Martinc ML, Morsea DL, Woods M, Sherry AD, Gillies RJ. NMR Biomed. 2011;24:1380–91.
Mastarone DJ, Harrison VSR, Eckermann AL, Parigi G, Meade TJ. J Am Chem Soc. 2011;133:5329–37.
Mayer D, Yen Y-F, Josan S, Park JM, Pfefferbaum A, Hurd RE, Spielman DE. NMR Biomed. 2012a;25: 1119–24.
Menchise V, Digilio G, Gianolio E, Cittadino E, Catanzaro V, Carrera C, Aime S. Mol Pharm. 2011;8:1750–6.
Merritt ME, Harrison C, Kovacs Z, Kshirsagar P, Malloy CR, Sherry AD. J Am Chem Soc. 2007a;129:12942–3.
Merritt ME, Harrison C, Storey C, Jeffrey FM, Sherry AD, Malloy CR. Proc Natl Acad Sci U S A. 2007b;104:19773–7.
Moats RA, Fraser SE, Meade TJ. Angew Chem Int Ed Engl. 1997;36:725–8.
Moller HE, Chen XJ, Saam B, Hagspiel KD, Johnson GA, Altes TA, de Lange EE, Kauczor HU. Magn Reson Med. 2002;47:1029–51.
Muller RN, Vander Elst L, Roch A, Peters JA, Csajbok E, Gillis P, Gossuin Y. Adv Inorg Chem. 2005;57:239–92.
Napolitano R, Pariani G, Fedeli F, Baranyai Z, Aswendt M, Aime S, Gianolio E. J Med Chem. 2013;56:2466–77.
Nasrallah FA, Pages G, Kuchel PW, Golay X, Chuang KH. J Cerebr Blood Flow Metab. 2013;33:1270–8.
Nelson SJ, Vigneron D, Kurhanewicz J, Chen A, Bok R, Hurd R. Appl Magn Reson. 2008;34:533–44.
Nelson SJ, Kurhanewicz J, Vigneron DB, Larson PEZ, Harzstark AL, Ferrone M, van Criekinge M, Chang JW, Bok R, Park I, Reed G, Carvajal L, Small EJ, Munster P, Weinberg VK, Ardenkjaer-Larsen JH, Chen AP, Hurd RE, Odegardstuen L-I, Robb FJ, Tropp J, Murray JA. Sci Transl Med. 2013a;5(198):198ra108.
Norek M, Kampert E, Zeitler U, Peters JA. J Am Chem Soc. 2008;130:5335–40.
Olatunde A, Cox JM, Daddario M, Spernyak JA, Benedict JB, Morrow JR. Inorg Chem. 2014;53:8311–21.
Paris J, Gameiro C, Humblet V, Mohapatra PK, Jacques V, Desreux J. Inorg Chem. 2006;45:5092–102.
Park I, Larson PEZ, Zierhut ML, Hu S, Bok R, Ozawa T, Kurhanewicz J, Vigneron DB, VandenBerg SR, James CD, Nelson SJ. Neuro Oncol. 2010;12:133–44.
Park I, Bok R, Ozawa T, Phillips JJ, James CD, Vigneron DB, Ronen SM, Nelson SJ. J Magn Reson Imaging. 2011;33:1284–90.
Pikkemaat JA, Wegh RT, Lamerichs R, van de Molengraaf RA, Langereis S, Burdinski D, Raymond AY, Janssen HM, de Waal BF, Willard NP, Meijer EW, Grull H. Contr Media Mol Imaging. 2007;2:229–39.
Raghunand N, Howison C, Sherry AD, Zhang S, Gillies RJ. Magn Reson Med. 2003;49:249–57.
Raghunand N, Jagadish B, Trouard TP, Galons JP, Gillies RJ, Mash EA. Magn Reson Med. 2006; 55:1272–80.
Raghunand N, Guntle GP, Gokhale V, Nichol GS, Mash EA, Jagadish B. J Med Chem. 2010;53:6747–57.
Reed GD, Larson PEZ, von Morze C, Bok R, Lustig M, Kerr AB, Pauly JM, Kurhanewicz J, Vigneron DB. J Magn Reson. 2012;217:41–7.
Rinck PA. Magnetic resonance in medicine. Blackwell Scientific: Publications; 1993.
Rinck PA. Magnetic resonance in medicine. Berlin: ABW Wissenschaftsverlag GmbH; 2003.
Rosen BR, Belliveau JW, Aronen HJ, Kennedy D, Buchbinder BR, Fischman A, Gruber M, Glas J, Weisskoff RM, Cohen MS, Hochberg FH, Brady TJ. Magn Reson Med. 1991;22:293–9.
Rummeny EJ, Marchal G. Acta Radiol. 1997;38: 626–30.
Saleh A, Schroeter M, Jonkmanns C, Hartung HP, Modder H, Jander S. Brain. 2004;127:1670–7.
Schmitt-Willich H, Brehm M, Evers CLJ, Michl G, Müller-Fahrnow A, Petrov O, Platzek J, Radüchel B, Sülzle D. Inorg Chem. 1999;38:1134–44.
Schroder L, Lowery TJ, Hilty C, Wemmer DE, Pines A. Science. 2006;314:446–9.
Schroeder MA, Atherton HJ, Ball DR, Cole MA, Heather LC, Griffin JL, Clarke K, Radda GK, Tyler DJ. FASEB J. 2009a;23:2529–38.
Schroeder MA, Clarke K, Neubauer S, Tyler DJ. Circulation. 2011;124:1580–94.
Schroeder MA, Atherthon HJ, Dodd MS, Lee P, Cochlin LE, Radda GK, Clarke K, Tyler DJ. Circ Cardiovasc Imaging. 2012;5:201–9.
Schumann-Giamperi G. Invest Radiol. 1993;28:753–61.
Senadheera L, Mayer D, Darpolor MM, Yen Y, Luong R, Spielman DM, Xing L. I J Rad Oncol Biol Physics. 2010;78:S116.
Shchepin RV, Coffey AM, Waddell KW, Chekmenev EY. Parahydrogen induced polarization of 1-(13) C-phospholactate-d(2) for biomedical imaging with >30,000,000-fold NMR signal enhancement in water. Anal Chem. 2014a;86:5601–5.
Shchepin RV, Pham W, Chekmenev EY. J Label Compd Radiopharm. 2014b;57:517–24.
Sipkins DA, Cheresh DA, Kazemi MR, Nevin LM, Bednarski MD, Li KCP. Nat Med. 1998;4:623–6.
Song Y, Kohlmeir EK, Meade TJ. J Am Chem Soc. 2008;130:6662–3.
Spence MM, Rubin SM, Dimitrov IE, Ruiz EJ, Wemmer DE, Pines A, Yaoi SO, Tiani F, Schultzi PG. Proc Natl Acad Sci U S A. 2001;98:10654–7.
Stevens TK, Palaniappan KK, Ramirez M, Francis MB, Wemmer DE, Pines A. Magn Reson Med. 2013;69:1245–52.
Strijkers GJ, Kluza E, Van Tilborg GAF, Geralda AF, van der Schaft DWJ, Griffioen AW, Mulder WJM, Nicolay K. Angiogenesis. 2010;13:161–73.

Swanson SD, Rosen MS, Agranoff BW, Coulter KP, Welsh RC, Chupp TE. Magn Reson Med. 1997; 38:695–8.
Taratula O, Dmochowski JJ. Curr Opin Chem Biol. 2010;14:97–104.
Terreno E, Delli Castelli D, Cravotto G, Milone L, Aime S. Invest Radiol. 2004;39:235–43.
Terreno E, Cabella C, Carrera C, Delli Castelli D, Mazzon R, Rollet S, Stancanello J, Visigalli M, Aime S. Angew Chem Int Ed. 2007a;46:966–8.
Terreno E, Cabella C, Carrera C, Delli Castelli D, Lanzardo S, Mazzon R, Rollet S, Visigalli M, Aime S Proceeding joint annual meeting ISMRM-ESMRM. 2007b, Berlin, Germany, p. 248.
Terreno E, Barge A, Beltrami L, Cravotto G, Delli Castelli D, Fedeli F, Jebasingh B, Aime S. Chem Commun. 2008a;7:600–2.
Terreno E, Delli Castelli D, Milone L, Rollet S, Stancanello J, Violante E, Aime S. Contrast Media Mol Imaging. 2008b;3:38–43.
Terreno E, Sanino A, Carrera C, Delli Castelli D, Giovenzana GB, Lombardi A, Mazzon R, Milone L, Visigalli M, Aime S. J Inorg Biochem. 2008c;102:1112–9.
Tsitovich PB, Burns PJ, McKay AM, Morrow JR. J Inorg Biochem. 2014;133:143–54.
Tweedle MF. In: Bünzli JCG, Choppin GR, editors. Lanthanide probes in life, chemical and earth sciences: theory and practice. Amsterdam: Elsevier; 1989.
Uggeri F, Aime S, Anelli PL, Botta M, Brocchetta M, de Haeen C, Ermondi G, Grandi M, Paoli P. Inorg Chem. 1995;34:633–43.
Vasalatiy O, Gerard RD, Zhao P, Sun X, Sherry AD. Bioconjug Chem. 2008;19:598–606.
Vengatesh HS, Chaumeil MM, Ward CS, Haas-Kogan DA, James CD, Ronen SM. Neuro Oncol. 2012;14:315–25.
von Morze C, Larson PEZ, Hu S, Keshari K, Wilson DM, Ardenkiaer-Larse JE, Goga A, Bok R, Kuhanewicz J, Vigneron DB. J Magn Reson Imaging. 2011;33:692–7.
von Morze C, Bok R, Sands JM, Kurhanewicz J, Vigneron DB. Am J Renal Physiol. 2012a;302:F1658–62.
von Morze C, Larson PEZ, Hu S, Yoshihara HAI, Bok R, Goga A, Ardenkjaer-Larsen JH, Vigneron DB. Magn Reson Imaging. 2012b;30:305–11.
Walker-Samuel S, Ramasawmy R, Torrealdea F, Rega M, Rajkumar V, Johnson SP, Richardson S, Goncalves M, Parkes HG, Arstad E. Nat Med. 2013;19:1067–72.
Ward KM, Balaban RS. Magn Reson Med. 2000;44:799–802.
Ward KM, Aletras AH, Balaban RS. J Magn Reson. 2000;143:79–87.
Weinmann HJ, Mühler A, Radüchel B. In: Young IR, editors. Biomedical magnetic resonance imaging and spectroscopy. Chichester: John Wiley & Sons LTD; 2000.
Weissleder R, Mahmood U. Radiology. 2001;219:316–33.
Wilson DM, Keshari KR, Larson PEZ, Chen AP, Hu S, Van Criekinge M, Bok R, Nelson SJ, Maddonald JM, Vigneron DB, Kurhanewicz J. J Magn Reson. 2010;205:141–7.
Winter PM, Cai K, Chen J, Adair CR, Kiefer GE, Athey PS, Gaffney PJ, Buff CE, Robertson JD, Caruthers SD, Wickline SA, Lanza GM. Magn Reson Med. 2006;56:1384–8.
Witney TH, Kettunen MI, Day SE, Hu D, Neves AA, Gallagher FA, Fulton SM, Brindle KM. Neoplasia. 2009;11:574–82.
Witney TH, Kettunen MI, Hu D-E, Gallagher FA, Bohndiek SE, Napolitano R, Brindle KM. Br J Canc. 2010;103:1400–6.
Woessner DE, Zhang S, Merritt ME, Sherry AD. Magn Reson Med. 2005;53:790–9.
Wolber J, Rowland IJ, Leach MO, Bifone A. Magn Reson Med. 1999;41:442–9.
Wolber J, Cherubini A, Leach MO, Bifone A. Magn Reson Med. 2000;43:491–6.
Woods M, Woessner DE, Zhao P, Pasha A, Yang MY, Huang CH, Vasalitiy O, Morrow JR, Sherry AD. J Am Chem Soc. 2006;128:10155–62.
Yen Y-F, Le Roux P, Mayer D, King R, Spielman D, Tropp J, Butts Pauly K, Pfefferbaum A, Vasanawala S, Hurd R. NMR Biomed. 2010;23:414–23.
Zacharias NM, Chan HR, Sailasuta N, Ross BD, Bhattacharya P. J Am Chem Soc. 2012a;134:934–943.
Zandt R. et al. Abstracts n. 4380 and 4381, 17th ISMRM scientific meeting & exhibition, Honolulu, Hawaii (USA), 18–24 Apr 2009.
Zhang SR, Wu KC, Sherry AD. Angew Chem Int Ed. 1999;38:3192–4.
Zhang S, Winter P, Wu K, Sherry AD. J Am Chem Soc. 2001;123:1517–8.
Zhang ZD, Greenfield M, Spiller TJ, McMurry RB, Lauffer RB, Caravan P. Angew Chem Int Ed. 2005;44:6766–9.

In Vivo Magnetic Resonance Imaging and Spectroscopy with Hyperpolarized Agents

Abragam A, Goldman M. Principles of dynamic nuclear-polarization. Rep Prog Phys. 1978;41(3):395–467.
Adams RW, Aguilar JA, Atkinson KD, Cowley MJ, Elliott PIP, Duckett SB, et al. Reversible interactions with Para-hydrogen enhance NMR sensitivity by polarization transfer. Science. 2009b;323(5922):1708–11.
Adams RW, Duckett SB, Green RA, Williamson DC, Green GGR. A theoretical basis for spontaneous polarization transfer in non-hydrogenative parahydrogen-induced polarization. J Chem Phys. 2009c;131(19):194505–15.
Adriany G, Gruetter R. A half-volume coil for efficient proton decoupling in humans at 4 Tesla. J Magn Reson. 1997;125(1):178–84.

Agraz J, Grunfeld A, Cunningham K, Li D, Wagner S. Improved PHIP polarization using a precision, low noise, voltage controlled current source. J Magn Reson. 2013;235:77–84.

Allouche-Arnon H, Lerche MH, Karlsson M, Lenkinski RE, Katz-Brull R. Deuteration of a molecular probe for DNP hyperpolarization – a new approach and validation for choline chloride. Contrast Media Mol Imaging. 2011;6(6):499–506.

Ardenkjær-Larsen JH, Fridlund B, Gram A, Hansson G, Hansson L, Lerche MH, et al. Increase in signal-to-noise ratio of > 10,000 times in liquid-state NMR. Proc Natl Acad Sci. 2003c;100(18):10158–63.

Ardenkjaer-Larsen J-H, Golman K, Brindle KM. Hyperpolarized 13C magnetic resonance imaging – principles and applications. In: Weissleder R, Ross, Rehemtulla A, Gambhir SS, editors. Molecular imaging: principles and practice. Shelton: PMPH-USA; 2010.

Ardenkjaer-Larsen JH, Johannesson H, Petersson JS, Wolber J. Hyperpolarized molecules in solutions. In: Faber C, Schroeder L, editors. In vivo MR imaging: methods and protocols. Methods in molecular biology. New York: Springer; 2011a.

Ardenkjaer-Larsen JH, Johanneson H, Petersson JS, Wolber J. Applications of hyperpolarized agents in solutions. In: Faber C, Schroeder L, editors. Methods in molecular biology. New York: Springer; 2011b.

Ardenkjaer-Larsen JH, Leach AM, Clarke N, Urbahn J, Anderson D, Skloss TW. Dynamic nuclear polarization polarizer for sterile use intent. NMR Biomed. 2011c;24(8):927–32.

Bachert P, Bellemann ME, Layer G, Koch T, Semmler W, Lorenz W. In vivo 1H, 31P-{1H} and 13C-{1H} magnetic resonance spectroscopy of malignant histiocytoma and skeletal muscle tissue in man. NMR Biomed. 1992;5:161–70.

Ball DR, Rowlands B, Dodd MS, Le Page L, Ball V, Carr CA, et al. Hyperpolarized butyrate: a metabolic probe of short chain fatty acid metabolism in the heart. Magn Reson Med Off J Soc Magn Reson Med Soc Magn Reson Med. 2014;71(5):1663–9.

Bär S, Lange T, Leibfritz D, Hennig J, von Elverfeldt D, Hövener J-B. On the spin order transfer from parahydrogen to another nucleus. J Magn Reson. 2012;225:25–35.

Barskiy DA, Shchepin RV, Coffey AM, Theis T, Warren WS, Goodson BM, Chekmenev EY. Over 20% 15N hyperpolarization in under one minute for metronidazole, an antibiotic and hypoxia probe. J. Am. Chem. Soc. 2016;138:8080–83.

Bastiaansen JAM, Cheng T, Mishkovsky M, Duarte JMN, Comment A, Gruetter R. In vivo enzymatic activity of acetylCoA synthetase in skeletal muscle revealed by 13C turnover from hyperpolarized [1-13C]acetate to [1-13C]acetylcarnitine. Biochim Biophys Acta BBA Gen Subj. 2013;1830(8):4171–8.

Bastiaansen JAM, Yoshihara HAI, Takado Y, Gruetter R, Comment A. Hyperpolarized 13C lactate as a substrate for in vivo metabolic studies in skeletal muscle. Metabolomics. 2014;6:1–9.

Bastiaansen JAM, Cheng T, Lei H, Gruetter R and Comment A. Direct noninvasive estimation of myocardial tricarboxylic acid cycle flux in vivo using hyperpolarized ^{13}C magnetic resonance. Journal of Molecular and Cellular Cardiology. 2015;87:129–37.

Bastiaansen JAM, Merritt M, Comment A. Measuring changes in substrate utilization in the myocardium in response to fasting using hyperpolarized [1-^{13}C]butyrate and [1-^{13}C]pyruvate. Scientific Reports. 2016; 6:25573. doi:10.1038/srep25573.

Batel M, Krajewski M, Weiss K, With O, Däpp A, Hunkeler A, et al. A multi-sample 94 GHz dissolution dynamic-nuclear-polarization system. J Magn Reson. 2012;214:166–74.

Beeson H, Woods S. Guide for hydrogen hazards analysis on components and systems. NASA Johns space cent tex 77058-3696. 2003;TP-WSTF-937.

Bhattacharya P, Chekmenev EY, Reynolds WF, Wagner S, Zacharias N, Chan HR, et al. Parahydrogen-induced polarization (PHIP) hyperpolarized MR receptor imaging in vivo: a pilot study of 13C imaging of atheroma in mice. NMR Biomed. 2011b;24(8):1023–8.

Bonhoeffer KF, Harteck P. Characteristics of parahydrogen. Z Elektrochem Angew Phys Chem. 1929;35:621–3.

Borowiak R, Schwaderlapp N, Huethe F, Fischer E, Lickert T, Bär S, et al. A battery-driven, low-field NMR unit for thermally and hyperpolarized samples. Magn Reson Mater Phys Biol Med. 2013;26(5):491–9.

Bowers CR. Sensitivity enhancement utilizing parahydrogen. Encyclopedia of magnetic resonance [Internet]. John Wiley & Sons, Ltd; 2007 [cited 2013 Jan 23]. Available from: http://onlinelibrary.wiley.com/doi/10.1002/9780470034590.emrstm0489/abstract.

Bowers CR, Weitekamp DP. Transformation of symmetrization order to nuclear-spin magnetization by chemical reaction and nuclear magnetic resonance. Phys Rev Lett. 1986;57(21):2645–8.

Bowers CR, Weitekamp DP. Para-hydrogen and synthesis allow dramatically enhanced nuclear alignment. J Am Chem Soc. 1987;109(18):5541–2.

Bretthorst GL. Bayesian analysis. I. Parameter estimation using quadrature NMR models. J Magn Reson 1969. 1990;88(3):533–51.

Cai C, Coffey AM, Shchepin RV, Chekmenev EY, Waddell KW. Efficient transformation of parahydrogen spin order into heteronuclear magnetization. J Phys Chem B. 2013;117(5):1219–24.

Canet D, Aroulanda C, Mutzenhardt P, Aime S, Gobetto R, Reineri F. Para-hydrogen enrichment and hyperpolarization. Concepts Magn Reson A. 2006;28A(5):321–30.

Cassidy MC, Chan HR, Ross BD, Bhattacharya PK, Marcus CM. In vivo magnetic resonance imaging of hyperpolarized silicon particles. Nat Nanotechnol. 2013;8(5):363–8.

Chekmenev EY, Hövener J, Norton VA, Harris K, Batchelder LS, Bhattacharya P, et al. PASADENA hyperpolarization of succinic acid for MRI and NMR spectroscopy. J Am Chem Soc. 2008b; 130(13):4212–3.

Chekmenev EY, Chow SK, Tofan D, Weitekamp DP, Ross BD, Bhattacharya P. Fluorine-19 NMR chemical shift probes molecular binding to lipid membranes. J Phys Chem. 2008c;112:6285–7.

Chen AP, Albers MJ, Cunningham CH, Kohler SJ, Yen Y-F, Hurd RE, et al. Hyperpolarized C-13 spectroscopic imaging of the TRAMP mouse at 3T—Initial experience. Magn Reson Med. 2007b;58(6):1099–106.

Chen AP, Kurhanewicz J, Bok R, Xu D, Joun D, Zhang V, et al. Feasibility of using hyperpolarized [1-13C] lactate as a substrate for in vivo metabolic 13C MRSI studies. Magn Reson Imaging. 2008b;26(6):721–6.

Cheng T, Capozzi A, Takado Y, Balzan R, Comment A. Over 35% liquid-state 13C polarization obtained via dissolution dynamic nuclear polarization at 7 T and 1 K using ubiquitous nitroxyl radicals. Phys Chem Chem Phys. 2013a;15(48):20819–22.

Cheng T, Mishkovsky M, Bastiaansen JAM, Ouari O, Hautle P, Tordo P, et al. Automated transfer and injection of hyperpolarized molecules with polarization measurement prior to in vivo NMR. NMR Biomed. 2013b;26(11):1582–8.

Chiavazza E, Kubala E, Gringeri CV, Düwel S, Durst M, Schulte RF, et al. Earth's magnetic field enabled scalar coupling relaxation of 13C nuclei bound to fast-relaxing quadrupolar 14N in amide groups. J Magn Reson San Diego Calif 1997. 2013;227:35–8.

Coffey AM, Kovtunov KV, Barskiy DA, Koptyug IV, Shchepin RV, Waddell KW, et al. High-resolution low-field molecular magnetic resonance imaging of hyperpolarized liquids. Anal Chem. 2014;86(18):9042–9.

Coffey AM, Shchepin RV, Truong ML, Wilkens K, Pham W, Chekmenev EY. Open-source automated parahydrogen hyperpolarizer for molecular imaging using 13C metabolic contrast agents. Anal Chem. 2016;88:8279–88.

Comment A. Chapter 9 hyperpolarization: concepts, techniques and applications. New applications of NMR in drug discovery and development [Internet]. 2013 [cited 2015 Jan 1]. Available from: http://pubs.rsc.org/en/content/chapter/bk9781849734448-00252/978-1-84973-444-8.

Comment A, Merritt ME. Hyperpolarized magnetic resonance as a sensitive detector of metabolic function. Biochemistry (Mosc). 2014;53(47):7333–57.

Comment A, van den Brandt B, Uffmann K, Kurdzesau F, Jannin S, Konter JA, et al. Design and performance of a DNP prepolarizer coupled to a rodent MRI scanner. Concepts Magn Reson Part B Magn Reson Eng. 2007b;31B(4):255–69.

Comment A, van den Brandt B, Uffmann K, Kurdzesau F, Jannin S, Konter JA, et al. Principles of operation of a DNP prepolarizer coupled to a rodent MRI scanner. Appl Magn Reson. 2008;34(3-4):313–9.

Cowley MJ, Adams RW, Atkinson KD, Cockett MCR, Duckett SB, Green GGR, et al. Iridium N-Heterocyclic carbene complexes as efficient catalysts for magnetization transfer from para-hydrogen. J Am Chem Soc. 2011;133(16):6134–7.

Cunningham CH, Lau JY, Chen AP, Geraghty BJ, Perks WJ, Roifman I, Wright GA, Connelly KA. Hyperpolarized 13C metabolic MRI of the human heart: initial experience. Circulation Research 2016:CIRCRESAHA.116.309769.

Cunningham CH, Chen AP, Albers MJ, Kurhanewicz J, Hurd RE, Yen Y-F, et al. Double spin-echo sequence for rapid spectroscopic imaging of hyperpolarized 13C. J Magn Reson. 2007;187(2):357–62.

Davies B, Morris T. Physiological parameters in laboratory animals and humans. Pharm Res. 1993;10(7):1093–5.

Day SE, Kettunen MI, Gallagher FA, Hu D-E, Lerche M, Wolber J, et al. Detecting tumor response to treatment using hyperpolarized 13C magnetic resonance imaging and spectroscopy. Nat Med. 2007b;13(11):1382–7.

Dementyev AE, Cory DG, Ramanathan C. Dynamic nuclear polarization in silicon microparticles. Phys Rev Lett. 2008;100(12):127601.

Diehl K-H, Hull R, Morton D, Pfister R, Rabemampianina Y, Smith D, et al. A good practice guide to the administration of substances and removal of blood, including routes and volumes. J Appl Toxicol. 2001;21(1):15–23.

Duarte JMN, Gruetter R. Glutamatergic and GABAergic energy metabolism measured in the rat brain by 13C NMR spectroscopy at 14.1 T. J Neurochem. 2013;126(5):579–90.

Duckett SB, Sleigh CJ. Applications of the parahydrogen phenomenon: a chemical perspective. Prog Nucl Magn Reson Spectrosc. 1999;34(1):71–92.

Duckett SB, Mewis RE. Application of parahydrogen induced polarization techniques in NMR spectroscopy and imaging. Acc Chem Res. 2012;45(8):1247–57.

Durst M, Koellisch U, Frank A, Rancan G, Gringeri CV, Karas V, Wiesinger F, Menzel MI, Schwaiger M, Haase A, Schulte RF. Comparison of acquisition schemes for hyperpolarised 13C imaging. NMR Biomed. 2015;28:715–25.

Eisenschmid TC, Kirss RU, Deutsch PP, Hommeltoft SI, Eisenberg R, Bargon J, et al. parahydrogen induced polarization in hydrogenation reactions. J Am Chem Soc. 1987;109(26):8089–91.

Emondts M, Ledbetter MP, Pustelny S, Theis T, Patton B, Blanchard JW, et al. Long-lived heteronuclear spin-singlet states in liquids at a zero magnetic field. Phys Rev Lett. 2014;112(7):077601.

Evelhoch JL, Crowley MG, Ackerman JJH. Signal-to-noise optimization and observed volume localization with circular surface coils. J Magn Reson 1969. 1984;56(1):110–24.

Farkas A. The thermal parahydrogen conversion. Z Phys Chem B Chem Elem Aufbau Mater. 1930;10(6):419–33.

Feng B, Coffey A, Colon R, Chekmenev EY, Waddell K. A pulsed injection parahydrogen generator and techniques for quantifying enrichment. J Magn Reson. 2012a;214:258–62.

Feng Y, Davis RM, Warren WS. Accessing long-lived nuclear singlet states between chemically equivalent spins without breaking symmetry. Nat Phys. 2012b;8(11):831–7.

Freundlich A, Bhattacharya P, Techy G, Ward B, Ingram M, Ross BD. Rapid toxicity screening of novel PASADENA MRI contrast agents. Proc Intl Soc Mag Reson Med 14. Seattle; 2006.

Gallagher FA, Kettunen MI, Day SE, Hu D-E, Ardenkjær-Larsen JH, Zandt R, et al. Magnetic resonance imaging of pH in vivo using hyperpolarized 13C-labelled bicarbonate. Nature. 2008c;453(7197):940–3.

Gallagher FA, Kettunen MI, Hu D-E, Jensen PR, Zandt R, Karlsson M, et al. Production of hyperpolarized [1,4-13C2]malate from [1,4-13C2]fumarate is a marker of cell necrosis and treatment response in tumors. Proc Natl Acad Sci. 2009;106(47):19801–6.

Gamliel A, Allouche-Arnon H, Nalbandian R, Barzilay C, Gomori J, Katz-Brull R. An apparatus for production of isotopically and spin-enriched hydrogen for induced polarization studies. Appl Magn Reson. 2010;39(4):329–45.

Glöggler S, Grunfeld AM, Ertas YN, McCormick J, Wagner S, Schleker PPM, et al. A nanoparticle catalyst for heterogeneous phase para-hydrogen-induced polarization in water. Angew Chem Int Ed. 2015;54:1–6.

Goldman M, Johannesson H. Conversion of a proton pair para order into C-13 polarization by rf irradiation, for use in MRI. Comptes Rendus Phys. 2005b;6(4-5):575–81.

Goldman M, Jóhannesson H, Axelsson O, Karlsson M. Hyperpolarization of 13C through order transfer from parahydrogen: a new contrast agent for MRI. Magn Reson Imaging. 2005b;23(2):153–7.

Goldman M, Johannesson H, Axelsson O, Karlsson M. Design and implementation of C-13 hyperpolarization from para-hydrogen, for new MRI contrast agents. Comptes Rendus Chim. 2006;9(3-4):357–63.

Golman K, Axelsson O, Jóhannesson H, Månsson S, Olofsson C, Petersson JS. parahydrogen-induced polarization in imaging: subsecond 13C angiography. Magn Reson Med. 2001b;46(1):1–5.

Golman K, Axelsson O, Johanneson H, Olofsson C, Mansson S, Petersson S. Para-hydrogen labelled agents and their use in magnetic resonance imaging [Internet]. 6574495, 2003a [cited 2012 Oct 29]. Available from: http://www.google.com/patents/US6574495.

Golman K, Olsson LE, Axelsson O, Mansson S, Karlsson M, Petersson JS. Molecular imaging using hyperpolarized 13C. Br J Radiol. 2003b;76:118–27.

Golman K, Zandt R, Thaning M. Real-time metabolic imaging. Proc Natl Acad Sci U S A. 2006b;103(30):11270–5.

Golman K, Zandt R, Lerche M, Pehrson R, Ardenkjaer-Larsen JH. Metabolic imaging by hyperpolarized C-13 magnetic resonance imaging for in vivo tumor diagnosis. Cancer Res. 2006c;66(22):10855–60.

Grant AK, Vinogradov E, Wang X, Lenkinski RE, Alsop DC. Perfusion imaging with a freely diffusible hyperpolarized contrast agent. Magn Reson Med. 2011;66(3):746–55.

Gruetter R, Tkáč I. Field mapping without reference scan using asymmetric echo-planar techniques. Magn Reson Med. 2000;43(2):319–23.

Haake M, Natterer J, Bargon J. Efficient NMR pulse sequences to transfer the parahydrogen-induced polarization to hetero nuclei. J Am Chem Soc. 1996;118(36):8688–91.

Happer W. Optical pumping. Rev Mod Phys. 1972;44(2):169–249.

Harrison C, Yang C, Jindal A, DeBerardinis RJ, Hooshyar MA, Merritt M, et al. Comparison of kinetic models for analysis of pyruvate-to-lactate exchange by hyperpolarized 13C NMR. NMR Biomed. 2012;25(11):1286–94.

Hirsch ML, Kalechofsky N, Belzer A, Rosay M, Kempf JG. Brute-force hyperpolarization for NMR and MRI. J Am Chem Soc. 2015;137:8428–34.

Hommeltoft SI, Berry DH, Eisenberg R. A metal-centered radical-pair mechanism for alkyne hydrogenation with a binuclear rhodium hydride complex – CIDNP without organic radicals. J Am Chem Soc. 1986;108(17):5345–7.

Hövener J-B. Strategies to prolong the T1 time of hyperpolarized molecules. Proceedings of the 16th annual meeting of ISMRM. Toronto; 2008. p. 336.

Hövener J-B, Chekmenev EY, Harris KC, Perman WH, Tran TT, Ross BD, et al. Quality assurance of PASADENA hyperpolarization for 13C biomolecules. Magn Reson Mater Biol Phys Med. 2009a;22(2):123–34.

Hövener J-B, Chekmenev E, Harris K, Perman W, Robertson L, Ross B, et al. PASADENA hyperpolarization of 13C biomolecules: equipment design and installation. Magn Reson Mater Phys Biol Med. 2009b;22(2):111–21.

Hövener J-B, Bär S, Leupold J, Jenne K, Leibfritz D, Hennig J, et al. A continuous-flow, high-throughput, high-pressure parahydrogen converter for hyperpolarization in a clinical setting. NMR Biomed. 2013a;26(2):124–31.

Hövener J-B, Schwaderlapp N, Lickert T, Duckett SB, Mewis RE, Highton LAR, et al. A hyperpolarized equilibrium for magnetic resonance. Nat Commun [Internet]. 2013 December [cited 2013 Dec 16];4:2946. Available from: http://www.nature.com/ncomms/2013/131216/ncomms3946/full/ncomms3946.html.

Hövener J-B, Knecht S, Schwaderlapp N, Hennig J, von Elverfeldt D. Continuous re-hyperpolarization of nuclear spins using parahydrogen: theory and experiment. Chemphyschem. 2014a;15:2451–7.

Hövener J-B, Schwaderlapp N, Borowiak R, Lickert T, Duckett SB, Mewis RE, et al. Toward biocompatible nuclear hyperpolarization using signal amplification by reversible exchange: quantitative in situ spectroscopy and high-field imaging. Anal Chem. 2014b;86(3):1767–74.

Hu S, Larson PEZ, VanCriekinge M, Leach AM, Park I, Leon C, et al. Rapid sequential injections of hyperpolarized [1-13C]pyruvate in vivo using a sub-kelvin,

multi-sample DNP polarizer. Magn Reson Imaging. 2013;31(4):490–6.
Hund F. On the explanation of molecular spectra I. Z Phys. 1927;40(10):742–64.
Hurd RE, Yen Y-F, Chen A, Ardenkjaer-Larsen JH. Hyperpolarized 13C metabolic imaging using dissolution dynamic nuclear polarization. J Magn Reson Imaging. 2012;36(6):1314–28.
Invento. Parahyperpol, [Internet]. Available from: http://www.invento-lab.com/ParaHyperpol.html.
Jannin S, Comment A, Kurdzesau F, Konter JA, Hautle P, van den Brandt B, et al. A 140GHz prepolarizer for dissolution dynamic nuclear polarization. J Chem Phys. 2008;128(24):241102.
Jensen PR, Peitersen T, Karlsson M, Zandt R, Gisselsson A, Hansson G, et al. Tissue-specific short chain fatty acid metabolism and slow metabolic recovery after ischemia from hyperpolarized NMR in vivo. J Biol Chem. 2009;284(52):36077–82.
Jindal AK, Merritt ME, Suh EH, Malloy CR, Sherry AD, Kovács Z. Hyperpolarized 89Y complexes as pH sensitive NMR probes. J Am Chem Soc. 2010;132(6):1784–5.
Johannesson H, Axelsson O, Karlsson M. Transfer of para-hydrogen spin order into polarization by diabetic field cycling. C R Phys. 2004b;5(3):315–24.
Jóhannesson H, Macholl S, Ardenkjaer-Larsen JH. Dynamic nuclear polarization of [1-13C]pyruvic acid at 4.6 tesla. J Magn Reson. 2009;197(2):167–75.
Johansson E, Månsson S, Wirestam R, Svensson J, Petersson JS, Golman K, et al. Cerebral perfusion assessment by bolus tracking using hyperpolarized 13C. Magn Reson Med. 2004b;51(3):464–72.
Johnson RT, Paulson DN, Giffard RP, Wheatley JC. Bulk nuclear polarization of solid3He. J Low Temp Phys. 1973;10(1-2):35–58.
Josan S, Yen Y-F, Hurd R, Pfefferbaum A, Spielman D, Mayer D. Application of double spin-echo spiral chemical shift imaging to rapid metabolic mapping of hyperpolarized [1-13C]-pyruvate. J Magn Reson San Diego Calif 1997. 2011;209(2):332–6.
Kadlecek S, Emami K, Ishii M, Rizi R. Optimal transfer of spin-order between a singlet nuclear pair and a heteronucleus. J Magn Reson. 2010;205(1):9–13.
Kadlecek S, Vahdat V, Nakayama T, Ng D, Emami K, Rizi R. A simple and low-cost device for generating hyperpolarized contrast agents using parahydrogen. NMR Biomed. 2011;24(8):933–42.
Keshari KR, Wilson DM. Chemistry and biochemistry of 13C hyperpolarized magnetic resonance using dynamic nuclear polarization. Chem Soc Rev. 2014;43(5):1627–59.
Keshari KR, Kurhanewicz J, Bok R, Larson PEZ, Vigneron DB, Wilson DM. Hyperpolarized 13C dehydroascorbate as an endogenous redox sensor for in vivo metabolic imaging. Proc Natl Acad Sci. 2011b;108(46):18606–11.
Khegai O, Schulte RF, Janich MA, Menzel MI, Farrell E, Otto AM, et al. Apparent rate constant mapping using hyperpolarized [1-(13)C]pyruvate. NMR Biomed. 2014;27(10):1256–65.
Kinrade SD, Swaddle TW. Mechanisms of longitudinal silicon-29 nuclear magnetic relaxation in aqueous alkali-metal silicate solutions. J Am Chem Soc. 1986;108(23):7159–62.
Koellisch U, Gringeri CV, Rancan G, Farell EV, Menzel MI, Haase A, et al. Metabolic imaging of hyperpolarized [1-13C]acetate and [1-13C]acetylcarnitine - investigation of the influence of dobutamine induced stress. Magn Reson Med. 2015;74:1011–8.
Kohler SJ, Yen Y, Wolber J, Chen AP, Albers MJ, Bok R, et al. In vivo 13carbon metabolic imaging at 3T with hyperpolarized 13C-1-pyruvate. Magn Reson Med. 2007;58(1):65–9.
Koptyug IV, Kovtunov KV, Burt SR, Anwar MS, Hilty C, Han S-I, et al. para-hydrogen-induced polarization in heterogeneous hydrogenation reactions. J Am Chem Soc. 2007;129(17):5580–6.
Koptyug IV, Zhivonitko VV, Kovtunov KV. New perspectives for parahydrogen-induced polarization in liquid phase heterogeneous hydrogenation: an aqueous phase and ALTADENA study. Chemphyschem. 2010;11(14):3086–8.
Kovtunov KV, Beck IE, Bukhtiyarov VI, Koptyug IV. Observation of parahydrogen-induced polarization in heterogeneous hydrogenation on supported metal catalysts. Angew Chem Int Ed. 2008;47(8):1492–5.
Kovtunov KV, Koptyug IV. Parahydrogen-induced polarization in heterogeneous catalytic hydrogenations. In: Codd SL, Seymour JD, editors. Magnetic resonance microscopy [Internet]. Wiley-VCH Verlag GmbH & Co. KGaA; 2009 [cited 22 Mar 2013]. p. 99–115. Available from: http://onlinelibrary.wiley.com/doi/10.1002/9783527626052.ch7/summary.
Kurhanewicz J, Vigneron DB, Brindle K, Chekmenev EY, Comment A, Cunningham CH, et al. Analysis of cancer metabolism by imaging hyperpolarized nuclei: prospects for translation to clinical research. Neoplasia N Y N. 2011;13(2):81–97.
Larson PE, Kerr AB, Chen AP, Lustig MS, Zierhut ML, Hu S, et al. Multiband excitation pulses for hyperpolarized 13C dynamic chemical-shift imaging. J Magn Reson. 2008b;194(1):121–7.
Lego D, Plaumann M, Trantzschel T, Bargon J, Scheich H, Buntkowsky G, et al. Parahydrogen-induced polarization of carboxylic acids: a pilot study of valproic acid and related structures. NMR Biomed. 2014;27(7):810–6.
Leupold J, Månsson S, Petersson JS, Hennig J, Wieben O. Fast multiecho balanced SSFP metabolite mapping of 1H and hyperpolarized 13C compounds. Magn Reson Mater Phys Biol Med. 2009;22(4):251–6.
Lickert T, Schwaderlapp N, Bär S, Leupold J, Hennig J, Korvink J, et al. 13C-hyperpolarization by transferring parahydrogen spin order on a 7 T MRI-system. 16 Jahrestagung der DS ISMRM. Freiburg, Germany; 2013.

Lingwood MD, Siaw TA, Sailasuta N, Abulseoud OA, Chan HR, Ross BD, et al. Hyperpolarized water as an MR imaging contrast agent: feasibility of in vivo imaging in a Rat model. Radiology. 2012;265(2):418–25.

Lumata LL, Martin R, Jindal AK, Kovacs Z, Conradi MS, Merritt ME. Development and performance of a 129-GHz dynamic nuclear polarizer in an ultra-wide bore superconducting magnet. Magn Reson Mater Phys Biol Med. 2014;14:1–11.

Mayer D, Levin YS, Hurd RE, Glover GH, Spielman DM. Fast metabolic imaging of systems with sparse spectra: application for hyperpolarized 13C imaging. Magn Reson Med Off J Soc Magn Reson Med Soc Magn Reson Med. 2006;56(4):932–7.

Mayer D, Yen Y-F, Josan S, Park JM, Pfefferbaum A, Hurd RE, et al. Application of hyperpolarized [1-13C] lactate for the in vivo investigation of cardiac metabolism. NMR Biomed. 2012b;25(10):1119–24.

McCarney ER, Armstrong BD, Lingwood MD, Han S. Hyperpolarized water as an authentic magnetic resonance imaging contrast agent. Proc Natl Acad Sci. 2007;104(6):1754–9.

McRobbie DW, Moore EA, Graves MJ, Prince MR. MRI from picture to proton. New York: Cambridge University Press; 2006. p. 416.

Merritt ME, Harrison C, Storey C, Jeffrey FM, Sherry AD, Malloy CR. Hyperpolarized 13C allows a direct measure of flux through a single enzyme-catalyzed step by NMR. Proc Natl Acad Sci. 2007c;104(50):19773–7.

Mewis RE, Atkinson KD, Cowley MJ, Duckett SB, Green GGR, Green RA, et al. Probing signal amplification by reversible exchange using an NMR flow system. Magn Reson Chem. 2014;52:358–69.

Nabuurs C, Huijbregts B, Wieringa B, Hilbers CW, Heerschap A. 31P saturation transfer spectroscopy predicts differential intracellular macromolecular association of ATP and ADP in skeletal muscle. J Biol Chem. 2010;285(51):39588–96.

Naressi A, Couturier C, Devos JM, Mangeat C, de Beer R, Graveron-Demilly D. Java-based graphical user interface for the MRUI quantitation package. Magn Reson Mater Biol Phys Med. 2001;2-3:141–52.

Natterer J, Bargon J. Parahydrogen induced polarization. Prog Nucl Magn Reson Spectrosc. 1997;31:293–315.

Nelson SJ, Kurhanewicz J, Vigneron DB, Larson PEZ, Harzstark AL, Ferrone M, et al. Metabolic imaging of patients with prostate cancer using hyperpolarized [1-13C]Pyruvate. Sci Transl Med. 2013b;5(198):198ra108.

Nelson SJ, Ozhinsky E, Li Y, Park IW, Crane J. Strategies for rapid in vivo 1H and hyperpolarized 13C MR spectroscopic imaging. J Magn Reson San Diego Calif 1997. 2013c;229:187–97.

Nonaka H, Hata R, Doura T, Nishihara T, Kumagai K, Akakabe M, et al. A platform for designing hyperpolarized magnetic resonance chemical probes. Nat Commun [Internet]. 2013 [cited 2013 Nov 8];4:2411. Available from: http://www.nature.com/ncomms/2013/130911/ncomms3411/full/ncomms3411.html.

Norton VA. Efficient generation of hyperpolarized molecules utilizing the scalar order of parahydrogen [Internet] [phd]. California Institute of Technology; 2010 [cited 2014 Mar 4]. Available from: http://resolver.caltech.edu/CaltechTHESIS:05212010-154212167.

Olsson LE, Chai C-M, Axelsson O, Karlsson M, Golman K, Petersson JS. MR coronary angiography in pigs with intraarterial injections of a hyperpolarized 13C substance. Magn Reson Med. 2006;55(4):731–7.

Pfeuffer J, Tkáč I, Provencher SW, Gruetter R. Toward an in vivo neurochemical profile: quantification of 18 metabolites in short-echo-time 1H NMR spectra of the rat brain. J Magn Reson. 1999;141(1):104–20.

Pileio G, Levitt MH. Theory of long-lived nuclear spin states in solution nuclear magnetic resonance. II. Singlet spin locking. J Chem Phys. 2009;130(21):214501 – 14.

Pravica MG, Weitekamp DP. Net Nmr alignment by adiabatic transport of Para-hydrogen addition-products to high magnetic-field. Chem Phys Lett Chem Phys Lett. 1988;145(4):255–8.

Reineri F, Viale A, Giovenzana G, Santelia D, Dastru W, Gobetto R, et al. New hyperpolarized contrast agents for 13C-MRI from para-hydrogenation of oligooxyethylenic alkynes. J Am Chem Soc. 2008;130(45):15047–53.

Reineri F, Santelia D, Viale A, Cerutti E, Poggi L, Tichy T, et al. Para-hydrogenated glucose derivatives as potential 13C-hyperpolarized probes for magnetic resonance imaging. J Am Chem Soc. 2010;132(20):7186–93.

Reineri F, Viale A, Ellena S, Boi T, Daniele V, Gobetto R, et al. Use of labile precursors for the generation of hyperpolarized molecules from hydrogenation with parahydrogen and aqueous-phase extraction. Angew Chem Int Ed. 2011;50(32):7350–3.

Reineri F, Boi T, Aime S. ParaHydrogen induced polarization of 13C carboxylate resonance in acetate and pyruvate. Nat Commun. 2015;6:5858.

Rodrigues TB, Serrao EM, Kennedy BWC, Hu D-E, Kettunen MI, Brindle KM. Magnetic resonance imaging of tumor glycolysis using hyperpolarized 13C-labeled glucose. Nat Med. 2014;20(1):93–7.

Roth M, Koch A, Kindervater P, Bargon J, Spiess HW, Munnemann K. (13)C hyperpolarization of a barbituric acid derivative via parahydrogen induced polarization. J Magn Reson. 2010;204(1):50–5.

Rovedo P, Knecht S, Bäumlisberger T, Cremer AL, Duckett SB, Mewis RE, Green GGR, Burns M, Rayner PJ, Leibfritz D, Korvink JG, Hennig J, Pütz G, von Elverfeldt D, Hövener J-B. Molecular MRI in the earth's magnetic field using continuous hyperpolarization of a biomolecule in water. J Phys Chem. B; 2016. doi:10.1021/acs.jpcb.6b02830.

Schlemmer H-PW, Sawatzki T, Sammet S, Dornacher I, Bachert P, van Kaick G, et al. Hepatic phospholipids in alcoholic liver disease assessed by proton-decoupled 31P magnetic resonance spectroscopy. J Hepatol. 2005;42(5):752–9.

Scholz DJ, Janich MA, Köllisch U, Schulte RF, Ardenkjaer-Larsen JH, Frank A, et al. Quantified pH imaging with hyperpolarized 13C-bicarbonate. Magn Reson Med. 2015;73:2274–82.

Schröder L, Lowery TJ, Hilty C, Wemmer DE, Pines A. Molecular imaging using a targeted magnetic resonance hyperpolarized biosensor. Science. 2006;314(5798):446–9.

Schroeder MA, Atherton HJ, Cochlin LE, Clarke K, Radda GK, Tyler DJ. The effect of hyperpolarized tracer concentration on myocardial uptake and metabolism. Magn Reson Med. 2009b;61(5):1007–14.

Shchepin RV, Coffey AM, Waddell KW, Chekmenev EY. PASADENA hyperpolarized 13C phospholactate. J Am Chem Soc. 2012;134(9):3957–60.

Shchepin RV, Coffey AM, Waddell KW, Chekmenev EY. Parahydrogen induced polarization of 1-13C-Phospholactate-d2 for biomedical imaging with >30,000,000-fold NMR signal enhancement in water. Anal Chem. 2014c;86:5601–5.

Shi F, Coffey AM, Waddell KW, Chekmenev EY, Goodson BM. Heterogeneous solution NMR signal amplification by reversible exchange. Angew Chem. 2014;53:7495–8.

Sriram R, Kurhanewicz J, Vigneron DB. Hyperpolarized carbon-13 MRI and MRS studies. eMagRes [Internet]. John Wiley & Sons, Ltd; 2007 [cited 2015 Jan 5]. Available from: http://onlinelibrary.wiley.com/doi/10.1002/9780470034590.emrstm1253/abstract.

Tam S, Fajardo ME. Ortho/para hydrogen converter for rapid deposition matrix isolation spectroscopy. Rev Sci Instrum Rev Sci Instrum. 1999;70(4):1926–32.

Theis T, Truong M, Coffey AM, Chekmenev EY, Warren WS. LIGHT-SABRE enables efficient in-magnet catalytic hyperpolarization. J Magn Reson. 2014;248:23–6.

Theis T, Truong ML, Coffey AM, Shchepin RV, Waddell KW, Shi F, et al. Microtesla SABRE enables 10% nitrogen-15 nuclear spin polarization. J Am Chem Soc [Internet]. 2015 [cited 2015 Jan 20];137:1404–7. Available from: http://dx.doi.org/10.1021/ja512242d.

Trantzschel T, Bernarding J, Plaumann M, Lego D, Gutmann T, Ratajczyk T, et al. Parahydrogen induced polarization in face of keto–enol tautomerism: proof of concept with hyperpolarized ethanol. Phys Chem Chem Phys. 2012;14(16):5601.

Truong ML, Shi F, He P, Yuan B, Plunkett KN, Coffey AM, et al. Irreversible catalyst activation enables hyperpolarization and water solubility for NMR signal amplification by reversible exchange. J Phys Chem B. 2014;118(48):13882–9.

Van Heeswijk RB, Uffmann K, Comment A, Kurdzesau F, Perazzolo C, Cudalbu C, et al. Hyperpolarized lithium-6 as a sensor of nanomolar contrast agents. Magn Reson Med. 2009;61(6):1489–93.

Vasos PR, Comment A, Sarkar R, Ahuja P, Jannin S, Ansermet J-P, et al. Long-lived states to sustain hyperpolarized magnetization. Proc Natl Acad Sci [Internet]. 2009 [cited 2013 Feb 18];106:18469–73. Available from: http://www.pnas.org/content/early/2009/10/16/0908123106.

Waddell KW, Coffey AM, Chekmenev EY. In situ detection of PHIP at 48 mT: demonstration using a centrally controlled polarizer. J Am Chem Soc. 2011;133(1):97–101.

Wagner S. Conversion rate of para-hydrogen to ortho-hydrogen by oxygen: implications for PHIP gas storage and utilization. Magn Reson Mater Phys Biol Med. 2014;27(3):195–9.

Wiesinger F, Weidl E, Menzel MI, Janich MA, Khegai O, Glaser SJ, et al. IDEAL spiral CSI for dynamic metabolic MR imaging of hyperpolarized [1-13C]pyruvate. Magn Reson Med. 2012;68(1):8–16.

Witney TH, Kettunen MI, Brindle KM. Kinetic modeling of hyperpolarized 13C label exchange between pyruvate and lactate in tumor cells. J Biol Chem. 2011;286(28):24572–80.

Witte C, Schröder L. NMR of hyperpolarised probes. NMR Biomed. 2013;26(7):788–802.

Xu V, Chan H, Lin A, Sailasuta N, Valencerina S, Tran T, et al. MR spectroscopy in diagnosis and neurological decision-making. Semin Neurol. 2008;28(4):407–22.

Yoshihara H, Bastiaansen JAM, Karlsson M, Lerche M, Comment A, Schwitter J. Myocardial fatty acid metabolism probed with hyperpolarized [1-13C]octanoate. J Cardiovasc Magn Reson. 2015;17(Supp. 1):O101.

Zacharias N, Chan H, Sailasuta N, Ross BD, Bhattacharya P. Real time molecular imaging of TCA cycle metabolism in vivo by hyperpolarized 1-13C diethyl succinate. J Am Chem Soc. 2012b;134(2):934–43.

Zierhut ML, Yen Y-F, Chen AP, Bok R, Albers MJ, Zhang V, et al. Kinetic modeling of hyperpolarized 13C1-pyruvate metabolism in normal rats and TRAMP mice. J Magn Reson. 2010;202(1):85–92.

MR Spectroscopy

Barker PB, Butterworth EJ, Boska MD, Nelson J, Welch KMA. Magnesium and pH imaging of the human brain at 3.0 tesla. Magn Reson Med. 1999;41:400–6.

Bollard ME, Garrod S, Holmes E, Lindon JC, Humpfer E, Spraul M, Nicholson JK. High-resolution 1H and 1H-13C magic angle spinning NMR spectroscopy of rat liver. Magn Reson Med. 2000;44:201–7.

Bottomley PA, Hardy CJ. Rapid, reliable in vivo assays of human phosphate metabolites by nuclear magnetic resonance. Clin Chem. 1989;35:392–5.

de Graaf R. In vivo NMR spectroscopy. New York: Wiley; 1998.

Dong Z, Dreher W, Leibfritz D. Toward quantitative short-echo-time in vivo proton MR spectroscopy without water suppression. Magn Reson Med. 2006;55:1441–6.

Neumann-Haefelin C, Kuhlmann J, Belz U, Kalisch J, Quint M, Gerl M, Juretschke P, Herling AW. Determinants of intramyocellular lipid concentrations in rat hind leg muscle. Magn Reson Med. 2003;50:242–8.

Ordidge RJ, Connelly A, Lohmann JAB. Image-selected in vivo spectroscopy (ISIS). A new technique for spatially selective nmr spectroscopy. J Magn Reson. 1986;66:283–94.

Pan DA, Lillioja S, Kriketos AD, Milner MR, Baur LA, Bogardus C, Jenkins AB, Storlien LH. Skeletal muscle triglyceride levels are inversely related to insulin action. Diabetes. 1997;46:983–8.

Petroff OAC, Prichard JW, Behar KL, Alger JR, den Hollander JA, Shulman RG. Cerebral intracellular pH by 31P nuclear magnetic resonance spectroscopy. Neurology. 1985;35:781–8.

Podo F. Tumour phospholipid metabolism. NMR Biomed. 1999;12(7):413–39.

Renema WKJ, Schmidt A, van Asten JJA, Oerlemans F, Ullrich K, Wieringa B, Isbrandt D, Heerschap A. NMR spectroscopy of muscle and brain in guanidinoacetate methyltransferase (GAMT)-deficient mice: validation of an animal model to study creatine deficiency. Magn Reson Med. 2003;50:936–43.

Street JC, Szwergold BS, Matei C, Kappler F, Koutcher JA. Study of the metabolism of choline and phosphatidylcholine in tumors in vivo using phosphonium-choline. MRM. 1997;3:769–75.

Ultrasound

14

Stuart Foster, J.M. Hyvelin,
Minalini Lakshman, Andrew Needles, I. Tardy,
and François Tranquart

Contents

S. Foster
Department of Medical Biophysics, Sunnybrook Health Sciences Centre, 2075 Bayview Avenue, Toronto, ON M4N 3M5, Canada
e-mail: stuart.foster@sw.ca

J.M. Hyvelin • I. Tardy
Bracco Suisse SA, Route de la Galaise, 31, Plan les Ouates 1228, Switzerland

M. Lakshman • A. Needles (✉)
VisualSonics Inc, 3080 Yonge Street, Suite 6100, Toronto, ON M4N 3N1, Canada
e-mail: aneedles@visualsonics.com

F. Tranquart, MD, PhD
Geneva Research Center and Manufacturing Site, Bracco Suisse SA, Route de la Galaise, 31, Plan-les-Ouates 1228, Switzerland

Bracco Suisse SA,
Route de la Galaise, 31, Plan les Ouates 1228, Switzerland
e-mail: francois.tranquart@bracco.com

14.1 Ultrasound Methods and Devices

Stuart Foster, Minalini Lakshman, and Andrew Needles

14.1.1 Introduction

Over the past several decades, mouse models have been used in cancer and cardiovascular research to aid in the investigation of the basic biological underpinnings of disease and as a tool for discovering new clinical agents and assays. Murine models are the most commonly used basic science and preclinical animal systems in

F. Kiessling et al. (eds.), *Small Animal Imaging*, DOI 10.1007/978-3-319-42202-2_14

academic and pharmaceutical research. This is due to the significant similarities and the plethora of commonly shared inherited diseases between humans and mice. Some of these diseases include atherosclerosis, cancer, heart disease, hypertension, obesity, bleeding disorders, asthma and neurological disorders. Notwithstanding, there are other mammals which also share this similarity. However, one of the major advantages of the mouse model is the wealth of resources available on its genetics and molecular and cellular pathways. Furthermore, mice are ideal for research environments as they are small and easy to maintain and cost-effective and have short gestation periods (~19–20 days) and, finally, genetically uniform inbred strains are readily obtained.

Imaging has contributed substantially to small animal research by enabling quantitative visualization of the living biology-associated development, growth and progression of disease. As in clinical imaging, no single imaging modality suits all biological applications. In fact, each imaging modality has its own strengths and weaknesses with respect to its temporal and spatial resolution, accessibility, sensitivity, ease of use, cost, the specific regions of the body and biological processes that can be imaged. The availability of suitable contrast agents is also important for each modality. Often preclinical imaging is performed using a multimodality format to allow researchers a more complete understanding of disease processes and/or the efficacy of a preclinical therapy.

Here, we will focus on micro-ultrasound as an imaging modality in preclinical research. Clinically, ultrasound is used in hospital departments for real-time imaging and quantification of soft tissue disease, cardiac function, foetal development and diagnosis, emergency medicine, and screening and assessment of tumours and as a tool for guidance of invasive procedures. The traditional strengths of ultrasound are its speed in image formation, high resolution, portability and low cost compared to other modalities. In recent years, preclinical ultrasound systems ("micro-ultrasound") have been developed that provide the functionality available clinically, yet allow for ultrahigh spatial resolution (30–150 mm) in order to view and quantify the detailed structures, flow dynamics and molecular biomarkers inherent in murine microimaging. In addition, these systems have been developed to minimize perturbation of the mouse, rat, or other small animal models while maximizing reproducibility of both the procedure and the data derived. Several hundred peer-reviewed papers using the single element scanned micro-ultrasound platform have now been published. In the area of cardiovascular research, refer to, Liu et al. (2007), Lee et al. (2008), Trivedi et al. (2007), Ino et al. (1996), and Zhou et al. (2003, 2004), and in the area of cancer, see, for example, Goessling et al. (2007), Kiguchi et al. (2007), Olive and Tuveson (2006), Wirtzfeld et al. (2005, 2006), and Xuan et al. (2007).

In this chapter, the basic technology of micro-ultrasound will be reviewed. Scanning techniques, animal handling and applications will be described in the context of relevant biological problems.

14.1.2 Micro-ultrasound Imaging Technology

There is only one manufacturer of dedicated preclinical high-resolution micro-ultrasound systems (VisualSonics, Toronto, Canada). These systems operate at frequencies between 15 and 70 MHz compared to frequencies of 3–15 MHz for clinical systems. Both mechanical and array technologies are currently available for ultrasound microimaging. A block diagram of the latest array system is illustrated in Fig. 14.1. It shows a 256-element transducer in combination with a 64-element beamformer. A high-speed bus transfers the multiplexed transducer aperture data to processing systems for calculation of B-mode and Doppler images. Figure 14.2 shows the consoles and scanheads for both the mechanical (Fig. 14.2a, b) and array (Fig. 14.2c, d) imaging systems. Each system is connected to a series of application-specific scanheads, (Fig. 14.2b, d) which transmit and receive high-frequency ultrasound signals that generate the real-time images. Operation of the scanner is illustrated in Fig. 14.3. As Fig. 14.3 shows, the scanhead is configured on an imaging platform called a rail system to allow for hands-free positioning and

capture of the images. The animal is anaesthetized and maintained on a heated platform to ensure the comfort and maintain body temperature of the animal during imaging. Key physiological parameters are captured from the platform including heart rate, temperature, respiration and ECG. These signals are gathered through paw and temperature probes and integrated with the real-time micro-ultrasound images. An additional accessory to this imaging station is an injection mount that allows for the guidance of precise injections or biopsies in vivo through the real-time imaging of the micro-ultrasound system. Figure 14.3b shows a typical abdominal cross section in a normal mouse. Visible structures include the right kidney, adrenal gland, liver and a variety of vascular structures. Figure 14.4 shows a cross section through an orthotopic hepatocellular carcinoma pre- and postcontrast injection showing the increase in signal intensity caused by the contrast agent (discussed in the Chap. 16).

The analytic software is designed to allow for study-based aggregation of animal data for longitudinal experiments with multiple animals, multiple time points and multiple therapeutic interventions. Over 500 disease-specific measurements are implemented within the software to allow for quantification and analysis of the images. Two-dimensional images are gathered and viewable in real time without any reconstruction or delay, while 3D images are acquired rapidly and reconstruction into a 3D image is done in seconds by the software. Animal physiological data can be stored with the imaging data for cardiotoxicity studies, for example. All images and measurements can easily be exported to databases for further analysis or archiving. The

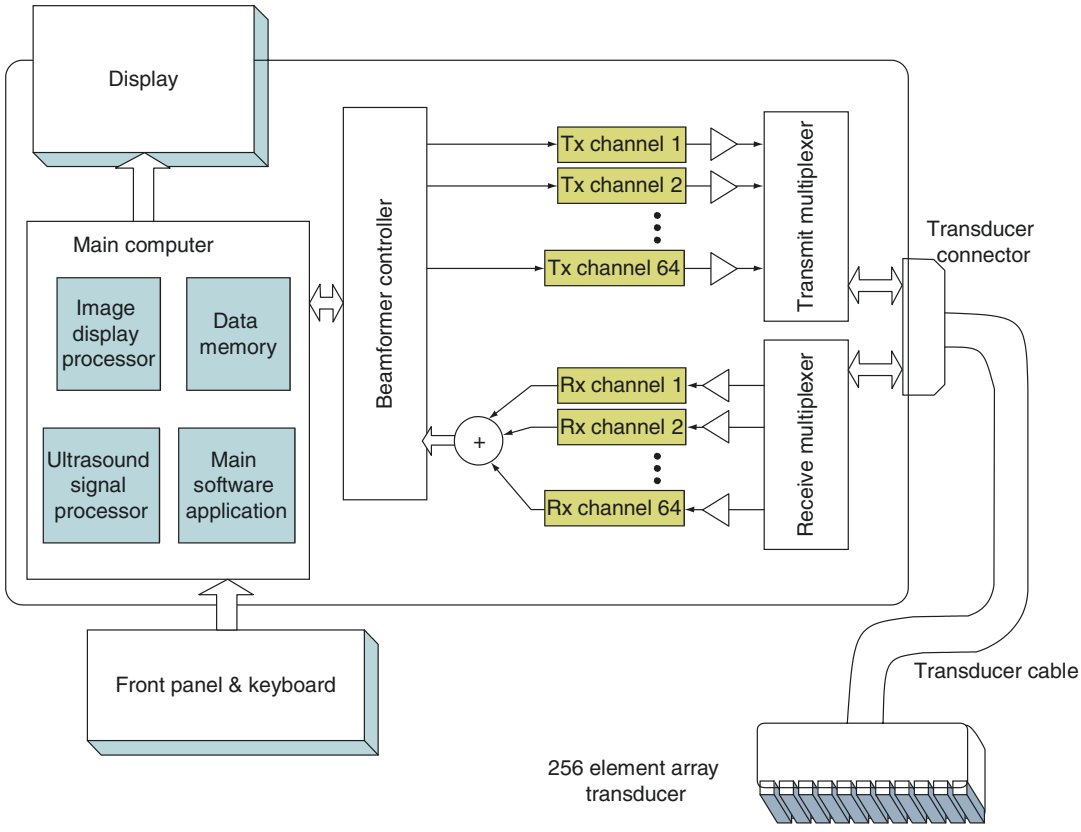

Fig. 14.1 Block diagram of the Vevo 2100 scanner architecture. The system consists of a 256-element transducer coupled to a 64-element beamformer. A high-speed data connection to the main processing computer enables B-mode and Doppler data to be computed in real time and displayed on the system monitor

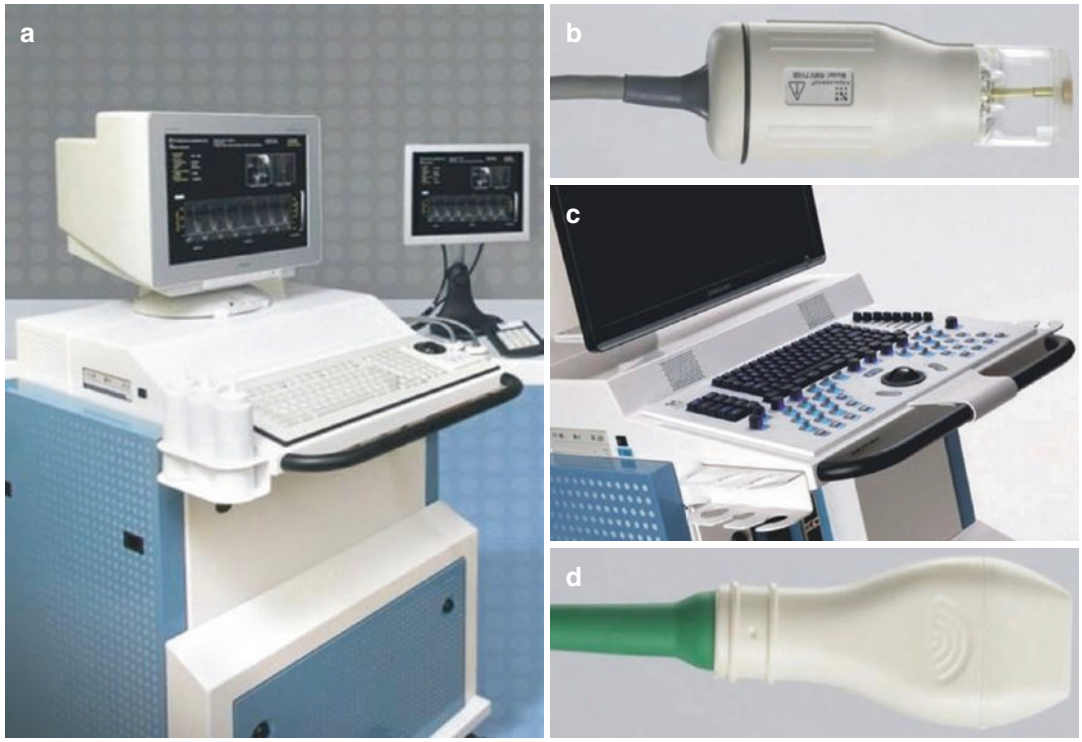

Fig. 14.2 Consoles for mechanical (**a**) and array-based (**c**) high-frequency ultrasound imagers. Corresponding probes for the two systems are given in (**b**) and (**d**), respectively

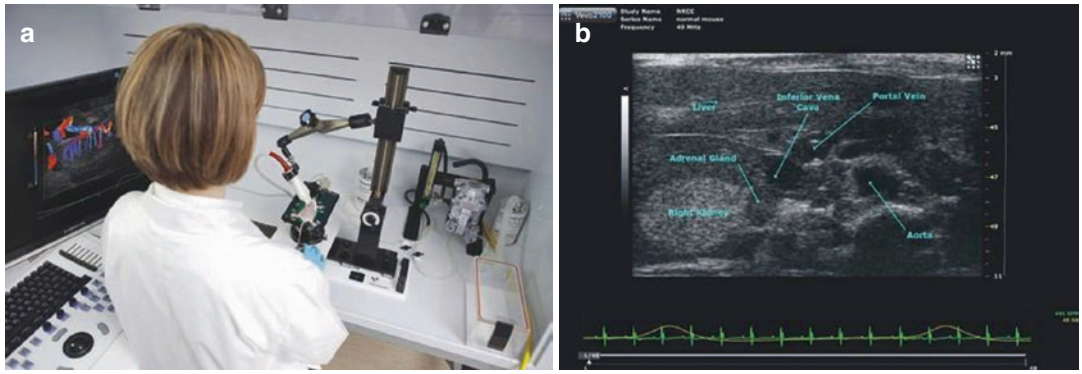

Fig. 14.3 Linear array scanhead positioned on rail system for imaging (**a**). The mouse is monitored for temperature, ECG and other physiologically relevant parameters, while the operator makes instrument adjustments during a scanning session. (**b**) A still frame from a typical abdominal cross section of a normal mouse

software is networked for high-throughput studies or for use in core imaging facilities where multiple researchers use the same instrument and can quickly image their animals and then review their data and perform measurements over the network.

High-frequency mechanical sector scanning for mice was originally developed by Foster et al. (2002). The mechanical scanhead shown in Fig. 14.2b has been optimized with sophisticated low inertia actuation and is capable of frame rates of over 100/s. The 15–55 MHz transducer

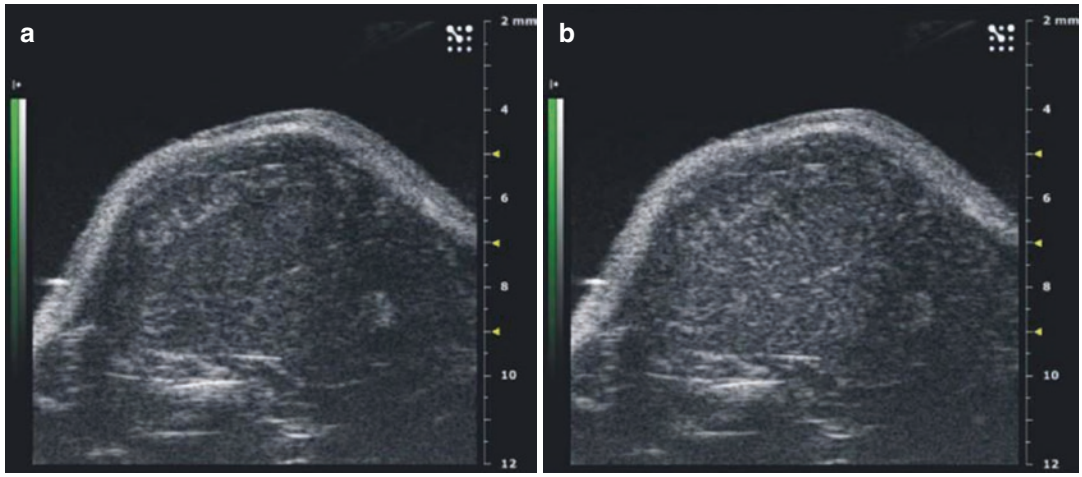

Fig. 14.4 Images of a hepatocellular tumour (**a**) pre and (**b**) postcontrast injection

executes a shallow sector scan over about a 15-mm field of view in these devices. The single-element transducers used in the mechanical probes are composed of PVDF copolymer devices configured as described by Sherar and Foster (1989) and Foster (2000) and optimized to achieve high sensitivity and bandwidth. Foster et al. introduced high- frequency linear arrays for mouse imaging in 2008 (Foster et al. 2009; Foster 2008). These scanheads (Fig. 14.2d) contain no moving parts, but rather create the ultrasound image through careful orchestration transmit and receive beamforming that is well described in numerous publications (Cobbold 2007). The choice of scanhead frequency for either the mechanical or array systems is driven by the required resolution and depth of penetration. Table 14.1 illustrates the expected resolution for various ultrasound frequencies. Resolution in the axial (depth) direction is approximately equal to the wavelength of ultrasound where as in the two lateral directions resolution is about twice the wavelength. Resolution is typically between 30 and 150 mm depending on the choice of frequency. Total depth of penetration is on the order of 30 mm at 20 MHz and is reduced to <10 mm at 50 MHz. A thorough description of resolution and depth of penetration for high-frequency imaging are given in (Foster et al. 2009).

14.1.3 Oncology Applications

For cancer research applications, micro-ultrasound is an imaging modality that, because of its high spatial resolution and real-time temporal resolution, can be used to visualize, characterize and quantify prepalpable orthotopic and subcutaneous tumours in a multitude of small animal models. Tumours can be monitored and quantified from tumorigenesis through their growth stages and through to metastases to surrounding organs, lymph nodes and tissues. Cheung et al. (2005) describe the use of micro-ultrasound in the assessment of xenograft growth analysis. The current software allows real-time visualization and measurement of the tumours in two and three dimensions. Blood flow, blood architecture and assessment of feeder vessels can be quantified using power Doppler (for vessels larger than 30 mm) and using contrast agents for tumour perfusion and microcirculatory flow in vivo. Early applications of flow analysis and measurement in tumour growth are provided by Franco et al. (2006), Shaked et al. (2006) and Cheung et al. (2007). Xuan et al. (2007) described neoangiogenic development and tumour blood flow in prostate tumours including visualization of each of the early stages of such development that can be clearly visualized and quantified in longitudinal studies.

Table 14.1 Resolution and other relevant parameters vs. frequency for ultrasound imaging

Frequency (MHz)	Wavelength (mm)	Axial resolution (mm)	Lateral resolution (mm)	Max imaging depth (mm)
1	1.5	1.5	3	150
5	0.3	0.3	0.6	90
10	0.15	0.15	0.3	45
20	0.075	0.075	0.15	22.5
50	0.03	0.03	0.06	9
100	0.015	0.015	0.03	4.5

14.1.4 Tumour Sizing and Quantification in Two and Three Dimensions

One of the most important measurements in oncology is quantifying the change in tumour size during disease progression and changes related to tumour response to anticancer therapy (Wirtzfeld et al. 2005; Feldmann et al. 2008; Wang et al. 2007). Because micro-ultrasound is noninvasive, tumour growth and changes can be monitored repeatedly and longitudinally in the same animal, which can serve as its own control, thereby increasing accuracy of the experiment and reducing the number of cohort animals required. Micro-ultrasound is routinely used in serial 2D and 3D volumetric quantification of tumour sizing in vivo in a variety of murine and nonrodent cancer models (Goessling et al. 2007; DeRosier et al. 2007; Graham et al. 2005; Huizen et al. 2005; Kiguchi et al. 2005; Lyshchik et al. 2007a; Wu et al. 2005). For example, Wirtzfeld et al. (2005) were the first to publish on the use of micro-ultrasound to track 3D tumour volumes in progression in a transgenic prostate cancer mouse model. 3D micro-ultrasound images correlated closely to serial histology (a correlation coefficient of 0.998 ($p < 0.001$)). Furthermore, 3D micro-ultrasound measurements accurately confirmed the size and shape of these tumour masses in vivo (Wirtzfeld et al. 2005). The technique is highly reproducible as tumour detection sensitivity and specificity were both >90 % when diagnoses were based on repeated micro-ultrasound examinations performed on separate days.

Further studies went on to show the utility of 3D micro-ultrasound to not only noninvasively track the growth of liver metastases (tumour diameter, volume and growth curve) but also evaluate potential chemotherapeutics on these parameters in a longitudinal murine metastasis model (Graham et al. 2005). In this particular study, the authors showed high accuracy in detecting tumour mass progression using four different cell lines: B16F1 (murine melanoma), PAP2 (murine H-ras-transformed fibroblast), HT-29 (human colon carcinoma) and MDA-MB-435/HAL (human breast carcinoma) in a liver metastasis model. Furthermore, the longitudinal imaging of B16F1 liver metastases revealed distinct textural changes which had anechoic regions found to be areas of liquefactive necrosis. The tracking of tumour volume and textural changes can be a useful tool in tracking subtle responses to different antiangiogenic therapeutic treatments. More importantly, this study illustrated that longitudinal micro-ultrasound imaging is a powerful tool in preclinical trials and drug development since liver metastases treated with doxorubicin, a cytotoxic chemotherapeutic agent, were found to have significant decreases in tumour volume at day 12 post cell injection. The authors concluded that micro-ultrasound improved the evaluation of therapeutic efficacy on sequential stages of tumour development (Graham et al. 2005).

14.1.5 Evaluation and Quantification of Blood Flow

A key component of studying cancer in animal models is understanding how specific drugs affect angiogenesis, tumour growth and metastases. As such, microimaging modalities that provide insight into how a drug influences tumour vasculature and molecular expression of specific biomarkers, such as those involved in angiogenesis,

have become important life science research tools. Micro-ultrasound provides such utility, allowing for the mapping and visualization of tumour vasculature using the power Doppler which can detect blood flow ranging from 2 mm/s up to 4 m/s in tumours at multiple time points (Xuan et al. 2007; Goertz et al. 2002; Jugold et al. 2008). Power Doppler can be used to detect subtle changes in tumour perfusion and blood vessel architecture in a noninvasive longitudinal manner (unpublished observation by Xuan et al. (2006), Robarts Research Institute, London, Canada). Studies by Goertz et al. (2002) reported the first use of high-frequency micro-ultrasound 2D power Doppler in studying the effects of an antivascular drug on blood flow in superficial human melanoma MeWo tumours. The authors reported a significant reduction in blood flow 4 h after injection of the tumour vascular targeting agent ZD6126 followed by a recovery of flow by 24 h after injection. They concluded that high-frequency power Doppler was a highly effective noninvasive quantitative tool for longitudinally following the effects of antivascular therapy on blood flow in superficial tumours (Goertz et al. 2002). Similarly, Xuan et al. (2007) recently reported the first application of high-frequency 3D power Doppler micro-ultrasound imaging in a genetically engineered mouse prostate cancer model. They showed that 3D power Doppler could sensitively, specifically and reproducibly depict functional neoangiogenic blood flow in prostate tumours when compared to normal prostate tissue which had little or no flow. These observations were confirmed using micro-CT and by correlation with microvessel distributions measured by immunohistochemistry and enhanced vascularity visualized by confocal microscopy. Figure 14.5 shows examples of the correlation between micro-ultrasound and micro-CT from this study. A separate study from Jugold et al. (2008) investigated the effects of blocking VEGF-mediated pathways using a VEGFR2-blocking antibody treatment. This study, using power Doppler imaging, showed that after 6 days of treatment of subcutaneous tumour (spontaneously immortalized human skin keratinocytes) in nude mice, tumour vascularity significantly decreased. These findings were additionally confirmed with immunohistochemistry staining for vascular markers, CD31 and smooth muscle actin (Jugold et al. 2008).

Finally, the high-resolution imaging capabilities of micro-ultrasound allow cancer researchers to study not only the effect of a novel drug on angiogenesis and tumour growth but also the influence of that drug on the surrounding tissues. This advantage is highly beneficial when monitoring side effects and determining the toxicity of therapeutics during drug development (Refer to Table 14.2)

14.1.6 Targeting Injections and Biopsies

Because of its real-time nature, a unique utility to micro-ultrasound is its ability to guide targeted injections or biopsies without having to do surgical intervention. As such, intricate procedures such as the placement of probes or invasive monitors in animals, the targeted injection of stem cells into specific tumour or anatomical targets or even the specific placement of probes in vivo can be visualized noninvasively using micro-ultrasound. As a result of this noninvasive guidance facilitated by micro-ultrasound, surgery and stress on the animal are minimized or eliminated, accuracy of the procedures and injections is increased significantly, and results are more quantitative and reproducible. This was illustrated by Goessling et al. (2007) who demonstrated image-guided tumour biopsy in adult zebrafish with hepatic tumours. A 23G needle was guided into the tumour and a sample was taken, and the sample was subsequently implanted in a separate recipient zebrafish (Goessling et al. 2007). The implanted tumour was still detected in vivo by micro-ultrasound 6 weeks later.

14.1.7 Contrast Agents for Performing Real-Time Tumour Perfusion and Targeted Molecular Imaging of Biomarkers

Microbubble contrast agents allow more sensitive detection of microvascular flow down to the capillary level. By adding ligands to endothelial cell surface markers, it is also possible to evaluate

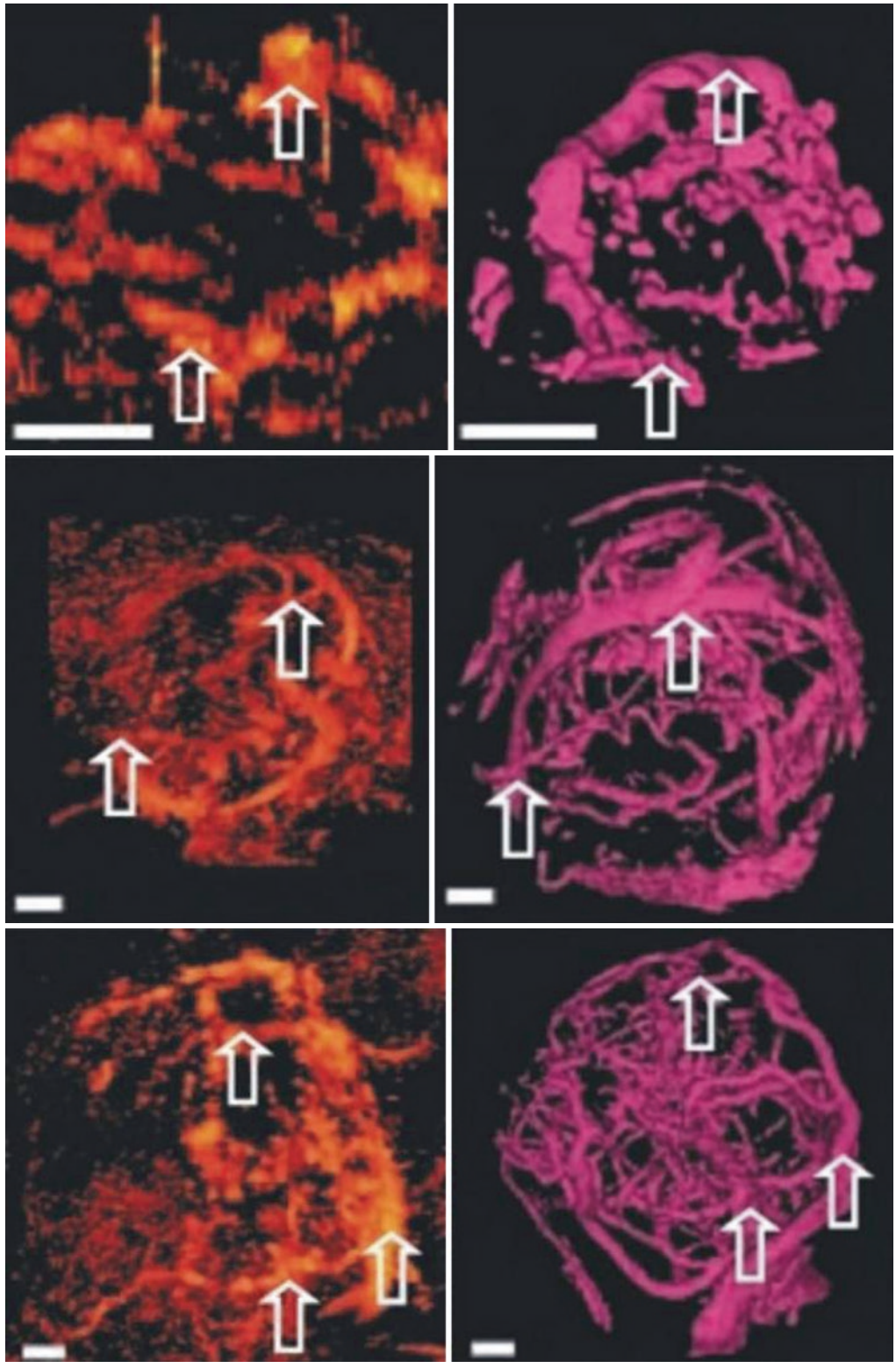

Fig. 14.5 Comparison of three-dimensional power Doppler (*left*) and three-dimensional micro-CT (*right*) for prostate tumours at early (*top*), middle (*centre*) and late (*bottom*) stages of development. *Arrows* point to common features in the vascular patterns. Bar = 1 mm (Image from Xuan et al. (2007) with permission)

Table 14.2 List of angiogensis drugs

Cancer drugs	Reference
First-generation angiogenesis inhibitors	
REGN910	Daly et al. (2013), *Cancer Res*
Aflibercept	Eichten et al. (2013), *Angiogenesis*
ABDNAZ	Ning et al. (2012), *Cancer Res*
Gemcitabine	Francia et al. (2012), *Mol Cancer Ther*
Sunitinib	Olson et al. (2011), *PNAS*
Paclitaxel	Hwang et al. (2010a), *J Ult Med*
Vascular disrupting agents	
STA-9584	Foley et al. (2012)
Vadimezan DMXAA/ASA404	Seshadri et al. (2011)

expression of important signalling, inflammation and adhesion molecules. In angiogenic studies, for example, the target-ready contrast agent (MicroMarker, VisualSonics) can be conjugated with an antibody against VEGFR2. The agent is then introduced into the animal through venous injection, and the animals are screened for relative expression of the tagged contrast agent. The animals can then be injected with an antiangiogenic drug, and the effect of the therapeutic on the expression of the VEGFR2 receptor can be quantified. This whole procedure can be performed in vivo in the same animals and at multiple time points over a longitudinal time course. For micro-ultrasound, this procedure was first described by Rychak et al. (2007) and subsequently by Lyshchik et al. (2007a), concluding that targeted contrast-enhanced high-frequency micro-ultrasound allows in vivo molecular imaging of VEGFR2 expression on the tumour vascular endothelium and may be used for noninvasive longitudinal evaluation of tumour angiogenesis in preclinical studies. More recently, Willmann et al. (2008a, b) showed high VEGFR2 expression in subcutaneous tumour (mouse angiosarcoma SVR cells) grown in nude mice using targeted VEGFR2 contrast agent. VEGFR2 expression was confirmed by immunohistochemistry. Furthermore, this contrast agent was mixed in in vitro cell culture to examine the binding affinity of the targeted contrast agent to angiosarcoma SVR cells. These results showed an average of two targeted VEGFR2 microbubbles binding to each angiosarcoma cell, suggesting very high binding affinity exists between targeted VEGFR2 microbubbles and angiosarcoma cell (Willmann et al. 2008a, b). More recent reports using ultrasound-guided injections addressed the need for relevant models of tumours. For example, Jäger et al. (2013) reported guided inoculation of bladder tumour cells to generate an orthotopic model and test efficacy of gemcitabine/cisplatin treatment, and this approach replaced complex laparotomy and decreased morbidity for mice.

14.1.8 Cardiovascular Applications

Another major application of micro-ultrasound is in the field of cardiovascular research (see, e.g., references Zhou et al. 2004; Franco et al. 2006; Kulandavelu et al. 2006). The principal advantages of ultrasound in this regard are real-time frame rates to image the rapidly beating (6/s) heart rate, functional imaging of blood flow hemodynamics via pulsed Doppler and the ability to achieve phenomenal (<1 ms) temporal resolution using ECG-registered reconstruction (Cherin et al. 2006). Figure 14.6 shows an example of a day 13 mouse embryo in which both ventricles are visible and the total size of the heart is little more than 1 mm in diameter. Other structures visible include neural tubes in the brain, the heart and the torso. Measurement of essential cardiac performance factors is possible using semiautomated methods in which the cardiac chambers are outlined in various phases of the cardiac cycle as illustrated in Fig. 14.7. Quantitative analysis of stroke volume, ejection fraction, fractional shortening, area change, fractional area change, cardiac output, LV mass and average wall thickness is possible. Pulsed Doppler is also important for the assessment of the hemodynamics of the heart. For example, peak velocity of zebrafish heart was assessed to report a molecular mechanism to cardiac function by Mishra et al. (2013). Fig. 14.8 shows the use of pulsed Doppler to measure flow velocity through the mitral valve. Visible are both the E and A waves critical for the assessment of diastolic function. Other features that are directly measureable include the isovolumic relaxation times.

ECG-registered reconstruction enables useful studies of myocardial biomechanics in which quantitative measurements of displacement and strain are needed. Speckle tracking studies (Li et al. 2007, 2008) have shown that high-resolution ultrasound image tracking methods provide for the detection of cardiac dyssynchrony in the noninfarcted regions in the murine left ventricles late after MI by identifying the temporal and spatial disparity of regional myocardial contraction. A recent publication on advanced speckle tracking has reported on restored synchrony in the adult heart with stem cell therapy (Yamada et al. 2013). Myocardial strain values have been recently reported in paediatric heart to study pathophysiology of paediatric cardiovascular diseases (Andrews et al. 2013). Elastography based on full-radiofrequency reconstructions has demonstrated capability of accurately characterizing normal myocardial function throughout an entire cardiac cycle, at high resolution, and detecting and localizing myocardial infarction in vivo (Luo et al. 2007; Luo and Konofagou 2008).

High-frequency ultrasound has also been used to assess right ventricular (RV) dysfunction and flow through the left (LCA), septal (SCA) and right (RCA) coronary arteries using colour and pulsed Doppler (Wu et al. 2013). Right ventricular dysfunction is prevalent in a variety of diseases/models including pulmonary insufficiency, pulmonary hypertension and COPD. Micro-ultrasound has been used to assess various RV parameters including cardiac output and stroke volume, RV wall thickness, and RV diastolic dysfunction using pulsed Doppler through the tricuspid valve and tricuspid annular plane systolic excursion (TAPSE), a clinical standard for assessing RV systolic function.

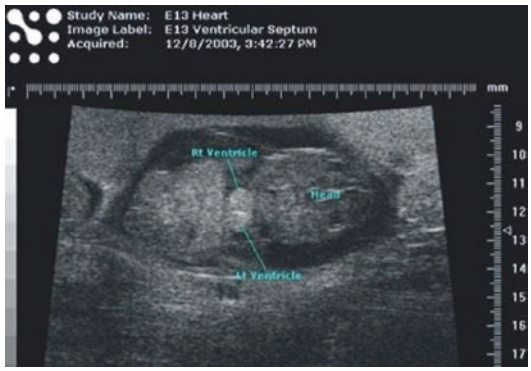

Fig. 14.6 Forty megahertz micro-ultrasound image of a day 13 mouse embryo showing the ventricles of the heart, neural and body structures. The field of view is about 12 × 10 mm

14.1.9 Photoacoustic Imaging and Its Applications

Recent reviews have described about photoacoustic imaging and its applications to meet translational research priorities such as understanding disease mechanisms and developing

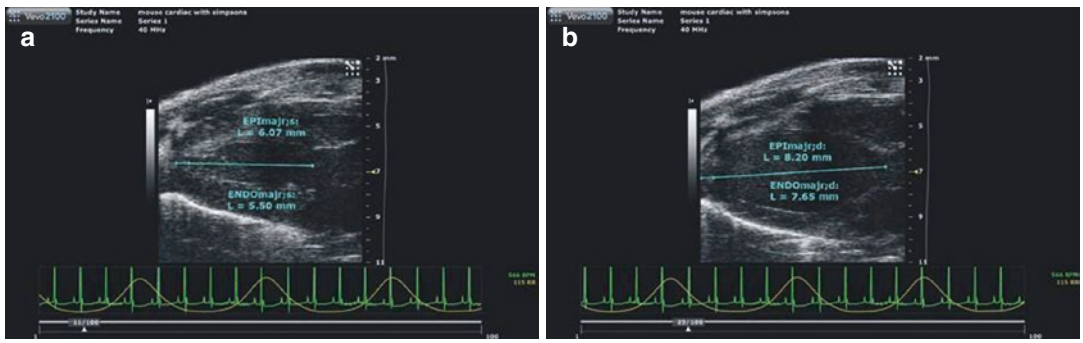

Fig. 14.7 Long-axis imaging of the left ventricle at end systole (**a**) and end diastole. (**b**) Data from these views are combined with measurements of endo- and epicardium in the short-axis view to generate quantitative estimates of stroke volume, ejection fraction, fractional shortening, fractional area change, cardiac output, stroke volume, LV mass and average wall thickness. These measures are transferred directly to Excel-compatible data files for analysis

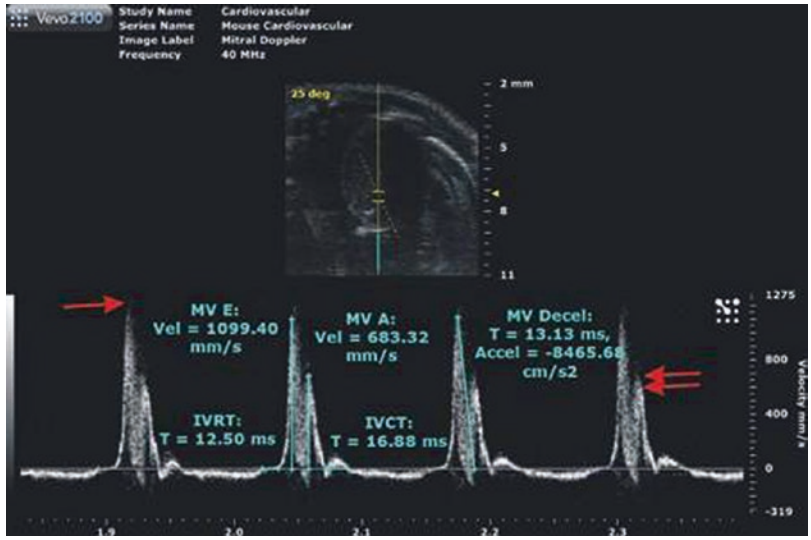

Fig. 14.8 Mitral valve flow waveforms such as that shown above can be obtained using the four-chamber view. The E (*arrow*) and A (*double arrow*) waveforms and isovolumic relaxation times (IVRT, IVCT) can be used for quantitative assessment of diastolic function

innovative therapies (Luke et al. 2012; Mallidi et al. 2011). Herein, we summarize recent advances using photoacoustic imaging with high-frequency ultrasound. We will focus on the principles of photoacoustic imaging and expand on its validation as it relates to key applications in in vivo imaging. Where applicable, photoacoustic data will be compared to existing imaging modalities to demonstrate multimodal imaging in key disease research areas.

14.1.9.1 Technology Overview

Photoacoustic imaging (also commonly optoacoustic imaging) has many parallels to ultrasound imaging; however, unlike ultrasound where the signal detection is based on acoustic backscatter, the underlying principle is due to the absorption of light in tissue. The optical absorption in tissue leads to a subsequent thermo-elastic expansion and vibration in the ultrasound frequency range. Relative to pure optical imaging techniques that have limited imaging depth (mm scale), photoacoustics offers the benefit of deep imaging (cm scale), but with sensitivity of optical imaging. Within the context of ultrasound imaging, photoacoustics offers the ability to add additional image contrast based on the optical absorption of tissues and other exogenous agents. Examples include the oxygen saturation content of haemoglobin and other spectral properties of tissues, such as melanin and fat. A general review of the topic and the various implementations of the technology can be found in the book by Wang et al. (2012). A common implementation of the technology is ultrasound-based photoacoustics. Using this approach, laser light is exposed to the tissue and photoacoustic waves are detected with the linear array ultrasound transducer. The main benefit of this technique, over other detection geometries, is that since it is inherently registered with an ultrasound transducer, both standard B-mode ultrasound and PA images can be fused into a single multimodal imaging display. A description of a commercial high-frequency system from VisualSonics is described by Needles et al. (2013). The applications described below will be related to this ultrasound-based implementation of photoacoustics. Additional and complimentary applications will be described in Sec. 14.1.9.1, along with the other various implementations of the technology.

14.1.9.2 Application of Photoacoustic Imaging

Photoacoustic imaging has emerged as a groundbreaking hybrid imaging modality in key disease research areas (summarized in Table 14.4). Many of these research areas utilize the ability of photoacoustics to evaluate oxygen content in blood. This is possible because the optical absorption of haemoglobin molecules, found in red blood cells, varies with the amount of bound oxygen and also as a function of optical wavelength. Thus, by imaging blood vessels at multiple wavelengths and knowing the absorption properties of haemoglobin, the relative level of oxygen saturation can be deduced. A simple two-wavelength approach is the most practical, yet effective method, and is described by Wang et al. (2006). Measurement of oxygen saturation by photoacoustic imaging has been validated with existing and relevant imaging modalities – summarized in Table 14.5. Highlighted in these publications is the fidelity and quality of photoacoustic data and rapid in vivo acquisition of data comparable to either BOLD-MRI or immunohistochemistry for hypoxia markers (Rich 2015; Qin et al. 2013)

In fact, in vivo imaging of oxygen saturation has shown tremendous growth in cancer therapy and regenerative medicine. Cancer therapy research has benefitted from the photoacoustic ability to detect hypoxic areas and response to therapy by restoration of oxygenation to these areas (Mallidi et al. 2015a, b). Tissue-engineered scaffolds using FDA-approved polymers were shown efficacious when oxygen saturation was restored to the underlying tissue (Talukdar et al. 2014). Photoacoustic imaging of oxygen saturation can benefit ischemic research in disease such as stroke and other neurological diseases, embryology and diabetes research to advance understanding of the underlying mechanism of disease progression (Figley et al. 2013; Guevara et al. 2013; Sethuraman et al, 2007).

Deep tissue imaging of cellular and molecular events is a tremendous benefit with photoacoustic imaging. This application demands localized imaging of the target organ in vivo and detection of discrete signals from one or more tagged contrast agents. Contrast agents are designed to exhibit a unique optical absorption spectrum that is different from the surrounding tissues. Using multispectral imaging (also referred to as spectroscopic imaging), photoacoustic data is collected at multiple wavelengths (typically 5–10) and then analysed to unmix the relative contributions from contrast agent signal and background tissue and provide an estimate of concentration. An overview of the technique and methods for optimizing the signal processing are given by Luke et al. (2012).

Particular to this application is the ability to track different cell types and their homing abilities for a better understanding of either disease progression mechanism or innovation in the design of targeted therapy. In this respect, photoacoustic imaging of tagged nanoparticles has benefitted in tracking stem cells, immune cells and metastatic cells (Jokerst et al. 2012; Swierczewska et al. 2012; Mallidi et al. 2015; Grootendorst et al. 2011; Luke et al. 2013; Prasad et al. 2014). Photoacoustic properties of gold and carbon nanoparticles have rendered them suitable contrast agents for cell tracking. Likewise, these nanoparticles when coated for conjugation to molecular markers can be used for molecular imaging as summarized in Tables 14.3, 14.4 and 14.5. More recently, photoacoustic imaging has made breakthroughs with the genesis of theranostics in which therapy can be deployed against a cell type when a targeted molecular marker is detected. In fact, Hollander et al. (2014) reported on the development of a nanobody-functionalized gold nanostar for photothermal treatment of HER2-positive cancer. An illustration comparing an optical image of tagged optical contrast agent by photoacoustic is shown in Fig. 14.9.

14.1.10 Discussion and Conclusion

The mechanical and array ultrasound technologies reported here extend the bandwidth of high-performance ultrasound imaging from 15 to 50 MHz enabling significant improvement in performance for preclinical and potentially clinical applications. The established value of the mechanical high-frequency imaging systems is now augmented by new systems based on a 256-element

Table 14.3 List of targeted contrast agents

Biomarker category	Molecular target	Cell types	Contrast agent
Clinically translatable	Human CD276	Ovarian cancer	MicroMarker *(Part # VS-11915)*
	Human BR55 (kinase domain)	Colon cancer	MicroMarker *(Part # VS-11915)*
Matrix proteins	Matrix metalloproteases (MMP)	Myocardial infarct Metastasis marker	MicroMarker *(Part # VS-11915)* Fluorescent activatable (Alexa Fluor)
Adhesion proteins	Integrin	Endothelial cells	MicroMarker *(Part # VS-11915)*
	Integrin	Tumour cells	IR800 CW[a]/SWCNTs (LICOR)/ De la Zerda A, et al. (2008)
	VCAM	Cell adhesion	SWCNTs
Receptors	EGFR	Metastatic cells	Gold Nanorods (Nanopartz Inc.)
	VEGFR2	Endothelial cell in angiogenesis	MicroMarker *(Part # VS-11915)*
Immune proteins	P-Selectin	Endothelial cell in inflammation	MicroMarker *(Part # VS-11915)*
	MAdCAM-1	Immune cell in inflammation	MicroMarker *(Part # VS-11915)*
	CD44	Immune cell or tumour cell	SWCNTs

[a]http://www.licor.com/clinical_translation/irdye_800CW_background

Table 14.4 Summary of photoacoustic applications

Applications	Oxygen saturation	Multi-spectral imaging
Oncology	√	√
Neurobiology	√	√
Diabetes	√	
Embryology	√	
Atherosclerosis		√
Regenerative medicine	√	√
Cell tracking		√
Molecular imaging		√

Table 14.5 Multimodal imaging with photoacoustics complements data from existing imaging modalities

	Photoacoustic imaging	
Existing imaging modalities	Oxygen saturation	Molecular imaging
Optical imaging	Mallidi et al. (2015a, b) Florian et al. (2014)	Levi et al. (2013) Lakshman et al. (2012) De la Zerda et al. (2008)
MRI/PET/CT	Rich (2015)	Qin et al. (2013) Kircher et al. (2012) Swierczewska et al. (2012)
Contrast-enhanced ultrasound	Gerling et al. (2014), Yin et al. (2013)	
Histology	Gerling et al. (2014) Lakshman et al. (2013) Yin et al. (2013)	Paproski et al. (2014)
Interstitial fibre optic probe	Campos et al. (2013)	

linear array configuration with a 64-channel beamformer. Laser machining is used to define the array structure providing narrowly spaced elements with only 5–10 mm between elements. The architecture of the transducer and beamformer enables beam profiles that approach the diffraction limit and ensure high image quality. One of the major advances associated with the development of the high-frequency array-based micro-ultrasound is the ability to perform real-time colour and power Doppler as demonstrated in Fig. 14.5. In the preclinical arena, the new technology will find immediate application in a wide range of small animal biomedical research and with over 1000+ publications. In addition to providing accurate measures of tumour burden in the parenchymal organs, micro-ultrasound and photoacoustic imaging enables real-time visualization of biological events at the

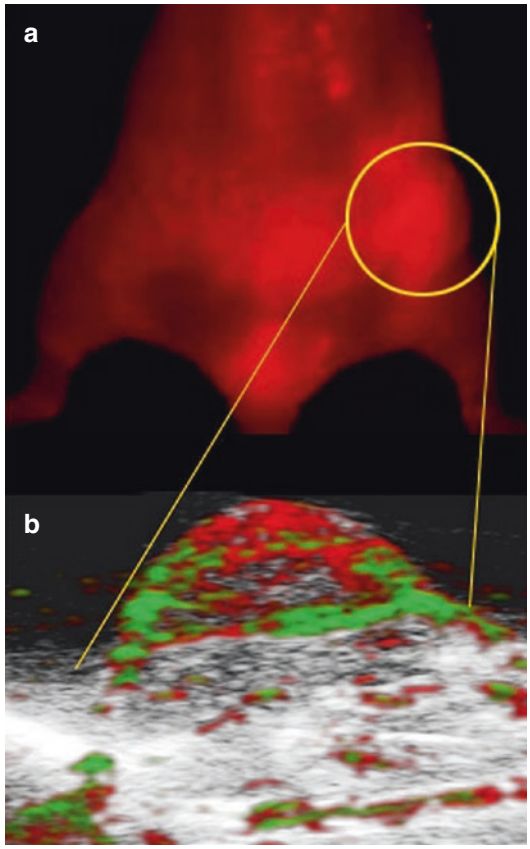

Fig. 14.9 What does the photoacoustic data of a taggable contrast agent look like? (**a**) shows a subcutaneous tumour positive for fluorescent signal from a nanoparticle, and (**b**) shows the complementary photoacoustic data within the microenvironment of the same tumour. The taggable nanoparticle is spectrally unmixed as *green* and is present in the axial and depth peripheries of the tumour. Endogenous blood is clearly unmixed and pseudo-coloured as *red*

physiological and molecular level that can be fused onto real-time anatomical information and in three dimensions over time. All applications that benefit from this image fusion approach including cardiovascular disease, developmental biology, musculoskeletal disease, inflammation, atherosclerosis, regenerative medicine using stem cells and engineered tissues and a wide variety of other mouse models of human disease are developing rapidly. In addition to providing accurate measures of tumour burden in the parenchymal organs, micro-ultrasound enables real-time visualization of flow in the tumour microcirculation. Other applications in cardiovascular disease, developmental biology, musculoskeletal disease, inflammation, atherosclerosis and a wide variety of other mouse models of human disease are developing rapidly.

14.2 Ultrasound Contrast Agents for Small Animal Imaging

François Tranquart, J.M. Hyvelin, and I. Tardy

14.2.1 Introduction

Focal imaging has been used for a while in the assessment of anatomic features both at clinical and preclinical levels. In vivo imaging of small laboratory animals is an outstanding component of new drug development, contributing to the validation of new animal models, the evaluation of drug effects together with a careful assessment of the safety profile. The noninvasive nature of imaging when compared to histopathology has reinforced the use of imaging for serial and longitudinal assays of rodent models of human diseases throughout the disease course.

Among the various imaging techniques available for small animals such as mice and rats, ultrasound imaging including B-mode, M-mode and Doppler mode is playing a major role. Ultrasound techniques have been well established and extensively used for assessing cardiac function and blood flow changes in animal models of cardiovascular or oncology diseases (Hanton et al. 2008; Palmowski et al. 2008). However, the limited sensitivity of Doppler ultrasound for accurate blood flow assessment with devices operating between 3 and 40 MHz is a weakness for examination in small animals.

Contrast agents are now extensively used in medical imaging to enhance visualization of specific cavities or tissue perfusion (Claudon et al. 2013). Even though computed tomography (CT), magnetic resonance imaging (MRI), single-photon emission computed tomography (SPECT) and positron emission tomography (PET) have made extensive use of contrast agents since their initial development, the use of ultrasound contrast agents (UCAs) is more recent and really emerged as a

routine technique in the early 2000s. Besides gross anatomy, lesion extent and other morphological information provided by ultrasound (US) imaging, UCAs are able, after intravenous administration, to provide valuable functional information about perfusion (Correas et al. 2006; Frinking et al. 2000), which often represents a key factor for a definitive diagnosis or for therapeutic guidance.

Since the first report made by Gramiak and Shah in 1968 (Gramiak et al. 1969), showing that air microbubbles could be used in vivo as strong ultrasound scatterers, many improvements have been made in bubble formulations (bubble stabilization methods based on various shell components or fluorinated gas) and in ultrasound equipment, with the introduction of specific imaging sequences to exploit the acoustic properties of these agents in an optimal way. Nowadays, this new method, called "contrast-enhanced ultrasound" (CEUS), is becoming more and more popular in almost all possible indications and organs, thanks to its performance, ease of use, real-time capabilities and low cost.

With the advent of targeted UCA, ultrasound imaging is gaining momentum in the field of molecular imaging due to practical advantages similar to those of CEUS and more particularly due to the simultaneous real-time anatomical and functional/molecular imaging capabilities (Deshpande et al. 2010; Hwang et al. 2010b; Kiessling et al. 2009; Inaba and Lindner 2012).

Despite the recognized added value of CEUS in clinical research, this imaging modality suffers from some limitations at preclinical level, mainly due to the lack of standardization. In preclinical imaging, minimizing variability in data acquisition is an important goal since scientists are eager to draw valid conclusions from their experiments for elucidating various pathophysiological mechanisms or for investigating new drug developments. As such, in-depth knowledge of interaction between ultrasound contrast agents and ultrasound waves together with animal physiology is required (Hyvelin et al. 2013). This will be the purpose of the present paper to present a state of the art on UCAs and related imaging technology for an appropriate use of CEUS imaging in small animals according to their specificities.

14.2.2 Specificities of Ultrasound Contrast Agents (UCAs)

Microbubble diameter sizes are in the micron range. After intravenous administration, microbubbles larger than 6–8 μm in diameter cannot pass the capillaries at the pulmonary level and thus do not reach the left heart and general circulation. Microbubble sizes should therefore preferably be in the 2–5 μm range, i.e. close to or below the size of red blood cells. Microbubbles in this size range are able to move freely in the entire vasculature, including the smallest capillaries. They act as strong ultrasound scatterers due to the fortunate coincidence that their resonance frequencies match well the range of ultrasound diagnostic frequencies (2–20 MHz).

Today, all commercially available ultrasound contrast agents (Fig. 14.10) for clinical use contain

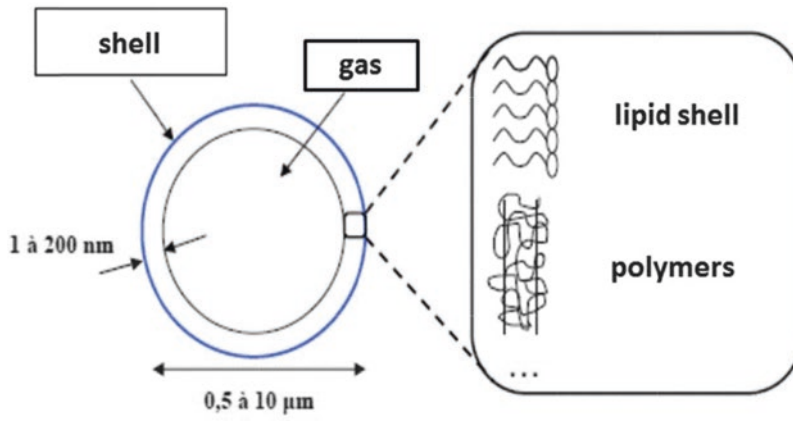

Fig. 14.10 Structure of microbubbles as ultrasound contrast agent. It is a bubble of gas from 0.5 to 10 μm in diameter, encapsulated by a lipid, protein or polymer-based biocompatible shell. The shell thickness can vary from 1 to 200 nm

high concentrations of micron-sized gas microbubbles (10^8–10^{10} microbubbles per mL) stabilized by phospholipids (SonoVue®, Bracco Imaging, Italy; DEFINITY®, Lantheus Medical Imaging Inc., MA, USA; Sonazoid™, Nycomed Amersham Imaging, Oslo, Norway) or heat-denatured albumin (Optison™, GE Healthcare Inc., Princeton, NJ, USA) (Claudon et al. 2013; Correas et al. 2006). The half-life of ultrasound contrast agents after intravenous administration is short, typically a few minutes. This duration is however in most cases sufficient for imaging purposes and has the added advantage that several consecutive injections can be performed during the same examination.

Only minute amounts of gas and stabilizing material are administered in an imaging dose, in the range of a few μL of gas and a few tens of micrograms of phospholipids per injection. These minute quantities reflect the remarkable potency of bubble-based ultrasound contrast agents combined with the high sensitivity of the ultrasound contrast imaging mode, significantly higher than the sensitivity reported for X-ray and magnetic resonance methods.

These clinical UCAs are also commonly used in small animal preclinical studies, and their characteristics are provided in Table 14.6. Few other UCAs have been developed specifically for preclinical research, such as Non-Targeted MicroMarker™ (VisualSonics Inc., Toronto, Canada) and Targestar® (Targeson Inc., San Diego, USA) (Hyvelin et al. 2013).

Ultrasound molecular imaging (US-MI) requires the use of targeted UCAs, which differ from those initially developed for blood pool imaging by the presence of a targeting moiety able to link the bubble to the selected cell biomarker (Kiessling et al. 2012). Once attached, these microbubbles are able to generate detectable echo signals similar to those obtained with blood pool agents, since the signal is generated by the bubble itself and not the ligand. It is important to highlight two characteristics:

- As the microbubbles remain strictly within the vascular compartment, targets of interest must be selected on the luminal side of the endothelial cells (Moestue et al. 2012).
- The attachment of microbubbles to the surface of endothelial cells must be strong enough for vascular areas where shear stress is high due to high blood velocity and viscosity.

Among targeted microbubbles, commercial preparations have been designed specifically for small animal imaging based on streptavidin-functionalized microbubbles (Target-Ready

Table 14.6 Main characteristics of ultrasound contrast agents already commercialized for clinical and preclinical use

	contrast agent	Manufacturer / Distributor	Shell	Gas	microbubble number (mL^{-1})	mean diameter (μm)	
clinical	Optison™	GE Healthcare	Albumin	C_3F_8	5-8 x 10^8	3.0-4.5	non-targeted UCA (vascualr perfusion)
	Definity®	Lantheus Medical Imaging	Lipid	C_3F_8	1.2 x 10^{10}	1.1-3.3	
	Sonazoid™	GE Healthcare	Lipid	C_4F_{10}	1.2 x 10^9	2.4-3.6	
	SonoVue®	Bracco Spa	phospholipid	SF_6	5 x 10^8	1.8	
pre-clinical	BR38[1]	Bracco Suisse SA	phospholipid	C_4F_{10}/ N_2	2 x 10^8	2	
	Non Targeted MicroMarker™	VisualSonics Inc	phospholipid	C_4F_{10}/ N_2	2 x 10^9	1.3	
	Targestar® P	Targeson Inc	phospholipid	C_4F_{10}	1 x 10^9	2.2	
	TargetReady MicroMarker™	VisualSonics Inc	phospholipid	C_4F_{10}/ N_2	2 x 10^9	1.3	targeted UCA (vascular perfusion +USMI)
	Targestar® SA	Targeson Inc	phospholipid	C_4F_{10}	1 x 10^9	2.2	
	Visistar® VEGFR2/Integrin/VCAM-1	Targeson Inc	phospholipid	C_4F_{10}	1 x 10^9	2.2	
	BR55[2]	Bracco Suisse SA	phospholipid	C_4F_{10}/ N_2	2 x 10^9	1.5	

To be noted is the information provided for two agents non-commercially available but largely used at preclinical level

MicroMarker™, VisualSonics Inc., Toronto, Canada; Targestar SA, Targeson Inc., San Diego, CA) (Hyvelin et al. 2013). The ligand can be a protein, an antibody or antibody fragment, an oligopeptide or even an organic small molecule, the only requirement being that a biotin residue be attached to the molecule selected. No separation stage is usually necessary since the amount of biotinylated ligand added can be adjusted in order to be captured entirely by the streptavidin microbubbles. This procedure is very flexible and convenient for small animal imaging, as it allows the preparation of microbubbles coated on their surface with a biotinylated molecule selected by the investigator.

Another strategy is the direct conjugation of the ligand on the PEG spacer. For covalent protein coupling, a maleimide reactive group on the shell is coupled to a thiol group on the ligand, forming a thio-ether bond (Unnikrishnan and Klibanov 2012). Taking advantage of these new approaches, targeted contrast agents, whose outer shell is functionalized with the direct incorporation of specific ligands, have been made available for preclinical research (Visistar® VEGFR2, Visistar® VCAM-1 and Visistar® Integrin, Targeson Inc., San Diego, USA).

Finally, small molecules such as peptides can be conjugated to the shell-forming material before UCA generation (Anderson et al. 2010). Targeted UCA BR55 (Bracco Suisse SA, Geneva, Switzerland), which has reached clinical trial stage, is using a pegylated lipopeptide construct that is inserted into the UCA shell. BR55's capacity to be used in many animal models and humans provides a major advantage when developing a new agent (Pillai et al. 2010; Pochon et al. 2010; Tardy et al. 2010).

14.2.3 Ultrasound Contrast Agent Preparation

Due to microbubble nature of UCAs, specific care must be taken when using these agents. Their use must strictly follow manufacturer's instructions. Non-Targeted MicroMarker™ and Target-Ready MicroMarker™ (VisualSonics Inc., Toronto, Canada), SonoVue® (Bracco Imaging, Italy) are provided in sealed vials as a lyophilized cake in an atmosphere of gas making them stable for several months when stored according to the manufacturer's instructions. These microbubbles are reconstituted by adding saline in the vials and shaking the vials for a few seconds until a milky suspension is obtained. Other UCAs, such as DEFINITY®, Optison™, Targestar® and Visistar® consist of a suspension of microbubbles within the vials. DEFINITY® requires vigorous mechanical shaking for microbubble activation, whereas Optison™, Sonazoid™, Targestar® and Visistar® require gentle homogenization by a top-bottom movement before use. Regarding the Target-Ready MicroMarker™ microbubbles, a biotinylated antibody in solution, usually 10–20 μg per vial, is added in saline at a low enough concentration to ensure no remaining free antibody after mixing. During reconstitution, it is crucial to avoid excessive pressure in the sealed vial, as this will destroy the microbubbles. After reconstitution, UCAs are stable in the sealed vial for a few hours (up to 6 h depending on the contrast agent and the number of withdrawals). The use of microbubbles after the recommended time post-dissolution could increase the variability related to a significantly lower number of microbubbles. Since the solution tends to become less homogeneous due to the natural buoyancy of microbubbles, it is mandatory to mix the vial contents before each retrieval by a top-bottom movement. UCAs can be further diluted with saline. Dilution should be performed into a clean Eppendorf Tube immediately prior to injection to prevent bubble destabilization. Any remaining diluted contrast agent should be discarded.

14.2.4 Contrast-Specific Imaging Modes

UCAs cannot be detected with conventional B-mode imaging. Conventional Doppler modalities, including colour, power and spectral Doppler imaging, are very sensitive to the presence of microbubbles in relation to the increased backscatter. However, this increased sensitivity is hampered by artefacts such as colour blooming and saturation requiring a decrease in the injected dose (bolus or infusion) or the machine gain.

The interaction between microbubbles and US beam is complex and offers a unique opportunity to specifically tune the signal processing to improve microbubble detection in solid tissues (Klibanov et al. 2002). Specific US imaging sequences have been designed to take advantage of the highly specific microbubble resonant properties by varying acoustic parameters such as acoustic power, transmit and receive frequencies, pulse frequency, pulse phase and amplitude (Fig. 14.11) (Frinking et al. 2000; Rafter et al. 2004).

Perfluorocarbon microbubbles present a significant resonance at low acoustic power (MI <0.3) related to the non-linear response to positive and negative pulse with a stronger expansion of the bubble with negative pulse than expected. This low acoustic pressure did not entail burst of the bubble maintaining the bubble almost intact and detected within the vessels, organs or lesions that can be studied in real time in many anatomical planes during a few minutes. This major development of using low MI techniques results in two improvements: (1) longer persistence and improved reliability of contrast enhancement and (2) scanning technique almost identical to that of non-contrast conventional US imaging.

When using high or very high acoustic pressure (MI >0.5), we could also obtain non-linear signals from microbubbles, but the enhancement duration is shortened by the disruption of microbubbles by excessive pressure. This did not allow real-time image. This method could be combined with low MI techniques to perform replenishment image: for this, after some pulses with high MI to destroy all microbubbles within an area of interest, we switched to low MI technique to detect a new arrival of microbubbles within the same area. It has been shown that replenishment is proportional to the local blood flow. In particular, both blood flow velocity and blood flow volume may be calculated by this method.

Among the specific US imaging sequences developed by the manufacturers, pulse or phase inversion imaging (PII), cadence contrast pulse sequencing (CPS) and pulse inversion amplitude modulation (PIAM) technology are at present the most efficient in our experience.

Pulse or phase inversion imaging was first introduced by ATL, Philips and Siemens and is now available in most high-end US systems. It relies on the different microbubble behaviour when the UCA is exposed to consecutive pulses of inverted phase. The reflected signals which contain reflection from background tissue and from microbubbles are stored and summed in the digital beamformer. The sum of the two out-of-phase

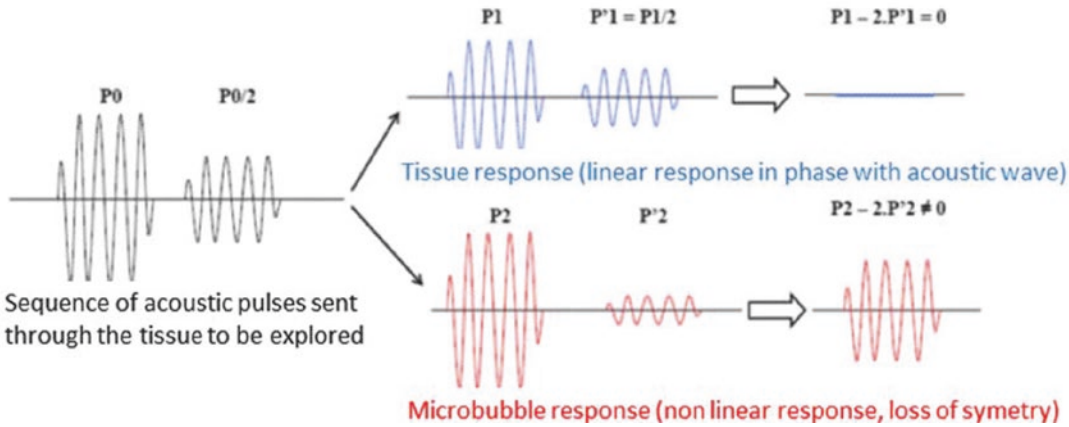

Fig. 14.11 Principle of amplitude modulation contrast imaging. A pulse amplitude P0 is sent on medium whose echo is recorded, followed by a second pulse amplitude P0/2. The tissue response to the pulse amplitude P0/2 (amplitude P'1) is two times lower than that to the pulse amplitude P0 (amplitude P1), due to the linearity of the response of the tissues with pressure. On the other hand, the response of microbubbles will not show this relationship of proportionality: the response to the pulse amplitude P0 (amplitude P2) is not twice the response to the pulse amplitude P0/2 (amplitude P'2). Thus, subtracting twice the response of the environment to the pulse amplitude response P0/2 from the response to the pulse amplitude P0 will cancel the component corresponding to the tissues without losing the component corresponding to the contrast agent

signals obtained from the background tissues is close to zero, cancelling the fundamental signals. On the contrary, the sum of the two signals obtained from the microbubbles differs from zero. The detection of the microbubbles is strongly enhanced, particularly if the microbubbles exhibit strong non-linear response and tissue displacement is negligible. This PI mode could be used with high and low MI according to the differences mentioned above.

Cadence CPS imaging, introduced by Acuson-Siemens, or PIAM combines amplitude and phase modulations in order to extract the non-linear fundamental signals. This technique should improve detection of microbubbles particularly in the deep field from which non-linear signals are extremely weak.

Real-time contrast imaging is now combined with simultaneous B-mode imaging by using a dual view with a split screen allowing us to see dynamic enhancement within a lesion on one side and the background tissue on the other one for anatomical support. This B-mode image is obtained with low acoustic pressure in order to preserve the microbubbles from disruption. This capability is mandatory to track the enhancement of small lesions that cannot be seen before the arrival of contrast by the absence of signal. It could be superimposed to background fundamental B-mode image.

At baseline, when contrast-specific imaging modes are used, the residual signal in an area of interest (AOI) is usually minimal, provided that proper ultrasound platform settings and animal preparation are used. Following administration of UCA, a very substantial enhancement of the vascular compartment can be seen. The enhancement observed for non-targeted contrast agents follows a very simple pattern (Fig. 14.12). The initial part of the curve (wash-in and early wash-out) is related to the vascular distribution of the agent in the organ/lesion of interest. The intensity of the detected signals is proportional to the local concentration of microbubbles interrogated by the acoustic beam. Since UCAs are pure blood pool agents, the wash-in curve can be used to quantify vascular parameters in that lesion, such as time for contrast arrival,

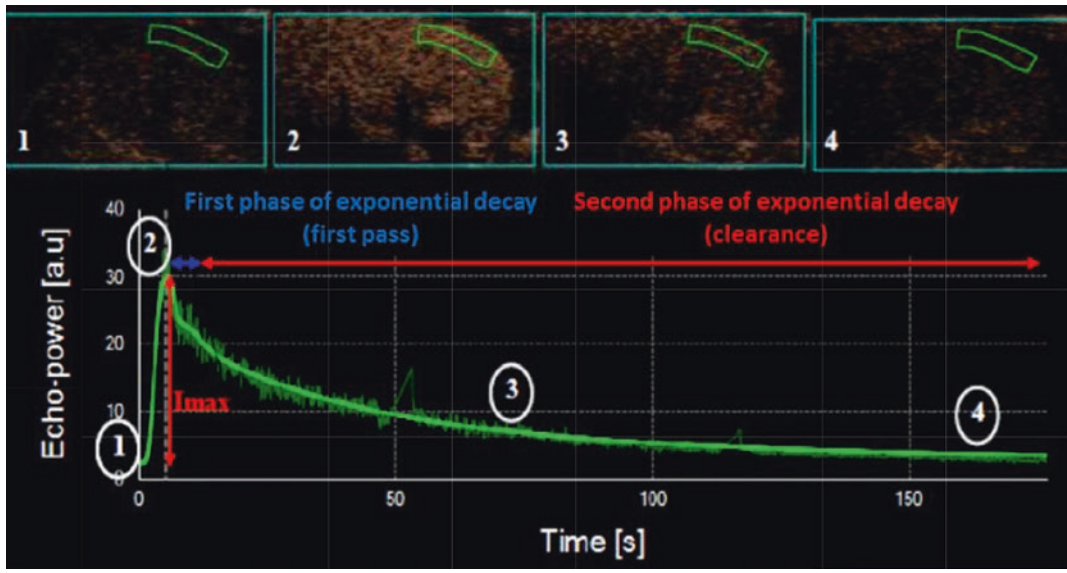

Fig. 14.12 Example of wash-in/wash-out curve and the bolus two-phase model allowing to extract the relevant parameters (agent SonoVue, ROI at the level of the upper cortex of the kidney, volume of agent injected 50 μL). There is an initial phase where the signal increases until the Imax value; it is the phase of filling (wash-in). There is then a first phase of exponential decay which corresponds to the first passage of the agent in the bloodstream. Then comes a second phase of decay exponentially, longest, which corresponds to the elimination of the agent by the animal (wash-out). We observe that in the case of SonoVue, elimination is very fast. Top panel images are contrast images acquired before contrast filling (1), at the time when the intensity is maximum (2), in the middle of the second phase of decay (3) and at the end of the elimination (4)

rise time, maximal peak enhancement and area under the wash-in curve. The second part of the curve (wash-out curve) which starts from the peak enhancement corresponds to the clearance of contrast agent from the vascular compartment in relation to reticulo-endothelial system capture, non-specific microbubble retention and bubble collapse. The clearance time (usually several minutes) will depend on the dose of UCAs used as well as on the UCAs circulation characteristics.

Basically, the imaging modes used for imaging targeted microbubbles are rather similar to those used for non-targeted agents. However, the simultaneous presence of bound and circulating microbubbles after injection has triggered the need to develop new imaging strategies for the specific detection of bound microbubbles, excluding those remaining in circulation. As a matter of fact, only a very small fraction of the injected site-specific microbubbles actually reach and stick to the endothelial receptors. The large majority will transit freely throughout the microcirculation for minutes after injection before complete clearance from the bloodstream. Therefore, one strategy could be to wait for a complete disappearance of circulating microbubbles from the vascular compartment but this would be time consuming and could expose the investigator to the detection of less bound bubbles due to their natural collapse. Therefore, the use of an alternative imaging sequence based on the destruction-replenishment concept has been proposed. Since these UCAs are relatively fragile, they can be destroyed within the imaging field by applying ultrasound pulses at sufficiently high mechanical index (MI >0.8) over five or more frames. Following the destruction within the imaging frame of both attached and circulating microbubbles, UCAs still in circulation will replenish the scan plane with an unbound bubble concentration close to the one immediately before destruction. Therefore, by subtracting the signal measured after the destructive pulses from the signal measured before this destructive pulse, the relative amount of bound microbubbles within the area of interest can be estimated. The name "differential targeted enhancement" was coined at Bracco Suisse for this method, as used in the VevoCQ™ software package (VisualSonics Inc., Toronto, Canada).

Other approaches to selectively visualize and quantify bound targeted microbubbles are under investigation such as image processing or the use of new acoustic methods like plane waves (Couture et al. 2012).

14.2.5 The Importance of Quantification

The quantification of perfusion has been proposed as an adjunct to the visualization of characteristic enhancement patterns to identify specific diseases, to differentiate benign from malignant focal lesions, to screen different molecules in an animal model or to characterize local response to specific treatments.

Following administration of blood pool agents, the measurement of the mean signal intensity in the AOI as a function of time provides information on the local concentration of microbubbles and hence – since UCAs are pure blood pool agents – on blood perfusion parameters in the scanning plane. Typically quantification tools operate as an off-line application after CEUS is performed (Pysz et al. 2012). These tools are using either raw data (obtained before signal processing) or linearized data from recorded DICOM clips before assessing perfusion using patented curve fitting models. When applying data linearization, the compression law is system- and settings-dependent, meaning that the appropriate law has to be selected prior to linearization of the video signal (Rognin et al. 2010; Mule et al. 2007). The validity of this approach has been confirmed for all tested systems based on the strict proportionality between the local bubble concentration and the measured echo signal (Payen et al. 2013). Further to the curve fitting, several parameters can be derived from the time intensity curve such as time to peak, peak intensity, mean transit time, area under the curve, etc. (Kiessling et al. 2009; Tranquart et al. 2012).

This is also of utmost importance for US-MI since a relatively low number of microbubbles are expected to bind to cellular biomarkers, and so it is important to be able to detect these few microbubbles with high sensitivity. The situation

is more complex than for perfusion quantification in the sense that there is no strict proportionality between the detected signal and the absolute level of expression of a given marker. As such, it is recommended to rely more on relative measurements than on absolute values, but, nowadays, no straightforward method is available for that purpose.

Nevertheless, some groups have already reported changes in the amount of microbubbles bound in a selected area which matched nicely the level of expression of a given receptor as assessed by immunohistochemistry. This means that US-MI might be used for treatment monitoring in order to assess treatment efficacy or to identify possible mechanisms underlying therapeutic effects.

14.2.6 Recommendations

14.2.6.1 Animal Handling During CEUS Imaging Session

Special care should be taken regarding animal preparation and handling during ultrasound imaging (Hyvelin et al. 2013). Skin hair must be completely removed, using depilatory cream, in order to avoid the lack of enhancement produced by hair particularly when using high ultrasound frequency. Warm acoustic gel should be applied all over the area between the animal and the transducer avoiding air microbubbles that will produce strong attenuation.

Body temperature control is of utmost importance (Fig. 14.13). During anaesthesia, animals are preferably placed on a heating pad to prevent a drop in their body temperature which can impact nega-

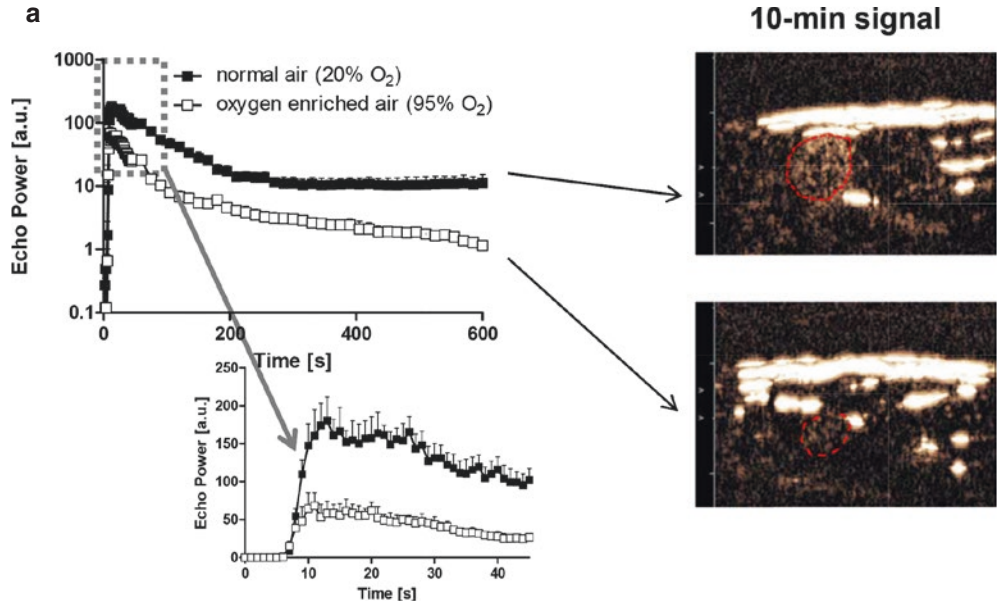

Fig. 14.13 Effect of speed rate of injection on ultrasound-enhanced signal (from 11). (**a**) In a rat model of prostate tumour, three successive injections of BR55 microbubbles (80 µL/kg of body weight of BR55 completed up to 50 µL with saline, i.v. injection, tail vein) were performed. Injections were made at different rates, and injection order was randomized. Lowering the rate of injection significantly decreased time to peak as well as maximal peak enhancement (*Imax*). Typical image of prostate tumour at *Imax* is shown on the right side. Red dotted line indicates the tumour. (**b**) Typical example demonstrating the added value of a semiautomated (controlled) system to inject UCA. In rats ($n=4$), four successive injections (tail vein) of UCA were performed manually or using an automated pump to maintain a constant speed rate set at 4 mL/min. Using the controlled injection system, the wash-in and wash-out phase of the TIC were more reproducible. (**c**). Effect of body temperature on contrast-enhanced signal was assessed in both rat and mice bearing mammary tumours. Graphs showed *Imax* and 10 min late phase signal in response to BR55 (80 µL of BR55/kg of body weight) in rat (MatBIII cells implanted in the mammary fat pad, $n=6$, *left graph*) and mouse (DA3 cells implanted in the mammary fat pad, $n=6$, *right graph*). Body temperature was either maintained using a heating pad *plus* heating lamp or a heating pad alone. In the latter case, both *Imax* and late phase signal, measured 10 min after microbubble injections, were lower

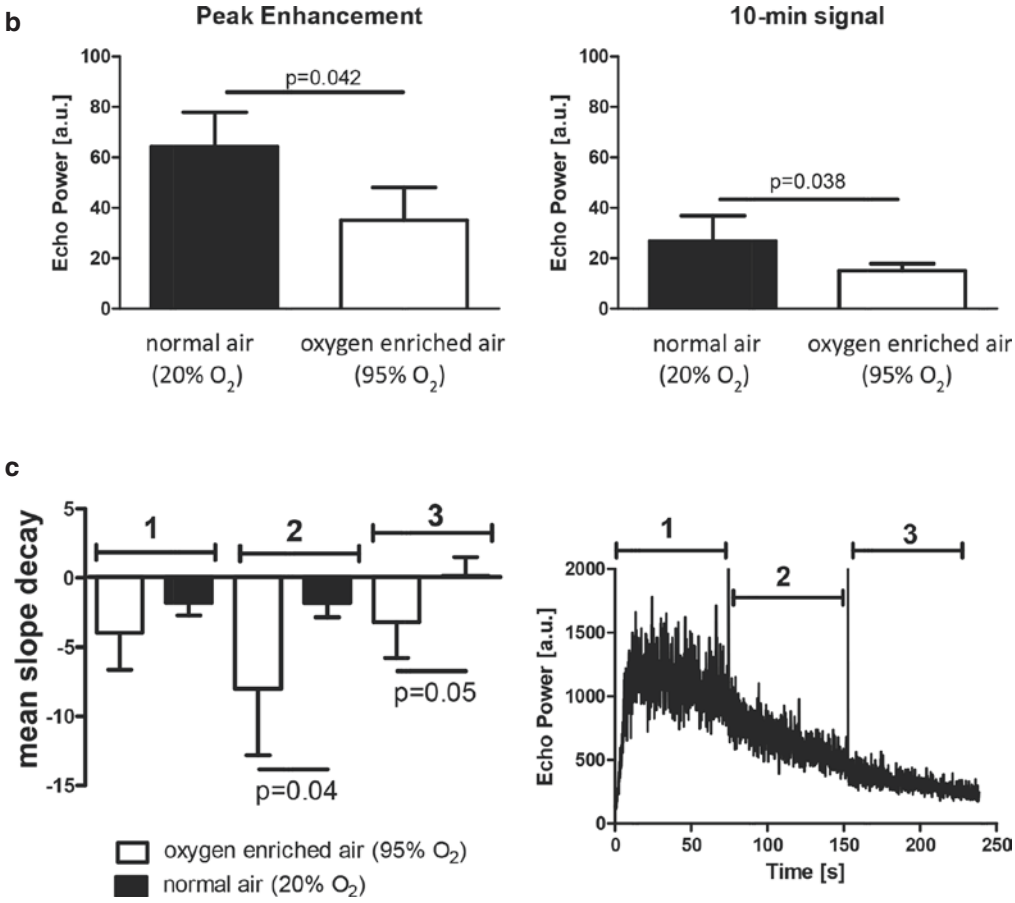

Fig. 14.13 (continued)

tively the enhancement. In this regard, previous study shown that hypothermia (32°C) significantly alters dorsal skin blood flow rate, as well as blood flow of subcutaneously implanted tumour. Alteration in blood flow will ultimately affect UCA distribution and might then impaired reproducibility of successive injection throughout an imaging session.

After anaesthesia induction in small animal when using isoflurane, it is recommended to perform ultrasound examinations under medical air to maintain a good lifetime of microbubbles and to improve reproducibility between experiments. Indeed it has been shown that the use of 100 % oxygen as carrier gas could significantly decrease

Fig. 14.14 Effect of anaesthesia carrier gas on contrast-enhanced ultrasound signal (from 11). (**a**) In a rat model of prostate cancer, both peak enhancement and late phase 10 min signal in response to two successive injections of BR55 (80 µL/kg of body weight) were performed. Between the two injections, the isoflurane anaesthetic gas was driven either by medical air (20 % oxygen) or oxygen-enriched air (>95 %). Under high oxygen concentration, both peak enhancement and late phase 10 min signal were decreased. Curves are the mean ± SD obtained from eight animals. (**b**) Similar experiments performed in a model of TNFα-induced mouse hindlimb inflammation. Twenty four hours after TNFα treatment, microbubbles specifically targeted to P-selectin were injected intravenously (50 µL Targeted MicroMarker™ specific for murine P-selectin). In mice anaesthetized with isoflurane/medical air, *Imax* and 10 min signal were higher compared to mice anaesthetized with isoflurane/oxygen-enriched air. (**c**) Effect of switching anaesthesia carrier gas during the wash-out phase of the time intensity curve in response to Non-Targeted MicroMarker in a large artery of mouse hindlimb. Experiment was performed on six mice, with randomized order of anaesthesia carrier gas. Bar graph shows mean slope decay for each condition

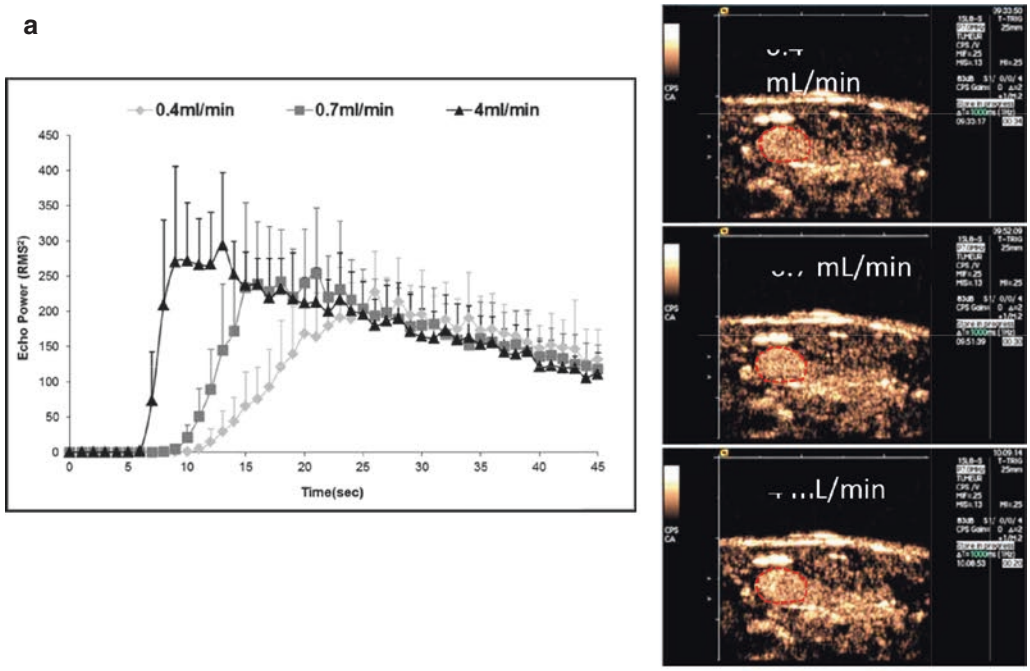
a
0.4ml/min
0.7ml/min
4ml/min
Echo Power (RMS²)
Time(sec)
mL/min

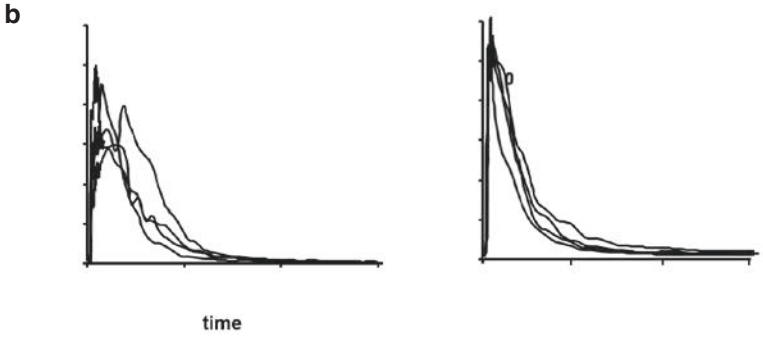
b
time

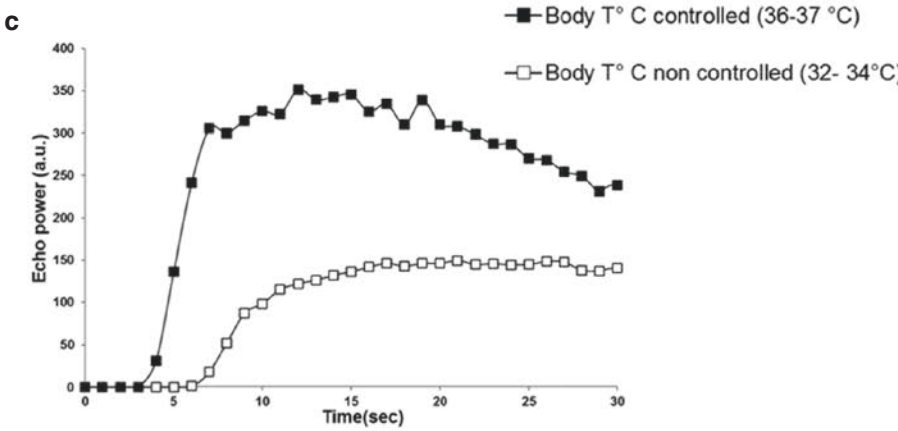
c
Body T° C controlled (36-37 °C)
Body T° C non controlled (32- 34°C)
Echo power (a.u.)
Time(sec)

the enhancement duration by promoting a faster exchange of gas between the core of the microbubbles and the vascular environment. Therefore, changing carrier gas from 100 % oxygen to medical air (20 % O_2) will dramatically impact the half-life on the UCA and thus the final results (Mullin et al. 2011) (Fig. 14.14).

14.2.6.2 Ultrasound Platform Settings

All changes in ultrasound platform settings will modify the detected ultrasound signal (Hyvelin et al. 2013). The acoustic power, or mechanical index (MI), is one of the most important parameters to be considered. CEUS requires low MI in order to minimize microbubble destruction, this being crucial when performing molecular imaging. Recommendations provided by ultrasound companies should be followed cautiously.

Continuous insonation at high frame rate of the organ/lesion of interest will increase microbubble destruction and therefore decrease the late phase signal, more particularly in tissues with low blood flow, such as tumours. When assessing only the perfusion parameters, using a non-targeted contrast agent, a frame rate of 1–2 Hz is recommended for a low blood flow organ, but for higher blood flow, as found in the kidney and heart, a higher frame rate (5–10 Hz) is preferable. For targeted agents, a significantly lower frame rate below 0.1 Hz is enough for detecting properly microbubble binding.

Among the other parameters to be considered, gain, focus position and tissue gain compensation (TGC) will also affect signal intensity. It is important to refer to user manual of the equipment as well as to keep constant these parameters when performing longitudinal follow-up studies. We recommend adjusting TGC settings in a fixed and reproducible pattern (preferably "flat" or linear). The use of automatic TGC is not recommended since different values could be obtained from time to time (Gauthier et al. 2011).

14.2.6.3 Determination of the Optimal Concentration of UCAs

In the setting of a new ultrasound imaging protocol, determination of the optimal dose of contrast agent is crucial, more particularly when quantitative perfusion parameters are needed (Hyvelin et al. 2013). It is essential to refer to companies recommendations to avoid artefacts such as weak enhancement due to a too low amount of microbubbles or shadowing due to an excessive amount of microbubbles in the organ of interest (Figs. 14.15 and 14.16). The recommendations have been established under strict conditions and as such must be followed in the absence of specific requirements. Typically the dose of UCAs should be adjusted for preclinical use since animal physiology, and the use of high ultrasound frequencies and slighter higher mechanical index will modify the conditions for an appropriate detection.

When it comes to the targeted contrast agent, the same recommendation applies. Furthermore, it is important to consider that targeted UCAs generally become detectable only after the large majority of unbound microbubbles cleared from the bloodstream. As a matter of fact, only a very small fraction of the injected targeted UCAs will actually reach and stick to the endothelial receptors. It is important to adjust the dose of targeted contrast agent to obtain a good signal from bound microbubbles after a rapid elimination of unbound microbubbles. A proper dose ideally allows measurement of targeted microbubbles 5–10 min after injection of contrast agents.

14.2.6.4 Injection Procedure of UCA

UCAs are injected intravenously (i.v.) in small animals, as in man (Hyvelin et al. 2013). In preclinical studies, UCAs are administered either preferably as a bolus, followed or not by a flush of saline, or less frequently as an infusion. The injected volume should remain typically lower than 100 μL to avoid overload which can modify physiology conditions. It is essential to remind each user the pressure sensitivity of UCAs leading to major caution during the injection. Indeed an overpressure could break a large part of the microbubbles within the syringe leading to the absence of contrast enhancement. Based on our experience, we are recommending a 25G for rat tail vein and a 27G for mouse tail vein connected to a Hamilton syringe. We recommend a device constituted of a three-way valve, with one end connected to a pump, a second end connected to the butterfly needle and the third end connected to a Hamilton syringe. UCAs are then loaded into the system and injected into the tail by mean of a flush of saline controlled by the syringe pump. The use of a flush whose volume is higher than the

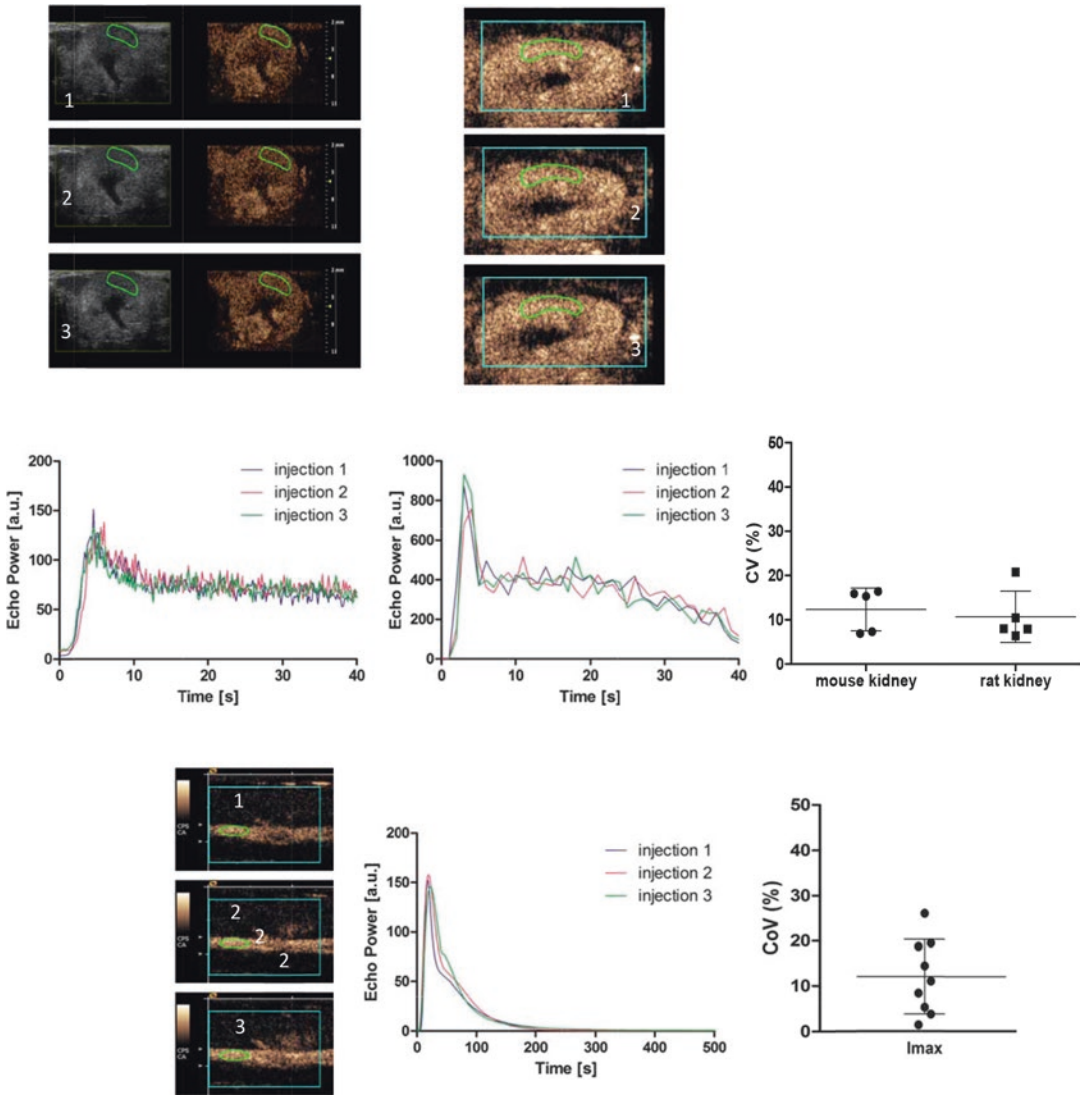

Fig. 14.15 Quantification of contrast enhancement within a rat renal cortex after intravenous injection of Non-Targeted MicroMarker. Two ROIs have been drawn, ROI 1 in *green* as a superficial ROI and ROI 2 in *yellow* as a deep ROI. When plotting the peak intensity (Imax in arbitrary units) in these two ROIs according to an increased dose of agents, we observed that until 10 μL, the measured enhancement was the same in the two ROIs, while over this dose, the enhancement in the deep ROI (in *blue*) reached a plateau due to an attenuation effect related to the superficial enhancement (which is still increasing in red)

injected volume of microbubbles ensures a complete injection of the dose, avoiding any loss of microbubbles trapped in the tubing and/or the access vein. Obviously it is important to standardize the injection mode based on local expertize since this might be a large source of variability between injections. As such the speed of injection should be kept constant (Fig. 14.13).

14.2.7 Applications of Ultrasound Contrast Agents

14.2.7.1 Vascular Imaging

After intravenous injection, UCAs will enhance all blood-containing compartments. Contrast-enhanced ultrasound of vessels is superior to colour or power Doppler for the detection of

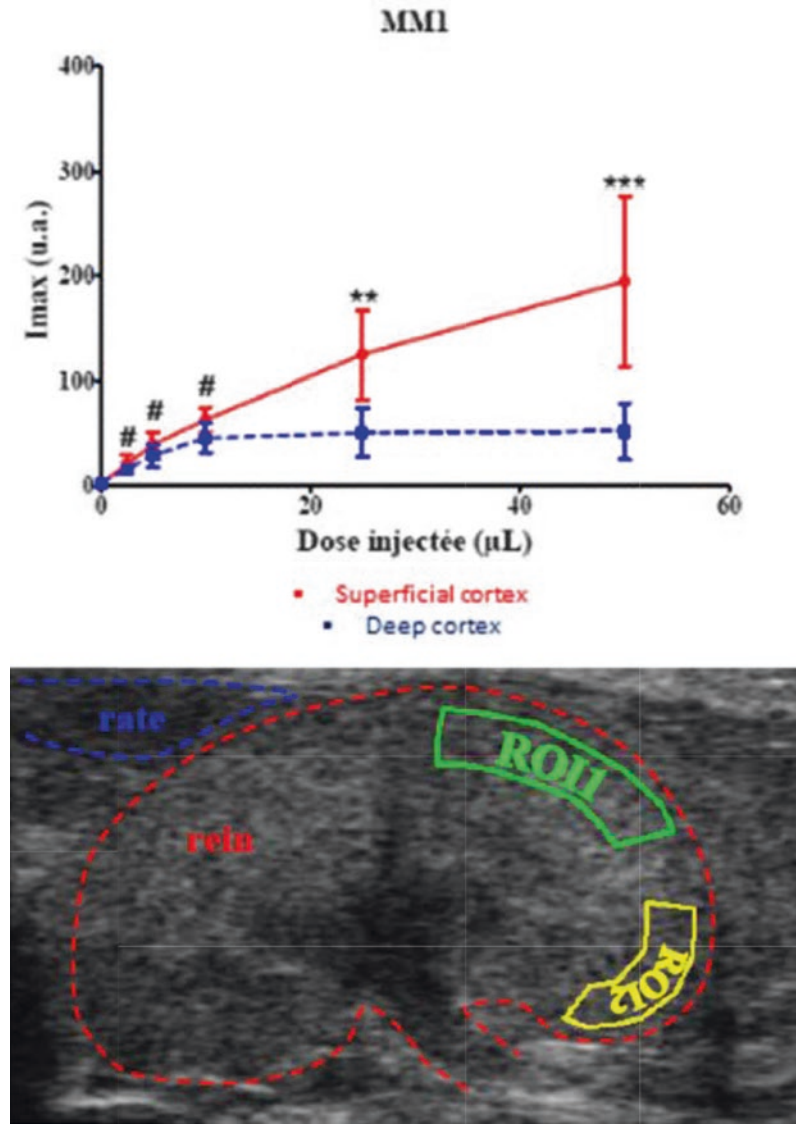

Fig. 14.16 Contrast-enhanced signal measured in normal organ/tissue in response to successive injection of UCA (from 11). (**a**) Typical example showing ultrasound contrast enhancement in a rat kidney in response to three successive injections of SonoVue® (0.03 mL/kg). Between each injection, 5 min latence period was observed. Graph on the right indicates the coefficient of variation (CoV) of *Imax* determined in three different rats. (**b**) Typical example TICs generated at the level of the renal artery in response to three successive injections of BR55 (0.08 mL/kg). CoV of Imax was determined in six different rats

microcirculation, due to a higher spatial and temporal resolution. These include heart ventricles and large vessels as in clinic. Left ventricle opacification and endocardial border delineation might help in identifying more precisely the endocardial border and therefore facilitates the detection of areas with abnormal ventricular contraction or the presence of abnormal structures. Similarly, in large vessels, the presence of contrast may help in determining precisely the size of the vessel, to evaluate the vessel wall thickness (intima-media thickness), to detect atherosclerotic plaque, stenosis, occlusion and blood leakages.

14.2.7.2 Tissue Perfusion

The level of tissue perfusion is the most important indicator of blood, oxygen and nutrient supply to parenchymal cells. Thanks to the high signal-to-noise ratio and to the exquisite sensitivity of contrast-specific imaging modes, it is now possible to detect microbubbles in small vessels, down to the capillary level. Real-time tissue perfusion assessment has opened large opportunities in the field of small animals by giving access to tumour blood flow assessment and monitoring under specific treatments, detection of abnormal local perfusion due to various procedures or simple physiological

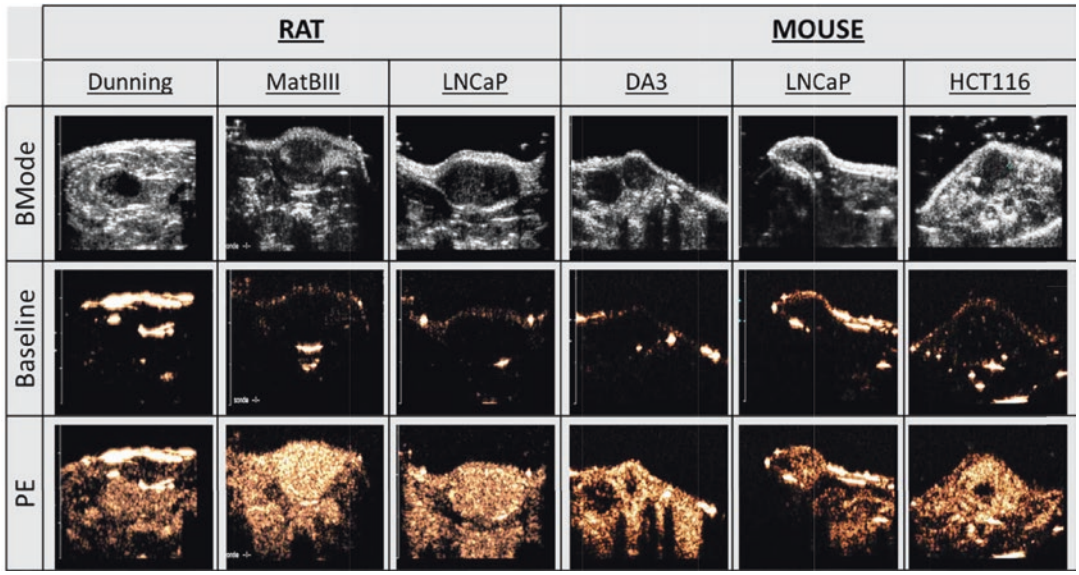

Fig. 14.17 Typical contrast enhancement obtained in various animal models in rats (Dunning, Mat B III, LNCaP) and mice (DA3, LNCap and HCT116). On *top panel* are presented B-mode images of each tumour in these animal models. On middle panel are presented images at baseline in contrast-enhanced ultrasound mode after injection of BR55 at a dose of 0.8 μL of gas/kg weight, while on the bottom panel are presented images obtained at peak enhancement after this injection. To be noted is the heterogeneity of enhancement in few models according to the degree of necrosis

response (Lucidarme et al. 2006; Thibault et al. 2005). This is a strong advantage over other imaging modalities which cannot provide such real-time assessment or easy monitoring. Changes in blood flow and vascular volume could be measured quantitatively in tumour-bearing rats providing useful data for treatment monitoring. This rapid effect of test drugs might also become important for identifying the optimal time window and dosing of drugs (Guibal et al. 2010; Seiler et al. 2007; Zhou et al. 2011) (Fig. 14.17).

14.2.7.3 Targeted Agents

The main areas of use of these targeted UCA are for the detection of neoangiogenesis and inflammation (Pysz and Willmann 2011; Pysz et al. 2010) (Figs. 14.18, 14.19, and 14.20). A large number of preclinical studies have been performed taking advantage of the commercially available biotinylated ligands and ready-to-use streptavidin microbubbles. In the course of the inflammatory process, various cell surface markers are expressed or upregulated on the luminal side of endothelium and therefore are accessible to targeted microbubbles. Several studies have demonstrated the feasibility of imaging inflammation (targeting ICAM-1, P-selectin and VCAM-1) in various cardiovascular diseases, including heart transplant rejection, atherosclerosis (Kaufmann et al. 2007), kidney ischemia/reperfusion (I/R) (Lindner et al. 2001) and cardiac I/R (Davidson et al. 2012, 2014; Hyvelin et al. 2014; Villanueva et al. 2007), inflammatory bowel disease (Wang et al. 2013; Deshpande et al. 2012) and more recently in inflamed endothelium of obese macaques (Takalkar et al. 2004). Among these markers, P-selectin plays critical role in the first cellular event of inflammatory processes. In a rat model of transient ischemia, we showed that US-MI using a targeted UCA specific for selectins based on rPSGL-Ig ligand (MB-selectin) allows the detection of a past myocardial I/R events (Hyvelin et al. 2014; Bettinger et al. 2012).

In addition to endothelial receptors, site targeted microbubbles can also be used for the visualization of thrombi associated with stroke. Immunobubbles bearing abciximab, a glycoprotein IIb/IIIa receptor inhibitor, were shown to improve visualization of human clots both in an in vitro and in an in vivo model of acute arterial

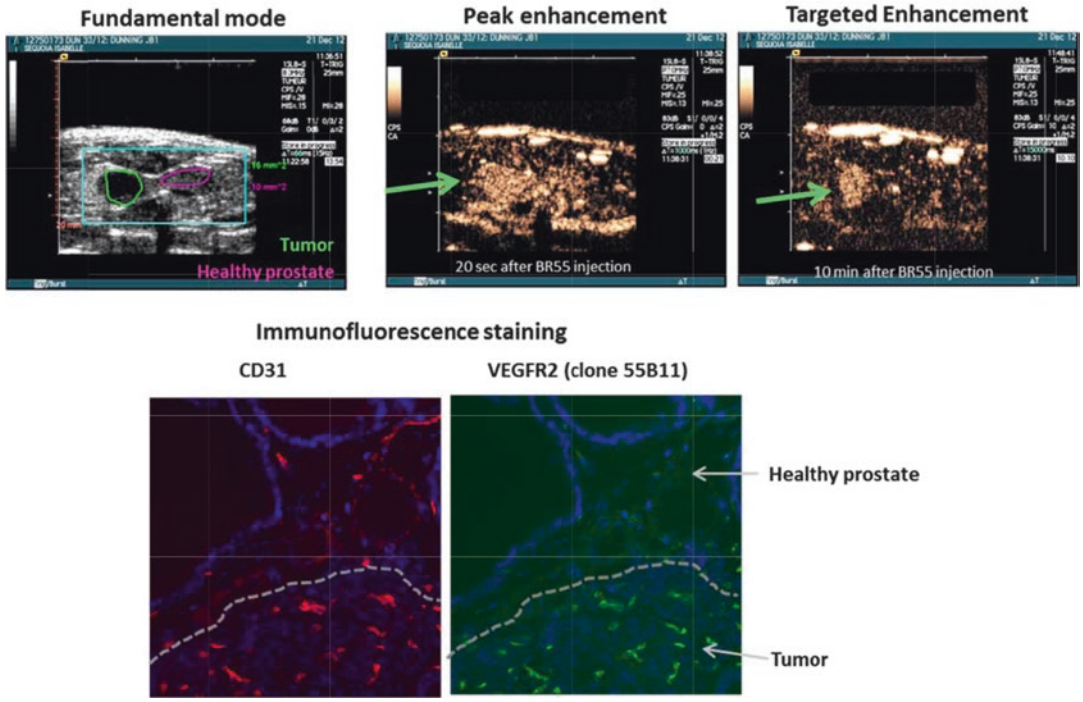

Fig. 14.18 Preclinical ultrasound molecular imaging of a Dunning prostate tumour with BR55 (ultrasound targeted agent for VEGFR2). *Top panel*: *Left*, B-mode image of the rat prostate with the tumoural part in *green* and the healthy part in *pink*. *Middle*, 20 s after BR55 injection the enhancement was slightly higher on the tumour side, indicating a higher vascularity. *Right*, 10 min after BR55 injection, only the tumour remains strongly enhanced. *Lower panel*: Immunohistochemistry confirmed the strong expression of VEGFR2 in the tumour vessels (identified by CD31 staining) compared to the basal level of VEGFR2 in the healthy prostate

thrombotic occlusion (Della et al. 2008; Alonso et al. 2007).

The second important area, in which US-MI has clearly emerged, is tumour detection and more particularly tumoural neoangiogenesis, i.e. the formation of new blood vessels, which is a fundamental process occurring during tumour progression. Among the key molecular pathways that regulate angiogenesis, the VEGF-A and its receptor VEGFR2 are the most important (Lyshchik et al. 2007b; Bachawal et al. 2013). A biotinylated anti-mouse VEGFR2 antibody coupled to streptavidin microbubbles showed significantly higher signal intensity in two murine models of breast cancer compared to control microbubbles (Willmann et al. 2008; Bzyl et al. 2013, 2011). In addition, the level of signal observed correlated well with the expression of VEGFR2 in these two tumour types. Similar results were reported in two murine models of angiosarcoma and malignant glioma (Forsberg et al. 2011). Many other biomarkers have been identified in this complex process such as neuropilin 2, the αvβ3 integrin and endoglin (CD105) (Willmann et al. 2010; Ellegala et al. 2003).

More recently, BR55, a clinical-grade UCA targeted to VEGFR2 (Bracco Suisse SA, Geneva, Switzerland), has been evaluated in animal models and also in man for the assessment of tumoural angiogenesis (Pochon et al. 2010; Tardy et al. 2010).

Several receptors can also be imaged in the same animals during tumour growth. For instance, VEGFR2 and αvβ3 integrin or endoglin (CD105) can be monitored separately during treatment. As shown in these studies, targeted microbubbles can be used not only to detect the presence of different markers expressed on endothelial cells but also to monitor changes in receptor levels longitudinally in response to therapy. Treatment with antiangio-

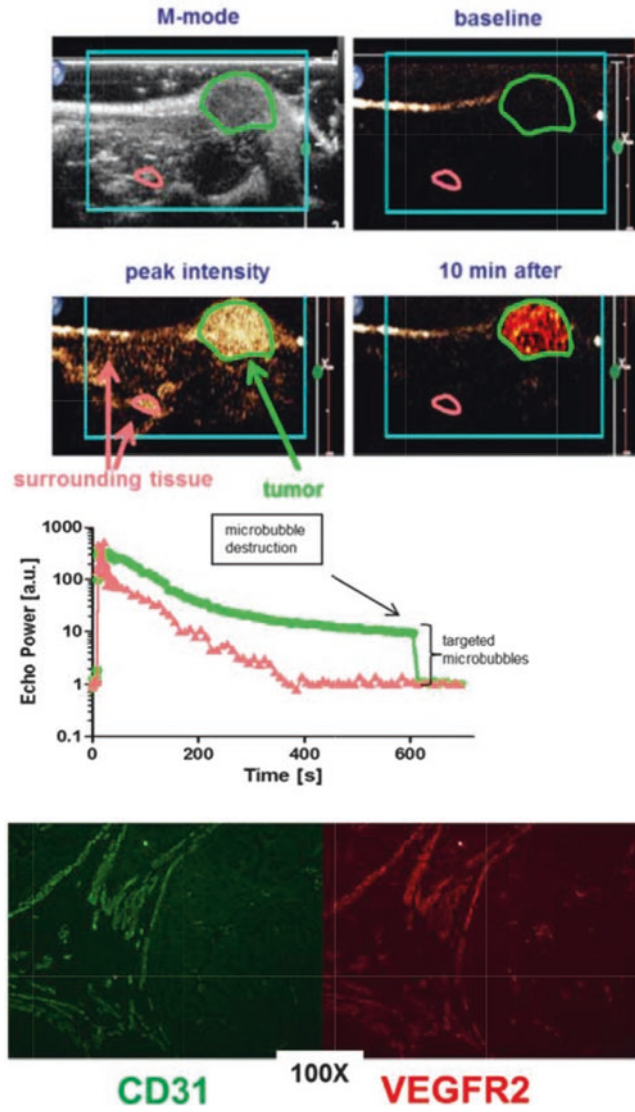

Fig. 14.19 This example refers to the use of BR55 microbubble in a mouse model of colon cancer tumour HCT116. On top left are presented image in B-mode with a clear delineation of the tumour and image at baseline before injection of BR55 (agent targeted for VEGFR2). Below is a presented image obtained at peak intensity demonstrating a strong and homogeneous enhancement (*left*) with a corresponding late phase enhancement obtained at 10 min after BR55 injection further to image processing and demonstrating an almost exclusive binding of BR55 in the area of the lesion. On *top right* is presented the acquisition mode with a time intensity curve which shows a progressive decrease in signal both in the lesion and surrounding tissue with a higher detected signal within the lesion. The specific binding is obtained after applying destructive pulses and replenishment to differentiate specific from non-specific detected signal. On *bottom right* are reported immunohistochemistry results of the lesion for both CD31 and VEGFR2 receptor illustrating the high vascularity and overexpression of VEGFR2 in this lesion

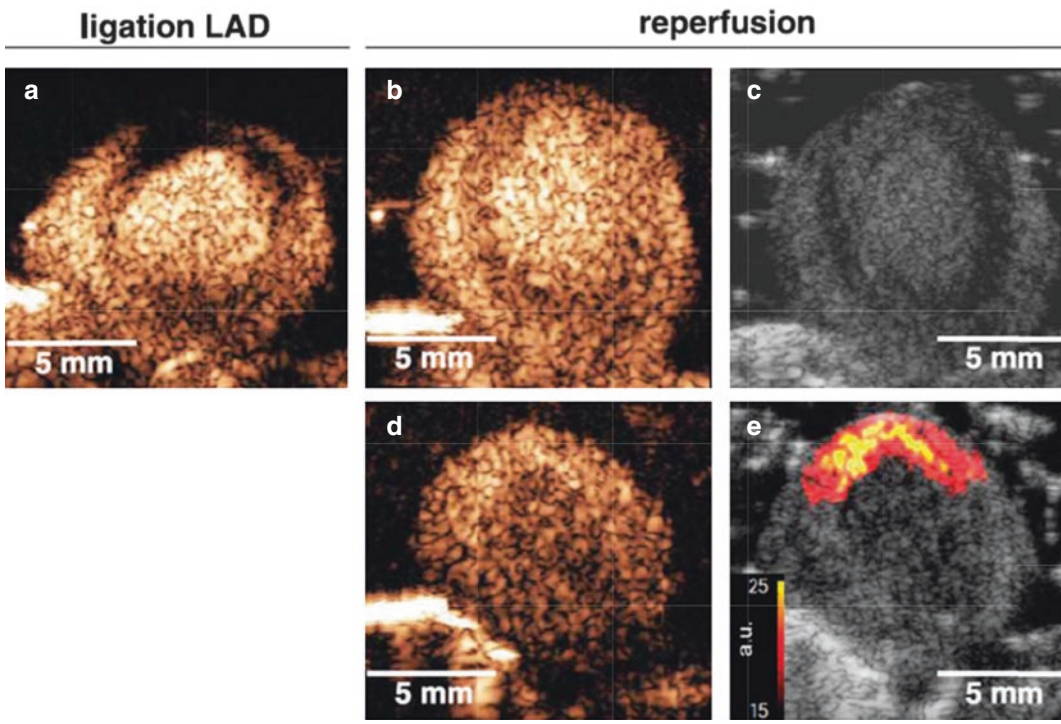

Fig. 14.20 Typical examples of US-MI of a transient ischemic event in rat subjected to 20 min LAD occlusion followed by 2 h reperfusion. (**a**), During LAD ligation, injection of BR38 allowed imaging of the ischemic territory within the anterolateral and free walls of the LV. (**b**), Late phase enhancement of BR38, 2 h after reperfusion, revealed uniform enhancement in the left myocardium, suggesting no binding of BR38. (**c**), Image obtained with a postprocessing US-MI method was overlaid on the corresponding B-mode (anatomical) image and revealed no bound BR38 MB. (**d**), The same rat, US-MI using MB-selectin, 2 h after reperfusion, revealed higher late phase enhancement whose location matched the ischemic area as determined with BR38 during LAD ligation. (**e**), Image obtained with a postprocessing US-MI method, identifying bound MB-selectin in the myocardium previously ischemic, was overlaid on the corresponding B-mode (anatomical) image (from 46)

genic or cytotoxic therapy resulted in a reduction in binding of microbubbles targeted to these receptors (Korpanty et al. 2007). This reduction correlated with a reduction in tumour microvessel density. Changes in receptor levels might be very early signs of treatment efficacy, well before any morphological and/or functional change is detected and might therefore be used as surrogate markers and good predictors of response to antiangiogenic or cytotoxic chemotherapy (Fig. 14.21).

14.2.8 Discussion and Conclusion

Ultrasound is a real-time imaging modality ideally suited for medical imaging, thanks to its very broad range of applications, its high spatial and temporal resolution and low cost. With the addition of a contrast agent, ultrasound imaging provides additional functional information on blood flow and tissue perfusion. The development of targeted UCAs has expanded the role of ultrasound and contrast-enhanced ultrasound beyond perfusion measurements into molecular imaging applications.

This exciting new area requires a multidisciplinary approach involving biologists, physiologists, physicists, engineers and clinicians to value the use of these agents and to provide valuable insights for pathophysiology and drug treatment development.

The combination of anatomic, functional and molecular information/data provided by contrast-enhanced ultrasound is a powerful tool for pathophysiological investigation as well as drug treatment development. This is paving the way for valuable use of these agents and these ultrasound techniques in several clinical domains.

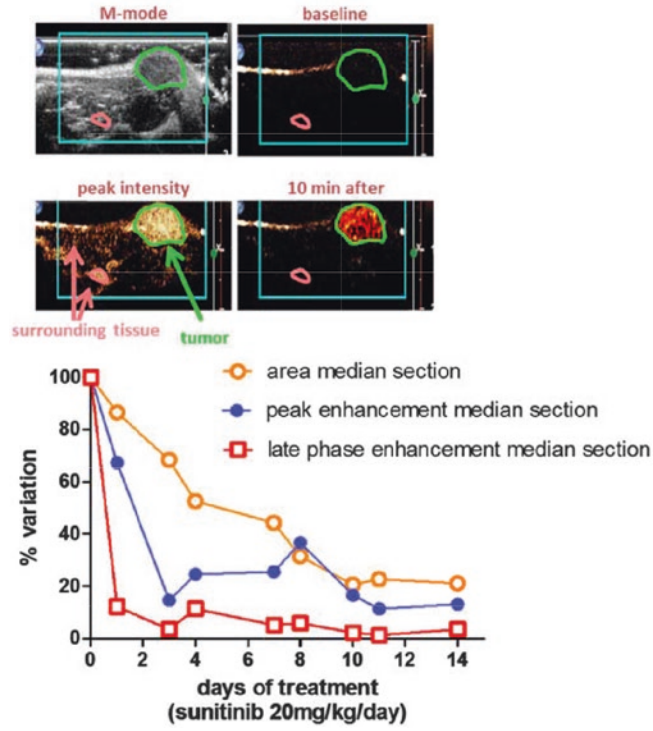

Fig. 14.21 BR55 US-MI imaging in a rat tumour model (breast cancer induced by NMU) under treatment with sunitinib at a dose of 20 mg/kg/day. (**a**), Representative images of the subcutaneous tumour in B-mode (*left upper*), before injection of BR55 (*right upper*), at peak intensity (*left lower*) and 10 min after BR55 injection (*right lower*). (**b**), Follow-up of these tumours undergoing sunitinib treatment demonstrated an early and rapid decrease in BR55 binding followed by a decrease in vascularity before an ultimate volume decrease

Acknowledgements The authors acknowledge contributions by Andrew Heinmiller and Dr. Kelly O'Connell with the preparation of this chapter.

References
Ultrasound Methods and Devices

Andrews TG, Lindsey ML, Lange RA, Aune GJ. Cardiac assessment in pediatric mice: strain analysis as a diagnostic measurement. Echocardiography (Mount Kisco, NY). 2013;31:375–84.

Campos D, Torres A, Lakshman M, Kissick MW, Kimple R, Jacques S, Yue Y, Jacques Y. In- vivo blood- oxygen content measurements via interstitial fiber optic probe and photoacoustic imaging. Conference proceeding of the American association of physicists in medicine, 1, 2013.

Cherin E, Williams R, Needles A, Liu G, White C, Brown AS, Zhou Y-Q, Foster FS. Ultrahigh frame rate ultrasound in micro-imaging and blood flow visualization in mice in vivo. Ultrasound Med Biol. 2006;32:683–91.

Cheung AM, Brown AS, Hastie LA, Cucevic V, Roy M, Lacefield JC, Fenster A, Foster FS. Three-dimensional ultrasound biomicroscopy for xenograft growth analysis. Ultrasound Med Biol. 2005;31:865–70.

Cheung AM, Brown AS, Cucevic V, Roy M, Needles A, Yang V, Hicklin DJ, Kerbel RS, Foster FS. Detecting vascular changes in tumour xenografts using micro-ultrasound and micro-ct following treatment with VEGFR-2 blocking antibodies. Ultrasound Med Biol. 2007;33:1259–68.

Cobbold RSC. Foundations of biomedical ultrasound. New York: Oxford University Press; 2007.

Daly C, Eichten A, Castanaro C, Pasnikowski E, Adler A, Lalani AS, Papadopoulos N, Kyle AH, Minchinton AI, Yancopoulos GD, Thurston G. Angiopoietin-2 functions as a Tie2 agonist in tumor models, where it limits the effects of VEGF inhibition. Cancer Res. 2013;73(1):108–18. doi:10.1158/0008-5472.CAN12-2064.

De la Zerda A, et al. Carbon nanotubes as photoacoustic molecular imaging agents in living mice. Nat Nanotechnol. 2008;3(9):557–62. d.

DeRosier LC, Buchsbaum DJ, Oliver PG, Huang ZQ, Sellers JC, Grizzle WE, Wang W, Zhou T, Zinn KR, Long JW, Vickers SM. Combination treatment with TRA-8 anti death receptor 5 antibody and CPT-11 induces tumor regression in an orthotopic model of pancreatic cancer. Clin Cancer Res. 2007;13:5535s–43.

Eichten A, Adler AP, Cooper B, Griffith J, Wei Y, Yancopoulos GD, Lin HC, Thurston G. Rapid decrease in tumor perfusion following VEGF blockade predicts long-term tumor growth inhibition in preclinical tumor models. Angiogenesis. 2013;16(2):429–41. doi:10.1007/s10456-012-9328-3.

Feldmann G, Fendrich V, McGovern K, Bedja D, Bisht S, Alvarez H, Koorstra JB, Habbe N, Karikari C, Mullendore M, Gabrielson KL, Sharma R, Matsui W, Maitra A. An orally bioavailable small-molecule inhibitor of Hedgehog signaling inhibits tumor initiation and

metastasis in pancreatic cancer. Mol Cancer Ther. 2008;7:2725–35.
Figley SA, Chen Y, Maeda A, Conroy L, McMullen JD, Silver JI, Stapleton S, Vitkin A, Lindsay P, Burrell K, Zadeh G, Fehlings MG, DaCosta RS. A spinal cord window chamber model for in vivo longitudinal multimodal optical and acoustic imaging in a murine model. PLoS One. 2013;8(3):e58081.
Raes F, Barre T, Jose J, Trochet P, Lerondel S, Pape AL. Characterization of tumor hypoxia by photoacoustic imaging and limitations of bioluminescence imaging in a Mia PaCa2-luc orthotopic model of pancreatic carcinoma. In: Background : photoacoustic principle : methods : results : discussion : conference proceedings of the American association of cancer research, 2014.
Foley KP, Zhou D, Borella C, Wu Y, Zhang M, Jiang J, Li H, Sang J, Korbut T, Ye J, Zhang X, Barsoum J, Sonderfan AJ. The vascular disrupting agent STA-9584 exhibits potent antitumor activity by selectively targeting microvasculature at both the center and periphery of tumors. J Pharmacol Exp Ther. 2012;343(2):529–38.
Foster FS. Transducers and probe construction. Ultrasound Med Biol. 2000;26S:2–5.
Foster FS. Micro-ultrasound takes off (in the biological sciences). IEEE international ultrasonics symposium, 2008. p. 120–5.
Foster FS, Zhang MY, Zhou YQ, Liu G, Mehi J, Cherin E, Harasiewicz KA, Starkoski BG, Zan L, Knapik DA, Adamson SL. A new ultrasound instrument for in vivo microimaging of mice. Ultrasound Med Biol. 2002;28:1165–72.
Foster FS, Mehi J, Lukacs J, Hirson D, White C, Chaggares C, Needles A. A new 15–50 MHz array-based micro-ultrasound scanner for preclinical imaging. Ultrasound Med Biol. 2009;35:1700–8.
Francia G, Shaked Y, Hashimoto K, Sun J, Yin M, Cesta C, Xu P, Man S, Hackl C, Stewart J, Uhlik M, Dantzig AH, Foster FS, Kerbel RS. Low-dose metronomic oral dosing of a prodrug of gemcitabine (LY2334737) causes antitumor effects in the absence of inhibition of systemic vasculogenesis. Mol Cancer Ther. 2012;11(3):680–9.
Franco M, Man S, Chen L, Emmenegger U, Shaked Y, Cheung AM, Brown AS, Hicklin DJ, Foster FS, Kerbel RS. Targeted anti-vascular endothelial growth factor receptor-2 therapy leads to short-term and long-term impairment of vascular function and increase in tumor hypoxia. Cancer Res. 2006;66:3639–48.
Gerling M, Zhao Y, Nania S, Norberg KJ, Verbeke CS, Englert B, Verbeke CS, Englert B, Kuiper RV, Bergström A, Hassan M, Neesse A, Löhr JM. Real-time assessment of tissue hypoxia in vivo with combined photoacoustics and high-frequency ultrasound. Theranostics. 2014;4(6):604–13.
Goertz DE, Yu JL, Kerbel RS, Burns PN, Foster FS. High-frequency Doppler ultrasound monitors the effects of antivascular therapy on tumor blood flow. Cancer Res. 2002;62:6371–5.
Goessling W, North TE, Zon LI. Ultrasound biomicroscopy permits in vivo characterization of zebrafish liver tumors. Nat Methods. 2007;4:551–3.
Graham KC, Wirtzfeld LA, MacKenzie LT, Postenka CO, Groom AC, MacDonald IC, Fenster A, Lacefield JC, Chambers AF. Three-dimensional high-frequency ultrasound imaging for longitudinal evaluation of liver metastases in preclinical models. Cancer Res. 2005;65:5231–7.
Grootendorst DJ, Langhout GC, Jose J, Fuchs D, Steenbergen W, Manohar S, Ruers TJM. Demarcation of human melanoma lymph node metastasis using photoacoustic spectral imaging. 2011, 096021, 96021.
Guevara E, Berti R, Londono I, Xie N, Bellec P, Lesage F, Lodygensky G a. Imaging of an inflammatory injury in the newborn rat brain with photoacoustic tomography. PLoS One. 2013;8(12):e83045.
Hollander D et al. Nanobody-functionalized gold nanostars as a theranostic agent for multimodal imaging and photothermal treatment of HER2 positive cancer. Conference proceedings, World Molecular Imaging Society, 2014.
Huizen IV, Wu G, Moussa M, Chin JL, Fenster A, Lacefield JC, Sakai H, Greenberg NM, Xuan JW. Establishment of a serum tumor marker for preclinical trials of mouse prostate cancer models. Clin Cancer Res. 2005;11:7911–9.
Hwang M, Hariri G, Lyshchik A, Hallahan DE, Fleischer AC. Correlation of quantified contrast-enhanced sonography with in vivo tumor response. J Ultrasound Med Off J Am Inst Ultrasound Med. 2010a;29(4):597–607.
Ino T, Akimoto K, Ohkubo M, Nishimoto K, Yabuta K, Takaya J, Yamaguchi H. Application of percutaneous transluminal coronary angioplasty to coronary arterial stenosis in Kawasaki disease. Circulation. 1996;93:1709–15.
Jäger W, Moskalev I, Janssen C, Hayashi T, Awrey S, Gust KM, So AI, Zhang K, Fazli L, Li E, Thüroff JW, Lange D, Black PC. Ultrasound guided intramural inoculation of orthotopic bladder cancer xenografts: a novel high-precision approach. PLoS One. 2013;8(3):e59536.
Jokerst JV, Cole AJ, Van de Sompel D, Gambhir SS. Gold nanorods for ovarian cancer detection with photoacoustic imaging and resection guidance via Raman imaging in living mice. ACS Nano. 2012;6(11):10366–77. doi:10.1021/nn304347g.
Jokerst JV, Thangaraj M, Kempen PJ, Sinclair R, Gambhir SS. Photoacoustic imaging of mesenchymal stem cells in living mice via silica-coated gold nanorods. ACS Nano. 2012;6(7):5920–30.
Jugold M, Palmowski M, Huppert J, Woenne EC, Mueller MM, Semmler W, Kiessling F. Volumetric high-frequency Doppler ultrasound enables the assessment of early antiangiogenic therapy effects on tumor xenografts in nude mice. Eur Radiol. 2008;18:753–8.
Kiguchi K, Ruffino L, Kawamoto T, Ajiki T, Digiovanni J. Chemopreventive and therapeutic efficacy of orally active tyrosine kinase inhibitors in a transgenic mouse model of gallbladder carcinoma. Clin Cancer Res. 2005;11:5572–80.
Kiguchi K, Ruffino L, Kawamoto T, Franco E, Kurakata S, Fujiwara K, Hanai M, Rumi M, DiGiovanni J. Therapeutic effect of CS-706, a specific cyclooxygenase-2 inhibitor, on gallbladder carcinoma in BK5. ErbB-2 mice. Mol Cancer Ther. 2007;6:1709–17.
Kircher MF, de la Zerda A, Jokerst JV, Zavaleta CL, Kempen PJ, Mittra E, Pitter K, Huang R, Campos C,

Habte F, Sinclair R, Brennan CW, Mellinghoff IK, Holland EC, Gambhir SS. A brain tumor molecular imaging strategy using a new triple-modality MRI-photoacoustic-Raman nanoparticle. Nat Med. 2012; 18(5):829–34.

Kulandavelu S, Qu D, Sunn N, Mu J, Rennie MY, Whiteley KJ, Walls JR, Bock NA, Sun JC, Covelli A, Sled JG, Adamson SL. Embryonic and neonatal phenotyping of genetically engineered mice. ILAR J. 2006;47:103–17.

Lakshman M, Heinmiller A, Lohse I, Hedley D, Needles A. Photoacoustic imaging for non invasive characterization of the tumor microenvironment. Proceeding of the world molecular imaging conference, (c), 100, 2013.

Lakshman M, Bu J, Maeda A, Zheng G, Needles A, Theodoropoulos C, C R. A validation study on photoacoustic imaging of fluorescent pyroporphysomes in vivo. Proceedings of the American association of cancer research. 40(2), 2012.

Lee DJ, Lyshchik A, Huamani J, Hallahan DE, Fleischer AC. Relationship between retention of a vascular endothelial growth factor receptor 2 (VEGFR2)-targeted ultrasonographic contrast agent and the level of VEGFR2 expression in an in vivo breast cancer model. J Ultrasound Med. 2008;27:855–66.

Levi J, Kothapalli S-R, Bohndiek S, Yoon J-K, Dragulescu-Andrasi A, Nielsen C, Tisma A, Bodapati S, Gowrishankar G, Yan X, Chan C, Starcevic D, Gambhir SS. Molecular photoacoustic imaging of follicular thyroid carcinoma. Clin Cancer Res Off J Am Assoc Cancer Res. 2013;19(6):1494–502.

Li Y, Garson CD, Xu Y, Beyers RJ, Epstein FH, French BA, Hossack JA. Quantification and MRI validation of regional contractile dysfunction in mice post myocardial infarction using high resolution ultrasound. Ultrasound Med Biol. 2007;33:894–904.

Li Y, Garson CD, Xu Y, French BA, Hossack JA. High frequency ultrasound imaging detects cardiac dyssynchrony in noninfarcted regions of the murine left ventricle late after reperfused myocardial infarction. Ultrasound Med Biol. 2008;34:1063–75.

Liu J, Du J, Zhang C, Walker JW, Huang X. Progressive troponin I loss impairs cardiac relaxation and causes heart failure in mice. Am J Physiol Heart Circ Physiol. 2007;293:H1273–81.

Luke GP, Yeager D, Emelianov SY. Biomedical applications of photoacoustic imaging with exogenous contrast agents. Ann Biomed Eng. 2012;40(2):422–37.

Luke GP, Bashyam A, Homan KA, Makhija S, Chen Y-S, Emelianov SY. Silica-coated gold nanoplates as stable photoacoustic contrast agents for sentinel lymph node imaging. Nanotechnology. 2013;24(45):455101.

Luo J, Konofagou EE. High-frame rate, full-view myocardial elastography with automated contour tracking in murine left ventricles in vivo. IEEE Trans Ultrason Ferroelectr Freq Control. 2008;55:240–8.

Luo J, Fujikura K, Homma S, Konofagou EE. Myocardial elastography at both high temporal and spatial resolution for the detection of infarcts. Ultrasound Med Biol. 2007;33:1206–23.

Lyshchik A, Fleischer AC, Huamani J, Hallahan DE, Brissova M, Gore JC. Molecular imaging of vascular endothelial growth factor receptor 2 expression using targeted contrast-enhanced high-frequency ultrasonography. J Ultrasound Med. 2007a;26:1575–86.

Mallidi S, Luke GP, Emelianov S. Photoacoustic imaging in cancer detection, diagnosis, and treatment guidance. Trends Biotechnol. 2011;29(5):213–21.

Mallidi S, Kim S, Karpiouk A, Joshi PP, Sokolov K, Emelianov S. Visualization of molecular composition and functionality of cancer cells using nanoparticle-augmented ultrasound-guided photoacoustics. Photoacoustics. 2015a;3:26–34. doi:10.1016/j.pacs.2014.12.003.

Mallidi S, Watanabe K, Timerman D, Schoenfeld D, Hasan T. Prediction of tumor recurrence and therapy monitoring using ultrasound-guided photoacoustic imaging. Theranostics. 2015;5(3):289–301.

Mishra S, Guan J, Plovie E, Seldin DC, Connors LH, Merlini G, Falk RH, MacRae CA, Liao R. Human amyloidogenic light chain proteins result in cardiac dysfunction, cell death, and early mortality in zebrafish. Am J Physiol Heart Circ Physiol. 2013;305(1):H95–103.

Needles A, Heinmiller A, Sun J, Theodoropoulos C, Bates D, Hirson D, Yin M, Foster F. Development and initial application of a fully integrated photoacoustic micro-ultrasound system. IEEE Trans Ultrason Ferroelectr Freq Control. 2013;60(5):888–97.

Ning S, Bednarski M, Oronsky B, Scicinski J, Saul G, Knox SJ. Dinitroazetidines are a novel class of anticancer agents and hypoxia-activated radiation sensitizers developed from highly energetic materials. Cancer Res. 2012;72(10):2600–8.

Olive KP, Tuveson DA. The use of targeted mouse models for preclinical testing of novel cancer therapeutics. Clin Cancer Res. 2006;12:5277–87.

Olson P, Chu GC, Perry SR, Nolan-Stevaux O, Hanahan D. Imaging guided trials of the angiogenesis inhibitor sunitinib in mouse models predict efficacy in pancreatic neuroendocrine but not ductal carcinoma. Proc Natl Acad Sci U S A. 2011;108(49):E1275–84.

Paproski RJ, Heinmiller A, Wachowicz K, Zemp RJ. Multi-wavelength photoacoustic imaging of inducible tyrosinase reporter gene expression in xenograft tumors. Sci Rep. 2014;4(5329):1–7.

Prasad P, Gordijo CR, Abbasi AZ, Maeda A, Ip A, Rauth M, DaCosta RS, Wu XY. Multifunctional albumin À MnO 2 nanoparticles modulate solid tumor microenvironment by attenuating enhance radiation response. ACS Nano. 2014;8:3202–12.

Qin C, Cheng K, Chen K, Hu X, Liu Y, Lan X, Zhang Y, Liu H, Xu Y, Bu L, Su X, Zhu X, Meng S, Cheng Z. Tyrosinase as a multifunctional reporter gene for Photoacoustic/MRI/PET triple modality molecular imaging. Sci Rep. 2013;3(1490):1490.

Rich LJ. Photoacoustic imaging of vascular hemodynamics: validation with blood oxygenation level-dependent MR imaging. Radiology. 2015;275:110–8.

Rychak JJ, Graba J, White C, Cheung AMY, Mistry B, Lindner JR, Kerbel RS, Foster FS. Micro-ultrasound molecular imaging of VEGFR-2 in a mouse model of tumor angiogenesis. Mol Imaging. 2007;6: 289–96.

Seshadri M, Sacadura NT, Coulthard T. Monitoring antivascular therapy in head and neck cancer xenografts using contrast-enhanced MR and US imaging. Angiogenesis. 2011;14(4):491–501.

Sethuraman S, Amirian JH, Litovsky SH, Smalling RW, Emelianov SY. Ex vivo characterization of atherosclerosis using intravascular photoacoustic imaging. Opt Express. 2007;15(25):16657–66.

Shaked Y, Ciarrocchi A, Franco M, Lee CR, Man S, Cheung AM, Hicklin DJ, Chaplin D, Foster FS, Benezra R, Kerbel RS. Therapy-induced acute recruitment of circulating endothelial progenitor cells to tumors. Science. 2006;313:1785–7.

Sherar MD, Foster FST. The design and fabrication of high frequency Poly(vinylidene fluoride) transducers. Ultrason Imaging. 1989;11:75–94.

Swierczewska M, Choi KY, Mertz EL, Huang X, Zhang F, Zhu L, Yoon HY, Park JH, Bhirde A, Lee S, Chen X. A facile, one step nanocarbon functionalization for biomedical applications. Nano Lett. 2012;12(7): 3613–20.

Talukdar Y, Avti P, Sun J, Sitharaman B. Multimodal ultrasound-photoacoustic imaging of tissue engineering scaffolds and blood oxygen saturation in and around the scaffolds.Tissue Eng Part C Methods. 2014;20(5):440–9.

Trivedi CM, Luo Y, Yin Z, Zhang M, Zhu W, Wang T, Floss T, Goettlicher M, Noppinger PR, Wurst W, Ferrari VA, Abrams CS, Gruber PJ, Epstein JA. Hdac2 regulates the cardiac hypertrophic response by modulating Gsk3 beta activity. Nat Med. 2007;13:324–31.

Wang LV. Photoacoustic tomography: in vivo imaging from organelles to organs. Science. 2012;335: 1458–62.

Wang XD, Xie XY, Ku GN, Wang LHV. Noninvasive imaging of hemoglobin concentration and oxygenation in the rat brain using high-resolution photoacoustic tomography. J Biomed Opt. 2006;11:024015.

Wang XF, Birringer M, Dong LF, Veprek P, Low P, Swettenham E, Stantic M, Yuan LH, Zobalova R, Wu K, Ledvina M, Ralph SJ, Neuzil J. A peptide conjugate of vitamin E succinate targets breast cancer cells with high ErbB2 expression. Cancer Res. 2007;67: 3337–44.

Wang B, Karpiouk A, Yeager D, Amirian J, Litovsky S, Smalling R, Emelianov S. Intravascular photoacoustic imaging of lipid in atherosclerotic plaques in the presence of luminal blood. Opt Lett. 2012;37(7):1244.

Willmann JK, Chen K, Wang H, Paulmurugan R, Rollins M, Cai W, Wang DS, Chen IY, Gheysens O, Rodriguez-Porcel M, Chen X, Gambhir SS. Monitoring of the biological response to murine hindlimb ischemia with 64Cu-labeled vascular endothelial growth factor-121 positron emission tomography. Circulation. 2008a; 117:915–22.

Willmann JK, Lutz AM, Paulmurugan R, Patel MR, Chu P, Rosenberg J, Gambhir SS. Dual-targeted contrast agent for US assessment of tumor angiogenesis in vivo. Radiology. 2008b;248:936–44.

Wirtzfeld LA, Wu G, Bygrave M, Yamasaki Y, Sakai H, Moussa M, Izawa JI, Downey DB, Greenberg NM, Fenster A, Xuan JW, Lacefield JC. A new three-dimensional ultrasound micro-imaging technology for preclinical studies using a transgenic prostate cancer mouse model. Cancer Res. 2005;65: 6337–45.

Wirtzfeld LA, Graham KC, Groom AC, Macdonald IC, Chambers AF, Fenster A, Lacefield JC. Volume measurement variability in three-dimensional high-frequency ultrasound images of murine liver metastases. Phys Med Biol. 2006;51:2367–81.

Wu G, Wang L, Yu L, Wang H, Xuan JW. The use of three-dimensional ultrasound micro-imaging to monitor prostate tumor development in a transgenic prostate cancer mouse model. Tohoku J Exp Med. 2005; 207:181–9.

Wu J, Zhou Y, Zou Y, Henkelman M. Evaluation of biventricular coronary flow patterns using high-frequency ultrasound in mice with transverse aortic constriction. Ultrasound Med Biol. 2013;39: 2053–65.

Xuan JW, Bygrave M, Jiang H, Valiyeva F, Dunmore-Buyze J, Holdsworth DW, Izawa JI, Bauman G, Moussa M, Winter SF, Greenberg NM, Chin JL, Drangova M, Fenster A, Lacefield JC. Functional neoangiogenesis imaging of genetically engineered mouse prostate cancer using three-dimensional power Doppler ultrasound. Cancer Res. 2007;67: 2830–9.

Yamada S, Nelson T, Kane G, Martinez-Fernandez A, Crespo-Diaz RJ, Ikeda Y, Perez-Terzic C, Terzic A. iPS cell intervention rescues wall motion disparity achieving biological cardiac resynchronization post-infarction. J Physiol. 2013;591:4335–49.

Yin M, Lakshman M, Foster FS. Quantitative functional assessment of tumour microenvironment using contrast enhanced ultrasound and photoacoustic imaging. IEEE Trans Ultrason Ferroelectr Freq Control. 2013:2–5.

Zhou YQ, Foster FS, Parkes R, Adamson SL. Developmental changes in left and right ventricular diastolic filling patterns in mice. Am J Physiol Heart Circ Physiol. 2003;285:H1563–75.

Zhou YQ, Foster FS, Nieman BJ, Davidson L, Chen XJ, Henkelman RM. Comprehensive transthoracic cardiac imaging in mice using ultrasound biomicroscopy with anatomical confirmation by magnetic resonance imaging. Physiol Genomics. 2004;18:232–44.

Ultrasound Contrast Agents for Small Animal Imaging

Alonso A, Della MA, Stroick M, Fatar M, Griebe M, Pochon S, et al. Molecular imaging of human thrombus with novel abciximab immunobubbles and ultrasound. Stroke. 2007;38(5):1508–14.

Anderson CR, Rychak JJ, Backer M, Backer J, Ley K, Klibanov AL. scVEGF microbubble ultrasound contrast agents: a novel probe for ultrasound molecular

imaging of tumor angiogenesis. Invest Radiol. 2010;45(10):579–85.
Bachawal SV, Jensen KC, Lutz AM, Gambhir SS, Tranquart F, Tian L, et al. Earlier detection of breast cancer with ultrasound molecular imaging in a transgenic mouse model. Cancer Res. 2013;73(6):1689–98.
Bettinger T, Bussat P, Tardy I, Pochon S, Hyvelin JM, Emmel P, et al. Ultrasound molecular imaging contrast agent binding to both E- and P-selectin in different species. Invest Radiol. 2012;47(9):516–23.
Bzyl J, Lederle W, Rix A, Grouls C, Tardy I, Pochon S, et al. Molecular and functional ultrasound imaging in differently aggressive breast cancer xenografts using two novel ultrasound contrast agents (BR55 and BR38). Eur Radiol. 2011;21(9):1988–95.
Bzyl J, Palmowski M, Rix A, Arns S, Hyvelin JM, Pochon S, et al. The high angiogenic activity in very early breast cancer enables reliable imaging with VEGFR2-targeted microbubbles (BR55). Eur Radiol. 2013;23(2):468–75.
Claudon M, Dietrich CF, Choi BI, Cosgrove DO, Kudo M, Nolsoe CP, et al. Guidelines and good clinical practice recommendations for contrast enhanced ultrasound (CEUS) in the liver – update 2012: a WFUMB-EFSUMB initiative in cooperation with representatives of AFSUMB, AIUM, ASUM, FLAUS and ICUS. Ultraschall Med. 2013;34(1):11–29.
Correas JM, Claudon M, Tranquart F, Helenon AO. The kidney: imaging with microbubble contrast agents. Ultrasound Q. 2006;22(1):53–66.
Couture O, Fink M, Tanter M. Ultrasound contrast plane wave imaging. IEEE Trans Ultrason Ferroelectr Freq Control. 2012;59(12):2676–83.
Davidson BP, Kaufmann BA, Belcik JT, Xie A, Qi Y, Lindner JR. Detection of antecedent myocardial ischemia with multiselectin molecular imaging. J Am Coll Cardiol. 2012;60(17):1690–7.
Davidson BP, Chadderdon SM, Belcik JT, Gupta S, Lindner JR. Ischemic memory imaging in nonhuman primates with echocardiographic molecular imaging of selectin expression. J Am Soc Echocardiogr. 2014;27:786–93.
Della MA, Allemann E, Bettinger T, Bussat P, Lassus A, Pochon S, et al. Grafting of abciximab to a microbubble-based ultrasound contrast agent for targeting to platelets expressing GP IIb/IIIa – characterization and in vitro testing. Eur J Pharm Biopharm. 2008;68(3):555–64.
Deshpande N, Needles A, Willmann JK. Molecular ultrasound imaging: current status and future directions. Clin Radiol. 2010;65(7):567–81.
Deshpande N, Lutz AM, Ren Y, Foygel K, Tian L, Schneider M, et al. Quantification and monitoring of inflammation in murine inflammatory bowel disease with targeted contrast-enhanced US. Radiology. 2012;262(1):172–80.
Ellegala DB, Leong-Poi H, Carpenter JE, Klibanov AL, Kaul S, Shaffrey ME, et al. Imaging tumor angiogenesis with contrast ultrasound and microbubbles targeted to alpha(v)beta3. Circulation. 2003;108(3):336–41.
Forsberg F, Ro RJ, Fox TB, Liu JB, Chiou SY, Potoczek M, et al. Contrast enhanced maximum intensity projection ultrasound imaging for assessing angiogenesis in murine glioma and breast tumor models: a comparative study. Ultrasonics. 2011;51(3):382–9.
Frinking PJ, Bouakaz A, Kirkhorn J, Ten Cate FJ, de Jong N. Ultrasound contrast imaging: current and new potential methods. Ultrasound Med Biol. 2000;26(6):965–75.
Gauthier TP, Averkiou MA, Leen EL. Perfusion quantification using dynamic contrast-enhanced ultrasound: the impact of dynamic range and gain on time-intensity curves. Ultrasonics. 2011;51(1):102–6.
Gramiak R, Shah PM, Kramer DH. Ultrasound cardiography: contrast studies in anatomy and function. Radiology. 1969;92(5):939–48.
Guibal A, Taillade L, Mule S, Comperat E, Badachi Y, Golmard JL, et al. Noninvasive contrast-enhanced US quantitative assessment of tumor microcirculation in a murine model: effect of discontinuing anti-VEGF therapy. Radiology. 2010;254(2):420–9.
Hanton G, Eder V, Rochefort G, Bonnet P, Hyvelin JM. Echocardiography, a non-invasive method for the assessment of cardiac function and morphology in preclinical drug toxicology and safety pharmacology. Expert Opin Drug Metab Toxicol. 2008;4(6):681–96.
Hwang M, Lyshchik A, Fleischer AC. Molecular sonography with targeted microbubbles: current investigations and potential applications. Ultrasound Q. 2010b;26(2):75–82.
Hyvelin JM, Tardy I, Arbogast C, Costa M, Emmel P, Helbert A, et al. Use of ultrasound contrast agent microbubbles in preclinical research: recommendations for small animal imaging. Invest Radiol. 2013;48:570–83.
Hyvelin JM, Tardy I, Bettinger T, von Wronski M, Costa M, Emmel P, et al. Ultrasound molecular imaging of transient acute myocardial ischemia with a clinically translatable P- and E-selectin targeted contrast agent: correlation with the expression of selectins. Invest Radiol. 2014;49(4):224–35.
Inaba Y, Lindner JR. Molecular imaging of disease with targeted contrast ultrasound imaging. Transl Res. 2012;159(3):140–8.
Kaufmann BA, Sanders JM, Davis C, Xie A, Aldred P, Sarembock IJ, et al. Molecular imaging of inflammation in atherosclerosis with targeted ultrasound detection of vascular cell adhesion molecule-1. Circulation. 2007;116(3):276–84.
Kiessling F, Huppert J, Palmowski M. Functional and molecular ultrasound imaging: concepts and contrast agents. Curr Med Chem. 2009;16(5):627–42.
Kiessling F, Bzyl J, Fokong S, Siepmann M, Schmitz G, Palmowski M. Targeted ultrasound imaging of cancer: an emerging technology on its way to clinics. Curr Pharm Des. 2012;18(15):2184–99.
Klibanov AL, Rasche PT, Hughes MS, Wojdyla JK, Galen KP, Wible Jr JH, et al. Detection of individual microbubbles of an ultrasound contrast agent: fundamental and pulse inversion imaging. Acad Radiol. 2002;9 Suppl 2:S279–81.

Korpanty G, Carbon JG, Grayburn PA, Fleming JB, Brekken RA. Monitoring response to anticancer therapy by targeting microbubbles to tumor vasculature. Clin Cancer Res. 2007;13(1):323–30.

Lindner JR, Song J, Christiansen J, Klibanov AL, Xu F, Ley K. Ultrasound assessment of inflammation and renal tissue injury with microbubbles targeted to P-selectin. Circulation. 2001;104(17):2107–12.

Lucidarme O, Kono Y, Corbeil J, Choi SH, Golmard JL, Varner J, et al. Angiogenesis: noninvasive quantitative assessment with contrast-enhanced functional US in murine model. Radiology. 2006;239(3):730–9.

Lyshchik A, Fleischer AC, Huamani J, Hallahan DE, Brissova M, Gore JC. Molecular imaging of vascular endothelial growth factor receptor 2 expression using targeted contrast-enhanced high-frequency ultrasonography. J Ultrasound Med. 2007;26(11): 1575–86.

Moestue SA, Gribbestad IS, Hansen R. Intravascular targets for molecular contrast-enhanced ultrasound imaging. Int J Mol Sci. 2012;13(6):6679–97.

Mule S, De CA, Frouin F, Lucidarme O, Herment A. An original methodology for quantitative assessment of perfusion in small animal studies using contrast-enhanced ultrasound. Conf Proc IEEE Eng Med Biol Soc. 2007;2007:347–50.

Mullin L, Gessner R, Kwan J, Kaya M, Borden MA, Dayton PA. Effect of anesthesia carrier gas on in vivo circulation times of ultrasound microbubble contrast agents in rats. Contrast Media Mol Imaging. 2011;6(3):126–31.

Palmowski M, Huppert J, Hauff P, Reinhardt M, Schreiner K, Socher MA, et al. Vessel fractions in tumor xenografts depicted by flow- or contrast-sensitive three-dimensional high-frequency Doppler ultrasound respond differently to antiangiogenic treatment. Cancer Res. 2008;68(17):7042–9.

Payen T, Coron A, Lamuraglia M, Le Guillou-Buffello D, Gaud E, Arditi M, et al. Echo-power estimation from log-compressed video data in dynamic contrast-enhanced ultrasound imaging. Ultrasound Med Biol. 2013;39(10):1826–37.

Pillai R, Marinelli ER, Fan H, Nanjappan P, Song B, von Wronski MA, et al. A phospholipid-PEG2000 conjugate of a vascular endothelial growth factor receptor 2 (VEGFR2)-targeting heterodimer peptide for contrast-enhanced ultrasound imaging of angiogenesis. Bioconjug Chem. 2010;21(3):556–62.

Pochon S, Tardy I, Bussat P, Bettinger T, Brochot J, von Wronski M, et al. BR55: a lipopeptide-based VEGFR2-targeted ultrasound contrast agent for molecular imaging of angiogenesis. Invest Radiol. 2010;45(2):89–95.

Pysz MA, Willmann JK. Targeted contrast-enhanced ultrasound: an emerging technology in abdominal and pelvic imaging. Gastroenterology. 2011;140(3): 785–90.

Pysz MA, Gambhir SS, Willmann JK. Molecular imaging: current status and emerging strategies. Clin Radiol. 2010;65(7):500–16.

Pysz MA, Guracar I, Foygel K, Tian L, Willmann JK. Quantitative assessment of tumor angiogenesis using real-time motion-compensated contrast-enhanced ultrasound imaging. Angiogenesis. 2012;15(3):433–42.

Rafter P, Phillips P, Vannan MA. Imaging technologies and techniques. Cardiol Clin. 2004;22(2):181–97.

Rognin NG, Arditi M, Mercier L, Frinking PJ, Schneider M, Perrenoud G, et al. Parametric imaging for characterizing focal liver lesions in contrast-enhanced ultrasound. IEEE Trans Ultrason Ferroelectr Freq Control. 2010;57(11):2503–11.

Seiler GS, Ziemer LS, Schultz S, Lee WM, Sehgal CM. Dose–response relationship of ultrasound contrast agent in an in vivo murine melanoma model. Cancer Imaging. 2007;7:216–23.

Takalkar AM, Klibanov AL, Rychak JJ, Lindner JR, Ley K. Binding and detachment dynamics of microbubbles targeted to P-selectin under controlled shear flow. J Control Release. 2004;96(3):473–82.

Tardy I, Pochon S, Theraulaz M, Emmel P, Passantino L, Tranquart F, et al. Ultrasound molecular imaging of VEGFR2 in a rat prostate tumor model using BR55. Invest Radiol. 2010;45(10):573–8.

Thibault H, Lafitte S, Timperley J, Tariosse L, Becher H, Roudaut R, et al. Quantitative analysis of myocardial perfusion in rats by contrast echocardiography. J Am Soc Echocardiogr. 2005;18(12):1321–8.

Tranquart F, Mercier L, Frinking P, Gaud E, Arditi M. Perfusion quantification in contrast-enhanced ultrasound (CEUS) – ready for research projects and routine clinical use. Ultraschall Med. 2012;33 Suppl 1:S31–8.

Unnikrishnan S, Klibanov AL. Microbubbles as ultrasound contrast agents for molecular imaging: preparation and application. AJR Am J Roentgenol. 2012;199(2):292–9.

Villanueva FS, Lu E, Bowry S, Kilic S, Tom E, Wang J, et al. Myocardial ischemic memory imaging with molecular echocardiography. Circulation. 2007;115(3):345–52.

Wang H, Machtaler S, Bettinger T, Lutz AM, Luong R, Bussat P, et al. Molecular imaging of inflammation in inflammatory bowel disease with a clinically translatable dual-selectin-targeted US contrast agent: comparison with FDG PET/CT in a mouse model. Radiology. 2013;267(3):818–29.

Willmann JK, Paulmurugan R, Chen K, Gheysens O, Rodriguez-Porcel M, Lutz AM, et al. US imaging of tumor angiogenesis with microbubbles targeted to vascular endothelial growth factor receptor type 2 in mice. Radiology. 2008;246(2):508–18.

Willmann JK, Kimura RH, Deshpande N, Lutz AM, Cochran JR, Gambhir SS. Targeted contrast-enhanced ultrasound imaging of tumor angiogenesis with contrast microbubbles conjugated to integrin-binding knottin peptides. J Nucl Med. 2010;51(3):433–40.

Zhou JH, Cao LH, Liu JB, Zheng W, Liu M, Luo RZ, et al. Quantitative assessment of tumor blood flow in mice after treatment with different doses of an antiangiogenic agent with contrast-enhanced destruction-replenishment US. Radiology. 2011;259(2):406–13.

PET and SPECT

15

Clemens Decristoforo, Uwe Haberkorn,
Roland Haubner, Walter Mier,
and Sibylle I. Ziegler

Contents

C. Decristoforo • R. Haubner (✉)
Medical University Innsbruck,
Anichstrasse 35, Innsbruck 6020, Austria
e-mail: roland.haubner@i-med.ac.at

U. Haberkorn • W. Mier
Department of Nuclear Medicine,
Heidelberg University Hospital,
INF 400, 69120 Heidelberg, Germany
e-mail: Uwe_Haberkorn@med.uni-heidelberg.de;
Walter.Mier@med.uni-heidelberg.de

S.I. Ziegler (✉)
Nuklearmedizinische Klinik und Poliklinik der TU München, Klinikum rechts der Isar,
Ismaninger Strasse 22, Munich 81675, Germany
e-mail: sibylle.ziegler@tum.de

15.1 PET and SPECT: Methods and Devices

Sibylle I. Ziegler

15.1.1 PET and SPECT Principles

Both positron emission tomography (PET) and single-photon emission computed tomography (SPECT) use radioactively labeled molecules that interact with a specific cellular target after injection. Images are formed by the detection of gamma rays, X-rays, or annihilation quanta (in the case of positron imaging). If single-photon emitters are used, the direction of flight has to be determined by geometric collimation. In contrast, coincidence detection exploits the unique feature of positron annihilation which results in two high-energy photons simultaneously emitted back to back.

In most cases, PET or SPECT instrumentation for small animals consists of scintillation crystals to convert photon energy into visible light, suitable light sensors, readout electronics, and image processing units. Depending on the application, PET and SPECT have different advantages and disadvantages, so there is not one technology superior for all cases.

F. Kiessling et al. (eds.), *Small Animal Imaging*, DOI 10.1007/978-3-319-42202-2_15

15.1.1.1 Positron Emitters Versus Single-Photon Emitters

Depending on the process to be imaged, adequate substances and labeling radioisotopes need to be selected. While PET nuclides offer the opportunity to label molecules without changing their biological behavior (e.g., ^{11}C labeling), for some slow biological processes it is advantageous to use SPECT tracers labeled with longer-lived radioisotopes, such as ^{99m}Tc or ^{125}I. This allows much longer scan sequences, following slow processes, which would not be possible with the short-lived positron emitting isotopes. Furthermore, labeling chemistry may be very different for SPECT and PET isotopes. Typically, it is much simpler and less expensive for SPECT.

A unique feature of SPECT imaging is the possibility to acquire data in several energy windows at the same time, offering the opportunity to coinject tracers with different radiolabels for simultaneous detection of different processes (Table 15.1).

The radiopharmaceuticals used in PET are labeled with beta emitters. The positron, depending on its initial energy, will travel a small distance in the surrounding material, losing energy until it annihilates with an electron resulting in the emission of two photons with 511 keV, each in the opposite direction. Imaging is based on the detection of the two annihilation photons by two opposing detectors with a short time window (ns) (Fig. 15.1). Every pair of opposing detectors defines a line of response along which the emission point of the two annihilation photons is located; this can be described as an electronic collimation in contrast to geometric collimation in SPECT. In case the positron and electron are not at rest during annihilation, the angle between the two annihilation quanta can deviate from 180° by up to 0.25°. Positron range and noncolinearity of annihilation quanta are physical limits of the spatial resolution in PET imaging. Obviously, these limits especially influence the quality of preclinical imaging.

There are no such limits for SPECT nuclides. The drawback in SPECT is found in the necessity of geometric collimation, which reduces detection sensitivity. Collimators are made of highly absorbing material, such as lead or tungsten, and their exact geometry needs to be defined according to the energy of the radionuclide and the spatial resolution. In clinical SPECT systems, collimators with parallel hole geometry are most widely used. For preclinical measurements, in which small structures are being measured, pinhole collimators offer excellent submillimeter spatial resolution (see Fig. 15.2). In general, caused by the geometric collimation, a strong dependence of spatial resolution vs. distance from the collimator is observed in SPECT. To improve sensitivity, there are systems available with many pinholes, measuring overlapping or nonoverlapping projections. Advanced image reconstruction techniques have been developed for these geometries (Schramm et al. 2003; Beekman and van der Have 2007).

Table 15.1 Characteristics of the most commonly used radionuclides in nuclear medicine

Radionuclide	Decay	Photon energy (keV)	Half-life
^{11}C	β^+	511	20.3 min
^{13}N	β^+	511	10.0 min
^{15}O	β^+	511	2.07 min
^{18}F	β^+	511	110 min
^{68}Ga	β^+	511	68 min
^{82}Rb	β^+	511	1.25 min
^{99m}Tc	IT	140	6.03 h
^{111}In	EC	172,247	2.81 day
^{123}I	EC	159	13.0 h
^{125}I	EC	27–35	59.4 day
^{201}Tc	EC	68–80	3.05 day

15.1.1.2 SPECT Imaging Devices

The main detector module of a SPECT imaging device is a gamma camera. A typical gamma camera consists of a collimator, a scintillator crystal, a light guide, and a number of photomultiplier tubes (PMTs). The energy information is acquired by the sum of the PMT signals, and the position information of the gamma ray interaction within the crystal is determined using a centroid algorithm (Anger 1958). A light guide is used in order to efficiently collect the scintillation light and distribute it among the PMTs. Segmented scintillator crystals and position-sensitive PMTs (PSPMTs) are also used in current systems in order to

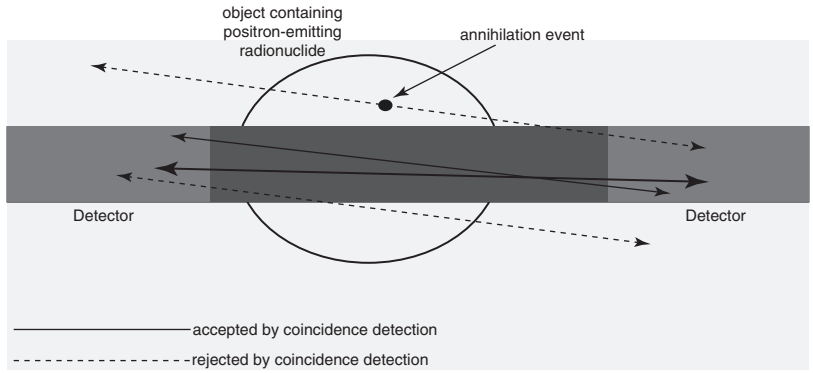

Fig. 15.1 Volume (*shaded area*) from which a pair of simultaneously emitted annihilation photons can be detected in coincidence by a pair of detectors. Not all decays in this volume will lead to recorded events, because it is necessary that both photons strike the detectors. Outside the shaded volume, it is impossible to detect annihilation photons in coincidence unless one or both undergo a Compton scatter in the tissue and change direction (After Cherry et al. 2003)

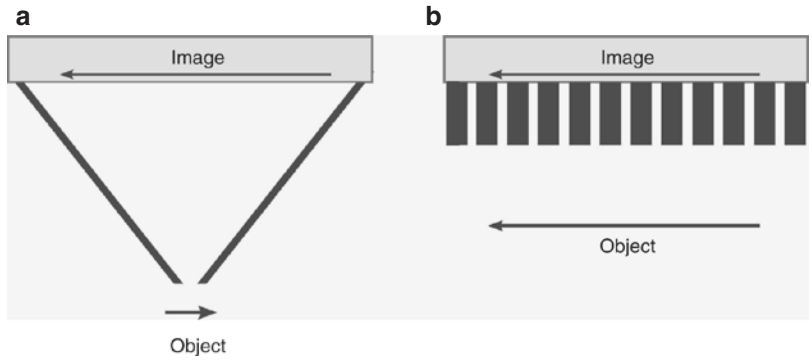

Fig. 15.2 (**a**, **b**) Two types of collimators used to project "γ-ray images" onto the detector of a gamma camera. (After Cherry et al. 2003)

improve the spatial resolution for the preclinical application (Zeniya et al. 2006).

A typical SPECT device contains one, two, or more gamma cameras which rotate around the object. Stationary systems with several detector heads are currently available for small animals (Wirrwar et al. 2005; van der Have et al. 2009). Cost-effective approaches implemented stationary detectors in combination with the possibility of rotating the animal inside the field of view.

15.1.1.3 PET Imaging Devices

Block detectors are traditionally used in clinical PET, which consist of a number of individual crystal elements read out by a small number of photomultiplier tubes (typically four). The sum of the four signals from the PMTs is used to determine the energy information, while the crystal where the interaction took place is determined by the four PMT signals using Anger logic (Casey and Nutt 1986). Another option is the readout of a large number of crystals with a continuous light guide and an array of PMTs, similar to a gamma camera (Surti and Karp 2004). Both concepts have been translated into preclinical tomograph designs (Cherry et al. 1997; Huisman et al. 2007), with the commercial version of the microPET concept currently being the most widely used principle (Kemp et al. 2009).

Alternative to the block detector concept is the individual crystal readout which can be achieved by using more compact photodetectors such as avalanche photodiodes (Lecomte et al. 1996;

Ziegler et al. 2001). The use of small-size crystals is advantageous in PET, since the crystal size will determine a lower limit in the achieved spatial resolution. However, the need of a large number of electronic channels to individually process the large number of detector signals significantly increases the cost of such a design. On the other hand, this concept was the base for developments toward integrated PET/MR imaging (e.g., (Judenhofer et al. 2007)).

The thickness of the crystal is critical for both PET and SPECT imaging. A thick crystal increases the gamma detection efficiency and hence the sensitivity of the imaging device. However, in SPECT large thickness enhances the spread of the scintillation light before reaching the PMT; therefore, a larger uncertainty in the localization of the photon interaction is introduced. In PET, and especially in small animal systems, making use of depth of interaction (DOI) information plays an important role in the improvement of the spatial resolution at the edges of the FOV when using long crystals. In order to minimize the crystal penetration effects and thus to determine the position along the crystal where the photon interaction took place, PET scanner geometries were suggested with two radial crystal layers of either the same or different material instead of a single scintillation radial crystal layer (Schmand et al. 1998; Seidel et al. 2003; Chung et al. 2004). Advanced readout schemes of the scintillation light spread in a continuous crystal offer continuous depth measurement. DOI measurement is not yet a standard feature of commercial systems but will become more important as the ring diameter becomes smaller and the reconstructed field of view covers a large fraction of the detector diameter.

15.1.2 Image Reconstruction: Quantification

15.1.2.1 Image Reconstruction Algorithms

Tomographic image reconstruction is based on measured estimation of the integral of radiotracer distribution as seen under different angles (projections). The reconstruction algorithms used for both SPECT and PET are the same, although, as previously described, the hardware and the principle of operation are different for the two modalities. These algorithms are used to produce a volume representation of the radiotracer distribution. The reconstruction algorithms can be divided into two groups: analytical and statistical.

For each projection, the acquired data are organized as number of counts along each line of response. In SPECT the lines are defined as the radial extensions of the collimator holes across the field of view, while in PET a line of response is the line connecting a detector pair. For the total number of projections, it is convenient to reorganize the data into a 2-D matrix called sinogram, which contains the number of counts for every LOR at each angular view, namely, for every radial distance r and every angle θ. Sinograms are then used as input to the reconstruction algorithms in order to generate the final image.

Analytical reconstruction algorithms model the measurement of radiotracer distribution in a simplified way so that an exact solution may be calculated analytically. However, these algorithms ignore a number of physical effects during acquisition such as limited sampling, Poisson statistics in photon counting, attenuation, or radiotracer decay, resulting in reduced image accuracy. Filtered back projection (FBP) has long been the most widely used analytical reconstruction algorithm. Data in each LOR are homogeneously back projected and filtered. The filter introduces negative contributions which cancel out the positive counts in areas of zero activity. The choice of filter and cutoff frequency determines resolution and noise level in the reconstructed image.

On the other hand, statistical, iterative reconstruction algorithms compensate for the inaccuracies introduced to the image by including in the initial estimate of the image the abovementioned physical processes. Thus, the model becomes more complicated and an analytical solution is impossible to compute. An iterative calculation is thus needed which starts with an estimate of tracer distribution, computes the forward-projection, and compares calculated and

measured projections. The image is updated according to the differences found between calculated and measured projections until the estimate agrees with the measured data. The model used in the algorithm can account for geometrical and detector effects, yielding improved image quality especially in the case of low counting statistics. Maximum likelihood expectation maximization (MLEM) is most commonly used. Since convergence is slow, accelerated algorithms have become most important in clinical routine, such as ordered subsets expectation maximization (OSEM) (Hudson and Larkin 1994).

15.1.2.2 Quantification

Quantification of activity concentration in the reconstructed images is most important, e.g., if changes of tracer accumulation are being measured during therapy. It is the basis for tracer kinetic modeling, which yields parameters characterizing the biological process under investigation. Several factors affect quantification. While PET is widely accepted to be a quantitative imaging method, this is not the case for SPECT, although reconstruction and correction techniques have become available for quantitative SPECT. The main effects which determine quantification are attenuation and scatter in the object of interest and spatial resolution of the imaging device.

Gamma rays traversing material undergo scattering and photoabsorption effects; the magnitude of these effects depends on the energy of the gamma rays. In tissue, annihilation quanta mainly interact via Compton scattering, while lower-energy gamma rays, typical for SPECT, undergo photo absorption as well. In either case, gamma ray intensity along a certain line is attenuated and needs to be corrected. Compton scattering in the object causes gamma rays to deviate from their original line of flight and to lose some energy. Depending on the energy resolution of the detector system, they may still be detected and falsely attributed to a different line.

In contrast to the clinical case, it can be questioned whether attenuation and scatter need to be corrected for when imaging small animals, since the amount of tissue through which the gamma rays pass is much smaller. It should be kept in mind that these effects are much more pronounced when imaging a low-energy nuclide such as I-125. For example, it has been shown for commercial small animal pinhole SPECT systems that for determination of activity within 5 %, appropriate correction methods need to be applied (Hwang et al. 2008; Chen et al. 2009).

Both, in PET and SPECT, attenuation and scatter correction algorithms rely on the availability of structural information, which can be gained from radionuclide transmission or CT scans. The latter is routinely used in dual-modality scanners (Chow et al. 2005; Hwang and Hasegawa 2005; Vanhove et al. 2009).

The distance-dependent spatial resolution of SPECT systems also needs to be taken into account if quantitative reconstruction is aimed for. Developments in SPECT reconstruction algorithms include descriptions of the resolution degradation, based on measurements, in order to minimize this effect (Liang et al. 1992).

In PET imaging, spatial resolution is nearly independent of the position along a line of response. For noncentral lines of response, the so-called parallax error introduces spatially variable resolution. Oblique angles cause the volume of coincidence to be much wider, thus worsening the spatial resolution. Parallax error is more pronounced for small detector ring diameters, as it is the case in devices for small animal imaging. Several schemes are being investigated for reducing the parallax effect in PET by exploiting DOI detection schemes.

The spatial resolution is also affecting quantification significantly due to the partial volume effect. The partial volume effect is the bias introduced to the estimation of the radiotracer concentration due to the limited spatial resolution of the imaging device and is dependent on both the size and shape of the object (Hoffman et al. 1979) and on the relative radiotracer concentration with respect to the surroundings. In general, the partial volume effect is minimized if the size of the object is relatively large in comparison to the system's spatial resolution. In order to acquire quantitative information about the radiotracer

distribution, compensation for partial volume effects is a prerequisite (Chen et al. 1999). Advanced reconstruction algorithms include the detector blur in the system matrix description, thus offering reconstructed images with enhanced resolution (e.g., (Rafecas et al. 2004)).

There are other less important effects which influence image quality. In the case of PET, the detection of random coincidences may increase background in the reconstructed image. Owing to the finite time resolution of the detectors, a coincidence event is the detection of two photons by two opposing detectors within a specific time window. This window is usually chosen to be twice the system's time resolution. Since from theory, the random coincidence rate is proportional to the width of the time coincidence window, the number of random events may be reduced by improving the system time resolution, namely, by choosing fast scintillators, photodetectors, and electronics. The detection and subtraction of random coincidences from measured data are performed by various methods which may be software or hardware based (Brasse et al. 2005).

15.1.3 Future Developments

Obviously, spatial resolution is the primary requirement for animal imaging instruments. But sensitivity is as important since the amount of activity which can be injected may be limited by the specific activity (ratio of labeled tracer to nonlabeled substance) of the radiotracer.

Highest spatial resolution in preclinical SPECT in the range of a few hundred μm can be achieved with pinhole collimators, which, on the other hand, have a very low sensitivity (Meikle et al. 2005). In order to increase sensitivity, several detectors are used. The spatial resolution of commercial PET devices for imaging small animals has reached the 1.0–1.5 mm region (Kemp et al. 2009), with sub-mm imaging possible (Schafers et al. 2005). Sensitivity of small animal PET scanners is increased by a long axial extent and 3D data acquisition.

Detector development will aim at cost-effective designs covering a large field of view. Parallel readout of many electronic channels with high count rate capability is a challenge. Both PET and SPECT reconstruction algorithms are continuously being refined, including models for improved system matrix generation, which will incorporate the specific detector configurations and characteristics.

15.2 PET and SPECT Tracers for Molecular Imaging

Uwe Haberkorn and Walter Mier

15.2.1 Introduction

Molecular imaging combines noninvasive imaging methods with tools of molecular and cellular biology. Traditional imaging approaches in nuclear medicine were solely based on the detection of anatomical and structural features. Complementary to these conventional methods, advances in biology made it possible to visualize cellular and biochemical processes. Until the event of PET imaging, the spectrum of nuclides used for tracers was largely restricted to iodine isotopes and 99 m-technetium (Dadparvar et al. 1993; Eckelman et al. 2013). Today several PET nuclides have largely extended the possibilities of tracer design. The uptake of several archetypical diagnostic radiopharmaceuticals is illustrated in Figs. 15.3, 15.4, and 15.5. Yet, most of the commonly used tracers are derivatives of natural products. At present, the main effort in the field of radiotracer development is the identification of specific probes for targeting cellular structures, e.g., tumor-associated receptors. These new ligands can be used for diagnosis as well as for treatment, a concept known as theranostics. Further, noninvasive imaging paradigms studied in small animals are currently being translated into the clinics (Benešová et al. 2015; Wüstemann et al. 2016). In the future molecular imaging will provide new ways in diagnosis of cancer and monitoring treatment response in oncology. For instance, studies using PET-based imaging of reporter genes have already been described in gene therapy approaches (Sara et al. 2012; Yaghoubi et al. 2012).

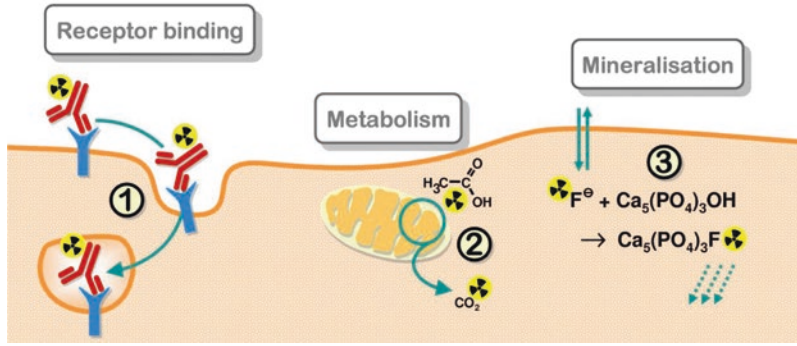

Fig. 15.3 Receptor binding, metabolism, and mineralization: *1* Receptor-mediated endocytosis of the antibody Zevalin allows the targeting of NHL. *2* Myocardial cells metabolize ^{11}C-acetate in the tricarboxylic acid (TCA) cycle. *3* ^{18}F-fluoride ions substitute hydroxide ions in hydroxyapatite of the cancellous bone matrix

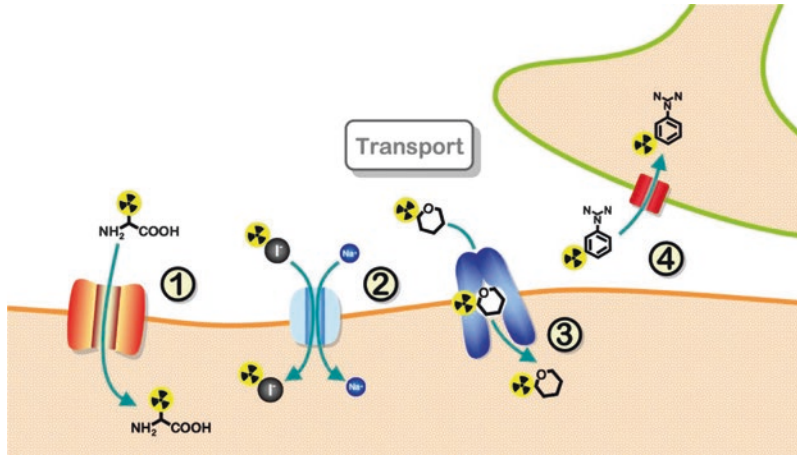

Fig. 15.4 Transport: *1* The amino acid ^{18}F-O-(2-fluoroethyl)-tyrosine (FET) is taken up into the cells by the L-type amino acid transporter system. *2* Iodide is taken up by the human sodium iodide symporter (NIS) on thyroid cancer tissues. *3* ^{18}F-Fluorodeoxyglucose (FDG) is taken up into cells by glucose transporters. *4* ^{123}I-Meta-iodobenzylguanidine (MIBG) is transported by the norepinephrine transporter (NET) into adrenergic neurons

15.2.2 PET Tracers

15.2.2.1 ^{18}F-FDG ([18F]-Fluoro-2-deoxy-2-D-glucose)

The glucose analog ^{18}F-FDG is the most versatile PET radiopharmaceutical with major applications in oncology, neurology, and cardiology (Fletcher et al. 2008; Hellwig et al. 2015; Hutchings et al. 2006). Most malignant tumors show an upregulation of glycolysis, resulting in increased glucose consumption. FDG is taken up into cells by glucose transporters and then phosphorylated to FDG-6-phosphate by the enzyme hexokinase, the first enzyme of glycolysis. FDG-6-phosphate is not metabolized within the cells because it is a poor substrate for the further enzyme systems of glycolysis. Since the dephosphatase activity is downregulated in tumors, a dephosphorylation does not occur. As a consequence FDG-6-phosphate is trapped in the cells because the charge prevents the diffusion through the cellular membrane (Fig. 15.6).

Target

Glucose utilization, cellular uptake predominantly by glucose transporter 1 (GLUT-1) followed by phosphorylation by hexokinase II (HK-II)

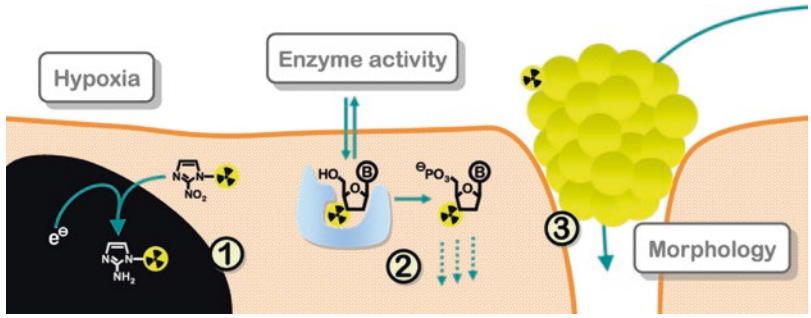

Fig. 15.5 Hypoxia, enzyme activity, and morphology: *1* ^{18}F-Fluoromisonidazole (FMISO) is reduced and covalently bound within hypoxic cells. *2* The nucleoside ^{18}F-3′-deoxy-3′-fluorothymidine (FLT) is phosphorylated by thymidine kinase-1. *3* ^{99m}Tc-labeled microspheres (i.e., macroaggregated human serum albumin) can be trapped in the sentinel lymph node

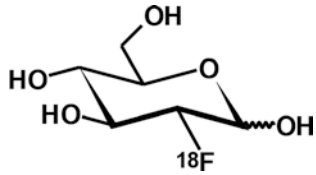

Fig. 15.6 Chemical structure of ^{18}F-FDG ([18F]-fluoro-2-deoxy-2-D-glucose)

Applications

The clinical impact of ^{18}F-FDG-PET has been reported for many different tumor types, such as lung tumors, colorectal carcinomas, breast carcinoma, and lymphomas (Rohren et al. 2004). Since PET allows quantitative values, the tracer has also been used for therapy monitoring by the assessment of changes in glucose metabolism (Huang et al. 1980). These changes usually occur very early during treatment thus allowing a rapid decision about the effectiveness of a specific treatment schedule. This may lead to early changes in therapy management. Furthermore, the values obtained with FDG-PET have been used as predictive markers in a couple of tumors including lymphomas and esophageal cancer. Non-oncological applications include the assessment of myocardial viability and inflammatory plaque detection in cardiovascular diseases, the diagnosis of dementia, and the detection of inflammatory foci in patients with fever of unknown origin.

15.2.2.2 ^{18}F-FLT (3′-Deoxy-3′-[18 F] fluorothymidine)

^{18}F-FDG uptake is not tumor specific, and false-positive findings can occur in inflammatory lesions. In contrast, nucleoside metabolism correlates with the proliferative activity of malignant tumors. ^{18}F-FLT is transported via nucleoside transporters and phosphorylated to 3′-fluorothymidine monophosphate by thymidine kinase 1 and reflects thymidine kinase 1 activity. The phosphorylated tracer is trapped in the tumor cells (Fig. 15.7).

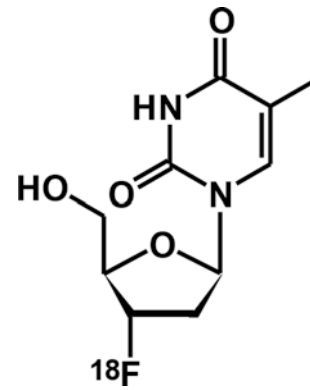

Fig. 15.7 Chemical structure of ^{18}F-FLT, 3′-Deoxy-3′-[^{18}F]fluorothymidine

Target

Proliferation, nucleoside uptake and phosphorylation by thymidine kinase-1 (TK-1)

Applications

The tracer has been used as a proliferation marker in a variety of tumors (Chen et al. 2005).

15.2.2.3 ^{18}F-FMISO ([18F] Fluoromisonidazole)

Large tumors show areas with low blood perfusion. The reduced oxygenation of these areas causes a reductive milieu. Tumor cells in hypoxic areas show reduced metabolism and sensitivity against radiation and chemotherapy (Moeller et al. 2007). The hydrophilic tracer ^{18}F-FMISO diffuses across cell membranes. It is subsequently reduced and covalently attached to macromolecules within hypoxic cells (Fig. 15.8).

Target

Hypoxia; reductive potential in hypoxic tissues

Applications

Used for the detection of hypoxia in tumors, myocardial infarcts, or cerebral ischemia (Koh et al. 1992).

15.2.2.4 ^{11}C-MET (L-[*methyl*-11C] Methionine)

The malignant transformation goes along with the overexpression of a variety of amino acid transporters (Kobayashi et al. 2008). Consequently radiolabeled amino acids can be used as functional biomarkers to visualize amino acid transport and to some extent protein synthesis. ^{11}C-Methionine, the most commonly used amino acid-based PET tracer, is considered be more tumor specific than FDG because its uptake in inflammatory cells is low (Kubota et al. 1995) (Fig. 15.9).

Target

Amino acid transport, by L-type amino acid transporters sodium-dependent transport systems as well as protein synthesis

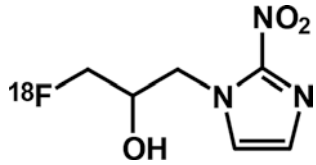

Fig. 15.8 Chemical structure of [^{18}F]fluoromisonidazole

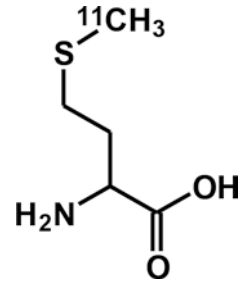

Fig. 15.9 Chemical structure of **^{11}C-MET**, L-[*methyl*-^{11}C]methionine

Applications

^{11}C-Methionine has been applied in brain tumors, head and neck tumors, and lung tumors, mainly for diagnosis but also in selected cases for therapy monitoring (Kubota et al. 1992).

15.2.2.5 ^{18}F-Fluoride ([18F]Fluoride)

^{18}F-Fluoride is a sensitive indicator of skeletal pathology. It is taken up by mineralizing bone in proportion to osteoblastic activity; normal bone structures demonstrate uniform uptake of ^{18}F-fluoride. The ^{18}F-fluoride ion exchanges with hydroxyl groups on hydroxyapatite to form fluorapatite. ^{18}F-fluoride is used as an alternative to the clinical bone scanning ^{99m}Tc-diphosphonate SPECT agents (Blake et al. 2001; Even-Sapir et al. 2004) (Fig. 15.10).

Target

Mineralization, malignant processes stimulate the osteoblastic activity; this causes increased fluoride incorporation.

Applications

Fluoride is increasingly used as an alternative to the classical bone scan for the detection bone metastases. The possibility to obtain quantitative values should also offer new aspects such as the therapy monitoring of benign bone diseases.

Fig. 15.10 Chemical structure of [^{18}F]fluoride

15.2.2.6 ^{18}F-FECH ([18F] Fluoroethylcholine)

FECH is a specific substrate of choline kinase, an enzyme commonly overexpressed in malignant lesions. Phosphorylation with choline kinase results in intracellular trapping of FECH. Phosphorylated choline derivatives can be incorporated into phospholipids. The major application of FECH is in prostate cancer as FDG-PET-CT is generally not suitable for diagnosing prostate cancer showing low glycolysis rates (Hara et al. 2002) (Fig. 15.11).

Target

Choline metabolism, phosphorylation by choline kinase and subsequent incorporation into phospholipids of cell membranes

Applications

Choline-based tracers are used for the diagnosis of primary and recurrent prostate carcinoma, the planning of biopsy, and therapy monitoring.

15.2.2.7 ^{13}N-Ammonia ([13N] Ammonia)

[^{13}N]-Ammonia allows to measure regional myocardial perfusion in normal and diseased states. The small molecule moves from the vascular space to the tissue both by active transport and by passive diffusion. Once in the myocardial cells, retention of ^{13}N-ammonia involves predominantly the enzymatic conversion of ^{13}N-ammonia and glutamic acid to ^{13}N-labeled. Because of the requirement for ATP for the metabolism, intracellular levels of ^{13}N-ammonia reflect cellular processes dependent on viable myocardium (Fig. 15.12).

Target

Myocardial blood flow followed by metabolism by the glutamic acid-glutamine pathway

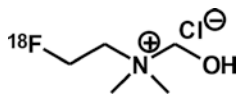

Fig. 15.11 Chemical structure of [^{18}F]fluoroethylcholine

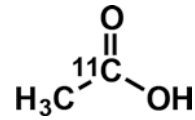

Fig. 15.12 Chemical structure of [^{13}N]ammonia

Applications

The tracer is used for the quantitative determination of myocardial blood flow (Schelbert et al. 1981).

15.2.2.8 ^{68}Ga-DOTATOC ([68Ga] (1,4,7,10-Tetraazacyclododecane -N,N′,N″,N‴-tetraacetic acid)-Tyr^3-octreotide)

Due to its excellent performance, the peptide derivative DOTATOC is the gold standard of peptide radiopharmaceuticals. A large number of carcinoid tumors have been shown to express receptors for somatostatin (Reubi, 2003). Somatostatin receptor-binding peptides containing chelators for various radiometals can be used for the diagnosis and therapy of somatostatin receptor-positive tumors. DOTATOC labeled with ^{68}Ga allows the diagnosis by PET; ^{90}Y-labeled DOTATOC has been proven to be effective for endoradiotherapy (Fig. 15.13).

Target

Peptide receptor binding, the binding to the somatostatin receptor subtypes SSTR2 and SSTR5 induces receptor-mediated endocytosis of the tracer.

Applications

DOTATOC is used for the diagnosis and therapy monitoring of neuroendocrine tumors (Waldherr et al. 2002).

15.2.2.9 ^{68}Ga-DKFZ-PSMA-11 (Glu-NH-CO-NH-Lys-(Ahx)-[68Ga(HBED-CC)])

Glu-NH-CO-NH-Lys-(Ahx)-[^{68}Ga(HBED-CC)] is used for the diagnosis and therapy monitoring of prostate tumors. The prostate-specific membrane antigen (PSMA), an enzyme highly overexpressed in prostate cancer, presents excellent properties as a tar-

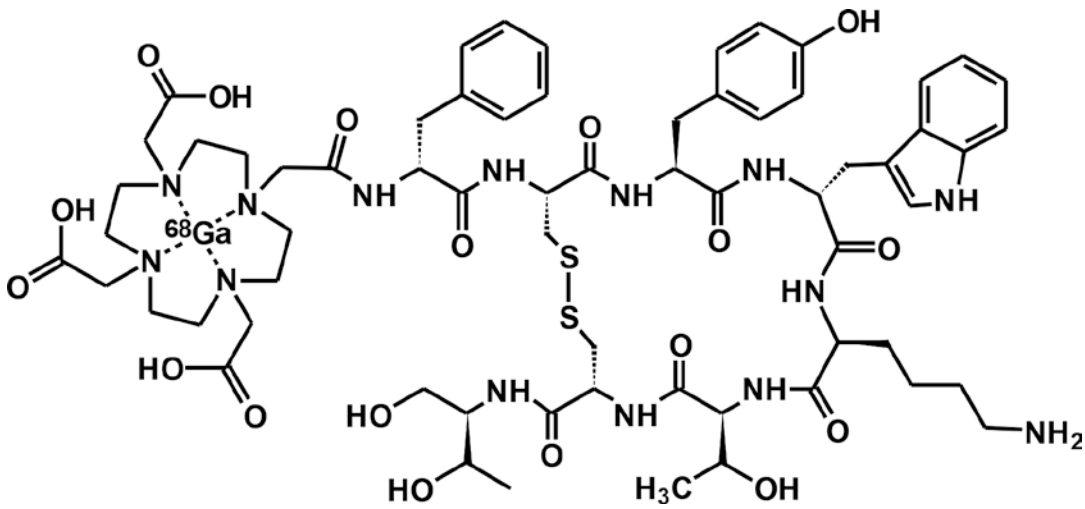

Fig. 15.13 Chemical structure of [^{68}Ga](1,4,7,10-tetraazacyclododecane-N,N′,N″,N‴-tetraacetic acid)-Tyr^3-octreotide

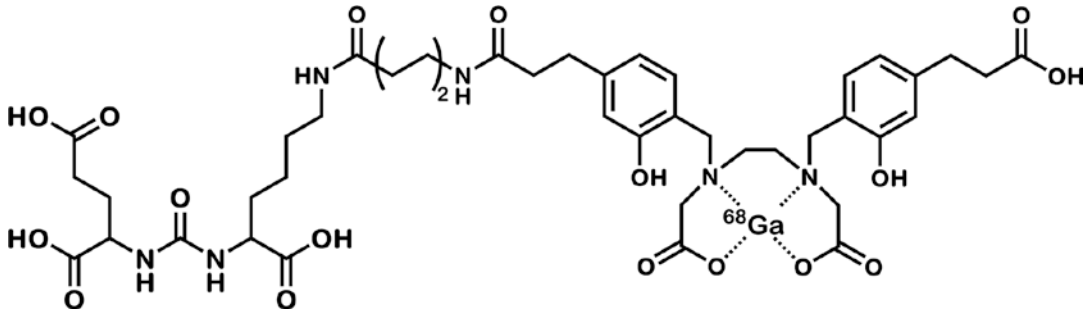

Fig. 15.14 Chemical structure of Glu-NH-CO-NH-Lys-(Ahx)-[^{68}Ga(HBED-CC)]

get. A urea-based binding motif has been shown to bind with high affinity to PSMA (Hillier et al. 2009). Conjugation to the chelator HBED-CC (N,N′-bis-[2-hydroxy-5-(carboxyethyl)benzyl] ethylenediamine-N,N′-diacetic acid) allows for labeling with ^{68}Ga and enhances the pharmacokinetics of the molecule (Fig. 15.14).

Target

Prostate-specific membrane antigen, an epitope overexpressed on prostate tumors

Applications

The tracer is applied for the diagnostics of prostate tumors (Afshar-Oromieh et al. 2015; Eder et al. 2014).

15.2.2.10 ^{11}C-Acetate ([11C]Acetate)

Fatty acids are the primary metabolic energy source for the myocardium. ^{11}C-acetate, a readily utilized myocardial substrate, is predominantly metabolized to carbon dioxide in the tricarboxylic acid cycle. Consequently, PET imaging of ^{11}C-acetate allows the measurement of both myocardial flow and oxidative lipid metabolism. In contrast to the predominant oxidative metabolism in myocardial cells, tumor cells involve the fatty acid synthesis pathway in ^{11}C-acetate metabolism. Consequently, ^{11}C-acetate can be used as a marker for the expression fatty acid synthetase, an enzyme overexpressed in prostate carcinomas and other cancers (Fig. 15.15).

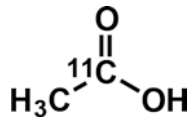

Fig. 15.15 Chemical structure of [^{11}C]acetate

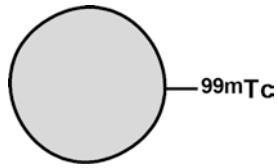

Fig. 15.16 Structure of [^{99}mTc]-microspheres

Target
Oxidative metabolism, *fatty acid metabolism*, tricarboxylic acid (TCA) cycle in myocardial cells, and fatty acid synthetase (FAS) in tumor cells

Applications
PET tracer for myocardial oxidative metabolism and regional myocardial blood flow as well as renal, pancreatic, and prostate tumors (Armbrecht et al. 1990; Oyama et al. 2002).

15.2.3 SPECT Tracers

15.2.3.1 ^{99m}Tc-Microspheres

Localization of the sentinel node can be achieved using a radiolabeled colloid such as ^{99m}Tc-HSA microspheres. The "sentinel" node is the very first lymph node(s) to receive drainage from a cancer-containing area; it can be the only site of lymphatic metastasis. A negative result from the intraoperative sentinel lymph node negates the possibility of more distant lymphatic metastatic spread. This process is part of "staging" the cancer. Once the labeled tracer has reached the nodes, the surgeon scans the area with a handheld gamma counter to detect the tracer. The sentinel node is removed and examined by a pathologist procedure. Thin intraoperative procedure is used to decide whether further dissection is required, most commonly for axillary lymph node dissection to avoid extensive removal of underarm nodes in case of breast cancer (Boni et al. 2000) (Fig. 15.16).

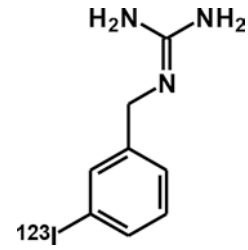

Fig. 15.17 Chemical structure of meta-[^{123}I] iodobenzylguanidine

Target
Filtration of particles from the lymphatic ducts that drain from a tumor into the sentinel lymph node

Applications
Breast cancer, melanoma, colon cancer, and prostate cancer

15.2.3.2 ^{123}I-MIBG (Meta-[123I] Iodobenzylguanidine)

Some tumors show a metabolic pathway, in which the hormones dopamine, adrenaline, and noradrenaline are synthesized from phenylalanine. The guanidine analog ^{123}I-MIBG is chemically similar to these hormones. It enters a metabolic pathway of noradrenaline, a catecholamine that acts as an adrenergic transmitter and is synthesized and stored in the storage granules (synaptosomes) of the sympathomedullary cells. MIBG uptake is studied in nuclear cardiology to demonstrate myocardial sympathetic innervation to characterize acute and chronic alterations in sympathetic nerve function (Kasama et al. 2005) (Fig. 15.17).

Target
Transport by the norepinephrine transporter followed by accumulation in neurosecretory storage granules of adrenergic tissue

Applications
Diagnosis of pheochromocytoma or paraganglioma, measurement of myocardial sympathetic innervation

15.2.3.3 ^{99m}Tc-Pertechnetate ([99mTc]TcO_4^-)

Due to its comparable charge/radius ratio, pertechnetate is incorporated into the thyroid gland similarly as iodide. This uptake is specific for tissues expressing the sodium iodide symporter such as the thyroid, the stomach, etc. ^{99m}Tc-pertechnetate has shown advantages over ^{123}I- and ^{131}I-iodide with respect to image quality, procedure, and radiation dose for examinations of thyroid uptake and scintigraphy (Zuckier et al. 2004). Consequently studies of the thyroid gland (morphology, vascularity, and function) are performed primarily using pertechnetate. The pertechnetate ion is not incorporated into thyroglobulin and therefore not stored in the thyroid gland. ^{99m}Tc-pertechnetate cannot pass the blood-brain barrier; it accumulates primarily in the choroid plexus. It is therefore used to study the blood perfusion, regional accumulation, and cerebral lesions in the brain. ^{99m}Tc pertechnetate can be used for the diagnosis of papillary and follicular thyroid carcinoma (Scott et al. 1995) (Fig. 15.18).

Target

Thyroid-specific uptake by the human sodium iodide symporter (hNIS)

Applications

Evaluation of thyroid diseases. Diagnosis of thyroid cancers and their metastases. Detection of ectopic gastric mucosa as a source of gastrointestinal bleeding

15.2.3.4 ^{99m}Tc-MIBI ([99mTc] Tc-2-Methoxyisobutylisonitrile)

The cationic, lipophilic complex ^{99m}Tc-MIBI enters the cell by passive diffusion across negatively charged plasma and mitochondrial membranes. It was originally developed for myocardial perfusion imaging, which is still its major application (Sun et al. 2003). However, it has been shown that ^{99m}Tc-MIBI can be used to evaluate oncological questions, i.e., overexpression of P-glycoprotein (Pgp), one of the primary mechanisms of multidrug resistance (MDR) in several diseases, including multiple myeloma (Fonti et al. 2004) (Fig. 15.19).

$$^{99m}[TcO_4]^{\ominus}$$

Fig. 15.18 Chemical structure of [^{99m}Tc]pertechnetate

Target

Passive diffusion across negatively charged membranes. The retention is influenced by transport proteins such as the P-glycoprotein pump and the multidrug resistance-associated protein pump.

Applications

Myocardial perfusion, detection of parathyroid adenoma, used to estimate drug efflux

15.2.3.5 ^{111}In Zevalin ([111-In] In-Ibritumomab Tiuxetan)

Due to its excellent performance, the protein derivative Zevalin is the gold standard of protein radiopharmaceuticals. Rituximab is a chimeric monoclonal antibody directed against the B-cell-specific antigen CD20 expressed which is primarily found on the surface of B cells. The high expression of CD20 on non-Hodgkin's lymphomas (NHL) allows the treatment with this protein. Zevalin is a derivative of rituximab; it can be radiolabeled via the chelator MX-DTPA. Zevalin labeled with ^{111}In allows the diagnosis by SPECT; ^{90}Y-labeled Zevalin has been proven to be effective for endoradiotherapy of NHL (Wiseman and Witzig, 2005) (Fig. 15.20).

Target

Antigen binding to the B-cell-specific antigen CD20 allows the targeting of NHL.

Applications

Non-Hodgkin's lymphomas (NHL)

15.2.3.6 ^{99m}Tc-MAG3 ([99mTc] Tc-Mercaptoacetyl-triglycine)

Radiotracers with low binding to plasma proteins that are filtrated through the glomerular

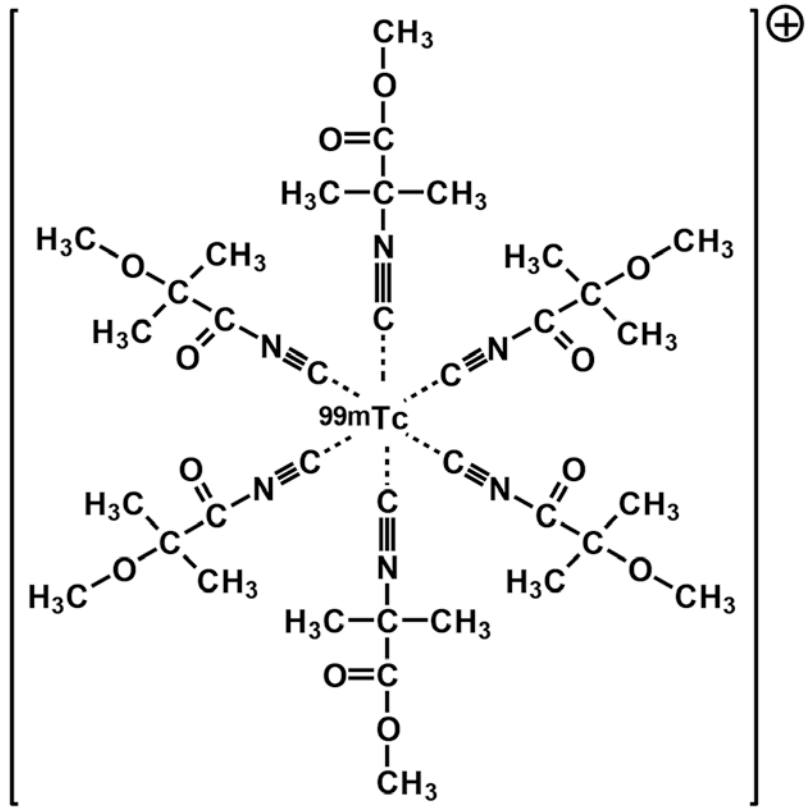

Fig. 15.19 Chemical structure of [^{99m}Tc] Tc-2-methoxyisobutylisonitrile

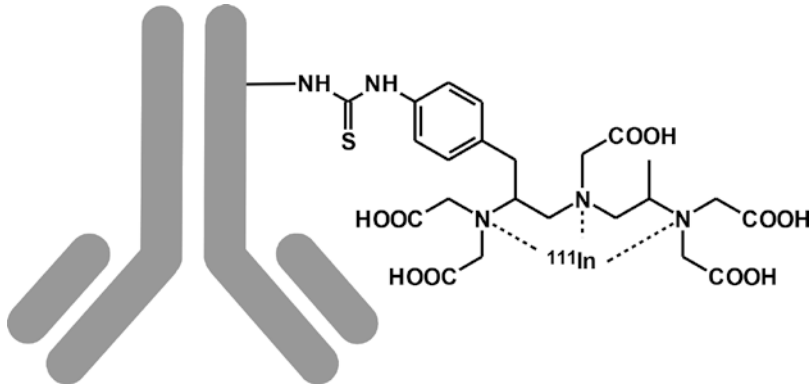

Fig. 15.20 Schematic structure of [^{111}In] In-Zevalin

capillary membranes and not secreted or absorbed by the renal tubules can be used to study renal function. ^{99m}Tc-MAG3 has a high extraction efficiency from functional kidneys, following active excretion by the tubular and glomerular system. It is used to determine the kidney function and kidney outflow rates (Shirasaki et al. 2004) (Fig. 15.21).

Target

Kidney perfusion due to a high glomerular filtration and low kidney retention

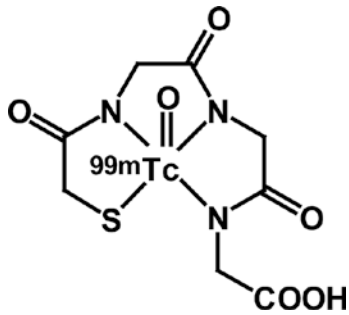

Fig. 15.21 Schematic structure of [^{99m}Tc] Tc-mercaptoacetyl-triglycine

Applications
Follow-up of kidney transplants. Kidney clearance rate (combined perfusion and functional scintigraphy)

15.3 Radiotracer

Clemens Decristoforo and Roland Haubner

15.3.1 Development and Evaluation of Peptide-Based Radiopharmaceuticals

15.3.1.1 Introduction

Recently, radiolabeled receptor-binding peptides have emerged as an important class of radiopharmaceuticals for diagnosis and therapy. Major advantages of peptides compared with antibodies are that they are not immunogenic, show fast diffusion and target localization, and can be modified concerning metabolic stability and pharmacokinetics. Advantages compared to small molecular weight compounds are that they are more tolerant concerning modification required for appropriate labeling (e.g., introduction of chelating systems for radio metalation) and strategies for optimizing pharmacokinetics. Most prominent members of this class of tracer are radiolabeled peptides for targeting somatostatin receptors. Some of them are already clinical routine for diagnosis as well as peptide receptor radionuclide therapy of somatostatin-receptor-expressing tumors. Currently a variety of other peptides such as bombesin derivatives, cholecystokinin/gastrin analogs, RGD-containing peptides, and chemokine receptor CXCR4 targeting peptides are evaluated.

In this chapter we want to give some guidelines for the development and evaluation of radiolabeled peptides. This includes a summary of strategies for lead structure finding, approaches for optimization of binding affinity, metabolic stability and pharmacokinetic behavior, possible labeling strategies, and discussion of techniques for in vitro and in vivo evaluation. Obviously, this chapter cannot cover all aspects of the different topics in detail. The first part is thought to give some brief insights in different strategies on how to find a new lead structure. The second part gives an overview of the different approaches to optimize tracer for the use in nuclear medicine and may help to choose appropriate strategies for the development of new peptide-based radiopharmaceuticals. The third part deals with labeling strategies and covers the most suitable labeling techniques for the most important isotopes used for labeling of peptides and will try to give the reader some guidelines for choosing the appropriate labeling techniques. The last part includes theoretical and practical details for carrying out corresponding in vitro and in vivo evaluations of peptide-based tracer.

15.3.1.2 Tracer Development

Lead Structure Finding
Human disease is often caused and/or associated with alterations in protein expression. Peptide-protein interactions play a central role in controlling and modulating cellular function, intracellular communication, immune response, and signal-transduction pathways. With some exceptions, like calcitonin, insulin, and oxytocin, naturally occurring peptides are not directly used as drugs. Especially for radiolabeling modifications are required. The different strategies for the design of peptides as drugs, drug candidates, and biological tools include structural, conformational, dynamic, and topographical considerations.

In general the development of new drugs is a challenging task. Many are discovered by chance observations, by the scientific analysis of folk

medicines, or by noting side effects of other drugs. More systematic methods include (a) the "classical" approach, where at least the structure of the ligand or the structure of the protein and the binding site is known; (b) approaches based on combinatorial chemistry, where synthetic libraries of peptides were produced and screened; and (c) approaches based on phage display libraries, where the properties of bacteriophages are used to produce a great diversity of binding epitopes. The following part gives a brief overview of these major strategies in lead structure finding and is not thought as a comprehensive review of the state of the art. Nevertheless, it should provide some basic information for those who are not familiar with this topic.

Rational Drug Design

This approach uses information about the structure of a drug receptor or one of its natural ligands to identify or create candidate drugs (for more information, see (Leach and Harren 2007)). The three-dimensional structure of a protein can be determined using methods such as X-ray crystallography or nuclear magnetic resonance spectroscopy. Based on this structural information, databases containing structures of many different chemical compounds can be searched. These approaches allow selection of those compounds that are most likely to interact with the receptor, which can subsequently be synthesized and tested in corresponding biological assays.

If the structure of the receptor's binding pocket is not known, the development can start by using the structure of a known ligand or, at least, binding sequence of the ligand. Resulting from these informations, by using structure activity relationship (SAR) studies, molecules with high binding affinity are synthesized. In this process searching of databases to identify compounds with similar properties can narrow down the search as much as possible to avoid large-scale screening.

For example, with the knowledge that the three-amino-acid sequence Arg-Gly-Asp is essential for binding of a variety of extracellular matrix proteins to the corresponding integrins, comprehensive SAR studies resulted in the cyclic pentapeptide cyclo(-Arg-Gly-Asp-ᴅPhe-Val-) (Haubner et al. 1997), which was the lead structure for development of a diversity of radiolabeled RGD-peptides for monitoring αvβ3 integrin expression.

Combinatorial Chemistry

About two decades ago, techniques became available to produce and screen a great variety of different compounds in an acceptable time frame. In the beginning the emphasis of combinatorial chemistry was to prepare enormous collections of compounds, but the kind of compounds resulting from this screening process did not have the kind of properties that drugs typically have. Even though large collections of compounds were being made, they were not much different from each other due to the limited variability of the synthetic routes used. Therefore, strategies changed and the emphasis now is on preparing smaller collections of compounds – not millions, but dozens to hundreds of compounds which are more varied, are pure, and based on basic chemical principles that are consistent with drugs. For example, Feher and Schmidt (Feher and Schmidt 2003) noted that combinatorial chemistry libraries suffer particularly from the lack of chirality, as well as structure rigidity, both of which are widely regarded as drug-like properties.

The concept of the high-throughput organic synthesis (HTOS) starts with preparing the core part of the molecules that constitutes the library by classical organic synthesis and then "decorating" this core by using databases which allow selection from a wide array of different variations (Chighine et al. 2007). Some key foci of HTOS are automation and development of standard procedures that are likely to work with a wide variety of different starting cores so that there is very minimal chemistry development time required for every new class of compounds.

Further improvements will lead more into automated multistep libraries. Currently a lot of effort is focused on libraries that involve only one chemical step. The automation in chemistry is now evolving to the point where multiple step synthesis on a single platform can be conducted.

Phage Display Libraries

The principle underlying all phage display systems is to physically link phenotypes of peptides to the corresponding genotypes (for overview see (Brissette and Goldstein 2007)). The single-stranded

DNA of the peptide to be expressed is packed inside bacteriophages. This allows expression of peptides as fusion proteins with the phage coat protein (e.g., pIII or pVIII) on the surface of the phage. Using this technique large phage display libraries containing up to 10^{10} individual members can be created from batch-cloned gene libraries. These phage libraries can be used for finding new peptide sequences that bind to a given target structure. The enrichment of phages presenting the binding peptide is achieved by affinity selection. For this "panning" process, the corresponding purified target receptor is immobilized, and phages binding to the target are isolated and amplified by reinfection of *E. coli* cells. Typically the panning and amplification step is repeated several times before the isolated phages are analyzed for the peptide they present.

In addition, phage display libraries are used to identify new peptides targeting particular cells or even organs without knowledge of the target receptor identity. Therefore cultured cells or biopsy specimens were used for in vitro panning. Even in vivo phage library selection was described. In this case, the intravenous administered phage display library is allowed to circulate for a certain period of time in the vascular system followed by perfusion and washing of the tissue to remove nonspecifically bound phage clones. Phages selectively homing to the vascular bed of the tissue of interest are recovered and amplified for subsequent rounds of selection. This approach has been used predominantly in murine models, where it mainly supplies information on changes in the expression patterns of the vasculature during tumor-induced angiogenesis or during the shift from benign to metastatic state. One limitation of this approach is that the screening is carried out in an animal model and data from such an experiment can normally not directly be transferred to the situation in humans. Thus, first attempts are made to use phage display systems in patients (Trepel et al. 2002). Anyway, this approach includes very strict regulatory and ethical requirements and has yet not been established as a routine procedure.

Tracer Optimization

After the lead structure is identified, strategies to optimize the labeling precursor concerning binding affinity, metabolic stability, and pharmacokinetics have to be considered. In many cases binding affinity of the lead structure is already sufficient for monitoring the corresponding target structure. Nevertheless, in some cases improvement of the binding affinity is of advantage. This may be achieved by modification of the peptide sequence or by the formation of multimeric compounds. For the improvement of pharmacokinetic properties, a variety of strategies are available. Additionally, especially peptide sequences derived from screening procedures may exhibit low stability toward metabolic degradation requiring modifications to stabilize the peptide. In the attempt to reach these goals, a major advantage of peptides as tracers is found in the greater tolerance concerning modification without effecting binding properties compared with small molecular weight compounds.

Optimization of Binding Affinity: Multimerization

A variety of strategies can be used to optimize binding affinities of biological active lead structures. Most are focused on modifications of the first-generation compounds resulting from the abovementioned lead structure finding process. This can be a comprehensive iterative process involving replacements and modifications within the found amino acid sequence and is out of the scope of this chapter.

Another approach introduces multimeric compounds presenting more than one receptor-binding sites in one molecule (Handl et al. 2004). This "multimerization" approach may result in an improved target affinity and prolonged target retention mainly due to an increased apparent ligand concentration and/or, especially by lager ligand molecules, due to strong cooperative binding (see Fig. 15.22). This strategy was successfully used for the improvement of the binding affinity of RGD-containing peptides.

In almost all approaches, the biological active cyclic pentapeptide with the general sequence cyclo(-Arg-Gly-Asp-DPhe/DTyr-Xxx-), where Xxx is either lysine or glutamic acid, was used and conjugated via different linker and/or spacer units. This includes lysine and glutamic acid as branching units and polyethylene glycol as spacer/pharmacokinetic modifier. Initially derivatives presenting two to

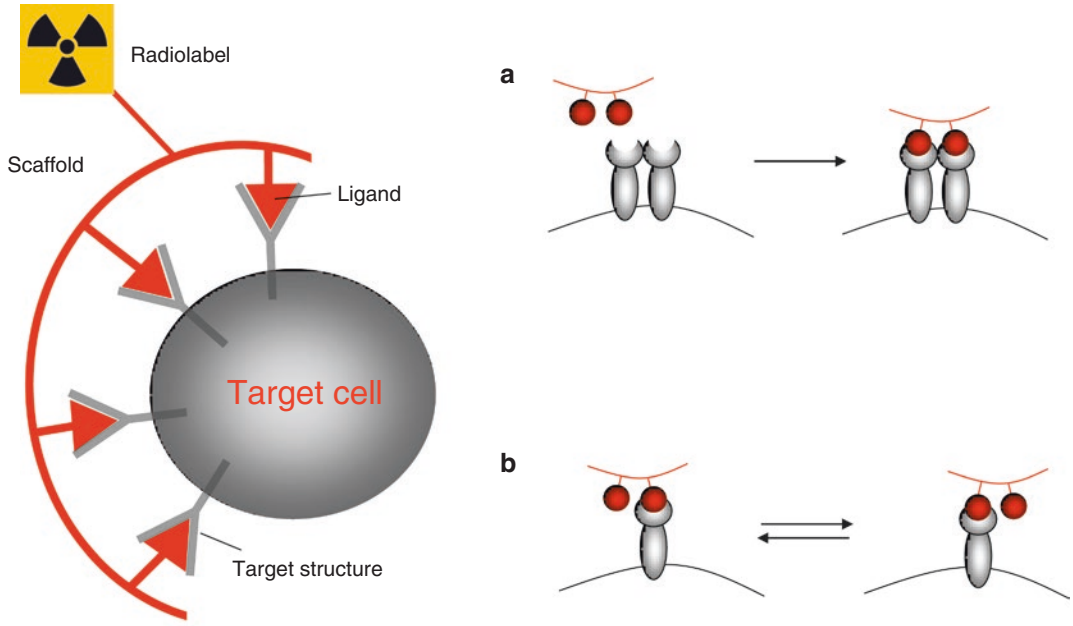

Fig. 15.22 Scheme showing the concept of multimerization to improve tumor uptake and retention. This concept includes that in one compound, multiple ligands binding to the same target are combined. The binding epitopes are connected via corresponding scaffolds (e.g., lysine trees) which also carries the radiolabel. The increased binding can be due to a strong cooperative binding, which is only possible if the designed molecule is large enough to bind two receptors the same time (**a**). Or binding affinity is increased due to an increased apparent ligand concentration (**b**)

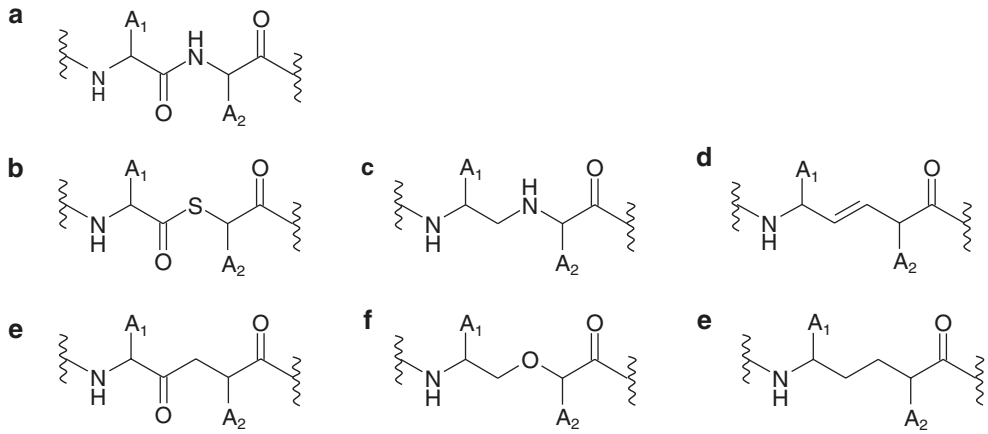

Fig. 15.23 Structure of some peptide bond isosteres (**b**–**g**) and comparison with a dipeptide fragment with classical peptide bond (**a**): thioamide ψ(CSNH) (**b**), methyleneamino ψ(CH_2NH) (**c**), E-alkene ψ(CH=CH) (**d**), ketomethylen ψ($COCH_2$) (**e**), methylenoxy ψ(CH_2O) (**f**), and carba ψ(CH_2CH_2) (**g**) bond (A_1 and A_2 indicate corresponding amino acid side chains)

eight binding epitopes per molecule have been studied. It was demonstrated in in vitro binding studies using immobilized integrin receptors that the affinity increased depending on the amount of cyclic RGD-peptides presented. Subsequent in vivo studies confirmed improved tracer accumulation and retention for some of the multimeric compounds.

For example, Janssen et al. (2002) synthesized a dimeric RGD-peptide by coupling two cyclo(-RGDfK) via a glutamic acid linker. For radiolabeling DOTA or HYNIC were conjugated to the free

amino function of the linker moiety. The dimeric ^{99m}Tc-HYNIC-E-[c(RGDfK)]$_2$ revealed a tenfold higher affinity for the αvβ3 integrin as the monomeric ^{99m}Tc-HYNIC-c(RGDfK). Moreover, also activity retention in the tumor was improved compared with the monomeric compound. However, activity retention was also high in the kidneys.

A more systematic study on the influence of multimerization on receptor affinity and tumor uptake was carried out by the groups of Kessler and Wester (Poethko et al. 2004b). They synthesized a series of monomeric, dimeric, tetrameric, and octameric RGD-peptides. These compounds contain different numbers of c(RGDfE) peptides which are connected via PEG linker and lysine moieties, which are used as branching units. Labeling was based on a chemoselective oxime formation between an amino-oxo function at the peptide site and an ^{18}F-labeled aldehyde. They found an increasing binding affinity in the series monomer, dimer, tetramer, and octamers in in vitro binding assay. Initial PET images confirmed these findings. The images of mice with both a receptor-positive and a receptor-negative melanoma showed an increasing activity accumulation only in the receptor-positive tumor in the series monomer, dimer, and tetramer.

Meanwhile a large set of different multimeric RGD-peptides have been introduced (Haubner et al. 2010). Maximum loading was achieved using a dentrimeric scaffold which results in compounds with up to 16 RGD units (Wangler et al. 2010). Again this study demonstrated increasing binding affinity in corresponding in vitro assays. Initial studies using multimeric RGD-peptides in lung cancer patients demonstrated specific imaging of αvβ3 expression with good contrast (Wan et al. 2013). Comparable findings were reported for other peptides, e.g., for minigastrin (Sosabowski et al. 2009) derivatives, where dimerization resulted in considerable improvement of binding affinity. However, this approach will mainly be helpful for radiopharmaceuticals targeting extracellular receptors, which only show limited internalization of their ligands. However, dimerization is not always accompanied by increase of binding affinity. Yu et al. (2013) studied dimeric bombesin derivatives and found lower binding affinity for the dimer. Despite lower affinity in vitro internalization of the compound was higher as found for the monomer. Anyway, tumor uptake in vivo could not be increased.

Optimization of Metabolic Stability

One major drawback when using peptide-based tracer is their low metabolic stability. A variety of peptidases specialized either to cleave N- or C-terminal amide bonds (exopeptidases) or amide bonds within the peptide sequence (endopeptidases) are found in the blood and other tissue such as the liver and kidneys. There are several strategies to overcome this problem. The easiest way to protect from degradation by exopeptidases is formation of cyclic peptides where the N-terminal end is conjugated with the C-terminus. This was carried out during the development of αvβ3-selective RGD-peptides. Radiopharmaceuticals based on this lead structure demonstrated high metabolic stability (for review see (Haubner and Decristoforo 2009)). The problem of this approach is that the biologically active sequence will be fixed in a certain spatial conformation. This can lead to improved target selectivity, as found in the case of the RGD-peptides, but may also result in a complete loss of binding affinity and, thus, cannot be used as a general strategy to improve metabolic stability. In some cases already modification of the C- or/and N-terminal amino acid via conjugation with corresponding chelating moieties required for labeling (e.g., DOTA) may improve stability toward degradation by exopeptidases.

Other approaches are focused on the replacement of natural amino acids by their enantiomeric D-analogs or by unnatural amino acids. For example, the sequence of octreotide includes DPhe at the N-terminus, DTrp at position 4, and threoninol (threonine where the carboxylate is reduced to an alcohol function) at the C-terminus (Heppeler et al. 2000). In other radiolabeled octreotide derivatives, DPhe^1 is replaced by the unnatural D-naphthylalanine. Some endopeptidases have special cleavage sites. For example, trypsin is specific for Arg and Lys and chymotrypsin for Trp, Tyr, and Phe; thus, replacement of these amino acids, if found in the corresponding sequence, will be of particular benefit.

Obviously, not all amino acids in a sequence can be replaced by either the corresponding D-amino acid or by an unnatural amino acid without influencing the binding affinity. In some cases the essential amino acids are already known; if not, an "alanine scan" (for details see (Nicole et al. 2000)) may supply this information.

Chemically much more challenging approaches deal with modifications of the amide bounds. A variety of peptide bond isosteres are possible (Vagner et al 2008). They range from replacement of the nitrogen by a methylene group via reduction of the carbonyl group to the replacement/modification of both the carbonyl group and the nitrogen (see Fig. 15.23). These modifications result in ketomethylene analogs, in reduced amid bonds, and in carba or alkene analogs, respectively. This approach has been successfully applied to stabilize neurotensin analogs to be used as tracers (Garcia-Garayoa et al 2009). Anyway, all of these modifications have drastic effects on the properties of the peptide. Depending on the modification carried out, this includes higher flexibility of the modified amide bond and changes in electron densities and, thus, changes in the hydrogen bridge donor-acceptor character. In many cases these modifications result in changes of the peptide structure and will influence the binding affinities of the peptides. Moreover, most of the modifications cannot be carried out on the final peptide, meaning that via complex synthesis routes the corresponding pseudo dipeptide including the peptide bond isostere has to be synthesized, which is in a second step included into the peptide sequence. The complexity of such synthetic routes strongly depends on the amino acids involved. Pseudo dipeptides including complex amino acids with additional side-chain functionalities are in general more difficult to produce than pseudo dipeptides including "simple" amino acids like Gly or Phe. In any case, determination of the binding affinity of the peptide after modification is a prerequisite.

A completely different approach to increase the in vivo stability of peptides is to block peptidases rather than stabilizing the peptide itself. Recently, it has been shown (Nock et al. 2014) that by coadministration of a peptidase inhibitor, the in vivo stability of otherwise highly metabolically labile radiolabeled peptides could be considerably enhanced resulting in significantly higher tumor uptake. This strategy holds the advantage of avoiding tedious synthetic stabilization strategies but requires further evaluation and standardization.

Optimization of Pharmacokinetics

Depending on their amino acid sequence, peptides can greatly differ in pharmacokinetic properties. In some cases, they already meet the needs of radiopharmaceuticals for molecular imaging and PRRT. In most cases, improvement of these properties (e.g., blood clearance, renal elimination, protein binding) is necessary. Here it is of advantage that normally not all amino acids of the sequence are required for high affinity binding. Usually there are parts of the peptide where modifications are tolerated. The strategies are manifold and include conjugation of carbohydrates, polyethylene glycol (PEG) moieties, or hydrophilic amino acids.

The conjugation of carbohydrates (glycosylation approach) was introduced to, e.g., optimize pharmacokinetics of RGD-peptides (Haubner et al. 2001b) and octreotide derivatives (Schottelius et al. 2005). For example, sugar amino acids (SAA) were conjugated via the ε-amino function of the lysine in the sequence cyclo(-Arg-Gly-Asp-DPhe-Lys-). In a murine tumor model, the resulting [*I]Gluco-RGD (Haubner et al. 2001a) and [^{18}F]Galacto-RGD (Haubner et al. 2001b) showed an initially increased activity concentration in the blood, very similar kinetics in the kidneys, a clearly reduced activity concentration in the liver, and an increased activity uptake and retention in the tumor compared to the first-generation, unmodified peptides.

In another approach hydrophilic D-amino acids were introduced to improve pharmacokinetics. Therefore, peptides containing three D-serine or D-aspartic acids and a γ-amino butyric acid for ^{18}F-labeling via prosthetic groups were coupled with the corresponding cyclic RGD-peptide. D-amino acids were used to improve the

metabolic stability of the compounds. The peptides showed high αvβ3 selectivity in vitro and receptor-specific accumulation in vivo. The tumor uptake in a murine melanoma model was lower as found with the glycosylated RGD-peptides. However, due to the rapid predominantly renal elimination of [^{18}F]DAsp$_3$-RGD, tumor/background ratios calculated from small animal PET images were comparable with [^{18}F] Galacto-RGD.

PEGylation is known to improve many properties of peptides and proteins including plasma stability, immunogenicity, and pharmacokinetics (Harris and Chess 2003). In many cases it is used to prolong median circulation times and half-lives of proteins and polypeptides by shifting the elimination pathway from renal to hepatobiliary excretion. Since renal filtration is dependent on both molecular mass and volume occupied, this effect strongly depends on the molecular weight of the PEG moiety.

For example, Chen et al. (2004b) attached a 2 kDa PEG moiety to the ε-amino function of cyclo(-Arg-Gly-Asp-DTyr-Lys-) and compared the ^{125}I-labeled PEGylated derivative (^{125}I-RGD-PEG) with the radioiodinated cyclo(-Arg-Gly-Asp-DTyr-Lys-) (^{125}I-RGD). ^{125}I-RGD-PEG showed a more rapid blood clearance, a decreased activity concentration in the kidneys, and a slightly increased activity retention in the tumor. However, tumor uptake for ^{125}I-RGD was higher as found for ^{125}I-RGD-PEG for all time points. Moreover, increased activity retention in the liver and intestine was found. In another study [^{18}F]FB-RGD, a [^{18}F]fluorobenzoyl-labeled RGD-peptide, and the PEGylated analog [^{18}F]FB-PEG-RGD (PEG, MW = 3.4 kDa) have been compared (Chen et al. 2004a). Again activity retention of the PEGylated peptide in the tumor was improved compared with the lead structure. However, initial elimination from the blood was slower and activity concentration in the liver and kidneys was higher as for [^{18}F] FB-RGD.

Altogether, these studies revealed very different effects of PEGylation on the pharmacokinetics and tumor uptake of RGD-peptides which seems to strongly depend on the nature of the lead structure, indicating that the effects are not completely predictable. Anyway, in general pharmacokinetic modifiers are helpful tools to adjust lipophilicity and charge toward the desired pharmacokinetic properties.

In some cases, however, radiolabeling strategies themselves can serve to modulate pharmacokinetics. The best example for this is the development of radiolabeled somatostatin analogs. Initially ^{123}I-labeled Tyr^3-octreotide was used to image neuroendocrine tumors in patients. This compound, although only showing very limited modification from the lead structure octreotide, showed considerable hepatobiliary excretion. By introducing DTPA as chelator for ^{111}In labeling, pharmacokinetics were switched to a predominant renal excretion pathway, which was a major breakthrough for imaging applications (Bakker et al. 1991). Also other chelator systems have shown to act as pharmacokinetic modifiers for octreotide derivatives. Especially HYNIC derivatization for radiolabeling with ^{99m}Tc allows using coligands, which can serve as pharmacokinetic modifiers (Decristoforo et al. 2006). Also hydrophilic chelating systems like DOTA for labeling with, e.g., ^{90}Y, ^{177}Lu, and ^{111}In have shown to serve this purpose.

In most cases the goal is to increase hydrophilicity of the peptide-based radiotracer to improve elimination from the body. Most recently a ^{68}Ga-labeled PSMA derivative was introduced (Eder et al. 2012). In this case higher tumor uptake was found using more lipophilic substituents. This was achieved by conjugating HBED-CC (N,N′-bis[2-hydroxy-5-(carboxyethyl)benzyl] ethylenediamine-N,N′-diacetic acid) to the target structure. This chelator allows straightforward labeling with ^{68}Ga, and the resulting ^{68}Ga-HBED-CC-PSMA showed excellent properties for imaging prostate cancer.

15.3.1.3 Labeling Strategies

Labeling strategies for peptides can be divided into two major groups. One includes halogens like ^{18}F-fluorine and iodine radioisotopes. The other includes radiometals like ^{99m}Tc-technetium, ^{111}In-indium, ^{68}Ga-gallium, ^{64}Cu-copper, ^{89}Zr-zirconium, ^{90}Y-yttrium, and ^{177}Lu-lutetium

Table 15.2 Overview of the most frequently used isotopes for peptide labeling and some physical characteristics

Nuclide	Half-life [h][a]	Decay mode	Max. β-energy [MeV][b]	γ-energy [MeV][b]	Production route
SPECT					
^{99m}Tc	6.01	100 % IT[c]	–	0.140	Generator
^{111}In	2.8 days	100 % EC[d]	–	0.171 0.245	Cyclotron
^{123}I	13.2	100 % EC	–	0.159	Cyclotron
^{125}I[e]	59.4 days	100 % EC	–	0.035	Reactor
PET					
^{18}F	1.83	97 % β^+ 3 % EC	0.63	–	Cyclotron
^{68}Ga	1.13	89 % β^+ 11 % EC	2.92 0.82	1.077	Generator
^{64}Cu	12.7	17 % β^+ 44 % EC 39 % β^-	1.67 0.58	1.345	Cyclotron
^{89}Zr	78.4	22.3 % β^+ 76.6 % EC	0.90	0.91	Cyclotron
^{124}I	4.2 days	23 % β^+ 77 % EC	1.53 2.14	0.603 1.691	Cyclotron
Therapy					
^{90}Y	64.1	100 % β^-	2.3	–	Generator
^{177}Lu	6.7 days	100 % β^-	0.50 0.38 0.18	0.208 0.113	Reactor
^{131}I	8.0 days	100 % β^-	0.61 0,33	0.636 0.364 0.284	Reactor

[a]As indicated for some nuclides, half-life is given in days
[b]If more only the most prominent decay energies are listed
[c]IT: internal transfer
[d]EC: electron capture
[e]Most commonly ^{125}I-iodine is used for biodistribution experiments, but small animal imaging using ^{125}I and SPECT is also possible

(for some physical characteristics of the different nuclides, see Table 15.2). Due to the different properties of halogens and metal isotopes, labeling of the first focuses on direct labeling (iodine) or labeling via prosthetic groups (^{18}F and iodine), whereas labeling of the latter is carried out via chelating systems conjugated to the peptides. Anyway, most recently also strategies to use ^{18}F-fluorine with chelating systems have been introduced. Here we want to summarize some standard labeling protocols for radioiodination, describe the most common prosthetic groups as well as new alternative labeling strategies for ^{18}F-labeling, and discuss major aspects of labeling with radiometals.

Halogens

Radioiodine

One of the easiest ways to label peptides is by direct labeling using radioiodine isotopes. For this approach at least one tyrosine in the amino acid sequence is necessary. Labeling is carried out via electrophilic substitution at the activated position 3/5 of the aromatic ring of the tyrosine (Fig. 15.24). Oxidation of the commercially available radioiodide can be carried out by different strategies (overview in Ref. (Coenen et al. 2006)). Standard procedures use chloramine-T or better chloramine-T on a polymeric support (Iodobeads$^{(R)}$) or Iodogen$^{(R)}$ for oxidizing *I^- to

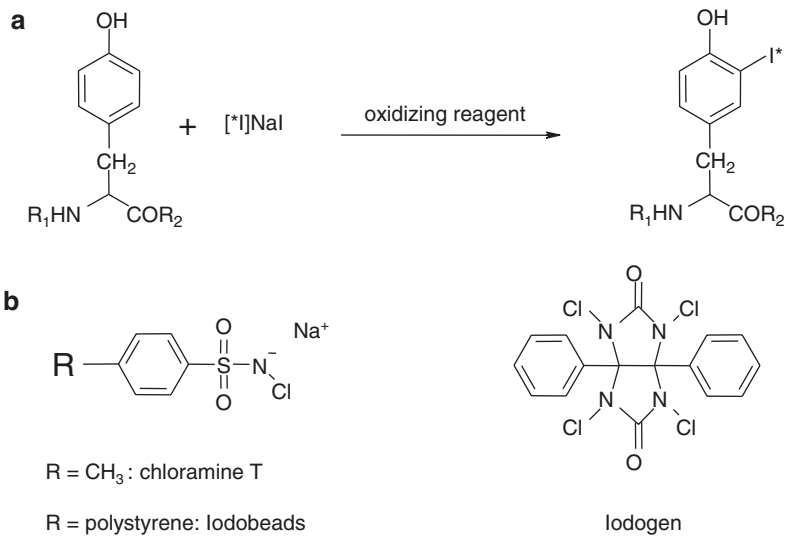

Fig. 15.24 (**a**) Radioiodine labeling of peptides via the phenol system of included tyrosine moieties. For electrophilic substitution the commercially available radioiodine has to be oxidized. (**b**) Structure of chloramine-T, Iodobeads (polymer-bound chloramine-T), and of Iodogen, which are the most commonly used oxidizing reagents for radioiodinations

$^{*}I^{+}$. Advantage of Iodobeads$^{(R)}$ and Iodogen$^{(R)}$ is that under standard conditions (labeling in puffer systems), these reagents are not soluble and can easily be separated from the solution containing the radiopharmaceutical after labeling. Of disadvantage, especially for chloramine-T, is that they can oxidize sensitive amino acids (e.g., methionine) in the peptide sequence, which may lead to changes in affinity. A gentler oxidation can be carried out via enzymatic systems (e.g., peroxidases) and hydrogen peroxide.

For labeling of peptides which do not include tyrosine and are sensitive toward oxidation or if direct labeling has negative effects on binding affinity, the Bolton-Hunter reagent, N-succinimidyl-3-(4-hydroxyphenyl) propionate, can be used. Labeling is a two-step reaction. In the first step, the Bolton-Hunter reagent is radioiodinated using, e.g., Iodobeads$^{(R)}$. In the second step, the radioiodinated reagent is conjugated to an amine function of the peptide sequence (e.g., α-amino function of the N-terminal amino acid or ε-amino function of lysine).

In many cases for the first evaluation of a new class of peptides, ^{125}I-iodine is used. The advantages are a comparable low radiation exposure due to the low energy and long half-life allowing experiments over a long period. Due to the availability of a great variety of iodine isotopes, depending on the isotope used, peptides can be utilized for SPECT (^{123}I), PET (^{124}I), and therapeutic approaches (^{131}I). However, in any case it has to be taken into account that the iodine-carbon bond can easily be cleaved by corresponding enzymes. Thus, radioiodinated peptides may show low metabolic stability reducing the applicability of this class of tracer. In some cases proof of principle is carried out with iodinated derivatives followed by modifications allowing labeling with ^{18}F or radiometals.

^{18}F-Fluorine

Direct labeling of peptides using ^{18}F-fluorine is in most cases not appropriate (harsh reaction conditions, formation of [^{18}F]HF in the presence of acidic protons). Thus, most approaches use prosthetic group labeling for introducing ^{18}F into peptides and proteins. Therefore, the nature of peptides, which include amino acids with multiple side-chain functionalities like amino, thiol, and alcohol groups, is exploited. Thus, standard labeling strategies are based on ^{18}F-fluoroalkylation, ^{18}F-fluoroacylation, and ^{18}F-fluoroamidation (Okarvi 2001; Wester and Schottelius 2007) (see also Fig. 15.25).

Most prosthetic groups for labeling of peptides focus on acylation of an amino function via an activated ester. One of the most prominent members is succinimidyl-4-[^{18}F] fluorobenzoate ([^{18}F]SFB) (Fig. 15.25). This prosthetic group can be produced via a three-step synthesis starting with the ^{18}F-labeling of

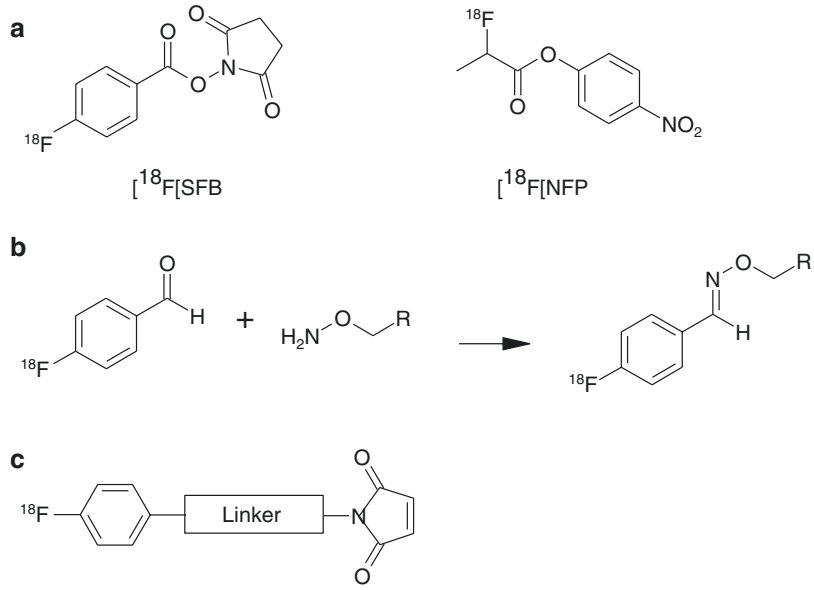

Fig. 15.25 (**a**) Structure of succinimidyl-4-[^{18}F]fluorobenzoate ([^{18}F]SFB) and 4-nitrophenyl-2-[^{18}F]fluoropropionate ([^{18}F]NFP), which belong to the most commonly used prosthetic groups for ^{18}F-labeling of peptides via fluoracylation. (**b**) Labeling of peptides via oxime formation using 4-[^{18}F]fluorobenzaldehyde and amino-oxo-modified peptides. By using this strategy, care has to be taken because of the high reactivity of the amino-oxo-function. Any aldehyde or keto function has to be avoided. Otherwise, quenching reactions can lead to the loss of the coupling group. (**c**) Schematic structure of a prosthetic group which is selective for thiol-containing peptides. Many of them combine an aromatic system for labeling via a linker system with the maleimido group which allows selective addition of HS groups to the double bond

4-N,N,N-trimethylammonium ethyl benzoate followed by the hydrolysis of the ethyl ester and subsequent activation using O-(N-succinimidyl)-N,N,N′,N′-tetramethyluronium tetrafluoroborate (TSTU). Another aliphatic prosthetic group is 4-nitrophenyl-2-[^{18}F]fluoropropionate (Fig. 15.25). Again synthesis includes ^{18}F-labeling of the corresponding precursor, hydrolysis of the ester, and subsequent activation. In many cases, at least, before conjugation with the peptide, a HPLC-separation is carried out making these labeling strategies very complex and time consuming. Anyway, for most of the yet described ^{18}F-labeled peptides, acylation is used for conjugation of the prosthetic group.

In the last decade, alternative strategies designed to optimize ^{18}F-labeling of peptides have been discussed. This includes oxime and hydrazone formation, conjugation via "click chemistry," or by using thiol-reactive groups. It has been demonstrated that amino-oxy functionalized peptides allow regioselective labeling using aldehydes and ketones. For example, it has been shown that multimeric RGD-peptides modified with amino-oxo acetic acid could be labeled successfully by using [^{18}F]fluorobenzaldehyde (Poethko et al. 2004a). Based on similar chemistry, HYNIC-modified peptides can be labeled with [^{18}F]fluorobenzaldehyde (Bruus-Jensen et al. 2006). Another concept, based on isotopic exchange reactions, uses p-(ditert butylfluorosilyl) benzaldehyde as labeling precursor (Schirrmacher et al. 2007). This compound allows isotopic exchange in almost quantitative yields leading to unexpected high specific activity. Similarly to the other aldehydes, the resulting prosthetic group is conjugated with the peptide via oxime formation.

Click chemistry, the 1,3-dipolar cycloaddition of an azide and an alkyne at room temperature using a Cu catalyst, was first introduced in radiochemistry to produce ^{99m}Tc(CO)$_3$-labeled compounds (Mindt et al. 2006). Meanwhile this

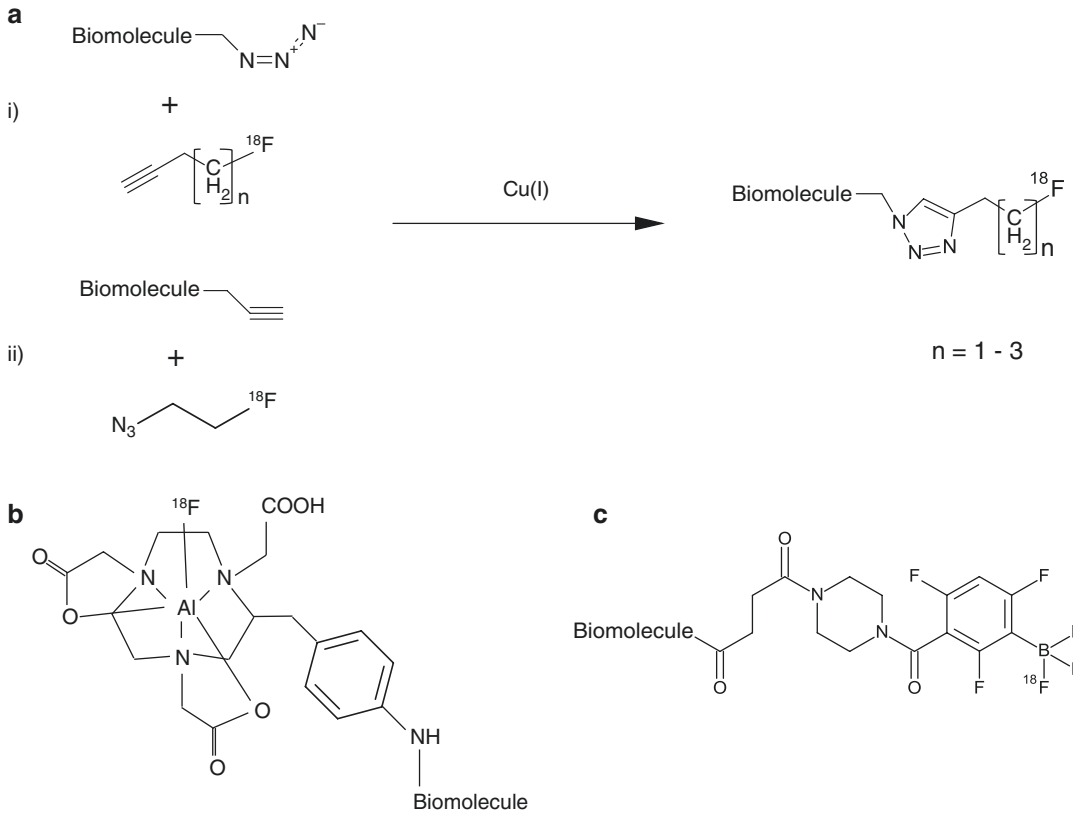

Fig. 15.26 (**a**) ^{18}F-labeling via Cu(I)-mediated click chemistry. (*i*) Prosthetic group is based on an alkyne. (*ii*) Prosthetic group is based on an azide. Mostly aliphatic derivatives with 1–3 carbon atoms are used. (**b**) Expected coordination of the aluminum fluoride species by NOTA derivatives. (**c**) Aryl trifluoroborate-containing peptide (^{18}F-labeling is carried out via isotopic exchange)

approach is also used for ^{18}F-labeling. For example, using the corresponding tosylate, ω-[^{18}F]fluoroalkynes were produced by nucleophilic fluorination and conjugated via cycloaddition to peptides functionalized with 3-azidopropionic acid. Other routes use propargylglycine for introducing an alkyne function into the peptide and [^{18}F]fluoroethylazide, again produced via the tosylate, as prosthetic group (Thonon et al. 2009) (Fig. 15.26a). Most recent approaches are focused on the introduction of copper-free, strain-promoted [3+2] azide-alkyne cycloaddition. The advantage is that this reaction can be carried out under mild conditions without the use of cytotoxic copper. Initial studies introduced [^{18}F]FB-DBCO which is synthesized by conjugating N-(3-aminopropionyl)-5,6-dihydro-11,12-didehydro-dibenzo-[b,f]azocine with [^{18}F]SFB (Bouvet et al. 2011) and chosen because of the availability of the aza-dibenzocyclooctyne derivative and the easy access to [^{18}F]SFB. Anyway, of disadvantage is the slow reaction rate resulting in long reaction times compared with the half-life of ^{18}F and the lipophilic character which might negatively influence the pharmacokinetic of corresponding labeled peptides. Thus, further studies have to demonstrate the potential of this approach. It has been found that glycosylation can improve pharmacokinetics of peptide-based tracer (for details see above). An elegant approach would combine introduction of the label and the sugar moiety in one step. Most elegant would be to use [^{18}F]FDG, which is available in almost all PET centers, as the prosthetic group. Because fluorodeoxyglucose exists in small amounts in the "aldehyde form," the chemoselective labeling

strategy via oxime formation with amino-oxy functionalized peptides can be used. Recently, by using this approach, Wester and coworkers produced an ^{18}F-labeled glycosylated RGD-peptide (Hultsch et al. 2009). Of importance for the production of larger activities is that n.c.a. [^{18}F]FDG is used, which means that after [^{18}F]FDG production, a separation of the radiolabeled sugar from excess glucose via HPLC is necessary. Other approaches modify [^{18}F]FDG before conjugation with the corresponding peptide (for review see (Haubner et al. 2014)). This can be carried out by producing thiosulfonate derivatives of the fluorodeoxyglucose which can form disulfide bridges with thiol-containing peptides, by synthesizing a thiol-reactive prosthetic group via oxime formation of the corresponding maleimide derivative and [^{18}F]FDG (Prante et al. 2007), or by using an "[^{18}F]FDG-azide" which is conjugated to a propargylglycine-containing peptide via click chemistry (Maschauer and Prante 2009). However, all these strategies have to be evaluated in more detail before it will become clear which will be the most useful labeling procedure.

Despite recent developments reduced the complexity of ^{18}F-labeling of peptides using prosthetic groups (see above), none of the prosthetic group approaches can compete with the simple and rapid labeling strategies based on ^{68}Ga. Thus, there is a keen interest in alternative ^{18}F-labeling strategies. This led to the development of new approaches based on ^{18}F-aluminum fluoride derivatives ("AlF") together with complexing agents (McBride et al. 2009) or an isotopic exchange reaction (Liu et al. 2013). The first technique transforms the halogen into a "pseudo" metal by utilizing the high affinity of fluorine to aluminum which allows straightforward production of the $(Al^{18}F)^{2+}$ species (Fig. 15.26b). The advantage is that this species forms stable complexes with NOTA-conjugated peptides in a one-step synthesis without HPLC purification comparable to radiometal labeling (see, e.g., McBride et al. (2010)). The second approach uses aryl trifluoroborate-containing peptides which were directly labeled using ^{18}F. Isotopic exchange rate is high resulting in high specific activity (Fig. 15.26c). However, initial in vivo experiments with an RGD-peptide showed only low uptake in the tumor. Thus, again further developments are needed to optimize this strategy. Anyway, the initial studies demonstrate that labeling can be carried out in a kit-like procedure within 1 h.

Metals

Today a number of radiometals are available for radiolabeling including labeling of peptides. Many radiometal-labeled peptides have proven to have a high stability in biological systems and residualizing properties in cells, once taken up.

In contrast to radiohalogens, metals have to be introduced via formation of a strong complex with the peptide structure. While direct labeling approaches of peptides have been described, it is today recognized that a specific metal chelator has to be introduced to achieve suitable targeting properties of the radiolabeled peptide in vivo in the great majority of cases. This is achieved by the so-called post labeling bifunctional chelate approach. Therefore, a metal chelating moiety is introduced into the peptide by chemical synthesis, either using peptide chemistry approaches using specific, chemically protected chelating moieties or alternatively by attaching the chelator using, e.g., activated ester functions after synthesis of the peptide. It is well recognized that an introduction of the chelating moiety will have considerable influence on specific interaction between the peptide sequence and the receptor, dependent on the individual targeting sequence. Information on the site of chelator attachment without impairing receptor-binding ability can be derived from basic research on the peptides themselves and their respective receptors.

Such derivatized peptides can be radiolabeled by incubating the radiometal with an excess of peptide-chelate conjugate directly, typically achieving almost quantitative labeling yields. In contrast to radiohalogenation, the radiolabeled peptide is usually not separated from excess of the labeling precursor (here peptide-chelate). As peptides bind to so-called low capacity targets, usually receptors, with high affinity, the total peptide amount has to be limited to avoid saturation of the target. Therefore, radiolabeling reactions have to be performed at very high specific

activities, meaning with very low amounts of peptide conjugate and radiometal. This limits the choice of both the radiometal and the chelator. Additionally, the chelator has to ensure a high in vivo stability, especially avoiding the release of the radiometal and should not deteriorate pharmacokinetic behavior or ideally even act as pharmacokinetic modifier (see section "Optimization of Pharmacokinetics").

Besides high specific activity, the radiometal should have a high chemical purity, mainly being free from other metallic impurities, and be easily available at reasonable costs.

The most frequently used radiometals applied in peptide labeling for imaging purposes are, on the one hand, ^{99m}Tc and ^{111}In for SPECT and, on the other hand, ^{68}Ga, ^{64}Cu, and recently ^{89}Zr for PET. ^{99m}Tc and ^{68}Ga show advantages in terms of availability, as they are generator products providing high flexibility and low cost in use. Whereas ^{99m}Tc requires the use of dedicated chelators and will be described separately in the following chapter, the other radiometals have some common properties in their coordination chemistry allowing the use of similar labeling strategies.

Technetium

Different chelating systems have been employed in an attempt to develop ^{99m}Tc-labeled peptides for targeting peptide receptors.

Early attempts for radiolabeling peptides using bifunctional chelators were based on propylenediamine-dioxime (PnAO) or so-called N_3S-ligands such as mercaptoacetyltriglycine (MAG_3). The relatively high lipophilicity of these chelating systems resulted in relatively low tumor and a high liver uptake with predominant excretion via the hepatobiliary system (Decristoforo and Mather 1999b). Only introduction of pharmacokinetic modifiers could improve properties to achieve suitable imaging properties, such as ^{99m}Tc-depreotide based on a N_3S monothiol-bisamide-monoamine ligand and multiple lysine residues to increase hydrophilicity (Vallabhajosula et al. 1996).

A very frequently used labeling moiety is 2-hydrazinonicotinic acid (HYNIC). It can be attached via the carboxylic function to a free amine group of the peptide either by using carboxylic group activation via succinimidyl-ester (succinimidyl-6-hydrazinopyridine-3-carboxylic acid) or by using, e.g., the hydrazine-BOC protected building block (6-BOC-hydrazinopyridine-3-carboxylic acid) during peptide synthesis (Fig. 15.27). In both cases the required HYNIC derivative is easily accessible via chemical synthesis or is commercially available.

In the radiolabeling process with HYNIC-derivatized peptides, a coligand is required that has shown to be of major importance for in vivo properties (Decristoforo and Mather 1999a). Coligands that allow radiolabeling at very high specific activities are usually aminocarboxylates such as tricine and ethylenediamine-N,N′diacetic acid (EDDA) or even ternary complexes with tricine and a monodentate ligand such a phoshines or N-heterocycles, imidazoles, or pyridines. Ternary complexes and EDDA have shown a higher stability especially resulting in a reduced plasma protein binding. Radiolabeling is achieved by reacting the HYNIC peptide with ^{99m}Tc-pertechnetate in the presence of stannous chloride; the choice of coligand may also be a matter of peptide stability as some coligands require heating.

Tetraamine (N_4)-based chelators are also suitable to prepare ^{99m}Tc-labeled peptides. Such a tetraamine chelator can be labeled at high specific activities under relatively mild alkaline conditions at room temperature and is hydrophilic, due to the formation of a positively charged Tc-dioxo unit. This ^{99m}Tc-labeling approach has shown to result in very suitable in vivo properties when attached, e.g., to octreotide derivatives (Maina et al. 2002). The N_4 chelator has to be introduced as protected building block during peptide synthesis, which is not commercially available.

A very versatile ^{99m}Tc-labeling approach is based on the so-called carbonyl core (Fig. 15.27). Therefore, ^{99m}Tc-pertechnetate is first reacted to the Tc-tricarbonyl-triaqua-ion ($[^{99m}Tc(CO)_3(H_2O)_3]^+$), where positively charged ^{99m}Tc in oxidation state (I) is bound very stable to three CO and weakly to three water molecules. This can be achieved by a commercially available kit (Isolink Covidien, NL) in a straightforward procedure.

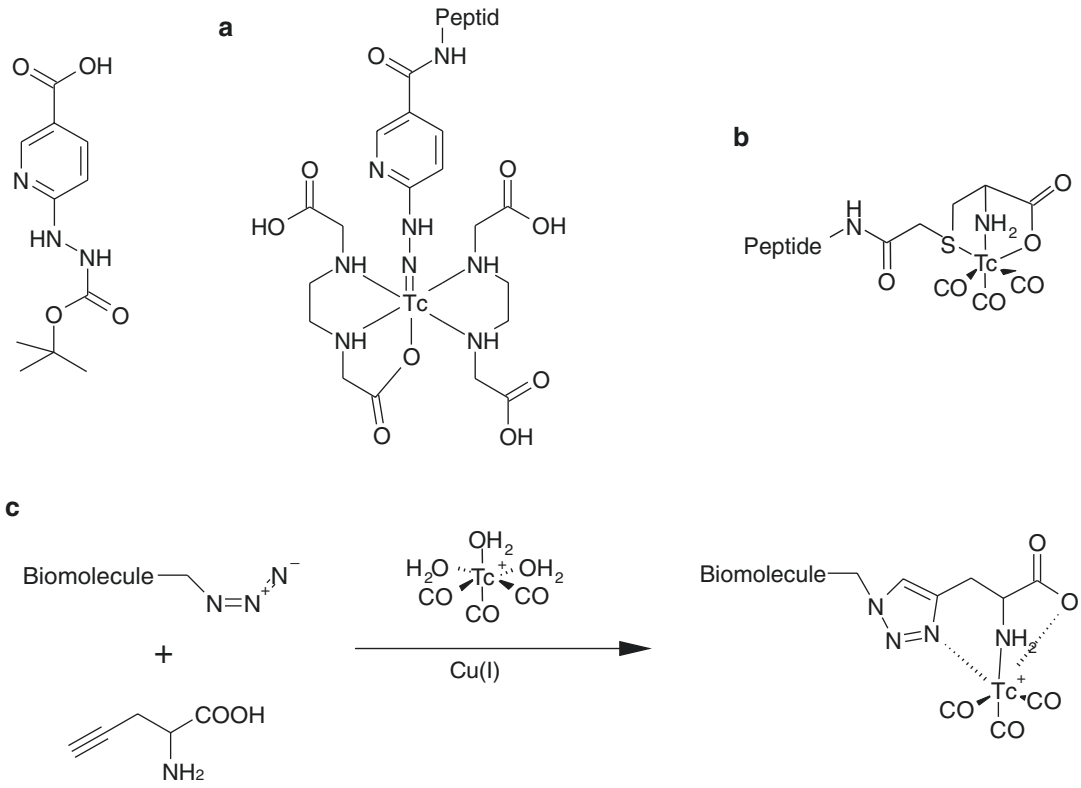

Fig. 15.27 (**a**) Structure of HYNIC-Boc, which can be directly used for conjugation of the carboxylate with amino functions in the peptide sequence. For complexation of ^{99m}Tc, the Boc-protection group has to be removed and coligands have to be added. Here EDDA was used as coligand. (**b**) Shows an example of a peptide labeled using the $Tc(CO)_3$-core. As tridentate ligand a thiol-modified cysteine is used. (**c**) The "click to chelate" approach uses the copper(I)-catalyzed 3 + 1 cycloaddition reaction to produce the triazole-based tridentate chelating system and subsequently the ^{99m}Tc-complex in a one-pot reaction

$[^{99m}Tc(CO)_3(H_2O)_3]^+$ is then reacted with a chelating system replacing the weakly bound water molecules by more stable bound chelator. It has been shown that some amino acids form very stable complexes with the ^{99m}Tc-$(CO)^3$ core with very high specific activities (Egli et al. 1999). Especially using histidine but also cysteine provides a tridentate ligand system. However, if these amino acids are incorporated into a peptide chain, one coordination site is lost and then these amino acids only act as bidentate chelators, resulting in a much lower in vivo stability. While complexes with tridentate coordinated ligand systems generally showed a fast and complete clearance from all organs and tissues, those complexes with only bidentate coordinated ligands showed a significantly higher retention of activity in the liver, the kidneys, and the blood pool (Schibli et al. 2000). The likely explanation for this behavior is that the coordination site which is unoccupied by these ligands become filled by donor atoms from circulating plasma proteins resulting in a high degree of protein binding and a radically altered pattern of biodistribution.

Therefore, specific building blocks for introduction into peptide chains for ^{99m}Tc-tricarbonyl labeling have been described, based on inverse histidine derivatives or by introducing chelators using click chemistry approaches resulting in triazole derivatives providing corresponding coordination sites for the ^{99m}Tc-tricarbonyl core (Mindt et al. 2006) (see also Fig. 15.27). To date, however, none of these chelator systems for ^{99m}Tc-tricarbonyl cores are commercially available and has to be synthesized individually. Whether the tricarbonyl approach offers advan-

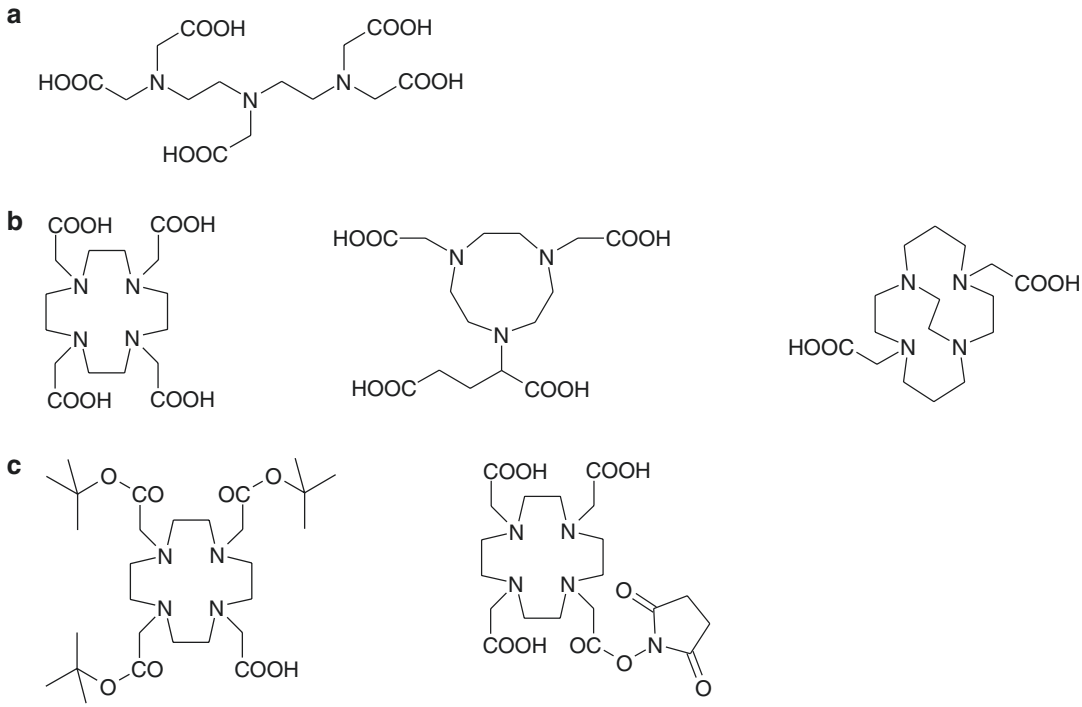

Fig. 15.28 (**a**) Structure of DTPA as an example of a linear chelating system. It can be used especially for ^{111}In-labeling. (**b**) Macrocyclic chelating systems: DOTA is used for ^{111}In, ^{90}Y, ^{177}Lu, and ^{68}Ga (*left*). NODAGA is a nine-membered ring which fits very well for ^{68}Ga and shows for this isotope a drastically increased complex binding affinity compared with DOTA (*middle*). TE2A is a bridged chelating system especially designed for complexing ^{64}Cu (*right*). (**c**) Special building blocks to introduce DOTA as chelator into peptides: *left*: Tris-BOC protected for conjugation in peptide synthesis with final deprotection, *right*: activated N-succinimidyl-ester that can be reacted with free amine groups of unprotected peptides

tages in terms of biological properties as, e.g., compared to HYNIC derivatization remains to be shown.

Other Radiometals

Labeling of other metals (e.g., ^{64}Cu, ^{68}Ga, ^{89}Zr, and ^{111}In) can be carried out by a class of very similar chelating systems. Basically they can be distinguished between open chain analogs and macrocyclic ligands.

The main open chain ligands used are based on diethylenetriamine-tetraacetic acid (DTPA) (Fig. 15.28), an octadentate ligand for many metals. DTPA anhydride can directly be coupled to free amino groups in the peptide chain. This, however, is not site specific and results in loss of one carboxylic group required for high stability coordination of many radiometals. To overcome this limitation, DTPA derivatives have been described, e.g., based on S-2(4-aminobenzyl)-diethylenetriamine pentaacetic acid. They are commercially available and can be used to introduce DTPA as a peptide building block or via active esters. It has to be considered that especially introduction of aromatic linking moieties will increase lipophilicity and may hamper pharmacokinetic properties.

A major advantage of DTPA derivatization of peptides is that it allows radiolabeling at room temperatures, thereby avoiding destruction of chemically sensitive moieties in the peptide. However, stability in vivo remains a challenge, especially in case of ^{68}Ga, ^{64}Cu, and ^{89}Zr derivatives.

In case of $^{68/67}$Ga, also deferoxamine (DFO) (Fig. 15.29a) as linear chelator has been used for radiolabeling through the included three hydroxamate groups. So far this approach was mainly used for proteins such as antibodies. However,

DFO-octreotide has been attempted to be used for tumor imaging labeled with ^{67}Ga (Smith-Jones et al. 1994) but was achieving only poor clinical results.

In contrast DFO is, at the moment, the most prominent chelating system for ^{89}Zr (van de Watering et al. 2014). In this case Zr^{4+} is coordinated by the six oxygen atoms of the hydroxamate groups of the DFO which is conjugated via an "amine tail" to peptides and proteins. Despite it demonstrates good stability ex vivo in serum (Holland et al. 2010; Meijs et al. 1992), in vitro some release and subsequent incorporation in bone is observed (Deri et al. 2013). Thus, there are attempts to find alternative chelating systems improving the binding of Zr^{4+}. Eventually, this can be achieved by introducing ligands with an oxygen-rich, octadentate chelation sphere.

The most frequently used chelating system for radiometal labeling of peptides is the cyclic chelator 1,4,7,10-tetraazacyclododecane-N,N′,N″,N‴-tetraacetic acid (DOTA) (Fig. 15.28). It contains four amino groups and four carboxylic groups for coordination of metals; the carboxylic group can be utilized for attachment to amino groups of peptides. This can be achieved either by specifically protected building blocks during the peptide synthesis or again via activated esters after the peptide has been prepared. Examples of commercially available building blocks are shown in Fig. 15.27.

Radiolabeling of DOTA-derivatized peptides is achieved under acidic conditions and requires elevated temperatures (Breeman et al. 2003). Temperature and pH vary dependent on the radionuclide being used. The ideal pH is a compromise between the tendency of the radiometal to form colloids at elevated pH and the reduced speed of complex formation at lower pH. Whereas for ^{111}In-labeling optimal pH is in the range between 4.5 and 5 usually achieved with acetate or ascorbate buffers, lower pH values are required for ^{68}Ga-labeling whereby HEPES or acetate buffers are frequently used to provide high radiolabeling yields (Velikyan et al. 2004). The prototype of a DOTA-derivatized peptide is DOTA-Tyr^3-octreotide (DOTATOC) and related derivatives that have been labeled with ^{111}In and ^{68}Ga for diagnostics but also with ^{90}Y and ^{177}Lu for therapeutic applications. However, coordination chemistry of DOTA may vary dependent on the radiometal. Whereas ^{111}In result in an octacoordinated complex, ^{68}Ga is hexacoordinated resulting in a free carboxylic group. This may result in different biological behavior of the radiolabeled peptides. In the case of DOTATOC, ^{68}Ga labeling resulted in higher tumor uptake and more rapid clearance (Froidevaux et al. 2002). In contrast a DOTA-RGD derivative showed higher blood levels and impaired tumor/background ratios when labeled with ^{68}Ga compared to the corresponding ^{111}In-labeled compound (Decristoforo et al. 2008).

Ga^{3+} is a relatively small cation and therefore cyclic chelators with smaller ring size may be more suitable for derivatization of peptides for radiolabeling. One alternative chelating system for radiolabeling with $^{68/67}$Ga is 1,4,7-triazacyclononane-1,4,7-triacetic acid (NOTA). In contrast to DOTA, all three carboxylic functions are involved in the stable hexacoordinated gallium complex. Therefore, specific derivatives of NOTA are required providing a coupling site with the peptide chain, an example hereof is NODAGA (1,4,7-triazacyclononane-1-glutaric acid-4,7-diacetic acid) (Eisenwiener et al. 2002) (Fig. 15.28); overall aliphatic substitutions should be preferred over aromatic linker due to comparably reduced lipophilicity values. An increasing number of NOTA building blocks are becoming commercially available allowing straightforward derivatization of peptides. A major advantage of NOTA derivatives is the possibility of radiolabeling at room temperature, therefore being suitable for sensitive peptide structures.

Recently, other alternatives have been introduced including 1,4,7-triazacyclononane-1,4,7-tris[(2-carboxyethyl)methylenephosphinic acid] (TRAP) (Fig. 15.29b) and 1,4,7-triazacyclononane-1,4-bis[methylene(hydroxymethyl)-phosphinic acid]-7-[methylene(2-carboxyethyl) phosphinic acid] (NOPO) as well as 1,2-[{6-(carboxylato-)pyridin-2-yl}methylamino]ethane (H_2dedpa) derivatives (Fig. 15.29b) (for review

see: (Haubner et al. 2014)). The first two chelating systems are based on the nine-membered ring system also found in NOTA derivatives but include phosphinic acid moieties instead of carboxylate groups. The advantage of the modification is found in the very high Ga^{3+} binding affinity of this class of chelators allowing labeling using very low peptide amounts resulting in very high specific activity. The major difference between TRAP (Notni et al. 2013) and NOPO (Simecek et al. 2014) is that the first allows conjugation of up to three ligands per chelating system, whereas for the latter only one phosphinic acid is functionalized allowing conjugation of corresponding ligands. The H_2dedpa system allows synthesis of monomeric or dimeric tracer (Boros et al. 2012). Performance was studied using RGD-peptides as model compounds. In vitro data (e.g., stability, affinity) was promising but in vivo studies demonstrated high activity concentration in blood even 2 h p.i. indicating inferior imaging properties compared with other RGD-peptides. This might be due to the estimated more lipophilic character of the chelating system which includes two pyridine moieties. Anyway, the applicability of the system for other target systems has to be verified in further studies.

DOTA has been used as chelator for ^{64}Cu-labeling of RGD-peptides (Chen et al. 2004c). Tumor/blood and tumor/muscle ratios of approximately 7 and 8, respectively, allowed acquisition of clear tumor/background contrast images 1 h p.i. using a small animal scanner. However, highest activity concentration was found in the liver, intestine, and bladder indicating that further optimization of the tracer is needed. Therefore alternative chelating systems have been described including 1,4,8,11-tetraazacyclotetradecane-1,4,8,11-tetraacetic acid (TETA) and 4-[(1,4,8,11-tetraazacyclotetradec-1-yl)methyl]benzoic acid (CPTA). Recently, cross-bridged tetraamine chelators such as 4,11-bis(carboxymethyl)-1,4,8,11-tetraazabicyclo[6.6.2]hexadecane (TE2A) (Fig. 15.28b) and

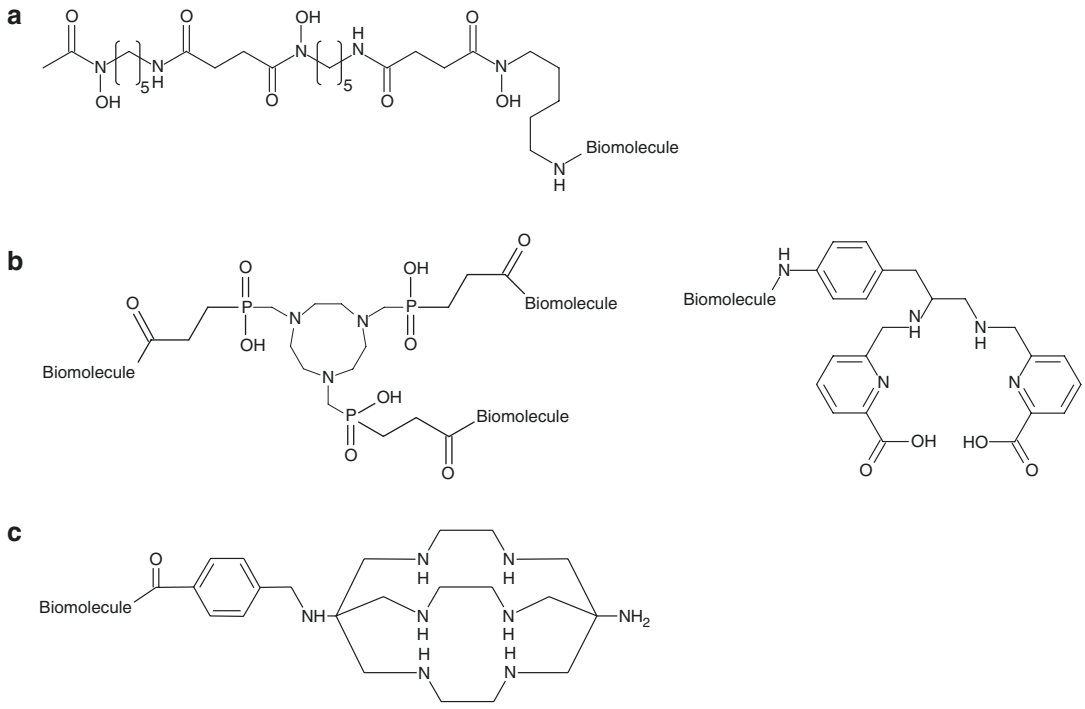

Fig. 15.29 (**a**) Structure of desferrioxamine (DFO) conjugated via an amino function with the biomolecule. (**b**, *left*) Structure of the phosphinic acid containing TRAP, which allows conjugation of up to three biomolecules. (**b**, *right*) Structure of a 1,2-[{6-(carboxylato-)pyridin-2-yl}methylamino]ethane (H_2dedpa) derivative. (**c**) Structure of the 3,6,10,13,16,19-hexaazabicyclo[6.6.]icocsan derivative AmBaSar

3,6,10,13,16,19-hexaazabicyclo[6.6.]icocsan derivatives like AmBaSar (Fig. 15.29c) have been proposed that show improved in vivo stability of radiolabeled peptides compared with their DOTA analogs (Garrison et al. 2007; Hausner et al. 2009). These chelators have been demonstrated to form extremely inert Cu^{2+}-complexes which results in increased in vivo stability compared to monocyclic chelator systems. However, there are also some drawbacks including very slow complexation kinetics and low electrochemical stability (Anderson et al. 2008). Thus, also NOTA derivatives have been tested as chelating systems for ^{64}Cu (Dumont et al. 2011). Using RGD-peptides as model structure, it has been demonstrated that the corresponding NODAGA-RGD possess superior properties as DOTA-RGD and similar properties as found for the CB-TE2A-RGD indicating that the NOTA system is an alternative in complexing ^{64}Cu. Recent approaches suggested picolinate modified cyclam derivatives as chelators for Cu^{2+} (Frindel et al. 2014). By conjugation of the picolinate to one of the nitrogen atoms in the ring, the complexation properties could be improved resulting in, e.g., rapid complexation time, high stability, and low transchelation rate. Anyway, initial activity concentrations of [^{64}Cu]TE1PA in kidneys and liver are high compared with [^{64}Cu]DOTA, but due to elimination after 24 h, values are comparable. For all other organs, activity concentration of [^{64}Cu]TE1PA is lower as found for [^{64}Cu]DOTA. Further studies of peptide-conjugated compounds have to demonstrate the potential of this new chelating system.

Overall if peptides are to be labeled with different radiometals for SPECT and PET applications, DOTA may be the chelator of initial choice allowing radiolabeling with ^{111}In, $^{68/67}Ga$, and ^{64}Cu and additionally with ^{177}Lu and ^{90}Y if therapeutic applications are to be considered.

15.3.1.4 Tracer Evaluation

For the evaluation of the radiolabeled peptides, adequate in vitro and in vivo studies have to be carried out. A comprehensive evaluation has to include studies determining affinity, selectivity, stability, and pharmacokinetic properties of the tracer. The most relevant assays to generate these data are discussed below. Besides the described studies, noninvasive imaging data resulting from studies using dedicated small animal scanner belong to the main criteria to determine the imaging properties of a new tracer. However, discussion of corresponding scanner, imaging techniques, and protocols are not included and described in detail in other chapters.

In Vitro Evaluation

Target (Receptor) Binding Assays

Binding affinity can be determined using a variety of radioligand binding assays, whereby description of all details is out of scope of this chapter. Theoretical and practical descriptions can be found in standard textbooks.

To determine the receptor binding, first a source for the receptors has to be found. This can either be:

- A cell line naturally expressing the receptor
- A cell line (stably) transfected with the receptor, such as CHO (Chinese hamster ovarian cancer) cells
- Fresh tissue or frozen tissue homogenates from animals
- Tissue sections from human or animal tissue (normal organs, tumors)
- Isolated receptors, ideally commercially available

Dependent on the source of the receptor, different experimental techniques have to be applied. However, receptor-binding assays always will include:

- A radioligand: This can either be the radiolabeled peptide itself or a known radiolabeled ligand for the respective receptor (e.g., commercially available as ^{125}I- or ^{14}C-labeled compound). A major requirement is that the concentration of the radioligand has to be very low to avoid saturation of the receptor system. A rule of thumb is that the radioligand should

be used in a concentration below the (expected or known) K_d value of the radioligand to the receptor. Therefore, radioligands of high specific activity are required still to provide sufficient count statistics in the assay.

- A suitable buffer system: This depends on the receptor system studied and specific additives such as metal ions, protease inhibitors, or additives to reduce nonspecific binding (e.g., albumin) that may have to be added.
- A competitor of the radioligand: This is a nonradioactive compound known to bind to the receptor and may serve in the simplest case to determine nonspecific binding; in this case, typically 1-10 μM of the competitor is used. In more complicated assays, different dilutions of the competitor are used.
- A washing buffer: Typically this is refrigerated before use to remove nonspecific binding but reduces the probability of loss of specific binding.
- A separation mechanism between bound and free radioligand: This may be in the simplest system pipetting of a supernatant, e.g., when tissue sections, coated receptors plates, or sticking cells are used. It may be achieved by centrifugation or more often by filtration, typically using glass fiber filters.

Some different assays can be designed that also require different values of complexity:

1. Simple binding assays, where a radioligand is incubated with receptors with and without competitor. This assay will provide answer whether a compound specifically binds to a receptor only in qualitative terms.
2. Competition assays: Here a radioligand is incubated with increasing concentration of a nonradioactive ligand. The results can be fitted in dedicated computer programs (such as ORIGIN or SIGMA-Plot) and are expressed as IC_{50} values in a concentration unit (typically nM). The IC_{50} value is a parameter for the binding affinity of the competitor (not the radioligand!).
3. Saturation assays: Here increasing concentrations of the radioligand are used and results are again fitted in a computer program. This assay results in K_d values, giving the binding affinity of the radioligand.
4. Internalization assays: Here the radioligand is incubated with intact cells, and after certain time points, cells are washed from unbound radioligand, followed by a washing step with an acidic buffer (typically acetate or glycine buffers) that removes cell surface receptor bound activity and at the end cells are collected and counted. In this assays information is gained on active cell uptake via receptor internalization, and results are expressed as internalized activity related to the total activity added or related to surface bound activity. Nonspecific cell uptake can be determined either by co-incubation with excess of cold receptor ligand or at 4 °C inhibiting energy-dependent internalization.
5. Washout assays: This assay may be performed if information is required whether an internalizing radioligand is released after intracellular metabolism or via active excretion mechanisms. To achieve this first a radioligand is incubated with the respective cells and then extracellular radioactivity is washed off. The cells are incubated again and samples of the supernatant are collected over time. The result may be expressed as % washout of total activity in the cell.

It must be stressed that for assays giving information on internalization and externalization, intact cells have to be used, whereas for determination of binding affinities, membranes or isolated receptor assays may be preferred as equilibrium required for exact determination of, e.g., a K_d value cannot be reached when the system is "open," e.g., by allowing internalization of ligands. In any case the nonspecific binding has to be determined, usually by co-incubation with an excess of a ligand blocking the target; without this no information on target binding whatsoever can be gained.

Special assays may also require additional techniques, such as when tissue sections are used. In this case determination of radioligand binding must be performed by autoradiography either

electronically or by means of classical film autoradiography.

Recently, also the receptor signaling has become of interest in receptor characterization of radiotracers based on peptides. Most peptides used traditionally were agonists, i.e., exhibiting the pharmacological action of the natural ligand when binding to the receptor including internalization. However, antagonists have shown to potentially have advantages in targeting with higher target/nontarget ratios. Radiolabeled somatostatin receptor antagonists are preferable to agonists for in vivo peptide receptor targeting of tumors (Ginj et al. 2006) and exhibiting no pharmacological effect, which can be challenging due to high potency of some agonistic peptides, such as bombesin derivatives. To characterize agonistic vs. antagonistic properties, several investigations can be made dependent on the target system, including internalization assays, Ca^{2+}-flux assays, or immunofluorescence assays combining peptide with antigen binding visualized by optical methods (Abiraj et al. 2011).

Partition Coefficient

One parameter, which is easy to determine and allows some prediction of the pharmacokinetics in vivo, is the partition coefficient (log P). It is a major parameter for the hydrophilicity and describes the distribution of the radiolabeled peptide between an octanol and a buffer phase. Especially for the partition of peptides, a defined pH value is of great importance (the protonation stage has influence on the hydrophilicity). Mostly phosphate-buffered saline pH 7.4 (PBS) is used as buffer system. The more hydrophilic the radiolabeled peptide is, the higher is the activity found in the buffer phase. It is difficult to define an optimal range for this parameter as it strongly depends on the particular nature and application of the radiolabeled peptide. In most cases radiolabeled peptides are developed to target receptors which are upregulated in tumor tissue. Thus, peptides that are rapidly accumulated in the tumor and eliminated from the body are searched for. It has been shown that peptides with very low logP values (typically below −3) are preferable in this case (see also section "Tracer Optimization"). Anyway, fast elimination from the blood is accompanied by a short time for tumor uptake. Thus, a balance between elimination and accumulation has to be found, which is best reflected in the tumor-to-background ratio (see later).

For the determination of the log P value, it is suggested to add approx. 500,000 cpm of the radiolabeled peptide in <50 µl aqueous solution to an Eppendorf cap containing 500 µl octanol and 500 µl PBS. After rigorous shaking for 10 min, samples of 100 µl from each phase are collected and counted. As peptides usually are very hydrophilic, most of the activity is found in the aqueous phase, and great care has to be taken during sample drawing to avoid cross contamination of the organic layer.

Protein Binding

A second important predictor of pharmacokinetics is the amount of radioligand bound to plasma proteins. High values of plasma protein binding will lead to prolonged blood circulation and reduced target to nontarget ratios. Plasma protein binding increases with increased lipophilicity, which is a known phenomenon for drugs. In the case of radiometal-labeled peptides, protein binding may also reflect reduced complex stability resulting in increased binding of the radiometal to proteins.

The protein-bound fraction is determined by incubation of the radiolabeled peptide in low concentration (<1 µM) at 37 °C in human or, if not available, rat plasma or serum for varying time points. Care has to be taken that the radioligand solution does not contain organic solvents or may contain buffers influencing the pH. The protein-bound fraction is determined by separation of the radiolabeled peptide from plasma proteins. This may be achieved by size exclusion, precipitation, or ultrafiltration. The latter two may overestimate the protein-bound fraction due to unspecific effects. A straightforward approach is to use miniaturized Sephadex-based size exclusion columns (Microspin). These can be loaded with the sample and centrifuged under controlled conditions, thereby only releasing the protein-bound fraction. Eluate and column are counted in a gamma counter and the protein-bound fraction is calculated as % protein bound of total activity. The assay should always be performed using a

negative control (i.e., incubation in buffer). Increase of protein binding over time may be an indicator of a limited complex stability (release of radiolabel over time). It should be stated that the method only is applicable if the molecular weight of the peptide is comparably low (i.e., < 5000). Low protein binding is usually of advantage; absolute values are difficult to give; however, e.g., for RGD-peptides low protein binding was considered to be clearly below 10 %.

Stability Assays

Stability assays should be performed for different reasons. First, they can give an indication of the stability of the radiolabel, especially when radiometal-based labels are used. On the other hand, they can provide information on the stability of the peptide itself. In general these assays are performed by incubation of the radiolabeled peptide in a certain medium, followed by analysis of the incubation solution at different time points, usually by radio-HPLC analysis; in certain cases TLC or SPE may be applied; however, it will only provide limited information (especially no information of the stability of the peptide is included).

Assays to determine the stability of the radiolabel, specifically when radiometals are used, should include incubation in different media. First stability in solution and in buffers at neutral pH (e.g., PBS) should be included. Additionally, so-called challenging assays should be performed. In this case an excess of a ligand with good chelating properties for the radiometal should be co-incubated. This can be DTPA in the case of ^{111}In, $^{67/68}$Ga, or ^{64}Cu. In the case of ^{99m}Tc, the challenging agent should be adapted to the radiolabeling approach used. In the case of ^{99m}Tc(V) ligands (e.g., N_3S and N_4 ligands), cysteine can be used as naturally occurring competing ligands. In case of ^{99m}Tc-tricarbonyl compounds, histidine may be a better choice.

Such assays can be designed in different ways. One possibility is co-incubation with a great excess of the competing ligand (e.g., 1000-fold molar excess of ligand over radiolabeled peptide) and determination of the stability at different time points (up to 24 h). Another possibility is to use one time point (e.g., 4 h) and different molar ratios of competing ligand and peptide. The amount of released radionuclide is usually determined by means of radio-HPLC but may be simplified by using, e.g., TLC methods. However, it should be validated whether the separation of radiolabeled peptide and released radiometal can be determined in this way.

Stability of the peptide itself is usually determined by incubation of the radiolabeled peptide in serum at 37 °C, followed by radio-HPLC analysis at different time points, expressing the result as half-lives of the radiolabeled peptide. To allow this analysis, first serum proteins have to be separated by means of precipitation (e.g., by pipetting the same volume ethanol or acetonitrile to the serum sample, followed by centrifugation). An alternative approach uses fixation of the peptide on a C-18 cartridge. In both cases the protein-bound fraction should be determined in parallel by one of the methods described above to avoid artifacts due to protein-bound material. Additionally to incubation in serum, other incubation media may be chosen such as tissue homogenates (e.g., from rat), as it is known that among other organs, the kidneys and liver are responsible for peptide degradation. It also may be of interest to determine stability in tumor cells expressing the respective target in a similar way. With such assays information on the metabolic stability can be gained. However, interpretation should be made very carefully, as stability can be very variable dependent on assay conditions (volume, age of serum, concentration). It therefore should be rather considered as an intra-laboratory standard rather than a comparison with published data or results from other laboratories.

In Vivo Evaluation

Normal Distribution/Metabolic Stability

First in vivo studies with a new tracer can be carried out using normal mice. This study will supply information about the overall biodistribution of the radiolabeled peptide. For example, it will show if tracer elimination is predominantly hepatobiliary or renal, if blood pool clearance is fast or slow, and if blood-brain barrier is penetrated.

For this study the tracer is injected into the tail vein of the mouse. At different time points (depending on the isotope used), the animals are sacrificed and dissected, and tissue of interest is weighed and activity is measured using a γ-counter. Activity concentration in the different organs will be expressed as percent injected dose per organ (%ID) and/or per gram tissue (%ID/g).

Further important data in tracer evaluation results from studies of the metabolic stability. A first indicator of tracer performance results already from determination of this parameter in serum/plasma. However, studying of the metabolic stability in whole body may supply a deeper insight in tracer properties. A standard protocol may include investigation of the metabolic stability of the tracer in the blood, tumor, kidney, and liver. Therefore, the tracer is injected i.v. and blood and organs are sampled at corresponding time points. Subsequently organs are homogenized (e.g., organs were frozen with liquid nitrogen and homogenized using a Mikro-Dismembrator) and suspended in buffer, and organ homogenates and blood are centrifuged. Workup of the supernatant follows the same protocols as described above (in vitro stability assays).

Murine Tumor Models

Most approaches using radiolabeled peptides are focused on targeting receptors involved in tumor biology. Most important in the development of these tracers is to choose the appropriate tumor model. One very important factor is that it is proven that the target molecule is expressed on the used tumor cell line as well as, and even more important, on the tumor grown in the corresponding animal. The latter can be carried out by dissecting the tumor and immunohistochemical staining of the tumor tissue sections using corresponding antibodies. If this is not possible, at least in Western blotting, determining that the mRNA is produced should be carried out.

In cases where a set of subtypes belongs to a receptor family (e.g., somatostatin receptors, integrins) and the development is focused on a subset or even on one special subtype out of the receptor family, it has to be guaranteed that only the target receptor is expressed. This can be achieved by using genetically modified cell lines where the target receptor is inserted into the host cell genome or by selecting cell lines which have already the desired expression pattern, e.g., by FACS.

Standard procedures to demonstrate selective receptor-mediated tracer accumulation are using blocking experiments (see below). However, these include in general that high peptide amounts have to be injected which may induce some downstream signals and/or influence the pharmacokinetics of the tracer. Thus, preferable assays will include negative control cell lines which are selected or modified not to express the target receptor. Such approaches will allow to grow receptor-positive as well as receptor-negative tumors; within the same animal, eliminating effects may be occurring due to injection of "cold" peptide or due to the fact that experiments are carried out in different sets of animals.

In most cases for the first in vivo evaluation, the animal models of choice are based on mice or in some cases rats, which are injected subcutaneously with the corresponding tumor cell line. One advantage is that adequate animal housing and handling is relatively easy. Moreover, a variety of immunodeficient nude mice strains, required for the use of human cell lines, are available.

In some cases transgenic mice may be included in the evaluation. Transgenic mice are very useful systems for studying mammalian gene function and regulation. Moreover, transgenic mice can be used to model human diseases that involve the over- or miss-expression of a particular protein. For example, the RIP-TAG model is a transgenic mouse model of carcinogenesis and angiogenesis where the oncogene SV40 T antigen is expressed under the control of the rat insulin promoter. The advantage of such a model is that the tumor arises from normal cells in its natural tissue environment and progresses through multiple stages as human cancer do. In the RIP-TAG model within 12–14 weeks, insulin-producing beta cells develop to islet cell hyperplasia, adenomas, and finally carcinomas. Anyway, production and handling of transgenic mice are not trivial and are not a

prerequisite in the evaluation of new radiolabeled peptide but can add additional information to get a deeper insight into the molecular mechanism of tracer accumulation.

Tumor Accumulation/Blocking Experiments

Information on the distribution of the tracer in normal tissue and the metabolic stability in vivo are important factors. But finally adequate and specific accumulation of the tracer at the target structure is the most important prerequisite of a radiopharmaceutical. Thus, a major step in radiotracer development is the evaluation of the radiolabeled peptide using corresponding disease models. As already mentioned most radiolabeled peptides yet are developed to target receptors which are overexpressed in tumor tissue. Thus, tumor xenografts grown in mice (or nude mice; depending on the origin of the tumor cells) are used in most cases. These were generated by either injection of tumor cells subcutaneously into the mouse or by directly transplanting tumor tissue from one animal to the next (which will not be discussed in detail here). For biodistribution studies, injection site is not important. Preferably the tumor cells (approx. five Mio but it strongly depends on the in vivo growth rate of the cell line) are injected subcutaneously at the *musculus femoris*. Mice are ready for biodistribution studies when the tumors reached a weight of approx. 100–200 mg. There is a great variation in the growth period, which strongly depends on the tumor cell type used. Many cell lines can be injected in buffer systems (e.g., PBS). For some cell lines, injection in Matrigel is recommended. Therefore, it is mixed with immortalized human cancer cells and the mixture is injected subcutaneously in immunodeficient mice. A human tumor usually forms in 2–4 weeks. Major components of Matrigel are structural proteins such as laminin and collagen. Additionally, it contains growth factors that promote differentiation and proliferation of many cell types as well as numerous proteins in small amounts. Anyway, its exact composition is unknown.

After the tumor reached desired size, distribution of the tracer will be studied following the same protocols as described above. An important parameter to draw conclusions regarding tracer performance is the tumor-to-background ratio, which can be extracted from this experiment.

Not only the absolute amount of tracer accumulation in tumor tissue is important but also it is even more important to show that accumulation is tumor or better receptor specific. As mentioned this can be confirmed by either using negative control tumors or, if not available, by carrying out blocking or competition experiments. Therefore, prior (approx. 10 min) or together with the radiolabeled peptide, a great excess of unlabeled peptide, which is known to bind with high affinity to the target structure, is injected. This has to lead to a significant reduction in tumor uptake. Sometimes not only tracer accumulation in the tumor but also in other organs decreases. This can be due to expression of the target structure on organs other than the tumor. Anyway, this has to be considered carefully, because the high amount of peptide can influence elimination, which also may result in changes of the distribution pattern.

References

PET and SPECT: Methods and Devices

Anger HO. Scintillation camera. Rev Sci Instr. 1958;29:27–33.

Beekman F, van der Have F. The pinhole: gateway to ultra-high-resolution three-dimensional radionuclide imaging. Eur J Nucl Med Mol Imaging. 2007;34(2):151–61.

Brasse D, Kinahan PE, et al. Correction methods for random coincidences in fully 3D whole-body PET: impact on data and image quality. J Nucl Med. 2005;46(5):859–67.

Casey ME, Nutt R. Multicrystal two dimensional BGO detector system for positron emission tomography. IEEE Trans Nucl Sci. 1986;33:460–3.

Chen CH, Muzic Jr RF, et al. Simultaneous recovery of size and radioactivity concentration of small spheroids with PET data. J Nucl Med. 1999;40(1):118–30.

Chen CL, Wang Y, et al. Toward quantitative small animal pinhole SPECT: assessment of quantitation accuracy prior to image compensations. Mol Imaging Biol. 2009;11(3):195–203.

Cherry SR, Shao Y, et al. MicroPET: a high resolution PET scanner for imaging small animals. IEEE Trans Nucl Sci. 1997;44:1161–6.

Cherry SR, Sorenson JA, et al. Physics in nuclear medicine. Philadelphia: Saunders; 2003.
Chow PL, Rannou FR, et al. Attenuation correction for small animal PET tomographs. Phys Med Biol. 2005;50(8):1837–50.
Chung YH, Choi Y, et al. Characterization of dual layer phoswich detector performance for small animal PET using Monte Carlo simulation. Phys Med Biol. 2004;49(13):2881–90.
Hoffman EJ, Huang SC, et al. Quantitation in positron emission computed tomography: 1. effect of object size. J Comput Assist Tomogr. 1979;3(3):299–308.
Hudson HM, Larkin RS. Accelerated image reconstruction using ordered subsets of projection data. IEEE Trans Med Imaging. 1994;13:601–9.
Huisman MC, Reder S, et al. Performance evaluation of the Philips MOSAIC small animal PET scanner. Eur J Nucl Med Mol Imaging. 2007;34(4):532–40.
Hwang AB, Hasegawa BH. Attenuation correction for small animal SPECT imaging using x-ray CT data. Med Phys. 2005;32(9):2799–804.
Hwang AB, Franc BL, et al. Assessment of the sources of error affecting the quantitative accuracy of SPECT imaging in small animals. Phys Med Biol. 2008;53(9):2233–52.
Judenhofer MS, Catana C, et al. PET/MR images acquired with a compact MR-compatible PET detector in a 7-T magnet. Radiology. 2007;244(3):807–14.
Kemp BJ, Hruska CB, et al. NEMA NU 2-2007 performance measurements of the Siemens Inveon preclinical small animal PET system. Phys Med Biol. 2009;54(8):2359–76.
Lecomte R, Cadorette J, et al. Initial results from the Sherbrooke avalanche photodiode positron tomograph. IEEE Trans Nucl Sci. 1996;43:1952–7.
Liang Z, Turkington T, et al. Simultaneous compensation for attenuation, scatter and detector response for SPECT reconstruction in three dimensions. Phys Med Biol. 1992;37:587–603.
Meikle SR, Kench P, et al. Small animal SPECT and its place in the matrix of molecular imaging technologies. Phys Med Biol. 2005;50(22):R45–61.
Rafecas M, Mosler B, et al. Use of Monte-Carlo based probability matrix for 3D iterative reconstruction of MADPET-II data. IEEE Trans Nucl Sci. 2004;51(5):2597–605.
Schafers KP, Reader AJ, et al. Performance evaluation of the 32-module quadHIDAC small-animal PET scanner. J Nucl Med. 2005;46(6):996–1004.
Schmand M, Eriksson L, et al. Performance results of a new DOI detector block for a high resolution PET-LSO research tomograph: HRRT. IEEE Trans Nucl Sci. 1998;45:3000–6.
Schramm NU, Ebel G, et al. High-resolution SPECT using multipinhole collimation. IEEE Trans Nucl Sci. 2003;50(3):315–20.
Seidel J, Vaquero JJ, et al. Resolution uniformity and sensitivity of the NIH ATLAS small animal PET scanner: comparison to simulated LSO scanners without depth-of-interaction capability. IEEE Trans Nucl Sci. 2003;50:1347–50.
Surti S, Karp JS. Imaging characteristics of a 3-dimensional GSO whole-body PET camera. J Nucl Med. 2004;45(6):1040–9.
van der Have F, Vastenhouw B, et al. U-SPECT-II: an ultra-high-resolution device for molecular small-animal imaging. J Nucl Med. 2009;50(4):599–605.
Vanhove C, Defrise M, et al. Improved quantification in single-pinhole and multiple-pinhole SPECT using micro-CT information. Eur J Nucl Med Mol Imaging. 2009;36(7):1049–63.
Wirrwar AK, Nikolaus S, et al. TierSPECT: performance of a dedicated small-animal-SPECT camera and first in vivo measurements. Z Med Phys. 2005;15(1):14–22.
Zeniya T, Watabe H, et al. Use of a compact pixellated gamma camera for small animal pinhole SPECT imaging. Ann Nucl Med. 2006;20(6):409–16.
Ziegler SI, Pichler BJ, et al. A prototype high resolution animal positron tomograph with avalanche photodiode arrays and LSO crystals. Eur J Nucl Med. 2001;28(2):136–43.

PET and SPECT Tracers for Molecular Imaging

Afshar-Oromieh A, Avtzi E, Giesel FL, Holland-Letz T, Linhart HG, Eder M, Eisenhut M, Boxler S, Hadaschik BA, Kratochwil C, et al. The diagnostic value of PET/CT imaging with the (68)Ga-labelled PSMA ligand HBED-CC in the diagnosis of recurrent prostate cancer. Eur J Nucl Med Mol Imaging. 2015;42:197–209.
Armbrecht JJ, Buxton DB, Schelbert HR. Validation of C-1 carbon-11 labeled acetate as a tracer for noninvasive assessment of oxidative metabolism with positron emission tomography in normal ischemic postischemic and hyperemic canine myocardium. Circulation. 1990;81:1594–605.
Benešová M, Schäfer M, Bauder-Wüst U, Afshar-Oromieh A, Kratochwil C, Mier W, Haberkorn U, Kopka K, Eder M. Preclinical evaluation of a tailor-made DOTA-conjugated PSMA inhibitor with optimized linker moiety for imaging and endoradiotherapy of prostate cancer. J Nucl Med. 2015;56:914–20.
Blake GM, Park-Holohan S-J, Cook GJR, Fogelman I. Quantitative studies of bone with the use of 18F-fluoride and 99mTc-methylene diphosphonate. Semin Nucl Med. 2001;31:28–49.
Boni G, Bellina CR, Grosso M, Lucchi M, Manca G, Ambrogi MC, Volterrani D, Menconi G, Melfi FMA, Gonfiotti A, et al. Gamma probe-guided thoracoscopic surgery of small pulmonary nodules. Tumori. 2000;86:364–6.
Chen W, Cloughesy T, Kamdar N, Satyamurthy N, Bergsneider M, Liau L, Mischel P, Czernin J, Phelps

ME, Silverman DHS. Imaging proliferation in brain tumors with F-18-FLT PET: comparison with F-18-FDG. J Nucl Med. 2005;46:945–52.

Dadparvar S, Krishna L, Brady LW, Slizofski WJ, Brown SJ, Chevres A, Micaily B. The role of iodine-131 and thallium-201 imaging and serum thyroglobulin in the management of differentiated thyroid carcinoma. Cancer. 1993;71:3767–73.

Eckelman WC, Jones AG, Duatti A, Reba RC. Progress using Tc-99m radiopharmaceuticals for measuring high capacity sites and low density sites. Drug Discov Today. 2013;18:984–91.

Eder M, Neels O, Müller M, Bauder-Wüst U, Remde Y, Schäfer M, Hennrich U, Eisenhut M, Afshar-Oromieh A, Haberkorn U, et al. Novel preclinical and radiopharmaceutical aspects of [68Ga]Ga-PSMA-HBED-CC: a new PET tracer for imaging of prostate cancer. Pharmaceuticals. 2014;7:779–96.

Even-Sapir E, Metser U, Flusser G, Zuriel L, Kollender Y, Lerman H, Lievshitz G, Ron I, Mishani E. Assessment of malignant skeletal disease: initial experience with 18F-fluoride PET/CT and comparison between 18F-fluoride PET and 18F-fluoride PET/CT. J Nucl Med. 2004;45:272–8.

Fletcher JW, Djulbegovic B, Soares HP, Siegel BA, Lowe VJ, Lyman GH, Coleman RE, Wahl R, Paschold JC, Avrill N, et al. Recommendations on the use of F-18-FDG PET in oncology. J Nucl Med. 2008;49:480–508.

Fonti R, Del Vecchio S, Zannetti A, De Renzo A, Catalano L, Pace L, Rotoli B, Salvatore M. Functional imaging of multidrug resistant phenotype by 99mTc-MIBI scan in patients with multiple myeloma. Cancer Biother Radiopharm. 2004;19:165–70.

Hara T, Kosaka N, Kishi H. Development of 18F-fluoroethylcholine for cancer imaging with PET: synthesis, biochemistry, and prostate cancer imaging. J Nucl Med. 2002;43:187–99.

Hellwig S, Frings L, Amtage F, Buchert R, Spehl TS, Rijntjes M, Tüscher O, Weiller C, Weber WA, Vach W, et al. 18F-FDG PET is an early predictor of overall survival in suspected atypical parkinsonism. J Nucl Med. 2015;56:1541–6.

Hillier SM, Maresca KP, Femia FJ, Marquis JC, Foss CA, Nguyen N, Zimmerman CN, Barrett JA, Eckelman WC, Pomper MG, et al. Preclinical evaluation of novel glutamate-urea-lysine analogues that target prostate-specific membrane antigen as molecular imaging pharmaceuticals for prostate cancer. Cancer Res. 2009;69:6932–40.

Huang SC, Phelps ME, Hoffman EJ, Sideris K, Selin CJ, Kuhl DE. Noninvasive determination of local cerebral metabolic rate of glucose in man. Am J Physiol. 1980;238:E69–82.

Hutchings M, Loft A, Hansen M, Pedersen LM, Buhl T, Jurlander J, Buus S, Keiding S, D'Amore F, Boesen A-M, et al. FDG-PET after two cycles of chemotherapy predicts treatment failure and progression-free survival in Hodgkin lymphoma. Blood. 2006;107:52–9.

Kasama S, Toyama T, Kumakura H, Takayama Y, Ichikawa S, Suzuki T, Kurabayashi M. Effects of candesartan on cardiac sympathetic nerve activity in patients with congestive heart failure and preserved left ventricular ejection fraction. J Am Coll Cardiol. 2005;45:661–7.

Kobayashi K, Ohnishi A, Promsuk J, Shimizu S, Kanai Y, Shiokawa Y, Nagane M. Enhanced tumor growth elicited by L-type amino acid transporter 1 in human malignant glioma cells. Neurosurgery (Hagerstown). 2008;62:493–503.

Koh WJ, Rasey JS, Evans ML, Grierson JR, Lewellen TK, Graham MM, Krohn KA, Griffin TW. Imaging of hypoxia in human tumors with fluorine-18 fluoromisonidazole. Int J Radiat Oncol Biol Phys. 1992;22:199–212.

Kubota K, Ishiwata K, Yamada S, Kubota R, Sato T, Takahashi J, Ito H, Ido T, Tada M. Dose-responsive effect of radiotherapy on the tumor uptake of L methyl-carbon-11-methionine feasibility for monitoring recurrence of tumor. Nucl Med Biol. 1992;19:27–32.

Kubota R, Kubota K, Yamada S, Tada M, Takahashi T, Iwata R, Tamahashi N. Methionine uptake by tumor tissue: a microautoradiographic comparison with FDG. J Nucl Med. 1995;36:484–92.

Moeller BJ, Richardson RA, Dewhirst MW. Hypoxia and radiotherapy: opportunities for improved outcomes in cancer treatment. Cancer Metastasis Rev. 2007;26:241–8.

Oyama N, Akino H, Kanamaru H, Suzuki Y, Muramoto S, Yonekura Y, Sadato N, Yamamoto K, Okada K. 11C-acetate PET imaging of prostate cancer. J Nucl Med. 2002;43:181–6.

Reubi JC. Peptide receptors as molecular targets for cancer diagnosis and therapy. Endocr Rev. 2003;24:389–427.

Rohren EM, Turkington TG, Coleman RE. Clinical applications of PET in oncology. Radiology. 2004;231:305–32.

Sara AC, Kei H, Akihito I, Noriyuki K, Mark T. PET imaging for gene & cell therapy. Curr Gene Ther. 2012;12:20–32.

Schelbert HR, Phelps ME, Huang SC, Macdonald NS, Hansen H, Selin C, Kuhl DE. Nitrogen-13 ammonia as an indicator of myocardial blood flow. Circulation. 1981;63:1259–72.

Scott GC, Meier DA, Dickinson CZ. Cervical lymph node metastasis of thyroid papillary carcinoma imaged with fluorine-18-FDG, technetium-99-m-pertechnetate and iodine-131-sodium iodide. J Nucl Med. 1995;36:1843–5.

Shirasaki Y, Tsushima T, Saika T, Nasu Y, Kumon H. Kidney function after nephrectomy for renal cell carcinoma. Urology. 2004;64:43–7.

Sun Y, Ma P, Bax JJ, Blom N, Yu Y, Han X, Wang Y, Van der Wall EE. 99mTc-MIBI myocardial perfusion imaging in myocarditis. Nucl Med Commun. 2003;24:779–83.

Waldherr C, Pless M, Maecke HR, Schumacher T, Crazzolara A, Nitzsche EU, Haldemann A, Mueller-Brand J. Tumor response and clinical benefit in neuroendocrine tumors after 7.4 GBq 90Y-DOTATOC. J Nucl Med. 2002;43:610–6.

Wiseman GA, Witzig TE. Yttriutm-90 (Y-90) ibritumomab tiuxetan (Zevalin (R)) induces long-term durable responses in patients with relapsed or refractory B-cell non-Hodgkin's lymphoma. Cancer Biother Radiopharm. 2005;20:185–8.

Wüstemann T, Bauder-Wüst U, Schäfer M, Eder M, Benešová M, Leotta K, Kratochwil C, Haberkorn U, Kopka K, Mier W. Design of internalizing PSMA-specific Glu-ureido-based radiotherapeuticals. Theranostics. 2016;6:1085–95.

Yaghoubi SS, Campbell DO, Radu CG, Czernin J. Positron emission tomography reporter genes and reporter probes: gene and cell therapy applications. Theranostics. 2012;2:374–91.

Zuckier LS, Dohan O, Li Y, Chang CJ, Carrasco N, Dadachova E. Kinetics of perrhenate uptake and comparative biodistribution of perrhenate, pertechnetate, and iodide by NaI symporter-expressing tissues in vivo. J Nucl Med. 2004;45:500–7.

Radiotracer

Abiraj K, Mansi R, Tamma ML, et al. Bombesin antagonist-based radioligands for translational nuclear imaging of gastrin-releasing peptide receptor-positive tumors. J Nucl Med. 2011;52:1970–8.

Anderson CJ, Wadas TJ, Wong EH, et al. Cross-bridged macrocyclic chelators for stable complexation of copper radionuclides for PET imaging. Q J Nucl Med Mol Imaging. 2008;52:185–92.

Bakker WH, Albert R, Bruns C, et al. [111In-DTPA-D-Phe1]-octreotide, a potential radiopharmaceutical for imaging of somatostatin receptor-positive tumors: synthesis, radiolabeling and in vitro validation. Life Sci. 1991;49:1583–91.

Boros E, Ferreira CL, Yapp DT, et al. RGD conjugates of the H2dedpa scaffold: synthesis, labeling and imaging with 68Ga. Nucl Med Biol. 2012;39:785–94.

Bouvet V, Wuest M, Wuest F. Copper-free click chemistry with the short-lived positron emitter fluorine-18. Org Biomol Chem. 2011;9:7393–9.

Breeman WA, De Jong M, Visser TJ, et al. Optimising conditions for radiolabelling of DOTA-peptides with 90Y, 111In and 177Lu at high specific activities. Eur J Nucl Med Mol Imaging. 2003;30:917–20.

Brissette R, Goldstein NI. The use of phage display peptide libraries for basic and translational research. Methods Mol Biol. 2007;383:203–13.

Bruus-Jensen K, Poethko T, Schottelius M, et al. Chemoselective hydrazone formation between HYNIC-functionalized peptides and (18)F-fluorinated aldehydes. Nucl Med Biol. 2006;33:173–83.

Chen X, Park R, Hou Y, et al. MicroPET imaging of brain tumor angiogenesis with 18F-labeled PEGylated RGD peptide. Eur J Nucl Med Mol Imaging. 2004a;31:1081–9.

Chen X, Park R, Shahinian AH, et al. Pharmacokinetics and tumor retention of 125I-labeled RGD peptide are improved by PEGylation. Nucl Med Biol. 2004b;31:11–9.

Chen X, Park R, Tohme M, et al. MicroPET and autoradiographic imaging of breast cancer alpha v-integrin expression using 18F- and 64Cu-labeled RGD peptide. Bioconjug Chem. 2004c;15:41–9.

Chighine A, Sechi G, Bradley M. Tools for efficient high-throughput synthesis. Drug Discov Today. 2007;12:459–64.

Coenen HH, Mertens J, Maziere B. Radioiodination reactions for pharmaceuticals - compendium for effective synthesis strategies. Dordrecht: Springer; 2006.

Decristoforo C, Faintuch-Linkowski B, Rey A, et al. [99mTc]HYNIC-RGD for imaging integrin alphavbeta3 expression. Nucl Med Biol. 2006;33:945–52.

Decristoforo C, Hernandez Gonzalez I, Carlsen J, et al. 68Ga- and 111In-labelled DOTA-RGD peptides for imaging of alphavbeta3 integrin expression. Eur J Nucl Med Mol Imaging. 2008;35:1507–15.

Decristoforo C, Mather SJ. 99m-Technetium-labelled peptide-HYNIC conjugates: effects of lipophilicity and stability on biodistribution. Nucl Med Biol. 1999a;26:389–96.

Decristoforo C, Mather SJ. Technetium-99m somatostatin analogues: effect of labelling methods and peptide sequence. Eur J Nucl Med. 1999b;26:869–76.

Deri MA, Zeglis BM, Francesconi LC, et al. PET imaging with (8)(9)Zr: from radiochemistry to the clinic. Nucl Med Biol. 2013;40:3–14.

Dumont RA, Deininger F, Haubner R, et al. Novel (64)Cu- and (68)Ga-labeled RGD conjugates show improved PET imaging of alpha(nu)beta(3) integrin expression and facile radiosynthesis. J Nucl Med. 2011;52:1276–84.

Eder M, Schafer M, Bauder-Wust U, et al. 68Ga-complex lipophilicity and the targeting property of a urea-based PSMA inhibitor for PET imaging. Bioconjug Chem. 2012;23:688–97.

Egli A, Alberto R, Tannahill L, et al. Organometallic 99mTc-aquaion labels peptide to an unprecedented high specific activity. J Nucl Med. 1999;40:1913–7.

Eisenwiener KP, Prata MI, Buschmann I, et al. NODAGATOC, a new chelator-coupled somatostatin analogue labeled with [67/68Ga] and [111In] for SPECT, PET, and targeted therapeutic applications of somatostatin receptor (hsst2) expressing tumors. Bioconjug Chem. 2002;13:530–41.

Feher M, Schmidt JM. Property distributions: differences between drugs, natural products, and molecules from combinatorial chemistry. J Chem Inf Comput Sci. 2003;43:218–27.

Frindel M, Camus N, Rauscher A, et al. Radiolabeling of HTE1PA: a new monopicolinate cyclam derivative for

Cu-64 phenotypic imaging. In vitro and in vivo stability studies in mice. Nucl Med Biol. 2014;41(Suppl):e49–57.
Froidevaux S, Eberle AN, Christe M, et al. Neuroendocrine tumor targeting: study of novel gallium-labeled somatostatin radiopeptides in a rat pancreatic tumor model. Int J Cancer. 2002;98:930–7.
Garcia-Garayoa E, Blauenstein P, Blanc A, et al. A stable neurotensin-based radiopharmaceutical for targeted imaging and therapy of neurotensin receptor-positive tumours. Eur J Nucl Med Mol Imaging. 2009;36:37–47.
Garrison JC, Rold TL, Sieckman GL, et al. In vivo evaluation and small-animal PET/CT of a prostate cancer mouse model using 64Cu bombesin analogs: side-by-side comparison of the CB-TE2A and DOTA chelation systems. J Nucl Med. 2007;48:1327–37.
Ginj M, Zhang H, Waser B, et al. Radiolabeled somatostatin receptor antagonists are preferable to agonists for in vivo peptide receptor targeting of tumors. Proc Natl Acad Sci U S A. 2006;103:16436–41.
Handl HL, Vagner J, Han H, et al. Hitting multiple targets with multimeric ligands. Expert Opin Ther Targets. 2004;8:565–86.
Harris JM, Chess RB. Effect of pegylation on pharmaceuticals. Nat Rev Drug Discov. 2003;2:214–21.
Haubner R, Beer AJ, Wang H, et al. Positron emission tomography tracers for imaging angiogenesis. Eur J Nucl Med Mol Imaging. 2010;37 Suppl 1:S86–103.
Haubner R, Decristoforo C. Radiolabelled RGD peptides and peptidomimetics for tumour targeting. Front Biosci. 2009;14:872–86.
Haubner R, Finsinger D, Kessler H. Stereoisomere Peptid-Bibliotheken und Peptidomimetika zum Design von selektiven Inhibitoren des αvβ3-Integrins für eine neuartige Krebstherapie. Angew Chem Int Ed Engl. 1997;36:1374–89.
Haubner R, Maschauer S, Prante O. PET radiopharmaceuticals for imaging integrin expression: tracers in clinical studies and recent developments. Biomed Res Int. 2014;2014:871609.
Haubner R, Wester HJ, Burkhart F, et al. Glycosylated RGD-containing peptides: tracer for tumor targeting and angiogenesis imaging with improved biokinetics. J Nucl Med. 2001a;42:326–36.
Haubner R, Wester HJ, Weber WA, et al. Noninvasive imaging of alpha(v)beta3 integrin expression using 18F-labeled RGD-containing glycopeptide and positron emission tomography. Cancer Res. 2001b;61:1781–5.
Hausner SH, Kukis DL, Gagnon MK, et al. Evaluation of [(64)Cu]Cu-DOTA and [(64)Cu]Cu-CB-TE2A chelates for targeted positron emission tomography with an alpha(v)beta(6)-specific peptide. Mol Imaging. 2009;8:111–21.
Heppeler A, Froidevaux S, Eberle AN, et al. Receptor targeting for tumor localisation and therapy with radiopeptides. Curr Med Chem. 2000;7:971–94.
Holland JP, Divilov V, Bander NH, et al. 89Zr-DFO-J591 for immunoPET of prostate-specific membrane antigen expression in vivo. J Nucl Med. 2010;51:1293–300.
Hultsch C, Schottelius M, Auernheimer J, et al. (18) F-Fluoroglucosylation of peptides, exemplified on cyclo(RGDfK). Eur J Nucl Med Mol Imaging. 2009;36(9):1469–74.
Janssen ML, Oyen WJ, Dijkgraaf I, et al. Tumor targeting with radiolabeled alpha(v)beta(3) integrin binding peptides in a nude mouse model. Cancer Res. 2002;62:6146–51.
Leach AR, Harren J. Structure-based drug discovery. Berlin: Springer; 2007.
Liu Z, Li Y, Lozada J, et al. Kit-like 18F-labeling of RGD-19F-arytrifluroborate in high yield and at extraordinarily high specific activity with preliminary in vivo tumor imaging. Nucl Med Biol. 2013;40:841–9.
Maina T, Nock B, Nikolopoulou A, et al. [99mTc] Demotate, a new 99mTc-based [Tyr3]octreotate analogue for the detection of somatostatin receptor-positive tumours: synthesis and preclinical results. Eur J Nucl Med Mol Imaging. 2002;29:742–53.
MaschauerS,PranteO.Aseriesof2-O-trifluoromethylsulfonyl-D-mannopyranosides as precursors for concomitant 18F-labeling and glycosylation by click chemistry. Carbohydr Res. 2009;344:753–61.
McBride WJ, D'Souza CA, Sharkey RM, et al. Improved 18F labeling of peptides with a fluoride-aluminum-chelate complex. Bioconjug Chem. 2010;21:1331–40.
McBride WJ, Sharkey RM, Karacay H, et al. A novel method of 18F radiolabeling for PET. J Nucl Med. 2009;50:991–8.
Meijs WE, Herscheid JD, Haisma HJ, et al. Evaluation of desferal as a bifunctional chelating agent for labeling antibodies with Zr-89. Int J Rad Appl Instrum A. 1992;43:1443–7.
Mindt TL, Struthers H, Brans L, et al. "Click to chelate": synthesis and installation of metal chelates into biomolecules in a single step. J Am Chem Soc. 2006;128:15096–7.
Nicole P, Lins L, Rouyer-Fessard C, et al. Identification of key residues for interaction of vasoactive intestinal peptide with human VPAC1 and VPAC2 receptors and development of a highly selective VPAC1 receptor agonist. Alanine scanning and molecular modeling of the peptide. J Biol Chem. 2000;275:24003–12.
Nock BA, Maina T, Krenning EP, et al. "To serve and protect": enzyme inhibitors as radiopeptide escorts promote tumor targeting. J Nucl Med. 2014; 55:121–7.
Notni J, Pohle K, Wester HJ. Be spoilt for choice with radiolabelled RGD peptides: preclinical evaluation of (6)(8)Ga-TRAP(RGD)(3). Nucl Med Biol. 2013;40:33–41.
Okarvi SM. Recent progress in fluorine-18 labelled peptide radiopharmaceuticals. Eur J Nucl Med. 2001;28:929–38.
Poethko T, Schottelius M, Thumshirn G, et al. Two-step methodology for high-yield routine radiohalogenation

of peptides: (18)F-labeled RGD and octreotide analogs. J Nucl Med. 2004a;45:892–902.

Poethko T, Schottelius M, Thumshirn G, et al. Chemoselective pre-conjugate radiohalogenation of unprotected mono- and multimeric peptides via oxime formation. Radiochim Acta. 2004b;92:317–27.

Prante O, Einsiedel J, Haubner R, et al. 3,4,6-Tri-O-acetyl-2-deoxy-2-[18F]fluoroglucopyranosyl phenylthiosulfonate: a thiol-reactive agent for the chemoselective 18F-glycosylation of peptides. Bioconjug Chem. 2007;18:254–62.

Schibli R, La Bella R, Alberto R, et al. Influence of the denticity of ligand systems on the in vitro and in vivo behavior of (99m)Tc(I)-tricarbonyl complexes: a hint for the future functionalization of biomolecules. Bioconjug Chem. 2000;11:345–51.

Schirrmacher E, Wangler B, Cypryk M, et al. Synthesis of p-(di-tert-butyl[(18)F]fluorosilyl)benzaldehyde ([(18)F]SiFA-A) with high specific activity by isotopic exchange: a convenient labeling synthon for the (18)F-labeling of N-amino-oxy derivatized peptides. Bioconjug Chem. 2007;18:2085–9.

Schottelius M, Rau F, Reubi JC, et al. Modulation of pharmacokinetics of radioiodinated sugar-conjugated somatostatin analogues by variation of peptide net charge and carbohydration chemistry. Bioconjug Chem. 2005;16:429–37.

Simecek J, Notni J, Kapp TG, et al. Benefits of NOPO as chelator in gallium-68 peptides, exemplified by preclinical characterization of (68)Ga-NOPO-c(RGDfK). Mol Pharm. 2014;11:1687–95.

Smith-Jones PM, Stolz B, Bruns C, et al. Gallium-67/gallium-68-[DFO]-octreotide–a potential radiopharmaceutical for PET imaging of somatostatin receptor-positive tumors: synthesis and radiolabeling in vitro and preliminary in vivo studies. J Nucl Med. 1994;35:317–25.

Sosabowski JK, Matzow T, Foster JM, et al. Targeting of CCK-2 receptor-expressing tumors using a radiolabeled divalent gastrin peptide. J Nucl Med. 2009;50:2082–9.

Thonon D, Kech C, Paris J, et al. New strategy for the preparation of clickable peptides and labeling with 1-(Azidomethyl)-4-[(18)F]-fluorobenzene for PET. Bioconjug Chem. 2009;20:817–23.

Trepel M, Arap W, Pasqualini R. In vivo phage display and vascular heterogeneity: implications for targeted medicine. Curr Opin Chem Biol. 2002;6:399–404.

Vagner J, Qu H, Hruby VJ. Peptidomimetics, a synthetic tool of drug discovery. Curr Opin Chem Biol. 2008;12:292–6.

Vallabhajosula S, Moyer BR, Lister-James J, et al. Preclinical evaluation of technetium-99m-labeled somatostatin receptor-binding peptides. J Nucl Med. 1996;37:1016–22.

van de Watering FC, Rijpkema M, Perk L, et al. Zirconium-89 labeled antibodies: a new tool for molecular imaging in cancer patients. Biomed Res Int. 2014;2014:203601.

Velikyan I, Beyer GJ, Langstrom B. Microwave-supported preparation of (68)Ga bioconjugates with high specific radioactivity. Bioconjug Chem. 2004;15:554–60.

Wan W, Guo N, Pan D, et al. First experience of 18F-alfatide in lung cancer patients using a new lyophilized kit for rapid radiofluorination. J Nucl Med. 2013;54:691–8.

Wangler C, Maschauer S, Prante O, et al. Multimerization of cRGD peptides by click chemistry: synthetic strategies, chemical limitations, and influence on biological properties. Chembiochem. 2010;11:2168–81.

Wester HJ, Schottelius M. Fluorine-18 labeling of peptides and proteins. In: Schubiger AP, Lehmann L, Friebe M, editors. PET chemistry - the driving force in molecular imaging. Berlin: Springer; 2007.

Yu Z, Carlucci G, Ananias HJ, et al. Evaluation of a technetium-99m labeled bombesin homodimer for GRPR imaging in prostate cancer. Amino Acids. 2013;44:543–53.

Optical Imaging

16

Frauke Alves, Julia Bode, Peter Cimalla, Ingrid Hilger, Martin Hofmann, Volker Jaedicke, Edmund Koch, Kai Licha, Timo Rademakers, Daniel Razansky, and Marc A.M.J. van Zandvoort

Contents

F. Alves
Department of Haematology and Medical Oncology and Institute for Diagnostic and Interventional Radiology, University Medical Center, Goettingen, Germany

Department Molecular Biology of Neuronal Signals, Max Plank Institute for Experimental Medicine, Goettingen, Germany

J. Bode (✉)
German Cancer Research Center (DKFZ), Molecular Mechanisms of Tumor Invasion (V077), Im Neuenheimer Feld 581, Heidelberg 69120, Germany

Department of Molecular Biology of Neuronal Signals, Max-Planck-Institute for Experimental Medicine, Herrmann-Rein-Str. 3, Goettingen 37075, Germany
e-mail: j.bode@dkfz.de

P. Cimalla • E. Koch
Klinisches Sensoring und Monitoring, Klinik für Anaesthesiologie und Intensivtherapie, TU Dresden, Dresden, Germany

I. Hilger (✉) • Marc A.M.J. van Zandvoort
Universitätsklinikum Jena, Am Klinikum 1, 07747, Jena, Germany
e-mail: ingrid.hilger@med.uni-jena.de

M. Hofmann (✉) • V. Jaedicke
Photonik und Terahertztechnologie, Ruhr Universität Bochum, Bochum, Germany

K. Licha (✉)
Institute of Chemistry and Biochemistry, Freie Universität Berlin, Takustr. 3, Berlin 14195, Germany
e-mail: kai.licha@fu-berlin.de

T. Rademakers (✉)
Cardiovascular Research Institute Maastricht (CARIM), Maastricht University, Maastricht, The Netherlands

D. Razansky (✉)
Institute for Biological and Medical Imaging, Technical University of Munich and Helmholtz Center Munich, Munich, Germany

F. Kiessling et al. (eds.), *Small Animal Imaging*, DOI 10.1007/978-3-319-42202-2_16

Abbreviations

µM	Micromolar
AAP23	Amyloid precursor protein-23
AD	Alzheimer's disease
apoE	Apoenzyme
Aß	Amyloid beta
BODIPY	Boron–dipyrromethene
CCD	Charged-coupled device
CCK2	Cholecystokinin-2
CEA	Carcinoembryonic antigen
CT	Computed tomography
CysLT1	Cysteinyl leukotriene-1
Da	Dalton
DNA	Deoxyribonucleic acid
EGFR	Epidermal growth factor receptor
EPR	Enhanced permeability and retention effect
FDA	Food and Drug Administration
fmol	Femto mol
FMT	Fluorescence-mediated tomography
FRET	Fluorescence energy transfer
IC50	Inhibitory concentration of how much of a particular drug (inhibitor) is needed to inhibit a given biological process by half
ICG	Indocyanine green
MMP	Matrix metalloproteinase
MRI	Magnetic resonance imaging
NADPH	Nicotinamide adenine dinucleotide phosphate
NIR	Near-infrared
nM	Nanomolar
PBS	Phosphate buffered saline
pH	Potential of hydrogen (strength of hydrogen)
PSMA	Prostate-specific membrane antigen
QDs	Quantum dots
SPECT	Single-photon emission computed tomography
TBR	Tumor-to-background ratio
uMUC-1	Underglycosylated mucin-1
UV–vis	*Ultraviolet–visible*
VEGF	Vascular endothelial growth factor receptor
WT	Wild type
Zn-DPA	Zinc-trisodium-pentetate
µm	Micrometer

16.1 Fluorescence Imaging

Ingrid Hilger

This chapter sets out to (a) describe the main techniques employed in current preclinical and clinical applications of fluorescence imaging, (b) define important aspects of using fluorescence reporters, and (c) describe current applications to diseases with high socioeconomic relevance.

16.1.1 Introduction

Fluorescence is the phenomenon by which certain molecules under illumination absorb light of a specific wavelength and normally react by emitting light of a comparatively longer wavelength.

This phenomenon relies on the production of excited single states. An electron in the excited

orbital is paired with a second electron (of opposite spin) in the ground-state orbital (Lakowicz 1999). A photon is emitted as a result, causing a rapid return to the ground state. Compared to phosphorescence (i.e., the emission of light from triplet excited states), fluorescence emission rates are very high, with fluorescence lifetimes in the 10 ns range.

Fluorescence occurs quite frequently in nature, in minerals such as benitoite, gypsum, and scapolite, for example. They emit visible light upon being illuminated by invisible ultraviolet light, X-rays, or electron beams. A number of marine animals – for example, lancelets, corals, jellyfish, and marine fish (Sparks et al. 2014) – are also capable of fluorescing, as are some land animals, namely, butterflies, parrots, etc.

Humans have exploited fluorescence by constructing chemical sensors, biological detectors, and cosmic ray detectors as well as by designing fluorescent lamps, etc. Fluorescence has also entered the field of life sciences and medicine, particularly for imaging purposes, as in microscopy. Initially, during the early twentieth century, this technique was primarily used to analyze selected tissue and cell samples with corresponding fixation. About 20 years later, a fluorescent contrast agent, fluorescein, was developed for use in neurosurgery applications (Moore et al. 1948) to improve the detection of brain tumors in patients. Expanding beyond microscopy, fluorescence featured prominently in the development of sophisticated mesoscopic and macroscopic optical imaging systems. This classification of optical imaging modalities from microscopy to macroscopy was originally proposed by (Ntziachristos et al. 2010) and was based on the tissue depth at which they operate (see below).

The success of fluorescence optical imaging methodology is in large part attributable to its (1) ease of use, (2) low cost, and (3) high sensitivity (up to the fmol range of detected dye molecule, depending on the method used) without requiring the use of radioactive tracers.

Nevertheless, even with all the technical developments of the last years, researchers and users still face the basic challenge that all tissues scatter light, which also leads to reduced resolution and difficulties in image formation (Yodh and Chance 1995). In particular, when exciting a specific optical probe localized within tissue, the signal intensity emerging from it will be affected by absorption and scattering (Arridge 1999; Schotland and Leigh 1992). To be exact, this means that the fate of excitation and emission photons depends on the tissue's scatter, anisotropy, and refractive indexes (Alfano et al. 1997). Therefore, the detection limits of fluoro-optical technologies within tissues are determined by a photon's main free path and the average angles at which photons scatter during each scattering event as stated by Ntziachristos et al. (2011).

Wavelengths are known to determine the degree of absorption and scattering in tissue and therefore the penetration depth in tissues. Using near-infrared light permits detecting tissue structures deeper under the surface than using visible light. In particular, near-infrared photons (wavelengths between 650 and 900 nm) were observed to travel more efficiently through tissues than ones in the visible light spectrum (Jobsis 1977). When wavelengths increase (i.e., red or infrared region of the optical spectrum), absorption and scattering of light in tissue are known to diminish. The longer the wavelength is, the lower is the delivered energy of the photons. Absorption is at its lowest between 500 and 800 nm (Osterman and Schutz-Geschwender 2007). By contrast, when increasing wavelength above 900 nm, increasing absorption by water results in markedly reduced transmission of light.

In normal tissue, the principal absorbers are water, oxyhemoglobin, deoxyhemoglobin, and lipids. The extent of absorption depends on the molar concentration of each constituent. For example, in a tissue with 8 % blood volume and 29 % lipid content, the dominant absorber will be hemoglobin, accounting for 39–64 % of total absorption at NIR wavelengths (Lim et al. 2003).

In addition to photon absorption and scattering in living tissues, tissue autofluorescence can also noticeably limit contrast in fluorescence optical imaging. The absorption of a photon is obtained by summing up all absorbing constitu-

ents present in tissue. Under visible light, fluorescence of intrinsic fluorophores such as NADPH, collagen, elastin, and flavin, etc., may occur (Frangioni 2003; Kovar et al. 2007), potentially interfering with that of xenogen reporters in the visible range of the light spectrum. NIR light solves this problem by reducing the autofluorescence background of intrinsic fluorophores.

With respect to NIR regions, tissue depths of several centimeters can be achieved, depending on the type of tissue, e.g., 10 cm in the human breast (Buehler et al. 2010a).

Most applications in recent years focused on preclinical whole-body imaging using near-infrared light. In this context, strategies employing NIR light typically included labeling specific high-affinity ligands with NIR fluorochromes, nanoparticles, and the like. Depending on the macroscopic imaging method used, less than 100 fmol of an NIR dye can be detected (Ntziachristos 2011). At present, a growing number of papers describe the introduction to the clinical field of fluorescence imaging, particularly for intraoperative (van Dam et al. 2011), endoscopic, and laparoscopic imaging applications (van der Poel et al. 2011) and intra-arterial imaging (Yoo et al. 2011).

16.1.2 In Vivo Fluorescence Imaging Systems

In this section, the focus will be on macroscopic fluorescence imaging that allows probing tissues to depths greater than 1 cm. Macroscopic imaging lets researchers probe organs, tissues, or entire small animals. For these applications, macroscopic fluorescence imaging systems have been used primarily as stand-alone devices for preclinical imaging. Recently, combining them with other imaging methods, such as MRI and CT, has also been suggested as a means for correlating the fluorescence signals with anatomical information. A comprehensive review of the advantages and current limitations of macroscopic imaging is found in (Ntziachristos 2010, 2011). The main imaging strategies are fluorescence reflectance imaging and fluorescence-mediated tomography, both of which will be discussed in greater detail below.

16.1.2.1 Epi-illumination or Reflectance Imaging

Preclinical fluorescence imaging devices include, among others, quite basic epi-illumination (photographic) systems. The typical epi-illumination system consists of a sensitive charge-coupled device (CCD) camera, a filter system operating at defined wavelengths, illumination systems for fluorophore excitation, macro lens systems, a lighttight imaging chamber, and the software needed to control the device. Among CCD cameras, silicon CCD cameras offer the best cost/performance ratio, but their sensitivity is rather poor above 800 nm. Increased sensitivity up to 900 nm can be achieved with more expensive arsenide CCD cameras. Also available are gallium arsenide cameras, but their sensitivity below 1,000 nm is poor (Frangioni 2003).

Typically, spectral bandwidths – resulting from filtering white light or use of a laser source or laser diode – are used to excite the fluorescing probes. The light source can also be used to produce an illumination image of an animal. The light falling on the surface of the tissue or animal will propagate into it for several millimeters (i.e., in the NIR) and excite the fluorophores. Similarly, the produced fluorescence signals will propagate to the surface. Epi-illumination systems can be used for both fluorescence and bioluminescence imaging.

Characteristic of epi-illumination systems is that the components used to illuminate and detect emitted fluorescence are lined up on the same side of the object of interest. The technique is mainly useful in detecting superficial tumors (e.g., tumor xenografts) in laboratory animals for preclinical research, since, depending on the type of tissue, probing is limited to depths of 3–7 mm from the tissue surface. In clinical practice, these systems are appropriate for open surgery and endoscopic procedures. The particular advantages are that the systems are simple to implement and operate. However, the fluorescence images will not exactly reflect probe localization since, as mentioned earlier, their fluorescence emission will be closely affected by absorption and scattering. Absorption and scattering will also impair full quantification of fluorescence signals (Boot et al. 2008). Therefore, semiquantitative analysis of

the fluorescence intensities is often performed to obtain rough approximations, particularly when taking repeated images from the same animal during the course of the disease (Haedicke et al. 2013; Kossatz et al. 2013). With this, the relative changes in probe accumulation can be deduced. Nevertheless, it must be taken into account that areas of high vascularization in tumors will certainly favor unspecific probe accumulation but will also absorb fluorescence emission due to the presence of blood (Huisken et al. 2004). The resolution of epi-illumination technique is approximately 2–3 mm with sensitivity in the nM to μM range.

16.1.2.2 Fluorescence-Mediated Tomography

Another type of fluorescence imaging methods utilizes fluorescence-mediated molecular tomography (FMT). In this method, the tissue of interest is illuminated from multiple angles, then the emitted fluorescence and excitation photons that have propagated through the tissue are collected and registered in different spectral bands. Using appropriate mathematical processing tools on the raw data, this method permits creating three-dimensional quantitative images of fluorescent probe localizations in the area of interest (Ntziachristos 2010). A comparatively high resolution can be achieved by illuminating the tissue surface with point light sources and by applying theoretical models and assumptions of photon propagation. In general, the sensitivity is in the nM-range, with an in vivo detection limit of 1 picomol fluorochrome (10 nM) (Ntziachristos et al. 2002). The resolution is at least 500 μm, and, despite some improvements, photon scattering remains a challenge. Consequently, to correlate the fluoro-optical signals with anatomical localization, the use of hybrid systems has been suggested. Feasible combinations include FMT with CT or MRI. These combinations can also be used to further improve image reconstruction and visualization (Ale et al. 2013; Gremse et al. 2014).

16.1.2.3 Multispectral Imaging

A particular advantage of fluorescence optical imaging is its ability to generate multiple images using different spectral regions or, alternatively, by applying methods for resolving different spectra (multispectral imaging). Different multispectral decomposition methods suggested can be applied either to the excitation light or to the fluorescing light. Corrections for absorption characteristics of various tissues, scattering variations, and depths are feasible. These methods have been summarized in a review (Ntziachristos 2010). The method has been applied to detect more than one molecular marker in cancer (Kossatz et al. 2013), cancer therapeutic efficiency (Haedicke et al. 2013) or for in vivo imaging of FRET (Busch et al. 2012) in edemas, etc. (Fig. 16.1).

16.1.2.4 Other Fluorescence Imaging Methods

Optoacoustic imaging is not based directly on fluorescence emissions by fluorophores but instead involves the detection of signals via optoacoustic impulses (for more details, see Sect. 16.5). The method allows the identification of intrinsic chromophores in tissue, such as oxyhemoglobin and deoxyhemoglobin (Allen and Beard 2006a; Eghtedari et al. 2007; Kolkman et al. 2004; Zemp et al. 2007). Optoacoustic imaging can also detect fluorochromes and fluorescent nanoparticles familiar from epi-illumination techniques (Razansky et al. 2007). Sensitivity is in the nM to μM-range, resolution is above 20 nm, the latter being limited by the attenuation of acoustic frequencies in the tissue (Ntziachristos 2010).

Further details on other fluorescence imaging methods such as bioluminescence imaging, optical coherence tomography, intravital microscopy can be seen in the following chapters of these book Sects. 16.2, 16.3, 16.4, 16.5, and 16.6.

16.1.3 Contrast Agents for Fluorescence Imaging

16.1.3.1 General Features

In addition to the fluorescence imaging devices themselves, appropriate contrast agents are an important complementary tool needed for probing organs, tissues, and whole animals. Most of the fluorescing contrast agents are aromatic

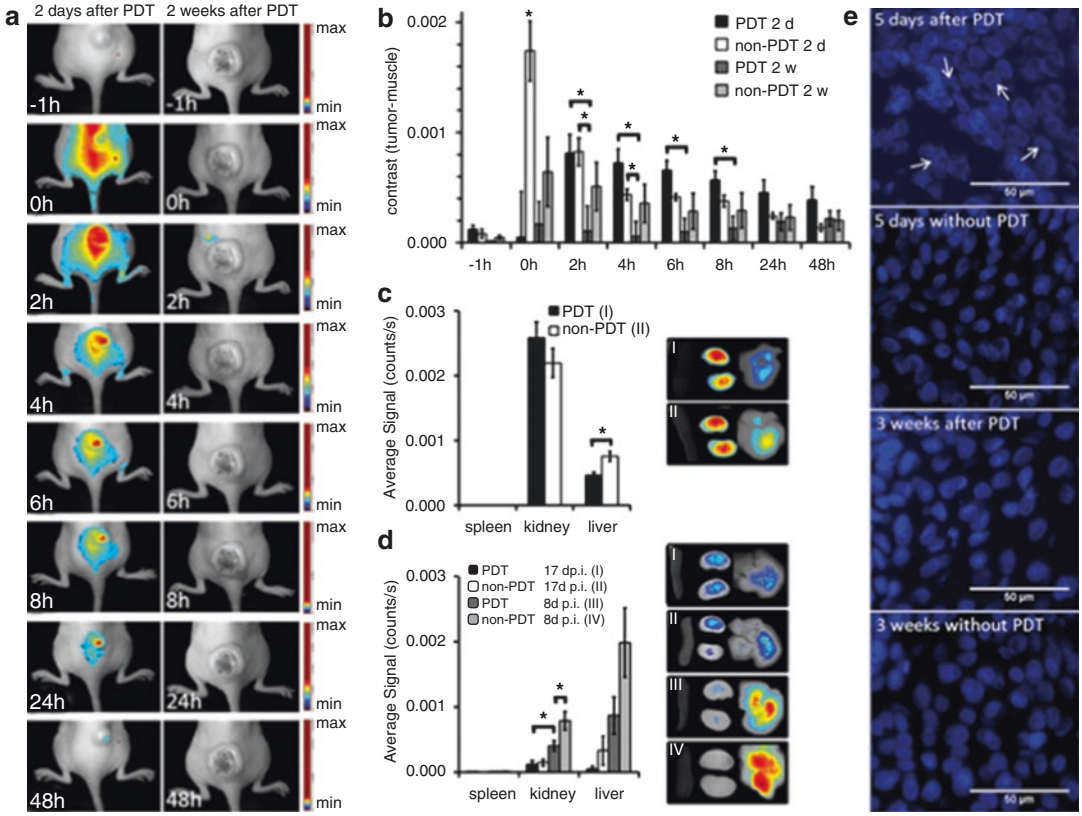

Fig. 16.1 Multispectral fluorescence imaging of apoptotic cells in tumors via photodynamic therapy. (**a**) Representative composite images of tumor-bearing mice injected with a fluorescent annexin V probe at 2 days (*left column*) or 2 weeks (*right column*) after therapy. (**b**) Semiquantitative analysis of fluorescence signals in tumors in treated or non-treated mice up to 48 h postinjection, 2 d, 2 days, or 2 w, 2 weeks (*$p<0.05$). (**c**) Biodistribution of the fluorescent annexin V 5 days after therapy and 3 days post probe injection in PDT-treated (*black*) and non-treated (*white*) mice, ex vivo organ fluorescence, *$p<0.05$. (**d**) Biodistribution of the annexin V probe at 3 weeks after therapy and 17 days (*black bars*) and 8 days (*dark gray bars*) after probe injection in treated mice or 17 days (*white bars*) and 8 days (*light gray bars*) after probe injection in non-treated mice, fluorescence signals of the organs, *$p<0.05$. (**e**) Cell nuclei of the cryo-frozen tumor slices 5 days (*upper images*) and 3 weeks (*lower images*). *Arrow*: condensed chromatin (Hoechst stain) (From Haedicke et al. (2013) with permission from Elsevier)

organic molecules (Fig. 16.2). Ideal fluorescence reporters should emit fluorescence in the near-infrared spectral range, as already noted. The fluorescent dyes most in use for in vivo imaging range between 550 and 900 nm in the diagnostic window. Typical examples are cyanines and their derivatives (i.e., Cy5.5 with an emission wavelength of 695 nm (Kovar et al. 2007)), hemicyanine dyes (Busch et al. 2012), and others. Increasingly popular are also Alexa Fluor 680, IRDye 680, and IRDye 700DX as well as the red chromophores Alexa 750 and IRDye 800CW (Kovar et al. 2007; Panchuk-Voloshina et al. 1999). Other fluorescent dyes are derivatives of squaraines, phthalocyanines, porphyrin, and borondipyrromethene analogues (BODIPY) (Ulrich et al. 2008). In recent years, much attention has been paid to the advent of quantum dots (QDs), nanoparticles constituted of heavy metals such as cadmium and selenite (see below).

A shared characteristic of fluorescent dyes is their high applicability potential, since (1) large-scale chemical synthesis is fundamentally feasible and (2) they are suited for rapid and efficient conjugation with specific molecules, such as DNA primers, nucleotides, proteins, small molecules, amino acids, etc. Most recently, modifications of their basic chemical structure

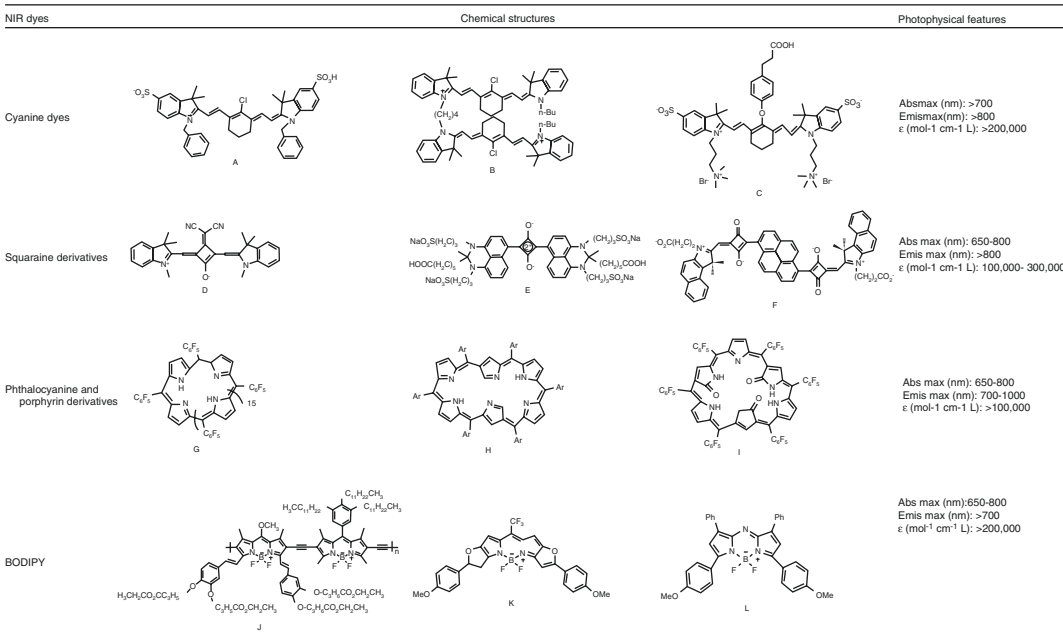

Fig. 16.2 Several of the newly developed NIR fluorescent dyes (From Luo et al. (2011a) with permission from Elsevier)

have produced improved chemical stability and photostability, long fluorescence life, and increased solubility with less aggregation propensity in biological systems (see below). Of particular significance is their adequate separation between excitation and emission wavelengths (Stokes shift), permitting effective filtering of emitted fluorescence from excitation light.

To be detected properly, fluorescence dyes should exhibit high quantum yields. The fluorescence quantum yield is defined as the efficiency of the fluorescence process. Mathematically, it is the ratio of the number of photons emitted to the number of absorbed photons. The ideal quantum yield is 1.0, indicating that every absorbed photon leads to a photon emission. In general, one can assume that all dyes between the values of 0.1 and 1 are fluorescent. Accordingly, this holds true for most of the NIRF dyes applied for in vivo imaging purposes, with values between 0.13 and 0.27 (Ohnishi et al. 2005). The highest quantum yields are achieved with QDs (around 0.50) (Frangioni 2003). All compounds below a value of 0.1 lack a detectable fluorescence emission. The values cited here should be regarded as rough estimates of fluorescence detection intensity, since the determination of quantum yield is highly susceptible to the features of the surrounding medium and lack of standardization.

Solubility of fluorescent probes is an important characteristic, as it assures an adequate dispersion in the body after intravenous application. Because of their basic molecular structure, hemicyanine and cyanine dyes lack solubilization. In order to boost it, attempts have been made to couple polar groups, such as sulfonates and others, with the basic configuration. Lack of solubility can lead to aggregation and agglomeration of the dye molecules, resulting in a reduction of the quantum yield (see below). As a result, the quantum dots produced initially were fairly insoluble, having been constructed with inorganic shells. New formulations use polar organic layers to make them water soluble. Due to their heavy metal constituents leading to low biocompatibility and degradability, QDs are restricted to preclinical applications.

Photobleaching is another phenomenon that needs to be considered in relation to the use of fluorescent probes. It is known to be associated with the reduction of fluorescence due to the molecule's destruction in the presence of light required to induce emission of fluorescence. Photobleaching is closely linked to the compound's stability. Most

of the known fluorophores are susceptible to it, although the light emitted by most fluorophores is adequate for successful optical imaging applications. QDs are more resistant to photobleaching than ICG and hemicyanine dyes.

Nonspecific binding is another important aspect, particularly in connection with detecting target-affine fluorescent probes. Nonspecific binding can occur as a result of interaction with cellular membranes as well as with extracellular matrix materials, etc. Nonspecific binding generally lowers the signal-to-noise ratio. Depending on their molecular configuration, most of the cyanines and hemicyanines have a tendency to bind proteins. For example, four members of the DY-67x cyanine family, composed of the same main chromophore but substituted with a sequentially increasing number of sulfonate groups (n 5 1–4; DY-675, DY-676, DY-677, DY-678, respectively), were shown to exhibit different bovine serum albumin binding constants: that of the most hydrophobic dye, DY-675, was 18 times higher than that of DY-678, the most hydrophilic fluorophore. In vivo biodistribution analysis revealed a considerable influence of dye hydrophilicity on biodistribution and excretion pathways. In this connection, the more hydrophobic dyes, DY-675 and DY-676, accumulate preferentially in the liver, followed by strong fluorescence signals in the bile and gut owing to accumulation in feces, while comparatively hydrophilic DY-678-COOH accumulates in the bladder (Hamann et al. 2011) (Fig. 16.3). QDs with a high number of charged surface groups exhibit pronounced nonspecific binding behavior (Bentzen et al. 2005). In contrast, hydroxyl-coated QDs were shown to be involved in a distinct reduction of nonspecific binding compared to carboxylated QDs (Kairdolf et al. 2008).

In order to achieve good signal-to-background ratios, fluoro-optical contrast agents should basically possess high-target affinity, good accessibility to the target molecule, and rapid clearance, since any uncleared molecule will contribute to the background signal. The commonly used dyes ICG, Cy5.5, and Cy7, IRdye800 CW, etc., are cleared very rapidly from the blood (Frangioni 2003). Polar hemicyanine dyes are

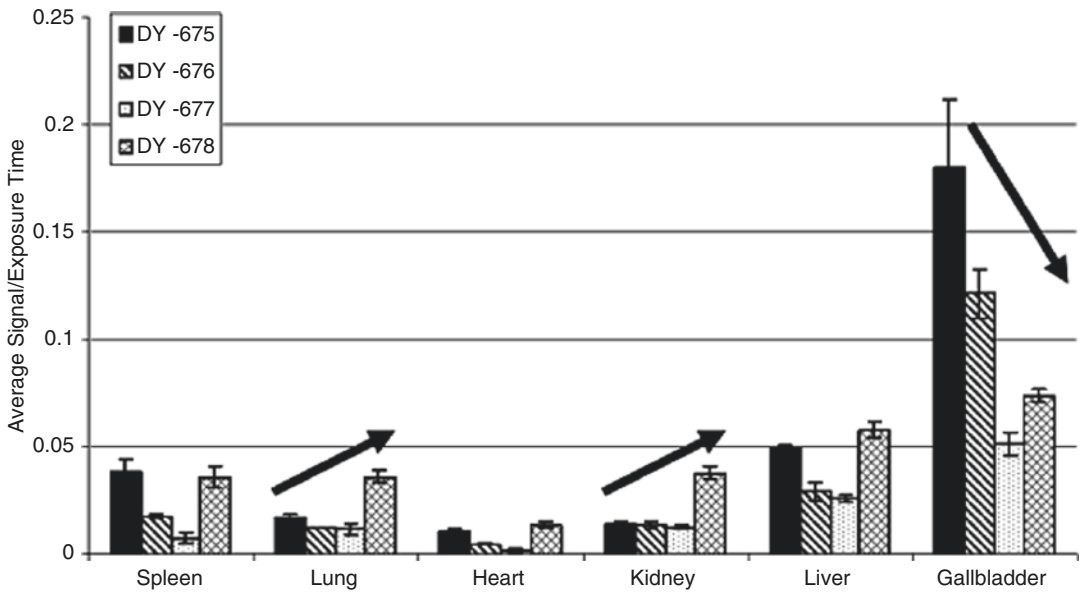

Fig. 16.3 Time-dependent dye organ distribution of one member of the DY-67x cyanine family composed of the same main chromophore, but substituted with a sequentially increasing number of sulfonate groups (DY-675, DY-676, DY-677, or DY-678, respectively) in living male NMRI mice. *Arrows* indicate the main accumulation behavior of the dyes with increasing hydrophilicity in selected organs (from Hamann et al. (2011) with permission from Decker Publishing)

cleared by renal filtration, nonpolar ones, such as ICG and nonpolar hemicyanines via the bile (Hamann et al. 2011; Recknagel et al. 2012). QDs with diameters over 3.5 nm cannot be cleared by renal filtration, which means that they circulate longer (Frangioni 2003).

Most fluorescent dyes have been shown to have low toxicity. However, so far, ICG is the only fluorescent dye approved by the FDA (Benya et al. 1989). The toxicity of hemicyanine dyes and ICG derivatives, such as Cy5.5, has not been fully evaluated. In some studies, the cytotoxicity and toxicity of Cy5.5 and the hemicyanine dyes were found to be lower than with ICG (Pauli et al. 2009a). QDs might be potentially dangerous because of the presence of cadmium and selenium (Hardman 2006). The features of the fluorescent dyes and QDs have been nicely summarized by te Velde et al. (2010). For more details, see Sect. 16.6.

16.1.3.2 The Most Popular Fluorescent Probes: Cyanine Dyes, Their Derivatives, and QDs

Cyanine dyes are synthetic dyes belonging to the group of polymethines. Other than cyanines with open chains, most of the cyanine molecules for biomedical applications are characterized by the presence of two aromatic heterocycles (symmetric cyanines), each of them containing a nitrogen molecule. Both nitrogen molecules can be part of a heteroaromatic moiety (e.g., pyrrole, pyridine, etc.). The heterocycles are linked by a polymethine bridge. The extension of the molecule by a vinylene moiety leads to a shift of absorption/emission to a longer wavelength (bathochromic shift) of about 100 nm (Mishra et al. 2000). In this context, mono- and trimethine cyanines absorb and emit in the visible region of the light spectrum and pentamethines in the near-infrared region.

In general, cyanine dyes and their derivatives are associated with a small Stokes shift and some aggregation in aqueous media (Landsman et al. 1976), which leads to rapid elimination from the blood through the liver. Despite being approved, ICG has in fact recently been reported as inducing transient cytotoxic effects (Ho et al. 2003; Ikagawa et al. 2005; Skrivanova et al. 2006). The introduction of carboxylic and sulfonic acid groups to the basic cyanine structure to address its low solubility in water led to a distinct improvement (Peng et al. 2005; Zhou et al. 2007). Interestingly, the heptamethine cyanine BHmC that is made up of two cyanine subunits exhibits a distinct increase in fluorescence after protein binding in contrast to solubilization in water (Kim et al. 2005).

Among currently available cyanines, *indocyanine green* (ICG, Cardiogreen) was already approved in 1958 for use in patients. The small molecule (775 Da) exhibits a short plasma half-life (1–2 min). It is heavily protein bound, has a low quantum yield in plasma, and diffuses readily from the vessels into the interstitium. It has been used for routine tests in retinal angiography (Chang et al. 1995) among others. It is also used in liver function testing (Cherrick et al. 1960; Weissleder and Ntziachristos 2003), for the identification of small and macroscopically invisible liver cancers in real time (Gotoh et al. 2009; Ishizawa et al. 2009), and in rheumatoid arthritis (Schafer et al. 2013). Typically, intravenous dosages of 25–50 mg ICG in saline are used. ICG has also been used to image the cerebrospinal fluid (Sakatani et al. 1997).

Hemicyanines are made up of at least one heterocycle instead of the two that are normally present in cyanine molecules (asymmetric cyanines). The fluorescence quantums of these dyes in aqueous solution depend on the substitution pattern of the benzopyrylium-type end group, which also significantly determines the aggregation tendency. Sterically demanding substituents and negatively charged sulfonate groups reduce the aggregation tendency (Pauli et al. 2011).

Squaraines are made up of an oxocyclobutenolate core and aromatic heterocyclic components at the two ends of the molecule (Volkova et al. 2007). These molecules present a high molar extinction coefficient and good photoconductivity (Dilek and Akkaya 2000; Oswald et al. 2000). However, water solubility is very poor due to their planar and hydrophobic molecular structure. Recently, stable and non-cytotoxic

supramolecular adducts of squaraines and the natural carrier protein, i.e., serum albumin, have been suggested for tumor-targeted imaging and photothermal therapy in vivo (Gao et al. 2014).

Phthalocyanines are porphyrin derivatives made up of four pyrrole moieties that were linked together through nitrogen atoms. These molecules are thermally and chemically very stable. Due to the feasibility of replacing the two central hydrogen atoms with metal atoms, plus the added possibility of incorporating substituents at the periphery and axial positions of the molecules, these molecules have been also used in optoelectronics and biomedicine applications (Cammidge and Gopee 2002). Of particular interest are applications as photosensitizers. When illuminated, they produce toxic singlet oxygen capable of killing target (tumor) cells (Haedicke et al. 2013). Several porphyrin derivatives such as porfimer sodium (Photofrin®), 5-aminolevulinic acid or ALA (Levulan®), and methyl aminolevulinate (Metvix®), chlorin (Foscan®), temoporfin, etc., are FDA-approved photosensitizers for photodynamic therapy. Photofrin is used intravenously for internal cancers, while Levulan® and Metvix® are applied in skin therapy (MedicineNet).

BODIPY (borondipyrromethene) dyes exhibit high quantum yield and excellent thermal and photochemical stability. However, most BODIPY dyes emit from yellow to deep-red emission with low extinction coefficients. Recent years have seen several attempts to shift the absorption spectrum to the NIR region of the spectrum (Rickert et al. 2010).

Quantum dots (QDs) Compared to organic dyes, QDs possess a series of interesting features such as high-absorption cross section, broadband absorption, narrow and symmetric luminescence band, simultaneous excitation with different emission wavelengths using a single excitation wavelength, etc. (Bruchez et al. 1998; Chan et al. 2002; Wu et al. 2003). Interestingly, by modulating the size of QDs made of a given material, different colors can be achieved. Doing so might make multiplexed imaging with differently sized QDs with the same excitation wavelength a versatile tool in preclinical imaging approaches. These nanoparticles are made up of heavy metal ingredients such as cadmium and selenite. To increase suspension in aqueous solution, nanoparticles are increasingly being coated with an organic material. They exhibit a high extinction coefficient combined with a quantum yield comparable to fluorescent dyes. They are highly stable (low photobleaching effects). In particular, QDs are 20 times brighter and 100 times more stable than traditional fluorescent reporters (Walling et al. 2009). However, their cytotoxicity in biological systems remains to be fully clarified. Additionally, they are quite expensive to prepare; moreover, difficulties in reproducibility and quantification have also been reported (e.g., (Nikoobakht and El-Sayed 2003; Tsung et al. 2006)).

16.1.4 Prospects of Macroscopic Fluorescence Imaging

Since it is a macroscopic imaging modality, fluorescence imaging is expected to be limited to the noninvasive detection in vivo of fluorescence signals in preclinical application to whole animals. In clinical settings, it has potential for use in imaging not only parts of the body with good accessibility to light, such as arthritic joints in hands, but also abnormalities in the gastrointestinal tract, gynecological cancers, cardiovascular diseases using specialized catheters, imaging of the eye, and intrasurgical imaging. In addition, it may serve as a valuable tool in the following applications: drug testing, understanding disease mechanisms in basic research, supporting translation of imaging approaches to clinical practice, pre-screening at key points in time during the course of diseases, etc.

16.1.4.1 Oncological Imaging

Most of the original preclinical oncological fluorescence imaging approaches aimed at demonstrating the feasibility of detecting vascular permeability and diffusion via nontargeted probes by exploiting the enhanced permeability and retention effect (EPR) (e.g., Duncan et al. 2006; Maeda et al. 2009) of tumor microvasculature and also at demonstrating the reliability of detecting molecular markers using targeted opti-

cal probes in whole animals. Active targeting has been achieved by conjugating fluorescent dyes (mostly cyanines or hemicyanines) with specific ligands made up of peptides, proteins, synthetic molecules, antibodies, aptamers, and others. Higher signal-to-background ratios were achieved with this approach when compared to nontargeted probes. Disadvantages of using target-affine probes in oncological imaging include bioconjugation that can affect the fluorescence of several dye molecules, impairment of ligand specificity because of the presence of comparatively large dye molecules when compared to radioactive tracers, and pharmacokinetics of conjugated ligands that may differ from those with free molecules. When using nanoparticles instead of small molecules, accessibility to the tumor interstitium may be impaired due to their comparatively large size (several nm). Particularly when imaging structures of the tumor interstitium, using small molecules is advantageous because of their high tissue penetrating behavior and rapid clearance of non-bound molecules from the tumor. Typical examples for active targeting in oncological fluorescence imaging address the tumor cell compartment per se, the tumor environment, extracellular compartment, and neovascularization, such as the detection of PSMA (Liu et al. 2010), folate (Tung et al. 2002), EGFR (Becker et al. 2000), CEA (Hilger et al. 2004), Her-1 and Her-2 (Ogawa et al. 2009), CCK2 receptor and Gut-1-receptor (Kossatz et al. 2013), apoptotic cells (Haedicke et al. 2013), uMUC-1 antigen (Pham et al. 2005), αvβ3-integrin (Wang et al. 2007a), etc. (Fig. 16.4).

Additional strategies for oncological imaging include the utilization of activatable probes that fluoresce upon activation or the incorporation of fluorescent dyes into (polymeric) nanoparticles with or without targeting moiety. Here, the encapsulation of dye molecules in nanoparticles offers the advantage of having a protective matrix cover the dyes and the ability to amplify the fluorescence signal. Moreover, encapsulation could help improve the stability of the dyes. Nevertheless, nanoparticles have a limited potential for extravasation into the tumor interstitium and might be of particular interest when address-

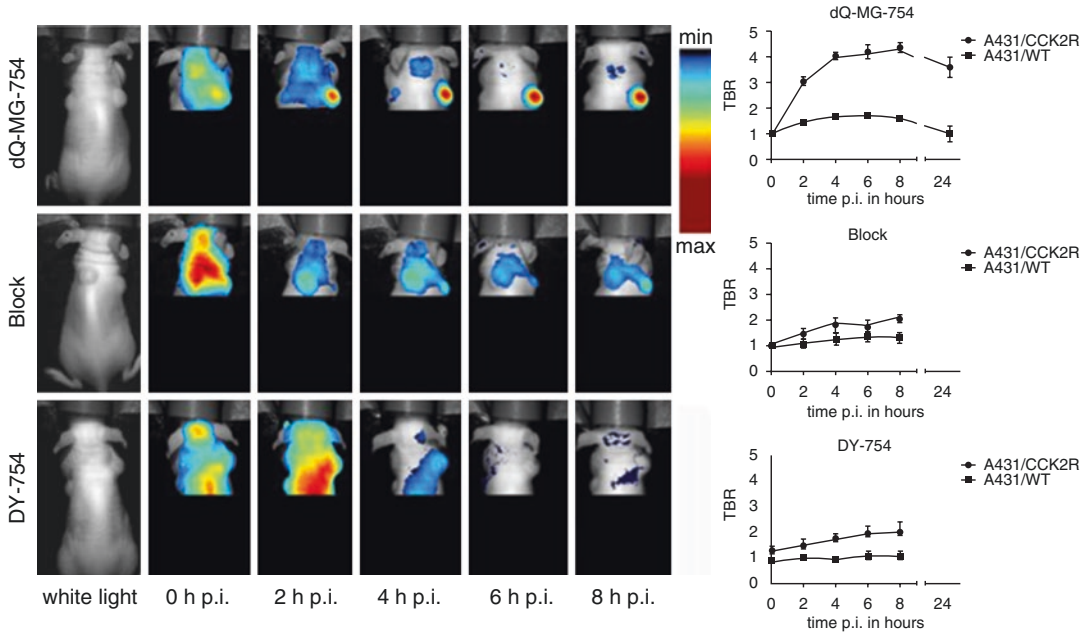

Fig. 16.4 Fluorescence imaging of the cholecystokinin-2 receptor in tumors. NIR fluorescence reflectance images of CCK2R expression in an A431/CCK2R (*right flank*) and A431/WT (*left flank*) xenograft model. The *left* panel displays representative intensity-scaled fluorescence images for each experimental group at indicated time points after probe injection. *TBR* tumor-to-background ratios (From Kossatz et al. (2013) with permission from Elsevier)

ing intravascular targets in the tumor. Numerous recent investigations focus on providing nanoparticles with multimodal capabilities for imaging and therapy, given that nanoparticles provide a good platform for multifunctional approaches. Nevertheless, uptake by the mononuclear phagocyte system limits specificity in several organs (liver, spleen, etc.), and reproducibility and the large-scale preparation of such formulations are challenging. For these reasons, application has been limited to the preclinical stage. Typically, silica nanoparticles conjugated with cyanines (He et al. 2007; Haedicke et al. 2015), liposomal nanoparticles for tumor imaging via the EPR effect in combination with photodynamic therapy (e.g., (Bendsoe et al. 2007), chitosan polymers (Backer et al. 2005), etc., have been proposed.

The tumor environment specifically has been addressed with so-called fluorescent activatable probes. The approach exploits the fact that tumor cells exhibit a different pH and different enzyme activity than normal cells. The corresponding probe does not fluoresce unless activated at the target site, which emits fluorescence from dequenching of the probe's dye molecules. Probes that are pH sensitive are based on the high sensitivity exhibited by chromophores to protonation and deprotonation (Wang et al. 2010a). Enzyme-activatable probes contain at least two chromophores in proximity to each other and connected by a specific peptide linker that serves as enzyme substrate. Due to the quenching (identical chromophores) or resonance energy transfer (differing chromophores) effects, no or very little fluorescence emission takes place in the non-activated stage. Sample applications include the detection of proteases in tumors such as matrix metalloproteinases, caspases, cathepsins, etc. (Bremer et al. 2001a; Messerli et al. 2004; Tung 2004).

16.1.4.2 Imaging of Infections

Infections represent a profound medical challenge worldwide, particularly when local infections turn into systemic ones. Here (fluorescence) optical imaging could help obtain new insights into the mechanisms of disease and prevention. For example, by utilizing bioluminescence sourced from the luc operon (e.g., from the firefly *Photinus pyralis* or the sea pansy *Renilla reniformis*) or lux operons (*Photorhabdus luminescens*, *Xenorhabdus luminescens*) on the bacterial strains of interest, their fate in the body and the disease mechanisms can be tracked via imaging. These operons express the luciferase enzyme which is not naturally present in mammalian cells. To produce light, the enzyme substrate luciferin is applied to the animals. In this context, several researchers found that bioluminescent bacteria could be tracked in vivo in murine models and that the bioluminescence intensity was closely related to the number of viable bacteria (Contag and Bachmann 2002). More recently, in vivo infection with *Pseudomonas aeruginosa* in an acute murine airway infection model was efficiently tracked with bioluminescence imaging (Munder et al. 2014). To study the liver stage development of malaria in humans and rodents, modified luciferase containing malaria parasites was used to analyze both hepatocytes in culture and in the livers of living mice (Ploemen et al. 2009).

In contrast to the analysis via utilization of genetic reporters, a more straightforward strategy designed for clinical applications is imaging with exogenous synthetic probes that target bacteria selectively. This methodology has a comparatively high potential for clinical translation at least for organs with good accessibility to light. In this connection, a deep-red fluorescent squaraine rotaxane scaffold with two appended (bis(zinc(II)-dicolylamine) (bis(Zn-DPA)) targeting ligands were used to track Gram-positive *Staphylococcus aureus* and Gram-negative *Salmonella enterica* serovar typhimurium in mice. The bis(Zn-DPA) ligands of the probe had high affinity for the anionic phospholipids and related biomolecules that reside within the bacterial envelope, and they are known to selectively target bacterial cells over the nearly uncharged membrane surfaces of healthy mammalian cells. Imaging of localized infections was possible, and the signal was independent of mouse humoral immune status. The probes did not respond to nonbacterial infections (White et al. 2010). Similarly, optical nanoprobes were designed that were composed of concanavalin A (Con A) as a bacterial targeting ligand, a nanoparticle carrier, and a near-infrared fluorescent dye. Using a murine wound and catheter infection model, nanoprobes could rapidly detect and quantify the extent of bacterial colonization

on wounds and catheters in real time (Tang et al. 2014). Additionally, detection of *Staphylococcus aureus* infection (5×10^7 cells) in a mouse is possible using a cationic antimicrobial peptide conjugated to a near-infrared dye ICG that targets the anionic surfaces of bacteria. This probe selectively accumulates in bacteria (Liu and Gu 2013).

Similarly, it was found that uptake and hepatobiliary excretion ICG and the hemicyanine dye DY635 are altered during sepsis, namely, by considering different variables including hepatic perfusion, hepatocellular energy state, and functional integrity of transporter proteins. In particular, with respect to hepatocellular transport of both dyes, excretion into bile was significantly delayed for both dyes and resulted in net accumulation of potentially cytotoxic xenobiotics in the liver parenchyma. Transcutaneous assessment of ICG fluorescence by whole-body NIRF imaging revealed a significant increase starting from the 30th minute of ICG fluorescence in the bowel region of the abdomen in sham but not in septic animals, confirming a sepsis-associated failure of canalicular excretion. These results have potential implications for monitoring liver function, critical care pharmacology, and the understanding of drug-induced liver injury in the critically ill (Recknagel et al. 2012; Gonnert et al. 2013) (Fig. 16.5).

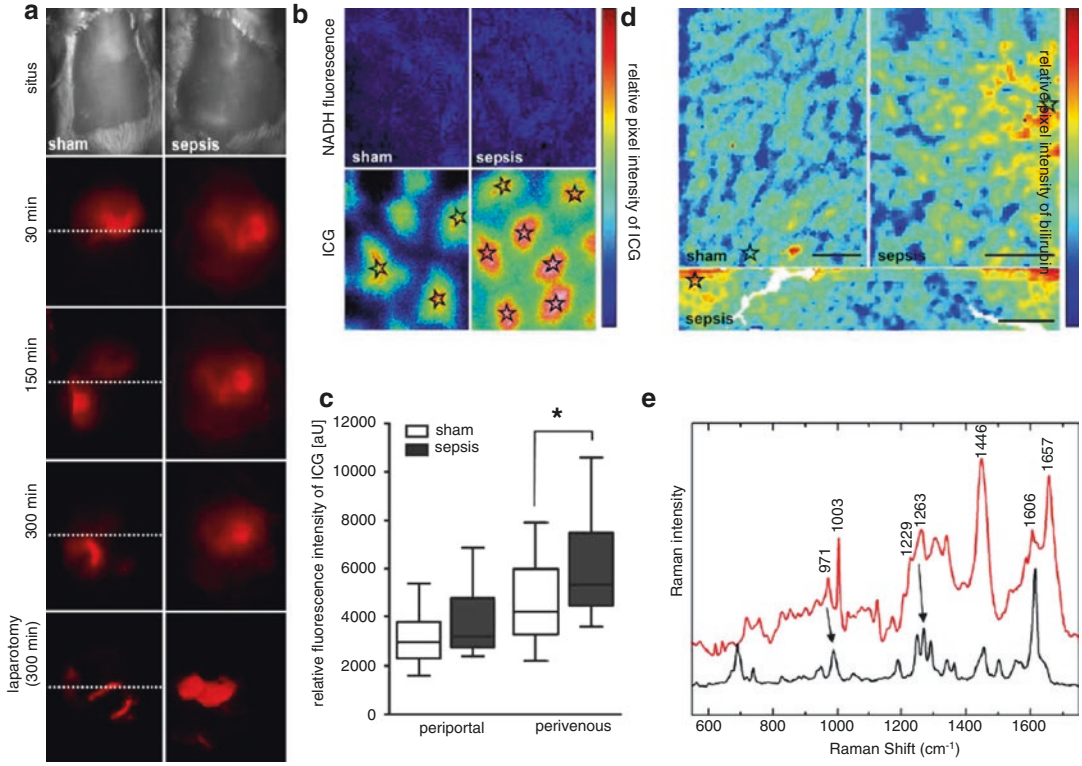

Fig. 16.5 Imaging of sepsis-induced excretory dysfunction, as visualized by accumulation of the xenobiotic indocyanine green and bilirubin. (**a**) NIRF imaging of ICG at 15 h after sepsis induction: ICG is eliminated via hepatobiliary excretion into the duodenum in sham animals, whereas the dye accumulates in the livers of septic animals, with an almost absence of fluorescence signal in the gut (the *dotted line* divides upper and lower abdominal quadrants for orientation). (**b**) Subsequent epifluorescence microscopic examination of liver surfaces after ICG administration in sham and septic animals. *Stars*: central veins (pseudo-colored). (**c**) ICG fluorescence intensities around central veins were significantly higher in septic compared to sham-operated animals (*$p=0.031$ compared to sham). (**d**) Micro-Raman images of tissue sections from liver sections obtained from sham-operated and septic rats. In the livers of the septic rats, elevated relative intensities of the bilirubin component were found in the perivenous region (*stars*), but only minor local spots of bilirubin were observed of control animals. *Scale bars*: 50 mm. (**e**) Raman spectrum of the bilirubin component (*red trace*) with crystalline bilirubin for comparison (*black trace*) (From Recknagel et al. (2012) (open-access article))

16.1.4.3 Preclinical Attempts at Alzheimer Imaging

Diagnosis of many neurodegenerative diseases continues to pose challenges. For example, a reliable discrimination of Morbus Alzheimer from other neurodegenerative diseases can only be accomplished *post-mortem.* For this purpose, the presence of amyloid plaques and tau fibrils in brains of AD patients is assessed. In living patients, the utilization of Florbetaben®, an 18 F-labeled amyloid ligand for image-based detection via PET, is currently in a phase III clinical trial (Barthel et al. 2011). The use of optical methods would bypass the use of radioactive tracers in AD image-based detection, which present a challenge given that they require a local cyclotron for production of positron-emitting radionuclides and a synthesis unit to produce radiolabeled agents.

Interestingly, tau and amyloid have been detected not only in the brain (e.g., cortex) but also in the retina (Koronyo-Hamaoui et al. 2011). In contrast to the brain, the eye is easily accessible to light thanks to its natural functions. Therefore, fluorescing small molecules with high affinity for aggregated proteins might be used to report protein aggregation in the retina. In this context, after intravenous injection of a fluorescent probe targeting amyloid plaques and/or tau fibrils, the subsequent illumination of the eye with light of defined wavelengths would presumably reveal the presence of molecular alteration in AD. Nevertheless, there are still several challenges to be overcome with regard to (1) passage of the fluorescence reporter to the brain barrier, (2) clearance of non-bound reporter molecules from the tissue, and (3) demonstrating a verified correlation of pathological changes in the brain and (cognitive) symptoms with pathological abnormalities in the retina. Of interest in this connection are several novel probes based on the bis(arylvinyl)pyrazine, bis(arylvinyl)pyrimidine, and the asymmetric hemicyanine family molecular structure. Among these, bis(arylvinyl)pyrazines represented the most promising UV–vis probes in terms of biocompatibility. Regarding their affinity to Aβ and tau, defined bis(arylvinyl) pyrimidines are the best ligands, endowed with good prospects for AD detection. Additionally, asymmetric hemicyanine exhibited good selectivity for amyloid plaques and tau fibrils at a level similar to that of bis(arylvinyl)pyrazines as well as low cytotoxic effects on human cell lines within the investigated NIR dyes. The data provides a solid base for further investigations of their applicability to image-based detection of AD in vivo (Bolander et al. 2012). Moreover, *a* series of rhodanine-3-acetic acids was synthesized and shown to bind to neurofibrillary tangles with a comparably high binding affinity (e.g., IC50 = 19 nM) (Anumala et al. 2013). Lastly, trimethine cyanine dyes bind to tau fibrils (Gu et al. 2013).

In other studies, oxazine dyes (Hintersteiner et al. 2005) have been used to track Aß in AAP23 transgenic mice, as have thiobarbitals (Okamura et al. 2011). The dimethylamine structural signature seems to favor binding affinity of compounds to Aß, and it is likely that this functionality is important for Aβ interaction. Dimethylamines can be found in chalcones, benzothiazoles, or imidazopyridines among others (Eckroat et al. 2013). In addition, other small-molecule fluorescent probes as reporters of amyloid formation, including single-molecule determinations such as JC-1, DCVJ, ANS derivatives, and luminescent conjugated polymers as well as site-specific probes such as pyrenes, have been suggested (Bertoncini and Celej 2011).

16.1.4.4 Imaging of Inflammation

Inflammation is basically associated with the release of exogenous and endogenous chemical mediators after tissue injury. Exogenous mediators (e.g., microbial peptides) act as chemoattractants which in turn recruit neutrophils to the target site. Typically, their aim is to phagocytize invading microorganisms and cellular debris. These response functions protect the host and normally they are self-limiting. Once the xenogen material has been removed, the inflammatory reaction will be resolved. In this context, leukocytes and debris from inflamed sites are removed in order to return to homeostasis. This tightly regulated biochemical and metabolic process can become chronic if the resolution of

the inflammation process is altered (Serhan et al. 2008).

Inflammation in the body can also be triggered by diverse intrinsic pathophysiological alterations leading to tissue lesions. A typical example is atherogenesis in blood vessels. In such a case, the inflammation process is triggered by infiltration of atherogenic lipoproteins into endothelial cells. This process ultimately leads to the formation of plaques. Acute thrombotic closures of coronary arteries can occur as a result of ruptures of the fibrous cap and exposure of the thrombogenic core to the blood (Jackson 2011).

For this reason, special attention was devoted to the examination of inflammatory plaques via imaging, since early detection and therapy can help reduce cardiovascular mortality and morbidity. To this end, fluorescence imaging was related to the development of fluorescence cardiovascular catheters for clinical application and/or to unveil important mechanisms of plaque formation in preclinical research activities designed to provide new insights into prevention and therapy. Specific fiber systems have been proposed; initially, they were based on one-dimensional systems and more recently on rotational ones. These developments have been summarized in several technical reviews (Jaffer et al. 2007; Lipinski et al. 2006; Nahrendorf et al. 2007). From the pathobiological point of view, the activity of matrix metalloproteinases and cathepsins, which are known to play an important role in rupture of vulnerable plaques, has been assessed (Chen et al. 2002). Subsequently, MMP-2, MMP-9, and cathepsin K und S were also efficiently imaged in atherosclerotic apoE mice (Jaffer et al. 2007; Deguchi et al. 2006; Galande et al. 2006) in preclinical research approaches using FMT, which provided deeper tissue penetration capabilities compared to epi-illumination techniques. Additionally, intensive research on the mechanisms of atherosclerosis and thrombosis formation is being performed at the high-resolution and high-speed intravital microscopic level, as reviewed by (Taqueti and Jaffer 2013).

Rheumatoid arthritis, a serious disease which can lead to pronounced activity limitation, disability, and reduced quality of life, is also known to be associated with inflammation. Diagnosis and individualized therapies are important factors in the fight against this disease. Primarily it is the wrists, hands, elbows, shoulder, knees, and ankles that are affected. Even with different imaging technologies in radiologic routines in use for detecting inflammatory arthritis and osteoarthritis, fluorescence imaging holds great promise since affected joints are located near the body surface and thus are mostly well accessible to light. It is expected that (fluorescence) optical imaging can contribute to detection and quantification of pathomorphologies and pathophysiologies in inflammatory rheumatic diseases such as angiogenesis, hypervascularization, hypoxia, and hypermetabolism – not only in the preclinical but also in the clinical stage. To this end, different optical modalities, such as spectroscopic methods, transillumination imaging, diffuse optical imaging, fluorescence and bioluminescence imaging, photoacoustic imaging, etc., have been analyzed. These research activities have been reviewed by Chamberland 2010. With regard to fluorescence optical imaging, the following have been studied: folate receptors (Chen et al. 2005), the F4/80 antigen present on the surface of macrophages (Hansch et al. 2004), cathepsin B (Lai et al. 2004), fluorescent-labeled leukocytes (Simon et al. 2006), perfusion in arthritic joints depending on the molecular weight of the probes (Dietzel et al. 2013), targeting glycosaminoglycans in cartilage degeneration via dipicolylamine (DPA) probes (Hu et al. 2014), and E-selectin (Jamar et al. 2002; Marshall and Haskard 2002). Image-based detection of rheumatoid arthritis in patients by using ICG as contrast agent is being analyzed in several clinical studies (Schafer et al. 2013).

In other studies, the mechanisms of inflammation have been investigated in different animal models. These encompassed granuloma formation using fluorescence-labeled macrophages (Eisenblatter et al. 2009), presence of CysLT1 in edema models (Busch et al. 2011), selective visualization of liposomal uptake by macrophages upon dequenching in endolysosomes (Tansi et al. 2013), the occurrence of FRET upon uptake of two exogenous probes in endolysosomes of phagocytes (Busch et al. 2012), and others (Fig. 16.6).

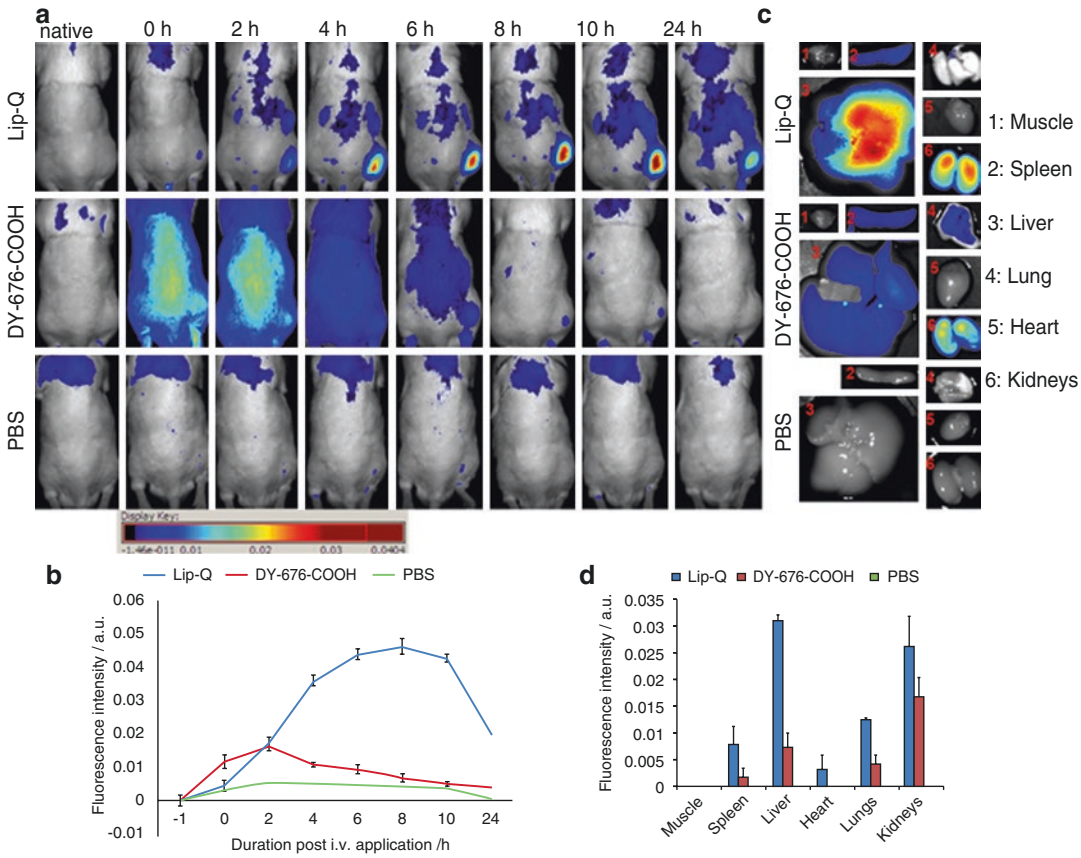

Fig. 16.6 Selective detection of liposomal uptake by macrophages upon dequenching endolysosomes. (**a**) Representative in vivo NIR fluorescence imaging of edema using quenched liposomes (Lip-Q) or the hemicyanine dye DY-676-COOH (concentration equivalent to Lip-Q content) or PBS, pH 7.2. (**b**) Semiquantitative analysis of fluorescence intensities of edema. (**c**) Bio-optical ex vivo images of organs from mice 6 h post probe application. (**d**) Semiquantitative analysis of fluorescence intensities of organs after ex vivo NIR imaging (from Tansi et al. (2013) with permission from Wiley and Sons)

16.1.5 Conclusion

Fluorescence imaging is an active and promising area of research and application in the preclinical and clinical field. NIRF imaging is especially promising thanks to greater tissue penetration depths of light and low interference by tissue autofluorescence. A wide spectrum of NIR fluorophores is now available. When utilizing contrast agents in vivo, several parameters influencing signal-to-background ratio are important for effective imaging applications. These include selection of excitation and emission wavelengths, solubility, photobleaching, target affinity, and pharmacokinetics, to name a few. Although several clinical studies with ICG are under way with a focus on detection of rheumatoid arthritis and certain tumors, the approval of other fluorescent probes, particularly for target-affine reporters, is a large undertaking. In this regard, probes with applicability in several disease frameworks (e.g., vascular targets in inflammation and cancer) will be of higher interest to pharmaceutical companies. With respect to hardware, epi-illumination techniques are widely used in preclinical research, although substantial advances have been made in producing tomographic systems, as well as other sophisticated systems (e.g., optoacoustic imaging). In the long term, clinical research, applications, and discrete fiber and

intraoperative systems will markedly improve the accuracy of interventional procedures.

16.2 Bioluminescence Imaging

Frauke Alves and Julia Bode

16.2.1 General Introduction

Optical imaging offers many unique opportunities in order to study biological processes in intact organisms. One option for the measurement of *in vivo* optical signals is bioluminescence. There has been a rapid growth of bioluminescence imaging applications in small animal models propelled by the approaches in technology during the last years.

In general, bioluminescence refers to the process of visible light emission in living organisms. Light as a form of energy consists of photons with different wavelengths. Light is not only the visible light that can be seen by the human eye with wavelength ranges from around 380 nm (violet) to about 740 nm (red), it also means that visible light is only a small part of the total electromagnetic light. This extends from gamma rays (10^{-12} m) through X-rays, ultraviolet, visible, and infrared or near-infrared light up to microwaves and radio waves (10^{3} m) (Sadikot et al. 2005).

There are two major groups where the emission of light can be classified in; one is thermal or heat radiation, whereas the other class consists of nonthermal radiation (Moreno et al. 2014).

16.2.2 Production of Light by Living Organisms

A variety of different bioluminescent systems have been identified in nature, every single one requires a specific enzyme and substrate. Living organisms produce light via luminescence. These luminescent species can be found across almost all major taxonomic groups ranging from bacteria via hydrozoa, fungi, or insects up to higher organisms such as fishes. Only few groups exist with no known luminescent forms such as spiders, birds, mammals, or flowering plants (Contag et al. 1998; Haddock et al. 2005, 2010).

The majority of luminescent organisms is of marine origin and indwells the ocean. They can be found all over the ocean depth, but the majority lives in the disphotic zone from 200 to 1000 m where only a small part of the sunlight from the surface reaches this area. The seawater above absorbs most wavelengths of light in the range of red, orange, and yellow. Only the light with a range of blue or blue-green light with a short wavelength of about 475 nm and more energy reaches the deeper area of the ocean, an almost completely dark place. That is why many of the organisms adapted to life there and have the ability to produce there own light now (Warrant and Locket 2004). Forms of luminescent terrestrial life can be found all over the world where they indwell different habitats and where they use light for diverse reasons. For example, swarms of glowworms or fireflies dance in the dark in order to impress the sexual partner with the blinking light (Li et al. 2013a; Close et al. 2011).

Armillaria species are other examples for terrestrial luminescence that is the most common source of foxfire. Out of about 40 known *Armillaria* species, five have been described as luminescent. The mycelium of one single *Armillaria* is able to reach tremendous dimensions with cases describing covering an area as large as 9 km^2 (Zhao et al. 2008; Mendes et al. 2008; Desjardin et al. 2008; Miller et al. 2005).

16.2.3 Production of Light and Mechanisms

In 1885, a French scientist, Raphael Dubois, verified the idea of bioluminescence being a result of a chemical process. He made a paste of the luminescent material from the clam *Pholas* and suspended it in cold water leading to the production of a glowing solution. Additionally, Dubois was able to show that this reaction was repeatable with extracts of the click beetle (*Pyrophorus*). Out of his studies, Dubois concluded that bioluminescence was chemical in nature and that there

is an organic molecule involved. He named this molecule *luciferin* and the responsible enzyme *luciferase* (Poisson 2010; de Wet et al. 1985).

Decades later the biochemical reaction of bioluminescence, when energy is converted into light, was solved. The substrate luciferin is oxidized by molecular oxygen, whereas the enzyme luciferase catalyzes the reaction towards a nonreactive product and the release of photons. Figure 16.7 shows a simplified scheme of the biochemical reaction.

In detail, luciferin is oxidized to oxyluciferin by luciferase – oxygen and ATP are needed for the reaction as well.

The most commonly used bioluminescent reporter for research purposes is luciferase from the North American firefly (*Photinus pyralis*). Other useful luciferases have also been cloned from jellyfish (*Aequorea*), sea pansy (*Renilla*), corals (*Tenilla*), click beetle (*Pyrophorus plagiophthalamus*), and several bacterial species (*Vibrio fischeri*, *V. harveyi*) (Hastings 1996).

In comparison to firefly and click beetle luciferase, *Gaussia* luciferase and *Renilla* luciferase use coelenterazine and oxygen. Here ATP is not needed since coelenterazine alone is a high-energy molecule that offers the energy for the reaction (Soling et al. 2004). All reactions have in common that they need oxygen.

During the reaction, a peroxyluciferin is built as an intermediate that provides energy for excitation. The peroxyluciferin holds the energy coming from the reaction only for nanoseconds, and afterwards the energy is released in the form of a photon.

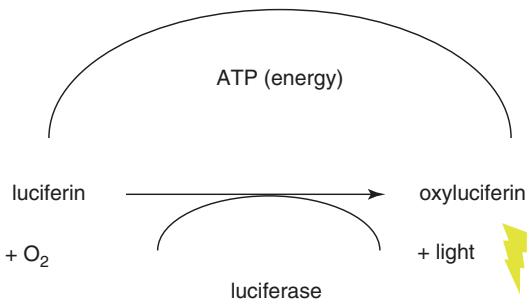

Fig. 16.7 Oxidation of luciferin and catalyzation of the reaction through luciferase. The side product light can be detected

With awareness of this phenomenon, different luciferases were generated by inducing mutations at important amino acids close to the enzymatic gap in order to emit light with different wavelengths. The energy conversion efficiency is with more than 80% of energy transformed into light that produces close to one photon per oxidized luciferin.

Since the differences in luciferin substrate utilization result in no crossover reactions, both techniques, the D-luciferin system and the coelenterazine system, can be used in parallel, for example, in the same animal. Each luciferase has its own substrate specificity, characteristic wavelength of light emission, and its optimal parameters.

Firefly luciferase was cloned in 1985 for the first time. Only 3 years later, an assay was invented that made it possible to detect luciferase activity in mammalian cell lysates. The development of this assay became a useful tool in order to set up *in vivo* studies of gene regulation with luciferase activity.

One of the many advantages of luciferase is that it is a perfect marker for gene expression because there is no posttranslational modification. Additionally, the halftime of luciferase *in vivo* is approximately 2 h (Ignowski and Schaffer 2004). The light emission from this firefly catalyzed luciferin reaction is broad band from 530 nm to 640 nm and peaks at 562 nm. The spectrum of this emission allows, together with the properties of biological tissues, the light to penetrate through several centimeters of tissue. This is true especially for light with spectral content of above 600 nm. This special feature can be used to detect light that is emitted from internal organs in mice expressing luciferase as a reporter.

There are several factors involved affecting the sensitivity of detecting internal light sources. One major factor is the level of luciferase expression of cells. Another one is the depth of cells expressing luciferase within the body because it influences the distance of photons that have to travel through the animal tissue. Last is the sensitivity of the detection system used for collecting the light signal.

Another big advantage of this method is the commercial availability of luciferin or D-luciferin. Several biochemical companies all

over the world sell it for research reasons (e.g., Life Technologies, Sigma-Aldrich, PerkinElmer, and many more).

For experimental handling, the first step in order to start a bioluminescence measurement is to place the animals in a dark chamber. To detect the light, emitted from the animal, photons are collected by a charge-coupled device (CCD) camera in combination with a computer for image acquisition and analysis of data. These CCD cameras first gather and then convert photons into electrons after striking silicon wafers. The intensity of incident photons is encoded into electrical charge patterns to generate an image.

During the last years, great advances have been made in order to improve detector technology to get better sensitivity and image quality. The background noise of the bioluminescence imaging machine is reduced by supercooling of the system and mounting the CCD camera in this light-tight dark box as mentioned before.

For the bioluminescence experiment itself, it is important that acquisition and analysis parameters remain constant when relative photons or counts are acquired. This includes, for example, the animal position relative to the CCD camera, the region of interest, and f-stop (the ration of lens focal length to the diameter of the entrance pupil). The absolute unit of radiance is photon/s/cm^2/steradian, and it refers to the photons per second of light that radiate from the mouse in a unit area (1 cm^2) and unit angle (1 steradian). This unit is more quantitative but enables an easier comparison of data in an experiment when image acquisition parameters are greatly different.

The concentration of administered luciferin also needs to be kept stable during experiments. Using the most commonly used concentration of 150 mg/kg per body weight for an animal, the experiment is cheap (with costs of around 300 Euro per 1 g D-luciferin), nontoxic for the laboratory animal, and easy to order. The D-luciferin solved in PBS can be stored in−20 °C for several months up to 1 year.

However, one problem for bioluminescence imaging is caused by D-luciferin itself. Since it is not produced by rodents, it needs to be injected systemically in order to travel through the bloodstream and needs to pass different membranes or barriers before it can reach the point or cells of interest. Different types of injections are discussed in the next chapter in more detail.

In addition, another disadvantage that D-luciferin causes itself is that it was first believed that for the rapidness of the enzyme luciferase, there is no restriction for the used D-luciferin. But it was reported that the detected *in vivo* signals correlate with the injected substrate dose, especially if there is a high number of cells expressing luciferase *in vivo*. This phenomenon shows that the higher the administered dose of D-luciferin in the animal is, the better the enzyme luciferase works close to its maximum velocity.

Because of the similarity of luciferin to albumin, it does not cause an immune response. Even though luciferin is able to freely cross the blood barrier and the placental barrier, toxicity appears low (Tiffen et al. 2010).

16.2.4 Luciferase as a Reporter Gene for *in vivo* imaging

The luciferase substrates need to be injected in rodents in order to be provided for the bioluminescence reaction *in vivo* as mentioned. There are different choices of injections that the experimenter can choose: intravenously and intraperitoneally are the most commonly used. Additionally, there are subcutaneous injections or less frequently used intratumoral injections or oral applications (Hiler et al. 2006; Inoue et al. 2009; Keyaerts et al. 2008, 2012; Wang and El-Deiry 2003). One advantage of intraperitoneally injections is the straightforwardness because the animal does not need to be anesthetized and the procedure itself is fast and easy. For injections in the tumor region, depending on the tissue or organ, or intravenously, the animal needs to be anesthetized. Before starting an experiment, several factors need to be considered. First, the injection site of the substrate needs to be discussed. This depends, for example, on the health situation of the animal and the question whether

there is an incubation time needed before starting a bioluminescence measurement. It takes several minutes for the substrate to reach the region of interest (ROI); therefore, the time of incubation need to be validated for every experimental approach. The time that is needed for the luciferin to reach the ROI may differ from tissue to tissue and in every experimental setup. For example, the incubation time of the substrate can differ depending on the organ or tissue where cells expressing luciferase are placed: the abdomen, neck, or brain of the animal.

One excellent example for the use of bioluminescence imaging in preclinical research is the detection of brain tumors in small rodents. D-luciferin readily crosses the blood–brain barrier and allows early examination of tumor growth in the brain tissue. Depending on the cell line and the strength of luciferase expression in the brain, tumor cells can be determined only hours after cell injection.

In addition to the time that is needed for the luciferin to cross the total body of the animal, the start point for the bioluminescence measurement needs to be determined because the bioluminescent signal proceeds over time. Imaging of the whole animal can be conducted 5–15 min after an intraperitoneally application of D-luciferin, with a relatively stable light emission level for 30–60 min, depending on the experimental conditions. Afterward the bioluminescence signal decrease and disappear after a maximum duration of three hours.

The reaction in the animal emerges in no background signal for the D-luciferin reaction in the absence of the enzyme. For example, for the coelenterazine reactions, an auto-oxidation of this high-energy molecule occurs at a low velocity. This results in a low background signal even if there is no luciferase present. For *in vitro* luciferase assays, it is described that with boundlessness of ATP, oxygen, and D-luciferin, the correlation between enzyme concentration and signal intensity is excellent.

In contradistinction to advantages by using bioluminescence imaging, the interpretation of data obtained from *in vivo* bioluminescence is not always straightforward.

For example, a mouse bearing a massive subcutaneous tumor expressing luciferase leads to a bioluminescence signal after injection of luciferin. This signal can be misinterpreted. Cells in the core of the tumor can be apoptotic or parts of the tumor necrotic. Necrotic tissue is not able to express luciferase or to provide oxygen or ATP. This leads to a reduction of the total bioluminescence signal, and the signal is not correlated to the real size of the tumor. In addition, parts of the tumor region that grow deeper in the tissue can lose maximal values of counts because of the depth. The emitted counts do not display a correlation of tumor cells, and therefore it can result in an imbalance between signals and real tumor volume. Furthermore, the density of vessel density or the leakiness of vessels that means reachability of luciferin for the luciferase expressing cells needs to be kept in mind because it can influence the bioluminescence signal as well. This has to be considered for the measurement of growth rates of brain tumors, for example. Questions that can arise while working with brain tumors are if the luciferin is crossing the blood–brain barrier up to 100 % or if the tumor region in the brain is reachable via newly developed vessels. In general, a highly vascularized tumor, independent from the tissue, might even give a much higher bioluminescence signal than a tumor of the same size with less vessel density.

A major point that is important for the experimental setup and the interpretation of data is the approximately ten-fold loss of photon intensity for each centimeter of tissue depth. Furthermore, images are surface weighted meaning that light sources closer to the surface of the animal appear brighter compared with deeper sources. In addition, changes in geometry can occur and can influence, for example, the growing tumor or scar tissue, or the optical properties of tissues can affect light scatter or absorption and therefore the detected bioluminescent signal.

In literature, there is one commonly used D-luciferin concentration described, 150 mg/kg, that is nontoxic for the animal and used by many researchers. For coelenterazine, a much lower concentration of 0.5–4 mg/kg is usually injected because of a limitation of solubility of the substrate in aqueous solution.

There are several parameters that can influence the sensitivity of bioluminescence imaging. Newly developed instruments, for example, with a new camera system are more sensitive in detection of small signals.

As mentioned before, the signal can be weakened by the depth of the tissue. Additionally, the hair of the rodent can disturb or weaken the signals.

Parameters for imaging, like acquisition time, binning, and the positioning of the animal, need to be optimized for every experimental approach. Also of high importance for the bioluminescence experiment is the level of promoter activity controlling the expression of luciferase. In addition, the amount of luciferin injected in the animals and the diet are sensitive parameters as the gut phosphorescence leads to an increase in the background signal in animals.

But in contrast to other *in vivo* preclinical imaging techniques, bioluminescence imaging is a versatile and cost-effective technique with high sensitivity. Three to five animals can be measured in parallel at the same time during one experiment, and the acquisition of data takes a few seconds up to some minutes. By reducing the amount of animals that can be investigated in parallel during one measurement and by lowering the distance to the CCD camera, the sensitivity can be increased. Optimizing settings and conditions leads to light detection only from areas that contain luciferase, and there is no or minimal background noise visible.

One critical point in BLI is the half-life time of luciferase. The half-life of luciferase activity in live cells was measured in real time and was 2 h (Ignowski and Schaffer 2004).

The enzyme has to be produced continuously for the detection of signals. When cells, that express the luciferase, die or when the promoter elements turn the luciferase "off" or inactivate the gene signals from the luciferase, activity disappears.

In comparison to other *in vivo* imaging techniques, the measurement time for bioluminescence is significantly less (Zinn et al. 2008). Data acquisition with PET, SPECT, or MRI takes 30–60 min, and only one rodent can be measured during that time. Therefore, there is a limitation of animals that can be monitored at one single day during one experiment. In comparison, five mice can be measured in parallel in a bioluminescence experiment, and the whole measurement takes only some minutes.

This fact increases the amount of animals that can be measured at one single day. Additionally in compared to PET, SPECT, or MRI, data analysis takes less time for BLI. In PET and SPECT, contrast agents are needed, and radiolabeled probes have to be prepared prior to the experiment. PET or SPECT result in background signals that reduce the sensitivity or signals in all locations, including those compounds that are metabolized or excreted by normal routes. Bioluminescence imaging can provide 2D and 3D images. But one major disadvantage of this method is the lack of translation to the application in humans because of the requirement for genetically encoded luciferase and the dependence of light signal on tissue depth.

16.2.5 Functions of Bioluminescence

The research that can be performed with bioluminescence imaging can be divided into two major parts. One includes routine investigations, in which a control element (promoter) for the luciferase that is always active in transfected cells is used. It is "on" under all conditions and in all tissue types. A highly active promoter that is often used and expressed in all tissue types is the cytomegalovirus (CMV) immediate-early promoter. Purposes for routine applications *in vivo* are detection of tumors or monitoring of their growth in cancer research. Gene therapy studies in combination with targeting of vectors or investigation of migration of adoptively transferred cells in cell therapy studies are also commonly performed.

For tumor imaging, plasmid or viral techniques are effective for the stable transfection of cancer cells with the luciferase reporter construct. This constitutive expression of luciferase is one strategy to use bioluminescence as a tool. These cells that constitutively express luciferase are

implanted in syngeneic animals, but in the case of human cancer cell lines, immunodeficient mice or rats are required and can be monitored over a specific time.

Studies in combination with bioluminescence imaging have been reported for human cancer cell lines of meningioma, bladder cancer, prostate adenocarcinoma, neuroblastoma, hepatocellular carcinoma, breast cancer, hematologic malignancy, lung cancer, melanoma, and glioma models and moreover encompass humanized as well as metastatic models (Maes et al. 2009).

For example, bioluminescence showed an excellent correlation between tumor size and light emission when human breast cancer cells, a subclone of MDA-MB-231, that stably express the luciferase gene under control of the CMV promoter, were implanted in the mammary fat pad of a mouse model. By bioluminescence imaging, the cells were detected in the mammary fat pads of nude mice, and later, tumor growth rates could be determined. This method has been described for the preclinical assessment of the effectiveness of novel therapies for ovarian cancer and for animal models of prostate cancer (Brakenhielm et al. 2007; Kanerva et al. 2003). Differences in obtained bioluminescence signals correlate with a reduction in tumor size after treatment.

One study showed a tumor determination in the mammary fat pad of a mouse 19 days after injection, but with bioluminescence imaging, tumor cells (1×10^6) could be detected immediately after implantation. 15 min after intraperitoneal D-luciferin administration, the bioluminescent signal could be measured. The same study defined the minimum amount that could be detected subcutaneously by BLI with only 5×10^3 cells (Zinn et al. 2008). This example shows the sensitivity of this detection method, and one advantage is the following: luciferase expressing tumor cells can be detected immediately after implantation in the animal model even weeks before the tumor can be detected by manual testing.

In comparison to monitoring a subcutaneous tumor that is visible or can be detected with manual testing, detection of metastasis of cancer cells within the whole body in rodents is not trivial. For this approach, bioluminescence imaging is particularly sensitive. Cowey et al. could show that immediately after injection of MDA-MB-435 breast cancer cells in the left ventricle of mouse hearts, the cells were detected in the blood pool with an overall body scan with BLI (Cowey et al. 2007). Forty-two days after injection of cells, bioluminescence imaging allowed the detection of metastases in the spine, joints, and head (mandibles).

For the detection of brain tumor growth *in vivo*, one of the best options besides MRI is bioluminescence imaging. The luciferin is able to cross the blood–brain barrier, and even days after tumor cell injection in the brain, signals can be measured. There are reports available that describe a detection of tumor cells even 7 days after injection in the brain.

In order to monitor the increasing luciferase expression and therefore increasing proliferation of human glioblastoma cells in a mouse model *in vivo* over time, 75,000 U87 MG cells, lentivirally transfected with luciferase, were injected in the right hemisphere of mouse brains according to Sabag, Bode, and Fink et al. (Sabag et al. 2012). The first bioluminescence signal was measured 12 days post injection. Figure 16.8 shows a representative image of a measurement of mice each bearing a glioblastoma multiforme. The expression of luciferase in the brain was detected after an incubation time of ten minutes after intraperitoneal injection of D-luciferin (150 mg/kg KG), exposure time of seven minutes, and binning of four. No expression of luciferase was detected initially after injection of PBS in a tumor-bearing mouse (Figure 16.8) (negative control, right mouse).

Intraperiotenal injection of D-luciferin resulted in bioluminescence signals in the here shown two mice (Figure 16.8). Both mice received with the same amount of tumor cells at the same day.

The obtained bioluminescence signals demonstrate the heterogeneity of glioblastoma growth *in vivo*. Mice were then chosen for MRI studies using a newly developed contrast agent for the detection of brain tumors in mouse models in vivo. The goal was to investigate the enrichment

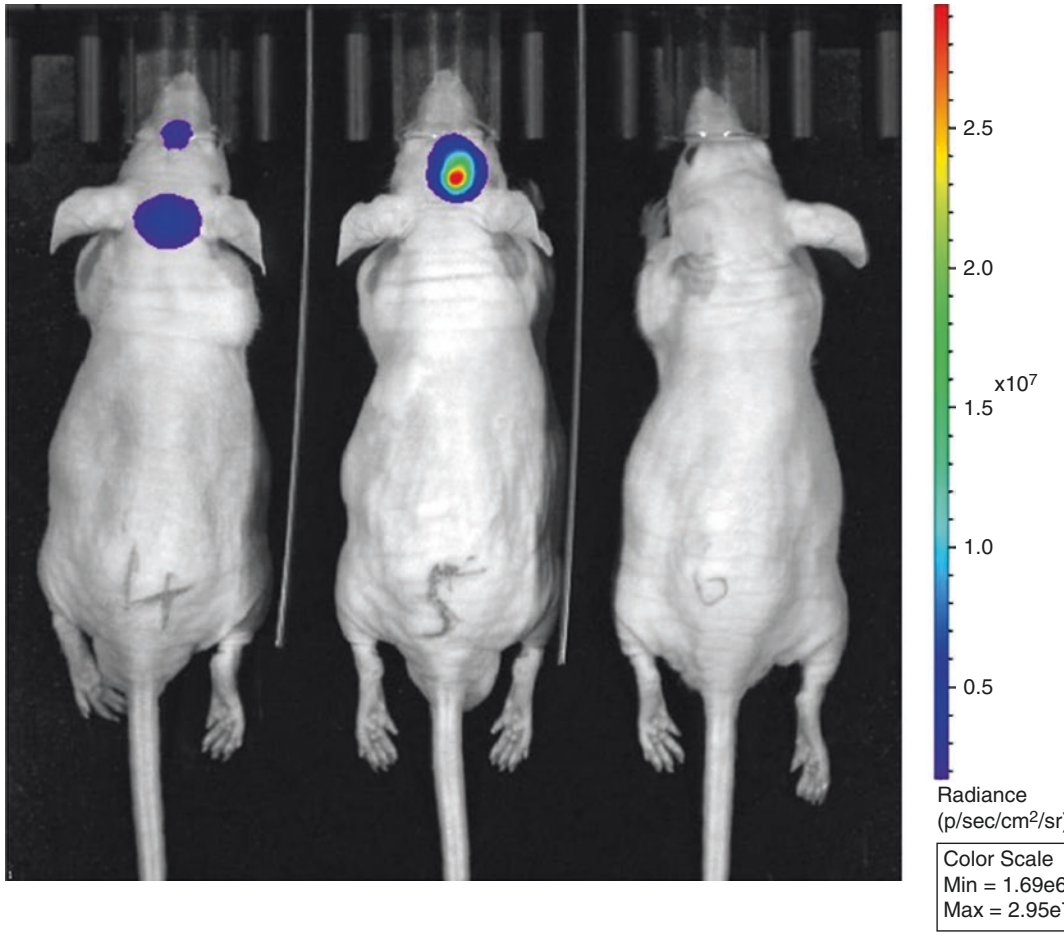

Fig. 16.8 Bioluminescence imaging of nude mice 12 days after injection of 75,000 luciferase-positive U87 MG glioblastoma multiforme cells into the right hemisphere. (*Left*, *middle*) Luciferin 150 mg/kg bw was given intraperitoneally; imaging times of 7 min and a binning of 4 were kept constantly A brain tumor-bearing mouse as control after injection of PBS shows no BLI signal (*right*). The pseudo-color scale bar represents the intensity of light emission with different colors (Unpublished data: T. Krüwel and J. Bode)

of contrast agent in brain tumors with different sizes in order to optimize the resolution of MRI and to find a correlation with obtained bioluminescence signals.

One disadvantage that we observed during this study was the deviation from the location of the tumor in the brain and the obtained bioluminescence signal. A tumor grown deeper in the brain tissue led to a smaller bioluminescence imaging signal compared to a tumor, smaller in size, that grew in a more cranial direction. The method is not suitable for monitoring treatment effects of brain tumor growth *in vivo*. The reason is the event of default of missing the right time of, for example, injection of a drug. The brain tumor is only detectable with bioluminescence imaging when (i) the size is big enough and (ii) the location is not too deep in the tissue.

One advantage of this technique is the fast and easy way of monitoring the proliferation of cells over time *in vivo* depending on the location of tumor cells in the tissue. It is a technique that allows to investigate tumor growth of a cancer type that cannot determined easily *in vivo*.

Noninvasive bioluminescence imaging was also applied to monitor preclinically pancreatic tumors, a tumor also not visible from the outside. Therefore, 1×10^6 luciferase-transfected

human pancreatic adenocarcinoma PancTu-I cells (PancTu-I-luc) were orthotopically injected into the head of the pancreas of nude mice. Whole-body scans 23 days after cell implantation using the IVIS Spectrum *in vivo* imaging system (Fig. 16.9) and 13 min after the intraperiotenal injection of 150 mg/kg D-luciferin show bioluminescence signals over the tumor areas corresponding to a distinct tumor growth and expansion in each mouse.

Another example for an application of bioluminescence imaging is the detection of bacteria (Burns-Guydish et al. 2005; Siragusa et al. 1999), for example, the colonization of *Citrobacter rodentium* in wild-type C57BL/6 mice. It was shown that the bacterial colonization of the animal after inoculation could be monitored over a time of over 15 days. The technique demonstrated that the pathogens are cleared from the body at day 9 or 10 post transfection that was complete by days 15 to 17. By applying a bioluminescent strain of *C. rodentium*, it was shown that after the removal of the abdominal wall and bacterial exposure of the cecum and colon, the *Citrobacter* preferentially colonized the cecal lymphoid patch and the mid and distal colon. The mice were kept in a chamber in a biosafety cabinet. The chamber was sealed to avoid bacterial exposure of other animals; therefore, bioluminescence signals and the position of bacteria in the

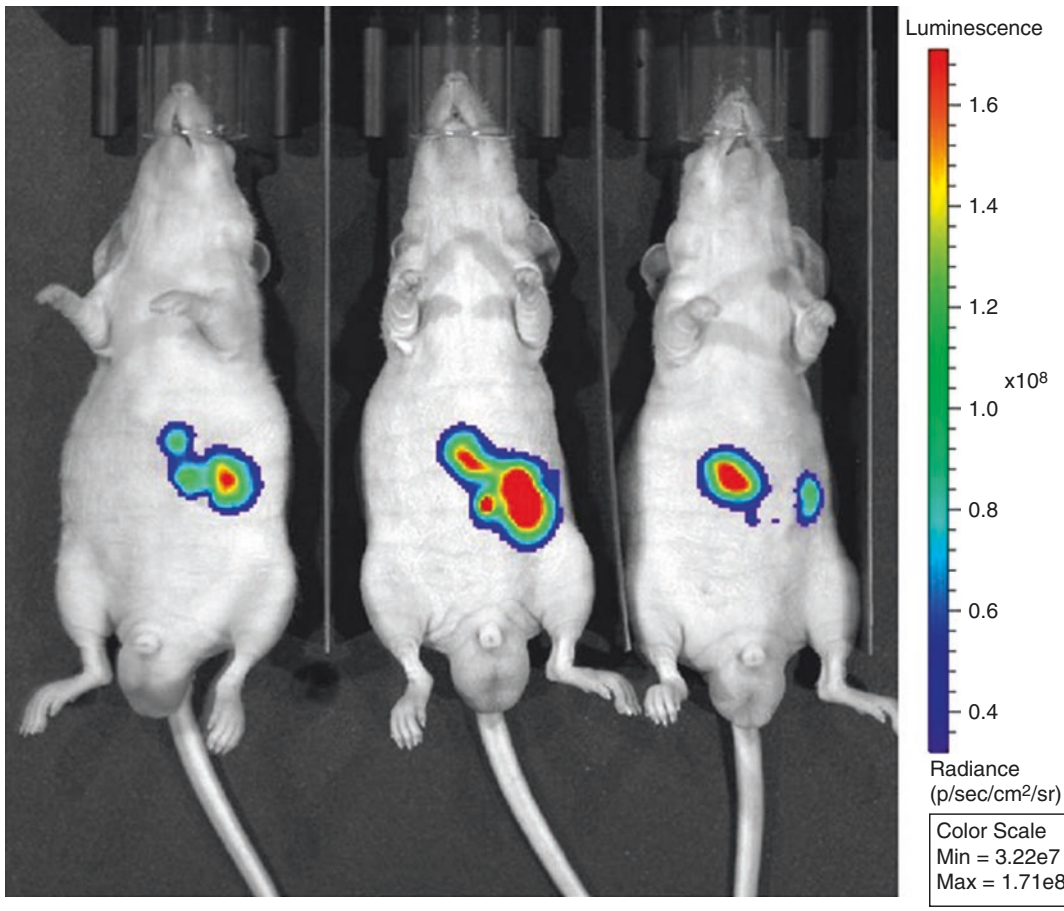

Fig. 16.9 Representative in vivo 2D bioluminescent images of three pancreatic tumor-bearing nude mice, 23 days after orthotopic implantation of 1×10^6 luciferase-transfected PancTu-I cells into the head of the pancreas. Bioluminescence signal was measured 13 min after i.p. injection of D-luciferin 150 mg/kg (Unpublished data: M. Saccomano)

animal were sensitively detected (Wiles et al. 2004, 2006).

There are specialized research applications for reporter constructs which are only active under defined conditions. For example, detection of apoptosis with bioluminescence signals can be realized to evaluate newly developed cancer therapies. In order to unravel gene regulation or to study other biological processes, one approach using bioluminescence imaging is to generate transgenic mice, expressing luciferase during developmental processes.

In another transgenic mouse model, firefly luciferase was expressed under the control of the VEGFR2 promoter in order to noninvasively elucidate the temporal profile of VEGFR2 expression after stroke as a biomarker for VEGF/VEGFR2 signaling (Adamczak et al. 2014). In their study they described that VEGFR2-related signaling is active at least up to 2 weeks after the infarct and results in increased vascular volume. Furthermore, this study presented a novel strategy for the noninvasive evaluation of angiogenesis-based therapies.

Bioluminescence imaging detects the expression of the luciferase as a genetic reporter. There are several opportunities to control the expression based on the activity of the promoter element, for example, monitoring the expression of luciferase in the liver under specific tissue conditions. The CMV promoter is only "on" or active when it is integrated in hepatocytes. A different promoter like cyclooxygenase 2 L (cox-2 L) is not active under normal conditions in the liver, but it is active or "on" in the presence of inflammation (Ishikawa et al. 2006). It was shown that the technique is sensitive enough to detect the inflammation caused after lipopolysaccharide (LPS) injection. After LPS injection, expression of luciferase was induced and could be measured. No expression in liver tissue was detected initially (Iyer et al. 2005, 2006).

Another well-characterized application of bioluminescence imaging is the investigation of tumor hypoxia.

Tumor hypoxia plays an important role in promoting malignant progression and affecting therapeutic response negatively. There is little knowledge about *in situ*, *in vivo*, tumor hypoxia during intracranial development of malignant brain tumors because of lack of efficient means to monitor it in these deep-seated orthotopic tumors. Bioluminescence imaging with a reporter gene system under the control of a promoter sequence can be used to monitor hypoxic stress in a noninvasive way. Under hypoxic stress, signaling responses are mediated mainly via the hypoxia-inducible factor-1α (HIF-1α) to drive transcription of various genes. For example, Saha et al. used a HIF-1α reporter construct, 5HRE-ODD-luc, stably transfected into human breast cancer MDA-MB231 cells (MDA-MB231/5HRE-ODD-luc) to study tumor hypoxia. *In vitro*, a HIF-1α bioluminescence assay was performed by incubating the transfected cells in a hypoxic chamber (0.1 % O_2) for 24 h before the bioluminescence signal measurement, while the cells in normoxia (21 % O_2) served as a control. Significantly higher photon flux observed for the cells under hypoxia suggests an increased HIF-1α binding to its promoter (HRE elements), as compared to those in normoxia. Cells were injected directly into the mouse brain to mimic a breast cancer brain metastasis model. In this model, *in vivo* bioluminescence imaging of tumor hypoxia dynamics is initiated 2 weeks after implantation and repeated once a week. Bioluminescence reveals increasing light signals from the brain as the tumor progresses, indicating a rise in intracranial tumor hypoxia (Saha et al. 2011).

In order to control luciferase expression with the help of promoter elements, one approach is to synthesize an inactive luciferase enzyme by linking a cleavable protein subunit to luciferase. For example, specific sequences within the subunit are activated by caspase 3. The caspase activates the luciferase, and this is one way to monitor apoptosis *in vivo* (Laxman et al. 2002). The application of this reporter in combination with bioluminescence imaging was used as an early detector of apoptosis (Rehemtulla et al. 2004), for example, in response to therapy.

A recently published paper by Cruz-Monserrate et al. showed that bioluminescence

imaging can be applied knowing that tumor cells and the surrounding tissue have different pH values. They utilized ph-sensitive probes determining primary tumors and metastasis of human pancreatic cancer xenografts (Cruz-Monserrate et al. 2014). They applied bioluminescence in order to validate signals from fluorescence-labeled insertion peptides they used for the localization of primary tumor and metastases in this particular mouse model.

Paulmurugan et al. described an inactive luciferase enzyme that responded to a drug to form an active luciferase under conditions of specific protein–protein interactions. This approach can be used to track interactions between proteins in living animals or cells (Paulmurugan et al. 2002).

The generation of transgenic mice, for example, can be established as a tool to track naïve T-cell populations in real time (Chewning et al. 2009). This is only one of the examples of transgenic mice with luciferase constructs that are available in academic research.

In this approach, the firefly luciferase gene was cloned into human cd2 genes, limiting the constitutive expression to all T-cells. Sorted cell populations clearly gave evidence for the T-cell-specific expression in CD4+ and CD8+ T-cells. *In vivo* this approach was deployed to image intact delineation of primary and secondary lymphoid organs.

16.2.6 Conclusions

There are several parameters that influence the sensitivity of bioluminescence imaging.

The most important determinants are:

- Instrumentation
- Hair
- Depth in tissue
- Imaging parameters (acquisition time, binning, animal position)
- Level of promoter activity controlling the luciferase expression
- Amount of luciferase substrate injection
- Diet

It is essential to optimize these parameters for each experiment. Of primary importance are especially the CCD camera and a position of the animal close to the camera. Together with longer acquisition times and higher binning, the sensitivity of the measurement can be increased.

Bioluminescence imaging is in summary a versatile and cost-effective technology that has high sensitivity and efficiency. Up to five mice can be imaged at the same time with acquisition times ranging from some seconds to some minutes. That means it is possible to image up to 150 mice in a single day if needed. By decreasing the number of mice in one measurement, the sensitivity can be increased. A simple ROI analyses can easily reduce the data.

Using optimal conditions for an experiment, light is only detected from areas that contain luciferase, and there is minimal or no background noise.

Since luciferase has a short biological half-life, it must be continuously produced for the measurement of signals. In the case of death of cells, the signal is lost. In a similar way, changes in luciferase levels can be discovered when promoter elements driving luciferase are turned off or on.

The majority of bioluminescence experiments take advantage of the well-characterized firefly luciferase or *Renilla* luciferase proteins, and when used in conjunction with alternate imaging technologies, they can provide extremely thorough and sophisticated datasets.

In comparison to other imaging systems such as SPECT, PET, or MRI, the cost of bioluminescence imaging systems is significantly less.

In future, an advancement of this method can lead to a higher sensitivity of tumor cell detection in animal models. Further developments could help to detect small metastasis and cell clusters in order to start treatments of diseases as soon as possible.

16.3 Optical Coherence Tomography (OCT)

Peter Cimalla, Martin Hofmann, Volker Jaedicke, and Edmund Koch

16.3.1 Tissue Properties and Ballistic Photons

Optical imaging of biological tissue suffers from the strong attenuation of light in the tissue. Therefore, standard optical imaging is limited to the tissue surface or to transparent tissue, for example, the eye. However, under certain circumstances, the attenuation is mostly not due to absorption but due to scattering of light. This enables advanced optical imaging technologies like optical coherence tomography which allows looking into biomedical tissue.

In more detail, the absorption coefficient and the scattering coefficient of tissue are shown as a function of wavelength in Fig. 16.10 (Roggan et al. 1999). The absorption coefficient drops from 300 nm to a minimum at 1100 nm and then rises again. The scattering coefficient exhibits a weaker wavelength dependence and slightly decreases from 300 nm to 2100 nm. But obviously, the scattering coefficient in the wavelength regime between 600 and 1300 nm is about two orders of magnitude higher than the absorption coefficient. Accordingly, light attenuation in tissue in this wavelength range is mostly due to scattering, and absorption plays a minor role. That is why this spectral range is also called "optical window."

As a consequence of these optical tissue properties, approaches for optical imaging in tissue have to operate in this optical window and have to make use of concepts to suppress or circumvent scattering.

To motivate the strategy used in OCT, we now look schematically at the scattering processes. This is shown schematically in Fig. 16.11.

All inhomogeneities inside the tissue represent potential scattering centers as indicated by the black dots in the schematic picture in Fig. 16.11. When photons of light enter the tissue, there is a small but finite probability that they propagate through the tissue without any scattering event. Of course, this probability drops strongly with increasing tissue thickness and with increasing density of scatterers. For practical biomedical tissue, the maximum path length or the penetration depth for these unscattered so-called ballistic photons (Yoo and Alfano 1990) is below 1 mm. More probably, the incoming photons will be multiply scattered before they leave the tissue. In between these extremes, there are also a few photons which are only weakly scattered. These are sometimes called "snakelike photons"(Yoo and Alfano 1990).

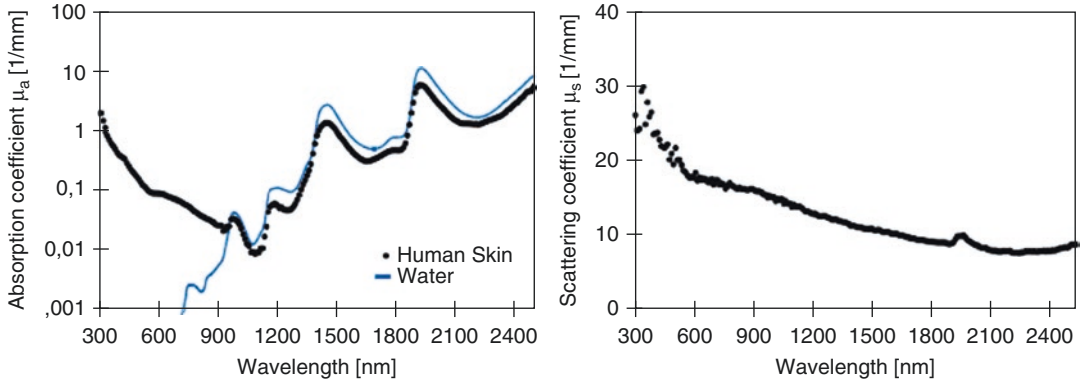

Fig. 16.10 Absorption coefficient and scattering coefficient of biomedical tissue as a function of wavelength (Roggan et al. 1999)

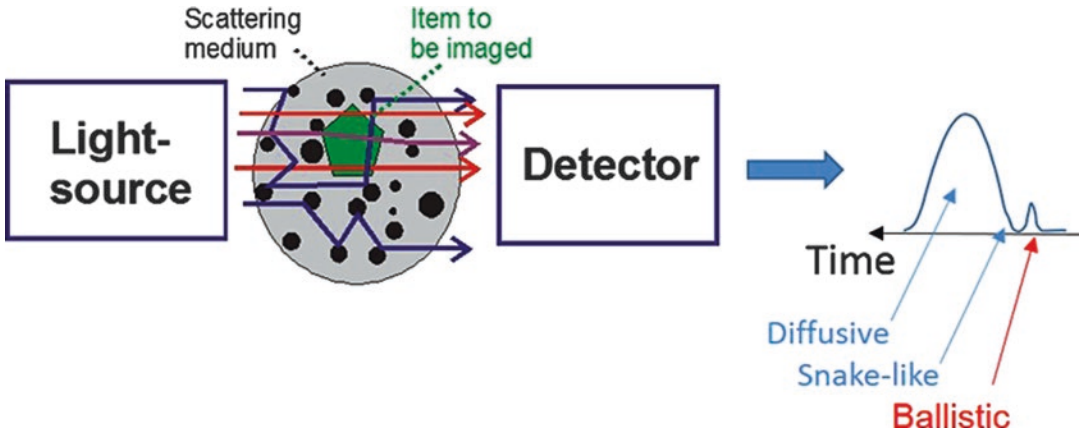

Fig. 16.11 Light scattering in tissue

If one aims to recover an image of the tissue from the transmitted photons, it is clear that the ballistic photons would contain the full image information. In contrast, the scattered photons would carry no image information anymore because of their arbitrary statistically distributed propagation paths. The snakelike photons may in some cases still contain some smeared-out image information.

Unfortunately, due to the high scattering coefficient, the transmitted light will mainly contain scattered photons. Any image information encoded in the ballistic photons is thus invisible by eye or with a standard camera because it is superimposed by a more or less unstructured background of scattered photons.

Accordingly, image concepts should be developed that separate the ballistic photons from the scattered ones or even suppress the scattered photons. Conceptually, one option is based on the fact that ballistic photons have a considerably shorter propagation path from the light source through the tissue to the detector than the multiply scattered photons. Accordingly, the ballistic photons have a much faster propagation time. If a pulsed light source is used, the ballistic photons might be filtered out with a fast enough camera that switches off after the arrival of the ballistic photons (Hee et al. 1993; Wang et al. 1991). But in practice, this approach suffers from enormous difficulties. For a clear separation of the ballistic photons, the light source should provide pulses considerably shorter than a picosecond (10^{-12}s), and the camera should detect only in a sub-picosecond time window. Though nonlinear optical schemes have been demonstrated to enable detection on such short-time scales (Wang et al. 1991), one fundamental problem cannot be overcome: the ultrashort pulses are substantially broadened in the tissue due to dispersion (i.e., wavelength dependence of the refractive index). Thus, the required temporal separation of the ballistic photons would not operate sufficiently in real biomedical tissue. Therefore, other separation schemes have to be implemented. In OCT, the coherence properties are used for separation of the ballistic photons (Huang et al. 1991). Before introducing the concept used in OCT, we first discuss the coherence of light sources.

16.3.2 Coherence, Interferometry, and Diffraction

Light is an electromagnetic wave. If its wavelength is exactly defined, the extension of this wave is infinite as indicated in Fig. 16.12a. In this case, the light is perfectly coherent that means all parts of the infinitely extended plane wave have well-defined phase relations to each other. Light from practical sources includes statistically distributed phase jumps as indicated in Fig. 16.12b.

In this case, the perfect phase relation of different parts of the wave is only maintained for the intervals in between two phase jumps. Accordingly, the perfect coherence is lost. To

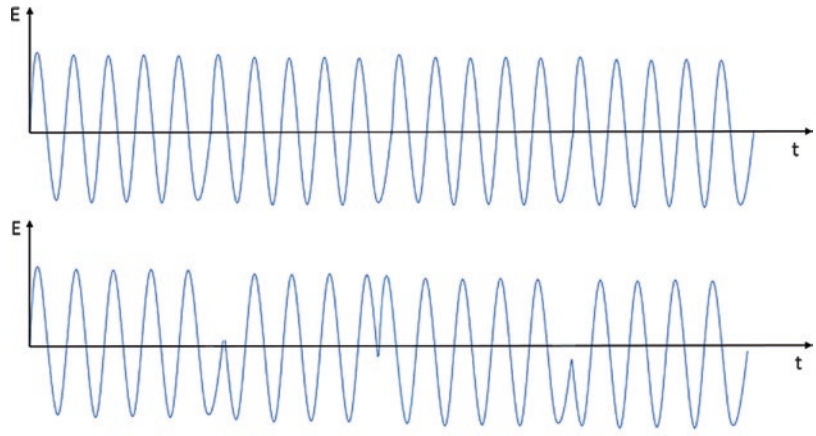

Fig. 16.12 $E(t)$ in a light wave with high (*top*) and low (*bottom*) temporal coherence

quantify the coherence, one defines the coherence length l_c of a light source as the average path length in between two phase jumps (Wolf 2007). Since light propagates with the speed of light c, the coherence length l_c is equivalent to a coherence time t_c given by $t_c = l_c/c$.

The coherence length of a light source is directly linked to its spectral distribution. As mentioned above, an ideal, perfectly coherent light source ($l_c = \infty$) consists of only one wavelength. For realistic light sources, the coherence length is finite and inversely proportional to the spectral width following $l_c = 0.44\frac{\lambda_0^2}{\Delta\lambda}$ (Wolf 2007) for a Gaussian-shaped spectrum with center wavelength λ_0 and spectral width $\Delta\lambda$.

Coherence is usually measured by autocorrelating the light source with itself in an interferometer arrangement, for example, a Michelson interferometer (Michelson 1881).

In a Michelson interferometer, a light beam is split into two parts with a beam splitter. The two parts propagate toward a mirror or retroreflector and are backreflected, recombined, and superimposed on a detector. The detector measures the time-integrated intensity of the superimposed light fields. One of the two interferometer arms can be changed in length, e.g., with a moveable mechanical stage. That means, the path length difference Δz or the time delay τ of the two arms can be varied. An interferogram corresponds to the signal $I(t)$ detected by the detector as a function of the delay time τ. When I_1 and I_2 are the intensities in the two arms, $I(t)$ is given by

$$I(\Delta z) = I_1 + I_2 + 2\sqrt{I_1 I_2}\,|\gamma(\Delta z)|\cos\frac{2\pi\Delta z}{\lambda},$$

$\gamma(\Delta z)$ being the coherence degree as a function of path delay (Hering and Martin 2006).

While I_1 and I_2 are independent of Δz, the third term that depends on Δz is called the interference term. Interference occurs when the two superimposed fields have a defined phase relation. If there is no phase relation, the time-integrated superposition averages out to zero, and the interference term disappears. In other words, an interference term is only detected if the path length difference between the two interferometer arms is shorter than the coherence length l_c. Thus, by measuring the interference signal as a function of Δz, one can determine the coherence length which is half the full width at half maximum of the coherence degree $\gamma(\Delta z)$.

So far, we have discussed the coherence of a light source in the propagation direction. This is usually called "temporal coherence" (Hecht 2005). In contrast, "spatial coherence" refers to the coherence in lateral direction (Hecht 2005). A light source with perfect spatial coherence exhibits no phase jumps along the lateral direction, i.e., perpendicular to the propagation direction. Spatially incoherent light sources are typically extended emitters, for example, standard light-emitting diodes with weak correlations between adjacent emission areas.

The important consequence for OCT is that the interference properties of the light source may be used to filter out the ballistic photons

carrying the image information. In particular, using light with a short coherence time or coherence length is advantageous (Huang et al. 1991). Let us consider to replace the short pulse light source in Fig. 16.11 by a light source with a short coherence length and to position the sample into one arm of an interferometer. Still, the ballistic photons have the shortest propagation path, and the multiply scattered photons have much longer propagation paths and require more time through the tissue. If the time difference between ballistic photons and scattered photons is larger than the coherence time, the interferometer can be moved to a position at which the ballistic photons contribute to the interference signal, while the scattered photons do not. This concept referred to as coherence filtering is the fundamental idea of optical coherence tomography (Huang et al. 1991). Its practical implementation will be discussed in the following section.

Before, let us briefly discuss what determines the spatial resolution in OCT. The coherence filtering implies that the resolution in propagation direction is determined by the coherence length of the light source. In a transmission geometry, the resolution would directly be given by the coherence length, while in the conventionally used reflection geometry, the resolution Δ_z in propagation direction or axial direction is given by $\Delta_z = l_c/2$. In OCT, the resolution in axial direction is decoupled from the resolution Δ_{xy} in lateral direction. Like in conventional optical imaging systems, the resolution Δ_{xy} in lateral direction, i.e., the minimum distance at which two objects can be separated, is given by Abbe's diffraction limit $\Delta_{xy} = \frac{\lambda}{2n\sin\alpha} = \frac{\lambda}{2\mathrm{NA}}$, λ being the wavelength of illumination, n the refractive index, α half the aperture angle of the optics, and NA the numerical aperture of the optics (Abbe 1873).

In practice, standard OCT systems provide axial resolutions in the range of a few µm, and their design usually provides similar values for the lateral resolution (Schmitt 1999) (Fig. 16.13).

In comparison to established nonoptical biomedical tomographic imaging concepts, OCT thus provides a uniquely high spatial resolution, while the penetration depth is significantly lower than for ultrasound imaging, magnetic resonance tomographic imaging (MRT), or computer tomography (CT) based on X-ray imaging.

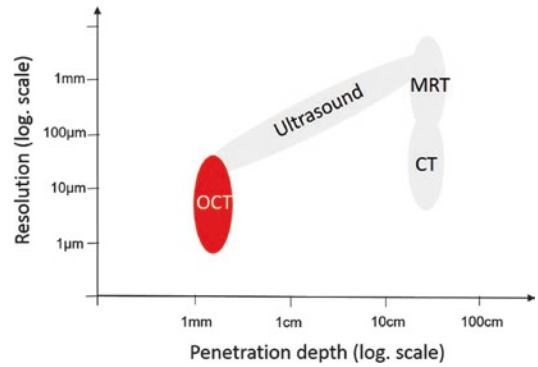

Fig. 16.13 Resolution versus penetration depth for OCT in comparison to ultrasound imaging, MRT imaging, and CT imaging

16.3.3 Fundamental Principles of Optical Coherence Tomography

Practical OCT systems are based on interferometers, typically on Michelson interferometers (Huang et al. 1991), but interferometers with different beam splitters for dividing and combining the beams allow higher flexibility and may use both rays from the second beam splitter, for instance, for differential detection. The various OCT concepts usually differ in the way the interferograms are recorded. The two main categories are time domain OCT (TD-OCT) (Huang et al. 1991) and frequency domain OCT (FD-OCT) sometimes called Fourier domain OCT (Leitgeb et al. 2003a). Both are schematically shown in Fig. 16.14

16.3.3.1 Time Domain OCT

A TD-OCT system consists of 3 main components: a broadband light source, the interferometer with sample arm and moveable reference arm, and the detector. As the broadband light source, one may use femtosecond laser systems (Morgner et al. 2000), white light continuum sources (Hartl et al. 2001), or superluminescent light-emitting diodes (LEDs) (Bayleyegn et al. 2012). Femtosecond lasers and white light continuum sources offer extremely broad spectra in excess of a few hundred nanometers (nm) and thus

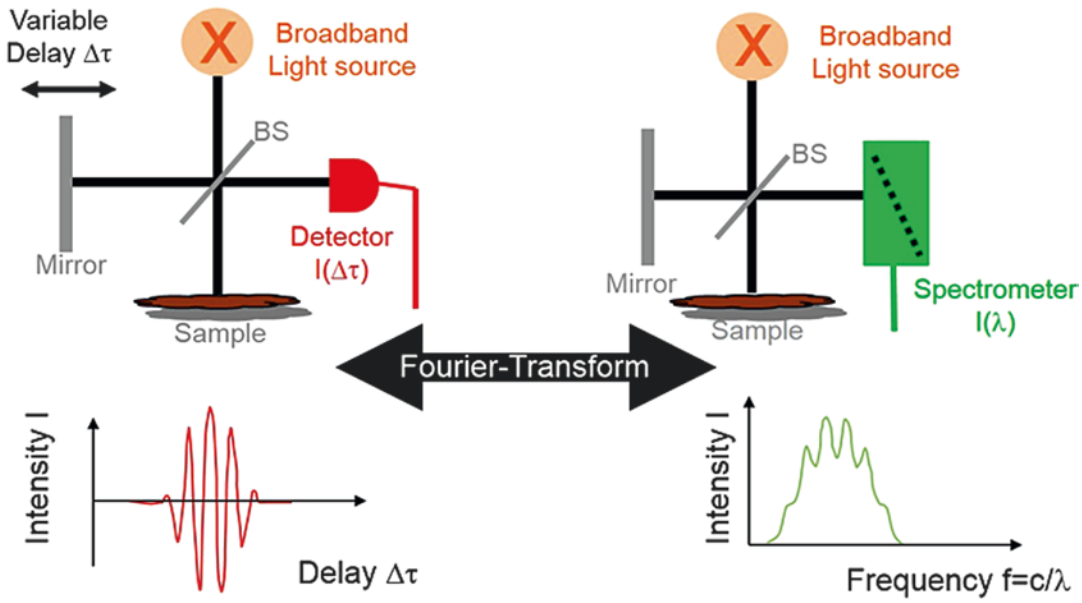

Fig. 16.14 TD-OCT (*left*) and FD-OCT (*right*). BS: beam splitter

enable axial resolutions down to the very few micrometer (μm) range (Bouma and Tearney 2002). But these systems are expensive and complex. In contrast, superluminescent LEDs provide spectral bandwidths of several tens of nm up to about 100 nm (Bayleyegn et al. 2012) and are much more compact and cost-effective than the other sources. Thus, most standard OCT systems use superluminescent LEDs as light sources.

The output beam of the broadband light source is coupled into the interferometer where a beam splitter divides it into two parts. One part propagates to the sample under investigation where it is backreflected and then it propagates back and is directed onto the detector. The other part of the beam propagates into the reference arm which contains a mirror or retroreflector on a moveable delay stage. After reflection, it propagates back via the beam splitter and is also directed to the detector where it interferes with the beam from the sample arm (Huang et al. 1991).

The detector is a standard photodetector in the easiest realization. Alternatively, photomultipliers or avalanche photodiodes may be used to increase sensitivity.

An interferogram is generated when the interference signal is measured as a function of the time delay Δt between reference arm and sample arm. When we consider that the sample is partially transparent and contains multiple reflecting interfaces inside, then the reflections of interfaces at different depths will appear at different times. Only when the propagation time to the corresponding interface and back corresponds within the coherence time of the light source to the propagation time through the reference arm, the backreflection from that interface will contribute to the interference signal. In other words, when the length of the reference arm is changed, only light reflected back from the sample that had the same propagation path length as that through the reference arm contributes to the interferogram. Accordingly, the position of the reference arm addresses a certain depth in the sample, and the strength of the interferogram at this position is a measure of the backreflection at that certain depth. In particular, interfaces between different substances in the sample will create stronger backreflections, so-called echoes of light (Drexler and Fujimoto 2008). Recording the strength of these echoes, i.e., the amplitude of the interference signal as a function of delay time or path length difference in the interferometer, provides a one-dimensional depth scan into the sample or a so-called A-scan (Drexler and Fujimoto 2008). In practical systems, the scanning of the reference

arm induces a Doppler shift in frequency which is used in the signal detection scheme (Drexler and Fujimoto 2008).

For a two-dimensional (so-called B-scan) or three-dimensional image, mechanical scanning in the two directions perpendicular to the axial direction is required. This might be done with mechanical delay stages or, more practically, with galvanometer scanners (Duma et al. 2011) and microelectromechanical systems (Sun et al. 2010).

A disadvantage of TD-OCT systems is the limited speed, specifying the number of A-scans per second. The speed is mostly limited by the mechanical scanning of the delay line (Kim and Kim 2010). Many efforts have been made by using multiple reflections, piezoelectric-driven fiber-optic delay lines, and more. The fastest systems achieve A-scan rates of a few kHz with rapid scanning optical delay lines (RSOD) using resonantly driven mirror systems (Gao 2007).

16.3.3.2 Frequency Domain OCT

The interference signal represents a correlation of the fields from the reference and from the sample arm. According to the Wiener–Khintchine theorem, the Fourier transform of this correlation provides the spectral power density (Goodman 1985). In other words, the interferogram and, correspondingly, an A-scan can also be obtained when the spectrum of the interference signal is recorded and then Fourier transformed. This is the principle of Frequency domain or Fourier domain OCT which is also referred to as spectral radar (Bail et al. 1996). Another explanation is that for each wavelength, interference occurs independent of the path difference, and the phase of the interference depends on the product of path difference and wave number (reciprocal value of the wavelength) of the light. One advantage of FD-OCT over TD-OCT is that no movement of a mirror in the interferometer arm is required. On the other hand, FD-OCT requires spectrally resolved detection. This can either be done with a spectrally resolving detector or with a spectrally scanning source (so-called swept source OCT) (Chinn et al. 1997).

In the first case, the spectrometer is mostly realized by a grating for dispersion and a line array detector for simultaneous detection of the different spectral components (Bail et al. 1996). These systems are often called spectral domain OCT (SD-OCT). For systems operating in the near-infrared range below 1 μm wavelength, this concept is well established because cost-effective line array detectors based on silicon technology are available. For wavelengths considerably above 1 μm, the silicon detector arrays have to be replaced by InGaAs detectors which are much more expensive.

Costly InGaAs line detectors can be avoided in the second case. In a swept source OCT system, also called optical frequency domain imaging (OFDI), one or two (in the case of differential detection) integrating detectors are used, and the source wavelength varies over time (Chinn et al. 1997). So the different wavelengths are detected sequentially, and no spectral resolution of the detector is required. Recently, extremely fast tunable swept sources have been demonstrated allowing up to 20 million A-scans per second enabling real-time 3D OCT imaging also called 4D imaging (Gora et al. 2009; Kottig et al. 2012; Wieser et al. 2010). Today's typical FD-OCT systems using commercially available swept sources or fast line scan cameras achieve A-scan rates in the range of 100 kHz.

While TD-OCT and FD-OCT systems generally provide similar physical information about the sample, FD-OCT systems have been shown to be more sensitive by a factor that scales with the square root of the number of spectral points (Choma et al. 2003; de Boer et al. 2003; Leitgeb et al. 2003a). To enable a fast processing of the data, the Fourier transformation is generally implemented as a FFT. Because neither the grating spectrometer nor the tunable source usually provides data linear in wave number, linearization of the data, often combined with oversampling, is applied before the FFT (Vergnole et al. 2010). For spectrometer-based systems of medium bandwidth, a combination of grating and prism can be used for linearization of the spectrum instead (Hu and Rollins 2007; Traub 1990). A further step in processing FD-OCT data is called spectral shaping. As the spectrum of the light source in combination with the sensitivity of

the detector and the spectral transmission of the interferometer is neither flat nor Gaussian, spectral shaping is used to produce a spectral form of the interference that leads to moderate artifacts after the FFT. Typical window functions used are Hanning and truncated Gaussian (Eigenwillig et al. 2009).

While TD-OCT detects only the interference between light from the reference arm and the sample, FD-OCT also detects the interference between different reflections within the sample arm or other unintended reflections in the optical setup. This can lead to ghost images, often caused by the strong Fresnel reflex of the first sample surface, and fixed pattern structures. Such artifacts can be suppressed by implementing enough dispersion between reference and sample arm (Kottig et al. 2012). While dispersion between both interferometer arms, broadening the interference signal and by this decreasing the axial resolution, can be numerically compensated in FD-OCT, this is more complicated in TD-OCT (Wojtkowski et al. 2004).

For systems with high lateral resolution, TD-OCT offers the advantage that the focus position can be shifted synchronously to the length of the reference arm allowing high lateral resolution over a large depth range (Schmitt et al. 1997).

TD-OCT and FD-OCT can be parallelized in one or two dimensions by using additional detector dimensions. Especially in TD-OCT, using camera-based systems allows sampling of complete frames which is then called full-field OCT (FF-OCT) providing en face images sequentially (Dubois et al. 2002). The disadvantage in FD-OCT is that due to the longer measurement time for the extra dimensions(s), the image will be more compromised by movement artifacts (Yun et al. 2004). Moreover, all parallel systems are more sensitive to artifacts due to multiple scattering because of the loss of the confocal advantage (Garini et al. 2006).

Besides central wavelength, resolution, speed, and measurement range, two more parameters are used to characterize OCT systems. The first is the sensitivity specifying the minimal reflectivity of a plain surface that results in a signal equivalent to the noise level. Because of the interference principle, very low levels can be detected and typical values of the minimal reflectivity are in the range of 10^{-10} corresponding to a sensitivity of 100 dB. Sometimes this parameter is called the signal-to-noise ratio (SNR) of the system as well. A second parameter is the dynamic range of the system which is the largest signal that does not saturate the detector or the electronics. Especially in FD-OCT, clipping of the signal, often caused by Fresnel reflexes, leads to strong artifacts and should be avoided. Due to the large dynamic range of OCT signals, mostly the logarithmic intensity data are visualized on a gray or false color map.

While in spectrometer-based FD-OCT systems, the limited resolution of spectrometers leads to a sensitivity roll off at the end of the measurement range of 10–20 dB (Bajraszewski et al. 2008), a similar degradation in swept source OCT systems is often caused by the limited frequency range of the detector and the coherence length of the sweeping light source. Additionally, the confocal principle leads to a signal drop outside of the focus that depends strongly on the used numerical aperture of the probe beam. Typical numerical apertures used in FD-OCT are therefore in the range of 0.05, yielding transversal resolutions of typically 10 wavelengths.

While alterations by transversal motion in images from SD-OCT and OFDI systems are similar, both are affected quite differently by axial sample motion (Yun et al. 2004). Axial motion will lead to fringe washout in the case of SD-OCT, while it leads to false positions in the case of OFDI. Oblique motion can in general not be treated as the sum of both effects (Walther et al. 2008).

16.3.4 Extended Functionalities

16.3.4.1 Spectroscopic OCT

Spectroscopic OCT (S-OCT) is an extension of the intensity-based backscattering images in standard OCT. Since OCT images are recorded with broadband light, the spectral distribution of the light will be affected by absorption and scattering in the tissue. In other words, if characteristic

absorbers or scatterers are present in the tissue, they will imprint characteristic features into the spectra of the backscattered light. These characteristic features may be analyzed to add spectroscopic information to the OCT images by an additional color map. This may enable a kind of "optical histology" including digital staining based on absorbing chromophores or characteristic sizes of scatterers (Kartakoullis et al. 2010; Robles and Wax 2010; Xu et al. 2005) inside the tissue. For example, in the near infrared, hemoglobin is a relevant substance for functional imaging with OCT (Faber et al. 2005; Faber and van Leeuwen 2009; Lu et al. 2008; Robles and Wax 2010) because its state of oxygenation influences its spectral properties. Other chromophores in the tissue with less pronounced spectral features in the optical window include melanin, bilirubin, and water (Anderson and Parrish 1981). The spectra are also sensitive to scatterers which are in the same order as the wavelength of the light. This may be used to analyze tissue structures below the resolution of the OCT system (Robles and Wax 2010; Yi et al. 2013). In addition to the existing tissue ingredients, contrast agents for S-OCT, for example, dyes (Xu et al. 2004) or nanoparticles (Lee et al. 2003; Oldenburg et al. 2009), may be used.

In principle, there are hardware-based and software-based S-OCT concepts. The hardware-based concepts use multi-band systems to obtain spectrally resolved OCT images in a differential manner (Cimalla et al. 2009; Storen et al. 2006). Software-based approaches use time-frequency distributions that extract the spectroscopic information from the raw OCT data, which can be recorded with standard OCT systems. In a first attempt, Morgner et al. performed spectroscopic analysis using a software-based approach on the basis of TD-OCT data (Morgner et al. 2000), while Leitgeb et al. used a FD-OCT system (Leitgeb et al. 2000). In practice, S-OCT still faces serious challenges. First, spectral features are often weak and superimposed by noise-like speckle and wavelength-dependent optical aberrations of the OCT system (Faber et al. 2005; Kasseck et al. 2010). Moreover, using time-frequency distributions, there is a tradeoff between spectral resolution and spatial resolution that has to be considered (Robles et al. 2009). But in spite of these difficulties, recent work has demonstrated that spectroscopic analysis may add significant contrast to the OCT images (Fleming et al. 2013; Jaedicke et al. 2013; Robles et al. 2011; Yi et al. 2014).

16.3.4.2 Polarization-Resolved OCT

In order to get more information or another contrast in OCT images, polarization-sensitive OCT (PS OCT) was introduced. Aligned structures like muscles or fibers show birefringence and thereby influence the polarization of the beam allowing depth-resolved measurement of the distribution and orientation of these structures. Birefringence of the sample might influence images even in normal OCT systems, resulting in horizontal stripes, as the polarization of sample and reference light from some depth will not be aligned, leading to a loss of signal (Cimalla et al. 2009). Most PS OCT systems detect at least two orthogonal linear polarization states of the reflected beam. In order to get similar intensities in both polarization states of the reference beam, a quarter wave plate is inserted into the reference arm. Moreover, a second quarter wave plate in the sample beam ensures circular polarization on the sample. Size and orientation of the birefringence can be calculated from amplitudes and phases of both interference signals (de Boer et al. 1997; Hee et al. 1992; Hitzenberger et al. 2001). While controlling the polarization is relatively easy in the case of bulk optics, the higher flexibility of fiber-coupled scanner heads demands for more complicated solutions (Al-Qaisi and Akkin 2010; Götzinger et al. 2009; Yamanari et al. 2008). One of the most important applications of PS OCT is the visualization of the retina. The retinal pigment epithelium (RPE) has the interesting property that it depolarizes the scattered light. Therefore, the homogeneity of polarization, called the degree of polarization uniformity (DOPU), is often shown as an additional contrast to differentiate this layer. PS OCT is also used to differentiate carcinoma and to distinguish between normal and burned tissue (Park et al. 2001).

16.3.4.3 Doppler-OCT

The visualization and quantification of flowing blood are one of the main applications of Doppler-OCT (DOCT). DOCT was first introduced in TD-OCT by detecting the frequency shift of the interference signal caused by axially moving scatterers (Xu et al. 2008). Much higher sensitivity to axial movement can be achieved by analyzing the phase of the interference signals in consecutive A-scans at the same or nearly the same position (Leitgeb et al. 2003b). This method, called phase resolved Doppler-OCT, is today used in TD-OCT and FD-OCT. A high spatial oversampling yielding a great overlap of the two beam profiles is beneficial for a good sensitivity of DOCT (Walther and Koch 2009). Other methods using phase modulators in the reference arm (Bachmann et al. 2007) or changing the length of the reference arm to highlight moving structures (Wang et al. 2007b) have shown remarkable results. As phase data are often very noisy, different ways of averaging have been suggested. Most commonly, the phase φ is calculated by calculating the phase of the sum of products of consecutive A-scans:

$$\varphi = \arg\left[\sum_{j} {}_{j+1}(z)\cdot\Gamma_{j}{}^{*}(z)\right]$$

$\Gamma_j(z)$ is the complex result of the FFT of the A-scan j at depth z and "*" denotes the complex conjugate. In the case of low SNR, analyzing a set of A-scans using a 2D Fourier transformation, called joint spectral and time domain OCT (STdOCT), may be beneficial (Szkulmowski et al. 2008). More sophisticated strategies for averaging Doppler data can be found in Chan et al. (2014) and Walther et al. (2014).

Doppler information is mostly visualized by a false color map, where the intensity is given by the logarithmic intensity of the signal and the color from blue over white to red indicates the phase in the interval of $\pm\pi$, with white indicating no axial motion. In the case of smooth velocity distribution, phase shifts much above $\pm\pi$ can be analyzed by unwrapping techniques, but in SD-OCT artifacts caused by the detector integration time may cause huge discrepancies at higher flow velocities depending on the angle of the flow (Walther et al. 2010).

An example of a phantom measurement, highlighting potentials and problems of the flow through different capillaries, is shown in Fig. 16.15. The different images show human blood or 1 % intralipid solution, often used as a substitute for blood in Doppler measurements, through a rectangular and a circular capillary in opposite directions. The angle of both capillaries was the same. While the top row shows only the intensities, the bottom row is colored as a function of the phase shift or velocity. To reduce the influence of the speckle noise, 256 B-scans are averaged. In spite of this averaging, the left images without flow still show the granularity of blood. The echo from intralipid is quite homogeneous as can be seen in the images on the right. Vice versa flowing blood shows echoes in the form of an hourglass, caused by the circular orientation of erythrocytes in flowing blood (Cimalla et al. 2011a). Especially at the backreflections from the capillaries in the case of blood, high phase shifts can be seen. This effect, called Doppler shadow (Bukowska et al. 2010), is attributed to multiple scattering (Kalkman et al. 2012) and is less pronounced in the case of intralipid.

Besides algorithms based on the phase shift, intensity-based algorithms evaluating the variance in repetitive scans have been used especially for angiography showing high contrast images of blood vessel structure in the hamster skin, for example (Liu et al. 2011). A comparison of different methods and their advantages and disadvantages is found in (Liu et al. 2012).

An application for Doppler imaging in small animals is the observation of blood flow in vessels of mice. Blood flow in these vessels is regulated by the contraction of the vessel muscles in the arteries. As the veins have no musculature, their diameter will only change passively by inner or outer pressure. While vasoconstriction may be caused by application of potassium, vessels will dilate after the application of sodium nitroprusside (SNP). A dysfunction of this regulation mechanism is associated with arteriosclerosis. Due to its advantageous position, imaging was performed at the arteria and vena saphena

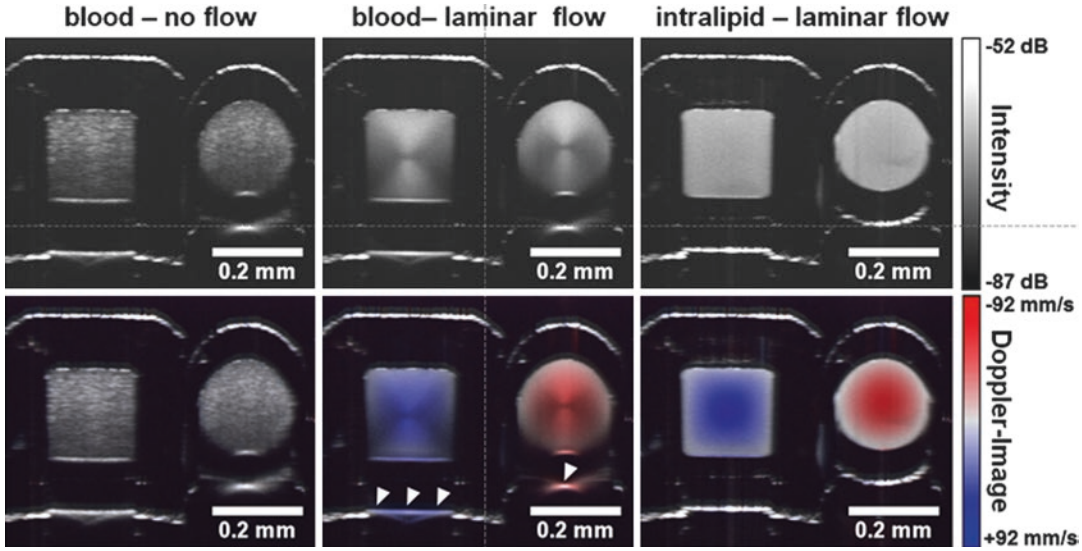

Fig. 16.15 Phantom measurement for Doppler imaging with OCT. The upper part on the left side shows the image of blood with no flow. Below additional Doppler processing shows no difference. The images in the middle show corresponding images for flowing blood. The square capillary and the circular capillary have opposite flow directions. Echoes behind the structure show the so-called Doppler echo which is attributed to multiple reflections. The inhomogeneous structure is attributed to the alignment of erythrocytes in the flowing blood. The images on the right side are taken with intralipid showing less Doppler echo and no inhomogeneity. To reduce the speckle noise, the images were averaged over 50 B-scans

with a dual-band OCT system. The dual-band system nicely shows the higher phase changes at the smaller wavelength. Quasi M-scans are shown in the middle and bottom of Fig. 16.16, showing the oscillating blood flow in the artery and the almost constant blood flow in the vein. The low amplitude of the backscattered signal in the center of the vessels is attributed to the alignment of the erythrocytes as stated above.

16.3.4.4 Contrast Enhancement by Nanoparticles: Photothermal OCT and Magnetomotive OCT

Compared to other optical imaging techniques such as fluorescence microscopy, OCT is a rather unspecific modality that provides only general information on the tissue structure based on light scattering on cells and cellular components such as the nuclei and mitochondria. Hence, to improve visibility of specific tissues or cells, OCT contrast agents are required. Several attempts have been made to find a suitable contrast agent for OCT including dyes and plasmon-resonant nanoparticles, which have distinct absorption spectra and therefore can be detected by means of spectroscopic OCT (Cang et al. 2005; Oldenburg et al. 2009; Xu et al. 2004; Yang et al. 2004a). However, these absorption-based methods always suffer from an inherent concentration-path length tradeoff. In order to detect a sufficient absorbance, either a long propagation length through the absorber is required, which consequently degrades axial resolution, or a high concentration of absorbing agents is necessary, which is often not tolerated by the specimen.

However, since OCT is very sensitive to motion due to the coherent nature of the illuminating light, the most promising approaches – photothermal and magnetomotive OCT – use dynamic contrast agents to enhance visualization of specific substances.

In photothermal OCT, gold nanoparticles inside the sample are remotely heated by illumination with intense laser light (>20 mW). For that purpose, the emission wavelength of the laser is matched to the plasmon resonance absorption maximum of the particles. The illuminated

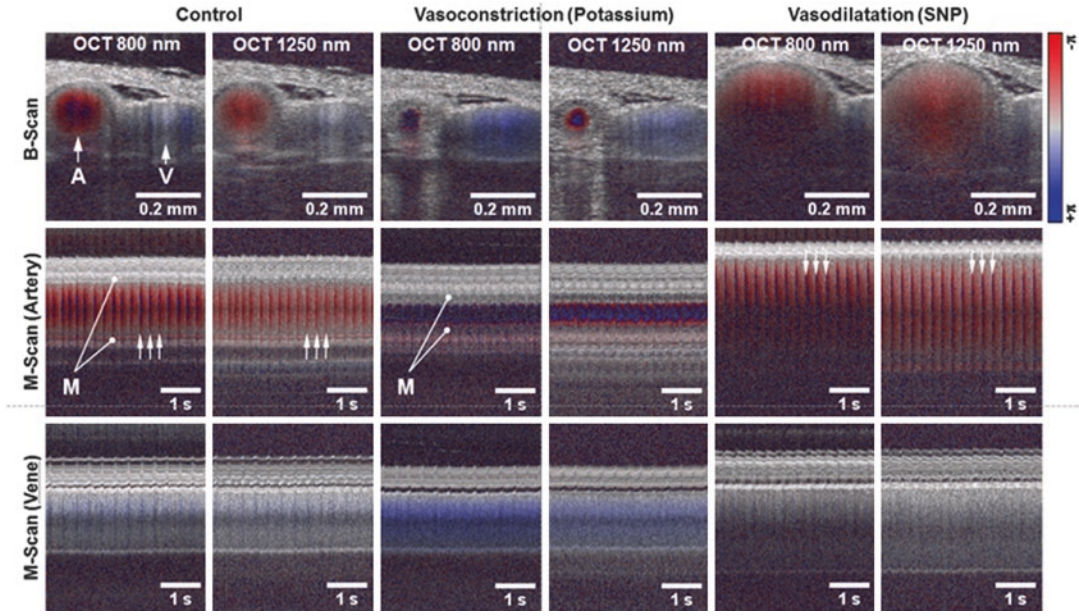

Fig. 16.16 *Top row*: single B-scans showing a cross section through the artery and vein in mice. *Left side* control, middle vasoconstriction after the application of potassium, *right side* vasodilatation caused by the application of SNP. As stated in the columns, images were taken at the same time at center wavelengths of 800 nm and 1250 nm. Due to the shorter wavelength, the phase change is larger in the 800 nm band. Related to this, a phase wrap (phase change more than $\pm\pi$) is first seen in the 800 nm band. Nevertheless, in the case of vasoconstriction, phase wrap is seen in both bands. A-scans selected in the center of the artery (*middle*) and vein (*bottom*), indicated by *A* and *V* in the upper *left part*, from sequential B-scans, forming a quasi M-scan, highlight the highly pulsating blood flow (see *arrows*) in the artery and the slightly modulated blood flow in the vein. The musculature of the artery (*M*) can be nicely seen, especially in the case of vasoconstriction

particles also heat their immediate vicinity causing thermal expansion of the microenvironment. Hence, resulting sample motion in the submicron regime is then detected by OCT using phase information (Adler et al. 2008). Sufficient sensitivity is achieved by modulating the laser (turn on/turn off periodically) and searching for the corresponding frequency in the OCT phase signal. Photothermal heating can be performed at relatively high frequencies of 0.5–20 kHz (Zhou et al. 2008), which enables fast image acquisition.

Therefore, among others, photothermal OCT was successfully applied for pharmacokinetic studies to noninvasively image nanoparticle accumulation in mouse mammary tumors (Tucker-Schwartz et al. 2014).

Furthermore, photothermal OCT is not necessarily bound to the presence of gold nanoparticles. Also, the absorption profile of endogenous chromophores such as hemoglobin can be used for imaging (Yim et al. 2014). Since the absorption spectra of oxy- and deoxyhemoglobin differ, photothermal OCT can be applied to assess the blood oxygenation level both in vitro (Kuranov et al. 2011a) and in vivo, e.g., in the murine brain cortex (Kuranov et al. 2011b).

However, attention must be paid to keep sample temperature below 44 °C to avoid thermal damage of biological tissue. Furthermore, photothermal OCT is not suited for imaging of photosensitive tissue such as the retina due to the use of intense light.

In magnetomotive OCT, magnetic micro- or nanoparticles are used as dynamic contrast agents, which are exited into motion by an external magnetic field. Contrast enhancement is then achieved by quantifying the displacement of the elastic tissue next to the particles using the amplitude or phase information of the OCT signal (Oldenburg et al. 2005a, 2008).

In this context, it was shown that magnetomotive OCT is a suitable method for contrast-enhanced imaging of single magnetically labeled cells in vitro (Oldenburg et al. 2005b). Proof-of-principle in vivo magnetomotive imaging was demonstrated in African frog (*Xenopus laevis*) tadpole (Oldenburg et al. 2005a) as well as in the mouse eye (Wang et al. 2010b). Furthermore, similar to photothermal OCT, magnetomotive OCT was also successfully applied to image the accumulation of targeted magnetic nanoparticles in rat mammary tumors (John et al. 2010).

Typically, superparamagnetic iron oxide particles are used for labeling of biological samples. Compared to ferromagnetic materials, these particles exhibit lower forces in a magnetic field due to their smaller magnetization capability. However, iron oxide is much better suited in terms of biocompatibility since pure iron in higher concentrations is cytotoxic.

In contrast to photothermal OCT, modulation of the magnetic field in magnetomotive OCT is restricted to relatively low frequencies of 0,1–1 kHz (Kim et al. 2013) since fast switching of sufficiently high magnetic fields is technically challenging. Furthermore, magnetomotive imaging is limited to small working distances because magnetic field strength rapidly degrades with distance from solenoid.

16.3.5 OCT for Small Animal Imaging

16.3.5.1 Retina Imaging

The retina was one of the first samples investigated with OCT, since it has the unique advantage to be visualized through the transparent ocular media. In this context, OCT provides in vivo cross-sectional visualization of the retinal microstructure that cannot be obtained by any other noninvasive imaging modality (Drexler and Fujimoto 2008). Therefore, the clinical application of OCT is mostly developed in ophthalmology for the diagnosis, staging, and monitoring of ocular diseases primarily macular pathologies such as age-related macular degeneration (AMD), central serous retinopathy, macular holes and edema, Stargardt disease, and retinitis pigmentosa but also optic neuropathies such as glaucoma. Today, several commercial ophthalmic OCT devices are available, which use high-speed spectral domain detection. All instruments have comparable performance with an axial resolution of 4–6 μm operating in the 800 nm wavelength range and imaging speeds of 25,000–40,000 axial scans per second (Wolf-Schnurrbusch et al. 2009), which enables real-time two-dimensional imaging of tissue cross sections.

As an alternative or extension to the conventional ophthalmic imaging at 800 nm, research OCT systems operating at 1050 nm have also been demonstrated. Due to less absorption of the retinal pigment epithelium and reduced tissue scattering on the one hand and still sufficiently low light absorption by means of the aqueous ocular media in front of the retina on the other hand, this spectral range allows depth-enhanced visualization of the choroid (Povazay et al. 2003; Unterhuber et al. 2005) and improved visibility of the retina in patients with opaque ocular media, i.e., cataract (Povazay et al. 2007).

As stated above, one particular feature of OCT is that the axial resolution is decoupled from the transverse or lateral resolution. The axial resolution is mainly given by the coherence length of the applied light source, while the lateral resolution is defined by the numerical aperture of the focusing optics, i.e., the beam diameter and the focal length, like in conventional microscopy. In ophthalmic imaging, the eye's cornea and lens are used as the imaging objective. Therefore, the lateral resolution is limited by the pupil size and the focal length of the eye and, in practice, even further reduced by ocular aberrations. In order to overcome this practical limitation, adaptive optics – well known in the field of astronomy – is applied in research OCT systems to correct ocular aberrations. These instruments measure the wavefront distortion caused by the ocular media and correct it by means of deformable mirrors or liquid crystal phase modulators. It was shown that adaptive optics can significantly improve lateral resolution to 2–3 μm compared to 15–20 μm in conventional ophthalmic OCT (Povazay et al. 2009). Furthermore, this technique increases

imaging sensitivity especially in the range of the photoreceptor layer and reveals single structures located at the inner/outer photoreceptor segment junction and the posterior tips of the photoreceptor outer segments, which are assumed to represent individual cone cells in humans (Fernández et al. 2008; Zhang et al. 2006) as well as in animal models such as mice (Jian et al. 2013). The combination of high axial resolution OCT with aberration-correcting adaptive optics is therefore often referred to as cellular imaging of the living retina.

For the understanding of the mechanisms underlying retinal degeneration and trial of potential therapeutic strategies, experimental animal models play an important role. In this context, OCT also enables noninvasive monitoring of the retina in small animals like rats (Nagata et al. 2009), mice (Horio et al. 2001) and even zebrafish (Bailey et al. 2012; Weber et al. 2013). The last-mentioned one is of particular interest for researchers and vision scientists since the zebrafish has the ability to regenerate neuronal tissue including the retina – a phenomenon that is not observed in mammals. Although animal imaging is mostly performed in the 800 nm wavelength range (Huber et al. 2009; Kocaoglu et al. 2007; Ruggeri et al. 2007) as in humans, OCT of the rodent retina is also reported at 1060 nm (Hariri et al. 2009) and 1300 nm (Li et al. 2001). It was shown that there is a good correlation between OCT data and histology (Huber et al. 2009), thus enabling OCT to be a valuable tool to analyze and monitor microstructural changes in the retina for noninvasive time-course studies in individual animals.

An example for in vivo OCT imaging and monitoring of the mouse retina is depicted in Fig. 16.17.

In human retinal imaging, the sample beam is conventionally relay imaged onto the pupil by means of a lens pair and focused onto the fundus by the eye itself, which was also applied for retinal imaging in mice and rats (Kocaoglu et al.

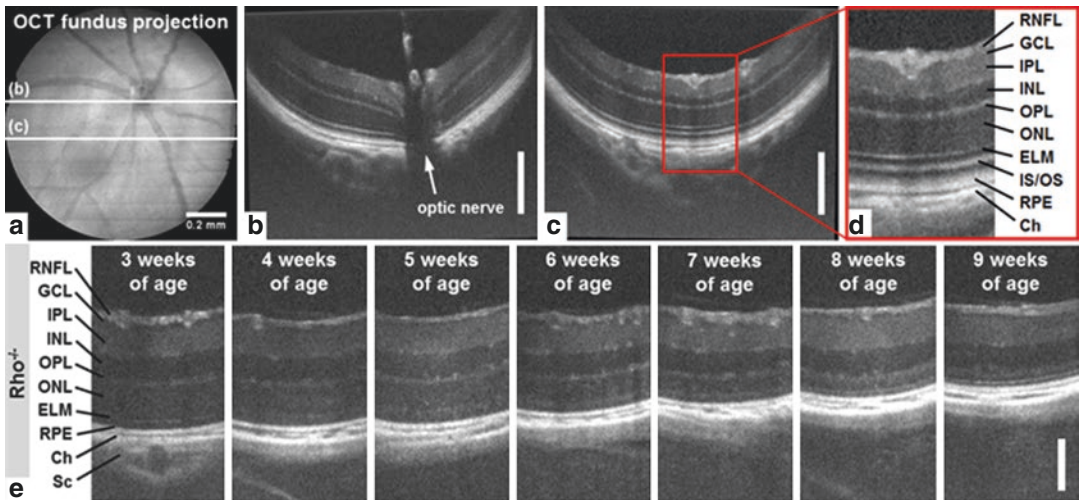

Fig. 16.17 High-resolution OCT imaging of the mouse retina in vivo. (**a**) OCT fundus projection and representative OCT cross sections (**b**, **c**) of the healthy mouse retina (*vertical bars*, 200 µm). (**d**) Detailed view of the retinal microstructure (abbreviations: *RNFL* retinal nerve fiber layer, *GCL* ganglion cell layer, *IPL* inner plexiform layer, *INL* inner nuclear layer, *OPL* outer plexiform layer, *ONL* outer nuclear layer, *ELM* external limiting membrane, *IS/OS* inner/outer photoreceptor segment junction, *RPE* retinal pigment epithelium, *Ch* choroid, *Sc* sclera). (**e**) Longitudinal OCT monitoring of genetic retinal degeneration in one individual rhodopsin-deficient ($Rho^{-/-}$) mouse at different ages (vertical bar, 100 µm). The $Rho^{-/-}$ degeneration as a model for recessive inherited retinitis pigmentosa is characterized by a progressive loss of the outer nuclear layer (ONL), which represents the nuclei of the photoreceptors. At an age of 9 weeks, the ONL has almost completely vanished, so that only a minor fraction of photoreceptors is left at this stage. All images were acquired with an experimental hybrid imaging system slightly modified in comparison to the one described in (Cimalla et al. 2012)

2007; Ruggeri et al. 2007). However, it is reasoned by others that this method is not optimal for small animals since the small size and short focal length of the eye imply a high numerical aperture objective lens design in order to cover a large measurement area on the retina. In addition, the short focal length of the eye increases aberration, which degrades the OCT signal and reduces image quality. Alternatively, a contact lens made from a microscope coverslip and hydroxypropyl methylcellulose solution is used, which effectively removes the refractive power of the air–cornea boundary and allows the sample beam to be focused directly onto the retina. Due to the corresponding enlargement of the eye's focal length, lower numerical aperture lens designs can be applied to cover a sufficient measurement area on the retina. Furthermore, this technique reduces corneal aberrations and prevents the eye from dehydration (Kim et al. 2008; Srinivasan et al. 2006), which would otherwise lead to corneal opacity.

Due to their small sizes, it is possible to image the entire eyes of mice and zebrafish from the cornea to the retina in one single OCT scan. This technique allows noninvasive quantitative assessment of biometric parameters such as intraocular distances and interface curvatures of ocular media, which is of interest in eye development research (Wang et al. 2010c; Zhou et al. 2008) and eye modeling for improved design of optical instruments (Gaertner et al. 2014).

Recent developments in the experimental and commercial sector tend toward multimodal imaging of the small animal retina using OCT in combination with other established methods such as scanning laser ophthalmoscopy (SLO), fluorescence angiography (FA), and fundus autofluorescence (FAF), which deliver additional information about fundus morphology, blood flow, and metabolism (Fischer et al. 2010; Huber et al. 2009, 2010; Seeliger et al. 2005).

An example for multimodal in vivo imaging of the mouse retina using OCT and fluorescence angiography is shown in Fig. 16.18.

In addition to the morphological and molecular contrast acquired by optical imaging techniques, functional information about photoreceptor and interneuron activity can be obtained by means of electroretinography (ERG). In this context, simultaneous OCT and ERG for parallel monitoring of the retinal structure and function in experimental animal models such as rats (Moayed et al. 2010) allows advanced analysis of retinal degeneration processes in vivo.

Furthermore, attempts have been made to retrieve functional information from the OCT signal itself. To that, local changes in the retina's optical properties following to light stimuli are detected by means of OCT. These intrinsic optical signals, which could by now be observed in the human retina (Schmoll et al. 2010) as well as in chicken (Moayed et al. 2011), were found to be restricted to the stimulated fundus region and to show some correlation with ERG recordings.

16.3.5.2 Lung Imaging

Due to a lack of imaging technologies having sufficient resolution for resolving single alveoli and delivering three-dimensional data at high frame rates, there is a high interest in using OCT for imaging airway wall and alveolar structures in animal studies. Lung function in healthy and diseased lungs is of high interest for several reasons. Some interest is related to the transport of inhaled particles for drug delivery and risk due to smoking (Yin et al. 2009). Further airway remodeling in connection with asthma may reduce the airway distensibility. Moreover, interest in visualization of alveoli and alveolar structures is related to the high morbidity of acute respiratory distress syndrome (ARDS) and ventilator-induced lung injury (VILI), which in spite of numerous efforts declines only slowly. A better understanding of processes during artificial ventilation might help in improving ventilation strategies.

Several strategies have been applied to image airway and alveolar structures with OCT. External scanning can be applied to isolated lungs visualizing the alveolar structure close to the pleura (Meissner et al. 2009b; Mertens et al. 2009). With some effort, this method can also be applied to anesthetized animals by opening the chest or by preparing a thoracic window in vivo (Meissner et al. 2010a). This method has been applied to

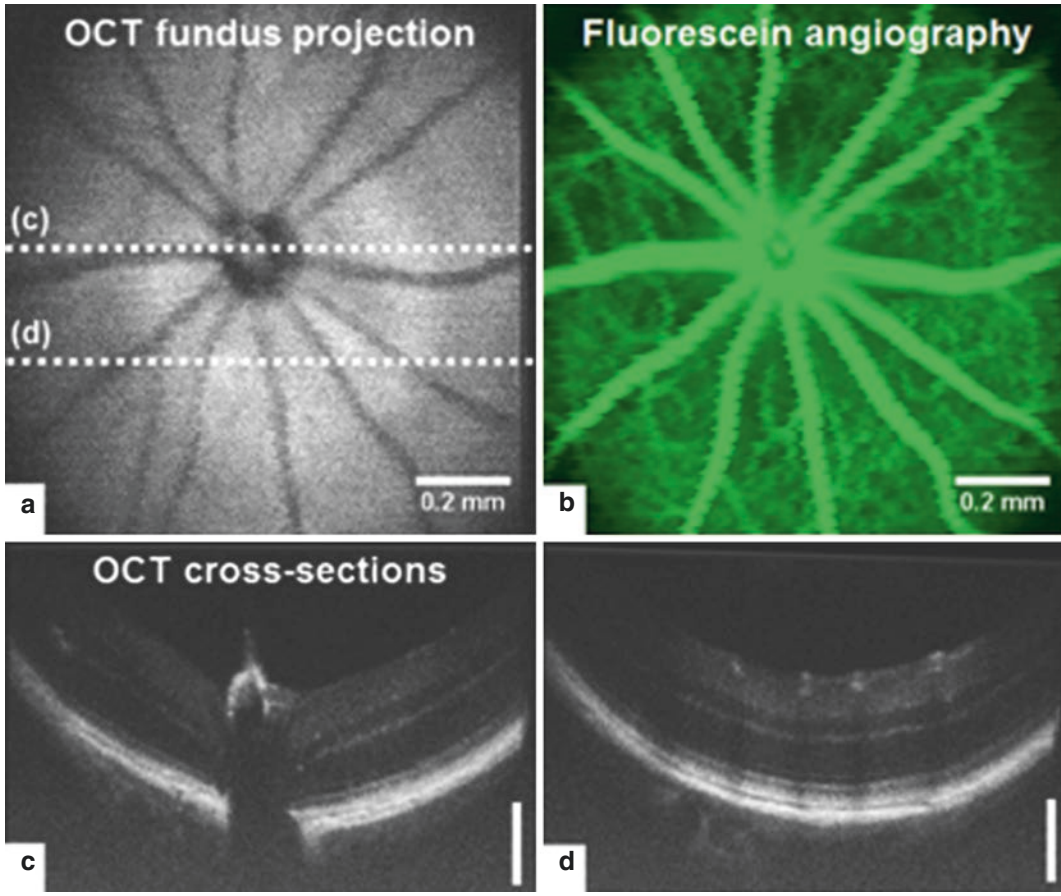

Fig. 16.18 *Multimodal* in vivo imaging of the mouse retina. (**a**) OCT fundus projection and (**b**) simultaneously acquired fluorescence angiography image of the healthy mouse retina. (**c**, **d**) Representative OCT cross sections (*vertical bars*, 200 µm). For fluorescence angiography, the approved in vivo dye fluorescein was used, which has its emission maximum in the green visible spectral range. All images were acquired with an experimental hybrid imaging system slightly modified to (Cimalla et al. 2012)

mouse and rabbit models to study alveolar sizes and the change during ventilation in healthy and injured lungs. While in the early systems, gated imaging was used to study the dynamic shape during the ventilation cycle (Meissner et al. 2010b), modern high-speed systems capture complete alveoli with some tens of frames per second, sufficient for breathing rates in the order of one per second (Kirsten et al. 2013). In larger animals the movement of the lung prevents following single alveoli during the complete ventilation cycle. Therefore, lightweight MEMS-based probes were developed resting on the lung and following the alveolar structures (Namati et al. 2013).

To access internal regions of the lung, endoscopic OCT probes have been used. Typically, such probes use radial scanning by rotating the entire probe or by using micromechanical motors placed in the probe (Yang et al. 2004b). While the rotation provides circumferential 2D images, the fiber may be retracted while accumulating subsequent radial images to provide three-dimensional information.

A third strategy uses miniaturized OCT needle probes. The needle probe can be inserted through the tissue into the region of interest that may be located several centimeters below the surface. Scanning is again performed by rotating the needle or the focusing optics inside the needle.

Although the size of needle probes has been reduced to a diameter of about 310 µm, the insertion of the needle will cause some trauma (Lorenser et al. 2011). As the needle can hardly be translated forth and back, the same tissue cannot be imaged during different states of the ventilation cycle. For repetitive scans, probes consisting of an inner part that translates rapidly back and forth multiple times per second were developed allowing two-dimensional image acquisition (McLaughlin et al. 2012).

Imaging alveolar structures is hampered by the repetitive refractive index change from air to liquid, limiting the useful depth to only one or two layers of alveoli. Therefore, several attempts have been made to fill the lung with an index matching fluid. For ex vivo imaging, the lung can be filled completely with saline water (Lorenser et al. 2011) or ethanol (Meissner et al. 2009a) increasing the useful imaging depth to 5 or more alveoli in depth. While these approaches are not suited for in vivo imaging, a small amount of fluid around the probe can enhance imaging without scarifying the animal (Quirk et al. 2014). Moreover, liquid ventilation using perfluorocarbons having a high transport capacity for oxygen and carbon dioxide can be used for ventilation allowing enhanced OCT imaging in vivo (Schnabel et al. 2013) (see Fig. 16.19).

16.3.6 Discussion and Conclusion

Optical coherence tomography is a contactless optical imaging concept enabling three-dimensional tomographic imaging with micrometer resolution. However, due to the strong scattering of light in biological tissue, the penetration depth and thus the image depth are limited to a few millimeters in the best case, when light in the optical window between 600 and 1300 nm is used. The imaging speed of state-of-the-art OCT systems is high enough to enable real-time video imaging.

Primarily, the contrast in OCT images is generated by refractive index variations at interfaces between different tissues that lead to backscattered light. Additional contrast mechanisms rely

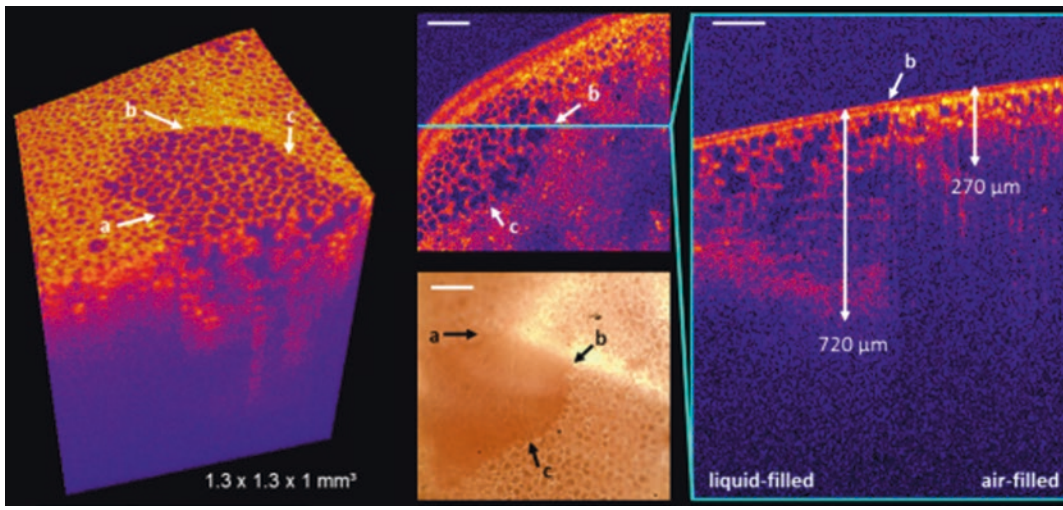

Fig. 16.19 Transition from an air-filled to a liquid-filled region in OCT and intravital microscopy (IVM). These pictures show the influence of liquid filling for OCT and IVM lung imaging after 18 min of total liquid ventilation. While image quality for OCT is considerably increased in the liquid-filled area, the contrast for IVM is decreased due to the refractive index matching. The depth of tissue visualization is nearly tripled in the liquid-filled area due to the reduction of scattering loss. The *arrows a*, *b*, and *c* in the 3D OCT image (*left*) were used for a better understanding of the OCT and IVM en face view (*middle row*) and the OCT cross section (*right*). For the 3D image, the pleura was hidden to get a look on the first layer of subpleural alveoli. Scale bar is 200 µm (From Schnabel et al. (2013) with permission)

on spectroscopic modifications of the backscattered light by spectrally dependent absorption or scattering or on variations of the polarization due to birefringence in aligned structures like fibers or muscles. Contrast enhancement by adding contrast agents like nanoparticles has also been demonstrated.

In addition to stationary images of the tissue structure, so-called Doppler-OCT also enables visualization of movements in the tissue, for example, the blood flow.

In terms of small animal imaging, OCT has been successfully used for retina imaging. The transparence of the ocular media enables noninvasive imaging of the retina not only for humans but also for rats, mice, and zebrafish. This imaging is not restricted to stationary morphological images but also extends to functional imaging by detecting local changes of the retina's optical properties due to light stimuli.

Imaging of vessels has been successfully demonstrated. A particular application is the investigation of traumatic brain injuries or strokes in rat models (Osiac et al. 2014). Also, cardiovascular defects in mutant mouse animal models have been analyzed by OCT. Even the development of whole mouse embryos can be monitored in vivo with OCT (Larina et al. 2011). In more recent studies, OCT has been successfully applied to monitor drug-induced changes of the tissue in mouse models (Bell et al. 2013). These recent developments demonstrate that OCT has become a powerful tool for small animal imaging and that its potential for this application is by far not completely explored.

16.4 Intravital Imaging in Small Animals

Timo Rademakers and Marc A.M.J. van Zandvoort

Over the last decades, molecular and cell biology has greatly advanced our knowledge of dynamic processes at a molecular level, especially by the use of (static) in vitro techniques. However, to gain an understanding of the in vivo implications hereof, a need for translation toward in vivo experiments developed, in which dynamic events could be studied in real time and in their specific microenvironment. Intravital microscopy (IVM) is one of the techniques which allow such studies. While the technique is (mostly) invasive, it is able to (depending on the system) study dynamic processes at a resolution of several micrometers and therefore has become a widely used technique in many fields of biomedical research.

The idea of studying (sub)cellular processes in small animals in vivo is not new. Already in the nineteenth century, the first rudimental intravital studies have been described, involving transillumination microscopy of leukocyte behavior in the mesentery of a frog (Julius Cohnheim 1839). From these initial intravital studies using transillumination, the field has developed greatly with aid of advances in microscopy, allowing at current detailed multicolor study of dynamic processes using the newest fluorescent techniques.

The purpose of this section is to give an overview of IVM techniques and applications, in which both classical intravital imaging and state-of-the-art multiphoton intravital imaging will be discussed, including examples from different fields of research.

16.4.1 Classical Intravital Imaging

Classical intravital imaging uses regular widefield microscopy systems, either using transillumination or fluorescence. These classical systems have been in use for several decades and are still being used to date. Classical IVM has mostly been applied in inflammation research (i.e., leukocyte adhesion and transmigration), but also in studies involving hemodynamics (Kiyooka et al. 2005) or thrombosis (Furie and Furie 2006). Classical IVM however has some intrinsic limitations, as will be discussed below.

16.4.1.1 Brightfield Imaging/ Transillumination

The first IVM studies were performed using brightfield illumination or transillumination in transparent tissues, eventually in combination with the use of differential interference contrast

(DIC) or phase contrast to enhance visualization of various structures within the tissue. The greatest advantage of this type of IVM is its relative ease of use, such that it can be performed on many regular light microscopes equipped with a high-speed detection system. Moreover, the lateral resolution (i.e., X-/Y-resolution) is generally good (±500 nm). One of the most obvious disadvantages, however, is the need for transparency in the tissue under study, which in most small laboratory animals is very limited. Also, in thicker tissues problems with image blurriness arise, caused by out-of-focus contributions. This significantly reduces image contrast and resolution. In practice, only few tissues like the cremaster muscle in male animals (Thorlacius et al. 1997) or the mesentery are transparent enough to allow transillumination. In these tissues, this type of IVM has been used to study, e.g., leukocyte adhesion to, rolling along, and transmigration through microvasculature. Figure 16.20 shows a typical image of a capillary in the cremaster muscle of a mouse, in which the capillary wall as well as the blood cells may be appreciated after applying a DIC filter.

16.4.1.2 Widefield Fluorescence and Confocal Microscopy

An approach which is similar to transillumination IVM is the use of widefield fluorescence microscopy. This technique offers a higher contrast at comparable resolution, since it only detects specifically labeled fluorescent structures or cells, while the background – with exception of autofluorescent molecules – remains black. In addition, since fluorescent markers are available in different colors, it is possible to study differentially labeled tissue/cells at the same time using dual or triple filters. Moreover, higher contrast allows imaging of a multitude of tissues and organs, e.g., the liver (Kubes et al. 2002), noninvasive imaging of the capillaries in the murine ear (Lammermann et al. 2013), or even larger vessels such as the carotid artery (Fig. 16.21) (Massberg et al. 2003). However, out-of-focus blurriness problems still arise, which in practice still limits penetration depth to several micrometers in most tissues.

To introduce axial resolution, confocal microscopy can be used. In confocal microscopy, a laser system is used for excitation of fluorophores at their specific wavelength. Out-of-focus emitted light is filtered out by the use of pinholes, which reduces blurring of images up to 50–100 μm of penetration depth depending on the type of tissue. Also, XY resolution is improved with a factor 2. It is however important to note that, when using line scanning systems, the acquisition speed is lower than in widefield systems due to the stepwise buildup of the image, instead of direct acquisition of the entire image. instead of direct acquisition of the entire image. To again gain imaging speed, systems can be fitted with a line scanning, resonant scanning, or spinning disk system, which

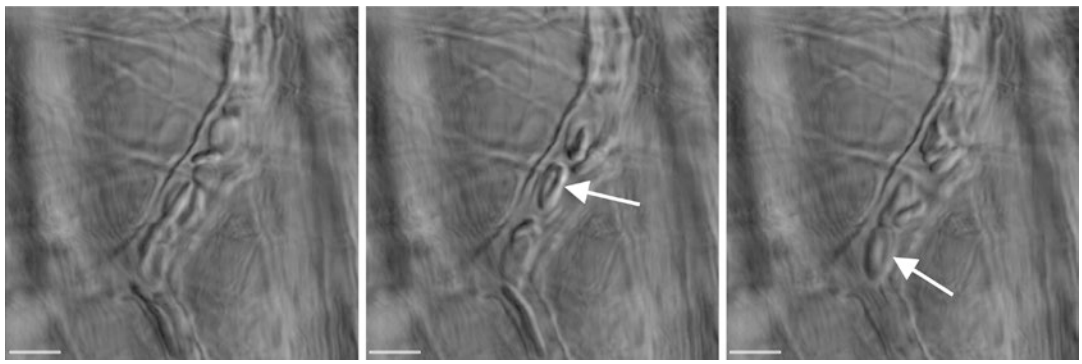

Fig. 16.20 IVM time series using transillumination microscopy. Thin tissue samples can be imaged by using DIC or phase contrast. Here, an erythrocyte (*white arrow*) can be seen passing through a capillary in the cremaster muscle. Upon an inflammatory stimulus, transmigration of leukocytes may also be determined

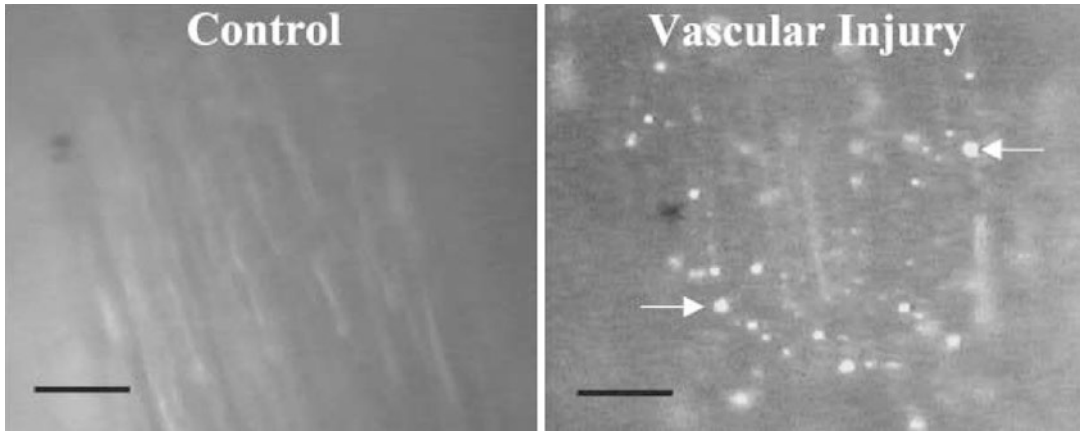

Fig. 16.21 IVM recording by widefield fluorescence microscopy of blood platelet (*white, arrow*) adhesion and aggregation in the common carotid artery of a mouse upon vascular injury. Widefield fluorescence IVM can be used to assess increases in platelet adhesion and aggregation. Nevertheless, axial resolution in widefield fluorescence IVM is low (Figure is adapted from Massberg et al. (2003) and reprinted with permission)

however causes some reduction in resolution and introduces noise. Alternatively, scanning multiple colors at the same time also enhances imaging speed, although not all systems are equipped for this task, as it requires specific fluorescent filters and/or dual-camera systems. Nevertheless, depending on the system setup, high-speed multicolor IVM can be achieved.

The applications of these types of IVM are numerous, as long as there is the possibility to introduce a fluorescent label (either genetically or via other means) which is required for detection. Obviously, these types of IVM can be applied to the previously mentioned applications in bright-field IVM, i.e., imaging of the microvasculature in different tissues. Yet, since transillumination is no longer an issue, larger structures such as the macrovasculature can be studied in fluorescence-based IVM. Indeed, this technique has, e.g., frequently been used to assess leukocyte adhesion to the vessel wall of the carotid artery under inflammatory conditions or after thrombosis (Massberg et al. 2003), also harboring the potential to study differentially labeled cells at the same time, e.g., wild-type vs. knockout cells. The same holds true for confocal IVM in, e.g., the cremaster muscle, in which leukocyte transmigration can be studied in detail in the microvasculature (Woodfin et al. 2011). Similarly in other fields like tumor biology, fluorescence-based IVM is often used in combination with dorsal skin chambers (Endrich et al. 1988; Menger et al. 2002).

16.4.2 Intravital Multiphoton Imaging

Even though classical intravital imaging is applicable in many cases, the intrinsic limitations with regard to axial resolution and penetration depth limit the use of these systems. New methods of intravital imaging, however, have become available over the past two decades. As a derivative of the confocal imaging systems, multiphoton microscopy was introduced early 1990s (Denk et al. 1990; Helmchen and Denk 2005). Multiphoton (MP) microscopy, mostly two-photon microscopy, uses multiple photons of higher wavelengths to excite fluorescent probes, in contrast to single-photon excitation in regular fluorescent techniques. Single-photon excitation comprises the transition of an electron in this fluorescent molecule to another molecular orbit, bringing the molecule from the ground state (S_0) to the excited state (S_1), as is depicted in the Jablonski diagram in Fig. 16.22. This transition is only transient, and upon return of the molecule to S_0, a fluorescent photon will be emitted. Since

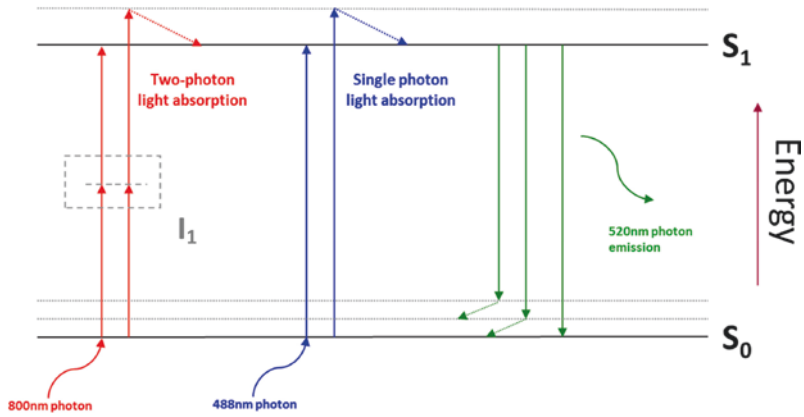

Fig. 16.22 Jablonski diagram showing single-photon excitation versus two-photon excitation. Single-photon excitation by, e.g., a solid-state laser in confocal setups uses a single photon to bring a fluorescent molecule from the ground state (S_0) to the excited stated (S_1), followed by fluorescence emission upon return of the electron from S_1 to S_0. Fluorescence emission can however also be achieved by two-photon excitation, in which two photons are required for transition from the ground state (S_0) to the excited stated (S_1) via the intermediate (I_1) state

some energy is lost in between absorption and emission, the emitted photon has lower energy that the absorbed photon, shifting the emission to the red (Stokes shift).

Single-photon excitation as used in confocal microscopy, however, causes photodamage and phototoxicity, while its penetration depth into tissue is limited. Therefore, single-photon excitation is not the most suitable technique to study thick and living samples. The use of (near-)infrared (IR) light, as used in MP microscopy, can circumvent these problems. However, near-IR light is not capable of exciting the molecule by itself, since it lacks the energy to induce the transition from S_0 to S_1. As a result, the molecule will end up in the intermediate I_1 state. Only if two infrared photons arrive virtually simultaneously (within 10^{-18}s, i.e., one attosecond) at the molecule, they can together bridge the energy gap between S_1 and S_0. In a continuous laser beam, however, the probability of photons to arrive simultaneously at the molecule is virtually zero. By increasing the photon density, it is possible to increase this probability and thus to allow the transition from S_0 to S_1 and, thus, perform deep-tissue fluorescence imaging. To achieve this, a pulsed laser is used (temporal confinement, Fig. 16.23a), which emits femtosecond pulses with a high photon density at a high frequency (80 MHz). Even under these prerequisites, effective two-photon excitation will happen only in the focal point (spatial confinement, Fig. 16.23b), as the probability of two-photon excitation decreases with a power of two with increasing distance to the focal point.

Especially in the recent 10–15 years, MP microscopy has been applied more frequently. At first, application was especially focused on deep-tissue imaging, since MP microscopy is one of the techniques which allows imaging up to 1 mm (1000 µm) in, e.g., brain tissue, without requiring tissue sectioning or extensive tissue handling and/or fixation.

MP microscopy has several advantages over confocal microscopy. The most important hereof are the use of a pulsed laser system and the use of higher excitation wavelengths. The use of a pulsed (femtosecond) laser causes less photobleaching and phototoxicity. This is caused by the fact that light of higher wavelengths is less absorbed by, and as a consequence interacts less with, the tissue itself. The reduction in photobleaching can be explained among others by the reduction in out-of-focus excitation due to the spatial confinement as well as by the relative reduced time of excitation of the fluorophore by the temporal confinement compared to continuous excitation in regular confocal systems. In addi-

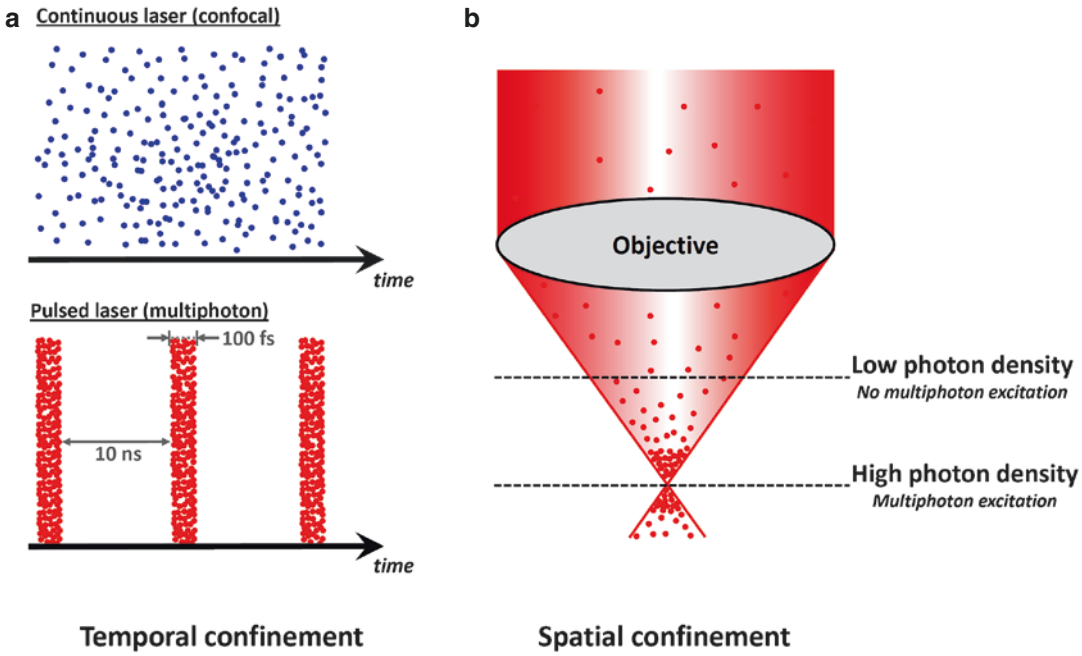

Fig. 16.23 Temporal (**a**) and spatial (**b**) confinement required for achieving fluorophore excitation in multiphoton microscopy. By temporal confinement, photon density is increased by creating narrow photon-dense pulses. Spatial confinement is caused by the focusing capacity of objective lenses, where, as a result, the photon density is solely high enough in the focal plane of the specimen

tion, excitation only occurs in focal point (i.e., no out-of-focus excitation as in confocal microscopy). Additionally, since there is no absorption in the out-of-focus plane, a higher penetration depth is achieved compared to confocal microscopy (Fig. 16.24).

The use of higher (near-)infrared light wavelengths also has distinct advantages. Firstly, it results in a higher penetration depth as discussed above, and, since these wavelengths are less damaging, they are very suitable for vital imaging. Moreover, since the two-photon excitation spectrum of many fluorescent probes is broader than its single-photon counterpart, simultaneous excitation of multiple probes often occurs as a result of off-peak excitation of these fluorophores using (near-) infrared light wavelengths. This may however also include excitation of autofluorescent molecules.

By combining the characteristics mentioned above with methods to allow high-speed image acquisition, intravital MP microscopy can be achieved. The two most well-established ways of achieving high-speed imaging are resonant scanning and multibeam-based imaging (Nielsen et al. 2001; Fan et al. 1999; Niesner et al. 2007). In resonant scanning, high scanning speeds are achieved by the use of resonant galvanometer mirrors, which can oscillate with a frequency up to 12 kHz. The high speed, however, comes at the cost of increased noise levels, which favor the use of better detectors which have as little noise as possible. An alternative is a multibeam approach, in which the excitation laser beam is split into multiple (up to 64) beams which can simultaneously scan the specimen, allowing a faster scanning time. Here however, there is a loss of resolution with increasing penetration depth. Alternatively, triggering based on the cardiac and/or respiratory cycle can be used as a means to compensate for tissue motion, allowing acquisition of stable images in time but at the cost of temporal resolution.

In recent years, the applications of MP-based IVM have expanded greatly, and MP microscopy has become a powerful technique for studying dynamic processes in, e.g., oncology, immunol-

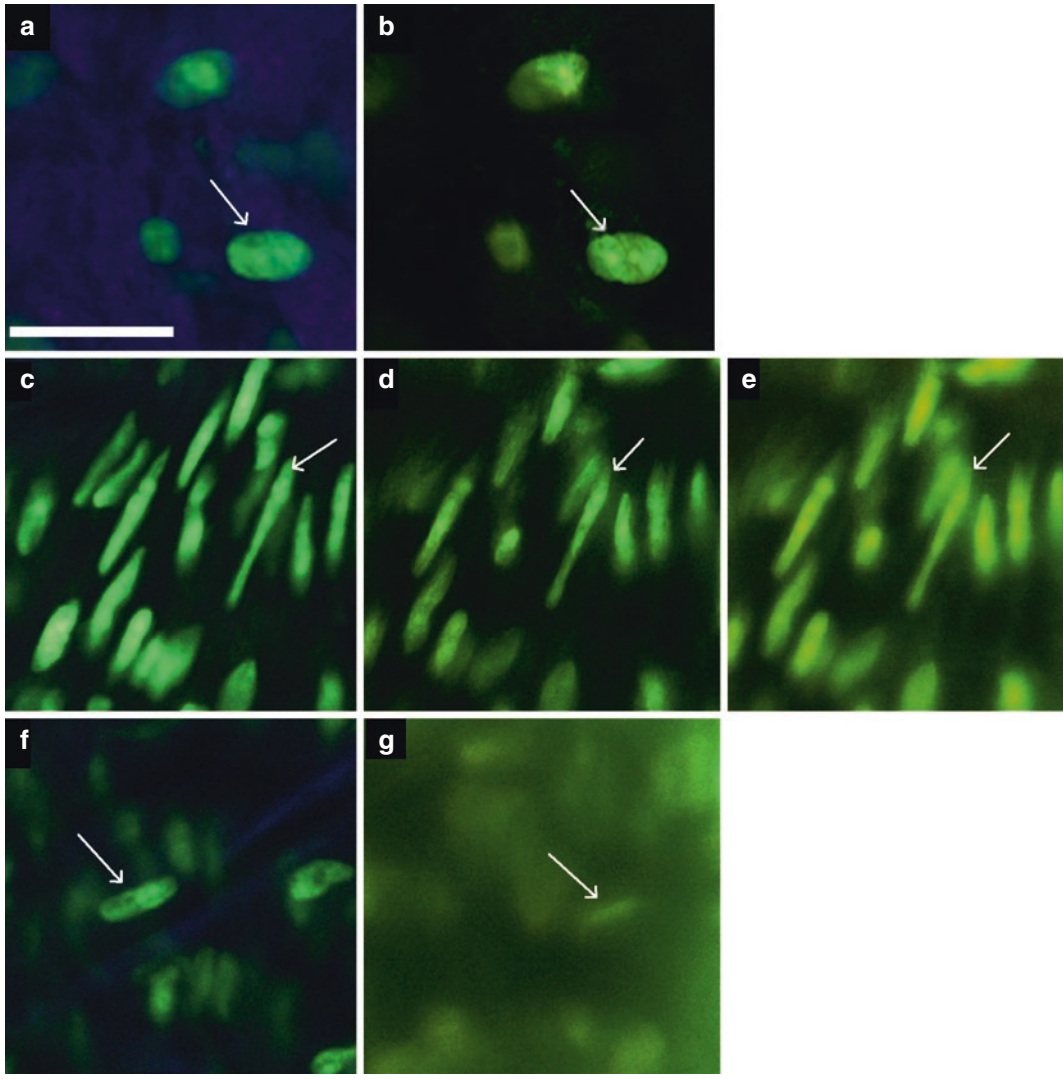

Fig. 16.24 Effect of penetration depth on the effective spatial resolution obtained with multiphoton microscopy (**a, c, f**) and confocal microscopy (**b, d, e, g**) as studied in a mouse carotid artery of which cell nuclei were labeled (*green*). Images are obtained at different depths: **a**, **b**, 15 μm depth; **c**–**e**, 40 μm depth; and **f**–**g**, 80 μm depth. Due to out-of-focus fluorescence in confocal microscopy, the effective resolution deteriorates far more with increasing depths as compared with MP microscopy. Confocal images obtained with optimal pinhole settings except for **e** in which the pinholes were fully open (Figure is adapted from van Zandvoort et al. (2004) and reprinted with permission)

ogy, neuroscience, gastroenterology, urology, and cardiovascular research, as is depicted below.

16.4.2.1 Cell Trafficking and Hemodynamics

Similar to classic intravital imaging, MP IVM imaging has been used to study live process, such as vascular permeability, leukocyte adhesion and transmigration, blood flow, shear rate, and hematocrit measurements in vivo. Significant progress has been made to allow imaging and quantification hereof. Nowadays, studies have been realized which are able to assess functional parameter in an entire tissue volume (Kamoun et al. 2010). By applying differential line scanning techniques, this can be achieved at several locations at the same time, allowing the generation of velocity maps and comparing the functional

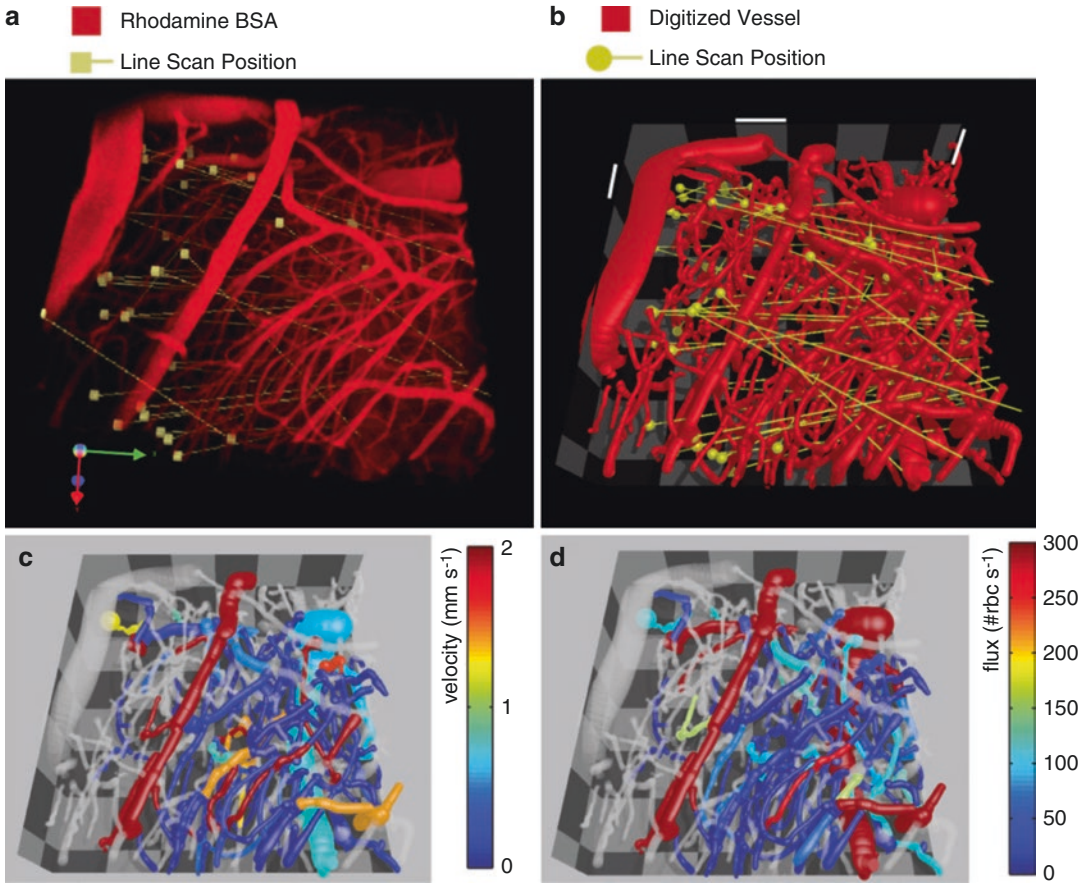

Fig. 16.25 Labeling both the cell-free blood volume and erythrocytes, it is possible to measure blood flow velocities in whole samples, e.g., the brain vasculature in a mouse, by using line scanning techniques (**a**). After image processing, involving post-processing of the acquired images (**b**), velocity maps (**c**), and maps revealing erythrocyte fluxes (**d**) within the vasculature can be constructed (Adapted from Kamoun et al. (2010); reprinted with permission)

makeup of vascular beds (Fig. 16.25). More recently, this technology has even been applied in tissues suffering from substantial motion artifacts, such as atherosclerotic carotid arteries (Rademakers et al. 2013), in which functional parameters of microvasculature surrounding the atherosclerotic lesion were assessed (Fig. 16.26). Moreover, heterotopic beating heart models have been studied using MP-based IVM, allowing intravital imaging of leukocyte transmigration in the beating heart (Li et al. 2013b).

Alternatively, by applying triggering for the cardiac and respiratory cycle, image resolution can be improved. When the residual tissue motion can then also be reduced, as was proposed recently for carotid artery imaging, spatial and temporal resolution are even high enough to permit 4D imaging, i.e., the acquisition of 3D images in time (Fig. 16.27) (Chevre et al. 2014).

16.4.2.2 Cell Tracking and Photoactivation

As part of intravital MP, new applications for dedicated cell tracking have been developed, inspired by developments of photoactivatable fluorescent probes (Shaner et al. 2007). These probes allow otherwise non-fluorescent proteins to be specifically activated in a certain cells in a piece of tissue or organ, after which these cells can be specifically traced. The great advantage of this technique is that no injections of labeled cells are required, which is especially useful for study-

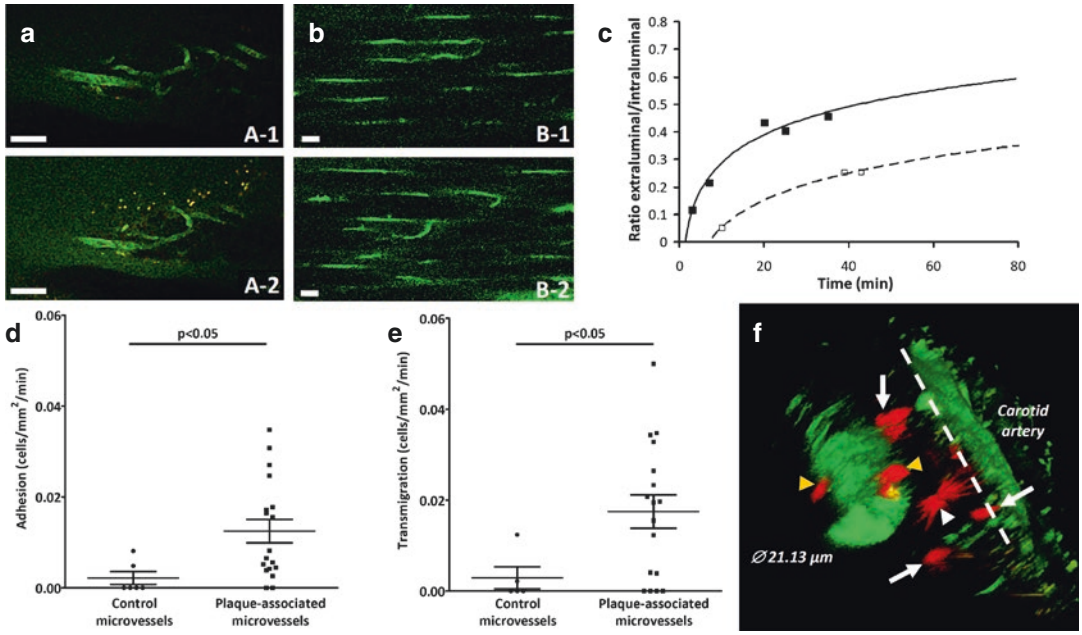

Fig. 16.26 Functional properties of the microvasculature can be studied in vivo in tissues suffering from substantial motion artifacts, such as atherosclerotic carotid arteries, by using resonant scanning MP-based IVM. Here, microvascular permeability for a 70 kDa dextran (*green*, **a,b**) was studied in local (**a**) and control (**b**) microvascular tissue, revealing an increased permeability in the local microvasculature in time (**c**). Moreover, leukocyte adhesion and transmigration could be assessed (**d**, **e**), with additional in situ z-scans allowing 3D study (**f**) of the leukocyte (*red*) transmigration process through the microvascular endothelium (*green*) (Adapted from Rademakers et al. (2013); reprinted with permission)

ing small and delicate tissues which would not allow injections. One of the most elegant examples hereof is a study investigating cell trafficking between different compartments within the germinal centers of lymph nodes (Fig. 16.28) (Victora et al. 2010).

16.4.2.3 Vascular Network Formation and Vascular Permeability

Similar to cell tracking, MP-based IVM also enables users to track development of vascular networks, a tool which is applied regularly in angiogenesis research (Brown et al. 2001). Transgenic animal models or labeling of blood vessels using fluorescent antibodies, lectins, or tracers which reside in the blood (e.g., high-molecular-weight dextrans) can be used to not only track the development of vessels in time but also determine properties like angiogenic activity, vascular surface area and volume, or vascular permeability. As such, functional parameters can be quantified which can be used to assess efficacy of interventions. Similarly, network formation and functionality can also be implemented in different biological systems, e.g., neuronal networks (Eichhoff and Garaschuk 2011; Grewe et al. 2010; Gobel et al. 2007).

16.4.2.4 Cellular Dynamics

Another development is Förster resonance energy transfer (FRET) imaging using MP microscopy, although FRET imaging has already been a frequently used tool in fluorescence microscopy. The basis of FRET imaging relies on a FRET pair, i.e., two fluorescent proteins, which can act as a donor-acceptor pair. In such a FRET pair, the fluorescent protein with the lowest emission wavelength will be excited. When the two fluorescent proteins are in close proximity, their electron orbits overlap, which causes direct energy transfer from the excited donor to the acceptor protein. This

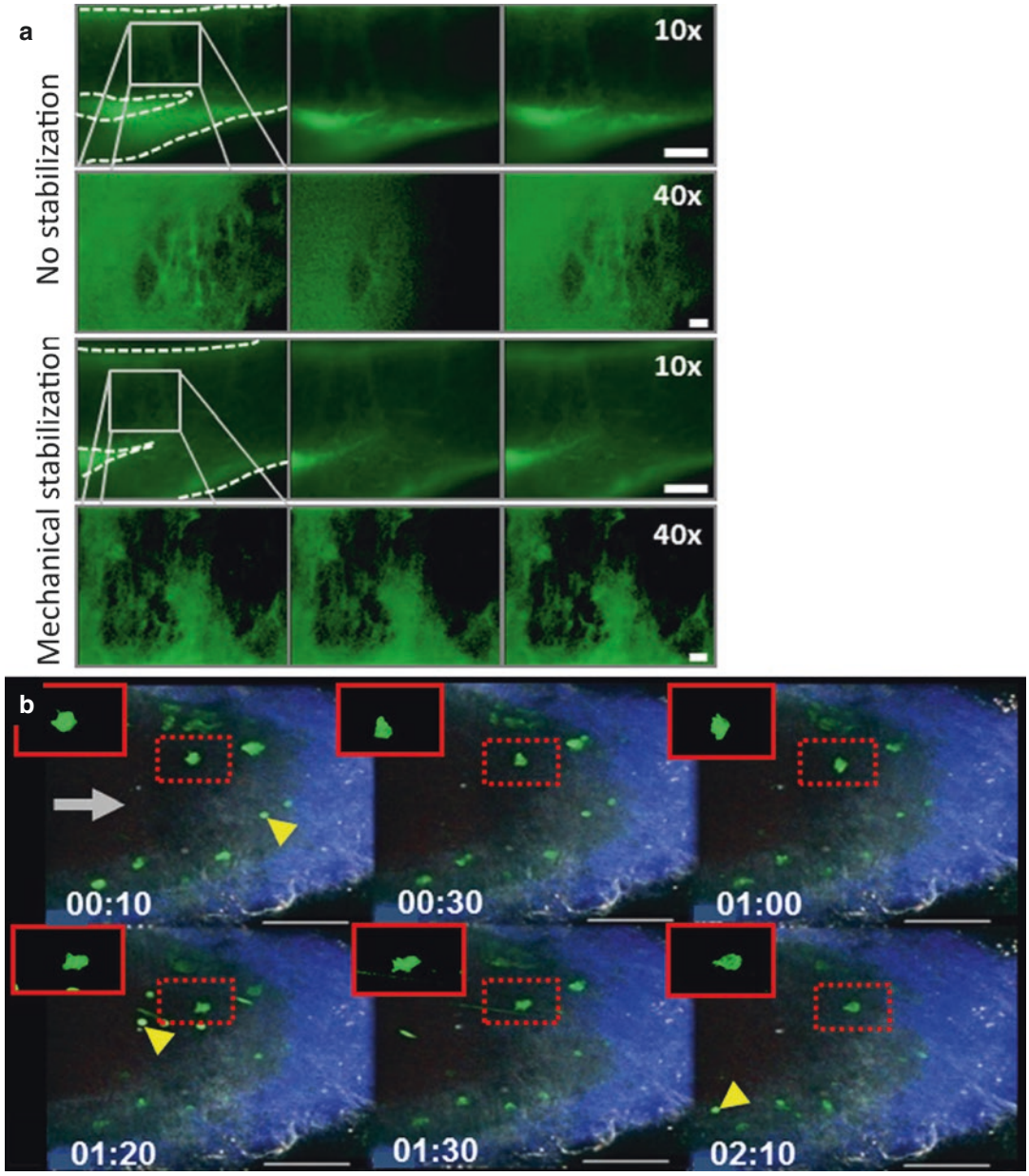

Fig. 16.27 Using triggered image acquisition and mechanical tissue stabilization, it is possible to greatly reduce the motion artifacts occurring during intravital imaging, hereby greatly enhancing image resolution (**a**). Such methods also allow imaging of tissue Z-stacks in time, i.e., 4D imaging. Maximum projection of time series shows the movement GFP$^+$ myeloid cells within a murine carotid artery (**b**) (Figure adapted from Chevre et al. (2014) and reprinted with permission)

fluorescent protein will, as a result, emit a fluorescent signal (Fig. 16.29). Since this process can only occur when both fluorophores are in close proximity to each other, this technique is well suited for studying receptor-ligand binding, protease/kinase activity, and other molecular interactions.

FRET imaging has been applied in isolated vital tissue (Kapsokalyvas et al. 2014), but recently FRET imaging has been implemented in

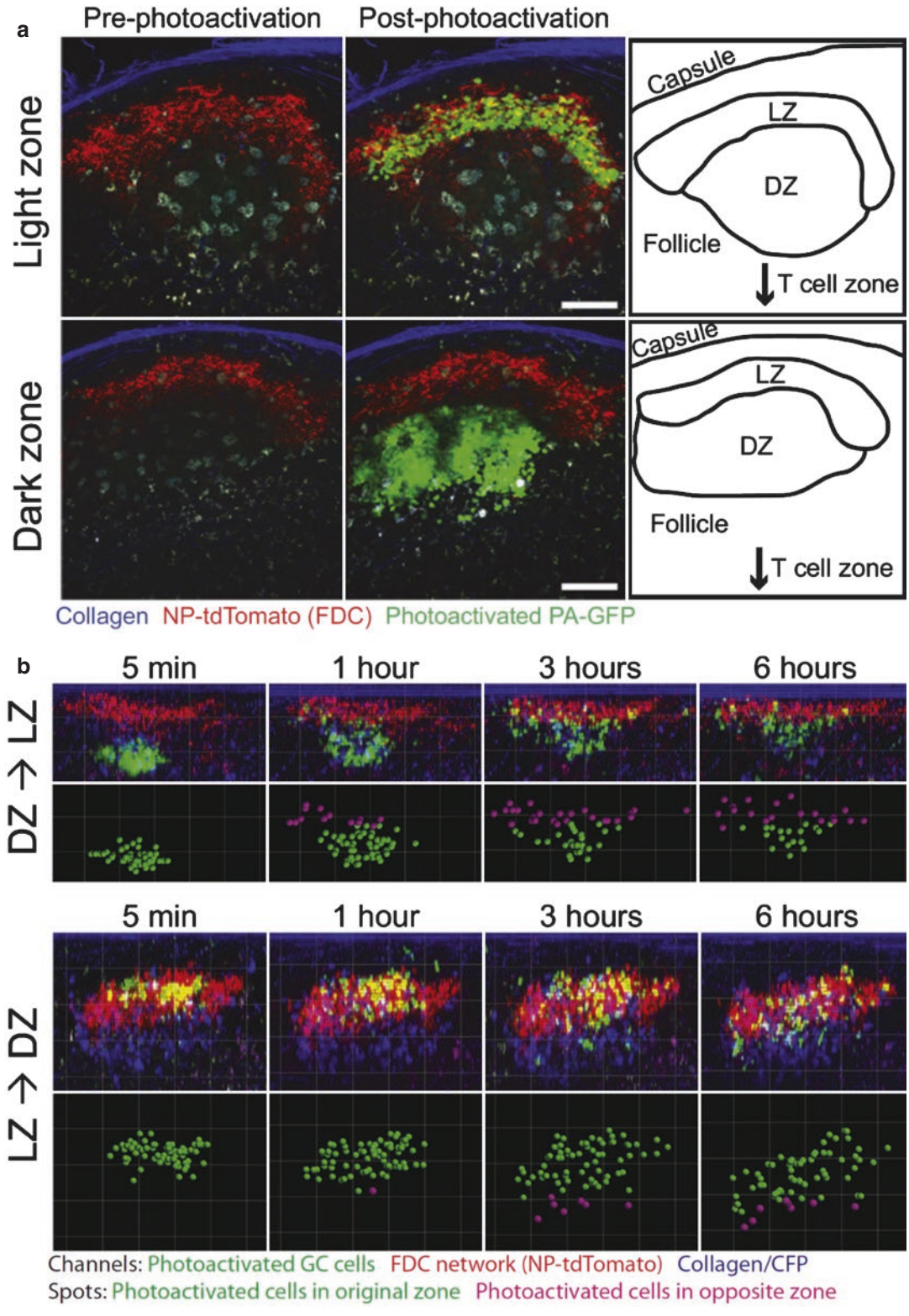
a
Pre-photoactivation
Post-photoactivation
Light zone
Dark zone
Capsule
LZ
DZ
Follicle
T cell zone
Collagen NP-tdTomato (FDC) Photoactivated PA-GFP
b
5 min
1 hour
3 hours
6 hours
DZ → LZ
LZ → DZ
Channels: Photoactivated GC cells FDC network (NP-tdTomato) Collagen/CFP
Spots: Photoactivated cells in original zone Photoactivated cells in opposite zone

intravital MP microscopy as well. FRET imaging in a multiphoton microscope can be performed either by measuring differences in fluorescent donor lifetime upon FRET activity or simply by measuring the emission signal of the FRET acceptor molecule relative to the emission signal of the donor molecule (i.e., ratio imaging), the latter of which is used in intravital FRET imaging. By intravital FRET, it is possible to study molecular interactions in tissue in vivo and has, e.g., been used to establish kinase activity of Erk during neutrophil recruitment under inflammatory conditions in mice (Fig. 16.30) (Mizuno et al. 2014).

Other examples of studying cellular dynamics are determining calcium fluxes. This technique is used, e.g., in neuroscience, to determine neuronal activity (Mittmann et al. 2011), but nowadays these experiments are also being applied to other organs like the kidney, in which podocyte calcium fluxes were determined in vivo (Burford et al. 2014).

16.4.2.5 Lineage Tracing

In the last years, novel animal models, genetic constructs, and probe developments have led to the possibility of mapping cell fate (or lineage tracing) by IVM. Here, also photoactivatable or photo-switchable probes have been used, while other studies rely on the Brainbow approach (Mahou et al. 2012) to achieve this. The principle of Brainbow technology is based on the stochastic expression of multiple copies of constructs which code for different fluorescent proteins (Livet et al. 2007). As such, a multitude of color combinations can be achieved, and this technique has been used especially in neuroscience settings, where individual neurons and their mutual connections were studied (Fig. 16.31). Similar approaches have been derived from the Brainbow principle, including RGB marking (Weber et al. 2011) or generation of so-called Confetti mice (Schepers et al. 2012), and have introduced these lineage tracing approaches in other fields of research as well.

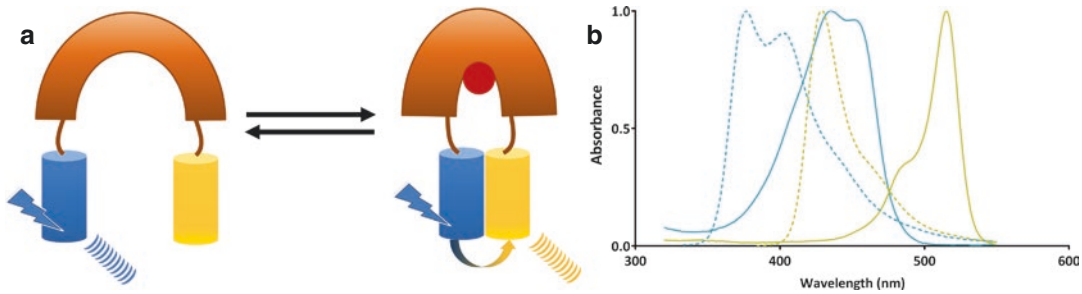

Fig. 16.29 FRET imaging is based on fluorescent proteins, e.g., cyan fluorescent protein (CFP, *blue*) and yellow fluorescent protein (YFP, *yellow*), which are linked together by a linker domain (**a**). Upon conformational changes (e.g., receptor activation), the two fluorescent proteins will come into close proximity, and energy transfer is possible between the two fluorescent proteins. Therefore, it is necessary that the emission wavelength (**b**, *solid blue line*) of the donor (i.e., CFP) overlaps with the excitation wavelength (**b**), *dotted yellow line*) of the acceptor (i.e., YFP)

Fig. 16.28 By using photoactivation in specific regions within a tissue, it is possible to study cellular dynamics between different tissue compartments, e.g., cell trafficking between the light (LZ) and dark zone (DZ) within the germinal centers of lymph nodes (**a**). After photoactivation, computational analysis can determine the movement of cells in time from DZ to LZ and vice versa (**b**) (Figure adapted from Victora et al. (2010) and reprinted with permission)

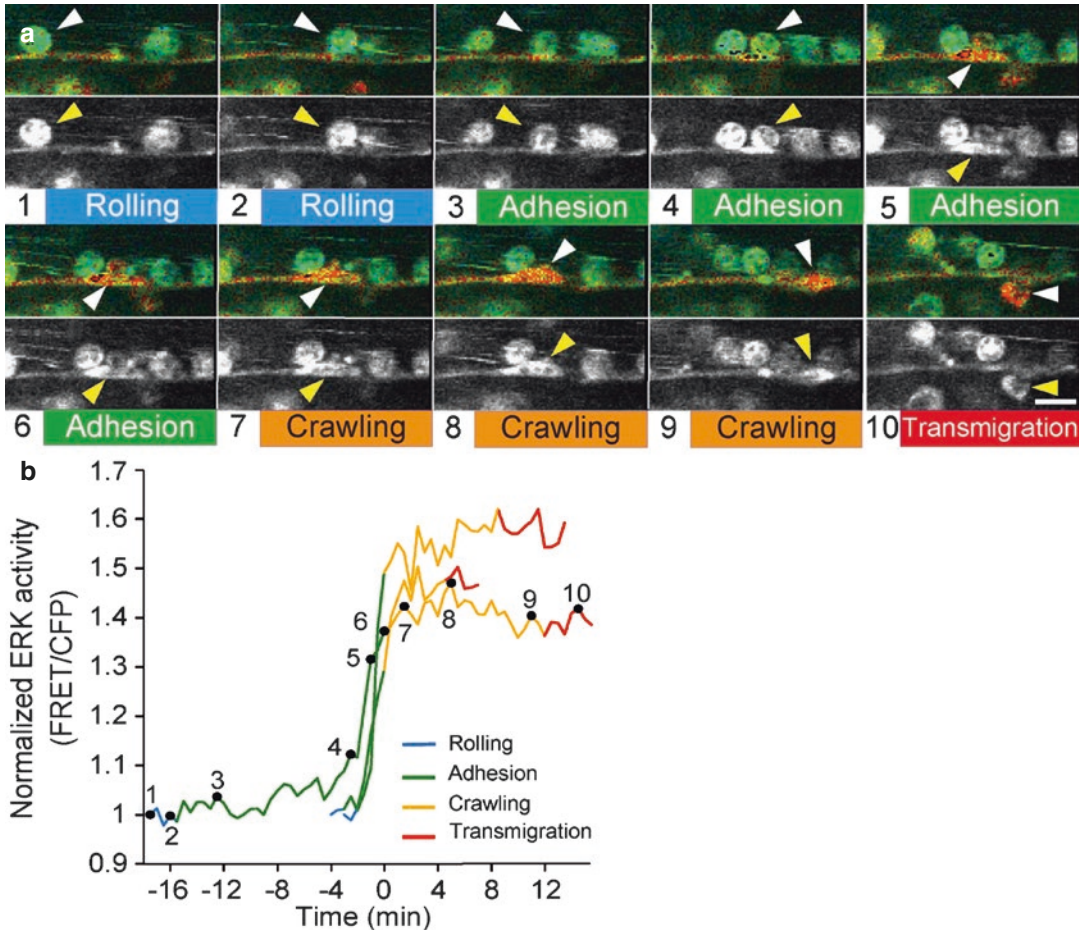

Fig. 16.30 FRET imaging has also been applied in IVM studies in mice, e.g., for studying kinase activity during neutrophil recruitment from the circulation to the intestine in a model of intestinal inflammation (**a**). These data can be quantified, giving a measure of kinase activity during the different phases of neutrophil recruitment (**b**) (Figure adapted from Mizuno et al. (2014) and reprinted with permission)

16.4.3 Perspectives and Considerations

In all, the field of intravital imaging has undergone considerable changes, even though to date, even the classical intravital approaches are still being used to some extent. The type of intravital microscopy one would want/need to use will depend on several factors (Table 16.1). MP-based IVM on the one hand can give an integrated approach of multicolor, deep-tissue imaging, but the equipment is far more expensive and requires considerable technical expertise. Moreover, often large datasets are acquired, which require substantial data processing like image deconvolution, because of the increased axial point spread function at higher wavelengths and increased depth in the tissue. Also data analysis in these larger datasets can be cumbersome. The classical techniques on the other hand are generally cheaper (depending on the specific setup) and easier to use and in many cases will be able to answer the research question at hand. The choice for the exact type of intravital imaging will therefore depend greatly on the research question at hand, as well as on the tissue/organ studied.

In line with these considerations, several other factors will influence the choice for intravital imaging, not unimportantly the availability of additional tools, e.g., adequate fluorescent probes, labeling strategies, or animal models.

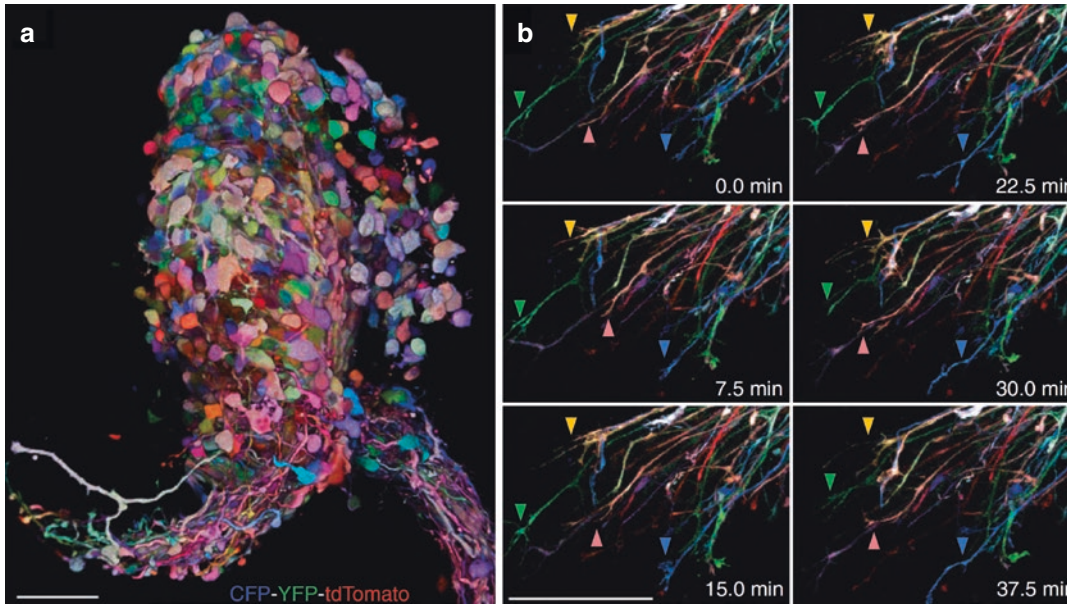

Fig. 16.31 By using a Brainbow approach, stochastic expression of multiple copies of constructs which code for different fluorescent proteins will lead to a multicolor mosaic. The color of a cell is dependent on the expression of these proteins, e.g., in the embryonic neural tube (**a**). In time, the growing motor neurons can be imaged (maximum intensity projections), allowing intravital lineage tracing of which cells induce axonal outgrowth (**b**) (Figure adapted from Mahou et al. (2012) and reprinted with permission)

Table 16.1 Comparison of the different IVM techniques with regard to acquisition speed, lateral and axial resolution, depth penetration into tissue, and possibility of multicolor imaging

	Acquisition speed	Lateral resolution	Axial resolution	Depth penetration	Multicolor imaging
Brightfield	++	+	−−	−−	−−
Fluorescence					
Widefield	++	++	−−	−−	+/−
Confocal	+	++	++	+/−	+
Spinning disk	++	++	+/−	−	+/−
Multiphoton	+	++	+/++	++	++

Based on Megens et al. (2011)
"−−" very low, "−" low, "+/−" moderate, "+" good, "++" very good

Especially in multiphoton setups, in which multiple fluorophores are excited simultaneously, there is a need for fluorescent probes with relative narrow emission spectra in order to distinguish between the fluorophores. Novel probes like quantum and carbon dots present promising tools (Douma et al. 2009). Next, the ability to label specific structures is an important issue (Progatzky et al. 2013). Usually, the vasculature and cells in circulation can be stained easily by intravenous injection of specific fluorescent antibodies, but other cell types are more challenging. The development of novel transgenic reporter mice as well as, e.g., FRET-sensor knock-in mice will provide an elegant tool for this purpose.

Yet, one of the greatest challenges still lies in achieving high-resolution imaging in vivo in various tissues. In fluorescence-based IVM, autofluorescence can significantly hinder proper image acquisition and requires careful consideration when selecting fluorescent probes. Worth mentioning, autofluorescence can also provide a means for label-free imaging. Imaging of, e.g., NAD(P)H has been used to assess mitochondrial

function in skeletal muscle in vivo (Rothstein et al. 2005). Also processes like second and third harmonics generation (SHG and THG, respectively) can be used to study different cell types, e.g., erythrocyte detection by THG, which can be used for label-free determination of hemodynamic factors (Dietzel et al. 2014).

Beyond autofluorescence, scattering properties of the tissue will also hinder image acquisition or limit penetration depth. Even though the inherent properties of tissue are not easy to alter, ex vivo attempts to induce optical clearing of tissue have proven to be quite successful, especially in brain tissue (Chung and Deisseroth 2013). First attempts to achieve optical clearing in vivo have been successful in, e.g., skin imaging using optical coherence tomography in rats (Genina et al. 2014), although application on an organ level in vivo – especially without altering function of the organ – remains tentative. Improvement of optics, like the development of graded index (GRIN) objectives, may however offer another way of improving imaging and even allow fiber-optic-based imaging, like intravascular or intracolon imaging. Also, applications of these objectives in brain and kidney imaging in vivo have given promising results (Levene et al. 2004; Li and Yu 2008).

Taken together, intravital imaging is a vital tool for studying dynamic process in small animal models. Depending on the research question, different variants of IVM may be used to answer this question. Ongoing and novel technical improvements on intravital imaging equipment as well as probes and animal models will provide valuable tools for many fields of research in the years to come.

16.5 Optoacoustic Imaging

Daniel Razansky

16.5.1 Introduction

The imaging depth limitation of optical microscopy related to light scattering in living tissues can be generally overcome by means of optoacoustic (OA) techniques (Razansky et al. 2012). By detecting pressure waves induced via transient absorption of short high-energy laser pulses, OA methods have recently enabled high-resolution imaging with optical contrast at depths of several millimeters to centimeters (Wang and Hu 2012), orders of magnitude deeper than possible with modern microscopy. OA sensing and imaging draw its roots from the discovery of the *photophone* by A. G. Bell and his assistant C. S. Tainter in 1880, which the inventors used as the first practical wireless telephony or, in fact, optical communication device (Tainter and Bell 1880). However, due to lack of appropriate laser sources and ultrasound detection technologies, utilization of optoacoustics to biomedical applications, such as spectroscopy or imaging, was first considered in the 1970s (Rosencwaig 1973) with first images from living small animals obtained in the past decade (Wang et al. 2003). By combining commercially available pulsed laser technology in the nanosecond range and sensitive acoustic detectors, it was shown possible to generate OA responses from tissue that carry spatially resolved spectroscopic information on the underlying absorption contrast (Ntziachristos and Razansky 2010). Nowadays, the terms *optoacoustic* and *photoacoustic* are equally used to describe the effect of acoustic wave generation by transient light absorption. Due to its hybrid nature combining optical excitation and acoustic detection, the OA imaging technology benefits both from the rich and versatile optical contrast and high (diffraction-limited) spatial resolution associated with low-scattering nature of ultrasonic wave propagation as compared to photon propagation (Wang and Hu 2012).

The ability to spatially resolve spectral information, i.e., location/size of unique tissue structures containing specific chromophores, provides added advantage of OA techniques. Rendering images at multiple excitation wavelengths and spectral unmixing allow for visualization of intrinsic tissue chromophores, such as melanin (Krumholz et al. 2011), oxy- and deoxyhemoglobin (Laufer et al. 2007), and lipids (Jansen

et al. 2014). Multispectral optoacoustic tomography thus holds a great promise for functional and molecular imaging, which is highlighted by the broad range of emerging biological applications of optoacoustics, including cardiovascular imaging (Taruttis et al. 2010), monitoring of organ perfusion and pharmacokinetics (Buehler et al. 2010b), targeted studies of inflammation and arthritis (Beziere et al. 2014; Vonnemann et al. 2014), cancer detection and staging (Mehrmohammadi et al. 2013), neuroimaging (Nasiriavanaki et al. 2013), and dermatologic imaging (Ida et al. 2014).

16.5.2 Principles of Optoacoustic Imaging

Optoacoustic (OA) imaging is based on absorption of light radiation in tissue and conversion of the deposited energy into heat, which in turn results in thermal expansion and mechanical stress propagating in the form of pressure waves (Fig. 16.32).

Similarly to most optical imaging modalities, light in the visible or near-infrared spectrum (400 nm–1200 nm) is normally used for excitation of OA responses due to the relatively weak absorption of biological tissues in this spectral region. Of particular importance is the near-infrared spectral window, which allows light penetration of up to several centimeters into optically dense tissues (Ntziachristos et al. 2005). Alternatively, tissue can be excited with energy in the radiofrequency and microwave spectra (Razansky et al. 2010), which is however not included in the scope of this chapter. Large variety of chromophores is absorbing at the optical wavelengths, which further leads to a high contrast between different tissues with varying chromophore concentration. Figure 16.33 shows absorption spectra of the most dominant intrinsic absorbers in tissue in the visible and near-infrared range (Yao and Wang 2014). For biomedical applications, except for intrinsic chromophores (e.g., hemoglobin in its oxygenated and deoxygenated form, melanin, fat), extrinsically administered agents, such as

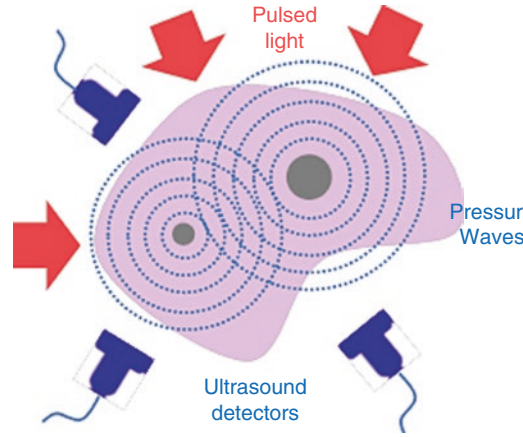

Fig. 16.32 Basic principle of optoacoustic imaging. Short pulses of light are absorbed by tissue absorbers, generating pressure (acoustic) waves propagating through the medium. The latter are recorded by ultrasonic detectors and used to form optoacoustic images by means of reconstruction methods

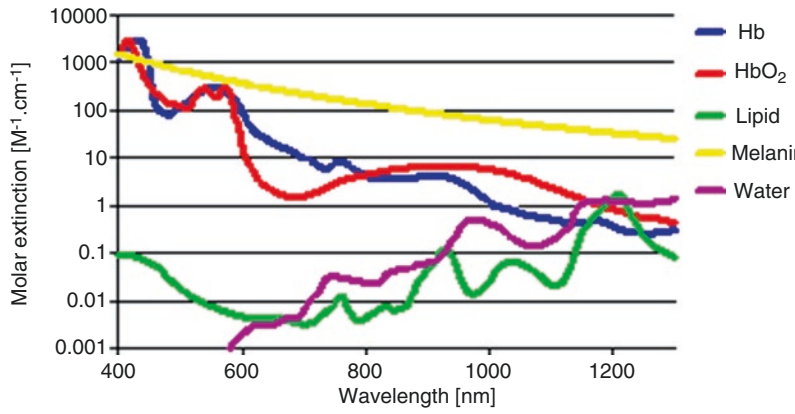

Fig. 16.33 Absorption spectral profiles of major intrinsic tissue chromophores responsible for generation of optoacoustic responses

nanoparticles or fluorophores (Amiot et al. 2008; Tong et al. 2009; De La et al. 2008), or genetically encoded markers (proteins) (Razansky et al. 2009), can be additionally employed for contrast enhancement.

Vast majority of the modern OA imaging setups utilize lasers that emit ultrashort pulses in the nanosecond range, mainly due to good signal-to-noise performance and ease of parallelization. Under thermal and stress confinement conditions (Lutzweiler and Razansky 2013), usually assumed with respect to the duration of the laser pulse in this regime, the initially induced pressure distribution $p_0(r)$ is generally proportional to the distribution of the absorbed optical energy density $H(r)$ via

$$p_0 = \Gamma \cdot H, \tag{16.1}$$

where Γ is the dimensionless Grüneisen parameter describing the thermal and mechanical properties of the imaged tissue. Since Γ does not exhibit significant variations among different soft tissues, is most often assumed to be constant at a constant temperature.

The initial goal of optoacoustic imaging and tomography is to retrieve the absorbed optical energy density inside the object. However, the generated pressure fields can normally only be measured outside the object, whereas propagation of pressure waves toward the detection point is described by the optoacoustic wave equation (Kruger et al. 1995). The way to obtain optoacoustic images therefore consists in reconstructing distribution of the energy density $H(r)$, i.e., solving or inverting the optoacoustic wave equation given the pressure variations measured around the imaged object.

For structural applications, it is the spatial distribution of the optical absorption coefficient $\mu_a(r)$ that is usually more directly related to the structural composition of the imaged tissue rather than the absorbed energy density. Both are related via

$$H = \mu_a \cdot \Phi \tag{16.2}$$

where Φ is the light fluence (or photon density) field. Although one may presume that H is a simple product, in fact depends nonlinearly on the absorption coefficient μ_a. This is because the light fluence generally depends on the underlying optical properties, including optical scattering and absorption coefficients. Thus, it is important for image quantification purposes to account for the light fluence since it may considerably vary as a function of depth.

16.5.3 Multispectral Optoacoustic Tomography

While reconstructing distribution of the optical absorption coefficient may provide valuable structural (anatomical) information on the underlying tissue contrast, it is the concentrations of different chromophores c_i, not the optical absorption coefficient μ_a, that are mainly of interest from the biological point of view. For instance, in many applications, the blood-related absorption is of particular interest, providing valuable physiological or functional information. The relation between concentrations of the different chromophores and the optical absorption coefficient may be expressed via linear superposition, namely,

$$\mu_a(\lambda) = \sum_i \varepsilon_i(\lambda) \cdot c_i + \mu_{\mathrm{BG}}(\lambda), \tag{16.3}$$

where $\varepsilon_i(\lambda)$ are the wavelength-dependent molar extinction coefficients of the different intrinsic tissue chromophores or extrinsically administered agents and μ_{BG} is the residual (background) absorption, which might also include noise. To differentiate between contributions of different chromophores, their distinct spectral dependence on wavelength can be assessed (Rosencwaig 1973; Kostli et al. 2000). This multiwavelength imaging approach is known as multispectral optoacoustic tomography (MSOT) or spectroscopic imaging (Laufer et al. 2007; Razansky et al. 2009; Sethuraman et al. 2008; Razansky 2012). The process of recovering c_i from multispectral measurements is known as spectral unmixing. It can be combined with calculation of the light fluence or treated as a separate image processing step.

Due to versatility and wide availability of optical molecular agents, sensitive and accurate spectral processing to recover concentration of extrinsically administered agents may enable longitudinal molecular imaging studies. This can be done by resolving accumulation of agents with specific spectral signatures, such as targeted and activatable fluorescent molecular agents, nanoparticles, or genetic markers.

Figure 16.34 summarizes the main contributions to the OA signal generation chain, which need to be accounted for when developing accurate image reconstruction algorithms.

16.5.4 Optoacoustic Imaging Instrumentation

A typical optoacoustic setup consists of several key components. In the pulsed excitation mode, the tissue is illuminated by laser emitting monochromatic pulses of light with typical duration of some nanoseconds. For deep-tissue imaging applications, optical parametric oscillators are often used to provide a tunable wavelength in the spectrum of interest with pulse repetition rate in the order of a few tens of Hertz and per-pulse energies in the millijoule range. In optoacoustic microscopy and other superficial applications, where such high per-pulse energies are not required, other types of sources in the microjoule and nanojoule range are considered as well, including high repetition dye lasers (Song et al. 2009), laser diodes (Allen and Beard 2006b), and fiber lasers (Wang et al. 2011).

For tomographic imaging, the optoacoustically generated pressure profiles are captured with detectors surrounding the object. In comparison to ultrasound (US) imaging, OA signals are broadband (from several tens of kHz up to a 100 MHz for small structures), while their amplitude is relatively low. Their frequency content is mainly dependent on the characteristic size of absorbers in the imaged volume. Due to the dominating low-frequency content of OA waves generated by common biological targets, utilization of physical or synthetic aperture focusing may turn inefficient. Moreover, while in US the focusing can be done in both transmission and detection, only the latter is relevant for OA. On the other hand, the optical absorption contrast may reach more than one order of magnitude for blood versus other tissues (Wang 2009). This is in contrast to up to 10% contrast between different soft tissues in pulse-echo US imaging (Duck 1990). As a result of both inefficient focusing and high-absorption contrast, OA image formation using linear phased arrays and other focusing techniques suffers from severe out-of-focus artifacts, impaired contrast, image blurring, and overall lack of quantification abilities (Lutzweiler and Razansky 2013). Thus, in contrast to pulse-echo US, correct image reconstruction in OA imaging is ideally achieved by an unfocused detection of OA responses from as many tomographic viewing angles as possible around the imaged object.

Acoustic coupling between object and detector is usually ensured by water or coupling gel. For acquisition of spatially resolved data, either a single detector is scanned around/along the object or multiple detectors acquire the data in parallel. The latter further allows for fast data acquisition, e.g., rendering images from single laser shots. The signals are then pre-amplified and digitized by a fast data acquisition system. Figure 16.35 illustrates the broad variety of OA setups employed for small animal imaging, including optical-resolution microscopy (Hu et al. 2011), endoscopy

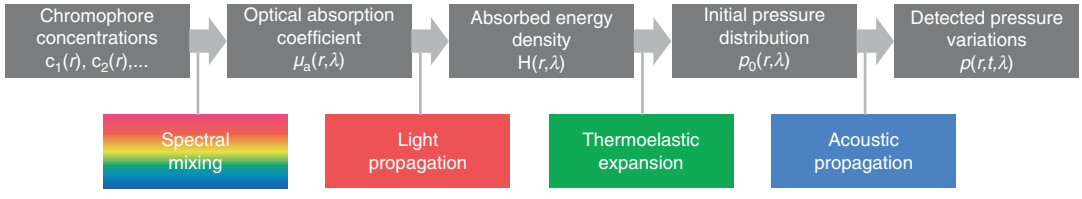

Fig. 16.34 Schematic representation of the sequence of generation and detection of optoacoustic signals

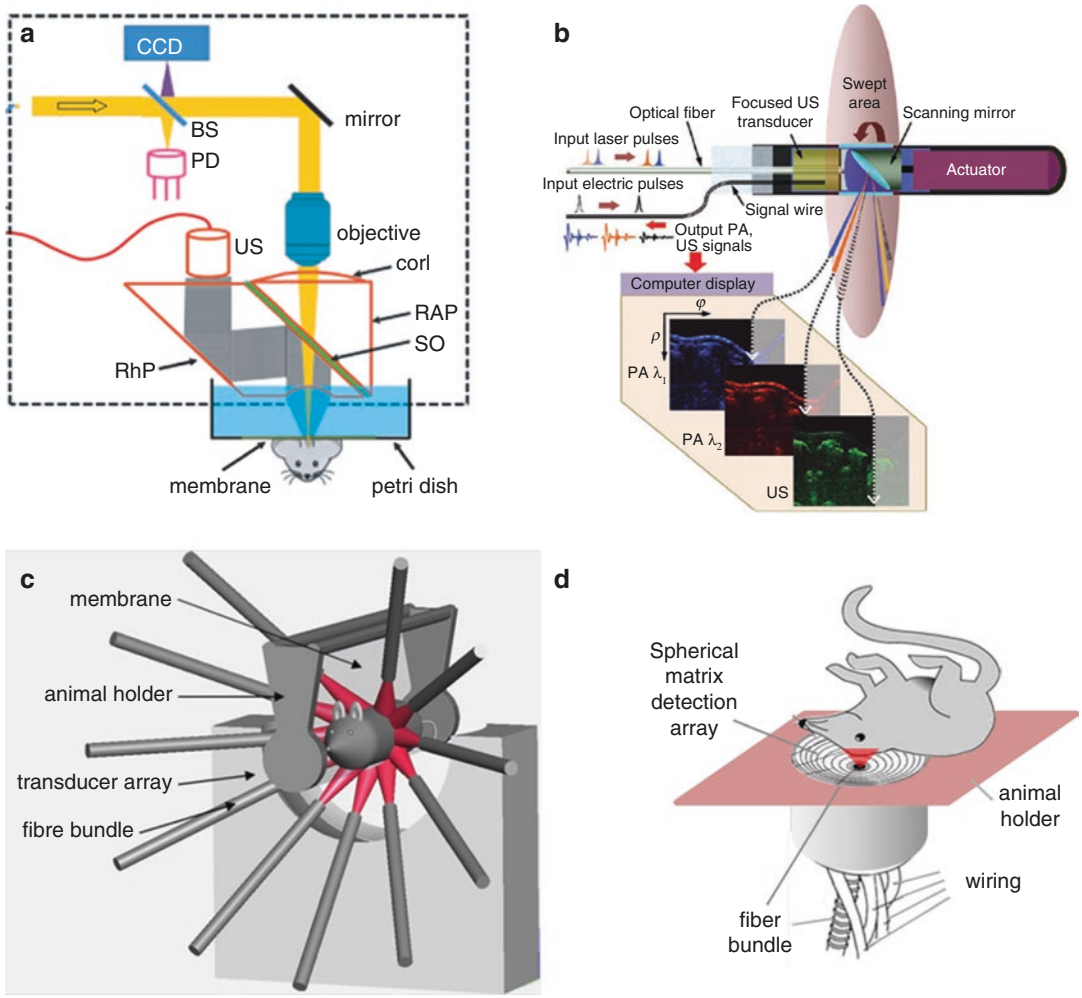

Fig. 16.35 Various types of optoacoustic imaging systems. (**a**) Optical-resolution photoacoustic microscopy (OR-PAM) scanner used for in vivo imaging of mice (Hu et al. 2011). Spatial resolution of the system in the lateral direction is determined by the size of the optical focus. Three-dimensional data is acquired by raster scanning of the optical beam along the imaged area. *BS* beam splitter, *PD* photodiode, *CorL* correction lens, *RAP* right-angle prism, *SO* silicone oil, *RhP* rhomboid prism, *US* ultrasonic transducer (central frequency – 50 MHz). The CCD is used to view the imaging region (Reprinted with permission from the Optical Society of America). (**b**) Combined endoscopic system for co-registered US and dual-wavelength functional OA imaging in vivo (Yang et al. 2012). The endoscope carries out circumferential sector scanning by rotating a scanning mirror, which reflects both the ultrasonic waves and laser pulses and enables static mounting of the associated illumination and ultrasonic pulse-generation detection units (Reprinted with permission from the Nature Publishing Group). (**c**) Schematic drawing of the real-time whole-body mouse scanner including the animal holder, illumination device, and transducer array (Razansky et al. 2011). A curved array of wide-band and cylindrically focused ultrasound transducers enables parallel data acquisition from the imaged cross-sectional plane. Optical fibers are used to homogeneously illuminate the object. By translating the animal holder, three-dimensional data can be acquired (Reprinted with permission from the Nature Publishing Group). (**d**) Real-time volumetric imaging system comprising of a spherical matrix ultrasound detection array with the laser illumination provided via a fiber bundle pulled through the center of the array. Rapid acquisition of multiwavelength data from an entire imaged volume, combined with real-time image reconstruction and spectral unmixing, provides four- and five-dimensional imaging capabilities by rendering volumetric unmixed images of individual chromophores in real time (Deán-Ben and Razansky 2014) (Reprinted with permission from the Nature Publishing Group)

(Yang et al. 2012), cross-sectional whole-body tomography (Razansky et al. 2011), as well as real-time volumetric (4D) and 5D imaging systems (Deán-Ben and Razansky 2014).

16.5.5 Small Animal Imaging Applications

Due to its rich optical contrast and high spatiotemporal resolution, optoacoustics can deliver multiple types of contrast from deep tissues. Naturally, the best intrinsic tissue contrast at the visible and near-infrared wavelengths arises from highly absorbing hemoglobin; thus, blood vessels are clearly visible in the optoacoustic images. OA microscopy is thus often geared toward investigation of vascular structures and neovascularization, providing an excellent intrinsic contrast and a high spatial resolution in the order of some tens of μm and penetration of several millimeters into scattering tissues. In this way, disease-related anatomical changes can be visualized, e.g., development of tumor neovasculature (Laufer et al. 2012) (Fig. 16.36a–c). While images can be generated at a single wavelength, multiwavelength illumination and spectral processing are necessary for optimally identifying the unique spectral signatures of intrinsic tissue chromophores, such as hemoglobin, water, and lipids. It is therefore natural for OA imaging to volumetrically visualize blood oxygenation levels in living tissues by resolving the contribution from oxygenated versus deoxygenated hemoglobin. This functional imaging capability is showcased in Fig. 16.36d where oxygen saturation status of individual blood vessels was visualized with the optical-resolution microscopy method (Hu et al. 2011).

Preclinical whole-body imaging of small animals with multispectral optoacoustic tomography (MSOT) systems is yet another key application of OA imaging. These systems can provide tomographic images with a resolution in the order of hundred μm for depths between several millimeters to several centimeters. Possible applications include monitoring of tumor hypoxia, drug response, or molecular targets in biological model organisms (Herzog et al. 2012; Lozano et al. 2014). The ability of MSOT to visualize deep-seated fluorescent proteins with high resolution has been also demonstrated (Razansky et al. 2009). Figures 16.36e, f show example of a study on kinetics and biodistribution of near-infrared contrast agent in a living mouse (Taruttis et al. 2012). The uptake of a carboxylate dye in separate regions of the kidneys was tracked in real time over 30 min post its systemic injection. The images indicate different dynamics in different areas of the kidneys, suggesting that two dependent processes are being imaged, firstly the filtration of agent in the cortex and subsequently the excretion toward the ureter.

Finally, Fig. 16.36g, h demonstrates the molecular imaging capabilities of MSOT, which was employed in this case to detect upregulated epidermal growth factor (EGF) receptor in orthotopic pancreatic xenografts using a near-infrared EGF-conjugated CF-750 fluorescent probe (Hudson et al. 2014). The images clearly indicate the region where EGF-750 probe has accumulated with high spatial resolution. In comparison, fluorescence imaging of the mice also validated the accumulation of the EGF-750 probe at 6 h with specific accumulation in the lower left quadrant of the tumor (Fig. 16.36h). However, due to intense light scattering in deep tissues, the fluorescence measurements were only able to provide diffuse signal pattern with no depth resolution.

16.5.6 Conclusions

Owing to its hybrid nature, optoacoustics benefits from both the rich and versatile optical contrast and high (diffraction-limited) spatial resolution associated with the scattering-free nature of ultrasonic wave propagation. Much like other optical imaging modalities, optoacoustics uses safe nonionizing radiation at the visible and near-infrared wavelengths. Thus, it provides an excellent platform for multiscale investigations using

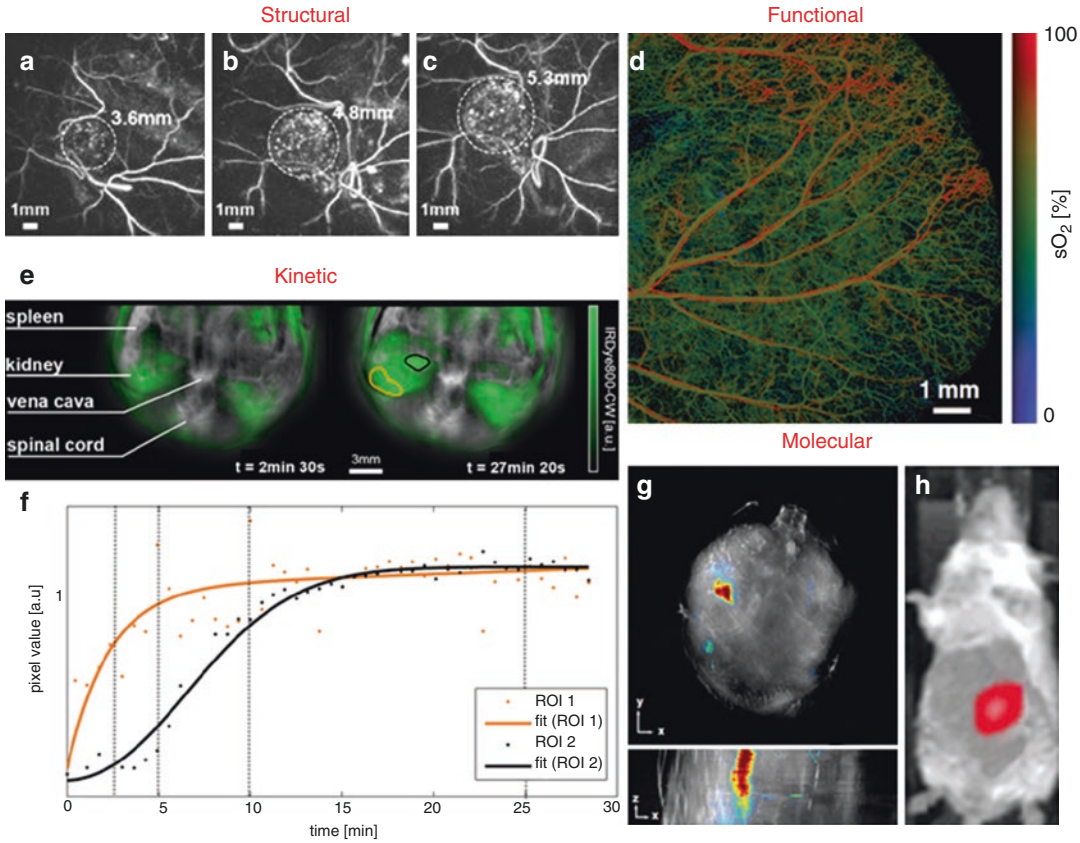

Fig. 16.36 Optoacoustic small animal imaging can provide multiple indications on in vivo structural, functional, kinetic, and molecular tissue profiles with a single modality. (**a**–**c**) show anatomical appearance of proliferating subcutaneous 293 T tumor and surrounding vasculature from day 7 to day 26 post inoculation (Laufer et al. 2012) (Reprinted with permission from SPIE). (**d**) Optical-resolution microscopy image representing distribution of blood oxygenation in a mouse ear (Hu et al. 2011) (Reprinted with permission from the Optical Society of America). (**e**) Time series of cross-sectional whole-body mouse images visualizing the biodistribution of IRdye800 near-infrared contrast agent in green overlaid on the anatomical image (Taruttis et al. 2012). (**f**) Temporal evolution of dye signal in the regions of interest highlighted in (**e**), orange showing a region in the renal cortex that displays early and steep signal pickup and black indicating a region in the renal pelvis where probe accumulation is delayed and has a smoother profile. Individual multispectral measurements acquired with a rate of approximately 2 per minute are shown as dots, while the solid line represents a fit to an analytical function (Reprinted with permission from the *Public Library of Science)*. (**g**) Multispectral optoacoustic tomography (MSOT) detection of upregulated epidermal growth factor (EGF) receptor in orthotopic pancreatic xenografts using a targeted near-infrared EGF-conjugated CF-750 fluorescent probe (Hudson et al. 2014). Three-dimensional biodistribution of targeted EGF-750 probe is shown in color at 6 h postinjection. While MSOT can localize distribution of the probe with high resolution and all three dimensions, epifluorescence images (**h**) from the same animal have highly blurred low-resolution appearance with no depth-resolved information (Reprinted with permission from the American Association for Cancer Research)

the same contrast, from microscopic observations at the single capillary and cell level to whole-body imaging of small animals and deep-tissue imaging of humans.

The optoacoustic effect relies on the absorption of light and is therefore ideally suited for vascular imaging since most of intrinsic contrast is obtained from high-hemoglobin-containing tissues like whole blood. This opens a multitude of potential applications in visualization of disease-related vascular changes, neovascularization, tumor microenvironment, and noninvasive

functional diagnostics of blood perfusion and oxygenation. Yet, the capacity to image spectrally distinctive photo-absorbing agents with high spatiotemporal resolution at depths far beyond the diffusive limit of light opens unprecedented capabilities for functional and molecular imaging.

Extensive research is underway to address technical challenges associated with the intriguing and highly promising combination of light and sound. Main limitations are currently associated with the lack of reliable and affordable laser and ultrasound detection technology that can optimally address the unique needs of optoacoustics, such as high per-pulse laser energy or repetition rate, ultrawideband detection, high detection sensitivity, and miniaturization. Multiple frontiers are also open in the algorithmic and inverse theory areas, trying to address challenges related to artifact removal, image quantification, reconstruction strategies in the presence of acoustically mismatched areas, real-time operation, and multispectral data processing.

All in all, optoacoustic imaging attracts growing interest from the biological and medical research communities, as manifested by the ever-increasing number of publications encompassing great variety of new applications that exploit the unique advantages offered by the technology. It is therefore expected to find broad applications in biological research and clinical practice in multiple fields, including cancer research, functional brain imaging, cardiovascular imaging, gastroenterology, ophthalmology, drug development, and treatment monitoring.

16.6 Optical Probes

Kai Licha

16.6.1 Introduction: Optical Probes for Animal Imaging

The application of optical imaging technologies for drug discovery research and the development of novel preclinical animal models have expanded with tremendous vigor in the past few years. The fact that fluorescent dyes can be detected at low concentrations and nonionizing and harmless radiation is applied with rather low technical effort makes optical techniques attractive for routine use in the animal imaging laboratory. Novel imaging probes and contrast agents have been designed in a broad variety addressing the various requirements given by the disease problem at the preclinical animal imaging stage. Moreover, the industry has identified this field as a market from the side both the imaging equipment and the fluorescent probes applied as readily injectable contrast agents or reactive labels for bioconjugation chemistry.

Imaging devices with powerful and versatile capabilities are now commercially available, addressing different needs of the customer, such as multicolor imaging, time-resolved imaging, planar or tomographic geometry, signal quantification, spectral unmixing for background correction, or zooming within macroscopic scale. A closer look into these topics is provided elsewhere in this book.

The design of fluorescent imaging probes for in vivo imaging applications has likewise emerged and is reflected by an increasing number of commercialized probes and labels. The underlying chemistries have been optimized for their capability to monitor disease-specific anatomic, physiological, and molecular parameters by way of directly applicable imaging probes or by specific reactive labels, which can be used by the customer to fluorescently label his own drug candidate for further studies or derivatize important biological ligands to investigate the basics of a given targeting approach.

The main objective of this contribution is to provide an overview on the different choices available when setting up an imaging protocol using optical probes. Hereby, the review sets a focus on practical aspects of the application of optical probes for animal imaging and drug discovery research. The state of the art of imaging probes is first discussed covering nontargeted and vascular agents, approaches to generate targeted agents via reactive fluorophores, the field of enzymatically activatable probes, and imaging agents

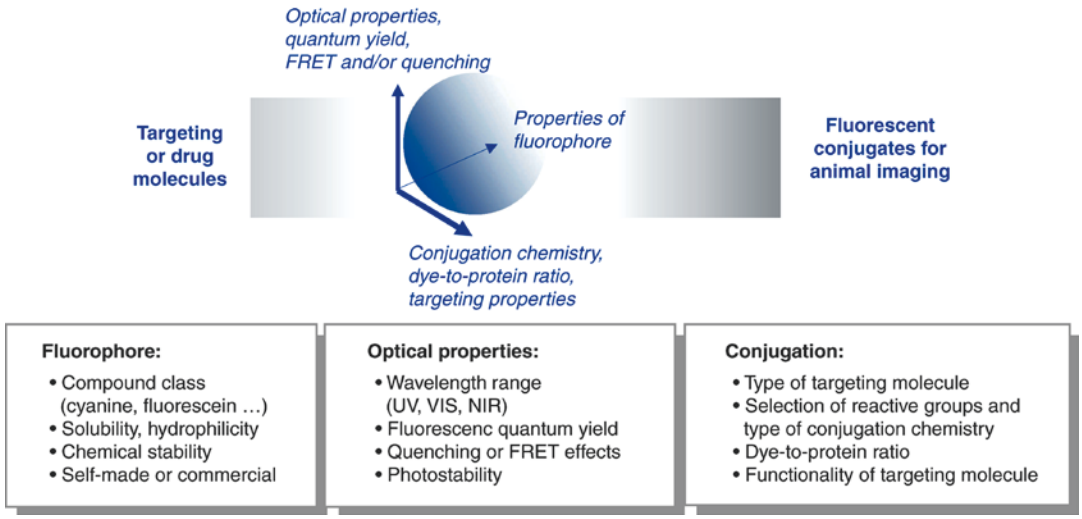

Fig. 16.37 Basic idea and general parameters for the generation of optical probes

based on particles. To facilitate the researcher's choice, a selection of relevant parameters is discussed in the subsequent chapter, discussing appropriate examples out of the literature. At this point, it is mentioned that examples include published work and refer to selected commercial compounds and companies as well. The intention of this review is neither to provide a comprehensive dataset on these probes nor to accentuate particular commercial suppliers. Figure 16.37 summarizes the general parameters that contribute to the design of optical imaging probes.

16.6.2 State-of-the-Art Technologies

16.6.2.1 Basics on Fluorescent Dyes

An efficient fluorescence imaging probe should employ a combination of different properties, which are (1) a high fluorescence quantum yield in the desired wavelength spectrum, (2) sufficient biological stability and photostability to permit unimpaired image acquisition, and (3) reasonable solubility in (most) aqueous environment to enable bioconjugation and labeling reactions without substantial triggering of aggregation and/or precipitation. Among the many possible organic fluorophore classes, the polymethine dyes (e.g., cyanines, hemicyanines, benzopyrylium dyes), xanthene dyes (rhodamines and fluoresceins), and also some oxazoles and thiazoles (e.g., methylene blue, Nile blue) are basically the ones that are widely established and have been contributing to the majority of scientific results (Licha and Resch-Genger 2011, 2014). Figure 16.38 illustrates typical absorption and fluorescence spectra of these types of fluorophores, thereby showing the wavelength range within imaging is possible. While xanthene dyes do not reach fluorescence emission far beyond 700 nm, they exhibit extremely high fluorescence quantum yields often close to 100 %. In turn, cyanine dyes are capable to cover the entire spectrum from VIS to NIR (>900 nm) with high extinction coefficients (up to 250,000 L/mol cm), but rather moderate fluorescence quantum yields (up to 30 %). Other interesting but less frequently applied organic dyes include squaraines (Luo et al. 2011b) and BODIPYs (Boens et al. 2012). Besides organic fluorophores, inorganic semiconductor nanoparticles have emerged as alternative fluorescent reporters (see Chap. 16.1.3).

As further detailed in the subsequent chapters, the most relevant applications for these dyes as imaging tools are the direct use as injectable contrast agents in a nontargeted or passively distributing format, the use as reactive fluorophore

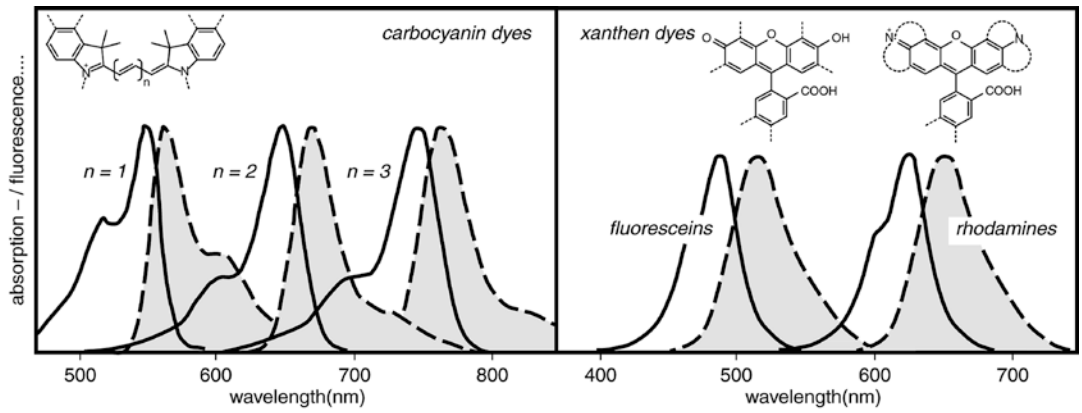

Fig. 16.38 Typical absorption and fluorescence spectra of cyanine dye and xanthenes dyes shown as idealized illustration

labels to create targeted conjugates of biological or synthetic origin, and the use as quenched components or non-fluorescent precursors as activatable imaging probes (also named "turn-on" probes) to monitor different kinds of enzyme activity. Furthermore, pH-responsive fluorophores enabling the sensing of pH in tissues have been approached as additional parameter in tumor models.

16.6.2.2 Nontargeted and Vascular Dyes as Contrast Agents

A variety of fluorescent dyes for passive targeting and vascular circulation have been applied as fluorescent imaging probes. These probes, most of them carbocyanine dyes, represent the basic chemicals for the design of labels and probes. Using these dyes as imaging agents by themselves, they act by their physicochemical and structural properties since they do not employ structures designed for a specific molecular interaction. However, the suitability for animal studies, e.g., the characterization of experimental tumor models, has been demonstrated in various publications.

The near-infrared dye indocyanine green (ICG, absorption ~780–800 nm) was approved in the 1960s as a diagnostic drug, was rediscovered in the 1990s as an imaging agent, and is today, together with fluorescein, frequently applied for fluorescence angiography in ophthalmology (Richards et al. 1998), as well as increasingly used for fluorescence methods in surgery (Alander et al. 2012). Similarly, novel cyanine dye derivatives have been created as passively targeted contrast agents of simple synthetic availability. Examples are the dye SIDAG, which leads to enhanced uptake in a variety of tumor models and permits differentiation of the degree of angiogenesis (Wall et al. 2008). Furthermore, the compound was shown to enable fluorescence imaging of inflammation in a model of rheumatoid arthritis (Fischer et al. 2006). It therefore provides a powerful tool for the validation of preclinical models, imaging equipment, and therapeutic studies (TryX750, mivenion). With the IRDyes (LI-COR Biosciences) or Cy5.5 (GE Healthcare Life Sciences), other examples of nontargeted or control dyes with published results for animal imaging and human applications, such as lymphatic mapping or studies on T-cell migration, accompany ICG (Foster et al. 2008; Rasmussen et al. 2009). Another class that has recently attracted attention is the benzopyrylium-based polymethine dyes (Dyomics) (Pauli et al. 2009b). In Fig. 16.39, a panel of selected chromophores is depicted. Beyond ICG, which by itself is not directly applicable to synthesize reactive derivatives for biolabeling due to the absence of chemical functionalities, the compounds discussed here represent basic structures to create in few further steps reactive labels and subsequently any desired bioconjugate.

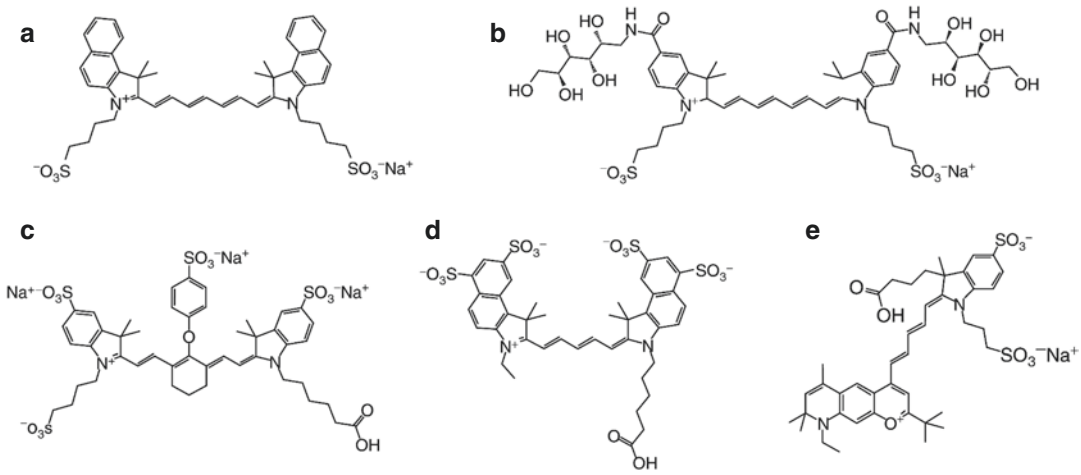

Fig. 16.39 Selected near-infrared fluorescent dyes, which have been used as nontargeted probes for in vivo fluorescence imaging: (**a**) indocyanine green, (**b**) SIDAG (Wall et al. 2008), (**c**) IRDye® 800CW (LI-COR, [394]), (**d**) Cy5.5® carboxylic acid (GE Healthcare) and (**e**) DY-750 (Dyomics)

Cyanine dye conjugates with substantially increased molecular weight have been designed to enable the visualization of vascular structures and to study effects on the vascularity. For this purpose, the dyes were covalently conjugated to macromolecular carriers, such as albumin, dextran, or other biopolymers (Klohs et al. 2009) or non-covalently entrapped into dendritic architectures used as passive drug delivery systems (Quadir et al. 2008). These conjugates have been useful for imaging tumors but also to visualize and characterize tissue architecture in vivo on a macro- to microscopic imaging level. Commercialized are, e.g., streptavidin, ovalbumin, protein A, and dextran conjugates with a variety of Alex Fluor® labels, marketed under the brand SAIVI™ (Invitrogen) as imaging probes and secondary detection materials. Other available probes are the Angio Sense® probes (Perkin Elmer) based on large, long-circulating macromolecules at 250 kD (type of macromolecular carrier not published).

16.6.2.3 Reactive Dyes and Labeled Targeting Molecules

This chapter addresses the increasing demand for fluorescently labeled drug candidates based on molecules of synthetic (small organic molecules, peptides, oligonucleotides) or biotechnological origin, such as engineered proteins, antibodies, and novel protein formats. In order to get an insight into the targeting capabilities of these drugs in vivo, optical imaging is establishing as a fast and easy-to-apply technology in the animal imaging laboratory. As further outlined in Chap. 16.6.3.2, fluorescence labeling offers the opportunity to study biological and physicochemical properties of a desired candidate along the entire path from synthesis, in vitro and cellular level to the in vivo application in higher organisms.

Generally, optical imaging probes in the format of bioconjugates range from protein conjugates, antibody conjugates, structures based on oligonucleotides to receptor-avid peptide conjugates. Furthermore, a large panel of small-molecule substrates and ligands, such as folate, cyanocobalamin, glucose, bisphosphonates, as well as rationally designed receptor ligands, has been conjugated with fluorophores for in vivo studies.

This work has ultimately led to a large variety of targeted imaging agents published in the past few years. A selection of different reactive dye labels and resulting conjugates is depicted in Fig. 16.40. Being not the intention of this chapter to discuss these versatile approaches in detail, the reader is referred to respective reviewing publications (Licha and and Resch-Genger 2014;

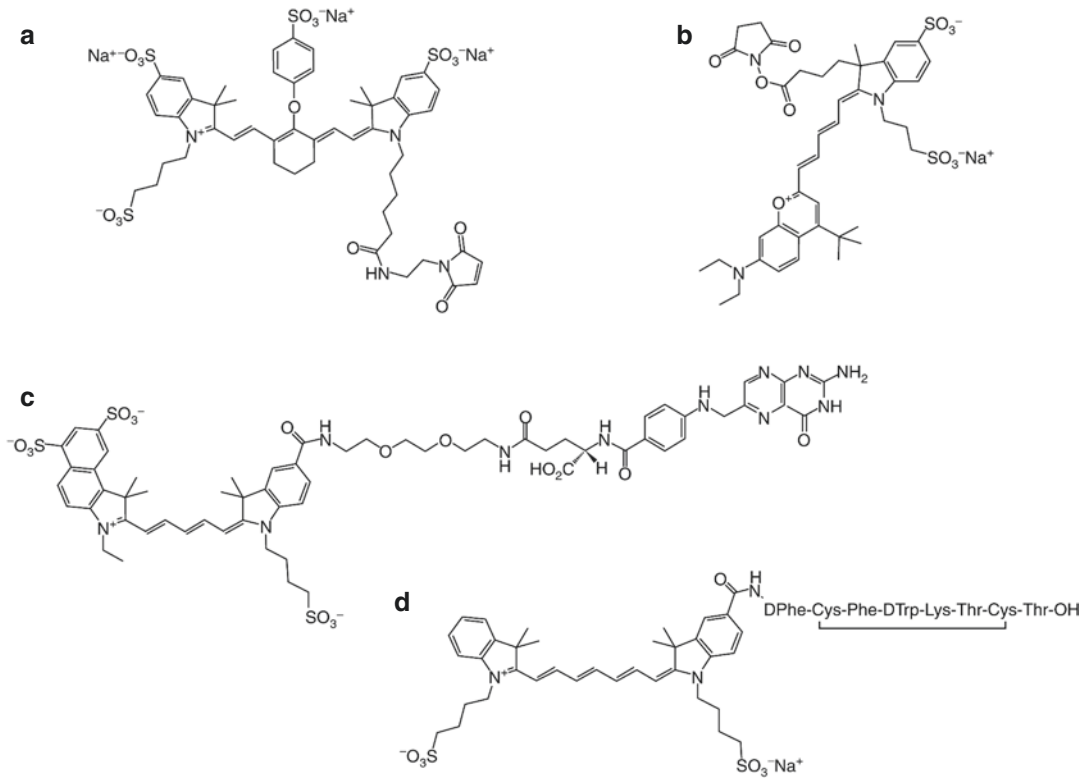

Fig. 16.40 Selected dyes in a reactive format for biolabeling and published bioconjugates: (**a**) IRDye® 800CW Maleimide (LI-COR), (**b**) DY-781 NHS-ester (Dyomics), (**c**) Cy5.5-folate conjugate (Moon et al. 2003), and (**d**) indotricarbocyanineoctreotate (Becker et al. 2001)

Umezawa et al. 2014). A number of conjugates have been made commercially available addressing fundamental pathways in cellular uptake, angiogenesis, and tumor growth, for instance, conjugates with EGF (LI-COR), transferrin, annexin V, bombesin, folate, glucose, or certain bisphosphonates with bone affinity (Perkin Elmer).

Oligonucleotides and small peptides, as opposed to, e.g., targeting molecules of biotechnological origin, are accessible via solid-phase synthesis with the fluorophore conjugation capable of being implemented into the synthetic protocol. Most of the dyes used have shown to be stable enough with respect to the chemical conditions required for peptide cleavage from the resin and other interventions (e.g., forming disulfide bridges via oxidation). Examples for the synthesis of low-molecular-weight peptide conjugates comprising different cyanine or rhodamine dyes have been published (Becker et al. 2001; Mier et al. 2002). For the 3′ and 5′ labeling of oligonucleotides, conjugation chemistry can be applied similarly. A broad set of labels and quenchers covering the entire VIS to NIR is, for instance, offered with the ATTO dyes (ATTO-TEC).

16.6.2.4 Activatable or "Turn-On" Probes

Weissleder and coworkers have introduced an optical imaging approach, which is of fundamental difference to the approaches described above and utilizes the unique opportunity of modulating optical signals through intramolecular fluorescence quenching effects (Hilderbrand and Weissleder 2010; Weissleder et al. 1999). These probes are "activatable" polymeric conjugates based on a poly-L-lysine/polyethylene glycol graft polymer, which are "switched on" when

single fluorochrome fragments are cleaved from the fluorescence-quenched polymeric structure by tumor-specific proteolytic enzymes, thus leading to signal amplification of up to 200-fold. In various preclinical disease models, the agents have demonstrated the imaging enzymatic activity and report the in vivo efficacy of enzyme-inhibiting drugs (Bremer et al. 2001b). The underlying imaging probes are based on cleavable graft polymers of high molecular weight and are commercialized by VisEn Medical Inc. Under different trade names (ProSense®, MMPSense®), the compounds are cleaved and activated by enzymes such as cathepsins and matrix metalloproteinases at spectral ranges of 680 and 750 nm, respectively.

Rationally designed conjugates of defined chemical structures, activatable photosensitizers for photodynamic therapy (Stefflova et al. 2007), as well as constructs sensitive to cleavage by other enzymes, such as thrombin and caspases (Barnett et al. 2009), have expanded this versatile technology. More recently, the capability to turn on fluorescence by an enzymatic conversion has been implemented into the fluorophore structure itself, thereby circumventing the need to employ a certain number of molecules to generate quenching (Kisin-Finfer et al. 2014). The advantage of such structures is the extremely low background in the switched-off state, simply because this precursor does not contain generate background due to the absence of a fully established chromophore.

16.6.2.5 Probes for Sensing of pH and Reactive Oxygen Species

The establishment and characterization of tumor models might benefit from knowledge about certain physiological parameters, such as tumor pH (extracellular or intracellular) and the level of oxidative stress (reactive oxygen species), both of which being valuable in combination with molecular conditions (Licha and Resch-Genger 2014).

Examples for pH-responsive xanthene dyes are BCECF (2′,7′-bis-(2-carboxyethyl)-5-(and-6-)-carboxyfluorescein) and BCPCF (2′,7′-bis-(2-carboxypropyl)-5-(and-6)-carboxyfluorescein) (see also the Oregon Green series from Life Technologies). Beyond fluoresceins and rhodamines, similarly, benzoxanthenes have been synthesized in many versions combining the advantages of fluoresceins and rhodamines, such as the SNARF and SNAFL dyes (semi-naphthorhodafluor and semi-naphthofluorescein derivatives, respectively). Typically, these dyes do not show significant pH-dependent changes in emission. Accordingly, these probes are termed dual or ratiometric excitation probes for pH, requiring excitation at two wavelengths.

More relevant for imaging purposes are NIR cyanine dyes which exhibit responsiveness to pH changes by omitting one substituent in the indole end groups. Recent examples include the commercially available CypHer5E dye label (Mathejczyk et al. 2012) and other similarly constructed NIR-emissive pH-responsive cyanine dyes (Lee et al. 2011), which have been applied for in vivo imaging thereby showing advantages in tumor detection and background suppression.

The term reactive oxygen species (ROS) encompasses oxygen radicals and peroxides such as $\bullet OH^-$, $\bullet O_2^-$, and •OOH which are important indicators for the oxidative state of cells, in particular as a result of certain therapeutic intervention. Thus, fluorescent sensors and stimuli-responsive fluorophores have emerged as imaging tools. An example are so-called hydrocyanines (Selvam et al. 2011) which change from a reduced, non-colored status to the chromophore structure upon oxidation in living systems.

16.6.2.6 Fluorescent Particles as Imaging Agents

Fluorescent imaging agents based on particles have shown great utility, especially for applications on cellular staining (in vitro) and vascular imaging (in vivo). In principle, there are two different groups of nanoparticle probes. On the one hand, nanosized materials based on organic and/or inorganic chemistry have been equipped with organic fluorophores, by either incorporating the dye molecules into the nanoshells or attaching it to surface functionalities (Azar and Intes 2008). Interesting nanomaterials, including semiconductor nanoparticles

(quantum dots), gold nanoparticles, and carbon-based particles (nanotubes), have emerged as powerful imaging tools with brilliant optical properties (Resch-Genger et al. 2008, Holzinger et al. 2014). Probably in a most advanced state of utility are quantum dots which consist of atoms such as Cd, Se, Te, S, and Zn. The fluorescence emission range depends on the diameter of the particles, which can be synthesized in a very controlled fashion with respect to size and surface modifications (Fig. 16.41). Surfaces employing stabilizing polymers as well as targeting molecules, such as antibodies and peptides, have expanded their applications for in vivo animal imaging (Bentolila et al. 2009).

Nanoparticles are particularly interesting for multimodality imaging purposes due to their modular composition. Magnetic cores for MRI imaging can be functionalized with additional fluorophores to allow fluorescent tracking and vice versa; fluorescent cores have been combined with paramagnetic complexes (Azar and Intes 2008).

16.6.3 The Choice of Parameters

16.6.3.1 Optical Properties

Generally, the choice of the spectral range of absorption and fluorescence of the dye determines whether it is detectable on tissue surfaces (UV–vis dyes, 400–700 nm) or from deeper-located tissue areas (NIR dyes, >700 nm). A prerequisite for sensitive detection of a contrast-enhancing dye is a high extinction coefficient at the desired absorption wavelength. If fluorescence is recorded within the UV/VIS spectral region, both autofluorescence and the administered contrast agent will contribute to the observed signal, while in the NIR spectral region, tissue autofluorescence is negligible due to the absence of endogenous NIR fluorophores. In the latter case, the detected signal nearly exclusively reveals the distribution of the optical imaging probe.

The broad availability of fluorophore labels allows the selection of probes exactly matching the technical parameters of a given analytical instrument. Under practical circumstances is the application of one particular fluorophore for a research program starting at the in vitro level with cell microscopy, FACS, and other assays, then reaching in vivo imaging studies in animals, often not possible. Analytical instruments are usually not equipped with excitation and detection components permitting detection with sufficient sensitivity over the entire spectral range. Therefore, a work-around strategy often involves the choice of an appropriate series of fluorophores that differ only in minor extent in their

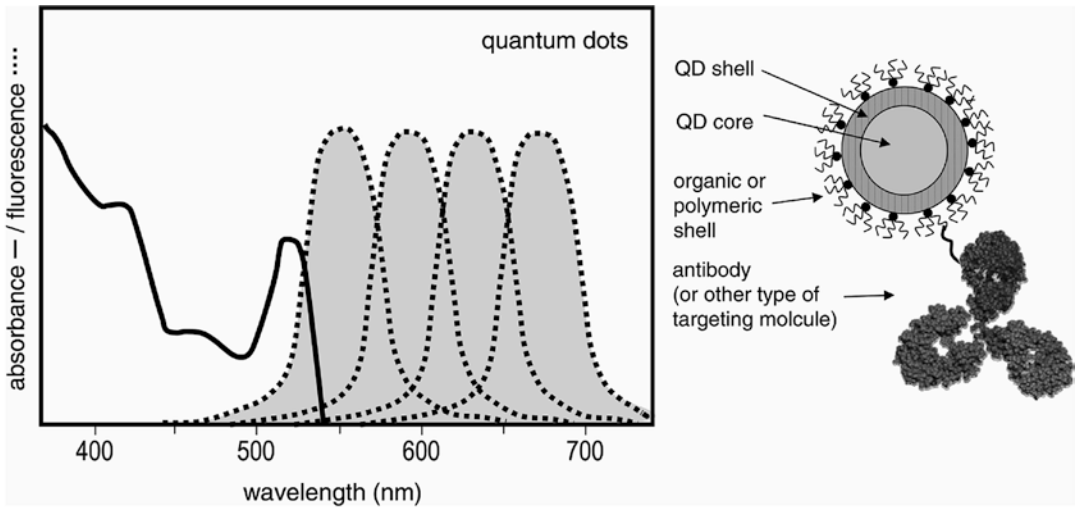

Fig. 16.41 Typical absorption and fluorescence spectra of quantum dots shown as idealized illustration; principal design of targeted quantum dot conjugates

chemical structures. This strategy minimizes unexpected effects on the resulting targeting conjugate when changing the fluorophore backbone. Here, cyanine dyes with their carbo-, dicarbo-, and tricarbocyanine homology are well suited. Examples of dyes offered as series are the CyDye™ series (GE Healthcare Life Sciences), which have been one of the first comprehensive product lines for fluorescence labeling (Cy3, Cy5, Cy5.5, Cy7).

The Alexa Fluor® Dye series (Invitrogen/Molecular Probes) have expanded the available spectral emission range from approximately 450 to 800 nm including derivatives (cyanine and xanthene) of improved photostability and fluorescence quantum yields. Alexa Fluor 488, Alexa Fluor 546, Alexa Fluor 555, and Alexa Fluor 750 are examples for products (consistently named by their excitation maximum). Similarly, highly hydrophilic Cy5.5-like pentamethine dyes have been reported in comparison to the known Cy5.5 label (LI-COR and (Pauli et al. 2013)). Another group is based on a different chromophore type, the borondipyrromethenes, known as BODIPY dyes (Invitrogen) (Boens et al. 2012). For a representative cyanine dye series, the typical color appearance of solutions (approximately 0.1 mM) in water is depicted in Fig. 16.42, which might facilitate the identification of the correct probe in case of some disorientation caused by too many flasks at the same time on the bench.

Generally, reactive dyes are offered in different version of chemoselectivity (see Chap. 16.6.3.3) so that the most reasonable labeling chemistry can be applied. The obtained amount of conjugate has to match the extent of the planned animal imaging study. Typically, fluorescent conjugates have been applied at doses in the range of 0.1–1 μmol/kg (i.v.), which corresponds to approximately 0.1–1 mg/kg amount of fluorophore (calculation based on the molecular weight of the fluorophore). Under technical aspects, the dose should be chosen such that a reasonable enhancement of the overall signal intensity in the animal directly after administration is detected (e.g., at least tenfold increase compared to background signal before injection).

16.6.3.2 Pathophysiological Paradigm

Viewing the applications of optical imaging probes from the angle of their pathophysiological function, it appears as common sense to group the probes into nontargeted or vascular agents, targeted conjugates, and activatable probes. As detailed in the preceding chapter

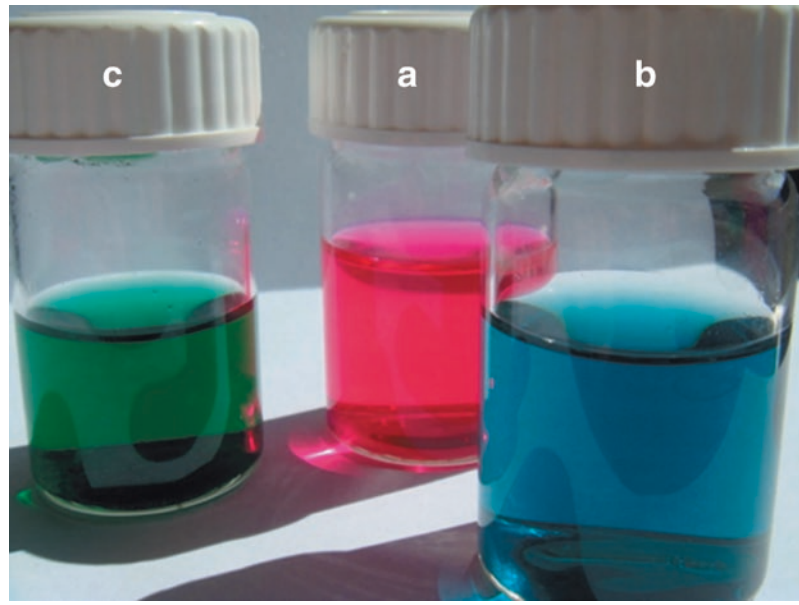

Fig. 16.42 Photograph of cyanine dye solutions: (**a**) indocarbocyanine with abs/fluor 550/580 nm, (**b**) indodicarbocyanine 650/680 nm, and (**c**) indotricarbocyanine 750/780 nm. Concentration of solutions approximately 0.1 mM in water

on state-of-the-art technologies, a host of compounds have been designed and studied for each of these three fundamental strategies. It depends on the rationale of the respective scientific problem to be solved by the application of in vivo optical imaging. Vascular or nontargeted fluorophores, as well as circulating fluorescent particles might be used first when a general imaging protocol is to be established, for the characterization of novel disease models (growth characteristics, vascularity, tumor sizes, formation of metastases, etc.). Other interesting aspects refer to the dose finding, detection limits, and image acquisition parameters. Targeted conjugates permit the imaging of molecular information, such as specific cellular expression profile. Fluorescently labeled drug candidates can be monitored with respect to their in vivo uptake into the target tissue and their capability to bind the molecular target. The underlying rationale is often to study the pharmacokinetic behavior of the probe, which has to fulfill certain properties with respect to their adsorption, distribution, metabolization, and excretion (ADME) for the living organism. Optical imaging can provide a fast and easy access to semiquantitative ADME data; however, a true quantification of drug amounts and the fate of metabolites in the organs are technically difficult. Here, radioactive techniques are a method of choice. Activatable probes provide insight into the third level of detecting protein function, such as the activity of proteolytic enzymes. Here, the injected imaging probe is silent until activated by the corresponding enzyme. Accordingly, a concentration ratio between diseased tissue and normal areas is not necessarily a requirement as long as the circulating fraction of the probe remains undetectable. This technology has shown to be applicable for the imaging of enzyme inhibitors in drug screening protocols (Fig. 16.43).

Probably, the combined exploitation of these mechanisms would allow that the deepest insight into the physiology and molecular biology of disease formation and progression be gained. At this point, it is worth to emphasize that a particular opportunity of fluorescence detection is the principal capability of multicolor imaging given that the imaging instrumentation permits multiple excitation and/or detection wavelengths. To give an example, the tumor vascularity would be detectable by a long-circulating vascular probe (e.g., 680 nm excitation), while the analysis of a certain receptor expression could be accomplished by a target-specific conjugate working at 750 or 800 nm.

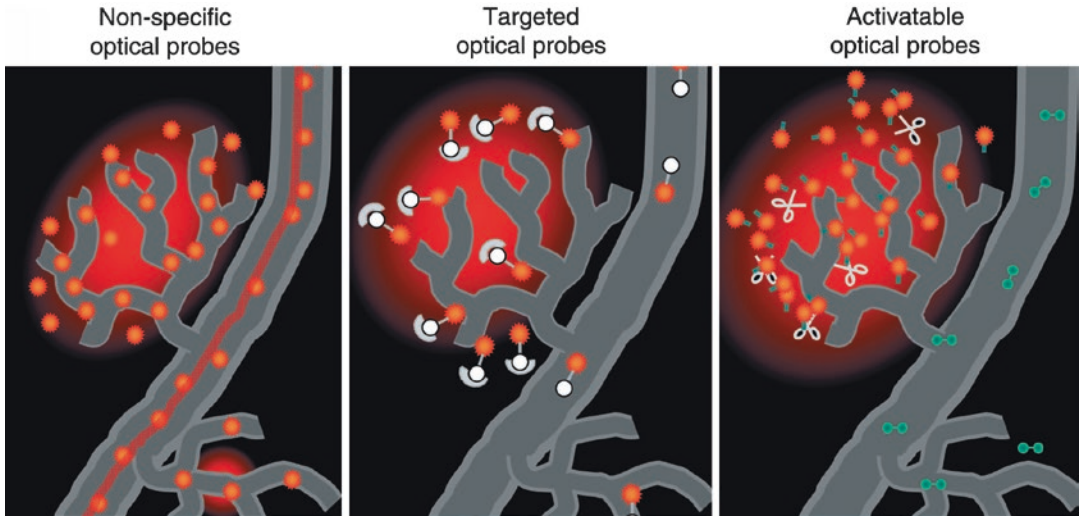

Fig. 16.43 Illustration of the different mechanisms of contrast generation by fluorescent imaging probes. In principle, the target-to-background ratios of signals and resulting imaging contrasts increase from nonspecific optical probes to targeted conjugates and activatable probes (Modified with permission from Sonja Vollmer)

16.6.3.3 Type of Labeling Chemistry

For the labeling of proteins, antibodies, or other macromolecules, the type of labeling reaction has to be considered. Generally, different residues in the macromolecule are available for covalent attachment to reactive fluorophores. The most relevant reaction sites are amino groups (lysines), thiol groups (cysteine), hydroxyl groups (threonine, serine, and glycans), and aldehydes (generated from oxidative cleavage of glycosylated structures). The principle pathways of covalent labeling of amino and thiol groups (provided by the amino acids, lysine, and cysteine, respectively) are illustrated in Fig. 16.44. Labeling of lysines is most established by using *N*-hydroxysuccinimidyl esters of dyes, easily accessible from carboxylic acid groups. Another approach is the utilization of isothiocyanate groups (most prominent is fluorescein isothiocyanate, FITC). Labeling of cysteines occurs most conveniently with maleimides or with pyridinium disulfides. A combined strategy involves the thiolation reagent iminothiolane (Traut's reagent), which enables the conversion of an amine group into a linker with free thiol group for subsequent maleimide labeling (Hermanson 1996).

Labeling usually occurs with high chemoselectivity, allowing that cysteines or lysines be targeted independently. In native proteins, labeling occurs statistically yielding an average dye-to-protein ratio with randomly distributed fluorophores due to the randomly located cysteines or lysines in the protein. In this respect, reactions at sensitive binding sites or amino acids involved in the molecular function can hamper the affinity of the biomolecule. Therefore, the labeling approach should consider the protein sequence in order to select the appropriate labeling reaction.

A complementary approach can be followed by employing structures of glycosylation by reducing sugar moieties in a way that aldehyde functionalities are generated. These aldehyde groups react readily with amino groups (forming imines) or hydrazine groups (forming hydrazones), both of which are acid cleavable but can be chemically stabilized by reduction with sodium cyanoborohydride (Hermanson 1996).

Thiols are usually accessible by reductive breaking of disulfide bonds in the protein. However, since these bonds are crucial for protein folding and stability, denaturation and loss of target binding capability can occur. A structurally more defined approach can be followed by using engineered antibodies with additional cysteine residues, which are not involved into protein structure and are free to be used for covalent labeling (Lee et al. 2008).

As outlined in Chap. 16.6.2, a host of fluorophores are available for the different bioconjugation chemistries. In a typical protein-labeling protocol, a buffered solution (pH 7.5–8) of the protein (1–10 mg/mL) is incubated with a molar excess of reactive dye (typically 10–50 moles of dye per mole biomolecule) for a few minutes to several hours depending on dye reactivity and desired labeling ratio. Purification and separation from unbound dye can be achieved by separation methods such as dialysis, ultrafiltration, or size exclusion chromatography. In order to determine the quality of the resulting conjugate, suitable analytical methods are needed subsequently.

16.6.4 Conclusion and Outlook

Optical imaging has an established role in preclinical research and animal imaging. The application of imaging techniques for the detection for fluorescence signals in living animals has emerged to a powerful routine level and utilizes a versatile set of commercially available imaging equipment. The detection of fluorophores as exogenously applied contrast agents can be accomplished with convenient handling and without a substantial effort regarding technical installation, safety issues, and training. A broad variety of fluorescent probes have been created and validated for their ability to facilitate the setup of imaging protocols, to support the characterization of disease models, and to accompany the drug discovery process from drug design, in vitro characterization to the in vivo proof of concept. Both the selection and application of commercially available products optimized for a

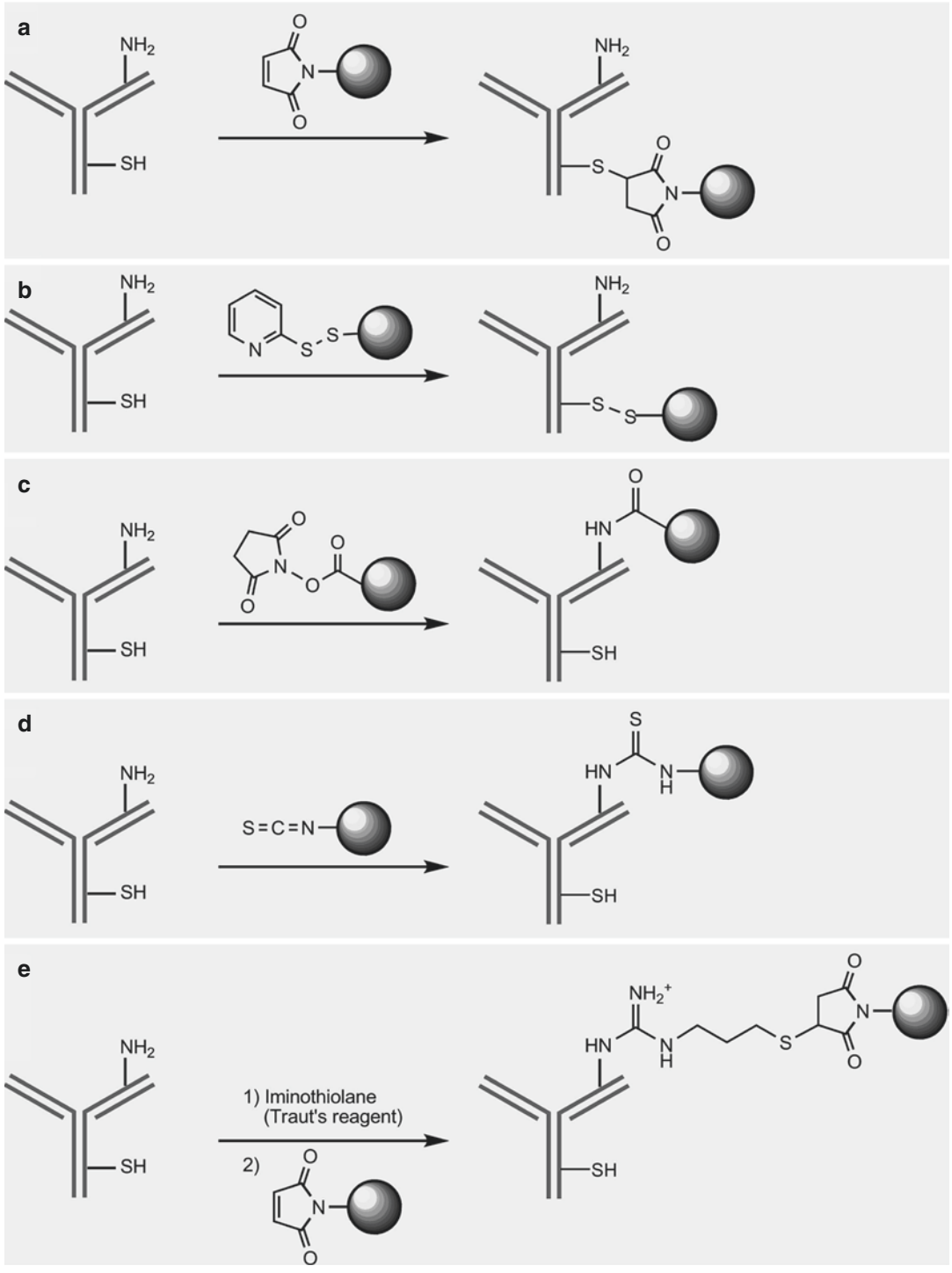

Fig. 16.44 Illustration of synthetic pathways for selective labeling of antibodies or other proteins; the fluorophore is simplified as bulb. Depicted are reactions of (**a**) maleimide dye with cysteine, (**b**) pyridinium disulfide dye with cysteine, (**c**) NHS-ester dye with lysine, (**d**) isothiocyanate dye with lysine, and (**e**) modification of lysine with Traut's reagent to give thiol, followed by reaction with maleimide dye

specific function as well as the implementation of self-induced synthetic chemistry adapting to the requirements in a given drug discovery project will play a central role in the optical imaging laboratory.

16.6.5 Laboratory Protocols

16.6.5.1 Labeling of Antibody with Dye NHS-Ester

Generally, antibodies should be used in a buffer free of amines. For instance, phosphate, acetate, or borate buffers are recommended, whereas TRIS and HEPES buffers are less suited. Incubation is performed with large excess of dye, followed by removal of excess nonreacted dye by using gel chromatography, dialysis, or ultracentrifugation. The latter two methods bring the dye conjugate into contact with material surfaces for which precipitation and loss of reaction yield are sometimes observed especially when using less hydrophilic dyes with tendency to aggregate. The following steps are recommended:

- Dissolve antibody or protein to be labeled in reaction buffer at concentration of 1–10 mg/mL depending on solubility (buffers, e.g., 100 mM sodium phosphate pH 7.4–8.0).
- Dissolve the reactive NHS-ester dye in a small amount of DMSO or DMF (concentration approximately 10 mM or 1 mg/100 μL). In case of high water solubility, the dye can be dissolved in buffer but should then be used immediately due to starting hydrolysis of the NHS-ester group.
- Add the stock solution of dye to the antibody/protein solution to achieve the desired molar excess. For instance, 15-fold molar excess is generated by adding 10 μL of dye solution (concentration 10 mM) to 1 mL of antibody solution (concentration 1 mg/mL, IgG molecular weight 150 kD).
- Incubate for 3–24 h under gentle shaking at room temperature and under protection from light.
- Remove excess dye by gel filtration, e.g., by using desalting columns. Best results are obtained when not loading the columns at the maximal possible volume, such as using a NAP10 column for not more than 0.5 mL.

16.6.5.2 Labeling of Antibody with Dye Maleimide

This example describes the labeling of a cysteine after reductive generation of free thiol. A mild reducing agent is, e.g., TCEP (triscarboxyethylphopshine), which reaches surface disulfides while leaving deeper bridges in the protein backbone intact. Usually, maleimide dyes can be used with less molar excess compared to NHS esters. The following steps are recommended:

- Dissolve antibody or protein to be labeled in reaction buffer at concentration of 1–10 mg/mL (buffers, e.g., 100 mM sodium phosphate pH 6.5–7.0).
- Dissolve TCEP in reaction buffer (concentration approximately 10 mM).
- Add the TCEP solution to the antibody/protein solution to achieve a molar excess of 5–10 molecules TCEP per disulfide to be reduced.
- Incubate for 2 h under gentle shaking at room temperature.
- Add the stock solution of dye to the freshly reduced antibody/protein solution to achieve the desired molar excess (five- to tenfold).
- Incubate for another 2–4 h under gentle shaking at room temperature.
- Remove excess dye by gel filtration, e.g., by using desalting columns.

Acknowledgments The authors (VJ and MH) thank ESA and the RW-TÜV foundation for financial support.

References

Fluorescence Imaging

Ale A, Ermolayev V, Deliolanis NC, et al. Fluorescence background subtraction technique for hybrid fluorescence molecular tomography/x-ray computed tomography imaging of a mouse model of early stage lung cancer. J Biomed Opt. 2013;18:56006. doi:10.1117/1.jbo.18.5.056006.

Alfano RR, Demos SG, Gayen SK. Advances in optical imaging of biomedical media. Imaging Brain Struct Funct. 1997;820:248–71. doi:10.1111/j.1749-6632.1997.tb46200.x.

Allen TJ, Beard PC. Pulsed near-infrared laser diode excitation system for biomedical photoacoustic imaging. Opt Lett. 2006a;31:3462–4. doi:10.1364/Ol.31.003462.

Anumala UR, Gu JM, Lo Monte F, et al. Fluorescent rhodanine-3-acetic acids visualize neurofibrillary tangles in Alzheimer's disease brains. Bioorg Med Chem. 2013;21:5139–44. doi:10.1016/j.bmc.2013.06.039.

Arridge SR. Optical tomography in medical imaging. Inverse Prob. 1999;15:R41–93. doi:10.1088/0266-5611/15/2/022.

Backer MV, Gaynutdinov TI, Patel V, et al. Vascular endothelial growth factor selectively targets boronated dendrimers to tumor vasculature. Mol Cancer Ther. 2005;4:1423–9. doi:10.1158/1535-7163.Mct-05-0161.

Barthel H, Gertz HJ, Dresel S, et al. Cerebral amyloid-beta PET with florbetaben (F-18) in patients with Alzheimer's disease and healthy controls: a multicentre phase 2 diagnostic study. Lancet Neurol. 2011;10:424–35. doi:10.1016/S1474-4422(11)70077-1.

Becker A, Riefke B, Ebert B, et al. Macromolecular contrast agents for optical imaging of tumors: comparison of indotricarbocyanine-labeled human serum albumin and transferrin. Photochem Photobiol. 2000;72:234–41. doi:10.1562/0031-8655(2000)072<0234:Mcafoi>2.0.Co;2.

Bendsoe N, Persson L, Johansson A, et al. Fluorescence monitoring of a topically applied liposomal temoporfin formulation and photodynamic therapy of nonpigmented skin malignancies. J Environ Pathol Toxicol oncol. 2007;26:117–26.

Bentzen EL, Tomlinson ID, Mason J, et al. Surface modification to reduce nonspecific binding of quantum dots in live cell assays. Bioconjug Chem. 2005;16:1488–94. doi:10.1021/Bc0502006.

Benya R, Quintana J, Brundage B. Adverse reactions to indocyanine green – a case-report and a review of the literature. Cathet Cardiovasc Diagn. 1989;17:231–3. doi:10.1002/ccd.1810170410.

Bertoncini CW, Celej MS. Small molecule fluorescent probes for the detection of amyloid self-assembly in vitro and in vivo. Curr Protein Pept Sc. 2011;12:206–20.

Bolander A, Kieser D, Voss C, et al. Bis(arylvinyl)pyrazines, −pyrimidines, and -pyridazines as imaging agents for tau fibrils and beta-amyloid plaques in Alzheimer's disease models. J Med Chem. 2012;55:9170–80. doi:10.1021/jm300653b.

Boot MJ, Westerberg CH, Sanz-Ezquerro J, et al. In vitro whole-organ imaging: 4D quantification of growing mouse limb buds. Nat Methods. 2008;5:609–12. doi:10.1038/Nmeth.1219.

Bremer C, Tung CH, Weissleder R. In vivo molecular target assessment of matrix metalloproteinase inhibition. Nat Med. 2001a;7:743–8. doi:10.1038/89126.

Bruchez M, Moronne M, Gin P, et al. Semiconductor nanocrystals as fluorescent biological labels. Science. 1998;281:2013–6. doi:10.1126/science.281.5385.2013.

Buehler A, Herzog E, Razansky D, et al. Video rate optoacoustic tomography of mouse kidney perfusion. Opt Lett. 2010a;35:2475–7.

Busch C, Passon M, Wenzel M, et al. Detection of leukotriene receptor CysLT(1)R in inflammatory diseases by molecular imaging with near-infrared fluorescence-based contrast agents. Mol Imaging. 2011;10:81–90. doi:10.2310/7290.2010.00023.

Busch C, Schroter T, Grabolle M, et al. An in vivo spectral multiplexing approach for the cooperative imaging of different disease-related biomarkers with near-infrared fluorescent Forster resonance energy transfer probes. J Nucl Med. 2012;53:638–46. doi:10.2967/jnumed.111.094391.

Cammidge AN, Gopee H. Macrodiscotic triphenylenophthalocyanines. Chem Commun. 2002; 966–7. doi:10.1039/B200978a.

Chamberland D, Jiang YB, Wang XD. Optical imaging: new tools for arthritis. Integr Biol-UK. 2010;2:496–509. doi:10.1039/B926506f.

Chan WCW, Maxwell DJ, Gao XH, et al. Luminescent quantum dots for multiplexed biological detection and imaging. Curr Opin Biotechnol. 2002;13:40–6. doi:10.1016/S0958-1669(02)00282-3.

Chang B, Yannuzzi LA, Ladas ID, et al. Choroidal neovascularization in 2nd eyes of patients with unilateral exudative age-related macular degeneration. Ophthalmology. 1995;102:1380–6.

Chen JQ, Tung CH, Mahmood U, et al. In vivo imaging of proteolytic activity in atherosclerosis. Circulation. 2002;105:2766–71. doi:10.1161/01.Cir.0000017860.20619.23.

Chen WT, Mahmood U, Weissleder R, et al. Arthritis imaging using a near-infrared fluorescence folate-targeted probe. Arthritis Res Ther. 2005;7:R310–7. doi:10.1186/Ar1483.

Cherrick GR, Stein SW, Leevy CM, et al. Indocyanine green – observations on its physical properties, plasma decay, and hepatic extraction. J Clin Invest. 1960;39:592–600. doi:10.1172/Jci104072.

Contag CH, Bachmann MH. Advances in vivo bioluminescence imaging of gene expression. Annu Rev Biomed Eng. 2002;4:235–60. doi:10.1146/annurev.bioeng.4.111901.093336.

Deguchi J, Aikawa M, Tung CH, et al. Inflammation in atherosclerosis - visualizing matrix metalloproteinase action in macrophages in vivo. Circulation. 2006;114:55–62. doi:10.1161/Circulationaha.106.619056.

Dietzel F, Boettger MK, Dahlke K, et al. Assessment of rat antigen-induced arthritis and its suppression during glucocorticoid therapy by use of hemicyanine dye probes with different molecular weight in near-infrared fluorescence optical imaging. Invest Radiol. 2013;48:729–37.

Dilek G, Akkaya EU. Novel squaraine signalling Zn(II) ions: three-state fluorescence response to a single input. Tetrahedron Lett. 2000;41:3721–4. doi:10.1016/S0040-4039(00)00474-3.

Duncan R, Ringsdorf H, Satchi-Fainaro R. Polymer therapeutics: polymers as drugs, drug and protein conjugates and gene delivery systems: past, present

and future opportunities. Adv Polym Sci. 2006;192:1–8. doi:10.1007/12_037.

Eckroat TJ, Mayhoub AS, Garneau-Tsodikova S. Amyloid-beta probes: review of structure-activity and brain-kinetics relationships. Beilstein J Org Chem. 2013;9:1012–44. doi:10.3762/Bjoc.9.116.

Eghtedari M, Oraevsky A, Copland JA, et al. High sensitivity of in vivo detection of gold nanorods using a laser optoacoustic imaging system. Nano Lett. 2007;7:1914–8. doi:10.1021/Nl070557d.

Eisenblatter M, Ehrchen J, Varga G, et al. In vivo optical imaging of cellular inflammatory response in granuloma formation using fluorescence-labeled macrophages. J Nucl Med. 2009;50:1676–82. doi:10.2967/jnumed.108.060707.

Frangioni JV. In vivo near-infrared fluorescence imaging. Curr Opin Chem Biol. 2003;7:626–34. doi:10.1016/j.cbpa.2003.08.007.

Galande AK, Hilderbrand SA, Weissleder R, et al. Enzyme-targeted fluorescent imaging probes on a multiple antigenic peptide core. J Med Chem. 2006;49:4715–20. doi:10.1021/Jm051001a.

Gao FP, Lin YX, Li LL, et al. Supramolecular adducts of squaraine and protein for noninvasive tumor imaging and photothermal therapy in vivo. Biomaterials. 2014;35:1004–14. doi:10.1016/j.biomaterials.2013.10.039.

Gonnert FA, Recknagel P, Hilger I, et al. Hepatic excretory function in sepsis: implications from biophotonic analysis of transcellular xenobiotic transport in a rodent model. Crit Care. 2013;17:R67. doi:10.1186/cc12606.

Gotoh K, Yamada T, Ishikawa O, et al. HOW I DO IT a novel image-guided surgery of hepatocellular carcinoma by indocyanine green fluorescence imaging navigation. J Surg Oncol. 2009;100:75–9. doi:10.1002/Jso.21272.

Gremse F, Theek B, Kunjachan S, et al. Absorption reconstruction improves biodistribution assessment of fluorescent nanoprobes using hybrid fluorescence-mediated tomography. Theranostics. 2014;4:960–71. doi:10.7150/thno.9293.

Gu JM, Anumala UR, Heyny-von Haussen R, et al. Design, synthesis and biological evaluation of trimethine cyanine dyes as fluorescent probes for the detection of tau fibrils in Alzheimer's disease brain and olfactory epithelium. Chemmedchem. 2013;8:891–7. doi:10.1002/cmdc.201300090.

Haedicke K, Grafe S, Lehmann F, et al. Multiplexed in vivo fluorescence optical imaging of the therapeutic efficacy of photodynamic therapy. Biomaterials. 2013;34:10075–83. doi:10.1016/j.biomaterials.2013.08.087.

Haedicke K, Kozlova D, Gräfe S, et al. Multifunctional calcium phosphate nanoparticles for combining near-infrared fluorescence imaging and photodynamic therapy. Acta Biomater. 2015;14:197–207.

Hamann FM, Brehm R, Pauli J, et al. Controlled modulation of serum protein binding and biodistribution of asymmetric cyanine dyes by variation of the number of sulfonate groups. Mol Imaging. 2011;10:258–69. doi:10.2310/7290.2011.00005.

Hansch A, Frey O, Sauner D, et al. In vivo imaging of experimental arthritis with near-infrared fluorescence. Arthritis Rheum. 2004;50:961–7. doi:10.1002/Art.20112.

Hardman R. A toxicologic review of quantum dots: toxicity depends on physicochemical and environmental factors. Environ Health Perspect. 2006;114:165–72. doi:10.1289/Ehp.8284.

He XX, Chen JY, Wang KM, et al. Preparation of luminescent Cy5 doped core-shell SFNPs and its application as a near-infrared fluorescent marker. Talanta. 2007;72:1519–26. doi:10.1016/j.talanta.2007.01.069.

Hilger I, Leistner Y, Berndt A, et al. Near-infrared fluorescence imaging of HER-2 protein over-expression in tumour cells. Eur Radiol. 2004;14:1124–9. doi:10.1007/s00330-004-2257-9.

Hintersteiner M, Enz A, Frey P, et al. In vivo detection of amyloid-beta deposits by near-infrared imaging using an oxazine-derivative probe. Nat Biotechnol. 2005;23:577–83. doi:10.1038/nbt1085.

Ho JD, Tsai RJF, Chen SN, et al. Cytotoxicity of indocyanine green on retinal pigment epithelium – Implications for macular hole surgery. Arch Ophthalmol-Chic. 2003;121:1423–9. doi:10.1001/archopht.121.10.1423.

Hu X, Wang Q, Liu Y, et al. Optical imaging of articular cartilage degeneration using near-infrared dipicolylamine probes. Biomaterials. 2014;35:7511–21. doi:10.1016/j.biomaterials.2014.05.042.

Huisken J, Swoger J, Del Bene F, et al. Optical sectioning deep inside live embryos by selective plane illumination microscopy. Science. 2004;305:1007–9. doi:10.1126/science.1100035.

Ikagawa H, Yoneda M, Iwaki M, et al. Chemical toxicity of indocyanine green damages retinal pigment epithelium. Invest Ophth Vis Sci. 2005;46:2531–9. doi:10.1167/Iovs-04-1521.

Ishizawa T, Fukushima N, Shibahara J, et al. Real-time identification of liver cancers by using indocyanine green fluorescent imaging. Cancer. 2009;115:2491–504. doi:10.1002/Cncr.24291.

Jackson SP. Arterial thrombosis-insidious, unpredictable and deadly. Nat Med. 2011;17:1423–36. doi:10.1038/Nm.2515.

Jaffer FA, Kim DE, Quinti L, et al. Optical visualization of cathepsin K activity in atherosclerosis with a novel, protease-activatable fluorescence sensor. Circulation. 2007;115:2292–8. doi:10.1161/Circulationaha.106.660340.

Jamar F, Houssiau FA, Devogelaer JP, et al. Scintigraphy using a technetium 99m-labelled anti-E-selectin Fab fragment in rheumatoid arthritis. Rheumatology. 2002;41:53–61. doi:10.1093/rheumatology/41.1.53.

Jobsis FF. Noninvasive, infrared monitoring of cerebral and myocardial oxygen sufficiency and circulatory parameters. Science. 1977;198:1264–7. doi:10.1126/science.929199.

Kairdolf BA, Mancini MC, Smith AM, et al. Minimizing nonspecific cellular binding of quantum dots with hydroxyl-derivatizied surface coatings. Anal Chem. 2008;80:3029–34. doi:10.1021/Ac800068q.

Kim JS, Kodagahally R, Strekowski L, et al. A study of intramolecular H-complexes of novel bis(heptamethine cyanine) dyes. Talanta. 2005;67:947–54. doi:10.1016/j.talanta.2005.04.025.

Kolkman RGM, Klaessens JHGM, Hondebrink E, et al. Photoacoustic determination of blood vessel diameter. Phys Med Biol. 2004;49:4745–56. doi:10.1088/0031-9155/49/20/006. Pii S0031-9155(04)83132-4.

Koronyo-Hamaoui M, Koronyo Y, Ljubimov AV, et al. Identification of amyloid plaques in retinas from Alzheimer's patients and noninvasive in vivo optical imaging of retinal plaques in a mouse model. Neuroimage. 2011;54:S204–17. doi:10.1016/j.neuroimage.2010.06.020.

Kossatz S, Behe M, Mansi R, et al. Multifactorial diagnostic NIR imaging of CCK2R expressing tumors. Biomaterials. 2013;34:5172–80. doi:10.1016/j.biomaterials.2013.03.073.

Kovar JL, Simpson MA, Schutz-Geschwender A, et al. A systematic approach to the development agents for optical imaging of mouse of fluorescent contrast cancer models. Anal Biochem. 2007;367:1–12. doi:10.1016/J.Ab.2007.04.011.

Lai WF, Chang CH, Tang Y, et al. Early diagnosis of osteoarthritis using cathepsin B sensitive near-infrared fluorescent probes. Osteoarthr Cartil. 2004;12:239–44. doi:10.1016/j.joca.2003.11.005.

Lakowicz JR. Principles of fluorescence spectroscopy. 2nd ed. New York: Kluwer Academic/Plenum Publishers; 1999.

Landsman MLJ, Kwant G, Mook GA, et al. Light-absorbing properties, stability, and spectral stabilization of indocyanine green. J Appl Physiol. 1976;40:575–83.

Lim YT, Kim S, Nakayama A, et al. Selection of quantum dot wavelengths for biomedical assays and imaging. Mol Imaging. 2003;2:50–64.

Lipinski MJ, Amirbekian V, Frias JC, et al. MRI to detect atherosclerosis with gadolinium-containing immunomicelles targeting the macrophage scavenger receptor. Magn Reson Med. 2006;56:601–10. doi:10.1002/Mrm.20995.

Liu CC, Gu YQ. Noninvasive optical imaging of Staphylococcus aureus infection in vivo using an antimicrobial petide fragment based near-infrared fluorescent probes. J Innov Opt Heal Sci. 2013;6:Artn 1350026. doi: 10.1142/S1793545813500260.

Liu TC, Wu LY, Hopkins MR, et al. A targeted low molecular weight near-infrared fluorescent probe for prostate cancer. Bioorg Med Chem Lett. 2010;20:7124–6. doi:10.1016/j.bmcl.2010.09.057.

Luo SL, Zhang EL, Su YP, et al. A review of NIR dyes in cancer targeting and imaging. Biomaterials. 2011a;32:7127–38. doi:10.1016/j.biomaterials.2011.06.024.

Maeda H, Bharate GY, Daruwalla J. Polymeric drugs for efficient tumor-targeted drug delivery based on EPR-effect. Eur J Pharm Biopharm. 2009;71:409–19. doi:10.1016/j.ejpb.2008.11.010.

Marshall D, Haskard DO. Clinical overview of leukocyte adhesion and migration: where are we now? Semin Immunol. 2002;14:133–40. doi:10.1006/smim.2001.0350.

Messerli SM, Prabhakar S, Tang Y, et al. A novel method for imaging apoptosis using a caspase-1 near-infrared fluorescent probe. Neoplasia. 2004;6:95–105. doi:10.1593/Neo.03214.

Mishra A, Behera RK, Behera PK, et al. Cyanines during the 1990s: a review. Chem Rev. 2000;100:1973–2011. doi:10.1021/Cr990402t.

Moore GE, Peyton WT, French LA, et al. The clinical use of fluorescein in neurosurgery – the localization of brain tumors. J Neurosurg. 1948;5:392–8. doi:10.3171/jns.1948.5.4.0392.

Munder A, Wolbeling F, Klockgether J, et al. In vivo imaging of bioluminescent Pseudomonas aeruginosa in an acute murine airway infection model. Pathog Dis. 2014;72:74–7. doi:10.1111/2049-632x.12184.

Nahrendorf M, Sosnovik DE, Waterman P, et al. Dual channel optical tomographic imaging of leukocyte recruitment and protease activity in the healing myocardial infarct. Circ Res. 2007;100:1218–25. doi:10.1161/01.Res.0000265064.46075.31.

Nikoobakht B, El-Sayed MA. Preparation and growth mechanism of gold nanorods (NRs) using seed-mediated growth method. Chem Mater. 2003;15:1957–62. doi:10.1021/Cm0207321.

Ntziachristos V. Going deeper than microscopy: the optical imaging frontier in biology. Nat Methods. 2010;7:603–14. doi:10.1038/Nmeth.1483.

Ntziachristos V. Clinical translation of optical and opto-acoustic imaging. Philos T R Soc A. 2011;369:4666–78. doi:10.1098/rsta.2011.0270.

Ntziachristos V, Bremer C, Tung C, et al. Imaging cathepsin B up-regulation in HT-1080 tumor models using fluorescence-mediated molecular tomography (FMT). Acad Radiol. 2002;9:S323–5. doi:10.1016/S1076-6332(03)80217-9.

Ogawa M, Kosaka N, Choyke PL, et al. Tumor-specific detection of an optically targeted antibody combined with a quencher-conjugated neutravidin "quencher-chaser": a dual "quench and chase" strategy to improve target to nontarget ratios for molecular imaging of cancer. Bioconjug Chem. 2009;20:147–54. doi:10.1021/bc8003765.

Ohnishi S, Lomnes SJ, Laurence RG, et al. Organic alternatives to quantum dots for intraoperative near-infrared fluorescent sentinel lymph node mapping. Mol Imaging. 2005;4:172–81.

Okamura N, Mori M, Furumoto S, et al. In vivo detection of amyloid plaques in the mouse brain using the near-infrared fluorescence probe THK-265. J Alzheimers Dis. 2011;23:37–48. doi:10.3233/Jad-2010-100270.

Osterman HL, Schutz-Geschwender A. Seeing beyond the visible with IRDye infrared dyes. LI-COR Biosci. 2007:1–8.

Oswald B, Lehmann F, Simon L, et al. Red laser-induced fluorescence energy transfer in an immunosystem. Anal Biochem. 2000;280:272–7. doi:10.1006/abio.2000.4553.

Panchuk-Voloshina N, Haugland RP, Bishop-Stewart J, et al. Alexa dyes, a series of new fluorescent dyes that yield exceptionally bright, photostable conjugates. J Histochem Cytochem. 1999;47:1179–88.

Pauli J, Vag T, Haag R, et al. An in vitro characterization study of new near infrared dyes for molecular imaging. Eur J Med Chem. 2009a;44:3496–503. doi:10.1016/j.ejmech.2009.01.019.

Pauli J, Grabolle M, Brehm R, et al. Suitable labels for molecular imaging – influence of dye structure and hydrophilicity on the spectroscopic properties of IgG conjugates. Bioconjug Chem. 2011;22:1298–308. doi:10.1021/bc1004763.

Peng XJ, Song FL, Lu E, et al. Heptamethine cyanine dyes with a large stokes shift and strong fluorescence: a paradigm for excited-state intramolecular charge transfer. J Am Chem Soc. 2005;127:4170–1. doi:10.1021/Ja043413z.

Pham W, Medarova Z, Moore A. Synthesis and application of a water-soluble near-infrared dye for cancer detection using optical imaging. Bioconjug Chem. 2005;16:735–40. doi:10.1021/Bc049700+.

Ploemen IHJ, Prudencio M, Douradinha BG, et al. Visualisation and quantitative analysis of the Rodent malaria liver stage by real time imaging. Plos One. 2009; 4:Artn E7881. doi:10.1371/Journal.Pone.0007881.

Razansky D, Vinegoni C, Ntziachristos V. Multispectral photoacoustic imaging of fluorochromes in small animals. Opt Lett. 2007;32:2891–3. doi:10.1364/Ol.32.002891.

Recknagel P, Gonnert FA, Westermann M, et al. Liver dysfunction and phosphatidylinositol-3-kinase signalling in early sepsis: experimental studies in rodent models of peritonitis. Plos Med. 2012;9:e1001338. doi:10.1371/journal.pmed.1001338.

Rickert EL, Oriana S, Hartman-Frey C, et al. Synthesis and characterization of fluorescent 4-hydroxytamoxifen conjugates with unique antiestrogenic properties. Bioconjug Chem. 2010;21:903–10. doi:10.1021/Bc900461h.

Sakatani K, KashiwasakeJibu M, Wang S, et al. Noninvasive optical imaging of the subarachnoid space and cerebrospinal fluid pathways based on near-infrared fluorescence. J Neurosurg. 1997;87:738–45. doi:10.3171/jns.1997.87.5.0738.

Schafer VS, Hartung W, Hoffstetter P, et al. Quantitative assessment of synovitis in patients with rheumatoid arthritis using fluorescence optical imaging. Arthritis Res Ther. 2013;15:Artn R124 doi:10.1186/Ar4304.

Schotland JC, Leigh JS. Photon diffusion imaging. Faseb J. 1992;6:A446–A.

Serhan CN, Chiang N, Van Dyke TE. Resolving inflammation: dual anti-inflammatory and pro-resolution lipid mediators. Nat Rev Immunol. 2008;8:349–61. doi:10.1038/Nri2294.

Simon GH, Daldrup-Link HE, Kau J, et al. Optical imaging of experimental arthritis using allogeneic leukocytes labeled with a near-infrared fluorescent probe. Eur J Nucl Med Mol I. 2006;33:998–1006. doi:10.1007/s00259-006-0081-y.

Skrivanova K, Skorpikova J, Svihalek J, et al. Photochemical properties of a potential photosensitiser indocyanine green in vitro. J Photoch Photobio B. 2006;85:150–4. doi:10.1016/j.jphotobiol.2006.06.004.

Sparks JS, Schelly RC, Smith WL, et al. The covert world of fish biofluorescence: a phylogenetically widespread and phenotypically variable phenomenon. Plos One. 2014;9:ARTN e83259. doi:10.1371/journal.pone.0083259.

Tang EN, Nair A, Baker DW, et al. In vivo imaging of infection using a bacteria-targeting optical nanoprobe. J Biomed Nanotechnol. 2014;10:856–63. doi:10.1166/jbn.2014.1852.

Tansi FL, Ruger R, Rabenhold M, et al. Liposomal encapsulation of a near-infrared fluorophore enhances fluorescence quenching and reliable whole body optical imaging upon activation in vivo. Small. 2013;9:3659–69. doi:10.1002/smll.201203211.

Taqueti VR, Jaffer FA. High-resolution molecular imaging via intravital microscopy: illuminating vascular biology in vivo. Integr Biol-UK. 2013;5:278–90. doi:10.1039/C2ib20194a.

te Velde EA, Veerman T, Subramaniam V, et al. The use of fluorescent dyes and probes in surgical oncology. Ejso-Eur J Surg Onc. 2010;36:6–15. doi:10.1016/j.ejso.2009.10.014.

Tsung CK, Kou XS, Shi QH, et al. Selective shortening of single-crystalline gold nanorods by mild oxidation. J Am Chem Soc. 2006;128:5352–3. doi:10.1021/Ja060447t.

Tung CH. Fluorescent peptide probes for in vivo diagnostic imaging. Biopolymers. 2004;76:391–403. doi:10.1002/Bip.20139.

Tung CH, Lin YH, Moon WK, et al. A receptor-targeted near-infrared fluorescence probe for in vivo tumor imaging. Chembiochem. 2002;3:784–6. doi:10.1002/1439-7633(20020802)3:8<784::Aid-Cbic784>3.0.Co;2-X.

van Dam GM, Themelis G, Crane LMA, et al. Intraoperative tumor-specific fluorescence imaging in ovarian cancer by folate receptor-alpha targeting: first in-human results. Nat Med. 2011;17:1315–U202. doi:10.1038/Nm.2472.

van der Poel HG, Buckle T, Brouwer OR, et al. Intraoperative laparoscopic fluorescence guidance to the sentinel lymph node in prostate cancer patients: clinical proof of concept of an integrated functional imaging approach using a multimodal tracer. Eur Urol. 2011;60:826–33. doi:10.1016/j.eururo.2011.03.024.

Volkova KD, Kovalska VB, Tatarets AL, et al. Spectroscopic study of squaraines as protein-sensitive fluorescent dyes. Dyes Pigm. 2007;72:285–92. doi:10.1016/j.dyepig.2005.09.007.

Walling MA, Novak JA, Shepard JRE. Quantum dots for live cell and in vivo imaging. Int J Mol Sci. 2009;10:441–91. doi:10.3390/Ijms10020441.

Wang W, Ke S, Kwon S, et al. A new optical and nuclear dual-labeled imaging agent targeting interleukin 11 receptor alpha-chain. Bioconjug Chem. 2007a;18:397–402. doi:10.1021/Bc0602679.

Wang R, Yu CW, Yu FBA, et al. Molecular fluorescent probes for monitoring pH changes in living cells. Trac-Trend Anal Chem. 2010a;29:1004–13. doi:10.1016/j.trac.2010.05.005.

Weissleder R, Ntziachristos V. Shedding light onto live molecular targets. Nat Med. 2003;9:123–8. doi:10.1038/Nm0103-123.

White AG, Fu N, Leevy WM, et al. Optical imaging of bacterial infection in living mice using deep-Red fluorescent squaraine rotaxane probes. Bioconjug Chem. 2010;21:1297–304. doi:10.1021/bc1000998.

Wu X, Liu H, Liu J, et al. Immunofluorescent labeling of cancer marker Her2 and other cellular targets with semiconductor quantum dots. Nat Biotechnol. 2003;21:41–6. doi:10.1038/nbt764.

Yodh A, Chance B. Spectroscopy and imaging with diffusing light. Phys Today. 1995;48:34–40. doi:10.1063/1.881445.

Yoo H, Kim JW, Shishkov M, et al. Intra-arterial catheter for simultaneous microstructural and molecular imaging in vivo. Nat Med. 2011;17:1680–U202. doi:10.1038/Nm.2555.

Zemp RJ, Bitton R, Li ML, et al. Photoacoustic imaging of the microvasculature with a high-frequency ultrasound array transducer. J Biomed Opt. 2007;12:Artn 010501. doi:10.1117/1.2709850.

Zhou LC, Zhao GJ, Liu JF, et al. The charge transfer mechanism and spectral properties of a near-infrared heptamethine cyanine dye in alcoholic and aprotic solvents. J Photoch Photobio A. 2007;187:305–10. doi:10.1016/j.jphotochem.2006.10.027.

Bioluminescence Imaging

Adamczak JM, et al. In vivo bioluminescence imaging of vascular remodeling after stroke. Front Cell Neurosci. 2014;8:274.

Brakenhielm E, et al. Modulating metastasis by a lymphangiogenic switch in prostate cancer. Int J Cancer. 2007;121(10):2153–61.

Burns-Guydish SM, et al. Monitoring age-related susceptibility of young mice to oral Salmonella enterica serovar Typhimurium infection using an in vivo murine model. Pediatr Res. 2005;58(1):153–8.

Chewning JH, et al. Bioluminescence-based visualization of CD4 T cell dynamics using a T lineage-specific luciferase transgenic model. BMC Immunol. 2009;10:44.

Close DM, et al. In vivo bioluminescent imaging (BLI): noninvasive visualization and interrogation of biological processes in living animals. Sens (Basel). 2011;11(1):180–206.

Contag PR, et al. Bioluminescent indicators in living mammals. Nat Med. 1998;4(2):245–7.

Cowey S, et al. Breast cancer metastasis to bone: evaluation of bioluminescent imaging and microSPECT/CT for detecting bone metastasis in immunodeficient mice. Clin Exp Metastasis. 2007;24(5):389–401.

Cruz-Monserrate Z, et al. Targeting pancreatic ductal adenocarcinoma acidic microenvironment. Sci Rep. 2014;4:4410.

de Wet JR, et al. Cloning of firefly luciferase cDNA and the expression of active luciferase in Escherichia coli. Proc Natl Acad Sci U S A. 1985;82(23):7870–3.

Desjardin DE, Oliveira AG, Stevani CV. Fungi bioluminescence revisited. Photochem Photobiol Sci. 2008;7(2):170–82.

Haddock SH, et al. Bioluminescent and red-fluorescent lures in a deep-sea siphonophore. Science. 2005;309(5732):263.

Haddock SH, Moline MA, Case JF. Bioluminescence in the sea. Ann Rev Mar Sci. 2010;2:443–93.

Hastings JW. Chemistries and colors of bioluminescent reactions: a review. Gene. 1996;173(1 Spec No):5–11.

Hiler DJ, Greenwald ML, Geusz ME. Imaging gene expression in live transgenic mice after providing luciferin in drinking water. Photochem Photobiol Sci. 2006;5(11):1082–5.

Ignowski JM, Schaffer DV. Kinetic analysis and modeling of firefly luciferase as a quantitative reporter gene in live mammalian cells. Biotechnol Bioeng. 2004;86(7):827–34.

Inoue Y, et al. Comparison of subcutaneous and intraperitoneal injection of D-luciferin for in vivo bioluminescence imaging. Eur J Nucl Med Mol Imaging. 2009;36(5):771–9.

Ishikawa TO, et al. Imaging cyclooxygenase-2 (Cox-2) gene expression in living animals with a luciferase knock-in reporter gene. Mol Imaging Biol. 2006;8(3):171–87.

Iyer M, et al. Non-invasive imaging of a transgenic mouse model using a prostate-specific two-step transcriptional amplification strategy. Transgenic Res. 2005;14(1):47–55.

Iyer M, et al. Bioluminescence imaging of systemic tumor targeting using a prostate-specific lentiviral vector. Hum Gene Ther. 2006;17(1):125–32.

Kanerva A, et al. Enhanced therapeutic efficacy for ovarian cancer with a serotype 3 receptor-targeted oncolytic adenovirus. Mol Ther. 2003;8(3):449–58.

Keyaerts M, et al. Dynamic bioluminescence imaging for quantitative tumour burden assessment using IV or IP administration of D: −luciferin: effect on intensity, time kinetics and repeatability of photon emission. Eur J Nucl Med Mol Imaging. 2008;35(5):999–1007.

Keyaerts M, et al. Inhibition of firefly luciferase by general anesthetics: effect on in vitro and in vivo bioluminescence imaging. PLoS One. 2012;7(1):e30061.

Laxman B, et al. Noninvasive real-time imaging of apoptosis. Proc Natl Acad Sci U S A. 2002;99(26):16551–5.

Li J, et al. Cage the firefly luciferin! - a strategy for developing bioluminescent probes. Chem Soc Rev. 2013a;42(2):662–76.

Maes W, et al. In vivo bioluminescence imaging in an experimental mouse model for dendritic cell based immunotherapy against malignant glioma. J Neurooncol. 2009;91(2):127–39.

Mendes LF, et al. Influence of culture conditions on mycelial growth and bioluminescence of Gerronema viridilucens. FEMS Microbiol Lett. 2008;282(1):132–9.

Miller SD, et al. Detection of a bioluminescent milky sea from space. Proc Natl Acad Sci U S A. 2005;102(40):14181–4.

Moreno JC, et al. Effect of the relative optical air mass and the clearness index on solar erythemal UV irradiance. J Photochem Photobiol B. 2014;138:92–8.
Paulmurugan R, Umezawa Y, Gambhir SS. Noninvasive imaging of protein-protein interactions in living subjects by using reporter protein complementation and reconstitution strategies. Proc Natl Acad Sci U S A. 2002;99(24):15608–13.
Poisson J. Raphael Dubois, from pharmacy to bioluminescence. Rev Hist Pharm (Paris). 2010;58(365):51–6.
Rehemtulla A, Taneja N, Ross BD. Bioluminescence detection of cells having stabilized p53 in response to a genotoxic event. Mol Imaging. 2004;3(1):63–8.
Sabag AD, et al. Semaphorin-3D and semaphorin-3E inhibit the development of tumors from glioblastoma cells implanted in the cortex of the brain. PLoS One. 2012;7(8):e42912.
Sadikot RT, et al. Pathogen-host interactions in Pseudomonas aeruginosa pneumonia. Am J Respir Crit Care Med. 2005;171(11):1209–23.
Saha D, et al. In vivo bioluminescence imaging of tumor hypoxia dynamics of breast cancer brain metastasis in a mouse model. J Vis Exp. 2011;56:e3175. DOI: 10.3791/3175.
Siragusa GR, et al. Real-time monitoring of Escherichia coli O157:H7 adherence to beef carcass surface tissues with a bioluminescent reporter. Appl Environ Microbiol. 1999;65(4):1738–45.
Soling A, et al. A dual function fusion protein of Herpes simplex virus type 1 thymidine kinase and firefly luciferase for noninvasive in vivo imaging of gene therapy in malignant glioma. Genet Vaccines Ther. 2004;2(1):7.
Tiffen JC, et al. Luciferase expression and bioluminescence does not affect tumor cell growth in vitro or in vivo. Mol Cancer. 2010;9:299.
Wang W, El-Deiry WS. Bioluminescent molecular imaging of endogenous and exogenous p53-mediated transcription in vitro and in vivo using an HCT116 human colon carcinoma xenograft model. Cancer Biol Ther. 2003;2(2):196–202.
Warrant EJ, Locket NA. Vision in the deep sea. Biol Rev Camb Philos Soc. 2004;79(3):671–712.
Wiles S, et al. Organ specificity, colonization and clearance dynamics in vivo following oral challenges with the murine pathogen Citrobacter rodentium. Cell Microbiol. 2004;6(10):963–72.
Wiles S, et al. In vivo bioluminescence imaging of the murine pathogen Citrobacter rodentium. Infect Immun. 2006;74(9):5391–6.
Zhao RL, et al. A new species of bird's nest fungi: characterisation of Cyathus subglobisporus sp. nov. based on morphological and molecular data. Persoonia. 2008;21:71–6.
Zinn KR, et al. Noninvasive bioluminescence imaging in small animals. ILAR J. 2008;49(1):103–15.

Optical Coherence Tomography (OCT)

Abbe E. Beiträge zur Theorie des Mikroskops und der mikroskopischen Wahrnehmung. Archiv F Mikrosk Anatomie. 1873;9:413–8.
Al-Qaisi MK, Akkin T. Swept-source polarization-sensitive optical coherence tomography based on polarization-maintaining fiber. Opt Express. 2010;18:3392–403.
Anderson RR, Parrish JA. The optics of human-skin. J Invest Dermatol. 1981;77:13–9.
Bachmann AH, Villiger ML, Blatter C, Lasser T, Leitgeb RA. Resonant Doppler flow imaging and optical vivisection of retinal blood vessels. Opt Express. 2007;15:408–22.
Bail MA, Haeusler G, Herrmann JM, Lindner MW, Ringler R. Optical coherence tomography with the "spectral radar": fast optical analysis in volume scatterers by short-coherence interferometry. In: Benaron DA, Chance B, Mueller GJ, editors. Vienna: SPIE; 1996. p. 298–303.
Bailey TJ, Davis DH, Vance JE, Hyde DR. Spectral-domain optical coherence tomography as a noninvasive method to assess damaged and regenerating adult zebrafish retinas. Invest Ophthalmol Vis Sci. 2012;53:3126–38.
Bajraszewski T, Wojtkowski M, Szkulmowski M, et al. Improved spectral optical coherence tomography using optical frequency comb. Opt Express. 2008;16:4163–76.
Bayleyegn MD, Makhlouf H, Crotti C, Plamann K, Dubois A. Ultrahigh resolution spectral-domain optical coherence tomography at 1.3 mu m using a broadband superluminescent diode light source. Opt Commun. 2012;285:5564–9.
Bell BA, Vincent KL, Bourne N, Vargas G, Motamedi M. Optical coherence tomography for assessment of microbicide safety in a small animal model. J Biomed Opt. 2013;18:046010.
Bouma BE, Tearney GJ. Handbook of optical coherence tomography. New York: Marcel Dekker; 2002.
Bukowska D, Szkulmowska A, Grulkowski I, Tamborski S, Szkulmowski M, Leitgeb R, Kowalczyk A, Wojtkowski M. Observation of blood optical inhomogeneity using joint Spectral and Time domain OCT. IN Izatt JA, Fujimoto JG, Tuchin VV, (eds.), Optical Coherence Tomography and Coherence Domain Optical Methods in Biomedicine XIV, View ResearcherID and ORCID. Proceedings of SPIE-The International Society for Optical Engineering. San Francisco, CA. 2010;7554. DOI: 10.1117/12.842203.
Cang H, Sun T, Li ZY, et al. Gold nanocages as contrast agents for spectroscopic optical coherence tomography. Opt Lett. 2005;30:3048–50.
Chan AC, Srinivasan VJ, Lam EY. Maximum likelihood Doppler frequency estimation under decorrelation noise for quantifying flow in optical coherence tomography. IEEE Trans Med Imaging. 2014;33:1313–23.
Chinn SR, Swanson EA, Fujimoto JG. Optical coherence tomography using a frequency-tunable optical source. Opt Lett. 1997;22:340–2.
Choma M, Sarunic M, Yang C, Izatt J. Sensitivity advantage of swept source and Fourier domain optical coherence tomography. Opt Express. 2003;11:2183–9.
Cimalla P, Walther J, Mehner M, Cuevas M, Koch E. Simultaneous dual-band optical coherence tomog-

raphy in the spectral domain for high resolution in vivo imaging. Opt Express. 2009;17:19486–500.
Cimalla P, Walther J, Mittasch M, Koch E. Shear flow-induced optical inhomogeneity of blood assessed in vivo and in vitro by spectral domain optical coherence tomography in the 1.3 mum wavelength range. J Biomed Opt. 2011a;16:116020.
Cimalla P, Burkhardt A, Walther J et al. Non-invasive imaging and monitoring of rodent retina using simultaneous dual-band optical coherence tomography. Proc. SPIE. 2011b;7889:788909–788909.
Cimalla P, Gaertner M, Weber A, et al. A hybrid imaging system for simultaneous ophthalmic optical coherence tomography and dual-channel fluorescence detection in small animal models. Biomed Tech. 2012;57:515–8.
de Boer JF, Milner TE, van Gemert MJC, Nelson JS. Two-dimensional birefringence imaging in biological tissue by polarization-sensitive optical coherence tomography. Opt Lett. 1997;22:934–6.
de Boer JF, Cense B, Park BH, et al. Improved signal-to-noise ratio in spectral-domain compared with time-domain optical coherence tomography. Opt Lett. 2003;28:2067–9.
Drexler W, Fujimoto JG. State-of-the-art retinal optical coherence tomography. Prog Retin Eye Res. 2008;27:45–88.
Dubois A, Vabre L, Boccara AC, Beaurepaire E. High-resolution full-field optical coherence tomography with a Linnik microscope. Appl Opt. 2002;41:805–12.
Duma VF, Lee KS, Meemon P, Rolland JP. Experimental investigations of the scanning functions of galvanometer-based scanners with applications in OCT. Appl Opt. 2011;50:5735–49.
Eigenwillig CM, Biedermann BR, Wieser W, Huber R. Wavelength swept amplified spontaneous emission source. Opt Express. 2009;17:18794–807.
Faber DJ, van Leeuwen TG. Are quantitative attenuation measurements of blood by optical coherence tomography feasible?, Opt Lett. 2009;34(9):1435–7.
Faber DJ, Mik EG, Aalders MC, van Leeuwen TG. Toward assessment of blood oxygen saturation by spectroscopic optical coherence tomography. Opt Lett. 2005;30:1015–7.
Fernández EJ, Hermann B, Povazay B, et al. Ultrahigh resolution optical coherence tomography and pancorrection for cellular imaging of the living human retina. Opt Express. 2008;16:11083–94.
Fischer MD, Huber G, Feng Y, et al. In vivo assessment of retinal vascular wall dimensions. Invest Ophthalmol Vis Sci. 2010;51:5254–9.
Fleming CP, Eckert J, Halpern EF, Gardecki JA, Tearney GJ. Depth resolved detection of lipid using spectroscopic optical coherence tomography. Biomed Opt Express. 2013;4:1269–84.
Gaertner M, Weber A, Cimalla P, KÂttig F, Brand M, Koch E. Towards a comprehensive eye model for zebrafish retinal imaging using full range spectral domain optical coherence tomography. p. 89342H–89342H, International Society for Optics and Photonics. 2014.
Gao W. Dispersion properties of grating-based rapid scanning optical delay lines. Appl Opt. 2007;46:986–92.
Garini Y, Young IT, McNamara G. Spectral imaging: principles and applications. Cytometry A. 2006;69:735–47.
Goodman JW. Statistical optics. New York: Wiley; 1985.
Gora M, Karnowski K, Szkulmowski M, et al. Ultra high-speed swept source OCT imaging of the anterior segment of human eye at 200 kHz with adjustable imaging range. Opt Express. 2009;17:14880–94.
Götzinger E, Baumann B, Pircher M, Hitzenberger CK. Polarization maintaining fiber based ultra-high resolution spectral domain polarization sensitive optical coherence tomography. Opt Express. 2009;17:22704–17.
Hariri S, Moayed AA, Dracopoulos A, et al. Limiting factors to the OCT axial resolution for in-vivo imaging of human and rodent retina in the 1060nm wavelength range. Opt Express. 2009;17:24304–16.
Hartl I, Li XD, Chudoba C, et al. Ultrahigh-resolution optical coherence tomography using continuum generation in an air-silica microstructure optical fiber. Opt Lett. 2001;26:608–10.
Hecht E. Optik. München: Oldenbourg; 2005.
Hee MR, Huang D, Swanson EA, Fujimoto JG. Polarization-sensitive low-coherence reflectometer for birefringence characterization and ranging. J Opt Soc Am B. 1992;9:903–8.
Hee MR, Izatt JA, Swanson EA, Fujimoto JG. Femtosecond transillumination tomography in thick tissues. Opt Lett. 1993;18:1107–9.
Hering E, Martin R. Photonik: Grundlagen, Technologie und Anwendung. Berlin: Springer; 2006.
Hitzenberger C, Goetzinger E, Sticker M, Pircher M, Fercher A. Measurement and imaging of birefringence and optic axis orientation by phase resolved polarization sensitive optical coherence tomography. Opt Express. 2001;9:780–90.
Horio N, Kachi S, Hori K, et al. Progressive change of optical coherence tomography scans in retinal degeneration slow mice. Arch Ophthalmol. 2001;119:1329–32.
Hu Z, Rollins AM. Fourier domain optical coherence tomography with a linear-in-wavenumber spectrometer. Opt Lett. 2007;32:3525–7.
Huang D, Swanson EA, Lin CP, et al. Optical coherence tomography. Science. 1991;254:1178–81.
Huber G, Beck SC, Grimm C, et al. Spectral domain optical coherence tomography in mouse models of retinal degeneration. Invest Ophthalmol Vis Sci. 2009;50:5888–95.
Huber G, Heynen S, Imsand C, et al. Novel rodent models for macular research. PLoS One. 2010;5:e13403.
Jaedicke V, Agcaer S, Robles FE, et al. Comparison of different metrics for analysis and visualization in spectroscopic optical coherence tomography. Biomed Opt Express. 2013;4:2945–61.
Jian Y, Zawadzki RJ, Sarunic MV. Adaptive optics optical coherence tomography for in vivo mouse retinal imaging. J Biomed Opt. 2013;18:056007–056007.
John R, Rezaeipoor R, Adie SG, et al. In vivo magnetomotive optical molecular imaging using targeted magnetic nanoprobes. Proc Natl Acad Sci. 2010;107:8085–90.

Kalkman J, Bykov AV, Streekstra GJ, van Leeuwen TG. Multiple scattering effects in Doppler optical coherence tomography of flowing blood. Phys Med Biol. 2012;57:1907–17.

Kartakoullis A, Bousi E, Pitris C. Scatterer size-based analysis of optical coherence tomography images using spectral estimation techniques. Opt Express. 2010;18:9181–91.

Kasseck C, Kratz M, Torcasio A, et al. Comparison of optical coherence tomography, microcomputed tomography, and histology at a three-dimensionally imaged trabecular bone sample. J Biomed Opt. 2010;15:046019.

Kim YK, Kim YP. High-speed time-domain optical coherence tomography with an imaging speed of ten frames per second with 2000 A-scan. Opt Eng. 2010;49:055601.

Kim KH, Puoris'haag M, Maguluri GN, et al. Monitoring mouse retinal degeneration with high-resolution spectral-domain optical coherence tomography. J Vision. 2008;8:1701–11.

Kim J, Ahmad A, Boppart SA. Dual-coil magnetomotive optical coherence tomography for contrast enhancement in liquids. Opt Express. 2013;21:7139–47.

Kirsten L, Gaertner M, Schnabel C, Meissner S, Koch E. Four-dimensional imaging of murine subpleural alveoli using high-speed optical coherence tomography. J Biophotonics. 2013;6:148–52.

Kocaoglu OP, Uhlhorn SR, Hernandez E, et al. Simultaneous fundus imaging and optical coherence tomography of the mouse retina. Invest Ophthalmol Vis Sci. 2007;48:1283–9.

Kottig F, Cimalla P, Gartner M, Koch E. An advanced algorithm for dispersion encoded full range frequency domain optical coherence tomography. Opt Express. 2012;20:24925–48.

Kuranov RV, Qiu JZ, McElroy AB, Estrada A, Salvaggio A, Kiel J, Dunn AK, Duong TQ, Milner TE. Depth-resolved blood oxygen saturation measurement by dual-wavelength photothermal (DWP) optical coherence tomography, View ResearcherID and ORCID. Biomed Opt Express. 2011a;5(3)491–504. DOI: 10.1364/BOE.2.000491.

Kuranov RV, Kazmi S, McElroy AB, Kiel JW, Dunn AK, Milner TE, Duong TQ. In vivo depth-resolved oxygen saturation by dual-wavelength photothermal (DWP) OCT, View ResearcherID and ORCID. Opt Express. 2011b;19(24):23831–44. DOI: 10.1364/OE.19.023831

Larina IV, Larin KV, Justice MJ, Dickinson ME. Optical coherence tomography for live imaging of mammalian development. Curr Opin Genet Dev. 2011;21:579–84.

Lee TM, Oldenburg AL, Sitafalwalla S, et al. Engineered microsphere contrast agents for optical coherence tomography. Opt Lett. 2003;28:1546–8.

Leitgeb R, Hitzenberger C, Fercher A. Performance of fourier domain vs. time domain optical coherence tomography. Opt Express. 2003a;11:889–94.

Leitgeb R, Schmetterer L, Drexler W, et al. Real-time assessment of retinal blood flow with ultrafast acquisition by color Doppler Fourier domain optical coherence tomography. Opt Express. 2003b;11:3116–21.

Leitgeb R, Wojtkowski M, Kowalczyk A, Hitzenberger CK, Sticker M, Fercher AF. Spectral measurement of absorption by spectroscopic frequency-domain optical coherence tomography, Opt Lett. 2000;25(11):820–2. DOI: 10.1364/OL.25.000820.

Li Q, Timmers AM, Hunter K, et al. Noninvasive imaging by optical coherence tomography to monitor retinal degeneration in the mouse. Invest Ophthalmol Vis Sci. 2001;42:2981–9.

Liu G, Chou L, Jia W, et al. Intensity-based modified Doppler variance algorithm: application to phase instable and phase stable optical coherence tomography systems. Opt Express. 2011;19:11429–40.

Liu G, Lin AJ, Tromberg BJ, Chen Z. A comparison of Doppler optical coherence tomography methods. Biomed Opt Express. 2012;3:2669–80.

Lorenser D, Yang X, Kirk RW, et al. Ultrathin side-viewing needle probe for optical coherence tomography. Opt Lett. 2011;36:3894–6.

Lu CW, Lee CK, Tsai MT, Wang YM, Yang CC. Measurement of the hemoglobin oxygen saturation level with spectroscopic spectral-domain optical coherence tomography. Opt Lett. 2008;33:416–8.

McLaughlin RA, Yang XJ, Quirk BC, et al. Static and dynamic imaging of alveoli using optical coherence tomography needle probes. J Appl Physiol. 2012;113:967–74.

Meissner S, Knels L, Koch E. Improved three-dimensional Fourier domain optical coherence tomography by index matching in alveolar structures. J Biomed Opt. 2009a;14:064037.

Meissner S, Muller G, Walther J, Morawietz H, Koch E. In-vivo Fourier domain optical coherence tomography as a new tool for investigation of vasodynamics in the mouse model. J Biomed Opt. 2009b;14:034027.

Meissner S, Knels L, Schnabel C, Koch T, Koch E. Three-dimensional Fourier domain optical coherence tomography in vivo imaging of alveolar tissue in the intact thorax using the parietal pleura as a window. J Biomed Opt. 2010a;15:016030.

Meissner S, Tabuchi A, Mertens M, Kuebler WM, Koch E. Virtual four-dimensional imaging of lung parenchyma by optical coherence tomography in mice. J Biomed Opt. 2010b;15:036016.

Mertens M, Tabuchi A, Meissner S, et al. Alveolar dynamics in acute lung injury: heterogeneous distension rather than cyclic opening and collapse. Crit Care Med. 2009;37:2604–11.

Michelson AA. The relative motion of the earth and the lumniferous ether. Am J Sci. 1881;22:120–9.

Moayed AA, Hariri S, Hyun C, et al. Combined optical coherence tomography and electroretinography system for in vivo simultaneous morphological and functional imaging of the rodent retina. J Biomed Opt. 2010;15:040506.

Moayed AA, Hariri S, Choh V, Bizheva K. In vivo imaging of intrinsic optical signals in chicken retina with functional optical coherence tomography. Opt Lett. 2011;36:4575–7.

Morgner U, Drexler W, Kärtner FX, et al. Spectroscopic optical coherence tomography. Opt Lett. 2000;25:111–3.

Nagata A, Higashide T, Ohkubo S, Takeda H, Sugiyama K. In vivo quantitative evaluation of the rat retinal nerve fiber layer with optical coherence tomography. Invest Ophthalmol Vis Sci. 2009;50:2809–15.

Namati E, Warger WC, Unglert CI, et al. Four-dimensional visualization of subpleural alveolar dynamics in vivo during uninterrupted mechanical ventilation of living swine. Biomed Opt Express. 2013;4:2492–506.

Oldenburg A, Toublan F, Suslick K, Wei A, Boppart S. Magnetomotive contrast for in vivo optical coherence tomography. Opt Express. 2005a;13:6597–614.

Oldenburg AL, Gunther JR, Boppart SA. Imaging magnetically labeled cells with magnetomotive optical coherence tomography. Opt Lett. 2005b;30:747–9.

Oldenburg AL, Crecea V, Rinne SA, Boppart SA. Phase-resolved magnetomotive OCT for imaging nanomolar concentrations of magnetic nanoparticles in tissues. Opt Express. 2008;16:11525–39.

Oldenburg AL, Hansen MN, Ralston TS, Wei A, Boppart SA. Imaging gold nanorods in excised human breast carcinoma by spectroscopic optical coherence tomography. J Mater Chem. 2009;19:6407–11.

Osiac E, Balseanu TA, Catalin B, et al. Optical coherence tomography as a promising imaging tool for brain investigations. Rom J Morphol Embryol. 2014;55:507–12.

Park BH, Saxer C, Srinivas SM, Nelson JS, de Boer JF. In vivo burn depth determination by high-speed fiber-based polarization sensitive optical coherence tomography. J Biomed Opt. 2001;6:474–9.

Povazay B, Bizheva K, Hermann B, et al. Enhanced visualization of choroidal vessels using ultrahigh resolution ophthalmic OCT at 1050 nm. Opt Express. 2003;11:1980–6.

Povazay B, Hermann B, Unterhuber A, et al. Three-dimensional optical coherence tomography at 1050 nm versus 800 nm in retinal pathologies: enhanced performance and choroidal penetration in cataract patients. J Biomed Opt. 2007;12:041211.

Povazay B, Hofer B, Torti C, et al. Impact of enhanced resolution, speed and penetration on three-dimensional retinal optical coherence tomography. Opt Express. 2009;17:4134–50.

Quirk BC, McLaughlin RA, Pagnozzi AM, et al. Optofluidic needle probe integrating targeted delivery of fluid with optical coherence tomography imaging. Opt Lett. 2014;39:2888–91.

Robles FE, Wax A. Separating the scattering and absorption coefficients using the real and imaginary parts of the refractive index with low-coherence interferometry. Opt Lett. 2010;35:2843–5.

Robles F, Graf RN, Wax A. Dual window method for processing spectroscopic optical coherence tomography signals with simultaneously high spectral and temporal resolution. Opt Express. 2009;17:6799–812.

Robles FE, Wilson C, Grant G, Wax A. Molecular imaging true-colour spectroscopic optical coherence tomography. Nat Photonics. 2011;5:744–7.

Roggan A, Beuthan J, Schründer S, Müller G. Diagnostik und therapie mit dem laser. Physikalische Blätter. 1999;55:25–30.

Ruggeri M, Wehbe H, Jiao S, et al. In vivo three-dimensional high-resolution imaging of rodent retina with spectral-domain optical coherence tomography. Invest Ophthalmol Vis Sci. 2007;48:1808–14.

Schmitt JM. Optical coherence tomography (OCT): a review. IEEE J Quantum Electron. 1999;5:1205–15.

Schmitt JM, Lee SL, Yung KM. An optical coherence microscope with enhanced resolving power in thick tissue. Opt Commun. 1997;142:203–7.

Schmoll T, Kolbitsch C, Leitgeb RA. In vivo functional retinal optical coherence tomography. J Biomed Opt. 2010;15:041513–041513.

Schnabel C, Gaertner M, Kirsten L, Meissner S, Koch E. Total liquid ventilation: a new approach to improve 3D OCT image quality of alveolar structures in lung tissue. Opt Express. 2013;21:31782–8.

Seeliger MW, Beck SC, Pereyra-Muñoz N, et al. In vivo confocal imaging of the retina in animal models using scanning laser ophthalmoscopy. Vision Res. 2005;45:3512–9.

Srinivasan VJ, Ko TH, Wojtkowski M, et al. Noninvasive volumetric imaging and morphometry of the rodent retina with high-speed, ultrahigh-resolution optical coherence tomography. Invest Ophthalmol Vis Sci. 2006;47:5522–8.

Storen T, Royset A, Svaasand LO, Lindmo T. Measurement of dye diffusion in scattering tissue phantoms using dual-wavelength low-coherence interferometry. J Biomed Opt. 2006;11:014017.

Sun JJ, Guo SG, Wu L, et al. 3D In Vivo optical coherence tomography based on a low-voltage, large-scan-range 2D MEMS mirror. Opt Express. 2010;18:12065–75.

Szkulmowski M, Szkulmowska A, Bajraszewski T, Kowalczyk A, Wojtkowski M. Flow velocity estimation using joint spectral and time domain optical coherence tomography. Opt Express. 2008;16:6008–25.

Traub WA. Constant-dispersion grism spectrometer for channeled spectra. J Opt Soc Am A. 1990;7:1779–91.

Tucker-Schwartz JM, Beavers KR, Sit WW, Shah AT, Duvall CL, Skala MC. In vivo imaging of nanoparticle delivery and tumor microvasculature with multimodal optical coherence tomography, Biomed Opt Express. 2014;5(6):1731–43. DOI: 10.1364/BOE.5.001731.

Unterhuber A, Povazay B, Hermann B, et al. In vivo retinal optical coherence tomography at 1040 nm - enhanced penetration into the choroid. Opt Express. 2005;13:3252–8.

Vergnole S, Levesque D, Lamouche G. Experimental validation of an optimized signal processing method to handle non-linearity in swept-source optical coherence tomography. Opt Express. 2010;18:10446–61.

Walther J, Koch E. Transverse motion as a source of noise and reduced correlation of the Doppler

phase shift in spectral domain OCT. Opt Express. 2009;17:19698–713.
Walther J, Koch E. Relation of joint spectral and time domain optical coherence tomography (jSTdOCT) and phase-resolved Doppler OCT. Opt Express. 2014;22:23129–46.
Walther J, Krüger A, Cuevas M, Koch E. Effects of axial, transverse, and oblique sample motion in FD OCT in systems with global or rolling shutter line detector. J Opt Soc Am A. 2008;25:2791–802.
Walther J, Mueller G, Morawietz H, Koch E. Signal power decrease due to fringe washout as an extension of the limited Doppler flow measurement range in spectral domain optical coherence tomography. J Biomed Opt. 2010;15:041511.
Wang L, Ho PP, Liu C, Zhang G, Alfano RR. Ballistic 2-D imaging through scattering walls using an ultrafast optical Kerr gate. Science. 1991;253:769–71.
Wang RK, Jacques SL, Ma Z, et al. Three dimensional optical angiography. Opt Express. 2007b;15:4083–97.
Wang J, Wang MR, Jiang H, et al. Detection of magnetic particles in live DBA/2J mouse eyes using magnetomotive optical coherence tomography. Eye Contact Lens. 2010b;36:346–51.
Wang L, Hofer B, Chen YP, et al. Highly reproducible swept-source, dispersion-encoded full-range biometry and imaging of the mouse eye. J Biomed Opt. 2010c;15:046004.
Weber A, Hochmann S, Cimalla P, et al. Characterization of light lesion paradigms and optical coherence tomography as tools to study adult retina regeneration in zebrafish. PLoS One. 2013;8:e80483.
Wieser W, Biedermann BR, Klein T, Eigenwillig CM, Huber R. Multi-Megahertz OCT: High quality 3D imaging at 20 million A-scans and 4.5 GVoxels per second. Opt Express. 2010;18:14685–704.
Wojtkowski M, Srinivasan V, Ko T, et al. Ultrahigh-resolution, high-speed, Fourier domain optical coherence tomography and methods for dispersion compensation. Opt Express. 2004;12:2404–22.
Wolf E. Introduction to the theory of coherence and polarization of light. Wolf E, editors. Cambridge: Cambridge University Press; 2007.
Wolf-Schnurrbusch UEK, Ceklic L, Brinkmann CK, et al. Macular thickness measurements in healthy eyes using six different optical coherence tomography instruments. Invest Ophthalmol Vis Sci. 2009;50:3432–7.
Xu C, Ye J, Marks DL, Boppart SA. Near-infrared dyes as contrast-enhancing agents for spectroscopic optical coherence tomography. Opt Lett. 2004;29:1647–9.
Xu CY, Carney PS, Boppart SA. Wavelength-dependent scattering in spectroscopic optical coherence tomography. Opt Express. 2005;13:5450–62.
Xu ZQ, Carrion L, Maciejko R. A zero-crossing detection method applied to Doppler OCT. Opt Express. 2008:16(7):4394–412. DOI: 10.1364/OE.16.004394.
Yamanari M, Makita S, Yasuno Y. Polarization-sensitive swept-source optical coherence tomography with continuous source polarization modulation. Opt Express. 2008;16:5892–906.
Yang C, McGuckin LEL, Simon JD, et al. Spectral triangulation molecular contrast optical coherence tomography with indocyanine green as the contrast agent. Opt Lett. 2004a;29:2016–8.
Yang Y, Whiteman S, van Pittius DG, et al. Use of optical coherence tomography in delineating airways microstructure: comparison of OCT images to histopathological sections. Phys Med Biol. 2004b;49:1247–55.
Yi J, Radosevich AJ, Rogers JD, et al. Can OCT be sensitive to nanoscale structural alterations in biological tissue? Opt Express. 2013;21:9043–59.
Yi J, Radosevich AJ, Stypula-Cyrus Y, et al. Spatially resolved optical and ultrastructural properties of colorectal and pancreatic field carcinogenesis observed by inverse spectroscopic optical coherence tomography. J Biomed Opt. 2014;19:036013–036013.
Yin JC, Liu GJ, Zhang J, et al. In vivo early detection of smoke-induced airway injury using three-dimensional swept-source optical coherence tomography. J Biomed Opt. 2009;14:060503.
Yim J, Kim H, Ryu S, Song S, Kim HO, Hyun KA, Jung HI, Joo C. Photothermal spectral-domain optical coherence reflectometry for direct measurement of hemoglobin concentration of erythrocytes. View ResearcherID and ORCID. Biosensors and Bioelectronics. 2014;57:59–64. DOI: 10.1016/j.bios.2014.01.052.
Yoo KM, Alfano RR. Determination of the scattering and absorption lengths from the temporal profile of a back-scattered pulse. Opt Lett. 1990;15:276–8.
Yun SH, Tearney G, de Boer J, Bouma B. Motion artifacts in optical coherence tomography with frequency-domain ranging. Opt Express. 2004;12:2977–98.
Zhang Y, Cense B, Rha J, et al. High-speed volumetric imaging of cone photoreceptors with adaptive optics spectral-domain optical coherence tomography. Opt Express. 2006;14:4380–94.
Zhou X, Xie J, Shen M, et al. Biometric measurement of the mouse eye using optical coherence tomography with focal plane advancement. Vision Res. 2008;48:1137–43.

Intravital Imaging in Small Animals

Adler DC, Huang SW, Huber R, Fujimoto JG. Photothermal detection of gold nanoparticles using phase-sensitive optical coherence tomography View ResearcherID and ORCID. Opt Express. 2008;16(7):4376–93.
Brown EB, Campbell RB, Tsuzuki Y, Xu L, Carmeliet P, Fukumura D, et al. In vivo measurement of gene expression, angiogenesis and physiological function in tumors using multiphoton laser scanning microscopy. Nat Med. 2001;7(7):864–8.
Burford JL, Villanueva K, Lam L, Riquier-Brison A, Hackl MJ, Pippin J, et al. Intravital imaging of podocyte calcium in glomerular injury and disease. J Clin Invest. 2014;124(5):2050–8.

Chevre R, Gonzalez-Granado JM, Megens RT, Sreeramkumar V, Silvestre-Roig C, Molina-Sanchez P, et al. High-resolution imaging of intravascular atherogenic inflammation in live mice. Circ Res. 2014;114(5):770–9.

Chung K, Deisseroth K. CLARITY for mapping the nervous system. Nat Methods. 2013;10(6):508–13.

Denk W, Strickler JH, Webb WW. Two-photon laser scanning fluorescence microscopy. Science. 1990;248(4951):73–6.

Dietzel S, Pircher J, Nekolla AK, Gull M, Brandli AW, Pohl U, et al. Label-free determination of hemodynamic parameters in the microcirculaton with third harmonic generation microscopy. PLoS One. 2014;9(6):e99615.

Douma K, Prinzen L, Slaaf DW, Reutelingsperger CP, Biessen EA, Hackeng TM, et al. Nanoparticles for optical molecular imaging of atherosclerosis. Small. 2009;5(5):544–57.

Eichhoff G, Garaschuk O. Two-photon imaging of neural networks in a mouse model of Alzheimer's disease. Cold Spring Harb Protoc. 2011;2011(10):1206–16.

Endrich B, Hammersen F, Messmer K. Capillary ultrastructure and microcirculatory function of malignant tumors. Adv Exp Med Biol. 1988;242:205–14.

Fan GY, Fujisaki H, Miyawaki A, Tsay RK, Tsien RY, Ellisman MH. Video-rate scanning two-photon excitation fluorescence microscopy and ratio imaging with cameleons. Biophys J. 1999;76(5):2412–20.

Furie B, Furie BC. Thrombus formation in a living mouse. Pathophysiol Haemost Thromb. 2006;35(1–2):1–4.

Genina EA, Bashkatov AN, Kolesnikova EA, Basko MV, Terentyuk GS, Tuchin VV. Optical coherence tomography monitoring of enhanced skin optical clearing in rats in vivo. J Biomed Opt. 2014;19(2):21109.

Gobel W, Kampa BM, Helmchen F. Imaging cellular network dynamics in three dimensions using fast 3D laser scanning. Nat Methods. 2007;4(1):73–9.

Grewe BF, Langer D, Kasper H, Kampa BM, Helmchen F. High-speed in vivo calcium imaging reveals neuronal network activity with near-millisecond precision. Nat Methods. 2010;7(5):399–405.

Helmchen F, Denk W. Deep tissue two-photon microscopy. Nat Methods. 2005;2(12):932–40.

Julius Cohnheim (1839–1884) experimental pathologist. JAMA :J Am Med Assoc. 1968;206(7):1561–2.

Kamoun WS, Chae SS, Lacorre DA, Tyrrell JA, Mitre M, Gillissen MA, et al. Simultaneous measurement of RBC velocity, flux, hematocrit and shear rate in vascular networks. Nat Methods. 2010;7(8):655–60.

Kapsokalyvas D, Schiffers P, Maij N, Suylen D, Hackeng T, Van Zandvoort M, et al. Imaging evidence for endothelin ETA/ETB receptor heterodimers in isolated rat mesenteric resistance arteries. Life Sci. 2014;111(1-2):36–41.

Kiyooka T, Hiramatsu O, Shigeto F, Nakamoto H, Tachibana H, Yada T, et al. Direct observation of epicardial coronary capillary hemodynamics during reactive hyperemia and during adenosine administration by intravital video microscopy. Am J Physiol Heart Circ Physiol. 2005;288(3):H1437–43.

Kubes P, Payne D, Woodman RC. Molecular mechanisms of leukocyte recruitment in postischemic liver microcirculation. Am J Physiol Gastrointest Liver Physiol. 2002;283(1):G139–47.

Lammermann T, Afonso PV, Angermann BR, Wang JM, Kastenmuller W, Parent CA, et al. Neutrophil swarms require LTB4 and integrins at sites of cell death in vivo. Nature. 2013;498(7454):371–5.

Levene MJ, Dombeck DA, Kasischke KA, Molloy RP, Webb WW. In vivo multiphoton microscopy of deep brain tissue. J Neurophysiol. 2004;91(4):1908–12.

Li X, Yu W. Deep tissue microscopic imaging of the kidney with a gradient-index lens system. Opt Commun. 2008;281(7):1833–40.

Li W, Goldstein DR, Kreisel D. Intravital 2-photon imaging, leukocyte trafficking, and the beating heart. Trends Cardiovasc Med. 2013b;23(8):287–93.

Livet J, Weissman TA, Kang H, Draft RW, Lu J, Bennis RA, et al. Transgenic strategies for combinatorial expression of fluorescent proteins in the nervous system. Nature. 2007;450(7166):56–62.

Mahou P, Zimmerley M, Loulier K, Matho KS, Labroille G, Morin X, et al. Multicolor two-photon tissue imaging by wavelength mixing. Nat Methods. 2012;9(8):815–8.

Massberg S, Gawaz M, Gruner S, Schulte V, Konrad I, Zohlnhofer D, et al. A crucial role of glycoprotein VI for platelet recruitment to the injured arterial wall in vivo. J Exp Med. 2003;197(1):41–9.

Megens RT, Kemmerich K, Pyta J, Weber C, Soehnlein O. Intravital imaging of phagocyte recruitment. Thromb Haemost. 2011;105(5):802–10.

Menger MD, Laschke MW, Vollmar B. Viewing the microcirculation through the window: some twenty years experience with the hamster dorsal skinfold chamber. Eur Surg Res Europaische chirurgische Forschung Recherches chirurgicales europeennes. 2002;34(1–2):83–91.

Mittmann W, Wallace DJ, Czubayko U, Herb JT, Schaefer AT, Looger LL, et al. Two-photon calcium imaging of evoked activity from L5 somatosensory neurons in vivo. Nat Neurosci. 2011;14(8):1089–93.

Mizuno R, Kamioka Y, Kabashima K, Imajo M, Sumiyama K, Nakasho E, et al. In vivo imaging reveals PKA regulation of ERK activity during neutrophil recruitment to inflamed intestines. J Exp Med. 2014;211(6):1123–36.

Nielsen T, Fricke M, Hellweg D, Andresen P. High efficiency beam splitter for multifocal multiphoton microscopy. J Microsc. 2001;201(Pt 3):368–76.

Niesner R, Andresen V, Neumann J, Spiecker H, Gunzer M. The power of single and multibeam two-photon microscopy for high-resolution and high-speed deep tissue and intravital imaging. Biophys J. 2007;93(7):2519–29.

Progatzky F, Dallman MJ, Lo CC. From seeing to believing: labelling strategies for in vivo cell-tracking experiments. Interface Focus. 2013;3(3):20130001.

Rademakers T, Douma K, Hackeng TM, Post MJ, Sluimer JC, Daemen MJ, et al. Plaque-associated vasa vasorum in aged apolipoprotein E-deficient mice exhibit pro-atherogenic functional features in vivo. Arterioscler Thromb Vasc Biol. 2013;33(2):249–56.

Rothstein EC, Carroll S, Combs CA, Jobsis PD, Balaban RS. Skeletal muscle NAD(P)H two-photon fluorescence microscopy in vivo: topology and optical inner filters. Biophys J. 2005;88(3):2165–76.

Schepers AG, Snippert HJ, Stange DE, van den Born M, van Es JH, van de Wetering M, et al. Lineage tracing reveals Lgr5+ stem cell activity in mouse intestinal adenomas. Science. 2012;337(6095):730–5.

Shaner NC, Patterson GH, Davidson MW. Advances in fluorescent protein technology. J Cell Sci. 2007;120(Pt 24):4247–60.

Thorlacius H, Lindbom L, Raud J. Cytokine-induced leukocyte rolling in mouse cremaster muscle arterioles in P-selectin dependent. Am J Physiol. 1997;272(4 Pt 2):H1725–9.

van Zandvoort M, Engels W, Douma K, Beckers L, Oude Egbrink M, Daemen M, et al. Two-photon microscopy for imaging of the (atherosclerotic) vascular wall: a proof of concept study. J Vasc Res. 2004;41(1):54–63.

Victora GD, Schwickert TA, Fooksman DR, Kamphorst AO, Meyer-Hermann M, Dustin ML, et al. Germinal center dynamics revealed by multiphoton microscopy with a photoactivatable fluorescent reporter. Cell. 2010;143(4):592–605.

Weber K, Thomaschewski M, Warlich M, Volz T, Cornils K, Niebuhr B, et al. RGB marking facilitates multicolor clonal cell tracking. Nat Med. 2011;17(4):504–9.

Woodfin A, Voisin MB, Beyrau M, Colom B, Caille D, Diapouli FM, et al. The junctional adhesion molecule JAM-C regulates polarized transendothelial migration of neutrophils in vivo. Nat Immunol. 2011;12(8):761–9.

Optoacoustic Imaging

Allen TJ, Beard PC. Pulsed near-infrared laser diode excitation system for biomedical photoacoustic imaging. Opt Lett. 2006b;31:3462–4.

Amiot L, Xu SP, Liang S, Pan LY, Zhao JXJ. Near-infrared fluorescent materials for sensing of biological targets. Sensors. 2008;8:3082–105.

Beziere N, von Schacky C, Kosanke Y, et al. Optoacoustic imaging and staging of inflammation in a murine model of arthritis. Arth Rheumatol. 2014;66:2071–8.

Buehler A, Herzog E, Razansky D, Ntziachristos V. Video rate optoacoustic tomography of mouse kidney perfusion. Opt Lett. 2010b;35:2475–7.

De La Z, Zavaleta C, Keren S, Vaithilingam S, Bodapati S, Liu Z, Levi J, Smith BR, Ma TJ, Oralkan O, et al. Carbon nanotubes as photoacoustic molecular imaging agents in living mice. Nat Nanotech. 2008;3:557–62.

Deán-Ben XL, Razansky D. Adding fifth dimension to optoacoustic imaging: volumetric time-resolved spectrally-enriched tomography. Light Sci Appl. 2014;3:e137.

Duck FA. Physical properties of tissues: a comprehensive reference book. San Diego: Academic; 1990.

Herzog E, Taruttis A, Beziere N, Lutich A, Razansky D, Ntziachristos V. Optical imaging of cancer heterogeneity with multispectral optoacoustic tomography. Radiology. 2012;263:461–8.

Hu S, Maslov K, Wang LV. Second generation optical-resolution photoacoustic microscopy with improved sensitivity and speed. Opt Lett. 2011;36:1134–6.

Hudson SV, Huang JS, Yin W, Albeituni S, Rush J, Khanal A, Yan J, Ceresa BP, Frieboes HB, McNally LR. Targeted noninvasive imaging of EGFR-expressing orthotopic pancreatic cancer using multispectral optoacoustic tomography. Cancer Res. 2014;74:6271–9.

Ida T, Kawaguchi Y, Kawauchi S, et al. Real-time photoacoustic imaging system for burn diagnosis. J Biomed Opt. 2014;19:086013.

Jansen K, Wu M, van der Steen AFW, van Soest G. Photoacoustic imaging of human coronary atherosclerosis in two spectral bands. Photoacoustics. 2014;2(1):12–20.

Kostli KP, Frenz M, Weber HP, Paltauf G, Schmidt-Kloiber H. Optoacoustic infrared spectroscopy of soft tissue. J Appl Phys. 2000;88:1632–7.

Kruger RA, Liu P, Fang YR, Appledorn CR. Photoacoustic ultrasound (PAUS)--reconstruction tomography. Med Phys. 1995;22:1605–9.

Krumholz A, Vanvickle-Chavez SJ, Yao J, et al. Photoacoustic microscopy of tyrosinase reporter gene in vivo. J Biomed Opt. 2011;16:80503.

Laufer J, Delpy D, Elwell C, Beard P. Quantitative spatially resolved measurement of tissue chromophore concentrations using photoacoustic spectroscopy: application to the measurement of blood oxygenation and haemoglobin concentration. Phys Med Biol. 2007;52(1):141–68.

Laufer J, Jathoul A, Johnson P, Zhang E, Lythgoe M, Pedley RB, Pule M, Beard P. In vivo photoacoustic imaging of tyrosinase expressing tumours in mice. Proc SPIE. 2012;8223, 82230M.

Lozano N, Al-Ahmady ZS, Beziere NS, Ntziachristos V, Kostarelos K. Monoclonal antibody-targeted PEGylated liposome-ICG encapsulating doxorubicin as a potential theranostic agent. Int J Pharm. 2014;482:2–10. doi:10.1016/j.ijpharm.2014.10.045.

Lutzweiler C, Razansky D. Optoacoustic imaging and tomography: reconstruction approaches and outstanding challenges in image performance and quantification. Sensors. 2013;13:7345–84.

Mehrmohammadi M, Yoon SJ, Yeager D, Emelianov SY. Photoacoustic imaging for cancer detection and staging. Curr Mol Imag. 2013;2:89–105.

Nasiriavanaki M, Xia J, Wan H, Bauer AQ, Culver JP, Wang LV. High-resolution photoacoustic tomography of resting-state functional connectivity in the mouse brain. Proc Natl Acad Sci U S A. 2013;111:21–6.

Ntziachristos V, Razansky D. Molecular imaging by means of multispectral opto-acoustic tomography (MSOT). Chem Rev. 2010;110:2783–94.
Ntziachristos V, Ripoll J, Wang LV, Weissleder R. Looking and listening to light: the evolution of whole-body photonic imaging. Nat Biotechnol. 2005;23:313–20.
Razansky D. Multispectral optoacoustic tomography - volumetric color hearing in real time. IEEE J Sel Top Quant Electron. 2012;18:1234–43.
Razansky D, Distel M, Vinegoni C, Ma R, Perrimon N, Köster RW, Ntziachristos V. Multi-spectral optoacoustic tomography of deep-seated fluorescent proteins in-vivo. Nat Photon. 2009;3:412–7.
Razansky D, Kellnberger S, Ntziachristos V. Near-field radio-frequency thermoacoustic tomography with impulse excitation. Med Phys. 2010;37:4602–7.
Razansky D, Buehler A, Ntziachristos V. Volumetric real-time multispectral optoacoustic tomography of biomarkers. Nat Prot. 2011;6:1121–9.
Razansky D, Deliolanis N, Vinegoni C, Ntziachristos V. Deep tissue optical and optoacoustic molecular imaging technologies for small animal research and drug discovery. Curr Pharm Biotechnol. 2012;13:504–22.
Rosencwaig A. Photoacoustic spectroscopy of biological materials. Science. 1973;181:657–8.
Sethuraman S, Amirian JH, Litovsky SH, Smalling RW, Emelianov SY. Spectroscopic intravascular photoacoustic imaging to differentiate atherosclerotic plaques. Opt Express. 2008;16:3362–7.
Song L, Kim C, Maslov K, Shung KK, Wang LHV. High-speed dynamic 3D photoacoustic imaging of sentinel lymph node in a murine model using an ultrasound array. Med Phys. 2009;36:3724–9.
Tainter CS, Bell AG. Selenium and the photophone. Nature. 1880;22:500–3.
Taruttis A, Herzog E, Razansky D, et al. Real-time imaging of cardiovascular dynamics and circulating gold nanorods with multispectral optoacoustic tomography. Opt Express. 2010;18:19592–602.
Taruttis A, Morscher S, Burton NC, Razansky D, Ntziachristos V. Fast multispectral optoacoustic tomography (MSOT) for dynamic imaging of pharmacokinetics and biodistribution in multiple organs. PLoS One. 2012;7:e30491.
Tong L, Wei QS, Wei A, Cheng JX. Gold nanorods as contrast agents for biological imaging: optical properties, surface conjugation and photothermal effects. Photochem Photobiol. 2009;85:21–32.
Vonnemann J, Beziere N, Böttcher C, et al. Polyglycerolsulfate functionalized gold nanorods as optoacoustic signal nanoamplifiers for in vivo bioimaging of rheumatoid arthritis. Theranostics. 2014;4:629–41.
Wang LV, editor. Photoacoustic imaging and spectroscopy. Boca Raton: CRC Press; 2009.
Wang LV, Hu S. Photoacoustic tomography: in vivo imaging from organelles to organs. Science. 2012;335:1458–62.
Wang XD, Pang YJ, Ku G, Xie XY, Stoica G, Wang LHV. Noninvasive laser-induced photoacoustic tomography for structural and functional in vivo imaging of the brain. Nat Biotechnol. 2003;21:803–6.
Wang Y, Maslov K, Zhang Y, Hu S, Yang LM, Xia YN, Liu JA, Wang LHV. Fiber-laser-based photoacoustic microscopy and melanoma cell detection. J Biomed Opt. 2011;16:011014.
Yang JM, Favazza C, Chen RM, Yao JJ, Cai X, Maslov K, Zhou QF, Shung KK, Wang LHV. Simultaneous functional photoacoustic and ultrasonic endoscopy of internal organs in vivo. Nat Med. 2012;18:1297–302.
Yao J, Wang LV. Sensitivity of photoacoustic microscopy. Photoacoustics. 2014;2:87–101.

Optical Probes

Alander JT, Kaartinen I, Laakso A, Pätilä T, Spillmann T, Tuchin VV, Venermo M, Välisuo P. A review of indocyanine green fluorescent imaging in surgery. Int J Biomed Imaging. 2012;2012:940585.
Azar S, Intes X. Translational multimodality optical imaging. Boston: Artech House; 2008.
Barnett EM, Zhang X, Maxwell D, Chang Q, Piwnica-Worms D. Single-cell imaging of retinal ganglion cell apoptosis with a cell-penetrating, activatable peptide probe in an in vivo glaucoma model. Proc Natl Acad Sci U S A. 2009;106:9391–6.
Becker A, Hessenius C, Licha K, Ebert B, Sukowski U, Semmler W, Wiedenmann B, Grötzinger C. Receptor-targeted optical imaging of tumors with near-infrared fluorescent ligands. Nat Biotechnol. 2001;19:327–31.
Bentolila LA, Ebenstein Y, Weiss S. Quantum dots for in vivo small-animal imaging. J Nucl Med. 2009;50:493–6.
Boens N, Leen V, Dehaen W. Fluorescent indicators based on BODIPY. Chem Soc Rev. 2012;41:1130–72.
Bremer C, Tung CH, Weissleder R. In vivo molecular target assessment of matrix metalloproteinase inhibition. Nat Med. 2001b;7:743–8.
Fischer T, Gemeinhardt I, Wagner S, Stieglitz DV, Schnorr J, Hermann KG, Ebert B, Petzelt D, Macdonald R, Licha K, Schirner M, Krenn V, Kamradt T, Taupitz M. Assessment of unspecific near-infrared dyes in laser-induced fluorescence imaging of experimental arthritis. Acad Radiol. 2006;13:4–13.
Foster AE, Kwon S, Ke S, Lu A, Eldin K, Sevick-Muraca E, Rooney CM. In vivo fluorescent optical imaging of cytotoxic T lymphocyte migration using IRDye800CW near-infrared dye. Appl Opt. 2008;47:5944–52.
Hermanson GT. Bioconjugate techniques. San Diego: Academic; 1996.
Hilderbrand SA, Weissleder R. Near-infrared fluorescence: application to in vivo molecular imaging. Curr Opin Chem Biol. 2010;14:71–9.
Holzinger M, Le Goff A, Cosnier S. Nanomaterials for biosensing applications: a review. Front Chem. 2014;2:63.
Kisin-Finfer E, Ferber S, Blau R, Satchi-Fainaro R, Shabat D. Synthesis and evaluation of new NIR-fluorescent probes for cathepsin B: ICT versus FRET

as a turn-ON mode-of-action. Bioorg Med Chem Lett. 2014;24:2453–8.

Klohs J, Steinbrink J, Bourayou R, Mueller S, Cordell R, Licha K, Schirner M, Dirnagl U, Lindauer U, Wunder A. Near-infrared fluorescence imaging with fluorescently labeled albumin: a novel method for non-invasive optical imaging of blood–brain barrier impairment after focal cerebral ischemia in mice. J Neurosci Methods. 2009;180(1): 126–32.

Lee SB, Hassan M, Fisher R, Chertov O, Chernomordik V, Kramer-Marek G, Gandjbakhche A, Capala J. Affibody molecules for in vivo characterization of HER2-positive tumors by near-infrared imaging. Clin Cancer Res. 2008;14:3840–9.

Lee H, Akers W, Bhushan K, Bloch S, Sudlow G, Tang R. Near-infrared pH-activatable fluorescent probes for imaging primary and metastatic breast tumors. Bioconjug Chem. 2011;22:777–84.

Licha K, Resch-Genger U. Probes for optical imaging: new developments. Drug Discovery Today: Technol. 2011;8:e87–94.

Licha K, Resch-Genger U. Fluorescent reporters and optical probes. In: Brahme A. (Editor in Chief) Comprehensive biomedical physics, vol. 4. Amsterdam: Elsevier; 2014. p. 85–109.

Licha K, Schirner M, Henry G. Optical agents. In: Schwaiger M, editor Handbook of experimental pharmacology, vol 185, part 2. Heidelberg: Springer, p. 203–22.

Luo S, Zhang E, Su Y, Cheng T, Shi C. A review of NIR dyes in cancer targeting and imaging. Biomaterials. 2011b;32:7127–38.

Mathejczyk JE, Pauli J, Dullin C, Resch-Genger U, Alves F, Napp J. High-sensitivity detection of breast tumors in vivo by use of a pH-sensitive near-infrared fluorescence probe. J Biomed Opt. 2012;17:076028.

Mier W, Beijer B, Graham K, Hull WE. Fluorescent somatostatin receptor probes for the intraoperative detection of tumor tissue with long-wavelength visible light. Bioorg Med Chem. 2002;10:2543–52.

Moon WK, Lin Y, O'Loughlin T, Tang Y, Kim DE, Weissleder R, Tung CH. Enhanced tumor detection using a folate receptor-targeted near-infrared fluorochrome conjugate. Bioconjug Chem. 2003;14: 539–45.

Pauli J, Vag T, Haag R, Spieles M, Wenzel M, Kaiser WA, Resch-Genger U, Hilger I. An in vitro characterization study of new near infrared dyes for molecular imaging. Eur J Med Chem. 2009b;44:3496–503.

Pauli J, Licha K, Berkemeyer J, Grabolle M, Spieles M, Wegner N, Welker P, Resch-Genger U. New fluorescent labels with tunable hydrophilicity for the rational design of bright optical probes for molecular imaging. Bioconjug Chem. 2013;24:1174–85.

Quadir QA, Radowski MR, Kratz F, Licha K, Hauff P, Haag R. Dendritic multishell architectures for drug and dye transport. J Control Release. 2008;132: 289–94.

Rasmussen JC, Tan IC, Marshall MV, Fife CE, Sevick-Muraca EM. Lymphatic imaging in humans with near-infrared fluorescence. Curr Opin Biotechnol. 2009;20: 74–82.

Resch-Genger U, Grabolle M, Cavaliere-Jaricot S, Nitschke R, Nann T. Quantum dots versus organic dyes as fluorescent labels. Nat Methods. 2008;9: 763–75.

Richards G, Soubrane G, Yanuzzi L. Fluorescein and ICG angiography. Germany: Thieme; 1998.

Selvam S, Kundu K, Templeman KL, Murthy N, Garcia AJ. Minimally invasive, longitudinal monitoring of biomaterial-associated inflammation by fluorescence imaging. Biomaterials. 2011;32:7785–92.

Stefflova K, Chen J, Zheng G. Using molecular beacons for cancer imaging and treatment. Front Biosci. 2007;12:4709–21.

Ulrich G, Ziessel R, Harriman A. The chemistry of fluorescent bodipy dyes: versatility unsurpassed. Angew Chem Int Ed. 2008;47:1184–201.

Umezawa K, Citterio D, Suzuki K. New trends in near-infrared fluorophores for bioimaging. Anal Sci. 2014;30:327–49.

Wall A, Persigehl T, Hauff P, Licha K, Schirner M, Müller S, von Wallbrunn A, Matuszewski L, Heindel W, Bremer C. Differentiation of angiogenic burden in human cancer xenografts using a perfusion-type optical contrast agent (SIDAG). Breast Cancer Res. 2008;10:R23.

Weissleder R, Tung CH, Mahmood U, Bogdanov Jr A. In vivo imaging of tumors with protease-activated near-infrared fluorescent probes. Nat Biotechnol. 1999;17: 375–8.

Multimodal Imaging and Image Fusion

17

Hans F. Wehrl, Mario Amend, and André Thielcke

Contents

17.1 Introduction

In multimodal imaging diverse imaging techniques are applied to the same subject usually within a limited time frame in order to capture the same functional, morphologic, and metabolic state of the subject. The historical most compelling need for multimodal imaging stems from the requirement to match functional or metabolic information captured with, e.g., positron emission tomography (PET) or single-photon emission computed tomography (SPECT) with morphological information about the subject obtained from computed tomography (CT) or magnetic resonance imaging (MRI).

Figure 17.1 shows an example of multimodal imaging in the case of a mouse bearing a subcutaneous tumor. The [^{64}Cu] monoclonal antibody (mAb)-PET images show increased uptake in the tumor and also in the liver. However, based on the PET images alone, it is difficult to set these metabolic highly active regions into an anatomical context. Morphological information from CT helps to clarify the position of the tumor within the mouse's body, which can be estimated in the fused PET/CT images. However, there is still space for improvement on the anatomical side of detail displayed. The combination of PET with MR (Fig. 17.1) allows also the utilization of the increased soft tissue contrast provided by the MR, which in return gives a much better anatomical clarification also of internal organs, which are not visible in the non-contrast-enhanced, small animal CT images.

17.2 Sequential and Simultaneous Imaging

Multimodal images have been historically acquired usually in a serial matter, i.e., the subject is first scanned in one modality (e.g., the PET)

H.F. Wehrl (✉) • M. Amend • A. Thielcke
University of Tuebingen, Department of Preclinical Imaging and Radiopharmacy, Werner Siemens Imaging Center, Tuebingen, Germany
e-mail: Hans.Wehrl@med.uni-tuebingen.de

F. Kiessling et al. (eds.), *Small Animal Imaging*, DOI 10.1007/978-3-319-42202-2_17

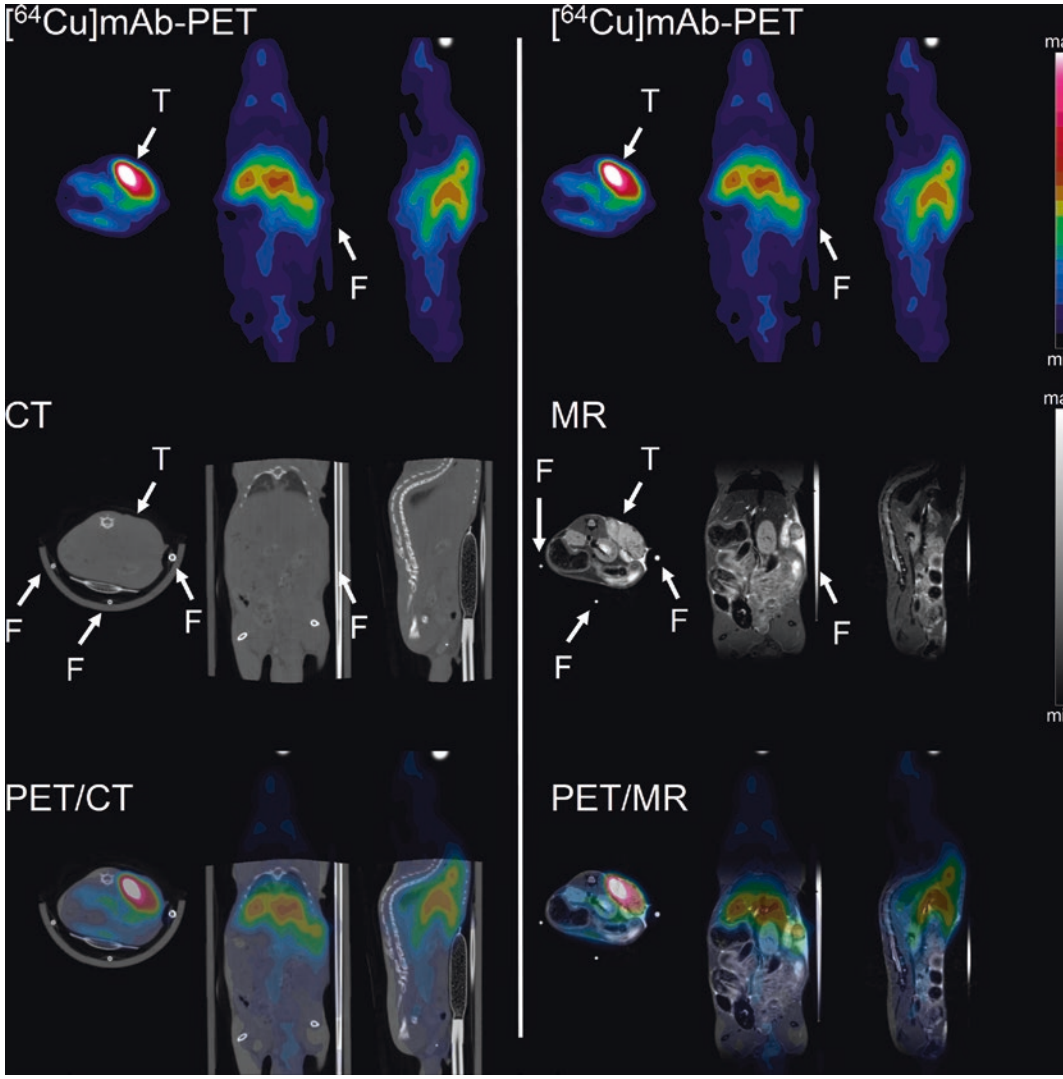

Fig. 17.1 *Left panel*: [^{64}Cu]mAb-PET in a mouse bearing a subcutaneous tumor. A high uptake of the PET tracer is observed in the areas of the liver and also the tumor (T). However, the metabolic information provided by PET alone makes a clear identification of the tumor, in terms of its anatomical context, difficult. CT images obtained in the same animal, using the same animal bed as well as fiducial markers (F), allow a fusion of PET and CT images. The CT depicts some soft tissue structures, but with low contrast, and bone structures in the animal (e.g., the spine). *Right panel*: The same animal imaged in PET and MR. A T2-weighted MR sequence delivers excellent soft tissue contrast and allows the identification of internal organs without the use of contrast agents. The subsequent PET/MR image fusion does not only allow to put the metabolic PET information into an anatomical framework but can also be used to define regions of interests based on anatomy that can guide the PET images analysis and yield a more reliable quantification

and afterwards transferred and scanned in the other modality (e.g., the CT, Fig. 17.2a). Image fusion is then accomplished by software tools that load the image data of both modalities and either fuse them manually with user interaction or automatically. Image fusion can be done using either common landmarks, e.g., regions that are identifiable in both image modalities, or fiducial markers, e.g., structures attached to the animal or the animal bed that are visible in both modalities. Recent

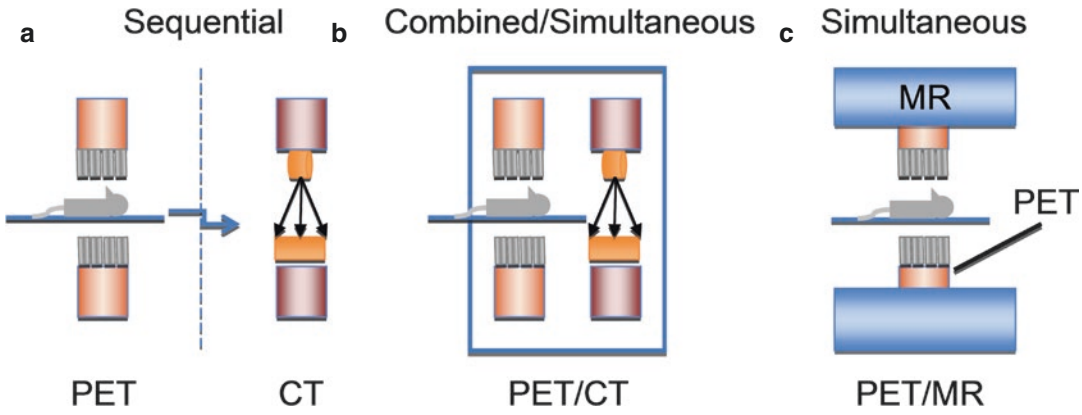

Fig. 17.2 Multimodal imaging options. (**a**) Sequential approach, e.g., sequential PET and CT. In theory the devices can be located in different rooms or even in different buildings. The animal is transferred from one modality to the next either using dedicated imaging beds and fiducial markers or just being placed on the respective animal holder. (**b**) Combined and pseudo simultaneous systems, e.g., for PET/CT, allow to scan the animal in both modalities during the same imaging session. However, the images are still acquired in a sequential manner. (**c**) Simultaneous imaging, e.g., PET/MR. The field of view (FOV) of both modalities is aligned; therefore, during MR acquisition also PET images can be acquired. This approach saves imaging time and allows also an excellent spatial co-registration

developments have, however, led to simultaneous multimodal imaging. Here, the subject is scanned ideally at the same time or only with a very small time offset (e.g., minutes) in two imaging modalities. Simultaneous multimodal imaging devices are designed in a way that either the animal is moved using the same animal bed in a conveyor-like style, without altering its position from one modality to the next, e.g., in PET/CT (Fig. 17.2b) (Lawrence et al. 2010), or that imaging data is acquired simultaneously in, e.g., simultaneous PET/MR systems (Fig. 17.2c) (Wehrl et al. 2015). True simultaneous acquisition is possible by concentrically arranging the imaging modalities around the animal (e.g., PET scanner as an insert into the MR scanner).

All of the above implementations of multimodal imaging have their respective pros and cons. The examples of most widespread multimodal modalities, PET, CT, and PET/MR, are used exemplarily to show these advantages and disadvantages. However, these points apply to all multimodal combinations.

A sequential approach (Fig. 17.2a), where, e.g., stand-alone PET and CT machines are used, has the advantage that both machines can be utilized in a separate manner, especially when no multimodal image information is needed – i.e., only PET or only CT information is required. The implementation costs and technical challenges are low for stand-alone solutions compared to combined imaging devices. However, there is the disadvantage that image fusion can be more difficult when images have been acquired in two separate devices. Motion artifacts of the animal, especially in the abdominal area, e.g., due to peristaltics, can make an exact fusion cumbersome. Moreover, there exists the risk of changes in the physiological state of the animal (e.g., anesthesia depth), when it is scanned at two different time points. This might not be a major implication when functional and metabolic information from one modality is matched with anatomical information from another modality; however, when functional processes should be assessed with two different modalities, these effects can be of interest – especially when small effects such as in the case of brain function are studied (Wehrl et al. 2013). Even for a sequential approach a common animal bed that can be used in both modalities (e.g., by means of dedicated mounting mechanisms) is mandatory, since otherwise the position of the animal is changed. This is especially important in the abdominal area, where nonrigid alterations of the body form can be expected when changing the positioning of the

animal. Also the ultimate scanning time is the time needed for both PET and CT scan or in the case of other combinations of the respective modalities.

Combined systems use the same animal bed as well as animal transportation mechanism in order to shift the animal from one modality to the next. These systems are usually mounted within the same gantry, e.g., as in the case of PET/CT devices (Fig. 17.2b). User interaction between scans is usually minimized and the animal is often automatically transported after the finishing of single scans, e.g., the PET scan into the CT part of the machine where subsequent anatomical scans and scans for PET attenuation correction are performed. Even though the data is acquired consecutively, the animal is imaged within the same anesthesia session and no manual transport of the animal bed is needed. This reduces greatly the possibility of motion and mispositioning artifacts induced by the user and also, to some extent, changes in physiology are minimized (e.g., by maintaining the animal body temperature by means of the same heating system). Disadvantages of such a combined but consecutive multimodality solution are that the respective modalities usually cannot be used in a stand-alone setting. During the PET scanning, e.g., the CT component is blocked. No true simultaneous acquisition is possible and also a substantial amount of engineering efforts is needed for such a multimodal integration. The total scanning time, needed for such a combined but consecutive examination, is the time needed for PET and CT.

Simultaneous multimodal systems, e.g., PET/MR, are able to acquire the imaging data of both modalities at the same time (Fig. 17.2c). This combination has a variety of advantages. Since, e.g., the time for a static PET scan (ca. 10 min) and for an anatomical MR image (ca. 10 min) are in the same order of magnitude, approximately 50 % of the total study time can be saved by acquiring PET and MR data simultaneously. This can be substantial especially in high-throughput studies. Moreover, in dedicated research application, functional processes can be monitored at the same time using PET and functional MRI (fMRI) techniques either to monitor multiple stages of metabolism or to cross-calibrate techniques (Wehrl et al. 2014). Since the animal physiology, but also possible animal motion, is the same in both modalities during acquisition, it is also feasible to use, e.g., MR information to correct for motion artifacts in PET imaging (Catana et al. 2011; Furst et al. 2015; Wurslin et al. 2013). The downsides of simultaneous multimodal systems are their usually very complex engineering efforts and the associated costs. Furthermore, as it is also the case for combined systems, the respective combined modalities can usually not be used in a stand-alone fashion. However, here, e.g., PET/MR is often an exception, since the current majority of systems are designed in a way that PET inserts are installed inside an MR system (Wehrl et al. 2011; Weissler et al. 2015; Yoon et al. 2012). The MR can then also be used without the installed PET insert.

17.3 Techniques

17.3.1 Multimodal Animal Beds and Fiducial Markers

To allow sequential multimodal imaging studies, e.g., in the case of separate PET, CT, and MR devices, it is advisable to use dedicated multimodal animal beds. Shifting the animal just from one modality to the next, without the use of the same animal bed, inevitably leads to changes in the animal position, which makes a later image fusion difficult. This is especially pronounced when areas outside the brain, e.g., in the abdominal part of the animal, are imaged. Also subcutaneous tumors tend to shift their location slightly if the animal is repositioned on different animal beds. A proper solution to this problem is to use either the animal bed from one modality in all other modalities by means of adapters and interconnectors or tape that allows to mount the bed on the often various animal holder devices found on imaging equipment. Dedicated small animal multimodal animal beds (Fig. 17.3) allow to transport and mount the bed on a multitude of imaging systems using dedicated adapter systems that can be permanently integrated to the

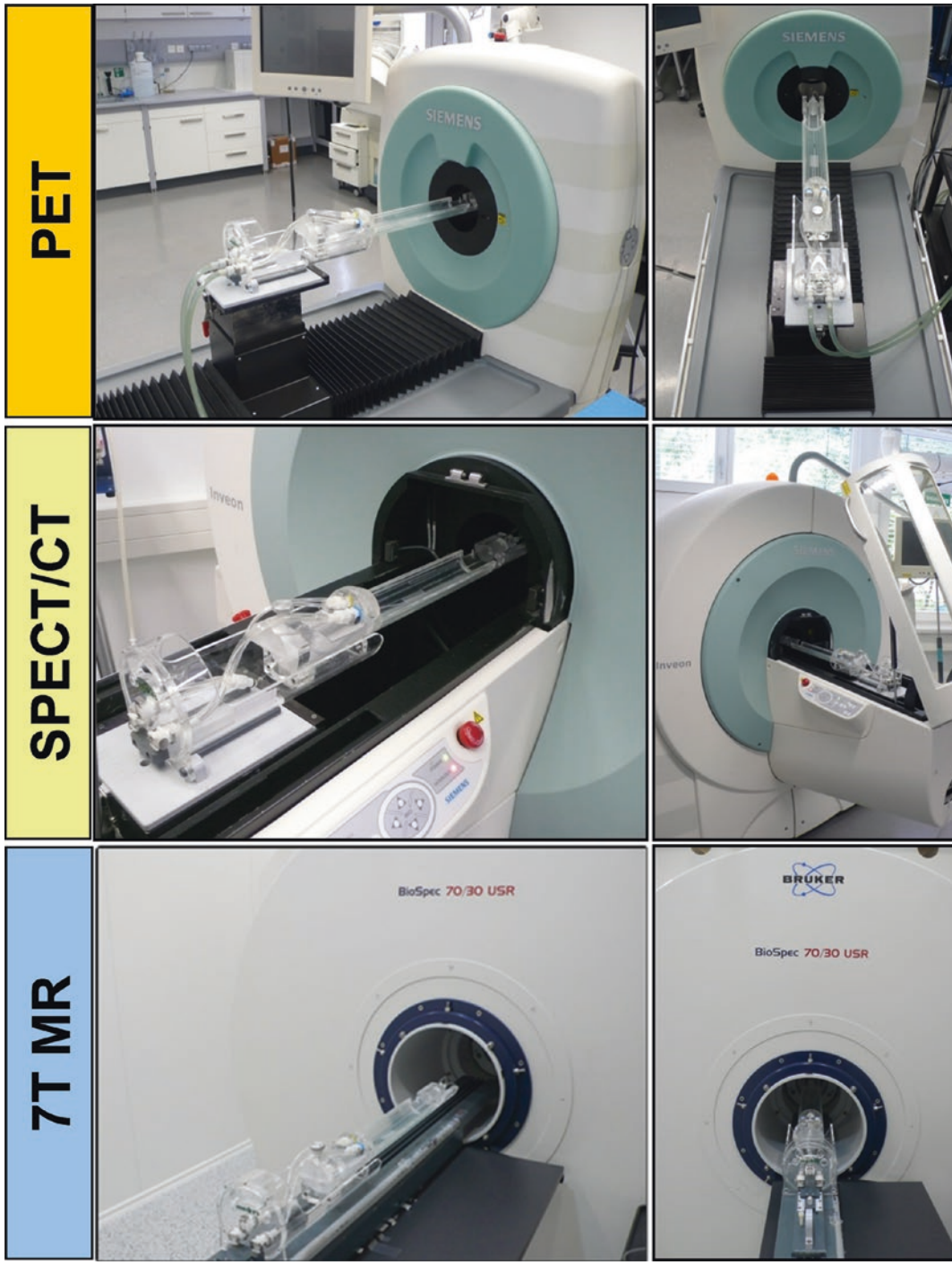

Fig. 17.3 Animal bed for multiparametric imaging. The dedicated animal bed can be easily installed at different scanner types such as PET (*first row*), SPECT/CT (*second row*), or MR scanners (*third row*). Thus, animals can be transferred from one scanner to another without changing its position on the animal bed, avoiding motion and repositioning artifacts. This approach allows also co-registration of images obtained by different modalities

respective modality. Finally, just the bed with the animal is moved between modalities, allowing a fast and easy transfer, also by means of standardized connectors for animal warming, temperature monitoring, and anesthesia agents. Here, it is important to emphasize on the role of body temperature stabilization to maintain a stable physiological condition of the animal during multimodal imaging. Changes in physiology can have significant impact on many parameters one wants to observe. A study by Winslow et al. showed that a slight increase in body temperature of the head and neck tumor in a xenograft-bearing mouse already lead to significant changes in tumor interstitial fluid pressure, perfused tumor blood vessels, and hypoxia status (Winslow et al. 2015). Such changes in body temperature should be avoided, since it can influence the results obtained, e.g., in PET and MR functional measurements such as the apparent diffusion coefficient (ADC), which is temperature dependent (Hasegawa et al. 1994). The same also applies to the used anesthesia regime and air mixture, which should also remain constant for all multimodal scans, since changes can also in some cases influence imaging outcomes, especially if multimodal functional and metabolic information are acquired (Mahling et al. 2015).

Fiducial markers (visible, e.g., in Fig. 17.1) are objects that are visible in a multitude of modalities. If a fusion between PET and MR is desired, these objects should have both a good PET contrast and good MR contrast. This can be achieved by using small glass or plastic capillary tubes. Hematocrit tubes that are widely available in most clinical and scientific laboratories have proven to be suitable for the production of fiducial markers. These tubes (inner diameter ca. 0.1–0.5 mm, length ca. 20–80 mm) are filled via the capillary effect with a solution of saline and PET tracer and sealed on both ends with plasticine-like sealant. The fiducial markers are then attached to the animal bed; usually the markers are placed at the inside position of the bed close to the animal. Typically two or three fiducial markers are used for each animal bed; their position should be chosen in a way that the fiducials are visible in the final images but do not interfere with important structures in the image (tumor, brain, etc.). Also care should be taken in MR imaging that no artifacts (e.g., backfolding or wrap-around artifact) are caused by the placement of fiducial markers – these artifacts are usually minimized by placing the fiducial marker close to the animal. The accuracy of fiducial markers has been studied in humans and has been found to be more accurate (mean offset 2.7 mm) than using the laser positioning system of the gantry (mean offset 10.7 mm) (Samarin et al. 2015). Fiducial markers can be constructed for a combination of many modalities and have been proven to be useful also in combining CT with ultrasound (Ng et al. 2015) or mass spectrometric imaging with optical imaging (Chughtai et al. 2012).

17.3.2 PET/CT

The combination of PET with CT is certainly one of the most successful combinations in multimodal imaging. Since its introduction in the late 1990s and early 2000s (Beyer et al. 2000; Kinahan et al. 1998), PET/CT has been become one of the most popular methods of choice in clinical oncological imaging using [^{18}F]fluorodeoxyglucose ([^{18}F]FDG) (Poeppel et al. 2009) and other PET tracers (Treglia et al. 2014). Similarly, PET/CT has been widely applied in small animal oncological imaging (Del Vecchio et al. 2010) and in other fields such as arthritis (van der Geest et al. 2015) or cardiovascular research (Greco et al. 2013).

In PET/CT the two imaging devices are usually mounted within the same gantry and coaxially, so that the PET and CT images can be acquired in the same imaging session. Depending on the performed PET scan (static, dynamic) but also on the performance of the CT system and the used resolution, the image acquisition times in both modalities can be the same or differ by an order of magnitude. Usually, when dynamic PET imaging is performed, the PET acquisition times are longer compared to the CT image acquisition time. The CT component is usually also applied to acquire the data needed for PET attenuation

correction; therefore, a combined PET/CT system does not need PET attenuation sources (Kinahan et al. 2003). However, it should be noted that a CT-based PET attenuation correction can still pose problems in some instances, e.g., cardiac imaging (Nekolla and Martinez-Moller 2015). The hardware problems of combined PET/CT systems can be regarded as being solved so that in practice usually no substantial challenges are encountered. In most cases functional and metabolic information derived from PET imaging is merged with anatomical details derived from CT. However, also functional parameters such as perfusion can be studied using dedicated contrast media with small animal CT (Bai et al. 2013). New CT techniques such as the use of dual energy CT in combination with nanoparticles can even allow characterizing more functional parameters using CT (Ashton et al. 2014). Another advantage of combined PET/CT is that the CT-derived anatomical information can be used to improve PET image reconstruction (Tang and Rahmim 2015).

The costs of a combined PET/CT system for a small animal can be considered to be high, albeit not as high as for combined PET/MR systems. A downside of PET/CT is the limited soft tissue contrast of CT if no contrast agents are used.

17.3.3 PET/MR

Combined PET/MR devices have been already proposed in the 1990s (Shao et al. 1997); however, elaborated small animal systems (Catana et al. 2008; Judenhofer et al. 2008) as well as the human brain (Schlemmer et al. 2008) and clinical whole body systems (Drzezga et al. 2012) have first appeared after 2005. This, in contrast to PET/CT relative late start, can be attributed to numerous technological challenges encountered when trying to combine PET with MR. These can be summarized on the one hand as effects of the MR on the PET side, such as the influence of strong magnetic fields on PET detectors, especially the photomultiplier tubes, effects of MR gradient switching and RF pulses on PET electronics and signal processing, as well as spatial constraints to fit the PET inside the limited space available in an MR system. On the other hand, the PET can have effects on the MR: homogeneity of the main magnetic field, the RF field, and also the gradient field in the presence of PET electronics within the MR bore, RF noise introduced by the PET electronics, temperature stability, and eddy currents imposed in PET components to name just a few. Also other challenges such as to derive a PET attenuation map based on MR data are encountered. Despite these technological hurdles, most of these problems can be considered to be solved at least to such an extent that combined PET/MR systems can now be applied in preclinical and clinical research and diagnostics (Wehrl et al. 2014, 2015; Bailey et al. 2015).

In contrast to PET/CT, many preclinical PET/MR devices are designed in a way that PET and MR images are acquired at the same time (Wehrl et al. 2015). This allows on the one hand to save image acquisition time, since PET and MR data are acquired simultaneously, so even if one modality takes longer to acquire (e.g., a dynamic PET scan with 60 min in comparison to an anatomical MR scan of just 10 min), effectively time is saved. This allows a larger throughput and saves time under anesthesia for the animal, which can be crucial in the case of long-term studies in certain disease models. This time can also be used to acquire additional information such as functional MR data to supplement the anatomical details. In addition to time savings, a simultaneous acquisition can also be used for cross-calibration and multiparametric imaging studies to monitor *in vivo* processes on multiple stages, e.g., brain activation using the blood oxygen level-dependent (BOLD) effect in fMRI and at the same time changes in blood flow using PET (Wehrl et al. 2009). The soft tissue contrast of MR is in many cases superior to the soft tissue contrast offered by small animal CT (Fig. 17.1), which is another plus for the combination of PET/MR in the field of small animal research.

Small animal PET/MR has also some disadvantages. A first and very important point is the system cost. Combined PET/MR is probably one of the most expensive multimodal imaging solutions in use, especially if high field (>4.7 T) MR

systems are used. Also the site planning requirements of such a system are complicated, since it usually requires also a dedicated room for the MR and PET electronics. From a methodological point of view, simultaneous imaging is often limited by the fact that PET tracer have certain uptake characteristics, which often make a direct, truly simultaneous acquisition difficult. However, within these limitations physiological parameters, animal positioning, etc., can be regarded as being constant.

17.3.4 Combined PET and Optical Imaging System

A system combining the detection of high energy γ-rays and optical wavelength photons allows to image small animal models noninvasively and repeatedly for the presence of PET and optical signals *in vivo*. Such a system, named OPET, is developed at the UCLA Crump Institute for Molecular Imaging (Alexandrakis et al. 2005).

Due to a poor penetration depth of visible light photons (Jacques 2013), optical imaging techniques are mostly limited to surface applications. However, optical imaging has still tremendous impact for the imaging of cellular and biochemical processes (Contag et al. 2000). The basis of optical imaging is, besides of fluorescent molecules, mostly a bioluminescent enzymatic reaction of genetically engineered cells expressing luciferase. After application of the enzyme-specific substrate luciferin, photons ranging from 510 to 700 nm are emitted, resulting in an emitted spectrum peak at around 610 nm (Rice et al. 2001). Due to the limited number of emitted photons, which is caused by significant light attenuation from the surface of the animal, cooled charge-coupled devices (CCD) are used. Optical imaging systems have the disadvantage of reduced intrinsic spatial resolution, because unabsorbed optical wavelength photons are highly scattered in animal tissue.

In contrast, a detector for PET imaging of small animals is built by a scintillation crystal array, which converts the annihilation γ-rays, emitted by a radioactive tracer, to low-energy, visible light photons. These photons are further detected by a multichannel or position-sensitive photodetector (Marriott et al. 1994). Contrary to the photons emitted from the animal, in the case of bioluminescence (600–750 nm), the low-energy, visible light photons detected in PET correspond to wavelengths in the region of 350–550 nm.

To combine the detection of both optical and PET signals into a single detector, it must be sensitive for both wavelength ranges. Furthermore, the detector needs to have enough sensitivity to detect single photons emitted by the bioluminescence reaction but also have a high dynamic range to detect the huge amount of photons produced in γ-ray interactions in the scintillation crystal (Prout et al. 2004).

In addition a single imaging probe, which can be detected by both PET and optical imaging, can contribute to the ease and speed of validation approaches (Fig. 17.4a). A possible vector can be generated by labeling a substrate with two different signatures such as a radioactive nuclide for PET imaging and a bioluminescent molecule for optical imaging (Fig. 17.4b) (Ray et al. 2003).

17.3.5 Combined Optical/MR Optical/CT Imaging

One desired advantage of multimodal imaging is the combination of modalities in order to provide functional as well as structural information.

An example for multimodality imaging pursuing this aim is the combination of optical imaging with MRI. The striking advantage of MRI, which is a very dynamic imaging field with constant progression, is not only the excellent spatial resolution for anatomical purposes but also the ability to measure functional properties using fMRI and the application of diffusion or perfusion imaging. Combining the information provided by MRI with the unique functional information obtained by optical imaging, a combination of both modalities can result in outstanding insights into biological processes in small animal models.

The main obstacle to overcome is the integration of an optical light detection system into the

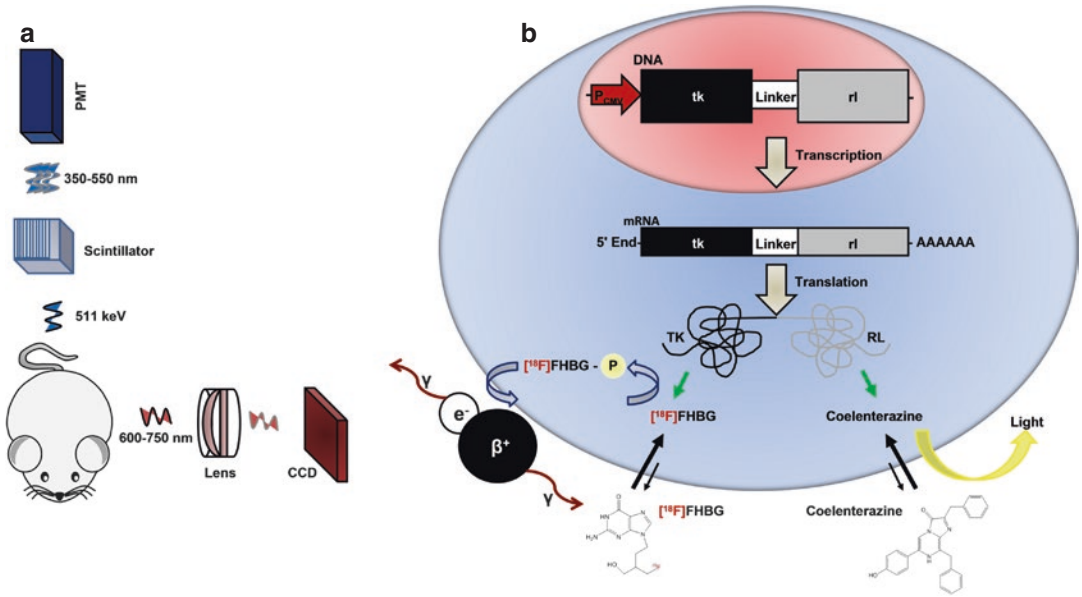

Fig. 17.4 Simultaneous optical/PET imaging. (**a**) Schematic of an optical/PET imaging system. To detect both PET and bioluminescence signals, a position-sensitive photon detector and optical coupling is required. PET images are usually acquired by segmented scintillators and photomultiplier tubes or avalanche photo diodes (APDs). In contrast, CCD cameras, using a lens for optical coupling are used for bioluminescence imaging (Figure inspired by Prout et al. (2004)). (**b**) Imaging probe for simultaneous optical/PET imaging (developed at Crump Institute for Molecular Imaging). Two reporter genes are simultaneously expressed in order to measure their expression with both modalities: PET as well as optical imaging. Therefore, tk, a PET reporter gene encoding for thymidine kinase, is fused with rl, an optical bioluminescence reporter gene encoding for Renilla luciferase. Both reporter genes are linked resulting in a 20-amino-acid linker to fuse both enzymes after transcription of the fusion vector and translation of the single mRNA. The resulting single polypeptide retains partial if not full activities of both enzymes fused. Reporter gene expression can then be imaged by trapping the PET reporter probe ^{18}F-labeled 9-[4-fluoro-3-(hydroxymethyl)butyl]guanine ([^{18}F]FHBG), phosphorylated by the thymidine kinase (PET), as well as by the light-producing enzymatic reaction of coelenterazine with Renilla luciferase (optical imaging) (Figure inspired by Ray et al. (2003))

MR scanner hardware without any interference with the high magnetic field of the MR system, as well as limited space capabilities inside the MR scanner. Silicon fiber bundles can be placed into the MR scanner and be integrated into the housing of the RF coil to measure optical light transmission simultaneously to the MR scan (Xu et al. 2005).

Besides emerging developments in multimodal imaging systems, there is also significant attention to develop multimodality imaging probes, especially for dual optical/MRI probes. An ideal multimodal imaging probe for dual optical/MRI should contain an optical component detectable by bioluminescence, fluorescence, or phosphorescence, as well as a component enhancing the MR signal comparable to a regular contrast agent. Therefore, organic dyes can be conjugated to iron oxide nanoparticles (Tombacz et al. 2015), or gadolinium chelates can be attached to quantum dots (Mulder et al. 2006) and fluorescently labeled polymers (Huber et al. 1998).

Similar to optical/MR the combination of *in vivo* optical and CT imaging is an advanced technique allowing the visualization of biochemical reactions obtained by optical imaging in an anatomical context provided by CT. Compared to dual-modality optical/MR systems, the integration of an optical system inside a CT is not as challenging. This is due to much more available space, since most CT scanners are constructed more openly compared to MR scanners and no

hardware interference with magnetic fields. Furthermore, CT equipment is often less costly compared to high-field MR systems.

A small animal system developed at Huazhong University combines a micro-CT unit with fluorescence diffuse optical tomography (fDOT) (Yang et al. 2010). Here, the dual-modality scanner is built using a microfocus X-ray tube and a near-infrared laser diode as sources. As sensors, a flat panel detector (FPD) and a cooled CCD camera are used. To ensure that fDOT and micro-CT scan the same field of view, a collimator and a concave lens, focusing the laser beam, are located on a linear stage (Yang et al. 2010).

17.3.6 SPECT with CT and MR

Single-photon emission computer tomography (SPECT) is a diagnostic method that is suitable for investigating, e.g., cancer, skeletal diseases, and especially for cardiac studies as well as neurologic and psychiatric diseases (Buck et al. 2008).

The first usable SPECT system was developed by David Edwards and Roy Kuhl in the 1960s (Kuhl and Edwards 1963). With SPECT it is possible to investigate biological processes *in vivo* by using radiolabeled molecules. Compared to clinical systems, SPECT scanners for small animal research are changed, considering the different body size between humans and small animals. Major changes become noticeable in regard to the smaller field of view (FOV) and higher spatial resolution or sensitivity. However, in general SPECT systems the spatial resolution of approximately 3 mm (Figueroa and et al. 2005) (in a single-pinhole system) is limited, which is why it is difficult to clarify morphological structures. Therefore, SPECT is mostly used in a combined version with CT (Fig. 17.3) based on the work pioneered by Hasegawa et al. (Hasegawa et al. 2002). Recently, SPECT is also used together with MRI (Goetz et al. 2008; Wagenaar et al. 2007). Likewise in SPECT/CT, MRI is also used to combine the functional information, based on SPECT, together with morphological information delivered by combined (Goetz et al. 2008; Schurrat et al. 2003; Booij et al. 2002) or simultaneously (Meier et al. 2011; Wagenaar et al. 2007) measured MR. Therefore, reconstructed images from SPECT and CT or MRI are realigned and co-registered to overlay the functional and morphological information in order to determine the location of biological processes. Furthermore, CT and MRI are also used to provide attenuation correction for SPECT images to allow an accurate quantification (Masood et al. 2005; Ruf et al. 2007; Dondi et al. 2004; Hwang and Hasegawa 2005).

The hybrid systems can be realized in two ways, either based on a combination of SPECT and CT or MRI (Hasegawa et al. 2002; Goetz et al. 2008; Schurrat et al. 2003; Booij et al. 2002) or by using a SPECT insert (Wagenaar et al. 2007). The former techniques use a sequential image acquisition procedure. Hence, first SPECT is recorded, followed by CT or MRI measurements. By using a SPECT insert inside a CT or MR system, images can be recorded simultaneously. Like simultaneous PET/MR systems, a SPECT insert system benefits from the co-registration between SPECT and CT or MR images and reduces the total measurement time. In contrast to a combined version, animals do not change their position, and all functional and morphological images are measured under the same physiological condition. In a sequential measurement, the location and positioning of the animal in the SPECT and CT or MR scanner can be slightly different. To co-register data from SPECT with CT or MR, landmarks or fiducial markers are used, which can be seen in SPECT images as well as in CT or MRI images. However, to co-register these images it is important that images have similar resolutions (Goetz et al. 2008).

17.3.6.1 SPECT/CT Versus SPECT/MRI

One reason to use SPECT in combination with MRI instead of CT is the fact that MRI causes no additional radiation exposure compared to CT. Furthermore, high-field MRI delivers often a better image contrast in brain measurements, and techniques such as the BOLD fMRI can be used (Marzola et al. 2003; Wagenaar et al. 2006). Therefore, in contrast to CT, MRI delivers often a multitude of additional information beyond morphology.

17.3.6.2 SPECT/CT Versus PET/ CT

SPECT/CT and PET/CT are used to perform three-dimensional tomographic imaging. In both hybrid systems, CT delivers morphological information and provides the attenuation correction needed for SPECT or PET quantification, respectively. SPECT and PET use radiolabeled tracers to detect biological processes. The choice for the right tracer depends on the biological process of interest (e.g., receptors in neurology or cell metabolism in oncology). One fundamental difference between SPECT/CT and PET/CT can be seen in the detection sensitivity (Franc et al. 2008). Since PET detectors receive more radiation than SPECT using single-pinhole collimators, PET has usually a higher sensitivity compared to SPECT. Therefore, SPECT/CT is often more suited for static than for dynamic measurements. In order to increase the detection sensitivity in SPECT, there are systems which consist of multiple-pinhole collimators (Franc et al. 2008).

17.3.6.3 Simultaneous EEG/fMRI

The electroencephalogram (EEG) is a powerful tool to investigate the temporal component of neuronal connectivity. Recently, in human studies, EEG has been combined with other modalities (e.g., PET, MR), which deliver additional morphological and functional information to increase the informational content within one measurement (Larson et al. 1998; Shah et al. 2013; Schreckenberger et al. 2004).

Simultaneous EEG/fMRI measurements enable the recording of electrical potential fluctuations combined with hemodynamic information (e.g., BOLD) delivered by fMRI. Particular in the investigation of epilepsy, animal studies are important for a better understanding of the ongoing processes during epileptic seizures. One of the first reported animal studies using simultaneous EEG/fMRI was done in 1995 by Busch et al. (1995). Interestingly, the first simultaneous EEG/fMRI system was established in human studies (Ives et al. 1993). This is founded on several facts. First, the human brain is much bigger than a small animal brain, e.g., rat brain. Therefore, the number of EEG channels can be much higher. In human studies, for instance, 256 channels can be placed; however, in small animals the scalp surface is extremely limited so only a few electrodes can be fixed. Second, it is easier to tell human subjects not to move during the whole measurement, because movement artifacts induce noisy EEG and fMRI data. However, animals must be anesthetized or at least motion restricted. Studies revealed that anesthesia has an influence on brain activity. For instance, it is well known that isoflurane, a common anasthetic in small animal research, changes the BOLD signal (Aksenov et al. 2015). Other than the already described combined systems, the EEG in combination with fMRI is only used to investigate processes in the brain. Considering both modalities separately, MRI has a high spatial resolution but a low temporal (about 1 s for standard BOLD imaging) resolution, whereas the EEG allows to follow up neuronal activity in a range of milliseconds (ms). Therefore, simultaneous EEG/fMRI combines the power of high spatial and fast temporal resolutions that deliver increased information, which is important to investigate and to understand neuronal diseases. The lower temporal resolution of fMRI can be explained by both the physiology of hemodynamic processes and limitations in imaging hardware and the detection sensitivity of the MR system itself. However, noninvasive EEG does not detect deep neuronal activation, which also results in a limited spatial resolution (Gloor 1985; Mirsattari et al. 2007).

In simultaneous EEG/fMRI invasive and noninvasive EEG can be used. The noninvasive EEG measures potential fluctuations of electrical fields at the scalp. These fluctuations arise due to different neuronal activations in different brain areas. Electrodes, which are fixed at the scalp, are used to measure these fluctuations that are caused by neuronal oscillation patterns in the brain. The noninvasively recorded EEG signal is influenced by physical and physiological conditions (Kempf 2009). Due to the resistance of the cranium, thousands of neurons have to fire simultaneously to deliver an EEG signal (Light et al. 2010). Therefore, neurons (especially pyramidal neurons) have to operate in parallel. This parallel operation results in a summation of the extracellular current, which generates the field potential on the scalp. Extracellular currents develop from the membrane

potential of every single neuron. These membrane potentials can be excitatory postsynaptic (EPSP) or inhibitory postsynaptic potentials (IPSP) (Coombs et al. 1955). The summation of membrane potentials is responsible for the spreading currents in the extracellular space that lead to measurable circulating currents at the scalp. Considering the different direction of neurons in gyri (vertical) and sulci (horizontal), the regional orientation of field potentials in sulci and gyri depends on their tangential and radial orientation (Srinivasan et al. 2006).

With focus on small animal research, it is challenging to integrate an EEG system into an MRI system. However, since the last 10 years, simultaneous EEG/fMRI has emerged as a helpful instrument to investigate neuronal diseases. The main challenge that needs to be solved in EEG/fMRI is that the instruments influence each other (Ives et al. 1993; Krakow et al. 2000). The EEG signal is very susceptible to the voltage induced by the MR gradient coils and the MR radio-frequency (RF) pulses. On the other side, the MRI signal can be influenced by the magnetic parts of EEG instrumentation, e.g., cable or metallic components in amplifiers (Krakow et al. 2000). Therefore, by using nonmagnetic components and putting the EEG amplifier as far as possible from the MR magnet, the mutual interference is reduced. Replacing conductive shielded cables with fiber-optic cables can further reduce interference (Ives et al. 1993). In small animals EEG, the electrodes are very closely spaced, and the used magnetic field and gradient field strengths are often higher compared to human studies; therefore, it is possible that EEG artifacts are enhanced.

An efficient simultaneous EEG/fMRI system consists of an MRI system combined with an adapted EEG system (Fig. 17.5). In order to

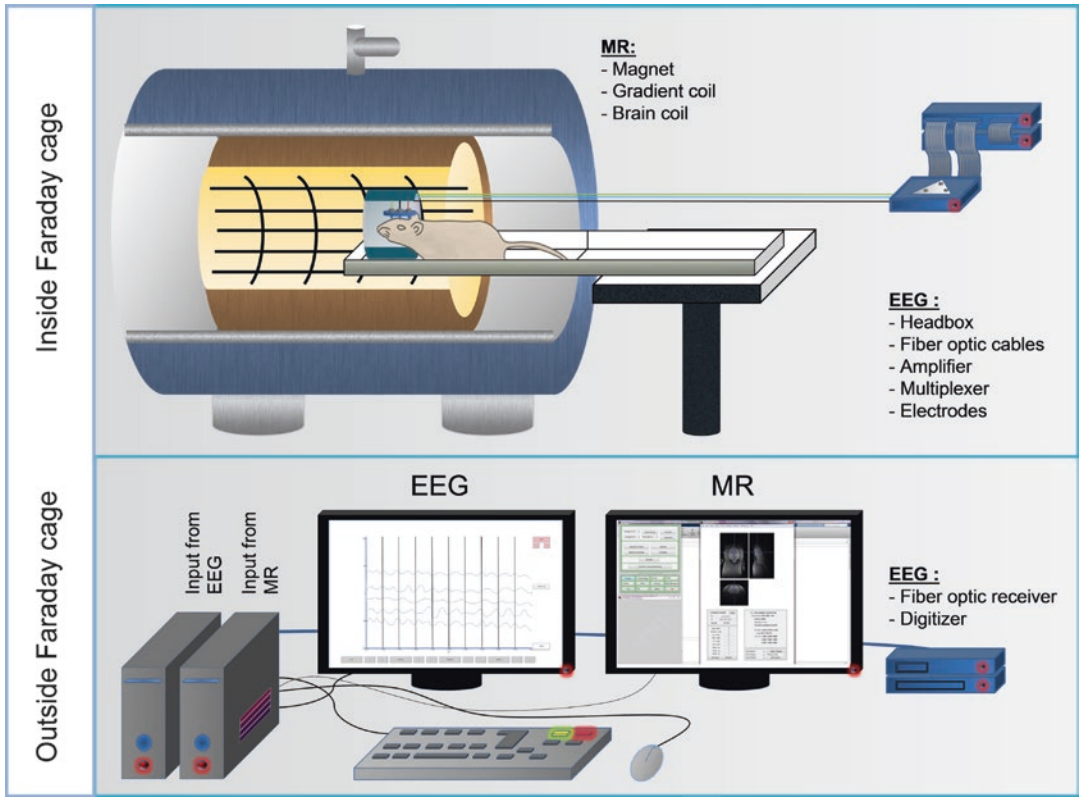

Fig. 17.5 Schematic illustration of a simultaneous EEG/MR system. The recorded EEG signal from the EEG electrodes in the magnet is sent to further EEG devices. The EEG is amplified by a factor 1000–100,000. Via fiber-optic cables, the amplified signal is transported to the fiber-optic receiver that is located outside the faraday cage. The receiver translates the optical signal into electrical and gets afterward digitized. After these hardware pathways, the data can be further analyzed. Simultaneously to the EEG acquisition, MR data is collected

investigate brain processes in small animals, e.g., in rats, the space between the head of the rat and the RF coil needs to be large enough in order to integrate the EEG electrodes. This EEG electrode system has also to be thin, because the larger the distance between head and RF coil, the smaller the received fMRI signal. The material of the electrodes depends on the EEG system, which means whether using invasive (intracranial) or noninvasive (scalp surface fixation) EEG electrodes. Invasive electrodes are made of nontoxic and nonmagnetic material like platinum or gold. However, in many animal studies, carbon is the material of choice for invasive and noninvasive EEG electrodes. For a general overview about simultaneous EEG/fMRI experiments in animals, see Mirsattari et al. (2007).

With intracranial electrodes a specific activity in areas of interest inside the brain will result in a meaningful EEG signal. However, the intracranial electrodes can damage the brain. In addition, the change of physiology state, caused by anesthesia or brain damage via electrodes, can have an effect in the BOLD-fMRI signal (Tenney et al. 2003; Austin et al. 2005).

The electrode signal in EEG gets amplified (with a factor 1000–100,000) and multiplexed and is transferred via fiber-optic cables to a fiber-optic receiver. The fiber-optic receiver translates the optical signals back into electrical signals. Afterwards, this analog electrical signal must be digitalized in order to analyze the data. Furthermore, the EEG signal gets filtered with a high- and low-pass filter. In order to reduce artifacts in the EEG signal, reference electrodes are used. The signal, recorded via surface electrodes, from the reference signal – common artifacts present on both the surface and reference electrode are therefore canceled.

17.4 Image Fusion Software

Multimodal imaging is ultimately performed to provide a multitude of functional, metabolic, and anatomical data from the same object. These images are often best interpreted when imaging data of the various modalities is fused together, so that the respective information can be superimposed. There are basically two ways of image fusion: One is a hardware-based approach, so that the respective offset values between imaging modalities are known, and images can be combined based on these known offsets, e.g., by including these offsets in the image header information so that it can be read directly by the respective image analysis and display program. Another way is a software-based fusion, e.g., the offsets of the images are not per se known, and images need to be manually or automatically transformed to match each other.

The manual or automatic software co-registration steps can be either rigid or nonrigid. In rigid transformations the source image (the image that is shifted) is only rotated and shifted relative to the target image (the image that remains static) (Hill et al. 2001). If nonrigid co-registration steps are involved and also local deformations, the so-called warping, are applied, the shape of the source image may therefore be altered. Warping is also applied if between-subject comparisons are made (Mazziotta et al. 1991). Even more challenging than a 3D image registration is a registration in time, e.g., 4D. This can be interesting when comparing complementary physiological information in domains such as cardiac imaging. Here, dedicated methods such as dynamic time warping are employed to compare dynamic PET and MR images (Betancur et al. 2015).

Image co-registration can be based on anatomical or artificial landmarks in the image. Anatomical structures include, e.g., the brain, bones, and certain organs, whereas artificial landmarks are often composed by fiducial markers (Fig. 17.6) visible in both modalities. Registration approaches using these landmarks are called feature based. Moreover, it is also possible to base the image co-registration on voxel intensity values, an approach utilized in automatic registration programs (Zaidi 2015).

There exists a plethora of image fusion programs. Some are offered by commercial vendors, and others are based on freeware or shareware developments. Most of the available software can be easily found by utilizing common Internet search engines using keywords such as PET, MR, image fusion, software, etc. Often, the software is mainly developed for

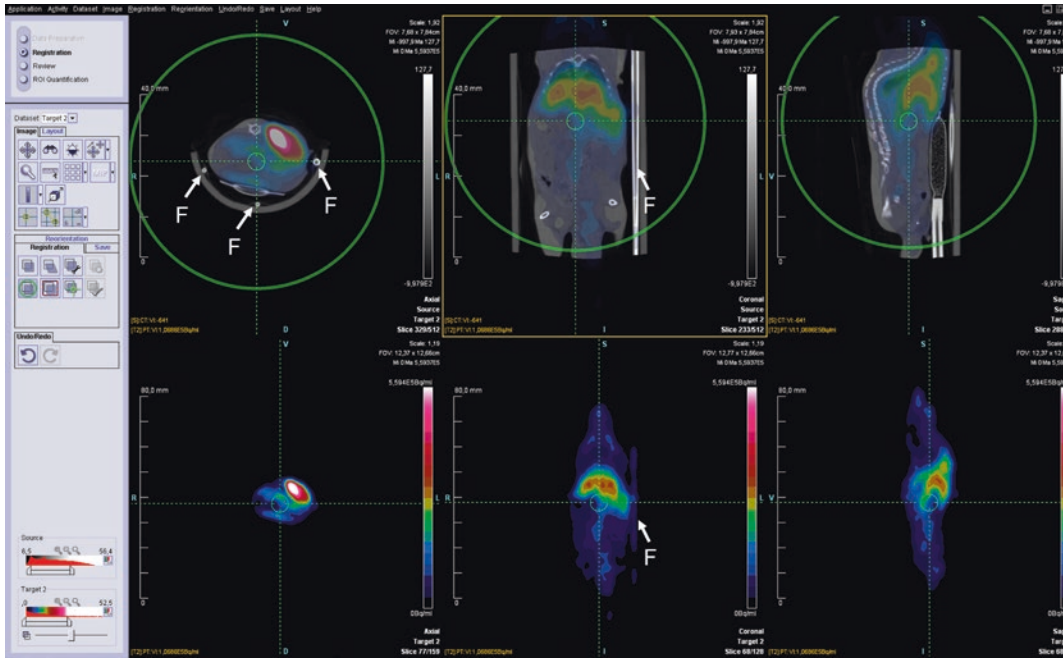

Fig. 17.6 A typical example of image fusion software. Fusion of CT (*upper part*) and PET (*lower part*) data obtained in a mouse. Fiducial markers (F), visible in both modalities, assist in the co-registration of both images. Datasets are viewed from three orientations, which allow an adequate manual co-registration workflow. Tools for image manipulation (e.g., control of the windowing parameters, zoom, rotation) can be found on the left side of the window

Table 17.1 List of selected software for small animal image fusion

Software name	Remarks	Website
Inveon Research Workplace	Commercial, multimodal, small animal, possibility for kinetic modeling, etc.	http://www.healthcare.siemens.com/molecular-imaging/preclinical-imaging/inveon-workplace/inveon-research-workplace
PMOD	Commercial, multimodal, small animal and human data, possibility for kinetic modeling, etc.	http://www.pmod.com
AFNI	Noncommercial, focus on fMRI and statistical mapping	http://afni.nimh.nih.gov/afni/
AMIDE	Noncommercial, image viewing and fusion	http://sourceforge.net/projects/amide/
FSL	Noncommercial, focus on fMRI and statistical mapping, main focus on functional calculations, focus on human data, image fusion possible	http://fsl.fmrib.ox.ac.uk
ImageJ	Noncommercial, image viewing, plugins for fusion	http://imagej.nih.gov/ij/
Mango	Noncommercial, image viewing and fusion	https://www.nitrc.org/projects/mango/

Table 17.1 (continued)

Software name	Remarks	Website
MRIcron	Noncommercial, image viewing and fusion, focus on MR images	www.mccauslandcenter.sc.edu/mricro/mricron/
OsiriX	Noncommercial and commercial versions available, image fusion	http://www.osirix-viewer.com/
SPM	Noncommercial, statistical parametric mapping, main focus on functional mapping and statistical calculations, focus on human data, image fusion possible	http://www.fil.ion.ucl.ac.uk/spm/
VINCI	Noncommercial, focus on multimodal image fusion	http://www.nf.mpg.de/vinci3/

Besides the mentioned programs, many more are available; therefore, this list should be considered as a starting point for further research by the reader

applications in humans; however, with most packages it is also relatively straightforward to process small animal imaging data. Table 17.1 represents an incomplete list of commonly used software and their web addresses. Some of these packages are also able to perform higher order image analysis such as statistical parametric mapping or kinetic data modeling. Ultimately, the user has to decide which software package fits the specific application best.

References

Aksenov DP, et al. Effects of anesthesia on BOLD signal and neuronal activity in the somatosensory cortex. J Cereb Blood Flow Metab. 2015;35(11):1819–26.

Alexandrakis G, Rannou FR, Chatziioannou AF. Tomographic bioluminescence imaging by use of a combined optical-PET (OPET) system: a computer simulation feasibility study. Phys Med Biol. 2005;50(17):4225–41.

Ashton JR, et al. Dual-energy micro-CT functional imaging of primary lung cancer in mice using gold and iodine nanoparticle contrast agents: a validation study. PLoS One. 2014;9(2):e88129.

Austin VC, et al. Confounding effects of anesthesia on functional activation in rodent brain: a study of halothane and alpha-chloralose anesthesia. Neuroimage. 2005;24(1):92–100.

Bai RJ, et al. Investigation on the optical scan condition for imaging of multi-slice spiral CT liver perfusion in rats. Chin Med J (Engl). 2013;126(24):4742–6.

Bailey DL, et al. Combined PET/MR: the real work has just started. Summary Report of the Third International Workshop on PET/MR Imaging; February 17–21, 2014, Tubingen, Germany. Mol Imaging Biol. 2015;17(3):297–312.

Betancur J, et al. Synchronization and registration of cine magnetic resonance and dynamic computed tomography images of the heart. IEEE J Biomed Health Inform. 2015.

Beyer T, et al. A combined PET/CT scanner for clinical oncology. J Nucl Med. 2000;41(8):1369–79.

Booij J, et al. Imaging of dopamine transporters in rats using high-resolution pinhole single-photon emission tomography. Eur J Nucl Med Mol Imaging. 2002;29(9):1221–4.

Buck AK, et al. SPECT/CT. J Nucl Med. 2008;49(8):1305–19.

Busch E, et al. Simultaneous recording of eeg, dc potential and diffusion-weighted nmr imaging during potassium induced cortical spreading depression in rats. NMR Biomed. 1995;8(2):59–64.

Catana C, et al. Simultaneous in vivo positron emission tomography and magnetic resonance imaging. Proc Natl Acad Sci U S A. 2008;105(10):3705–10.

Catana C, et al. MRI-assisted PET motion correction for neurologic studies in an integrated MR-PET scanner. J Nucl Med. 2011;52(1):154–61.

Chughtai K, et al. Fiducial markers for combined 3-dimensional mass spectrometric and optical tissue imaging. Anal Chem. 2012;84(4):1817–23.

Contag CH, et al. Use of reporter genes for optical measurements of neoplastic disease in vivo. Neoplasia. 2000;2(1–2):41–52.

Coombs J, Eccles JC, Fatt P. The specific ionic conductances and the ionic movements across the motoneuronal membrane that produce the inhibitory post-synaptic potential. J Physiol. 1955;130(2):326–73.

Del Vecchio S, et al. PET/CT in cancer research: from preclinical to clinical applications. Contrast Media Mol Imaging. 2010;5(4):190–200.
Dondi M, et al. Myocardial SPECT: what do we gain from attenuation correction (and when)? Q J Nucl Med Mol Imaging. 2004;48(3):181.
Drzezga A, et al. First clinical experience with integrated whole-body PET/MR: comparison to PET/CT in patients with oncologic diagnoses. J Nucl Med. 2012;53(6):845–55.
Figueroa, SD, et al. Performance characteristics of an integrated small animal SPECT/CT unit. in Nuclear Science Symposium Conference Record, 2005 IEEE. 2005. IEEE.
Franc BL, et al. Small-animal SPECT and SPECT/CT: important tools for preclinical investigation. J Nucl Med. 2008;49(10):1651–63.
Furst S, et al. Motion correction strategies for integrated PET/MR. J Nucl Med. 2015;56(2):261–9.
Gloor P. Neuronal generators and the problem of localization in electroencephalography: application of volume conductor theory to electroencephalography. J Clin Neurophysiol. 1985;2(4):327–54.
Goetz C, et al. SPECT low-field MRI system for small-animal imaging. J Nucl Med. 2008;49(1):88–93.
Greco A, et al. High-resolution positron emission tomography/computed tomography imaging of the mouse heart. Exp Physiol. 2013;98(3):645–51.
Hasegawa Y, et al. Temperature dependent change of apparent diffusion coefficient of water in normal and ischemic brain of rats. J Cereb Blood Flow Metab. 1994;14(3):383–90.
Hasegawa BH, et al. Dual-modality imaging of cancer with SPECT/CT. Technol Cancer Res Treat. 2002;1(6):449–58.
Hill DL, et al. Medical image registration. Phys Med Biol. 2001;46(3):R1–45.
Huber MM, et al. Fluorescently detectable magnetic resonance imaging agents. Bioconjug Chem. 1998;9(2):242–9.
Hwang AB, Hasegawa BH. Attenuation correction for small animal SPECT imaging using x-ray CT data. Med Phys. 2005;32(9):2799–804.
Ives JR, et al. Monitoring the patient's EEG during echo planar MRI. Electroencephalogr Clin Neurophysiol. 1993;87(6):417–20.
Jacques SL. Optical properties of biological tissues: a review. Phys Med Biol. 2013;58(11):R37–61.
Judenhofer MS, et al. Simultaneous PET-MRI: a new approach for functional and morphological imaging. Nat Med. 2008;14(4):459–65.
Kempf W. Forschungsmethoden der Psychologie: zwischen naturwissenschaftlichem Experiment und sozialwissenschaftlicher Hermeneutik. Band I: Theorie und Empirie. Berlin: Regener; 2009.
Kinahan PE, et al. Attenuation correction for a combined 3D PET/CT scanner. Med Phys. 1998;25(10):2046–53.
Kinahan PE, Hasegawa BH, Beyer T. X-ray-based attenuation correction for positron emission tomography/computed tomography scanners. Semin Nucl Med. 2003;33(3):166–79.
Krakow K, et al. EEG recording during fMRI experiments: image quality. Hum Brain Mapp. 2000;10(1):10–5.
Kuhl DE, Edwards RQ. Image separation radioisotope scanning 1. Radiology. 1963;80(4):653–62.
Larson CL, et al. Relations between PET-derived measures of thalamic glucose metabolism and EEG alpha power. Psychophysiology. 1998;35(2):162–9.
Lawrence J, Rohren E, Provenzale J. PET/CT today and tomorrow in veterinary cancer diagnosis and monitoring: fundamentals, early results and future perspectives. Vet Comp Oncol. 2010;8(3):163–87.
Light GA, et al. Electroencephalography (EEG) and event-related potentials (ERPs) with human participants. Curr Protoc Neurosci. 2010;6(25):1–24. doi: 10.1002/0471142301.ns0625s52.
Mahling M, et al. A comparative pO2 probe and [18F]-Fluoro-Azomycinarabino-Furanoside ([18F]FAZA) PET study reveals anesthesia-induced impairment of oxygenation and perfusion in tumor and muscle. PLoS One. 2015;10(4):e0124665.
Marriott CJ, et al. High-resolution PET imaging and quantitation of pharmaceutical biodistributions in a small animal using avalanche photodiode detectors. J Nucl Med. 1994;35(8):1390–6.
Marzola P, Osculati F, Sbarbati A. High field MRI in preclinical research. Eur J Radiol. 2003;48(2):165–70.
Masood Y, et al. Clinical validation of SPECT attenuation correction using x-ray computed tomography–derived attenuation maps: multicenter clinical trial with angiographic correlation. J Nucl Cardiol. 2005;12(6):676–86.
Mazziotta JC, et al. Relating structure to function in vivo with tomographic imaging. Ciba Found Symp. 1991;163:93–101; discussion 101–12.
Meier D, et al. A SPECT camera for combined MRI and SPECT for small animals. Nucl Instrum Methods Phys Res A. 2011;652(1):731–4.
Mirsattari SM, et al. EEG monitoring during functional MRI in animal models. Epilepsia. 2007;48(s4):37–46.
Mulder WJ, et al. Quantum dots with a paramagnetic coating as a bimodal molecular imaging probe. Nano Lett. 2006;6(1):1–6.
Nekolla SG, Martinez-Moller A. Attenuation correction in cardiac PET: to raise awareness for a problem which is as old as PET/CT. J Nucl Cardiol. 2015;22(6):1296–9.
Ng SK, et al. SU-E-J-42: Evaluation of Fiducial Markers for Ultrasound and X-Ray Images used for motion tracking in Pancreas SBRT. Med Phys. 2015;42(6):3273.
Poeppel TD, et al. PET/CT for the staging and follow-up of patients with malignancies. Eur J Radiol. 2009;70(3):382–92.
Prout DL, Silverman RW, Chatziioannou A. Detector concept for OPET-a combined PET and optical imaging system. IEEE Trans Nucl Sci. 2004;51(3):752–6.
Ray P, Wu AM, Gambhir SS. Optical bioluminescence and positron emission tomography imaging of a novel

fusion reporter gene in tumor xenografts of living mice. Cancer Res. 2003;63(6):1160–5.
Rice BW, Cable MD, Nelson MB. In vivo imaging of light-emitting probes. J Biomed Opt. 2001;6(4):432–40.
Ruf J, et al. Impact of image fusion and attenuation correction by SPECT-CT on the scintigraphic detection of parathyroid adenomas. Nuklearmedizin. 2007;46(1): 15–21.
Samarin A, et al. Image registration accuracy of an in-house developed patient transport system for PET/CT+MR and SPECT+CT imaging. Nucl Med Commun. 2015;36(2):194–200.
Schlemmer HP, et al. Simultaneous MR/PET imaging of the human brain: feasibility study. Radiology. 2008;248(3):1028–35.
Schreckenberger M, et al. The thalamus as the generator and modulator of EEG alpha rhythm: a combined PET/EEG study with lorazepam challenge in humans. Neuroimage. 2004;22(2):637–44.
Schurrat T, et al. Molecular gastrin receptor localisation in mice using high-resolution SPET-MRI image fusion. Eur J Nucl Med Mol Imaging. 2003;30(5):800.
Shah NJ, et al. Advances in multimodal neuroimaging: hybrid MR–PET and MR–PET–EEG at 3T and 9.4 T. J Magn Reson. 2013;229:101–15.
Shao Y, et al. Simultaneous PET and MR imaging. Phys Med Biol. 1997;42(10):1965–70.
Srinivasan R, Winter WR, Nunez PL. Source analysis of EEG oscillations using high-resolution EEG and MEG. Prog Brain Res. 2006;159:29–42.
Tang J, Rahmim A. Anatomy assisted PET image reconstruction incorporating multi-resolution joint entropy. Phys Med Biol. 2015;60(1):31–48.
Tenney JR, et al. Corticothalamic modulation during absence seizures in rats: a functional MRI assessment. Epilepsia. 2003;44(9):1133–40.
Tombacz E, et al. Magnetic iron oxide nanoparticles: recent trends in design and synthesis of magnetoresponsive nanosystems. Biochem Biophys Res Commun. 2015;468(3):442–53.
Treglia G, et al. Diagnostic performance of PET/CT with tracers other than F-18-FDG in oncology: an evidence-based review. Clin Transl Oncol. 2014;16(9):770–5.
van der Geest T, et al. [(18)]F FDG PET/CT imaging to monitor the therapeutic effect of liposome-encapsulated prednisolone in experimental rheumatoid arthritis. J Control Release. 2015;209:20–6.
Wagenaar DJ, et al. Rationale for the combination of nuclear medicine with magnetic resonance for pre-clinical imaging. Technol Cancer Res Treat. 2006;5(4):343–50.
Wagenaar D, et al. A multi-ring small animal CZT system for simultaneous SPECT/MRI imaging. in Society of Nuclear Medicine Annual Meeting Abstracts. 2007. Soc Nuclear Med.
Wehrl HF, et al. Pre-clinical PET/MR: technological advances and new perspectives in biomedical research. Eur J Nucl Med Mol Imaging. 2009;36 Suppl 1:S56–68.
Wehrl HF, et al. Assessment of MR compatibility of a PET insert developed for simultaneous multiparametric PET/MR imaging on an animal system operating at 7 T. Magn Reson Med. 2011;65(1):269–79.
Wehrl HF, et al. Simultaneous PET-MRI reveals brain function in activated and resting state on metabolic, hemodynamic and multiple temporal scales. Nat Med. 2013;19(9):1184–9.
Wehrl HF, et al. Preclinical and translational PET/MR imaging. J Nucl Med. 2014;55(Supplement 2):11S–8.
Wehrl HF, et al. Combined PET/MR: a technology becomes mature. J Nucl Med. 2015;56(2):165–8.
Weissler B, et al. A digital preclinical PET/MRI insert and initial results. IEEE Trans Med Imaging. 2015;34(11): 2258–70.
Winslow TB, et al. A pilot study of the effects of mild systemic heating on human head and neck tumour xenografts: analysis of tumour perfusion, interstitial fluid pressure, hypoxia and efficacy of radiation therapy. Int J Hyperthermia. 2015;31(6):1–9.
Wurslin C, et al. Respiratory motion correction in oncologic PET using T1-weighted MR imaging on a simultaneous whole-body PET/MR system. J Nucl Med. 2013;54(3):464–71.
Xu H, et al. Magnetic-resonance-imaging-coupled broadband near-infrared tomography system for small animal brain studies. Appl Opt. 2005;44(11):2177–88.
Yang X, et al. Combined system of fluorescence diffuse optical tomography and microcomputed tomography for small animal imaging. Rev Sci Instrum. 2010;81(5): 054304.
Yoon HS, et al. Initial results of simultaneous PET/MRI experiments with an MRI-compatible silicon photomultiplier PET scanner. J Nucl Med. 2012;53(4):608–14.
Zaidi H. Molecular imaging of small animals. New York: Springer; 2015.

Part IV

Ex Vivo Validation Methods

18 In Vitro Methods for In Vivo Quantitation of PET and SPECT Imaging Probes: Autoradiography and Gamma Counting

David Stout and Cinthia Pastuskovas

Contents

D. Stout (✉)
UCLA School of Medicine,
4297 Motor Ave, Culver City, CA 90232, USA
e-mail: davidstoutphd@gmail.com

C. Pastuskovas
Pharmacokinetic and Pharmacodymic Sciences,
Genentech, Inc., South San Francisco, CA, USA
e-mail: pastuskovas.cinthia@gene.com

18.1 Introduction

The development of noninvasive imaging methods such as positron emission tomography (PET) and single-photon emission computed tomography (SPECT) has opened up tremendous opportunities to investigate biological function in vivo. These methods applied to small animals enable the whole body to be imaged over time, so the biodistribution of labeled probes can be followed within the same animal for hours or days (Phelps 2004; Rudin and Weissleder 2003). This is in sharp contrast to previous biodistribution methodology, where many animals had to be injected and groups sacrificed at various time points to see where the probe localized. The ability to observe changes within the same animal over time drastically reduces the number of animals and complexity of the experiment, while at the same time providing better temporal sampling and the ability to track individual metabolic function.

One drawback of in vivo small animal PET and SPECT systems is the limited spatial resolution. When various factors such as blurring due to respiratory and cardiac motion, positron range, and image reconstruction methods are considered, most in vivo imaging systems have a resolution in the 1–2 mm range. Higher resolution is possible, but may be prohibitively expensive in terms of costs, time, radiation dose, and image noise (Cherry and Gambhir 2001). While this resolution is excellent for many purposes, it is not sufficient to discriminate exactly where the signal

F. Kiessling et al. (eds.), *Small Animal Imaging*, DOI 10.1007/978-3-319-42202-2_18

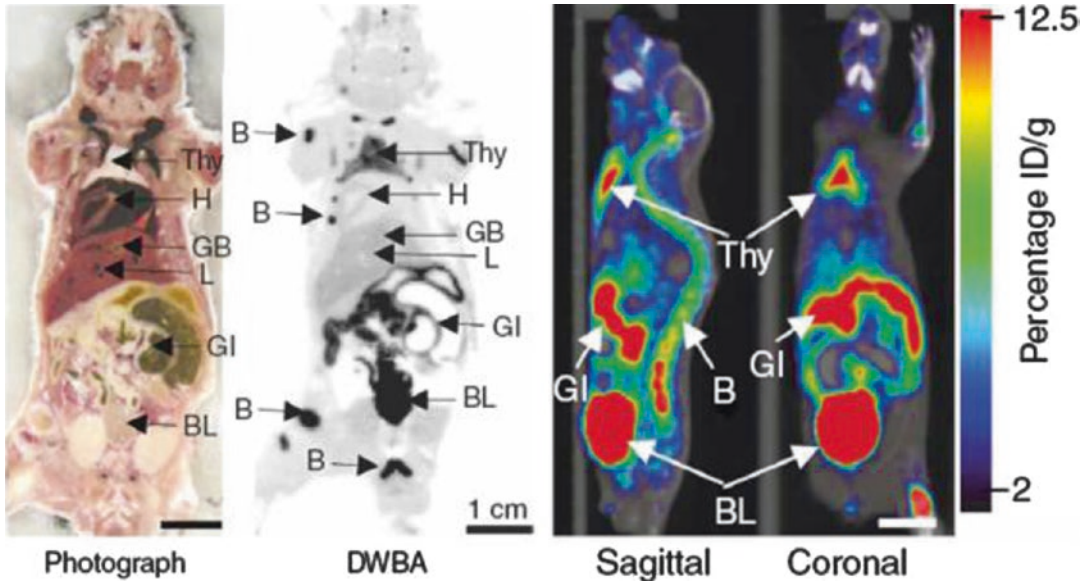

Fig. 18.1 Cryosection photograph, autoradiography, and PET image of a F-18 imaging probe used in a mouse

originated. Precise localization is particularly important in the development of new imaging probes, where the uptake, clearance, and metabolism must be understood in order to know exactly what information the images are providing. A good example of this is in Fig. 18.1, where the PET signal shows uptake in the bowel (Radu et al. 2008). Only with the use of higher-resolution autoradiography (AR) could we see that the uptake was in the intestinal wall, rather than the bowel contents. This is important, since it means the probe was delivered by the bloodstream, not through hepatobiliary excretion through the liver and bile duct.

The radiolabeling of compounds to assess tissue distribution is a common practice in research and drug development. The fate of radiolabeled probes can be determined by directly counting the radioactivity in dissected tissues using a gamma or liquid scintillation counting, for gamma- or beta-related isotopes, respectively. This methodology is known as "tissue dissection" or "cut and count." For SPECT and PET probe biodistributions, the two most common methods used are gamma counting of tissues and autoradiography. Gamma counting is relatively simple, with individual samples placed in tubes to measure radioactivity; however, this method typically only provides organ level information. Autoradiography is the process of visualizing radioactivity distributions in either tissue samples or over the whole body. Systems used for autoradiography can image over a range of resolutions, from 200 to 5 microns; thus activity distributions can be seen down to the cellular level.

18.2 Autoradiography

18.2.1 Tissue Distribution of Radiolabeled Compounds

Autoradiography is used to determine the distribution of radiolabeled molecules from whole-body sections or specific tissues of interest by exposing the sample to an energy-capturing matrix such as photographic film, phosphor-imagers, or emulsions. There are two types of autoradiography: whole-body and micro or tissue sectioning. Whole-body autoradiography is increasingly popular in the pharmaceutical industry as it allows an accurate evaluation of the tissue distribution in the intact animal. Whole-body sections also can be matched with in vivo imaging

data. In addition to the qualitative assessment, it offers the capability of quantitating the concentrations of radioactivity in tissues by the use of standard curves, accounting for the commonly used terminology, quantitative whole-body autoradiography (QWBA). Micro-autoradiography (MAR) detects radioactivity at a microscopic level providing information about the cellular, subcellular, and topographical tissue deposition of the radiolabeled compound (Stumpf 2003).

The advantages of whole-body autoradiography relative to traditional cut-and-count strategies are severalfold. First, whole-body autoradiography allows for a comprehensive and quantitative anatomical survey of compound tissue distribution within the intact animal. This avoids the need to preselect tissues of interest and aids in the identification of distribution to unexpected tissues. Second, the methodology enables localization of compound in organ substructure, which can be important for better understanding compound mechanism of action and toxicity. Third, by virtue of this methodology, the animals are quickly frozen at completion of prespecified time points, which immediately arrests potential compound redistribution. When performing cut and count, the time from time-point completion to tissue dissection is often variable. Lastly, this methodology allows for the in situ evaluation of placental transfer of a compound, melanin binding, and penetration of the blood/brain barrier. The key disadvantages of QWBA are that the methodology is labor-intensive, expensive, and time-consuming.

18.2.2 QWBA Methodology

Tissue distribution and fate of radiolabeled molecules by QWBA were introduced by Ullberg (1954). Immediately after euthanasia, animals are pinned onto a stationary board and immersed in an alcohol bath at −70 °C until completely frozen. Unpinned frozen animal carcasses are then embedded in 3 % carboxymethyl cellulose (CMC) and placed into a freezing chamber at −70 °C. Whole-body cryosections are obtained by using a cryostat microtome at −20 °C. The section thickness depends on the strength of the energy emitted by the radioisotope in use (i.e., 20 µm (^{3}H, ^{125}I) and 40 µm (^{14}C)).

Several sectioning levels can be collected, with each level representing the various major tissues (organs and fluids) (see Fig. 18.2, as an example). Sectioning levels to be collected are selected according to the tissues of interest. A digital picture of the level is taken before sectioning to be used as anatomical reference during imaging analysis (see Fig. 18.3). The collection of multiple sectioning levels not only permits for a wide tissue sampling but also captures the possible heterogeneity of the distribution within the same tissue. A minimum of three sections per level allow for a statistically meaningful value at the time of quantitation. Although sagittal sections are the standard practice, other planes can be adopted to better represent the tissues of interest. As an example, Fig. 18.4 depicts coronal sections of a mouse bearing two tumors, in the left and right flanks,

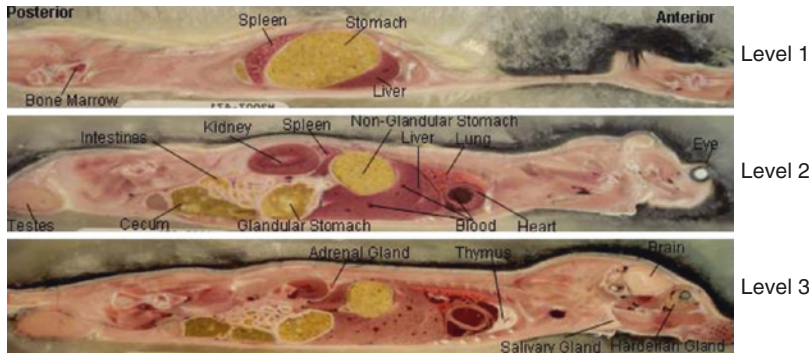

Fig. 18.2 Digital images of sagittal whole-body sections of a male rat at different sectioning levels

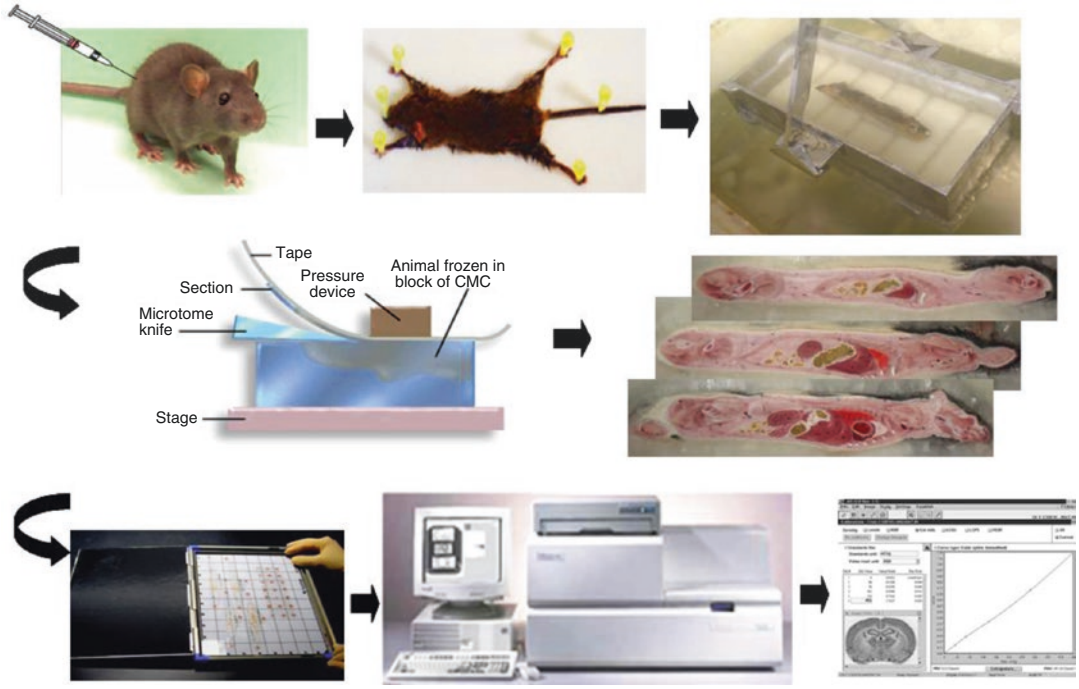

Fig. 18.3 Diagram showing the steps required in a QWBA study, starting with injection of a radiolabeled probe, freezing and embedding, sectioning, exposure of whole-body sections, and image analysis for quantification

respectively. Unlike PET or SPECT, where the same animals can be observed over time, autoradiography measurements at different time points must be done using different animals for each sampling time.

Whole-body sections are collected by placing a layer of clear tape on the animal, then cutting the tissue free, leaving the tissue slice mounted on the tape. The tissue sections are lyophilized at −20 °C for 24–48 h before exposing them on film or phosphor-imaging plates (PIs). Suitable imaging plates for each specific isotope are commercially available and have replaced the X-ray films used in the past for autoradiography. The PIs are composed of phosphors designed to absorb radiation (Miyahara 1989; Hamaoka 1990). To avoid contamination of the plates, tissue samples can be covered with thin sheets of Mylar film, so the tissue is not in direct contact with the plate. However, this step does not apply to samples containing ^{3}H as the low-energy radioactivity emission of this isotope requires direct contact of the tissue to the plate to avoid quenching of the signal.

For quantitation purposes there are two types of standards: a separate quantitation block and internal standards within the animal block. Polymer calibration standards are commercially available; however, standards prepared with biological matrixes are more reliable. Whole blood is the preferred matrix, as it is similar to most tissues in the body (Solon and Kraus 2002). Thus, several known concentrations of radioactivity are spiked into whole blood according to the concentration range expected in the whole-body samples. Blood standards are placed into drilled holes in the frozen CMC block and allowed to freeze at −20 °C prior to sectioning. Quantitation standards are placed in an independent block and the section thickness should match that of the whole-body sections. The internal standard consists of few concentrations that are placed along the animal block (where the animal is embedded), and they are used as a parameter to determine the section thickness variations in any given section.

Exposure time of the whole-body sections to the PIs is determined by the radioisotope used and the concentration of radioactivity adminis-

trated to the animals. In general, recommended exposure times are 2–24 h for ^{125}I, ^{124}I, ^{64}Cu, ^{18}F, and ^{11}C, 3–8 days for ^{14}C, and 15–30 days for ^{3}H. Longer exposure times can improve detection of low radioactivity signals; however, caution should be applied as flare intensity, nonlinear response of high radioactivity signal, and increased signal-to-noise ratio may occur.

Exposure conditions such as artificial light, environmental radiation, and temperature of the room where the tissue samples are exposed can affect the drug-related radioactivity detection. Because light and environmental radiation are absorbed by the PIs, lead- and copper-lined cabinets are recommended to decrease background signals. Typically, exposure of sections to PIs at room temperature is sufficient. With short-lived PET isotopes, there is not sufficient time to dehydrate overnight, so the exposure process must be conducted below freezing to prevent the tissues from thawing and loss of signal localization. This requires that the cassettes and the PIs be precooled to the exposure temperature to avoid water condensation (Maas et al. 2000) and to prevent the tissue sections from thawing. After exposure, PIs are scanned by a phosphorimager, and the digital autoradiogram image is obtained. These digital images are then analyzed and can be quantified using various software programs available from several sources. A diagram of the steps involved in a typical QWBA study is shown in Fig. 18.3.

The ability to quantify the radioactivity concentration in tissues has made QWBA an important tool in drug discovery and development. The quantitation is done by densitometry, pairing the optic density values of the standard to the corresponding radioactivity concentration values. A resulting standard curve converts the tissue density values to units of radioactivity concentration as described by Potchoiba et al. (1995). The quantitation method described above has been demonstrated to be as accurate and precise as the values obtained from the gamma or liquid scintillation counters (Potchoiba et al. 1995, 1998; Steinke et al. 2000; Busch et al. 2000). Results of tissue distribution by QWBA of a ^{14}C-labeled molecule are demonstrated in Fig. 18.5.

18.2.3 Special Considerations for the Design of a QWBA Study

The radioactive concentration of the dose will depend on the isotope. Suggested doses are ^{14}C = 100–300 μCi/kg, ^{3}H = 1000–2500 μCi/kg, and ^{125}I = 100–800 μCi/kg. Either too high or too low radioactivity doses can impact imaging quality, quantitation, and overall outcome of the study (Maas et al. 2000; Potchoiba and Nocerini 2004). To accomplish the desired dose of the drug or test article, the total concentration can be adjusted by mixing radiolabeled

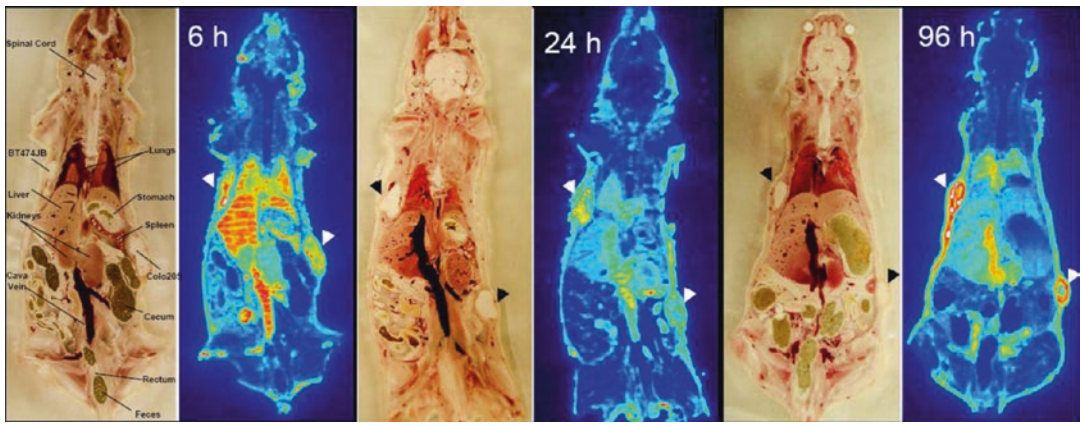

Fig. 18.4 Representative whole-body images and autoradiograms of mice bearing two tumors (*arrows*) at different time points after an IV bolus injection I-125-labeled SPECT imaging agent. Uptake by tumors increased over time, showing specific localization of the probe

Fig. 18.5 Phosphor-imaging plate and cassette (*left*), Fujifilm BAS 5000 plate reader (*right*)

with non-radiolabeled material. Caution must be exercised when the drug formulation contains any oil-based component as the oil may impair complete tissue freezing.

Other considerations are when working with tumor-bearing models, the localization of the tumor tissue in the autoradiograms can be challenging (i.e., when working with orthotopic tumors). In this case, a complementary histological staining of adjacent whole-body sections may be a useful tool to discriminate normal from diseased tissue. Similarly, tumor detection can become more difficult in studies where drug administration affects tumor size. Lastly, artifacts can influence the outcome of QWBA data: one of the most common causes of misreading tissue-related radioactivity is due to variations of the sectioning thickness within the whole-body section. Thus, internal standards placed in the animal block can help to identify thickness variations among the section. Another common artifact is caused by the conditions and length of the tissue exposure, as detailed above, which can result in poor signal-to-noise ratio or flare induced by very high radioactivity uptake in a given tissue. Flare will not only impact the ability to accurately quantitate radioactive signal in the tissue of origin but also in surrounding tissues. In addition, tissues not properly frozen or tissues affected by surgical manipulation (e.g., bile, venous catheter; Zimmer 2007) can result in a false radioactivity signal.

It is important to consider that incomplete erasing of residual radioactivity on plates will result in the so-called phantom images where new whole-body sections appear in the mist of old exposures. Plates are reusable if properly protected and blanked between uses. Given their high cost ($800–1200), it is worth the effort to keep the tissue and radiation from contaminating the surface.

There are many challenges with QWBA experiments, so many that an entire society and conference has been created around this topic. For more information, refer to http://www.autoradiography.net/index.html

18.2.4 Combination of QWBA with Other Imaging Approaches

A multimodal approach to assessing distribution is often useful, as QWBA can complement in vivo imaging strategies such as positron emission tomography (PET) or single-photon emission computed tomography (SPECT). QWBA adds to PET and SPECT imaging by enabling an enhanced resolution of the distribution of radioactivity to tissues. An example of QWBA complementing SPECT/CT imaging is depicted in Figs. 18.6 and 18.7 (Pastuskovas et al. 2008).

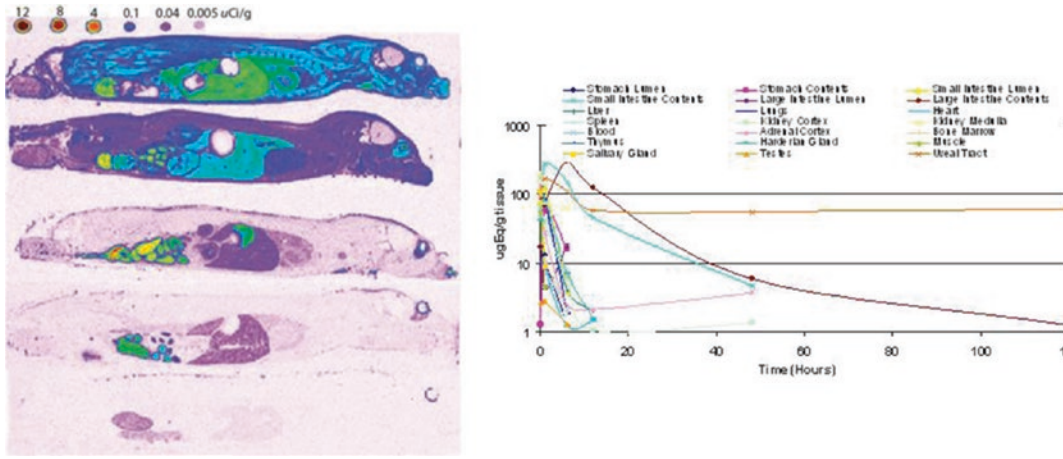

Fig. 18.6 Representative whole-body rat autoradiograms at different time points (0.083, 1, 6, 12, and 120 h, respectively) after an IV bolus injection of C-14-labeled compound. Quantitation of tissue radioactivity concentrations (*dots* in *upper left* side of image), converted to μEq/g of tissues, was obtained

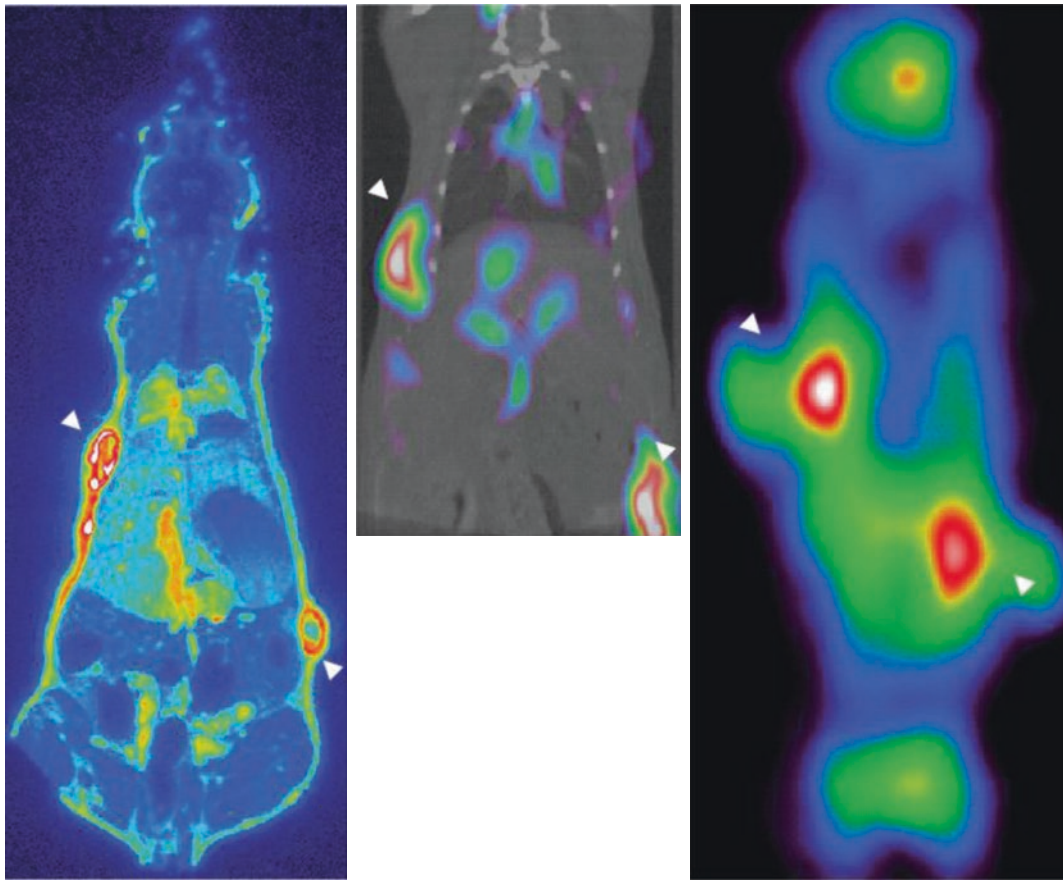

Fig. 18.7 Coronal views of whole-body autoradiography (*left*), SPECT/CT (*center*) and SPECT (*right*) images of the same two tumor-bearing mouse at 96 h post-dose of a ^{125}I-labeled compound. Tumors are shown by the *arrows*

18.3 Gamma Counters

18.3.1 Principles of Detection

Gamma counters are sensitive instruments designed to measure very small quantities of radioactivity, usually less than 18.5 kBq (0.5 microcuries). Unlike dose calibrators, which measure a wide range of activities and are proportional gas detectors that measure a total signal, gamma counters are made of solid scintillator material, typically sodium iodide (NaI). Each gamma ray interacts within the scintillation crystal and creates many light photons, which are collected by a photomultiplier tube (PMT). The PMT has a photocathode that converts the light photons into electrons, then accelerates them using an electric field through a series of anodes to amplify the charge sufficiently for electronic processing. The electrical pulse is then processed using both hardware and software to determine a count rate. Software settings can be used to set energy thresholds and windowing, to identify certain isotopes, and to eliminate spurious background noise (Knoll 1989).

Each isotope has a characteristic emission of gamma rays, alpha or beta particles, positrons, or electrons. The gamma counter is not able to detect alpha or most beta particles. Alpha particles cannot penetrate the plastic sample tube. Beta particles are typically stopped within a few millimeters, so again the tube and housing for the crystal will stop those emissions. Gamma counters, as the name implies, are only suitable for detecting gamma emissions. The rays must be strong enough to penetrate into the scintillator and deposit energy, roughly a minimum of 25 keV.

The ability of the detector to stop the gamma ray and deposit its energy is called the stopping power, which is determined by both the energy of the gamma rays and the density of the detector material. Over a certain energy threshold required to penetrate completely through the detector, as gamma energy increases, there will be less activity detected as more rays pass completely through the scintillator or only deposit some of their energy. This can be compensated by knowing the isotope, thus knowing the energy emissions and accounting for scintillator penetration using a calibration factor. For SPECT imaging, typical energies range from ~30 to 200 keV, with the most common isotope Tc-99 m at 140 keV. With PET isotopes, there are always 511 keV gammas from the annihilation process, which may also sum to 1022 keV. Some PET isotopes may emit multiple types of radiation, such as both positrons and gammas. These “dirty” isotopes often deliver more dose to animals; however they can be quite useful for their biological applications and longer half-lives (Cu-64, 12 h; I-124, 4 days) compared to the more frequently used F-18 (2 h) and C-11 (20 min) isotopes. A reasonable tradeoff for both cost and stopping power for NaI detectors is 2 in. (5 cm), which is suitable for both SPECT and PET isotopes. For a 5 cm NaI detector measuring PET isotopes at 511 keV, the detection efficiency is around 55%. To convert the counts measured to the true activity, this efficiency must be taken into account, converting counts per second to disintegrations per second or becquerel.

18.3.2 Geometric Efficiency

Two types of detector configurations are possible: a pass-through hole in the center of a cylinder and a cylinder with a hole going only part way through, commonly called a well detector (Fig. 18.8). The pass-through design has an advantage for automated sample handling, since samples can be pushed or raised into a counting position, then lowered and moved aside to make room for the next sample. Well configurations have an advantage of more detector material, thus higher efficiency for stopping more activity. Unfortunately, well configurations often have problems with sample handling, since the sample must be held from the top, requiring very specific tubes and positioning. If anything drops out of the holder, it can be tricky to try and fish out things from the well.

Sample positioning is a crucial consideration for any gamma counting work. Ideally the

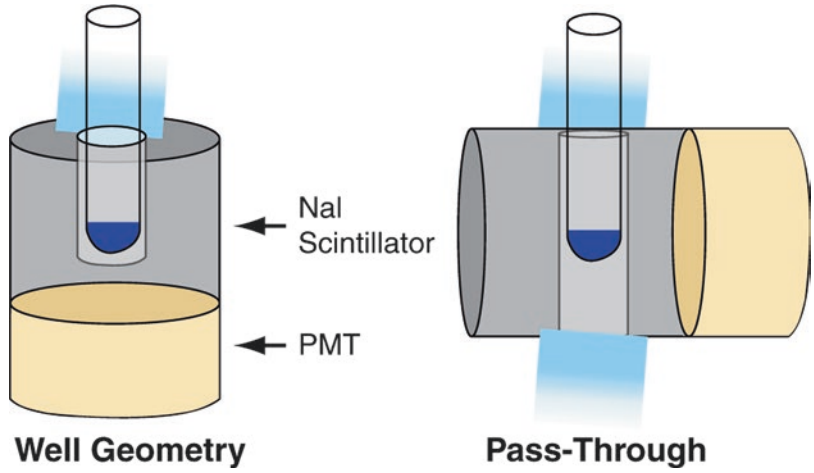

Fig. 18.8 Two geometries used in gamma counters: well and pass-through. Some of the solid angle emitted from the blue source is not covered, shown in light blue. Light from the scintillation crystal is collected, converted to an electrical signal, and amplified by the photomultiplier tube (PMT)

sample should be placed in the center of the detector for a pass-through configuration or at the bottom of a well detector, where the maximum geometric efficiency is located for signal measurements. The solid angle of detector coverage directly affects the signal measured (Katz and Blantz 1972). As the sample moves toward the opening, the signal strength decreases and counts are lost, making the measurements inaccurate. For this reason, it is important to make sure all sample materials containing radiation are placed at the bottom of the test tube used to hold samples. Sample volume can also affect measurements through attenuation and displacement toward the top of the detector, where the geometric efficiency drops off. Attenuation is more important for lower-energy isotopes such as thallium, as they will be more subject to this effect compared to either PET or higher-energy SPECT isotopes.

18.3.3 Factors Altering Measurement Values

Aside from the geometric positioning of samples, there are several other factors that can alter the signals measured from the gamma counters. There are specific settings and counting protocols used that may specify certain energy windows, calibration files used to correct measurements for specific isotopes, and the duration of how long the samples are counted. The longer samples are counted, the lower the noise will be in the measurements (Knoll 1989). Often there is a trade-off in how long to count each sample versus the half-life of the isotope and the potential for very low activity in some of the samples. The clock in the counter computer should also be configured to match those of other related imaging systems, so that the timing is precisely known and decay corrections are accurate.

The ability to detect small or weak sources relies mainly upon the background radiation level where the counter is located. Ideally the gamma counter is located well away from other sources of radioactivity, or at a minimum that other sources nearby be adequately shielded. A common rule of thumb is that samples are only significant if they have three times background, so the background level plays an important role in the data analysis. Commercial gamma counters are well shielded using a substantial amount of lead to reduce background. This shielding is necessary and important, but it also can make servicing and moving the system difficult.

The maximum amount of activity that can be counted is vendor specific, but is generally in the range of 0.5 uCi. High activity levels can saturate the electronics, causing system dead time and loss of counts. Systems typically have a software-encoded limit of ~20 % dead time and give some sort of error message rather than providing an inaccurate reading. One way to work with a wide range of activities is to have samples automatically counted numerous times until the activity decays to a working range. This enables measurements of both weak samples at early times and strong samples at a later time.

Another factor is how samples are prepared and located in the counter. Blood or HPLC samples may be fractionated into individual samples, or various tissues might be collected and placed in tubes for measurements. If a high activity sample is located immediately adjacent to a low activity sample, there may be shine contamination from the hot sample to the cold one. A simple solution could be separating the samples by several spaces in the holding rack, to enable the shielding of the detector to function better.

18.3.4 QC Measurements

Gamma counters should be checked periodically to make sure the response to a known standard is consistent with the expected measurement, corrected for decay. Various calibration standards for a range of energies are commercially available in vials suitable for either well or pass-through geometries. Most often Cs-137 and Co-57 are used for PET and SPECT energy ranges. For short-lived isotopes, the measurements can be compared to those obtained with a dose calibrator using either dilutions or waiting for decay to bring the sample activity down from the minimum accurate dose calibrator range (~10 uCi) to the reasonable range of the gamma counter (<0.5 uCi). Keep in mind that dose calibrators have a stated accuracy in the 10–15 % range and that there are both instrument settings and geometric factors that also affect these measurements. Dilutions add another source of potential error; however this is perhaps the only viable option for short- to medium-lived isotopes (hours to days).

18.4 PET and SPECT Quantitation Issues

18.4.1 Factors Related to Image Data

An in-depth review of PET and SPECT instrumentation and image reconstruction is beyond the scope of this chapter; nonetheless, there are some settings and choices that must be considered when comparing image data with gamma counter or autoradiography data. Foremost is that the image data must be as accurate as possible to account for any differences in how the data is measured. This means all the necessary correction factors must be applied, factors such as detector normalization, dead-time correction, random count correction, isotope decay and decay scheme, attenuation and scatter corrections, partial volume effects related to system resolution, and possibly probe metabolism. The amount of dose injected needs to be accurately known, accounting for any residual in the syringe or any activity stuck in the injections site that is not bioavailable.

The choice of image reconstruction method can also change image values, depending on the filtering used, iterations, and the use of system performance parameters. Although the use of filtered back projection (FBP) is common, there is an increasing use of iterative methods such as ordered subset maximum likelihood (OSEM) or for some systems maximum a posteriori (MAP), which makes use of the system response to activity to create higher-resolution images (Chatziioannou et al. 2000).

If an object is small relative to the resolution, roughly 3× the resolution or less in size, then there will be partial volume effects that blur the uptake into adjacent voxels, resulting in both a larger apparent size and a lower uptake measurement (Hoffman et al. 1979). For objects with mostly spherical shapes, such as tumors or the left ventricle (LV), a recovery coefficient can

be used to correct the activity level to account for the resolution loss.

18.4.2 Calibration Constant

To compare image values and gamma counter results, the best method is to measure a known volume and amount of radioactivity in both the scanner and gamma counter. Knowing the true activity and measured counts, the gamma counter efficiency can be determined, which should be very stable over time. The corresponding measurement in the imaging system allows the system response to activity to be assessed and a calibration constant determined, which can be used to convert the counts per voxel per second to activity amounts. These two measurements can be done in one process, using a small vial approximating the size of a mouse (a liquid scintillation vial works well). By weighing the vial empty and full of a known amount of radiation, the concentration is known and can be compared to the image data. Aliquots of the vial can be carefully weighed and measured in the gamma counter to provide the counter efficiency measurement. Measurement of the efficiency and calibration constant is an excellent quality control process to ensure that each system is functioning as expected, primarily because the process follows exactly that used to image animals and samples. The same process is used with autoradiography using known radioactivity standards or measured standards embedded within the sectioning block.

Figure 18.9 shows how each type of measurement system has its own efficiency for data collection. Using the appropriate correction factor, the measurements can be converted into the same unit of measure, enabling comparisons between divergent data sets. There are many corrections and steps involved in this process, so careful measurements and reproducible protocols are essential. If the temperature and environmental conditions remain constant, these efficiency values should be very stable over time. When using these values with data, a running average is best to use, to avoid the noise coming from any one measurement. In general, these systems should have a variability of less than 3–5 %; thus, any errors greater than this probably can be attributed to human measurements and might be best repeated.

18.4.3 Blood Sampling

One place where gamma counters and SPECT or PET imaging often overlap is the measurement of blood or plasma radioactivity samples taken during the imaging process. The blood time activity profile is needed for kinetic modeling of

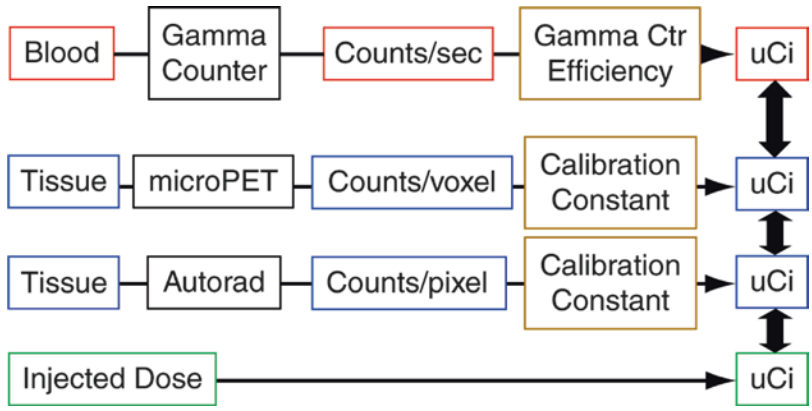

Fig. 18.9 To compare information from different sources, measurements need to be calibrated to the same unit of measure. Calibration constants and gamma counter efficiency are needed to compare PET, autoradiography, and gamma counter data

metabolic rate constants. The ability to measure in vivo metabolism is the primary purpose and most valuable application of SPECT and PET systems. Blood sampling is unfortunately not easy in small animals, especially mice (Laforest et al. 2005). While a simple poke of the tail may be good for obtaining a small amount of blood for a glucose measurement, a well-sampled blood time activity curve requires 15–20 samples, with accurate known timing and sufficient volume to enable handling, counting, and perhaps plasma separation and metabolite analysis. The most challenging part is sampling fast enough over the first few seconds to adequately sample the initial rise and fall of activity during the first pass extraction by the tissues (Raylman et al. 1993). Sometimes it is possible to use the image-derived input function using the left ventricle (Shoghi and Welch 2007); however this approach may not work well for fluorodeoxyglucose (FDG) in mice, where there is substantial myocardial muscle uptake over time, causing spillover of heart muscle signal into the late low activity blood pool values. Several people have validated using both the LV and liver signals to get an accurate input function using FDG (Ferl et al. 2007). Others have worked on microfluidic blood sampling systems that can take relatively fast and tiny samples (Wu et al. 2007).

If blood samples are to be used in a gamma counter, then several factors must be considered. First is that an accurate sampling time must be recorded. Second is that the sample needs to be large enough to accurately weigh in order to get the volume. Most analytical balances are only useful to a few microliters, so it may be necessary to have 25 uL or more for the sample size. Third is that the samples must contain only blood and not any saline or other solutions that might be flushed into the catheter between sampling to keep the line open and free from blood clots. A good clean sample requires first flushing with about three times the volume of the tubing and any valves before taking the sample. This flush can either be discarded or reinjected after the sample has been taken. For small animals, it is therefore very important to minimize the sampling system. Often a short piece of PE-10 tubing and a TB syringe with a fixed needle are used, since the dead volume associated with a Luer fitting and three-way stopcock can easily add up to volumes over 500 uL. As mentioned previously, to get a good measurement of the sample, it must be placed at the bottom of the test tube used in the gamma counter so that there be reproducible and optimal geometric efficiency.

18.5 PET and Autoradiography Combined

18.5.1 Working Fast: Using PET Isotopes with Autoradiography

Conducting a SPECT or PET imaging session followed immediately by autoradiography is truly a logistical challenge. Each imaging method requires careful and timely attention to many details, so the combination of the two makes for an intensive experiment (Dogdas et al. 2007). Practice and experience are essential for success. The in vivo imaging is conducted first, then the animal must be quickly euthanized, frozen, and cut, and the sections are exposed to the imaging plates. Usually autoradiography experiments have the luxury of time, often 3 days or so to prepare everything for cutting. Timing only matters for the injection and subsequent sacrifice, since after freezing the tissues are stable and the half-life of C-14 or tritium is measured in years. The most common isotope used with PET is F-18, with a 2-h half-life, so the entire process of autoradiography must be sped up accordingly.

Figure 18.10 shows the linear autoradiography process and the corresponding times often required for each step. On the right are the times required for working quickly with F-18 in only a few hours. One group in Sweden has even sped this up for working with C-11, though the number of sections that can be imaged is very limited (Sihver et al. 1999).

Something worth considering when conducting both in vivo imaging and QWBA is that animals are typically anesthetized during the imaging process, often for an hour or more. The

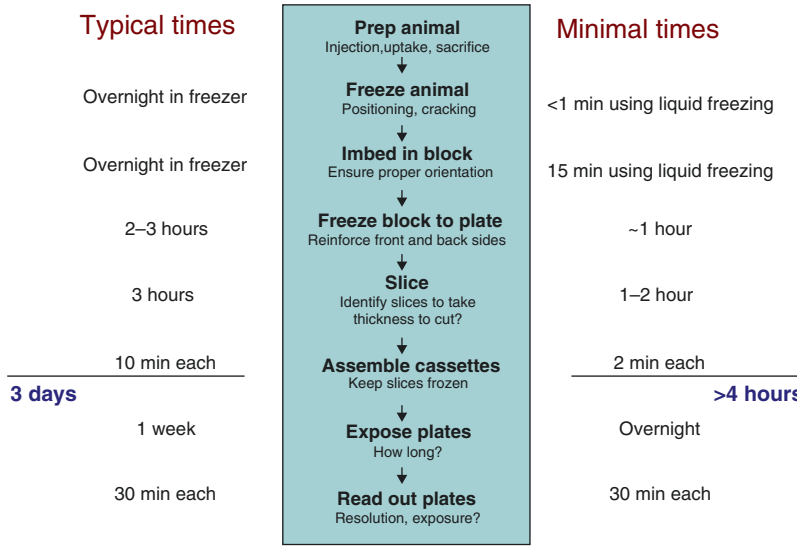

Fig. 18.10 Typical autoradiography processing times and steps required versus the fast times required for working with short-lived isotopes. The minimal process here was optimized for F-18, with a 2-h half-life

physiology and possibly the probe biodistribution may be different compared with animals injected and left conscious for the uptake period. One way to test this is to inject the probe into two groups: unconscious animals and conscious animals that are anesthetized only right before the imaging process. Comparing the resulting images will show the difference between anesthetized and awake animals. Another option is to inject two groups of animals, one left awake for QWBA work and another group anesthetized for in vivo imaging, though this will mean the in vivo image data will not necessarily match the QWBA data coming from different animals. Different anesthetics also have different effects in vivo, so the anesthetic choice may be necessary to consider during the experimental design phase.

For long-lived isotopes, sections can be hung on a rack inside the cryostat and a defrost cycle run overnight to dehydrate the samples. Once dry, the tape can be moved to phosphor-imaging plates at room temperature for exposure. With short-lived isotopes, this is not an option, so the sections must be placed immediately on the PI plates. To keep the sections from melting and losing all the valuable positioning information, the PI plates and cassettes must be kept frozen. Exposure must be done in a −20 or −80 freezer, typically overnight for F-18. Condensation needs to be kept at a minimum to prevent water from collecting on any surfaces, which can degrade the image quality. Most of the signal on the PI plates will come from the positron, which only has a short range. The plates are relatively insensitive to the 511 keV gamma rays, so it is best to keep the sections as close as possible to the PI plates with only minimal material between them, usually just a thin layer of plastic wrap. Cassette enclosures for AR are useful to both block light from exposing the plates and to provide pressure to keep the sections in close contact with the plates (Fig. 18.11).

18.5.2 Quantitation Comparisons

Using the calibration constant and QWBA standards, the amount of radioactivity in tissues can be determined. The challenge then becomes trying to match up the locations from the two methods. A minor technical hurdle is that images are in different formats and will have different resolutions, slice thicknesses, and orientations. More problematic is that the freezing and slicing process deforms the tissues, so that they are no longer in the same orientation as in the in vivo

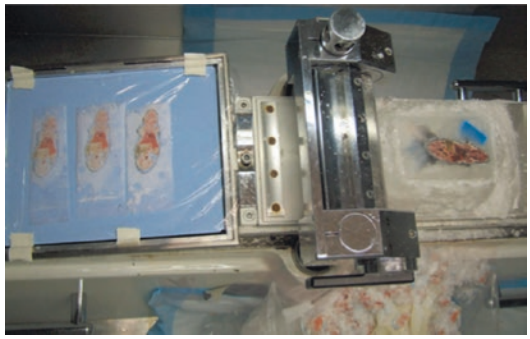

Fig. 18.11 Sectioning of animal using F-18. Note that the phosphor plate and cassette are placed within the freezer compartment to keep the sections completely frozen after slicing

imaging experiment. The mismatch in resolution may make image warping and coregistration difficult. Often QWBA experiments only look at specific sections within the animal to get a representative sampling of the activity. One option is to survey the entire animal; however this is very time-consuming and may not be feasible given the short half-life of the isotope. A reasonable trade-off might be to take several back-to-back slices to acquire data from a representative thick section of the tissue, which may give sufficient information for coregistration or cover the entire area of interest. Fiducial markers have also been used to help with this difficult process.

Often tissue sections are stained for histology and pathology work. For whole-body QWBA, a problem is posed in that the sections are acquired directly on to tape as a support surface. If the tape does not stick to the section, then it is not useful as the tissues curl and fall off or get wrinkled. If samples stick properly, then it is hard to do the staining process. A solution has been devised where a degradable polymer is used as the tape, which is then dissolved by exposure to UV light. Using this process, it is possible to both image and stain the same section, rather than resorting to adjacent sections each going to one method (CryoJane tape-transfer system, Instrumedics http://www.instrumedics.com/cryojane.htm).

Fortunately exact image coregistration is not often necessary. Looking back at Fig. 18.1, simply being fairly close in orientation and location is sufficient to derive useful information about the content of both in vivo and cryosection images. QWBA plus PET or SPECT is a challenging process, but fortunately one that might only need to be used sparingly to validate probe biodistributions, then perhaps no longer necessary at all or only as an end point to following the same animal over time. The challenges of radiolabeling probes may prevent the easy use of in vivo methods, plus the cost and complexity may not be warranted. QWBA remains a reasonable alternative, though one requiring more animals and a known optimal timing sequence for when to look at the biodistribution.

18.6 Summary

By measuring the efficiencies of each radioactivity sensing device, the resulting data can be converted into a common unit of reference, usually either becquerel or curies. This conversion into the same unit makes it possible to compare values across different types of measurement systems, making use of the value of each system, whether it be high spatial resolution or in vivo measurements over hours or days. To be accurate, the various corrections and calibration factors must be carefully measured and applied. Fortunately, regular assessments of the calibration factors are an excellent quality control measure and they are relatively simple to obtain. Combining autoradiography with in vivo imaging is challenging but certainly possible, enabling more exact knowledge of the precise location of the imaging probe used in vivo.

References

Busch U, Heinzel G, Nehmiz G. Precision of measurement of tissue concentration by radioluminography. Regul Toxicol Pharmacol. 2000;31:S45–50.

Chatziioannou A, Qi J, Moore A, Annala A, Nguyen K, Leahy R, Cherry S. Comparison of 3-D maximum a posteriori and filtered backprojection algorithms for high-resolution animal imaging with microPET. IEEE Trans Med Imaging. 2000;19(5):507–12.

Cherry SR, Gambhir SS. Use of positron emission tomography in animal research. ILAR J. 2001;42(3): 219–32.

Dogdas B, Stout D, Chatziioannou A, Leahy R. Digimouse: a 3D whole body mouse atlas from and cryosection data. Phys Med Biol. 2007;52(3):577–87.

Ferl GZ, Zhang X, Wu H-M, Huang S-C. Estimation of the ^{18}F-FDG input function in mice by use of dynamic small-animal PET and minimal blood sample data. J Nucl Med. 2007;48(12):2037–45.

Hamaoka T. Autoradiography of a new era replacing traditional X-ray film. Cell Technol. 1990;9:456–562.

Hoffman E, Huang SC, Phelps M. Quantitation in positron emission computed tomography: 1. Effects of object size. J Comput Assist Tomogr. 1979;3(3): 299–308.

Katz M, Blantz R. Geometric error in tissue gamma-counting: methods for minimization. J Appl Physiol. 1972;32(4):533–4.

Knoll G. Radiation detection and measurement. New York: John Wiley & Sons; 1989.

Laforest R, Sharp TL, Engelbach JA, Fettig NM, Herrero P, Kim J, Lewis JS, Rowland DJ, Tai Y-C, Welch MJ. Measurement of input functions in rodents: challenges and solutions. Nucl Med Biol. 2005;32(7): 679–85.

Maas J, Binder R, Steinke W. Quantitative whole-body autoradiography: recommendations for the standardization of the method. Regul Toxicol Pharmacol. 2000;31:S15–21.

Miyahara J. Visualizing things never seen before. The imaging plate: a new radiation image sensor. Chem Today. 1989;223:29–36.

Pastuskovas CV, Williams S, McFarland L, Khawli L. A multimodal imaging approach for the characterization of antibody distribution in a preclinical model of mice bearing high and low Her2 expressing tumors. Abstract 1415, The Society of Nuclear Medine 55th Annual Meeting. 2008.

Phelps M. PET: molecular imaging and its biological applications. Secaucus: Springer; 2004.

Potchoiba MJ, Nocerini M. Utility of whole-body autoradiography in drug discovery for the quantification of tritium-labeled drug candidates. Drug Metab Dispos. 2004;26(3):1190–8.

Potchoiba MJ, Tensfeldt TG, Nocerini MR, Silber BM. A novel quantitative method determining the biodistribution of radiolabeled xenobiotics using whole-body cryosectioning and autoradioluminography. J Pharmacol Exp Ther. 1995;272:953–62.

Potchoiba MJ, West M, Nocerini MR. Quantitative comparison of autoradioluminography and radiometric tissue distribution studies using carbon-14 labeled xenobiotics. Drug Metab Dispos. 1998;26:272–7.

Radu CG, Shu CJ, Nair-Gill E, Shelly SM, Barrio JR, Satyamurthy N, Phelps ME, Witte ON. Molecular imaging of lymphoid organs and immune activation using positron emission tomography with a new ^{18}F-labeled 2′-deoxycytidine analog. Nat Med. 2008;14(7):783–8.

Raylman R, Caraher J, Hutchins G. Sampling requirements for dynamic cardiac PET studies using image-derived input functions. J Nucl Med. 1993;34:440–7.

Rudin M, Weissleder R. Molecular imaging in drug discovery and development. Nat Rev Drug Discov. 2003;2:123–31.

Shoghi KI, Welch MJ. Hybrid image- and blood-sampling (HIBS) input function for quantification of microPET data. Nucl Med Biol. 2007;34(8):989–94.

Sihver S, Sihver W, Mats B, Höglund AU, Sjöberg P, Långström B, Watanabe Y. Quantitative autoradiography with short-lived positron emission tomography tracers: a study on muscarinic acetylcholine receptors with N-[^{11}C]methyl-4-piperidylbenzilate. J Pharmacol Exp Ther. 1999;290(2):917–22.

Solon EG, Kraus L. Quantitative whole-body autoradiography in the pharmaceutical industry. Survey results on study design, methods, and regulatory compliance. J Pharmacol Toxicol Methods. 2002;46:73–81.

Steinke W, Archimbaud Y, Becka M, Binder R, Busch U, Dupont P, Maas J. Quantitative distribution studies in animals: cross-validation of radioluminography versus liquid-scintillation measurements. Regul Toxicol Pharmacol. 2000;31:S33–43.

Stumpf WE. Drug localization in tissues and cells. Receptor microscopic autoradiography. International Institute of Drug Distribution, Cytopharmacology and Cytotoxicology (IDDC) Press; 2003.

Ullberg S. Studies on the distribution and fate of 35S-labeled benzylpenicillin in the body. Acta Radiol Suppl. 1954;118:1–110.

Wu H-M, Sui G, Lee C-C, Prins ML, Ladno W, Lin H-D, Yu AS, Phelps ME, Huang S-C. In vivo quantitation of glucose metabolism in mice using small-animal PET and a microfluidic device. J Nucl Med. 2007;48(5): 837–45.

Zimmer M. Catheter rats: Influence of surgery quality on distribution pattern. Abstract, The Society for Whole-Body Autoradiography, 2007 Meeting.

Part V

Data Postprocessing

Qualitative and Quantitative Data Analysis

19

Felix Gremse

Contents

F. Gremse
Institute for Experimental Molecular Imaging,
RWTH Aachen University Hospital,
Aachen, Germany
e-mail: fgremse@ukaachen.de

19.1 Introduction

Scientific preclinical imaging studies are usually conducted to gain evidence about novel probes, therapies, pathologies, biologic mechanisms, mouse models, imaging devices, or analysis methods. Usually representative images are good to explain a phenomenon but need to be backed up by a statistical analysis based on quantitative or at least comparable measurements. The extraction of quantitative measurement often poses a major challenge for imaging studies. Figure 19.1 shows the required steps toward achieving a significant statistical result for typical studies involving small animal imaging.

After preparation of the animal models, which already may require considerable effort and expertise, these are imaged with one or more devices which capture raw data. Subsequently, reconstructions are performed to generate image data suitable for interpretation and analysis. Typically, the internal details of the reconstruction software are hidden to the user but may be configured, e.g., by selecting a reconstruction kernel for μCT. This configuration can have severe effects on the resulting images as it may affect the resolution, the noise level, and the presence of artifacts and other properties relevant for quantitative image analysis. Therefore, Sect. 19.2 provides an overview about the properties of reconstructed images.

Modern preclinical imaging devices can generate data sets that are too large to be processed

F. Kiessling et al. (eds.), *Small Animal Imaging*, DOI 10.1007/978-3-319-42202-2_19

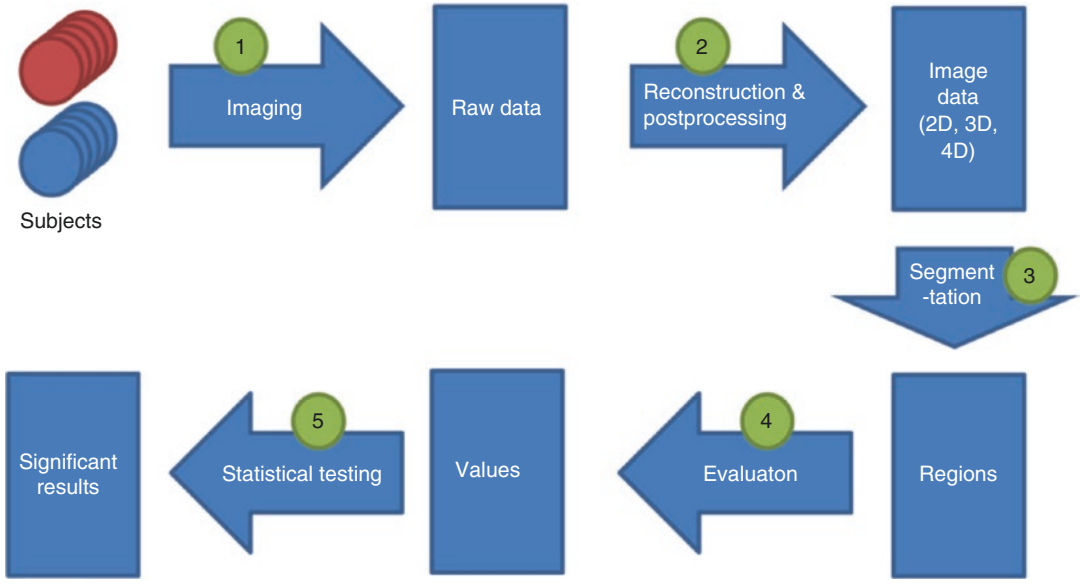

Fig. 19.1 Steps during typical imaging studies. *1* Imaging devices acquire raw data of subjects of one or more groups. *2* Images are reconstructed from the raw data and post-processed. *3* To analyze the data, regions are defined or segmented. *4* Regions are evaluated to extract measurement values such as the volume or the amount of probe accumulation. *5* Statistical tests are applied to check if differences or relationships between groups are significant or coincidental

directly. Then image transformations such as down-sampling or cropping may be required. Image transformations are also needed to fuse and analyze multimodal data sets. Therefore, these aspects and their relationship to quantification are treated in Sect. 19.3.

Often, the voxel intensities have too many influencing factors to be used as quantitative measurements directly. A good example is a T2-weighted MRI image whose voxel intensities depend on the proton density, the partial volume effect, the position in the coil, and finally the T2 relaxation time, which may be the quantity of interest. To resolve this, parametric fitting may be performed, to which Sect. 19.4 is devoted.

Only few measurements can be performed directly on the image data, e.g., measurement of the diameter of a blood vessel. Typically, regions of interest (ROIs) are defined corresponding to tissue types, organs, or lesions. Subsequently, the regions are evaluated to extract quantitative values such as volumes or probe concentrations. Segmentation can be performed interactively or even automatically, if such a method is available for the particular problem. To avoid a systematic or user-dependent bias, several aspects need to be considered, which are discussed in Sect. 19.5.

Finally a statistical test is selected and applied to the extracted measurement values to generate a qualitative, and "significant," statement, e.g., that the tumor size is significantly lower in the therapy group compared to a control group. Therefore, Sect. 19.6 provides an introductory overview for the statistical tests that are most commonly used for preclinical imaging studies.

This introduction shows that a broad amount of interdisciplinary expertise is required to successfully plan and execute small animal imaging studies. To achieve a significant result with the often parsimonious allocation of animals, the measurement error should be as low as possible. Unfortunately, the error accumulates throughout the intermediate steps, in addition to the unavoidable biologic variability. Common sources of variability are animal positioning, variations in the measurement time points due to unexpected delays, reconstruction artifacts, and variations that occur during the segmentation step. Therefore, this chapter aims to provide a broad introduction into the concept, terminology, and

pitfalls of steps that are typical for many preclinical imaging studies.

19.2 Image Properties

Most preclinical and clinical scanners provide, after reconstruction, an image that consists of a regular grid of voxels. A voxel is a generalization of a pixel for three-dimensional or four-dimensional images. Voxels have a rectangular shape and a fixed width, height, and depth, e.g., in [mm]. The volume of a voxel is the product of these three quantities. If the width, height, and depth are equal, the voxels are called isotropic; otherwise, they are anisotropic. μCT and FMT usually provide isotropic voxels, while MRI and US often generate anisotropic voxels (Fig. 19.2). Isotropic voxels can be advantageous for image analysis because the data set has the same resolution in all slicing directions. The three dimensions of the image are called the x, y, and z dimensions and correspond to three orthogonal spatial dimensions. The spatial extent of the entire three-dimensional image is called the field of view.

Furthermore, each voxel has an intensity value representing a physical property of the tissue region corresponding to the voxel. Usually, the voxel is much larger than the granularity of the tissue heterogeneity. Therefore, the voxel intensity represents an average value of the tissue regions which is called "partial volume effect." These voxel values are often stored as 8 or 16 bit integers. These types have a limited range, e.g., a 16 bit unsigned integer can only represent values in the range [0–65,535], which should be considered when performing arithmetic operations such as image subtractions, which can result in negative values. To resolve this issue, the image should be converted to store voxels as floating point values which requires storage of 32 or 64 bits per voxel, however.

19.2.1 Dimensionality

Many devices are capable of acquiring multiple images successively, which jointly comprise a four-dimensional image where the fourth dimension is the time. Single slices, e.g., acquired by an MRI or US device, can be considered as special case where the third dimension is one. Most ultrasound devices acquire a single slice only at each time point, and the resulting data set is called a cine loop. The time points may be equidistant, e.g., commonly for US and μCT devices, or non-equidistant, e.g., for PET devices. Furthermore, multiple channels may be acquired, e.g., by the use of dual-energy CT or by applying different scanning protocols successively. Then the number of channels can be considered as fifth dimension.

19.2.2 Intensity and Contrast

Imaging modalities have different physical principles to generate signal, i.e., the voxel intensities. μCT intensities depend on the electron density, MRI T1 images depend on the proton density and the T1 relaxation rate, PET images require radioactive tracers, and FMT is based on fluorescent molecules. While μCT and MRI can be used without contrast agents, PET and FMT require the application of contrast agents or, for the latter, some other sources of fluorescence such as transfected fluorescence-expressing cells. The ability to perform imaging without contrast agent is useful because an injection of contrast agent is not required. It complicates the analysis of contrast-enhanced scans because the native and induced signals need to be distinguished. One approach is to perform a scan before injection and subtract this image from the scans after injection. This technique is problematic in praxis because even slight motion can cause strong artifacts at edges of bright regions. Devices that only generate signal based on contrast agent are difficult to analyze, because of the lack of anatomical reference information. Therefore, multimodal combinations, e.g., PET–μCT, PET–MRI, or μCT–FMT, are a commonly used approach.

19.2.3 Noise and Sharpness

Two important quality criteria of images are noise and sharpness, and they are often competing with each other. The noise level can be

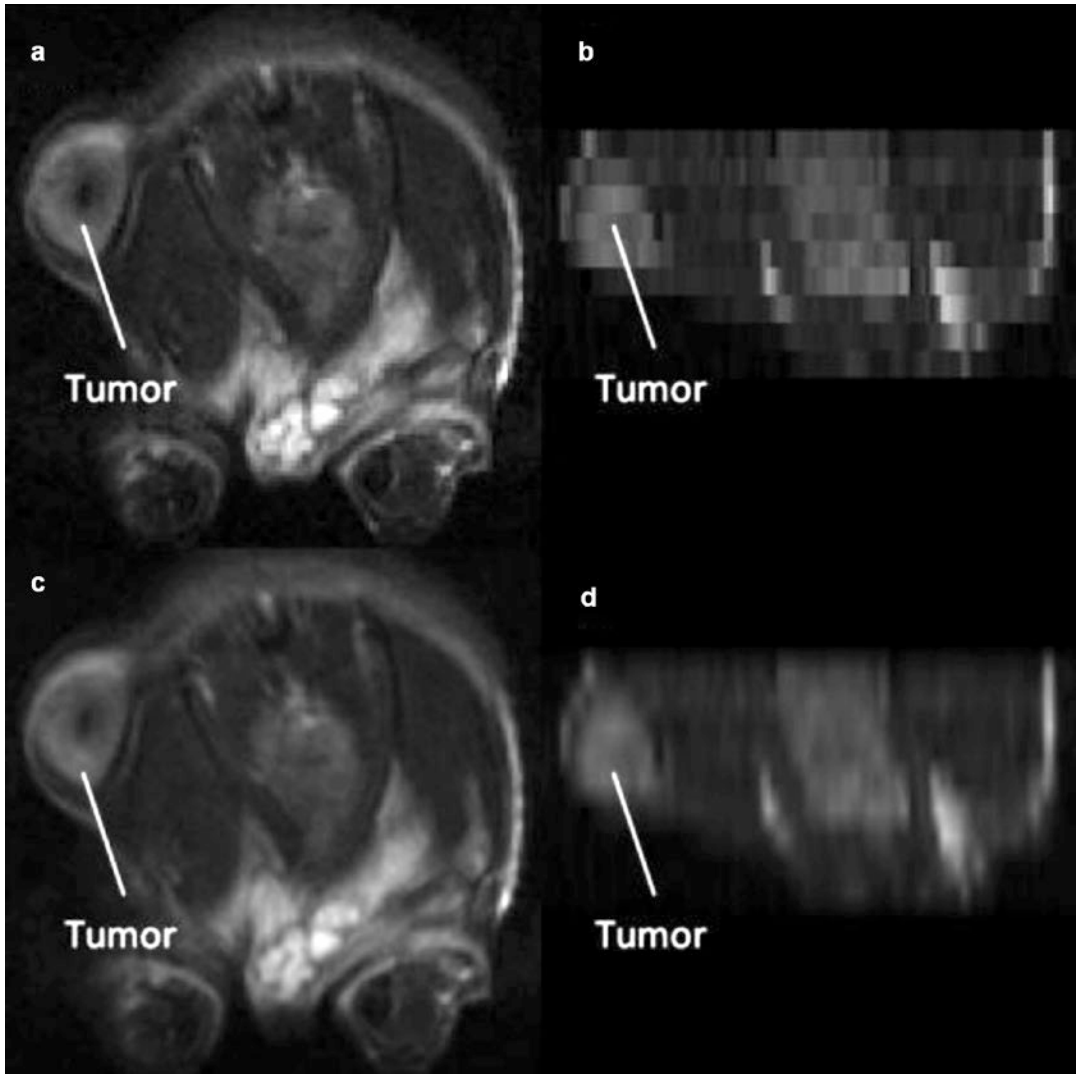

Fig. 19.2 Anisotropic voxels. (**a**) Transversal slice through a mouse with a subcutaneous tumor which appears bright in a T2-weighted image. (**b**) Coronal slice through the tumor showing elongated (anisotropic) voxels. Anisotropic voxels can complicate image analysis. (**c**, **d**) Same as (**a**, **b**) with linear interpolation to give a more pleasant visualization (Data is used from Abou-Elkacem et al. (2011))

described by the signal-to-noise ratio (SNR) which is experimentally determined as the ratio of the mean intensity of a region of interest, e.g., using a water phantom for μCT or MRI, and the standard deviation of the voxel intensities in a homogeneous region, e.g., in the air. The contrast-to-noise ratio (CNR) is used to describe the contrast between two regions or tissue types, e.g., between fat and muscle in μCT images, and is defined as the signal difference divided by the standard deviation of the noise. SNR and CNR can be increased by applying a smoothing filter or by using a smooth reconstruction kernel, e.g., for μCT (Fig. 19.3), at the expense of decreased sharpness, however.

The sharpness of rasterized images is limited by the voxel size. Small details or sharp edges cannot be accurately represented with a coarse resolution. Real objects being imaged have sharp contrast borders, e.g., between the cortical bone

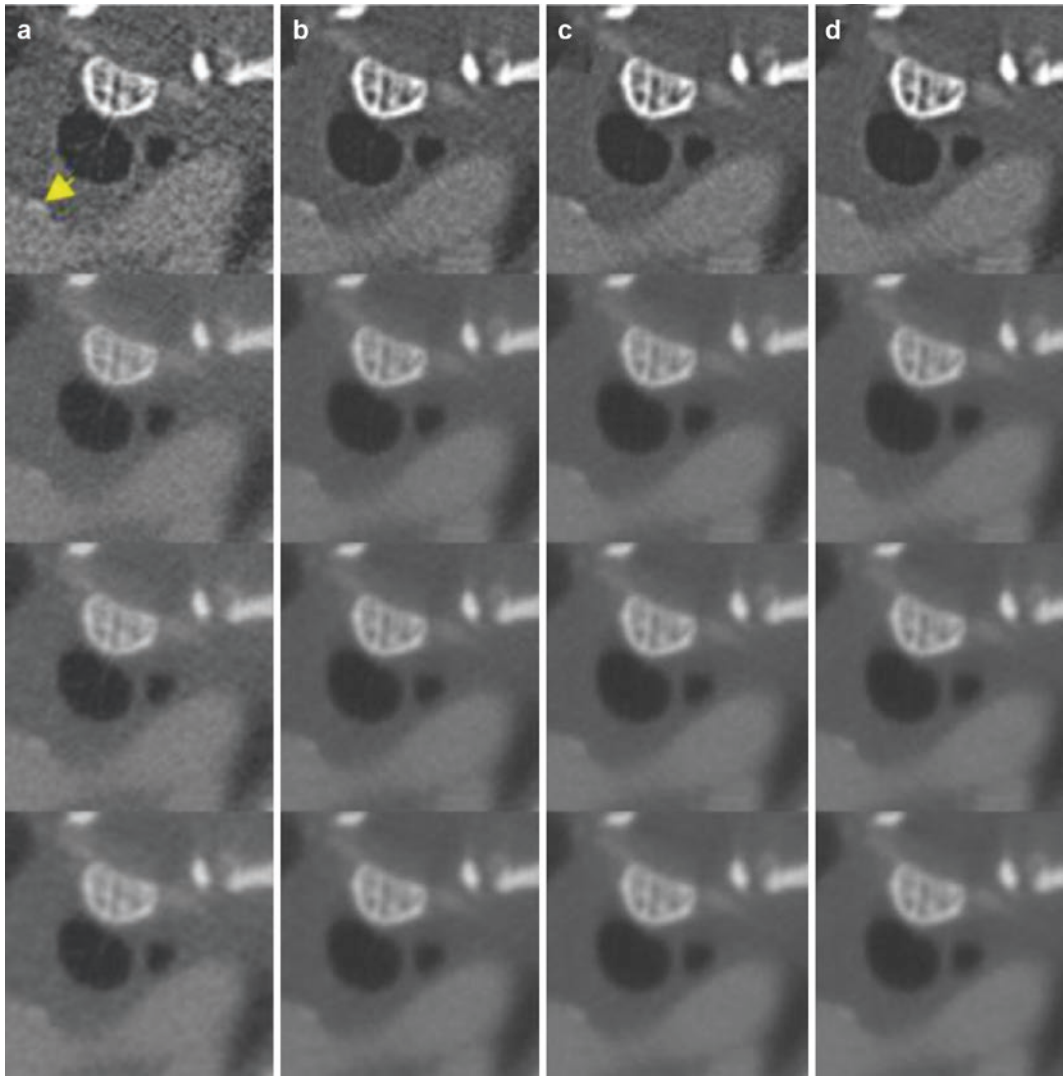

Fig. 19.3 µCT kernel selection and scanning duration. (**a**) Axial slices through a µCT scan of mouse showing a vertebra (*white*), bronchi (*dark*), and the aortic arch (*gray*) with a calcified plaque (*arrow*). A single revolution is used for reconstruction. A blood pool contrast agent enhances the blood vessels. The µCT reconstruction kernel is varied from top to bottom (sharp to smooth). Smooth kernels reduce the noise at the expense of sharpness. (**b**–**d**) Two, three, and four µCT revolutions are used for reconstruction resulting in reduced noise; however, ring artifacts are not reduced. The scanning protocol is described in (Gremse et al. 2011)

and tissue, and therefore would ideally require an infinite resolution, i.e., infinitely small voxel size. It is important to distinguish between the digital resolution of an image, i.e., the voxel size, and the effective resolution that can be achieved by an imaging device. The latter is limited by technical constraints such as sensor size, aperture size, motion blur, size of a "point" light source, scanning duration, or the reconstruction algorithm and is typically coarser than the digital resolution. Seen from the other side, the digital resolution should always be higher than the effective resolution to not lose any valuable information. The blurring effect caused by the physical constraints can be thought of as a smoothing operation that is applied to the true image during the process of acquisition. The result of scanning a (theoretically infinitely) small object is called the

"point spread function" (PSF) of a device. For many devices, it can be approximated by a Gaussian filter whose full width at half maximum (FWHM) is a good indication of the effective resolution. This limit of resolution through physical constraints is often also called partial volume effect; however, "intensity diffusion" would be a better term (Skretting 2009). It has a larger relative effect on small objects which will appear larger or may be smoothed away completely into the background. In particular, in combination with thresholding, this will lead to an under- or overestimation of the size of small objects. For many devices, it is possible to reduce the noise by increasing the scanning duration or to trade off noise against resolution, by configuring the reconstruction. The optimal decision may depend on the type of analysis that is intended, however.

19.2.4 Metadata

Other properties like the type of device, date of acquisition, subject name, capturing protocol, room temperature, etc., are called metadata. Information about the position and orientation of the field of view is particularly important for automated image fusion because the field of view is not necessarily identical for the involved modalities. Many image file formats do not foresee storage of metadata, however.

19.3 Image Transformation and Fusion

In many situations, an image transformation such as upsizing, downsizing, or rotation is necessary for processing, registration, or visualization. Several problems can arise with respect to a quantitative evaluation, however.

19.3.1 Resizing

In vivo μCT images can have sizes of several GB which poses a challenge for many analysis tools due to limited memory and processing power. The situation is even more aggravated for ex vivo μCT scanners which can generate images with several hundred GB (Ehling et al. 2014a). To allow analysis with available software and computers, these images can be down-sampled, e.g., by averaging (binning) eight neighboring voxels into one larger voxel. This increases the voxel size by a factor of two in each dimension and therefore reduces the number of voxels and the total memory size by a factor of eight. Consequently, the image looses fine details but also the noise is reduced. If this down-sampling is performed multiple times, it results in an image pyramid. Storage overhead of the pyramid is usually negligible, i.e., around 15 % more compared to the original image, because the size of the lower levels decreases exponentially. Particularly for whole-animal organ analysis, a reduced resolution (e.g., 140 μm) is often sufficient (Gremse et al. 2014). If the fine-grained structure of a region, e.g., the bone trabecula, needs to be analyzed, cropping may be a solution to reduce the image size by focusing on a relevant part only.

19.3.2 Affine Transformations

During analysis image data sets might have to be resized, rotated, translated, flipped, or more generally transformed by an affine transform. Registration of scans from two different devices can also be achieved through an affine transform. Any combination of rotation, translation, isotropic scale, anisotropic scale, and shear transformations can be combined into one affine transformation, which can be expressed with 12 parameters in 3D. Any combination of rotations, translations, and isotropic scaling results in a rotate, scale, and translate (RST) transform, which is a special affine transform. RST transforms require seven parameters and preserve angles. This can be further restricted to a rigid body transformation which consists only of rotation and translation and requires six parameters in 3D. Aligning two partial scans from one device might require only a translation which also is a special affine transformation. These four groups, affine transformation, RST, rigid

transformation, and translation, are closed under composition, which means that any sequential composition of two or more transformations results in a transformation of the same group.

19.3.3 Image Registration

Rigid body transformations are commonly used for registration of multimodal images because the geometric scaling factor is known and determined by the voxel size. Affine transformations or RST transformations should be avoided because they would estimate a different scaling factor than the one which is given by the voxel sizes. The parameters of the transformation can be estimated using markers or some minimization criterion based on the pixel intensities. For a rigid body transformation, at least three corresponding markers are required in each of the two data sets. To get an accurate transformation, markers should be chosen that are as distant as possible from each other and are not positioned along a line. Selecting more than three markers further reduces the alignment error. The average registration error is region dependent and can be estimated using phantom studies or approximated from the markers. After computing the transformation between multimodal images, e.g., μCT and FMT (Doleschel et al. 2012), one image can be resampled to match the voxel size and field of view of the other. Alternatively the transformation can be stored as metadata and considered during analysis.

19.4 Parametric Fitting

Many imaging modalities do not provide voxel intensities with a calibrated unit. For MRI images, the intensity may depend on the position inside the coil, for example. Therefore, the intensities cannot directly be used for quantitative measurements. Parametric fitting may be an adequate solution to derive quantitative voxels. Usually, this technique requires 4D images, where the fourth dimension may be the time or another parameter that is varied. Then the intensities over time are described as a parametric function, e.g., as mono-exponential curve. By linear or nonlinear fitting, the parameters that best match the actual measurements are computed. If this is performed for each voxel, parametric maps can be generated and visualized. Alternatively, the fitting can be performed after segmentation, i.e., for the average values of a given segment.

19.4.1 MRI Relaxometry

For magnetic resonance images, the voxel intensities of T1- and T2-weighted images depend on many factors, including the proton density, the relaxivity, and the position in the coil. MRI relaxometry is a technique to derive quantitative T1, T2, and T2* relaxation times and is clinically used to image multiple sclerosis, liver iron content, and acute myocardial infarction (Cheng et al. 2012). For T2-weighted images, the signal falls off exponentially with increasing echo time (Fig. 19.4). This can be modeled by a mono-exponential curve $y = ae^{(-\mathrm{R2}*\mathrm{TE})}$, where TE is the known echo time, a is the amplitude, and $\mathrm{R2} = 1/\mathrm{T2}$ the relaxivity, i.e., the inverse relaxation T2 time. By performing parametric fitting, the relaxivity is determined quantitatively, i.e., in [1/s], while the amplitude describes the other factors such as position-dependent sensitivity and the proton density. By using logarithmic conversion, the R2 value can be computed by fast linear fitting; however, severe problems arise in practical applications due to noise. Therefore, iterative nonlinear fitting is advised (Otto et al. 2011). Even then, noise may cause systematic errors which may put segment-wise approach at an advantage over voxel-wise modeling, because larger segments have lower noise levels than voxels (Marro et al. 2011). Recently, a model was proposed that corrects for noise by including it into the model, however (Feng et al. 2013).

T1 relaxometry is more complicated because the T1-based signal recovers as a function of the repetition time. Furthermore, the acquisition may be prolonged because each measurement has an effect on the proton flip angle, and long pauses are required for total relaxation after reading each

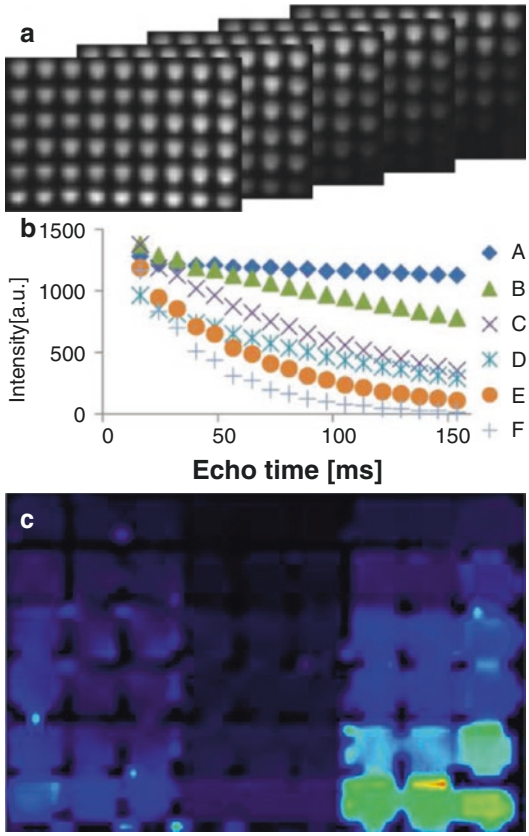

Fig. 19.4 Parametric fitting for MRI relaxometry. (**a**) T2-weighted images of a well plate filled with contrast agent dilutions. Images are acquired at different echo times. The voxel intensity depends on the R2 relaxivity but also on other effects, e.g., the position in the coil and the partial volume effect. (**b**) Voxel intensities of the rightmost column are plotted as function of the echo time. These curves are modeled as parameterized exponential functions $y = ae^{(-R2*TE)}$). (**c**) The R2 relaxivity is determined for each voxel and shown as a parametric map. The influence of the position in the coil and the partial volume effect is removed

line in k-space. There are faster methods, however, which take this interaction into account (Deichmann et al. 1999).

19.4.2 Diffusion-Weighted Imaging

Diffusion-weighted imaging (DWI) is a special MRI technique to image the degree of diffusion of water molecules, e.g., cysts result in lower signal than tumors, because in the latter the water cannot diffuse as freely because of the cell membranes (Taouli and Koh 2010). DWI is widely clinically applied for abdominal and, in particular, liver imaging where it is more sensitive for focal liver lesion detection than other MRI imaging methods, e.g., T2-weighted turbo spin echo methods (Morana et al. 2008). The voxel intensities depend on many influencing factors, however, but they can be described with the formula $y = ae^{-b*ADC}$ with the known gradient factor b, the amplitude a, and the apparent diffusion coefficient (ADC). Then amplitude and ADC can be determined by parametric fitting, similar as for T2 relaxometry. Voxels usually contain multiple tissue types due to the partial volume effect, e.g., tumor tissue and blood vessels. Then the fitted apparent diffusion coefficient (ADC) contains two effects inside the voxel, the actual diffusivity of the tumor tissue and an additional effect caused by the blood perfusion. Therefore, the ADC is systematically higher than the true diffusion coefficient of the soft tissue. To compensate for this, a model with two additive exponential functions can be used (Yamada et al. 1999).

19.4.3 Contrast-Enhanced Ultrasound

Ultrasound contrast agents are predominantly used for intravascular imaging, since they hardly extravasate. Not only microbubbles provide signal; however, the signal from regular tissue is quite strong already. To avoid repositioning, one cineloop is usually acquired during injection and the enhancement phase, while the anesthetized mouse is kept in a fixed position. Unfortunately, there still are breathing artifacts, and sometimes the mouse is irritated by the injection and twitches, which complicates the analysis. The region of interest, e.g., a tumor, can be segmented and the mean intensity be plotted as function over time. The curve appears to consist of three phases, a plateau before injection, a phase of rising intensity during injection until the bubbles are well distributed in the blood, and another plateau which slowly decreases because the bubbles are cleared from the blood eventually. The user can

select beginning and end of the increasing phase to compute parameters such as the enhancement which correlates with the relative blood volume. To enable a more user-independent analysis, an approach was developed which automatically fits a three-segment curve to the measurements (Rix et al. 2014). The free parameters are the two kink positions and the levels of the two plateaus. The fitting algorithm exhaustively searches through the kink positions. For each pair, it determines the means of the plateaus, connects the plateaus with a linearly increasing segment for the rising phase, and computes the squared error between the three-segment curve and the measurements. Off all pairs, the parameters with minimal squared error are chosen. A variant of the algorithm determines the median instead of the mean to be more robust to outliers caused by twitching and breathing. Based on the fitted three-segment curve, the enhancement, time to peak, slope, and area under the curve are computed in a more user-independent way than when the user would have to position the plateaus himself.

19.4.4 Kinetic Modeling

Kinetic modeling is the most complex parametric fitting technique discussed in this chapter. Its purpose is to analyze the behavior of probes with low molecular weight which diffuse into and out of the interstitial space and eventually accumulate in specific regions such as tumors. Mice are scanned during and after intravenous injection to acquire a four-dimensional image set, i.e., multiple 3D images over time. The contrast agent interchanges between the tissue compartments, i.e., blood, interstitial space, and tumor cells, either by diffusion or active transport. After some time, the blood level drops below the interstitial level because the contrast agent is usually cleared via kidneys and liver. Then the contrast agent diffuses from the interstitial space back into the blood. If it was possible to measure both blood concentration and interstitial concentration, the latter would appear to follow the blood concentration with a certain delay. A kinetic model describes the exchange between compartments with certain exchange rates that correspond to physiologic parameters. Unfortunately, the concentration in the interstitial space cannot be measured directly, because voxels contain an unknown amount of blood vessels which are below the resolution of the scanner. Therefore, the measured intensity of a voxel represents a mixture of the blood concentration and the tissue concentration. Fortunately, it is possible to measure the pure blood concentration, called the arterial input function (AIF), by placing a region into a large artery or even the heart. The task of kinetic model fitting is then to derive the model parameters from the measurement curve and the AIF which poses an iterative nonlinear optimization problem (Kadrmas and Oktay 2013). If the model is well selected, the estimated parameters correspond to physiological parameters such as relative blood volume, blood flow, blood perfusion, permeability, metabolic rate, or receptor expression levels (Hoff 2011).

For MRI and CT contrast agents, which typically do not accumulate in cancer cells, two-tissue compartment models are used, i.e., one compartment for the blood and one for the tissue where the contrast agent diffuses into (Brix et al. 2004; Kiessling et al. 2007). Using this approach, it is possible to assess the tumor vascularization and how it changes during antiangiogenic therapy (Pöschinger et al. 2014). For PET tracers, models with three compartments are frequently used to assess the specific binding and accumulation (Fig. 19.5). Besides the blood compartment, these models include a compartment for the interstitial space and the intracellular space; therefore, they are also called two-tissue compartment models instead of three-compartment models (Innis et al. 2007).

19.5 Segmentation

Segmentation is the process of defining regions of interest (ROIs) such as organs and lesions in images. It is an intermediate step to derive quantitative measurements such as volumes or mean intensities of ROIs.

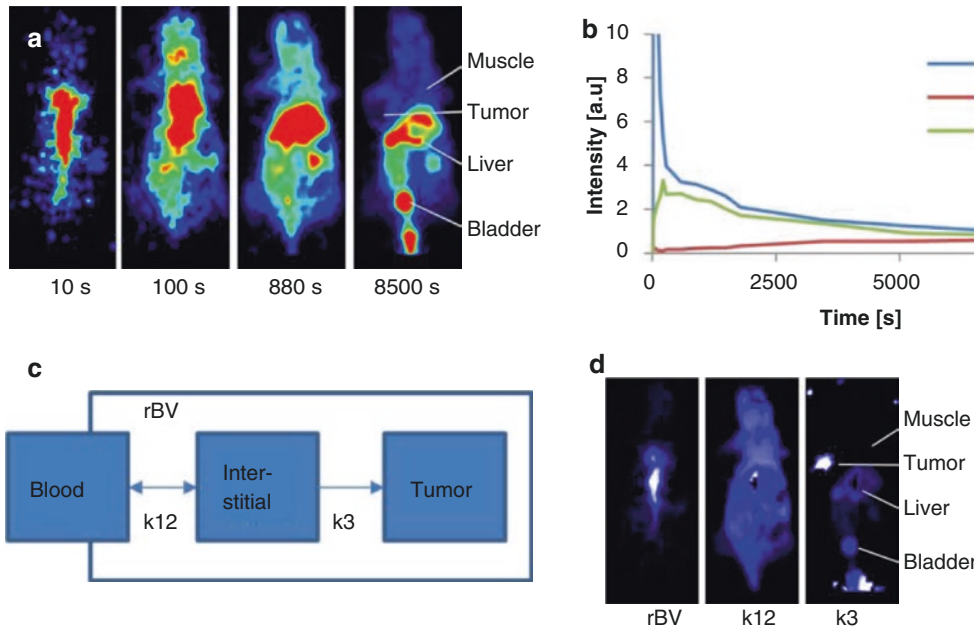

Fig. 19.5 Kinetic modeling. (**a**) Coronal slices through a PET scan of a mouse at multiple time points after intravenous injection of a tracer that accumulates in hypoxic tissues. The mouse has a large and poorly blood-perfused tumor on the shoulder which is hardly visible. (**b**) Voxel intensities of different tissue regions are plotted as function of measurement time. The arterial input function (AIF) is derived from a large blood vessel. The tracer slowly accumulates in the tumor. (**c**) The behavior of the tracer is modeled using a three-compartment model. The exchange rate between the blood and interstitial space is assumed to be symmetric and the exchange between interstitial space and tumor is irreversible, resulting in three degrees of freedom (*rBV* or relative blood volume, k12, and k3). (**d**) Model fitting is performed for each voxel to compute parametric maps. The tumor appears hyperintense in the k3 map due to the irreversible accumulation

19.5.1 Types of ROIs

Two different types of ROIs are commonly used, geometric ROIs and voxel-wise segmentations. Geometric ROIs are defined by geometric primitives such as spheres, ellipses, boxes, or cylinders. A 3D sphere, for example, is defined as the set of points within a certain distance from a center point. This sphere has four parameters, i.e., three for the center point and one for the radius. Many programs, e.g., the free software AMIDE (Loening and Gambhir 2003), allow manual definition of simple geometric ROIs. These simple ROIs are typically entered by the user through clicking and dragging until covering the desired region. They are well suited for simple cases, but to cover more complicated shapes, a voxel-wise segmentation is advantageous (Gremse et al. 2015).

A voxel-wise segmentation is a subset of the voxels and is typically represented as a binary mask or integer mask if multiple segmentations are required. Each segment is given a class name, e.g., liver, kidney, or tumor. If the segments do not overlap, the segmentation is called a partition.

19.5.2 Interactive Segmentation

One common approach to perform segmentation is to create and adjust the ROIs interactively (Gremse et al. 2016). A set of intuitive interactive operations, which can be combined in a flexible way, can solve the needs for many small animal imaging studies (Gremse et al. 2015). The combination of thresholding, cutting, and region growing is useful for bone and lung segmentation in μCT images, for example. Bones appear as

hyperintense regions in µCT images due to their strong x-ray absorption. Other bright regions may be metal implants or minerals in the stomach and intestine (Fig. 19.6). By thresholding, these bright regions can be segmented. Region growing is an operation that requires a seed point provided by the user and determines the connected subset of a segmented region. It can be used to separate the large connected parts of the skeleton from the smaller bright spots in the stomach and intestine. Another example is the lung which can be segmented in µCT images by a sequence of thresholding, cutting, and region growing because it is a dark region that is only connected to the outer dark air through the trachea.

Regions with a convex shape such as the bladder and kidneys can be segmented by manually delineating their boundaries by drawing so-called scribbles (Fig. 19.7). The interactive segmentation software then connects the scribbles in 3D and fills them to determine the convex shape. For organs whose boundaries are visible in µCT, this approach enables a more user-independent segmentation and analysis of µCT-FMT images compared to a workflow without anatomical reference data from µCT (Kunjachan et al. 2013).

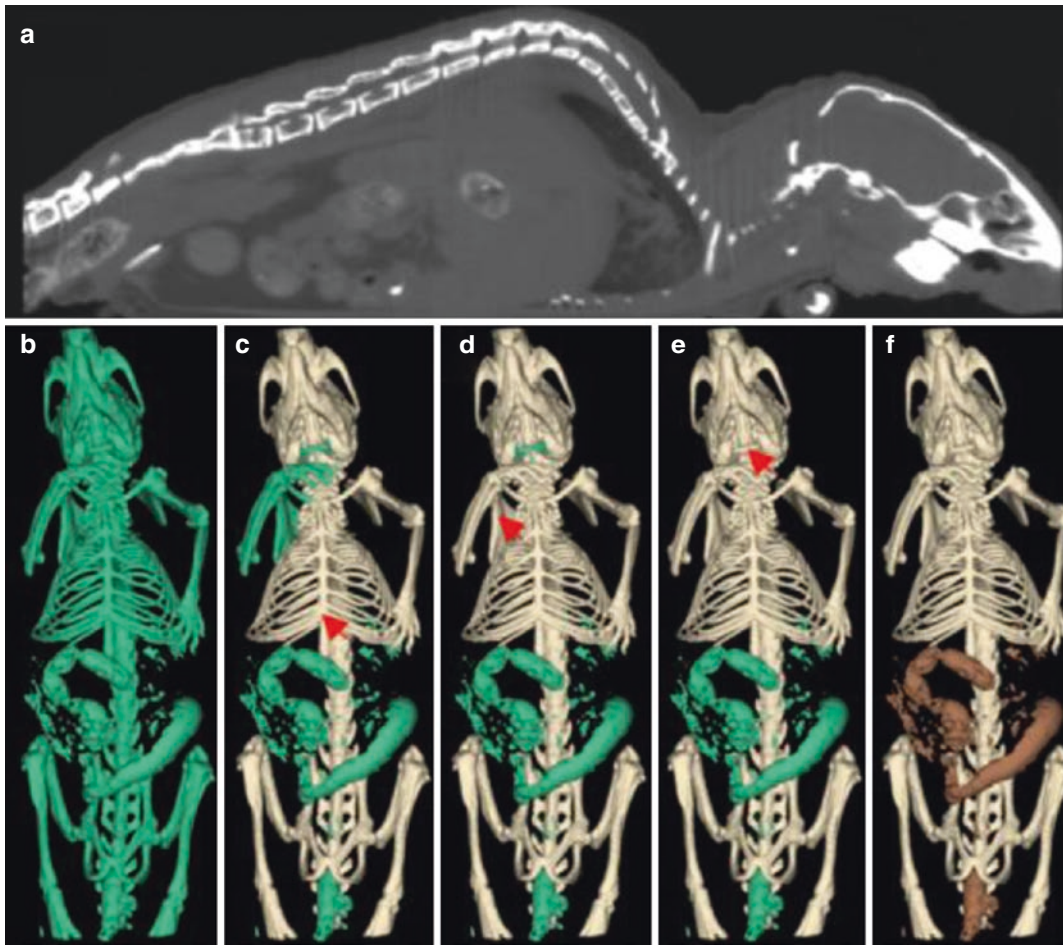

Fig. 19.6 Thresholding and region growing. (**a**) Sagittal slice through a native µCT scan of a mouse. Bones and feces appear bright. (**b**) Bones and feces are segmented into a green temporary class by thresholding. (**c**) A part of the skeleton is segmented by region growing (seed point is the *red arrow*). (**d**, **e**) More components of the skeleton are segmented by region growing. (**f**) The remaining regions are assigned to the feces class (*brown*). The software for interactive segmentation is described in Gremse et al. 2016

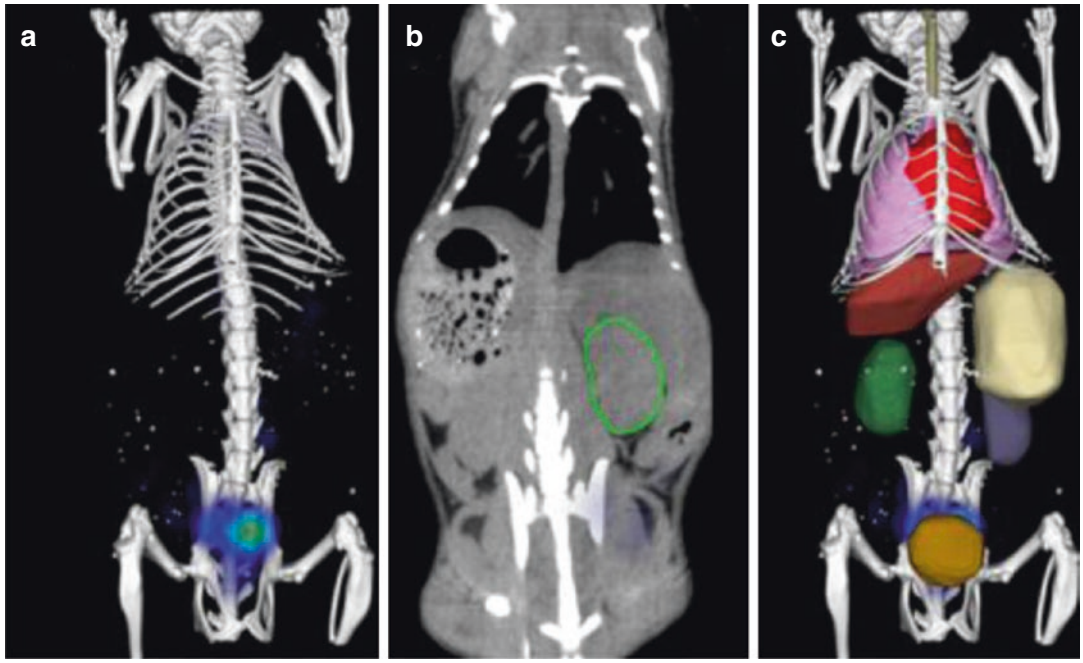

Fig. 19.7 Interactive ROI definition. (**a**) Fused µCT–FMT data sets with high accumulation in the urinary bladder. µCT and FMT data sets are registered through a geometric transformation. (**b**) Organs are interactively segmented by delineating the organ boundaries using the µCT data. (**c**) Each region of interest (ROI) is defined by a voxel mask. The amount of fluorescent probe in a particular ROI is computed by iterating over the voxels of the ROI and fetching the fluorescence concentration through the geometric transformation (Data from Gremse et al. (2015))

Many studies require assessment of the state of the vasculature or its change as consequence of pathologies. For µCT, the use of a blood pool contrast agent is necessary to distinguish blood from the surrounding soft tissue. Clinical contrast agents who rely on fast renal clearance to reduce toxic side effects are rarely suitable because the mouse metabolism is much faster than the human metabolism and preclinical devices are much slower than clinical ones. Therefore, long circulating blood pool contrast agents have been developed (de Vries et al. 2010). The blood vessels appear enhanced and can be segmented using thresholding (Fig. 19.8). This approach cannot capture small blood vessels, e.g., capillaries, because these are far below the resolution of in vivo µCTs. The effect of large and small vessels on the relative blood volume (rBV) can be assessed indirectly, however, because even small blood vessels contribute to the overall enhancement of a region, such as the tumor. To determine the rBV quantitatively, the enhancement of the region is determined by subtracting the pre-injection intensity and computing the ratio of the tumor enhancement and the enhancement of pure blood which can be determined from a large blood vessel (Ehling et al. 2014b).

19.5.3 Automated Segmentation

Interactive segmentation can be used for many different studies, but several problems persist. First, an amount of user dependence remains because the segmentation often depends at least partially on subjective estimations or on a particular workflow the user is accustomed to. Second, in many experiments, a large number of data sets are generated which all need to be segmented independently because the mouse is repositioned over and over again. This is particularly relevant

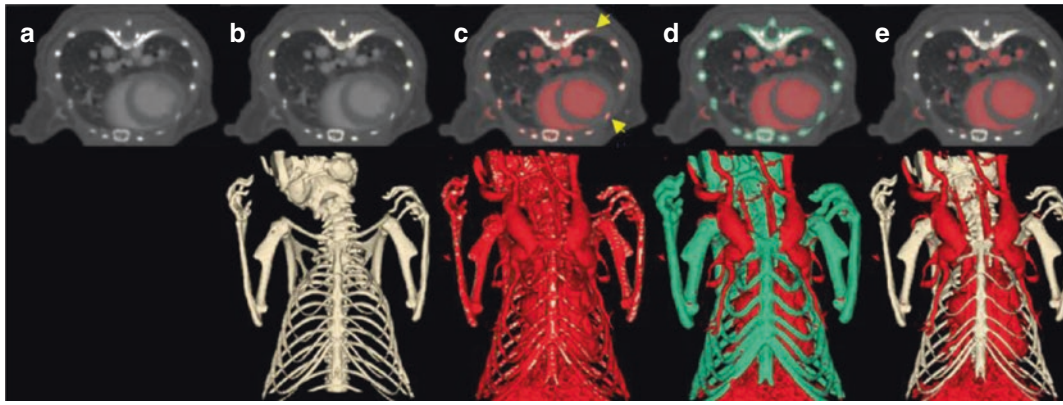

Fig. 19.8 Segmentation of large blood vessels in µCT images. (**a**) Transversal slice through a murine chest showing the rib cage, lungs, and heart. Blood appears brighter than other soft tissues due to the use of a blood pool µCT contrast agent. (**b**) Bones are segmented using a high threshold; the 3D segmentation is shown on the bottom. (**c**) Blood vessels are segmented by applying a second threshold between soft tissue intensity and the blood intensity. Due to the smooth intensity transition, a thin region around the bones is misclassified as blood vessels. (**d**) This is corrected by applying a coating operation on the bone class which results in a temporary green class. (**e**) The temporary class is removed showing the result. This approach fails to find small blood vessels and blood vessels that are very close to bones, however. The imaging protocol is described in Gremse et al. (2011)

for longitudinal µCT-FMT experiments where multiple mice of different groups are scanned at several time points (Kunjachan et al. 2014). Therefore, automated whole-animal segmentation software would be very useful to reduce effort and potential user-dependent bias. Previous attempts involved a so-called atlas, i.e., a known segmentation of one or more example scans, which is transformed to the data at hand (Baiker et al. 2010; Gutierrez and Zaidi 2012). Usage of an atlas is likely to introduce bias when anatomical abnormalities such as pathologies occur, however. Another approach (Fig. 19.9) uses a set of intuitive rules in combination with anatomical and functional image data (Baatz et al. 2009). Particularly for µCT, automated segmentation is difficult because of low soft tissue contrast. Fatty mice which are commonly used for cardiovascular research provide an advantage because fat and other soft tissues can be discriminated well in MRI and µCT and provide a contrasted boundary around the other organs (Ranefall et al. 2009; Li et al. 2014). Oncologic mouse models are rather lean, however, which is further aggravated by side effects of chemotherapies. Contrast agents may help to separate organ boundaries, but the contrast agent has its own kinetic which complicates the usage for longitudinal imaging. Therefore, robust whole-animal segmentation remains to be an unsolved challenging problem.

19.6 Statistical Testing

The previous sections explained how quantitative or at least comparable measurements can be extracted from preclinical images. To derive a qualitative and "significant" statement, a statistical test needs to be selected and applied. In the following, a basic overview over the most common statistical tests in the context of small animal imaging is given. A thorough treatment can be found in established sources such as Lane (2006), Motulsky (2007), and Lehmann and Romano (2008).

19.6.1 Principle of Statistical Tests

All image-derived measurements contain a random error, e.g., caused by operator-dependent handling or electronic noise. Furthermore, the

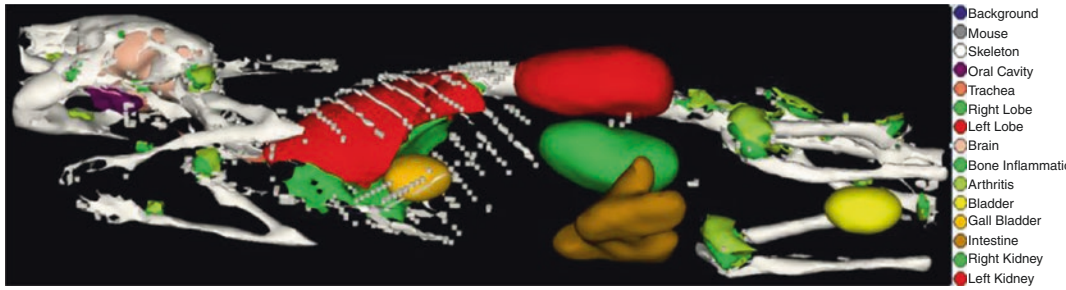

Fig. 19.9 Automated segmentation. Fully automated segmentation of a mouse scanned with a SPECT/CT device using the Tc99m-GCA tracer. The algorithm was developed by Baatz et al. (2009) and used 11 mice to compute volume and tracer activities of regions such as the skeleton, brain, kidney, lungs, and bladder

biologic variability is a considerable source of variance. Therefore, the comparison of single measurements, e.g., the tumor sizes of one treated vs. one control animal, is rarely useful. Instead, multiple animals are required to estimate the means of measurements which will be more accurate the more animals are used. Still, one mean will always be higher than the other, and it remains unclear whether this is caused by the effect under investigation or by chance through the incurred randomness. The purpose of a statistical test is to resolve this question by estimating the probability that the measurements occur by chance only, i.e., without any real difference between the groups. This probability is called the *P* value of the test and the assumption that there is no difference is called the null hypothesis. A low *P* value, below a significance level of, e.g., 0.05, i.e., 5 %, means that there probably is a difference because the measurements would be too unlikely if there was no difference. Then the difference between groups is called significant. A high *P* value on the other hand does not prove the absence of a difference; it just means that the experiment and the statistical test failed to prove a difference, maybe because too few animals were used. The mentioned value of 0.05, i.e., 5 %, is called a significance level. Typical significance levels are 5, 1, and 0.1 %, which are commonly indicated by one to three stars in a chart. The probability to achieve a significant *P* value, which is often required for a publishable result, depends on several aspects. First, a strong effect is more likely to result in significant *P* values than a weak effect. Furthermore, the probability to achieve a significant result can be increased by using more animals or by reducing or eliminating sources of variance.

Usually, statistical tests require that independent measurements are used. This means that any random factors acting on one value have no effect on other values. Therefore, repeated measurements of the same animal are not independent. It is however possible to average multiple measurements from the same animal to reduce the noise, and then use these averages as input for the statistical test.

19.6.2 Tests for Two Groups

The most often used statistical test is the *t*-test, or student's *t*-test, which was published by William Gosset in 1908 under the synonym "student" because using statistics was considered a trade secret by his employer, the Guinness brewery in Dublin. The *t*-test can be used to test if the means of two groups differ significantly, i.e., not just by chance. The null hypothesis is that the true means are identical. There are variants for paired and unpaired samples. Paired samples are measurements with a strict one-to-one association, e.g., tumor volumes before and after treatment that were noninvasively measured in the same animal. An example for unpaired data is the tumor volume of treated and untreated animals. The paired *t*-test should be used for paired samples because it is stronger than the unpaired *t*-test, i.e., more likely to generate a significant *P* value. Both variants of the *t*-test assume that the samples are

Table 19.1 Statistical tests for two groups

	Parametric	Nonparametric
Paired	Paired *t*-test	Wilcoxon test
Unpaired	Unpaired *t*-test	Mann–Whitney test

Paired tests require paired data, e.g., the probe uptake of tumor and liver within the same mouse. Unpaired tests are used to compare data of different groups, e.g., tumor sizes of treated and untreated animals. Parametric tests are stronger, i.e., require less samples, if the values have a normal distribution, but may fail for values without normal distribution

drawn from a normal distribution, however. Therefore, they are called parametric tests because the normal distribution can be described with two parameters, mean and standard deviation. While the *t*-tests are the strongest possible tests for normally distributed samples, their power is impaired by off-scale samples, or "outliers," or simply when the sample distributions differ much from a normal distribution. In such cases, nonparametric tests such as the Wilcoxon test and the Mann–Whitney test may be more powerful, which are for paired and unpaired data, respectively (Table 19.1). These tests sort the measurement values and operate on the ranks, i.e., the order established by the sorting. This makes them robust to off-scale values, but on the other hand the information about the magnitude of the samples is lost. Nonparametric tests that apply such a rank conversion are therefore less powerful than their parametric counterparts, i.e., may require more samples to result in a significant *P* value.

The choice about which statistical test to use should be made during the experimental design phase, however. If all possible tests are tried during analysis until a significant result is found, this is likely to be misleading.

19.6.3 Multiple Groups

Special care is advised if many groups are compared. If the *t*-test or the Mann–Whitney test is used to compare each group to each other, this may lead to some significant *P* values just by chance, especially if there are many comparisons. Therefore, special multigroup tests should be used, such as one-way ANOVA and the *Kruskal–Wallis test*, which are extensions of the *t*-test, and Mann–Whitney test for multiple groups, respectively. A low *P* value of a multigroup test means that differences exist between some groups, but it does not mean that all groups differ significantly to each other. This can be checked by a posttest. A simple and conservative method is the *Bonferroni correction*, which multiplies the *P* values by the number of comparisons. The Bonferroni correction results in a loss of power, however, particularly if many groups are involved. The Tukey posttest is a more powerful alternative to the Bonferroni correction. The Dunnett posttest can be used if there is one control group against which the other groups are compared and is even more powerful. If the groups are arranged in a natural order, e.g., over time, a test for linear trends can be used (Motulsky 2007). All posttests have a reduced power compared to a two-group test, however, and this means that adding more groups should be compensated by increasing the number of animals per group.

19.6.4 Correlative Tests

All tests mentioned so far are meant to test for differences between sample sets. Often, a relationship, i.e., statistical dependency, between two measurements is hypothesized, e.g., between the relative blood volume and the drug accumulation in a tumor (Theek et al. 2014). Another example is to compare noninvasive measurements with results from histology from the same subject to show that one is related to the other or can even be replaced if the dependence is strong enough. Measurements are statistically dependent if the chances at guessing one can be improved knowing the other which means that there has to be some kind of connection between them. If the relationship is linear, it can be characterized using Pearson's correlation analysis. In order to visualize the correlation, the bivariate measurements can be plotted as scatter plots. The strength of the correlation is described by the coefficient of determination r^2, a value between 0

and 1. If r^2 is 1, then there is a direct functional dependency between the measurements. If there is no statistical dependency between the variables, r^2 will converge toward 0. Even a high r^2 can occur by mere chance, particularly if there are few measurements only. To test this, a P value can be computed, and a low P value indicates an actual statistical dependency between the variables. Similar to the t-test, the Pearson's correlation is optimal for normally distributed samples. The Spearman correlation is a nonparametric alternative that is more robust to deviations from the normal distributions. Sometimes, two r^2 need to be compared, e.g., to show that a semiautomated method results in stronger correlation between users than a manual method (Gremse et al. 2011). Then the Fisher z-test can be used to test if this difference is significant.

References

Abou-Elkacem L, Gremse F, Barth S, et al. Comparison of µCT, MRI and optical reflectance imaging for assessing the growth of GFP/RFP-expressing tumors. Anticancer Res. 2011;31:2907–13.

Baatz M, Zimmermann J, Blackmore CG. Automated analysis and detailed quantification of biomedical images using definiens cognition network technology. Comb Chem High Throughput Screen. 2009;12:908–16.

Baiker M, Milles J, Dijkstra J, et al. Atlas-based whole-body segmentation of mice from low-contrast micro-CT data. Med Image Anal. 2010;14:723–37.

Brix G, Kiessling F, Lucht R, et al. Microcirculation and microvasculature in breast tumors: pharmacokinetic analysis of dynamic MR image series. Magn Reson Med. 2004;52:420–9.

Cheng H-LM, Stikov N, Ghugre NR, Wright GA. Practical medical applications of quantitative MR relaxometry. J Magn Reson Imaging. 2012;36:805–24.

De Vries A, Custers E, Lub J, et al. Block-copolymer-stabilized iodinated emulsions for use as CT contrast agents. Biomaterials. 2010;31:6537–44.

Deichmann R, Hahn D, Haase A. Fast T1 mapping on a whole-body scanner. Magn Reson Med. 1999;42:206–9.

Doleschel D, Mundigl O, Wessner A, et al. Targeted near-infrared imaging of the erythropoietin receptor in human lung cancer xenografts. J Nucl Med Off Publ Soc Nucl Med. 2012;53:304–11.

Ehling J, Bartneck M, Wei X, et al. CCL2-dependent infiltrating macrophages promote angiogenesis in progressive liver fibrosis. Gut. 2014a;63:1960–71.

Ehling J, Theek B, Gremse F, et al. Micro-CT imaging of tumor angiogenesis: quantitative measures describing micromorphology and vascularization. Am J Pathol. 2014b;184:431–41.

Feng Y, He T, Gatehouse PD, et al. Improved MRI R2 * relaxometry of iron-loaded liver with noise correction. Magn Reson Med. 2013;70:1765–74.

Gremse F, Grouls C, Palmowski M, et al. Virtual elastic sphere processing enables reproducible quantification of vessel stenosis at CT and MR angiography. Radiology. 2011;260:709–17.

Gremse F, Theek B, Kunjachan S, et al. Absorption reconstruction improves biodistribution assessment of fluorescent nanoprobes using hybrid fluorescence-mediated tomography. Theranostics. 2014;4:960–71.

Gremse F, Doleschel D, Zafarnia S, et al. Hybrid µCT-FMT imaging and image analysis. J Online Vis Exp. 2015;100:52770.

Gremse F, Stärk M, Ehling J, et al. Imalytics Preclinical: Interactive Analysis of Biomedical Volume Data. Theranostics. 2016;6(3):328–41.

Gutierrez DF, Zaidi H. Automated analysis of small animal PET studies through deformable registration to an atlas. Eur J Nucl Med Mol Imaging. 2012;39:1807–20.

Innis RB, Cunningham VJ, Delforge J, et al. Consensus nomenclature for in vivo imaging of reversibly binding radioligands. J Cereb Blood Flow Metab. 2007;27:1533–9.

Kadrmas DJ, Oktay MB. Generalized separable parameter space techniques for fitting 1K–5K serial compartment models. Med Phys. 2013;40:072502.

Kiessling F, Jugold M, Woenne EC, Brix G. Non-invasive assessment of vessel morphology and function in tumors by magnetic resonance imaging. Eur Radiol. 2007;17:2136–48.

Kunjachan S, Gremse F, Theek B, et al. Noninvasive optical imaging of nanomedicine biodistribution. ACS Nano. 2013;7:252–62.

Kunjachan S, Pola R, Gremse F, et al. Passive versus active tumor targeting using RGD- and NGR-modified polymeric nanomedicines. Nano Lett. 2014;14:972–81.

Lane DM Online statistics education: a multimedia course of study (http://onlinestatbook.com/). Rice University. 2006.

Lehmann EL, Romano JP. Testing statistical hypotheses. 3rd ed. New York: Springer; 2008.

Li X, Zhu M, Penfold ME, et al. Activation of CXCR7 limits atherosclerosis and improves hyperlipidemia by increasing cholesterol uptake in adipose tissue. Circulation. 2014;129:1244–53.

Loening AM, Gambhir SS. AMIDE: a free software tool for multimodality medical image analysis. Mol Imaging. 2003;2:131–7.

Marro K, Otto R, Kolokythas O, et al. A simulation-based comparison of two methods for determining relaxation rates from relaxometry images. Magn Reson Imaging. 2011;29:497–506.

Morana G, Cugini C, Mucelli RP. Small liver lesions in oncologic patients: characterization with CT, MRI and contrast-enhanced US. Cancer Imaging. 2008;8(Spec No A):S132–5.

Motulsky HJ. Prism 5 statistics guide. San Diego: GraphPad Software Inc.; 2007.

Otto R, Ferguson MR, Marro K, et al. Limitations of using logarithmic transformation and linear fitting to estimate relaxation rates in iron-loaded liver. Pediatr Radiol. 2011;41:1259–65.

Pöschinger T, Renner A, Eisa F, et al. Dynamic contrast-enhanced micro-computed tomography correlates with 3-dimensional fluorescence ultramicroscopy in antiangiogenic therapy of breast cancer xenografts. Invest Radiol. 2014;49:445–56.

Ranefall P, Bidar AW, Hockings PD. Automatic segmentation of intra-abdominal and subcutaneous adipose tissue in 3D whole mouse MRI. J Magn Reson Imaging. 2009;30:554–60.

Rix A, Palmowski M, Gremse F, et al. Influence of repetitive contrast agent injections on functional and molecular ultrasound measurements. Ultrasound Med Biol. 2014;40:2468–75.

Skretting A. "Intensity diffusion" is a better description than "partial volume effect". Eur J Nucl Med Mol Imaging. 2009;36:536–7.

Taouli B, Koh D-M. Diffusion-weighted MR imaging of the liver. Radiology. 2010;254:47–66.

Theek B, Gremse F, Kunjachan S, et al. Characterizing EPR-mediated passive drug targeting using contrast-enhanced functional ultrasound imaging. J Controlled Release. 2014;182:83–9.

van den Hoff J. Kinetic modelling. In: Kiessling PDF, Pichler PDBJ, editors. Small anim. Imaging. Berlin/Heidelberg: Springer; 2011. p. 387–403.

Yamada I, Aung W, Himeno Y, et al. Diffusion coefficients in abdominal organs and hepatic lesions: evaluation with intravoxel incoherent motion echo-planar MR imaging. Radiology. 1999;210:617–23.

Guidelines for Nuclear Image Analysis

20

Martin S. Judenhofer, Stefan Wiehr,
Damaris Kukuk, Kristina Fischer,
and Bernd J. Pichler

Contents

M.S. Judenhofer (✉)
Department of Biomedical Engineering,
University of California Davis,
One Shields Avenue, Davis, CA 95616, USA
e-mail: msjudenhofer@ucdavis.edu

S. Wiehr • D. Kukuk • K. Fischer • B.J. Pichler
Werner Siemens Imaging Center, Department of Preclinical Imaging and Radiopharmacy, Eberhard Karls University Tübingen, Tübingen, Germany

20.1 Quantitative Image Analysis

The information of nuclear emission images depends mainly on the used radiolabeled biomarker, which interacts – in an ideal case – specifically with the in vivo target. Although several sections of this chapter are applicable for single-photon emission computed tomography (SPECT), the major focus of this chapter is on positron emission tomography (PET) imaging since accurate quantification is more complicated in SPECT which is why SPECT is often considered as a semiquantitative imaging modality. Figure 20.1 shows examples of PET images of the same rat, scanned on 2 consecutive days with different tracers, the glucose analog ^{18}F-FDG and the proliferation marker ^{18}F-FLT. The rat bears a xenograft tumor on the right flank. Figure 20.1 clearly shows the strength of PET imaging, which delivers information based on the molecular target of the tracer. However, it depicts also a major weakness of PET, which is the limited availability of anatomical references. This drawback makes the quantitative analysis sometimes very difficult as the tumor size, displayed in the image, does not only depend on the physical lesion size and metabolic rate but also on the image contrast, noise, as well as the chosen upper and lower image intensity threshold for display. Figure 20.2 highlights this effect and shows an example of a rodent displayed at two different upper thresholds using an image analysis software.

F. Kiessling et al. (eds.), *Small Animal Imaging*, DOI 10.1007/978-3-319-42202-2_20

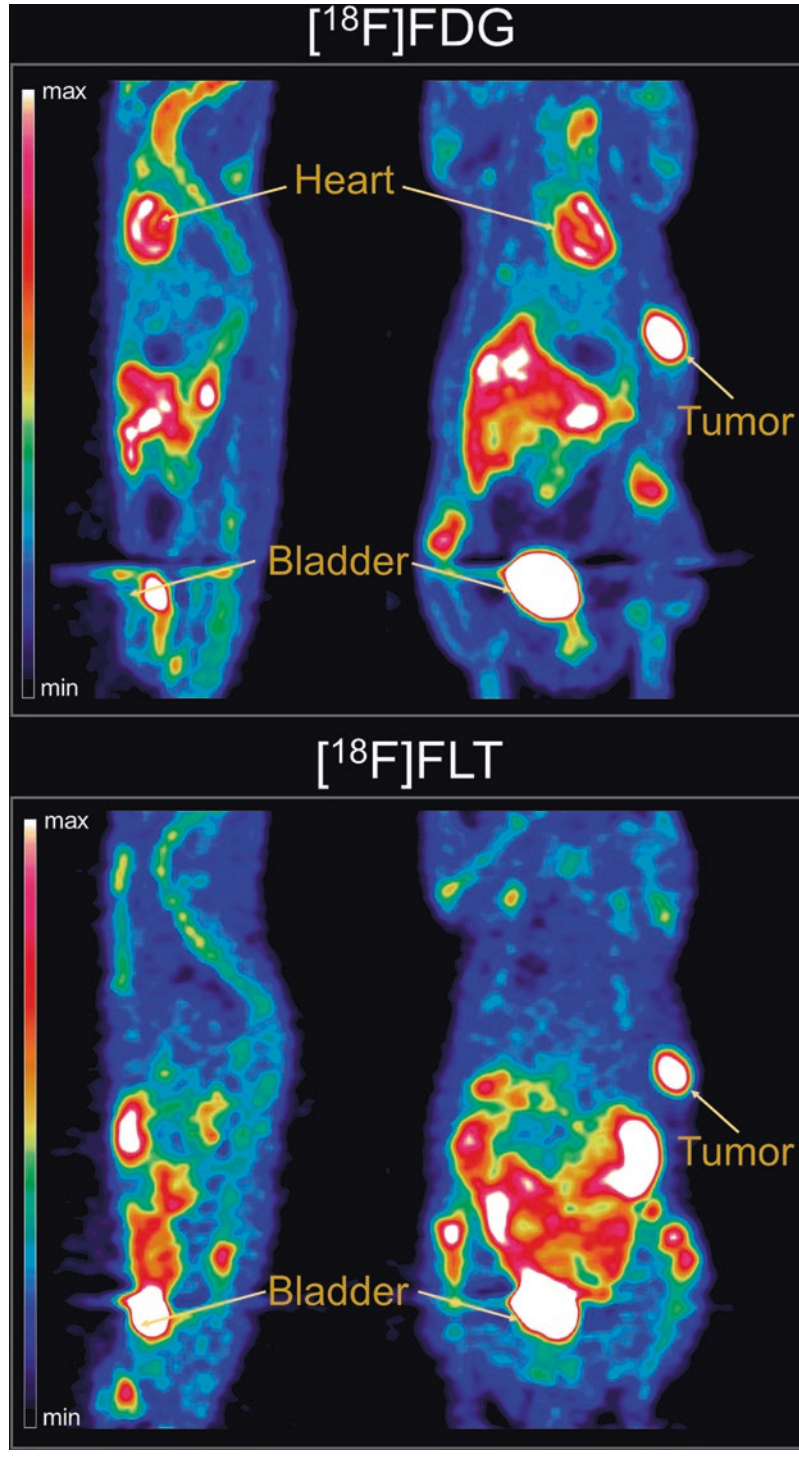

Fig. 20.1 The strength of PET lies in the ability to acquire the in vivo biodistribution of different tracers in one single animal. This example shows two different tracers commonly used in oncology. The rat, bearing a subcutaneous tumor, was imaged for 20 min on two consecutive days. Each tracer shows different uptake patterns

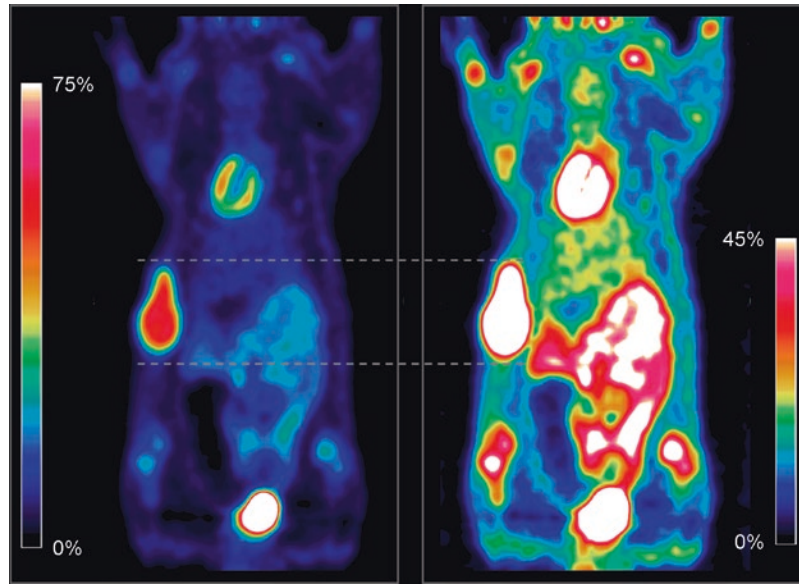

Fig. 20.2 The appearance of PET images and the size of organs or lesions are determined by upper (max) and lower (min) image intensity thresholds. The same PET image is displayed at different lower and upper intensity levels showing clearly the change of tumor size which would influence the quantification when ROIs are based on these different displayed images

As shown in Fig. 20.2, it is obvious that the intensity threshold for image analysis needs to be chosen very carefully. Too low thresholds might lead to blasting of the image, which makes the tumor larger than it is. Drawing the region of interest (ROI) for quantification based on such an image would result in an underestimation of the average tumor activity due to the large volume. However, on the other hand, displaying the image too dim by choosing a very wide display range (low lower and high upper threshold) would lead to smaller visual depiction of the tumor and subsequently to a too small ROI, which would then not represent the real tracer uptake distribution in the entire tumor. Therefore, different approaches are used to minimize bias of the image quantification by the chosen threshold:

- Using an anatomical reference like a CT or MR scan of the same subject (Fig. 20.3).
- Using an anatomical atlas to define the ROIs.
- Normalizing all images of one study to each other and use of a ROI size based on visual, color-based boarders. The normalization factor needs to account for the individual injected radioactivity and half-life of the isotope. However, the uptake time and physiological parameters need to be maintained constant for all animals, especially if the tracer has a fast or time-variant pharmacokinetic.
- Placing ROIs automatically using a region growth algorithm-based predefined isocontours (e.g., 50 % of the maximum value within a seeding point) (Fig. 20.4).

There is no ideal approach or gold standard for PET or SPECT image analysis; choosing the best option depends on the study design and target area. For example, in brain studies where the striatum or cerebellum is the region being investigated, an atlas-based ROI positioning in combination with the use of a fixed ROI size might be ideal since the brain has a fairly constant spatial distribution of regions across a group of subjects. However, an anatomical atlas would not necessarily be a prudent choice for a tumor study. Here, the size and location of the tumor are more random and have most of the time significant size variations within a group of subjects.

Besides the variations arising from the biological effects of the model being investigated, there is also a major source of user-determined factors which influence the measured activity in nuclear imaging. It is therefore helpful to adhere to the following suggestions if the study design allows for it:

- Normalize all images within one study to the injected dose (keep the injected dose as constant as possible among a group of animals).

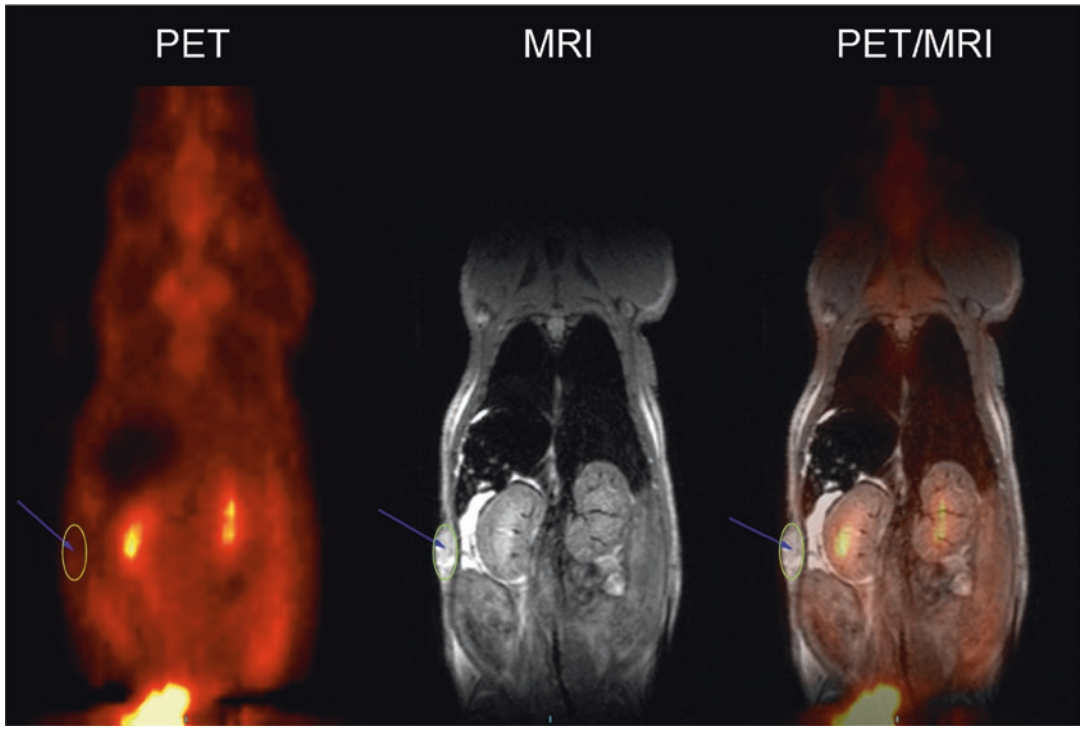

Fig. 20.3 Example of the importance of using a MR image as anatomical reference for defining a PET ROI. Since in this example the PET tracer uptake in the tumor is very low, the tumor cannot be visualized. However, if the MR image, which clearly shows the subcutaneous tumor, is used to delineate a ROI around the tumor volume, the PET data can be quantified

- Keep the scan time for each animal within a study constant.
- Keep the tracer uptake time for each animal within a study constant.
- If more than one PET or SPECT scanner is used for a study, the scanner needs to be cross-calibrated.
- For quantitative studies, the dose calibrator, animal scanners, and gamma counter need to be cross-calibrated.

Figure 20.3 (animals 1–4, injection, dynamic scan, uptake time, static scan time, TX time)

20.2 Quantification Errors

There are several error sources which can limit the image quantification accuracy. Although other chapters deal more specifically with these errors, this chapter will provide some more practical related guidelines on how to account for these errors in small animal imaging studies.

20.2.1 Photon Attenuation and Scattering

A major predicament in nuclear imaging, especially if accurate quantification is required, is the attenuation and scattering of the gamma quanta in tissue or scanner materials. Photon attenuation and scatter are driven by the gamma energy (PET annihilation photons have 511 keV) as well as the tissue density and volume of the subject being measured. Neglecting the effect of attenuation and scatter will always lead to an underestimation of the total amount of measured activity as well as additional blurring from scattering. For PET, on average the underestimation in a mouse-sized object can range between 10 and 20 %,

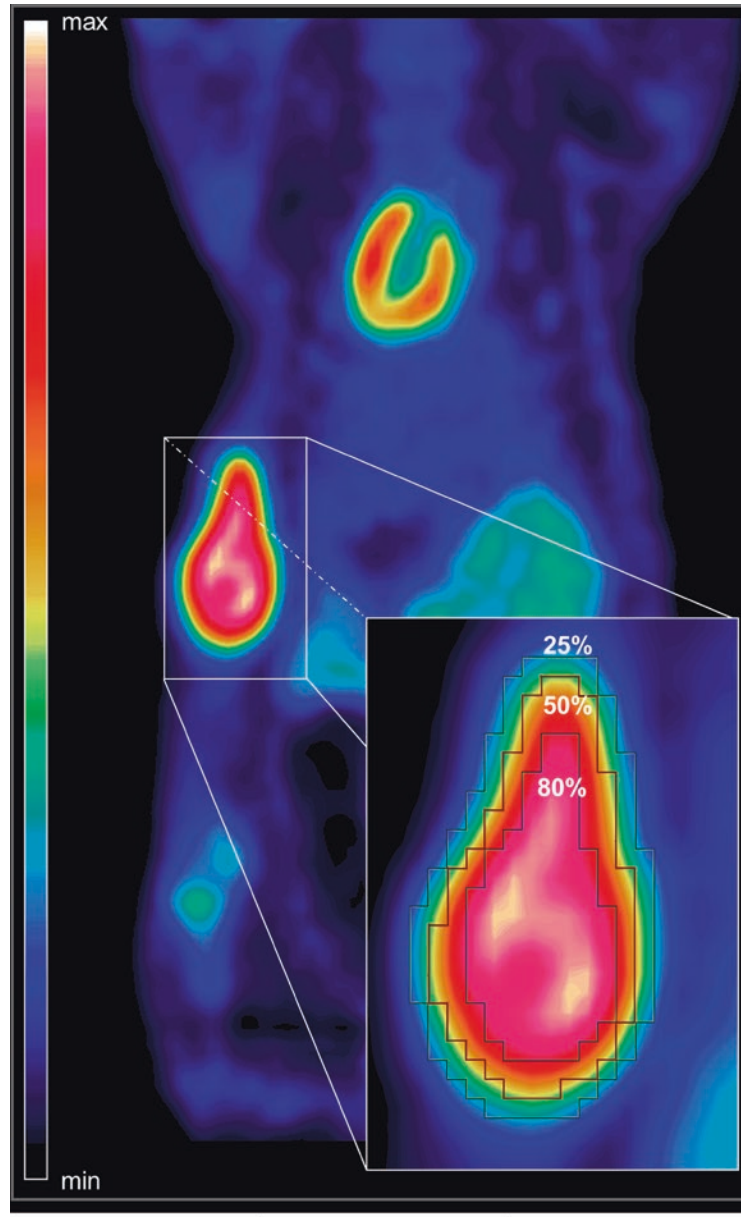

Fig. 20.4 Isocontours are often used as non-user-biased method for generating ROIs. This ^{18}F-FDG PET image of a tumor-bearing rat shows the different-sized volumes which are generated for different chosen 3D isocontour levels (percentage of the maximum pixel intensity). The table shows that this can lead to significant differences in volume and estimated mean activity

Region level	Volume [μL]	Mean Activity [kBq/mL])
25%	890	44,5
50%	499	57,7
80%	214	68,2

whereas in rat-sized object tracer quantification is underestimated by 20–35 %. The scatter fraction is typically on the order of 10 % and 20–30 % for a mouse-sized or rat-sized object, respectively (in PET). With SPECT the attenuation is also varying for the different isotopes depending on

their respective gamma energies. Here, a lower-energy isotope, such as I-125, will be much more affected by attenuation than an isotope with higher gamma energy (e.g. Tc-99 m).

For a proper correction of the attenuation effects and subsequent scatter correction, information about the size and density of the object have to be acquired. In PET this is generally achieved by measuring the transmission (attenuation) properties for gamma rays at 511 keV for the specific object (Ostertag et al. 1989). There are several ways how this can be achieved. The most straightforward approach is simply by using an external radioactive source (preferably with the same gamma energy as the used isotope) which is rotated around the object and then measures the transmitted photons. By this, the attenuation properties of the object can be estimated for all necessary projectional angles resulting in a so-called μ-map. For PET, the use of a 511 keV transmission source delivers images with a very limited contrast which is why alternatively some small animal PET systems provide the use of a lower-energy transmission source (e.g., ^{57}Co). In this case the measured values need to be rescaled to match the energy of the 511 keV photons.

Scatter events can typically not be measured or detected directly. For the purpose of a scatter correction, usually a scatter is estimated performing a Monte Carlo simulation for the underlying scanner and object (i.e., the mouse or rat). For this purpose subject attenuation data as well as the emission data are employed and will provide a best estimate for the profile and distribution of scattered events.

As more and more PET systems are combined with CT scanners, the CT images can also be used to obtain PET attenuation data (Townsend 2001). This has the benefit of reducing the examination time significantly since a CT acquisition is performed faster than a regular transmission scan on a PET system.

As an alternative to directly measured transmission data, the required attenuation information can also be obtained by using other available image data (e.g., MRI scan, PET emission data) which delineate the exact shape and size of the scanned object in the FOV. In this case, the image data are segmented, and known tissue-specific attenuation factors can be assigned to provide proper attenuation information for PET.

For PET imaging in mice, attenuation and scatter correction are often neglected, and a quantification error of 10–20 % is often accepted to save transmission scan time and therefore shorten the time under anesthesia of the animal. In addition, a non-proper performed transmission measurement can add significant noise to the emission image. Thus, mouse attenuation and scatter correction are only recommended when the study design mandates most accurate quantification or when the scanner periphery, such as the bed, adds significant attenuation. However, especially for larger animals like rats, attenuation correction is recommended, especially when inter-object variations, e.g., different tumor positions, have to be considered.

20.2.2 Partial Volume Effect

Besides photon attenuation and scattering, a second source for false estimations of absolute activity values is the partial volume effect which is also described in more details in another chapter of this book. In brief, since the PET or SPECT system has a finite spatial resolution on the order of 1–1.5 mm, it cannot properly depict structures that are smaller than this resolution. Therefore, the whole image and especially sharp edges will always appear blurred. The effect of this can be seen in Fig. 20.5 which shows that all shapes suffer the same amount of blurring at the edges; however, the smaller the overall structures are, the more severe this effect is propagated when the values are quantified. This is demonstrated by the profiles through the spheres in Fig. 20.5.

As this effect is intrinsic to the system and cannot be avoided, it is difficult to correct for. Currently, there are only a few experimentally used algorithms which allow for corrections of the partial volume effect in the image data (Srinivas et al. 2009). However, standard systems do currently not provide any sort of correction. It is therefore in the responsibility of the investigator to consider this effect if results are compared

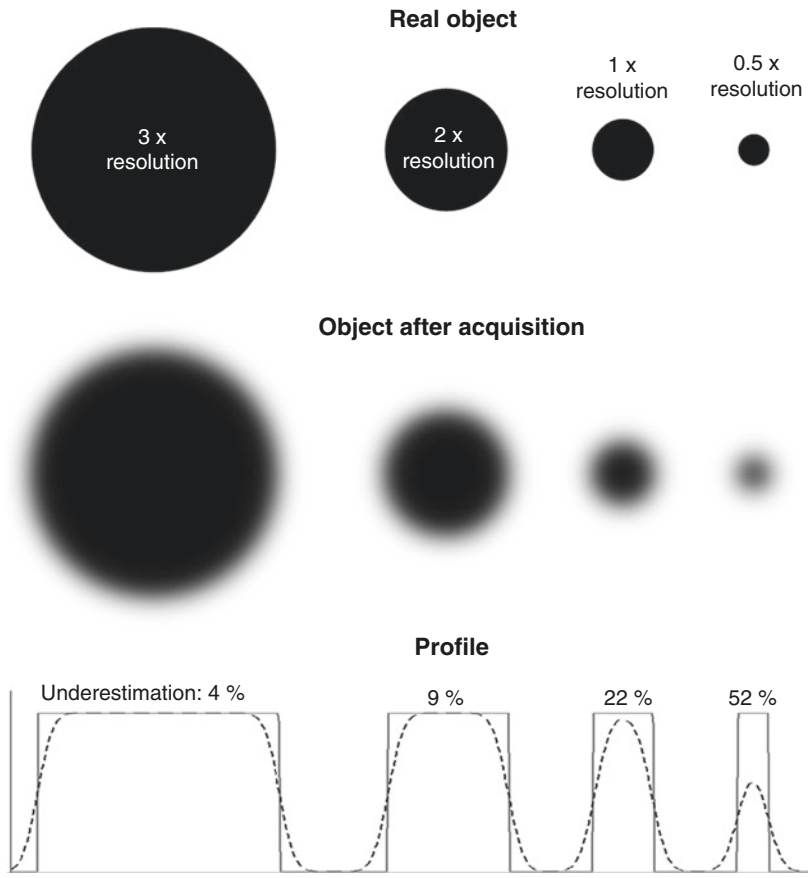

Fig. 20.5 Schematic overview demonstrating the partial volume effect. Objects with the same activity concentrations but different sizes suffer from partial volume effect when imaged by a scanner with finite spatial resolution. The profile on the bottom shows severe underestimation in the smaller objects and only full recovery for lesion sizes reaching three times the scanner's spatial resolution

to other methods like in vitro gamma counting of tracer uptake in isolated organs. Ex vivo gamma counting is in many ways advisable to be done whenever possible, in terminal studies, to cross-validate the in vivo measured results with the gold standard of tracer distribution measurement. As in vivo PET is a convolution of several parameters, superimposed by errors such as attenuation or partial volume effects, the in vivo and ex vivo results can differ significantly. Figure 20.6 shows an example of in vivo PET results and ex vivo biodistribution measurements by gamma counting from the same mouse. The animal was bearing a 250 μL tumor and was injected with a Cu-64-labeled, tumor-specific antibody. The PET scan was performed 2 days after the injection, and the animal was sacrificed immediately after the PET scan to limit any further tracer biodistribution. Interestingly, the in vitro and in vivo quantification differ by a factor of approximately 2.5. Based on phantom scans, one can expect that the underestimation from not performing attenuation scans is approximately 20 % and that approximately 50 % underestimation is a result of the partial volume effect. This was quite surprising as the tumor had a size of ~5 mm in diameter, being more than three times larger than the PET scanner's resolution of 1.4 mm. Further measurements confirmed that partial volume effects in small animal scanners are more predominate than in larger clinical scanners. The underestimation can reach values of ~65 % for 3 mm and 30 % for 8 mm diameter lesions. Thus, the common rule of thumb for clinical scanners that the recovery of a scanned object in PET is close to 100 % of the real activity concentration, if the lesion size is 2.5 times the scanner's resolution, does not necessarily apply for the geometry and intrinsic physical parameters of small animal PET scanners. It is therefore advised that for accurate PET

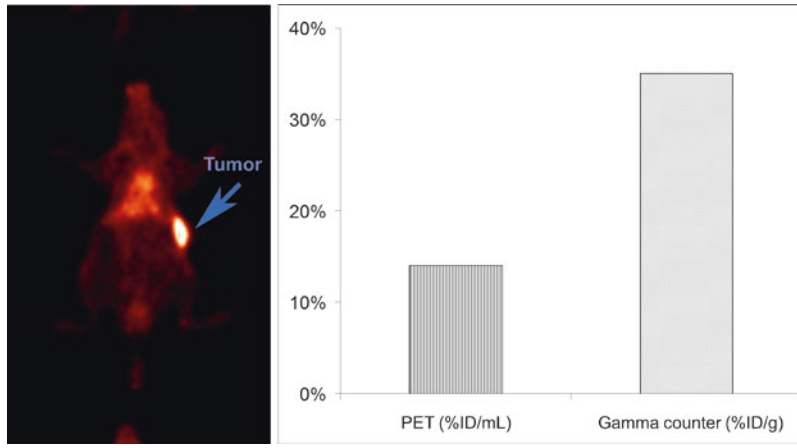

Fig. 20.6 In vivo PET example of the partial volume effect. Due to the small tumor volume of approximately 250 mm^3, the quantification based on the PET image reveals a much lower activity (%ID/cc) than what was found by examining the same tumor by ex vivo gamma counting (%ID/g), which is considered as the gold standard

quantification, the impaired recovery for a specific lesion size, caused by partial volume effect, should be known.

20.3 Reporting of Nuclear Image Quantification

There are different ways to report the quantitative tracer uptake in specific organs of interest. A PET scanner is usually calibrated to deliver values of activity per volume (e.g., kBq/mL) from the image data. Based on this, tracer uptake of specific organs can be easily reported as percent injected dose per volume (%ID/mL) if the values are put in relation to the total injected amount of activity. The %ID/mL can be calculated according to equation (Eq. 20.1):

$$a_{\%\mathrm{ID}} = \frac{a_{\mathrm{Abs}}}{A_{\mathrm{Injected}}} \tag{20.1}$$

where:

a_{Abs} = measured activity within a defined ROI in the PET image [kBq/mL].

A_{Injected} = injected activity [kBq].

$a_{\%\mathrm{ID}}$ = measured value in PET [%ID/mL].

The beauty of reporting the tracer uptake of a specific organ in %ID/cc is the direct link of this value to the quantification measured by ex vivo biodistribution with a gamma counter, which is usually reported in %ID/g. Assuming a density of 1, meaning that 1 mL tissue is equal to 1 g, the two values %ID/mL and %ID/g can be directly compared. A prerequisite to compare biodistribution from in vivo PET and ex vivo gamma counting results is that the tracer's kinetics are known or, alternatively, that the animal is immediately sacrificed during or directly after the PET scan to inhibit the tracer's pharmacokinetic distribution.

Another way of quantitatively reporting values in PET, which is mainly used in the clinical field, is the so-called standard uptake value (SUV), which is a simplification of the more complex Patlak analysis (Weber et al. 2000) used mainly for FDG. The SUV is defined as specified in equation (Eq. 20.2). Even though the SUV does not provide a "cutoff" value which would allow for a sharp separation of malignant and benign tumors, it can be very well used to compare values among patients with the same type of tumor and especially for follow-up studies within the same patient to determine a response to a certain therapy:

$$\mathrm{SUV} = \frac{a_{\mathrm{Abs}}}{A_{\mathrm{Injected}}} \times m \tag{20.2}$$

where:

SUV = standard uptake value [1/1].

a_{Abs} = measured value in PET image [kBq/mL].

A_{Injected} = injected activity [kBq].

m = object's body weight [g].

Note: The assumption is made that the density of the tissue is 1 which is why the SUV is dimensionless.

Since the SUV is a frequently used parameter in clinical diagnosis, it is also applied in the preclinical field. However, in most cases, the clinical SUV values are not comparable with SUVs reported in preclinical studies. For example, a prostate xenograft tumor of 200 μL grown in a nude mouse can provide an SUV of only 0.5, which is a value measured in most mouse tumors. In sharp contrast, ^{18}F-FDG PET SUV values measured in tumors of humans are typically between 2 and 5 and higher.

20.4 PET Images from Miscellaneous Tracer

Figure 20.7 shows an example of PET being used in brain research experiments. The in vivo biodistribution of different commonly used PET brain receptor tracers in mice has been investigated by performing a dynamic acquisition over 1 h. A time series of PET images was reconstructed, and based on ROIs, a so-called time activity curve (TAC) was generated which shows quantitatively the regional tracer uptake over time. These TAC data can later be used as input data to perform kinetic modeling. It should also be noted that advanced iterative reconstruction algorithms are currently researched which try to fit the time-distributed projection data to a specific kinetic model during the reconstruction process, thus providing an image output in terms of kinetic parameters. These reconstruction algorithms can provide 3D parametric maps and usually outperform simple pixel-wise modeling of a conventionally reconstructed time series.

For small animal PET studies, the amount of required injected activity depends on the size of the animal, the tracer and its specific activity, the isotope, and the detection sensitivity of the animal PET scanner. For scanner sensitivities of <5 %, in mice, injected dose of 5–13 MBq for a F-18 tracer is a good lead, while the dose is escalated to approximately 11–18 MBq in larger animals like rats. For these amounts of tracer, static scan times of 10 min are sufficient. Using C-11 compounds and data analysis by kinetic modeling requiring dynamic data analysis and time framing over 1 h, injected activities of 11–18 MBq for mice are advisable. In rats, amounts of up to 1 mCi should be considered. However, for longer-living isotopes like Cu-64 (12.7 h half-life), amounts of 150–350 mCi are sufficient providing enough activity to perform scans over 24 h. When using Cu-64, one has to keep in mind that only ~20 % of the decay is by positrons, requiring more injected activity or longer scan times than isotopes with a higher positron decay branch.

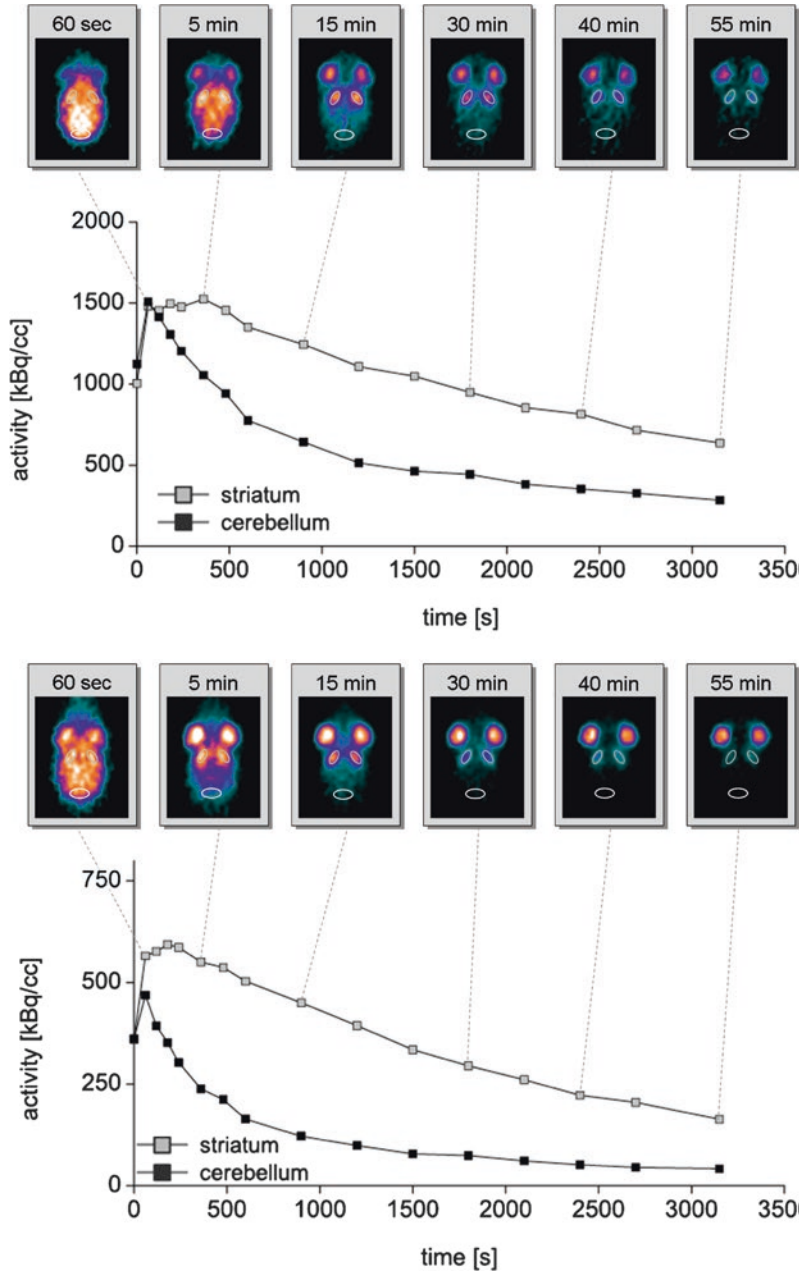

Fig. 20.7 The strength of PET lies in its ability to track the in vivo biodistribution of a tracer over time. This example shows the application of dynamic PET acquisitions performed over 1 h with two common tracers used in brain research. The top row shows an acquisition with the C-11-labeled dopamine transporter ligand ^{11}C-methylphenidate. The bottom shows a similar acquisition when using the ^{11}C-D2 receptor ligand ^{11}C-raclopride. The small image icons show visually the tracer uptake in the mouse brain at specific time points. While images at early time points after tracer injection are dominated by perfusion, later time points show specific tracer uptake in the striatum. The cerebellum is the reference tissue region where no specific tracer binding is found. The harderian glands behind the eyes light up in all images; most of the PET tracers accumulate in these glands. In both acquisitions, quantitative time activity curves were derived based on ROIs (white circles in the images) in the striatum and cerebellum of the animal

References

Ostertag H, et al. Measured attenuation correction methods. Eur J Nucl Med. 1989;15(11):722–6.
Srinivas SM, et al. A recovery coefficient method for partial volume correction of PET images. Ann Nucl Med. 2009;23(4):341–8.
Townsend DW. A combined PET/CT scanner: the choices. J Nucl Med. 2001;42(3):533–4.
Weber WA, Schwaiger M, Avril N. Quantitative assessment of tumor metabolism using FDG-PET imaging. Nucl Med Biol. 2000;27(7):683–7.

Kinetic Modeling

21

J. van den Hoff

Contents

J. van den Hoff
PET Center, Helmholtz-Zentrum Dresden-Rossendorf (HZDR), Bautzner Landstrasse 400,
Dresden 01328, Germany
e-mail: j.van_den_hoff@hzdr.de

21.1 Introduction

A mathematical description of the time-dependent tissue uptake and tissue clearance after injection of contrast agents or radioactively labeled tracers with suitable models (kinetic modeling) allows a detailed analysis of transport processes and metabolism in vivo.

Such an analysis can provide at once quantitative information for several interesting parameters such as local blood volume, blood flow, distribution volumes, metabolic rates, binding potentials, and so forth.

While the mathematical techniques are – with some reservations – in principle suited for data analysis in other tomographic modalities as well (notably CT and MRI), the broadest field of application is found in PET. We will focus especially on small animal PET in the following.

Small animal PET is a quantitative tomographic imaging technique enabling noninvasive and repeated determination of regional accumulation and distribution of suitable radioactively labeled tracers in vivo. The full potential of this quantitative capability is only utilized if the well-established techniques of tracer kinetic modeling are used to derive from the measurements of regional tracer concentrations quantitative values of relevant physiological and biochemical transport constants. This chapter provides an introduction to the basic techniques while drawing attention to some specific problems of translating techniques established in human investigations to small animals.

F. Kiessling et al. (eds.), *Small Animal Imaging*, DOI 10.1007/978-3-319-42202-2_21

For reasons of limited space, this chapter cannot cover all aspects of kinetic modeling. A comprehensive discussion of concepts in classical tracer kinetic experiments can be found in Lassen and Perl (1979). Some recent references, which partly cover complementary aspects of tracer kinetic modeling in PET, are Carson (2003), Carson et al. (2003), van den Hoff (2005), Müller-Schauenburg and Reimold (2008), Willemsen and van den Hoff (2002). A useful reference regarding the physics and mathematics of physiological transport processes in general is Weiss (1996).

What are the benefits of kinetic modeling? This is a justified and important question since – as we will see – kinetic modeling requires substantial methodological effort both during data acquisition and during data evaluation. The answer is that only in this way we are able to really *measure* relevant parameters. Valuable information can be derived from the image data solely by visual inspection, determination of regional contrast, or computation of regional values for the accumulated percentage of injected dose. But all these approaches are essentially qualitative and purely phenomenological. They are frequently not suited to gain a deeper understanding of the investigated processes.

Moreover, tracer experiments are investigating inherently time-dependent processes, namely the transport and metabolism of certain substrates. Only by suitable evaluation of the whole time course is it possible to actually get information concerning the nature of these processes.

What are the limits and pitfalls of kinetic modeling? One serious danger lies in the attempt to derive "too much" information from the data by using too complex models. Noninvasive PET imaging provides only an integral signal, namely the time-dependent total tracer concentration in the target region. This signal is in general the sum over several compartments. Only for very simple models is it possible to derive from this superposition all the contributing curves (and thus the corresponding rate constants connecting the compartments).

Another danger is a wrong interpretation of the model parameters that is related to the fact that the parameters always express relative rates (of concentration changes) with respect to total volume and not with respect to the individual pools.

21.2 Mathematical Basics of Tracer Kinetic Models

This section presents the principles of pharmacokinetic modeling, more specifically those of tracer kinetic compartment modeling. Although the formalism is usually considered in the context of PET, certain aspects can equally well be applied to CT or MRI, for example, for evaluation of dynamic contrast agent enhanced (DCE) or arterial spin labeling (ASL) measurements. This of course requires to take into account the rather different properties of the respective tomographic technique and of the resulting image data regarding spatial and temporal resolution, quality of linear correlation between concentration and signal intensity, physical half life/relaxation time of the considered "label," and, accordingly, the time window accessible to the measurement.

Basically, pharmacokinetic modeling is concerned with the mathematical description of physiological and metabolical transport processes by analysis of mass balance equations. Contrary to classical pharmacokinetics, which is essentially dealing with whole body kinetics such as blood clearance of a substance, tracer kinetic modeling of tomographic data is investigating regional processes. No attempt is made to account for the body as a whole. A direct consequence is that the concentration in the arterial blood $c_a(t)$ (the so-called *arterial input function* or AIF) is treated as a given known quantity. $c_a(t)$ has to be determined either via arterial blood sampling or in the tomographic image data.

The fundamental mass balance is given by

$$\frac{\mathrm{d}m_s(t)}{\mathrm{d}t} = Fc_a(t) - Fc_v(t) \qquad (21.1)$$

or equivalently, if $m_s(t \le 0) = 0$, in integral form

$$m_s(t) = F\int_0^t c_a(u)\,du - F\int_0^t c_v(u)\,du, \quad (21.2)$$

where $m_s(t)$ is the tracer amount (mass, activity, …) residing in the system at a time t and is measured, for example, in Becquerel (Bq). So far the "system" can be considered to represent a whole organ (say the heart or the brain) or just a single voxel of the tomographic data set., F denotes the total blood flow (units: mL/min) through the system and $c_a(t)$, $c_v(t)$ are the tracer concentrations in (inflowing) arterial and (outflowing) venous blood (units, e.g., Bq/mL), respectively. Equation (21.2) expresses the simple fact of mass conservation: the amount $m_s(t)$ of tracer in the system at time t is the difference between cumulative inflow and outflow until this time.[1]

Since the tomographic techniques yield concentration proportional data (e.g., tracer amount per image voxel), it is necessary to divide Eq. (21.1) on both sides by the system volume, which leads to

$$\frac{dc_s(t)}{dt} = fc_a(t) - fc_v(t), \quad (21.3)$$

where $f = F/V$ (units: mL/min/mL) is called specific blood flow or *perfusion* and represents the blood flow per unit system volume.[2] For local quantification Eq. (21.3) is not directly usable since the *local* venous concentration $c_v(t)$ can generally not be measured. On the other hand, $c_a(t)$ is the same in all arteries (apart from a possible bolus delay and dispersion that can be accounted for during further data evaluation). Thus, it might be measured directly either via blood sampling from an accessible peripheral artery or, using the image data, possibly in the cavum of the left ventricle although for small animals such image-based determination of the input function is heavily affected by partial volume effects (PVE) and limited signal recovery. Hybrid imaging has some obvious potential here by deriving the geometric information required for reliable PVE correction from the CT or MR component of the imaging system.

Quite obviously $c_v(t)$ is determined by how the tracer is transported back and forth between the capillary blood space and tissue. Thus, $c_v(t)$ is not an independent quantity and should be eliminated from the equations. It is exactly at this point that specific model assumptions have to be used to proceed. A central, still rather general assumption of tracer kinetic modeling is that we are dealing with a so-called *linear system*. The following section discusses the implications of this assumption.

21.2.1 Linear Systems and Convolution

A linear system "translates" the given *input function* $c_a(t)$ into the corresponding *system response function* c_s, which might be expressed symbolically as $c_a \to c_s$, in such a way that a scaling of the input leads to an identical scaling of the response and, more generally, the response to the sum of two inputs $c_a^{(1)}$, $c_a^{(2)}$ equals the sum of the responses $c_s^{(1)}$, $c_s^{(2)}$ to the separate inputs: $c_a^{(1)} + c_a^{(2)} \to c_s^{(1)} + c_s^{(2)}$.

This "translation" from input to response is mediated by the system's (unit) *impulse response function (IRF)*, which we denote as h:

$$c_a \xrightarrow{h} c_s.$$

Mathematically, linear systems are described by linear differential equations whose formal solution can be expressed with the help of a so-called *convolution integral*. In their most general form, the model equations are partial differential equations for the time- and space-dependent tracer concentration $c(x, y, z, t)$ at each point in the system (*distributed modeling*), but it turns out that explicit treatment of the spatial concentration variations is not necessary when analyzing

[1] If the tracer is finally completely washed out from the system, i.e., $\lim_{t\to\infty} m_s(t) = 0$, mass conservation implies that the areas under the curves (*AUCs*) of inflow and outflow are identical: $\int_0^\infty c_a(t)\,dt = \int_0^\infty c_v(t)\,dt$.

[2] It is rather common to use both terms (perfusion and blood flow) synonymously to denote specific blood flow per unit volume. We will adopt this custom in this chapter.

tomographic image data. Instead it suffices to subdivide the system into a number of *compartments*, which eliminates the spatial coordinates from the mathematical description. We are thus left with solely time-dependent functions. The resulting *compartment models* are described by *ordinary differential equations* for the time-dependent concentrations $c_1(t)$, $c_2(t)$,…,$c_N(t)$ in the different compartments constituting the model.

Since, furthermore, all concentrations are equal to zero before $t=0$, the solution is given by this specific convolution integral:

$$c_s(t) = c_a(t) \otimes h(t) = \int_0^t c_a(u) \cdot h(t-u)\, du. \quad (21.4)$$

A linear system is completely characterized by its IRF. Once you know the IRF, you can compute the system response for any input $c_a(t)$. This special property of linear systems separates the specific system properties that control the functional shape of $h(t)$ and the influence of the specific input function actually used in an experiment. Equation (21.4) is a direct consequence of the linearity of the system. Simply speaking, for any given observation time t, the convolution integral is adding up time-shifted impulse responses $h(t-u)$ to successive short pulses of intensity $c_a(u)$ and duration du occurring at all times between $u=0$ and the observation time $u=t$. An illustration of this process is given in Fig. 21.1.

21.3 Compartment Models

Compartment modeling is definitely the most important kinetic modeling technique used for quantification of PET investigations.

In this approach, it is assumed that we can decompose the system into a finite (preferably small) number of components – the compartments – that correspond to distinguishable states of the tracer. Compartments might represent different spatial components where the tracer resides

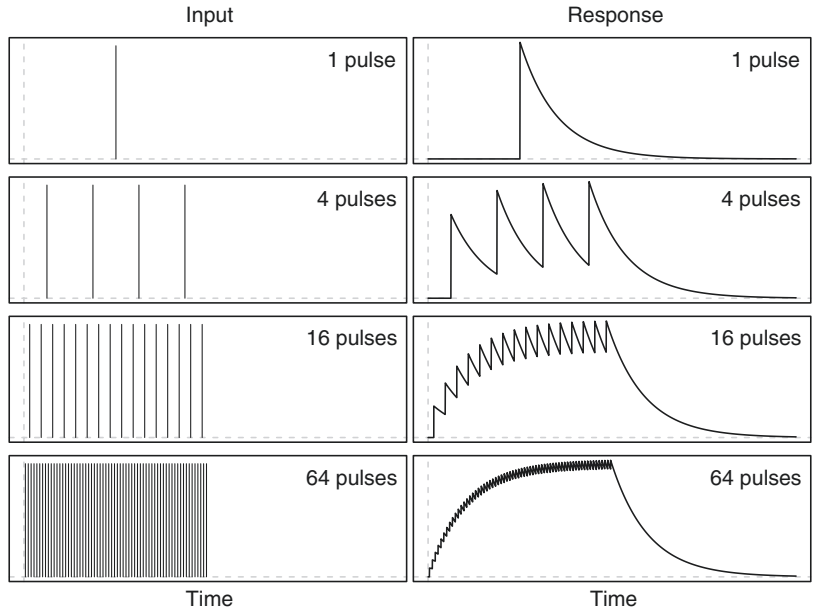

Fig. 21.1 Response of a linear system characterized by a mono-exponential IRF $h(t)=e^{-\lambda t}$ to a fixed input dose respectively distributed over different numbers of discrete pulses with negligible duration. Pulse positions are indicated by vertical lines (*left column*). The system response (*right column*) is obtained by superposition of the impulse responses to the separate input pulses. Plots are individually scaled for better visualization. With increasing number of pulses the input approaches a "boxcar function" (finite-duration constant infusion) while the system response asymptotically approaches the convolution of this boxcar function with the impulse response according to Eq. (21.4).

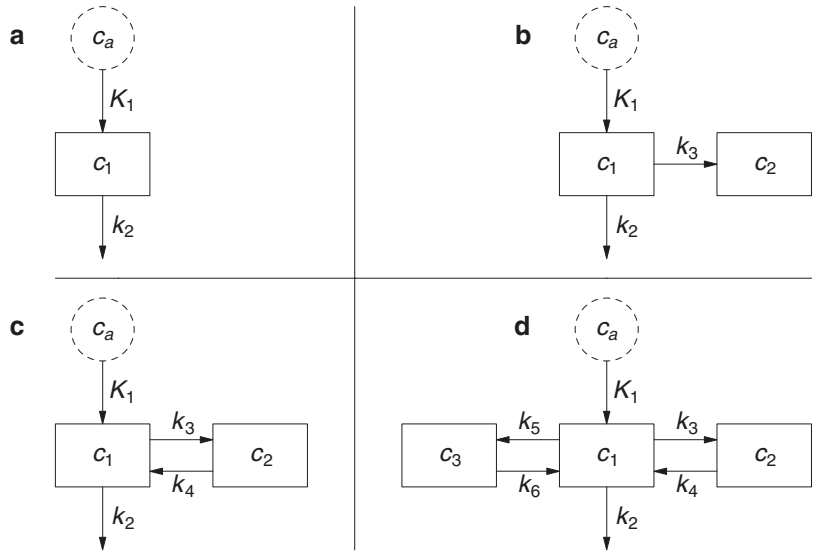

Fig. 21.2 Examples of compartment models. (**a**) reversible one-compartment model. This model is very frequently used and includes the case of freely diffusible (flow) tracers. (**b**) irreversible two-compartment model. This is the well-known "FDG-model". (**c**) reversible two-compartment model. Configurations *B* and *C* are used broadly for description of tracers which are first entering a free pool (c_1) and are then metabolized, either irreversibly or reversibly, which is represented by the second compartment (c_2). (**d**) three-compartment model. This model is suitable, for example, for receptor ligands with competitive specific (c_2) and nonspecific (c_3) binding to different sites. Typical response curves for these models are shown in Figs. 21.3 and 21.4

(e.g., extra- and intracellular space) or different chemical modifications of the tracer. In any case, the central assumption is that a compartment does not exhibit any internal structure, but is completely characterized by the (generally time-dependent) tracer concentration in this compartment. In other words, there are no internal concentration differences: a compartment is by definition a space with homogeneous tracer concentration ("well-stirred pool"). All concentration differences are attributed to transitions from one compartment to another.

Even complex systems can be described by compartment models if one is willing to accept a large number of compartments.[3] The real value and usefulness of compartment models depends, however, on sufficient model simplicity. This is especially true for noninvasive imaging, where one cannot access the individual compartments directly but has to deduce their properties via their contribution to the total tracer concentration in the system.

21.3.1 General Properties of Compartment Models

The structure of compartment models can be illustrated as shown in Fig. 21.2.

Compartments are represented by boxes. Tracer exchange is represented by arrows labeled with the *transport constants* K_1,k_2,….[4] The input into the system is given by the time-dependent arterial tracer concentration $c_a(t)$. In the examples from Fig. 21.2, tracer is lost from the system via

[3] The so-called *distributed models* (Bassingthwaighte et al. 1984; Bassingthwaighte and Holloway 1976; Bassingthwaighte et al. 1992), which permit description of tracer transport in the presence of spatial concentration gradients, can be seen as limiting cases of compartment models where the number of compartments tends to infinity.

[4] Actually, constancy of these parameters (i.e., time invariance of the investigated process during the measurement) is *assumed* and not to be taken for granted. Variability of the transport constants during the measurement does complicate the situation considerably.

a single outlet characterized by the rate constant k_2. Each model is mathematically defined by a certain differential equation. For instance, the reversible two-compartment model of Fig. 21.2c[5] has the model equation

$$\begin{aligned}\frac{\mathrm{d}c_1}{\mathrm{d}t} &= K_1 c_a - \left(k_2 + k_3\right)c_1 + k_4 c_2,\\ \frac{\mathrm{d}c_2}{\mathrm{d}t} &= k_3 c_1 - k_4 c_2.\end{aligned} \tag{21.5}$$

Remember that all concentrations are specified with respect to the same volume, and Eq. (21.5) thus describes the fundamental mass balance for the system: the rate of concentration change in a compartment equals the difference of inflow into and outflow from the compartment which in turn are proportional to the respective "source" concentrations.

Inspection of Eq. (21.5) shows that the transport constants have dimensions of inverse time. They are typically specified in units of min^{-1}. From dimensional considerations alone, it appears that K_1 is measured in the same units as the rate constants k_2,k_3,…. But contrary to all other model parameters K_1 relates c_a, the tracer concentration in blood, to the rate of concentration change in a tissue compartment. For this reason, the units are commonly specified as

$$\left[K_1\right] = \frac{\dfrac{mL\left(\text{blood}\right)}{\text{min}}}{mL\left(\text{tissue}\right)}$$

and formal cancelation of the volume units is not performed. From this one might construct the following interpretation of a given numerical value of K_1: it represents that volume of arterial blood whose tracer content is *completely* extracted and transferred within 1 min to 1 mL of tissue. Note that in general tracer extraction during the capillary transit is actually incomplete, so that the blood volume flowing through the tissue per unit time will be larger than K_1 (cf. Sect. 21.3.2).

A noninvasive experiment does not allow separate determination of individual compartment concentrations. Rather we only can measure the average tracer concentration in tissue. For example, in the case of a two-compartment model, this is given by the sum $c_t = c_1 + c_2$ (remember that all concentrations refer to a common volume). The IRF of the system, $h(t)$, is correspondingly given by the sum of the IRFs in the individual compartments: $h = h_1 + h_2$.

The IRF in *each* compartment of an N-compartment system is a sum over N decreasing exponentials: $h_m\left(t\right) = \sum_{n=1}^{N} a_{mn} \cdot e^{-\lambda_n t}\left(\lambda_n \geq 0\right)$. The decay constants λ_n are identical in all compartments, but the amplitudes a_{mn} differ between compartments (and some amplitudes might be negative or zero). The IRF of the whole system is given by summing over all compartments:

$$\begin{aligned}h\left(t\right) &= \sum_{m=1}^{N} h_m\left(t\right) = \sum_{m=1}^{N}\sum_{n=1}^{N} a_{mn} \cdot e^{-\lambda_n t}\\ &= \sum_{n=1}^{N}\left(\sum_{m=1}^{N} a_{mn}\right)\cdot e^{-\lambda_n t} = \sum_{n=1}^{N} a_n \cdot e^{-\lambda_n t}.\end{aligned} \tag{21.6}$$

As can be seen, the IRF of a N-compartment model has $2N$ free parameters (N amplitudes, N decay constants). This is the maximum number of parameters derivable from an experiment that only accesses the total concentration in the system.[6] In the case of Eq. (21.5), the IRF is explicitly given by

[5] In the older literature, the blood pool was frequently counted (erroneously) as one of the compartments, so that this model was called a three-compartment model. In order to be completely unambiguous, it might be wise to use the notation two *tissue* compartment model (Innis et al. 2007), but omitting the explicit reference to "tissue" should not lead to misunderstandings anymore.

[6] Theoretically, the number of transport constants in a N-compartment model can get larger than $2N$ (in the most general case there are N^2 rate constants and N blood-to-tissue uptake constants). In this case, determination of all model parameters from a noninvasive experiment would be principally impossible. In practice, this usually poses no problem since the relevant models have more specific configurations, such as those given in Fig. 21.2, where the number of rate constants never exceeds $2N$.

$$
\begin{aligned}
h_1 &= \frac{K_1}{\lambda_1-\lambda_2}\left[(k_4-\lambda_2)e^{-\lambda_2 t}+(\lambda_1-k_4)e^{-\lambda_1 t}\right],\\
h_2 &= \frac{K_1}{\lambda_1-\lambda_2}\left[k_3 e^{-\lambda_2 t}-k_3 e^{-\lambda_1 t}\right],\\
h_1+h_2 \equiv h &= a_2 e^{-\lambda_2 t}+a_1 e^{-\lambda_1 t}\\
&= \frac{K_1}{\lambda_1-\lambda_2}\left[(k_3+k_4-\lambda_2)e^{-\lambda_2 t}+(\lambda_1-k_3-k_4)e^{-\lambda_1 t}\right],
\end{aligned}
\tag{21.7}
$$

where

$$
\lambda_{1/2} = \frac{(k_2+k_3+k_4)\pm\sqrt{(k_2+k_3+k_4)^2-4k_2k_4}}{2}. \tag{21.8}
$$

As can be seen, the analytical relation between the parameters a_n, λ_n of Eq. (21.6) and the transport constants (K_1, k_2,…) already is rather complicated even for this simple model. For multicompartment models, these relations are usually no longer obtainable in closed form.[7] The Appendix gives some hints on the numerical methods that can be used to derive the IRF in these cases.

It is straightforward to deduce the IRF for the simpler model in Fig. 21.2b by letting $k_4=0$ in Eqs. (21.7 and 21.8). Hence, $\lambda_1=k_2+k_3$, $\lambda_2=0$, and we obtain

$$
\begin{aligned}
h_1 &= K_1 e^{-(k_2+k_3)t},\\
h_2 &= \frac{K_1}{k_2+k_3}\left[k_3-k_3 e^{-(k_2+k_3)t}\right],\\
h &= \frac{K_1}{k_2+k_3}\left[k_3+k_2 e^{-(k_2+k_3)t}\right].
\end{aligned}
\tag{21.9}
$$

For models with irreversible binding such as this one (the well-known "FDG-model" developed for description of the tracer [^{18}F]2-fluoro-2-deoxy-D-glucose, which is routinely used for investigating glucose metabolism), the IRF approaches a nonzero value at sufficiently late times, which corresponds to the rate of binding in the irreversible pool. For example, for the above model, this metabolic binding rate is given by

$$
K_m = \frac{K_1 k_3}{k_2+k_3}. \tag{21.10}
$$

Additionally letting $k_3=0$ in Eq. (21.9) yields the solution for the one-compartment model in Fig. 21.2a:

$$
h = K_1 e^{-k_2 t}. \tag{21.11}
$$

The typical shape of the IRF for different models is shown in Fig. 21.3. The corresponding responses to a finite input are presented in Fig. 21.4. One further remark concerning the interpretation of the impulse response Eq. (21.6): in this equation we started by summing over the contributions $h_m(t)$ from the N individual compartments and ended up with a sum over the N exponentials $a_n \cdot e^{-\lambda_n t}$. This has the important implication that one always can envisage an artificial compartment model consisting of N noninteracting ("decoupled") one-compartment systems independently exchanging tracer with the blood pool with uptake constants a_n and clearance rate constants λ_n that always exhibits exactly the same total tissue response curve as the original compartment model. This is exemplified in

[7] Note, however, that the basic functional form of the IRF always remains the sum of exponentials according to Eq. (21.6).

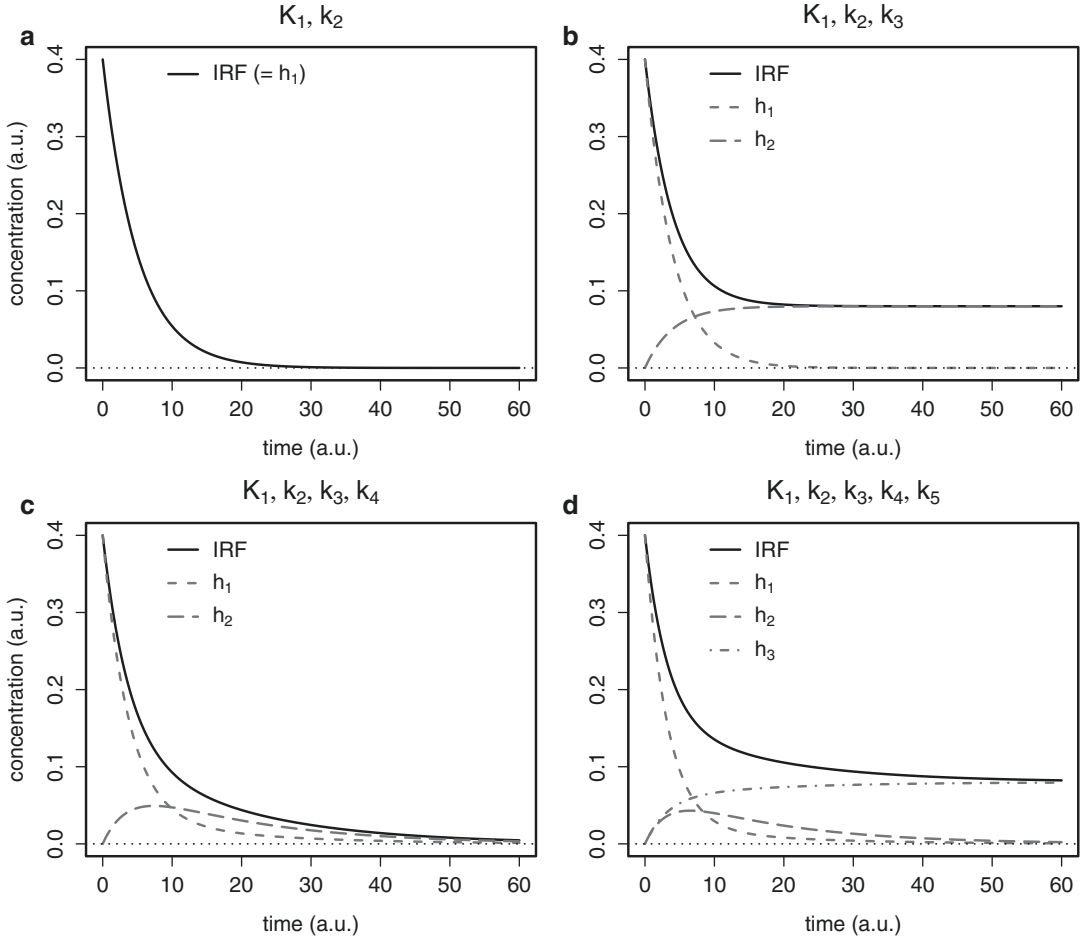

Fig. 21.3 Total impulse response (*IRF*), $h = \sum_{n=1}^{N} h_n$, of the models from Fig. 21.2. Non-zero transport constants in each case are indicated on top of the plots (*a.u.*: arbitrary units). The transport constants were set to the following values (in the appropriate units): $K_1 = 0.4$, $k_2 = 0.2$, $k_3 = 0.05$, $k_4 = 0.075$, $k_5 = 0.05$, $k_6 = 0$. Note how the impulse responses h_n in the different compartments change from *a* to *d* and how the different compartments contribute to the tissue response. Further note the rather similar but not identical shape of the tissue responses in *a*, *c* and *b*, *d*, respectively

Fig. 21.5. The indistinguishability between different models containing the same number of compartments has the following consequences:

- By measuring only the total tissue response (rather than the concentration in the individual compartments), one cannot determine the actual compartmental structure of the system under investigation but only the number *N* of kinetically discriminable compartments. In order to be able to derive specific model parameters, the model structure must be decided a priori.
- In general, it would be an error to interpret individual exponentials in the impulse response as representation of individual compartments. This would only be true if the actual structure of the system were that of a decoupled model.

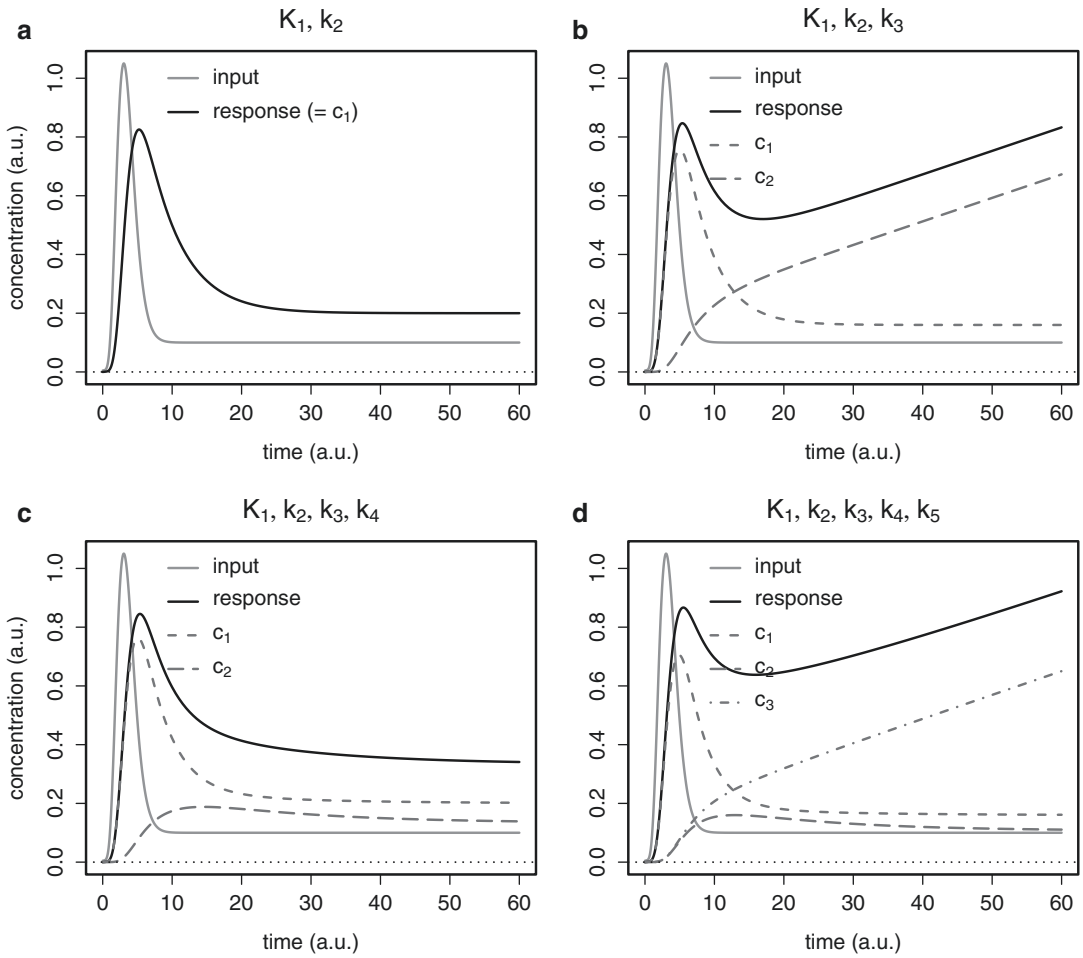

Fig. 21.4 Response curves $c_t = c_a \otimes h$ for the models from Fig. 21.2 to an idealized bolus input with recirculation using the impulse responses from Fig. 21.3

- The qualitative behavior of the system under consideration can frequently be more easily understood in terms of the equivalent decoupled model.

21.3.2 Extraction Fraction and the Renkin-Crone Formula

The unidirectional tracer uptake rate K_1 can never exceed the tissue perfusion f. The ratio of these parameters is called the (unidirectional) extraction fraction:

$$E(f) = \frac{K_1(f)}{f}. \tag{21.12}$$

As indicated, the extraction fraction is generally flow dependent (as is K_1). Under certain assumptions, the flow dependence is given by the Renkin-Crone formula (Crone 1963; Renkin 1959):

$$E(f) = 1 - e^{-PS/f} \quad \text{and} \quad K_1(f) = f\left(1 - e^{-PS/f}\right), \tag{21.13}$$

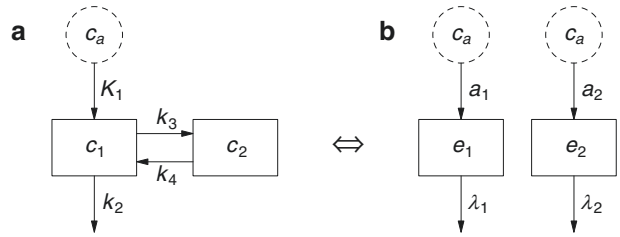

Fig. 21.5 A reversible two-compartment model (**a**) and the equivalent decoupled model (**b**). Each compartment e_n of (**b**) corresponds to one of the exponentials in the tissue response of (**a**). The parameters of both models are related according to Eqs. (21.7 and 21.8). Both models are equivalent in the sense that for all times $c_1(t)+c_2(t) \equiv e_1(t)+e_2(t)$ so that they behave completely identical with respect to the total tissue response

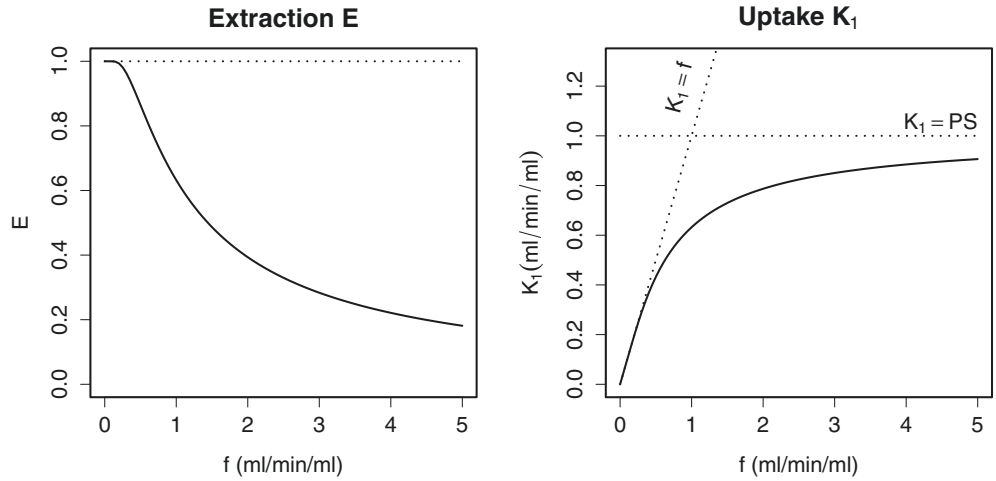

Fig. 21.6 Unidirectional extraction fraction and uptake rate according to the Renkin-Crone formula for $PS = 1$ mL/min/mL. In this example, the uptake rate K_1 essentially equals perfusion f below $f \approx 0.3$ mL/min/mL and becomes nearly constant beyond $f \approx 3$ mL/min/mL

where PS is called the *permeability surface area product*, which is specific of the given tracer and diffusion boundary. The two limiting cases of very high and very low permeability are of special interest:

$$K_1 \rightarrow \begin{cases} f & \text{for } f \ll PS \ \left(\text{flow limited transport}\right) \\ PS & \text{for } f \gg PS \ \left(\text{diffusion limited transport}\right), \end{cases}$$

which are a direct consequence of the Renkin-Crone formula.[8] A perfect perfusion tracer thus would allow to identify K_1 with f while the uptake of a "metabolic" marker should yield a K_1 that is completely flow-independent. Note that the discrimination between a "flow tracer" such as ^{15}O-water and a "metabolic tracer" such as FDG is not an absolute one, but rather depends on the considered perfusion level (and possibly also the targeted tissue): ^{15}O-water transport across the

[8]The low permeability limit follows from first order Taylor expansion $x \ll 1 \Rightarrow e^{-x} \approx 1 - x$ in the Renkin-Crone formula.

blood brain barrier, for example, is known to deviate increasingly from a linear relation between K_1 and f at very high flow levels (while this does not happen in the myocardium). FDG uptake, on the other hand, might very well become flow limited at sufficiently low perfusion levels such as those present in resting peripheral muscle tissue.

Figure 21.6 shows the flow dependence of E and K according to Eq. (21.13) for $PS = 1$ mL/min/mL.

In practice, deviations from Eq. (21.13) are frequently observed under high flow conditions and the modified formula

$$E(f) = 1 - T_\infty \cdot e^{-PS_0/f} \qquad (21.14)$$

is empirically more appropriate. This equation might be derived from Eq. (21.13) by assuming a flow dependence of PS according to

$$PS(f) = PS_0 + \ln\left(\frac{1}{T_\infty}\right) \cdot f. \qquad (21.15)$$

PS_0 is the low-flow limit of the PS-product and T_∞ represents the nonextracted ("transmitted") fraction at very high flows. One way in which such a flow dependence of PS could be understood is successive capillary recruitment (increasing S) with increasing flow (but not in the brain, where capillary recruitment is not operational).

21.3.3 Perfusion Measurements

Perfusion measurements in PET require the use of highly extracted tracers (cf. Sect. 21.3.2). Ideally, a perfusion tracer is freely diffusible between blood and tissue. In this case, $K_1 = f$ and in the one-compartment case one gets the *Kety-Schmidt model*

$$\frac{dc_t}{dt} = f c_a - \frac{f}{V_d} c_t. \qquad (21.16)$$

This model results directly from the primary mass balance Eq. (21.3) using a single but rather restrictive assumption, namely, that the tracer entering the system equilibrates so rapidly between blood and tissue space that the venous outflow $c_v(t)$ is proportional to $c_t(t)$ at *all* times:

$$c_v(t) = \frac{1}{V_d} c_t(t).$$

This very simple model usually works well in PET, since the time resolution of the measurements is relatively low in comparison to the capillary tracer transit time ($\approx 1-2$ s), so that violations of the model assumptions do not manifest themselves in the data.

21.3.4 Fractional Blood Volume

Up to now we have silently assumed that we are really able to measure directly the tracer concentration in tissue when performing a PET measurement. Actually, we are measuring the concentration in a macroscopic *Region of Interest (ROI)*[9] and are thus averaging over the enclosed tissue space as well as the microvasculature. In order to account for this, we introduce the *Fractional Blood Volume (fbv)* as a further parameter. The measured PET-signal is then given by

$$c_s(t) = (1 - fbv) \cdot c_t(t) + fbv \cdot c_a(t), \qquad (21.17)$$

that is, the volume weighted average of tissue and blood concentration. Since one finds $fbv \approx 0.03 - 0.05$ in most tissues, the scaling of $c_t(t)$ with $(1 - fbv)$ is generally only a small correction and sometimes omitted in the literature. This omission amounts to a redefinition of K_1 by referring it (and $c_t(t)$) not to the unit of *tissue* volume but rather to the unit of *total* volume (including blood space). As explained, the difference is usually (although not always) small, but conceptually noteworthy.

From the mathematical side, *fbv* simply represents an additional model parameter which has to be determined together with the transport constants of the compartment model. The inclusion of *fbv* in the operational equations is primarily important to avoid serious bias in the estimates of the other parameters. On the other hand, *fbv* might be interesting in itself since it provides direct information regarding the degree of regional vascularization, for example, in tumors. The identifiability of *fbv* in the measured data depends on

[9] The smallest possible ROI being a single image voxel.

sufficiently rapid variation of $c_a(t)$ in some time window, usually the early phase of bolus transit.

A further remark seems necessary: Eq. (21.17) *assumes* that the tracer concentration in the whole enclosed microvasculature follows the arterial tracer concentration. This assumption is only sensible for sufficiently low extraction of the tracer. For highly extracted ("perfusion") tracers, on the other hand, one usually assumes rapid equilibration between capillary and tissue space, so that the distinction between both spaces vanishes completely for perfectly diffusible tracers (cf. Sect. 21.3.3). This is the reason why the fractional blood volume usually is *not* included in this case (although one might argue that there still is a very small fractional blood volume contribution from the arterial part of the microvasculature).

Formally, Eq. (21.17) amounts to assuming an instantaneous impulse response of the capillary space to the arterial input. If this assumption is dropped, one is led to more elaborate models, one example being the two-compartment system (Fig. 21.5a), where in this case the first compartment represents the capillary and the rate constants can be expressed in terms of perfusion f, PS-product PS and the fractional blood and tissue spaces. These types of models become relevant, for example, in the context of dynamic contrast agent enhanced CT (DCE-CT).

21.3.5 Distribution Volume

For reversible (untrapped) tracers, the regional *distribution volume*[10] V_d can be defined as[11]

$$V_d = \lim_{t\to\infty} \frac{\int_0^t c_t(u)\,du}{\int_0^t c_a(u)\,du}. \tag{21.18}$$

If $c_a(t)$ approaches zero at late times, this is simply the ratio of the (finite) total areas under both time activity curves. This definition implies that V_d is also identical to the equilibrium (i.e., time-independent) tissue to blood concentration ratio

$$\frac{c_t^{eq}}{c_a^{eq}} \tag{21.19}$$

if (and only if) $c_a(t)$ – and consequently $c_t(t)$ – approaches a finite *constant* value at late times.[12] V_d is related to the impulse response of the system according to

$$V_d = \int_0^\infty h(t)\,dt, \tag{21.20}$$

which follows from the definition Eq. (21.18) together with Eq. (21.4). For our compartment models, $h(t)$ is given by Eq. (21.6) and computation of the above integral yields

$$V_d = \sum_{n=1}^{N} \frac{a_n}{\lambda_n}. \tag{21.21}$$

In terms of the equivalent decoupled model (cf. Fig. 21.5), this is directly understandable considering the equilibrium at late times, when all compartments e_n have equilibrated with the blood. The tissue-blood concentration ratio is then equal to the ratio of the forward/backward transport rates, hence equal to a_n/λ_n. By summing over the independent components, Eq. (21.21) follows. Expressed in terms of the rate constants of the original model, this leads, for example, to

$$V_d = \frac{K_1}{k_2}\cdot\left(1+\frac{k_3}{k_4}+\frac{k_5}{k_6}\right)$$

for the reversible three-compartment model of Fig. 21.2d, which includes the simpler models of Fig. 21.2a, c by setting either $k_3=k_5=0$ or only $k_5=0$.

Apart from deriving V_d from a determination of all transport constants, there are other strategies such as the Logan approach which make use of the asymptotic behavior of the system at sufficiently late times (Logan et al. 1990).

[10] The terms *distribution volume* and *tissue-blood partition coefficient*, although conceptually different, denote essentially equivalent quantities. We choose the former.

[11] If tracer is irreversibly trapped in the system the ratio of the above integrals tends towards infinity with increasing time, so that V_d formally would become infinite.

[12] The tissue to blood ratio can also become constant for sufficiently slowly varying $c_a(t)$, but this ratio can deviate substantially from V_d and is thus not suitable for estimation of this parameter.

Bolus-plus-infusion techniques (see, e.g., (Carson et al. 1997)) aiming at speeding up the approach to equilibrium Eq. (21.19) are another way to facilitate V_d determination.

21.3.6 Reference Tissue Methods

Reference tissue methods have gained considerable importance in receptor imaging. In other settings, there usefulness is questionable. The basic idea is to use a reference region devoid of receptors as an indirect input function for the target region. This is achieved by assuming one-compartment kinetics in the reference region and an identical K_1/k_2 ratio in, both, target and reference region (note that these are nontrivial assumptions). $c_a(t)$ is then expressed in terms of the tissue response and rate constants of the reference region, and the resulting expression is substituted in the model equation of the target region. For details, we refer the reader to the literature (e.g., Lammertsma and Hume 1996; Müller-Schauenburg and Reimold 2008 and references given therein). Here, we only want to draw attention to the fact that reference tissue approaches must be carefully validated in each individual case before reliable results can be derived from measurements.

21.4 Specific Problems of Quantitative Small Animal Imaging

While the principal techniques of tracer kinetic modeling are equally valid for human and small animal PET, there are a number of important practical differences which generally make quantification distinctly more difficult in the latter case.

21.4.1 Spatial Resolution

Probably the most obvious difference is the fact that the limited spatial resolution of the PET scanner is potentially more problematic in small animal investigations: the reconstructed spatial resolution of small animal scanners is about a factor of three better than in clinical PET scanners (about 1.5–2 mm vs. 4.5–6 mm), while the body size of a mouse and a human differs by a factor of about 20. Therefore, in small animal PET the relative spatial resolution is reduced by a factor of about 7.

Consequently, in small animal PET the size of many target structures is not much larger than the spatial resolution and the limited recovery of true signal intensity frequently plays a much larger role than in human PET. Figure 21.7 illustrates how serious this effect becomes when the 3D object size approaches the resolution limit. It is very important to realize that incomplete signal recovery directly translates into a corresponding reduction of the derived uptake parameters (perfusion f or, more generally, uptake K_1). It is thus at least very difficult, if not unfeasible, to reliably quantify tracer uptake in structures whose size approaches the tomographic resolution: accurate recovery correction becomes mandatory, which in turn necessitates precise knowledge of the object size and shape. In real data, the situation becomes even more complicated by the spill-over of signal intensity from the surrounding background into the target region.

The different model parameters are affected differently by recovery effects. Actually, *only* the uptake parameter K_1 is directly affected. All other rate constants are not altered as long as no sizable spill-over from the vicinity into the target region occurs. The latter assumption is of course only valid if the actual target to background contrast is sufficiently high.

21.4.2 Timescales

Naturally, circulation time is much smaller in small animals than in humans. Moreover, many metabolic processes are occurring on shorter timescales, too. These differences have to be taken into account, when designing optimal scan and reframing protocols.

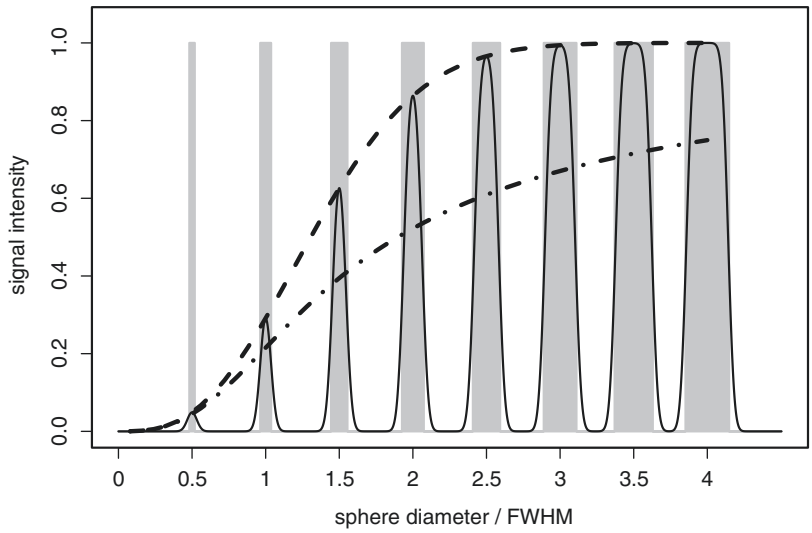

Fig. 21.7 Cross sections through the centers of differently sized homogeneous spheres of unit intensity (*solid gray*) together with the corresponding measured line profiles (*solid black curve*). Sphere diameter is specified in units of the *FWHM* (full width at half maximum) of the scanner's point spread function. The dashed curve shows the variation of the maximum measured signal for each sphere (as fraction of true intensity) with varying size, the so-called peak recovery. The dash-dotted curve shows the variation of the signal averaged over the sphere volume, the so-called mean recovery. A sphere with a diameter of twice the *FWHM*, for instance, has a peak recovery of 86 % and a mean recovery of 52 %

21.4.3 Arterial Input Function

Accurate knowledge of the input function is mandatory for many quantification approaches. The practical limitations (e.g., limited available blood volume) usually prevent direct determination by arterial blood sampling in small animal experiments. Continuous or repeated arterial blood sampling in small animals requires advanced techniques that minimize the sampled blood volume or allow direct reinjection of the blood after the measurement. Such techniques are currently far from being routinely available.

The apparently obvious solution to this problem is determination of the input function from the cavum of the left heart ventricle, since contrary to human investigations the heart is nearly always included in the field of view. But this solution is hampered by the already mentioned problems of limited recovery (of the blood signal) and spill-over (from the myocardium and other tissues in the vicinity). Using this approach requires serious effort to avoid massive bias in the derived input functions.

The critical importance of a correct input function should be re-emphasized: each overall scaling error of $c_a(t)$ directly translates into a corresponding (reciprocal) scaling error of K_1 and f. Erroneous curve shape (e.g., by spill-over from neighboring regions into an image-derived input function) effects all model parameters. Erroneous input functions do not necessarily manifest themselves in bad fits of the used model to the data: scaling errors, for example, do not affect the goodness of fit at all. Two plausibility checks can be performed, however: if the fitted fractional blood volume is much larger than expected, this is a strong indication of a scaling error (e.g., due to limited recovery) in $c_a(t)$. *If* there are strong deviations of the data from the fit of a model known to be correct for the given tracer, this might be an indication of shape errors in the input function.

21.5 Practical Considerations

21.5.1 Computing the Convolution Integral

The special convolution integral occurring in compartment modeling is computed by summing over the contributions from the different

exponentials in Eq. (21.6). We end up with a sum over integrals of the form

$$a_n \cdot c_a(t) \otimes \mathrm{e}^{-\lambda_n t} = a_n \cdot \int_0^t c_a(u)\,\mathrm{e}^{-\lambda_n (t-u)} du.$$

Only for very special choices of $c_a(t)$, this integral can be computed analytically.[13] Otherwise, one must resort to numerical methods. In this case, computation of the tissue response for all interesting time points directly from the above formula would imply repeated integrations between $u=0$ and $u=t$ since the integrand itself depends on the upper integration boundary t. This is disadvantageous since it increases computation time substantially. The obvious solution is to rewrite the integral as

$$\int_0^t c_a(u)\,\mathrm{e}^{-\lambda_n (t-u)} du = \mathrm{e}^{-\lambda_n t} \int_0^t c_a(u)\,e^{\lambda_n u} du.$$

The actual problem, then, is to accurately compute

$$I_n(t) = \int_0^t c_a(u)\,\mathrm{e}^{\lambda_n u} du, \qquad (21.22)$$

which can be done incrementally for all given time points t_m thus saving computation time. This comes at a cost, however: the naive approach would be direct numerical integration of Eq. 21.22 on the grid t_m of the measured time points using the trapezoidal rule. This approach is prone to substantial error in the resulting integral, since due to the exponential the integrand increases, for realistic input functions, very rapidly with increasing $\lambda_n u$ and the implied piecewise linear approximation continuously overestimates the actual $I_n(t)$.

A solution to this problem is to choose a suitable phenomenological model for the input function and use this in integration of Eq. 21.22. The easiest approach is to approximate $c_a(t)$ itself by a piecewise linear function, that is, to describe it by a polygon connecting the measured data points. One can then proceed by piecewise analytical integration of Eq. 21.22 using *integration by parts*. This is generally much more accurate than the naive approach.

[13] notably, if $c_a(t)$ is a sum of exponentials or piecewise linear (this includes $c_a(t) = \text{const.}$ as a special case).

21.5.2 Input Function Delay and Dispersion

Frequently, the input function has to be determined remote from the investigated tissue region or derived by arterial blood sampling. In small animal imaging, especially the latter approach will introduce a sizable time delay and shape modification (dispersion) of the input function relative to the true input function as it arrives in the target tissue.

These two parameters (delay and dispersion) have to be corrected or incorporated in the operational equations (cf., e.g., van den Hoff et al. 1993; Meyer 1989) in order to avoid potentially significant errors in the derivation of the relevant model parameters. This is at least true for perfusion measurements with freely diffusible tracers, since in this case the correct modeling of the early phase of the tracer kinetic is most important.

21.5.3 Interpolation of the Measured Data

It is frequently necessary to interpolate the measured time activity curves to a common time grid. Quite generally it can be said that linear interpolation is sufficient, if the temporal sampling of the curves is adequate. More elaborate techniques (e.g., spline interpolation) might even be dangerous by deviating locally to much from the data.

21.5.4 Influence of Metabolites

If local or systemic metabolism leads to accumulation of sizable amounts of radioactive metabolites in the blood, there are two possibilities:

1. The metabolites do not enter the target tissue at all.
2. The metabolites do enter the target tissue in parallel to the original tracer.

In the first case, the effect of the metabolites is restricted to modifying the time activity curve in the blood. If the time dependency of metabolite accumulation in the blood is known (either individually or at least in a representative control

group), the metabolites can be subtracted from the whole blood time activity curve in order to derive the true input function for the used compartment model. Note, however, that in the fractional blood volume term in Eq. (21.17), one has nevertheless to use the *uncorrected* blood curve.[14]

In the second case (metabolites do enter target tissue), one usually has to give up on the tracer, since synchronous determination of all model parameters (including those describing the metabolite kinetics) is in general out of the question.

21.5.5 Model Fitting

The actual determination of the model parameters is usually achieved by adjusting the parameters in such a way that the sum of squared differences between data and fit are minimized (*Least Squares Fitting*). In the case of compartment modeling, the model functions are nonlinearly dependent on the rate constants k_2, k_3,…, which necessitates nonlinear Least Squares Fits. It is strongly advisable to use dedicated fitting routines instead of general purpose function minimizers, since the special properties of Least Squares Problems can be used to improve stability and runtime of the fit.

The central problem with a nonlinear fit (apart from sizable runtime, which prevents use for generation of parametric maps) is that the algorithms are iterative procedures which depend on reasonable start values for all parameters. Moreover, convergence to the best parameter estimate (in the least squares sense) is not guaranteed.

For these reasons, trying to avoid nonlinear fits is worthwhile. One possibility of achieving this is to concentrate on the asymptotic behavior of the model equations. The so-called Logan-Plot (Logan et al. 1990) for determination of distribution volumes and the Patlak-Plot (Patlak et al. 1983) for determination of irreversible binding rates are the most important examples. These approaches have in common that they do not provide complete information for all model parameters but rather only for certain ratios of the parameters (which frequently can be estimated more reliably than the individual parameters).

Another possibility consists in directly using the integral versions of the model equations which *are* linear in all parameters (cf., e.g., Blomqvist 1984). This approach also allows inclusion of corrections for input function delay and dispersion (van den Hoff et al. 1993). These *linearized* fits provide estimates for all model parameters. The procedure is fast and thus well suited for generation of parametric maps. One notable disadvantage is the fact that it is in general not possible to impose constraints on the fit (e.g., by fixing some of the parameters to known nonzero values or demanding positive parameter estimates). Moreover, the parameter estimates are not optimal in the least squares sense, although in practice this does seldom lead to sizable effects.

21.5.6 How to Decide Which Model to Use

Assume you have performed an investigation with a new tracer and managed to measure a good arterial input function as well as tissue response curves. Now the question arises which kinetic model to use for further data evaluation. There are two ways to approach this task.

1. Set up the model from first principles based on your knowledge of the transport and metabolization of the tracer. Use this model for data evaluation.
2. Choose a phenomenological model of minimum complexity which is able to describe the data adequately.

There is of course no clear-cut difference between both approaches. More often than not

[14] A related problem, which can lead to substantial errors if ignored, should be mentioned: sizable plasma protein binding of the tracer (e.g., neuroreceptor ligands), which necessitates to distinguish between plasma concentration of the tracer and the free fraction in plasma that actually defines the input function.

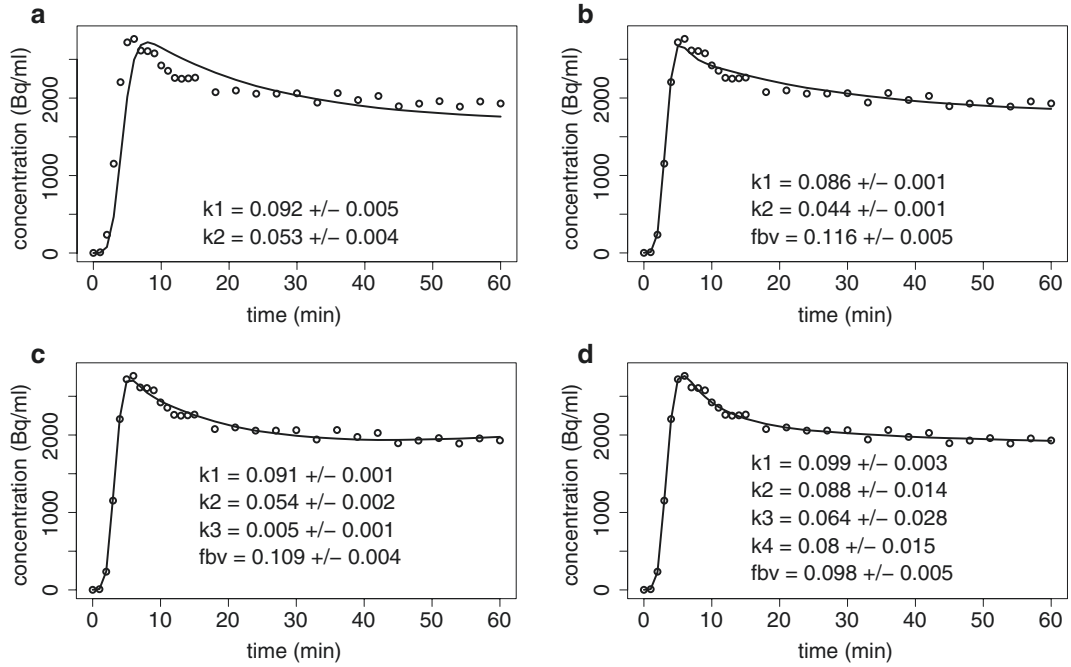

Fig. 21.8 Comparison of the performance of different models in fitting a simulated noisy tissue response of a reversible two-compartment model including a fractional blood volume parameter. The fitted model parameters are indicated in the respective subplot. All model parameters were set to a value of 0.1 in the simulation. The data were simulated using a bolus input with a shape similar to that used in Fig. 21.4. In this example, identification of the correct underlying model (**d**) is difficult, which is signaled, for example, by the substantial estimation errors of k_2 and k_3 in (**d**)

one has no complete a priori knowledge of the tracer's fate. Moreover, even if possible, a detailed description of the tracer's fate will lead to model configurations far too complex to use directly in data evaluation. It will therefore be necessary to simplify the model sufficiently.

What *is* sufficient in this context can be decided by the second approach: clarify how complex the model has to be in order to completely describe the data. It does not make sense to use a complex model whose parameters can no longer be determined with adequate accuracy from the data. It is therefore not a good idea to start with a too complex model. Rather start with a simple configuration. A pragmatic approach is the following[15]:

1. Start with a very simple model. Usually this will be the reversible one-compartment model.
2. Try to fit this model to the data. Inspect the residues (differences between data and fit). If you get systematic deviations of the fit from the data, analyze these. For example, a sharp peak in the tissue response during the bolus passage of the input is a sure sign of sizable fractional blood volume. Continuously rising tissue uptake in the late phase, whereas the fit tries to "level out," is a rather sure sign of additional compartments. According to your analysis successively increase model complexity and add further parameters. Repeat the fit.
3. Inspect the parameter estimation errors (it is mandatory that the used algorithm does provide these!). If the estimation error approaches or even exceeds the parameter estimate itself, this is indication that the parameter is not identifiable in the data and should therefore be eliminated from the model. A difficult case is shown in Fig. 21.8 were simulated noisy data

[15] There are also statistical criteria, notably the F-test and the Akaike information criterion, that can help to decide whether an increase in model complexity is justified by the concomitant improvement in the goodness of fit.

are fitted with different models. Identification of the correct model (Fig. 21.8d) is possible, but requires great care. The one-compartment model (Fig. 21.8b) cannot be ruled out with certainty.

21.6 Simplified Quantification Procedures

As has been explained previously, full compartmental modeling above all requires accurate knowledge of the full arterial input function (AIF). For small animal imaging, this poses considerable problems due to the small size of the systemic blood volume which limits the tolerable total volume and number of blood samples on the one hand and on the other hand the rather low spatial resolution which makes generation of reliable imaged-derived AIFs very difficult if not impossible. Nevertheless, for many investigations including evaluation of new tracers, there is no sensible alternative but to try to overcome these difficulties in order to obtain the required information from the investigation.

However, there are also many investigations utilizing well-known tracers with well-understood kinetics where it might be possible to avoid the aforementioned difficulties by focusing on the determination of more easily derivable quantities that can serve as surrogate of the actually targeted metabolic parameters. The definition of such surrogate parameters should always be based on a thorough analysis of the kinetic models and given experimental conditions rather than on phenomenological ad hoc approaches.

A prominent example where such a strategy can be useful is the well-known PET tracer FDG ([^{18}F]2-fluoro-2-deoxy-D-glucose). In one of the previous sections, we have reviewed the corresponding irreversible 2-compartment model, frequently called simply the "FDG-model" due to the ubiquitous use of this tracer in neurological, cardiological, and oncological PET. While FDG will serve as the concrete example here, many tracers obey a similar irreversible two-compartment kinetics and the following considerations principally apply to such tracers as well.

Although the rate constants of the FDG-model (K_1, k_2, k_3 plus *fbv*) can be derived individually from dynamic investigations (and might provide the actually needed information in special cases), it is much more frequent to only ask for a determination of the metabolic rate K_m given by Eq. (21.10), especially in the context of oncological investigations where the total glucose consumption of the tumor is the targeted quantity.

However, determination of K_m still requires to perform a dynamic PET investigation including reliable measurement of the full AIF. The method of choice for K_m determination then is the so-called *Patlak approach* (Patlak et al. 1983) which states that the relation

$$\begin{aligned}\mathrm{SUR}(t) &= \frac{c_t(t)}{c_a(t)} = K_m \cdot \frac{\int_0^t c_a(s)\,ds}{c_a(t)} + V_r \\ &= K_m \cdot \Theta(t) + V_r \end{aligned} \tag{21.23}$$

asymptotically holds at sufficiently late times after injection for the time dependence of the ratio of tissue to arterial blood concentration, called the *Standard Uptake Ratio* (SUR) in the following.

The parameter V_r (the "apparent volume of distribution") is a certain function of the three rate constants $K_1 - k_3$ – just as K_m – but of no immediate interest since it does have no straightforward interpretation in terms of physiologically relevant quantities. Plotting SUR versus the quantity $\Theta(t)$ (also called "Patlak's funny time" since dimensionally it is indeed a time) is called a Patlak Plot. It becomes linear at later times, typically around 15 min p.i., so that K_m can be determined by simple linear regression in that time window. This approach frequently works very well in practice but requires, as already mentioned, availability of dynamic data in tissue at least for the time window used in the fit as well as the *full* AIF starting at time of injection since its integral is entering the Patlak equation. Despite being numerically easier, the Patlak approach thus suffers in the same way as full compartmental modeling from the difficulties to derive the full AIF in small animal investigations.

One solution to this problem has been proposed in the context of human whole body PET

(van den Hoff et al. 2013a) by reducing the required amount of dynamic data to just two time points (DTP: *"dual time point"*) both in tissue and in blood. Regarding small animal imaging, this approach could be of interest since acquiring just two arterial samples might be considered still practicable even if sampling of the full AIF is not an option. The DTP approach in principle then allows to derive an estimate of K_m (or a closely related quantity, see van den Hoff et al. 2013a) from the secant slope between both DTP measurements.

The only possible further simplification is restriction of the quantification to what is derivable from a static scan/single time point. It is still common practice to restrict quantification either to normalization of regional tracer activity to injected dose (PID: percent of injected dose) or – slightly more sensible – to normalization of regional tracer concentration to injected dose per body weight (BW). The latter quantity is well known in clinical oncological whole body PET where for more than a decade now quantification has been limited to specifying this so-called *Standardized Uptake Value* (SUV):

$$\mathrm{SUV}(t) = \frac{c_t(t)}{\mathrm{Dose}/\mathrm{BW}}. \qquad (21.24)$$

The rationale (or hope…) underlying this approach of normalizing local tracer uptake to injected dose per body weight is that the resulting SUV should be approximately proportional to K_m so that it can serve as a surrogate parameter describing relative changes in FDG (and thus glucose) metabolism: twice the SUV thus should reflect a twofold increase of metabolic trapping. However, two potentially serious flaws of this assumption are rather obvious:

- According to Eq. 21.23 the relevant quantity is SUR rather than SUV since only for the former parameter a linear relationship and possibly – if V_r is negligible – even an approximate proportionality to K_m can be expected if the inter-study variability of the AIF shape is not too large. However, a linear relation between K_m and SUV would require *identical* AIFs (when normalized to SUV units) across subjects, an assumption which is known to be not fulfilled.
- The SUV exhibits the same time dependence as the "raw" activity concentration in the targeted tissue so its value depends on the chosen evaluation time point, which therefore needs to be strictly standardized. Where this is not possible (which is the case quite generally in clinical PET and can happen in small animal PET as well), additional nonnegligible variability of the results is caused if no suitable correction procedures are applied.

These issues have been investigated in two recent papers (van den Hoff et al. 2013b; van den Hoff et al. 2014) to which the reader is referred for a detailed exposition. The main findings are outlined in the following.

One important empirical observation is that typically AIFs of FDG and many other tracers exhibit a remarkably similar shape across different scans of the same or different subjects. This approximate shape invariance has been noted time and again, and it is of course a prerequisite to justify the use of population-averaged input functions. It can be understood in terms of similarities of systemic glucose metabolism even if pronounced pathological changes occur locally in the organism. Obviously, this shape invariance is not a "natural law" and might not always be valid, but it seems to hold remarkably well in practice.

Accepting this shape invariance as a fact, one can immediately conclude that $\Theta(t)$ in Eq. 21.23 becomes a unique, although not necessarily known function of time across different investigations. In this case (and only then…) for any chosen scan time point an essentially invariant linear relation between SUR and K_m exists since V_r is numerically small ($V_r \approx 0.5$ is a typical value in humans) and its intersubject variability is modest (and much smaller than that of K_m) so that a constant average value can be used. To a first approximation, V_r might even be neglected completely in which case SUR simply becomes proportional to K_m with the *same* scan time-dependent factor of proportionality $\Theta(t)$ across all scans and subjects.

As detailed in van den Hoff et al. (2013b), the described behavior can indeed be demonstrated in actual human PET data by comparing K_m derived from fully dynamic Patlak analysis with SUR at some fixed time point of the dynamic investigation. This makes SUR a rather attractive choice as a surrogate of K_m that can be derived from static scans and a single sample of the AIF. In human investigations, the latter can easily be derived from a large arterial vessel. In small animal imaging, it would be possible to resort to acquiring a *single*, ideally truly arterial blood sample. In passing it might also be noted that to the extent that a solely image-based determination of SUR is possible it has the further advantage over SUV that an image-derived ratio is completely unaffected by any errors in scanner calibration.

The relation between SUR and SUV is most easily understood if SUV-normalized quantities are used in its computation, i.e.,

$$\mathrm{SUR}(t) = \frac{\mathrm{SUV}_{\mathrm{tis}}(t)}{\mathrm{SUV}_{\mathrm{bld}}(t)}. \qquad (21.25)$$

It is then immediately obvious that even if SUR is indeed linearly related to K_m in an invariant way across different investigations the same would be true for SUV *only* if the blood SUVs at the time of measurement were identical across all investigations – but this is simply not the case. Rather, the inter-study variability (single standard deviation) of blood SUV is of the order of about ± (20–25)% in humans which is quite severe, especially for the purposes of follow-up investigations in the same subject, for example, in the context of therapy response control. It is the elimination of the blood SUV variability in combination with the approximate shape invariance of the AIF which makes SUR a distinctly superior surrogate parameter of K_m in comparison to SUV.

21.7 Appendix: A Short Outlook on General Compartmental Theory

We give here a short overview of general compartmental theory, which is intended to provide some background for the topics covered in Sect. 21.3.1. It moreover shows the way for efficient simulations of multicompartment models which otherwise rapidly becomes tedious and numerically inaccurate. If the reader does not feel comfortable with the mathematics, this Appendix can be skipped without problem.

We use lower case boldface for vectors and upper case boldface for matrices. In matrix notation, the general N-compartment model is then defined by:

$$\frac{\mathrm{d}\mathbf{c}(t)}{\mathrm{d}t} = \mathbf{b}(t) + \mathbf{K}\mathbf{c}(t) \qquad (21.26)$$

or abbreviated:

$$\dot{\mathbf{c}} = \mathbf{b} + \mathbf{K}\mathbf{c},$$

where $\mathbf{c}$ is a (column) N-vector of concentrations in the different compartments, $\mathbf{b}$ is the corresponding vector of inputs into the different compartments, and $\mathbf{K}$ is the $N \times N$ *transfer matrix* defining the structure of the model. All concentrations are assumed to be zero until $t = 0$. With this notation one gets, for example, for the reversible two-compartment model (Fig. 21.2c)

$$\begin{pmatrix} \dot{c}_1 \\ \dot{c}_2 \end{pmatrix} = \begin{pmatrix} K_1 c_a \\ 0 \end{pmatrix} + \begin{pmatrix} -(k_2 + k_3) & k_4 \\ k_3 & -k_4 \end{pmatrix} \begin{pmatrix} c_1 \\ c_2 \end{pmatrix},$$

which is just another way of writing Eq. (21.5). Very generally, one could consider differing time-dependent input functions $c_a^{(n)}(t)$ with different uptake rates q_n from arterial blood into the N compartments (superscript T denotes matrix transposition):

$$\mathbf{b} = \left(q_1 c_a^{(1)}, \ldots, q_N c_a^{(N)}\right)^T \qquad (21.27)$$

This kind of situation could, for instance, arise, if metabolites of the tracer accumulate in the blood and do then enter the system as well. But to keep the situation a bit simpler, we assume instead a common input function for all compartments:

$$\mathbf{b} = \mathbf{q} c_a = \left(q_1, \ldots, q_N\right)^T c_a. \qquad (21.28)$$

The IRF in the N different compartments can be expressed via a so-called *matrix exponential*. With the input vector of Eq. (21.28), the IRF is given by the vector

$$\mathbf{h} = \left(h_1, \ldots, h_N\right)^T = \mathrm{e}^{\mathbf{K}t}\mathbf{q}. \qquad (21.29)$$

The response to a finite input is obtained by (component-wise) convolution of the IRF with the

input function: $\mathbf{c} = \mathbf{h} \otimes c_a$.[16] Due to the appearance of the matrix $\mathbf{K}$ in the exponent, the precise meaning of the matrix exponential might not be immediately clear. In fact, it is defined as the $N \times N$ matrix obtained by the formal Taylor expansion

$$e^{\mathbf{K}t} = \sum_{n=0}^{\infty} \frac{(\mathbf{K}t)^n}{n!},$$

where $(\mathbf{K}t)^n$ is the n-fold matrix product of the matrix $(\mathbf{K}t)$ with itself. Accurate computation of the matrix exponential is far from trivial in the general case, but reliable algorithms are known (Moler and Loan 2003). Freely available implementations can be found, for example, in the numerical *Open Source* systems *Octave* (Eaton et al. 2014) and *R* (R Core Team 2015). For more details concerning the matrix exponential formalism in the context of compartment modeling cf. Sect. 21.5.2 in (Bates and Watts 2007).

Given a reliable matrix exponential implementation, the formalism allows an easy, efficient, and accurate computation of the IRF for arbitrary compartment models via Eq. (21.29) irrespective of their complexity. This is a very valuable tool, for example, for simulation of complex systems in order to gain insight into consequences of model simplifications. Concerning numerical accuracy (and speed) the matrix exponential approach is especially superior to numerical integration of the model equations.

For reference, we finally look a bit closer at the case where $\mathbf{K}$ is diagonalizable. The matrix exponential can then be expressed via the eigenvector matrix $\mathbf{V}$, its inverse $\mathbf{V^{-1}}$, and the eigenvalues $(-\lambda_n)$ of $\mathbf{K}$. Equation (21.29) then becomes

$$\mathbf{h} = \mathbf{V}\mathbf{E}\mathbf{V}^{-1}\mathbf{q} \text{ with } E_{mn} = \begin{cases} e^{-\lambda_n t} & m = n, \\ 0 & m \neq n. \end{cases} \quad (21.30)$$

This implies that the IRF in each compartment is a weighted sum over the exponentials $e^{-\lambda_n t}$. Explicit evaluation of Eq. (21.30) yields:

$$h_m = \sum_{n=1}^{N} a_{mn} e^{-\lambda_n t} \text{ with } a_{mn} = V_{mn} \sum_{k=1}^{N} V_{nk}^{-1} q_k, \quad (21.31)$$

which simplifies to

$$a_{mn} = V_{mn} V_{n1}^{-1} K_1 \quad (21.32)$$

if there is input only into the first compartment with a rate $q_1 = K_1$. The total system response is finally given by

$$h = \sum_{m=1}^{N} h_m = \sum_{n=1}^{N} a_n e^{-\lambda_n t} \text{ with } a_n = \sum_{m=1}^{N} a_{mn}.$$

Equation (21.30) also shows the relation to the equivalent "decoupled" model introduced earlier. The latter is defined in such a way that its transfer matrix is already diagonal (namely $\mathbf{K} = diag(\lambda_1, \ldots, \lambda_N)$) and has the input vector $\mathbf{a} = (a_1, \ldots, a_N)^T$. The corresponding impulse response is

$$\mathbf{g} = \mathbf{E}\mathbf{a}, \quad (21.33)$$

which leaves the total system response unaltered:

$$g = \sum_{n=1}^{N} g_n = \sum_{n=1}^{N} a_n e^{-\lambda_n t} \equiv h.$$

[16] For the general case of input according to Eq. (21.27) one gets:

$$\mathbf{c} = e^{\mathbf{K}t} \otimes \mathbf{b} = \int_0^t e^{\mathbf{K}(t-u)} \cdot \mathbf{b}(u)\, du,$$

where integration of the vector function is performed component-wise.

References

Bassingthwaighte J, Holloway Jr G. Estimation of blood flow with radioactive tracers. Semin Nucl Med. 1976;6:141–61.

Bassingthwaighte J, Goresky C. Modeling in the analysis of solute and water exchange in the microvasculature. In: Handbook of physiology, Sect. 2. The rcardiovascular system, vol. IV. The Microcirculation, Bethesda; 1984. p. 549–626.

Bassingthwaighte J, Chan I, Wang C. Computationally efficient algorithms for convection-permeation-diffusion models for blood-tissue exchange. Ann Biomed Eng. 1992;20:687–725.

Bates D, Watts D. Nonlinear regression analysis and its applications (Wiley Series in Probability and Statistics); 2007. ISBN 0470139005.

Blomqvist G. On the construction of functional maps in positron emission tomography. J Cereb Blood Flow Metab. 1984;4:629–32.

Carson R. Tracer Kinetic Modeling in PET. In: Positron emission tomography. London: Springer; 2003. p. 147–79. ISBN 1852334851.

Carson R, Breier A, de Bartolomeis A, Saunders R, Su T, Schmall B, Der M, Pickar D, Eckelman W. Quantification of amphetamine-induced changes in [11 C] raclopride binding with continuous infusion. J Cereb Blood Flow Metab. 1997;17:437–47.

Carson R, Cunningham V, Gunn R, van den Hoff J, Knudsen G, Lammertsma A, Leenders K, Maguire R, Müller-Schauenburg W. PET Pharmacokinetic course manual. Groningen/Montreal: University of Groningen/McGill University; 2003.

Crone C. The permeability of capillaries in various organs as determined by the use of the indicator diffusion method. Acta Physiol Scand. 1963;58:292–305.

Eaton JW, Bateman D, Hauberg S, Wehbring R. GNU Octave version 3.8.1 manual: a high-level interactive language for numerical computations. CreateSpace Independent Publishing Platform; 2014. URL http://www.gnu.org/software/octave/doc/interpreter. ISBN 1441413006.

Innis R, Cunningham V, Delforge J, Fujita M, Gjedde A, Gunn R, Holden J, Houle S, Huang S, Ichise M, et al. Consensus nomenclature for in vivo imaging of reversibly binding radioligands. J Cereb Blood Flow Metab. 2007;27(9):1533–9.

Lammertsma A, Hume S. Simplified reference tissue model for PET receptor studies. Neuroimage. 1996;4(3):153–8.

Lassen N, Perl W. Tracer kinetic methods in medical physiology. New York: Raven; 1979. ISBN 0-89004-114-8.

Logan J, Fowler J, Volkow N, Wolf A, Dewey S, Schlyer D, MacGregor R, Hitzemann R, Bendriem B, Gatley S, et al. Graphical analysis of reversible radioligand binding from time-activity measurements applied to [n-11c-methyl]-(−)-cocaine PET studies in human subjects. J Cereb Blood Flow Metab. 1990;10:740–7.

Meyer E. Simultaneous correction for tracer arrival delay and dispersion in CBF measurements by the H215O autoradiographic method and dynamic PET. J Nucl Med. 1989;30(6):1069–78.

Moler C, Loan CV. Nineteen dubious ways to compute the exponential of a matrix, twenty-five years later. SIAM Rev. 2003;45(1):3–49.

Müller-Schauenburg W, Reimold M (2008) PET pharmacokinetic modelling. In: Molecular imaging: computer reconstruction and practice. p. 189–210. ISBN 978-1-4020-8751-6 (Print) 978-1-4020-87523 (Online).

Patlak C, Blasberg R, Fenstermacher J. Graphical evaluation of blood-to-brain transfer constants from multiple-time uptake data. J Cereb Blood Flow Metab. 1983;3:1–7.

R Core Team. R: a language and rnvironment for statistical computing. R Foundation for Statistical Computing, Vienna; 2015. ISBN 3-900051-07-0. URL http://www.R-project.org/.

Renkin E. Transport of potassium-42 from blood to tissue in isolated mammalian skeletal muscles. Am J Physiol. 1959;197:1205–10.

van den Hoff J. Principles of quantitative positron emission tomography. Amino Acids. 2005;29(4):341–53.

van den Hoff J, Burchert W, Müller-Schauenburg W, Meyer G, Hundeshagen H. Accurate local blood flow measurements with dynamic PET: fast determination of input function delay and dispersion by multilinear minimization. J Nucl Med. 1993;34:1770–7.

van den Hoff J, Hofheinz F, Oehme L, Schramm G, Langner J, Beuthien-Baumann B, örg Steinbach J, örg Kotzerke J. Dual time point based quantification of metabolic uptake rates in 18 F-FDG PET. EJNMMI Res. 2013a;3:16.

van den Hoff J, Oehme L, Schramm G, Maus J, Lougovski A, Petr J, Beuthien-Baumann B, Hofheinz F. The PET-derived tumor-to-blood standard uptake ratio (SUR) is superior to tumor SUV as a surrogate parameter of the metabolic rate of FDG. EJNMMI Res. 2013b;3:77.

van den Hoff J, Lougovski A, Schramm G, Maus J, Oehme L, Petr J, Beuthien-Baumann B, Kotzerke J, Hofheinz F. Correction of scan time dependence of standard uptake values in oncological PET. EJNMMI Res. 2014;4:18.

Weiss T. Cellular biophysics, vol. 1. Cambridge: Transport; 1996. ISBN 0-262-23183-2.

Willemsen A, van den Hoff J. Fundamentals of quantitative PET data analysis. Curr Pharm Des. 2002;8:1513–26.

Data Management in Small Animal Imaging: Conceptual and Technical Considerations

22

J. Maus and F. Hofheinz

Contents

J. Maus (✉) • F. Hofheinz
Department of Positron Emission Tomography, Institute of Radiopharmaceutical Cancer Research, Bautzner Landstrasse 400, Dresden 01328, Germany
e-mail: j.maus@hzdr.de; f.hofheinz@hzdr.de

22.1 Introduction

Small animal imaging in general and multimodal tomographic imaging in particular generate a substantial amount of heterogeneous data that can be challenging to handle. Besides computed tomographic images, there are also the primarily acquired raw data such as listmode data in positron emission tomography (PET), projection data in X-ray computed tomography (CT), or even k-space data in magnetic resonance imaging (MRI). Additionally, further image data might be created by postprocessing (e.g., filtering) or by using alternative image reconstruction methods. All these data have to be stored; thus, the required disk space can easily exceed several terabyte (TB) over time. Therefore, good data storage planning and management strategies are required. In this context, data management obviously does not just mean storing the data. Rather, the data have to be easily accessible for all involved researchers, they also have to remain accessible years after the measurement, and the data have to be backed up in a save and secured place.

Therefore, data management is not just a matter of hardware and software but also of data organization and discipline. In the following, we will discuss several aspects related to this issue which might be considered when setting up a data management strategy for small animal imaging departments.

F. Kiessling et al. (eds.), *Small Animal Imaging*, DOI 10.1007/978-3-319-42202-2_22

22.2 Estimating Storage Requirements

The optimal choice of a data management environment strongly depends on the type and amount of data to be stored. A few examinations per week investigated with a single imaging modality are of course much less demanding in this respect than is the case of many examinations per week investigated with multiple imaging modalities. Therefore, the very first step to perform is a thorough estimation of the expected disk space requirements. An important question in this context is: which data *should* and which data *must* be stored permanently? For example, is it sufficient to store only the final image data or is it necessary to store also the raw data? Table 22.1 shows typical figures regarding required storage space for some common imaging modalities. Obviously, storing raw data drastically increases the required storage space, especially for PET where the list-mode data contain information on the level of each single coincidence event.

Of course, the raw data are required for image reconstruction and, therefore, have to be stored at least temporarily. However, raw data might not be needed permanently under all circumstances, and deleting these data after image generation can save a lot of space. On the other hand, without the raw data it is not possible to regenerate image data, for example, using different image reconstruction parameters. Therefore, it cannot simply be recommended to delete the raw data after initial routine image reconstruction, but rather – if at all – only after final evaluation of the data or if a particular project is finished. One might also consider to archive the raw data in compressed or condensed formats using standard lossless file compression (e.g., the zip file format) or more application-specific compressed formats like *sinograms* instead of list mode data which does, however, come at the cost of some information loss but might still be acceptable to save the option to reuse the data at a later point in time.

Table 22.1 Typical numbers of required disk space for different imaging modalities in megabyte (MB) and gigabyte (GB)

Modality	Image data	Raw data
Dynamic PET	150 MB	5 GB
Static CT	2 GB	4 GB
Static MRI	50 MB	500 MB
Static SPECT	2 MB	20 MB
Optical imaging	20 MB	—

Another aspect which directly influences the amount of data that have to be managed is the voxel size or, more specifically, the matrix dimensions of the final image data. For example, the stated storage space for CT data as shown in Table 22.1 corresponds to matrix dimensions of 1024^3. Decreasing the matrix dimensions to 512^3 already reduces the required space by a factor of 8, and for matrix dimensions 256^3 it is even reduced by a factor 64. Therefore, it is always advisable to determine the actually needed matrix size by deciding on the maximally tolerated voxel size for the required field of view. Ultimately the voxel size needs to be somewhat smaller than the actual spatial resolution of the imaging device in order not to compromise effective resolution. These decisions should be made already during the planning phase of the project, which can include test scans to determine the required matrix dimensions and thus the required amount of storage space. Avoiding the use of unsensible huge matrix dimensions does not only reduce storage space requirements but also the time needed for data postprocessing and evaluation – think, for example, of image coregistration.

It should be reiterated that increasing the matrix dimensions does not necessarily increase image quality or spatial resolution of the images and thus does not automatically provide more image detail or information. For example, the PET entry in Table 22.1 corresponds to image data with voxel size 0.5 mm and matrix dimensions $190^2 \times 70$. Since small animal PET data typically have a spatial resolution of $\approx$1.5–2 mm a further decrease of the voxel size – and corresponding increase of matrix dimensions – would not be sensible. Even an increase of voxel size to 1 mm would not have serious adverse affects on the effective image resolution – actually, it could improve the signal to noise ratio.

Table 22.2 shows an estimate of storage space for a 5 years period based on the data

Table 22.2 Disk space requirement estimate for a 5 years period

	Image data small matrix	Image data large matrix	Raw data
One animal	250 MB	2.1 GB	9.5 GB
20 animals per project	5 GB	42 GB	190 GB
10 projects per year	50 GB	420 GB	1.9 TB
After 5 years	250 GB	2.1 TB	9.5 TB

shown in Table 22.1. In this example, we assume that for each animal a dynamic PET, a CT, and an MRI are performed. The shown storage space estimates are given for two typical "small" and "large" matrix sizes as well as for the raw data. As can be seen, if the raw data are stored they dominate the space requirements, while the image data only generate a comparatively modest additional overhead in this case. In this example, the overall required storage space is approximately 10 TB which is substantial, especially when keeping in mind that these data also need dedicated backup space and a reasonably fast data access for postprocessing. The table also shows that once the raw data are *not* stored permanently, the matrix dimensions strongly influence the required storage space.

It is obvious that for low data storage demands a dedicated storage space might not be required and storing the data locally on the workstations associated with the imaging devices might be sufficient. For larger storage demands or when several team members are evaluating the data in parallel such an approach is insufficient and a dedicated and centralized storage solution becomes a clear necessity. In any case, a dedicated backup solution is required.

To summarize, a careful estimation of the required storage space is essential for selecting adequate hardware. If storage space demands are high, storage systems such as direct attached storage (DAS) or network attached storage (NAS) systems are required which usually have to be installed and maintained by an IT expert. Therefore, storage space demands directly influence the costs for data storage. However, some costs can be reduced by carefully selecting the data, which need to be stored permanently and by avoiding excessively large image matrix sizes beyond what is actually required to utilize the actual spatial resolution of the respective imaging system. Therefore, a thorough data estimation (e.g., in terms of performing test scans) should already be considered during the planning phase of projects.

22.3 Efficient Data Management

For efficient data evaluation, easy data access is important and data consistency and possibilities to store data in an indexable/searchable way are mandatory. For a single imaging device and a small project, this can usually be achieved by using the storage system of the imaging device itself. If more than one imaging device is involved or complex usage scenarios are being used, this approach is, however, not sensible any more. For example, if an animal is investigated with PET, CT, and MRI, the data are initially stored on different imaging systems without any logical link between these data apart from manually chosen identifiers or examination names. This situation complicates data evaluation and also increases the potential of mistakes. Therefore, other approaches to data management are obviously required. In the following section, we discuss different possible solutions.

22.3.1 Data Hierarchies

Properly organizing data is a prerequisite for efficient data management and evaluation. A useful approach in this context is to use a hierarchical storage layout. From an abstract point of view, it is not relevant whether such hierarchical structures are simply utilizing directly the file system of a storage system or are implemented via complex database solutions. For instance, one could decide to use a structure similar to the one illustrated in Fig. 22.1 either way.

In this example, separate project folders contain subfolders for storing data of a certain

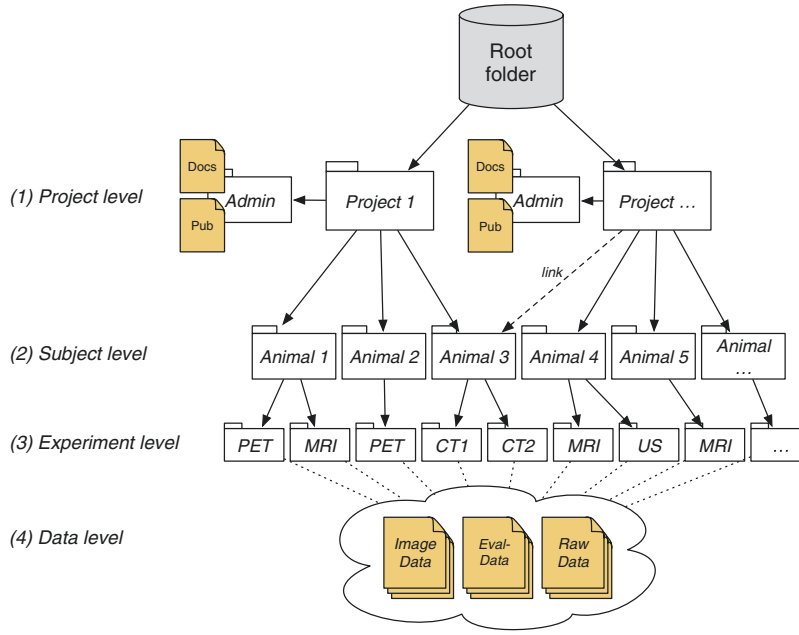

Fig. 22.1 Example of hierarchically organizing data in small animal imaging. Here, data are structured in four different levels: (*1*) all metadata belonging to a certain project (e.g., documentation and publications are stored in a separate "Admin" subfolder); (*2*) within each project folder, subfolders for each examined animal are generated; (*3*) within each animal folder another level of subfolders is created containing the actual data; and (*4*) the actual data can either be stored flat within a experiments' folder or further subfolders can be generated to separate, for example, image data from raw data. The number of levels in such hierarchical structures should be kept small. Too many levels lead to complex and untransparent setups. Also note the indicated possibility to keep all experiment data for one animal ("*Animal 3*") in a single folder while linking the subject to two different projects (thus avoiding unnecessary data redundancy)

experiment or animal. In addition, supplemental data can be organized at the same level allowing to keep administrative data (project description, planning documents, etc.) easily accessible. Finally, within the experiment or animal folder, the individual image data are stored. If appropriate, this could also mean encapsulating data from different modalities and/or raw data in separate folders.

It should be noted that while it is very helpful to use such hierarchical structures for storing/organizing data, the number of hierarchy levels should be kept rather small. If too complex, too deep hierarchical structures are built manual localization of the data within the "storage tree" becomes increasingly difficult. In such cases, dedicated search programs have to be consulted, which could complicate the data management process. In our experience, it is, therefore, a good idea not to exceed 4–5 levels.

22.3.2 Data Formats

Most older imaging devices store image data only in system specific, mostly proprietary data formats while more recent devices increasingly support storage of the image data in standardized formats, especially the "Digital Imaging and Communications in Medicine" (DICOM) standard. Still, one frequently faces a situation where multiple storage formats have to be handled within a single study. A reasonable approach, then, is to convert all data sets to a common format. Since many image data evaluation programs can read DICOM today, one possibility is to convert everything to DICOM. One drawback of this approach is the fact that the DICOM format historically is a 2D (planar) image format so that a single dynamic PET or CT investigation will be stored in thousands of separate files. This can increase access time to the data massively,

especially if the data reside on nonlocal disks. For example, for a dynamic PET scan with 70 slices and 30 time frames, 2100 DICOM files are necessary to store the data of a single experiment. To store the data shown in Table 22.2, several millions of DICOM files would be necessary. For handling such a large number of files, a powerful DICOM server and fast data storage is required both of which can be quite expensive. Therefore, it is worthwhile to consider other data formats that store all data in a single or a small number of files and are thus better suited for efficient storage and retrieval of volumetric data. For example, *Interfile* (Cradduck et al. 1989), *Analyze* (Mayo-Foundation 2007), or *NIfTI* (Strother 2007) should be named here (most of which are open data formats) that are accessible by many commercial and noncommercial software products. One example is the open source software *XMedCon* (Nolf 2003), which supports a substantial number of data formats including several vendor-specific formats and allows to convert them to the desired target format.

It should be emphasized that many things can go wrong during conversion from one format to another – and even when just reading a given format. This implies that the data conversion/import should always be thoroughly validated against the vendor-provided software tools. One recurring problem is the fact that relevant metadata might be overlooked or incorrectly converted. A good consistency check is usually to delineate regions-of-interest (ROIs) and to determine the maximum intensity values in these ROIs with the vendor software and with the actually used software. Both values should then agree within tight limits. Small residual relative deviations (e.g., below 10^{-5}) are usually no indication of malfunctioning but will rather reflect unavoidable numerical inaccuracies of the conversion process. Further checks need to be performed regarding the correct translation of the embedded metadata (e.g., scan duration, activity doses, etc.).

Despite the unquestionable advantages of using one's own choice of image display and data evaluation software – which necessitates suitable import capabilities for different formats or, alternatively, the mentioned conversion of all data to a common format – this approach is not feasible all the time or for all groups. The fallback solution in this situation is of course to use the different vendor-provided software tools. While this superficially might look like the most easy route, it frequently has the manifest disadvantage that merging of data from different modalities within a single data evaluation becomes much more cumbersome and error prone. Last not least, the vendor-provided software more often than not is severely limited in functionality, thus possibly excluding more advanced data evaluation. Overall, it thus depends heavily on circumstances which approach should be pursued.

22.3.3 DICOM Server Storage

As most modern imaging devices generate data in DICOM format storing these data on a *DICOM server* seems natural. A DICOM server can be set up very fast since server communication is part of the DICOM standard. Thus, the set up only requires a network connection of the respective imaging devices and data evaluation workstations with the DICOM server. The image data can then be easily transferred from the imaging device to the server and are immediately available for data evaluation on all suitably configured workstations.

Actually, to some extent, a DICOM server can be considered as a database which stores metadata for a certain experiment in terms of standardized DICOM tags and usually also embeds the images into the database. The latter point is the reason why DICOM servers usually require substantial hardware due to the fact that several thousands of DICOM slices have to be accessed via the database protocols. On the other hand, in principle the complete information stored in DICOM tags is accessible via suitable DICOM-aware evaluation software. This, however, does not usually imply that all this information can also be indexed and searched for. Rather, the DICOM provided search functionality is very limited: only some basic information about the animal, the image data, and the series and study

description can be queried in a search request. If more detailed information is required, it is necessary to retrieve the whole image data set in order to get access to all DICOM tags which is time-consuming, uncomfortable, and error prone. Furthermore, even DICOM certified data evaluation software in general will not provide access to all metadata tags since according to the DICOM standard vendors are allowed to optionally define so-called private tags whose correct interpretation primarily is only known to the vendor. Handling of these private tags necessitates continuous adaption of the respective evaluation software since they might be changed or augmented by the vendor as he sees fit, for example, during new software or hardware releases.

Another point to consider is that many DICOM servers are not designed to handle large number of images well. Only servers storing the data efficiently in databases or via highly cached file systems can cope with such a situation, while more basic DICOM servers (e.g., embedded DICOM server functionality of image devices themselves) will run into trouble: everything works fine when the DICOM server is first set up, but after some time data access becomes slower and slower until the latency becomes intolerable. It is therefore of crucial importance to carefully select suitable DICOM server hardware and a dedicated *DICOM server* software. It is, however, fortunate that even freely available open-sourced DICOM servers can be quite powerful today. One appropriate example is *Orthanc* (Jodogne et al. 2013).

An even more advanced option for an enterprise DICOM server setup is the use of a full *Picture Archiving and Communication System* (PACS). Such a system usually combines a powerful DICOM server in hardware and software as well as a full data archiving and backup system. Thus, if very advanced search functionality is required, the use of a plain but powerful DICOM server – or even better a full PACS – should be considered. However, while basic DICOM servers can be setup quite easily and with low costs, full PACS systems are usually quite expensive due to the fact that they are mostly target at large clinics.

22.3.4 File System Storage

Probably the most frequently chosen approach to management of the acquired image data is direct storage within the file system using sufficiently capable hardware. This allows fast and direct data access if a few conditions are met:

1. The storage solution (e.g., a DAS system connected to a file server or a NAS system) has to be directly accessible by all workstations and participants. Usually one of the best solutions is to connect such a storage system to a dedicated server providing shared file system capabilities to other systems/users.
2. Where possible, data stored in a large number of separate files (notably DICOM data) should be converted to a better manageable data format to allow file systems to operate more efficiently (sequential I/O on file systems shows usually better performance than random I/O).
3. The data have to be stored in a hierarchically organized directory tree with meaningful directory/file names.
4. Meta data supplied together with information about experiments should be stored in human readable text/data files rather than in binary formats. Together with meaningful directory/file names, this usually allows to quickly search and extract information using scriptable applications which provides functionality almost in a similar way how databases perform their search.

There are of course many ways to set up a file system-based directory tree. As long as directory/file names directly refer to project identifiers, even substantial amounts of imaging data can be handled in this way. As a side effect, the directory tree also provides a structure for storing results of data evaluation. For example, the results of an imaging data analysis (e.g., a region-of-interest (ROI) analysis) can be stored in the project directory (or within an additional "analysis" subdirectory) and can be easily located and accessed. A clear advantage of this solution is easy and rapid direct access to the image data. It is also easy to reorganize such data

structures, and it allows automated/scriptable data evaluation all of which is hardly possible if all data are stored in a database or are only accessible via a DICOM server.

It should be noted, however, that a purely file system-based data handling might not be suitable for very large imaging departments with complex data analysis procedures, for example, if many team members are working with the same data and/or the same subject belongs to several projects. In such a case, the relevant information is usually hard to be encoded in directory names or metadata files, and, therefore, the data might be usually better organized using a carefully designed database structure. At least metadata should then be handled by a database solution.

We think it is, nevertheless, fair to say that for most use cases keeping a clear and rigorous data structure on file system level probably is the best approach to maintain a good data management and reduce the probability of human errors during data evaluation. The only important prerequisite in this context is a properly defined file system structure and adequate discipline of all participants working with the data.

22.3.5 Database Storage

We have previously discussed the need for adequately structured data storage. Apart from realizing this via the file system, it might also be contemplated to use a *database* instead in the hope that it might provide the required functionality (easy lookup, rapid access, etc.) more easily or more efficiently. However, while databases in general are good in providing a centralized storage of data, especially if there are relations between them, their use has a couple of disadvantageous aspects as well.

For one, databases usually are only suitable to store the metadata but not the actual image data. Storing the metadata allows indexing and searching these data via dedicated user interfaces more efficiently and more easily than on the file system level. At the same time, the huge amount of binary image data is not suitably for efficient storage in a database.

In any case, it is not trivial to decide on a suitable database solution. There are hundreds of different products available today. They range from products claiming to be full-fledged databases but failing to provide crucial features over products combining database functionality with integrated configurable user interfaces to big SQL-based relational databases which require substantial expertise for setup and maintenance. Suitable intuitive user interfaces can also not be taken for granted. In addition, the efficient use of database products to store a large amount of data usually requires to also think about proper storage hardware which can handle the amount of I/O operations such a database based solution usually requires. Last not least, the database schema/layout has to be carefully defined in the very beginning as redefining the database schema afterwards is far from easy and should only be performed by a database expert.

Considering all these things, we believe uncritical reliance on databases as the best technology for the problem at hand should be avoided. Only if the database product is carefully selected, the initial database layout is competently designed and qualified maintenance performed this approach will be able to provide real advantages in comparison to the previously discussed approach of "just" using a file system-based hierarchy. Otherwise the disadvantages will – in our opinion – outweigh the advantages.

22.4 Data Storage Hardware

So far we have mostly discussed only software-related aspects of data management without considering the necessary hardware aspects. This will be done in the present section.

The principle rapid access storage units are hard disks. Single disks do not offer any safeguard against fatal data loss in case of hardware failure. For these reasons, so-called *Redundant Array of Independent Disks* (RAID) storage systems have found wide-spread distribution. Such systems use multiple hard drives to achieve redundant distributed storage of the data in such a way that failure of single or even multiple

drives – which frequently can be "hot-swapped" without shutting down the system – does not lead to data loss. Beside this basic functionality of providing redundancy in case of hard drive failure RAID systems also offers different "RAID levels" of combining drives to maximize storage space or performance. The most prominent RAID levels (RAID 0, RAID 1, RAID 5) are illustrated in Fig. 22.2.

Today they also often can provide more advanced enterprise features like *Deduplication* and *Thin Provisioning*. Deduplication enables a storage system to save only the differences between different data sets. This can significantly reduce the required disk space in case data have to be replicated in different project/study directories. Thin Provisioning, on the other hand, can greatly reduce the burden of having to reorganize a file system, or the whole storage system in case space is limited by utilizing all available storage space for all subvolumes without reserved space for a specific volume.

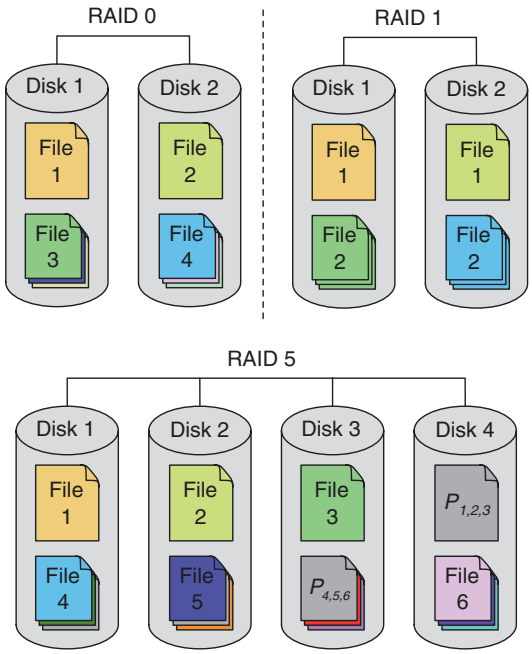

Fig. 22.2 Schematic illustration of the three most prominent RAID levels (*RAID 0*, *RAID 1*, *RAID 5*) which provide disk *striping* and *mirroring* at certain levels. RAID 0 (*striping*): maximized disk space while risking to lose all data in case of a single drive failure (not recommended). RAID 1 (*mirroring*): full data replication at the price of only providing disk space as large as a single drive. RAID 5: combination of *striping* and *mirroring* functionality by distributing parity information throughout all disks allowing data to survive a single disk drive failure while providing more disk space at the same time

While 15–20 years ago RAID systems, due to their high costs, were available only at large data centers, they have reached even the consumer market today. Thus, there is a multitude of different systems being available. Even small RAID systems can greatly improve storage access availability and access times today. This is especially true for setups where a large amount of files (e.g., DICOM server setups) have to be stored and accessed. Care has to be taken, however, that hardware RAID systems are used rather than software-based solutions which are commonly quite cheap and easy to setup but do not provide enough bandwidth and only have very limited fault tolerance functionality.

Another important question in this context is *how* the storage can be accessed by all participants of a project or study. For single hard drive-based solutions, this usually means that a certain folder or directory can be enabled to be *shared* via the workstation system of an imaging device. This has the advantage that it is quite easy and straightforward to setup. The bandwidth is limited in this case, however, and assigning suitably restricted user access permissions can be difficult. Even if a workstation comes with an embedded small-sized RAID system, it usually is not advisable to use the workstation as a file server because this setup usually will not provide appropriate backup functionality and performance under serious load or could even have a negative effect on the stability of the imaging device itself.

Instead, it is advisable to setup a dedicated file/storage server system providing a centralized and efficient path for accessing image data from several workstations and users. Such a file server should utilize a dedicated RAID system which makes it a so-called *Direct-Attached Storage* (DAS) solution. Another possibility is so-called *Network-Attached Storage* (NAS) systems. Today, they are even available with enterprise RAID features. Such systems have the advantage

that the burden to setup a dedicated file server is removed while still providing a basic set of management tools to setup shares, assign users, and provide project-based access rights while also allowing fault tolerance setups. Still, if more flexibility and dedicated control over the file system is required or if an efficient DICOM server setup is required, the use of a separate server connected to a DAS system usually remains the better choice.

22.5 Data Archiving and Backup

A final important point in data management is proper data backup which is essential to prevent fatal data loss through hardware failure, severe events like fire and water damages, or through theft. A RAID-based storage solution does not solve this problem alone, since RAID systems only provide fault tolerance functionality that reduces the risk of having data inaccessible for a longer period of time due to a disk drive failure. They are not suitable as a backup system protecting from data loss or as a data archiving system making sure data are still readable after a time period of 10+ years.

Strictly speaking, a proper backup solution includes regular copying the data to a physically remote location in order to minimize the probability of data loss. For this purpose, large institutions often establish mirrored storage systems at different geographical locations. Where this is not possible, the use of specialized backup tape drives with the possibility to regularly create a mirrored copy of all data and placing these tapes at safe and secured locations might be an option as well. This, however, often requires a manual transport of these tapes to secure locations. Using data encryption in such use cases is of course mandatory to protect from data theft.

Furthermore, *data backup* should not be confused with *data archiving*. In the latter case, the current state of data is not only mirrored, but the actual changes of data over a certain period of time are preserved. By using proper data archiving mechanisms, any data change over time can be restored within a certain time frame. Data archiving often involves storing of data on media systems such as tape drives, which are known to remain accessible over long periods of time (e.g., 25+ years). This, for example, cannot be guaranteed for most optical data storage systems: for example, a DVD is known to have a maximum life time of ≈ 5–10 years. In addition, such specialized data archiving solutions also often come with vendor guarantees that the hardware necessary to access these tapes will remain available in the future.

Altogether, it is thus important to keep in mind that a sound backup and archiving strategy is mandatory. Whether this is realized via specialized hardware and software solutions is not important in the first place. It is, however, important to refrain from relying on manual ad hoc procedures or to choose too limited backup/archiving solutions which sooner or later will lead to irrecoverable loss of valuable data which could easily set a whole project or institution at risk.

22.6 Summary

After reading this chapter, it should be clear that there certainly is not a single optimal solution for efficient data management and organization. Rather, the best approach depends on the amount of data generated, the data processing work-flow, and the utilized data evaluation software. And it is to some extent also a matter of taste.

Using appropriate tools for data management and storage can significantly contribute to successful and efficient data processing. Considering the possibility of fatal data loss or serious delays caused by deficiencies in this area, it even might be critical for a project's success. Selection of the appropriate tools, however, usually requires substantial expertise, making consulting of an IT professional advisable, at least in the planning and setup phase of a new facility.

At the same time, it should be kept in mind that simple, well thought-out and straightforward solutions usually will work better than overly complex enterprise solutions. The central point in our view is to implement a sound and clear organizational structure for the data handling and

management task which is understood, respected, and followed by all team members of a small animal imaging department.

References

Cradduck T, Bailey D, Hutton B, De Conninck F, Busemann-Sokole E, Bergmann H, Noelpp U. A standard protocol for the exchange of nuclear medicine image files. Nucl Med Commun. 1989;10(10): 703–14.

Jodogne S, Bernard C, Devillers M, Lenaerts E, Coucke P. Orthanc – a lightweight, RESTful DICOM server for healthcare and medical research. In: Biomedical imaging (ISBI), IEEE 10th International Symposium on, San Francisco; 2013. p. 190–3. URL http://orbi.ulg.ac.be/handle/2268/163949.

Mayo-Foundation. Analyze 7.5 file format. Mayo Foundation, Biomedical Imaging Resource; 2007. URL http://www.mayo.edu/bir/PDF/ANALYZE75.pdf.

Nolf E. Xmedcon – an open-source medical image conversion toolkit. Eur J Nucl Med. 2003;30:246. URL http://xmedcon.sourceforge.net/.

Strother S. Neuroimaging Informatics Technology Initiative (NIfTI); 2007. URL http://nifti.nimh.nih.gov/.

Part VI

Special Applications

Cell Tracking and Transplant Imaging

23

Laura C. Rose and Jeff W.M. Bulte

Contents

Abbreviations

^{19}F MRI	^{19}F Magnetic resonance imaging
^{1}H MRI	^{1}H Magnetic resonance imaging
^{64}Cu-PTSM	^{64}Cu-pyruvaldehyde-bis(N4-methyl-thiosemicarbazone)
CA	Contrast agent
CBG99	*Pyrophosphorus* luciferase
CT	Computed tomography
FDG	Fluorodeoxyglucose
FITC	Fluorescein isothiocyanate
GFP	Green fluorescent protein
hNIS	Human sodium iodide symporter
Luc2	Firefly luciferase
MR	Magnetic resonance
MRI	Magnetic resonance imaging
MSC	Mesenchymal stem cell
NMR	Nuclear magnetic resonance
PET	Positron emission tomography
pg	Picogram
PpyRE9	Mutant red-shifted firefly luciferase
RLuc	*Renilla* luciferase
SPIO	Superparamagnetic iron oxide

L.C. Rose • J.W.M. Bulte (✉)
Russell H. Morgan Department of Radiology and Radiological Science, Division of MR Research, Cellular Imaging Section and Vascular Biology Program, Institute for Cell Engineering, The Johns Hopkins University School of Medicine, Baltimore, MD 21205, USA
e-mail: jwmbulte@mri.jhu.edu

23.1 Introduction

There is an increased need to determine the fate of transplanted cells, owing in part to the great promise of cell therapy in contrast to the lim-

F. Kiessling et al. (eds.), *Small Animal Imaging*, DOI 10.1007/978-3-319-42202-2_23

ited successful clinical trials. Imaging allows investigations into the survival and biodistribution of implanted cells necessary to understand the mechanisms of action. Ultimately, this allows studies to correlate a biological response or therapeutic outcome with the presence of transplanted cells. Such correlation is critical to understanding both the progression of disease pathology and effect of cell therapies. Studies can be longitudinal, where cells can be noninvasively monitored over time delivery (Fan et al. 2012), or singular, where the immediate needs to be determined (Gorelik et al. 2012), or a combination of both (Baligand et al. 2009). For longitudinal studies, serial images are taken over time are migrating away from and are most suitable when as cells the engraftment site relevant to the disease or therapy (Fan et al. 2012). Biodistribution studies focus on migration of cells to targeted injured or diseased tissue, typically following systemic delivery (Azzabi et al. 2014).

The type of study, disease model, and available imaging modalities, among other considerations, dictate the tracking system. The cell type in particular affects label selection, as some cells may be less amenable to certain modifications. Immortalized cells are particularly suitable to transplantation due to a robust viability that enables exposure to strenuous labeling conditions followed by transplantation in a small animal model. Transgenic protein production is generally higher in cell lines compared to primary cells (Garikipati et al. 2014), allowing for increased sensitivity and detection of fewer cells. In addition to immune considerations, however, the process of immortalizing cells can alter cellular characteristics and potentially diminish the physiological relevance and necessitate use of alternative cell sources. Primary cells may present a more physiologically relevant model that better recapitulates the biological processes in vivo required to investigate the research question. More effort is typically needed to develop protocols appropriate for primary cells, as they can be more fragile and more resilient to genetic modification or label uptake.

Cells for transplantation are modified ex vivo and then transplanted into the animal, with workflow dictated by the label. The resources and extent of technical expertise required by the modification protocol are highly dependent on the label selected, with some labeling complete within hours and other requiring days or weeks to modify and confirm proper expression or detection. Cultures are collected to obtain a single-cell suspension that is injected into the animal. Alternatively, cells can be implanted together with a biomaterial where cells are grown or loaded on biomaterial substrates or encapsulated and the loaded graft surgically implanted. Following administration of the cell transplant, animals can generally be imaged on the same day.

This chapter will focus on the most widely used methods for tracking cells transplanted into small animals. Tracking methods are divided into genetic expression systems for optical detection with a focus on fluorescent proteins and bioluminescence and exogenous labeling systems with a focus on gadolinium, iron oxide, fluorine labels, and radioactive tracers.

23.2 Optical Imaging with Genetic Expression Systems

Cells can be genetically modified to express a gene that can be optically detected following transplantation. The lack of transgene in native tissue ensures that signal originates only from implanted cells, as the genetic modification in transplanted cells is not transferred to host cells. Cell tracking with genetic modifications has the added benefit that only living cells express the transgenic protein as cells that die cease to express the transgenic protein, leading to the absence of signal. When a cell divides, both daughter cells will continue to express the transgenic protein, increasing the number of cells expressing the protein of interest and corresponding to a signal increase (Qin et al. 2013). Viable cells can be tracked for as long as they remain alive and express the transgene. For this reason, transgenes are particularly well suited for long-term cell tracking studies. Bioluminescence is predominantly

used for pre-clinical cell tracking studies, but fluorescence can be a suitable choice and is frequently included as a reporter gene during construction of bioluminescent cells for imaging validation with microscopy. It is desirable to co-register the bioluminescent or fluorescent signal from transplanted cells with anatomical structures, e.g., as can be obtained using a micro-computed tomography (CT) scan. Low spatial resolution remains the main restriction for use of bioluminescent and fluorescent in vivo cell tracking in small animals, especially in deeper tissues.

Construction of cell cultures expressing the desired tracking genes can be an arduous task, but there are countless genetically modified cells available to researchers, allowing for widespread adoption of these systems. For most purposes, the stable production of transgenic protein over extended periods of time is desirable (Zhong et al. 2013) to ensure that changes in signal correlate with changes in cell number, and not altered gene expression. Differentiation along certain lineages (Elhami et al. 2013) and disease pathology (Katsumata et al. 2013) can alter transgene expression, and the effect of these variables on transgene production should also be investigated. The choice of promoter, the genetic element that controls transcription of the gene, is also an important factor to consider as stem cells in particular can show large decreases in the transgenic gene expression with viral promoters (Norrman et al. 2010). Modified cells should be tested to confirm there is no change in expression for at least the intended duration study or conditions (Cao et al. 2006). Once cells express the transgene and the stability of its expression confirmed, cultures are expanded for transplantation.

23.2.1 Bioluminescence

Due to its comparatively low background and high sensitivity, the majority of genetically modified in vivo cell tracking studies in small animals employ bioluminescence. Cells express the enzyme luciferase and, in the presence of a substrate, catalyze a reaction during which light is emitted. No excitation signal is required for light emission. After substrate administration, the animal is imaged in a dark, closed chamber, and the light emitted from the transplanted cells is detected. The lack of excitation beam results in a lowered background signal and high sensitivity (Fig. 23.1a). The most commonly employed luciferase is firefly luciferase (Luc2), but others such as *Renilla* luciferase (RLuc), *Pyrophosphorus* luciferase (CBG99), and mutant red-shifted firefly luciferase (PpyRE9) are frequently reported. Longer wavelength (>600 nm) emitting luciferases may by

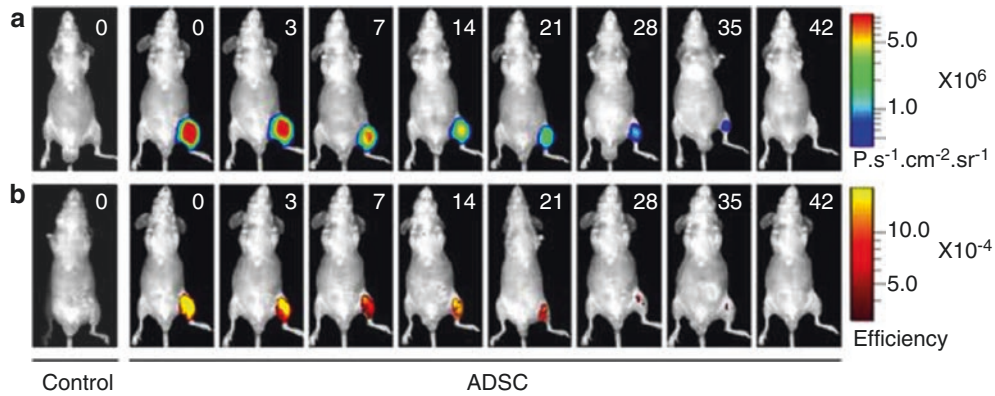

Fig. 23.1 Bioluminescent and fluorescent cell tracking. Adipose stromal cells were modified to express firefly luciferase (**a**) and green fluorescent protein (GFP, **b**) and were injected into a hind limb ischemia mouse model. Longitudinal monitoring shows gradual loss of graft viability as indicated by the decrease in signal, with agreement between the two reporter gene systems (Reproduced, with permission, from Fan et al. (2012))

more suitable for imaging transplanted cells, as shorter wavelength light is absorbed by cellular components, but these luciferases generally show lower signal strength (Mezzanotte et al. 2013; Liang 2012).

Bioluminescence data are normally shown with different time points or treatment groups normalized to a control. Since the number of implanted cells correlates with the bioluminescent signal, the signal intensity can be used to determine the fate of transplanted cells. With standard luciferase constructs, a minimum of 10^3–10^4 cells are needed for in vivo detection (Aswendt et al. 2013; Martens et al. 2014; Mezzanotte et al. 2014).

The sensitivity of bioluminescent cells depends greatly on the imaging system, animal (e.g., white vs. dark haired), and anatomical transplant site, but other external factors can be optimized to improve sensitivity. Animals can be imaged at several intervals following substrate administration to ensure maximum signal is measured, along with optimizing the dose of substrate (Aswendt et al. 2013). Sensitive applications that require detection of very small numbers of cells can be attempted using specifically engineered cells that yield increased light emission. Selected clones with multiple modifications have outputs of 10^3–10^4 photons per second per cell compared to 10^1–10^2 with unmodified luciferase expression systems and allow detection of fewer than ten cells (Rabinovich et al. 2008; Kim et al. 2010). Such sensitive imaging must be accompanied by more stringent tests to confirm the signal source, including imaging the animal before and after cell delivery to identify areas of autofluorescence (Kim et al. 2010).

23.2.2 Fluorescence

Genetically modified cells can express a fluorescent protein, which emits light when excited by the suitable wavelength. The excitation and emission wavelength, along with the signal strength, are dependent on the selected fluorescent protein. Since an excitation signal is required for production of emission signal, the background can also be high. As with bioluminescence, red and infrared fluorescent proteins are better suited for imaging in tissue. Both the excitation and emission signals of shorter wavelength green and yellow fluorescent proteins are impeded in tissue. Even with longer excitation and emission red and infrared fluorescent proteins, fluorescence imaging is also limited by scattering of both the excitation and emission signals, which can severely impact the imaging accuracy. Although not as frequently used as bioluminescence, fluorescence imaging can be used to track distribution of transplanted cells (Wang et al. 2014) and cell survival over time (Fan et al. 2012) (Fig. 23.1b). Fluorescent systems are advantageous because the presence of fluorescently labeled cells in vivo can be easily confirmed with fluorescent microscopy of fixed tissue sections or flow cytometry of cells harvested from tissue. For this reason, fluorescent labels are extensively used concurrently for confirmation with other tracking systems and during construction of other genetic tracking systems. The number of cells required for imaging is slightly higher than bioluminescence, with around 10^4 fluorescently labeled cells required for detection (Mezzanotte et al. 2014; Tam et al. 2007).

23.3 Exogenous Labels

Cells labeled with exogenous compounds not normally present or found only at low concentrations allow detection of transplantations. As neither compound is found in the body in large amounts, radioactive tracers or nonradioactive fluorine-19 (^{19}F) form hot spots that are detected with positron emission tomography (PET) and ^{19}F magnetic resonance imaging (^{19}F MRI), respectively (Bulte 2005). The MR contrast agents (CA) paramagnetic gadolinium (Gd^{3+}) and superparamagnetic iron oxide (SPIO) alter the local magnetic field, allowing detection of transplanted cells on MRI. For hot spot imaging, the signal produced by the transplanted cells is easily co-registered with anatomical structures of interest with either ^{1}H MRI or CT scans. Furthermore, labeling is generally faster and requires less technical expertise. Modification occurs either the same day or a few days prior to cell transplantation.

Exogenous labels are frequently employed in small animal models because many are suitable

for imaging cells transplanted in deep tissue. They also offer a potentially accelerated route for clinical translation, unlike most genetic-based tracking systems that are not suitable for use in humans. While it is not necessary and may not be prudent to use clinically relevant labels for tracking cells in small animals, studies aiming for clinical application may benefit from using labels approved for use in humans with relevant results and development of clinically applicable protocols.

For some label types, the signal will decline as cells die. For transplants that survive or increase in cell number, the total signal typically remains the same as long as cells do not migrate away, as the label is diluted between daughter cells as the cells divide (Guenoun et al. 2012; Danhier et al. 2014). Appropriate selection is necessary to ensure accurate cell tracking, as some labels remain at the transplant site following cell death, resulting in signal originating not from the transplanted cells but from free label or inadvertent labeling of the animal's own cells.

Cell cultures are typically incubated with the label for a period of hours to days. Free or unbound label should be removed with multiple washes, after which cultures can be harvested for transplantation. In addition to the cell type, labeling efficiency is influenced by the length of exposure, label concentration, and presence of serum in media. Although many labeling protocols are applicable across a variety of cell types, optimizing uptake is required when labeling a new cell culture. As the efficiency of labeling is paramount to imaging sensitivity, optimization is critical. The method to determine uptake efficiency is highly dependent on the particular label, but many commercially available labels have a conjugated form containing a fluorescent probe such as fluorescein isothiocyanate (FITC) or rhodamine to allow facile preliminary assessment with microscopy or flow cytometry (Helfer et al. 2013; Sibov et al. 2014; Chen et al. 2013). For cells that are difficult to modify, the label can be mixed with a carrier or transfection reagent to facilitate transfer across the cell membrane, but carriers may impart more toxicity than the label itself.

23.3.1 Gadolinium

Gadolinium (Gd^{+3}) is a T1-shortening CA for tracking cells with MRI, with labeled cells appearing as bright areas on T1-weighted MRI (Fig. 23.2a).

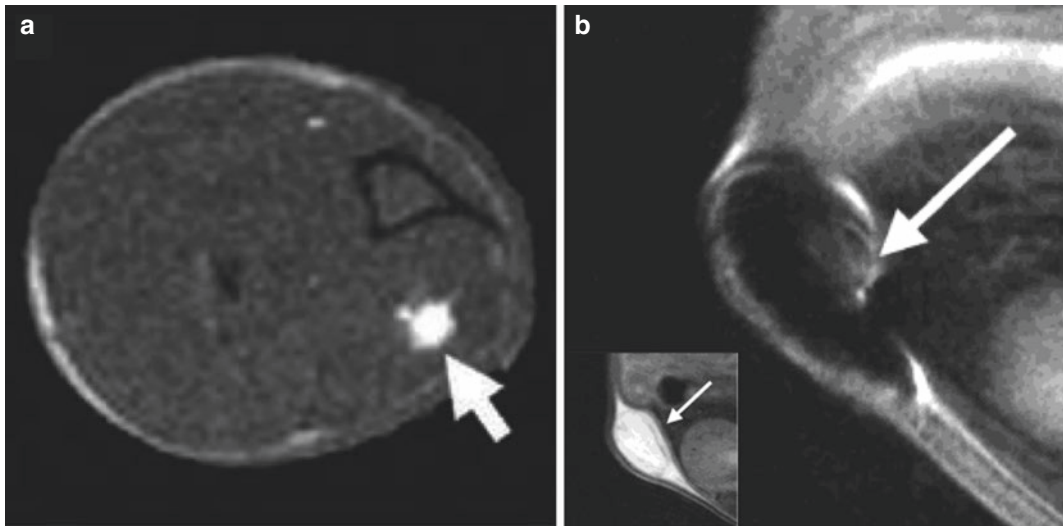

Fig. 23.2 ^{1}H MRI tracking with contrast agents. Gadolinium-labeled myoblasts transplanted into leg muscle show increased contrast on T1-weighted MRI (**a**), while SPIO-labeled cells appear as a signal void on T2-weighted MRI (**b**). Inset in panel (**b**) shows injection of unlabeled control cells transplanted for comparison. *Arrows* indicate the cell transplant (Reproduced, with permission, from Baligand et al. (2009), Azzabi et al. (2014))

Due to the toxicity of free Gd^{+3}, gadolinium is usually bound to a chelate or nanoparticle, such as gadolinium diethylenetriaminepentaacetic acid (Gd-DTPA) (Guenoun et al. 2012; Pan et al. 2014) or gadolinium oxide nanoparticles (Faucher et al. 2012). Although regulatory approved formulations for systemic delivery in patients can be used to label cells transplanted in small animals, the risk of Gd^{+3} release during long-term studies makes clinical translation of gadolinium cell tracking uncertain. A carrier is typically required to facilitate transfer across the cell membrane (Shuai et al. 2014), but some formulations can be used without need for uptake assistance (Nolte et al. 2008). Internalized gadolinium complexes can be observed with transmission electron microscopy of cultures (Pan et al. 2014). Alternatively, fluorescently tagged gadolinium complexes can be used for routine fluorescent microscopy or flow cytometry investigations.

The number of gadolinium atoms per cell can be quantified with spectrometry of lysed cultures (Faucher et al. 2012; Guenoun et al. 2012). Loading is around tens of picograms (pg) of gadolinium per cell (Faucher et al. 2012; Guenoun et al. 2012), an average of 10^{10} gadolinium atoms per cell. The content per cell becomes diluted with cell division, but the sum of the signal remains the same as long as cells don't migrate away, indicating that little if any probe is lost during cell division (Guenoun et al. 2012; Tachibana et al. 2014). With the high field strength required for small animals, transplants of 10^4 labeled cells are typically required for detection (Guenoun et al. 2012; Aspord et al. 2013). Because Gd^{3+} can be detected at the transplant site following death of cell graft, this label may not be suitable for long-term cell tracking (Baligand et al. 2009).

23.3.2 SPIO

Superparamagnetic iron oxide (SPIO) is referred to as a negative contrast agent, as it reduces the local MRI signal. Labeled cells appear as hypointense regions or signal voids on T2-weighted MR images. Cells are labeled with SPIO in culture and then transplanted for detected with MRI (Fig. 23.2b). Care must be taken in interpretation of signal, since other sources of field inhomogeneity can produce similar signal decreases, including surrounding structures or hemorrhage (van den Bos 2006) due to biological sources of iron such as hemoglobin (Josephson et al. 1991). Uptake of SPIO is on the order of tens of picograms (pg) of iron per cell (Heyn et al. 2005; Cianciaruso et al. 2014), corresponding to a calculated 10^{11} iron atoms per cell. Following SPIO labeling, the iron content of cultures can be obtained by spectroscopy of acid-treated cultures (Markides et al. 2013). SPIO particles in cell culture or tissue sections can be visualized with Prussian blue staining. Because particles can remain at the transplant site long after death of transplanted cells and can be taken up by the animal's own cells, SPIO is not recommended for long-term cell tracking of cell viability (Baligand et al. 2009; Cianciaruso et al. 2014). The number of cells required for detection depends greatly on the magnetic field strength as well as the labeling efficiency, and typical values are 10–100 cells (Ahrens and Bulte 2013). Single macrophages labeled with SPIO have been tracked in the brain, with its comparatively homogenous background, but required high iron loadings of 60 pg of iron per cell (Heyn et al. 2005) that may not be possible for all types.

23.3.3 Radiolabels

Cells labeled with radioactive tracers can produce images with good spatial resolution and, due to the lack of background signal, very good sensitivity (Fig. 23.3a, b). Commonly used tracers for cell tracking in small animals include fluorine-18 (^{18}F) or copper-64 (^{64}Cu) for detection with positron emission tomography (PET) and technetium-99 (^{99}Tc) or indium-111 (^{111}In) for detection with single-photon emission computed tomography (SPECT). Radiotracers are limited by short half-lives, which limits the length of time cells can be observed, and cellular toxicity particularly for sensitive cultures including stem cells (Tarantal et al. 2011) and T cells (Berglund et al. 2013). Unmodified cells can be preincu-

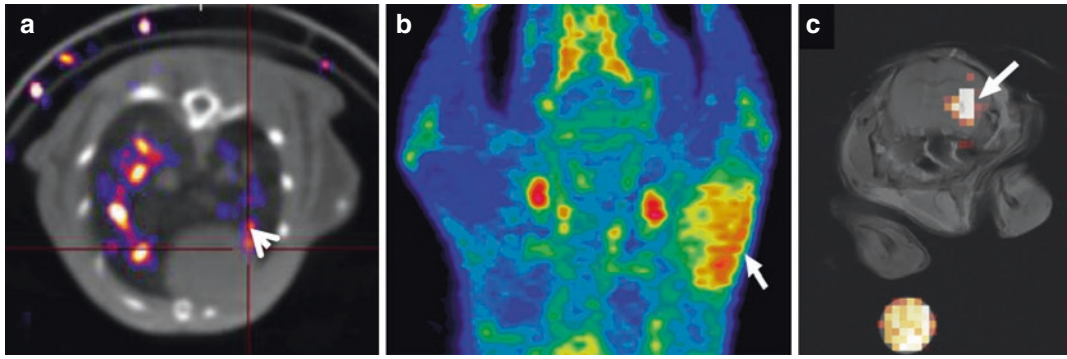

Fig. 23.3 Hot spots with radiotracers or ^{19}F-labeled cells. Mesenchymal stem cells (MSCs) labeled with ^{99}Tc were imaged with SPECT in a myocardial infarction mouse model (**a**), overlaid with CT scan. *Arrow* indicates cells that accumulated in damaged cardiac tissue, while other signals are from cells entrapped in the lungs. MSCs transfected with hERL were injected into the foreleg and imaged with PET following an intravenous injection of ^{18}F tracer (**b**). *Arrow* indicates tracer in MSC expressing hERL, while no signal is seen from the contralateral side containing unmodified MSCs, lacking hERL. ^{19}F-labeled cells were injected into the striatum and detected with ^{19}F MRI (**c**). The fluorine image is overlaid onto a ^{1}H MR image and shows a fluorine standard in the bottom as a reference with *arrow* indicating injected cells (Reproduced, with permission, from Garikipati et al. (2014), Qin et al. (2013), Zhong et al. (2013))

bated with the tracer for direct labeling, or cells can be tracked in an indirect manner, where cells modified to take up the tracer at an increased rate are implanted and labeled in vivo following intravenous injection of tracer in a manner similar to detection of luciferase expressing cells.

The glucose analogue ^{18}F-fluorodeoxyglucose (FDG) is actively taken up by glucose transporters and is approved for clinical applications, making it a suitable albeit short-term tracking label. Studies are limited to 4–6 h, due to the 100 min half-life and leakage from labeled cells (Zhang et al. 2012). Cells can be tracked for several days using ^{64}Cu and ^{111}In with half-lives of 12.7 and 67 h, respectively. Both lipophilic ^{64}Cu-pyruvaldehyde-bis(N4-methylthiosemicarbazone) (^{64}Cu-PTSM) and ^{111}In in indium oxine easily cross the plasma membrane (Griessinger et al. 2014) (Tarantal et al. 2011). Delivery of these tracers using a nanoparticle formulation or with assistance of electroporation can increase uptake, but may be associated with some cellular damage or loss of viability (Li et al. 2013).

Genetic modification of cells for transplantation can increase uptake of tracers and provide more flexibility with imaging schedule. Cells are modified to express a reporter gene, such as human sodium iodide symporter (hNIS) (Varma et al. 2012; Wolfs et al. 2014) or human estrogen receptor ligand-binding domain (hERL) (Qin et al. 2013) that facilitate the uptake of tracers in transplanted cells. Once transplanted, cells accumulate signal when the radiolabel is injected intravenously. The systemically injected radiolabel, however, produces a signal independent of its uptake in the modified cells and may give rise to a higher background signal. These indirect labeling studies employing reporter genes should include controls with radiolabel injected in the animal without modified cells to account for uptake into nontarget cells and buildup in secretory organs (Fig. 23.3b).

23.3.4 Fluorine-19

Due to the negligible background signal in vivo, fluorine-19 (^{19}F) is emerging as an alternative to radioactive tracers, as labeled cells form similar hot spots (Fig. 23.3c) but without the cytotoxic radioactivity. Cells are labeled with fluorinated compounds, such as perfluorinated polyethers or cyclic crown ethers (Kadayakkara et al. 2014, Rose et al. 2015), by incubation with the label for

1 or 2 days. Labeled cells are then transplanted and detected with MR. Due to the frequency difference between ^{1}H and ^{19}F, a dedicated coil is typically required for fluorine cell tracking imaging. The images from ^{19}F-MR can be co-registered with ^{1}H MR images to show localization to anatomical structures. A perfluorinated carbon for cell tracking is under investigation for clinical applications.

The uptake of fluorine content in cell cultures can be measured with nuclear magnetic resonance (NMR). A separate fluorine-containing compound with a different chemical shift is added as a reference, and the fluorine content from the label can be quantified and normalized to the cell number. Typical uptake is in the range of 10^{12} fluorine atoms per cell (Helfer et al. 2013; Ribot et al. 2014; Zhong et al. 2013). Fluorescently conjugated formulations allow detection of labeled cells with microscopy or flow cytometry. In high field strengths typical of small animal imaging, cells required for detection range from 10^{4} to 10^{5} cells (Boehm-Sturm et al. 2011; Helfer et al. 2013). The sensitivity of fluorine imaging currently remains the limiting factor for cell tracing, as large quantities of ^{19}F are needed to ensure detection.

23.4 Additional Validations and Differentiation of Multiple Cell Populations

Multimodal imaging can be employed to ensure the veracity of results (Fig. 23.4) (Danhier et al. 2014), where cells can be modified with more than one label to exploit the benefits of each imaging modalities (Elhami et al. 2013). Multimodal imaging study is especially prudent for labels that do not distinguish between live and dead or free labels or are highly subject to artifacts. Labeling genetically modified cells with SPIO allows MR detection of iron particles in transplanted cells, allowing for better resolution in deep tissue, but fluorescent protein expression still allows confirmation of live cells in tissue sections (Cianciaruso et al. 2014; Taylor et al. 2014). Dual labeling cells with SPIO for MR detection and FDG for PET detection combine the spatial resolution of MR (Fig. 23.4a) with sensitivity of PET (Fig. 23.4b) to confirm signal from transplanted cells (Fig. 23.4c) (Elhami et al. 2013).

Careful selection of specific labels can also allow tracking of different populations of cells in the same animal (Fig. 23.5). With bioluminescence, populations of cells labeled with different luciferases can be detected in the same animal. Cells expressing firefly luciferase can be distinguished from cells expressing with *Renilla* luciferase by exploiting the minimal cross-reactivity of substrates (Bhaumik and Gambhir 2002), as each luciferase requires its own substrate. Due to overlapping emission spectra for these luciferases, the imaging protocol includes a 3-h "washout" between administration of the first and second substrate. This ensures elimination of the first substrate to prevent errant detection of the first luciferase (Bhaumik and Gambhir 2002; Mezzanotte et al. 2013). Alternative configurations for imaging individual popula-

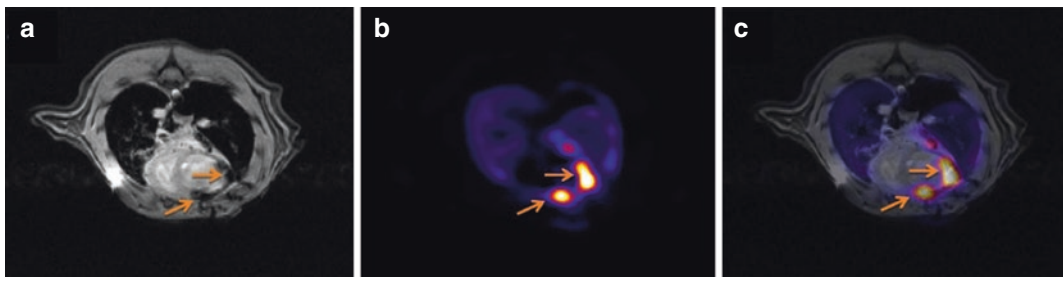

Fig. 23.4 Dual labeling of cells with SPIO and radiotracer. Adipose stromal cells were co-labeled with SPIO and the radiotracer FDG. Cells appear as voids on ^{1}H MRI (**a**) due to SPIO or areas of high signal with PET (**b**) due to FDG, as indicated by *arrows*. Co-registration of the MR and PET images (**c**) shows overlap of MR and PET signals, indicating that signals originate from the same source (Reproduced, with permission, from Elhami et al. (2013))

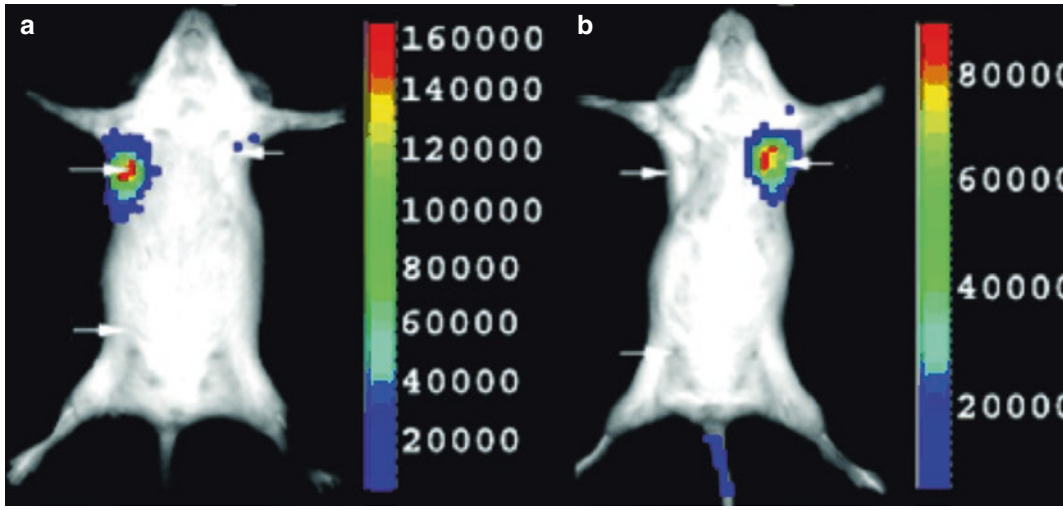

Fig. 23.5 Tracking multiple cell populations. Cells expressing firefly luciferase (FLuc) and *Renilla* luciferase (RLuc) were injected into the left and right forearm, respectively, along with cells expressing no luciferase in the left thigh. *Arrows* indicate injection sites. The mouse was imaged once after administration of D-luciferin (**a**) and once after coelenterazine (**b**). Cells expressing FLuc were detected only following administration of D-luciferin, whereas cells expressing RLuc were detected following administration of coelenterazine. These results show each luciferase's high specificity for its substrate and demonstrate the feasibility of tracking multiple cell populations in a single animal with bioluminescence (Reproduced, with permission, from Bhaumik and Gambhir (2002))

tions in the same animal include the use of the one substrate with two luciferases, such as the CBG99 and PpyRE9, and exploiting the different emission spectral patterns (Mezzanotte et al. 2011, 2013). Since these luciferases do have spectral overlap, the analysis is only qualitative (Mezzanotte et al. 2013) but provides useful information on co-localization of different cell populations in the same imaging session. Similar approaches can be applied to other systems, provided sufficient controls are included.

23.5 Functional Assessment of Labeled Cells

As with any modification, labeling for tracking purposes has the potential to modify key characteristics, and labeled cultures should be tested to ensure relevant physiologies are not impeded or altered. Both genetic modifications and exogenous labels should be investigated, but the extent of testing is mostly dependent on the cell type. Standard assessments include cell viability and proliferation to ensure that cells will grow and divide in a manner comparable to unmodified cells following transplantation. Phenotypes pertinent to the cell and the outcome of the study, such as migration (Diana et al. 2013) or motility (Cromer Berman et al. 2013), should be tested before and after labeling. For pluripotent and multipotent cells, cultures should be tested for differentiation into germ layers or appropriate lineages, respectively (Kostura et al. 2004), as some labels can interfere with differentiation along certain lineages. Additional assays should be included in the assessment as needed, especially if the label is known to affect a phenotype or essential for the study's outcomes.

Conclusions

A plethora of methods are available for cell tracking in small animals, and careful label selection based on cell type and study design allows detection of engrafted cells. Validation to confirm signal can be equally important to increase imaging confidence and confirm presence of live cells. More complex studies,

such as tracking multiple cell populations, are also possible with novel application of current tracking methods discussed in this chapter.

References

Ahrens ET, Bulte JWM. Tracking immune cells in vivo using magnetic resonance imaging. Nature Rev Immunology. 2013;13(10):755–63.

Aspord C, et al. Paramagnetic nanoparticles to track and quantify in vivo immune human therapeutic cells. Nanoscale. 2013;5(23):11409.

Aswendt M, et al. Boosting bioluminescence neuroimaging: an optimized protocol for brain studies S. L. Sensi, ed. Plos One. 2013;8(2):e55662.

Azzabi F, et al. Viability, differentiation capacity and detectability of super-paramagnetic iron oxide labeled muscle precursor cells for magnetic-resonance imaging. Tissue Eng Part C Methods. 2014. doi:10.1089/ten.tec.2014.0110.

Baligand C, et al. Discrepancies between the fate of myoblast xenograft in mouse leg muscle and NMR label persistency after loading with Gd-DTPA or SPIOs. Gene Ther. 2009;16(6):734–45.

Berglund D, et al. Imaging the in vivo fate of human T cells following transplantation in immunoincompetent mice – implications for clinical cell therapy trials. Transpl Immunol. 2013;29(1–4):105–8.

Bhaumik S, Gambhir SS. Optical imaging of Renilla luciferase reporter gene expression in living mice. Proc Natl Acad Sci U S A. 2002;99(1):377–82.

Boehm-Sturm P, et al. In vivo tracking of human neural stem cells with 19F magnetic resonance imaging C. Kleinschnitz, ed. Plos One. 2011;6(12):e29040.

Bulte J. Hot spot MRI emerges from the background. Nat Biotechnol. 2005;23(8):945–6.

Cao F, et al. In vivo visualization of embryonic stem cell survival, proliferation, and migration after cardiac delivery. Circulation. 2006;113(7):1005–14.

Chen YC, et al. Magnetic resonance and near-infrared imaging using a novel dual-modality nano-probe for dendritic cell tracking. Cytotherapy 2014;16(5):699–710.

Cianciaruso C, et al. Cellular magnetic resonance with iron oxide nanoparticles: long-term persistence of SPIO signal in the CNS after transplanted cell death. Nanomedicine 2014;9(10):1457–74.

Cromer Berman SM, et al. Cell motility of neural stem cells is reduced after SPIO-labeling, which is mitigated after exocytosis. Magn Reson Med Off J Soc Magn Reson Med Soc Magn Reson Med. 2013;69(1):255–62.

Danhier P, et al. Multimodal cell tracking of a spontaneous metastasis model: comparison between MRI, electron paramagnetic resonance and bioluminescence. Contrast Media Mol Imaging. 2014;9(2):143–53.

Diana V, et al. Dose dependent side effect of superparamagnetic iron oxide nanoparticle labeling on cell motility in two fetal stem cell populations P. Rameshwar, ed. Plos One. 2013;8(11):e78435.

Elhami E, et al. Assessment of three techniques for delivering stem cells to the heart using PET and MR imaging. EJNMMI Res. 2013;3(1):72.

Fan W, et al. Adipose stromal cells amplify angiogenic signaling via the VEGF/mTOR/Akt pathway in a Murine Hindlimb Ischemia Model: a 3D multimodality imaging study R. Kirchmair, ed. Plos One. 2012;7(9):e45621.

Faucher L, et al. Rapid synthesis of PEGylated ultrasmall gadolinium oxide nanoparticles for cell labeling and tracking with MRI. ACS Appl Mater Interfaces. 2012;4(9):4506–15.

Garikipati VNS, et al. Mesenchymal stem cells from fetal heart attenuate myocardial injury after infarction: an in vivo serial pinhole gated SPECT-CT study in rats R. Johnson, ed. Plos One. 2014;9(6):e100982.

Gorelik M, et al. Use of MR cell tracking to evaluate targeting of glial precursor cells to inflammatory tissue by exploiting the very late antigen-4 docking receptor. Radiology. 2012;265(1):175–85.

Griessinger CM, et al. In vivo tracking of Th1 cells by PET reveals quantitative and temporal distribution and specific homing in lymphatic tissue. J Nucl Med. 2014;55(2):301–7.

Guenoun J, et al. Cationic Gd-DTPA liposomes for highly efficient labeling of mesenchymal stem cells and cell tracking with MRI. Cell Transplant. 2012;21(1):191–205.

Helfer BM, et al. 19F MRI tracer preserves in vitro and in vivo properties of hematopoietic stem cells. Cell Transplant. 2013;22(1):87–97.

Heyn C, et al. In vivo magnetic resonance imaging of single cells in mouse brain with optical validation. Magn Reson Med Off J Soc Magn Reson Med Soc Magn Reson Med. 2005;55(1):23–9.

Josephson L, Bigler J, White D. The magnetic properties of some materials affecting MR images. Magn Reson Med Off J Soc Magn Reson Med Soc Magn Reson Med. 1991;22:204–8.

Kadayakkara DK, et al. 19F spin–lattice relaxation of perfluoropolyethers: dependence on temperature and magnetic field strength (7.0–14.1T). J Magn Reson. 2014;242:18–22.

Katsumata T, et al. Bioluminescence imaging of β Cells and intrahepatic insulin gene activity under normal and pathological conditions B. He, ed. Plos One. 2013;8(4):e60411.

Kim J-B, et al. Non-invasive detection of a small number of bioluminescent cancer cells in vivo A. Swarbrick, ed. Plos One. 2010;5(2):e9364.

Kostura L, et al. Feridex labeling of mesenchymal stem cells inhibits chondrogenesis but not adipogenesis or osteogenesis. NMR Biomed. 2004;17(7):513–7.

Li H, et al. In vivo imaging of T cells loaded with gold nanoparticles: a pilot study. Radiol Med. 2013;119(4):269–76.

Liang Y. Comparison of red-shifted firefly luciferase Ppy RE9 and conventional Luc2 as bioluminescence

imaging reporter genes for in vivo imaging of stem cells. J Biomed Opt. 2012;17(1):016004.
Markides H, et al. Whole body tracking of superparamagnetic iron oxide nanoparticle-labelled cells – a rheumatoidarthritis mouse model. Stem Cell Res Ther. 2013;4(5):1–1.
Martens A, et al. Substantial early loss of induced pluripotent stem cells following transplantation in myocardial infarction. Artif Organs. 2014;38(11):978–84.
Mezzanotte L, et al. Sensitive dual color in vivo bioluminescence imaging using a new red codon optimized firefly luciferase and a green click beetle luciferase A. Herrera-Estrella, ed. Plos One. 2011;6(4):e19277.
Mezzanotte L, et al. Evaluating reporter genes of different luciferases for optimized in vivo bioluminescence imaging of transplanted neural stem cells in the brain. S. Aime & R. N. Muller, eds. Contrast Media Mol Imaging. 2013;8(6):505–13.
Mezzanotte L, et al. A novel luciferase fusion protein for highly sensitive optical imaging: from single-cell analysis to in vivo whole-body bioluminescence imaging. Anal Bioanal Chem. 2014;406(23):5727–34.
Nolte IS, et al. In vitro labeling of glioma cells with gadofluorine M enhances T1 visibility without affecting glioma cell growth or motility. Magn Reson Med Off J Soc Magn Reson Med Soc Magn Reson Med. 2008;59(5):1014–20.
Norrman K, et al. Quantitative comparison of constitutive promoters in human ES cells D. S. Milstone, ed. Plos One. 2010;5(8):e12413.
Pan H, et al. Biologic properties of gadolinium diethylenetriaminepentaacetic acid-labeled and PKH26-labeled human umbilical cord mesenchymal stromal cells. J Cytotherapy. 2014;16(1):74–83.
Qin C, et al. An in vitro and in vivo evaluation of a reporter gene/probe system hERL/18F-FES R. Kirchmair, ed. Plos One. 2013;8(4):e61911.
Rabinovich BA, et al. Visualizing fewer than 10 mouse T cells with an enhanced firefly luciferase in immunocompetent mouse models of cancer. Proc Natl Acad Sci. 2008;105(38):14342–6.
Ribot E, et al. In vivo MR detection of fluorine-labeled human MSC using the bSSFP sequence. Int J Nanomedicine. 2014;9:1731–9.
Rose LC et al. Fluorine-19 labeling of stromal vascular fraction cells for clinical imaging applications. Stem Cells Transl Med. 2015;4:1472–81.
Shuai H-L, et al. Analysis of feasibility of in vitro nuclear magnetic resonance tracking human umbilical cord mesenchymal stem cells by Gd-DTPA labeled. Magn Reson Imaging. 2014;32(7):934–40.
Sibov T, et al. Umbilical cord mesenchymal stem cells labeled with multimodal iron oxide nanoparticles with fluorescent and magnetic properties: application for in vivo cell tracking. Int J Nanomedicine. 2014;9:337–50.
Tachibana Y, et al. Long-term/bioinert labeling of rat mesenchymal stem cells with PVA-Gd conjugates and MRI monitoring of the labeled cell survival after intramuscular transplantation. Bioconjug Chem. 2014;25(7):1243–51.
Tam JM, et al. Improved in vivo whole-animal detection limits of green fluorescent protein-expressing tumor lines by spectral fluorescence imaging. Mol Imaging 2007;6(4):1–9.
Tarantal AF, et al. Radiolabeling and in vivo imaging of transplanted renal lineages differentiated from human embryonic stem cells in fetal rhesus monkeys. Mole Imaging Bio MIB Off Pub Acad Mole Imaging. 2011;14(2):197–204.
Taylor A, et al. Assessing the efficacy of nano- and microsized magnetic particles as contrast agents for MRI cell tracking M. Yamamoto, ed. Plos One. 2014;9(6):e100259.
van den Bos EJ. Magnetic resonance imaging of haemorrhage within reperfused myocardial infarcts: possible interference with iron oxide-labelled cell tracking? Eur Heart J. 2006;27(13):1620–6.
Varma NRS, et al. Endothelial Progenitor Cells (EPCs) as gene carrier system for rat model of human Glioma J. G. Gelovani, ed. Plos One. 2012;7(1):e30310.
Wang N, et al. A red fluorescent nude mouse model of human endometriosis: advantages of a non-invasive imaging method. Eur J Obstet Gynecol. 2014;176(5):25–30.
Wolfs E, et al. Optimization of multimodal imaging of mesenchymal stem cells using the human sodium iodide symporter for PET and cerenkov luminescence imaging P. Rameshwar, ed. Plos One. 2014;9(4):e94833.
Zhang Y, et al. (18)F-FDG cell labeling may underestimate transplanted cell homing: more accurate, efficient, and stable cell labeling with hexadecyl-4-[(18)F]Fluorobenzoate for in vivo tracking of transplanted human progenitor cells by positron emission tomography. Cell Transplant. 2012;21(9):1821–35.
Zhong J, et al. In vivo intracellular oxygen dynamics in murine brain glioma and immunotherapeutic response of cytotoxic T cells observed by fluorine-19 magnetic resonance imaging R. L. Mosley, ed. Plos One. 2013;8(5):e59479.

Beta Cell Imaging as Part of "Imaging on Metabolic Diseases"

24

M. Brom, W.A. Eter, I. van der Kroon, S.M.A. Willekens, A. Eek, M. Boss, M. Buitinga, and M. Gotthardt

Contents

M. Brom (✉) • W.A. Eter • I. van der Kroon
S.M.A. Willekens • A. Eek • M. Boss • M. Buitinga
M. Gotthardt
Department of Radiology and Nuclear Medicine,
Radboud University Medical Center,
Nijmegen, The Netherlands
e-mail: maarten.brom@radboudumc.nl

24.1 Introduction

Currently, radionuclide imaging after injection of radiolabeled tracers seems to be the most promising approach to noninvasively determine the beta cell mass (BCM) in vivo. Despite the limited resolution of positron emission tomography (PET) and single photon emission computed tomography (SPECT), the very high sensitivity of these imaging modalities allows detection of very low radiotracer concentrations. Since the noninvasive imaging modalities that offer the highest spatial resolution, i.e., computed tomography (CT) and magnetic resonance imaging (MRI), are not able to resolve single islets in vivo, radionuclide imaging would be the method of choice for beta cell imaging. However, noninvasive visualization of the pancreatic beta cells is a highly challenging endeavor. The beta cells are located in the islets of Langerhans in the pancreas. The islets are small (usually between 50

F. Kiessling et al. (eds.), *Small Animal Imaging*, DOI 10.1007/978-3-319-42202-2_24

and 400 μm), only account for 1–2 % of the total pancreatic mass, and are spread throughout the pancreas (Bonner-Weir 1994; Weir et al. 1990). Targeting of these small structures spread through an organ is highly challenging when compared to tumor imaging, where a focal solid mass containing the target cells is visualized. Moreover, the islets consist of several cell types (beta cells, alpha cells, delta cells, and pp cells) with the beta cells representing around 60–80 % of the islet mass, making specific visualization of beta cells even more difficult. Since PET and SPECT cannot resolve single islets, let alone beta cells, a highly beta cell-specific radiotracer is required. Only when the radiotracer specifically accumulates in beta cells and not in other cell types of the endocrine or exocrine pancreas, the accumulation of the radiotracer in the pancreas could be used as a surrogate measure of the beta cell mass. To enable this, a target specifically expressed on beta cells and an optimal respective ligand should be selected for the development of beta cell targeting radiotracers. In contrast to tumor imaging, where several targets are overexpressed, beta cells express endogenous levels of receptors leading to generally lower accumulation of radiotracers when compared to tumor cells. In this book chapter, the challenges regarding tracer development and preclinical and clinical characterization will be discussed in detail.

24.2 Specific Requirements for Radiotracers Used in Diabetes Imaging

Development of a radiotracer for specific targeting of beta cells in vivo requires the consideration of many aspects, such as target and ligand selection, radiolabeling strategies, specific activity and post-labeling purification, and the effect of the administered radiotracer dose on accumulation and side effects.

24.2.1 Target Definition

Expression levels of beta cell-specific targets are performed by sequencing, quantitative (RT) PCR, western blot, FACS, and immunohistochemical staining. A complicating factor is that most of the techniques require pure preparations of beta cells, which are challenging to obtain. Purification of dispersed cells of the islets of Langerhans is highly demanding, and purities exceeding 80 % are rarely achieved. Due to the difficulty of obtaining pure beta cells, the expression levels in the endocrine and exocrine pancreas, isolated after enzymatic digestion of the pancreas, are widely used. However, the procedure of enzymatic digestion of the pancreas and subsequent purification of the islets of Langerhans is also characterized by impurities in the preparation, resulting in contamination with exocrine cells in the endocrine preparation and vice versa. These contaminations should be taken into account in the interpretation of the expression patterns determined in these preparations.

Immunohistochemical staining of the target of interest on pancreatic tissue specimens is highly desirable to confirm beta cell specificity. Beta cell specificity can be confirmed by counterstaining for proteins specific for beta cells and other endocrine cells in the islets of Langerhans (e.g., insulin for beta cells, glucagon for alpha cell, and somatostatin for delta cells). However, the availability of appropriate antibodies might be a concern, especially for novel targets. Also the specificity of certain antibodies might be an issue, for example, for the glucagon-like peptide 1 receptor (GLP-1R) where the specificity of most commercially available antibodies remains a matter of debate.

24.2.2 Ligand Selection

After selection of a candidate target for beta cell imaging, the appropriate ligand needs to be selected. For radionuclide imaging, several types of ligands were successfully used, such as antibodies and antibody fragments, peptides, and small molecules. Complete antibodies usually exhibit high specificity, but due to their size, the circulatory half-life is long, while the penetration rate in (healthy) solid tissue is low. When coupled to a radionuclide, this might lead to undesirable high radiation doses to the (study) subject. Moreover,

the large antibodies might have limited penetration through the basement membrane of the islets to the beta cells, which is of minor importance in tumor targeting where usually "leaky vessels" allow effective penetration of the antibodies in tumorous tissue. Alternatively, antibody fragments (Fab_2 and Fab fragments) could be used to reduce the circulation time and improve tissue penetration.

In contrast to antibodies, peptides are relatively small and rapidly excreted from the circulation. Often natural peptidic ligands are utilized for targeting of receptors, but these natural ligands might have low metabolic stability. High metabolic stability is required for successful in vivo targeting, since this increases the bioavailability of the ligands and thus will increase the accumulation in the target tissue. Therefore, peptides can be stabilized by addition of protective groups at the N-terminus or the substitution of certain amino acids by D-amino acids to prevent enzymatic degradation. Care should be taken with these modifications, since these changes could influence the binding affinity or internalization properties of the ligands.

Small molecules also allow rapid targeting and fast clearance. The excretion route is determined by the hydrophilicity of the compound (which is also the case for peptides). While hydrophilic compounds are cleared via the kidneys, lipophilicity is characterized by clearance via the hepatobiliary system. Clearance via the liver will lead to excretion of the radioactive compound and its metabolites in the intestinal tract resulting in high background activity concentrations in the abdomen potentially hampering the delineation of the pancreas. However, renal clearance might result in high kidney accumulation and could also hamper visualization of the tail of the pancreas (due to the close proximity to the left kidney). Furthermore, accumulation of radiotracer and metabolites due to clearance in nontarget organs potentially leads to increased radiation doses to the patient.

24.2.3 Radiolabeling Strategies

In general two radiolabeling strategies can be defined: direct labeling and indirect labeling. In direct labeling the radionuclide is directly coupled to a reactive moiety in the ligands, for example, by an oxidation reaction or a substitution reaction. Oxidation reactions are frequently used to label antibodies with a radioactive iodine isotope. Prerequisite for this strategy is that the compounds contain one or more reactive moieties in the structure to allow radiolabeling. Although this labeling strategy is relatively simple usually without the need of modification of the ligand, the labeling site might be located in the binding domain of the compound and in this way interfere with target binding.

Indirect labeling requires the coupling of a moiety to the chosen ligand to enable radiolabeling. A well-known example is radiometal labeling after conjugation of a chelator to the ligand. The chelator binds the radiometal with high affinity and efficiency, and the formed complex is highly stable, when the appropriate chelator-radiometal combination is selected. The chelator can be coupled to a desired position of the compound to avoid interference with the binding domain of the ligand. The chelators are relatively large and therefore the feasibility for labeling of very small molecules is limited. A major advantage of the radiometal labeling strategy is the high accumulation of the chelator-radiometal complex after internalization. After internalization, the radiolabeled compounds bound to the receptor are enclosed in the lysosomes in the cell, the compound is degraded, and the degradation products will be excreted. Due to the lack of a specific excretion route or metabolic pathway for the radiometal-chelator complex, a high accumulation in the target cells will occur (the so-called metabolic trapping), leading to high target-to-background ratios (Brom et al. 2010a). This phenomenon is not observed in most direct labeling strategies, for example, for radioiodinated antibodies, where the radioiodine is washed out rapidly from the cells. Other examples for metabolic trapping are tracer molecules that cannot be processed by the cell and get trapped, for example, ^{18}FDG (Andralojc et al. 2012).

The choice of the radionuclide depends on several factors, such as the labeling strategy as described above. Moreover, the imaging modality to be used is a major determinant for the

choice of radionuclides (positron emitters for PET and gamma emitters for SPECT). The energy of the emitted gamma photons or positrons, another physical aspect of radioisotopes, should be considered. In general, gamma photons with a high energy will result in poorer image quality, whereas gamma photons with too low energy will be absorbed and attenuated to a larger extent. Positrons emitted with a higher energy will travel longer in tissue and decrease the resolution of the obtained images.

The half-life is also of importance when selecting a radionuclide for radiolabeling of a compound. The half-life of the radionuclide should match with the half-life of the compound. In other words, at the optimal time point for imaging, when the target-to-background ratio is optimal, the radioactivity concentration in the target organs should be sufficient for proper image quality. Long-lived radionuclides attached to ligands with a short circulatory half-life will require high amounts of radioactivity injected, while short-lived radionuclides coupled to compounds with a long circulatory half-life will result in very poor target-to-background ratios.

24.2.4 Specific Activity, Pharmacological Dose

Unlike tumors, targets on healthy beta cells are not overexpressed but expressed at physiological levels. This is challenging for in vivo targeting of beta cells, since the relatively low number of receptors can easily be saturated by administration of high doses of radiotracers. To overcome the problem of decreased radiotracer uptake due to saturation, a high specific activity of the radiolabeled compound is required (i.e. the amount of radioactivity per molecule) in order to administer a sufficient radioactivity dose for appropriate image quality. Previous studies showed the effect of the administered doses on the accumulation of radiotracers and underline the importance of administration of doses of compound (Brom et al. 2010b; Selvaraju et al. 2013). This is of special importance when pharmacologically active ligands are used, since they can cause unwanted (pharmacological) side effects.

24.3 Development of Radiotracers for Diabetes Imaging: From Bench to Bedside (The Requirements for Preclinical Characterization)

After identification of a suitable target for beta cell imaging and optimization of the radiolabeling procedure of the tracer, the novel radiotracer should be extensively characterized both in vitro and in vivo. The ideal radiotracer for diabetes imaging should bind to a receptor specifically expressed on the beta cells in high numbers. In an optimal situation, the expression should be stable in healthy and diabetic conditions. The uptake of the tracer molecule should correlate with beta cell mass, and high target-to-background ratios (both exocrine versus endocrine tissue and also the pancreas versus adjacent organs) are needed to accurately quantify tracer uptake. Therefore, high affinity and specificity of the binding of the radiotracer to the beta cells are required. Preferably, the radiotracer is internalized upon receptor binding to increase target-to-background ratios. The affinity, specificity, and binding kinetics for the target receptor are initially determined in vitro, followed by in vivo characterization to determine the biological behavior.

24.3.1 In Vitro Characterization

In general in vitro radiotracer characterization is performed on cell lines known to express the target receptor. Commonly used assays to characterize the radiotracer are saturation binding assays, competition binding assays, and internalization assays. In these assays the binding kinetics, the specificity for the receptor, the dissociation constant (K_d), and the maximum receptor density on the cells (B_{max}) are determined.

24.3.1.1 Internalization Assay

An internalization assay provides information on the binding kinetics of the radiotracer. Cells are incubated with a fixed amount of radiolabeled tracer for a certain time. The bound fraction can be separated from the internalized fraction with an acid wash. Measurement of the bound and internalized fraction after several time points provides information on the internalization rate of the radiotracer. As only agonists are internalized upon binding the receptor, agonists are in general assumed to be more suitable as a radiotracer than antagonists. The internalization of the receptor-agonist complex leads to intracellular accumulation of the radiotracer resulting in high target-to-background ratios. However, recent studies showed favorable in vivo accumulation of bombesin (Abd-Elgaliel et al. 2008; Cescato et al. 2008; Mansi et al. 2009) and somatostatin (Ginj et al. 2006) antagonist in tumor-bearing mice, and the optimal tracer (agonist/antagonist) for every ligand-receptor combination should be exploited. By addition of an excess of unlabeled tracer (~100-fold) to block the receptors, the amount of nonspecific uptake in the target tissue can be determined. This assay is usually performed at 37 °C as internalization is slower at lower temperatures.

24.3.1.2 Saturation Binding Assay

To determine the receptor density (B_{max}) and the dissociation constant (K_d), which is a measure for the strength of the interaction between the radiotracer and the target receptor, saturation binding assays can be performed. In these assays cells expressing the target receptor are incubated with increasing concentrations of the radiotracer. With high concentrations of the radiotracer, the nonspecific binding to other proteins and lipids is likely to increase, leading to more nonspecific uptake. Therefore, separate cell preparations that are co-incubated with an excess unlabeled compound are used to correct for nonspecific binding for each experimental concentration.

The K_d is defined as the amount of radiotracer necessary to occupy 50 % of the receptors. A radiotracer with a K_d below 1 nM is considered a tracer with high affinity for the receptor and a K_d above 1 mM is assumed to be a tracer with low affinity (Davenport and Russell 1996). To be suitable for imaging, radiotracers should have an affinity in the nanomolar or subnanomolar range. The B_{max} is estimated from the graph with the saturation curve plateaus and is expressed in the amount of tracer bound per milligram tracer peptide. These assays are usually performed on ice to prevent internalization of the radiotracer.

24.3.1.3 Competition Binding Assay

In competition binding assays, the ability of unlabeled or non-radioactive labeled tracers of interest to compete with a fixed concentration of a radiotracer known to bind to the receptor of interest is assessed. This assay can, for example, be used to test if radiolabeling of the tracer has influenced the affinity for the receptor. Therefore, the radiotracer is incubated with increasing concentrations of the unlabeled tracer to determine the IC_{50} value of the unlabeled tracer. The IC_{50} value is the concentration needed to replace 50 % of the radiotracer. If there is a large difference between the K_d of the radiotracer (determined with the saturation binding assay) and the IC_{50} value of the unlabeled tracer, the labeling procedure might have affected the affinity of the radiotracer.

A competition binding assay can also be used to compare the affinity of several unlabeled tracers for the same receptor. Different concentrations of each unlabeled tracer are co-incubated with a control radiotracer (with affinity for the same receptor). The affinities of each unlabeled tracer can be directly compared, and the tracer with the highest affinity for the receptor can be selected.

24.3.1.4 In Vitro Autoradiography

In vitro autoradiography can be performed to gain more insight in the distribution of the receptor expression in the target tissue (Reubi and Waser 2003). Freshly frozen tissue sections are incubated with the radiotracer. After a fixed time, the excess of radiotracer is washed away, and the tissue sections are exposed to a light sensitive film in the dark. After a certain time (1 day–

several weeks), depending on the specific activity and amount of the radiotracer added, the amount of binding to the tissue of interest, and the isotope used, the film is developed, and distribution of the radiotracer uptake in the target tissue can be analyzed. Specificity of the uptake can be tested by adding an excess of unlabeled tracer.

24.3.1.5 Radiotracer Stability

Measurement of the percentage of intact radiolabeled tracer remaining after incubation of the radiotracer in several physiological solutions, like phosphate-buffered saline (PBS) and, for example, mouse serum, will give more insight in the in vivo tracer stability.

In general in vitro assays provide useful information on the binding kinetics and stability of the radiotracer. However, these assays are carried out in a controlled environment and therefore do not necessarily reflect in vivo behavior. Radiotracers should be further characterized in vivo to demonstrate the true potential of the developed radiotracer.

24.3.2 In Vivo Characterization

To gain insight in the pharmacokinetics of the tracer, biodistribution studies should be performed. These studies give information on:

- Stability of the radiotracer in vivo
- Specificity of the radiotracer in vivo
- Clearance rate and excretion route of the tracer
- Information on the accumulation and retention of the radiotracer in the target tissue

In biodistribution studies, the radiotracer is typically injected intravenously, the animal is euthanized after a fixed time, the organs and other relevant tissues are dissected, and the amount of radioactivity in each organ is measured. The amount of radioactivity in the organs is usually expressed as the percentage injected dose per gram tissue (%ID/g).

These biodistribution results give indications on the stability of the tracer in vivo and information on the excretion route of the radiotracer as well as information in respect to pancreatic uptake or uptake in an islet graft. Euthanizing animals at different time points will give insight in the clearance rate of the radiotracer and the optimal time point for imaging (highest target-to-background ratios). Injecting animals with different radiotracer doses (amount of peptide/antibody) will provide information on the optimal dose for imaging. Enough radiotracer should be injected to bind in high concentrations to the target receptor, but saturation of the receptor should be prevented, since the "excess" of radiotracer would increase uptake in other organs (and thus potentially reduce visibility of the target), requiring dose escalation studies. Furthermore, the specificity of the uptake in the organs and tissue can be tested by co-injection of an excess of unlabeled tracer. The unlabeled tracer saturates the target receptor and blocks the receptor-mediated uptake of the radiotracer. In this way specific uptake and unspecific uptake in organs and tissues can be distinguished.

24.3.2.1 Preliminary In Vivo Imaging Studies

If specific uptake of the radiotracer in the target tissue is observed in biodistribution studies, the uptake can still be too low for in vivo imaging. Animals should be injected with the radiotracer with a high specific activity with the optimal pharmacological dose and imaged at the time point that results in the highest target-to-background ratios as determined in the biodistribution studies. The scan time is depending on the amount of activity injected and the uptake expected in the target organ.

After imaging, the animals are euthanized and the organs and other relevant tissues are collected for ex vivo analysis. The tissues expected to express the target receptor are used for autoradiography. Macro autoradiography can show the global tracer uptake in the tissue, and micro-autoradiography can show radiotracer uptake at the cellular level. For micro-autoradiography, tissue sections are dipped in a photographic emulsion, containing silver grains, stored in the

dark, and developed after several weeks. After developing the emulsion, the silver grains exposed to radiation will show the location of the bound radiotracer in the tissue on the cellular level. Tissue sections adjacent to the sections used for micro-autoradiography can be stained for the target receptor, and the distribution of tracer accumulation can be compared to the distribution of the target receptor and confirm specific uptake in vivo.

To enable accurate interpretation of the in vivo imaging results, ex vivo scans of the pancreas and other organs can be performed after dissection of the organs.

In vivo imaging of the pancreas with radiotracers using small animal models is challenging, given the random shape of their pancreas, which cannot easily be identified by anatomical imaging modalities, such as CT and MRI. The rodent pancreas includes the splenic, duodenal, and gastric lobes (Alanentalo et al. 2007; Eriksson et al. 2013), named after their neighboring abdominal organs and representing the tail, body, and head of the human pancreas, respectively. Due to preferred renal excretion of radiotracers for beta cell imaging, signal originating from the left kidney can obscure the pancreatic uptake, since they are located in close proximity. This limitation is less of a problem in humans, where radiotracer uptake by the head and the body of the pancreas can be easily differentiated from kidney uptake due to the larger size of the organs and the larger spatial distance between the kidneys and the pancreas. Several approaches to enhance the visibility of the pancreas were suggested in rodents to evaluate the in vivo targeting properties of beta cell radiotracers.

One possibility is the use of a dual tracer method, where one tracer is selected with high accumulation in the (exocrine) pancreas to enable accurate delineation. This will allow quantification of the beta cell-specific agent in the pancreatic region. ^{99m}Tc-demobesin and ^{123}I-2-iodo-L-Phe have high uptake in the exocrine tissue and were previously used for this approach (Brom et al. 2014; Mathijs et al. 2015). A second approach is to perform (unilateral) nephrectomy before in vivo scanning, thereby omitting radioactivity originating from the left kidney which improves the visibility of the pancreas. Performing nephrectomy alone or in combination with the dual isotope tracer method could only be applied in rodents, to study the potential of a radiotracer for BCM quantification. Finally, compounds such as plasma expander succinylated gelatin/lysine/arginine can be coinfused to reduce kidney signal by competing with radiotracers that undergo renal reabsorption in the proximal tubule (Vegt et al. 2010), enhancing the visibility of the pancreas.

After complete characterization of the radiotracer in a healthy setting, the potential of the radiotracer in diabetes imaging should initially be investigated in a well-controlled diabetes model (chemically induced). After complete characterization of the radiotracer in healthy animals and controlled diabetes models, more realistic diabetes models can be used to investigate the true potential of the tracer in a clinical setting. Several animal models, spontaneously developing diabetes, are available, some more resembling type 1 diabetes (T1D) and others more similar to type 2 diabetes. Commonly used models are nonobese diabetic (NOD) mice, biobreeding diabetes-prone (BBDP) rats (for type 1 diabetes), Zucker Diabetic Fatty (ZDF) rats, or ob/ob mice (type 2 diabetes) (Rees and Alcolado 2005).

24.4 Models and Considerations for Small Animal Imaging in Diabetes

24.4.1 Implications of Interspecies Differences for Optimizing BCM Imaging

Mouse and rat harbor distinctive features related to their pancreas gene expression profile, if not the beta cell target receptor that is under investigation. Choosing the appropriate animal model is therefore an additional criterion to consider when identifying potential targets for nuclear imaging of beta cells in humans. Interspecies differences

can be illustrated by the use of glucagon-like peptide 1 receptor (GLP-1R) and vesicular monoamine transporter 2 (VMAT2) which are experimentally targeted for beta cell imaging in small animal models or diabetic patients (Brom et al. 2014; Simpson et al. 2006).

The GLP-1R is expressed at high densities on the beta cells of rodents and humans, which can be targeted in vivo with the radioligand ^{111}In-exendin for quantification of BCM. While tracer uptake in rats is predominantly originating from the beta cells, with insignificant uptake being observed in the exocrine tissue, tracer accumulation in mouse pancreas originates from both beta cells and the exocrine tissue. On the other hand, endocrine-to-exocrine GLP-1R mRNA expression levels are similar in mouse and rat, suggesting that ^{111}In-exendin could bind to a receptor other than the GLP-1R in the mouse exocrine pancreas, which does not occur in rats (Willekens et al. 2016). Rat is therefore more suitable model than mouse to quantify BCM using ^{111}In-exendin, implying that interspecies differences could lead to different conclusions about the clinical potential of the radiotracer to quantify BCM.

The vesicular monoamine transporter 2 (VMAT2) is expressed by human beta cells and can be specifically targeted with the radiolabeled analogue dihydrotetrabenazine (DTBZ). Whether the radiotracer is suitable to quantify BCM remains to be elucidated. In view of the considerable efforts to quantify BCM using DTBZ, mouse and rat models were used to characterize the targeting properties of the radiotracer to the receptor. The gene expression profile of VMAT2 in rodents was, however, not consistent with the human situation, since the receptor was absent in the beta cells, and was rather highly expressed by the sympathetic nerves of the pancreas when compared to human. In such a situation, mouse and rat are not suitable models to characterize the targeting properties of the radiotracer to the beta cells (Schäfer et al. 2013). Alternatively, larger animal models such as pigs and primates can be used.

24.4.2 Chemically Induced Diabetes Models

To investigate the potential of the radiotracer in diabetes imaging, a simple and controlled model for diabetes should be used. Chemically induced diabetes models are an excellent option. It is possible to induce diabetes in most strains of rat and mice, although the sensitivity for the chemicals differs per strain (Deeds et al. 2011). In these models, a high percentage of the beta cells is destroyed, resulting in hyperglycemia. After administration of the chemical, it takes 5–7 days to reach stable hyperglycemia. Several chemicals can be used, but the two most commonly used compounds to induce diabetes are alloxan and streptozotocin (STZ). Both compounds have a structure similar to glucose and compete with the glucose present in the body. Therefore, fasting animals are in general more susceptible to treatment with these chemicals (King 2012).

The use of alloxan and STZ is well described in the literature, although most studies do not provide accurate information on the severity of diabetes and the mortality rate in their animals (Deeds et al. 2011).

24.4.2.1 Alloxan

Alloxan (2,4,5,6-tetraoxypyrimidine; 5,6-dioxyuracil) is a urea derivative with a chemical structure similar to glucose.

Alloxan is taken up in the beta cells by the glucose transport 2 (GLUT2) receptor. After uptake in the beta cells, the alloxan is reduced to dialuric acid, reoxidized to alloxan, creating a redox cycle resulting in the formation of free radicals. These free radicals induce DNA damage, leading to beta cell death. Alloxan is also taken up by the liver, but this organ is less sensitive to the free radicals (King 2012). Besides formation of free radicals, alloxan leads to oxidation of essential –SH groups and causes a disturbance in the calcium homeostasis in the beta cells leading to beta cell death (Szkudelski 2001).

Alloxan doses to induce diabetes are in the range of 40–200 mg/kg for both mice and rats, but the actual required dose depends on strain,

route of administration, and nutritional status of the animal (King 2012). In general intraperitoneally and subcutaneously administered doses required to induce diabetes are up to three times higher than intravenously administered doses. The most commonly used dose in literature is around 60 mg/kg intravenously administered. By varying the administered dose of alloxan, different grades of diabetes can be induced.

Alloxan is very unstable and light sensitive, with only a half-life of several minutes at room temperature and neutral pH; therefore the solution should be freshly prepared immediately prior to injection and protected against exposure to light until injection. Furthermore, administration of high doses of alloxan can lead to damage to other organs, especially the kidneys (although kidney toxicity appears to be less pronounced than in the case of streptozotocin).

24.4.2.2 STZ

STZ (2-deoxy-2-(3-methyl-3-nitrosoureido)-D-glucopyranose, streptozotocin) is produced from the *Streptomyces achromogenes* bacterium.

The chemical structure of STZ is also recognized by the GLUT2 receptor. After entering the beta cell, STZ causes alkylation of the DNA resulting in beta cell death. In addition to the alkylation of the DNA, free radicals also contribute to the DNA damage and subsequent beta cell death. In contrast to alloxan, calcium is not involved in the diabetogenic action of STZ (Szkudelski 2001).

STZ doses required to induce diabetes are in the range of 40–60 mg/kg i.v (Szkudelski 2001), 80 mg/kg i.p in rats, and 150 mg/kg i.p in mice (Etuk 2010). Accurate doses depend on strain and species. In literature some evidence is found that female mice are less susceptible to STZ compared to male mice (Etuk 2010).

STZ is stable for up to 1 h at 37 °C and at neutral pH. Stability can be increased by decreasing pH and temperature. It is suggested that regeneration of beta cells can occur after administration of STZ (King 2012); this should be taken into account when performing long-lasting experiments. Another problem in long follow-up studies is the oncogenic activity (Etuk 2010) of STZ. It is reported in literature that high doses of STZ can induce kidney and liver tumors (Etuk 2010). Kidney toxicity of high doses of STZ can lead to relevant changes in the biodistribution of tracer molecules with renal excretion.

24.4.3 Spontaneous Models of Beta Cell Loss

Spontaneous models for type 1 and type 2 diabetes are crucial for validating the utility of beta cell radiotracers in monitoring the beta cells in diabetes-specific pathophysiological conditions. The most commonly used animal models for T1D are nonobese diabetic (NOD) mouse and the biobreeding diabetes-prone (BBDP) rat (Greiner et al. 2001). NOD mouse exhibits insulitis around 3–4 weeks of age, where B and T lymphocytes start infiltrating the islets and cause the specific destruction of beta cells. Onset of hyperglycemia takes places at 11–14 weeks of age, and the incidence of diabetes is 90–100 % by 30 weeks of age in female mice. The onset of diabetes is later in male mice, and the incidence is lower (40–60 % by 30–40 weeks of age). BBDP rats develop insulitis and a selective destruction of beta cells followed by severe hyperglycemia, which requires insulin treatment, between 7 and 16 weeks of age. Although the course of insulitis and the severity of hyperglycemia differ between NOD mouse and BBDP rat, the natural course of the disease is similar in both models. The inflammatory and the pre-/post-inflammatory phases will allow validating the use of the radiotracer in monitoring changes in beta cell mass in the progress of the disease.

Widely used monogenic models of obesity and type 2 diabetes are ob/ob mice and ZDF rats (Lindström 2007; Peterson et al. 1990). The ob/ob mouse does not produce leptin, and ZDF rat is deficient in the leptin receptor, and since leptin signaling is involved in regulating food intake, deficiency in this pathway will induce hyperphagia and obesity in both models.

Ob/ob mice exhibit islet hyperplasia and hyperinsulinemia within 2 weeks of age in response to increased demands in insulin and due to their genetic background. Despite hyperinsulinemia, mice will develop hyperglycemia during the fourth week because insulin production becomes insufficient to maintain normoglycemia. Hyperglycemia peaks between 3 and 5 months of age, where mice are under rapid weight gain due to very high food intake, and blood glucose levels start decreasing gradually between 5 and 7 months of age, where weight gain has ceased. Insulin levels peak after 8 months (Westman 1968).

In ZDF rats, beta cells will respond to increased blood glucose through hyperplasia and massive insulin release in the blood, which is evident at 8 weeks of age, followed by a decline in beta cell mass, which results in uncontrolled hyperglycemia at 8–12 weeks of age.

The changes in beta cell mass and function in these models allow studies to investigate to the relation between BCM and beta cell function.

24.4.4 Imaging of Islet Transplants

Since the establishment of the Edmonton protocol, intrahepatic islet transplantation has become a promising approach to reverse hyperglycemia in type 1 diabetic patients (Ryan et al. 2005). However, islets are lost in large amounts immediately after transplantation (Biarnés et al. 2002). Indeed, the presence of the islets in the hepatic vascular system triggers an instant blood-mediated inflammatory reaction (IBMIR) which compromises islet engraftment, blood supply, and survival (Nilsson et al. 2011; Moberg et al. 2002). Other factors such as islet lipo-/glucotoxicity and (auto)immune rejection are involved in long-term graft failure (Biarnés et al. 2002; Lee et al. 2007). Finally, the excessive use of immunosuppressive drugs for maintaining immune tolerance toward the islets can cause graft failure (Campbell et al. 2007; Barlow et al. 2013). Current functional tests cannot determine whether graft failure is caused by beta cell functional impairment or death. Noninvasive imaging methods could enable measurement of the amount of beta cells in the islet graft and in this way discriminate between loss of beta cell function and mass. Before implementation in clinical studies, these imaging techniques should be characterized in (small) animal models for islet transplantation.

In contrast to the clinical setting in small animal models, islets are transplanted at a variety of sites for islet graft imaging with radiotracers. These transplantation sites are chosen based on the following criteria: They should exhibit an environment that allows beta cell survival and proper function. They should offer an environment with high signal-to-background ratio for easy visualization and quantification of tracer uptake by the islets. The background signal can result from the preferred excretion routes of the radiotracer or the expression of the target receptor in the organs of the recipient. Finally, the transplantation site should allow easy histological evaluation of complete transplants, for accurate correlation of tracer uptake with the graft volume that is determined by the area of beta cell markers (e.g., insulin, nkx6.1, pdx1). Typically, fast and accurate histological evaluation of BCM can be achieved when islets are engrafted in a small area rather than being scattered across the transplantation site.

The kidney capsule has been the site of choice for in vivo monitoring of islet transplants that are prelabeled in vitro with super-paramagnetic iron oxide (SPIO), which can be easily detected by T2-weighed MRI acquisitions (Medarova and Moore 2009). Conversely, the kidney capsule is not suitable for imaging of islet transplants through in vivo injection of radioactive beta cell tracers, due to the preferred renal clearance of the tracers that may obscure beta cell-mediated signal. Several alternative sites (muscle, liver) are therefore used in radionuclide of islet grafts.

24.4.4.1 Transplantation Sites for Monitoring of Islet Grafts by Radionuclide Imaging

Imaging of human islets transplanted in the liver using ^{64}Cu-labeled exendin was achieved in NOD/SCID mice (Wu et al. 2013). Animals transplanted with the islets showed higher PET signal when compared to the control group, demonstrating the potential of this strategy for

imaging of intra-portally transplanted islets. However, in this model islets are spread in a large engraftment area, which renders histological determination of BCM difficult as it requires assessment of the whole organ.

The skeletal muscle was previously used as a clinical transplantation site to accommodate islet transplants and reverse hyperglycemia (Pattou et al. 2010; Espes et al. 2011; Christoffersson et al. 2010). The organ has high angiogenic potential allowing the establishment of intra-islet blood flow that is comparable to the native environment of pancreatic islets (Christoffersson et al. 2010). The transplantation procedure is minimally invasive and relatively easy to perform. Furthermore, the islets can be transplanted in muscles located far away from the radiotracer excretion routes (e.g., renal excretion) and organs that are known to express the target receptor. Finally, easy in vivo quantification of tracer uptake and fast histological analysis of complete transplants are possible, due to the focal transplant in the muscle. Using this model, islet imaging was achieved by ^{111}In-exendin in a mouse model, where islet-mediated uptake of the tracer was clearly visualized and the accumulation of the tracer correlated linearly with transplant size (Eter et al. 2015).

The subcutaneous space has been used for islet transplantation in humans given its easy accessibility and the safety of the procedure. However, the site exhibits low angiogenic potential, which represents an obstacle for proper graft survival and functioning. The large availability of subcutaneous spaces and the possibility to transplant islets into a small distribution area offer similar advantages as described above for the skeletal muscle. Using this model, previous studies demonstrated that human islets transduced with the simplex virus type 1 thymidine kinase (HSV1-tk) can be targeted in vivo with [^{18}F]FHBG and visualized by PET in mice (Lu et al. 2006).

24.4.4.2 Validation Strategies of Radiotracers to Monitor Islet Graft Survival

Radiotracers that are validated for imaging of endogenous beta cells could potentially also be used for monitoring of islet grafts. Before application of the imaging technique, several experiments should be performed to validate the potential to visualize transplanted islets.

As a first step, the performance of a beta cell tracer in quantifying islet numbers can be validated in syngeneic models, where various amounts of islets are transplanted and compared to tracer uptake in healthy (normoglycemic) recipients. The advantage of this approach is that validation of the radiotracer for BCM assessment would not be influenced by confounding factors, such as immune assaults and hyperglycemia.

Most islet transplantations are performed in patients with long history of brittle type 1 diabetes. Moreover, islets are transplanted in immune-incompatible recipients, requiring immunosuppressive drugs for successful islet engraftment. Therefore, as a second step, immune-incompatibility and hyperglycemia are parameters to consider when validating radiotracers for monitoring islet transplants. Ideally, radiotracer uptake should not be significantly influenced by inflammatory assaults, the immune-suppression regimen, and hyperglycemia. Here, syngeneic models can be used to study the effect of hyperglycemia on tracer uptake by islet grafts, where recipients are rendered diabetic by injection of alloxan or STZ prior to islet transplantation (Deeds et al. 2011). Allotransplantation and xenotransplantation models can be used to verify if the tracer can detect beta cell loss during immune rejection or quantify beta cell survival in animals that receive immunosuppressive treatment.

24.5 Current Status of Radiotracers for Preclinical Diabetes Imaging

In the following section, an overview of potential targets and their corresponding tracers for beta cell imaging is provided.

24.5.1 Exendin

The GLP-1R is a prominent target for noninvasive in vivo beta cell imaging. The receptor belongs to

a 7-transmembrane-spanning, heterotrimeric G-protein-coupled receptor family that also contains the receptors for glucagon, glucagon-like peptide 2 (GLP-2) and glucose-dependent insulinotropic polypeptide (GIP). GLP-1R expression is present in pancreatic beta cells, where receptor activation stimulates insulin secretion, insulin gene transcription, and biosynthesis. In all other endocrine cell types, however, receptor expression is absent. Furthermore, very limited expression is found in the exocrine pancreas and the surrounding organs, such as the stomach, lung, and duodenum (Baggio and Drucker 2007). These expression profiles make the GLP-1R an excellent potential target for beta cell imaging.

Since the half-life of GLP-1, the natural ligand of the GLP-1R, is less than 2 min in circulation, it is unsuitable for GLP-1R targeting in vivo. Therefore, stable GLP-1R agonists, such as exendin-3 and exendin-4, are applied for in vivo beta cell imaging via GLP-1R targeting. Initial studies were performed with ^{123}I-labeled exendin and showed high uptake in the pancreas and in insulinomas. However, ^{111}In-labeled exendin displays much higher uptake and retention in insulinomas since the radiometal is trapped in the lysosomes, while ^{123}I is cleared after degradation. Nowadays, ^{111}In-exendin SPECT can be successfully applied to visualize neuroendocrine tumors in both rodents and patients (Brom et al. 2010b; Eriksson et al. 2014a; Wild et al. 2008, 2010).

Radiolabeled exendin cannot only target insulinomas, but it can also target GLP-1R on beta cells, both in the native pancreas and after transplantation in the liver or the muscle (Wu and Kandeel 2010). Pancreatic ^{111}In-exendin uptake can be visualized in vivo using SPECT, and quantitative SPECT analysis shows a linear correlation of tracer uptake in the pancreas and BCM in a rat model with alloxan-induced diabetes.

In alloxan-treated rats, pancreatic ^{111}In-exendin uptake drops to the level observed in rats co-injected with an excess of unlabeled exendin. Furthermore, pancreatic uptake of radiolabeled exendin is not influenced by the alpha cells (Brom et al. 2015). These observations demonstrate the high specificity of ^{111}In-exendin for the beta cells. The potential of the radiotracer to visualize the beta cells in the pancreas was not only proven in rodents but also in humans. The uptake in the pancreas of type 1 diabetic patients was clearly decreased when compared to healthy volunteers (Brom et al. 2014). In diabetic subjects, pancreatic uptake dropped to background levels, indicating beta cell specificity.

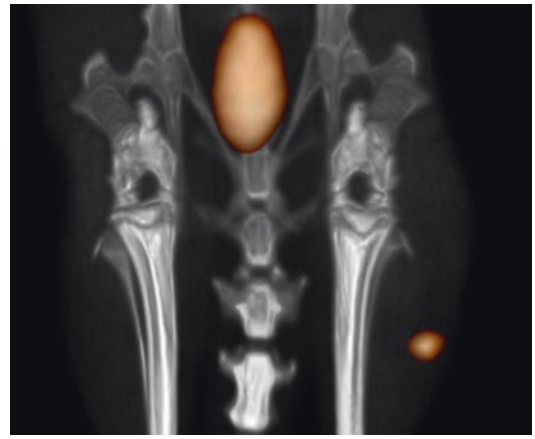

Fig. 24.1 ^{111}In-exendin SPECT/CT image of an islet transplant in the left hind leg of a mouse. The other structure showing radiotracer uptake is the urinary bladder (Image obtained 2 h p.i. 15 MBq ^{111}In-DTPA-Lys40-exendin)

Another application of radiolabeled exendin is noninvasive in vivo imaging of transplanted islet of Langerhans. After transplantation in the liver and the muscle, islet grafts could be visualized by ^{111}In-exendin SPECT and ^{18}F-TTCO exendin PET, respectively (Eriksson and Alavi 2012). In addition to radiolabeling for PET and SPECT imaging, exendin can also be coupled to an iron oxide nanoparticle for in vivo MRI or with fluorescent dyes for optical imaging (Reiner et al. 2010; Wang et al. 2014) (Fig. 24.1).

24.5.2 5-Hydroxytryptophan (5-HTP)

Some neurotransmitters found in the central nervous system are also expressed in the endocrine pancreas. One of these neurotransmitters, present in the islets of Langerhans, is serotonin (5-HT). Serotonin has a function in insulin secretion and influences beta cell proliferation during pregnancy. Furthermore, alterations in the serotonergic system

are observed in diabetic animal models and patients, suggesting involvement of serotonin in diabetes pathogenesis. 5-HTP, a precursor of serotonin, can be taken up in the islets via L-type amino acid transporters (LATs) and decarboxylated by L-amino acid decarboxylase (AADC) to form serotonin which is then stored in secretory vesicles via the vesicular monoamine transporter 2 (VMAT2). Interestingly, the serotonin pathway is absent in the exocrine pancreas, which renders it an attractive target for beta cell imaging.

^{11}C-5-HTP is a PET tracer originally designed for in vivo assessment of serotonin biosynthesis in the central nervous system. Nowadays, ^{11}C-5-HTP PET is clinically applied for the localization of neuroendocrine tumors (Rufini et al. 2012). For specific islet cell tumor detection, it may even perform better than ^{18}F-DOPA PET. Apart from tumor imaging, ^{11}C-5-HTP can also be applied for quantitative islet imaging. In mixtures of isolated human islets and exocrine cells, ^{11}C-5-HTP uptake correlates linearly with the amount of islets. Initially, ^{11}C-5-HTP is taken up by both endocrine and exocrine tissue via LATs. However, the tracer only accumulates in cells harboring the serotonin synthesis pathway. Therefore, the tracer accumulates in the islets and exits the exocrine tissue rapidly. Theoretically, ^{11}C-5-HTP is a marker for all endocrine cells since these cell types are serotonin positive. However, tracer retention is significantly higher in beta cells, resulting in increased accumulation in the beta cells 1 h p.i.

In streptozotocin-induced diabetic rats with 10–20 % remaining BCM, ^{11}C-5-HTP uptake is reduced by 66 % when compared to healthy animals. Furthermore, the tracer can discriminate between rats with severe and less severe beta cell loss. Both in type 1 and type 2 diabetic patients, ^{11}C-5-HTP uptake was decreased compared to healthy volunteers. Clinical studies in type 1 diabetic patients show a decrease in tracer uptake of 66 % 1 h p.i., and the main decrease is observed in beta cell-rich areas of the pancreas (Eriksson et al. 2014b). Furthermore, in vivo ^{11}C-5-HTP uptake correlates with C-peptide levels in type 1 diabetic patients. These findings clearly indicate negligible nonspecific uptake in vivo and preferential beta cell targeting. Nevertheless, one should keep in mind that total beta cell depletion will only partly reduce endocrine ^{11}C-5-HTP uptake due to the presence of other neuroendocrine pancreatic tissues retaining ^{11}C-5-HTP.

24.5.3 L 3-,4-Dihydroxyphenylalanine (DOPA)

A second neurotransmitter system expressed in the islets of Langerhans is the dopaminergic system. Furthermore, dopamine receptors are expressed in the islets of rodents and humans, and receptor expression co-localizes with insulin secretion. It is known that dopamine exerts an effect on insulin secretion, but its exact function remains to be elucidated. Ever since the presence of dopamine receptors on islets was revealed, it was pointed out as a potential target for beta cell imaging.

^{18}F-DOPA is a PET radioligand which has been used extensively to investigate dopaminergic transmission in patients with neurodegenerative diseases. The tracer accumulates in the islets through the same mechanism as ^{11}C-HTP. After ^{18}F-DOPA is taken up via LATs, it is decarboxylated by AADC, and ^{18}F-dopamine is stored in the secretory granules in the islets. However, specific in vitro beta cell binding is rather low. Furthermore, ^{18}F-DOPA displays high uptake in the exocrine pancreas which precludes islet imaging in the native pancreas using this tracer. Nevertheless, ^{18}F-DOPA PET is successfully applied to visualize neuroendocrine tumors such as insulinomas and to noninvasively distinguish between the focal and diffuse form of congenital hyperinsulinism of infancy (Souza et al. 2006). In these conditions, elevated L-DOPA decarboxylase activity is observed, which results in increased tracer accumulation. Although islet imaging using ^{18}F-DOPA PET is not feasible in the native pancreas due to exocrine pancreatic uptake, it might be a valuable tool to visualize the islets after transplantation. Indeed, islets transplanted subcutaneously could be imaged successfully using ^{18}F-DOPA PET. Also using other dopamine receptor ligands such as ^{18}F-fallypride and ^{123}I-IBZM, it is possible to visualize islet grafts.

24.5.4 Dihydrotetrabenazine (DTBZ)

DTBZ is a specific inhibitor of vesicular monoamine storage and binds with high affinity to VMAT2. Thereby, it precludes storage of monoamines, such as dopamine and serotonin, in secretory vesicles. It is therefore not surprising that VMAT2 expression is observed in pancreatic islets, making it a potential target for islet imaging.

^{11}C-DTBZ is a PET tracer, originally developed to visualize the striatum in patients suffering from neurodegenerative diseases. Both in streptozotocin-induced and spontaneously developing (BBDP) diabetic rats ^{11}C-DTBZ uptake was decreased compared to healthy animals. In BBDP rats, ^{11}C-DTBZ uptake decreased with further progression toward diabetes. Also in patients with long-standing type 1 diabetes, a reduction in tracer uptake was observed in comparison with pancreatic uptake healthy volunteers (Souza et al. 2006). Conversion of ^{11}C-DTBZ to ^{18}F-DTBZ and later to ^{18}F-FP-(+)-DTBZ resulted in improved target-to-background ratios. However, tracer uptake was never correlated with BCM (Wu and Kandeel 2010).

Although radiolabeled DTBZ can visualize the pancreas by PET and uptake is reduced in type 1 diabetic patients, significant tracer uptake was still present in these subjects. When compared to healthy controls, tracer uptake only decreased 14 % in type 1 diabetic patients, which rises questions concerning the beta cell specificity of the tracer. Residual tracer uptake might be caused by VMAT2 expression in the PP cells and the sympathetic nerve endings in the pancreas. Furthermore, it is suggested that pancreatic uptake of radiolabeled DTBZ is mainly due to nonspecific exocrine uptake since extensive displacement studies failed to show specific VMAT2 binding (Eriksson et al. 2014b; Fagerholm et al. 2010). Another study even showed that VMAT2 protein might not be expressed in the beta cells of adult mice and rats, raising concerns about the significance of results obtained in rodent models (Schafer et al. 2013).

24.5.5 IC2

Islet cell surface autoantibodies precede the onset of type 1 diabetes and are found in a majority of patients. Since these autoantibodies are responsible for autoimmune beta cell destruction, their corresponding antigens might be potential targets for beta cell imaging. IC2 is a monoclonal antibody (IgM) produced in a rat-rat hybridoma specific for the islet cell surface of rats and binds to a sulfatide epitope galactose-3 sulfate, present in the insulin granula (Wu and Kandeel 2010). The antibody shows binding to normal rat islet cells and insulinomas. Furthermore, the expression of islet cell surface antigen corresponding to IC2 is dependent on the metabolic state of the islets.

Pancreatic uptake of both ^{125}I-IC2 and ^{111}In-IC2 correlates with BCM, and no binding to exocrine tissue was observed. Furthermore, higher tracer accumulation is observed ex vivo in pancreata of healthy rats compared to uptake in streptozotocin-induced diabetic rats (Souza et al. 2006). Nevertheless, the feasibility of IC2 for noninvasive determination of the BCM in vivo needs to be determined.

24.6 Radiopharmaceuticals for Beta Cell Imaging: From Bench to Bedside

The development of a promising radiopharmaceutical for clinical use is a lengthy process, which involves several steps including both animal and human efficacy and safety studies. The extent of this process is dependent on the type of radiopharmaceutical and its intended application in humans.

In Europe, radiopharmaceuticals are considered as a special group of medicines. Their preparation and use are therefore regulated by a number of European Union (EU) directives. With the 2001/20/EC directive, the EU has provided a specific legislative framework, which defines a guideline for the use of radiopharmaceuticals in

clinical trials. The European Association of Nuclear Medicine (EANM) has provided some guidelines for the radiopharmaceutical community on how to comply with the EU legislation. These guidelines involve preclinical development and production of the radiopharmaceutical as well as documentation (EMA 2009; Verbruggen et al. 2008; Todde et al. 2014; Committee EAoNMR 2007).

In this section the different steps in the process in clinical translation of a new radiopharmaceutical will be described. The clinical translation of the radiolabeled tracers exendin-4 and 5-HTP will be provided as examples to illustrate the process.

24.6.1 Regulations: The Necessary Steps to Take

The first phase of development of a radiopharmaceutical consists of nonclinical safety assessment. This assessment includes pharmacology studies, toxicity studies, and pharmacokinetic studies. The nonclinical safety studies have to provide sufficient information to be able to characterize potential adverse effects which might occur under the intended conditions of use in patients.

The exact amount and type of nonclinical supporting data necessary for the translation to exploratory clinical studies is dependent on the extend of proposed human exposure, both with respect to the maximum clinical dose and the duration of dosing (EMA 2009).

Table 24.1 summarizes the nonclinical safety studies, which are appropriate in case of an intended single i.v. dose of less than 100 μg in humans.

24.6.2 Regulations on Production of Radiopharmaceuticals for Clinical Use

To ensure the quality of the drug product and its precursor, the production of radiopharmaceuticals must adhere to current good manufacturing process (CGMP) compliance.

Guidelines for CGMP are related to personnel and resources, equipment, facilities, and documentation. All personnel must possess appropriate education, background, training, and experience, and all operations should be carried out under the control of a responsible person. Specific rules with regard to techniques and safety are in place to ensure radiation protection. Furthermore, it is necessary to carry out quality assurance to oversee the preparation operations to secure the preparation of a radiopharmaceutical of sufficient quality.

Table 24.1 Nonclinical safety studies for microdose trials (adapted from EMA 2009)

Clinical dose to be administered	Start and maximum doses	Pharmacological data	General toxicity data	Genotoxicity and other data
Total dose ≤100 μg	Can be the same	In vitro target/receptor profiling	Extended single-dose toxicity study in one species (usually rodent) by intended route of administration with toxicokinetic data	Not recommended, but any studies or SAR[b] assessments conducted should be included in the clinical trial application
Total dose ≤1/100th of the NOAEL[a]	Cannot exceed a total accumulated dose of 100 μg	Appropriate characterization of primary pharmacology in a pharmacodynamically relevant model to support human dose selection	Maximum of 1000-fold the clinical dose on a mg/kg basis can be used	
Total dose ≤1/100th of the pharmacologically active dose				

[a]No observed adverse effect level
[b]Structure activity relationship

Dedicated self-contained facilities, complying with specific regulations, have to be in place in which the preparations are performed. Workstations and equipment must be regularly monitored, must be easy to clean, must be disinfected and decontaminated, and must be qualified. A further prerequisite is a system planned preventative maintenance and calibration.

There is also a need for thorough documentation of the entire operation, including training of personnel, calibration of equipment, production procedures, and product release. Finished radiopharmaceuticals are only allowed to be released after a formal, recorded decision of approval by a responsible person according to a written release procedure (Committee EAoNMR 2007).

24.6.3 Preparation of Clinical Trial Application

The first time that the new radiopharmaceutical will be used in humans, the first-time-into-man (FTIM) application, requires the classification of the radiopharmaceutical as an "investigational medicinal product" (IMP) and necessitates, besides a detailed study protocol, thorough documentation in a so-called Investigators Brochure (IB) and Investigational Medical Product Dossier (IMPD). All of these documents are required by the competent authority and the research ethics committee.

The IB is intended to provide the investigator and others who are involved in the clinical trial with relevant information regarding the chemical structure of the IMP and all available (non)clinical data. It should also deal with adverse reactions that are observed so far or that can be expected and their frequency of occurrence, provide valuable safety information and guidance to the investigator regarding the identification and reporting requirements of suspected serious adverse reactions (SUSARs). When the IMP has a marketing authorization in one of the member states, a Summary of Product Characteristics (SmPC) can replace the IB. Of note, the conditions of use should not differ from those authorized (Commission E 2008).

The sponsor of the clinical trial should submit an IMPD when no information regarding the IMP has been sent to the competent authority concerned and no cross-reference can be made to information submitted by another sponsor. An IMPD contains a detailed description of the chemical pharmaceutical data, such as the drug substance (e.g., structure, general properties, stability) and the finished drug product (e.g., pharmaceutical development, manufacturing process, control of medicinal product) (Verbruggen et al. 2008). If there is some special aspect about the (pre)clinical data that requires detailed expert explanation or discussion beyond what would be included in the IB, this has to be submitted as part of the IMPD. When a radiopharmaceutical is intended for marketing authorization, the IMPD has to focus particularly on the risk aspects (Todde et al. 2014). In Europe, the preparation of the IMPD is regulated by the European Medicines Agency (EMEA). However, it is recommended to always contact the competent authority to verify specific national requirements and regulations, if applicable. Both the IB and IMPD must be reviewed on at least an annual basis and updated if necessary.

When the clinical trial and accompanying documents are approved by the ethics committee and the competent authority has raised no grounds of nonacceptance, one can proceed with the trial.

24.6.3.1 Radiation Exposure

Another aspect that needs to be considered using radiopharmaceuticals for clinical research is the radiation exposure of the study participants. Usually a clear justification of activities that could cause or affect radiation exposure is required in advance, taking into account the specific objectives of the exposure and the characteristics of the individual involved. Furthermore, the dose should be limited by (1) constraining the dose and (2) optimizing the protection to keep the dose as low as possible (Verbruggen et al. 2008). The total amount of ionizing radiation exposure of study participants must comply with the Helsinki declaration and the guidelines of its application prepared by the Council for International Organizations of Medical Sciences (Verbruggen et al. 2008). The International Commission on

Table 24.2 ICRP categories of risk and corresponding societal benefit (from ICRP 62) (adapted from Verbruggen et al. 2008)

Level of risk	Risk category[a]	Corresponding effective dose range (adults; mSv)	Levels of expected social benefit
Trivial	Category I (~10^{-6} or less)	<0.1	Minor
Minor to intermediate	Category IIa (~10^{-5})	0.1–1	Intermediate to moderate
	Category IIb (~10^{-4})	1–10	
Moderate	Category III (~10^{-3})	>10[b]	Substantial

[a]Expressed as absolute risk probability (number if events/population)

Radiological Protection (ICRP) has formulated categories of risk and corresponding societal benefit (Table 24.2). The lowest risk is a probability in the order of one in a million to have direct consequences from the exposure and is considered trivial. The highest risk category corresponds to an effective dose of 10 mSv or more with a probability of 1 in 1,000 that the participant is experiencing direct consequences of the exposure.

Trials in this category can be justified if the expected benefit is substantial and related to the saving of life or the prevention or mitigation of serious disease. Justification for the intermediate category can be based on the ability to gain knowledge leading to health benefit or benefits directly aimed at the cure or prevention of the disease. This category has two subdivisions depending on exposure levels: Category IIa involves exposure levels similar to those received by members of the public from controlled sources, whereas study participants in category IIb receive exposure levels up to ten times higher. Finally, specific caution should be taken concerning pregnant woman. Because of the irradiation of the fetus and the accompanying risks, pregnant women should not be included for early phase clinical trials with radiopharmaceuticals, unless the pregnancy itself is central to the research and only if any alternative, less-risky techniques cannot be used (Verbruggen et al. 2008).

24.6.4 Clinical Application of ^{111}In-DTPA-Exendin-4 and ^{11}C-5-HTP

For clinical translation of a radiotracer, preclinical data regarding toxicity and specificity of the tracer have to be collected. In case of exendin, single-dose toxicity studies were performed to assess the acute toxicity of DTPA-exendin. Intravenous administration of ^{111}In-DTPA-exendin was well tolerated by mice and rats with no signs of toxicity (Gotthardt et al. 2006; Wild et al. 2006). Biodistribution studies in rodents have been performed showing that ^{111}In-labeled exendin specifically accumulates in GLP-1R positive tissues, such as the lung, stomach, and pancreas. Furthermore, it was shown that the pancreatic uptake of ^{111}In-labeled exendin was reduced in alloxan-induced diabetic rats (Brom et al. 2014; Gotthardt et al. 2006). The first-time-into-man application was in 2008 (Wild et al. 2008). In this proof-of-concept study, 90 MBq of ^{111}In-DTPA-exendin-4 was injected into two patients with insulinomas that could not, or unsatisfactory, be localized with conventional imaging methods. With a radiation exposure between 1 and 10 mSv, the risk category was considered intermediate. With this study, the authors provided the first evidence of the potential of this tracer for GLP-1R imaging for insulinoma detection in human patients. After these initial results, more clinical studies followed (Brom et al. 2014; Wild et al. 2008; Christ et al. 2009, 2013), also with other applications, such as the detection and quantification of beta cell mass in healthy volunteers and in patients with type 1 diabetes (Brom et al. 2014). In this study ^{111}In-DTPA-exendin SPECT imaging was performed in five healthy volunteers and in five patients with type 1 diabetes showing a marked decrease (about 60 %) in pancreatic tracer uptake in patients with type 1 diabetes.

^{11}C-5-HTP was originally developed as a PET tracer for assessing the rate of serotonin

biosynthesis in health and disease (Lundquist et al. 2006). ^{11}C-5-HTP is used in the clinic for localization of NET. An increased uptake of ^{11}C-5-HTP in tumorous tissue is observed resulting in better tumor visibility. As a consequence more lesions are found than with CT and somatostatin receptor scintigraphy (Orlefors et al. 1998, 2005). However, the observation that 5-HTP was taken up by pancreatic islets, leading to an accumulation of the radioisotope (Gylfe et al. 1973), has driven the characterization of this tracer as a possible marker for the endocrine pancreas (Lee et al. 2007; Campbell et al. 2007). These studies show that 5-HTP is taken up in the exocrine as well as in the endocrine pancreas, but that retention of 5-HTP in the cell only occurs when it is further metabolized. Retention therefore demands the presence of the entire molecular machinery involved in serotonin synthesis, which is present in islet cells, but not in the exocrine pancreas causing rapid washout of 5-HTP from exocrine cells. Eriksson et al. have shown that 5-HTP uptake in the entire pancreas of nonhuman primates was specific for serotonin biosynthesis and that the uptake was significantly reduced in rats with induced diabetes, indicating a negligible nonspecific uptake of ^{11}C-5-HTP in the exocrine pancreas (Eriksson et al. 2014c). Focusing on the endocrine pancreas, 5-HTP targets both alpha and beta cells, but the retention in the beta cells is four times higher compared to that in alpha cells (Barlow et al. 2013). Based on these preclinical results, the use of ^{11}C-5-HTP as an endocrine marker was examined in a clinical trial, published in 2014, in which ^{11}C-5-HTP PET imaging was performed in ten patients with type 1 diabetes and nine healthy volunteers. In this study an average 66% reduction of ^{11}C-5-HTP accumulation in patients with type 1 diabetes was found compared to the healthy volunteers (Eriksson et al. 2014b), a reduction which is comparable to the results shown with ^{111}In-DTPA-exendin.

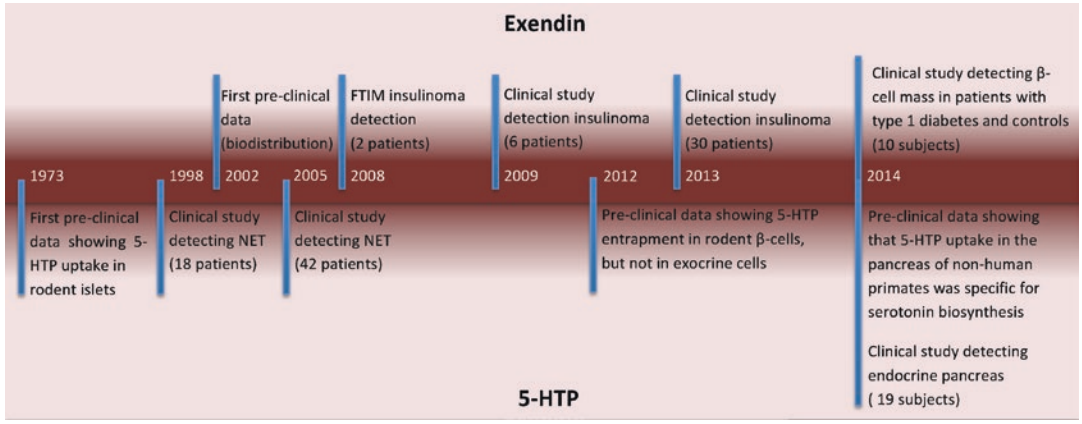

References

Abd-Elgaliel WR, Gallazzi F, Garrison JC, Rold TL, Sieckman GL, Figueroa SD, et al. Design, synthesis, and biological evaluation of an antagonist-bombesin analogue as targeting vector. Bioconjug Chem. 2008; 19(10):2040–8.

Alanentalo T, Asayesh A, Morrison H, Loren CE, Holmberg D, Sharpe J, et al. Tomographic molecular imaging and 3D quantification within adult mouse organs. Nat Meth. 2007;4(1):31–3.

Andralojc K, Srinivas M, Brom M, Joosten L, de Vries IJ, Eizirik DL, et al. Obstacles on the way to the clinical visualisation of beta cells: looking for the Aeneas of molecular imaging to navigate between Scylla and Charybdis. Diabetologia. 2012;55(5): 1247–57.

Baggio LL, Drucker DJ. Biology of incretins: GLP-1 and GIP. Gastroenterology. 2007;132(6):2131–57.

Barlow AD, Nicholson ML, Herbert TP. Evidence for rapamycin toxicity in pancreatic β-cells and a review of the underlying molecular mechanisms. Diabetes. 2013;62(8):2674–82.

Biarnés M, Montolio M, Nacher V, Raurell M, Soler J, Montanya E. β-cell death and mass in syngeneically transplanted islets exposed to short- and long-term hyperglycemia. Diabetes. 2002;51(1):66–72.

Bonner-Weir S. Regulation of pancreatic beta-cell mass in vivo. Recent Prog Horm Res. 1994;49:91–104.

Brom M, Andralojc K, Oyen WJ, Boerman OC, Gotthardt M. Development of radiotracers for the determination of the beta-cell mass in vivo. Curr Pharm Des. 2010a;16(14):1561–7.

Brom M, Oyen WJ, Joosten L, Gotthardt M, Boerman OC. 68Ga-labelled exendin-3, a new agent for the detection of insulinomas with PET. Eur J Nucl Med Mol Imaging. 2010b;37(7):1345–55.

Brom M, Woliner-van der Weg W, Joosten L, Frielink C, Bouckenooghe T, Rijken P, et al. Non-invasive quantification of the beta cell mass by SPECT with in-labelled exendin. Diabetologia. 2014;57(5):950–9.

Brom M, Joosten L, Frielink C, Boerman O, Gotthardt M. (111)In-exendin uptake in the pancreas correlates with the beta-cell mass and not with the alpha-cell mass. Diabetes. 2015;64(4):1324–8.

Campbell PM, Senior PA, Salam A, LaBranche K, Bigam DL, Kneteman NM, et al. High risk of sensitization after failed islet transplantation. Am J Transplant. 2007;7(10):2311–7.

Cescato R, Maina T, Nock B, Nikolopoulou A, Charalambidis D, Piccand V, et al. Bombesin receptor antagonists may be preferable to agonists for tumor targeting. J Nucl Med. 2008;49(2):318–26.

Christ E, Wild D, Forrer F, Brandle M, Sahli R, Clerici T, et al. Glucagon-like peptide-1 receptor imaging for localization of insulinomas. J Clin Endocrinol Metab. 2009;94(11):4398–405.

Christ E, Wild D, Ederer S, Behe M, Nicolas G, Caplin ME, et al. Glucagon-like peptide-1 receptor imaging for the localisation of insulinomas: a prospective multicentre imaging study. Lancet Diabetes Endocrinol. 2013;1(2):115–22.

Christoffersson G, Henriksnäs J, Johansson L, Rolny C, Ahlström H, Caballero-Corbalan J, et al. Clinical and experimental pancreatic islet transplantation to striated muscle: establishment of a vascular system similar to that in native islets. Diabetes. 2010;59(10):2569–78.

Commission E. Detailed guidance for the request for authorization of a clinical trial on a medicinal product for human use to the competent authorities, notification of substantial amendments and declaration of the end of the trial. 2008.

Committee EAoNMR. Guidelines on current good radiopharmacy practice (cGRPP) in the preparation of radiopharmaceuticals, version 2. 2007.

Davenport A, Russell F. Radioligand binding assays: theory and practice. In: Mather S, editor. Current directions in radiopharmaceutical research and development. Developments in nuclear medicine, vol. 30. Springer; Doordrecht, The Netherlands. 1996. p. 169–79.

Deeds MC, Anderson JM, Armstrong AS, Gastineau DA, Hiddinga HJ, Jahangir A, et al. Single dose streptozotocin-induced diabetes: considerations for study design in islet transplantation models. Lab Anim. 2011;45(3):131–40.

EMA. ICH guideline M3(R2) on non-clinical safety studies for the conduct of human clinical trials and marketing authorization for pharmaceuticals. EMA/CPMP/ICH/286/1995. 2009.

Eriksson O, Alavi A. Imaging the islet graft by positron emission tomography. Eur J Nucl Med Mol Imaging. 2012;39(3):533–42.

Eriksson AU, Svensson C, rnblad A, Cheddad A, Kostromina E, Eriksson M, et al. Near infrared optical projection tomography for assessments of β-cell mass distribution in diabetes research. J Vis Exp. 2013;(71):e50238.

Eriksson O, Velikyan I, Selvaraju RK, Kandeel F, Johansson L, Antoni G, et al. Detection of metastatic insulinoma by positron emission tomography with [(68)ga]exendin-4-a case report. J Clin Endocrinol Metab. 2014a;99(5):1519–24.

Eriksson O, Espes D, Selvaraju RK, Jansson E, Antoni G, Sorensen J, et al. Positron emission tomography ligand [11C]5-hydroxy-tryptophan can be used as a surrogate marker for the human endocrine pancreas. Diabetes. 2014b;63(10):3428–37.

Eriksson O, Selvaraju RK, Johansson L, Eriksson JW, Sundin A, Antoni G, et al. Quantitative imaging of serotonergic biosynthesis and degradation in the endocrine pancreas. J Nuclear Med Off Pub Soc Nuclear Med. 2014c;55(3):460–5.

Espes D, Eriksson O, Lau J, Carlsson PO. Striated muscle as implantation site for transplanted pancreatic islets. J Transplant. 2011;2011:352043.

Eter WA, Bos D, Frielink C, Boerman OC, Brom M, Gotthardt M. Graft revascularization is essential for non-invasive monitoring of transplanted islets with radiolabeled exendin. Sci Rep. 2015;5:15521.

Etuk EU. Animals models for studying diabetes mellitus. Agric Biol J N Am. 2010;1(2):130–4.

Fagerholm V, Mikkola KK, Ishizu T, Arponen E, Kauhanen S, Nagren K, et al. Assessment of islet specificity of dihydrotetrabenazine radiotracer binding in rat pancreas and human pancreas. J Nucl Med. 2010;51(9):1439–46.

Ginj M, Zhang H, Waser B, Cescato R, Wild D, Wang X, et al. Radiolabeled somatostatin receptor antagonists are preferable to agonists for in vivo peptide receptor targeting of tumors. Proc Natl Acad Sci U S A. 2006;103(44):16436–41.

Gotthardt M, Lalyko G, van Eerd-Vismale J, Keil B, Schurrat T, Hower M, et al. A new technique for in vivo imaging of specific GLP-1 binding sites: first results in small rodents. Regul Pept. 2006;137(3):162–7.

Greiner DL, Rossini AA, Mordes JP. Translating data from animal models into methods for preventing human autoimmune diabetes mellitus: caveat emptor and primum non nocere. Clin Immunol. 2001;100(2):134–43.

Gylfe E, Hellman B, Sehlin J, Taljedal IB. Amino acid conversion into 5-hydroxytryptamine in pancreatic beta-cells. Endocrinology. 1973;93(4):932–7.

King AJ. The use of animal models in diabetes research. Br J Pharmacol. 2012;166(3):877–94.

Lee Y, Ravazzola M, Park B-H, Bashmakov YK, Orci L, Unger RH. Metabolic mechanisms of failure of intraportally transplanted pancreatic β-cells in rats: role of lipotoxicity and prevention by leptin. Diabetes. 2007;56(9):2295–301.

Lindström P. The physiology of obese-hyperglycemic mice [ob/ob mice]. ScientificWorldJ. 2007;7:666–85.

Lu Y, Dang H, Middleton B, Campbell-Thompson M, Atkinson MA, Sam Gambhir S, et al. Long-term monitoring of transplanted islets using positron emission tomography. Mol Ther. 2006;14(6):851–6.

Lundquist P, Blomquist G, Hartvig P, Hagberg GE, Torstenson R, Hammarlund-Udenaes M, et al. Validation studies on the 5-hydroxy-L-[beta-11C]-tryptophan/PET method for probing the decarboxylase step in serotonin synthesis. Synapse (New York). 2006;59(8):521–31.

Mansi R, Wang X, Forrer F, Kneifel S, Tamma ML, Waser B, et al. Evaluation of a 1,4,7,10-tetraazacyclododecane-1,4,7,10-tetraacetic acid-conjugated bombesin-based radioantagonist for the labeling with single-photon emission computed tomography, positron emission tomography, and therapeutic radionuclides. Clin Cancer Res. 2009;15(16):5240–9.

Mathijs I, Xavier C, Peleman C, Caveliers V, Brom M, Gotthardt M, et al. A standardized method for in vivo mouse pancreas imaging and semiquantitative beta cell mass measurement by dual isotope SPECT. Mole Imaging Biol MIB Off Pub Academy Mole Imaging. 2015;17(1):58–66.

Medarova Z, Moore A. MRI as a tool to monitor islet transplantation. Nat Rev Endocrinol. 2009;5(8):444–52.

Moberg L, Johansson H, Lukinius A, Berne C, Foss A, Källen R, et al. Production of tissue factor by pancreatic islet cells as a trigger of detrimental thrombotic reactions in clinical islet transplantation. Lancet. 2002;360(9350):2039–45.

Nilsson B, Ekdahl KN, Korsgren O. Control of instant blood-mediated inflammatory reaction to improve islets of langerhans engraftment. Curr Opin Organ Transplant. 2011;16(6):620–6.

Orlefors H, Sundin A, Ahlstrom H, Bjurling P, Bergstrom M, Lilja A, et al. Positron emission tomography with 5-hydroxytryprophan in neuroendocrine tumors. J Clini Oncol Off J Am Soc Clini Oncol. 1998;16(7):2534–41.

Orlefors H, Sundin A, Garske U, Juhlin C, Oberg K, Skogseid B, et al. Whole-body (11)C-5-hydroxytryptophan positron emission tomography as a universal imaging technique for neuroendocrine tumors: comparison with somatostatin receptor scintigraphy and computed tomography. J Clin Endocrinol Metab. 2005;90(6):3392–400.

Pattou F, Kerr-Conte J, Wild D. GLP-1–receptor scanning for imaging of human beta cells transplanted in muscle. N Eng J Med. 2010;363(13):1289–90.

Peterson RG, Shaw WN, Neel M-A, Little LA, Eichberg J. Zucker diabetic fatty rat as a model for non-insulin-dependent diabetes mellitus. ILAR J. 1990;32(3):16–9.

Rees DA, Alcolado JC. Animal models of diabetes mellitus. Diabetic Med J Br Diabetic Assoc. 2005;22(4):359–70.

Reiner T, Kohler RH, Liew CW, Hill JA, Gaglia J, Kulkarni RN, et al. Near-infrared fluorescent probe for imaging of pancreatic beta cells. Bioconjug Chem. 2010;21(7):1362–8.

Reubi JC, Waser B. Concomitant expression of several peptide receptors in neuroendocrine tumours: molecular basis for in vivo multireceptor tumour targeting. Eur J Nucl Med Mol Imaging. 2003;30(5):781–93.

Rufini V, Baum RP, Castaldi P, Treglia G, De Gaetano AM, Carreras C, et al. Role of PET/CT in the functional imaging of endocrine pancreatic tumors. Abdom Imaging. 2012;37(6):1004–20.

Ryan EA, Paty BW, Senior PA, Bigam D, Alfadhli E, Kneteman NM, et al. Five-year follow-up after clinical islet transplantation. Diabetes. 2005;54(7):2060–9.

Schäfer MKH, Hartwig NR, Kalmbach N, Klietz M, Anlauf M, Eiden LE, et al. Species-specific vesicular monoamine transporter 2 (VMAT2) expression in mammalian pancreatic beta cells: implications for optimising radioligand-based human beta cell mass (BCM) imaging in animal models. Diabetologia. 2013;56(5):1047–56.

Schafer MK, Hartwig NR, Kalmbach N, Klietz M, Anlauf M, Eiden LE, et al. Species-specific vesicular monoamine transporter 2 (VMAT2) expression in mammalian pancreatic beta cells: implications for optimising radioligand-based human beta cell mass (BCM) imaging in animal models. Diabetologia. 2013;56(5):1047–56.

Selvaraju RK, Velikyan I, Johansson L, Wu Z, Todorov I, Shively J, et al. In vivo imaging of the glucagonlike peptide 1 receptor in the pancreas with 68Ga-labeled DO3A-exendin-4. J Nucl Med. 2013;54(8):1458–63.

Simpson NR, Souza F, Witkowski P, Maffei A, Raffo A, Herron A, et al. Visualizing pancreatic β-cell mass with [11C]DTBZ. Nucl Med Biol. 2006;33(7):855–64.

Souza F, Freeby M, Hultman K, Simpson N, Herron A, Witkowsky P, et al. Current progress in non-invasive imaging of beta cell mass of the endocrine pancreas. Curr Med Chem. 2006;13(23):2761–73.

Szkudelski T. The mechanism of alloxan and streptozotocin action in B cells of the rat pancreas. Physiol Res Academia Scientiarum Bohemoslovaca. 2001;50(6):537–46.

Todde S, Windhorst AD, Behe M, Bormans G, Decristoforo C, Faivre-Chauvet A, et al. EANM guideline for the preparation of an investigational medicinal product dossier (IMPD). Eur J Nucl Med Mol Imaging. 2014;41(11):2175–85.

Vegt E, de Jong M, Wetzels JFM, Masereeuw R, Melis M, Oyen WJG, et al. Renal toxicity of radiolabeled peptides and antibody fragments: mechanisms, impact on radionuclide therapy, and strategies for prevention. J Nucl Med. 2010;51(7):1049–58.

Verbruggen A, Coenen HH, Deverre JR, Guilloteau D, Langstrom B, Salvadori PA, et al. Guideline to regulations for radiopharmaceuticals in early phase clinical trials in the EU. Eur J Nucl Med Mol Imaging. 2008;35(11):2144–51.

Wang P, Yoo B, Yang J, Zhang X, Ross A, Pantazopoulos P, et al. GLP-1R-targeting magnetic nanoparticles for pancreatic islet imaging. Diabetes. 2014;63(5):1465–74.

Weir GC, Bonner-Weir S, Leahy JL. Islet mass and function in diabetes and transplantation. Diabetes. 1990;39(4):401–5.

Westman S. Development of the obese-hyperglycaemic syndrome in mice. Diabetologia. 1968;4(3):141–9.

Wild D, Behe M, Wicki A, Storch D, Waser B, Gotthardt M, et al. [Lys40(Ahx-DTPA-111In)NH2]exendin-4, a very promising ligand for glucagon-like peptide-1 (GLP-1) receptor targeting. J Nuclear Med Off Pub Soc Nuclear Med. 2006;47(12):2025–33.

Wild D, Macke H, Christ E, Gloor B, Reubi JC. Glucagon-like peptide 1-receptor scans to localize occult insulinomas. N Engl J Med. 2008;359(7):766–8.

Wild D, Wicki A, Mansi R, Behe M, Keil B, Bernhardt P, et al. Exendin-4-based radiopharmaceuticals for glucagonlike peptide-1 receptor PET/CT and SPECT/CT. J Nucl Med. 2010;51(7):1059–67.

Willekens SMA, Joosten L, Boerman OC, Balhuizen A, Eizirik DL, Gotthardt M, et al. Strain differences determine the suitability of animal models for non-invasive in vivo beta cell mass determination using radiolabeled exendin. Mol Imaging Biol. 2016. doi:10.1007/s11307-016-0936-y.

Wu Z, Kandeel F. Radionuclide probes for molecular imaging of pancreatic beta-cells. Adv Drug Deliv Rev. 2010;62(11):1125–38.

Wu Z, Liu S, Hassink M, Nair I, Park R, Li L, et al. Development and evaluation of 18F-TTCO-Cys40-exendin-4: a PET probe for imaging transplanted islets. J Nucl Med. 2013;54(2):244–51.

In Vivo Preclinical Imaging of Developmental Biology

25

Katrien Vandoorne, Tal Raz, Stav Sapoznik,
Inbal E. Biton, Joel R. Garbow, and Michal Neeman

Contents

K. Vandoorne
Biomedical NMR, Department of Biomedical Engineering, Eindhoven University of Technology, Eindhoven NL-5600 MB, The Netherlands
e-mail: k.vandoorne@tue.nl

T. Raz
Koret School of Veterinary Medicine, The Hebrew University of Jerusalem, Rehovot 76100, Israel
e-mail: tal.raz@mail.huji.ac.il

S. Sapoznik
Sheba Cancer Research Center, Chaim Sheba Medical Center, Ramat Gan 52621, Israel
e-mail: stav.sapoznik@sheba.health.gov.il

I.E. Biton
Department of Veterinary Resources, Weizmann Institute, Rehovot 76100, Israel
e-mail: inbal.biton@weizmann.ac.il

J.R. Garbow
Biomedical Magnetic Resonance Laboratory, Mallinckrodt Institute of Radiology, Washington University, St. Louis, MO 63110, USA
e-mail: garbow@wustl.edu

M. Neeman (✉)
Department of Biological Regulation, Weizmann Institute, Rehovot 76100, Israel
e-mail: michal.neeman@weizmann.ac.il

25.1 Animal Models for Developmental Imaging

Biological imaging studies of fetal development are frequently conducted on small laboratory animals, which offer the advantages of rapid

F. Kiessling et al. (eds.), *Small Animal Imaging*, DOI 10.1007/978-3-319-42202-2_25

reproductive cycle and multiparity. In addition to having the ability to provide basic information using available imaging modalities, animal models aiming to study human physiology or disease by noninvasive imaging should also exhibit genetic, anatomical, and physiological similarities to humans. Many developmental studies utilized the rapid reproduction, easy access, and optical clarity of developing avian and fish embryos for high-resolution fluorescence microscopy, while studies of mammals were frequently limited to ex vivo imaging. However, over the last years, new imaging tools also allow in vivo monitoring of development in the mouse, which is the most common mammalian model for the study of development, genetics, immune response, pathology, neurology, and cellular mechanisms of action. The following section of this chapter will screen the most widely used animal models for developmental imaging.

25.1.1 Imaging Development in Fish and Frogs

An important animal model for optical imaging of developmental processes is the transparent zebrafish embryo (Ingham 2009). The adult zebrafish is small (3 cm in length) and can therefore be easily maintained in large numbers. The generation time is short, as sexual maturity is achieved within 3 months after conception. Spawning is external and easily controlled, resulting in about 200 eggs per event. Hatching occurs within 2–3 days, and the entire developmental process is rapid, as the major organ systems largely develop by 6 days postfertilization.

By regulation of the environmental temperature, it is possible to alter the rates of physiological processes, including embryonic development. Contrary to mammals, the entire embryogenesis of the zebrafish takes place outside the maternal body, facilitating optical imaging and enabling direct manipulations. The transparency of the embryos persists naturally for 32 h postfertilization but can be extended experimentally for several days. Importantly, many fundamental morphogenetic processes are evolutionary conserved between zebrafish and mammals (Ingham 2009). Genetically engineering the zebrafish embryos to express fluorescent protein reporters, or injection of vital dyes or microscopic particles, can be used for molecular imaging. In vivo optical imaging is feasible by anesthetizing the embryos and mounting them in agarose to reduce movements.

Various physiological systems of the zebrafish embryo have been studied by optical imaging. Taking advantage of the superficial ventral position of the heart, cardiovascular development, and its response to either pharmacological or genetic manipulations were investigated. For example, the anatomical patterning of the primary vascular network was imaged using EGFP encoding embryos under the regulation of the *fli1* promoter (Vogt et al. 2009). Mechanism of action of macrophages and the development of the nerve system in zebrafish embryos were studied by using differential interference contrast microscopy and harmonic generation microscopy, respectively. Two photon microscopy of zebrafish was utilized for delineating the formation of the lymphatic vasculature (Yaniv et al. 2006) (Fig. 25.1a–g). In addition to optical imaging, zebrafish development was also followed by ultrasound, magnetic resonance imaging (MRI; Fig. 25.1h), and computerized tomography (CT).

Similar to zebrafish embryos, developing frog embryos are transparent and can be easily imaged using light microscopy; therefore, they are extensively used in development studies. Notably, the *Xenopus* oocytes were used for imaging development by MRI, using the reporter probe EgadMe that reveals the activity of the reporter gene beta-galactosidase (Louie et al. 2000). Furthermore, MRI microscopy was used to record the ongoing differentiation in the *Xenopus laevis* embryos in vivo (Lee et al. 2007).

25.1.2 Imaging Avian Development

Another widely used animal model for embryonic developmental studies is the avian egg, particularly chicken and quail embryos. Chick embryos are relatively transparent and flat and,

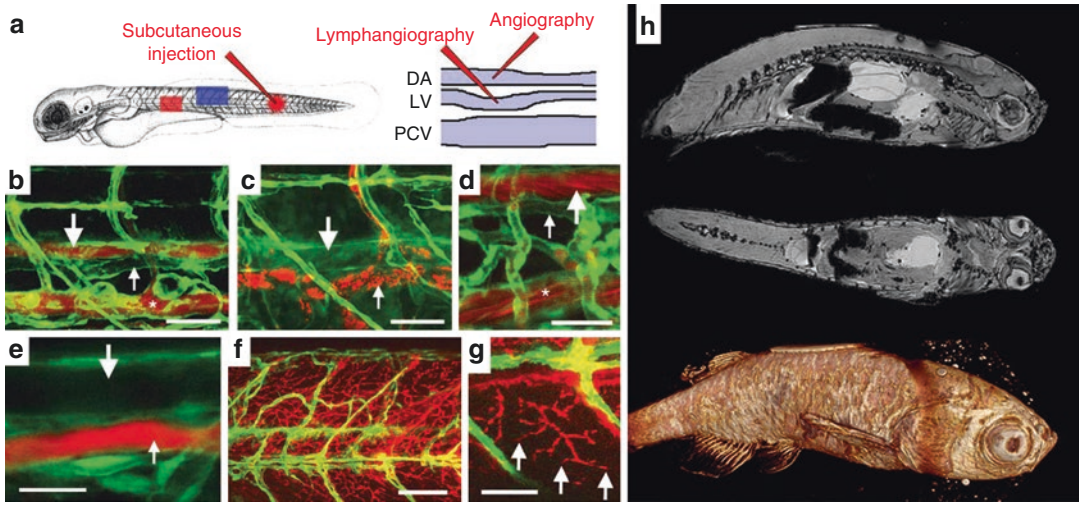

Fig. 25.1 Functional characterization of zebrafish lymphatic vessels. (**a**) Methods used to image blood or lymphatic vessels. *Red*, approximate region of the trunk imaged in **b**–**e** and **g**. *Blue*, approximate region of the trunk imaged in f. LV, lymphatic vessel (thoracic duct). (**b**) Angiography of a 14-d.p.f. Tg(*fli1*:EGFP)yl zebrafish (*green*) injected with fluorescent microspheres (*red*), labeling the dorsal aorta (DA, *large arrow*) and PVC (*asterisk*), but not the lymphatic thoracic duct (*small arrow*). (**c**) Lymphangiography of 3-week(s) postfertilization Tg(*fli1*:EGFP)yl zebrafish (*green*) injected with fluorescent microspheres (*red*), labeling the thoracic duct (*small arrow*), but not the dorsal aorta (*large arrow*). (**d**) Time-averaged confocal image of a 7-d.p.f. Tg(*fli1*:EGFP)yl (*green*) and TG(*gata1*:dsRed) (*red*) zebrafish, showing red fluorescence in the dorsal aorta (*large arrow*) and cardinal vein (CV; *asterisk*), but not the lymphatic thoracic duct (*small arrow*). (**e**–**g**) Confocal imaging of an 18-d.p.f. Tg(*fli1*:EGFP)yl zebrafish (*green*) injected subcutaneously with 2 Md rhodamine-dextran (*red*). (**e**) Subcutaneously injected rhodamine-dextran drains into the thoracic duct (*small arrow*), but does not label the adjacent dorsal aorta (*large arrow*). (**f**) Numerous rhodamine-dextran-labeled vessels (*red*) are visible between the blood vessels (*green*). (**g**) Higher-magnification image of blind-ended rhodamine-dextran-labeled vessels. Scale bars in **b**–**d**, **g**, 50 μ; in **e**, 20 μ; in **f**, 100 μ (**a**–**g**) (Reprinted by permission from Macmillan Publishers Ltd: [*Nature Medicine*] (Yaniv et al. 2006)). (**h**) 2D and 3D MRI images of zebrafish scanned at 9.4 T (Biton I., unpublished 2009)

like the zebrafish embryos, develop outside the maternal reproductive system (Ezin and Fraser 2008). The developmental process is relatively rapid, as blastulation, gastrulation, and early neurulation are completed within 36 h. The quail embryonic development is slightly faster.

Optical imaging takes advantage of the embryo's transparency and the many possibilities for cell labeling. Fluorescent labeling of avian embryos is often induced by microinjection of either lipophilic dyes or hydrophilic polysaccharides into living cells. Furthermore, microinjection, electroporation, or viral transfection of fluorescent proteins is commonly utilized. Interestingly, quail cells transplanted into chick embryos can be easily distinguished from the host cells due to a unique nuclear characteristic. In this way, cell-lineage studies can be carried out, avoiding the need for staining (Kulesa 2004; Tirosh-Finkel et al. 2006; Rinon et al. 2007).

Several experimental procedures were developed to allow avian embryogenesis imaging. Many studies are based on in vitro culturing of the embryos, where the embryo is collected with its vitelline membrane and laid ventral side up in an incubator, which controls the temperature, humidity, and CO_2 concentration. Nutrition of the embryo is provided by culturing it on a pool of thin egg white, Bacto agar, or culture medium (Ezin and Fraser 2008). This in vitro method allows experimental manipulations of the embryo, as well as both dorsal and ventral imaging.

Alternatively, in ovo embryos can be imaged through a window opened in the eggshell. This method allows a long imaging duration, with

minimal disruption of embryonic tissues. Newly developed sagittal slice culture procedures enable imaging of deep structures previously optically unexposed, such as the developing peripheral nervous system (Kulesa 2004). Furthermore, the chick embryo model was used to investigate developmental processes such as cell lineage and migration during axis formation, as well as cardiovascular, craniofacial, limb, skeletal, and vascular patterning (Kulesa 2004; Tirosh-Finkel et al. 2006; Rinon et al. 2007).

Avian development tracking by MRI is feasible and provides the advantage that the eggshell can remain unperturbed (Hogers et al. 2009). Thus, wild-type quail embryos imaged by MRI showed the entire process of heart development. Cardiac malformations, including ventricular septal defects and aortic arch interruptions, could be visualized in venous clipped embryos (Hogers et al. 2009). Furthermore, MRI was recently applied for monitoring the developing smooth muscle fiber by diffusion tensor imaging (Xu et al. 2012).

25.1.3 Imaging Development in Mice

The genetic, anatomical, and physiological similarity to human has led to the adoption of the laboratory mouse as the most widely used model for the study of reproduction and development. Sexual maturity of mice is achieved early in postnatal development; most commonly at 5–8 weeks of age, depending on the mouse strain. The estrus cycle lasts for 4–5 days, and once the female is pregnant, the whole gestation period lasts for only 19–21 days. The average litter size is usually six to eight pups, but can reach much higher depending on the mouse strain.

The cardiovascular and respiratory systems of mice are very similar to human (Schneider and Bhattacharya 2004). Both have a four-chambered heart, with a septated outflow tract, resulting in physical separation of the pulmonary and systemic circulations. The respiratory systems in both cases consist of the lungs, containing alveoli, and of a diaphragm, being the major respiratory muscle. Similarities between the two organisms are found also in other physiological processes, including reproduction and skeletogenesis. Importantly, a high degree of phylogenetic similarity between human and murine genomes facilitates identification of genetic homologues between the two species. This kind of homology provides justification for major efforts to identify roles of human genes by understanding their function in mouse model. An example of such a research strategy resulted in the identification of numerous genes involved in congenital heart defects (Schneider and Bhattacharya 2004). Moreover, manipulations of known human genes can be carried out in the mouse, enabling a better understanding of the genes function, spatiotemporal expression, and mutagenesis.

Methods for genetic manipulation in mice include overexpression of genes for studying gain-of-function-related phenomena, and deletion or replacement of a specific gene by another sequence (knockout or knock-in, respectively), for studying loss-of-function-related phenomena. Mutagenesis is often used for identification of a specific locus within a gene, bearing a unique feature, which is important for the gene's function.

Supplementary techniques, often used in embryology to study development processes, may also be combined with imaging techniques. An example is the tetraploid complementation method, which is used to create an embryo of a specific genetic background bearing extraembryonic tissues of a different genetic background (Tanaka et al. 2009; Plaks et al. 2011a); it is commonly used for analysis and prevention of in utero lethality in transgenic mice due to defects in placental function.

The fact that the entire embryonic development occurs in utero entails major challenges for in vivo imaging. Thus, most studies resorted to invasive methods, such as ex vivo culture and imaging of preimplantation embryos, static postimplantation embryos culture on a microscope stage, collection and fixation of embryos for ex vivo analysis, and culturing of embryonic slices (Passamaneck et al. 2006). Novel imaging methodologies, predominantly MRI and

ultrasound, now offer the possibility for longitudinal noninvasive in vivo imaging of the mouse embryonic development.

25.2 Imaging Modalities

During the very early stages of embryo development, prior to implantation in the uterus, the mammalian embryo can be cultured in vitro, allowing easy imaging by light and fluorescence microscopy. Using these tools, it is possible to track individual cells during the very early stages of fate specification and differentiation.

Previously, most imaging studies of postimplantation developing mouse and rat embryos and neonates were performed ex vivo. The main ex vivo techniques for mouse imaging are optical projection tomography (OPT), micro-computed tomography (μCT), micro-magnetic resonance imaging (μMRI), and microscopic imaging techniques (Weninger et al. 2006; Gerneke et al. 2007). OPT is well suited for whole mouse embryo during the early stages of development and can produce three-dimensional (3D) reconstruction of embryonic tissue. OPT has a spatial resolution of 10 μm, and it allows mapping of gene expression patterns through the visualization of immunofluorescent staining (Dickinson 2006) or autofluorescence (Gleave et al. 2012). Micro-computed tomography can distinguish between air, fatty, nonfatty, and bone tissues. Furthermore, by injecting radiopaque polymers into the vascular space, blood vessels can be imaged with a resolution of 10 μm. With the use of contrast media, CT can be used to visualize the entire vascular network of embryos and their placentas ex vivo (Degenhardt et al. 2010; Kulandavelu et al. 2006).

The imaging modalities that are currently available for in vivo analysis of pregnancy in rodents include ultrasound biomicroscopy (UBM), MRI, fluorescence and bioluminescence imaging, CT, positron emission tomography (PET), and single-photon emission tomography (SPECT). In selecting imaging modalities for developmental biology, it is important to take into consideration physiological side effects on the pregnant mice and the embryos, particularly in longitudinal in vivo studies. In this respect, MRI and UBM appear to be the tools of choice for most studies (Table 25.1). The exposure to high ionizing radiation (X radiation), such as in CT, may cause embryonic abnormalities (Bang et al. 2002), thus, limiting the use of CT for longitudinal monitoring of fetal development. Specifically, exposure at embryonic day (E) E11.5 to radiation dose of 0.5–4 gray (Gy) led to developmental defects, such as dilatation of the cerebral ventricles, cleft palate, growth retardation, and reduced head size with increased radiation dose. Failed pregnancies, including embryonic mortality and resorptions, were significantly more frequent when animals were exposed to radiation levels above 4 Gy. Similarly, the repeated use of radioactive tracer material and detection of gamma rays, another type of ionizing radiation, in SPECT/PET can be potentially harmful for embryos. However, the feasibility of CT imaging in vivo has been demonstrated in near-term pregnant rats and mice, showing exquisite bone contrast, and through the use of contrast media for visualization of the maternal circulation in the placenta (Winkelmann and Wise 2009) (Figs. 25.2 and 25.3).

25.2.1 Ultrasound Biomicroscopy

Ultrasound imaging is a safe method commonly used to monitor human pregnancy, clinically. In the last decade, ultrasound biomicroscopy (UBM) has emerged as a key in vivo imaging tool for noninvasive, in utero imaging of live rodent embryos, allowing ultrasonic visualization of living tissue. UBM transducers use higher frequencies (10–70 MHz) than diagnostic clinical transducers (typically 2–15 MHz). To date, there is no significant evidence for deleterious effects of UBM on the developing mouse embryo. However, slight growth retardation was documented for mice exposed to high-frequency ultrasound between E8.5 and 10.5 (Brown et al. 2004).

Similar to clinical imaging modalities, UBM-Doppler imaging modalities include cross-sectional or two-dimensional (B-mode) imaging, one-dimensional M-mode imaging, color Doppler, and spectral pulsed-wave Doppler. The

Table 25.1 UBM and MRI for in vivo imaging of prenatal development

	Ultrasound biomicroscopy (UBM) (Phoon 2006)	Magnetic resonance imaging (MRI) (Turnbull and Mori 2007)
Applications: Early stage embryo Late-stage embryo Neonates	Transabdominal: limited number of embryos visible Semi-invasive: transuterine, all embryos visible	Implantation visible with contrast-enhanced (CE) MRI (Plaks et al. 2006)
	Live embryo imaging: both transabdominal and transuterine imaging Late embryonic brain imaging not possible (mineralization of the skull)	Manganese-enhanced MRI (MEMRI) for imaging the central nervous system (CNS) (Deans et al. 2008) Cardiac imaging (Nieman et al. 2009) Molecular imaging of reporter gene expression (Cohen et al. 2007) Noninvasive position of the embryos (Avni et al. 2012) Placental imaging (Solomon et al. 2014)
	Cardiovascular system and other soft tissues	Diffusion tensor (DTI) and MEMRI for CNS
Advantages	Dynamic, real time Functional data: Doppler M-mode Quantitative information on structure and function Temporal resolution/image acquisition time Portable, versatile	Three-dimensional (3D) Nondestructive, excellent tissue contrast Contrast resolution by administration of contrast agents Mn2+, macromolecular Gd, cell tracking
Disadvantages	Images limited by gas, bone, depth Operator-dependent image acquisition No information on biochemical, metabolic processes Limited depth of penetration and poor tissue contrast	Temporal resolution/image acquisition time Physiological motion Limited SNR Low contrast resolution with difficulty in administration of the contrast agent High cost of the equipment
Image resolution Spatial Temporal	30–40 µm axial and 70–90 µm lateral resolution Depth of penetration close to 5–15 mm	Spatial resolution 100–200 µm
	Real time, but each embryo needs to be scanned separately	Several minutes per scan, but whole uterus imaged

Fig. 25.2 Micro-CT imaging of rat fetuses. (**a**) In vivo imaging of a pregnant rat (E21). A single coronal slice is shown on the left with multiple fetal skeletons visible (*white arrows*). On the right, a volume rendering of the same data set indicating individual fetuses (*red arrows*). (**b**) In vivo contrast-enhanced imaging of a pregnant rat (E21). The coronal slice on the left shows multiple contrast-enhanced placentas (*white arrows*). Individual fetal sacs can be visualized, as well as the urinary bladder (*red arrow*). The volume rendering on the right details the placental structure and vascular supply (*red arrows*). (**c**) Volume renderings of ex vivo imaging of a single rat fetus show detailed anatomical features. Scale bars = 1 cm (Reprinted from *J Pharmacol Toxicol Methods* (Winkelmann and Wise 2009) with permission from Elsevier)

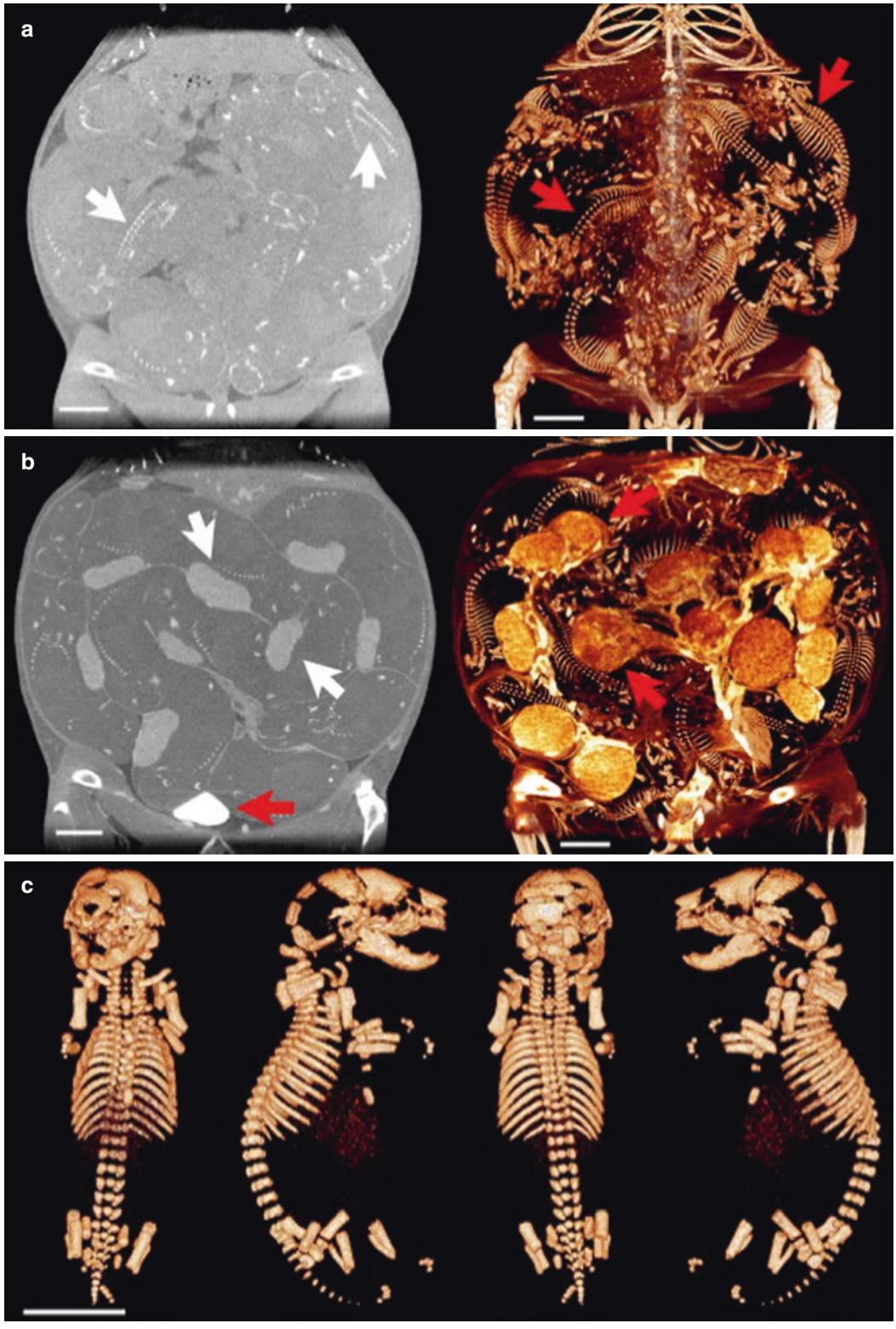
a
b
c

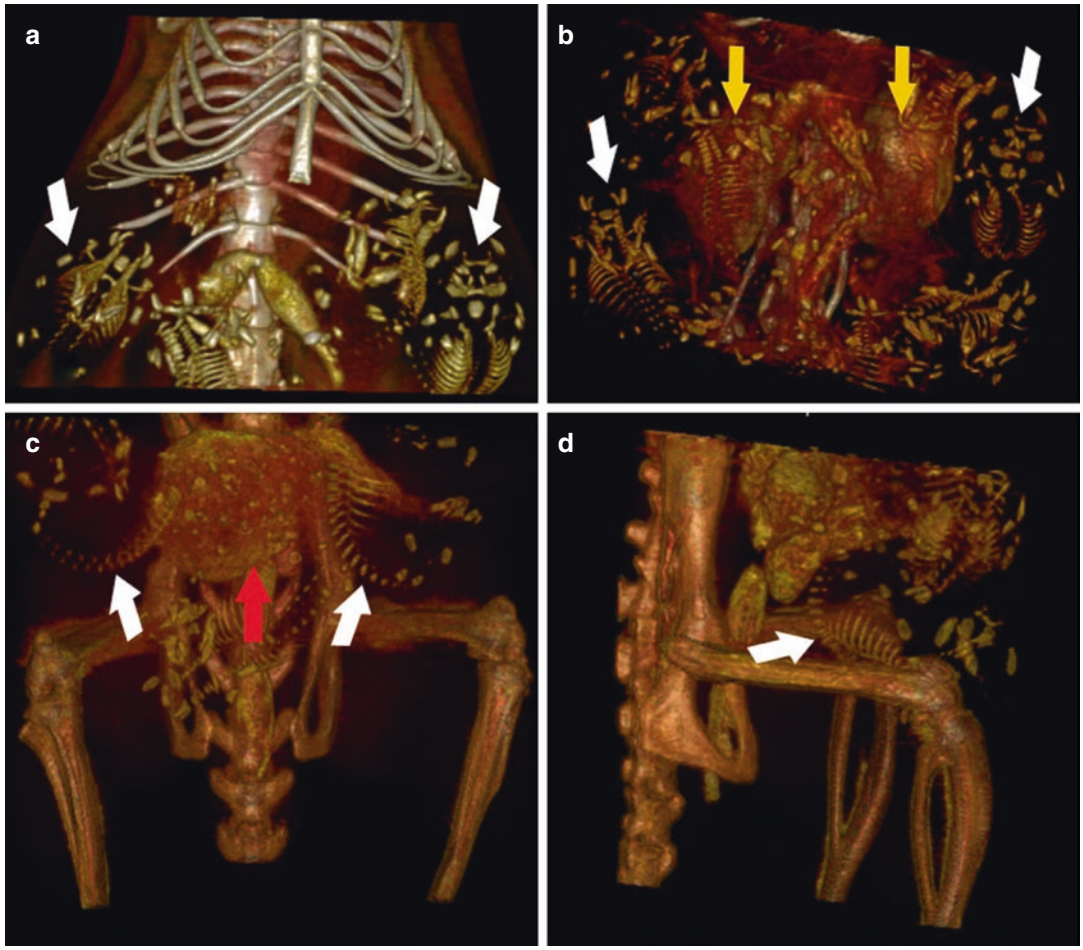

Fig. 25.3 In vivo CT imaging of late-stage pregnancy in mice (E18). 3D-rendered images of a pregnant mouse showing mineralized bone in late-stage fetal mice (*white arrows*) without contrast enhancement (**a**, **c**, **d**) and 15 min after i.v. injection of radiopaque contrast (**b**). (**a**) Volume-rendered image showing the rostral part of a pregnant mouse visualizing the mineralized rib cage of the mother cranially, and several fetuses, caudally (*white arrows*). (**b**) Abdomen of a pregnant mouse 15 min after contrast-agent injection, in which the contrast is washed out of the blood into the kidneys (*yellow arrows*) and both urethras appear radiopaque. (**c**, **d**) Volume renderings of the caudal part of a pregnant mouse picturing the fetuses (*white arrows*), the bladder (*red arrow*), and the mineralized femora and pelvis of the mother (Vandoorne et al. unpublished 2009)

latter permits the detection of flow velocities within a specified region of interest, or sample volume. Two important determinants of the capabilities for embryonic imaging are the size of the sample volume and the frequency of the Doppler incident beam; the smaller the sample volume, the more specific the flow detection of regions within the developing embryo.

In very small rodents, imaging developmental processes mandates high transducer frequencies to achieve adequate spatial resolution. UBM scanners cover high spatial resolution of 30–40 μm axial and 70–90 μm lateral, depending on the frequency. Lower frequencies used for clinical transducers appear ideal for deeper tissue penetrations, whereas high-frequency UBM imaging penetrates only 5–15 mm deep; this range, however, is considered sufficient for subsurface, in utero imaging of embryonic mouse (Fig. 25.4).

Transabdominal visualization of early stage embryos does not allow imaging of all embryos

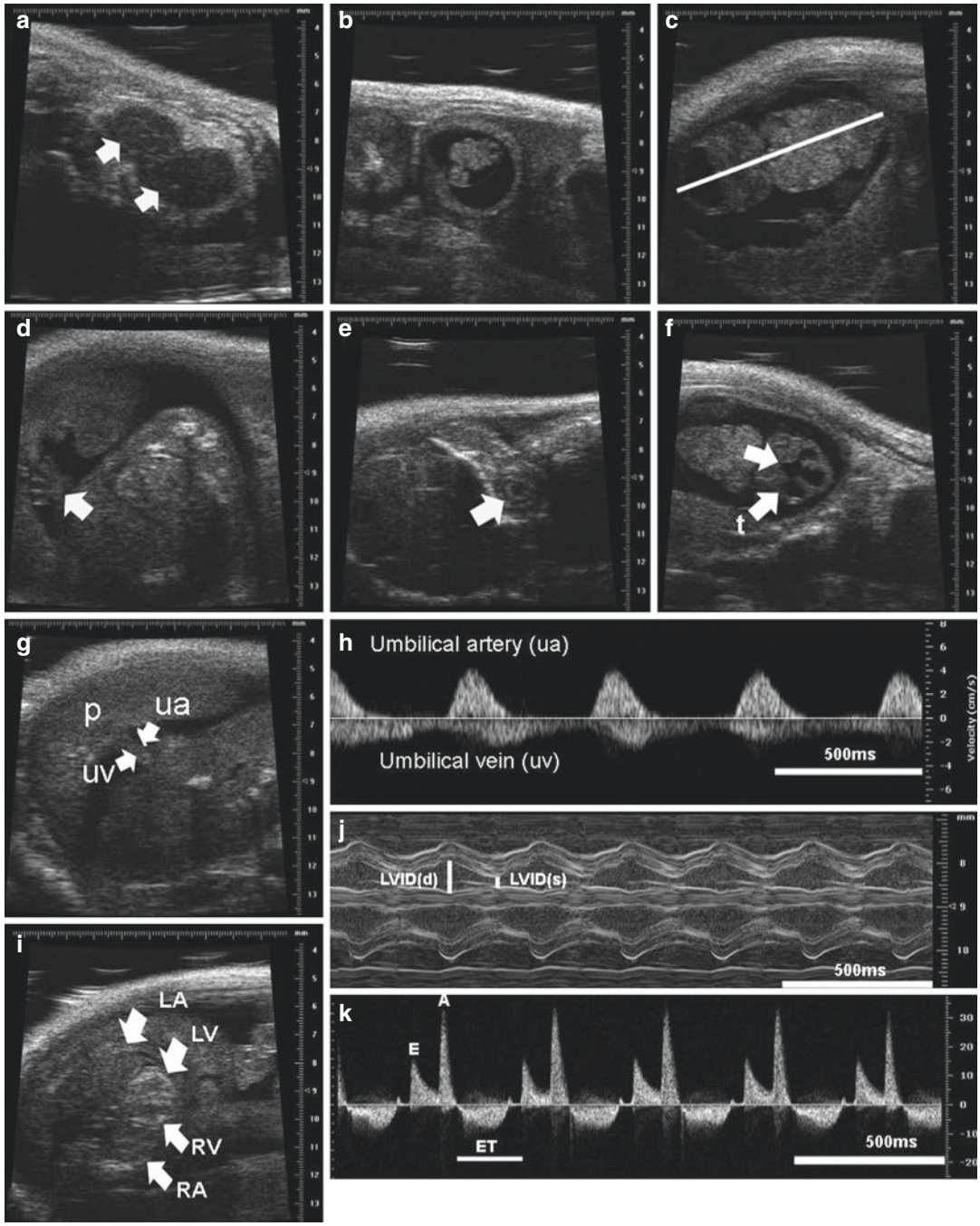

Fig. 25.4 Functional and structural ultrasound imaging of mice embryos. B-mode (**a**–**g**, **l**), pulse-wave Doppler mode (**h** and **k**), and M-mode (**j**). (**a**) Implantation at E5.5 can be visualized at the level of the uterine cavity as a bright hyper-echogenic spot (*arrows*); (**b**) Living embryo at E9.5; (**c**) Long-axis view of embryo at E11.5 allows its length to be to quantified; (**d**) E14.5 the forepaw; (**e**) E18.5 the eye; (**f**) E10.5 the brain with the third ventricle and telencephalic vesicle (t, future aqueduct); (**g**) E14.5 the placenta (*p*), with the umbilical vein (*uv*) and umbilical artery (*ua*); (**h**) Doppler velocity waveforms of E14.5 umbilical vein (uv) and umbilical artery (ua); (**i**) E16.5 the embryonic heart with the left ventricle (*LV*), right ventricle (*RV*), left atrium (*LA*), and right atrium (*RA*); (**j**) M-mode of E16.5 embryonic heart with diastolic internal diameter (LVID (d)) and systolic diameter (LVID(s)) of the LV; (**k**) Doppler waveforms showing LV inflow and outflow velocities of E16.5 embryonic heart. The inflow includes the passive E wave and the active A wave, whereas the ejection time (ET) contains the outflow into the aorta. (*E* embryonic day) (Vandoorne et al., unpublished 2009)

in a litter at once and cannot be used for identifying a particular embryo in a genetically heterogeneous litter. To overcome these technical limitations, a semi-invasive approach was established in which the uterine sac is exteriorized into warmed physiologic saline in a petri dish through an incision in the abdominal wall. Apart from the perturbating nature of this procedure, this technique has yielded excellent physiological imaging conditions, and it allows better resolution of embryonic structures. Furthermore, the technique allows longitudinal follow-up of early stage embryos and the possibility of microinjection.

Temporal resolution is important for moving objects, such as the rapidly beating embryonic heart (Kulandavelu et al. 2006) (Fig. 25.5). Historically, the temporal resolution was better on clinical ultrasound systems than on UBM systems; however, the frame rates of modern UBM systems (up to 1000 fps), using mechanical sector scanning, approach those of clinical systems. Current transducer technology yields a relatively narrow zone of focus (depth of field; up to 15 mm) (Phoon 2006). Fast, respiratory-gated, in utero acquisition of 3D data from individual embryos allowed high-resolution high-throughput characterization of volumetric changes associated with mouse brain development (Aristizabal et al. 2013).

25.2.2 Magnetic Resonance Imaging

Magnetic resonance imaging (MRI) provides isotropic, 3D, noninvasive morphological imaging; acquisition of dynamic, functional information; and the possibility of longitudinal studies of development. Ex vivo μMRI offers high spatial resolution (25–50 μm), albeit at long acquisition times (6–24 h). Spatial resolution for in vivo imaging is limited by physiological motion, signal-to-noise ratio (SNR), and scanning time and is typically on the order of 100–200 μm (Deans et al. 2008; Nieman et al. 2009; Turnbull and Mori 2007). Respiratory, cardiac gating, self-gating, and image co-registration are commonly required for in vivo studies to reduce motion artifacts (Fig. 25.6) (Nieman et al. 2009; Turnbull and Mori 2007). The available resolution may be sufficient for analyzing the developing brain and heart of mid- to late-stage mouse embryos (E13.5–18.5 days). However, effective analysis of organogenesis is limited, as early stage mouse embryo (E9.5–12.5 days) imaging requires better spatial resolution of at least 50 μm (isotropic); therefore, advances in hardware and techniques for small-animal MRI imaging would be beneficial (Turnbull and Mori 2007).

Contrast resolution is as important as spatial resolution for detection of anatomical features. Contrast resolution presents a special challenge in the developing mouse, where many cells and tissues are undifferentiated or immature, resulting in minimal differences in their endogenous MR relaxation properties. Sequence design, in combination with administration of targeted or physiologically relevant contrast agents, can improve MRI contrast (Turnbull and Mori 2007). The effective maternal-fetal barrier provided by the placenta excludes the transfer of most contrast materials from the fetal circulation. Early stage pregnancy can be detected by contrast-enhanced MRI, which highlights the maternal vasculature in the implantation sites (Fig. 25.7), while at later phases of pregnancy, contrast-enhanced MRI highlights the maternal circulation of the developing placenta (Taillieu et al. 2006; Salomon et al. 2005, 2006; Plaks et al. 2006, 2008; Tomlinson et al. 2010; Chalouhi et al. 2011; Alison et al. 2013).

Using albumin-based macromolecular MRI, contrast material revealed the uptake of maternal albumin by fetal-derived trophoblast cells lining the maternal vascular space in the placenta (Plaks et al. 2011b). The different compartmental behavior of this contrast material, when combined with analysis of water motion by pulsed gradient diffusion MRI, could be used for parametric mapping of the relative volume contribution of the maternal and fetal circulation in the placenta, and the rate and type of flow in each compartment (Solomon et al. 2014).

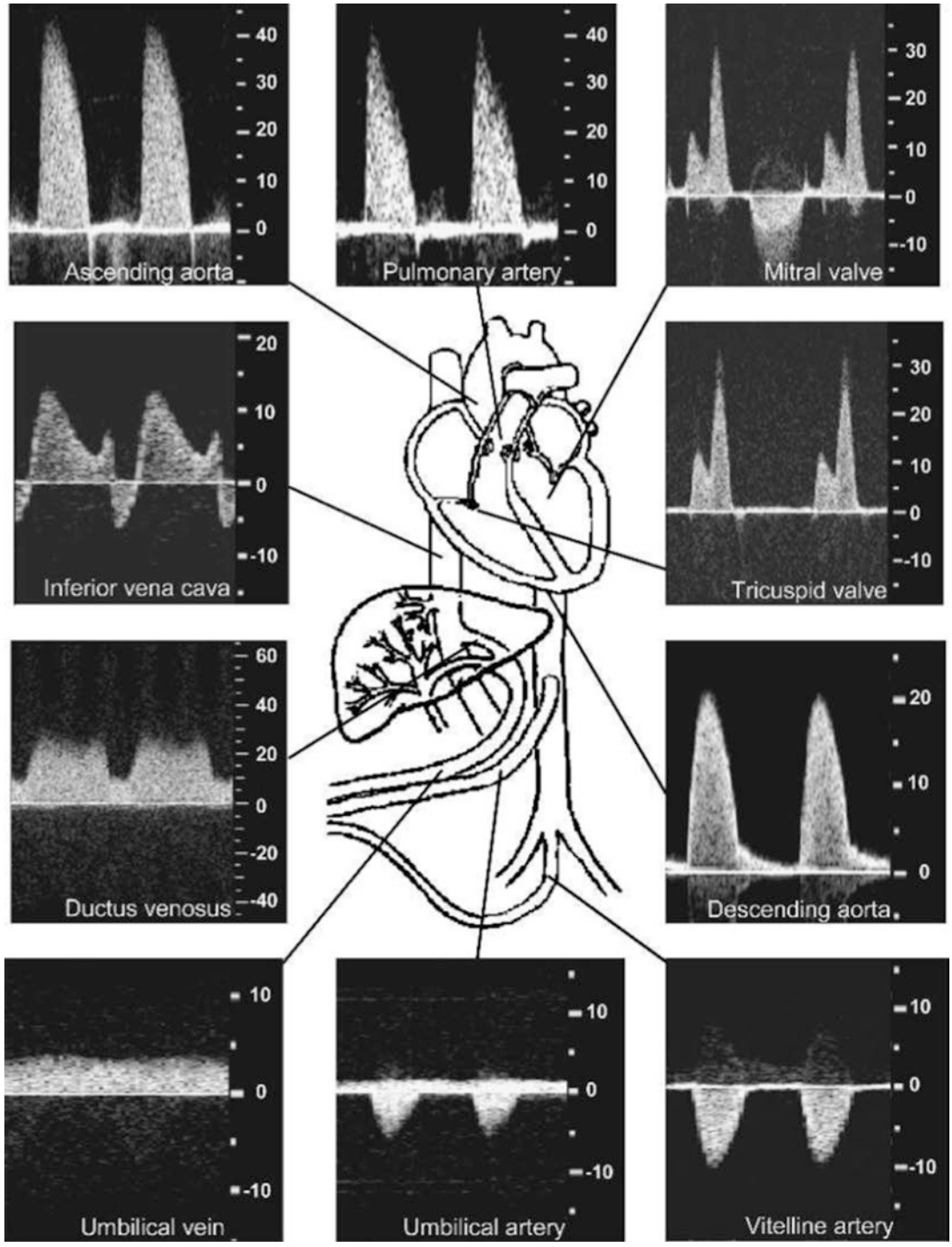

Fig. 25.5 Doppler blood velocity waveforms obtained at various sites in the embryonic circulation. Scale bars in cm/s (This figure originally appeared in an article by Shathiyah Kulandavelu et al. in *ILAR Journal* 47(2). It is reprinted with permission from the *ILAR Journal*, Institute for Laboratory Animal Research, The National Academies, Washington DC (www.nationalacademies.org/ilar) (Kulandavelu et al. 2006))

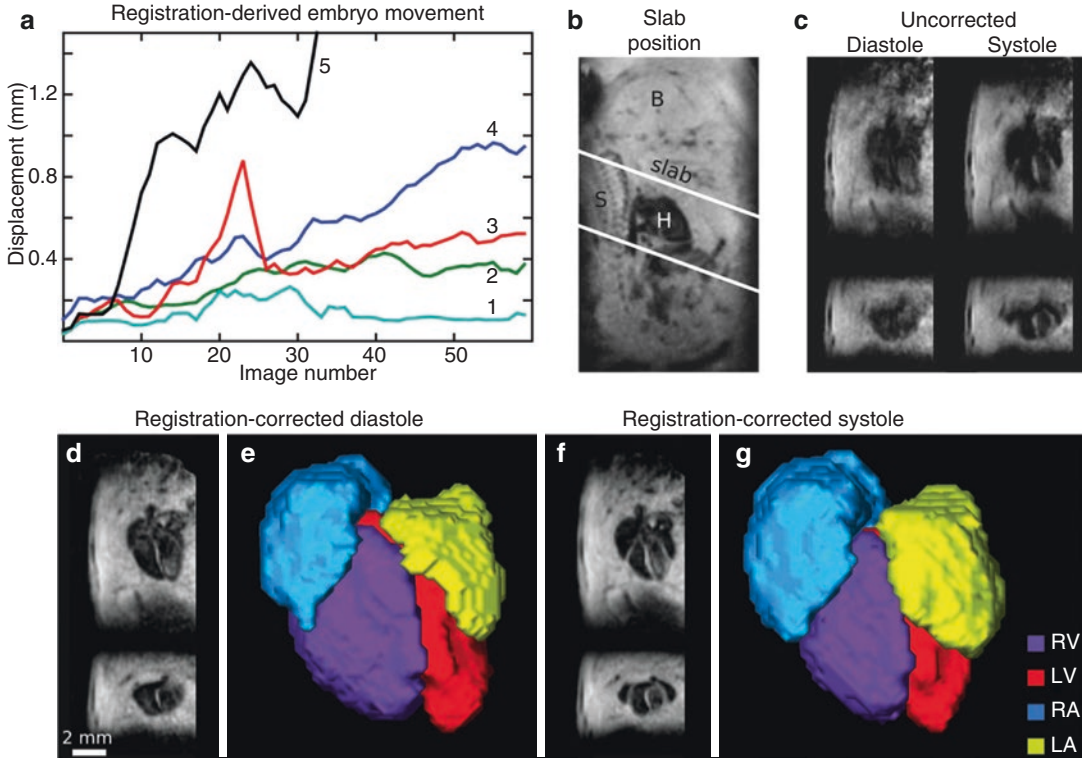

Fig. 25.6 In utero cardiac MRI of E17 mouse embryo. Embryonic displacement during the cardiac scan was followed by image registration of serially acquired 3D images. (**a**) Five examples of distance displacements within the initial imaging slab (**b**) (curve 5 shows displacement outside the imaging slab). Not correcting for embryo displacement results in blurred images (**c**), where long- and short-axis images from the same 3D data set are shown at both diastole and systole. (**d**, **f**) Correction of image displacement with registration improves image quality. (**e**, **g**) Segmentations of the chambers emphasize the changes in 3D shape over the cardiac cycle. Image parameters: TE/TR = 6.0/40 ms, flip angle = 16°, matrix size = 192 × 78 × 48, NR = 64, TA = 2 h 40 min, isotropic resolution = 130 μ, reconstructed with six 3D image frames per cardiac cycle. In (**b**), *B* brain, *S* spine, *H* heart (Reproduced with permission from (Nieman et al. 2009))

The central nervous system of in vivo late-stage embryos was imaged using manganese-enhanced MRI (MEMRI), which passes the placental barrier and can depict neuronal activity in the developing brain (Fig. 25.8) (Deans et al. 2008). The pre-myelinated neonatal mouse brain provides little relaxation-based (T_1, T_2) contrast, which is generally dominated in adult mice by regional myelin concentration. Neuronal-specific contrast can be achieved using MEMRI showing neuronal function or diffusion tensor imaging (DTI), which is sensitive to the structural formation of neuronal bundles (Turnbull and Mori 2007). DTI was applied in order to elucidate brain development in neonatal mice (Zhang et al. 2003; Mori et al. 2006).

25.3 Parametric Mapping of Development

25.3.1 Anatomical Imaging of Development

The most widely used application of noninvasive imaging in development is for detection of anatomical structures. MRI, CT, and ultrasound provide 3D information that can be used for parametric analysis of fetal anatomy in mice. These three

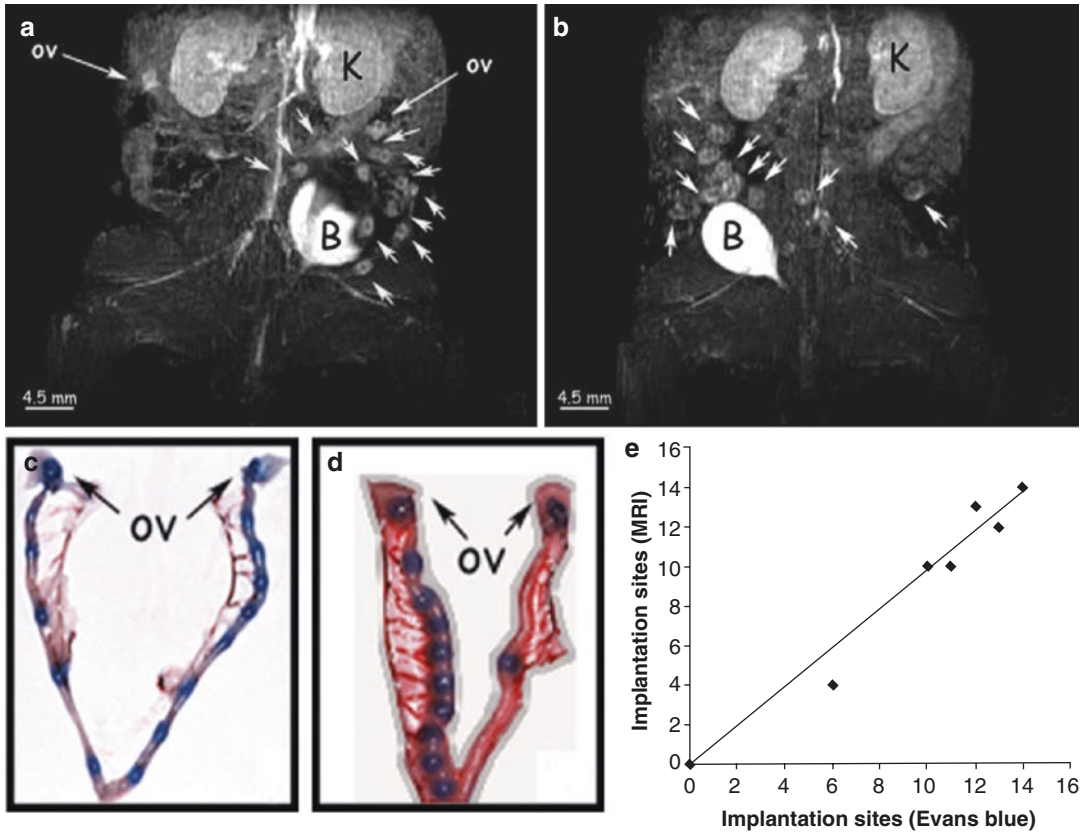

Fig. 25.7 Quantitative MRI assessment of mouse fetal implantation. Maximal intensity projections acquired 7.5 min after i.v. injection of biotin-BSA-GdDTPA of E4.5 (**a**) and E5.5 (**b**) implantation sites (*arrows*; individual implantation sites). (**c**, **d**) Ex vivo visualization of implantation sites highlighted by i.v. administration of Evans blue for the mice shown in (a) and (b), respectively. (**e**) Correlation between the number of implantation sites detected by MRI in vivo and the number detected ex vivo ($N = 11$ total mice; $N = 5$ spontaneously nonpregnant; overlapping points at 0, 0). *ov* ovaries, *K* kidney, *B* bladder (Reproduced with permission from (Plaks et al. 2006))

methodologies are complementary due to the differences in image contrast, as well as spatial and temporal resolution. MRI provides high contrast for soft tissues and high spatial resolution, but relatively low temporal resolution. Ultrasound provides better temporal resolution, while CT provides the best resolution for mineralized bones.

25.3.1.1 Following Anatomy by Ultrasound Biomicroscopy (UBM)

Like clinical monitoring of pregnancy, embryonic size and cross-sectional area can be determined by UBM (Fig. 25.4). Similarly, UBM can be used to obtain real-time images, providing quantitative measurements of dimensions and morphological information of different fetal organs of the mouse, such as the eye, brain, heart, and placenta (Phoon 2006). Acquiring in vivo cardiac morphology is difficult because of the small size of individual structures (valves or myocardial wall) and the rapid beating (200–300 beats/min). However, major events in cardiac morphogenesis can be visualized, such as cardiac looping (E9.5), outflow tract septation (E11.5, E12.5), and ventricular chamber septation (E12.5, E13.5), including the appearance of the atrioventricular valves (E13.5) (Fig. 25.5). Nevertheless, it remains difficult to determine the internal anatomy of the embryonic heart at early gestational

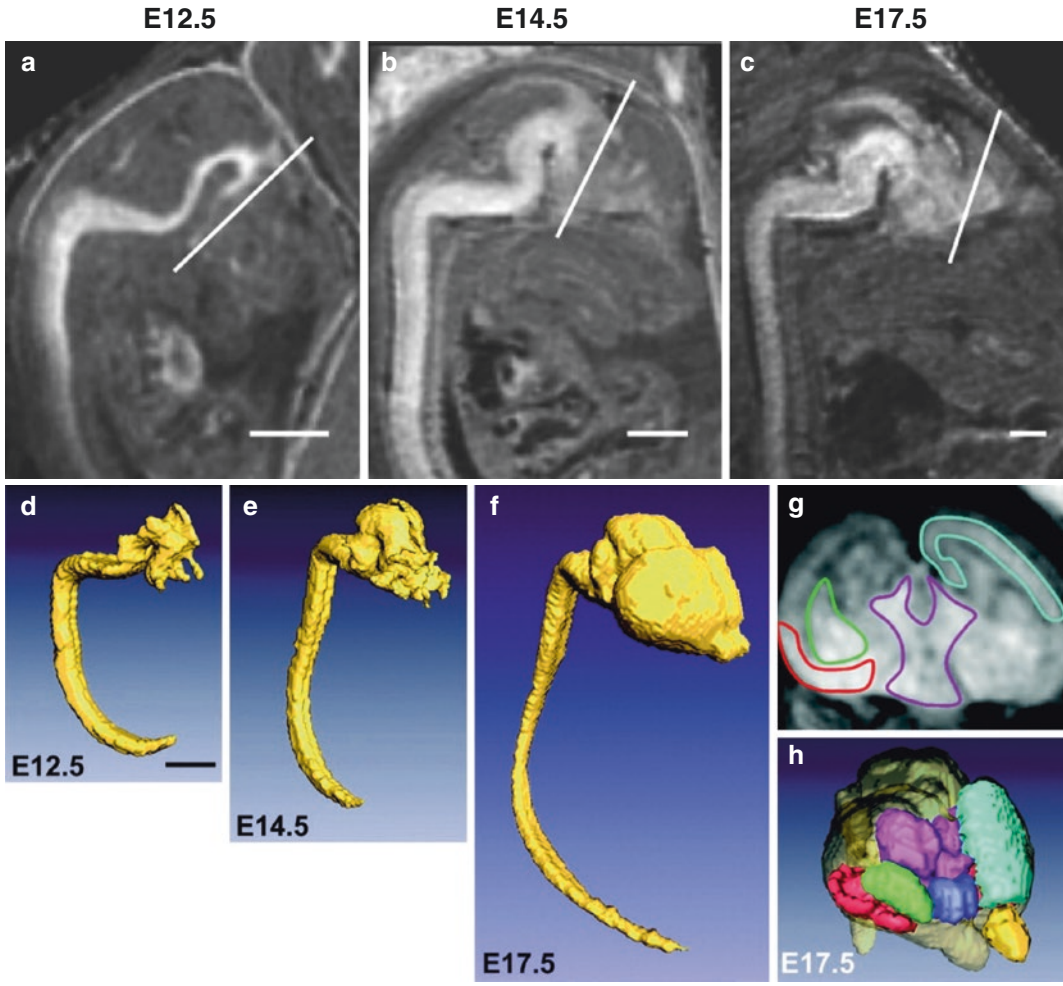

Fig. 25.8 Manganese-enhanced MRI of the mouse embryonic CNS. Developmental stage-dependent changes were detected by Mn enhancement (Mn dose 80 mg/kg). (**a**–**c**) Sagittal images of E12.5, E14.5, and E17.5 embryos showed increasing forebrain enhancement with age (scale bar, 0.5 mm). The spinal cord (SC) and ventral brain enhanced at all time points (**d**–**f**), with progressive enhancement from the posterior to anterior and ventral to dorsal with increasing age (scale bar is 1 mm). At E17.5, the boundaries of brain subregions, including the cortex (*aqua*), thalamus (*magenta*), BG (*green*), and pyriform cortex (*red*) could be appreciated (**g**), enabling semiautomated segmentation and 3D analysis of these structures, as well as the olfactory bulbs (*orange*) and SE (*blue*) (**h**) (Reproduced with permission from (Deans et al. 2008))

stages before E15.5, since the nucleated red blood cells in the mouse embryo are echo-dense (Le Floc'h et al. 2004), thus reducing the ability to discriminate boundaries (Phoon 2006).

The developing neural tube (brain, spine) in early- and mid-gestational embryo can be visualized, although UBM is not well suited for imaging late embryonic brain development, because of the limited penetration of high-frequency ultrasound through the skull (Deans et al. 2008). Developmental processes such as implantation, growth, and placentation have been imaged in a qualitative manner; the inner cell mass of recently implanted embryos (E5.5) and the three cavities of the embryo, the amniotic cavity, the coelomic cavity, and the ectoplacental cavity (E7.5), could be visualized. The placenta could be imaged as it formed during gestation. Embryonic structures such as the lungs, liver, limbs, and eye can also be imaged,

illuminating the process of embryonic patterning and development (Fig. 25.4) (Phoon 2006).

Ultrasound biomicroscopy allowed detection and longitudinal monitoring of fetal development of the retina lens and cornea in the mouse eye (Foster et al. 2003). The rate of growth of the major axis was linear throughout development, starting at E8.5 when the eye was close to the system spatial resolution limit. At E11–12, blood vessels were still not detectable by ultrasound.

25.3.1.2 Following Anatomy by Magnetic Resonance Imaging (MRI)

MRI studies of fetal development exploit the exquisite endogenous soft tissue contrast mechanisms to depict specific anatomical features beyond measurements of fetal and organ size. Postnatal development was studied by DTI and MEMRI, for maximizing contrast in the central nervous system (CNS) in mice from the earliest postnatal stages. Recently, diffusion-weighted MRI has been used to study uteroplacental compartments (Solomon et al. 2014). Employing respiratory gating to decrease motion artifacts, in utero MEMRI was used in studies of the embryonic CNS and allowed MEMRI-facilitated CNS segmentation and 3D analysis in mid- and late-stage embryos. Moreover, quantitative MEMRI analysis of *Nkx2-1* knockout mice demonstrated volumetric changes in the septum and basal ganglia, as well as alterations in hypothalamic structures (Fig. 25.8) (Deans et al. 2008; Turnbull and Mori 2007).

A method for in utero cardiac imaging has been described using self-gating data and image co-registration to permit reconstruction of images in the presence of both periodic physiological motion and nonperiodic rigid-body motion, including gastrointestinal peristalsis, uterine contractions, shifts of the head or torso, and embryonic movement in utero (Fig. 25.6). Long-axis and short-axis slices at systole and diastole were reconstructed, along with 3D rendering of the heart chambers (Fig. 25.5) (Nieman et al. 2009). Neonatal cardiac MRI has been described to accurately follow postnatal cardiac function (Wiesmann et al. 2000).

Another way to assess fetal well-being in utero involves measurements of specific skeletal parameters, such as limb length, crown-to-rump length, and cranial size. High-throughput, ex vivo morphological phenotyping of mouse embryos and neonates by MRI and automated segmentation has been used to evaluate soft tissue with or without gadolinium staining (Petiet et al. 2008; Norris et al. 2013). Digital atlases of normal development are available for the identification of subtle phenotypic differences (Cleary et al. 2011).

In a recent study, MRI, UBM, and CT were applied for monitoring cardiovascular function during development. Reduced contractile function detected by UBM in *Akt1* null fetuses was consistent with dilated cardiomyopathy, and ventricular septum defects were detected ex vivo by CT and histology, as well as reduced myocardial capillaries and coronary vessels (Vandoorne et al. 2013).

25.3.1.3 Following Anatomy by Micro-computerized Tomography (μCT)

Ex vivo μCT provides images of radiopaque structures with a voxel resolution of up to 10 μm (Oest et al. 2008). Iodine staining can be used to phenotype the embryonic cardiovascular system (Degenhardt et al. 2010, 2013; Vandoorne et al. 2013). μCT replaced the more conventional histological method used previously to assess skeletal development and growth. Compared with histology, μCT enables fast, 3D imaging, and reconstruction of the entire bone. Using μCT, parameters such as material density, bone volume fraction, and trabecular architecture (including trabecular thickness, number, separation, connectivity, and orientation) can be retrieved and analyzed.

The endogenous contrast of bones can be used for anatomical in vivo imaging of fetal skeletal development in pregnant rats (Fig. 25.2) (Winkelmann and Wise 2009). This methodology is particularly valuable during the last stages of pregnancy, when bone mineralization is a critical determinant of fetal size. The inherently low soft tissue contrast and the lack of transfer of contrast media across the placenta limit the use of CT for

soft tissue fetal analysis. When considering longitudinal monitoring by μCT, the cumulative effects of the administered radiation dose should be considered.

25.4 Functional Parametric Mapping

While anatomical information can be derived from noninvasive imaging, it can also be acquired ex vivo. However, one of the key strengths of in vivo imaging is access to functional physiological information that is lost when analyzing fixed specimens.

25.4.1 Functional Imaging of Development by UBM

Fetal blood velocity can be detected through the Doppler frequency shift in the signal reflected from the moving red blood cells and is routinely used to assess developmental cardiovascular physiology. UBM is well suited to study embryonic and postnatal developmental cardiovascular physiology (Figs. 25.4 and 25.5). It can be used as soon as the heart starts to beat on E8.5 in the mouse. From this moment onward, it is possible to use Doppler to measure heart rate and to detect heart failure. Blood-flow velocity in the vitelline circulation to the yolk sac is also first detected at this stage. By E9.5, the umbilical circulation is formed, and Doppler arterial waveforms can be obtained from the umbilical artery and from the inflow or outflow tracts of the heart. By E13.5, when embryos are in a suitable orientation to obtain a four-chamber view of both ventricles and both atria, the pulsed Doppler sample volume can be placed within either the left or right ventricular chamber to record the mitral or tricuspid inflow, or within the ascending aorta to record the outflow blood velocity waveforms. Doppler waveforms can also be obtained at other sites, such as the ascending and descending aorta, the pulmonary artery, the umbilical and vitelline arteries, the umbilical vein, the ductus venosus, and the inferior vena cava (Phoon 2006; Kulandavelu et al. 2006).

To obtain information on the motion and dimensions of the cardiac chambers over time, the M-mode cursor can be placed over the heart. By E13.5, when fetuses are in a suitable orientation to obtain a long-axis view of the left and right ventricles, it is possible to obtain M-mode recordings of the motion of the heart walls, in addition to the intraventricular waveforms. The UBM (both Doppler and M-mode) gives similar information in newborn mice. Because the operator has more freedom to position and change the transducer or body angle to obtain the best imaging plane, imaging of postnatal animals might be easier. UBM can characterize the pathophysiology of embryonic cardiovascular system and has been applied to define in utero heart and vascular malformations (Vandoorne et al. 2013; Phoon et al. 2004).

25.4.2 Functional Imaging of Development by MRI

Functional imaging by MRI has been used to identify fetal implantation sites and to analyze early vascular changes during implantation (Plaks et al. 2006). This approach was used to study implantation failure. Contrast-enhanced (CE) MRI using high molecular weight contrast media allowed high-resolution detection and quantitative assessment of mouse embryo implantation sites as early as E4.5, and subsequent vascular expansion at E5.5. Vessel permeability was elevated in E4.5 implantation sites, relative to the non-implanted uterus, followed by increased blood volume in implantation sites between E4.5 and E5.5 (Fig. 25.7) associated with ablation of dendritic cells from the implantation site (Plaks et al. 2008). A similar MRI approach was recently applied for detection of failure of implantation of blastocysts derived from oocytes that are deficient in Cx43 (Plaks et al. 2014).

Blood oxygenation provides another important endogenous contrast mechanism that can be utilized by MRI. While oxygenated hemoglobin is diamagnetic, deoxyhemoglobin is paramagnetic, resulting in reduced signal

intensity in R_2*-weighted images. Blood oxygenation level-dependent (BOLD) contrast MRI was applied for monitoring changes in blood oxygenation in rat embryos (Girsh et al. 2007). Cloprostenol, a prostaglandin-F2α analog, reduced fetal blood oxygenation, which resulted in increased deoxyhemoglobin concentration and decreased signal in R_2*-weighted MRI images. The changes in BOLD contrast correlated with placental expression of vascular endothelial growth factor (VEGF) (Girsh et al. 2007).

BOLD contrast was recently used for detection of the response to hyperoxia in a rat model of in utero growth retardation (IUGR). BOLD MRI at 1.5 T showed significant response to maternal hyperoxygenation, but response was lower for IUGR fetuses (Aimot-Macron et al. 2013).

25.5 Molecular and Cellular Mapping of Development

Significant progress in imaging technologies in recent years has led to the possibility of mapping molecular and cellular events in live animals. A number of these technologies have also been utilized for imaging fetal development. In particular, UBM provides the ability to manipulate and deliver materials to embryos, while MRI permits monitoring of reporter gene expression during cell differentiation and tracking of cell migration.

25.5.1 Molecular and Cellular Imaging of Development Using UBM

Ultrasound biomicroscopy can facilitate the manipulation of the mouse embryo, especially at the early stages of pregnancy, to help gain insight into specific developmental processes. Cells, viruses, or other agents can be injected under UBM guidance, into precise locations in the developing embryo at various developmental stages. Following microinjections into specific sites within the embryonic mouse brain, for example, investigators have studied progenitor engraftment, ectopic gene expression with gain-of-function, cell lineages, and tumor induction. Nevertheless, these intraembryonic injections are perturbing even for the normal embryo and may carry a substantial mortality rate of approximately 50 % (Phoon 2006).

25.5.2 Molecular and Cellular Imaging of Development Using MRI

In vivo cell tracking and imaging of gene expression can supply critical new insights into the dynamics of developmental processes. In vivo imaging of gene expression and cell tracking after magnetic labeling with gadolinium has been carried out in studies of frog embryo development using single-cell microinjection and micro-MRI (Louie et al. 2000). Such cell tracking has not yet been done in vivo for fetal development of mice. However, ex vivo MRI of fixed mouse embryos was recently used to detect micron-sized iron oxide particles, internalized in cells of mouse blastocyst-stage embryos, more than a week later in E11.5 embryos (Shapiro et al. 2004; Turnbull and Mori 2007).

MRI contrast can be generated by overexpression of ferritin, the iron storage protein, which can serve as a reporter for the detection of gene expression by MRI. Tetracycline-regulated overexpression of ferritin resulted in specific alterations of the transverse relaxation rate ($R2$) of water. Transgene-dependent changes in $R2$ were detectable by MRI in fetal developmental induction of transgene expression in utero. Specific endothelial cell differentiation was visualized using mice in which expression of ferritin was regulated by the promoter of vascular endothelial cadherin (VE-cadherin). Thus, tet-hfer MRI reporter mice provide a new transgenic mouse platform for in vivo molecular imaging of reporter gene expression by MRI during embryonic development (Fig. 25.9) (Cohen et al. 2007).

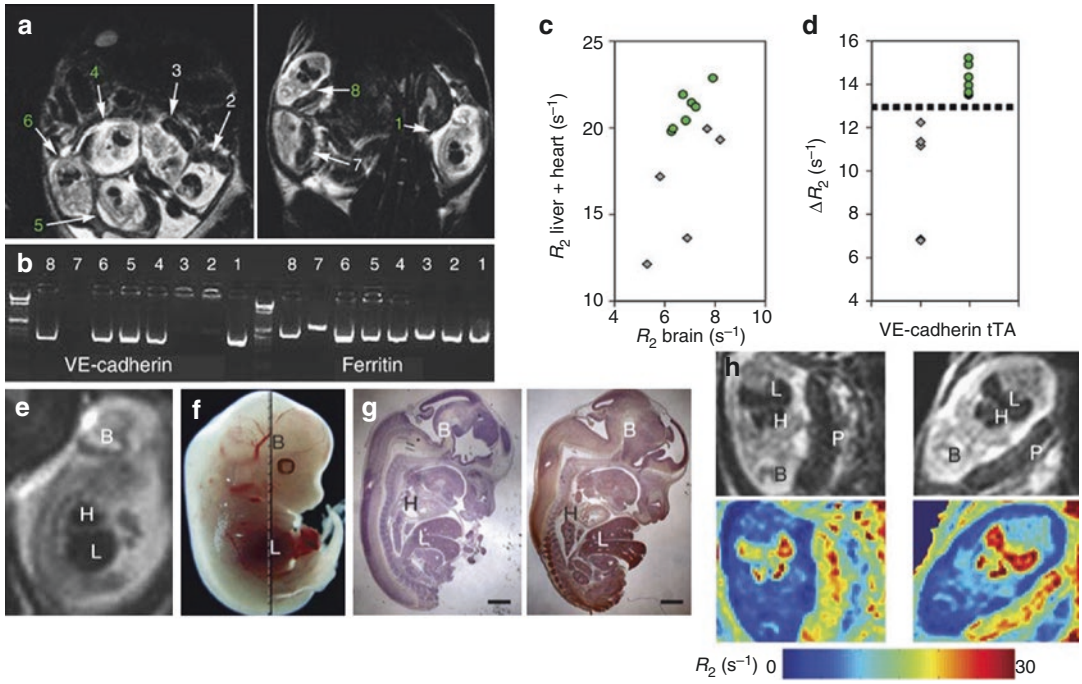

Fig. 25.9 In utero MRI detection of VE-cadherin mediated expression in E13.5 fetal liver and heart. (**a**) MRI of a pregnant homozygous tet-hfer transgenic dam mated with a heterozygous VE-cadherin-tTA male (8 embryos at E13.5). (**b**) Embryos were genotyped as dTG (VE-cadherin-hfer; *green*) or sTG (tet-hfer; *white*). (**c**) R_2 relaxation rate was significantly elevated in the liver and heart, but not in the brain, of dTG (*green*) embryos. (**d**) R_2 difference values ($\Delta R_2 = (R_2$ in liver + heart) – R_2 in brain) differentiated between the sTG (*gray*) and dTG (*green*) embryos. (**e**, **f**) Sagittal MRI and whole embryo (line, coronal slice, as in **g**, **h**). (**g**) No EGFP was detected in sTG (*left*) and high EGFP in the liver, with lower expression in the brain in dTG (*right*) embryos. (**h**) Coronal images (*top*) and R_2 maps (*bottom*) of sTG (*left*) and dTG embryo (*right*) show elevated R_2 in the liver, heart, and posterior region of the dTG embryo. *P* placenta, *H* heart, *L* liver, *B* brain (Reprinted by permission from Macmillan Publishers Ltd: [*Nature Medicine*] (Cohen et al. 2007), copyright (2007))

25.6 Specific Applications

25.6.1 Detection of Interventions

An important role for imaging lies in the analysis of the consequence of interventions on the developing embryo. In particular, longitudinal, multiparametric imaging is critical for those interventions that result in variable response such that the dynamic changes cannot be inferred from comparison of histological specimens taken from different embryos. Multiple studies have evaluated the use of imaging as part of the phenotyping efforts on genetically modified mice (Turnbull and Mori 2007; Phoon 2006; Dickinson 2006; Kulandavelu et al. 2006). A specific type of intervention providing important insight is the selective ablation of cells. Such manipulation can be achieved by genetic introduction of suicide genes or by selective introduction of specific toxins. Using this approach, dynamic contrast-enhanced MRI revealed that ablation of dendritic cells resulted in failure of fetal implantation, due to impaired decidual angiogenesis (Plaks et al. 2008).

25.6.2 Detection of Fluorescent and Bioluminescent Reporter Genes

Another study examined the role of invading fetal precursor cells in maternal angiogenesis using bioluminescence imaging (BLI) (Nguyen Huu et al. 2007). During pregnancy, fetal endothelial

precursor cells invade the maternal circulation. Using *Vegfr2*-luciferase males mated with wild-type females, it was possible to detect bioluminescence of endothelial cells originating from the embryo in sites of inflammation and in newly formed blood vessels.

High-resolution fluorescence microscopy provides additional possibilities for imaging-based analysis of development. Recent studies described the generation of a novel transgenic mice line, in which the endothelial cell membranes were labeled with the red fluorescent protein mCherry, and the nuclei of the same embryonic endothelial cells were labeled with the yellow fluorescent protein EYFP (Larina et al. 2009). The combination of the two proteins enabled imaging of the entire vasculature, as well as identification of specific endothelial cells within the blood vessels. Using confocal microscopy of E7.5–E12.5 cultured mouse embryos, the authors were able to image ex vivo the vascular plexus in the yolk sac, the blood vessels in the embryo trunk, the brain, the eye, and the endocardium of the heart. Rapid image acquisition enabled imaging of the beating heart in cultured E8.5 embryos.

25.6.3 Detection of Fluorescent Probes

Detailed electrophysiological analysis of heart development can be conducted ex vivo using optical probes for cell membrane potential, namely, voltage-sensitive dyes (Efimov et al. 2004; Rothenberg et al. 2004). These dyes bind the plasma membrane of cardiac cells and exhibit changes in fluorescence as a result of transmembrane voltage alternations. Unlike traditional microelectrode recordings, optical signals derived from voltage-sensitive dyes enable simultaneous detection of electrical activation from multiple sites within the embryonic heart.

Optical mapping was applied to study the patterning and organization of the conduction system and working myocardium in the developing avian and mammalian hearts. In mice, as it is impossible to apply this method in utero, the embryonic heart must be excised and bathed in a solution of voltage-sensitive dyes. A light source then excites the cells and causes emission of a fluorescent signal, proportional to the change in cell membrane voltage. Disadvantages of this method are the inability to retrieve absolute transmembrane potentials due to the absence of standard calibration, as well as its invasiveness, which prevent follow-up studies of the same embryos throughout pregnancy.

25.6.4 Imaging of Brain Development

Both voltage-sensitive dyes and MRI methods have been used to follow embryonic brain development (Mori et al. 2006). MRI allows a 3D characterization of the brain, consisting of different contrast mechanisms, usually based on water relaxation parameters T_1, T_2, and T_2*. Adjusting acquisition parameters enables detection of different anatomical structures within the brain, including the ventricles, and the large white and gray matter structures. However, various white matter tracts cannot be detected using these conventional MR contrast mechanisms, and their analysis requires application of diffusion tensor imaging (Zhang et al. 2003).

25.6.5 Imaging Skeletogenesis

Imaging of transgenic mice is important for understanding skeletogenesis and the genes involved in this process, as well as quantification of structure-function relationships in the bone. Vascularization of the bone growth plate is important for its adequate development during embryogenesis and during bone repair and regeneration following injury in the adult. Imaging of this process reveals a precise spatial regulation of vascularity, based on vascular regression and invasion to the hypertrophic zone of the growth plate. Using contrast agents, 3D vascular networks within the bone can be imaged by μCT either in vivo or postmortem. Micro-CT further allows imaging of skeletogenesis of E17–E19

mouse embryos (Oest et al. 2008; Guldberg et al. 2004). The overall increase in fetal size throughout development was detected, as well as the increase in bone volume and the changes in quantity of mineralized tissue. Measurements of specific bones lengths were found to be well correlated with measurements taken using the standard clear-stained technique, suggesting μCT as an appropriate technique for skeletogenesis analysis. Although most studies were done ex vivo, fetal bone mineralization can also be detected in utero in both rats and mice (Figs. 25.2 and 25.3) (Winkelmann and Wise 2009; Vandoorne et al. 2010).

25.7 Animal Preparation

Pregnancy and fetal development are sensitive to many of the procedures that are routinely included in in vivo imaging studies.

25.7.1 Anesthesia Procedures

Anesthetic agents are frequently used to immobilize mice to reduce motion artifacts during image acquisition or other procedures. For imaging procedures under 30–45 min in length, injectable anesthetics are successfully used. Most commonly, a combination of ketamine with a tranquilizer such as xylazine is administered i.p., although i.m. or i.v. administration is also possible. Ketamine increases cardiac output, heart rate, and blood pressure in normal patients. On the other hand, xylazine causes an initial increase in total peripheral resistance of the cardiovascular system, with increased blood pressure followed by a longer period of hypotension. Cardiac output may be reduced, but respiration is unaffected by xylazine. Because this adrenergic-α2 agonist may increase uterine tone, xylazine should be used with caution during pregnancy. Xylazine depresses thermoregulatory mechanisms, which might cause considerable mortality. Diazepam is also commonly mixed with ketamine but has been implicated as a teratogen in humans and, thus, is less appropriate for pregnant mice. Barbiturate anesthetics, such as pentobarbital, have a widely variable response to anesthetic dose and a narrow therapeutic index, which lead to considerable anesthetic mortality with i.p. injections in mice. Barbiturate anesthesia in the mouse is much safer by i.v. injection than by i.p. injection (Lukasik and Gillies 2003). For newborns, injectable anesthetics proved to be unsafe, whereas hypothermia is used as an effective and safe long-term method for reducing motion (Danneman and Mandrell 1997).

For procedures lasting longer than 30–45 min, inhalant anesthetics are preferred to injectable drugs. Inhaled anesthesia results in reduced risk for intrauterine injury that can occur with intraperitoneal administration, readily adjustable dosage, precise control of the duration of anesthesia, and rapid anesthetic induction and recovery (Kulandavelu et al. 2006). Also, in newborns, inhalation anesthetics are reported to be safer than injectable anesthetics (Kulandavelu et al. 2006).

The most commonly used inhalant anesthetic today is isoflurane. All of the inhalant anesthetics cause some degree of myocardial and respiratory depression but undergo very little hepatic metabolism. Elimination is via the lung. Consequently, recovery is usually rapid after discontinuing inhalant administration and takes just a few minutes, regardless of the length of anesthesia, as long as the animals are supported (e.g., temperature) while anesthetized. Additionally, in contrast with injectable anesthesia where depth is continuously decreasing as drug metabolism takes place (Lukasik and Gillies 2003), isoflurane provides a stable depth of anesthesia during the entire length of the anesthetic episode.

Pregnant rodents are typically induced with 5 % isoflurane in oxygen and maintained with 1–2 % isoflurane in oxygen. Isoflurane is relatively safe when used at appropriate concentrations. Single or repeated exposure to anesthesia may have long-term effects on embryonic and newborn mice, but these effects have not been studied in detail. It has been reported that chronic exposure to light isoflurane anesthesia (4 h/day daily from E6–15) reduced embryonic growth and increased the incidence of cleft palate;

however, the effect of repeated exposure to deeper levels of anesthesia is largely unexplored. Furthermore, isoflurane was not found to reduce pregnancy rates and fetal survival significantly, so that it is unlikely that isoflurane induces severe cardiac malformations. However, there may be an increased incidence of anomalies and mild growth retardation, and exposed preimplantation embryos exhibit arrested development (Kulandavelu et al. 2006).

25.7.2 Animal Preparation and Physiological Monitoring

Sedated and anesthetized animals will not close their eyelids completely, which may lead to drying of the corneas, to corneal ulcer, and eventually even to blindness. Therefore, it is advised to protect the animal's eyes with a sterile eye lubricating ointment prior to the imaging session. All animals are susceptible to hypothermia while under anesthesia, which can be a source of considerable variation in the animal physiology and may even lead to mortality. Maternal body temperature should be monitored using a rectal thermometer and maintained between 36 and 38 °C by wrapping the animal or its extremities in an insulator, like a plastic wrap, or using an external heat source such as heating pad and/or infrared lamp. The latter should be used with caution due to increased risk of thermal injury. Body temperature in newborns can be monitored using a rectal probe only when older than 14 days of age, since insertion of probes in younger mice is unsafe. Ventilation and oxygenation are critically important for maintaining normal maternal and embryonic cardiovascular function, and thus, monitoring the depth of the anesthesia by electrocardiography (ECG) and respiration is vital. Even in newborns ECG monitoring have been reported (Lukasik and Gillies 2003; Kulandavelu et al. 2006).

Motion such as spontaneous uterine contractions, respiratory motion of the mother, or motion of later stage embryos can be minimized pharmacologically or taken into account through gating or ex post facto data processing (Deans et al. 2008; Turnbull and Mori 2007; Akselrod-Ballin et al. 2016).

25.7.3 Fetal Identification and Genotyping

A requirement of longitudinal studies is the ability to identify individual animals and their contributions to the study data. This is particularly difficult for longitudinal studies at early stages of pregnancy, due to the extensive motion of the uterus at this stage.

Newborns can be labeled on a short-term basis using permanent marker. The label must be refreshed daily. Tattooing on the bottom of the paw provides a longer-lasting label. Tattooing lasts for a minimum of a month, and at this stage, mice are weaned; an ear clipping can be used for subsequent identification. Ideally, embryos studied in utero should be "tattooed" so they can be identified after birth. Inter-litter variance is important. Thus, it is necessary to compare embryos within and between pregnancies. As a rule, it has been suggested that 1–4 embryos should be evaluated from at least three litters (Kulandavelu et al. 2006).

Some of the problems of identification and restraint can be resolved through the use of cultured embryos (Phoon 2006). Isolated mouse embryos remain viable and show normal growth in culture for 1–2 days despite the disruption of the placental circulation.

Recently, bidirectional arterial spin labeling MRI has succeeded in identifying fetal position within the murine uterus and in identifying positional and interfetal effects in mouse pregnancies (Raz et al. 2012; Avni et al. 2012). These studies were consistent with dual arterial maternal blood supply to each placenta from the descending uterine branch of the ovarian artery and from the ascending uterine artery, each irrigating distinct regions of each placenta. This functional description stands in contrast with the accepted view of anastomosis of these two maternal arteries to form a uterine arterial loop (Raz et al. 2012).

25.8 Summary

Noninvasive, in utero fetal imaging of small laboratory animals offers a growing portfolio of parameters that can aid in developmental biology.

In particular, imaging is valuable for physiological, functional, and molecular mapping of fetal development of genetically modified mice. Exciting insights are obtained by imaging perturbations of development in transgenic and knockout mice and mice carrying specific reporter genes, allowing migration and differentiation of cells during organ formation to be followed. It is clear, however, that the current limitations on contrast and on temporal and spatial resolution restrict the range of questions that can be addressed. Thus, improved technologies would be welcome for meeting the challenges of functional mapping of the genome using large-scale efforts for genetic modifications in mice.

Acknowledgments We acknowledge the support of the Israel Science Foundation ISF 93/07 and ISF Converging Technologies Equipment Award, the European Commission Seventh Framework ERC Advanced Project IMAGO 232,640, the US-Israel Binational Science Foundation and the National Institutes of Health (grant 1R01HD086323-01). MN is incumbent of the Helen and Morris Mauerberger Chair.

References

Aimot-Macron S, Salomon LJ, Deloison B, Thiam R, Cuenod CA, Clement O, et al. In vivo MRI assessment of placental and foetal oxygenation changes in a rat model of growth restriction using blood oxygen level-dependent (BOLD) magnetic resonance imaging. Eur Radiol. 2013;23(5):1335–42. doi:10.1007/s00330-012-2712-y.

Alison M, Quibel T, Balvay D, Autret G, Bourillon C, Chalouhi GE, et al. Measurement of placental perfusion by dynamic contrast-enhanced MRI at 4.7 T. Invest Radiol. 2013;48(7):535–42. doi:10.1097/RLI.0b013e3182856a25.

Akselrod-Ballin A, Dafni H, Addadi Y, Biton I, Avni R, Brenner Y, Neeman M. Multimodal correlative preclinical whole body imaging and segmentation. Sci Rep. 2016;6:27940. doi:10.1038/srep27940.

Aristizabal O, Mamou J, Ketterling JA, Turnbull DH. High-throughput, high-frequency 3-D ultrasound for in utero analysis of embryonic mouse brain development. Ultrasound Med Biol. 2013;39(12):2321–32. doi:10.1016/j.ultrasmedbio.2013.06.015.

Avni R, Raz T, Biton IE, Kalchenko V, Garbow JR, Neeman M. Unique in utero identification of fetuses in multifetal mouse pregnancies by placental bidirectional arterial spin labeling MRI. Magn Reson Med. 2012;68(2):560–70. doi:10.1002/mrm.23246.

Bang DW, Lee JH, Oh H, Kim SR, Kim TH, Lee YS, et al. Dose-incidence relationships on the prenatal effects of gamma-radiation in mice. J Veter Sci (Suwon-si Korea). 2002;3(1):7–11.

Brown AS, Reid AD, Leamen L, Cucevic V, Foster FS. Biological effects of high-frequency ultrasound exposure during mouse organogenesis. Ultrasound Med Biol. 2004;30(9):1223–32.

Chalouhi GE, Deloison B, Siauve N, Aimot S, Balvay D, Cuenod CA, et al. Dynamic contrast-enhanced magnetic resonance imaging: definitive imaging of placental function? Semin Fetal Neonatal Med. 2011;16(1):22–8. doi:10.1016/j.siny.2010.09.001.

Cleary JO, Modat M, Norris FC, Price AN, Jayakody SA, Martinez-Barbera JP, et al. Magnetic resonance virtual histology for embryos: 3D atlases for automated high-throughput phenotyping. Neuroimage. 2011;54(2):769–78. doi:10.1016/j.neuroimage.2010.07.039.

Cohen B, Ziv K, Plaks V, Israely T, Kalchenko V, Harmelin A, et al. MRI detection of transcriptional regulation of gene expression in transgenic mice. Nat Med. 2007;13(4):498–503.

Danneman PJ, Mandrell TD. Evaluation of five agents/methods for anesthesia of neonatal rats. Lab Anim Sci. 1997;47(4):386–95.

Deans AE, Wadghiri YZ, Berrios-Otero CA, Turnbull DH. Mn enhancement and respiratory gating for in utero MRI of the embryonic mouse central nervous system. Magn Reson Med. 2008;59(6):1320–8.

Degenhardt K, Singh MK, Aghajanian H, Massera D, Wang Q, Li J, et al. Semaphorin 3d signaling defects are associated with anomalous pulmonary venous connections. Nat Med. 2013;19(6):760–5. doi:10.1038/nm.3185.

Degenhardt K, Wright AC, Horng D, Padmanabhan A, Epstein JA. Rapid 3D phenotyping of cardiovascular development in mouse embryos by micro-CT with iodine staining. Circ Cardiovasc Imaging. 2010;3(3):314–22. doi:10.1161/CIRCIMAGING.109.918482.

Dickinson ME. Multimodal imaging of mouse development: tools for the postgenomic era. Dev Dyn. 2006;235(9):2386–400.

Efimov IR, Nikolski VP, Salama G. Optical imaging of the heart. Circ Res. 2004;95(1):21–33. doi:10.1161/01.RES.0000130529.18016.3595/1/21[pii].

Ezin M, Fraser S. Time-lapse imaging of the early avian embryo. Methods Cell Biol. 2008;87:211–36.

Foster FS, Zhang M, Duckett AS, Cucevic V, Pavlin CJ. In vivo imaging of embryonic development in the mouse eye by ultrasound biomicroscopy. Invest Ophthalmol Vis Sci. 2003;44(6):2361–6.

Gerneke DA, Sands GB, Ganesalingam R, Joshi P, Caldwell BJ, Smaill BH, et al. Surface imaging microscopy using an ultramiller for large volume 3D reconstruction of wax- and resin-embedded tissues. Microsc Res Tech. 2007;70(10):886–94. doi:10.1002/jemt.20491.

Girsh E, Plaks V, Gilad AA, Nevo N, Schechtman E, Neeman M, et al. Cloprostenol, a prostaglandin F(2alpha) analog,

induces hypoxia in rat placenta: BOLD contrast MRI. NMR Biomed. 2007;20(1):28–39.
Gleave JA, Wong MD, Dazai J, Altaf M, Henkelman RM, Lerch JP, et al. Neuroanatomical phenotyping of the mouse brain with three-dimensional autofluorescence imaging. Physiol Genomics. 2012;44(15):778–85. doi:10.1152/physiolgenomics.00055.2012.
Guldberg RE, Lin AS, Coleman R, Robertson G, Duvall C. Microcomputed tomography imaging of skeletal development and growth. Birth Defects Res C Embryo Today. 2004;72(3):250–9. doi:10.1002/bdrc.20016.
Hogers B, van der Weerd L, Olofsen H, van der Graaf LM, Deruiter MC, Groot AC, et al. Non-invasive tracking of avian development in vivo by MRI. NMR Biomed. 2009;22(4):365–73.
Ingham PW. The power of the zebrafish for disease analysis. Hum Mol Genet. 2009;18(R1):R107–12. doi:10.1093/hmg/ddp091. ddp091 [pii].
Kulandavelu S, Qu D, Sunn N, Mu J, Rennie MY, Whiteley KJ, et al. Embryonic and neonatal phenotyping of genetically engineered mice. ILAR J Nat Res Council Inst Lab Animal Resour. 2006;47(2):103–17.
Kulesa PM. Developmental imaging: insights into the avian embryo. Birth Defects Res C Embryo Today. 2004;72(3):260–6.
Larina IV, Shen W, Kelly OG, Hadjantonakis AK, Baron MH, Dickinson ME. A membrane associated mCherry fluorescent reporter line for studying vascular remodeling and cardiac function during murine embryonic development. Anat Rec (Hoboken). 2009;292(3):333–41.
Le Floc'h J, Cherin E, Zhang MY, Akirav C, Adamson SL, Vray D, et al. Developmental changes in integrated ultrasound backscatter from embryonic blood in vivo in mice at high US frequency. Ultrasound Med Biol. 2004;30(10):1307–19. doi:10.1016/j.ultrasmedbio.2004.07.018. S0301-5629(04)00195-4 [pii].
Lee SC, Mietchen D, Cho JH, Kim YS, Kim C, Hong KS, et al. In vivo magnetic resonance microscopy of differentiation in Xenopus laevis embryos from the first cleavage onwards. Diff Res Bio Divers. 2007;75(1):84–92. doi:10.1111/j.1432-0436.2006.00114.x.
Louie AY, Huber MM, Ahrens ET, Rothbacher U, Moats R, Jacobs RE, et al. In vivo visualization of gene expression using magnetic resonance imaging. Nat Biotechnol. 2000;18(3):321–5. doi:10.1038/73780.
Lukasik VM, Gillies RJ. Animal anaesthesia for in vivo magnetic resonance. NMR Biomed. 2003;16(8):459–67. doi:10.1002/nbm.836.
Mori S, Zhang J, Bulte JW. Magnetic resonance microscopy of mouse brain development. Methods Mol Med. 2006;124:129–47.
Nguyen Huu S, Oster M, Uzan S, Chareyre F, Aractingi S, Khosrotehrani K. Maternal neoangiogenesis during pregnancy partly derives from fetal endothelial progenitor cells. Proc Natl Acad Sci U S A. 2007;104(6):1871–6.
Nieman BJ, Szulc KU, Turnbull DH. Three-dimensional, in vivo MRI with self-gating and image coregistration in the mouse. Magn Reson Med. 2009;61(5):1148–57.
Norris FC, Modat M, Cleary JO, Price AN, McCue K, Scambler PJ, et al. Segmentation propagation using a 3D embryo atlas for high-throughput MRI phenotyping: comparison and validation with manual segmentation. Magn Reson Med Off J Soc Magn Reson Med Soc Magn Reson Med. 2013;69(3):877–83. doi:10.1002/mrm.24306.
Oest ME, Jones JC, Hatfield C, Prater MR. Micro-CT evaluation of murine fetal skeletal development yields greater morphometric precision over traditional clear-staining methods. Birth Defects Res. 2008;83(6):582–9.
Passamaneck YJ, Di Gregorio A, Papaioannou VE, Hadjantonakis AK. Live imaging of fluorescent proteins in chordate embryos: from ascidians to mice. Microsc Res Tech. 2006;69(3):160–7.
Petiet AE, Kaufman MH, Goddeeris MM, Brandenburg J, Elmore SA, Johnson GA. High-resolution magnetic resonance histology of the embryonic and neonatal mouse: a 4D atlas and morphologic database. Proc Natl Acad Sci U S A. 2008;105(34):12331–6. doi:10.1073/pnas.0805747105.
Phoon CK. Imaging tools for the developmental biologist: ultrasound biomicroscopy of mouse embryonic development. Pediatr Res. 2006;60(1):14–21.
Phoon CK, Ji RP, Aristizabal O, Worrad DM, Zhou B, Baldwin HS, et al. Embryonic heart failure in NFATc1-/- mice: novel mechanistic insights from in utero ultrasound biomicroscopy. Circ Res. 2004;95(1):92–9. doi:10.1161/01.RES.0000133681.99617.28.
Plaks V, Berkovitz E, Vandoorne K, Berkutzki T, Damari GM, Haffner R, et al. Survival and size are differentially regulated by placental and fetal PKBalpha/AKT1 in mice. Biol Reprod. 2011a;84(3):537–45. doi:10.1095/biolreprod.110.085951.
Plaks V, Birnberg T, Berkutzki T, Sela S, BenYashar A, Kalchenko V, et al. Uterine DCs are crucial for decidua formation during embryo implantation in mice. J Clin Invest. 2008;118(12):3954–65.
Plaks V, Gershon E, Zeisel A, Jacob-Hirsch J, Neeman M, Winterhager E, et al. Blastocyst implantation failure relates to impaired translational machinery gene expression. Reproduction. 2014;148(1):87–98. doi:10.1530/rep-13-0395.
Plaks V, Kalchenko V, Dekel N, Neeman M. MRI analysis of angiogenesis during mouse embryo implantation. Magn Reson Med. 2006;55(5):1013–22.
Plaks V, Sapoznik S, Berkovitz E, Haffner-Krausz R, Dekel N, Harmelin A, et al. Functional phenotyping of the maternal albumin turnover in the mouse placenta by dynamic contrast-enhanced MRI. Mol Imaging Biol. 2011b;13(3):481–92. doi:10.1007/s11307-010-0390-1.
Raz T, Avni R, Addadi Y, Cohen Y, Jaffa AJ, Hemmings B, et al. The hemodynamic basis for positional- and interfetal dependent effects in dual arterial supply of mouse pregnancies. PloS One. 2012;7(12):e52273. doi:10.1371/journal.pone.0052273.
Rinon A, Lazar S, Marshall H, Buchmann-Moller S, Neufeld A, Elhanany-Tamir H, et al. Cranial neural crest cells regulate head muscle patterning and differentiation during vertebrate embryogenesis.

Development. 2007;134(17):3065–75. doi:10.1242/dev.002501. dev.002501 [pii].

Rothenberg F, Efimov IR, Watanabe M. Functional imaging of the embryonic pacemaking and cardiac conduction system over the past 150 years: technologies to overcome the challenges. Anat Rec A Discov Mol Cell Evol Biol. 2004;280(2):980–9. doi:10.1002/ar.a.20076.

Salomon LJ, Siauve N, Balvay D, Cuenod CA, Vayssettes C, Luciani A, et al. Placental perfusion MR imaging with contrast agents in a mouse model. Radiology. 2005;235(1):73–80.

Salomon LJ, Siauve N, Taillieu F, Balvay D, Vayssettes C, Frija G, et al. In vivo dynamic MRI measurement of the noradrenaline-induced reduction in placental blood flow in mice. Placenta. 2006;27(9–10):1007–13.

Schneider JE, Bhattacharya S. Making the mouse embryo transparent: identifying developmental malformations using magnetic resonance imaging. Birth Defects Res C Embryo Today. 2004;72(3):241–9.

Shapiro EM, Skrtic S, Sharer K, Hill JM, Dunbar CE, Koretsky AP. MRI detection of single particles for cellular imaging. Proc Natl Acad Sci U S A. 2004;101(30):10901–6. doi:10.1073/pnas.0403918101 0403918101[pii].

Solomon E, Avni R, Hadas R, Raz T, Garbow JR, Bendel P, et al. Major mouse placental compartments revealed by diffusion-weighted MRI, contrast-enhanced MRI, and fluorescence imaging. Proc Natl Acad Sci U S A. 2014;111(28):10353–8. doi:10.1073/pnas.1401695111.

Taillieu F, Salomon LJ, Siauve N, Clement O, Faye N, Balvay D, et al. Placental perfusion and permeability: simultaneous assessment with dual-echo contrast-enhanced MR imaging in mice. Radiology. 2006;241(3):737–45.

Tanaka M, Hadjantonakis AK, Vintersten K, Nagy A. Aggregation chimeras: combining ES cells, diploid, and tetraploid embryos. Methods Mol Biol. 2009;530:287–309. doi:10.1007/978-1-59745-471-1_15.

Tirosh-Finkel L, Elhanany H, Rinon A, Tzahor E. Mesoderm progenitor cells of common origin contribute to the head musculature and the cardiac outflow tract. Development. 2006;133(10):1943–53. doi:10.1242/dev.02365. dev.02365 [pii].

Tomlinson TM, Garbow JR, Anderson JR, Engelbach JA, Nelson DM, Sadovsky Y. Magnetic resonance imaging of hypoxic injury to the murine placenta. Am J Physiol Regul Integr Comp Physiol. 2010;298(2):R312–9. doi:10.1152/ajpregu.00425.2009.

Turnbull DH, Mori S. MRI in mouse developmental biology. NMR Biomed. 2007;20(3):265–74.

Vandoorne K, Magland J, Plaks V, Sharir A, Zelzer E, Wehrli F, et al. Bone vascularization and trabecular bone formation are mediated by PKBalpha/Akt1 in a gene-dosage-dependent manner: in vivo and ex vivo MRI. Magn Reson Med. 2010;64(1):54–64. doi:10.1002/mrm.22395.

Vandoorne K, Vandsburger MH, Weisinger K, Brumfeld V, Hemmings BA, Harmelin A, et al. Multimodal imaging reveals a role for Akt1 in fetal cardiac development. Physiol Rep. 2013;1(6):e00143. doi:10.1002/phy2.143.

Vogt A, Cholewinski A, Shen X, Nelson SG, Lazo JS, Tsang M, et al. Automated image-based phenotypic analysis in zebrafish embryos. Dev Dyn. 2009;238(3):656–63. doi:10.1002/dvdy.21892.

Weninger WJ, Geyer SH, Mohun TJ, Rasskin-Gutman D, Matsui T, Ribeiro I, et al. High-resolution episcopic microscopy: a rapid technique for high detailed 3D analysis of gene activity in the context of tissue architecture and morphology. Anat Embryol. 2006;211(3):213–21. doi:10.1007/s00429-005-0073-x.

Wiesmann F, Ruff J, Hiller KH, Rommel E, Haase A, Neubauer S. Developmental changes of cardiac function and mass assessed with MRI in neonatal, juvenile, and adult mice. Am J Physiol Heart Circ Physiol. 2000;278(2):H652–7.

Winkelmann CT, Wise LD. High-throughput microcomputed tomography imaging as a method to evaluate rat and rabbit fetal skeletal abnormalities for developmental toxicity studies. J Pharmacol Toxicol Methods. 2009;59(3):156–65. doi:10.1016/j.vascn.2009.03.004. S1056-8719(09)00230-5 [pii].

Xu J, Delproposto Z, Zhou Z, Shen H, Xuan SY, Li QH, et al. In ovo monitoring of smooth muscle fiber development in the chick embryo: diffusion tensor imaging with histologic correlation. PLoS One. 2012;7(3):e34009. doi:10.1371/journal.pone.0034009.

Yaniv K, Isogai S, Castranova D, Dye L, Hitomi J, Weinstein BM. Live imaging of lymphatic development in the zebrafish. Nat Med. 2006;12(6):711–6. doi:10.1038/nm1427. nm1427 [pii].

Zhang J, Richards LJ, Yarowsky P, Huang H, van Zijl PC, Mori S. Three-dimensional anatomical characterization of the developing mouse brain by diffusion tensor microimaging. Neuroimage. 2003;20(3):1639–48. S1053811903004105 [pii].

Imaging in Gynecology Research

26

Matthias W. Laschke and Michael D. Menger

Contents

26.1 Introduction

Rodents are widely used as model animals in gynecology research for several reasons. Their breeding and maintenance is uncomplicated and cost-efficient. They exhibit a short and regular estrous cycle, including the stages of proestrus, estrus, metestrus, and diestrus, which can reliably be determined by cytological analysis of vaginal lavage samples. Accordingly, the selection of animals in the same cycle stage allows for the performance of standardized studies, excluding discrepancies between individual animals due to different sex hormone levels. Alternatively, rodents can easily be ovariectomized and substituted with defined doses of estrogen and progesterone to induce constant hormonal conditions. Moreover, they exhibit a short life cycle, which reduces the time of puberty, pregnancy, and delivery and, thus, facilitates research focusing on reproductive function and dysfunction. Mainly in mice, there is the possibility of genetic manipulations for the investigation of gene functions and the establishment of novel gynecological disease models. The use of immunocompromised nude or SCID mice further bears the advantage of studying pathophysiological processes in xenografts, such as endometriotic lesions or tumor tissue of human origin.

In the past, gynecology research in rodents was mainly based on histological, immunohistochemical, or gene expression analyses of tissue samples, which were isolated after surgery or necropsy.

M.W. Laschke, PhD (✉) • M.D. Menger
Institute for Clinical & Experimental Surgery,
Saarland University, Homburg/Saar 66421, Germany
e-mail: matthias.laschke@uks.eu

F. Kiessling et al. (eds.), *Small Animal Imaging*, DOI 10.1007/978-3-319-42202-2_26

Accordingly, this invasive approach provided data based on single observation time points, not allowing sequential dynamic studies performed in the same animals. However, such studies are especially important for the examination of the female reproductive organs, which are continuously changing during the estrous cycle. Moreover, to assess the increasing amounts of novel, targeted therapies for the treatment of severe gynecological diseases, such as gynecologic cancer or endometriosis, it is desirable to measure changes in tissue proliferation and regression over time in clinically relevant rodent models. Therefore, sophisticated small animal imaging technologies have been introduced in the field of gynecology research during the last years, which allow for the noninvasive and repetitive analysis of physiological and pathological processes within the female reproductive organs. These include the technique of intravital fluorescence microscopy, bioluminescence, ultrasound biomicroscopy, computed tomography (CT), and magnetic resonance imaging (MRI). All of these technologies contribute to limit the statistical variability of preclinical studies, to reduce the number of animals required for each study, and to maximize the amount of data obtained from each animal according to the philosophy of the 3Rs model (refinement, reduction, and replacement) of Russel and Burch (Flecknell 2002). This chapter highlights some of the most interesting and relevant small animal models and imaging technologies, applied in central gynecology research fields, including physiology of the ovary and ovarian tissue transplantation, placental pathology, gynecologic oncology, as well as endometriosis.

26.2 Physiology of the Ovary and Ovarian Tissue Transplantation

The ovary is beside the uterus one of the dynamic organs in the adult, which exhibit periodic growth and regression. In fact, the ovarian cycle is characterized by the growth of individual ovarian follicles, which continually leave the large pool of resting, primordial follicles. During their development, they produce increasing amounts of estrogens and finally approach ovulation. Subsequently, the remaining cells of ruptured follicles form the corpus luteum, which is critical for successful maintenance of pregnancy in mammals, because it is the primary source of progesterone. All of these steps are tightly regulated by the hypothalamic-pituitary axis via the release of the gonadotropins follicle-stimulating hormone (FSH) and luteinizing hormone (LH). Accordingly, folliculogenesis and corpus luteum formation are essential for the regulation of physiological reproductive function and hormonal state.

Recently, the technique of high-resolution ultrasound imaging has been introduced for the noninvasive imaging of follicles and corpora lutea in rodents. By means of ultra-high frequencies of 25–70 MHz, this technique allows the generation of images with a resolution, which is near to conventional microscopy. Therefore, it is also called ultrasound biomicroscopy. Using this imaging tool, it is possible to easily localize the ovaries in rabbits, rats, and mice, to assess their volume, and to count and measure non-proliferating and preovulatory follicles as well as corpora hemorrhagica and corpora lutea due to their different echogenic patterns (Pallares and Gonzalez-Bulnes 2008) (Fig. 26.1). Importantly, the ultrasound waves do not induce tissue damage and genetic alterations, such as X-rays, and thus can be applied without the risk of negative effects on the reproductive process. Moreover, repeated exposure to anesthesia during ultrasound imaging does not affect the estrous cycle (Jaiswal et al. 2009).

A major prerequisite for cyclic folliculogenesis and corpus luteum formation is angiogenesis, which is defined as the formation of new capillaries from preexisting blood vessels. During the ovarian cycle, vascular changes are tightly regulated by the expression of numerous pro- and anti-angiogenic growth factors in that angiogenesis is turned on for brief periods and then completely inhibited. Correspondingly, the ovary represents a unique system for the study of physiological angiogenesis and blood vessel regression in the adult, where angiogenesis is normally restricted to pathological processes, such as tumor growth, wound healing, or inflammation. Moreover, some types of infertility may directly be caused by disturbed follicular angiogenesis.

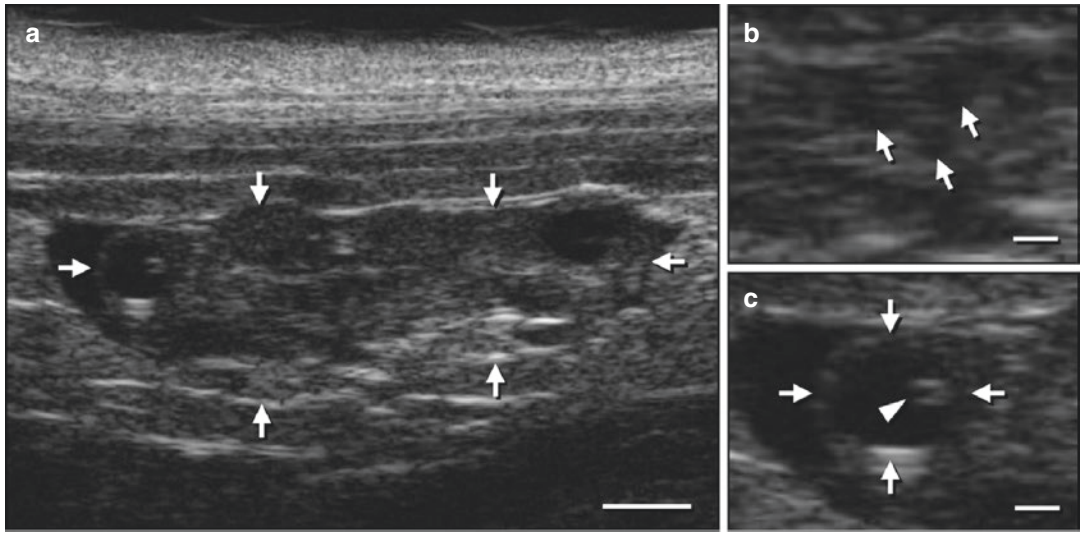

Fig. 26.1 High-resolution ultrasound imaging of a rat ovary (**a**, borders marked by *arrows*) by means of a Vevo 770 high-resolution imaging system (VisualSonics) and a 704 scan-head with a center frequency of 40 MHz and a focal depth of 6 mm. (**b**, **c**): Higher magnification shows typical stages of folliculogenesis, such as premature ovarian follicles (**b**, *arrows*) and mature, preovulatory follicles (**c**, border marked by *arrows*), which are characterized by a large anechoic antral cavity and an echogenic cumulus oocyte complex (**c**, *arrowhead*). Scale bars: **a** = 1.2 mm; **b**, **c** = 350 µm

For instance, the polycystic ovarian syndrome is associated with excessive development of new blood vessels, while the ovarian hyperstimulation syndrome is characterized by an increase in capillary permeability. Thus, the analysis of ovarian angiogenesis and its regulation is also of major importance for the establishment of new therapies in gynecology, which control inappropriate follicle development due to enhanced or decreased angiogenesis.

The rapid changes in blood vessel development and regression within the ovary are accompanied by equally rapid changes in rates of blood perfusion. Measurement of ovarian blood flow and volume by means of color-coded Doppler ultrasound imaging or ultrasound biomicroscopy with microbubbles as a contrast agent may therefore be useful for studying dynamic angiogenesis and vascular remodeling associated with the ovarian cycle or for detecting chemotherapy-induced side effects on the ovary (Bar-Joseph et al. 2011). Alternatively, pulsed arterial spin labeling MRI has been suggested for the analysis of ovarian tissue perfusion in small animal studies (Tempel-Brami and Neeman 2002). In this type of measurement, the MRI signal is tagged in the upstream of the ovary by pulsed slice selective saturation. By this, perfusion within the ovary can be calculated by monitoring the saturation transfer due to perfusion without the need for exogenous administration of contrast agents. Pulsed arterial spin labeling MRI of the rat ovary showed that preovulatory follicles exhibit poorly perfused regions, indicating that physiological hypoxia may play a crucial role in the ovulation process (Tempel-Brami and Neeman 2002). Of interest, the MRI technology may not only be used to assess perfusion rates. Dynamic contrast-enhanced MRI additionally enables the noninvasive analysis of vascular density, vessel permeability, and interstitial convection in ovarian tissue (Israely et al. 2004). Moreover, the novel generation of MRI scanners with high field strengths of 11.7 T even allows for the in vivo imaging of preovulatory follicles (Stephenson et al. 2012).

For the detailed in vivo analysis of the morphology and perfusion of individual microvessels within ovarian tissue, follicles, and corpora lutea can be transplanted into the dorsal skinfold chamber (Vollmar et al. 2001) (Fig. 26.2). This well-established rodent model allows for the repetitive analysis of microcirculatory processes in mice, hamsters, and rats by means of intravital multi-fluorescence microscopy over a time period of 3–4 weeks (Menger et al. 2002). For the implantation of the chamber, the back of the anesthetized

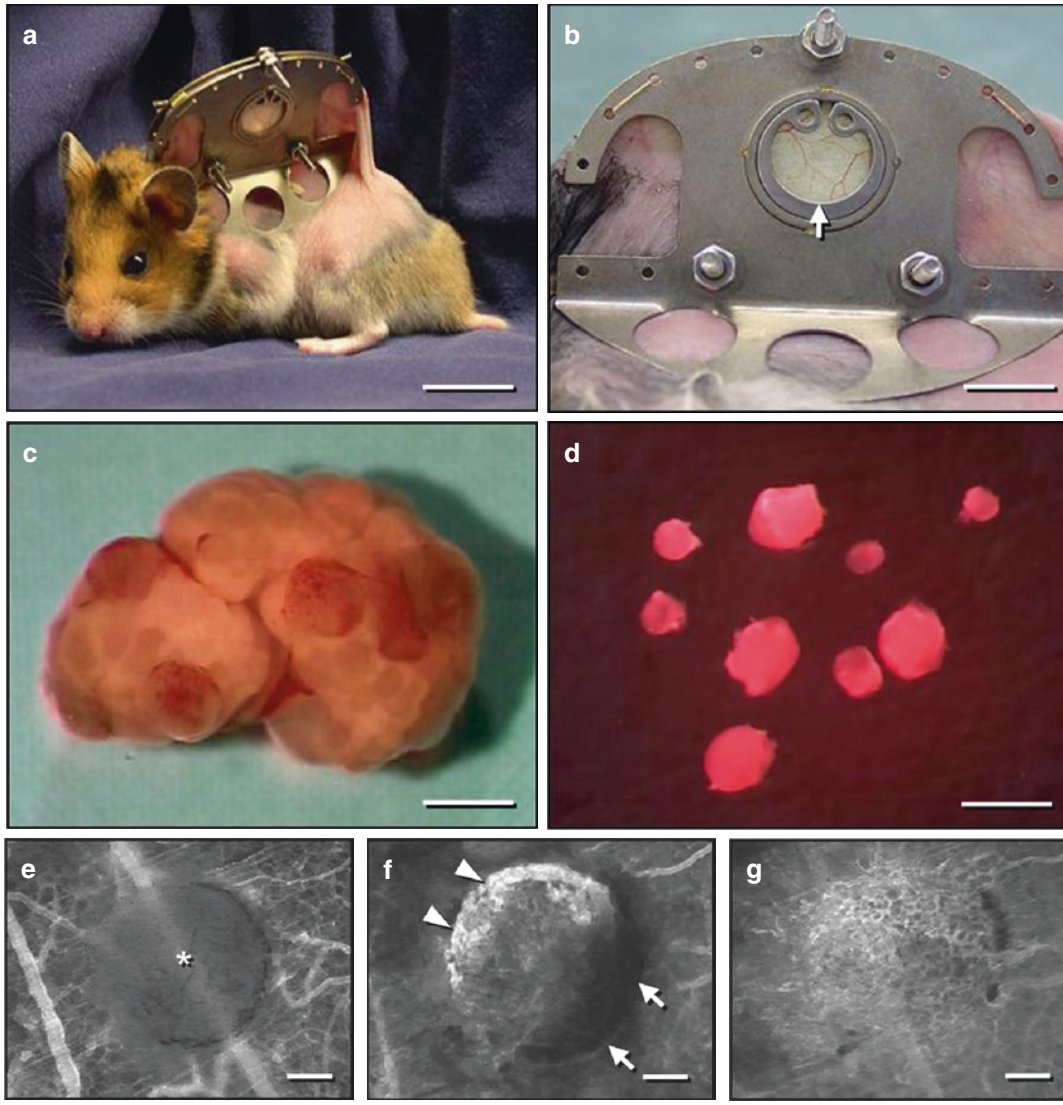

Fig. 26.2 Dorsal skinfold chamber model for the noninvasive and repetitive in vivo imaging of physiological angiogenesis in ovarian follicles by means of intravital fluorescence microscopy. (**a**) Syrian golden hamster equipped with a dorsal skinfold chamber (chamber weight ~ 4 g). (**b**) Within the observation window of the chamber (*arrow*), all segments of the microcirculation including arterioles, capillaries, and venules of the striated skin muscle and subcutaneous tissue can be directly visualized. (**c**, **d**) For the analysis of ovarian follicles, the ovary of a donor hamster (**c**) is carefully microdissected using 27-gauge needles under a stereomicroscope. A handpicking procedure guarantees single connective tissue-free follicles (**d**), which subsequently can be transplanted onto the striated muscle within the dorsal skinfold chamber. (**e**–**g**) Intravital fluorescence microscopic images of an ovarian follicle directly after transplantation (**e**) as well as at day 2 (**f**) and day 4 (**g**) after transplantation into the hamster dorsal skinfold chamber. Note the initial lack of nutritive capillaries within the freshly transplanted graft (**e**, *asterisk*). On day 2 after transplantation parts of the follicular graft display newly formed microvessels (**f**, *arrowheads*), while some areas still lack vascularization (**f**, *arrows*). On day 4 a dense glomerulum-like network of newly formed microvessels covers the entire graft (**g**). (**e**–**g**): Blue light epi-illumination with contrast enhancement by 5% FITC-labeled dextran 150,000 iv. Scale bars: **a** = 2.2 cm; **b** = 9 mm; **c**, **d** = 1.1 mm; **e**–**g** = 200 µm

animal is shaven and depilated before two symmetrical titanium frames are implanted on the extended dorsal skinfold, so that they sandwich the double layer of skin. One layer of skin is completely removed in a circular area of ~15 mm in diameter, and the remaining layers consisting of striated skin muscle, subcutaneous tissue, and skin are covered with a removable coverslip incorporated into the observation window of one of the titanium frames. The coverslip of the observation window can be temporarily removed to transplant ovarian follicles or corpora lutea onto the striated muscle within the chamber. After application of the fluorochrome fluorescein-isothiocyanate (FITC)-labeled dextran (MW 150,000 Da) for contrast enhancement by staining of blood plasma, intravital fluorescence microscopy can be performed to visualize in vivo angiogenic sprouting and network formation within the ovarian tissue and to quantify in vivo morphological (vascularized area, functional capillary density) and microhemodynamic (vessel diameters, red blood cell velocity, volumetric blood flow) parameters of follicular and luteal microcirculation. Using additional fluorochromes, this microscopic in vivo approach also enables for the assessment of cellular and molecular aspects, such as leukocyte-endothelial cell interaction, platelet adhesion, or apoptotic cell death (Menger et al. 2002). By means of the dorsal skinfold chamber model of Syrian golden hamsters, it could be demonstrated that the theca interna is essential for the vascularization of follicles (Vollmar et al. 2001). Moreover, bilateral ovariectomy of the animals accelerates angiogenesis and improves vascular blood perfusion, which may be best interpreted in that lack of steroid negative feedback and high gonadotropin secretion contribute to vascular growth and nutritive perfusion of ovarian follicles (Laschke et al. 2002).

However, ovarian tissue transplantation is not only an experimental approach for the noninvasive in vivo analysis of physiological angiogenesis but also represents a clinical treatment strategy for preservation of ovarian function in women, who suffer from premature ovarian failure due to aggressive chemotherapy or radiation therapy. For this purpose, small ovarian tissue fragments are isolated from patients and are cryopreserved until their transplantation back into the patients after successful cancer therapy. A major prerequisite for the restoration of the grafts' hormonal and fertility function after cryopreservation is the development of a new vasculature. Therefore, the aforementioned imaging technologies have also been used to study angiogenesis and blood perfusion within cryopreserved ovarian grafts and to establish approaches, which may accelerate and improve the angiogenic process. In this context, intravital fluorescence microscopic studies revealed that cryopreservation does not affect angiogenesis and revascularization of freely grafted ovarian follicles (Laschke et al. 2003). In addition, dynamic contrast-enhanced MRI analyses of the vascular permeability of rat ovarian xenografts demonstrated that intramuscular implantation provides a better maintenance of functional blood vessels compared to subcutaneous implantation (Israely et al. 2003). Finally, high-resolution ultrasonography and bioluminescence imaging have been shown to be reliable methods to trace the survival and follicular development of ovarian grafts with excellent sensitivity and spatial resolution (Fassbender et al. 2007; Lin et al. 2011).

26.3 Placental Pathology

During pregnancy, the placenta ensures nearly all exchanges of respiratory gases, nutrients, and metabolites between the fetal and maternal organism. Thereby, the rate of transplacental exchange is critically dependent on the maternal (uteroplacental) and the fetal (umbilicoplacental) circulation. Abnormalities in placental blood perfusion are associated with serious pregnancy disorders, such as maternal preeclampsia or fetal intrauterine growth restriction. To establish preventive strategies and effective therapies for these diseases, sophisticated small animal models are needed, which allow for the study of the mechanisms underlying placental pathology. For this purpose, mice are an appropriate species, because their placenta is quite similar to the human placenta regarding cellular and circulatory architecture

as well as gene expression. In addition, mutant mouse lines have already been identified, which exhibit different pathological placenta phenotypes (Rossant and Cross 2001). To adequately analyze the pathogenesis of human pregnancy disorders in these mice, noninvasive imaging methods have been introduced in gynecology research, including ultrasound biomicroscopy and dynamic contrast-enhanced MRI.

High-resolution Doppler ultrasound imaging is an easy and reliable tool to quantify blood flow velocities in the uterine artery as well as in the uteroplacental and umbilicoplacental circulation throughout gestation in mice (Mu and Adamson 2006; Khankin et al. 2012). Importantly, blood flow velocity waveforms in mice are similar in shape and show similar changes during gestation when compared to those observed in human pregnancy (Mu and Adamson 2006). This indicates that abnormal uterine hemodynamics, which are typically associated with severe preeclamptic and fetal intrauterine growth restriction pregnancies in humans, may be phenocopied in corresponding mutant mouse models. For this purpose, high-resolution Doppler ultrasound imaging represents an attractive technology, because it parallels the routine ultrasound imaging used in clinical practice. Due to its high resolution, it further allows for the visualization of the calcification of the placenta (Akirav et al. 2005). Finally, placental size of pregnant mice, which is also an early predictor for poor pregnancy outcome in humans, can be repetitively quantified in vivo (Mu et al. 2008).

Dynamic contrast-enhanced MRI offers the possibility to quantify the rate at which a contrast agent crosses from the intravascular compartment into other compartments. Accordingly, this technology ideally suits for the noninvasive determination of placental perfusion and permeability in mice (Taillieu et al. 2006). For this purpose, gadolinium should be used as contrast agent, because it can easily cross the placental barrier due to its low molecular weight and small particle size. Moreover, high gadolinium doses of 0.5 mmol/kg body weight are recommended in mice to increase fetal uptake and, thereby, facilitate permeability measurements. By means of dynamic contrast-enhanced MRI it could be demonstrated that noradrenaline, which has been implicated in the pathogenesis of preeclampsia, reduces placental perfusion in mice (Salomon et al. 2006). Exposure to hypoxia near the end of mouse pregnancy also reduces placental perfusion, which is associated with fetal growth restriction (Tomlinson et al. 2010). These results indicate that dynamic contrast-enhanced MRI is an interesting technology for functional evaluation of the placenta in small animal models, which may help to gain new insights into the pathology of severe pregnancy disorders. The technology may even be a future diagnostic tool in clinical practice, although the routine use of contrast agents in humans during pregnancy is to date not recommended in order to prevent potential deleterious effects to the fetus.

26.4 Gynecologic Oncology

Breast cancer and cancer of the female reproductive organs belong to the most common types of cancer in women. In the United States approximately 82,000 women per year are diagnosed with gynecologic cancer. Small animal models are important experimental tools to investigate mechanisms of tumor development and to evaluate the efficacy of novel therapeutic strategies. For this purpose, noninvasive approaches to analyze angiogenesis, metastasis, and tumor growth have also been introduced in the field of gynecologic oncology during the last years.

For a long time, the standard technique for the study of different gynecologic tumor types was the subcutaneous implantation of human tumor cells or tissue fragments into immunodeficient mice. By this, the growth of the xenografts could be determined in vivo by external caliper measurement where the tumor volume is calculated by means of the modified ellipsoid formula $0.5 \times \text{length} \times \text{width}^2$. However, this method is often affected by errors, because of variability in tumor shape or skin thickness. Moreover, it is associated with a large interobserver variability. To overcome these problems, high-resolution ultrasound imaging, microCT, or MRI may alternatively be

used for growth measurements of subcutaneous tumors in rodents. Nonetheless, one should be aware that such subcutaneous tumor models often do not reflect the real clinical situation, because they are usually based on the analysis of larger tumors. For instance, the majority of newly diagnosed breast cancers in women are very early tumor stages, such as preinvasive ductal carcinoma in situ (DCIS), which can nowadays be detected in clinical practice due to improved mammography techniques. However, in the past most imaging studies of mouse mammary cancer have focused on large tumors that were extremely advanced and, thus, do not realistically reflect early breast cancer. In contrast, spontaneous developing rodent tumors progress through all disease stages and thus mimic their human counterpart much better. Interesting examples of such tumor models in gynecology research are the uterine leiomyoma model of the Eker rat (Walker et al. 2003) or the transgenic mouse models of mammary and ovarian cancer (Hensley et al. 2007; Jansen et al. 2008).

Preclinical studies of spontaneous gynecologic tumors in rodents present unique challenges, including variable latency of tumor formation and detection of very small tumors, which are located deep within the female reproductive organs. Accordingly, numerous noninvasive imaging techniques have been proposed for the in vivo analysis of gynecologic tumors, such as ultrasound biomicroscopy, bioluminescence, MRI, microCT, and recently also flat-panel detector volume CT. Each technique bears many specific advantages and disadvantages relating to the analysis of tumors, whose detailed description would go beyond the scope of this section and can be found in other chapters of this book.

26.5 Endometriosis

Endometriosis is a frequent gynecological disorder, which affects approximately 10–15 % of all women in reproductive age. The disease is diagnosed by clinical evidence of proliferating endometrium–like tissue outside the uterine cavity. Classical symptoms of endometriosis are dysmenorrhea, dyspareunia, dysuria, severe abdominal or pelvic pain, as well as infertility. Despite the high prevalence of endometriosis, many questions about its etiology and pathogenesis are still unanswered. However, the disease is most likely caused by retrograde menstruation, i.e., reflux of endometrial fragments in the fallopian tubes during menstruation and their implantation and development to endometriotic lesions in the peritoneal cavity. Because the growth of these lesions is estrogen dependent, current medical therapies aim on the suppression of endogenous estrogen production, which may be associated with substantial side effects such as osteoporosis or episodes of depression. Alternatively, endometriotic lesions are surgically removed, however, with a high recurrence rate of up to ~50–70 %. Accordingly, current endometriosis research focuses on the development of more effective treatment strategies. For this purpose, genetically well-defined rodent models, which allow for standardized preclinical studies, are an important approach.

Because the development of spontaneous endometriosis is dependent on menstruation and thus restricted to humans and subhuman primates, endometriotic lesions in rodents are usually induced iatrogenically by grafting isolated endometrium from the uterus to ectopic sites (Grümmer 2006). For this purpose, the dorsal skinfold chamber model can be used, which allows for the repetitive in vivo analysis of implantation, growth, and angiogenesis of the ectopic endometrial tissue using the combination of epi-illumination multi-fluorescence microscopy and computer-assisted off-line analysis techniques (see also Sect. 26.2) (Fig. 26.3). Because this experimental approach enables for the visualization of individual microvessels with a high resolution, it is of particular interest for studies focusing on the analysis of blood vessel development and regression in endometriotic lesions as well as on the establishment of novel anti-angiogenic treatment strategies for endometriosis therapy (Laschke and Menger 2007). However, a major disadvantage of the chamber model is the fact that it is restricted in use to a time period of only 3–4 weeks. In addition, the

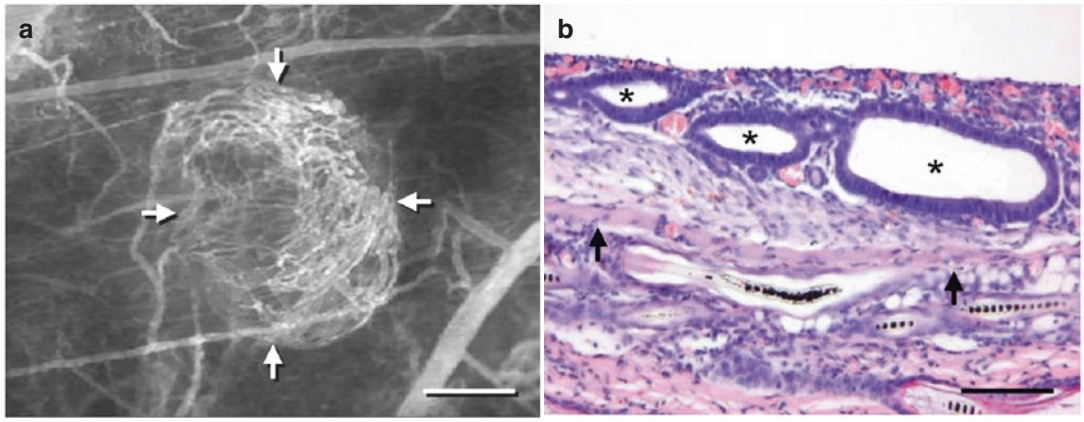

Fig. 26.3 Typical microangioarchitecture and histomorphology of endometriotic lesions induced in the dorsal skinfold chamber model. (**a**) Intravital fluorescence microscopy of an endometrial graft (borders marked by *arrows*) at day 10 after transplantation into the dorsal skinfold chamber of a Syrian golden hamster. The graft exhibits a dense network of newly formed blood vessels with a glomerulum-like angioarchitecture. Blue light epi-illumination with contrast enhancement by 5% FITC-labeled dextran 150,000 i.v. (**b**) Hematoxylin-eosin stained cross section of an endometrial graft at day 14 after transplantation onto the striated muscle (*arrows*) of the dorsal skinfold chamber of a Syrian golden hamster, displaying typical histomorphological signs of an endometriotic lesion such as cyst-like dilated endometrial glands (*asterisks*) with an intact glandular epithelium surrounded by a richly vascularized endometrial stroma. Scale bars: **a** = 270 µm; **b** = 80 µm

environment within the chamber may not exactly reflect the physiological profile of cytokines and growth factors of the peritoneal fluid and the intra-abdominal immune system.

To fulfill these criteria, endometrium has to be transplanted directly into the peritoneal cavity. For the noninvasive monitoring of intraperitoneal endometriotic lesions in mice, the technique of bioluminescence has been introduced (Becker et al. 2006). For this purpose, luciferase-expressing transgenic mice are generated by inserting the human ubiquitin C promoter coupled to the firefly luciferase reporter. The transgenic endometrial tissue from these mice is subsequently transplanted into the peritoneal cavity of wild-type mice. By this, systemic injection of luciferin evokes a specific light signal within the endometrial grafts, which can be detected and quantified through the abdominal wall by a bioluminescence imaging system. Importantly, transabdominal luminescence correlates well with the grafts' implantation, reflecting onset of angiogenesis and tissue growth. Accordingly, it could be shown by this imaging technology that systemic treatment with the angiogenesis inhibitors endostatin peptide mP-1 and caplostatin significantly delays and suppresses angiogenesis within endometriotic lesions (Becker et al. 2006). These results indicate that bioluminescence may be a useful tool to monitor the efficacy of anti-angiogenic drugs in the treatment of endometriosis, especially in combination with the first genetic mouse model of spontaneous endometriosis (Dinulescu et al. 2005). However, a major disadvantage of this approach is the fact that it is dependent on specific transgenic mice. Moreover, bioluminescence lacks a high spatial resolution.

Another possibility to analyze intraperitoneal endometriotic lesions in rodents is the use of MRI. Thereby, detection of the lesions has been shown to be markedly facilitated by the application of contrast agents such as gadofosveset trisodium (Schreinemacher et al. 2012) or ultrasmall superparamagnetic iron oxides (Lee et al. 2012). Accordingly, these contrast agents may be also promising tools for future MRI-based endometriosis diagnosis under clinical conditions.

Alternatively, intraperitoneal endometriotic lesions may be analyzed by high-resolution

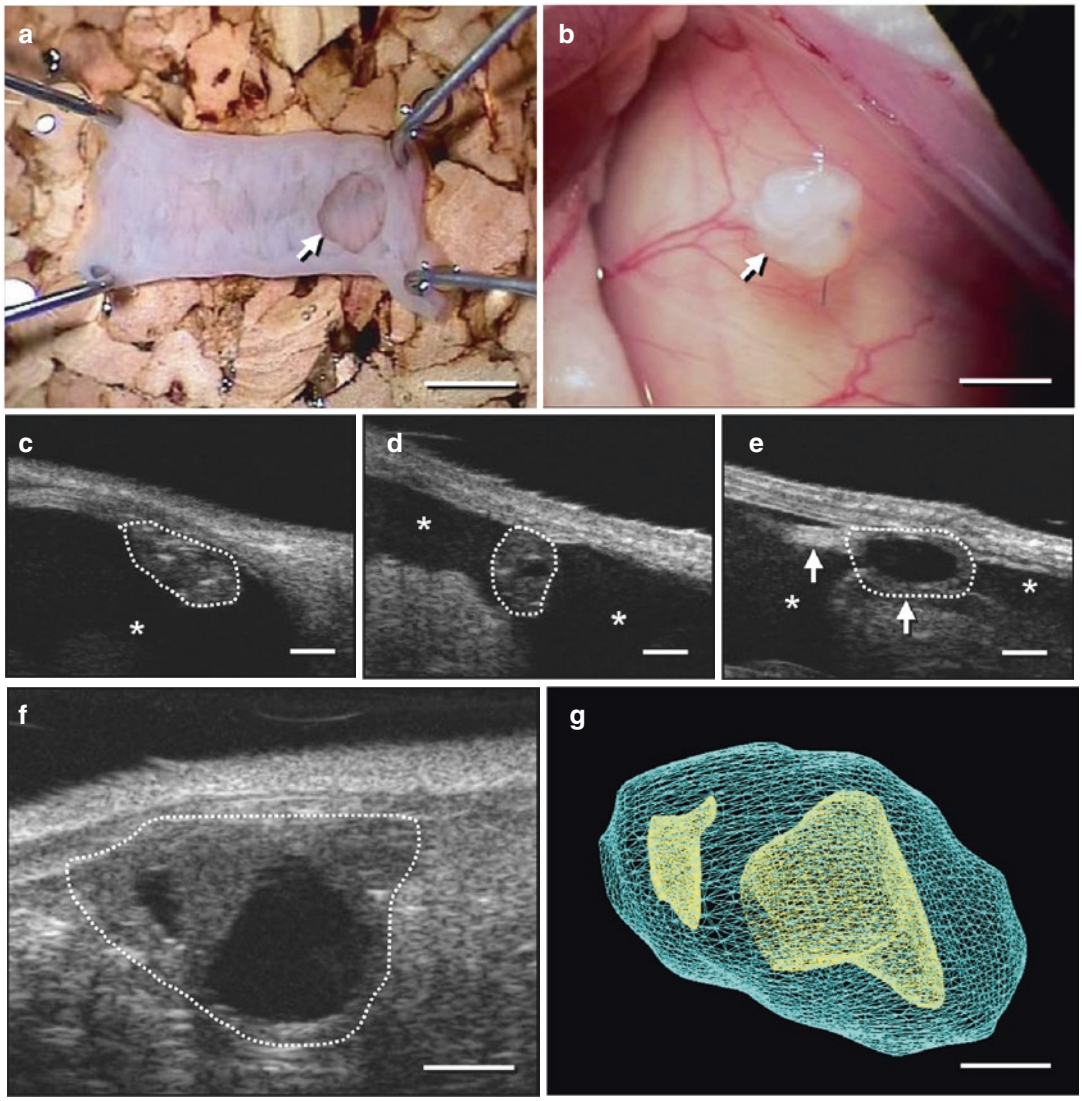

Fig. 26.4 (**a**, **b**) Surgical induction of intraperitoneal endometriosis in mice. For this purpose, a uterine tissue sample (**a**, *arrow*) is harvested from a longitudinally opened uterine horn of a donor animal by means of a biopsy punch. The tissue sample is then sutured to the peritoneal wall of a recipient animal (**b**, *arrow*). (**c**–**e**) High-resolution ultrasound imaging of a developing endometriotic lesion (borders marked by white broken line) directly (**c**) as well as 14 and 28 days (**e**) after fixation of an uterine tissue sample to the abdominal wall. Note that the formation of an anechoic cyst (**d**, **e**) within the lesion can be visualized with this noninvasive technique. Moreover, adhesion formation (**e**, *arrows*) around the lesion can easily be detected by injecting 1 ml saline solution (**c**–**e**, *asterisks*) into the peritoneal cavity, which separates the endometriotic lesion at the abdominal wall from the surrounding intra-abdominal organs. (**f**, **g**) Three-dimensional reconstruction of an endometriotic lesion (**g**, *blue polygon*) with two cysts (**g**, *yellow polygon*) based on manual image segmentation of two-dimensional ultrasound images of the lesion (**f**, borders marked by white *broken line*). Scale bars: **a** = 2.9 mm; **b** = 1.6 mm; **c**–**e** = 800 µm; **f** = 1 mm; **g** = 900 µm

ultrasound imaging (Laschke et al. 2010) (Fig. 26.4). Using high-frequency scanheads, this technology allows for the noninvasive analysis of endometriotic lesions in mice with good soft tissue contrast and without the application of i.v. contrast agents. To provide optimal conditions for ultrasound imaging, endometrial tissue samples should be sutured to the abdominal wall,

which makes it easy to detect them and to differentiate them from adjacent intra-abdominal organs during repetitive analyses. Importantly, this technique provides complete new information about endometriotic lesions. The localization and extension of anechoic cysts can nicely be visualized in three-dimensional image reconstructions. Furthermore, it is possible to detect noninvasively adhesion formation around the developing lesions. Tissue perfusion can be monitored by color-coded Doppler ultrasound imaging. In addition, microbubbles targeted to specific neovascular endothelial receptors such as α_v-integrins may be used to assess angiogenesis in endometriotic lesions. Accordingly, high-resolution ultrasound imaging is a reliable and easy method to gain new insights in the pathogenesis of endometriosis. Moreover, it is an excellent tool in preclinical research to test the efficacy of novel medical therapies for the treatment of this frequent gynecological disease.

26.6 Outlook

Rapid progress in the development of high-resolution imaging technologies for small animals allows now for the noninvasive and repetitive in vivo analysis of physiological and pathological processes within the female reproductive organs. This option will not only contribute to the reduction of animals required for future preclinical studies but will also significantly increase our knowledge about the physiology of reproduction and the pathogenesis of numerous gynecological diseases. In contrast to the ex vivo analysis of isolated tissue samples by means of genetic, biochemic, or histological techniques, noninvasive imaging methods bear the major advantage that they enable for the assessment of functional parameters in highly dynamic tissues, as they can typically be found within the ovary, the uterus, and the placenta. Important examples are the measurement of placental perfusion and permeability by dynamic contrast-enhanced MRI or the determination of functional capillary density in developing endometriotic lesions by intravital fluorescence microscopy. Accordingly, small animal imaging technologies have already a major impact on gynecology research and will essentially contribute in the future to the establishment of novel diagnostic and therapeutic strategies in clinical gynecology.

26.7 Lab Protocol

The following protocol describes an easy model for the surgical induction of standardized intraperitoneal endometriotic lesions in mice and their noninvasive analysis by means of high-resolution ultrasound imaging:

1. To exclude discrepancies of sex hormone levels between individual mice, female animals of the same stage of the estrous cycle are selected. For this purpose, 15 µl of 0.9% saline are carefully pipetted into the vagina and subsequently transferred on a glass slide for examination under a phase contrast microscope. The four different cycle stages can easily be distinguished by their typical cytology: Proestrus (nucleated epithelia and leukocytes), estrus (cornified epithelia), metestrus (cornified epithelia and leukocytes), and diestrus (leukocytes).
2. Donor mice are anesthetized by i.p. injection of ketamine (75 mg/kg body weight) and xylazine (15 mg/kg body weight).
3. Both uterine horns are removed and transferred in a Petri dish containing 37 °C warm Dulbecco's modified Eagle medium (DMEM; 10% fetal calf serum, 100 U/mL penicillin, 0.1 mg/mL streptomycin).
4. The uterine horns are opened longitudinally with micro-scissors under a stereomicroscope and tissue samples of comparable size are removed using a 2-mm dermal biopsy punch.
5. For induction of intraperitoneal endometriotic lesions, the recipient animals are anesthetized by i.p. injection of ketamine/xylazine. After midline incision one tissue sample per quadrant is fixed with a 7–0 Prolene suture to the peritoneal wall.
6. The laparotomy is closed again with a 6–0 Prolene muscle and skin suture. During the

following weeks to months, the developing endometriotic lesions can be repetitively analyzed by high-resolution ultrasound imaging.

7. For ultrasound image acquisition, mice are anesthetized with 2 % isoflurane in oxygen and fixed in supine position on a heated stage.
8. After chemical depilation of the abdomen to prevent air trapped in the fur from interfering with ultrasound coupling into the animal, ultrasound coupling gel is applied to the skin.
9. Subsequent ultrasound imaging of developing endometriotic lesions, their cysts and adhesion formation can, for example, be performed with a Vevo 770 high-resolution imaging system and a 704 scanhead (VisualSonics, Toronto, ON, Canada) with a center frequency of 40 MHz and a focal depth of 6 mm (Fig. 26.4).

References

Akirav C, Lu Y, Mu J, Qu DW, Zhou YQ, Slevin J, Holmyard D, Foster FS, Adamson SL. Ultrasonic detection and developmental changes in calcification of the placenta during normal pregnancy in mice. Placenta. 2005;26(2-3):129–37.

Bar-Joseph H, Ben-Aharon I, Tzabari M, Tsarfaty G, Stemmer SM, Shalgi R. In vivo bioimaging as a novel strategy to detect doxorubicin-induced damage to gonadal blood vessels. PLoS One. 2011;6(9):e23492.

Becker CM, Wright RD, Satchi-Fainaro R, Funakoshi T, Folkman J, Kung AL, D'Amato RJ. A novel noninvasive model of endometriosis for monitoring the efficacy of antiangiogenic therapy. Am J Pathol. 2006;168(6):2074–84.

Dinulescu DM, Ince TA, Quade BJ, Shafer SA, Crowley D, Jacks T. Role of K-ras and Pten in the development of mouse models of endometriosis and endometrioid ovarian cancer. Nat Med. 2005;11(1):63–70.

Fassbender M, Hildebrandt TB, Paris MC, Colenbrander B, Jewgenow K. High-resolution ultrasonography of xenografted domestic cat ovarian cortex. J Reprod Dev. 2007;53(5):1023–34.

Flecknell P. Replacement, reduction and refinement. ALTEX. 2002;19(2):73–8.

Grümmer R. Animal models in endometriosis research. Hum Reprod Update. 2006;12(5):641–9.

Hensley H, Quinn BA, Wolf RL, Litwin SL, Mabuchi S, Williams SJ, Williams C, Hamilton TC, Connolly DC. Magnetic resonance imaging for detection and determination of tumor volume in a genetically engineered mouse model of ovarian cancer. Cancer Biol Ther. 2007;6(11):1717–25.

Israely T, Dafni H, Granot D, Nevo N, Tsafriri A, Neeman M. Vascular remodeling and angiogenesis in ectopic ovarian transplants: a crucial role of pericytes and vascular smooth muscle cells in maintenance of ovarian grafts. Biol Reprod. 2003;68(6):2055–64.

Israely T, Dafni H, Nevo N, Tsafriri A, Neeman M. Angiogenesis in ectopic ovarian xenotransplantation: multiparameter characterization of the neovasculature by dynamic contrast-enhanced MRI. Magn Reson Med. 2004;52(4):741–50.

Jaiswal RS, Singh J, Adams GP. High-resolution ultrasound biomicroscopy for monitoring ovarian structures in mice. Reprod Biol Endocrinol. 2009;7:69.

Jansen SA, Conzen SD, Fan X, Krausz T, Zamora M, Foxley S, River J, Newstead GM, Karczmar GS. Detection of in situ mammary cancer in a transgenic mouse model: in vitro and in vivo MRI studies demonstrate histopathologic correlation. Phys Med Biol. 2008;53(19):5481–93.

Khankin EV, Mandala M, Colton I, Karumanchi SA, Osol G. Hemodynamic, vascular, and reproductive impact of FMS-like tyrosine kinase 1 (FLT1) blockade on the uteroplacental circulation during normal mouse pregnancy. Biol Reprod. 2012;86(2):57.

Laschke MW, Menger MD. In vitro and in vivo approaches to study angiogenesis in the pathophysiology and therapy of endometriosis. Hum Reprod Update. 2007; 13(4):331–42.

Laschke MW, Menger MD, Vollmar B. Ovariectomy improves neovascularization and microcirculation of freely transplanted ovarian follicles. J Endocrinol. 2002;172(3):535–44.

Laschke MW, Menger MD, Vollmar B. Cryopreservation does not affect neovascularization of freely transplanted ovarian follicles. Fertil Steril. 2003;79(6):1458–60.

Laschke MW, Körbel C, Rudzitis-Auth J, Gashaw I, Reinhardt M, Hauff P, Zollner TM, Menger MD. High-resolution ultrasound imaging: a novel technique for the noninvasive in vivo analysis of endometriotic lesion and cyst formation in small animal models. Am J Pathol. 2010;176(2):585–93.

Lee HJ, Lee HJ, Lee JM, Chang Y, Woo ST. Ultrasmall superparamagnetic iron oxides enhanced MR imaging in rats with experimentally induced endometriosis. Magn Reson Imaging. 2012;30(6):860–8.

Lin YH, Yeh YC, Tzeng CR, Shang WJ, Liu JY, Chen CH. Evaluating the effects of immunosuppression by in-vivo bioluminescence imaging after allotransplantation of ovarian grafts. Reprod Biomed Online. 2011;22(2):220–7.

Menger MD, Laschke MW, Vollmar B. Viewing the microcirculation through the window: some twenty years experience with the hamster dorsal skinfold chamber. Eur Surg Res. 2002;34(1–2):83–91.

Mu J, Adamson SL. Developmental changes in hemodynamics of uterine artery, utero- and umbilicoplacental, and vitelline circulations in mouse throughout gestation. Am J Physiol Heart Circ Physiol. 2006;291(3):H1421–8.

Mu J, Slevin JC, Qu D, McCormick S, Adamson SL. In vivo quantification of embryonic and placental growth

during gestation in mice using micro-ultrasound. Reprod Biol Endocrinol. 2008;6:34.
Pallares P, Gonzalez-Bulnes A. The feasibility of ultrasound biomicroscopy for non-invasive and sequential assessment of ovarian features in rodents. Reprod Biol. 2008;8(3):279–84.
Rossant J, Cross JC. Placental development: lessons from mouse mutants. Nat Rev Genet. 2001;2(7):538–48.
Salomon LJ, Siauve N, Taillieu F, Balvay D, Vayssettes C, Frija G, Ville Y, Cuénod CA, Clément O. In vivo dynamic MRI measurement of the noradrenaline-induced reduction in placental blood flow in mice. Placenta. 2006;27(9-10):1007–13.
Schreinemacher MH, Backes WH, Slenter JM, Xanthoulea S, Delvoux B, van Winden L, Beets-Tan RG, Evers JL, Dunselman GA, Romano A. Towards endometriosis diagnosis by gadofosveset-trisodium enhanced magnetic resonance imaging. PLoS One. 2012;7(3):e33241.
Stephenson AP, Tyler DJ, Carr CA, Williams SA. Magnetic resonance imaging for the study of ovarian follicles in the mouse. Theriogenology. 2012;78(6):1190–8.
Taillieu F, Salomon LJ, Siauve N, Clément O, Faye N, Balvay D, Vayssettes C, Frija G, Ville Y, Cuenod CA. Placental perfusion and permeability: simultaneous assessment with dual-echo contrast-enhanced MR imaging in mice. Radiology. 2006;241(3):737–45.
Tempel-Brami C, Neeman M. Non-invasive analysis of rat ovarian angiogenesis by MRI. Mol Cell Endocrinol. 2002;187(1–2):19–22.
Tomlinson TM, Garbow JR, Anderson JR, Engelbach JA, Nelson DM, Sadovsky Y. Magnetic resonance imaging of hypoxic injury to the murine placenta. Am J Physiol Regul Integr Comp Physiol. 2010;298(2):R312–9.
Vollmar B, Laschke MW, Rohan R, Koenig J, Menger MD. In vivo imaging of physiological angiogenesis from immature to preovulatory ovarian follicles. Am J Pathol. 2001;159(5):1661–70.
Walker CL, Hunter D, Everitt JI. Uterine leiomyoma in the Eker rat: a unique model for important diseases of women. Genes Chromosomes Cancer. 2003;38(4):349–56.

Imaging in Cardiovascular Research

27

Michael Schäfers, Michael Kuhlmann,
Lars Stegger, Klaus Schäfers, and Sven Hermann

Contents

M. Schäfers (✉) • L. Stegger
Department of Nuclear Medicine, University Hospital Münster, UKM, Münster, Germany
e-mail: michael.schaefers@uni-muenster.de

M. Kuhlmann • K. Schäfers • S. Hermann
European Institute for Molecular Imaging – EIMI
University of Münster Mendelstr, Münster, Germany

27.1 Clinical Challenges in Cardiovascular Medicine: Rationale for Basic Cardiovascular Research Involving Small Animal Imaging

Cardiovascular events most frequently stem from vascular diseases, namely, atherosclerosis, with the clinical sequelae myocardial infarction or stroke. These clinical scenarios result from complex inflammatory changes in the vascular wall (atherosclerotic plaques). If these plaques are mechanically unstable ("vulnerable"), a rupture or erosion of the plaque surface may eventually lead to thrombosis with partial or complete occlusion of the respective vessel. Organs heavily depending on the blood supply by arteries such as the heart or the brain thus suffer from severe acute ischaemia. Despite optimised therapy regimes (acute PCI, thrombolytic therapies, anti-ischaemic medical strategies, etc.), a significant loss of cells due to apoptosis and necrosis is observed in many cases with clinical consequences ranging from dysfunction to disability to death.

The incidence of chronic heart failure, a widespread cardiac disease resulting from acute or recurrent myocardial infarctions, long-term hypertension, valve diseases or cardiomyopathies is dramatically increasing worldwide. The risk for heart failure approximately doubles with each decade of life. Although the progressive decline in cardiac contractile function is responsible for

F. Kiessling et al. (eds.), *Small Animal Imaging*, DOI 10.1007/978-3-319-42202-2_27

the majority of deaths due to heart failure, other deadly events might also occur from acute severe tachyarrhythmias. Despite highly potent medical therapies, the prognosis of heart failure patients is as poor as for patients with advanced tumour diseases. Prognosis in heart failure is influenced by vascular and myocardial factors.

The armamentarium of established diagnostic clinical tools (ECG, angiography, perfusion SPECT and other stress tests, etc.) together with recently emerging improvements in imaging technologies such as three-dimensional echocardiography, multi-slice/dual source computed tomography (MSCT) or magnetic resonance imaging (MRI) allows for a detailed characterisation of the cardiovascular system in men. However, these imaging modalities only provide insight into the morphological and/or functional consequences of cardiovascular diseases (coronary artery stenoses, cardiac dilation and hypertrophy, arrhythmias, perfusion deficits, impaired contractile function, etc.) and do not assess the underlying cellular and molecular pathophysiology of the respective diseases. On the other hand, significant new insight into the molecular basis of cardiovascular diseases has been gained from genetic screening and the development and application of transgenic animal models.

Atherosclerosis associated with the life-threatening risk of plaque ruptures is a good example of a cardiovascular disease where individual risk stratification is currently impossible. The initial atherosclerotic lesion can be triggered by various noxae, hypercholesterolaemia, arterial hypertension, smoking and such, primarily damaging the endothelium (endothelial dysfunction). In the course of the disease, the endothelium aims at neutralisation of the initial noxae. If this is unsuccessful, a chronic inflammation of the vessel wall results. The inflammation is characterised and driven by infiltration of cells into the vessel wall, resulting in the long term in a complex lesion (plaque) composed of activated macrophages/foam cells, T lymphocytes, mast cells, etc. around a necrotic lipid-rich core. Plaques can be occlusive and be detected by clinical signs such as pectoral angina and shortness of breath. The much more dangerous type of an atherosclerotic lesion is the unstable "vulnerable" plaque, which can suddenly rupture expelling the thrombogenic plaque content into the blood stream triggering a thrombotic vessel occlusion and the clinical sequelae myocardial infarction or stroke.

A clinically available strategy towards risk stratification of individuals is based on analysing known risk factors for atherosclerosis such as age, sex, smoking, positive family history, diabetes and such, which were identified by large epidemiological studies. These findings have been implemented into risk calculators, which can excellently predict risk for a group of patients (e.g. HeartScore of the European Society of Cardiology, http://www.heartscore.org). However, even these approaches finally fail to identify individual risk. This means that current medicine will have to treat more patients than needed. For example, in a typical high-risk group of patients, which is identified by risk factor analysis, the maximum 10-year risk for cardiovascular events can only be as high as 20–40 %. This implies that only every third to fifth patient will suffer from the event. Since we cannot identify these patients, we will preventively have to treat all patients.

Amongst other strategies such as blood biomarker analysis, vascular imaging for direct assessment/visualisation of the specific processes involved in atherosclerosis in a single patient is expected to contribute to the individual risk assessment in the future. Current imaging technologies, which are predominantly based on morphological and functional imaging approaches of vessels and the myocardium, seem to fail in this respect. Conventional angiography can only detect coronary artery stenoses and is blinded to the vessel wall, whereas high-resolution MSCT can add information on calcium deposition and even non-calcified soft plaques in the vessel wall. However, although these diagnostic tools can identify coronary artery disease with high sensitivity, their specificity with respect to the prediction of individual outcome and future cardiovascular events remains limited. Again, the weakness of the morphological imaging approaches might be explained by the fact that these see only secondary disease processes but

not the molecular mechanisms that are decisive for the progression and outcome of the disease. In the case of atherosclerosis, it is now well understood that the molecular composition of an atherosclerotic plaque is determining its fate rather than its size. About 50 % of cardiovascular events result from low-degree stenosis – diameter narrowing of the vessel of less than 50 % (Falk et al. 1995). Molecular targets are therefore the focus of research; the development of both target-specific molecular imaging and therapies promises substantial clinical innovations and improvements.

Another example for a clinical challenge unmet by imaging of the basic pathophysiology is the field of life-threatening tachyarrhythmias, which can occur in a broad spectrum of diseases ranging from idiopathic diseases including the inherited cardiomyopathies to coronary artery disease. Although these tachyarrhythmias can be described and characterised by Holter recordings, electrophysiological studies, etc., prediction of the individual risk for future arrhythmic events remains a challenge currently unmet by any diagnostic technology. In the case of tachyarrhythmias, it is well known that amongst others electrical changes on the level of the affected myocardium and disturbances in nerve function can trigger events. In the latter respect, sympathetic nerves play an important role. Again, their function can be assessed by molecular imaging technologies quantifying catecholamine recycling, β-adrenoceptor density and such. First studies have already demonstrated that these molecular imaging approaches can identify patients at risk for future cardiovascular events. The combination of molecular imaging with emerging knowledge about the genetic background of various different types of tachyarrhythmias may pave the way for a better risk estimation for future arrhythmic events.

These facts justify an intense research effort towards both new diagnostic and therapeutic approaches with a special focus on the prevention of cardiovascular events. In this field of basic and translational cardiovascular research, high-resolution imaging in small animals recently became a substantial tool; an overview is given here.

Small animal imaging can be and is frequently used in different aspects of basic and translational cardiovascular research:

- *Phenotyping*. Imaging to characterise genetic or surgical mouse models mimicking human cardiovascular diseases. Phenotyping of new and existing animal models is substantially supported by functional and molecular small animal imaging, especially since small animal imaging characteristically can be performed non-invasively and serially in individual animal. Furthermore, whole-body imaging is a particular value to discover pathologies developing in organs "outside" the focus of the study.
- *Monitoring*. Imaging to monitor morphological, functional and molecular changes induced by interventional studies (pharmaceutical treatment, surgical intervention, gene therapy, stem cell therapy). Again, serial non-invasive imaging studies do allow to assess intra-individual changes in a few animals.
- *Development*. Since the majority of clinical cardiovascular imaging devices are now available in a "miniaturised" fashion for small animal imaging with similar imaging characteristics, it seems straightforward to use small animal imaging in validation studies to characterise new imaging approaches in animal models first and then translate into clinical imaging by using the analogous clinical imaging modality. This is especially useful when testing new imaging probes for molecular imaging (contrast agents, radiopharmaceutical, optical dyes, etc.).

27.2 Mouse Models of Human Cardiovascular Diseases: Basis for Small Animal Imaging in Cardiovascular Research

Appropriate animal models, mimicking the pathology of cardiovascular human diseases, are essential for progress in the field of cardiovascular research and for the transfer of preclinical

results into the clinical setting. In principle, a variety of animal species can be used in cardiovascular research. Although larger animals such as pigs (a classical model for myocardial infarction) are used in cardiovascular research, in the context of this book, only small animal models in rats and mice are being discussed.

Animal models of cardiovascular diseases can rely both on genetic manipulations and surgical interventions and do nowadays cover the wide spectrum of cardiovascular human diseases. In this context, examples for relevant human cardiovascular diseases, myocardial infarction and atherosclerosis, already being studied by small animal imaging rather than a complete overview, are given.

27.2.1 Myocardial, Peripheral and Cerebral Ischaemia

Induction of acute myocardial infarction – permanent and transient occlusion Acute myocardial infarction can be induced in mice by a surgical intervention, in which the left ventricular blood supply will be interrupted by a permanent or transient ligation of the left anterior descending (LAD) coronary artery (Kuhlmann et al. 2006). Depending on the length of ischaemia and the length of reperfusion in the case of non-permanent ligation, the degree of ischaemic damage and scar formation can be varied. However, reproducibility with respect to the amount of ischaemic tissue, scarring and localisation is limited by a quite variable coronary anatomy in mice. These models can either be performed in wild-type or transgenic mouse models.

Induction of cerebral ischaemia – stroke model The classical animal model resembling human stroke is the so-called middle cerebral artery occlusion (MCAO) model. In this model, a thin thread is inserted into the A. carotis interna and guided into the A. cerebri media, which in turn is occluded by the thread. The resulting ischaemia in the media territory causes focal lesions resembling the clinical situation of stroke. The procedure is typically controlled by measuring the regional brain perfusion by a specialised laser Doppler device (Klohs et al. 2009).

Peripheral ischaemia – hind limb model In the hind limb model, permanent unilateral ligation of the A. femoralis induces chronic peripheral ischaemia – a pathophysiological situation often associated with diabetes and smoking in patients. This model drives neoangiogenesis to circumvent the femoral artery ligation and is therefore often employed when imaging of angiogenesis is in the focus (Dobrucki et al. 2009).

27.2.2 Non-ischaemic Heart Failure

Transverse Aortic Constriction (TAC) Non-ischaemic heart failure can be induced in mice by a surgical intervention, the so-called transverse aortic constriction (TAC) model. Here, the aortic arch is partially constricted by using a surgically introduced thread inducing cardiac pressure overload, finally resulting in pathological hypertrophy and subsequently dilative cardiomyopathy (Tsujita et al. 2005).

Genetically triggered heart failure Besides the surgical approaches to induce heart failure, different genetically determined models have been developed. A good example is the survivin-knockout mouse. Survivin belongs to the class of inhibitors of apoptosis proteins (IAPs); its knockout is resulting in a spontaneous progressive heart failure (Levkau et al. 2008).

27.2.3 Atherosclerosis

Transgenic mouse models to produce spontaneous atherosclerosis When fed a normal and species-appropriate diet, mice or rats do typically not develop any human-like atherosclerosis in their lifetime. Therefore, metabolic changes incurred by gene knock-in or knockout with additional diets, e.g. cholesterol-rich food, have to be employed to produce atherosclerosis. Typical examples are the apolipoprotein E-knockout

(ApoE$^{-/-}$) and the lipoprotein receptor knockout mouse, which both do spontaneously present with hypercholesterolaemia when compared with their littermates, which in the long runs (weeks) results in atherosclerosis at predilection sites such as the aortic root, the aortic arch and the brachiocephalic artery. When feeding high-cholesterol diets, the progression of the atherosclerosis is accelerated, and the inflammation within the vascular lesions is enhanced (Zhang et al. 1992).

Surgical local induction of atherosclerotic lesions Based on the above-mentioned genetically determined atherosclerosis models, local lesions can be triggered by surgical interventions aiming at endothelial damage. Unilateral ligation of the common carotid artery in ApoE$^{-/-}$knockout mice causes a vascular remodelling, resulting in highly inflammatory plaque-like vascular lesions within 4 weeks (Ivan et al. 2002). Another model for inducing endothelial damage, thrombosis and vascular remodelling is the wire-induced endothelial disruption, where the endothelium of the carotid artery is surgically injured by a wire (Manka et al. 2000). In contrast to the carotid ligation model, the surgical procedure is more sophisticated, but has the advantage of affecting the common carotid artery on its whole run. Since these models are based on relatively harsh, non-pathophysiological interventions, another model of carotid atherosclerosis induction was recently introduced, the shear stress-induced arteriosclerotic plaque development ("cast" model). This model employs the surgical placement of a small plastic collar (cast), consisting of two longitudinal halves of a cylinder, forming together a cone-shaped lumen, around one common carotid artery producing a carotid stenosis. Upstream of the site of constriction, lowered shear stress induces plaque development in the western diet-fed ApoE$^{-/-}$ mouse (Cheng et al. 2006).

Models for spontaneous myocardial infarction The above-described models of atherosclerosis typically do not exhibit signs of unstable plaques and plaque rupture and do not result in the clinical sequelae myocardial infarction or stroke. Therefore, a great interest exists with respect to new models. A good example towards more human-like models is the model of diet-induced occlusive coronary atherosclerosis in SrB1$^{-/-}$/ApoE-R61$^{h/h}$ mice. In this mouse, two genes involved in lipid metabolism are modified: the HDL scavenger receptor class B, type 1 (SrB1), is knocked out, and in addition, mice of that strain express a mutant form of murine ApoE, Thr61 → Arg61 (Arg-61ApoE) (Zhang et al. 2005). When fed with a high-fat/high-cholesterol (HFC) diet, atherosclerosis rapidly progresses, including massive plaque deposition, plaque rupture, occlusive coronary events and myocardial infarctions, causing death within approximately 4 weeks after onset of the HFC diet (Hermann et al. 2016).

27.3 Applications of High-Resolution Small Animal Imaging in Cardiovascular Research: Examples

27.3.1 Computed Tomography

Over the past three decades, micro-CT imaging has rapidly advanced with higher quality resolution, the introduction of the cone beam reconstruction algorithm and an increased availability of dedicated scanners for non-invasive small animal imaging research. To achieve the same resolution in relation to object size between human and small animal CT systems, small animal CTs have to be designed with spatial resolutions of 100 μm or better. This is especially true when it comes to imaging of the heart and vessels in mice in vivo, where respiratory and cardiac movement additionally degrades image quality. Currently CT imaging of the heart and vessels of a living mouse therefore remains a huge challenge. The typical design of a micro-CT involves a tube and a detector array which are rotated around the object slowly and noncontinuously (minutes), which results in a low or non-existent temporal resolution. With a heart rate of ~400 bpm under anaesthesia in mice, the movement of the heart and the vessels cannot be assessed by micro-CT, leading to blurring artefacts. It has been recently

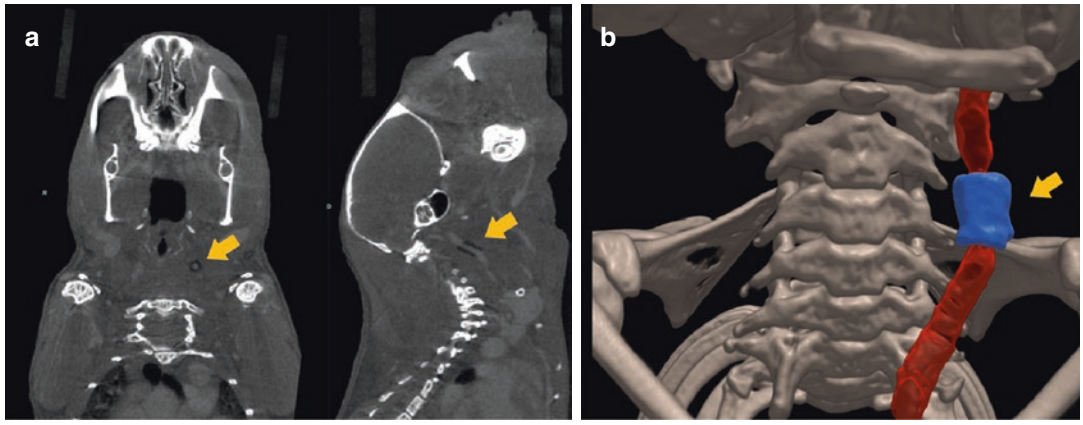

Fig. 27.1 High-resolution contrast-enhanced CT (Ultravist 300®) of a 25 g mouse where a small plastic cast is placed around the left carotid artery (*arrow*). (**a**) Shows horizontal and sagittal sections and (**b**) shows a segmentation and rendering of the left common carotid artery (*red*) and the surrounding cast (*blue*)

shown that using special prospective triggering algorithms or employing fast flat panel technology CT imaging of the heart cycle is feasible (Dinkel et al. 2008). However, these scans do characteristically increase radiation dose and need a stable contrast enhancement resulting in an intravenously injected iodinated contrast agent to achieve good image contrast between vessels, the myocardium and surrounding tissues. While the radiation dose is primarily an important issue when studying individual animals serially over time, the use of contrast agents remains a challenge. Contrast agents with a long blood circulation time, which are unfortunately currently rather expensive, can be used or are clinically available. The latter have to be combined with an "intelligent" infusion protocol to balance a stable contrast with a volume limited as much as possible.

With these prerequisites, small animal CT in cardiovascular applications so far has mainly been used in comparative studies, where a PET, SPECT or fluorescence signal is overlaid on the CT to project a molecular signal onto morphology.

Vascular anatomy As detailed above, the imaging of small-calibre arteries in mice and rats remains a significant challenge. Therefore, publications describing micro-CT applications in the aorta or coronary arteries in mice are rare to nonexistent. The principal feasibility of imaging small arteries was recently nicely demonstrated by Kiessling et al. and Schambach et al., which imaged tumour-supplying vessels and cerebrovascular structures at resolutions of 50 µm and better in mice (Kiessling et al. 2004; Schambach et al. 2009).

New CT technology will most likely further advance the field. Recently, using a novel carbon nanotube (CNT)-based x-ray source, it has been demonstrated that vascular calcifications in the course of atherosclerosis can be imaged in ApoE$^{-/-}$ mice (Wait et al. 2013) (see Fig. 27.1).

Imaging of the heart As is true for vascular CT applications in mice, small animal CT in mouse or rat hearts has been only rarely reported. However, studies have shown the principle feasibility of imaging heart anatomy and infarct size by delayed contrast enhancement employing long-circulating contrast agents (Dinkel et al. 2008; Nahrendorf et al. 2007) (see Fig. 27.2).

27.3.2 Ultrasound

Ventricular morphology and function Due to substantial technical improvements, ultrasound has become a key imaging technology for phenotypisation of murine models in cardiovascular research. Echocardiography is ideally suited for cardiac phenotypisation and assessment of left

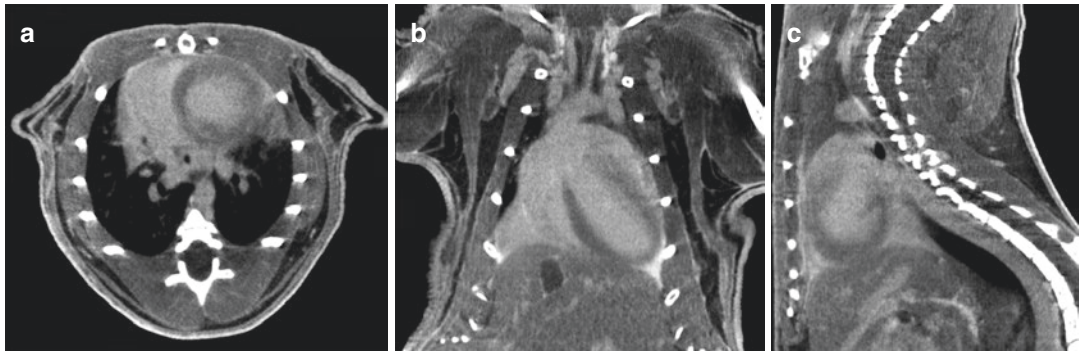

Fig. 27.2 Contrast-enhanced CT of a 23 g mouse (Ultravist 300®). Sectional images (**a** transaxial, **b** horizontal, **c** sagittal) show a good contrast of the blood in the vessels and the ventricles of the heart to the surrounding tissues and the myocardium

ventricular function since it is a real-time method which requires minimal instrumentation of the mouse, allows fast imaging protocols and can be thereby applied even in models with severely impaired physical conditions. Most recent transducer technology ranges from single-element transducers which offer a unique spatial resolution to linear array probes which allow duplex or triplex imaging to 4D matrix transducers. This wide range of available systems.

A major hallmark in phenotypisation is systolic left ventricular function. Higher transducer frequencies as well as higher frame rates allow proper assessment of chamber dimensions, wall thickness and global as well as regional left ventricular function (Collins et al. 2003; Gao et al. 2000). In adult mice, the symmetric shape of the ventricle allows proper assessment of LV wall thickness, LV mass and global-regional function assessed by M-mode using the Teichholz formula. However, in asymmetrically shaped ventricles (e.g. newborn or juvenile mice) or particularly in infarct models, M-mode technology is not adequate for the assessment of left ventricular mass and function (Ghanem et al. 2006). 2D and most recently 3D echocardiographies have been proposed as the ideal technology for the assessment of mass and function in transgenic models presenting with asymmetrically shaped ventricles or most importantly cardiac infarction models (Gao et al. 2000; Dawson et al. 2004; Ghanem et al. 2008). High-resolution ultrasound was found to be suitable to characterise the scar border zone in infarct models and to precisely assess regional ventricular function (Ghanem et al. 2008). Specialised imaging acquisition algorithms allow frame rates of up to 1,000 Hz and offer thereby a unique inside into regional ventricular function. Stress echocardiography has been found to be suitable to identify viable myocardium and to assess contractile reserve. In general, 2D echocardiography applying mathematical models such as the area-length method or the truncated ellipsoid model is sufficient for the assessment of global left ventricular function and left ventricular mass (Collins et al. 2001; Tiemann et al. 2003). In more complex models, reconstructive or real-time 3D echocardiography is more accurate and superior to 1D or 2D echocardiography (Ghanem et al. 2006; Dawson et al. 2004). LV chamber dimensions, wall thickness and function can be assessed either in conscious mice or using volatile anaesthesia to avoid cardiodepressive effects as seen by, e.g. ketamine/xylazine.

2D echocardiography can be used to analyse the shape and the ventricular geometry, allows identifying missing or extra structures and is suited to identify structures such as thrombus formation or pericardial effusion. In addition, diastolic function can be assessed using Doppler technology (PW Doppler of mitral inflow), tissue Doppler imaging (TDI) or volume-time curves derived by 4D echocardiography. These techniques have been applied in models of hypertrophy, heart failure and others. Doppler ultrasound, particularly colour Doppler, allows to demonstrate shunt flow in congenital

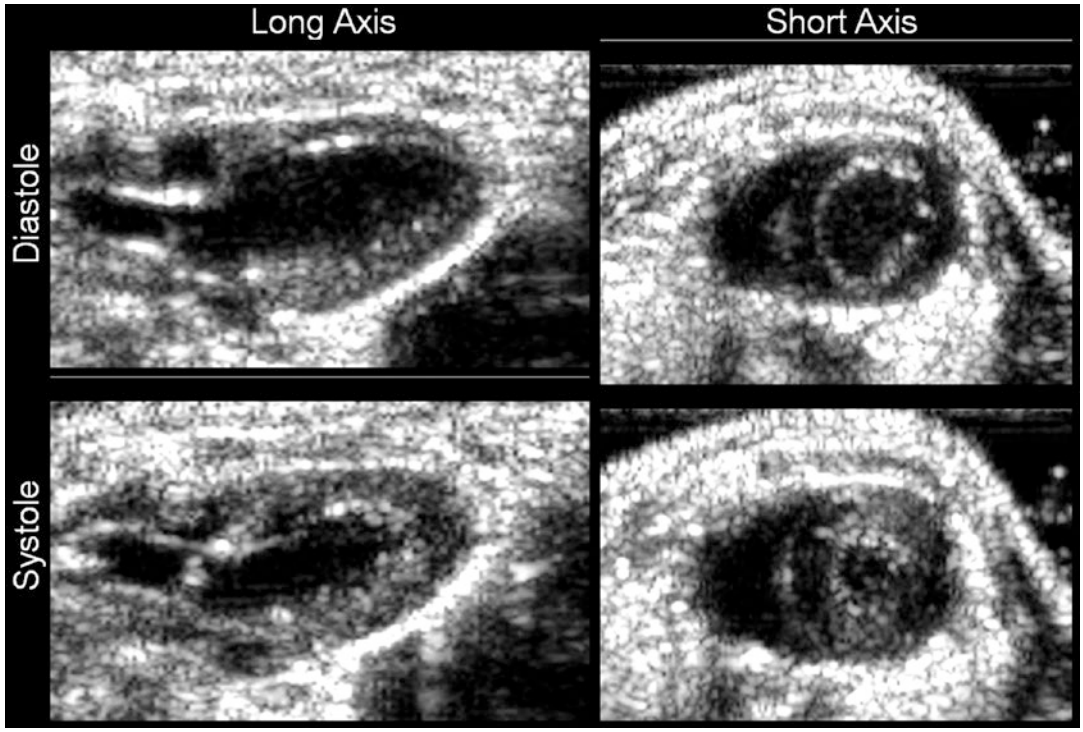

Fig. 27.3 High-resolution murine echocardiography (30 MHz). Morphology and function of the murine heart can be nicely visualised and quantitatively assessed. Frame rates of up to 1,000 Hz provide an excellent temporal resolution

heart disease. In adult mice, morphology and function of the heart valves, particularly the mitral valve and aortic valve, can be assessed by 2D echocardiography. In addition, regurgitated or stenotic flow can be quantified and characterised by PW Doppler technology. However, morphological and visual assessment of valvular geometry and function is limited due to spatial and temporal resolution. Thus, the current gold standard for evaluation is Doppler technology. New high-resolution imaging probes allow the morphological and functional assessment of left ventricular structures even in utero (Gui et al. 1996; Yu et al. 2008). Due to constant movements, quantification is, however, limited (see Fig. 27.3).

Vascular anatomy There are several mouse models of arteriosclerosis available today which mimic lesion phenotypes comparable to human disease. Transgene murine models as well as operative manipulations (wire injury, balloon injury or constrictive models) require high-resolution imaging technology for follow-up. Recent technical advances now offer real-time ultrasound imaging of vascular structures with a special resolution which allows the assessment of single plaques as well as total plaque burden (Gan et al. 2007). Larger structures such as the aorta and larger blood vessels can be easily identified by this technology. Branches from the aortic arch as well as intravascular thrombi can be assessed. Vessel morphology and wall thickness, pulse wave propagation and blood flow within the arteries can be analysed by 2D imaging, colour Doppler and PW Doppler technology. Identification and quantification of regional and total plaque burden are feasible by ultrasound biomicroscopy (Gan et al. 2007). This technology allows follow-up investigations in atherosclerotic models and thereby characterisation and quantification of plaque location and growth. Intracerebral blood vessels can be identified by PW Doppler technology, colour Doppler technology or even contrast ultrasound.

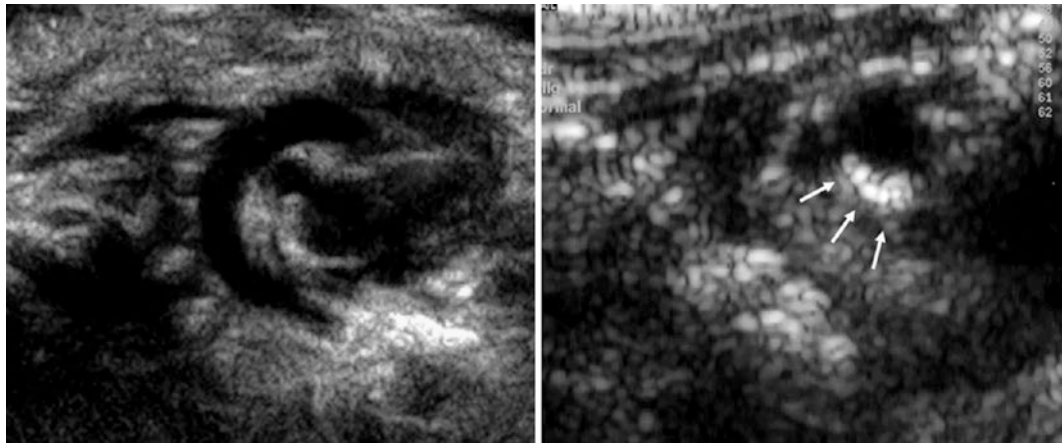

Fig. 27.4 *Left*: aortic arch in a healthy mouse. *Right*: cross-sectional view of the aortic arch demonstrating plaque formation (*arrows*) in a mouse model of atherosclerosis ($ApoE^{-/-}$)

Atherosclerotic plaques can be visualised and measured en face. Reconstructive 3D technology allows quantification of plaque volume/plaque burden. Close correlation between histomorphometry and ultrasonic assessment has been demonstrated (Gan et al. 2007). Reproducibility (intra- and interobservability) was very good using this new technology. Blood vessels down to the level of the coronary arteries can be assessed in real time, and blood flow within these vessels can be obtained. Assessment of intima-media thickness and elasticity of the blood vessel in atherosclerotic plaques is feasible by ultrasound biomicroscopy with the advent of high-resolution linear area transducers; the limitation in even smaller blood vessels needs to be elucidated. In vivo assessment of plaque formation allows further insight in plaque development, particularly since, e.g. intravital thrombus formation can be visualised, which is somehow difficult to assess by histological techniques (see Fig. 27.4).

Perfusion Contrast-specific imaging modalities opened new arena for murine echocardiography. Tissue perfusion at the level of coronary microcirculation has become possible and allows visual assessment of regional perfusion, perfusion defects, quantification of risk area and infarct size (Scherrer-Crosbie et al. 2000). It has been demonstrated that perfusion imaging is superior to wall motion analysis in the assessment of infarct size and risk area. Contrast-specific imaging probes allow sufficient spatial and temporal resolution for perfusion imaging and provide real-time segmentation of tissue and regional blood volume. Commercially available as well as custom-made microbubbles have been used for this purpose (Scherrer-Crosbie et al. 2007). Besides qualitative assessment of tissue perfusion, infarct size and risk area, quantitative approaches have been proposed. This technology relies on the ultrasound-mediated destruction of contrast microbubbles and the assessment of replenishment rate at the level of microcirculation. Mathematical modelling of contrast replenishment allows the assessment of regional blood volume as well as replenishment rate and therefore allows the assessment of even absolute myocardial blood flow (Thibault et al. 2005; Vogel et al. 2005) (see Fig. 27.5).

Molecular targeting Molecular targeting, particularly of vascular epitopes, has become feasible due to the introduction of contrast microbubbles and contrast-specific imaging modalities. Ultrasound contrast agents (microbubbles) remain strictly intravascular after intravenous or intraarterial injection. Different shell properties and the gas content characterise their resonance behaviour and therefore their contrast-specific detection by ultrasound as well as their stability within the sound field. Inert gases such

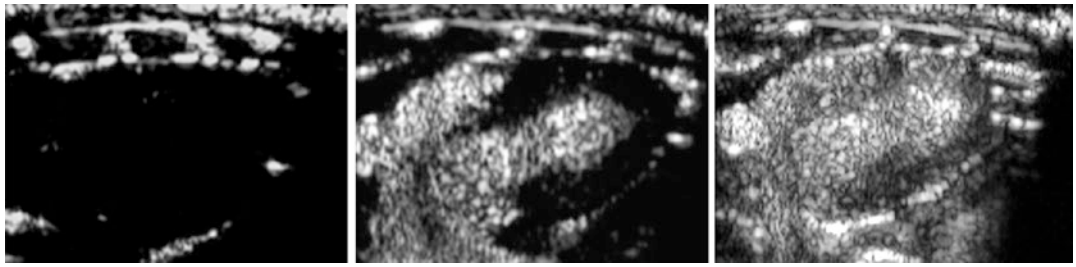

Fig. 27.5 Contrast-enhanced ultrasound (CEUS). *Left*: long-axis view of a murine heart in harmonic imaging mode. Note that almost no signals from the myocardium are visible in this mode. *Centre*: following i.v. injection of 0.05 ml of Optison®, opacification of the atria and chambers allows delineation of endocardial borders. Since the myocardium appears still black, an optimal signal-to-noise ratio is achieved. *Right*: intermittent imaging with refreshing the image once per cardiac cycle allows visualisation of myocardial microcirculation by CEUS

as perfluorocarbons make them ideally suited for ultrasound imaging. Particularly their destructive behaviour within the sound field provides a unique technology to visualise even single microbubbles (loss of correlation imaging). Molecular targeting relies either on intrinsic properties of the microbubble shell or the attachment of binding ligands. Phosphatidylserine-coated microbubbles, for example, stimulate the uptake of these particles by macrophages and have been therefore used for in vivo imaging of inflammatory cells. This type of imaging ("hotspot imaging") has been used to characterise inflammation in ischaemia-reperfusion models (Kunichika et al. 2003). Positively or negatively charged microbubbles can be used in addition to facilitate unspecific binding. In contrast, specific binding ligands have been added to microbubbles for target-specific binding. In cardiovascular models, particularly selectins and integrins have been used today to characterise early stages of atherosclerosis and to image various stages of the adhesion cascade (Lindner 2009). Intracellular adhesion molecules (ICAM-1, VCAM) and selectins such as P-selectin have been targeted (Kaufmann 2009). When combined with myocardial perfusion imaging, P-selectin has been found to serve as an "ischaemic memory". P-selectin-specific binding demonstrated a late-phase effect due to upregulation of P-selectin in a previously ischaemic area. Multimodality imaging (contrast perfusion imaging, 2D wall motion assessment and molecular imaging) allows further insights and provides valuable information in addition to the molecular signal. Besides inflammation and early stages of atherosclerosis, $\alpha_v\beta_3$ has been addressed as a target for angiogenesis in infarct models. Again, in combination with perfusion and functional imaging, this molecular information can contribute to the understanding of vascular and ventricular remodelling after myocardial infarction. Although this technology was suitable in areas of microcirculation, a general problem of contrast microbubbles was the inability to bind in high-flow scenarios such as the aorta or larger arteries. The addition of Sialyl Lewis^X has been found to overcome this limitation. Mimicking, rolling and sticking of leucocytes by Sialyl Lewis^X, the attachment of targeted microbubbles even in high-flow settings such as the aorta could be demonstrated. Kaufmann et al. used P-selectin as an early marker of atherosclerosis with Sialyl Lewis^X-labelled microbubbles and could demonstrate specific binding to P-selectin even in the aortic arch (Kaufmann 2009). Smaller particles (contrast nanoparticles) have been used to image thrombus formation in the blood vessels. However, there are technical limitations to image contrast particles which are smaller than 500 nm in size due to the resonance behaviour of these particles. Newer imaging strategies which might even address intracellular targets rely on the release of gas bubbles from these nanoparticles which might result in specific detection of even intracellular contrast agents.

Multimodality imaging taking advantage of contrast ultrasound for molecular targeting is a very interesting approach since imaging of

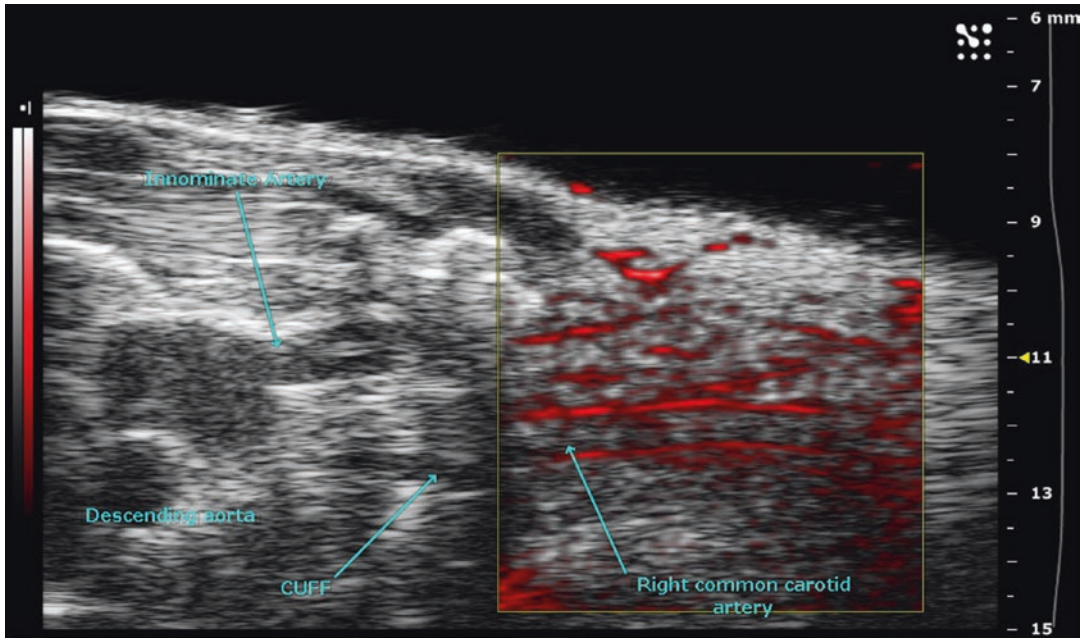

Fig. 27.6 Ultrasound-based imaging (40 MHz, *greyscale*) and photoacoustic window (850 nm, *coloured*) in an ApoE$^{-/-}$ mouse after implantation of a carotid cuff. Note the strong photoacoustic signal delineating the vascular wall of the right common carotid artery even without fluorochrome injection

strictly intravascular targets can be compared with technologies such as PET or optical imaging aiming for intracellular compartments. This complementary approach might offer new insights in the development of cardiovascular disease. The advent of smaller particles, the new imaging technologies including the active release of gas bubbles and the development of new ligands have to be evaluated for future research projects.

Photoacoustic imaging

A currently very actively promoted new, ultrasound-based imaging technology is the photoacoustic imaging, which also has a high potential for molecular imaging of vessels and the heart. As with fluorescence reflectance imaging, a pulsed laser is used to activate fluorochromes in tissues; however, the readout is not through emitted light but through waves being emitted from the heating of the fluorochromes by the laser. These waves are in the ultrasound range and can travel much longer distances in tissue than light, which results in a deeper imaging window in organisms (Razansky et al. 2012). Photoacoustic signals can be recorded even without contrast agents, e.g. haemoglobin has a very specific signal, which even differentiates between its oxygenated and deoxygenated form. Amongst others, Rouleau et al. recently provided a feasibility study for photoacoustic molecular imaging of the VCAM-1 expression in atherosclerotic plaques in vivo (Rouleau et al. 2013) (see Fig. 27.6).

27.3.3 Magnetic Resonance Imaging

As for the other imaging modalities discussed here, for small animal cardiovascular imaging, the heart and vessels of a mouse-/rat-sized animal pose significant challenges for the MRI technology with respect to spatial and temporal resolution. Since, per se, signal-to-noise ratios are dependent on the strength of the magnetic field of an MRI scanner, typically scanners with field strengths above 3 T have been used for small animal cardiovascular MRI studies (Tsui and Kraitchman 2009). Because of the small object size and fast heart rates in small animals,

MRI of the heart and vessels typically must be performed, employing both ECG and respiratory gating, which in itself is not straightforward in an MRI scanner on the basis of space restriction, influence of the MRI field on the ECG and other effects. This dual-gating approach provides unblurred images from either one stage of the cardiac cycle or a dynamic series of stages from the cardiac cycle. MRI is therefore often stated as the reference for the assessment of left and right ventricular volumes, myocardial wall thickness and ejection fraction. However, since – in contrast to clinical scanners – small animal MRI scanners are not able to acquire a three-dimensional volume in a short time but do a rather slow slice-by-slice filling of the k-space, significant inaccuracies (shifts, inconstistencies etc.) can be detected between slices of the volume due to unequal timing of the data acquisition in different slices. Furthermore, image acquisition time for multiple short- and long-axis views can result in imaging times, ranging from 30 min to several hours per animal also restricting an efficient "high-throughput" phenotyping of mouse models. New methods to image multiple mice simultaneously such as employing individual receiver coil arrays and parallel imaging techniques have been reported (Ramirez and Bankson 2007; Ramirez et al. 2007). However, these are currently not routinely available. To shorten acquisition time, image acquisition protocols without cardiac gating, where images are retrospectively reconstructed on the basis of a separately acquired navigator or the image data itself, have been proposed (Heijman et al. 2007). Herewith, imaging times can be reduced from several hours to a few minutes per imaging slice.

Vascular anatomy Starting already over 10 years ago, multiple studies have shown that the assessment of atherosclerosis progression in aortas of genetically engineered mice is feasible (Manka et al. 2000; Fayad et al. 1998). In the context of high-resolution imaging of small plaques in animal models of atherosclerosis, higher field strengths have been found advantageous for enhanced spatial resolution of the components of atherosclerotic plaques. With the use of paramagnetic blood-pool contrast agents (e.g. Gd-DTPA), MRI is well suited to visualise the lumen of arterial and venous vessels throughout the whole body in humans and animals. Conventional high-resolution MRI is furthermore capable of detecting lipid-rich atherosclerotic plaques in both human atherosclerosis and animal models of atherosclerosis. However, the spontaneous tissue contrast of the atherosclerotic vascular wall against neighbouring tissues is often limited. Therefore, new contrast agents have been tested. A good example is the use of paramagnetic liposomes. While in conventional multispectral MRI neointimal lesions in an ApoE$^{-/-}$ carotid cast model were not distinguishable from the surrounding neck tissue, Mulder et al. found that injecting paramagnetic liposomes with a mean size of 90 nm resulted in a pronounced signal enhancement of >100 % immediately after injection, which was sustained largely until 24 h postinjection (Mulder et al. 2006). In contrast, the vessel wall of all controls (left carotid artery and animals injected with Gd-DTPA) did not show significant contrast enhancement at those time points. Further alternative contrast agents to delineate atherosclerotic plaques are currently under investigation in humans and will most likely also be used in small animals soon (Ibrahim et al. 2009) (see Fig. 27.7).

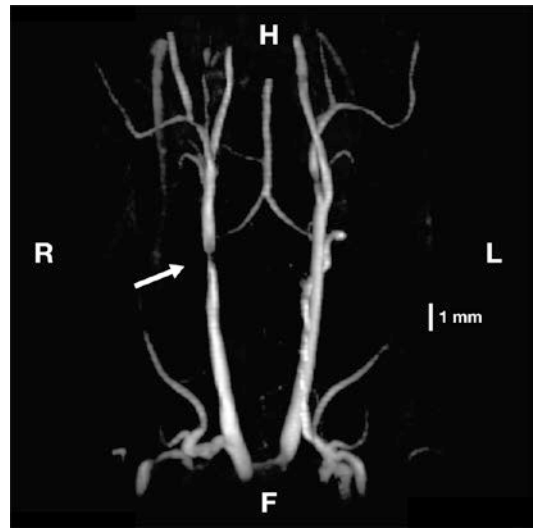

Fig. 27.7 MR angiography of the neck regions in a mouse showing constriction of the right carotid artery by a tapered cast (Image is a courtesy of G. Strijkers, TU Eindhoven, The Netherlands)

Ventricular anatomy and function As a first attempt to characterise the murine heart, various ECG-gated MRI sequences have been developed for quantifying left ventricular (LV) mass in mice. These methods have been shown to be highly accurate (Berr et al. 2005). In addition to LV mass, state-of-the-art sequences can also quantify wall thickness, wall thickening, LV volume for each cardiac phase and, subsequently, end-diastolic volume, end-systolic volume, stroke volume, cardiac output and EF. Multiple studies have employed this technology in wild-type and animal models of ischaemic or non-ischaemic heart failure (Levkau et al. 2008; Franco et al. 1999). Recently, it was demonstrated that measuring morphological and functional cardiac parameters in mice is also feasible with the use of a clinical 3 T-MRI with a dedicated small animal coil (Bunck et al. 2009). Although the wall is significantly thinner and the geometry is more complex, the right ventricle can also be assessed by cine MRI. Indeed, it has been shown that cine MRI at 7 T with in-plane spatial resolution of approximately 0.1*0.1 mm^2 can be used to quantify right ventricle function (Wiesmann et al. 2002). Similarly, high-resolution cine MRI at 7 T has also been successfully applied in the neonatal and juvenile mouse heart (Wiesmann et al. 2000).

Apart from the LV morphology and contractile function, left ventricular perfusion can be regionally assessed by first-pass imaging of contrast agents such as Gd-DTPA or quantitatively by arterial spin labelling (ASL). For long ASL has been the only quantitative MRI technique that has been developed for imaging myocardial perfusion in mice and was well validated by comparison to microspheres (Streif et al. 2005). However, high-end MRI techniques such as ASL have not seen many preclinical applications so far. Recently, a quantitative technique based on first-pass perfusion measurements in mice has been demonstrated (van Nierop et al. 2013).

The same is true for the imaging of myocardial viability in ischaemia/infarction mouse models by MRI. Conventional methods to quantify infarct size after myocardial infarction in mice are not ideal, requiring either tissue destruction for histology or relying on nondirect measurements such as wall motion. Bohl et al. therefore successfully implemented a fast, high-resolution method to directly measure infarct size in vivo using three-dimensional late gadolinium enhancement small animal MRI resembling the clinically established late enhancement protocol (Bohl et al. 2009). Established and emerging applications of contrast-enhanced MRI to characterise post-infarct myocardium have been reviewed (Coolen et al. 2012; Geelen et al. 2012) (see Fig. 27.8).

Molecular and cellular targeting Experience with cardiovascular molecular MRI in the myocardium and vessels is significantly less extensive than that with nuclear imaging agents, although in principle the characteristics of MRI make it well suited for myocardial imaging.

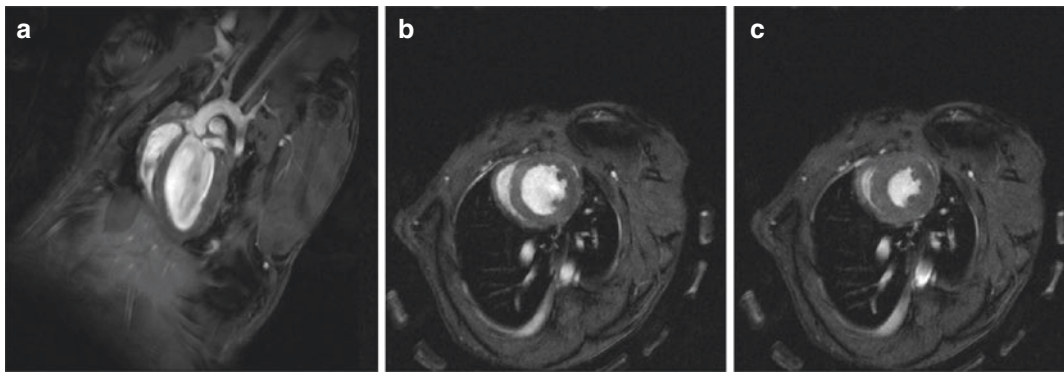

Fig. 27.8 Horizontal long-axis (**a**) and two short-axis images (**b**=end diastole, **c**=end systole) of a murine heart (Images are courtesy of G. Strijkers, TU Eindhoven, The Netherlands)

As reported above, MRI is able to assess a range of anatomical, physiological and functional parameters in the myocardium. Although the spatial resolution of MRI is excellent, its limitation when it comes to molecular imaging applications lies in its low sensitivity for the detection of conventional imaging agents (Sosnovik et al. 2007). To increase the sensitivity for cardiovascular molecular imaging, a variety of new gadolinium-containing contrast agents consisting of either small molecules or large supramolecular structures such as liposomes were developed (Mulder et al. 2007a). Furthermore, iron oxide-based magnetic nanoparticles have been developed and are now available for functionalisation by antibodies or other target-affine ligands (McAteer et al. 2009). Their small size (20–50 nm), long blood circulation and detectability at nanomolar sensitivity with T2-weighted pulse sequences make them particularly well suited for targeted imaging in the cardiovascular system.

An early attempt to targeted molecular cardiovascular MRI was the use of antimyosin antibodies labelled with iron oxide-based magnetic nanoparticles to image myocardial necrosis following acute myocardial infarction in rats (Weissleder et al. 1992).

In the same scenario of ischaemia/infarction as well as in heart failure, apoptosis plays an important role in cardiovascular pathophysiology. Small animal MRI in vivo using AnxCLIO-Cy5.5, an annexin-labelled magneto-fluorescent nanoparticle, has been successfully employed to study apoptosis in mice (Sosnovik et al. 2005).

Besides molecular targeting by functionalised contrast agents, non-functionalised contrast agents have also been used to label and track cells. For example, carbohydrate-coated magnetic nanoparticles are efficiently phagocytosed by macrophages and other cells. Using these myocardial macrophage infiltrations in infarct, healing was demonstrated recently (Nahrendorf et al. 2007). Using similar contrast agent constructs, stem cells injected into the myocardium can be followed and tracked by MRI (Ly et al. 2008). Flögel et al. showed that fluorocarbons which are phagocytosed by macrophages can be used in combination with ^{19}F-MRI to image macrophages with high contrast due to the lack of significant background noise in ^{19}F-MRI imaging (Flogel et al. 2008).

Besides myocardial applications of molecular MRI, a variety of applications are already pursued or can be foreseen for molecular MRI of atherosclerotic plaques, where inflammatory cells and molecular targets are of great interest (Te Boekhorst et al. 2012). Similar to their use in myocardial infarction, iron oxide-based nanoparticles can be used to detect macrophages invading atherosclerotic plaques in mouse models (Tang et al. 2009). A broad spectrum of liposome or nanoparticle-based molecular MRI approaches to characterise atherosclerotic plaques ranging from the targeting of proteases over integrins for assessment of angiogenesis to cell apoptosis has been described in the literature and was recently excellently reviewed by Mulder et al. (Mulder et al. 2007b). Recently, den Adel et al. showed that retrospectively gated cine MRI allows only for quantifying contrast enhancement in the aorta of ApoE$^{-/-}$ mice, but from the same scan, plaque-correlated changes of arterial wall stiffness can be analysed. In ApoE$^{-/-}$ a correlation of both signals could be demonstrated (den Adel et al. 2013) (see Fig. 27.9).

27.3.4 Scintigraphic Imaging: SPECT and PET

With the general development and excitement of molecular imaging, scintigraphic imaging, one of the traditional functional and molecular imaging modalities, has recently again received novel attention. Together with fluorescence optical imaging, scintigraphic approaches provide the highest molecular sensitivity of all imaging modalities in vivo. With this extraordinarily high sensitivity, radionuclide imaging can be based on the injection of only trace amounts of target-affine ligands with radioisotopes (radiopharmaceuticals), which do not influence the organism under investigation. Scintigraphic imaging allows the functional and molecular study of various functional aspects of the heart, including

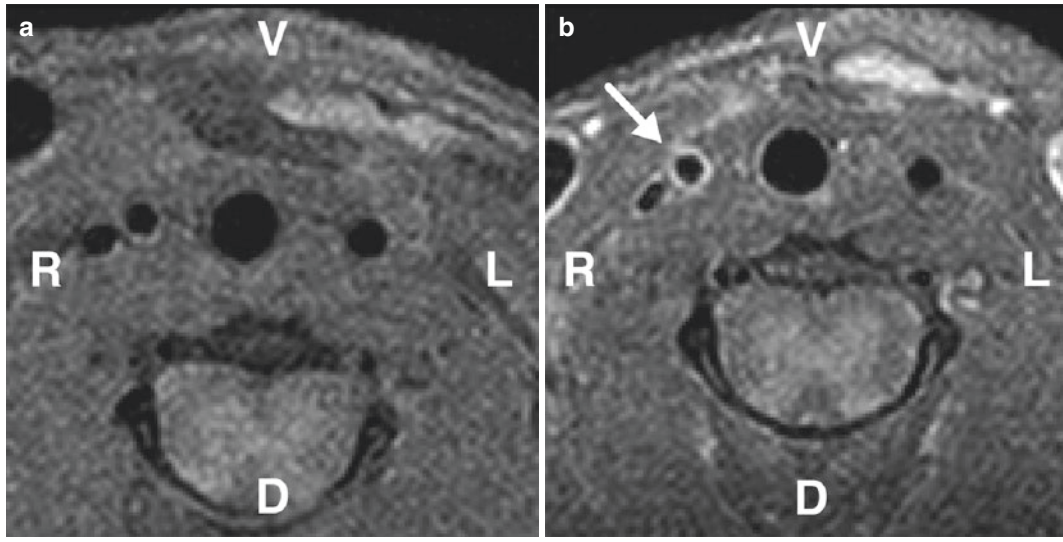

Fig. 27.9 Mouse carotid artery with atherosclerotic plaque at baseline (**a**) and 24 h (**b**) after injection with collagen-targeted CNA35-micelles (Images are courtesy of G. Strijkers, TU Eindhoven, The Netherlands)

ejection fraction, regional wall motion, perfusion, viability, oxygen consumption, glucose and fatty acid metabolism and such. Also, coronary artery functions and related diseases, such as ischaemia, infarction and atherosclerosis, can be investigated.

In contrast to any other imaging modality, a broad spectrum of commercially available radiolabelled tracers or cyclotron-produced radiopharmaceuticals is clinically available for functional and molecular imaging and used in routine algorithms. Scintigraphic methods are currently the only clinical molecular imaging tools. Preclinical molecular imaging can straightforwardly make use of these existing radionuclide techniques and apply these using dedicated small animal devices to animal models of cardiovascular diseases and has therefore enjoyed much progress. Furthermore, new radioactive biomarkers and radiopharmaceuticals have been developed for cardiovascular imaging. These prerequisites have fuelled the application of preclinical scintigraphic imaging in the past years. Besides "pure" preclinical applications to test new radiopharmaceuticals or to characterise mouse models, successful preclinical molecular scintigraphic imaging can be directly translated to clinical studies, where the same trace amount principle is realised. Scintigraphic methods therefore gained particular importance for drug development and translational molecular imaging from in vitro to patients (McAteer et al. 2009; Riemann et al. 2008).

To accustom the clinical scintigraphic technology to the preclinical scenario with small object sizes and – especially true for the murine heart – fast and significant motion, dedicated SPECT and PET devices have been designed in the past years. In SPECT, an adequate spatial resolution for cardiovascular studies can only be achieved by using pinhole techniques, which nowadays allow for spatial resolution well beyond 1 mm FWHM (Pissarek et al. 2009; van der Have et al. 2009). The same is true for PET: while the widely installed state-of-the-art crystal-based small animal PET systems provide spatial resolution close to 1 mm FWHM only in the centre of the field of view, a so-called multiwire chamber-based system (quadHIDAC, Oxford Positron Ltd., UK) offers a submillimetre (0.7 mm FWHM) homogeneous resolution in a large field of view (16 * 28 cm) (Schafers et al. 2005; Rowland and Cherry 2008). The resolution of all existing SPECT and PET devices in comparison to a wall thickness of ~1.0 mm in the left murine heart, of ~0.5 mm in the right murine heart and of ~0.1 mm in the

murine aorta leads to significant partial volume artefacts when imaging the murine heart and vessels. These have to be corrected for quantitative measurements and for improving detectability of small lesions.

A significant improvement of cardiac small animal scintigraphic imaging was realised by the introduction of gated SPECT and PET acquisitions. Besides improvement in spatial resolution in the single gates of the acquisition, functional parameters can be derived from scans with myocardium-affine tracers such as ^{18}F-FDG. When using contour-finding algorithms adapted from clinical gated SPECT and PET to small animal imaging, end-diastolic and end-systolic volumes and ejection fraction can be reliably and reproducibly derived with high-resolution scanners even in the mouse heart (Schafers et al. 2006; Stegger et al. 2009; Vanhove et al. 2005; Constantinesco et al. 2005). The drawback of gated imaging in scintigraphic imaging is the loss in statistics in a single gate, which is even worse when gating for both cardiac and respiratory cycles. Currently, for human and preclinical use, methods are being developed to detect and compensate myocardial motion to come up with an optimal non-blurred and maximum-statistics image (Dawood et al. 2008). These algorithms seem to be mandatory for the future imaging of novel radiopharmaceuticals especially in coronary artery plaques, which are small and heavily moving.

Myocardial perfusion and metabolism Translated from clinical algorithms to diagnose myocardial parameters, the field of small animal SPECT and PET was initially established using clinically available tracers. Still, a majority of cardiovascular applications are based on the use of various perfusion tracers and ^{18}F-fluorodeoxyglucose; the latter is regularly available in PET centres through in-house production involving a cyclotron or through distribution networks worldwide.

Several studies have used pinhole SPECT in combination with ^{99m}Tc-labelled clinically available perfusion tracers to obtain high-quality myocardial perfusion images in rats and mice (Constantinesco et al. 2005; Hirai et al. 2000). This technique can achieve excellent quantitative accuracy for in vivo measurement of even small myocardial infarctions in rats (Acton et al. 2006).

In the ninetieth to the twentieth century with the improved resolution of the developed small animal PET systems imaging of the heart of a rat and later of mice became feasible; $^{13}NH_3$ ammonia was mostly used in a transfer of clinical PET protocols to study regional and absolute myocardial perfusion in rats and mice by small animal PET, which is especially interesting when studying the effect of pharmaceutical interventions on myocardial perfusion (Inubushi et al. 2004; Croteau et al. 2004) (see Fig. 27.10).

Myocardial FDG uptake is heavily determined by the concentration of glucose in the plasma at the time of injection, insulin levels, depth and type of anaesthesia (isoflurane increases uptake), temperature and such. Reproducible and standardised preparation of the animals (starved vs. fed, baseline vs. insulin/glucose load, awake vs. anaesthetised, etc.) is therefore crucial to compare between individuals and to optimise the myocardial signal according to the scientific question (see Fig. 27.11).

Multiple studies have shown the principle feasibility of using FDG-PET to measure infarct size and to metabolically characterise myocardial infarctions in rats (Higuchi et al. 2007) or mice (Stegger et al. 2006). Results for the quantification of myocardial infarct size were typically validated against histology and/or MRI/echocardiography (see Fig. 27.12).

Apart from analysis of relative glucose utilisation in the heart of small animals, PET was also employed to study absolute cardiac substrate metabolism. To assess absolute myocardial glucose uptake, either compartmental modelling or quantification in correlation to the injected radioactive dose (% injected dose) can be used. Shoghi et al. have shown that Zucker diabetic fatty (ZDF) rats utilise significantly less glucose in the myocardium than their lean littermates (Shoghi et al. 2008). Levkau et al. demonstrated that in a knockout mouse model resulting in

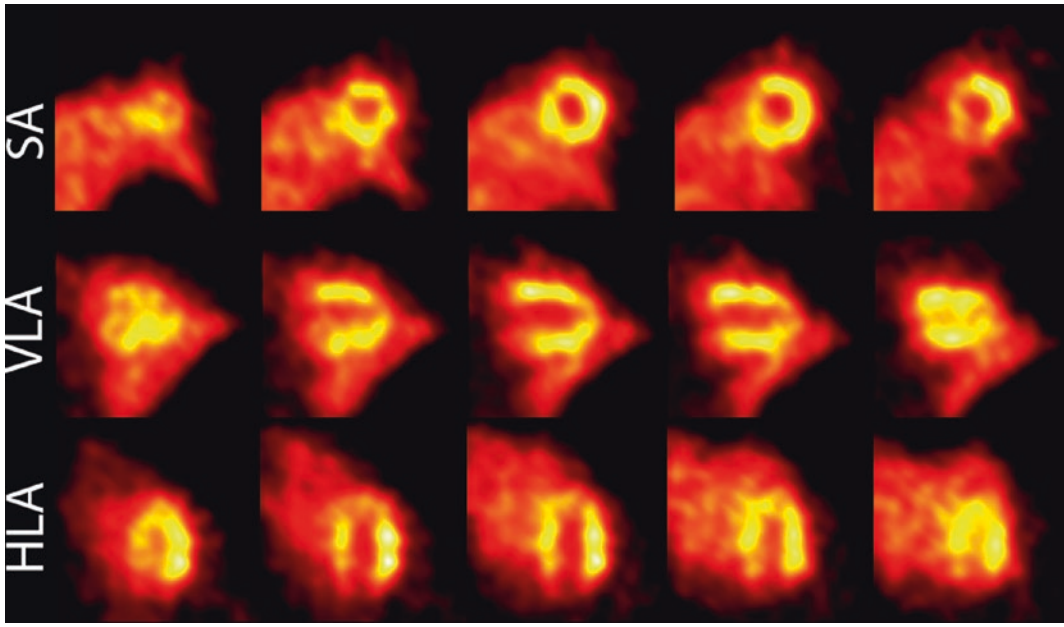

Fig. 27.10 Perfusion tracers such as ^{13}N-ammonia for PET in man can also be used in mice to study myocardial ischaemia. The figure shows representative 0.4 mm thick sections of the reoriented murine left ventricle (*SA* short axis, *VLA* vertical long axis, *HLA* horizontal long axis) with a physiological perfusion

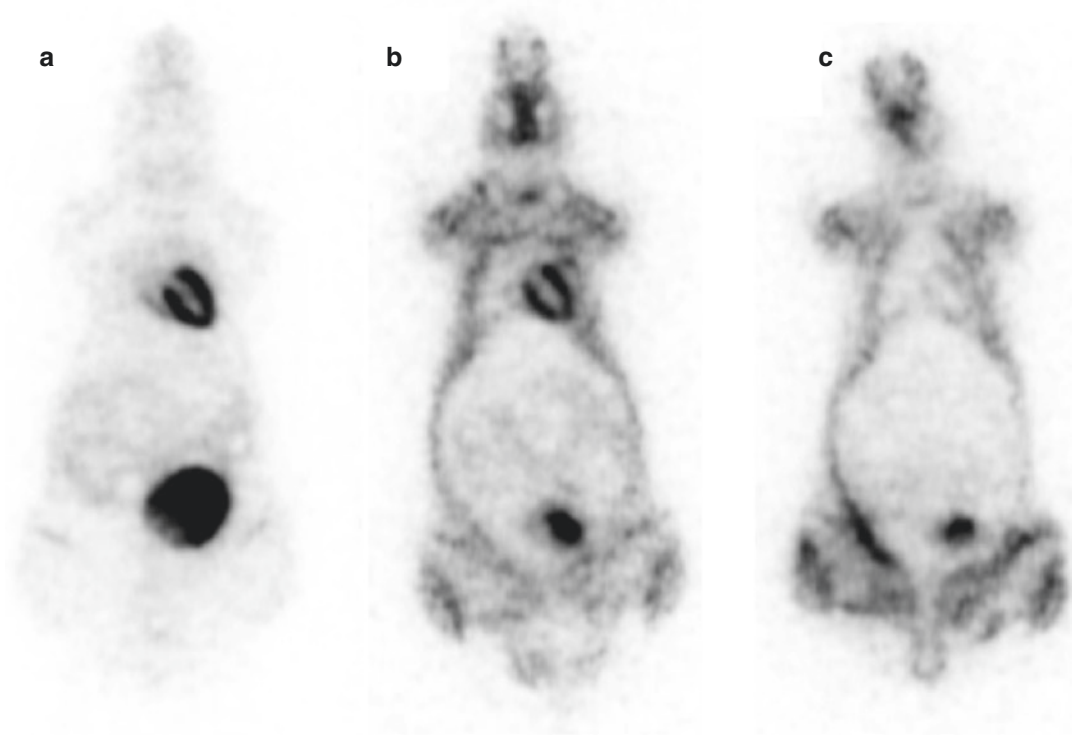

Fig. 27.11 Myocardial uptake of ^{18}F-FDG is heavily dependent on animal preparation. This figure displays typical horizontal whole-body slices of the same mouse with a good heart uptake following i.v. injection under isoflurane anaesthesia (**a**) or i.p. co-injection with an insulin/glucose cocktail in the awake animal (**b**) and virtually no heart uptake in the case of i.p. injection in the awake mouse (**c**). In all cases, the animal was allowed food ad libitum before the start of the protocols

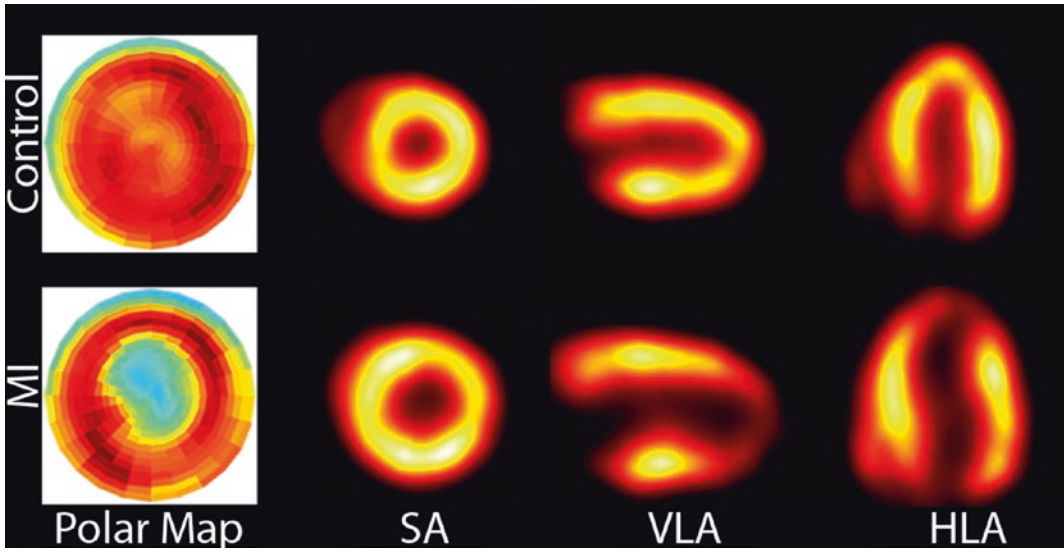

Fig. 27.12 Polar maps (*left*) and single slices (*SA* short axis, *VLA* vertical long axis, *HLA* horizontal long axis) of high-resolution ^{18}F-FDG-PET in a control mouse (*upper row*) and a mouse following myocardial infarction (*bottom row*) nicely depicting the loss of myocardial viability in the apex of the left ventricle

progressive heart failure myocardial ^{18}F-FDG uptake was increasing with the degree of heart failure (Levkau et al. 2008). FDG-PET was also used to show a switch in cardiac substrate utilisation towards glucose in myoglobin$^{-/-}$ mice, which was correlated with an overexpression of GLUT4 (Flogel et al. 2005).

Further tracers for assessing the myocardial metabolism were and are studied by small animal PET and SPECT. For instance, in a dual-tracer PET study in rats, Herrero et al. compared ^{11}C-acetate and $H_2{}^{15}O$-water to quantitatively assess myocardial perfusion (Herrero et al. 2006); ^{11}C-acetate was also used by the same group to measure free fatty acid utilisation in ZDF rats (Welch et al. 2006). Free fatty acid metabolism in the myocardium was studied in the course of ischaemia/reperfusion in the rat heart by ^{123}I-BMIPP (Higuchi et al. 2005).

Because of the anatomic information, soft tissue differentiation and additional functional information offered by coregistered MR images, dual-modality preclinical small animal SPECT/MRI and PET/MRI systems are under active research and development (Wehrl et al. 2009). These developments should aid both the molecular imaging of the myocardium and of the vessels (see Fig. 27.13).

27.3.5 Emerging Cardiovascular Applications of Molecular and Cellular Targeting by Small Animal PET and SPECT

Myocardial innervation The autonomic nervous system plays an important role in regulating cardiac function and is implicated in many cardiac diseases, ranging from coronary heart disease, congestive heart failure and cardiomyopathies to life-threatening arrhythmias. Although less established in clinical practice than perfusion and metabolic imaging, examination of the cardiac autonomic nervous system is potentially equally valuable. A variety of tracers targeting the pre- and postsynaptic sympathetic innervation of the heart is available and further developed. Since for imaging of receptors such as the beta-adrenoceptors on the myocardium maximum sensitivity is needed to avoid interference between the tracer dose and the receptor, imaging of myocardial innervation remains an exclusive field of SPECT and PET. ^{11}C-HED-PET and ^{123}I-MIBG-SPECT can be employed to study sympathetic innervation in rats or mice (Tipre et al. 2008; Goethals et al. 2009). PET and SPECT studies investigating postsynaptic

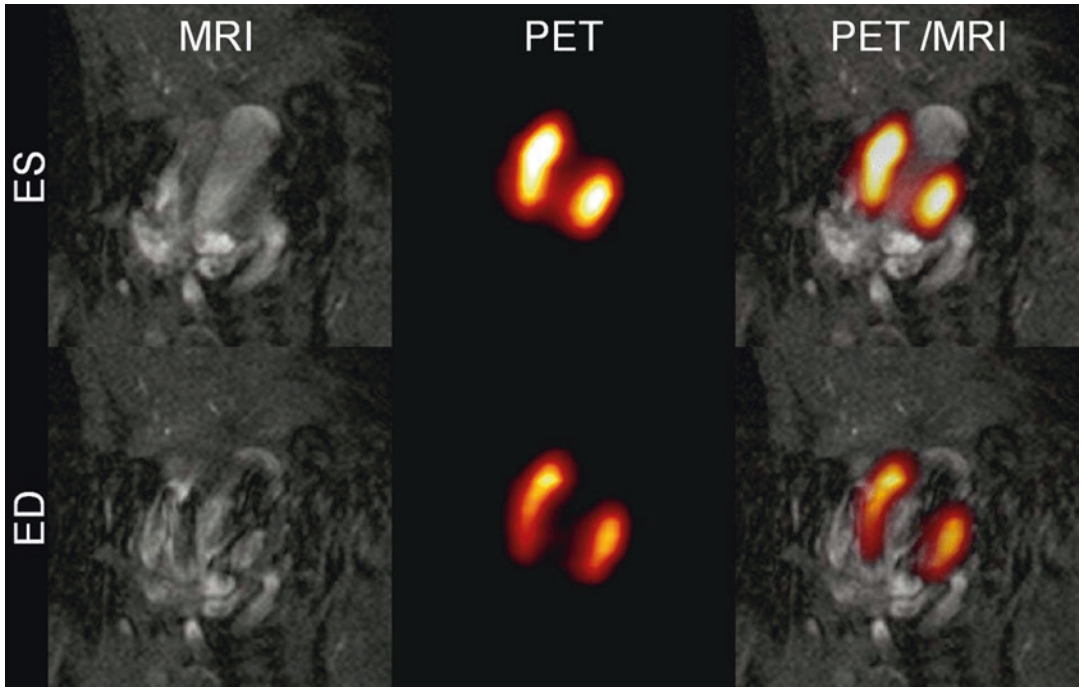

Fig. 27.13 Pilot-integrated MRI/^{18}F-FDG-PET scan of a murine heart in vivo. The scan was acquired on an experimental APD-PET insert in a 7 T preclinical MRI scanner developed at the University of Tübingen (Prof. Bernd Pichler). ECG-gated images depict a myocardial infarction with an apical aneurysm (*ED* end diastole, *ES* end systole)

beta-adrenoceptor density in small animals have not been reported so far.

Apoptosis Apoptosis, or programmed cell death, occurs in many cardiovascular diseases such as myocardial infarction, atherosclerosis, cardiomyopathies and post heart transplantation. As for other imaging methodologies, radiolabelled annexin V targeting phosphatidylserine occurring in the course of apoptosis on the outer cell membrane was used to image apoptosis in animal models and patients. Annexin V has been labelled with ^{99m}Tc for SPECT and ^{18}F, ^{64}Cu or ^{124}I for PET studies (Cauchon et al. 2007; Yagle et al. 2005; Kietselaer et al. 2004; Keen et al. 2005). Kietselaer and coworkers have already successfully applied ^{99m}Tc-annexin V in humans (Kietselaer et al. 2004). However, phosphatidylserine is not an exclusive in vivo target for apoptosis. It is also elevated in other forms of cell stress not necessarily leading to apoptosis. Activation of caspases inside the cells signals the initiation of the pivotal cascade towards apoptosis. Caspases, therefore, are likely to be better targets for molecular imaging of apoptosis. Targeting an intracellular enzyme with a radiotracer, e.g. a radiolabelled caspase inhibitor, is conceptually more challenging than targeting a cell surface receptor such as phosphatidylserine. First approaches have recently been reviewed (Faust et al. 2009).

Angiogenesis In cardiovascular medicine, there is tremendous interest not only in therapeutic approaches that strive for preventing angiogenesis, e.g. in the context of restenoses after angioplasty with or without stent implantation, but also in approaches that promote angiogenesis either by administration of angiogenic factors, such as the vascular endothelial growth factor (VEGF), or by gene therapeutic approaches in patients with ischaemic heart disease. The non-invasive molecular imaging of angiogenesis is a formidable means to improve therapy monitoring. VEGF is a key mediator of angiogenesis. Lu et al. have shown in an in vivo animal experiment in rabbits that uptake of VEGF121 labelled with the SPECT radionuclide ^{111}In is considerably higher in an ischaemic hind

leg compared to the contralateral non-ischaemic hind leg (Lu et al. 2003). Another important mediator is the $\alpha_v\beta_3$ integrin receptor, a heterodimeric transmembrane glycoprotein with α and β subunits that mediates not only adhesion but also proliferation and differentiation of endothelial cells. Since the expression of $\alpha_v\beta_3$ integrin is upregulated with angiogenesis, it should be a suitable target for molecular imaging. Peptides containing the amino acid sequence arginine-glycine-aspartic acid (RGD) can interact with the $\alpha_v\beta_3$ integrin receptor. Consequently, a large number of radiotracers containing the RGD sequence have been developed and evaluated. The iodinated compound *I-gluco-RGD, where * can stand for any of ^{123}I, ^{124}I, ^{125}I and ^{131}I, and the fluorinated PET radiotracer ^{18}F-galacto-RGD have been applied in several preclinical and clinical imaging studies (Beer et al. 2014; Laitinen et al. 2013; Gaertner et al. 2012). Most recently, ^{18}F-galacto-RGD was employed for imaging of vascular inflammation in atherosclerotic mice (Laitinen et al. 2009).

Vascular inflammation in atherosclerosis One rapidly growing area of cardiovascular molecular imaging is the development of methods to characterise atherosclerotic plaques, which are the pathophysiological basis for most of the cardiovascular events. As detailed above, the vulnerability/instability of atherosclerotic plaques is dependent rather on the cellular and molecular composition of these plaques than their size. Inflammatory targets play an utmost role and are therefore in the focus of new radioligand developments to image plaque vulnerability. Here, besides imaging of apoptosis and angiogenesis, both processes are involved in the progression of plaques; the molecular imaging of proteases such as matrix metalloproteinases (MMPs) and other inflammatory pathways is of great interest. A variety of MMP inhibitors typically based on small non-peptidic compounds such as hydroxamates or barbiturates was labelled in the past years by different radioligands for SPECT and PET (Wagner et al. 2006). These have been successfully applied to different animal models of atherosclerosis and are now awaiting their first clinical application (Schafers et al. 2004; Fujimoto et al. 2008). Comprehensive overviews of various inflammatory targets and tracers can be found here (Orbay et al. 2013; Tarkin et al. 2014; Hag et al. 2013).

Although small animal SPECT and PET offer unique molecular sensitivity, these techniques are often difficult to interpret on their own because of the lack of correlation with anatomic structures or biologic landmarks. This is especially true for the imaging of atherosclerosis in animal models. Because CT images provide excellent anatomic information, multimodality SPECT/CT and PET/CT or even SPECT/PET/CT has become available for clinical and small animal molecular imaging systems. However, even with these novel technologies, perfect coregistration which is needed for high-resolution imaging of the murine vessel wall is not straightforward, since motion detection and correction are currently not implemented. Furthermore, the resulting complex multimodal datasets need special workup to be visualised and interpreted. As an example, a dedicated software to analyse mouse aorta PET/CT data was published (Ropinski et al. 2009) (see Fig. 27.14).

Gene reporter imaging Therapeutic strategies based on the introduction of genes into the genome of living organisms have been developed for several cardiac diseases, e.g. atherosclerosis, myocardial infarction, heart failure and arrhythmias. To monitor efficiency, safety, etc., there is a considerable interest in molecular imaging techniques that offer the unique possibility to closely monitor gene distribution and gene expression in vivo non-invasively as a direct way to assess the efficacy of gene transfer. SPECT and PET can be used in combination with a reporter gene which is co-expressed with the gene of interest. Several reporter gene/probe systems have been developed for molecular radiotracer imaging, which utilise different kinds of interaction, such as enzyme-based reporter gene imaging using the herpes simplex virus type 1 thymidine kinase reporter gene (HSV1-tk) or its mutant derivative HSV1-sr39tk to induce thymidine kinase which phosphorylates nucleoside reporter probes such as 5-iodo-1-(2-deoxy-2-fluoro-β-D-arabinofuranosyl)uracil (FIAU) and 9-(4-fluoro-3-hydroxymethylbutyl) guanine (FHBG). This reporter gene/probe

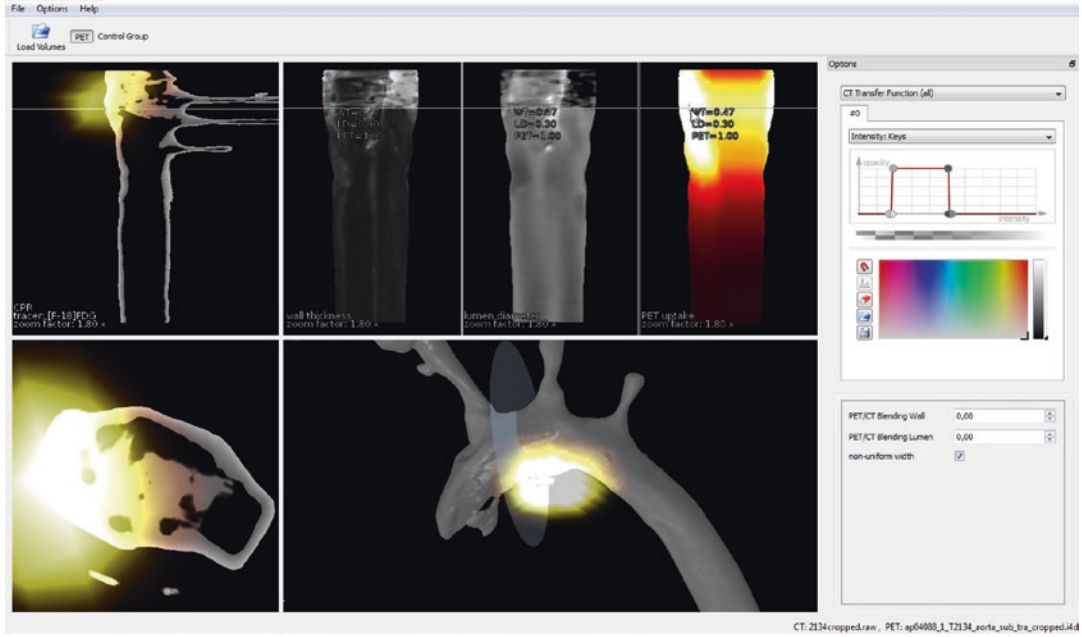

Fig. 27.14 Post-processing of high-resolution multimodal imaging data is needed for integrated analysis and potential future diagnostics. These figures show an example of multiple linked views which are employed to allow a comparative visualisation of aortic arches of mice scanned by PET and CT. For more detailed information, visit http://www.uni-muenster.de/Voreen/

system has seen application in small animal PET imaging and even in humans (Wu et al. 2002). A variety of further approaches is summarised elsewhere (Min and Gambhir 2008).

Cell tracking With the development and evaluation of novel algorithms for regenerative cardiovascular medicine involving stem cells and other cells in various cardiovascular diseases, molecular imaging and tracking of the biodistribution and fate of the applied cells have become an important research area. Here, challenges for imaging are the dynamic localisation and quantification of the number of such cells in vivo, over long periods. For tracking cells with radioactive isotopes, two principal strategies exist: one is the direct labelling of cells, e.g. by incubation with ^{111}In-oxine or ^{18}F-FDG in vitro, and the other is the use of gene reporters as detailed above (Zhang et al. 2008). For instance, by taking advantage of radionuclides with relatively long half-lives, small animal SPECT has been used to track the migration of radiolabelled stem cells to myocardial infarction (Brenner et al. 2004). Newer approaches involve labelled antibodies that are internalised and target immune cells specifically. A recent example is targeting of T cells by a T-cell-specific antibody labelled with ^{64}Cu for PET imaging (Griessinger et al. 2015).

27.3.6 Optical Imaging

In the last decade, the existing molecular imaging armamentarium is being strengthened by the development of fluorescent imaging approaches. With the heart and most vessels being located deep in tissues, especially in men, scattering of light plays an important role and is limiting the applications of optical imaging in cardiovascular research. Furthermore, absorption of light by haemoglobin in the well-perfused organs heart and vessels is another thread for the technology. The development of near-infrared sensors and imaging probes has broadened this technique's scope. Further developments aim at novel catheter-based approaches for imaging of vascular signals. While having a theoretically similar sensitivity, the main advantages of fluorescence

imaging over radioisotope-based imaging are the stability of the imaging agents as well as the ability to activate/switch-on imaging agents in vivo. Furthermore, fluorescence can also be measured by high-resolution microscopy of the same tissue sample, allowing an accurate correlation of in vivo molecular imaging signals and histology parameters (Megens et al. 2015).

As is true for radioisotope-based imaging, fluorescence imaging has the potential to provide a wealth of cellular and molecular information. However, although this technique has seen a tremendous variety of applications in tumours and other applications, cardiovascular applications in vivo in small animals such as mice and rats comparable to those involving the other imaging modalities reviewed here are still rare. Review on the status and the potential can be found here (Sinusas et al. 2008; Nahrendorf et al. 2009).

As detailed above, photoacoustic imaging holds promise for vascular and cardiac imaging due to its ability to penetrate deep tissues. Especially intravascular photoacoustic imaging seems feasible and should see its first application in mice and men (Jansen et al. 2014) (see Fig. 27.15).

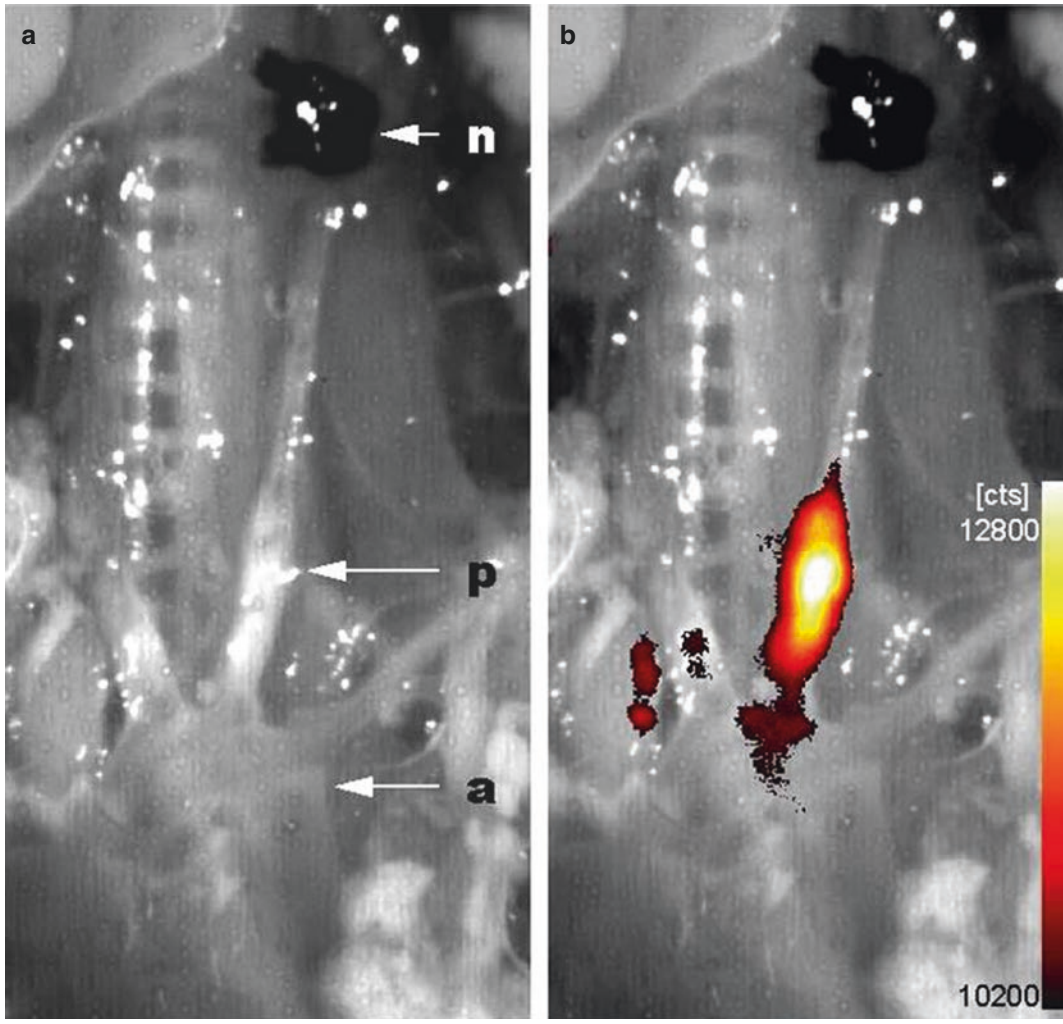

Fig. 27.15 White light (**a**) and fluorescence reflectance imaging (**b**) of an atherosclerotic plaque (*P*) developing after left carotid ligation in an ApoE$^{-/-}$ mouse using Cy5.5-labelled RGD (Reproduced from Waldeck et al. 2008). In this case, the skin was opened to get direct imaging access to the carotid arteries

References

Acton PD, Thomas D, Zhou R. Quantitative imaging of myocardial infarct in rats with high resolution pinhole SPECT. Int J Cardiovasc Imaging. 2006;22(3–4):429–34.

Beer AJ, Pelisek J, Heider P, et al. PET/CT imaging of integrin alphavbeta3 expression in human carotid atherosclerosis. JACC Cardiovasc Imaging. 2014;7(2):178–87. doi:10.1016/j.jcmg.2013.12.003.

Berr SS, Roy RJ, French BA, et al. Black blood gradient echo cine magnetic resonance imaging of the mouse heart. Magn Reson Med. 2005;53(5):1074–9.

Bohl S, Lygate CA, Barnes H, et al. Advanced methods for quantification of infarct size in mice using three-dimensional high-field late gadolinium enhancement MRI. Am J Physiol Heart Circ Physiol. 2009;296(4):H1200–8.

Brenner W, Aicher A, Eckey T, et al. 111In-labeled CD34+ hematopoietic progenitor cells in a rat myocardial infarction model. J Nucl Med. 2004;45(3):512–8.

Bunck AC, Engelen MA, Schnackenburg B, et al. Feasibility of functional cardiac MR imaging in mice using a clinical 3 tesla whole body scanner. Invest Radiol. 2009;44(12):749–56.

Cauchon N, Langlois R, Rousseau JA, et al. PET imaging of apoptosis with (64)cu-labeled streptavidin following pretargeting of phosphatidylserine with biotinylated annexin-V. Eur J Nucl Med Mol Imaging. 2007;34(2):247–58.

Cheng C, Tempel D, van Haperen R, et al. Atherosclerotic lesion size and vulnerability are determined by patterns of fluid shear stress. Circulation. 2006;113(23):2744–53.

Collins KA, Korcarz CE, Shroff SG, et al. Accuracy of echocardiographic estimates of left ventricular mass in mice. Am J Physiol Heart Circ Physiol. 2001;280(5):H1954–62.

Collins KA, Korcarz CE, Lang RM. Use of echocardiography for the phenotypic assessment of genetically altered mice. Physiol Genomics. 2003;13(3):227–39.

Constantinesco A, Choquet P, Monassier L, Israel-Jost V, Mertz L. Assessment of left ventricular perfusion, volumes, and motion in mice using pinhole gated SPECT. J Nucl Med. 2005;46(6):1005–11.

Coolen BF, Paulis LE, Geelen T, Nicolay K, Strijkers GJ. Contrast-enhanced MRI of murine myocardial infarction – part II. NMR Biomed. 2012;25(8):969–84. doi:10.1002/nbm.2767.

Croteau E, Benard F, Bentourkia M, Rousseau J, Paquette M, Lecomte R. Quantitative myocardial perfusion and coronary reserve in rats with 13N-ammonia and small animal PET: impact of anesthesia and pharmacologic stress agents. J Nucl Med. 2004;45(11):1924–30.

Dawood M, Buther F, Jiang X, Schafers KP. Respiratory motion correction in 3-D PET data with advanced optical flow algorithms. IEEE Trans Med Imaging. 2008;27(8):1164–75.

Dawson D, Lygate CA, Saunders J, et al. Quantitative 3-dimensional echocardiography for accurate and rapid cardiac phenotype characterization in mice. Circulation. 2004;110(12):1632–7.

den Adel B, van der Graaf LM, Strijkers GJ, Lamb HJ, Poelmann RE, van der Weerd L. Self-gated CINE MRI for combined contrast-enhanced imaging and wall-stiffness measurements of murine aortic atherosclerotic lesions. PLoS One. 2013;8(3):e57299. doi:10.1371/journal.pone.0057299.

Dinkel J, Bartling SH, Kuntz J, et al. Intrinsic gating for small-animal computed tomography: a robust ECG-less paradigm for deriving cardiac phase information and functional imaging. Circ Cardiovasc Imaging. 2008;1(3):235–43.

Dobrucki LW, Dione DP, Kalinowski L, et al. Serial noninvasive targeted imaging of peripheral angiogenesis: validation and application of a semiautomated quantitative approach. J Nucl Med. 2009;50(8):1356–63.

Falk E, Shah PK, Fuster V. Coronary plaque disruption. Circulation. 1995;92(3):657–71.

Faust A, Hermann S, Wagner S, et al. Molecular imaging of apoptosis in vivo with scintigraphic and optical biomarkers – a status report. Anticancer Agents Med Chem. 2009;9(9):968–85.

Fayad ZA, Fallon JT, Shinnar M, et al. Noninvasive in vivo high-resolution magnetic resonance imaging of atherosclerotic lesions in genetically engineered mice. Circulation. 1998;98(15):1541–7.

Flogel U, Laussmann T, Godecke A, et al. Lack of myoglobin causes a switch in cardiac substrate selection. Circ Res. 2005;96(8):e68–75.

Flogel U, Ding Z, Hardung H, et al. In vivo monitoring of inflammation after cardiac and cerebral ischemia by fluorine magnetic resonance imaging. Circulation. 2008;118(2):140–8.

Franco F, Thomas GD, Giroir B, et al. Magnetic resonance imaging and invasive evaluation of development of heart failure in transgenic mice with myocardial expression of tumor necrosis factor-alpha. Circulation. 1999;99(3):448–54.

Fujimoto S, Hartung D, Ohshima S, et al. Molecular imaging of matrix metalloproteinase in atherosclerotic lesions: resolution with dietary modification and statin therapy. J Am Coll Cardiol. 2008;52(23):1847–57.

Gaertner FC, Kessler H, Wester HJ, Schwaiger M, Beer AJ. Radiolabelled RGD peptides for imaging and therapy. Eur J Nucl Med Mol Imaging. 2012;39 Suppl 1:S126–38. doi:10.1007/s00259-011-2028-1.

Gan LM, Gronros J, Hagg U, et al. Non-invasive real-time imaging of atherosclerosis in mice using ultrasound biomicroscopy. Atherosclerosis. 2007;190(2):313–20.

Gao XM, Dart AM, Dewar E, Jennings G, Du XJ. Serial echocardiographic assessment of left ventricular dimensions and function after myocardial infarction in mice. Cardiovasc Res. 2000;45(2):330–8.

Geelen T, Paulis LE, Coolen BF, Nicolay K, Strijkers GJ. Contrast-enhanced MRI of murine myocardial infarction – part I. NMR Biomed. 2012;25(8):953–68. doi:10.1002/nbm.2768.

Ghanem A, Roll W, Hashemi T, et al. Echocardiographic assessment of left ventricular mass in neonatal and adult mice: accuracy of different echocardiographic methods. Echocardiography. 2006;23(10):900–7.

Ghanem A, Troatz C, Elhafi N, et al. Quantitation of myocardial borderzone using reconstructive 3-D echocardiography after chronic infarction in rats: incremental value of low-dose dobutamine. Ultrasound Med Biol. 2008;34(4):559–66.

Goethals LR, Weytjens CD, De Geeter F, et al. Regional quantitative analysis of small animal myocardial sympathetic innervation and initial application in streptozotocin induced diabetes. Contrast Media Mol Imaging. 2009;4(4):174–82.

Griessinger CM, Maurer A, Kesenheimer C, et al. 64Cu antibody-targeting of the T-cell receptor and subsequent internalization enables in vivo tracking of lymphocytes by PET. Proc Natl Acad Sci U S A. 2015;112(4):1161–6. doi:10.1073/pnas.1418391112.

Gui YH, Linask KK, Khowsathit P, Huhta JC. Doppler echocardiography of normal and abnormal embryonic mouse heart. Pediatr Res. 1996;40(4):633–42.

Hag AM, Ripa RS, Pedersen SF, Bodholdt RP, Kjaer A. Small animal positron emission tomography imaging and in vivo studies of atherosclerosis. Clin Physiol Funct Imaging. 2013;33(3):173–85. doi:10.1111/cpf.12017.

Heijman E, de Graaf W, Niessen P, et al. Comparison between prospective and retrospective triggering for mouse cardiac MRI. NMR Biomed. 2007;20(4):439–47.

Hermann S, Kuhlmann MT, Starsichova A, et al. Imaging Reveals the Connection Between Spontaneous Coronary Plaque Ruptures, Atherothrombosis, and Myocardial Infarctions in HypoE/SRBI-/- Mice. J Nucl Med. 2016;57(9):1420–7. doi: 10.2967/jnumed.115.171132. PMID: 27127225.

Herrero P, Kim J, Sharp TL, et al. Assessment of myocardial blood flow using 15O-water and 1-11C-acetate in rats with small-animal PET. J Nucl Med. 2006;47(3):477–85.

Higuchi T, Taki J, Nakajima K, Kinuya S, Namura M, Tonami N. Time course of discordant BMIPP and thallium uptake after ischemia and reperfusion in a rat model. J Nucl Med. 2005;46(1):172–5.

Higuchi T, Nekolla SG, Jankaukas A, et al. Characterization of normal and infarcted rat myocardium using a combination of small-animal PET and clinical MRI. J Nucl Med. 2007;48(2):288–94.

Hirai T, Nohara R, Hosokawa R, et al. Evaluation of myocardial infarct size in rat heart by pinhole SPECT. J Nucl Cardiol. 2000;7(2):107–11.

Ibrahim T, Makowski MR, Jankauskas A, et al. Serial contrast-enhanced cardiac magnetic resonance imaging demonstrates regression of hyperenhancement within the coronary artery wall in patients after acute myocardial infarction. JACC Cardiovasc Imaging. 2009;2(5):580–8.

Inubushi M, Jordan MC, Roos KP, et al. Nitrogen-13 ammonia cardiac positron emission tomography in mice: effects of clonidine-induced changes in cardiac work on myocardial perfusion. Eur J Nucl Med Mol Imaging. 2004;31(1):110–6.

Ivan E, Khatri JJ, Johnson C, et al. Expansive arterial remodeling is associated with increased neointimal macrophage foam cell content: the murine model of macrophage-rich carotid artery lesions. Circulation. 2002;105(22):2686–91.

Jansen K, van Soest G, van der Steen AF. Intravascular photoacoustic imaging: a new tool for vulnerable plaque identification. Ultrasound Med Biol. 2014;40(6):1037–48. doi:10.1016/j.ultrasmedbio.2014.01.008.

Kaufmann BA. Ultrasound molecular imaging of atherosclerosis. Cardiovasc Res. 2009;83(4):617–25.

Keen HG, Dekker BA, Disley L, et al. Imaging apoptosis in vivo using 124I-annexin V and PET. Nucl Med Biol. 2005;32(4):395–402.

Kiessling F, Greschus S, Lichy MP, et al. Volumetric computed tomography (VCT): a new technology for noninvasive, high-resolution monitoring of tumor angiogenesis. Nat Med. 2004;10(10):1133–8.

Kietselaer BL, Reutelingsperger CP, Heidendal GA, et al. Noninvasive detection of plaque instability with use of radiolabeled annexin A5 in patients with carotid-artery atherosclerosis. N Engl J Med. 2004;350(14):1472–3.

Klohs J, Steinbrink J, Bourayou R, et al. Near-infrared fluorescence imaging with fluorescently labeled albumin: a novel method for non-invasive optical imaging of blood-brain barrier impairment after focal cerebral ischemia in mice. J Neurosci Methods. 2009;180(1):126–32.

Kuhlmann MT, Kirchhof P, Klocke R, et al. G-CSF/SCF reduces inducible arrhythmias in the infarcted heart potentially via increased connexin43 expression and arteriogenesis. J Exp Med. 2006;203(1):87–97.

Kunichika H, Peters B, Cotter B, et al. Visualization of risk-area myocardium as a high-intensity, hyperenhanced "hot spot" by myocardial contrast echocardiography following coronary reperfusion: quantitative analysis. J Am Coll Cardiol. 2003;42(3):552–7.

Laitinen I, Saraste A, Weidl E, et al. Evaluation of alphavbeta3 integrin-targeted positron emission tomography tracer 18F-galacto-RGD for imaging of vascular inflammation in atherosclerotic mice. Circ Cardiovasc Imaging. 2009;2(4):331–8.

Laitinen I, Notni J, Pohle K, et al. Comparison of cyclic RGD peptides for alphavbeta3 integrin detection in a rat model of myocardial infarction. EJNMMI Res. 2013;3(1):38. doi:10.1186/2191-219X-3-38.

Levkau B, Schafers M, Wohlschlaeger J, et al. Survivin determines cardiac function by controlling total cardiomyocyte number. Circulation. 2008;117(12):1583–93.

Lindner JR. Molecular imaging of cardiovascular disease with contrast-enhanced ultrasonography. Nat Rev Cardiol. 2009;6(7):475–81.

Lu E, Wagner WR, Schellenberger U, et al. Targeted in vivo labeling of receptors for vascular endothelial growth factor: approach to identification of ischemic tissue. Circulation. 2003;108(1):97–103.

Ly HQ, Frangioni JV, Hajjar RJ. Imaging in cardiac cell-based therapy: in vivo tracking of the biological fate of therapeutic cells. Nat Clin Pract Cardiovasc Med. 2008;5 Suppl 2:S96–102.

Manka DR, Gilson W, Sarembock I, Ley K, Berr SS. Noninvasive in vivo magnetic resonance imaging of injury-induced neointima formation in the carotid artery of the apolipoprotein-E null mouse. J Magn Reson Imaging. 2000;12(5):790–4.

McAteer MA, Akhtar AM, von Zur Muhlen C, Choudhury RP. An approach to molecular imaging of atherosclerosis, thrombosis, and vascular inflammation using microparticles of iron oxide. Atherosclerosis. 2009;209(1):18–27.

Megens RT, Bianchini M, Schmitt MM, Weber C. Optical imaging innovations for atherosclerosis research: multiphoton microscopy and optical nanoscopy. Arterioscler Thromb Vasc Biol. 2015;35(6):1339–46. doi:10.1161/ATVBAHA.115.304875.

Min JJ, Gambhir SS. Molecular imaging of PET reporter gene expression. Handb Exp Pharmacol. 2008;(185 Pt 2)(185 Pt 2):277–303.

Mulder WJ, Douma K, Koning GA, et al. Liposome-enhanced MRI of neointimal lesions in the ApoE-KO mouse. Magn Reson Med. 2006;55(5):1170–4.

Mulder WJ, Griffioen AW, Strijkers GJ, Cormode DP, Nicolay K, Fayad ZA. Magnetic and fluorescent nanoparticles for multimodality imaging. Nanomed. 2007a;2(3):307–24.

Mulder WJ, Strijkers GJ, Vucic E, Cormode DP, Nicolay K, Fayad ZA. Magnetic resonance molecular imaging contrast agents and their application in atherosclerosis. Top Magn Reson Imaging. 2007b;18(5):409–17.

Nahrendorf M, Badea C, Hedlund LW, et al. High-resolution imaging of murine myocardial infarction with delayed-enhancement cine micro-CT. Am J Physiol Heart Circ Physiol. 2007;292(6):H3172–8.

Nahrendorf M, Sosnovik DE, French BA, et al. Multimodality cardiovascular molecular imaging, part II. Circ Cardiovasc Imaging. 2009;2(1):56–70.

Orbay H, Hong H, Zhang Y, Cai W. Positron emission tomography imaging of atherosclerosis. Theranostics. 2013;3(11):894–902. doi:10.7150/thno.5506.

Pissarek M, Meyer-Kirchrath J, Hohlfeld T, et al. Targeting murine heart and brain: visualisation conditions for multi-pinhole SPECT with (99m)tc- and (123)I-labelled probes. Eur J Nucl Med Mol Imaging. 2009;36(9):1495–509.

Ramirez MS, Bankson JA. A practical method for 2D multiple-animal MRI. J Magn Reson Imaging. 2007;26(4):1162–6.

Ramirez MS, Ragan DK, Kundra V, Bankson JA. Feasibility of multiple-mouse dynamic contrast-enhanced MRI. Magn Reson Med. 2007;58(3):610–5.

Razansky D, Deliolanis NC, Vinegoni C, Ntziachristos V. Deep tissue optical and optoacoustic molecular imaging technologies for pre-clinical research and drug discovery. Curr Pharm Biotechnol. 2012;13(4):504–22. BSP/CPB/E-Pub/0000184-13-8 [pii].

Riemann B, Schafers KP, Schober O, Schafers M. Small animal PET in preclinical studies: opportunities and challenges. Q J Nucl Med Mol Imaging. 2008;52(3):215–21.

Ropinski T, Hermann S, Reich R, Schafers M, Hinrichs K. Multimodal vessel visualization of mouse aorta PET/CT scans. IEEE Trans Vis Comput Graph. 2009;15(6):1515–22.

Rouleau L, Berti R, Ng VW, et al. VCAM-1-targeting gold nanoshell probe for photoacoustic imaging of atherosclerotic plaque in mice. Contrast Media Mol Imaging. 2013;8(1):27–39. doi:10.1002/cmmi.1491.

Rowland DJ, Cherry SR. Small-animal preclinical nuclear medicine instrumentation and methodology. Semin Nucl Med. 2008;38(3):209–22.

Schafers M, Riemann B, Kopka K, et al. Scintigraphic imaging of matrix metalloproteinase activity in the arterial wall in vivo. Circulation. 2004;109(21):2554–9.

Schafers KP, Reader AJ, Kriens M, Knoess C, Schober O, Schafers M. Performance evaluation of the 32-module quadHIDAC small-animal PET scanner. J Nucl Med. 2005;46(6):996–1004.

Schafers KP, Lang N, Stegger L, Schober O, Schafers M. Gated listmode acquisition with the quadHIDAC animal PET to image mouse hearts. Z Med Phys. 2006;16(1):60–6.

Schambach SJ, Bag S, Steil V, et al. Ultrafast high-resolution in vivo volume-CTA of mice cerebral vessels. Stroke. 2009;40(4):1444–50.

Scherrer-Crosbie M, Liel-Cohen N, Otsuji Y, et al. Myocardial perfusion and wall motion in infarction border zone: assessment by myocardial contrast echocardiography. J Am Soc Echocardiogr. 2000;13(5):353–7.

Scherrer-Crosbie M, Rodrigues AC, Hataishi R, Picard MH. Infarct size assessment in mice. Echocardiography. 2007;24(1):90–6.

Shoghi KI, Gropler RJ, Sharp T, et al. Time course of alterations in myocardial glucose utilization in the zucker diabetic fatty rat with correlation to gene expression of glucose transporters: a small-animal PET investigation. J Nucl Med. 2008;49(8):1320–7.

Sinusas AJ, Bengel F, Nahrendorf M, et al. Multimodality cardiovascular molecular imaging, part I. Circ Cardiovasc Imaging. 2008;1(3):244–56.

Sosnovik DE, Schellenberger EA, Nahrendorf M, et al. Magnetic resonance imaging of cardiomyocyte apoptosis with a novel magneto-optical nanoparticle. Magn Reson Med. 2005;54(3):718–24.

Sosnovik DE, Nahrendorf M, Weissleder R. Molecular magnetic resonance imaging in cardiovascular medicine. Circulation. 2007;115(15):2076–86.

Stegger L, Hoffmeier AN, Schafers KP, et al. Accurate noninvasive measurement of infarct size in mice with high-resolution PET. J Nucl Med. 2006;47(11):1837–44.

Stegger L, Heijman E, Schafers KP, Nicolay K, Schafers MA, Strijkers GJ. Quantification of left ventricular volumes and ejection fraction in mice using PET, compared with MRI. J Nucl Med. 2009;50(1):132–8.

Streif JU, Nahrendorf M, Hiller KH, et al. In vivo assessment of absolute perfusion and intracapillary blood volume in the murine myocardium by spin labeling magnetic resonance imaging. Magn Reson Med. 2005;53(3):584–92.

Tang TY, Muller KH, Graves MJ, et al. Iron oxide particles for atheroma imaging. Arterioscler Thromb Vasc Biol. 2009;29(7):1001–8.

Tarkin JM, Joshi FR, Rudd JH. PET imaging of inflammation in atherosclerosis. Nat Rev Cardiol. 2014;11(8):443–57. doi:10.1038/nrcardio.2014.80.

Te Boekhorst BC, van Tilborg GA, Strijkers GJ, Nicolay K. Molecular MRI of inflammation in atherosclerosis. Curr Cardiovasc Imaging Rep. 2012;5(1):60–8. doi:10.1007/s12410-011-9114-4.

Thibault H, Lafitte S, Timperley J, et al. Quantitative analysis of myocardial perfusion in rats by contrast echocardiography. J Am Soc Echocardiogr. 2005;18(12):1321–8.

Tiemann K, Weyer D, Djoufack PC, et al. Increasing myocardial contraction and blood pressure in C57BL/6 mice during early postnatal development. Am J Physiol Heart Circ Physiol. 2003;284(2):H464–74.

Tipre DN, Fox JJ, Holt DP, et al. In vivo PET imaging of cardiac presynaptic sympathoneuronal mechanisms in the rat. J Nucl Med. 2008;49(7):1189–95.

Tsui BM, Kraitchman DL. Recent advances in small-animal cardiovascular imaging. J Nucl Med. 2009;50(5):667–70.

Tsujita Y, Kato T, Sussman MA. Evaluation of left ventricular function in cardiomyopathic mice by tissue doppler and color M-mode doppler echocardiography. Echocardiography. 2005;22(3):245–53.

van der Have F, Vastenhouw B, Ramakers RM, et al. U-SPECT-II: an ultra-high-resolution device for molecular small-animal imaging. J Nucl Med. 2009;50(4):599–605.

van Nierop BJ, Coolen BF, Dijk WJ, et al. Quantitative first-pass perfusion MRI of the mouse myocardium. Magn Reson Med. 2013;69(6):1735–44. doi:10.1002/mrm.24424.

Vanhove C, Lahoutte T, Defrise M, Bossuyt A, Franken PR. Reproducibility of left ventricular volume and ejection fraction measurements in rat using pinhole gated SPECT. Eur J Nucl Med Mol Imaging. 2005;32(2):211–20.

Vogel R, Indermuhle A, Reinhardt J, et al. The quantification of absolute myocardial perfusion in humans by contrast echocardiography: algorithm and validation. J Am Coll Cardiol. 2005;45(5):754–62.

Wagner S, Breyholz HJ, Faust A, et al. Molecular imaging of matrix metalloproteinases in vivo using small molecule inhibitors for SPECT and PET. Curr Med Chem. 2006;13(23):2819–38.

Wait JM, Tomita H, Burk LM, et al. Detection of aortic arch calcification in apolipoprotein E-null mice using carbon nanotube-based micro-CT system. J Am Heart Assoc. 2013;2(1):e003358. doi:10.1161/JAHA.112.003358.

Waldeck J, Hager F, Holtke C, et al. Fluorescence reflectance imaging of macrophage-rich atherosclerotic plaques using an alphavbeta3 integrin-targeted fluorochrome. J Nucl Med. 2008;49(11):1845–51.

Wehrl HF, Judenhofer MS, Wiehr S, Pichler BJ. Preclinical PET/MR: technological advances and new perspectives in biomedical research. Eur J Nucl Med Mol Imaging. 2009;36 Suppl 1:S56–68.

Weissleder R, Lee AS, Khaw BA, Shen T, Brady TJ. Antimyosin-labeled monocrystalline iron oxide allows detection of myocardial infarct: MR antibody imaging. Radiology. 1992;182(2):381–5.

Welch MJ, Lewis JS, Kim J, et al. Assessment of myocardial metabolism in diabetic rats using small-animal PET: a feasibility study. J Nucl Med. 2006;47(4):689–97.

Wiesmann F, Ruff J, Hiller KH, Rommel E, Haase A, Neubauer S. Developmental changes of cardiac function and mass assessed with MRI in neonatal, juvenile, and adult mice. Am J Physiol Heart Circ Physiol. 2000;278(2):H652–7.

Wiesmann F, Frydrychowicz A, Rautenberg J, et al. Analysis of right ventricular function in healthy mice and a murine model of heart failure by in vivo MRI. Am J Physiol Heart Circ Physiol. 2002;283(3):H1065–71.

Wu JC, Inubushi M, Sundaresan G, Schelbert HR, Gambhir SS. Positron emission tomography imaging of cardiac reporter gene expression in living rats. Circulation. 2002;106(2):180–3.

Yagle KJ, Eary JF, Tait JF, et al. Evaluation of 18F-annexin V as a PET imaging agent in an animal model of apoptosis. J Nucl Med. 2005;46(4):658–66.

Yu Q, Leatherbury L, Tian X, Lo CW. Cardiovascular assessment of fetal mice by in utero echocardiography. Ultrasound Med Biol. 2008;34(5):741–52.

Zhang SH, Reddick RL, Piedrahita JA, Maeda N. Spontaneous hypercholesterolemia and arterial lesions in mice lacking apolipoprotein E. Science. 1992;258(5081):468–71.

Zhang S, Picard MH, Vasile E, et al. Diet-induced occlusive coronary atherosclerosis, myocardial infarction, cardiac dysfunction, and premature death in scavenger receptor class B type I-deficient, hypomorphic apolipoprotein ER61 mice. Circulation. 2005;111(25):3457–64.

Zhang Y, Ruel M, Beanlands RS, deKemp RA, Suuronen EJ, DaSilva JN. Tracking stem cell therapy in the myocardium: Applications of positron emission tomography. Curr Pharm Des. 2008;14(36):3835–53.

Imaging in Neurooncology

28

Yannic Waerzeggers, Bastian Zinnhardt, Alexandra Winkeler, Parisa Monfared, Sonja Schelhaas, Thomas Viel, and Andreas H. Jacobs

Contents

Y. Waerzeggers • B. Zinnhardt • P. Monfared
S. Schelhaas
European Institute for Molecular Imaging (EIMI), Westfälische Wilhelms University of Münster (WWU), Germany

A. Winkeler
Imagerie Moléculaire In Vivo, IMIV, CEA, Inserm, CNRS, Univ. Paris-Sud, Université Paris Saclay, CEA-SHFJ, Orsay, France

T. Viel
European Institute for Molecular Imaging (EIMI), Westfälische Wilhelms University of Münster (WWU), Germany

PARCC, INSERM U970, Université Paris Descartes, Paris, France

A.H. Jacobs, MD (✉)
European Institute for Molecular Imaging (EIMI), Westfälische Wilhelms University of Münster (WWU), Waldeyerstr. 15, Münster 48149, Germany

Department of Geriatrics, Johanniter Hospital, Evangelische Kliniken, Bonn, Germany
e-mail: ahjacobs@uni-muenster.de

28.1 Introduction

Over the last decades, the development of animal models of neurological disorders and cancer has progressed rapidly. Many in vitro and in vivo models of brain tumours have been developed and have proven to be important tools for our understanding of human cancer. Progression in neurosciences, especially in neurooncology, also increasingly required improvements in imaging methodologies to provide non-invasive measures of a broad range of tumour-relevant parameters, both at the cellular and the molecular level.

In recent years there has been a rapid increase in the variety of ways to non-invasively monitor animal tumour models. Refinement in specialised hardware dedicated to small-animal imaging that overcomes the limitations of spatial resolution and sensitivity associated with the use of clinical scanners for imaging small-sized laboratory animals (dedicated small-animal computed tomography (CT) (Paulus et al. 2000), positron emission

F. Kiessling et al. (eds.), *Small Animal Imaging*, DOI 10.1007/978-3-319-42202-2_28

or single-photon emission computed tomography (PET/SPECT), magnetic resonance imaging (MRI) and PET/MRI scanners (Pichler et al. 2008; de Kemp et al. 2010; Thompson et al. 2014; Fine et al. 2014)) has taken place. Moreover, there has been a further development of new imaging techniques for non-invasive imaging on the cellular and subcellular level (optical imaging (OI), intravital imaging, confocal microscopy, two-photon microscopy, fibred fluorescence microscopy, Raman spectroscopy and photoacoustic tomography (Pierce et al. 2008; Wang 2008; Yao and Wang 2014; Pittet and Weissleder 2011)). Furthermore, the application of improved imaging probes for selective accumulation in tumours or for activation by tumour-specific molecules and of new imaging methodologies such as detection of reporter transgene expression in vivo had great impact on versatility, sensitivity and specificity of tumour imaging in living subjects. Moreover, as repetitive measurements can be performed in the same animal over time, a dynamic picture of the progressive changes of biological parameters under investigation can be generated, and statistical significance can be achieved using far less animals than with conventional laboratory experiments. These developments profoundly influenced our basic understanding of in vivo tumour biology and comprise a strong tool which should be used to test the in vivo efficacy of new therapeutic intervention strategies (e.g. molecular-targeted, gene and cell-based therapies) and to characterise factors that influence chemo- or radioresistance.

This chapter will give an overview of the recent developments in the application of small-animal imaging in neurooncology. Particular emphasis has been placed on the use of MRI, PET/SPECT and OI, since these approaches had the most significant impact on small-animal cancer research in recent years (Table 28.1).

28.2 Brain Tumour Models

Many in vitro and in vivo models of brain tumours have been developed. The ideal animal tumour models should be able to accurately recapitulate all aspects of human tumour physiology such as angiogenesis, tumour-stroma and tumour-host interaction and tumour environment and should also address the various factors that underlie the molecular and genetic lesions associated with tumour heterogeneity.

The study of brain tumour models have increased our understanding of brain tumour initiation, formation, progression and metastasis and provide an excellent experimental system to discover novel therapeutic targets and test various therapeutic agents (Fomchenko and Holland 2006). Many tumour-derived cell lines have been established, and they are often employed for screening of novel drugs in cell culture or xenograft experiments because of their ready availability and ease of use. Xenograft models, induced either by subcutaneous or by orthotopic (into native tumour sites) injection of primary tumour cells or tumour cell lines, represent the most frequent in vivo cancer model system. However, both cell culture and xenograft model systems lack the stepwise genetic alterations thought to occur during tumour progression and do not recapitulate the genetic and cellular heterogeneity of primary tumours and the complex tumour-stroma interaction. Increasing knowledge of human cancer biology and technical improvements has led to tumour models that better reflect human disease, such as genetically engineered mouse models and orthotopic patient-derived xenograft models. These models recapitulate more accurately the causal genetic events and subsequent molecular evolution in situ. They give rise to tumour-stroma interactions resembling those of the native tumours and also harbour cellular subpopulations like cancer stem cells thought to be of central importance to the development, maintenance and drug resistance of brain cancer (Huse and Holland 2009). In recent years, a variety of such mouse models have been developed and for in-depth information, several excellent reviews exist (Fomchenko and Holland 2006; Huse and Holland 2009; Simeonova and Huillard 2014; de Jong et al. 2014; McNeill et al. 2014; Tentler et al. 2012). However, it should be kept in mind that till now no true ‘humanised’ animal tumour model has been developed that-

Table 28.1 Overview of the main non-invasive imaging systems commonly used to image tumours in rodents

Technique (and used energy window)	Spatial resolution	Depth penetration	Time scale	Primary target interrogated	Cost	Main advantages	Main disadvantages	Clinical use
CT (X-rays)	50 μm	No limit	Minutes	A,P	€€	Primarily lung and bone imaging of tumours and metastases	Poor soft tissue contrast	Yes
US (high-frequency sound)	50 μm	Centimeters	Minutes	A,P	€	Primarily vascular and soft tissue imaging	Difficult to image through bone or lungs	Yes
PET (high-energy γ-rays)	1–2 mm	No limit	Minutes-hours	P,M	€€€	High sensitivity, quantitative, variety of available probes	Cyclotron needed, short-lived radioisotopes, low resolution, single-to-noise ratio	Yes
SPECT (low-energy γ-rays)	1–2 mm	No limit	Minutes-hours	P,M	€€	Radioisotopes have longer half-lives than those used in PET, multiple probes can be detected simultaneously	Sensitivity 10–100 times lower than PET	Yes
MRI (radio-waves)	10–100 μm	No limit	Minutes-hours	A,P,M	€€€	High spatial resolution and soft tissue contrast, functional information, versatile	Low sensitivity, long acquisition and image processing times	Yes
BLI (visible light)	Several mm	Centimeters	Minutes	M	€	High sensitivity, high through-put, transgene-based approach confers versatility	Light emission prone to attenuation and scatter with increased tissue depth	No
FI (visible and NIR light)	1 mm	<10 cm	Seconds-minutes	P,M	€	Potential for multiplex imaging, high through-put, transgene-based approach confers versatility	Excitation and emission light < 600 nm prone to attenuation with increased tissue depth, autofluorescence	In development

The main advantages and disadvantages associated with each system are listed. Primary targets of the respective imaging system: *A* anatomical, *P* physiological, *M* molecular

fully imitates the human disease or a particular disease stage. Consequently, the translational value of many animal studies remains controversial, and obtained results in these models will not necessarily be translatable to 100 % in the human situation.

Many cancer cell lines used in xenograft models are transgenic cell lines that exhibit overexpression, depression or complete inactivation of a gene of interest to provide insights in the molecular and functional impact of this specific gene on tumour pathophysiology. Moreover, in addition to this gene of interest, often a reporter gene is introduced and allows for non-invasive phenotyping of the effects of the induced molecular alterations by molecular imaging techniques.

28.3 Imaging Through Transgene-Based Approaches

Many recent advances associated with imaging tumours in small animals have arisen from the application of non-invasive reporter gene imaging.

Reporter transgenes have been developed for optical, nuclear and to a lesser extent also for MR imaging modalities. The choice of a reporter gene is dependent on the question to be addressed, the available imaging modality, the need for translationability to larger animals or humans and the desired throughput of the analyses (Gross and Piwnica-Worms 2006; Youn and Chung 2013; Brader et al. 2013). Reporter genes can be used to visualise the levels of expression of particular exogenous and endogenous genes and several intracellular biologic phenomena such as specific signal transduction pathways, nuclear receptor activities, protein–protein interactions and post-translational protein modifications (Kang and Chung 2008).

Regardless of the examined process, any strategy for imaging genetically encoded reporters is comprised of three major components: (i) a reporter gene that generates an imageable signal, (ii) a regulatory element governing the activity of the reporter gene and therefore generating contrast, and (iii) a detection device able to non-invasively sense and quantify the signal produced by the reporter gene within the intact cell or organism (Gross and Piwnica-Worms 2005).

Genetically encoded reporters can produce signal: (i) Intrinsically by the reporter (e.g. fluorescent proteins). (ii) Through enzymatic activation of an inactive substrate by the reporter (e.g. firefly luciferase (FLuc) that catalyses the light-producing reaction from the substrate D-luciferin in the presence of O2, Mg2+ and ATP, β-galactosidase that enzymatically cleaves an inactive paramagnetic chelate or quenched fluorophore into an active contrast agent). (iii) By enzymatic modification of an active (e.g. radiolabelled) substrate resulting in its selective trapping in the reporter cells (e.g. selective retention of [^{18}F]-labelled 9-[4-fluoro-3-(hydroxymethyl) butyl]guanine, [^{18}F]FHBG, or [^{124}I]-labelled 2′-fluoro-2′-deoxy-1-β-D-arabinofuranosyl-5-iodouracil, [^{124}I]FIAU, by the herpes simplex virus type 1 thymidine kinase enzyme, HSV-1-*tk*). (iv) By direct binding or import of an active substrate by intracellular or extracellular receptors and/or transporters (e.g. binding of radiolabelled somatostatin to somatostatin receptor type 2 [SSTR2]-expressing cells, accumulation of radioactive iodine in cells expressing the human thyroid sodium/iodide symporter (hNIS) gene or accumulation of superparamagnetic transferrin probe or iron in cells expressing an engineered human transferrin receptor or the metalloprotein ferritin, respectively) (Youn and Chung 2013; Gross and Piwnica-Worms 2005; Gilad et al. 2007; Lee et al. 2012; Vandsburger et al. 2013).

A common feature of all reporter constructs is the cDNA expression cassette containing the reporter transgenes of interest. The versatility of reporter gene imaging results in part from the flexibility to tailor the expression cassette to an individual need. Regulation of the reporter genes can be achieved at the transcriptional level (e.g. a constitutively active or inducible promoter or an upstream *cis*-regulatory element) or at the post-transcriptional/post-translational level (e.g. a regulatory polypeptide sequence fused in frame with the reporter). Conditional elements regulating transgene expression can restrict their expression to a certain time frame, a desired organ or a certain

biological event (e.g. tetracycline and mifepristone responsive elements, Cre-recombinase/lox and Gal4-dependent transactivation) (Waerzeggers et al. 2009a).

One major disadvantage of reporter gene imaging is the need to transduce or transfect the target tissue, which limits its clinical use. The cDNA containing vector can be used directly to transfect the cells, mostly facilitated by cationic lipid-based transfection agents or electroporation; or the vectors can be wrapped into a recombinant viral vector which is then used to transduce the cells. Several currently available vector types can be used (e.g. retrovirus, adenovirus, adeno-associated virus, lentivirus, herpes simplex virus). Reporter transgenes can be introduced in vitro into xenografted or allografted cells, directly delivered to tissues by somatic gene transfer or cloned into the genomes of transgenic animals.

28.4 Imaging Tumour Growth and Metabolism

Tumour growth and survival are dependent on the maintenance of cell energy metabolism and on protein and DNA synthesis and are governed by the adequate delivery of necessary metabolites (glucose, amino acids and nucleosides) through development of a tumour vascular network. Conventional PET and MR techniques have been the imaging techniques of choice for diagnosis and staging of patient with brain tumours by monitoring the above-mentioned mechanisms (Gao and Jiang 2013; Suchorska et al. 2014). The increased cell metabolism in tumour cells results in a strongly increased glucose uptake and metabolism (glycolysis) compared to normal tissue. In the past, PET imaging with [^{18}F]-labelled glucose ([^{18}F]FDG) has been used to diagnose or to assist in the evaluation of malignancy in patients with known or suspected abnormalities (Oriuchi et al. 2006). The molecular targets of FDG are glucose transporters, such as the insulin-dependent GLUT1 transmembrane transporter, and hexokinase, both of which are overexpressed in many cancers. Once phosphorylated, FDG-6 phosphate is retained in cells in proportion to their glycolytic activity. [^{18}F]FDG has been widely used for imaging glucose transporter expression and hexokinase activity and is commonly used for brain tumour diagnosis (Herholz et al. 2007). In clinical neurooncology, [^{18}F]FDG has been used to detect the metabolic differences between normal brain tissue, low-grade and high-grade gliomas and radionecrosis. Moreover, increased intratumoural glucose consumption correlates with tumour grade, cell density, biological aggressiveness and patient survival in both primary and recurrent gliomas. However, due to the relatively high glucose metabolism in normal grey matter, clear tumour localisation and delineation with [^{18}F]FDG PET is difficult. The use of [^{18}F]FDG is further limited due to its non-specific uptake in proliferating non-cancerous cells or tissues (such as inflammatory cells or granulation tissue) and to the high glucose metabolism of normal brain tissue. Together these factors reduce its detection sensitivity and compromise the ability of [^{18}F]FDG PET to monitor the therapeutic response of intracranial lesions (Oriuchi et al. 2006; Herholz et al. 2007). Therefore, other PET and SPECT probes have been developed for tumour identification via a variety of different tumour-specific mechanisms.

Because of the uncontrolled and accelerated growth of cancer, the process of protein synthesis in tumours is increased. As a consequence, the demand for amino acids, the building blocks of proteins, is increased. Amino acids that have been used for cancer imaging include [^{11}C]methionine (MET), [^{18}F]fluoroethyl tyrosine (FET) and [^{18}F]fluoromethyltyrosine (FMT). In neurooncology, radiolabelled methionine and tyrosine compounds have been shown to be more specific tracers in tumour detection, delineation and staging owing to their relatively low uptake in normal brain (Herholz et al. 2007; Singhal et al. 2008; Juhasz et al. 2014; Crippa et al. 2012).

As a high rate of cellular proliferation is a key feature of malignant tumours, in recent years much attention has been attracted to the search for cellular proliferation markers, the uptake of which would accurately reflect DNA synthesis. Thereby, most emphasis is put on the development of tracers based on thymidine. There are two

main pathways involved in thymidine metabolism: (i) the exogenous or 'salvage' pathway, which utilises thymidine from outside the cell that is phosphorylated by thymidine kinase 1 (TK1); and (ii) the endogenous, de novo pathway, in which uridine monophosphate can enter DNA synthesis after reductive methylation by thymidylate synthase (Sherley and Kelly 1988).

A variety of nucleic acids have been radiolabelled as PET tracers for cellular proliferation such as ^{11}C-labelled thymidine and ^{18}F-labelled 3′-deoxy-3′-fluoro-thymidine (FLT) (Herholz et al. 2007). After its intravenous administration, [^{18}F]FLT is distributed extracellularly and is subsequently transported into the cytosol, where it is phosphorylated by TK1, a cytosolic enzyme that is expressed during the S phase of the cell cycle (Sherley and Kelly 1988). In its phosphorylated form, [^{18}F]FLT is metabolically 'trapped' in the cell, with essentially no incorporation into DNA. It has been demonstrated in many types of cancer, including glioblastoma, that [^{18}F]FLT uptake in vivo is a measure of tumour proliferation activity and that there exists a significant correlation between [^{18}F]FLT uptake and the proliferation marker Ki-67 (Ullrich et al. 2008; Chalkidou et al. 2012). Bradbury et al. investigated whether [^{18}F]FLT can be used to detect and assess proliferative activity in genetically engineered mouse high-grade glioma models (Bradbury et al. 2008). The authors characterised the intracranial gliomas by both static and dynamic small-animal PET imaging of [^{18}F]FLT uptake and developed and implemented a compartmental modelling approach, using a three-compartment, four-parameter model that permits the discrimination of tracer transport and delivery from tumour proliferation. The ability to distinguish between the delivery and retention components of radiotracer uptake may become particularly important in the evaluation of treatment responses. Without information on the relative contributions of the delivery and metabolic trapping of [^{18}F]FLT to overall uptake, incorrect interpretations regarding tumour proliferation status can result, particularly under conditions in which delivery largely dictates overall tumour uptake; for example, reduced delivery of [^{18}F]FLT to hypoperfused tumours may result in a spuriously low estimate of proliferation status. Other limitations of [^{18}F]FLT have been recognised, such as blood–brain barrier (BBB) permeability restrictions (Viel et al. 2012) and a lower sensitivity than other tumour tracers (FDG or FET) (Gulyas and Halldin 2012; Nowosielski et al. 2014). Moreover, [^{18}F]FLT uptake reflects tumour proliferation as a function of thymidine salvage pathway utilisation resulting in the fact that [^{18}F]FLT PET cannot discriminate moderately proliferative, thymidine salvage-driven tumours from those of high proliferative index that rely primarily upon de novo thymidine synthesis (McKinley et al. 2013). Furthermore, it was demonstrated that endogenous thymidine can compete with [^{18}F]FLT for binding to nucleoside transporters or the catalytic site of TK1 (Zhang et al. 2012a). It was also shown that thymidine phosphorylase can influence endogenous thymidine levels and hence uptake of [^{18}F]FLT (Schelhaas et al. 2014; Lee et al. 2014). Accordingly, the magnitude of [^{18}F]FLT uptake cannot be considered a universal surrogate of proliferative index (McKinley et al. 2013). Nevertheless, [^{18}F]FLT PET seems to be a valuable method to detect early treatment responses in glioma, in the preclinical (Viel et al. 2013a) as well as the clinical (Corroyer-Dulmont et al. 2013) setting. For instance, in an orthotopic mouse model of glioblastoma multiforme (GBM) treated with temozolomide (TMZ, an alkylating agent that induces DNA methylation) chemotherapy, our group could demonstrate that as early as 2 days after TMZ treatment, significant changes in [^{18}F]FLT accumulation can be observed in TMZ-treated vs. control tumours. The changes in [^{18}F]FLT accumulation at early stage (day 2) correlated positively with changes in tumour size later on (day 7) (Fig. 28.1) (Viel et al. 2013a).

Although PET tracers based on altered tumour metabolism are most commonly used in the clinical setting, they are not always suitable for the precise identification and differentiation of various tumour states (Gao and Jiang 2013). Therefore, researchers have attempted to develop alternative diagnostic probes, directed to more specific tumour characteristics such as surface

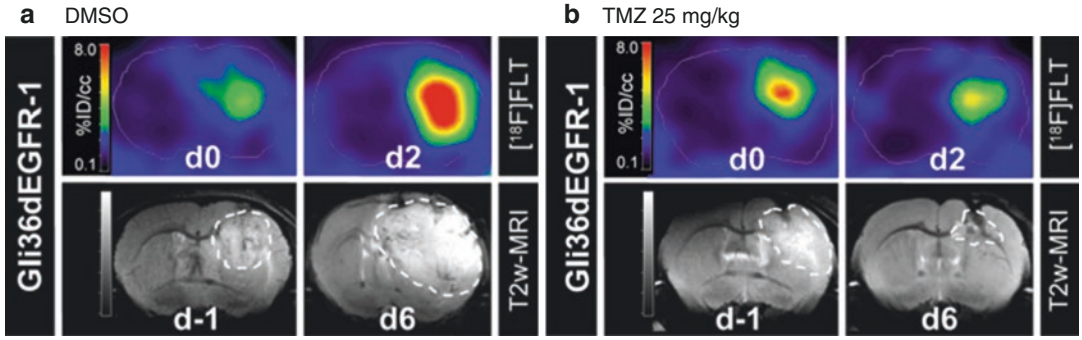

Fig. 28.1 Early assessment of the efficacy of TMZ chemotherapy in experimental GBM using [^{18}F]FLT PET imaging. Representative [^{18}F]FLT PET images at days 0 and 2 and corresponding T2w MR images at day 1 and day 6 of two mice bearing an orthotopic i.c. Gli36dEGFR xenograft and who received daily injections of DMSO (**a**) or 25 mg/kg TMZ (**b**). [^{18}F]FLT PET indicates response of i.c. growing gliomas to TMZ as early as 2 days after treatment (This research was originally published in *Plos One*. Viel et al. (2013a))

receptors or signalling pathways, which will be discussed more in detail further in this chapter.

MR imaging is the most common technique to assist the management of patients with brain tumours. MRI techniques, such as T1- and T2-weighted imaging, contrast-enhanced T1-weighted imaging, dynamic contrast-enhanced (DCE) imaging and diffusion-weighted imaging (DWI), have excellent soft tissue specificity and provide information on tumour localisation and extent, local BBB damage and brain invasiveness, regional blood flow and blood volume and tumour cellularity which, in the clinical setting, are known to be associated with glioma grade and prognosis (Herholz et al. 2007). Also, secondary changes associated with tumour growth, such as oedema, brain shift or hydrocephalus, can be determined on two- or three-dimensional MR images. Not only in the clinical settings but also in preclinical research, MR imaging has been used increasingly to characterise murine brain tumour models (Borges et al. 2012). Recently, McConville et al. demonstrated that MRI can be used to predict tumour grade and survival in a genetically engineered mouse model of glioma (McConville et al. 2007). In the employed Ntv-a model, approximately 100 % of mice spontaneously develop gliomas by 3 weeks of age, with 30 % of these tumours displaying high-grade histologic features. T2-weighted and T1-weighted gadolinium-enhanced MRI could distinguish between high- and low-grade tumours on the basis of their growth rate and contrast enhancement. However, care should be taken when interpreting contrast leakage as an indicator of BBB breakdown due to malignant degeneration as this sign can be absent in diffuse infiltrative tumour regions, non-specific or induced by therapeutic intervention (Herholz et al. 2007). Especially, the treatment with antiangiogenic compounds can restore the BBB in angiogenic regions without concomitant tumour regression. This underlines the need for alternatives to gadolinium-based contrast-enhanced MRI to detect progressing tumour portions that are not associated with angiogenesis and thus BBB disruption, but are based on an angiogenesis-independent tumour growth, for instance, via co-option of pre-existent vasculature (Leenders et al. 2004). Although these infiltrative lesions cannot be detected with gadolinium-based contrast-enhanced MRI, the relatively low vascular volume in these tumours, as compared to the surrounding tissue, can be exploited to detect these lesions using blood pool contrast agents such as ultrasmall superparamagnetic particles of iron oxide (USPIO) and to evaluate the response to antiangiogenic therapy (Claes et al. 2008). Furthermore, it has been shown that the rim of contrast enhancement at the margins of brain tumours detectable on MRI 24 h after intravenous injection of USPIOs correlates to the presence of iron-loaded macrophages and

microglia and can be used for tumour delineation and evaluation of tumour aggressiveness as the level of contrast enhancement seems to correlate with tumour proliferation and tumour growth (Kremer et al. 2007). When conjugating such an MR-detectable iron oxide nanoparticle to an optically detectable NIRF fluorochrome, this multimodality approach permits the correlation of preoperative MR images to intraoperative optical images to guide accurate tumour resection (Kircher et al. 2003). Another technique to follow indirectly in vivo tumour angiogenesis as a necessary component of tumour expansion, invasion and possible metastasis is DCE MRI that enables the longitudinal investigation of changes in tumour vascular permeability, vascular density and vessel morphology. Veeravagu et al. demonstrated in an orthotopic murine (GL26) glioblastoma model that in vivo changes in blood vessel permeability, as shown by DCE MRI, correlate with histologic quantification of vascular density and vessel diameter as well as with the molecular expression of angiogenic factors such as VEGF and angiopoietins (ANG-1 and ANG-2) (Veeravagu et al. 2008). An alternative MR approach to DCE was introduced by Dennie et al. based on the ratio of gradient and spin echo relaxation rate changes ($\Delta R2^*/\Delta R2$) after injection of an iron oxide-based superparamagnetic contrast agent of high molecular weight (Dennie et al. 1998). Since $\Delta R2^*/\Delta R2$ increases with increasing vessel size, this method enables calculation of the average vessel size within a voxel, which reveals an additional important parameter of the angiogenic process. Based on these findings, Jensen and Chandra proposed to map the ratio of $Q = \Delta R2/(\Delta R2^*)$ (2/3). For a certain concentration threshold of the contrast agent, in combination with appropriate echo times, Q has the advantage of being independent of the concentration of the contrast agent and correlates with vessel density (Jensen and Chandra 2000). This MR protocol has been used by our group in a rodent model of human brain tumour to enable non-invasive assessment of parameters related to the blood volume in tumour microvessels, to the total tumour blood volume, to the tumour vessel densities and to the tumour vessel size (Viel et al. 2013b). Finally, diffusion-weighted imaging (DWI) can be used in cancer imaging to assess tumour cellularity and infiltration and to monitor response to therapy. The apparent diffusion coefficient (ADC) of water has been found to increase in the early phase of anticancer therapies. Treatment-induced killing of tumour cells in a 9L brain glioma model, leading to a decrease of cell density in tumour tissue, results in an increase of the ADC that may be explained by destruction of tumour cells, widening of the extracellular space and a consequent increase in extracellular, relatively mobile water (Chenevert et al. 1997). Moreover, the treatment-induced increase in ADC values might occur as early as 4–5 days after therapy onset and precedes volumetric tumour changes (McConville et al. 2007). By depicting patterns of anisotropic diffusion, diffusion tensor imaging (DTI) and fibre tractography permit the visualisation of the structural integrity and connectivity of neuronal fibres surrounding brain tumours, and this approach can be used to discriminate the different patterns of aggressiveness between C6 or 9L gliomas and F98 gliomas (Asanuma et al. 2008; Kim et al. 2008) and to evaluate the neuroprotective effect of a free radical trapping compound against invasive glioma growth (Asanuma et al. 2008).

Tumour metabolism can be approached non-invasively by means of MR spectroscopy (MRS). MRS metabolic profiling has shown a good correlation between metabolic phenotypes and tumour type, proliferation index, metabolic activity and cell death (Griffin and Kauppinen 2007) and can be used for assessment of glioma grading (Bulik et al. 2013). Metabolic changes associated with intracranial tumour growth can be monitored with MRS and can be used to evaluate cell damage as early as 2–4 days after ganciclovir treatment in gene therapy of experimental gliomas (Hakumaki et al. 1999) and to predict and monitor clinical response to TMZ therapy (Guillevin et al. 2011). Nevertheless, most information on the metabolic state of intracranial gliomas can be gained with PET imaging, as stated above.

Another, rapidly expanding approach to non-invasively and sensitively image tumour load in intact animals is optical imaging, especially bioluminescence imaging (BLI). In general BLI of

tumour load is based on the conversion of a substrate by a specific enzyme called luciferase. This chemical reaction is accompanied by the production of light. The most prominent example is the ATP-dependent conversion of luciferin into the light-emitting product oxyluciferin by firefly luciferase (FLuc). The ATP, which is required for the enzyme reaction, is endogenously present in viable cancer cells, and thus the bioluminescence signal is only derived from living cancer cells and not from necrotic areas in the tumour (Klerk et al. 2007). Several validation studies that correlated BLI signals with the amount of inoculated tumour cells, with tumour volume measurements using callipers, with MRI volume measurements, with tumour weight measurements or with fluorescence-activated cell sorting (FACS) analysis of cancer cells in affected tissues indicate that BLI is useful to determine tumour load in the course of time, with each animal serving as its reference (Dinca et al. 2010). However, BLI is less suited for the determination of absolute tumour mass because of scatter and absorption of light by tissue components. Furthermore, the determination of exact tumour location is hampered because of the limited spatial resolution (Klerk et al. 2007). Nevertheless, BLI is particularly useful for longitudinal follow-up of tumour growth during therapy intervention studies (Dinca et al. 2010). Rehemtulla et al. (2000) investigated the ability of BLI to non-invasively quantify the growth and therapeutically induced cell death of orthotopic rat brain tumours derived from 9L gliosarcoma cells genetically engineered to stably express FLuc. Quantitative comparison of tumour cell death determined from serial MRI volume measurements and BLI photon counts following 1,3-bis(2-chloroethyl)-1-nitrosourea (BCNU) treatment revealed a statistically significant correlation between both modalities, providing direct validation of BLI imaging as a powerful and quantitative tool for high-throughput assessment of antineoplastic therapies. In a similar approach, Szentirmai et al. evaluated the antiangiogenic treatment effect of adenoviruses encoding antiangiogenic soluble vascular endothelial growth factor (VEGF) receptors in nude mice bearing U87MG glioma cells genetically engineered to express the firefly luciferase gene (Szentirmai et al. 2006).

28.5 Imaging Response to Therapy

Conventional PET and MR techniques have been used for a long time to evaluate response to therapy. Most commonly used is T1- and T2-weighted MR imaging that relies on the detection of morphological (volume) changes related to therapy. In a rat central nervous system lymphoma model, Jahnke et al. recently compared T2/fluid-attenuated inversion recovery (FLAIR) and gadolinium contrast-enhanced T1 MRI sequences for their ability to monitor response to chemotherapy by evaluating image-derived changes in tumour volume before and 1 week after treatment (Jahnke et al. 2009). In untreated control animals, tumour histological volumes correlated well with T2/FLAIR and contrast-enhanced T1 images; however, after treatment, only T2/FLAIR correlated significantly with histology. Tumour shrinkage is usually a late response and dependent on cell apoptosis and clearance of non-viable cells. By tracking changes in the molecular motion of water (designated as apparent diffusion coefficient, ADC), diffusion-weighted MRI gives insights into changes in tumour cellularity and membrane permeability that can occur well before changes in tumour volume or tumour contrast enhancement (McConville et al. 2007) and provides a sensitive means to assess dynamic therapy-induced responses, including the appearance of changes in drug sensitivity (Lee et al. 2006). Also [^{18}F]FDG PET has proven to be a relative early response marker in a variety of tumours (breast cancer, ovarian cancer, rectal cancer, oesophageal cancer, lung cancer), with significant detectable changes in [^{18}F]FDG uptake after a few cycles or a few weeks of chemotherapy treatment (Pantaleo et al. 2008). However, not all tumours are rapidly dividing and glycolytic, and many emerging targeted therapies are cytostatic or do not influence tumour glucose metabolism. As a result, other more specific imaging approaches are necessary that are also capable of evaluating directly the effects of novel targeted therapies and not only secondary, relatively non-specific changes. Examples of such specific imaging approaches are the direct

non-invasive evaluation of apoptosis, angiogenesis or growth factors and related signal transduction pathways.

28.5.1 Apoptosis Imaging

Apoptosis is an essential component of normal human growth and development, immunoregulation and tissue homeostasis by providing a means for elimination of redundant, damaged or diseased cells. Apoptosis may be initiated in response to cellular stress and DNA-damaging events, such as growth factor deprivation, hypoxia, heat, cold or chemical injury (Coppola et al. 2008). Furthermore, several genetic alterations associated with cancer, such as bcl-2 activation, MDM2 overexpression or p53 mutations, dysregulate apoptosis and facilitate neoplastic transformation. Apoptotic cell death can be initiated through an extrinsic pathway involving activation of cell surface death receptors or by an intrinsic pathway via mitochondria (Kelloff et al. 2005). Both pathways lead to activation of initiator (e.g. caspase-1, caspase-8, caspase-10) and effector (e.g. caspase-3, caspase-6, caspase-7) caspases that trigger a proteolytic cascade resulting in fragmentation of intracellular components and appearance of apoptotic morphology. One of the earliest effects of caspase activation is the disruption of the translocase system that normally maintains phosphatidylserine (PS) on the interior of the cell membrane. This results in the redistribution of phosphatidylserine to the outer membrane leaflet, where it serves as a signal to phagocytic cells to engulf and digest the membrane-enclosed apoptotic cells. Because many current cancer therapies promote cell death by reinstituting the apoptotic pathways, the ability to detect apoptosis by direct imaging of caspase activity or PS expression would aid significantly in the development and evaluation of such apoptotic pathway modulators (Blankenberg 2008).

Caspase peptide substrates containing either a nuclear (a ^{18}F-labelled caspase-inhibiting analogue) or a bioluminescence label or a far-red or near-infrared optical fluorochrome have been developed to detect apoptosis (Blankenberg 2008; Nicholls and Hyman 2014). The caspase-3-/caspase-7-specific PET radiotracer [^{18}F]ICMT-11 (^{18}F-(*S*)-1-((1-(2-fluoroethyl)-1H-[1,2,3]-triazol-4-yl)methyl)-5-(2(2,4-difluorophenoxymethyl)-pyrrolidine-1-sulfonyl)isatin) has shown promise for the early detection of drug-induced tumour apoptosis in xenograft models of lymphoma and breast and colon cancer, in which drug treatment increased probe retention in the tumours by 1.5- to twofold as early as 24 h post-treatment (Nguyen et al. 2009, 2013). Further evaluation of this tracer in preclinical models and humans is ongoing (Nguyen et al. 2012). Using firefly luciferase-based bioluminescence imaging in nude mice, Laxman et al. developed a caspase-cleavable reporter probe able to detect tumour apoptosis following chemotherapy (Laxman et al. 2002). In this study, a recombinant luciferase reporter molecule was developed in which luciferase activity was silenced via steric hindrance by the oestrogen receptor (ER) regulatory domain. Inclusion of a protease cleavage site for caspase-3 (DEVD) between the luciferase domain and the silencing domain allowed for protease-mediated activation of the reporter molecule. In vivo studies using a human glioma cell line stably expressing the reporter molecule revealed that caspase-3 activity by activation upon tumour necrosis factor-related apoptosis-inducing ligand (TRAIL) treatment could be imaged non-invasively by using BLI. Furthermore, the temporal pattern of caspase-3 activity in response to TRAIL treatment has been followed: sustained TRAIL administration only results in a transient induction of apoptosis, whereas concomitant treatment with 5-fluorouracil and TRAIL produces a synergistic and prolonged enhancement in apoptosis activation and a prolonged growth delay (Lee et al. 2007). In an attempt to develop an improved apoptosis reporter with increased signal to noise, the same group recently used the split firefly reporter strategy (Coppola et al. 2008). The developed reporter, ANLucBCLuc, constitutes a fusion of small interacting peptides (peptide A and peptide B) with the NLuc and CLuc fragments of luciferase and with the caspase-3 cleavage site DEVD between pepANLuc (ANLuc) and pepBCLuc (BCLuc).

During apoptosis, caspase-3 cleaves the reporter, enabling separation of ANLuc from BCLuc. A high-affinity interaction between peptide A and peptide B then restores luciferase activity by NLuc and CLuc complementation. Treatment of live cells and mice carrying D54 glioma tumour xenografts with chemotherapeutic agents such as temozolomide and perifosine (an alkylphospholipid that exerts its cytotoxic effect by interfering with Akt activation) resulted in a dose-dependent induction of bioluminescence activity, which correlated with activation of caspase-3 as determined by Western blot analysis and caspase-3 immunohistochemical staining. Furthermore, treatment of mice bearing glioma xenografts with combination therapy of temozolomide and radiation resulted in increased bioluminescence activity over individual treatments and increased therapeutic response (tumour shrinkage) due to enhanced apoptosis. A follow-up study of adenovirus-mediated TRAIL gene therapy in human D54 glioma cells stably expressing the same caspase-3 biosensor as well as the *Renilla* luciferase (R*Luc*) gene could visualise and evaluate the induction of apoptosis (by means of BLI of the caspase-3 sensor) and the therapeutic response (by means of RLuc activity as surrogate marker for cell viability) (Singh et al. 2014). A multimodality caspase-3 sensor has been developed, composed of a fluorescence reporter (monomeric red fluorescent protein, mRFP), a PET reporter (HSV-1-sr39 thymidine kinase, tTK) and firefly luciferase (FLuc), each joined by DEVD as peptide linker (Ray et al. 2008). In the fused form, all the three reporter proteins had markedly attenuated activity. However, upon cleavage by activated caspase-3 (induced by staurosporine), a significant gain in mRFP1, FLuc and tTK enzyme activity could be observed by fluorescence-activated cell sorting (FACS), enzyme-based assays and in vivo BLI and microPET imaging. Also a cyclic herpes simplex virus type 1 thymidine kinase reporter (cTK266) containing a caspase-3 cleavage domain has been developed and used for successful real-time PET imaging of apoptosis (Wang et al. 2014).

PS exposure has been the most pursued target for the detection for cell death using molecular imaging methods (Blankenberg 2008; Neves and Brindle 1766). The 40-kDa vesicle-associated protein annexin V (AnxV) has been the most widely used PS-targeting moiety. AnxV binds PS in a calcium-dependent manner and with high (nanomolar) affinity. Initially, AnxV was coupled to fluorescent dye molecules and used as an apoptosis detection reagent for fluorescence microscopy and flow cytometry. Subsequently, AnxV was coupled to a radionuclide (^{99m}Tc) and used to detect apoptosis non-invasively in animals and in the clinic using radionuclide imaging techniques. Recent studies in oncology suggest that a single scan 24–48 h after the start of treatment can identify patients with response after one course of chemotherapy. Other radionuclide derivatives of AnxV have been developed, including AnxV labelled for SPECT with ^{123}I or for PET labelled with ^{18}F or ^{124}I and ^{64}Cu-labelled streptavidin for PET imaging after pretargeting of PS with biotinylated annexin V. Photonic imaging methods have also been used to image AnxV labelled with fluorochromes or near-infrared (NIR) fluorochromes, and Schellenberger et al. were the first to label AnxV with SPIO nanoparticles for MR detection (Schellenberger et al. 2003). Later also Gd-containing AnxV-coated liposomes for positive or bimodal MR contrast have been developed as well as multimodality contrast agents for combined MRI and fluorescent imaging.

Besides annexin V, other imaging probes have been developed and investigated to visualise PS exposure in vivo, including PS binding proteins, peptides and small molecules (Niu and Chen 2010). For instance, the smaller PS-targeting protein synaptotagmin-I, which also binds PS with nanomolar affinity in a calcium-dependent manner, has been labelled with SPIO nanoparticles and Gd^{3+} chelates for MRI-based detection (Zhao et al. 2001; Krishnan et al. 2008) as well as with ^{18}F and ^{99m}Tc for radionuclide-based detection of PS exposure in vivo after chemotherapy (Wang et al. 2008, 2011).

28.5.2 Angiogenesis Imaging

A variety of genetic anomalies that trigger glioma-associated angiogenesis, such as overexpression of vascular endothelial growth

factor (VEGF), epidermal growth factor (EGF), platelet-derived growth factor (PDGF) and their receptors or chronic activation of the hypoxia-inducible transcription factor-1 (HIF-1), have been identified and can be measured directly or indirectly by non-invasive imaging techniques and used as read-outs for targeted tumour treatment. Conventional imaging techniques like MRI and PET focus on the measurement of physiologic parameters, such as blood flow, blood volume, vascular perfusion, permeability and/or structure, and represent the radiographic tools in current clinical trials of antiangiogenic therapy (Waerzeggers et al. 2009b). In glioma patients antiangiogenic approaches might initiate transformation from an angiogenic to an infiltrative phenotype (Verhoeff et al. 2009). Therefore, our group investigated the feasibility of PET and MRI to differentiate both phenotypes non-invasively with clinically relevant imaging parameters such as [^{18}F]FDG, [^{18}F]FLT, [^{11}C]MET, T2-weighted, contrast-enhanced T1-weighted and diffusion-weighted MRI (Fig. 28.2) (Viel et al. 2012). The study showed that these imaging techniques are very well suited to evaluate the angiogenic GBM phenotype (high uptake of [^{18}F]FLT and [^{11}C]MET, relatively low uptake of [^{18}F]FDG, clear tumour delineation on T1- and T2-weighted MRI with strong gadolinium enhancement). However, they fail to detect the infiltrative tumour growth especially in the absence of BBB breakdown (no accumulation of [^{18}F]FLT and [^{11}C]MET, impaired uptake of [^{18}F]FDG, absent gadolinium enhancement, low contrast on T1- and T2-weighted MRI). We also evaluated the MR approach introduced by Dennie et al. (Dennie et al. 1998) relying on the gradient and spin echo relaxation changes after injection of an iron oxide-based superparamagnetic contrast agent of high molecular weight (Viel et al. 2013b). This method enables non-invasive assessment of the anatomy and physiology of the vasculature of experimental gliomas. Combined with [^{11}C]MET and [^{18}F]FLT PET for monitoring biochemical markers of angiogenesis and proliferation in addition to vessel anatomy, this imaging protocol is particularly useful to improve our understanding of antiangiogenic therapy response of gliomas and in particular how tumours can escape therapy despite normalisation of vasculature (Fig. 28.3).

Although imaging of physiologic parameters related with tumour-associated angiogenesis is viable and widely practised, the use of contrast agents targeted to molecular cancer markers is more straightforward and facilitates early and accurate diagnosis and treatment follow-up, leading to improved and personalised patient management. Especially with the rising use of targeted antiangiogenic therapies like bevacizumab (Avastin), the possibility to directly image the molecular markers of angiogenesis (and thus the targets of the antiangiogenic therapy) has become increasingly important.

During the last years, intense research focused on VEGF/VEGFR-targeted molecular imaging, and a wide variety of targeting molecules (peptides, proteins, antibodies and nanoparticles) have been labelled with various imaging labels (such as radioisotopes, fluorescent dyes, T1/T2 agents and microbubbles) for PET, SPECT, optical, MR or contrast-enhanced ultrasound imaging of tumour angiogenesis (Cai and Chen 2008; Toy et al. 2014). Hsu et al. (Hsu et al. 2007) used multimodality (BLI, MRI and PET) molecular imaging to determine the antiangiogenic and antitumour efficacy of a vasculature-targeting fusion toxin (VEGF(121)/rGel) composed of the VEGF-A isoform VEGF(121) linked with a G(4)S tether to recombinant plant toxin gelonin (rGel) in an orthotopic glioblastoma mouse model. In this study, the level of target expression was monitored before therapy by [^{64}Cu]-1,4,7,10-tetraazacyclododedane-N,N′,N″,N‴-tetraacetic acid (DOTA)-VEGF(121)/rGel PET, whereas [^{18}F]FLT scans were obtained before and after treatment to evaluate VEGF(121)/rGel therapeutic efficacy. In VEGF(121)/rGel-treated mice, a significant decrease in [^{18}F]FLT uptake and peak BLI tumour signal intensities could be observed as compared to non-treated mice, and these results were validated by histologic analysis.

Also expression of cell adhesion molecules, such as integrins, is significantly upregulated during tumour growth and angiogenesis, and αvβ3 expression has been correlated with tumour aggressiveness. αvβ3 integrin expression can be

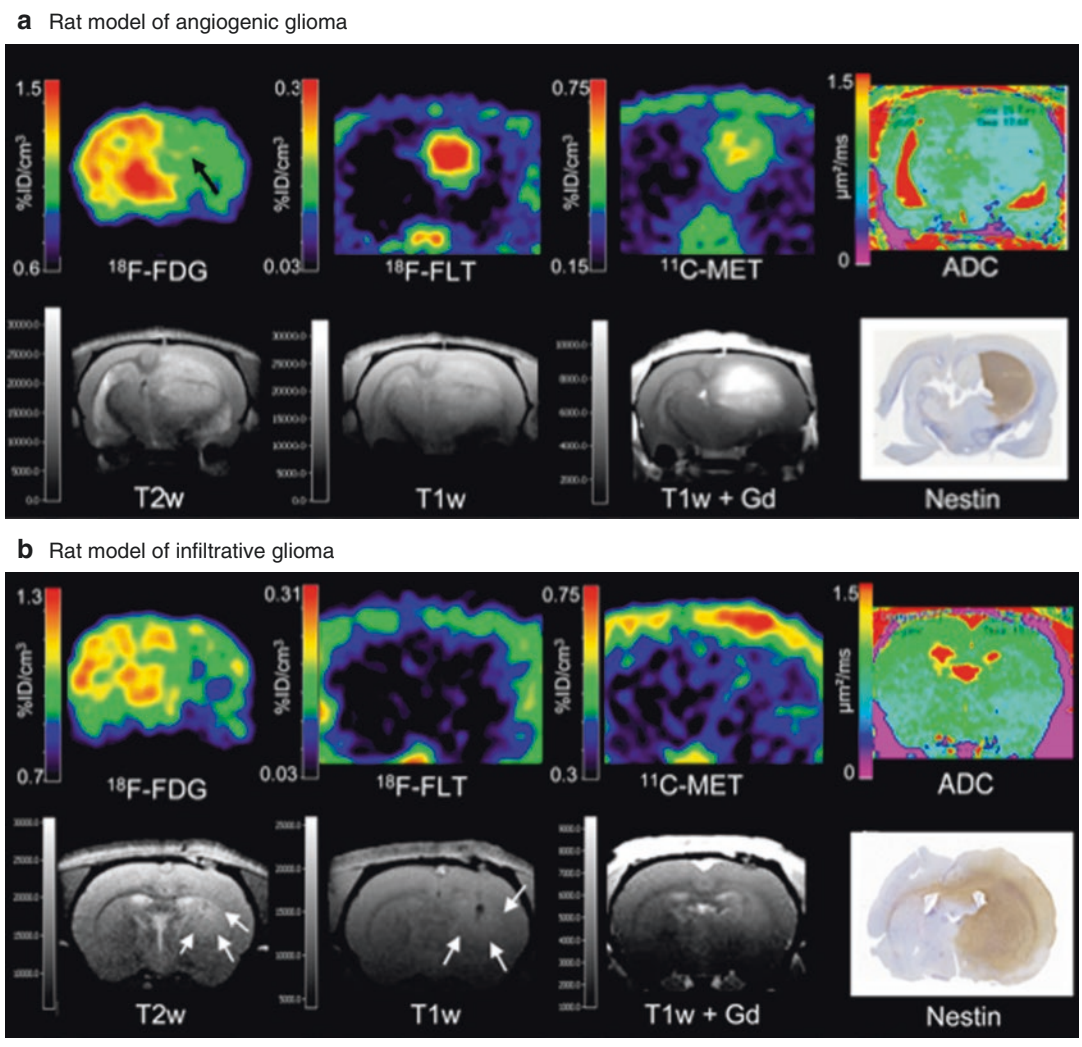

Fig. 28.2 Non-invasive assessment of glioma phenotype by multi-tracer PET and MRI. Nude rats were implanted with spheroids derived from two human glioblastoma, giving an angiogenic and an infiltrative glioma model. [^{18}F]FDG, [^{18}F]FLT and [^{11}C]MET PET scans, together with T2w, T1w, gadolinium-enhanced T1w and diffusion-weighted MR scans were performed during week 6 after glioma implantation. PET and MR images were coregistered based on anatomical MR information using the software Vinci (http://www.nf.mpg.de/vinci3/). (**a**) For the angiogenic model, [^{18}F]FDG uptake was reduced in the entire ipsilateral hemisphere but was heterogeneous (*black arrow*), whereas [^{18}F]FLT and [^{11}C]MET uptake increased substantially. Tumours were discernible on T2- and T1-weighted MRI scans before injection of gadolinium contrast agent and were enhanced after injection. Reduced ADC in tumour, compared with contralateral brain, revealed dense tumours. Nestin staining of brain sections confirmed the presence of circumscribed tumour. (**b**) For the infiltrative phenotype, only the low [^{18}F]FDG uptake revealed clearly the presence of tumour. Only minor [^{11}C]MET uptake was observed, while [^{18}F]FLT failed to detect this glioma. Extent of infiltrative tumours was observed by T2- and T1-weighted MRI (*white arrows*), but contrast was low and did not enhance after gadolinium injection. Nestin staining of brain sections confirmed the presence of an infiltrative tumour (This research was originally published in *JNM*. Viel et al. (Viel et al. 2012). © by the Society of Nuclear Medicine and Molecular Imaging, Inc)

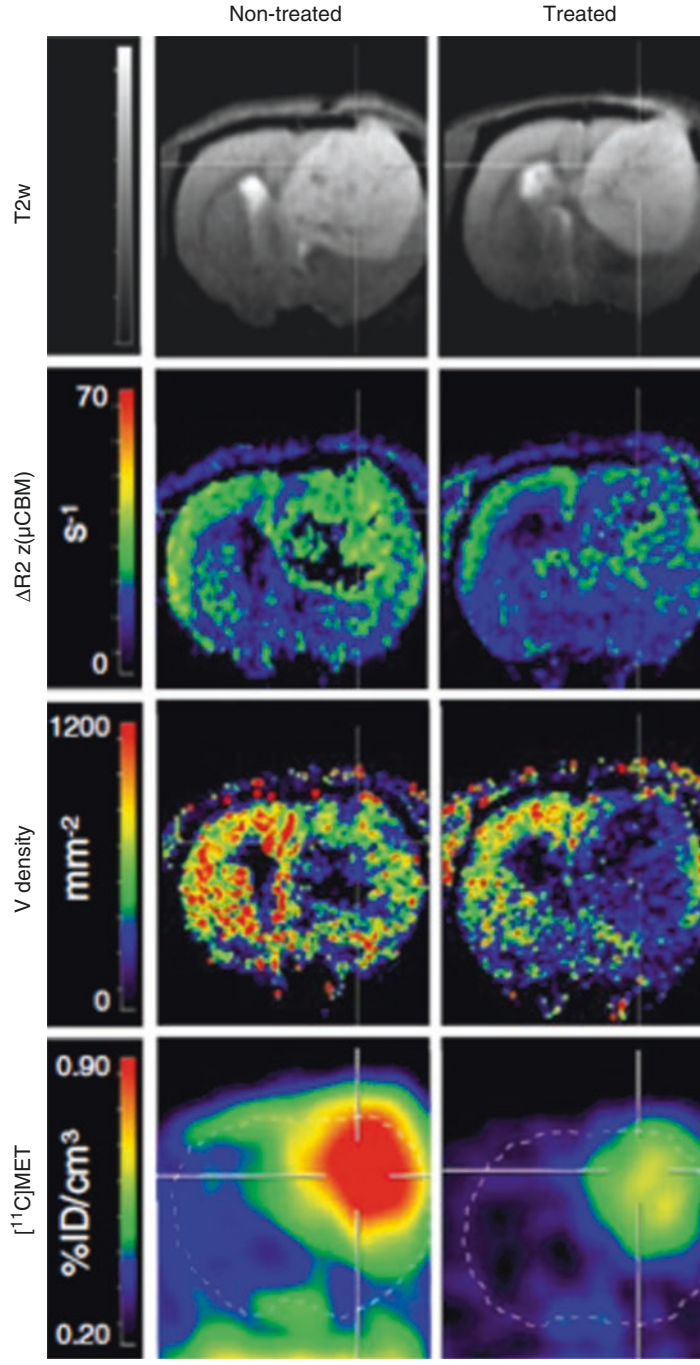

Fig. 28.3 Non-invasive imaging of glioma vessel size and densities in correlation with tumour cell proliferation by small-animal PET and MRI. T2w, T2*w and diffusion-weighted MR sequences were performed with injection of iron oxide contrast agent to calculate maps of parameters related to microvessel blood volume (μCBV) or vessel densities in rats developing orthotopic glioma and treated with an antiangiogenic compound (bevacizumab). This MR protocol was combined with [^{11}C]MET PET. A transaxial section of the different coregistered images of the brain of two rats are presented here. A reduction of the tumour microvessel blood volume, the tumour vessel density and the [^{11}C]MET tumour accumulation upon treatment could be observed, while no reduction of the tumour volume could be measured at this stage (Modified from Viel et al. (2013b) with permission)

measured by targeted radiolabelled, paramagnetic or fluorescent molecules (cyclic arginine-glycine-aspartic acid RGD peptides), and this method can be used to selectively target suicide gene therapy or drug delivery (Cai and Chen 2008) and to non-invasively monitor therapy response (Zhang et al. 2012b).

Non-invasive imaging of HIF-1 activity in vivo has been performed for the first time using a HIF-1-dependent reporter system for PET imaging.

Serganova et al. (Serganova et al. 2004) developed a dual reporter gene cassette to monitor non-invasively the dynamics and spatial heterogeneity of HIF-1-specific transcriptional activity in tumours and showed that HIF-1-mediated activation of thymidine kinase green fluorescent protein (TKGFP) reporter gene expression in hypoxic tumour tissue can be non-invasively and repeatedly visualised in living mice using PET imaging with [^{18}F]-2′-fluoro-2′-deoxy-1β-D-arabionofuranosyl-5-ethyl-uracil (FEAU). Tumour cells transfected with this construct may be used to study how treatment modulates hypoxia and subsequent HIF-1-mediated gene expression. Since then, several approaches for non-invasive PET imaging of HIF-1 activity have been reported (Ueda and Saji 2014). Also a HIF-1-sensitive bioluminescence reporter system has been developed and used for the detection of spontaneous solid tumour development (Goldman et al. 2011).

28.5.3 Imaging Growth Factors

The epidermal growth factor receptor (EGFR) is one of the most studied molecules as a target for cancer therapy (Brandes et al. 2008). EGFR is a cell surface receptor with tyrosine kinase (TK) activity that belongs to the c-erb family. Dysregulation of EGFR is associated with several key features of cancer, such as autonomous cell growth, inhibition of apoptosis, angiogenic potential, invasion and metastases (Fig. 28.4), and aberrant EGFR pathway activation may be the result of different molecular abnormalities which include gene amplification, receptor mutations, growth factor overexpression or cross-link activation of downstream signalling pathways. EGFR has been shown to be differentially deregulated, overexpressed, mutated or amplified in many types of cancer, including 40–60 % of glioblastoma, and has been associated with a poor prognosis, especially when occurring in younger glioblastoma patients (Brandes et al. 2008). The EGFR family comprises four members: EGFR (also known as HER1), HER2 (also known as Neu), HER3 and HER4. They share similar structures, with an extracellular ligand-binding domain, a transmembrane domain and a functional intracellular TK domain (except for HER3). Two main categories of EGFR mutations exist: deletion or point mutations in the extracellular domain and somatic mutations in the TK domain (Brandes et al. 2008). The type III EGFR mutant (EGFRvIII), which lacks the amino acid residues 6–273 in the extracellular domain, is the most common one and is observed in 60–70 % of EGFR-overexpressing glioblastomas. Since EGFRvIII lacks a large portion of the ligand-binding domain and hence is unable to bind either EGF or other EGFR ligands, it is constitutively active and can initiate downstream signalling because the deletion results in a conformational change that mimics the one induced by ligand binding in wild-type EGFR. These EGFRvIII-positive tumours are reported to be associated with a worse prognosis and shorter life expectancy. The other category of EGFR mutations involves changes in the TK domain that can influence the binding of TK inhibitors (TKIs). These mutants exhibit increased activation compared to wild-type EGFR, but at the same time are much more sensitive to inhibition by EGFR TKIs. However, mutations in the tyrosine kinase domain could not be shown in malignant gliomas so far (Brandes et al. 2008). Monoclonal antibodies (mAbs) against EGFR and small molecule inhibitors targeting tyrosine kinases that bind to the intracellular part of the receptor and thereby block receptor phosphorylation are the two major strategies for inhibiting the EGFR pathway and have been introduced in clinical practice for patients with malignant gliomas (Waerzeggers et al. 2009c). However, findings reported in studies evaluating EGFR inhibitors are surprisingly contradictory, and no clear predictive role of receptor status on anti-EGFR drug response could be found (Brandes et al. 2008). These results indicate the need for the development and validation of non-invasive imaging techniques targeted to EGFR expression to predict which patients will likely respond to anti-EGFR therapy and to monitor patient response to such personalised cancer management. Different imaging approaches have been developed to specifically detect EGFR expression, from OI

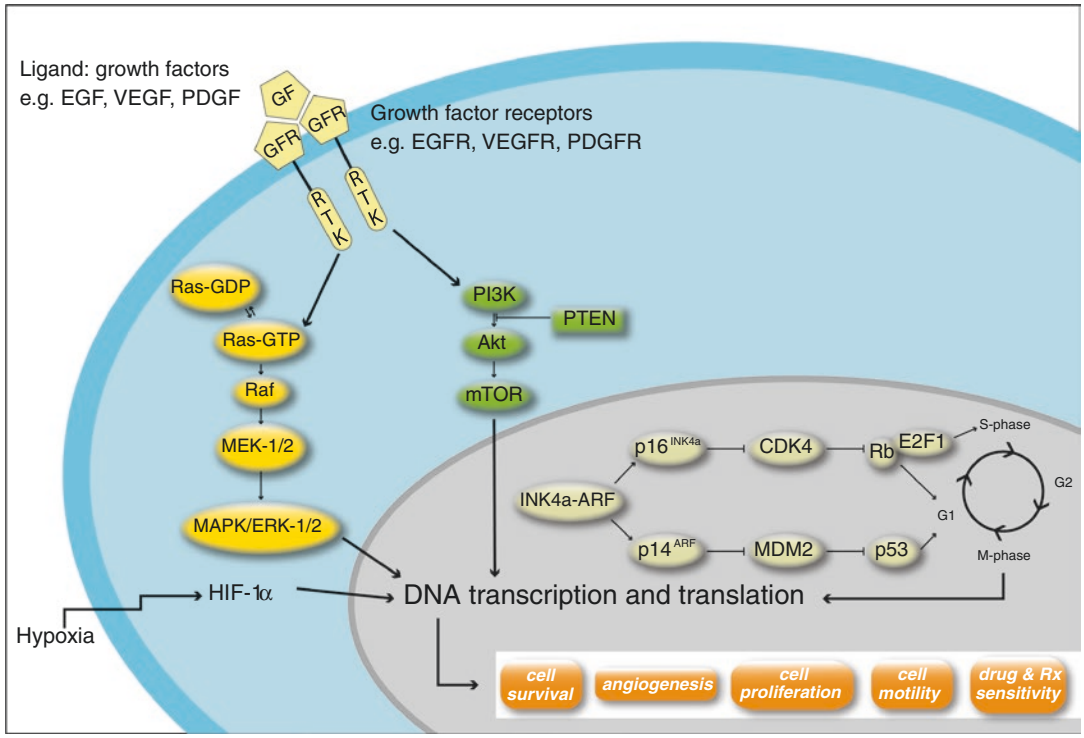

Fig. 28.4 Schematic representation of relevant signal transduction pathways and cell cycle control pathways known to be dysregulated and involved in glioma initiation and growth. *GF* growth factor; *GFR* growth factor receptor; *RTK* receptor tyrosine kinase; *EGF* epidermal growth factor; *VEGF* vascular endothelial growth factor; *PDGF* platelet-derived growth factor and their respective receptors EGFR, VEGFR and PDGR; *MAPK* mitogen-activated protein kinase; *ERK* extracellular signal-regulated kinase; *MEK* MAPK/ERK kinase; *PLC* phospholipase C; *PKC* protein kinase C; *PI3K* phosphatidylinositol-3-kinase; *PTEN* phosphatase and tensin homology deleted on chromosome 10; *Akt* protein kinase B; *mTOR* mammalian target of rapamycin; *HIF-1* hypoxia-inducible factor-1; *INK4a/ARF* inhibitor of kinase 4/alternative reading frame tumour suppressor genes; *CDK4* cyclin-dependent kinase 4; *MDM2* murine double minute 2 oncogene; *p53* protein 53 transcription factor; *Rb* retinoblastoma tumour suppressor protein; *E2F1* transcription factor (activator) from E2F family of transcription factors

modalities to nuclear and MR technologies, and two different labelling strategies have been studied so far: labelling small molecules such as TK inhibitors or analogues and labelling antibodies directed to the extracellular domain of the receptor (Pantaleo et al. 2009; Gelovani 2008; Cai et al. 2008; Qiao et al. 2014; Corcoran and Hanson 2014).

A number of ^{11}C, ^{18}F and radioiodine-labelled EGFR kinase inhibitors that bind reversibly or irreversibly to the EGFR kinase ATP-binding pocket have been developed. The radiolabelled irreversible EGFR inhibitors demonstrate the greatest potential for derivatisation into effective EGFR kinase imaging agents, as compared to those developed based on reversible inhibitors due to the rapid washout of the latter. Especially, PET imaging with (E)-but-2-enedioic acid [4-(3[^{124}I] iodoanilino)-quinazolin-6-yl]-amide-(3-morpholin-4-yl-propyl)-amide (morpholino[^{124}I] IPQA) seems to be very promising as this tracer binds covalently to the ATP-binding site in activated EGFR but not in inactive EGFR (Pal et al. 2006). In vitro studies demonstrated rapid accumulation and progressive retention post washout of morpholino[^{123}I]IPQA in A431 cells and in U87MG human glioblastoma cells genetically modified to express EGFRvIII (U87ΔEGFR), but not in the wild-type U87MG cells (which have low kinase activity) under serum-starved conditions. Also, the in vivo studies demonstrated a significant difference in the accumulation of the radiotracer in A431 carcinoma xenografts that reflected the EGFR expression and EGFR activity

in comparison to K562 control xenografts. The authors concluded that PET imaging with morpholino-^{124}I-IPQA should allow for identification of tumours with high EGFR signalling activity, such as brain tumours expressing the EGFRvIII mutant and non-small cell lung cancer (NSCLC) expressing gain-of-function EGFR mutants expected to have an increased sensitivity to EGFR TKIs (Cai et al. 2008). However, it should be pointed out that PET imaging was not carried out in U87ΔEGFR human glioma xenograft mice. Also, pegylation of known irreversible compounds with various lengths of polyethylene glycol (PEG) chains seems very promising due to increased stability and solubility of the radiolabelled tracers (Dissoki et al. 2007).

Labelling monoclonal antibodies with radioisotopes represents another strategy for the in vivo visualisation of EGFR tumour expression, but it seems more complicated. In comparison to labelling TK inhibitors, fewer studies have been conducted with the attempt of synthesising monoclonal antibody-based probes (Pantaleo et al. 2009; Cai et al. 2008; Corcoran and Hanson 2014). The natural ligand of EGFR, EGF, has been labelled with ^{76}Br or ^{68}Ga for direct targeted PET imaging or with ^{99m}Tc (Cornelissen et al. 2005) or ^{131}I for tumour detection and evaluation of therapy response with SPECT imaging. Also, monoclonal antibodies (mAbs) against EGFR, used for anti-EGFR therapy such as cetuximab, have been labelled with positron emitters, e.g. ^{64}Cu, or gamma-emitters, e.g. ^{99m}Tc and ^{111}In, with good tumour contrast and good correlation between tumour uptake and tumour EGFR expression level as measured by Western blot (Sihver et al. 2014). However, MRI with a ferromagnetic anti-EGFR mAb in athymic rats bearing EGFR-positive tumours revealed that the targeted contrast agent only gave modest EGFR-specific MR contrast in vivo (Suwa et al. 1998). Additionally, optical imaging studies on EGFR expression have been carried out with fluorescently labelled EGF or anti-EGFR mAbs (Diagaradjane et al. 2008). In an attempt to follow the role of growth factor receptor expression in glioma progression and to image therapeutic efficacy of targeted therapies, Arwert et al. genetically engineered glioma cells to visualise the dynamics of EGFR and targeted therapies in real time in vivo (Arwert et al. 2007). The authors created lentiviral (LV) reporter constructs containing fusions between EGFR or EGFRvIII and the bioluminescent-fluorescent fusion protein marker GFP-RLuc to transduce Gli36 glioma cells expressing FLuc-DsRed2. In vivo imaging of mice bearing EGFR-GFP-RLuc/FLuc-DsRed2 or EGFRvIII-GFP-RLuc/FLuc-DsRed2 gliomas in the right frontal lobe revealed that there is a direct correlation between EGFR expression (RLuc activity) and glioma cell proliferation (FLuc activity) in the initial stages of glioma progression. Using the same tumour model, the authors also could show that EGFR-targeted therapies (short hairpin RNAs, shRNA, targeting the two variants of EGFR or a monoclonal EGFR-antibody, cetuximab) result in a considerable reduction in glioma cell proliferation in culture and glioma burden in vivo that can be monitored in real time. Similar results have been obtained with HSV-1 amplicon vector-mediated shRNA targeting EGFR and evaluation by BLI (Saydam et al. 2005).

Another tyrosine kinase receptor that is implicated in the malignant progression of glioblastomas is c-Met, the receptor for the hepatocyte growth factor (HGF). Expression of HGF has been shown to be associated with poor prognosis of malignant gliomas, and both HGF and c-Met have emerged as key determinants of brain tumour growth and angiogenesis (Arrieta et al. 2002; Abounader and Laterra 2005). C-Met expression can be non-invasively imaged with MRI by specifically tagging the receptor with an anti-c-Met antibody linked to biotinylated gadolinium (Gd)-diethylene triamine penta acetic acid (DTPA)-albumin (anti-c-Met-Gd-DTPA-albumin) (Towner et al. 2008).

28.5.4 Imaging Signal Transduction Pathways

Recent advances in preclinical research have led to the development of several targeted reporters to interrogate the activity of other receptors or elements in intracellular signalling cascades related to cell growth and proliferation. Direct non-invasive imaging of therapy-induced changes in the cell cycle regulatory pathways controlled by PI3K/Akt/mTOR or further downstream

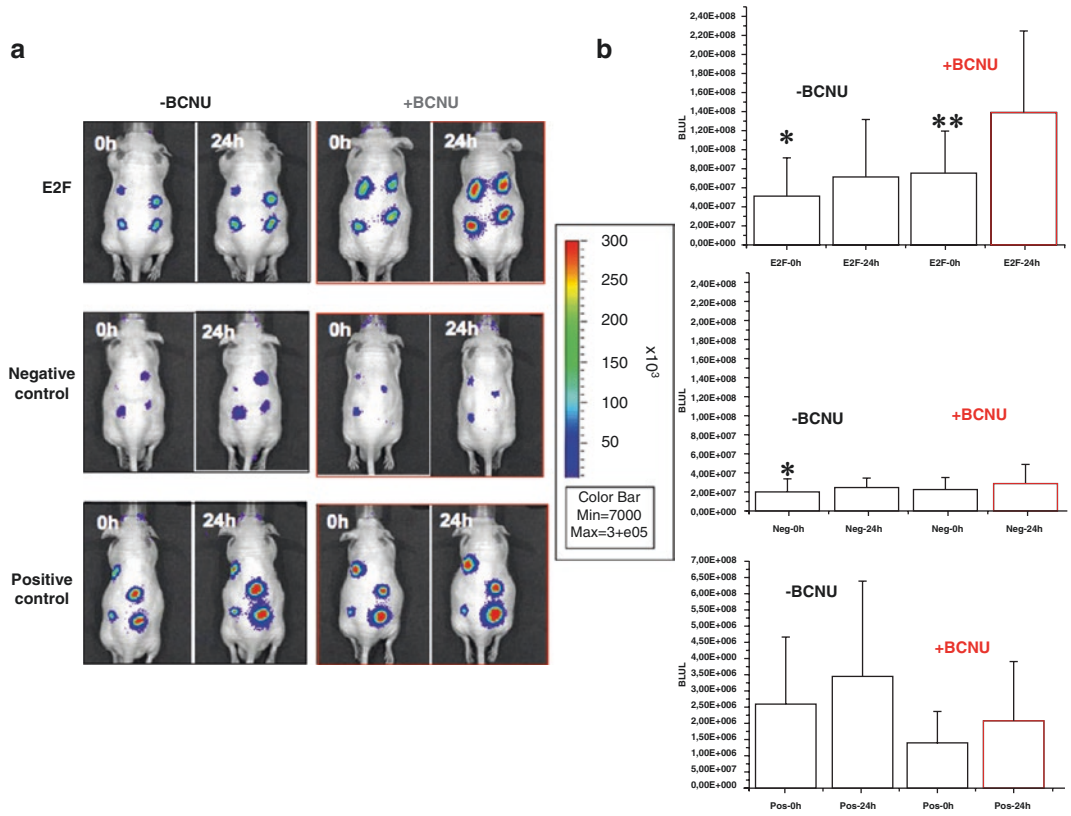

Fig. 28.5 Imaging E2F-1 signal transduction. (**a**) E2F-regulated cells and negative and positive control cells were implanted as a set of four tumours in the back of different groups of experimental mice. Mice were followed over time by bioluminescence imaging until tumours could be clearly visualised. Mice were then subjected to BCNU treatment (50 %) or control treatment (50 %), and repeat imaging was performed 24 h later. An increased luciferase signal was observed only in mice bearing E2F-1-regulated cells and not in mice bearing negative and positive control cells. Colour scale, luminescent signal intensity; blue, least intense signal; red, most intense signal. (**b**) Mean of the total bioluminescent signals emitted from E2F-1-regulated tumours and negative and positive control tumours in response to BCNU administration. Columns, mean of three independent experiments with $n=6$ animals per group; bars, SD. Significant differences are indicated by * ($P<0.05$) and ** ($P<0.05$) (Modified from Monfared et al. (2008) with permission)

signalling moieties such as p53 or E2F offers additional strategies for cancer diagnosis and to develop and evaluate targeted therapies directed to specific cancer-related molecular alterations (Fig. 28.4) (Gaikwad and Ray 2012).

Our group constructed a Cis-E2F/LucIRESTKGFP reporter system to non-invasively assess E2F-1-dependent transcriptional regulation in culture and in vivo (Monfared et al. 2008). In this reporter system the reporter genes firefly luciferase, HSV-1 thymidine kinase and green fluorescent protein are placed under control of an artificial cis-acting E2F-specific enhancer element. We could show that this reporter system is sensitive to non-invasively monitor various changes in cellular E2F-1 levels following DNA damage-induced upregulation of E2F-1 activity (Fig. 28.5). Following retroviral transduction of U87 glioma cells, exposure to 1,3-bis(2-chloroethyl)-1-nitrosourea leads to increased E2F-1 expression levels in a dose- and time-dependent manner, which can be quantified by in vivo imaging in established xenografts. Activation of the transcription factor E2F-1 via alteration of the p16-cyclin D-Rb pathway is one of the key molecular events in the development of gliomas and represents a promising anticancer target.

In a similar model system, Doubrovin et al. used the HSV-1 thymidine kinase reporter gene to image p53-dependent gene expression in an animal tumour xenograft model system, following DNA damage induced by the alkylating chemotherapeutic agent carmustine (Doubrovin et al. 2001). Damage-induced upregulation of p53 transcriptional activity, measured by elevated transgene HSV-1-thymidine kinase enzyme activity in vivo, correlated with the expression of p53-dependent downstream genes.

The PI3K/Akt/mTOR signalling cascade is one of the prime cell survival pathways involved in oncogenesis and chemoresistance, and its theranostic value is gaining increased attention. Zhang et al. (Zhang et al. 2007) constructed a recombinant bioluminescent Akt reporter containing an Akt consensus substrate peptide, consisting of a domain that binds phosphorylated amino acid residues (FHA2) flanked by the amino-(NLuc) and carboxyl-(CLuc) terminal domains of the firefly luciferase reporter molecule. In the presence of Akt kinase activity, phosphorylation of the Akt consensus substrate sequences within the reporter results in its interaction with the FHA2 domain, thus sterically preventing reconstitution of a functional luciferase reporter molecule. In the absence of Akt kinase activity, release of this steric constraint allows reconstitution of the luciferase reporter molecule whose activity can be detected non-invasively by bioluminescent imaging. By the use of this reporter, the authors could monitor quantitatively and dynamically Akt activity (Akt phosphorylation) in cultured cells and human glioma xenografts in response to upstream signalling pathway modulators such as EGF or PI3K inhibitors. On the other hand, mTOR inhibitors acting downstream of Akt did not result in reporter bioluminescence alteration. These results indicate the utility of the reporter to determine the pharmacodynamics of compounds that modulate this signalling pathway. Based on the fact that Akt is recruited to the plasma membrane upon activation, the same authors also constructed a modified membrane bound version of this reporter molecule whose bioluminescence activity enables monitoring Akt activity at the cell membrane (Zhang et al. 2008). This membrane-targeted Akt reporter was demonstrated to be more sensitive and quantitative. Furthermore, the reporter seemed to be sensitive to inhibition of upstream signalling kinases such as EGFR and PI3K. In another study, Chan et al. developed an Akt sensor based on a split firefly luciferase complementation strategy to monitor Akt phosphorylation (Chan et al. 2009). The authors demonstrated a temporal- and dose-dependent increase in complementation of firefly luciferase activities upon treatment with kinase inhibitors. Although optical imaging strategies are very useful for high-throughput screening in preclinical research, the translational potential of such strategies for human application is rather low for which nuclear or MR strategies would be more favourable. Recently, 1-(4-(4-(8-oxa-3-azabicyclo[3.2.1]octan-3-yl)-1-(2,2,2-trifluoroethyl)-1*H*-pyrazolo-[3,4-*d*]pyrimidin-6-yl)phenyl)-3-(2-fluoroethyl)urea (ATPFU), a highly potent and specific inhibitor of mTOR, could be radiolabelled with ^{18}F, opening the possibility for mTOR-specific PET imaging (Majo et al. 2014). However, most PET and MR studies evaluating the treatment of PI3K/Akt/mTOR modulators image the downstream effects of such therapies, e.g. changes in proliferation ([^{18}F]FLT PET) or metabolism ([^{18}F]FDG PET, MRS) (Keen et al. 2014; Beloueche-Babari et al. 2011).

Elevated expression of the translocator protein (TSPO) has been detected in various cancer types, including brain tumours, and associated with disease progression, invasiveness and survival (Vlodavsky and Soustiel 2007; Batarseh and Papadopoulos 2010). Several studies investigated the quantitative assessment of brain-tumour-related TSPO expression with selective and highly specific TSPO ligands such as [^{18}F]PBR06 (Buck et al. 2011) and [^{18}F]DPA-714 in syngeneic and allogeneic rat glioma models (Tang et al. 2012; Winkeler et al. 2012), thereby confirming the potential of TSPO tracers to act as a predictive cancer imaging modality. Furthermore, [^{18}F]DPA-714 has been used to non-invasively and quantitatively evaluate the treatment efficacy of proapoptotic treatment. Awde and colleagues could detect a statistically significant reduction of [^{18}F]DPA-714 uptake in intracranial rat 9L gliomas 8 days after treatment with erucylphosphohomocholine (ErPC3), an apoptosis-inducing

alkylphosphocholine (Awde et al. 2013). These findings could be validated with autoradiography and immunolabelling of brain sections of ErPC3-treated animals showing reduced [^{18}F]DPA-714 and TSPO expression.

28.6 Imaging Gene and Cell-Based Therapies

Classic gene therapy approaches for oncological application relied on two prodrug systems (cytosine deaminase/5-FC and HSV-1-*tk*/ganciclovir) and used viral particles for transgene transfer (Pulkkanen and Yla-Herttuala 2005; Altaner and Altanerova 2012). In recent years, much effort has been made to increase the efficacy of gene therapy, including the development of more effective delivery systems with increased tumour tropic properties, such as cellular or targeted delivery vehicles, the delivery of more effective therapeutic molecules, such as cytokines or proapoptotic genes, or the development of more effective monitoring systems. Especially the development of effective non-invasive in vivo imaging techniques for monitoring vector delivery and subsequent gene expression and treatment efficacy has received particular attention over the last years (Waerzeggers et al. 2009a). For this purpose, a reporter gene is commonly linked to the therapeutic gene by a shared promoter, which results in a proportional coexpression of both genes. This means that from the activity of the reporter gene (level of signal intensity), the activity of the therapeutic gene can be deduced. Several reporter gene systems have been developed for nuclear, optical and MR imaging. Especially, the herpes simplex virus type 1 thymidine kinase gene, HSV-1-*tk*, has been studied extensively for gene therapy purposes due to the fact that it can serve as suicide and reporter gene simultaneously depending on the administered substrate (the prodrug ganciclovir or the radiolabelled ligands [^{18}F]FHBG, [^{18}F]FIAU or [^{18}F]FEAU, respectively) (Kang and Chung 2008; Waerzeggers et al. 2009a). Our group has successfully applied small-animal PET imaging to monitor gene expression and to evaluate gene therapy in vivo. Employing an "imaging-guided" suicide gene therapy protocol, we showed in a subcutaneous glioblastoma model a response rate of 68 % of tumours in vivo transduced with an HSV-1 amplicon vector proportionally co-expressing *E. coli* cytosine deaminase (*cd*) as a therapeutic gene and HSV-1-*tk* as a combined PET marker and therapeutic gene (Jacobs et al. 2007). In this study, MRI was used for tumour localisation, and PET, using the radiotracers [^{18}F]FDG, [^{18}F]FLT and [^{11}C]MET, was used for identification of actively proliferating tumour tissue and guidance of targeted vector application (Fig. 28.6a). The latter is an important aspect in a gene therapy protocol as only viable tumour tissue is likely to respond to the introduced therapeutic genes, whereas necrotic tissue will show no benefit. These radiotracers displayed

Fig. 28.6 Imaging-guided gene therapy paradigm. (**a**) Experimental protocol for identification of viable target tissue and assessment of vector-mediated gene expression in vivo in a mouse model with three subcutaneous gliomas. *Row 1*: localisation of tumours is displayed by MRI. *Row 2*: the viable target tissue is displayed by [^{18}F]FDG PET; note the signs of necrosis in the lateral portion of the left-sided tumour (*arrow*). Rows 3+4: following vector application into the medial viable portion of the tumour (*arrow*), the tissue dose of vector-mediated gene expression is quantified by [^{18}F]FHBG PET. *Row 3* shows an image acquired early after tracer injection, which is used for co-registration; row 4 displays a late image with specific tracer accumulation in the tumour that is used for quantification. (**b**) Response to gene therapy correlates to therapeutic gene expression. The intensity of cdIREStk39gfp expression, which is equivalent to transduction efficiency and tissue dose of vector-mediated therapeutic gene expression, is measured by [^{18}F]FHBG PET (in %ID/g), and the induced therapeutic effect is measured by [^{18}F]FLT PET ($R=0.73$, $P<0.01$). Therapeutic effect ([^{18}F]FLT) was calculated as the difference between [^{18}F]FLT accumulation after and before therapy. (**c**) Relation between changes in volumetry and [^{18}F]FLT uptake. Changes in tumour volume and [^{18}F]FLT uptake were plotted for tumours grown in 11 nude mice. There is a strong correlation between volumetry and change in [^{18}F]FLT uptake ($R=0.83$) for those tumours responding to therapy (complete responders) and a weaker correlation ($R=0.57$) for those tumours not responding to therapy (nonresponders). No correlation was found for those tumours where focal alterations of [^{18}F]FLT uptake occurred which did not lead to a reduction in overall tumour volume (Partial responders; adapted from Jacobs et al. (2007) with permission)

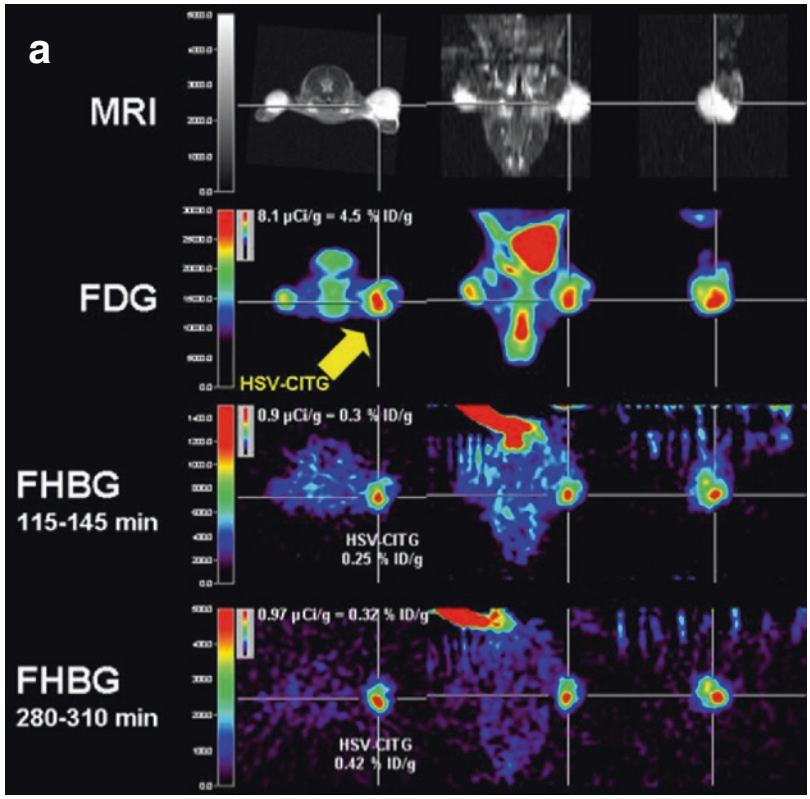
a
MRI
FDG
8.1 µCi/g = 4.5 % ID/g
HSV-CITG
FHBG
115-145 min
0.9 µCi/g = 0.3 % ID/g
HSV-CITG
0.25 % ID/g
FHBG
280-310 min
0.97 µCi/g = 0.32 % ID/g
HSV-CITG
0.42 % ID/g

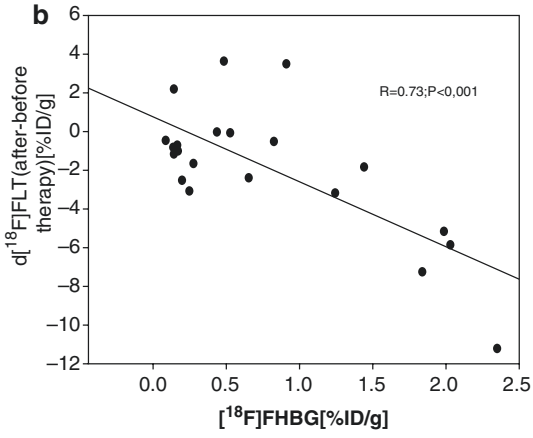
b
R=0.73;P<0,001
d[18F]FLT(after-before therapy)[%ID/g]
[18F]FHBG[%ID/g]

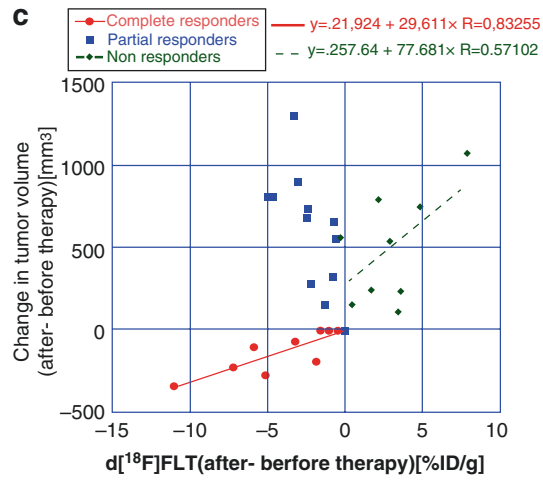
c
Complete responders
Partial responders
Non responders
y=.21,924 + 29,611× R=0,83255
y=.257.64 + 77.681× R=0.57102
Change in tumor volume (after- before therapy)[mm3]
d[18F]FLT(after- berfore therapy)[%ID/g]

homogeneous uptake in small tumours and heterogeneous uptake in larger tumours. In the latter, no radiotracer uptake occurred in the central part of the tumours indicative of central necrosis. For image validation, transaxial PET images were coregistered with histology showing a correlation between the lack of tracer accumulation and the histological signs of necrosis, whereas positive tracer accumulation correlated with viable tumour tissue. Tumour-to-background ratios for the various radiotracers ranged from 1.9 to 8.0 in viable tumour tissue and from 0.4 to 1.2 in necrosis. In this study [^{18}F]FLT was also used to determine the gene therapy-induced inhibition of proliferative activity of the tumour and thus therapeutic efficacy. Furthermore, [^{18}F]FHBG was used as a marker for the exogenously introduced therapeutic (HSV-1-*tk*) gene expression and to predict response to therapy (Fig. 28.6a). Specific [^{18}F]FHBG accumulation could localise the transduced tissue dose of therapeutic gene expression. Moreover, the primary transduction efficiency as measured by [^{18}F]FHBG PET was correlated to the induced therapeutic effect as measured by [^{18}F]FLT PET (Fig. 28.6b, c). Overall, this study showed the feasibility of a multimodal imaging approach for (i) identification of viable target tissue that might benefit from gene therapy, (ii) quantification of the transduction efficiency and (iii) monitoring of therapeutic efficacy. Wang et al. compared various PET tracers for their ability to assess response in tumours undergoing HSV-1-*tk* plus ganciclovir (GCV) prodrug activation gene therapy (Wang et al. 2006). The tracers evaluated interrogated therapy-induced changes in tumour glucose metabolism ([^{18}F]FDG), protein synthesis ([^{18}F]FET) and cell proliferation/DNA synthesis (5-[^{18}F]-fluoro-29-deoxyuridine, [^{18}F]FUdR). In addition, [^{123}I]FIAU SPECT imaging was performed to evaluate HSV-1-*tk* gene expression. In agreement with the study of Jacobs et al., the authors found that [^{123}I]FIAU SPECT imaging was the most reliable method for prediction of tumour response to GCV therapy, which was proportional to the magnitude of HSV-1-*tk* expression in tumour tissue. Furthermore, the authors showed that PET imaging with [^{18}F]FUdR reliably visualises proliferating tumour tissue and is most suitable for the assessment of responses in tumours undergoing HSV-1-*tk* plus GCV prodrug activation gene therapy, whereas PET imaging with [^{18}F]FDG or [^{18}F]FET can be used as additional 'surrogate' biomarkers of the treatment response, although these radiotracers are less sensitive than [^{18}F]FUdR for monitoring tumour responses to prodrug activation gene therapy with HSV-1-*tk* and GCV in this model.

Especially bioluminescent reporter genes have emerged as particularly useful for evaluation of therapeutic gene transfer and treatment response due to the operational ease, low cost and high-throughput of OI. For example, our group introduced the F*Luc* gene in a lentivirus expressing shRNA against the DNA repair protein O6-methylguanine-DNA methyltransferase (MGMT) (Viel et al. 2013c). MGMT is responsible for resistance against temozolomide treatment, the standard chemotherapy in clinical application. The goal of the study was to use the highly specific and efficient RNA interference pathway to modulate MGMT expression to increase temozolomide efficiency in resistant gliomas. In this study, we used BLI to follow the success of viral transduction as well as the combined treatment effect (Fig. 28.7). In another study, Söling and co-workers monitored suicide gene therapy in malignant glioma employing the prodrug activating system HSV-1-*tk*/GCV with BLI (Soling et al. 2004). The authors developed a fusion construct of HSV-1-*tk* and F*Luc* and showed that GCV-induced cytotoxicity in U87MG glioma xenografts stably expressing the fusion construct could be monitored by serial bioluminescence imaging and that bioluminescent signal intensities correlated to tumour volume changes measured with callipers. Especially the ability to image two or more biological processes in a single animal greatly increases the utility of luciferase imaging for gene therapy purposes. Dual luciferase imaging takes advantage from the fact that the luciferases from *Renilla* and firefly have different substrates, coelenterazine and D-luciferin, respectively, and thus can be imaged in the same living mouse with kinetics of light production being separable in time by separate injections of these two substrates

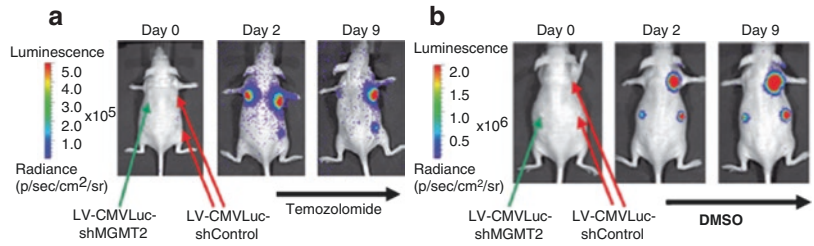

Fig. 28.7 BLI to follow up a combined gene and chemotherapy protocol. Combined MGMT gene therapy and TMZ chemotherapy induces an inhibition of the tumour growth of resistant glioblastoma xenografts. LN18 wild-type cells were xenografted in nude mice. The lentiviral vector expressing the luciferase reporter gene and the shMGMT2 sequence (LV-CMVLuc-shMGMT2) was injected into the left tumours. The lentiviral vector expressing the luciferase reporter gene and the control small hairpin RNA (shRNA) sequence (LV-CMVLuc-shControl) were injected into the right tumours. Two days after virus injection, mice were divided in two groups and treated with daily intraperitoneal injections of 50 mg/kg TMZ (**a**) or dimethyl sulfoxide (DMSO) (**b**) (Modified from Viel et al. (2013c) with permission)

(Waerzeggers et al. 2009a). Dual bioluminescence imaging has been used to monitor gene delivery via a therapeutic vector and to follow the effects of the proapoptotic therapeutic protein TRAIL in gliomas (Shah et al. 2003). Glioma cells stably expressing FLuc were implanted subcutaneously into nude mice, and the tumour growth was monitored in vivo over time by luciferin administration and BLI. HSV amplicon vectors bearing the genes for TRAIL and R*Luc* were injected directly into the FLuc-positive gliomas allowing superimposition of gene delivery to the tumour by coelenterazine administration and BLI. In contrast to mock-injected gliomas, tumour regression could be monitored with BLI after luciferin administration in TRAIL-treated gliomas over time. In a subsequent study, the same authors took advantage of the glioma tracking capabilities of neural progenitor cells (NPCs) to deliver therapeutic molecules to intracranial tumours (Shah et al. 2005). The authors engineered mouse NPCs to simultaneously express FLuc and deliver a secreted form of TRAIL (sTRAIL) (NPC-FL-sTRAIL). By using a highly malignant human glioma model expressing *Renilla* luciferase, they showed that intracranially implanted NPC-FL-sTRAIL expressing both firefly luciferase and sTRAIL migrated into the tumours and induced profound antitumour effects. Again, using the dual luciferase imaging method, both NPC migration and tumour burden could be monitored in the same animal over time. Recently, a triple luciferase reporter system has been developed and characterised for in vivo monitoring of three distinct biological phenomena over time with BLI using three different specific substrates (Maguire et al. 2013). In this system a codon-optimised luciferase from *Vargula hilgendorfii* (V*Luc*) is multiplexed with *Gaussia* (G*Luc*) and firefly (F*Luc*) luciferase, and the activity of these three reporter genes can be visualised after injection of the substrates, vargulin, coelenterazine and D-luciferin, respectively. The triple luciferase reporter system has been used to monitor the response of glioma cells to a gene therapeutic approach using the secreted soluble variant of the anticancer agent TRAIL. In this study, VLuc imaging showed efficient sTRAIL gene delivery to the brain, while FLuc imaging revealed a robust antiglioma therapy. Further, nuclear factor-kB (NF-kB) activation in response to sTRAIL binding to death receptors in glioma cells was monitored by GLuc imaging (Maguire et al. 2013).

For gene therapy protocols to be effective, not only the level and duration of transgene expression are important. Even more essential are selective delivery and expression of the therapeutic transgenes in the tissue of interest, mostly cancer cells, with sparing of the surrounding normal cells to reduce side effects and the possibility of temporal induction of therapeutic gene expression to turn on/off therapeutic gene expression at the desired time point (e.g. when

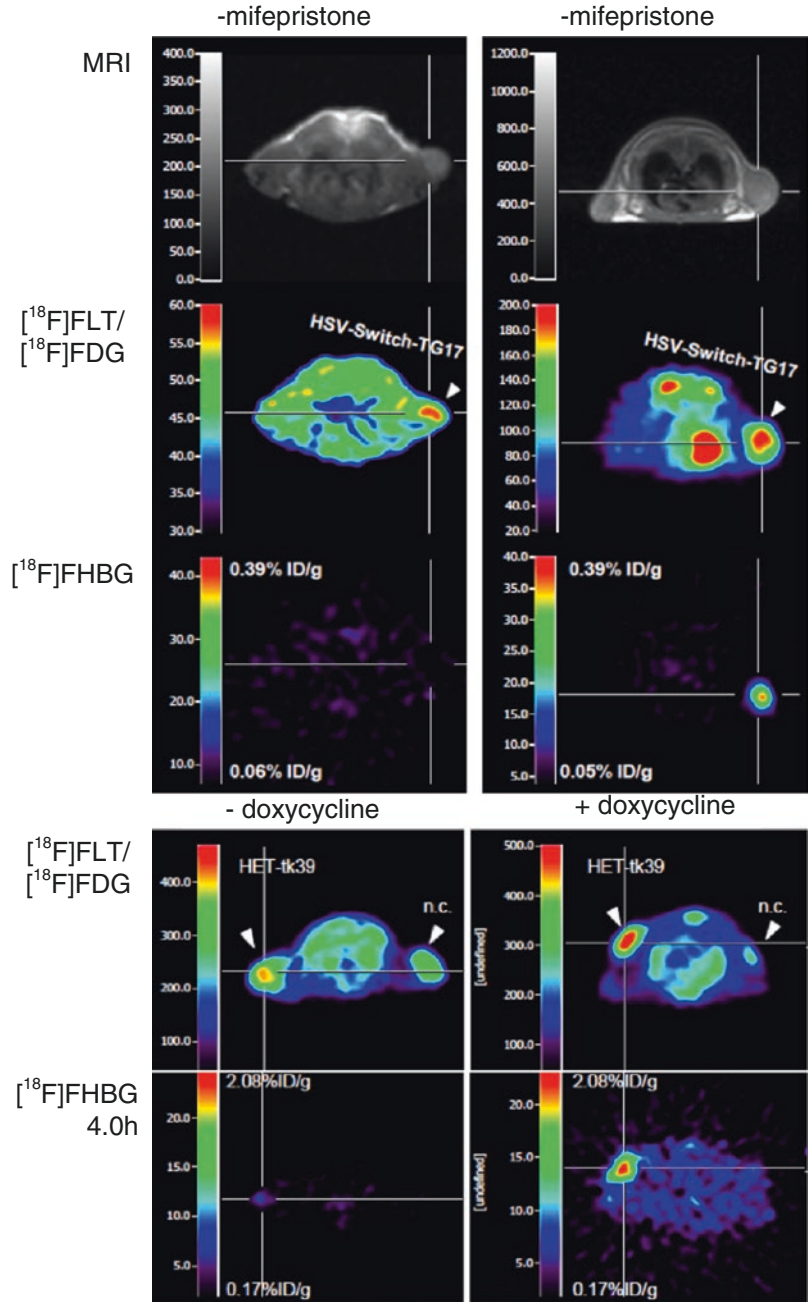

Fig. 28.8 In vivo imaging of regulated gene expression. Multimodal imaging ([18F]FLT, [18F]FDG and [18F]FHBG PET) of inducible gene expression by PET in nude mice bearing subcutaneous human Gli36dEGFR xenografts employing HSV-Switch-TG17 or HET6C-tk39. Mice were randomised to mifepristone- or doxycycline-treated (each group $n=7$) and mifepristone- or doxycycline-untreated (n-mif = 8; n-dox = 12) groups. Indicated xenografts (*arrowhead*) were injected with HSV-Switch-TG17 and HET6C-tk39, respectively, 48 h prior to PET imaging resulting in high accumulation of [18F]FHBG in HSV-Switch-TG17 or HET6C-tk39-infected and mifepristone- or doxycycline-treated tumours as compared to some background activity in non-treated tumours (This research was originally published in *Plos One*. Winkeler et al. (2007))

vectors maximally reached the target tissue or when the desired therapeutic effect has been reached). To demonstrate that non-invasive imaging of regulated expression of any type of gene after in vivo transduction by versatile vectors is feasible, our group generated regulable HSV-1 amplicon vectors carrying hormone (mifepristone) or antibiotic (tetracycline)-regulated promoters driving the proportional coexpression of two marker genes (a fluorescent gene [*rfp* or *egfp*] with either a PET [HSV-1-*tk*] or an optical [*fluc*] imaging gene) (Winkeler et al. 2007). Inducible and regulated gene expression could be monitored by fluorescence microscopy in culture and by PET (Fig. 28.8) or BLI in vivo (Fig. 28.9). Moreover, several strategies

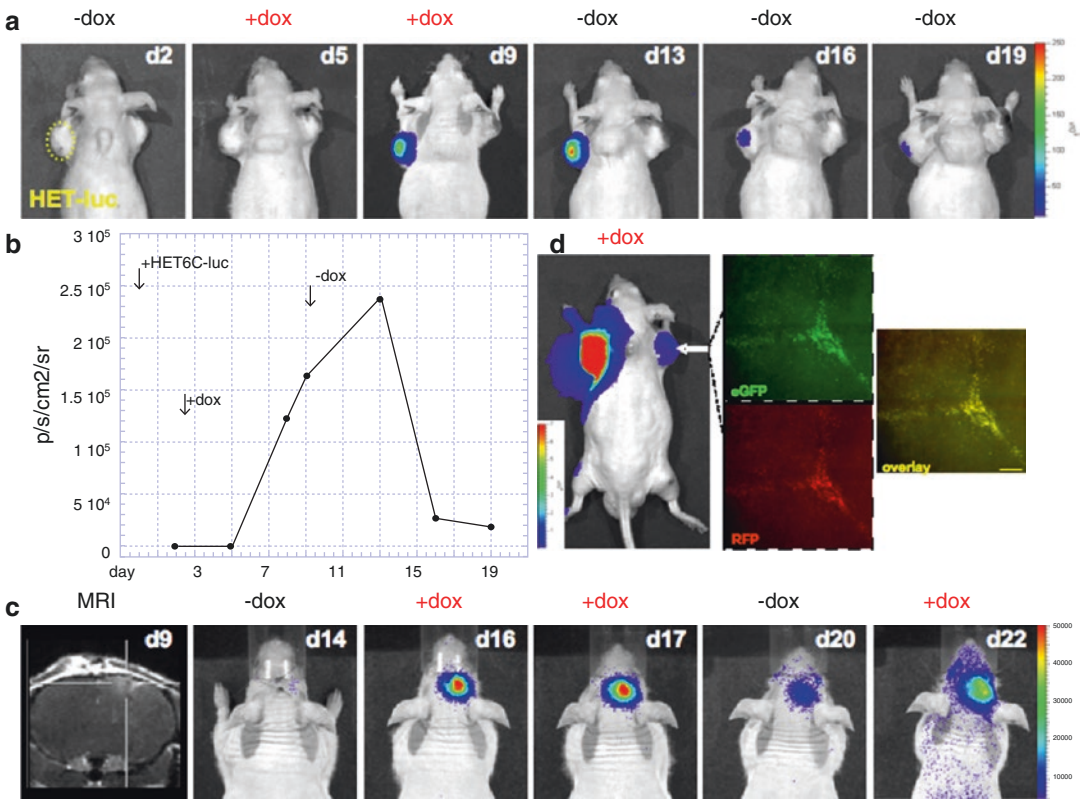

Fig. 28.9 In vivo bioluminescence imaging of doxycycline-dependent gene expression over time. Bioluminescence imaging of induced Luc expression and image validation by histology. Unit for all colour scales as well as the histogram on temporal analysis was defined as photons/s/cm2/sr (p/s/cm2/sr). (**a**) Temporal analysis of up- and downregulation of Luc expression. HET-6C injection was performed intratumourally at day 0. Days where bioluminescent images were obtained are indicated at the upper right corner, days of doxycycline treatment at the top. (**b**) Quantitative analysis of luciferase signal (OFF-ON-OFF) in response to doxycycline. (**c**) Temporal analysis of up- and downregulation of Luc expression in the intracranial glioma model (OFF-ON-OFF-ON). Indicated are the days of tumour growth. (**d**) Image validation by histology. BLI of a mouse bearing a subcutaneous glioma stably expressing Luc on its left shoulder after in vivo transduction with HET6C-Luc in the tumour on the right shoulder. Representative histological sections taken from the in vivo transduced tumour showing co-localisation of eGFP, expressed constitutively from the herpes viral immediate early 4/5 promoter, and RFP, expressed from the bidirectional regulated promoter (scale bar overlay, 150 mm; exposure time, 0.5 s) (This research was originally published in *Plos One*. Winkeler et al. (2007))

have been developed and evaluated to selectively deliver and/or express transgenes in the tissue of interest. These strategies either utilise tissue- or tumour-specific promoters to drive transgene expression (transcriptional targeting) or use a variety of modifications on vector tropism (transductional targeting) (Waerzeggers et al. 2009a). For instance, Liang et al. coated an adenovirus expressing firefly luciferase from the CMV early promoter (AdCMVFLuc) with a recombinant, bi-specific molecule containing the soluble portion of coxsackie- and adenovirus receptor (CAR) fused to epidermal growth factor (EGF). By this procedure CAR-dependent adenovirus infection to normal tissue could be blocked and redirected to specific, EGFR-expressing, target cells (Liang et al. 2004a, b). After systemic administration of coated AdCMVFLuc, luciferase expression was reduced in the liver and was facilitated in tumour xenografts expressing high levels of the EGFR, as quantitatively demonstrated by BLI.

The use of neural and mesenchymal stem cells for the treatment of brain tumours has attracted

much interest in recent years (Waerzeggers et al. 2009a; Altaner and Altanerova 2012). The characteristics of neural stem cells (NSCs) that make them attractive vehicles for targeted delivery are their tropic behaviour towards neoplasms. Aboody and colleagues (Aboody et al. 2000) first documented that modified exogenous NSCs injected into the contralateral hemispheres migrate over long distances to sites of gliomas in mice. Several groups have reported promising results with extended survival or reduced tumour growth after neural stem cell-based gene therapy in animal models of high-grade gliomas (Brekke et al. 2007). An intrinsic tumour-inhibition effect of neural stem cells has been observed after co-inoculation of NSCs with glioma cells or grafting into established gliomas. Also, due to the pluripotency of neural stem cells, their potential role may be to repair the damage caused by the brain tumours themselves and the neurological impairment that is frequently associated with traditional cancer treatment approaches (Brekke et al. 2007). Until recently, the in vivo study of particular populations of cells, such as NSCs, was mainly based on snapshot images from ex vivo histology. Thus, imaging techniques for in vivo longitudinal detection of the dynamics of these cells became desirable. Over the past years, the tumour-targeting abilities of implanted neural stem and progenitor cells have been monitored non-invasively with various imaging modalities, and most extensive information has been gained with reporter genes and optical imaging. Also cellular MR imaging techniques have been used increasingly, and even PET imaging has been applied to detect stem cell migration and therapy in intracranial glioma models. By the use of bioluminescence imaging systems, Shah and co-workers simultaneously monitored both the migration of NSCs towards gliomas and the efficacy of sTRAIL on the glioma burden in real time by dual enzyme substrate (RLuc/FLuc) imaging (Shah et al. 2005). However, in general, BLI offers poor tissue penetration and poor spatial resolution. Miletic et al. (Miletic et al. 2007) together with our group used a multimodal imaging protocol combining multi-tracer PET and MRI to demonstrate that a subpopulation of bone marrow-derived mesenchymal stem cells can be used as tumour-infiltrating therapeutic cells against malignant glioma. The stem cells genetically engineered to express HSV-1-TK were injected into rat intracranial 9L gliomas. After transplantation, stem cell localisation and distribution could be monitored non-invasively by means of the HSV-1-TK-specific PET radioligand [^{18}F]FHBG. In addition, the therapeutic effect of ganciclovir treatment could be monitored sequentially by MRI and [^{11}C]MET PET (Fig. 28.10) and strongly correlated with histological analysis.

Cellular imaging by magnetic resonance imaging (cellular MRI) provides another non-invasive dynamic method for evaluating the seeding, migration and homing of magnetically labelled NSCs (Modo et al. 2005), as well as an excellent soft tissue differentiation with a high spatial resolution. This led Zhang and co-workers

Fig. 28.10 Multimodal imaging of cell-based therapy. Representative three-dimensional MRI (T1-weighted FLASH, echo time = 5 ms, repetition time = 70 ms, 60° pulse, resolution 121 × 121 × 242 µm, postadministration of gadopentetic acid [Gd-DTPA]), [^{11}C]MET PET and [^{18}F]FHBG PET scans. Time points after tumour implantation: (**a**–**c**) 6 days, MRI before ganciclovir (GC) treatment; (**d**–**f**) 7–8 days, [^{11}C]MET PET before GC treatment; (**g**–**i**) 12 days, [^{18}F]FHBG PET during GC treatment; (**j**–**l**) 13 days, MRI during GC treatment; (**m**–**o**) 14 days, [^{11}C]MET PET during GC treatment; (**p**) 21 days, MRI after GC treatment; (**q**) 22 days, [^{11}C]MET PET after GC treatment. The three different groups were treated as described: (**a**, **d**, **g**, **j**, **m**, **p**, **q**) with injection of bone marrow-derived tumour-infiltrating cells expressing the genes for thymidine kinase and green fluorescent protein (BM-TIC-*tk-gfp*) injection and GCV treatment; (**b**, **e**, **h**, **k**, **n**) with BM-TIC-*tk-gfp* injection without GCV treatment; (**c**, **f**, **i**, **l**, **o**) 9LDsRed only with GC treatment (daily intraperitoneal injections of 30 mg per kg GC for 10 days, starting at day 4 after BM-TIC-*tk-gfp* implantation) (Adapted from Miletic et al. (2007) with permission)

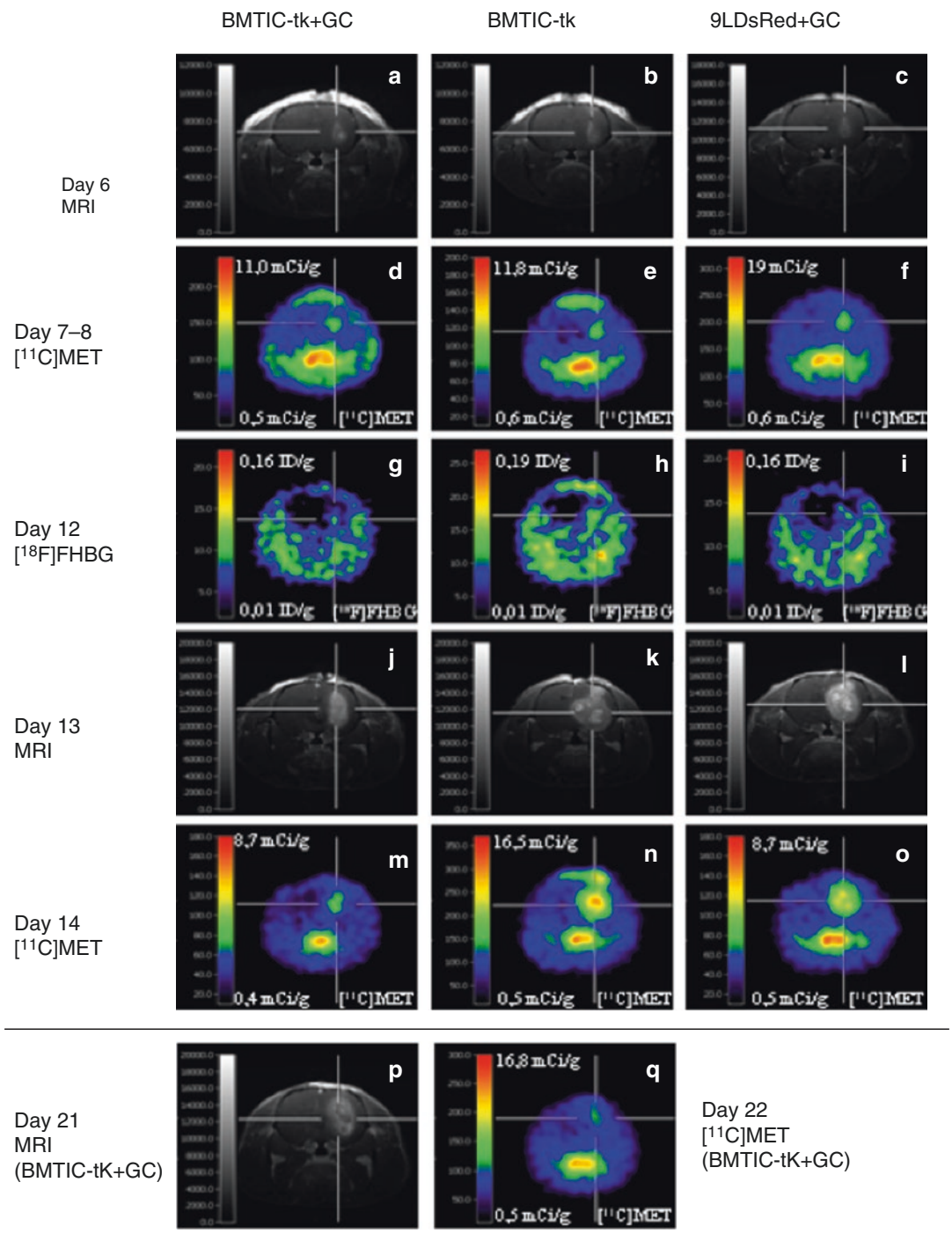
BMTIC-tk+GC
BMTIC-tk
9LDsRed+GC
Day 6
MRI
a
b
c
Day 7–8
[11C]MET
11,0 mCi/g
d
0,5 mCi/g
[11C]MET
11,8 mCi/g
e
0,6 mCi/g
[11C]MET
19 mCi/g
f
0,6 mCi/g
[11C]MET
Day 12
[18F]FHBG
0,16 ID/g
g
0,01 ID/g
0,19 ID/g
h
0,01 ID/g
0,16 ID/g
i
0,01 ID/g
Day 13
MRI
j
k
l
Day 14
[11C]MET
8,7 mCi/g
m
0,4 mCi/g
[11C]MET
16,5 mCi/g
n
0,5 mCi/g
[11C]MET
8,7 mCi/g
o
0,5 mCi/g
[11C]MET
Day 21
MRI
(BMTIC-tK+GC)
p
16,8 mCi/g
q
0,5 mCi/g
[11C]MET
Day 22
[11C]MET
(BMTIC-tK+GC)

(Zhang et al. 2004) to successfully monitor neural progenitor cells labelled with superparamagnetic iron oxide particles (SPIO) in a rat gliosarcoma model using in vivo MRI as they infiltrated the tumour mass or as they tracked down invading tumour cells. Also, migration and incorporation of magnetically labelled NSCs into the angiogenic vasculature of brain tumours has been studied (Modo et al. 2005). Brekke and colleagues (Brekke et al. 2007) investigated the potential of cellular MR imaging to monitor in vivo the migration and infiltration of GRID-labelled murine NSCs (MHP36) from the seeding site to the tumour region in a rat glioma model using longitudinal multiparametric MR imaging. Additionally, the authors were able to demonstrate the therapeutic potential of the mere injection of neural stem cells through an MRI-based measurement of tumour growth and development of vasogenic oedema. Fulci et al. (2006) used cellular MRI to non-invasively monitor innate immune response (iron oxide nanoparticle-loaded macrophages) after glioma virotherapy in a syngeneic rat glioma model. Furthermore, the applied image protocol enabled the authors to image the increased efficiency of oncolytic virotherapy after preadministration of cyclophosphamide. The increased efficiency was credited to the immunosuppressive action of cyclophosphamide. Other studies used a combination of cellular MRI and nuclear imaging to evaluate the administration of stem cells as combined gene carrier and imaging systems (e.g. stem cells expressing the human sodium iodide symporter, hNIS, or HSV-1-*tk* and labelled with iron oxide or gadolinium) (Varma et al. 2012, 2013; Ribot et al. 2011).

Simultaneous tracking of transplanted stem cell fate and function non-invasively in vivo has gained increased attention as it can address many safety aspects of the use of these cells as targeting vehicles for gene therapy (stem cell distribution, normal or aberrant stem cell proliferation, extent and duration of transgene expression, response to therapy). To address this issue, Cao et al. (2007) stably transduced murine embryonic stem (ES) cells with double or triple fusion reporter gene constructs expressing monomeric RFP, firefly luciferase and truncated HSV-1-TK, respectively, injected these cells subcutaneously into nude mice and tracked cell survival non-invasively by bioluminescence and PET imaging. Such multimodality imaging approaches are successful to monitor transplanted stem cell survival and proliferation in vivo and to assess the efficacy of suicide gene therapy as a backup safety measure (death switch) against teratoma formation or for selective elimination of the cellular vehicles post tumour treatment (Alieva et al. 2012; Martinez-Quintanilla et al. 2013). Also our group addressed the feasibility of multimodal imaging for non-invasive and early detection of the safety aspects related with the use of stem cells as delivery vectors for gene therapy. In this study, mouse NPCs genetically engineered to express HSV-1-TKGFP and FLuc (C17.2-LITG) were injected in the brains of mice bearing highly malignant human gliomas, either within the tumours or within the opposite brain hemisphere, or mice not bearing intracranial gliomas (Waerzeggers et al. 2008). BLI could not only detect migration of injected NPCs towards gliomas growing in the contralateral hemisphere but was also able to detect aberrant cell migration towards the cerebellum and the spine, even in animals not bearing intracranial gliomas (Fig. 28.11). Furthermore, BLI and [^{18}F]FHBG PET imaging showed excessive proliferation of intratumourally injected NPCs. These results highlight the importance of non-invasive imaging as safety switch in cell-based studies. Most importantly, multimodal imaging of these cells transplanted into pre-established gliomas was obtained by MRI, PET and OI demonstrating for the first time that cells can be detected and followed by multimodal imaging in a clinically applicable imaging protocol (Fig. 28.12).

28.7 Imaging Tumour Chemo- and/or Radiosensitivity

Resistance to chemoradiotherapy is an important cause of treatment failure in patients with cancer, including brain tumours, and one of the most significant obstacles in improving the efficacy of cancer treatment. Non-invasive imaging

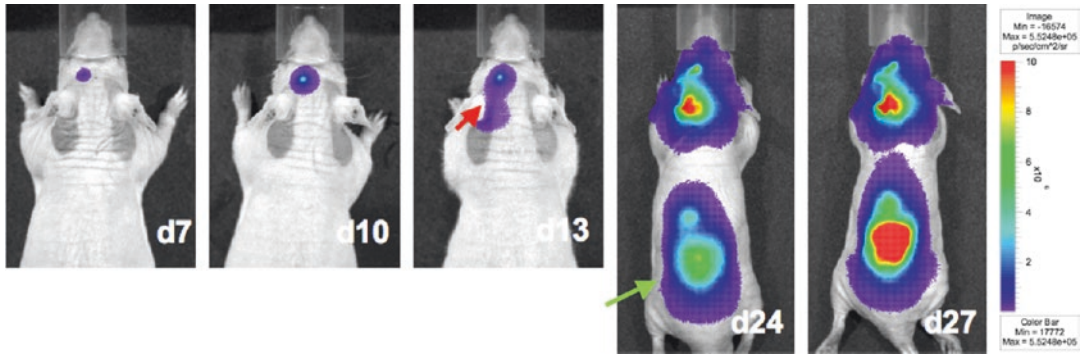

Fig. 28.11 Bioluminescence imaging of aberrant stem cell migration. C17.2-LITG cells were injected into the left striatum of a non-glioma-bearing mouse, and their behaviour over time was monitored with optical imaging. NPC migration in the direction of the cerebellar hemispheres (*red arrow*) could be demonstrated 13 days after injection (*red arrow*); at 3 weeks, NPCs also localised at the level of the thoracolumbar spine (*green arrow*) (Adapted from Waerzeggers et al. (2008) with permission)

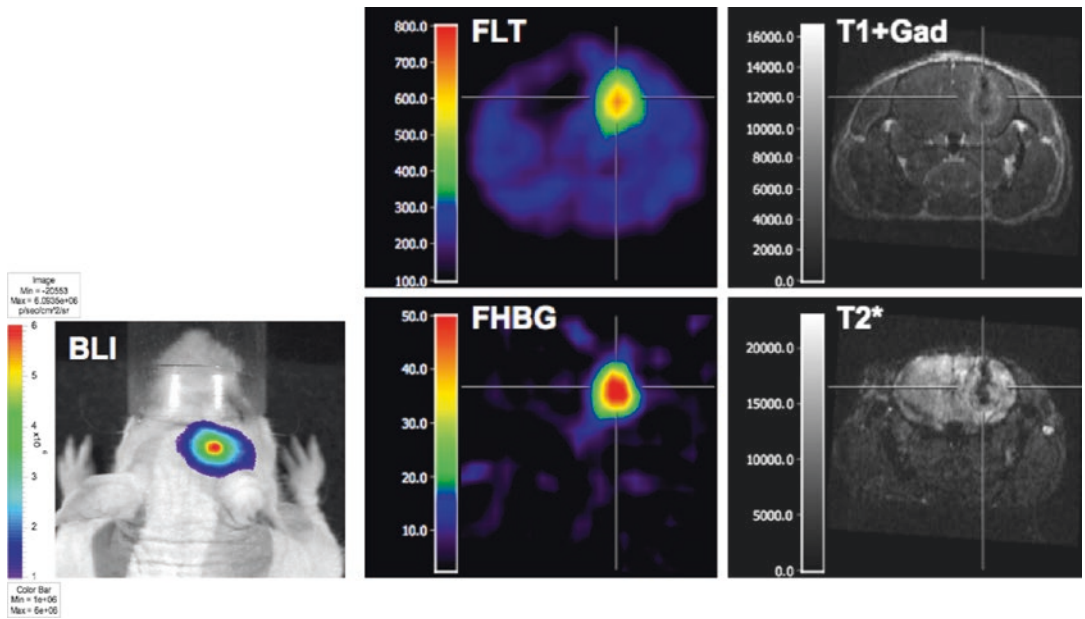

Fig. 28.12 Multimodal imaging of intracranially injected C17.2-LITG cells. FeO-labelled C17.2-LITG cells were co-injected together with Gli36dEGFR human glioma cells (2×10^5 cells, 1:1) into the right striatum of a nude mouse, and in vivo imaging was performed by OI, PET and MRI to detect glioma growth ([^{18}F]FLT PET and Gd-enhanced T1-weighted MRI) and stem cell survival and location (BLI, [^{18}F]FHBG PET and T2*-weighted MRI)

approaches to predict response to chemo- or radiotherapy would significantly aid in guiding more efficient clinical management at an early time point.

Chemotherapeutic failure is a multifactorial phenomenon related to initial resistance intrinsic to the tumour cells, resistance acquired by tumours during treatment or physiologic factors extrinsic to tumours (e.g. individual variations and pharmacokinetic behaviours of drugs). Moreover, resistance may be heterogeneous with respect to either different tumours in the same individual or even different cells in the same tumour (Hsueh et al. 2006). The term multidrug

resistance (MDR) is commonly used to indicate an overexpression of the transmembrane protein P-glycoprotein (P-gp) encoded by the *mdr1* gene. P-gp acts as an energy-dependent efflux transporter that efficiently enhances outward transport and/or prevents entry of compounds such as anticancer drugs, thereby resulting in decreased intracellular accumulation and thus decreased cytotoxicity. P-Glycoprotein confers cross-resistance to unrelated drugs that differ widely with respect to molecular structure and target specificity, including many natural product agents (e.g. paclitaxel, vincristine, doxorubicin, verapamil), as well as targeted anticancer agents (e.g. Gleevec, a kinase inhibitor) (Pichler et al. 2005). P-gp is not only expressed in tumour cells but also in normal, non-malignant tissue involved in drug excretion and absorption such as the kidneys, liver and colon. Furthermore, P-gp is highly expressed in endothelial cells at the blood–brain interface and is an essential element of its barrier function and protects against neurotoxicity. The mechanism of *mdr1* regulation in these tissues, particularly in response to xenobiotics and other environmental and physiologic stimuli, is not fully understood.

Several radiopharmaceuticals have been used as general probes for functional imaging of MDR pumps by measuring the efflux of these probes via the P-gp and other membrane transporters. The most commonly applied tracers are [^{99m}Tc]sestamibi and [^{99m}Tc]tetrofosmin for SPECT imaging and [^{11}C]verapamil and [^{18}F]fluoropaclitaxel for PET imaging, which can be used to quantify P-gp activity to predict response to chemotherapy (Kelloff et al. 2005; Hsueh et al. 2006) or to monitor P-gp inhibition by cyclosporine (Sasongko et al. 2005). Also coelenterazine, the bioluminescent substrate of the reporter gene *Renilla* luciferase, is a well-known substrate for the multidrug transporter P-gp thereby enabling P-gp transport activity to be monitored in intact cells and living animals with non-invasive bioluminescence imaging. This approach has been used to non-invasively image the reversal of multidrug resistance in mice (Pichler et al. 2004). In cultured living cells, stably transfected with a codon-humanised *Renilla* luciferase, it was shown that low baseline coelenterazine-mediated bioluminescence could be fully enhanced (reversed) to non-P-gp-matched control levels with potent and selective P-gp inhibitors. This study emphasises the role of coelenterazine as a P-gp substrate, but at the same time raises concerns regarding the indiscriminative use of *Renilla* luciferase and aequorin as reporters in intact cells and transgenic animals, since P-gp-mediated alterations in coelenterazine permeability may affect results (Gross and Piwnica-Worms 2005). Inhibition of the activity or expression of P-gp represents a valuable means to circumvent the drug resistance of cancer cells, and several approaches have been tested. In a study by Pichler et al., the effectiveness of a P-gp inhibition strategy using shRNA interference against human MDR1 mRNA was tested and could be monitored by direct bioluminescence imaging using coelenterazine (Pichler et al. 2005). Recently Park et al. investigated the feasibility of a combination of chemo- and radioiodide therapy and non-invasive imaging with a dual therapeutic vector expressing MDR1 shRNAi and a human sodium iodide symporter (hNIS) (Park et al. 2008). The authors showed that shMDR-NIS-expressing cells showed a significant decrease in the expression of MDR1 messenger RNA and P-glycoprotein and that this inhibition enhanced the intracellular accumulation of paclitaxel, resulting in increased sensitivity to this chemotherapeutic agent. Furthermore, the shMDR-NIS-expressing cells showed a significant increase of ^{125}I uptake and a marked decrease in cell survival rate after ^{131}I treatment. Interestingly, the combination of doxorubicin and ^{131}I displayed synergistic cytotoxicity that correlated with MDR1 inhibition and NIS expression in shMDR-NIS-expressing cells. In mice with shMDR-NIS-expressing tumour xenografts, small-animal PET with ^{124}I clearly visualised shMDR1-NIS-expressing tumours.

To gain a better understanding of mdr1 transcriptional regulation, Gu and colleagues recently developed a knock-in mouse model that uses a firefly luciferase gene inserted by homologous recombination into the murine mdr1a genetic locus and flanked by loxP sites, so that

Cre-mediated recombination is required to configure the F*Luc* gene directly under the control of the endogenous mdr1a promoter (Gu et al. 2009). The authors showed that this knock-in model can be used for non-invasive assessment of basal and xenobiotic-induced regulation of mdr1aFLuc expression in real time. With the chosen vector design, which requires Cre-mediated recombination to achieve the FLuc knock-in, it should also be possible to control mdr1aFLuc expression spatially by mating mdr1aflox mice with Cre-donor mice that express Cre in a tissue-restricted way. Therefore, this mouse model represents a unique tool to study the magnitude and kinetics of mdr1a induction under a variety of physiologic, pharmacologic, genetic and environmental conditions.

Since over 40 years, it is known that tumour cells at low oxygen tension are relatively radioresistant (Belkacemi et al. 2007). In recent years, more and more studies indicate that hypoxia can also induce the expression of specific genes and promote a more aggressive tumour phenotype. These findings suggest that procedures which could accurately measure the hypoxic fraction of individual tumours before, during and after therapy would permit valuable predictive information about tumour response and identification of subgroups of patients that would benefit from hypoxia-targeted therapies, such as hyperbaric oxygen treatment, neutron radiotherapy or hypoxic radiosensitiser administration. As with chemoresistance, tumour radioresistance can be constitutional or acquired during treatment. The hypoxic fraction of individual tumours can be defined by microelectrode techniques or non-invasive imaging assays using different radiolabelled products of the imidazole family. These markers are selectively reduced and accumulate in hypoxic cells and tissues. Most studied are ^{18}F-labelled 2-nitroimidazole derivates (MISO, FAZA, HX4) or the copper chelate Cu-diacetyl-bis(N4-methylthiosemicarbazone) (Cu-ATSM), and a significant correlation between tumour ligand uptake and radioresistance could be demonstrated (Belkacemi et al. 2007; Wijsman et al. 2013). Tumour hypoxia can also be measured indirectly with reporter genes sensitised to overexpress genes being induced under hypoxic/anoxic conditions, such as HIF-1. Hypoxic glioma tumour tissue has been imaged non-invasively and repeatedly in vivo through HIF-1-mediated activation of HSV-1-TKGFP reporter gene expression and PET imaging with [^{18}F]FEAU (Serganova et al. 2004). Furthermore, Wen et al. showed the equivalence between hypoxia detection by the intratumoural distribution of [^{124}I]FIAU or by [^{18}F]MISO (Wen et al. 2004). Furthermore, several MR imaging techniques can be applied to evaluate tissue oxygenation and tumour hypoxia, such as dynamic contrast-enhanced (DCE) MRI, blood oxygen level dependent (BOLD) MRI, tissue oxygen level dependent (TOLD) MRI, mapping of oxygen by imaging lipid relaxation enhancement (MOBILE) MRI or a combination thereof, and these techniques have been reviewed in depth by Price et al. (2013).

Conclusion

Continuous refinements in available brain tumour models together with improvements in small-animal imaging techniques have led to a rapid progress in a variety of ways by which tumour biology can be monitored non-invasively in living animals. Insights into the pathophysiological processes related to disease initiation and progression resulted in the identification of new molecular targets or treatment strategies. Functional and molecular imaging probes directed to disease-specific alterations have been developed and optimised. These advances greatly increased our knowledge of disease dynamics and refined the design of effective therapeutic interventions in a true translational manner. Ultimately, application of non-invasive imaging in animal brain tumour models will result in improved patient-tailored care by an individualised imaging-guided therapy approach.

Acknowledgements Our work has received funding from the European Union's Seventh Framework Programme (FP7/2007-2013) under grant agreement n° HEALTH-F2-2011-278850 (INMiND) and from the EU FP7- and EFPIA-funded IMI project QuIC-ConCePT (grant agreement n° 115151).

Literature

Aboody KS, Brown A, Rainov NG, et al. Neural stem cells display extensive tropism for pathology in adult brain: evidence from intracranial gliomas. Proc Natl Acad Sci U S A. 2000;97:12846–51.

Abounader R, Laterra J. Scatter factor/hepatocyte growth factor in brain tumor growth and angiogenesis. Neuro Oncol. 2005;7:436–51.

Alieva M, Bago JR, Aguilar E, et al. Glioblastoma therapy with cytotoxic mesenchymal stromal cells optimized by bioluminescence imaging of tumor and therapeutic cell response. PLoS One. 2012;7:e35148.

Altaner C, Altanerova V. Stem cell based glioblastoma gene therapy. Neoplasma. 2012;59:756–60.

Arrieta O, Garcia E, Guevara P, et al. Hepatocyte growth factor is associated with poor prognosis of malignant gliomas and is a predictor for recurrence of meningioma. Cancer. 2002;94:3210–8.

Arwert E, Hingtgen S, Figueiredo JL, et al. Visualizing the dynamics of EGFR activity and antiglioma therapies in vivo. Cancer Res. 2007;67:7335–42.

Asanuma T, Doblas S, Tesiram YA, et al. Visualization of the protective ability of a free radical trapping compound against rat C6 and F98 gliomas with diffusion tensor fiber tractography. J Magn Reson Imaging. 2008;28:574–87.

Awde AR, Boisgard R, Theze B, et al. The translocator protein radioligand 18F-DPA-714 monitors antitumor effect of erufosine in a rat 9L intracranial glioma model. J Nucl Med Off Publ Soc Nucl Med. 2013;54:2125–31.

Batarseh A, Papadopoulos V. Regulation of translocator protein 18 kDa (TSPO) expression in health and disease states. Mol Cell Endocrinol. 2010;327:1–12.

Belkacemi Y, Tsoutsou P, Magne N, Castadot P, Azria D. Metabolic functional imaging for tumor radiosensitivity monitoring. Crit Rev Oncol Hematol. 2007;62:227–39.

Beloueche-Babari M, Workman P, Leach MO. Exploiting tumor metabolism for non-invasive imaging of the therapeutic activity of molecularly targeted anticancer agents. Cell Cycle. 2011;10:2883–93.

Blankenberg FG. In vivo detection of apoptosis. J Nucl Med. 2008;49 Suppl 2:81S–95.

Borges AR, Lopez-Larrubia P, Marques JB, Cerdan SG. MR imaging features of high-grade gliomas in murine models: how they compare with human disease, reflect tumor biology, and play a role in preclinical trials. AJNR Am J Neuroradiol. 2012;33:24–36.

Bradbury MS, Hambardzumyan D, Zanzonico PB, et al. Dynamic small-animal PET imaging of tumor proliferation with 3′-deoxy-3′-18F-fluorothymidine in a genetically engineered mouse model of high-grade gliomas. J Nucl Med. 2008;49:422–9.

Brader P, Serganova I, Blasberg RG. Noninvasive molecular imaging using reporter genes. J Nucl Med Off Publ Soc Nucl Med. 2013;54:167–72.

Brandes AA, Franceschi E, Tosoni A, Hegi ME, Stupp R. Epidermal growth factor receptor inhibitors in neuro-oncology: hopes and disappointments. Clin Cancer Res. 2008;14:957–60.

Brekke C, Williams SC, Price J, Thorsen F, Modo M. Cellular multiparametric MRI of neural stem cell therapy in a rat glioma model. Neuroimage. 2007;37:769–82.

Buck JR, McKinley ET, Hight MR, et al. Quantitative, preclinical PET of translocator protein expression in glioma using 18F-N-fluoroacetyl-N-(2,5-dimethoxybenzyl)-2-phenoxyaniline. J Nucl Med Off Publ Soc Nucl Med. 2011;52:107–14.

Bulik M, Jancalek R, Vanicek J, Skoch A, Mechl M. Potential of MR spectroscopy for assessment of glioma grading. Clin Neurol Neurosurg. 2013;115:146–53.

Cai W, Chen X. Multimodality molecular imaging of tumor angiogenesis. J Nucl Med. 2008;49 Suppl 2:113S–28.

Cai W, Niu G, Chen X. Multimodality imaging of the HER-kinase axis in cancer. Eur J Nucl Med Mol Imaging. 2008;35:186–208.

Cao F, Drukker M, Lin S, et al. Molecular imaging of embryonic stem cell misbehavior and suicide gene ablation. Cloning Stem Cells. 2007;9:107–17.

Chalkidou A, Landau DB, Odell EW, Cornelius VR, O'Doherty MJ, Marsden PK. Correlation between Ki-67 immunohistochemistry and 18F-fluorothymidine uptake in patients with cancer: a systematic review and meta-analysis. Eur J Cancer. 2012;48:3499–513.

Chan CT, Paulmurugan R, Reeves RE, Solow-Cordero D, Gambhir SS. Molecular imaging of phosphorylation events for drug development. Mol Imaging Biol MIB Off Publ Acad Mol Imaging. 2009;11:144–58.

Chenevert TL, McKeever PE, Ross BD. Monitoring early response of experimental brain tumors to therapy using diffusion magnetic resonance imaging. Clin Cancer Res. 1997;3:1457–66.

Claes A, Gambarota G, Hamans B, et al. Magnetic resonance imaging-based detection of glial brain tumors in mice after antiangiogenic treatment. Int J Cancer. 2008;122:1981–6.

Coppola JM, Ross BD, Rehemtulla A. Noninvasive imaging of apoptosis and its application in cancer therapeutics. Clin Cancer Res. 2008;14:2492–501.

Corcoran EB, Hanson RN. Imaging EGFR and HER2 by PET and SPECT: a review. Med Res Rev. 2014;34:596–643.

Cornelissen B, Kersemans V, Burvenich I, et al. Synthesis, biodistribution and effects of farnesyltransferase inhibitor therapy on tumour uptake in mice of 99mTc labelled epidermal growth factor. Nucl Med Commun. 2005;26:147–53.

Corroyer-Dulmont A, Peres EA, Petit E, et al. Detection of glioblastoma response to temozolomide combined with bevacizumab based on muMRI and muPET imaging reveals [18F]-fluoro-L-thymidine as an early and robust predictive marker for treatment efficacy. Neuro Oncol. 2013;15:41–56.

Crippa F, Alessi A, Serafini GL. PET with radiolabeled amino acid. Q J Nucl Med Mol Imaging Off Publ Ital Assoc Nucl Med. 2012;56:151–62.

de Jong M, Essers J, van Weerden WM. Imaging preclinical tumour models: improving translational power. Nat Rev Cancer. 2014;14:481–93.

de Kemp RA, Epstein FH, Catana C, Tsui BM, Ritman EL. Small-animal molecular imaging methods. J Nucl Med Off Publ Soc Nucl Med. 2010;51 Suppl 1:18S–32.

Dennie J, Mandeville JB, Boxerman JL, Packard SD, Rosen BR, Weisskoff RM. NMR imaging of changes in vascular morphology due to tumor angiogenesis. Magn Reson Med Off J Soc Magn Reson Med Soc Magn Reson Med. 1998;40:793–9.

Diagaradjane P, Orenstein-Cardona JM, Colón-Casasnovas NE, et al. Imaging epidermal growth factor receptor expression in vivo: pharmacokinetic and biodistribution characterization of a bioconjugated quantum dot nanoprobe. Clin Cancer Res. 2008;14:731–41.

Dinca EB, Voicu RV, Ciurea AV. Bioluminescence imaging of invasive intracranial xenografts: implications for translational research and targeted therapeutics of brain tumors. Neurosurg Rev. 2010;33:385–94.

Dissoki S, Aviv Y, Laky D, Abourbeh G, Levitzki A, Mishani E. The effect of the [18F]-PEG group on tracer qualification of [4-(phenylamino)-quinazoline-6-YL]-amide moiety--an EGFR putative irreversible inhibitor. Appl Radiat Isot. 2007;65:1140–51.

Doubrovin M, Ponomarev V, Beresten T, et al. Imaging transcriptional regulation of p53-dependent genes with positron emission tomography in vivo. Proc Natl Acad Sci U S A. 2001;98:9300–5.

Fine EJ, Herbst L, Jelicks LA, Koba W, Theele D. Small-animal research imaging devices. Semin Nucl Med. 2014;44:57–65.

Fomchenko EI, Holland EC. Mouse models of brain tumors and their applications in preclinical trials. Clin Cancer Res. 2006;12:5288–97.

Fulci G, Breymann L, Gianni D, et al. Cyclophosphamide enhances glioma virotherapy by inhibiting innate immune responses. Proc Natl Acad Sci U S A. 2006;103:12873–8.

Gaikwad SM, Ray P. Non-invasive imaging of PI3K/Akt/mTOR signalling in cancer. Am J Nucl Med Mol Imaging. 2012;2:418–31.

Gao H, Jiang X. Progress on the diagnosis and evaluation of brain tumors. Cancer Imaging Off Publ Int Cancer Imaging Soc. 2013;13:466–81.

Gelovani JG. Molecular imaging of epidermal growth factor receptor expression-activity at the kinase level in tumors with positron emission tomography. Cancer Metastasis Rev. 2008;27:645–53.

Gilad AA, Winnard Jr PT, van Zijl PC, Bulte JW. Developing MR reporter genes: promises and pitfalls. NMR Biomed. 2007;20:275–90.

Goldman SJ, Chen E, Taylor R, et al. Use of the ODD-luciferase transgene for the non-invasive imaging of spontaneous tumors in mice. PLoS One. 2011;6:e18269.

Griffin JL, Kauppinen RA. A metabolomics perspective of human brain tumours. FEBS J. 2007;274:1132–9.

Gross S, Piwnica-Worms D. Spying on cancer: molecular imaging in vivo with genetically encoded reporters. Cancer Cell. 2005;7:5–15.

Gross S, Piwnica-Worms D. Molecular imaging strategies for drug discovery and development. Curr Opin Chem Biol. 2006;10:334–42.

Gu L, Tsark WM, Brown DA, Blanchard S, Synold TW, Kane SE. A new model for studying tissue-specific mdr1a gene expression in vivo by live imaging. Proc Natl Acad Sci U S A. 2009;106:5394–9.

Guillevin R, Menuel C, Taillibert S, et al. Predicting the outcome of grade II glioma treated with temozolomide using proton magnetic resonance spectroscopy. Br J Cancer. 2011;104:1854–61.

Gulyas B, Halldin C. New PET radiopharmaceuticals beyond FDG for brain tumor imaging. Q J Nucl Med Mol Imaging Off Publ Ital Assoc Nucl Med. 2012;56:173–90.

Hakumaki JM, Poptani H, Sandmair AM, Yla-Herttuala S, Kauppinen RA. 1H MRS detects polyunsaturated fatty acid accumulation during gene therapy of glioma: implications for the in vivo detection of apoptosis. Nat Med. 1999;5:1323–7.

Herholz K, Coope D, Jackson A. Metabolic and molecular imaging in neuro-oncology. Lancet Neurol. 2007;6:711–24.

Hsu AR, Cai W, Veeravagu A, et al. Multimodality molecular imaging of glioblastoma growth inhibition with vasculature-targeting fusion toxin VEGF121/rGel. J Nucl Med. 2007;48:445–54.

Hsueh WA, Kesner AL, Gangloff A, et al. Predicting chemotherapy response to paclitaxel with 18F-Fluoropaclitaxel and PET. J Nucl Med. 2006;47:1995–9.

Huse JT, Holland EC. Genetically engineered mouse models of brain cancer and the promise of preclinical testing. Brain Pathol. 2009;19:132–43.

Jacobs AH, Rueger MA, Winkeler A, et al. Imaging-guided gene therapy of experimental gliomas. Cancer Res. 2007;67:1706–15.

Jahnke K, Muldoon LL, Varallyay CG, et al. Efficacy and MRI of rituximab and methotrexate treatment in a nude rat model of CNS lymphoma. Neuro Oncol. 2009;11:503–13.

Jensen JH, Chandra R. MR imaging of microvasculature. Magn Reson Med Off J Soc Magn Reson Med Soc Magn Reson Med. 2000;44:224–30.

Juhasz C, Dwivedi S, Kamson DO, Michelhaugh SK, Mittal S. Comparison of amino acid positron emission tomographic radiotracers for molecular imaging of primary and metastatic brain tumors. *Mol Imaging* 2014;13:7290.2014.00015.

Kang JH, Chung JK. Molecular-genetic imaging based on reporter gene expression. J Nucl Med. 2008;49 Suppl 2:164S–79.

Keen HG, Ricketts SA, Maynard J, et al. Examining changes in [18 F]FDG and [18 F]FLT uptake in U87-MG glioma xenografts as early response biomarkers to treatment with the dual mTOR1/2 inhibitor AZD8055. Mol Imaging Biol MIB Off Publ Acad Mol Imaging. 2014;16:421–30.

Kelloff GJ, Krohn KA, Larson SM, et al. The progress and promise of molecular imaging probes in oncologic drug development. Clin Cancer Res. 2005;11: 7967–85.

Kim S, Pickup S, Hsu O, Poptani H. Diffusion tensor MRI in rat models of invasive and well-demarcated brain tumors. NMR Biomed. 2008;21:208–16.

Kircher MF, Mahmood U, King RS, Weissleder R, Josephson L. A multimodal nanoparticle for preoperative magnetic resonance imaging and intraoperative optical brain tumor delineation. Cancer Res. 2003;63:8122–5.

Klerk CP, Overmeer RM, Niers TM, et al. Validity of bioluminescence measurements for noninvasive in vivo imaging of tumor load in small animals. Biotechniques. 2007;43:7–13, 30.

Kremer S, Pinel S, Vedrine PO, et al. Ferumoxtran-10 enhancement in orthotopic xenograft models of human brain tumors: an indirect marker of tumor proliferation? J Neurooncol. 2007;83:111–9.

Krishnan AS, Neves AA, de Backer MM, et al. Detection of cell death in tumors by using MR imaging and a gadolinium-based targeted contrast agent. Radiology. 2008;246:854–62.

Laxman B, Hall DE, Bhojani MS, et al. Noninvasive real-time imaging of apoptosis. Proc Natl Acad Sci U S A. 2002;99:16551–5.

Lee KC, Hall DE, Hoff BA, et al. Dynamic imaging of emerging resistance during cancer therapy. Cancer Res. 2006;66:4687–92.

Lee KC, Hamstra DA, Bhojani MS, Khan AP, Ross BD, Rehemtulla A. Noninvasive molecular imaging sheds light on the synergy between 5-fluorouracil and TRAIL/Apo2L for cancer therapy. Clin Cancer Res. 2007;13:1839–46.

Lee SW, Lee SH, Biswal S. Magnetic resonance reporter gene imaging. Theranostics. 2012;2:403–12.

Lee SJ, Yeo JS, Lee HJ, et al. Thymidine phosphorylase influences [(18)F]fluorothymidine uptake in cancer cells and patients with non-small cell lung cancer. Eur J Nucl Med Mol Imaging. 2014;41:1327–35.

Leenders WP, Kusters B, Verrijp K, et al. Antiangiogenic therapy of cerebral melanoma metastases results in sustained tumor progression via vessel co-option. Clin Cancer Res. 2004;10:6222–30.

Liang Q, Yamamoto M, Curiel DT, Herschman HR. Noninvasive imaging of transcriptionally restricted transgene expression following intratumoral injection of an adenovirus in which the COX-2 promoter drives a reporter gene. Mol Imaging Biol. 2004a;6:395–404.

Liang Q, Dmitriev I, Kashentseva E, Curiel DT, Herschman HR. Noninvasive of adenovirus tumor retargeting in living subjects by a soluble adenovirus receptor-epidermal growth factor (sCAR-EGF) fusion protein. Mol Imaging Biol. 2004b;6:385–94.

Maguire CA, Bovenberg MS, Crommentuijn MH, et al. Triple bioluminescence imaging for in vivo monitoring of cellular processes. Mol Ther Nucleic Acids. 2013;2:e99.

Majo VJ, Simpson NR, Prabhakaran J, Mann JJ, Kumar JS. Radiosynthesis of [(18) F]ATPFU: a potential PET ligand for mTOR. J Label Compd Radiopharm. 2014;57:705–9.

Martinez-Quintanilla J, Bhere D, Heidari P, He D, Mahmood U, Shah K. Therapeutic efficacy and fate of bimodal engineered stem cells in malignant brain tumors. Stem Cells. 2013;31:1706–14.

McConville P, Hambardzumyan D, Moody JB, et al. Magnetic resonance imaging determination of tumor grade and early response to temozolomide in a genetically engineered mouse model of glioma. Clin Cancer Res. 2007;13:2897–904.

McKinley ET, Ayers GD, Smith RA, et al. Limits of [18F]-FLT PET as a biomarker of proliferation in oncology. PLoS One. 2013;8:e58938.

McNeill RS, Vitucci M, Wu J, Miller CR. Contemporary murine models in preclinical astrocytoma drug development. Neuro Oncol. 2014;17:12–28.

Miletic H, Fischer Y, Litwak S, et al. Bystander killing of malignant glioma by bone marrow-derived tumor-infiltrating progenitor cells expressing a suicide gene. Mol Ther. 2007;15:1373–81.

Modo M, Hoehn M, Bulte JW. Cellular MR imaging. Mol Imaging. 2005;4:143–64.

Monfared P, Winkeler A, Klein M, et al. Noninvasive assessment of E2F-1-mediated transcriptional regulation in vivo. Cancer Res. 2008;68:5932–40.

Neves AA, Brindle KM. Assessing responses to cancer therapy using molecular imaging. Biochim Biophys Acta. 1766;2006:242–61.

Nguyen QD, Smith G, Glaser M, Perumal M, Arstad E, Aboagye EO. Positron emission tomography imaging of drug-induced tumor apoptosis with a caspase-3/7 specific [18F]-labeled isatin sulfonamide. Proc Natl Acad Sci U S A. 2009;106:16375–80.

Nguyen QD, Challapalli A, Smith G, Fortt R, Aboagye EO. Imaging apoptosis with positron emission tomography: 'bench to bedside' development of the caspase-3/7 specific radiotracer [(18)F]ICMT-11. Eur J Cancer. 2012;48:432–40.

Nguyen QD, Lavdas I, Gubbins J, et al. Temporal and spatial evolution of therapy-induced tumor apoptosis detected by caspase-3-selective molecular imaging. Clin Cancer Res Off J Am Assoc Cancer Res. 2013;19:3914–24.

Nicholls SB, Hyman BT. Measuring caspase activity in vivo. Methods Enzymol. 2014;544:251–69.

Niu G, Chen X. Apoptosis imaging: beyond annexin V. J Nucl Med Off Publ Soc Nucl Med. 2010;51:1659–62.

Nowosielski M, DiFranco MD, Putzer D, et al. An intra-individual comparison of MRI, [18F]-FET and [18F]-FLT PET in patients with high-grade gliomas. PLoS One. 2014;9:e95830.

Oriuchi N, Higuchi T, Ishikita T, et al. Present role and future prospects of positron emission tomography in clinical oncology. Cancer Sci. 2006;97:1291–7.

Pal A, Glekas A, Doubrovin M, et al. Molecular imaging of EGFR kinase activity in tumors with 124I-labeled small molecular tracer and positron emission tomography. Mol Imaging Biol. 2006;8:262–77.

Pantaleo MA, Nannini M, Maleddu A, et al. Conventional and novel PET tracers for imaging in oncology in the era of molecular therapy. Cancer Treat Rev. 2008;34: 103–21.

Pantaleo MA, Nannini M, Maleddu A, et al. Experimental results and related clinical implications of PET detection of epidermal growth factor receptor (EGFr) in cancer. Ann Oncol. 2009;20:213–26.

Park SY, Kwak W, Thapa N, et al. Combination therapy and noninvasive imaging with a dual therapeutic vector expressing MDR1 short hairpin RNA and a sodium iodide symporter. J Nucl Med. 2008;49: 1480–8.

Paulus MJ, Gleason SS, Kennel SJ, Hunsicker PR, Johnson DK. High resolution X-ray computed tomography: an emerging tool for small animal cancer research. Neoplasia. 2000;2:62–70.

Pichler A, Prior JL, Piwnica-Worms D. Imaging reversal of multidrug resistance in living mice with bioluminescence: MDR1 P-glycoprotein transports coelenterazine. Proc Natl Acad Sci U S A. 2004;101:1702–7.

Pichler A, Zelcer N, Prior JL, Kuil AJ, Piwnica-Worms D. In vivo RNA interference-mediated ablation of MDR1 P-glycoprotein. Clin Cancer Res. 2005;11: 4487–94.

Pichler BJ, Wehrl HF, Judenhofer MS. Latest advances in molecular imaging instrumentation. J Nucl Med. 2008;49 Suppl 2:5S–23.

Pierce MC, Javier DJ, Richards-Kortum R. Optical contrast agents and imaging systems for detection and diagnosis of cancer. Int J Cancer. 2008;123:1979–90.

Pittet MJ, Weissleder R. Intravital imaging. Cell. 2011;147:983–91.

Price JM, Robinson SP, Koh DM. Imaging hypoxia in tumours with advanced MRI. Q J Nucl Med Mol Imaging Off Publ Ital Assoc Nucl Med. 2013;57: 257–70.

Pulkkanen KJ, Yla-Herttuala S. Gene therapy for malignant glioma: current clinical status. Mol Ther J Am Soc Gene Ther. 2005;12:585–98.

Qiao J, Xue S, Pu F, et al. Molecular imaging of EGFR/HER2 cancer biomarkers by protein MRI contrast agents. J Biol Inorg Chem JBIC Publ Soc Biol Inorg Chem. 2014;19:259–70.

Ray P, De A, Patel M, Gambhir SS. Monitoring caspase-3 activation with a multimodality imaging sensor in living subjects. Clin Cancer Res. 2008;14:5801–9.

Rehemtulla A, Stegman LD, Cardozo SJ, et al. Rapid and quantitative assessment of cancer treatment response using in vivo bioluminescence imaging. Neoplasia. 2000;2:491–5.

Ribot EJ, Miraux S, Konsman JP, et al. In vivo MR tracking of therapeutic microglia to a human glioma model. NMR Biomed. 2011;24:1361–8.

Sasongko L, Link JM, Muzi M, et al. Imaging P-glycoprotein transport activity at the human blood-brain barrier with positron emission tomography. Clin Pharmacol Ther. 2005;77:503–14.

Saydam O, Glauser DL, Heid I, et al. Herpes simplex virus 1 amplicon vector-mediated siRNA targeting epidermal growth factor receptor inhibits growth of human glioma cells in vivo. Mol Ther. 2005;12: 803–12.

Schelhaas S, Wachsmuth L, Viel T, et al. Variability of proliferation and diffusion in different lung cancer models as measured by 3′-deoxy-3′-18F-fluorothymidine PET and diffusion-weighted MR imaging. J Nucl Med Off Publ Soc Nucl Med. 2014;55:983–8.

Schellenberger EA, Bogdanov Jr A, Petrovsky A, Ntziachristos V, Weissleder R, Josephson L. Optical imaging of apoptosis as a biomarker of tumor response to chemotherapy. Neoplasia. 2003;5:187–92.

Serganova I, Doubrovin M, Vider J, et al. Molecular imaging of temporal dynamics and spatial heterogeneity of hypoxia-inducible factor-1 signal transduction activity in tumors in living mice. Cancer Res. 2004;64:6101–8.

Shah K, Tang Y, Breakefield X, Weissleder R. Real-time imaging of TRAIL-induced apoptosis of glioma tumors in vivo. Oncogene. 2003;22:6865–72.

Shah K, Bureau E, Kim DE, et al. Glioma therapy and real-time imaging of neural precursor cell migration and tumor regression. Ann Neurol. 2005;57:34–41.

Sherley JL, Kelly TJ. Regulation of human thymidine kinase during the cell cycle. J Biol Chem. 1988;263: 8350–8.

Sihver W, Pietzsch J, Krause M, Baumann M, Steinbach J, Pietzsch HJ. Radiolabeled cetuximab conjugates for EGFR targeted cancer diagnostics and therapy. Pharmaceuticals. 2014;7:311–38.

Simeonova I, Huillard E. In vivo models of brain tumors: roles of genetically engineered mouse models in understanding tumor biology and use in preclinical studies. Cell Mol Life Sci CMLS. 2014;71:4007–26.

Singh TD, Lee HW, Lee SW, et al. Noninvasive imaging of apoptosis induced by adenovirus-mediated cancer gene therapy using a caspase-3 biosensor in living subjects. Mol Imaging 2014;13:7290.2014.00019.

Singhal T, Narayanan TK, Jain V, Mukherjee J, Mantil J. (11)C-L: -Methionine positron emission tomography in the clinical management of cerebral gliomas. Mol Imaging Biol. 2008;10:1–18.

Soling A, Theiss C, Jungmichel S, Rainov NG. A dual function fusion protein of Herpes simplex virus type 1 thymidine kinase and firefly luciferase for noninvasive in vivo imaging of gene therapy in malignant glioma. Genet Vaccin Ther. 2004;2:7.

Suchorska B, Tonn JC, Jansen NL. PET imaging for brain tumor diagnostics. Curr Opin Neurol. 2014;27:683–8.

Suwa T, Ozawa S, Ueda M, Ando N, Kitajima M. Magnetic resonance imaging of esophageal squamous cell carcinoma using magnetite particles coated with anti-epidermal growth factor receptor antibody. Int J Cancer. 1998;75:626–34.

Szentirmai O, Baker CH, Lin N, et al. Noninvasive bioluminescence imaging of luciferase expressing intracranial U87 xenografts: correlation with magnetic resonance imaging determined tumor volume and longitudinal use in assessing tumor growth and antiangiogenic treatment effect. Neurosurgery. 2006;58:365–72; discussion -72.

Tang D, Hight MR, McKinley ET, et al. Quantitative preclinical imaging of TSPO expression in glioma using N, N-diethyl-2-(2-(4-(2-18F-fluoroethoxy)phenyl)-5,7-dimethylpyrazolo[1,5-a]pyrimi din-3-yl)acetamide. J Nucl Med Off Publ Soc Nucl Med. 2012;53:287–94.

Tentler JJ, Tan AC, Weekes CD, et al. Patient-derived tumour xenografts as models for oncology drug development. Nat Rev Clin Oncol. 2012;9:338–50.

Thompson CJ, Goertzen AL, Thiessen JD, et al. Development of a PET scanner for simultaneously imaging small animals with MRI and PET. Sensors. 2014;14:14654–71.

Towner RA, Smith N, Doblas S, et al. In vivo detection of c-Met expression in a rat C6 glioma model. J Cell Mol Med. 2008;12:174–86.

Toy R, Bauer L, Hoimes C, Ghaghada KB, Karathanasis E. Targeted nanotechnology for cancer imaging. Adv Drug Deliv Rev. 2014;76:79–97.

Ueda M, Saji H. Radiolabeled probes targeting hypoxia-inducible factor-1-active tumor microenvironments. ScientificWorldJournal. 2014;2014:165461.

Ullrich R, Backes H, Li H, et al. Glioma proliferation as assessed by FLT-PET in patients with newly diagnosed high grade glioma. Clin Cancer Res. 2008;14:2049–55.

Vandsburger MH, Radoul M, Cohen B, Neeman M. MRI reporter genes: applications for imaging of cell survival, proliferation, migration and differentiation. NMR Biomed. 2013;26:872–84.

Varma NR, Janic B, Iskander AS, et al. Endothelial progenitor cells (EPCs) as gene carrier system for rat model of human glioma. PLoS One. 2012;7:e30310.

Varma NR, Barton KN, Janic B, et al. Monitoring adenoviral based gene delivery in rat glioma by molecular imaging. World J Clin Oncol. 2013;4:91–101.

Veeravagu A, Hou LC, Hsu AR, et al. The temporal correlation of dynamic contrast-enhanced magnetic resonance imaging with tumor angiogenesis in a murine glioblastoma model. Neurol Res. 2008;30:952–9.

Verhoeff JJ, van Tellingen O, Claes A, et al. Concerns about anti-angiogenic treatment in patients with glioblastoma multiforme. BMC Cancer. 2009;9:444.

Viel T, Talasila KM, Monfared P, et al. Analysis of the growth dynamics of angiogenesis-dependent and -independent experimental glioblastomas by multimodal small-animal PET and MRI. J Nucl Med Off Publ Soc Nucl Med. 2012;53:1135–45.

Viel T, Schelhaas S, Wagner S, et al. Early assessment of the efficacy of temozolomide chemotherapy in experimental glioblastoma using [18F]FLT-PET imaging. PLoS One. 2013a;8:e67911.

Viel T, Boehm-Sturm P, Rapic S, et al. Non-invasive imaging of glioma vessel size and densities in correlation with tumour cell proliferation by small animal PET and MRI. Eur J Nucl Med Mol Imaging. 2013b;40:1595–606.

Viel T, Monfared P, Schelhaas S, et al. Optimizing glioblastoma temozolomide chemotherapy employing lentiviral-based anti-MGMT shRNA technology. Mol Ther J Am Soc Gene Ther. 2013c;21:570–9.

Vlodavsky E, Soustiel JF. Immunohistochemical expression of peripheral benzodiazepine receptors in human astrocytomas and its correlation with grade of malignancy, proliferation, apoptosis and survival. J Neurooncol. 2007;81:1–7.

Waerzeggers Y, Klein M, Miletic H, et al. Multimodal imaging of neural progenitor cell fate in rodents. Mol Imaging. 2008;7:77–91.

Waerzeggers Y, Monfared P, Viel T, Winkeler A, Voges J, Jacobs AH. Methods to monitor gene therapy with molecular imaging. Methods. 2009a;48:146–60.

Waerzeggers Y, Jacobs A, Monfared P, Viel T. Molecular imaging in patient-tailored cancer therapies. Eur Pharm Review Digital. 2009b;3:27–37.

Waerzeggers Y, Jacobs AH, Monfared P, Viel T. Molecular imaging in patient-tailored cancer therapies. Eur Pharm Rev Digital. 2009(3):27–37.

Wang LV. Prospects of photoacoustic tomography. Med Phys. 2008;35:5758–67.

Wang HE, Yu HM, Liu RS, et al. Molecular imaging with 123I-FIAU, 18F-FUdR, 18F-FET, and 18F-FDG for monitoring herpes simplex virus type 1 thymidine kinase and ganciclovir prodrug activation gene therapy of cancer. J Nucl Med. 2006;47:1161–71.

Wang F, Fang W, Zhao M, et al. Imaging paclitaxel (chemotherapy)-induced tumor apoptosis with 99mTc C2A, a domain of synaptotagmin I: a preliminary study. Nucl Med Biol. 2008;35:359–64.

Wang F, Fang W, Zhang MR, et al. Evaluation of chemotherapy response in VX2 rabbit lung cancer with 18F-labeled C2A domain of synaptotagmin I. J Nucl Med Off Publ Soc Nucl Med. 2011;52:592–9.

Wang F, Wang Z, Hida N, et al. A cyclic HSV1-TK reporter for real-time PET imaging of apoptosis. Proc Natl Acad Sci U S A. 2014;111:5165–70.

Wen B, Burgman P, Zanzonico P, et al. A preclinical model for noninvasive imaging of hypoxia-induced gene expression; comparison with an exogenous marker of tumor hypoxia. Eur J Nucl Med Mol Imaging. 2004;31:1530–8.

Wijsman R, Kaanders JH, Oyen WJ, Bussink J. Hypoxia and tumor metabolism in radiation oncology: targets visualized by positron emission tomography. Q J Nucl Med Mol Imaging Off Publ Ital Assoc Nucl Med. 2013;57:244–56.

Winkeler A, Sena-Esteves M, Paulis LE, et al. Switching on the lights for gene therapy. PLoS One. 2007; 2:e528.

Winkeler A, Boisgard R, Awde AR, et al. The translocator protein ligand [(1)(8)F]DPA-714 images glioma and activated microglia in vivo. Eur J Nucl Med Mol Imaging. 2012;39:811–23.

Yao J, Wang LV. Photoacoustic brain imaging: from microscopic to macroscopic scales. Neurophotonics. 2014;1(1):011003.

Youn H, Chung JK. Reporter gene imaging. AJR Am J Roentgenol. 2013;201:W206–14.

Zhang Z, Jiang Q, Jiang F, et al. In vivo magnetic resonance imaging tracks adult neural progenitor cell targeting of brain tumor. Neuroimage. 2004;23:281–7.
Zhang L, Lee KC, Bhojani MS, et al. Molecular imaging of Akt kinase activity. Nat Med. 2007;13:1114–9.
Zhang L, Bhojani MS, Ross BD, Rehemtulla A. Enhancing Akt imaging through targeted reporter expression. Mol Imaging. 2008;7:168–74.
Zhang CC, Yan Z, Li W, et al. [(18)F]FLT-PET imaging does not always "light up" proliferating tumor cells. Clin Cancer Res Off J Am Assoc Cancer Res. 2012a;18:1303–12.
Zhang F, Huang X, Zhu L, et al. Noninvasive monitoring of orthotopic glioblastoma therapy response using RGD-conjugated iron oxide nanoparticles. Biomaterials. 2012b;33:5414–22.
Zhao M, Beauregard DA, Loizou L, Davletov B, Brindle KM. Non-invasive detection of apoptosis using magnetic resonance imaging and a targeted contrast agent. Nat Med. 2001;7:1241–4.

Imaging in Neurology Research II: Exploring Plasticity and Cognitive Networks by In Vivo MRI

29

J. Hamaide, L. Van Ruijssevelt, F. Kara,
G. De Groof, and A. Van der Linden

Contents

Abbreviations

ADC	Apparent diffusion coefficient
AIM-MRI	Activity-induced manganese-enhanced magnetic resonance imaging
ASL	Arterial spin labeling
BBB	Blood-brain barrier
BDNF	Brain-derived neurotrophic factor
BOLD	Blood-oxygen-level dependent
CA 1/2/3	Cornu ammonis part 1/2/3
CBF	Cerebral blood flow
CBV	Cerebral blood volume
Cho	Choline
$CMRO_2$	Cerebral metabolic rate of oxygen
CNS	Central nervous system
Cr	Creatine
CT	Computed tomography
DCM	Dynamic causal modeling
DTI	Diffusion tensor imaging
EEG	Electroencephalography
EPI	Echo planar imaging
FA	Fractional anisotropy
FID	Free induction decay
fMRI	Functional magnetic resonance imaging
GABA	Gamma-aminobutyric acid
Gln	Glutamine
Glu	Glutamate
GRASE	Gradient and spin echo
HARDI	High angular resolution diffusion imaging
HRF	Hemodynamic response function
ICA	Independent component analysis

J. Hamaide • L. Van Ruijssevelt • F. Kara
G. De Groof • A. Van der Linden (✉)
Bio-Imaging Lab, Department of Biomedical Sciences, University of Antwerp, Universiteitsplein 1, 2610 Wilrijk, Belgium
e-mail: annemie.vanderlinden@uantwerpen.be

F. Kiessling et al. (eds.), *Small Animal Imaging*, DOI 10.1007/978-3-319-42202-2_29

Lac	Lactate
LFF	Low-frequency fluctuations
LTD	Long-term depression
LTP	Long-term potentiation
MD	Mean diffusivity
ME	Monocular enucleation
MEG	Magnetoencephalography
MEMRI	Manganese-enhanced magnetic resonance imaging
MPIO	Micron-sized paramagnetic iron oxide (particle)
MRI	Magnetic resonance imaging
MRS	Magnetic resonance spectroscopy
MTC	Magnetization transfer contrast
NAA	N-Acetylaspartate
NIRS	Near-infrared spectroscopy
Otx2	Orthodenticle homeobox 2 gene
PCr	Phosphocreatine
PET	Positron emission tomography
phMRI	Pharmacological magnetic resonance imaging
PRESS	Point-resolved spectroscopy
RF	Radio frequency
ROI	Region of interest
rsfMRI	Resting state functional magnetic resonance imaging
SNR	Signal-to-noise ratio
STEAM	Stimulated echo acquisition mode
tCr	Total creatine
TE	Echo time
TI	Inversion time
TR	Repetition time
VBM	Voxel-based morphometry
λ1 λ2, λ3	Three eigenvalues

The aim of this chapter is to introduce several models of neuroplasticity and to illustrate how basic neuroplastic events including learning and cognition can be unraveled with different in vivo magnetic resonance imaging (MRI) tools.

29.1 Neuroplasticity and Cognition in Animal Research

One of the most crucial paradigm shifts in the field of neurosciences of the twentieth century was the notion that the adult brain is not fixed or immutable but can adapt structurally and functionally in response to experience or injury. Today, this phenomenon is defined as experience-dependent neuroplasticity and is regarded as an interaction between innate genotype and environmental stimuli to ensure proper functioning of neural networks and to maintain homeostasis upon changing surroundings (Butz et al. 2009; Nagy and Turecki 2012).

29.1.1 Timing: Critical Period Versus Adult Neuroplasticity

The brains' ability to adapt is highest throughout infancy and adolescence. When reaching adulthood, neuroplasticity is dramatically downregulated to stabilize and consolidate the patterns of cortical connectivity shaped by prior experience (Jon 2012). Although plasticity becomes downregulated, the adult organism is still able to acquire novel skills, to learn and retain memory (Takesian et al. 2013; Lövdén et al. 2013; Lamprecht and LeDoux 2004), and to overcome possible functional losses due to, e.g., stroke or trauma (May 2011; Overman and Carmichael 2014).

29.1.1.1 Critical Period Plasticity

Numerous examples exist illustrating the crucial importance of early life experiences on shaping adult behavior. Children suffering congenital cataract or deafness should receive medical treatment before, respectively, 6 weeks or 2 years after birth as to ensure, respectively, visual acuity (Fledelius et al. 2014) or auditory perception and language acquisition in later life (Svirsky et al. 2004; Kral 2013). These observations can be explained by the existence of critical periods or precisely delineated time windows in early life during which environmental stimuli most potently shape cortical brain circuitries responsible for the acquisition of various skills needed later in life (Jon 2012). Interestingly, if the same stimulus is applied prior to or post opening or closure of the critical period, it will have a reduced effect (Jon 2012; Berardi et al. 2000), implying that the brain is only receptive to the specific input at the respective maturational window. Up to today, most research on critical period

mechanisms was dedicated to the development of the sensory systems such as the visual (critical period for ocular dominance plasticity (Hensch 2004; Levelt and Hübener 2012)), auditory (Kral 2013), and somatosensory system (whisker-barrel pathway (Erzurumlu and Gaspar 2012)) in mammals.

A very interesting model which displays a remarkable analogy with the critical period for human speech learning can be found in songbirds, especially zebra finches (Doupe and Kuhl 1999; Brainard and Doupe 2013). Indeed, similar to humans, zebra finches learn the tutor song during two well-described partly overlapping critical periods in early life (for review, see Doupe and Kuhl (1999)). When the critical period for vocal learning closes, male zebra finches will sing one stereotyped song for the rest of their lives. The advantage of songbirds in plasticity research is that they produce an easily quantifiable behavioral output, i.e., song, which reflects the respective phase of song learning and which can be easily related to the observed functional and structural brain changes. This makes songbirds a highly attractive model to study critical period plasticity beyond the acquisition of basic sensorimotor skills.

29.1.1.2 Maladaptive Critical Period Plasticity

Many neurological disorders result from improper critical period neuroplasticity. Evidence for this statement has been put forward by Berger and colleagues who postulate that besides the involvement of genetic mechanisms, early closure of the critical period for integration of sensory input, language, and social skills may lay at the basis of the behavioral phenotype of autism spectrum disorder (Berger et al. 2013). Furthermore, several other neurodevelopmental disorders have been linked to maladaptive critical period plasticity, i.e., developmental intellectual disabilities such as Down and Rett syndrome (Fernandez and Garner 2007), schizophrenia (Bitanihirwe and Woo 2014), epilepsy (Coghlan et al. 2012), etc. In addition, animal models for drug addiction (Lüscher 2013), chronic pain (Petersen-Felix and Curatolo 2002), stress, and depression (Stepanichev et al. 2014) display maladjustive functional, structural, and biochemical brain plasticity along the course of pathology.

29.1.1.3 Learn and Retain Memory in Adulthood

Fortunately, neuroplasticity necessary for the establishment of higher cognitive skills is never entirely downregulated enabling adult organisms to learn in adult life. Pavlov described one of the first reports on animal learning when he noticed that dogs started salivating upon hearing the sound of the bell that previously always coincided with serving food. From then onward an array of different learning and conditioning paradigms have been developed, e.g., defensive withdrawal reflex, eyeblink conditioning, operant conditioning, taste aversion conditioning, and fear conditioning. Other experimental procedures exist to assess the ability of laboratory animals to learn and retain memory, e.g., dry and water-based mazes, to investigate spatial learning.

A natural model, displaying spontaneous neuroplasticity throughout adulthood, is found in seasonal songbirds like the canary and the starling. The neural substrate in control of singing displays substantial seasonal plasticity, i.e., the volume and interconnectivity between the song control nuclei dramatically increases in anticipation of the breeding season, preparing birds to sing (Tramontin and Brenowitz 2000; De Groof et al. 2008). Moreover, most seasonal songbirds are capable of adapting and extending their song repertoire on a yearly basis. Therefore, it leaves no surprise that seasonal songbirds have been studied extensively as a superior model for adult neuroplasticity related to learning and memory (De Groof et al. 2008, 2009, 2013a; De Groof and Van der Linden 2010; Van der Linden et al. 2009a).

29.1.2 Recovery from Functional Loss

The brains' ability to recuperate from injury is highest in early life but is not completely vanished during adulthood (Nahmani and Turrigiano 2014). Interesting in this context is the importance of experience-dependent plasticity to promote recovery (Hannan 2014; Särkämö et al.

2014). Another example related to functional recovery post injury can be found in crossmodal plasticity defined as an adaptive reorganization of cortical circuitries in order to reallocate a specific brain area to process a new function after loss of the original one, following, e.g., congenital blindness or peripheral deafferentation (for review, see Frasnelli et al. (2011), Bavelier and Hirshorn (2010)).

29.1.3 Neurogenesis

Goldman and Nottebohm were the first to relate memory acquisition and retention to adult neurogenesis both in the context of song learning (Goldman and Nottebohm 1983; Nottebohm 1985) and in spatial memory of food caching in songbirds (Barnea and Nottebohm 1994, 1996; Leuner et al. 2006). Only by the late 1990s, this idea was supported in mammals by findings showing that newly generated cells are incorporated in the hippocampus and olfactory bulb (Carlén et al. 2002). Despite this information, the exact implication of neurogenesis in (hippocampal) memory formation and retention remains elusive (Leuner et al. 2006; Stuchlik 2014).

Interestingly, several studies have found a positive correlation between physical exercise and the rate of hippocampal neurogenesis (Olson et al. 2006). Moreover, environmental enrichment, i.e., supplying the basic animal housing conditions with supplementary species-specific challenges such as running wheels, labyrinths, etc. (Baumans 2005), has been shown to increase the extent of neurogenesis (Brown et al. 2003) (for review of human and animal studies discussing the effects of exercise and environment on learning and cognition, see Hötting and Röder (2013), Voss et al. (2013)). Since neurogenesis alters the number of neurons in a given network and neurogenesis is promoted upon physical exercise or upon housing in a more stimulating enriched environment, one can conclude that neurogenesis can be regarded as experience-dependent neuroplasticity as well.

29.2 Mechanisms Underlying Neuroplasticity

One of the most vital concepts describing the essence of all neuroplastic events can be found in the postulates of Donald Hebb summarized as "Cells that fire together, wire together." Indeed, neuroplasticity relates to functional adaptations, such as long-term potentiation (LTP) and depression (LTD) (Malenka and Bear 2004), over microscale structural alterations such as the formation of dendritic protrusions (Anthony and Karel 2009; Chen et al. 2014), to the establishment of axonal projections, neurogenesis, and macroscale reorganization of functional and structural connectivity between distinct brain areas (De Groof et al. 2008; Oboti and Peretto 2014; Gheusi et al. 2014; Barnes and Finnerty 2010). Using invasive methodologies, several targets in control of creating a permissive environment for plasticity to take place have been put forward, i.e., (i) structural factors, e.g., myelination and perineuronal nets; (ii) metabolic mechanisms, e.g., excitation-inhibition balance through GABA and glutamate; and (iii) molecular elements, e.g., BDNF, Otx-2, etc. (for review, see Tropea et al. (2009)). Recently, epigenetic mechanisms were proposed to be part of the interface between environmental stimuli experienced during early life critical periods and the sustained molecular, cellular, and complex behavioral phenotypes (Fagiolini et al. 2009).

The ultimate goal of studying neuroplasticity would be to "*unlock the brain*" (Jon 2012) and restore levels of early neuroplasticity in adulthood as strategy to treat certain CNS disorders. Several attempts have been made (Jon 2012; Sale et al. 2010; Gervain et al. 2013), yet, further investigation is highly necessary and requires the appropriate tools to track the functional, biochemical, and structural changes. In vivo noninvasive magnetic resonance imaging (MRI) strongly complies with this and has proven to be an exquisite tool to guide more localized invasive methods to disentangle the observed neuroplastic events and cognitive processes up to the molecular level.

29.3 In Vivo MRI: The Method of Choice to Study Neuroplasticity

MRI is a commonly used (pre)clinical imaging modality to visualize soft tissues such as the brain (for principle of MRI: Chapter 12). Most often the field of view occupies the entire brain, where high-resolution three-dimensional information can be obtained, and the datasets can be viewed and virtually sliced along any possible plane. The noninvasive nature of this method allows performing dynamic longitudinal studies where functional, structural, and metabolic brain changes can be followed up in vivo over time or upon treatment where each animal serves as its own reference. This essential feature makes MRI an exceptional tool to observe neuroplastic adaptations both acutely and in more extended time frames and to establish causal correlations between the observed MRI findings and behavioral to even molecular data from the same animal.

29.3.1 MRI: A Wide Range of Possibilities

A variety of MRI pulse sequences exist which exploit different characteristics of water protons in tissue. The most conventional and widely used MRI contrasts are found in T_1-, T_2-, T_2^*-, and proton density-weighted images. The resulting images provide superior anatomical contrast allowing a qualitative assessment of overall brain anatomy easily distinguishing gray and white matter. Slight adaptation of the basic T_1- and T_2-weighted MRI pulse sequences enables a quantitative evaluation of tissue properties reflecting tissue density, myelination, etc. (Deoni 2010). Besides anatomical assessment, specialized MRI techniques entail information on blood flow (arterial spin labeling, dynamic susceptibility contrast), diffusion properties (diffusion-weighted imaging, diffusion tensor imaging, diffusion kurtosis imaging), functional activation (functional MRI, resting state functional MRI, pharmacological MRI), and even the metabolic profile of tissues (magnetic resonance spectroscopy, chemical exchange saturation transfer). Most of these imaging contrasts do not require the administration of exogenous contrast agents as opposed to, e.g., PET (radioactive tracers), and do not rely on hazardous ionizing radiation, e.g., CT, making MRI a truly noninvasive and safe imaging tool.

29.3.2 Spatial and Temporal Resolution

The spatial and temporal image resolution is determined by the MRI modality of choice, the corresponding imaging pulse sequence, the signal-to-noise ratio, the acquisition time, and the available hardware. Temporal resolution primarily affects functional imaging modalities. Despite many efforts to speed up acquisition by, e.g., echo planar imaging pulse sequences, multiband acquisition, and parallel imaging, fMRI still relies on the detection of the intrinsic hemodynamic response of neural tissue to a given stimulus which is markedly slower than the actual neural activity experienced by neurons, i.e., hemodynamic response situated in the order of seconds, whereas neuronal activity goes well beyond this frequency (Logothetis and Wandell 2004; Logothetis et al. 2001). Besides its relatively low temporal resolution, fMRI provides an excellent three-dimensional spatial resolution (0.2–1.0 mm) covering the entire brain and excluding the need for an a priori selection of brain regions involved. This strongly contrasts to other functional imaging techniques such as EEG, MEG, NIRS, and PET which in turn benefit from a substantially higher temporal resolution (sampling frequency: ms).

Recently, in vivo microscopic imaging techniques such as two-photon laser imaging have been applied to study the dynamics of synapse formation, synaptic reorganization, and cortical spine mobility (Vivo et al. 2013; Denk and Svoboda 1997; Majewska 2013). Unfortunately, this falls beyond the resolution of structural

MRI. In theory, the physical limitation of MR image voxel size is situated around 10 μm (Mori and Zhang 2006). In practice, however, achieving a reasonable signal-to-noise ratio coming from a (isotropic) resolution of 10–100 μm requires a large number of averages which results in a long acquisition time, merely confining such spatial precision to ex vivo experiments (for details: Part IV*:* Ex Vivo Validation Methods). On average, in vivo MRI experiments take up to 0.5–3 h and are characterized by a spatial resolution of 100–200 μm (in plane).

29.4 In Vivo Imaging Techniques to Visualize Key Features of Neuroplasticity and Cognition

The previous sections discussed several biological phenomena implicated in neuroplasticity as well as a few arguments in favor of using MRI to follow up neuroplasticity and cognition in vivo. The following paragraphs will provide an overview of each imaging modality with (1) a brief introduction, explaining the origin of the obtained tissue contrast in combination with its major advantages and disadvantages; (2) practical examples of the application of in vivo MRI to assess functional, structural, and metabolic aspects of neuroplasticity and cognition in relevant animal models; and (3) references to papers or reviews concerned with practical details on how to optimize experimental protocols – from animal procedures to MRI pulse sequences – and how to analyze and interpret the data.

29.4.1 Functional MRI

Since its introduction over 20 years ago (Ogawa et al. 1992; Kwong et al. 1992), functional magnetic resonance imaging (fMRI) has become one of the most popular techniques in the field of cognitive neurosciences for studying the localization, pattern, and time course of brain activity in (pre) clinical and fundamental research (for reviews on the technique, see Di Salle et al. (1999), Logothetis (2008), Bandettini (2012)). To infer brain activity, fMRI measures activity-driven changes in local cerebral blood flow (CBF), blood volume (CBV), and metabolic rate of oxygen ($CMRO_2$). This makes fMRI an indirect indicator of neuronal activity assessing what is commonly referred to as the hemodynamic response function (HRF). The complex interplay between CBF, CBV, and $CMRO_2$ comprised in the HRF can be measured using blood-oxygen-level-dependent (BOLD) fMRI. BOLD is by far the most popular contrast used for fMRI and is based on the paramagnetic properties of deoxygenated hemoglobin. Figure 29.1 illustrates how neural activation can give rise to altered BOLD signals in fMRI (for review, see Logothetis and Wandell (2004b), Logothetis and Pfeuffer (2004), Malonek et al. (1997)). In order to accurately sample the hemodynamic response to a specific task, MRI pulse sequences with a sufficient temporal resolution are required. Over recent years, numerous variations to the well-established EPI and GRASE pulse sequences have been developed realizing a repetition time up to 0.500 s (for review of recently implemented fast- and high-resolution fMRI sequences, see Feinberg and Yacoub (2012)).

Besides the BOLD contrast, it is possible to specifically detect brain activity based on changes in CBF or CBV. For CBV-weighted fMRI, an exogenous intravascular contrast agent is administered to increase the sensitivity of the functional imaging protocol (for review, see Smirnakis et al. (2007) and Kim et al. (2013) and chapter contrast agents). Using arterial spin labeling (ASL), a method in which blood protons in the brain-feeding arteries are magnetically tagged to serve as endogenous tracer, activity-induced changes in CBF can be measured directly (Detre and Wang 2002). One can use fMRI to study neuronal activity in response to a certain task (activity-induced fMRI), during rest (resting state fMRI, rsfMRI) or in response to acute drug challenges (pharmacological MRI, phMRI).

29.4.1.1 Activity-Induced fMRI

The primary and most exploited use of fMRI is the inference of neural activity in response to a certain sensorimotor or cognitive task. Along

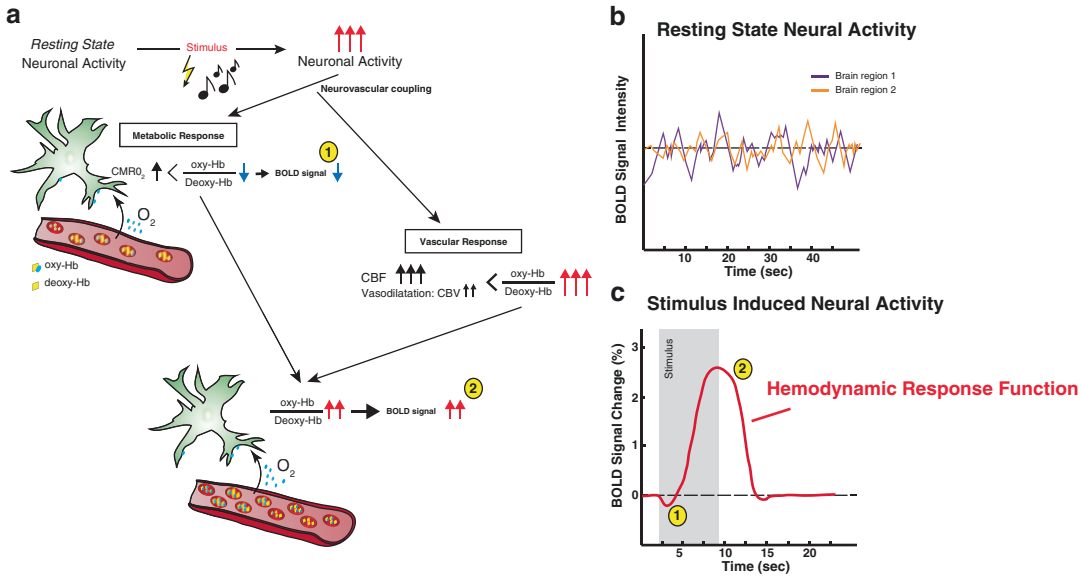

Fig. 29.1 Schematic overview of the principle of BOLD fMRI. (**a**) When the brain is stimulated, local neural activity gives rise to a cascade of events which result in local changes in oxygen consumption and blood flow. This translation from neural to vascular signals is termed the 'neurovascular coupling'. First, the increased local metabolic activity (including cerebral metabolic rate of O_2 ($CMRO_2$)) results in a decrease in the ratio between oxygenated (oxy-Hb) to deoxygenated hemoglobin (deoxy-Hb) in the blood. The paramagnetic properties of deoxy-Hb will induce an initial small dip in the BOLD signal reflected in changing T_2(*) contrast (number 1 in panel **a** and **c**). Second, the initial, activity-induced oxygen consumption will be compensated by a massive increase in local blood flow (CBF) and vasodilatation resulting in an increased cerebral blood volume (CBV). The net increase in oxy-Hb/deoxy-Hb ratio will overcompensate the metabolic O_2 demand resulting in a large peak in the BOLD signal (number 2 in panel **a** and **c**). (**b**) Small fluctuations in the BOLD response are present when no stimulus is given. The time course of the BOLD signal measured in resting state fMRI (rsfMRI) experiments can be extracted from different brain regions and is used to study functional connectivity. (**c**) A typical time course of stimulus-induced BOLD signal changes. The percentage signal change compared to the rest condition is indicated. When the temporal resolution allow it, the first small dip at the initiation of the stimulation followed by a peak in the BOLD signal can be picked up. The shape of the response follows the theoretical model of the hemodynamic response function

with the choice of the right stimulus associated with the hypothesis, the way these stimuli are presented to the subject should be judiciously determined. The most commonly used stimulus presentation designs for fMRI experiments are (i) a block design and (ii) an event-related design (for review on fMRI study designs, see (Amaro and Barker (2006)). Most small animal fMRI studies are performed while animals are anesthetized. This creates difficulties as anesthetics often affect vasculature and/or neuronal signaling to different extents (Masamoto and Kanno 2012). Therefore, depending on the animal model, the type of stimulus, and the expected effect, different anesthetics might be preferred (Schroeter et al. 2014; Tsurugizawa et al. 2010; Williams et al. 2010; Boumans et al. 2007). In case of phMRI, when the stimulation paradigm is combined with or consists of a pharmacological challenge, not only the effect of the anesthetic on the neurovascular coupling should be evaluated but also the impact of the anesthesia on the targeted neurotransmitter system as well as the possible interactions between the anesthetic and the drug of interest. Although the use of anesthesia seems necessary to reduce motion and stress, efforts are being made to train animals, including rats (King et al. 2005; Ferris et al. 2006), mice (Jonckers et al. 2014; Desai et al. 2011), and even birds (De Groof et al.

2013b), to be scanned awake and to design adapted restraining setups (Lahti et al. 1998). The possibility of using awake animals in fMRI experiments extends the type of questions that can be addressed, but as the training is very time-consuming, its implementation is not feasible for all fMRI studies. Finally, instabilities in physiological parameters can greatly influence the HRF (Birn et al. 2006; Kalisch et al. 2001; Wise et al. 2004). During the experiment one should therefore strive to maximal physiological stability or at least allow to account for instabilities within the data analysis steps by monitoring parameters such as body temperature, breathing rate, etc., closely while scanning.

To date, no consensus has been reached on the method of choice for fMRI data processing to extract activated brain regions from the fMRI time series. Typically, a voxel-based approach is opted. Prior to the voxel-based statistical modeling, some basic procedures are performed including (1) slice-timing correction and realignment, (2) co-registration of functional and structural images and normalization to a standardized stereotactic space, and (3) smoothing. A clear overview of these processing steps can be found in, e.g., Amaro and Barker 2006, Lindquist 2008, James et al. 2014. After preprocessing, the applied stimulation design (e.g., block design: box-car function) is convolved with a function which best describes how the BOLD signal evolves (e.g., HRF) in order to have a better estimation of the true design-related BOLD signal (Lindquist et al. 2009). Finally, statistics can be performed via parametric or nonparametric methods resulting in statistical maps indicating areas of activation surviving a preset statistical threshold. These maps are first created on single-subject level (first-level analysis) after which they are used in second-level analysis to perform group statistics. Besides maps indicating activated regions, alternative processing techniques are available, e.g., dynamic causal modeling (DCM) which models interactions between activated regions to infer effective connectivity (Friston et al. 2003).

Various human fMRI studies demonstrated altered neuronal activity caused by pathological conditions and/or associated with learning and memory processes. In early blind subjects, for example, fMRI studies have been very valuable in the study of crossmodal plasticity by visualizing neuronal activity in the visually deprived cortex in response to a wide variety of nonvisual sensory inputs (e.g., Ptito et al. (2012)). Translational fMRI studies in animal models are of inestimable value to further elucidate the mechanisms controlling (the degree of) such neuronal plasticity and their temporal profile (Van der Linden et al. 2009b; Pelled 2011).

Cortical reorganization after injury or disease can be reflected in changes in localization and magnitude of task-induced fMRI responses. Using fMRI in rodents, neuroplastic coping or recovery mechanisms were observed in models with lesions in the central and peripheral nervous system (Li et al. 2013; Pelled et al. 2007; Pawela et al. 2010; Yu et al. 2010; Endo et al. 2007). Indeed, after complete transection of the mid-thoracic spinal cord in rats, Endo et al. showed an enlarged region of activation partly invading the adjacent sensory-deprived hind limb cortical territory when stimulating the non-affected forelimb (Endo et al. 2007). At present (experimental) stroke is one of the most popular models to study altered cortical activation using fMRI (Dijkhuizen et al. 2012; Pelled et al. 2002). Using contrast-enhanced CBV-weighted fMRI, Dijkhuizen et al. (2003) demonstrated an increased contralesional activation in the sensorimotor cortex early post-stroke which evolved into a partial recovery of ipsilesional and diminished contralesional activation patterns in the chronic phase (Dijkhuizen et al. 2003). This study indicates that activation patterns can also inform on lateralization of brain function. Alongside surgical interventions, maladaptive plasticity has also been assessed in models of drug addiction (fMRI and/or phMRI).

In the healthy brain, fMRI can be used to study the effect of experience on shaping brain functional organization and activity. Researchers at Columbia University demonstrated in human subjects that fMRI activation patterns within the hippocampal formation changed over the course of an associative memory task (Small et al. 2001). Subsequently, they proved the contribution of

CA3 hippocampal neurons to the observed experience-dependent shift in brain activation by repeating the fMRI experiment in CA3 NMDA receptor knockout mice using an adapted sensory task, i.e., olfactory stimulation (Kent et al. 2007).

The mechanisms behind experience-dependent plasticity have been explored with fMRI by mapping functional network reorganization acutely after artificial induction of LTP in the hippocampus of adult rats. This study provided the first evidence of LTP-mediated global changes in brain activity and the feasibility of detecting rapid LTP-induced changes by in vivo BOLD fMRI (Alvarez-Salvado et al. 2014, Canals et al. 2009) (Fig. 29.2). In awake rabbits, fMRI was used to map changes in cerebellar

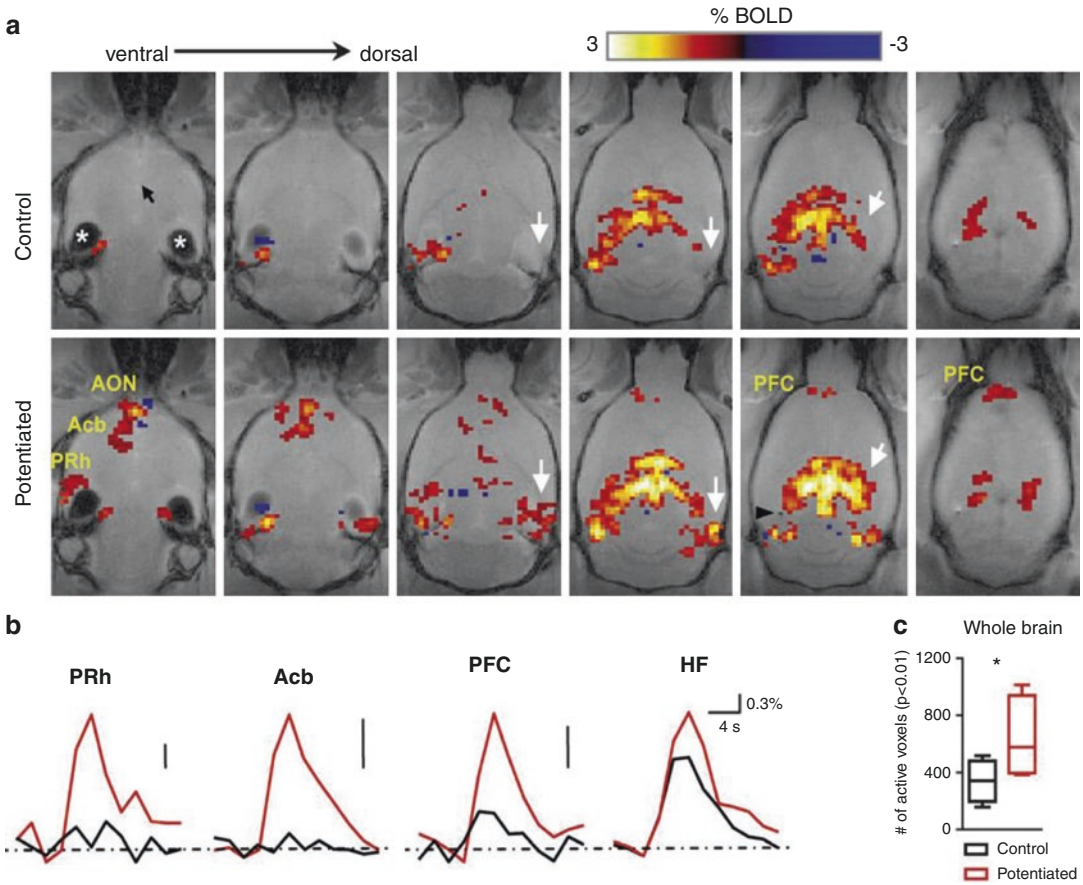

Fig. 29.2 Visualization of long-term potentiation (LTP) induced network reorganization using fMRI. LTP was induced in urethane-anesthetized rats with a protocol of high-frequency stimulation (HFS) of the perforant path, the main cortical input of the hippocampal formation (HF). (**a**) Functional maps thresholded and overlaid on anatomical scans, showing brain areas active during perforant path stimulation before (control) and after LTP induction (potentiation). The *black arrowhead* indicates the position of the tip of the stimulation electrode. LTP of hippocampal synapses resulted in increased responses in the hippocampus itself including areas contralateral to the stimulated perforant path (*white arrows*) illustrating increased interhemispheric communication. In addition, fMRI revealed recruitment of new structures including the nucleus accumbens (Acb), the anterior olfactory nucleus (AON), and the perirhinal (PRh) and prefrontal cortex (PFC). The *black arrow* points to the anterior commissure, and *asterisks* mark image artifacts due to the ear channel. The color-coded scale represents positive and negative BOLD response in percent change from baseline. Potentiation of the responses is further illustrated by (**b**) changes in the BOLD signal time courses at different ROIs and (**c**) the number of significantly ($p<0.01$) active voxels, indicating the volume of activated brain, before (*black*) and after (*red*) LTP induction. *$p<0.05$, paired t-test (Reprinted from Canals et al. (2009) with permission from Elsevier)

activity during an associative learning eyeblink paradigm. Evolution was seen in the laterality, location, and time course of the response within the cerebellum, demonstrating the latter's involvement in eyeblink conditioning (Miller et al. 2003).

So far, most small animal fMRI studies are performed in adult animals. As a starting point for future fMRI studies in rodent ontogeny, age-related changes in the hemodynamic response itself were studied by using parallel fMRI and electrophysiological techniques with somatosensory stimulation in the rat between postnatal day 13 and adulthood. The results of this study showed a systematic decrease in latency and increase in amplitude of the BOLD signal over the studied time period and can be used as prerequisite in the interpretation of BOLD imaging data acquired in ontogeny (Colonnese et al. 2008).

As mentioned before, songbirds are an excellent model to study plasticity induced by hormonal influences, vocal learning processes, and even memory (Van der Linden et al. 2009). The review by Van Ruijssevelt et al. (Van Ruijssevelt et al. 2013) discusses the implementation of auditory fMRI in zebra finches along with the encountered technical challenges and applications so far (Van Ruijssevelt et al. 2013). Songbirds can be used to investigate brain activation patterns in response to simple and complex learned acoustic communication signals (De Groof et al. 2013a; Boumans et al. 2008; van der Kant et al. 2013; Poirier et al. 2009). In the paper by De Groof et al. (2013a), the technique was used to demonstrate hormone-induced (seasonal) changes in the fMRI activation patterns in response to songs with different social relevance even without changing the spectro-temporal properties of the songs (De Groof et al. 2013a) (Fig. 29.3).

29.4.1.2 Resting State fMRI

Brain activity continues even beyond participation to explicit tasks; as a result, activity-independent or spontaneous fluctuations of the BOLD signal can be observed when the subject is at rest. Since brain regions with comparable fluctuation patterns are thought to be functionally connected (Lowe et al. 2000), these spontaneous low-frequency fluctuations of the BOLD signal (LFFs; typically ranging from 0.01 to 0.10 Hz) are used to investigate the functional architecture of the brain. Dedicated resting state fMRI sequences – most often gradient echo EPI – benefit from a higher temporal resolution and shorter scan times as compared to stimulus-induced fMRI. In recent years, rsfMRI has become a sensitive marker to study changes in brain circuitry beyond direct structural connections that are usually evaluated with anatomical techniques. For a more rigorous and detailed explanation of this method, we wish to refer to the many excellent textbooks and review articles available, e.g., van den Heuvel and Hulshoff Pol (2010); Kelly et al. (2012).

When performed in small animals, the subjects are usually anesthetized during acquisition with varying effects of the used compound on functional connectivity (Williams et al. 2010; Jonckers et al. 2014; Peltier et al. 2005). Therefore, similar to stimulus-induced fMRI, caution should be taken when choosing the type of anesthetic for a particular study. Alternatively, the technique can also be performed in awake animals after habituation training (Jonckers et al. 2014; Liang et al. 2011).

Preprocessing of resting state fMRI time series may include motion correction, slice-timing correction, global signal regression, spatial normalization, temporal filtering, and spatial smoothing. The benefit of using these preprocessing steps remains, however, a controversial topic (Weissenbacher et al. 2009; Gavrilescu et al. 2008; Chang and Glover 2009). For the post-processing of rsfMRI data, various software packages exist supporting different processing strategies (van den Heuvel and Hulshoff Pol 2010; Margulies et al. 2010). The most widely used methods in the analysis of resting state data to infer functional connectivity are ROI-based (Biswal et al. 1995), seed-based analyses, and model-free, data-driven approaches such as independent component analysis (ICA) (Calhoun et al. 2001; Beckmann et al. 2005). Besides ICA, other model-free methods include: hierarchical, partitional, and spectral clustering approaches and graph analysis (for methodological reviews, see

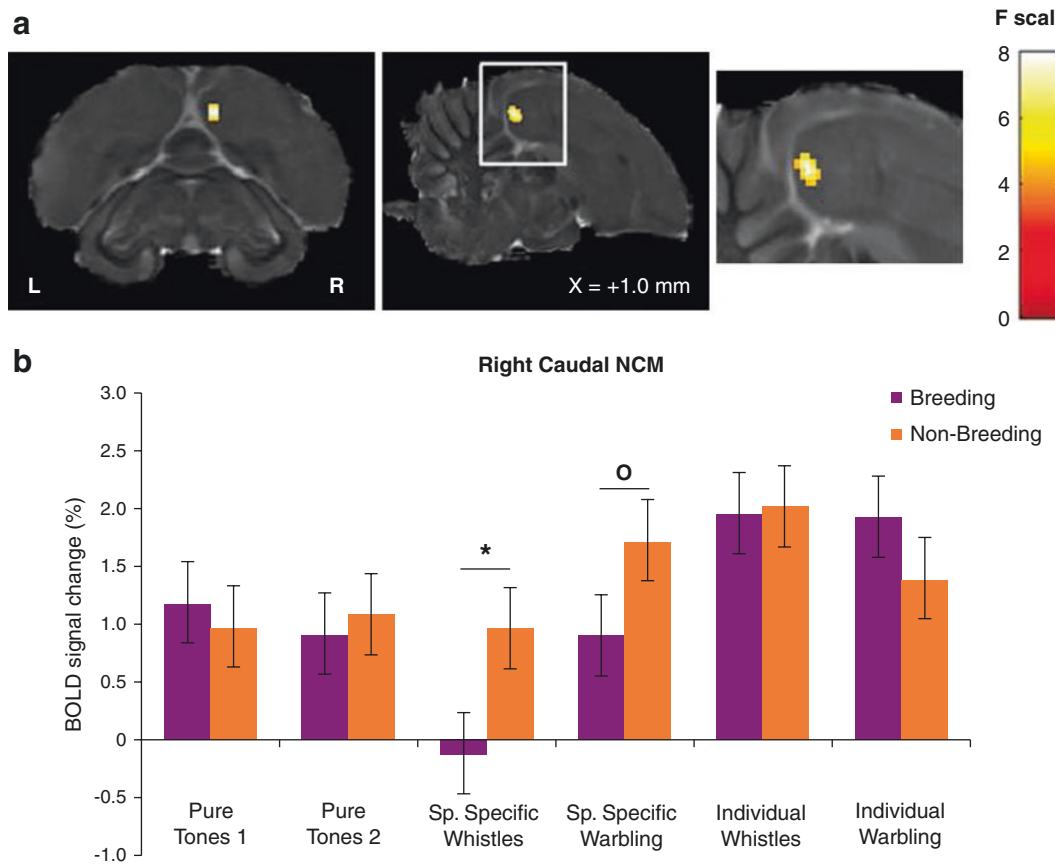

Fig. 29.3 The effect of season on differential song processing. (**a**) Statistical map of voxels displaying a significant seasonal difference in differential song processing i.e. a stronger response to songs used for individual recognition (INDIV) compared to songs used for species-specific recognition and sharing within the group (SPEC) between breeding and nonbreeding season ([INDIV vs. SPEC] breeding vs. [INDIV vs. SPEC] nonbreeding); *F*-test from repeated measures ANOVA; $N=5$). *F*-values are color coded according to the scale displayed on the *right*. The position of the slice along the *X* (*left/right*)-axis is indicated (the + sign indicates that results are from the right hemisphere). (**b**) Estimates of the relative (vs. rest) response amplitude (+ SEM) of neural activations elicited by the different song stimuli in the cluster illustrated in (**a**) (values from the voxel with the maximum *F*-value). The zero level corresponds to the estimated mean activation during rest periods. The *circle* indicates that the difference between seasons shows a trend ($^{\circ}p<0.1$), and the *star* indicates statistically significant difference between seasons ($*p<0.05$) (Reprinted from De Groof et al. (2013a) with permission from Frontiers)

van den Heuvel and Hulshoff Pol (2010), Margulies et al. (2010)). Over the last years, graph analysis has gained substantial interest as rsfMRI data analysis approach (especially in combination with MRI contrasts sensitive to structural connectivity such as diffusion tensor imaging (Bullmore and Sporns 2009)). Finally, by applying Granger causality analysis, rsfMRI data can be used to approach effective connectivity in which the directionality of the connectivity between regions is considered (Roebroeck et al. 2005).

Functional connectivity assessed using rsfMRI is believed to reflect the basic and intrinsic organization of the resting brain. In humans and to some extent also in rodents, large-scale "resting state networks" can be detected including brain regions involved in, e.g., auditory processing, motor function, visual processing, memory, executive functioning (Damoiseaux et al. 2006; Jonckers et al. 2011), and the so-called default mode network which is active during rest and deactivated during goal-directed

behavior (Lu et al. 2012; Fransson 2005). These large-scale networks can be further divided in subregions reflecting network topology. By examining alterations in functional connectivity within or between these networks, rsfMRI is a powerful tool to study aspects of plasticity involving cortical reorganization, global network rearrangements, and changes in region-to-region functional connectivity. As such, rsfMRI has emerged as a useful tool to study large-scale brain network maturation in infants and young children (Uddin et al. 2010). The utility of the technique for the assessment of maladaptive neuroplasticity in neurodegenerative disease is illustrated in a study investigating a transgenic mouse model for Alzheimer's disease in which increased functional connectivity was revealed between CA1 and cortical areas after environmental enrichment (Little et al. 2012) which might be linked to previously demonstrated increased hippocampal neurogenesis in similar circumstances (Herring et al. 2009). Furthermore, in a rat model of stroke, behavioral recovery of sensorimotor function was correlated to a re-establishment of resting state interhemispheric functional connectivity in the same animals (van Meer et al. 2010). Interhemispheric neuroplasticity was also studied following peripheral nerve injury in rats (Pawela et al. 2010) and following transcranial direct current stimulation in humans where increased interhemispheric connectivity is believed to be associated with the beneficial effects of the stimulation on cognitive functions such as working memory and planning ability (Park et al. 2013).

Review

- Di Salle F, et al. Exploring brain function with magnetic resonance imaging. Eur J Radiol. 1999;30(2):84–94.
- Logothetis NK. What we can do and what we cannot do with fMRI. Nature. 2008;453(7197):869–78.
- Amaro E Jr, Barker GJ. Study design in fMRI: basic principles. Brain Cogn. 2006;60(3):220–32.
- Van der Linden A, et al. MRI in small brains displaying extensive plasticity. Trends Neurosci. 2009;32(5):257–66.
- van den Heuvel MP, Hulshoff Pol HE. Exploring the brain network: a review on resting-state fMRI functional connectivity. Eur Neuropsychopharmacol. 2010;20(8):519–34.
- Margulies DS, et al. Resting developments: a review of fMRI post-processing methodologies for spontaneous brain activity. MAGMA. 2010;23(5–6):289–307.

29.4.2 Structural MRI

The most well-established relationship between functional and structural brain changes is found in the physiological mechanism underlying learning and memory, i.e., the effects of LTP on synapse formation (Butz et al. 2009; Muller et al. 2002). The following paragraphs will discuss different MRI contrasts designed to evaluate brain volume and shape, intrinsic tissue properties and microarchitecture, overall structural connectivity, and neuronal migration.

29.4.2.1 Quantitative Anatomy

Volumetry and Morphometry

Conventional T_1-, T_2-, and proton density-weighted images provide qualitative information on overall (brain) anatomy, realizing a clear structural segmentation between gray and white matter and facilitating the localization of abnormalities, e.g., tumors or traumata. In case of sufficient image resolution, volumetric (volume, size) and morphometric (shape) analyses can be performed by very simple delineation of brain ROIs. In addition to manual delineation, several automated segmentation procedures exist which are perfectly suited for volumetric and morphometric analyses (Galinsky and Frank 2014; Focke et al. 2014). The latter include three main approaches: (1) deformation-based morphometry, focused on finding differences in relative position of structures within the brain (Chung et al. 2001); (2) tensor-based morphometry,

concentrated on local shape changes of distinct brain regions (Freeborough and Fox 1998); and (3) voxel-based morphometry (VBM) which infers group differences in gray and white matter concentration after discounting for individual differences in overall anatomy and position (Ashburner and Friston 2000; Whitwell 2009). VBM is the most commonly used method. A subset of different preprocessing steps needs to be fulfilled before a statistical map indicating structural differences is obtained. In brief, all structural images need to be segmented (in gray matter, white matter and CSF) and spatially normalized to a common stereotactic frame (i.e., template or atlas) after which the resulting images are smoothed (a clear overview of the different preprocessing steps can be found in (Whitwell 2009; Mechelli and et al. 2005)).

One of the first applications of VBM in a research setting was a study by Maguire et al. who revealed a size difference in the posterior hippocampus of London taxi drivers compared to age-matched controls suggesting that the posterior part of the hippocampus is involved in spatial navigation and memory (Maguire et al. 2000). The first VBM studies showed the power of using a voxel-based approach and inspired many other researchers to apply this technique to reveal anatomic changes induced by, e.g., motor learning such as juggling in healthy subjects (Sampaio-Baptista et al. 2014; Boyke et al. 2008), structural changes resulting from daily music listening to facilitate recovery after stroke (Särkämö et al. 2014), as well as volumetric and morphometric alterations of brains suffering from, e.g., Alzheimer's disease (Li et al. 2012; Busatto et al. 2008). Also in animal research, where it is often more difficult to "mathematically" discriminate between gray and white matter, VBM revealed an increased hippocampal volume after a prolonged period of voluntary wheel running in mice (Biedermann et al. 2012) (Fig. 29.4) and widespread gray matter volume changes after 7 days of voluntary wheel running in rats (Sumiyoshi et al. 2014). In addition, VBM was successfully implemented in several species to assess the neuroanatomical characteristics of healthy aging in, e.g., dogs (Tapp et al. 2006) and primates (Sawiak et al. 2014). Hopkins and coworkers identified gray matter asymmetries in the chimpanzee cortex using VBM (Hopkins et al. 2008). Alternatively, deformation-based morphometry has been applied in high-resolution ex vivo three-dimensional datasets to examine rapid structural neuroplastic adaptations elicited by different maze training protocols (Lerch et al. 2011), to uncover the structural correlate of memory loss in Alzheimer mice (Lau et al. 2008), and to assess early structural shape differences in the striatum of Huntington mice compared to wild types (Lerch et al. 2008).

One should bear in mind that when studying developing or injured brains, the overall brain architecture and intrinsic tissue properties undergo massive changes either due to maturation or recovery which directly affect T_1- and T_2-relaxation properties (Paus et al. 2001; Dubois et al. 2014). Changing T_1 and T_2 properties implies that the ideal TR and TE evolve over ontogeny, which indicates that if a constant combination of TR and TE is applied over the entire development, this might lead to suboptimal image contrast thus interfering with accurate delineation of brain ROIs. Moreover, certain neuroplastic events might involve very subtle alterations in volume or shape that can easily be missed when merely considering volumes or shapes of tissue. Interestingly, since the longitudinal and transverse relaxation rates are intricately linked to tissue microstructure and biochemistry, quantitative analysis of the T_1- and T_2- relaxation times provides a wealth of information on neuroplastic changes associated with brain maturation, disease, etc.

Quantitative Relaxometry

Slight adaptation of the basic T_1- and T_2-weighted inversion recovery and spin-echo pulse sequences allows quantitative assessment of T_1- and T_2-relaxation times which are intrinsically linked to ultrastructural tissue characteristics in terms of local tissue density, concentration of paramagnetic atoms, protein and lipid constitution, and abundance of macromolecules (Deoni 2010). Quantitative T_1 and T_2 mapping is often referred to as "quantitative relaxometry" and is commonly

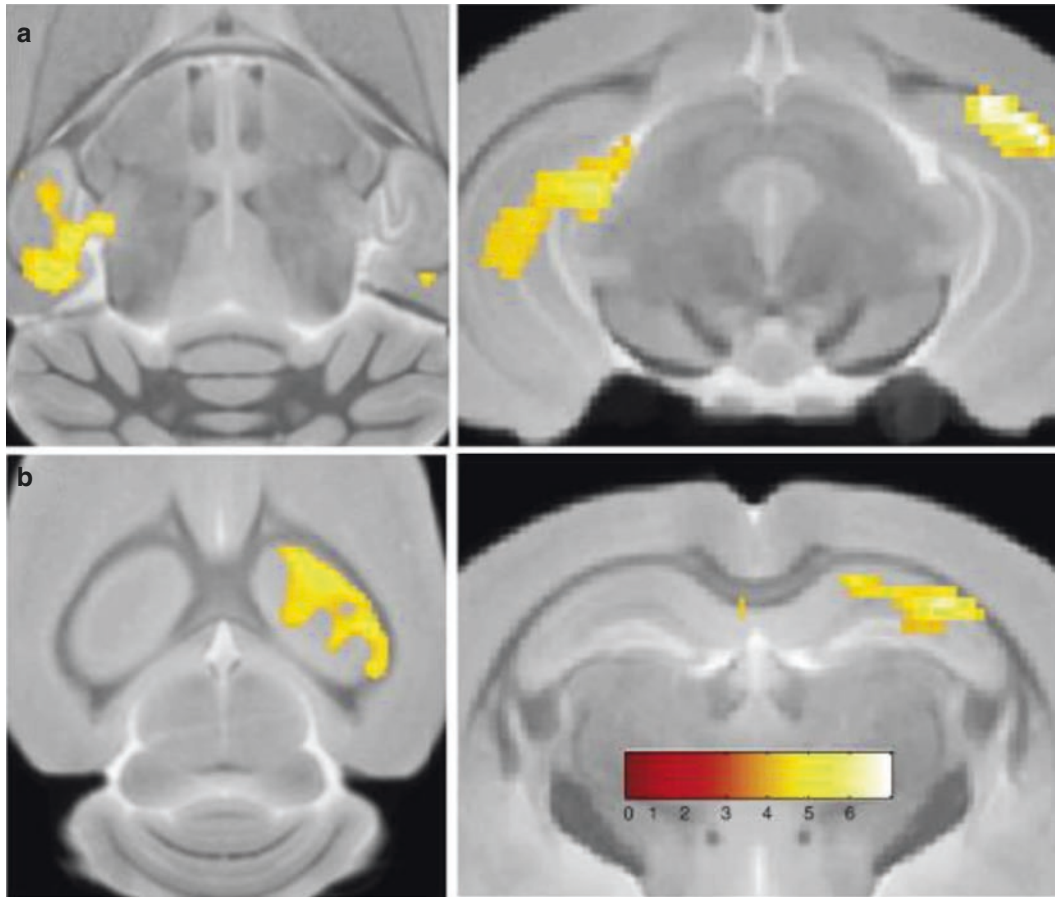

Fig. 29.4 Visualization of the outcome of voxel-based morphometry statistics comparing a group of voluntary running and sedentary mice. (**a**, **b**) are color-coded statistical maps indicating all voxels where the exercise group showed significantly higher gray matter volumes compared to the control group. Both clusters can be colocalized with either the left or the right hippocampus. The results are overlaid to a T_2-weighted template image ($p < 0.001$ uncorrected, 200 voxels cluster size) (Reprinted from Biedermann et al. (2012) with permission from Elsevier)

used to follow up early brain development and aging as well as disease-related tissue alterations involving myelination and/or demyelination, inflammation-edema, necrosis, iron accumulation, axonal growth, gyrification, etc. (for methodological review, see Deoni (2010)).

In order to determine the T_1- or T_2-relaxation time of a specific brain region of interest, the same dataset needs to be acquired several times where each acquisition is performed with a different TI or TE, respectively. Then, a voxel-wise exponential fitting of the obtained datasets is performed, where for each acquisition the signal intensities of a given voxel are set out to the proper TI or TE. Based on this exponential fit, a map is created where each voxel encodes the actual (absolute) relaxation time (T_1 or T_2). A more elaborate discussion of the acquisition and processing of T_1 and T_2 maps can be found in Deoni (2011), Dula et al. (2009), Crawley and Henkelman (1987), Shrager et al. (1998). Besides the advantage of assessing quantitative parameters which directly relate to specific tissue characteristics, relaxometry is independent of the MR system or hardware used, enabling to compare results obtained in different institutions.

Similar to the volumetric and morphometric analyses mentioned above, regions of interest can be delineated on the estimated T_1 and T_2 maps after which quantitative indices (T_1- or T_2-relaxation

time) can be extracted and statistically analyzed. In addition, also voxel-based approach has been introduced in this field (Pell et al. 2004). Instead of using the actual transformation parameters, e.g., the deformation fields, the voxel intensities of normalized datasets to which the deformation fields have been applied provide the necessary input for statistics. In other words, after successful spatial normalization, macroscopic shape and volume differences are discounted leaving only differences in voxel intensity – relaxation time – to be tested.

Several research groups have used quantitative relaxometry to follow up developmental brain changes in ontogeny in both healthy subjects and mice (Dubois et al. 2014; Kara et al. 2013; Ding et al. 2004). Kharatishvili and colleagues revealed that T_2-relaxation alterations could be linked to acute and long-term neurodegenerative changes resulting from epileptic seizures evoked by pilocarpine treatment (Kharatishvili et al. 2014) or TBI (Kharatishvili et al. 2009). Myelination characteristic to brain maturation during ontogeny is regarded as one of the major critical period delineators since it structurally inhibits neuroplasticity. Besides T_2 relaxometry, several other methods exist which extend information on different aspects of myelin content and organization within the brain. Recently, multicomponent relaxometry has been introduced (MacKay et al. 1994). This method is used to determine the myelin water fraction or the water trapped in between myelin sheets as in indirect measure of myelin content (MacKay et al. 2006). For a technical review on water-based myelin imaging tools, we refer to Alonso-Ortiz et al. (2015). Besides relaxometry, alternative methods are available to monitor white matter changes, e.g., magnetization transfer imaging (MTC) and diffusion tensor imaging (DTI).

Review

- Deoni SCL. Quantitative relaxometry of the brain. Top Magn Reson Imaging. 2010;21(2): 101–13.doi:10.1097/RMR.0b013e31821e56d8.
- Dula et al. Optimal echo spacing for multi-echo imaging measurements of bi-exponential T2 relaxation. J Magn Reson. 2009.
- Crawley and Henkelman. Errors in T2 estimation using multislice multiple-echo imaging. Magn Reson Med. 1987.
- Shrager et al. Optimal time spacings for T2 measurements: monoexponential and biexponential systems. NMR Biomed. 1998.

29.4.2.2 DTI

Diffusion tensor imaging (DTI) was introduced in the 1990s by the research group of Le Bihan (Basser et al. 1994). As compared to conventional MRI, DTI provides a noninvasive means for characterizing tissue microstructure and macroscopic fiber orientation in, e.g., muscle (Longwei 2012) and nervous tissue (Le Bihan et al. 2001), by measuring the random molecular Brownian motion (diffusion) of water molecules. The quantification of diffusion in tissues is achieved by supplementing a standard spin-echo pulse sequence with diffusion-encoding gradients (Stejskal and Tanner 1965). The phase difference induced by the translational motion of water molecules (during the two diffusion-encoding gradients) forms the basis of quantifying the diffusion properties of tissue (detailed description in Mori and Zhang (2006)).

By characterizing the overall three-dimensional diffusion profile of water molecules within a voxel, inferences can be made concerning the tissue microarchitecture situated within that voxel. For example, cerebrospinal fluid imposes few boundaries on the movement of water molecules resulting in a direction-independent or *isotropic* diffusion profile. In contrast, white matter contains myelinated axons and cell membranes which force water molecules to move along fibers as compared to traveling perpendicular to them; this is referred to as an *anisotropic* diffusion profile (Beaulieu 2002). Then the question remains how to "measure" the three-dimensional diffusion profile.

The simplest diffusion-weighting experiment consists of two acquisitions: firstly a regular dataset without diffusion weighting and secondly the same dataset with application of a diffusion gradient is acquired. This way an apparent diffusion coefficient (ADC) map can be calculated where

the intensity of each voxel is proportional to the extent of diffusion. ADC maps are a valuable tool in the clinic to detect brain areas affected by, e.g., acute stroke (Campbell and Macrae 2015). The combination of the strength, duration, and shape of the applied diffusion gradient defines the diffusion weighting and is represented by the "b value" (expressed in s/mm^2). ADC maps, however, only inform about the overall diffusion in a given voxel without deriving any information on specific character of interactions between tissue and water molecules or on the three-dimensional spatial diffusion profile. Moreover, the ADC contrast and thus diffusion measurement per se are highly dependent on the direction of the applied diffusion gradient: only water motion along the applied diffusion gradient axis can be detected. This observation leads to the notion that the three-dimensional diffusion profile of water molecules within one voxel can be characterized when at least six independent measurements are performed, each applying a diffusion gradient along a different noncoplanar direction (Basser et al. 1994). This is exactly what is aimed for in DTI (for detailed information, see Jones (2010), Mori and Tournier (2013)).

Starting from the raw diffusion-weighted data, several quantitative indices can be extracted which inform on the estimated diffusion profile of water molecules within one voxel, i.e., the three diffusion tensor eigenvalues (λ_1, λ_2, λ_3), mean diffusivity (MD), and fractional anisotropy (FA; for detailed overview of DTI (pre)processing pipeline, see Soares et al. (2013)). These parameters are computed for each voxel in the dataset, which results in different maps, each containing information on a specific DTI parameter. In general, a diffusion gradient sampling scheme including at least 30 unique and evenly distributed diffusion gradient orientations is needed to robustly estimate FA, MD, and the tensor orientation represented by the eigenvalues (Jones 2004). Again several basic processing techniques can be applied, i.e., histogram analysis, extraction of quantitative DTI parameters from manual or automatic delineation of ROIs, or comparing DTI-parameter maps between groups on a voxel-based level (for technical comparison between two most often used voxel-based DTI processing tools, see Abe et al. (2010)). The latter two techniques, ROI- and voxel-based analyses, are in line with the previously described principles. Histogram distributional analysis on the other hand informs on global diffusion alterations enabling to detect subtle changes that affect the entire brain (after removal of CSF signal). An elaborate discussion on the different processing strategies in a group-versus-group study design can be found in Chapter 29 of Jones (2010). In addition to these basic processing techniques, also more advanced methods exist, e.g., tractography (Chung et al. 2011) and graph theory-based connectivity mapping (especially interesting when performed together with functional MRI (Bullmore and Sporns 2009)). For these more advanced applications such as fiber tractography, it is recommended to acquire as many diffusion gradient directions (high angular resolution) as possible within the experimental time frame (Jones 2004; Mangin et al. 2013). The estimation of more complex spatial diffusion profiles can be realized by alternative methods, e.g., HARDI (high angular diffusion imaging (Tuch et al. 2002)), Q-ball imaging (Tuch 2004), etc. The latter method is expected to resolve subvoxel geometries such as multiple intra-voxel fiber orientations such as crossing, bending, twisting, or fanning fibers.

A low signal-to-noise ratio (SNR) – due to diffusion weighting – and a long acquisition time are inherent to DTI. The first can be overcome by increasing the number of diffusion gradient directions within a given experiment, which then again results in a longer acquisition time. SNR should be closely evaluated since low SNR can cause underestimation of the diffusion anisotropy of the effective diffusion tensor (Jones and Basser 2004). The latter can partly be overcome by utilization of state-of-the art rapid imaging techniques such as EPI (echo planar imaging) and parallel imaging. Although EPI markedly reduces the total acquisition time (100–150 ms/image), this sequence induces severe image distortion which markedly aggravates with higher magnetic field strengths. This imposes several practical challenges for in vivo small animal research. In

addition, EPI sequences can only achieve a limited spatial resolution, which is often confined to 0.2 mm slice thickness for in vivo preclinical imaging and is extremely prone to movement artifacts evoked by, e.g., breathing. Similar to quantitative relaxometry, DTI is highly sensitive but unfortunately notoriously unspecific to a wide range of biological phenomena making that the biological interpretation of the obtained results is not always straightforward (Mori and Zhang 2006; Jones et al. 2013), especially since different microscopic tissue properties might result in a similar parameter readout. Consequently, in order to establish a profound knowledge of the underlying neuroplastic events, additional measures need to be undertaken.

DTI has been thoroughly explored in the field of small animal MRI. Concha 2014 provides an extensive overview of how diffusion MRI data can inform on biological tissue remodeling and white matter pathologies both in clinical and research environments (Concha 2014). Ample evidence of structural remodeling in response to motor and spatial maze learning has been published as well (Sampaio-Baptista et al. 2014; Sagi et al. 2012; Hofstetter et al. 2013; Blumenfeld-Katzir et al. 2011). Disregarding the often long acquisition times needed for acquiring high-resolution DTI datasets, several groups report on using in vivo DTI to study early ontogeny. Olaverria and colleagues propose to use DTI as a tool to predict the critical period for the visual system in different species by targeting callosal and cortical projections related to the visual system in young animals (Jaime et al. 2012). In line with this statement, Chan and coworkers investigated the effects of early visual impairment on retinal and callosal projections in rats by using DTI in combination with MEMRI. They showed that the anterior and posterior retinal projection projecting from the deprived (enucleated) eye possessed a significantly lower FA, whereas the non-deprived eye was characterized with a higher FA as compared to controls (Chan et al. 2012). Another study by Cai and colleagues reported on acquiring high-resolution DTI data in rat pups at the fifth postnatal day. By inducing a state of mild-to-moderate hypothermia, they succeeded in lowering physiological motion-related artifacts. Their main research interest was focused on investigating the (micro)structural effects of cocaine exposure to dams on their offspring (Cai et al. 2011). However, since the water diffusion constant is highly dependent on the temperature (Einstein 1905), changes or fluctuations in body temperature strongly affect diffusion per se and thus will change the DTI outcome (diffusion MRI thermometry (Le Bihan et al. 1989)). This stresses the need to strictly control the animals' body temperature during acquisition.

Besides its use in mammalian species, DTI has proven to be the perfect tool to noninvasively assess morphological and cellular changes of the songbird brain in different conditions both relating to the photoperiod (season) and to specific endocrine status (reviewed by De Groof and Van der Linden (2010)). In brief, De Groof and coworkers succeeded in detecting seasonal changes in connectivity between distinct parts of the neural circuitry in control of singing behavior (De Groof et al. 2008) (Fig. 29.5); moreover, they were the first to describe seasonal plasticity in the optic chiasm, interhemispheric connectivity, and the avian analogue of the social behavioral network directing aggressive and courtship behavior (De Groof et al. 2009).

Review

- Jones DK. Diffusion MRI: theory, methods, and applications. Oxford University Press: USA; 2010.
- Mori S, Tournier J. Introduction to diffusion tensor imaging 2e: and higher order models. Elsevier Science & Technology Books;2013.
- Jones DK, Knösche TR, Turner R. White matter integrity, fiber count, and other fallacies: the do's and don'ts of diffusion MRI. NeuroImage. (0).
- Mori S, Zhang J. Principles of diffusion tensor imaging and its applications to basic neuroscience research. Neuron. 2006;51(5):527–39.
- Soares J, et al. A hitchhiker's guide to diffusion tensor imaging. Front Neurosci. 2013; 7.
- Concha L. A macroscopic view of microstructure: using diffusion-weighted images to infer

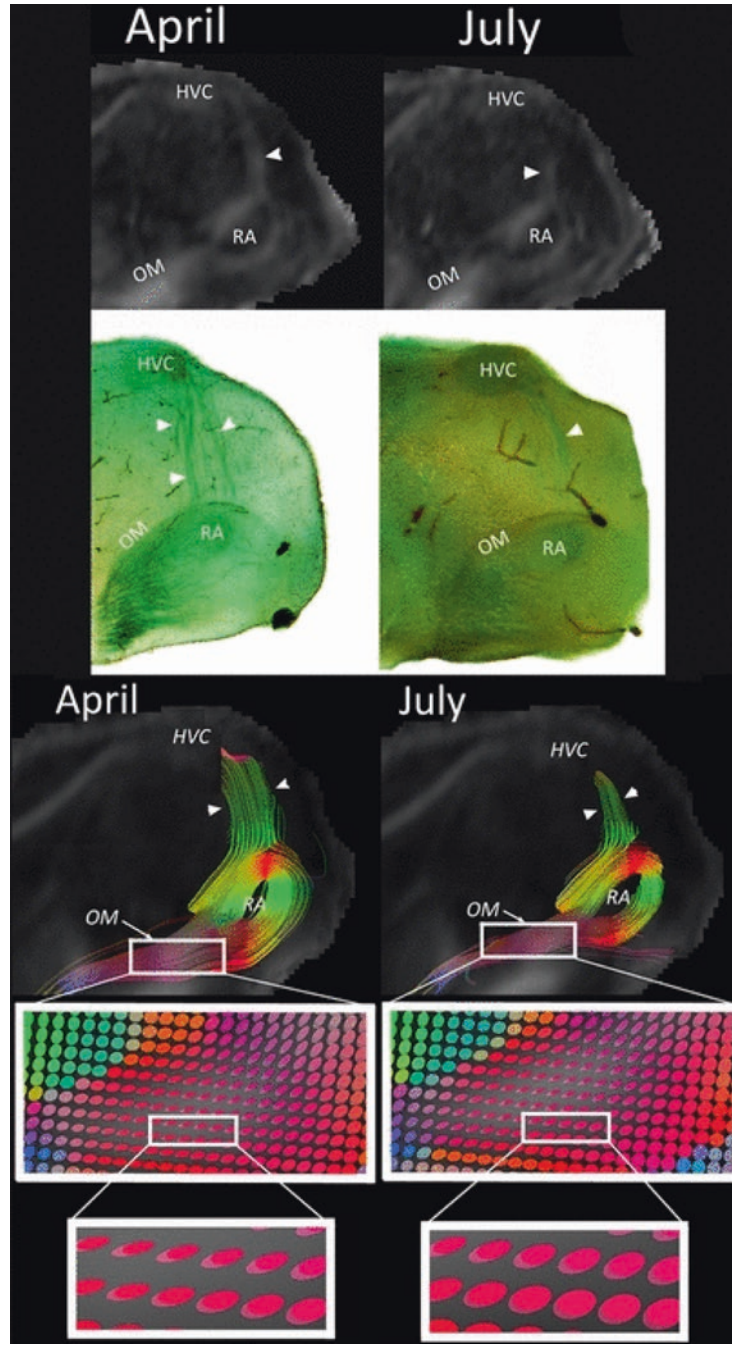

Fig. 29.5 Seasonal reinforcement of the pathway directly responsible for the motoric aspect of song production in adult male starlings. The *top row* displays two sagittal FA maps (left rostral, right caudal) of the same starling in spring (*left*) and summer (*right*). The tract connecting two nuclei of the song control system (HVC and RA) is indicated by an *arrowhead*. The *second row* presents two histological tissue sections stained with Luxol (myelin), at the same anatomical location as the first row. The *third row* contains fiber tracking results with a seed point near nucleus RA. The inserts below present voxel-wise glyphs (schematic representation of the diffusion tensor) of the OM tract connecting the HVC-RA tract to the downstream vocal organ. The main finding of this study was that the connectivity between both nuclei strongly changed over the season, indicated by in vivo DTI and confirmed by postmortem histology (Reprinted from De Groof et al. (2008) with permission from John Wiley and Sons)

damage, repair, and plasticity of white matter. Neuroscience. (0).
- Abe O, et al. Voxel-based analysis of the diffusion tensor. Neuroradiology. 2010;52(8): 699–710.

29.4.2.3 Contrast-Enhanced MRI

The intrinsic MR contrast attributable to differences in relaxation properties of water molecules in the tissues is not always sufficient to accurately differentiate brain architecture; moreover, the

MR signal is not always sensitive enough to pick up specific biological phenomena including activity-dependent neural connectivity, neurogenesis, and cell migration. This highlights the need for exogenous specific contrast-enhancing agents.

In general two main groups of MR contrast agents can be distinguished. The first group of compounds directly reduce the T_1 relaxation of the tissue where they accumulate, resulting in hyperintense (bright) signal on T_1-weighted images (positive MRI contrast, e.g., gadolinium or manganese). The latter contrast agents induce local magnetic field inhomogeneities which actively shorten T_2-/T_2*-relaxation time of protons in close vicinity of the administered contrast agent. This results in a faster signal decay visible as hypointense (dark) signal on conventional images (negative MRI contrast, e.g., iron oxide particles). A more elaborate discussion of MR contrast agents can be found in Sect. 13.2 MR Contrast Agents of this book; in the following sections, specific applications of manganese-enhanced MRI (MEMRI) and iron oxide particles will be discussed in detail.

MEMRI

Pautler and colleagues (1998) were the first to successfully visualize murine olfactory and visual pathways by using in vivo manganese-enhanced MRI (MEMRI) (Pautler et al. 1998). Manganese (Mn^{2+}) is an essential trace metal element (Erikson et al. 2005) vital for controlling a number of different cellular reactions (Erikson and Aschner 2003). In the brain, it primarily functions as a cofactor for various enzymes (Santamaria 2008). Consequently, Mn^{2+} deficiency or toxicity can lead to various pathological phenotypes (Erikson et al. 2005; Avelino et al. 2014; Dobson et al. 2004). Interestingly, besides its many biological functions, Mn^{2+} also acts as a Ca^{2+} analogue. As a result, Mn^{2+} can be transported across the blood-brain barrier (BBB), into excitable cells such as neurons and cardiac cells, upon activation of several types of Ca^{2+} channels (Roth et al. 2013; Gavin et al. 1990). In addition to these passive and active transporters, Mn^{2+} is also able to enter the CNS through leaky vasculature at the circumventricular organs and the choroid plexus (Aschner 2006) and via the olfactory and retinal receptor neurons as well (Chan et al. 2012; Tjälve et al. 1996). Once inside glial cells and neurons, Mn^{2+} can follow axons by anterograde microtubule-dependent transport (Sloot and Gramsbergen 1994) and is able to cross synapses to neighboring neurons (Takeda et al. 1998).

Another remarkable physical feature of Mn^{2+} is that it is paramagnetic. Consequently, Mn^{2+} evokes a positive contrast on T_1-weighted (and T_2*-weighted) images by markedly reducing the T_1 relaxation of water molecules in the adjacent tissue (where it accumulates). The combination of both physical and biochemical properties makes Mn^{2+} an exceptionally suited MRI contrast agent (1) to study brain anatomy using the tissue-specific distribution of Mn^{2+} (similar to other contrast agents such as gadolinium), (2) to highlight brain regions activated upon certain task (activity-induced MEMRI or AIM-MRI), and (3) to assess neuronal connectivity (tract tracing (Pautler et al. 1998)). The latter two characteristics rely on an activity-dependent accumulation of Mn^{2+} in cells (through voltage-gated Ca^{2+} channels). This implies that the signal intensity is a direct readout for neural activity, as opposed to fMRI which is an indirect measure for brain activation since it relies on the detection of the hemodynamic response of the brains' vasculature to a given stimulus. In addition, Mn^{2+} ($MnCl_2$) can be administered peripherally after which the animal is exposed to a certain stimulus during wakefulness, without the need for anesthesia in contrast to most small animal BOLD fMRI (Bissig and Berkowitz 2009). The disadvantage of AIM-MRI as compared to fMRI is that Mn^{2+} does not easily cross the BBB in nonphysiological concentrations. Therefore, it is often administered in combination with a BBB-disrupting chemical such as mannitol. Interestingly, alternative routes of administration have been described when the auditory, visual, somatosensory, and olfactory systems were the topic of investigation (Pautler et al. 1998; Bissig and Berkowitz 2009; Yu et al. 2005). The second

main disadvantage of AIM-MEMRI is that only one stimulus can be assessed per imaging experiment. This is in contrast to fMRI where several different stimuli can be presented within the same imaging session. In addition, before applying a second stimulus, the brain needs to be cleared from the previously applied Mn^{2+}, which entails that the second measurement cannot take place earlier than 1 week after the first.

Anatomical MEMRI has been used to visualize brain regions which otherwise appear indiscernible from its surrounding tissue, e.g., distinct cortical layers in rats and mice (Silva et al. 2008) and individual glomeruli in the olfactory bulb of rats (Chuang et al. 2010). Anatomical MEMRI has also been applied to visualize tissue remodeling at the cellular level acutely post-status epilepticus in a rat model for temporal lobe epilepsy, where the difference in Mn^{2+} signal in the dentate gyrus and CA3 subfield of the hippocampus corresponded to sites displaying mossy fiber sprouting, confirmed by postmortem histology (Nairismägi et al. 2006) (Fig. 29.6). The obtained anatomical contrast can also be used for volumetric assessments. Golub and coworkers described a volumetric decline in the hippocampus and amygdala of mice suffering posttraumatic stress; moreover, they also observed trophic changes upon housing the traumatized mice in an enriched environment (Golub et al. 2011).

Interestingly, because of the ability of Mn^{2+} to travel transsynaptically to neighboring neurons, Mn^{2+} can be used to investigate cortical projection fields of sensory neurons. This has been shown in several sensory systems such as the auditory (tonotopic mapping in inferior colliculus in mice (Yu et al. 2005)), visual (retinotopic mapping in superior colliculus (Chan et al. 2011)), and olfactory network (connectivity between olfactory bulb and downstream brain areas (Gutman et al.

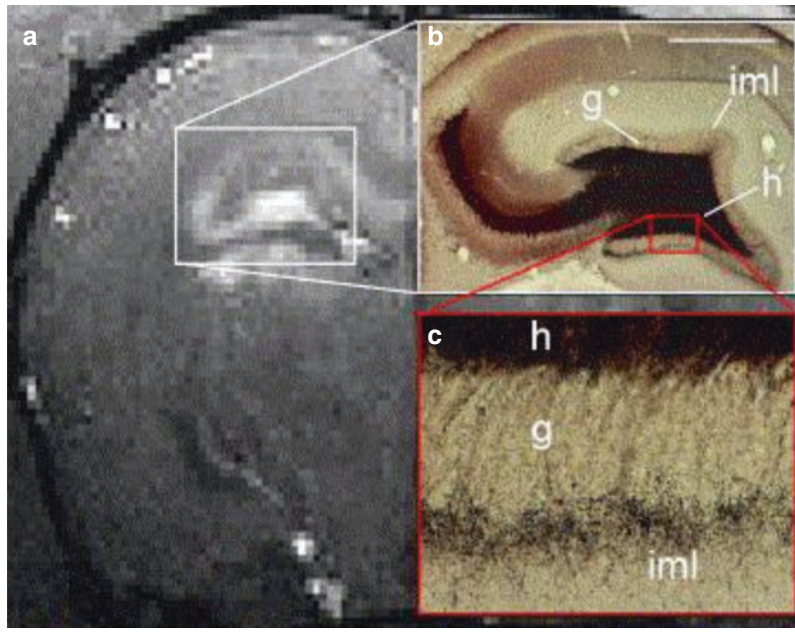

Fig. 29.6 The detection of acute mossy fiber sprouting evoked by *status epilepticus* in rats. T_1-weighted manganese-enhanced MRI (**a**) and Timm-stained histological sections of the corresponding brain area (**b** and inset **c**) clearly show that the hyperintensities found in vivo correspond to hippocampal brain areas displaying extensive mossy fiber sprouting. MRI datasets and sacrification for histology were performed at, respectively, 14 and 20 days post induction of status epilepticus. Abbreviations: *iml* molecular layer of the dentate gyrus, *h* dentate hilus, *g* granule cell layer. Scale bar *panel B* represents 1 mm (Reprinted from Nairismägi et al. (2006) with permission from Elsevier)

2013)). Also in vivo cortico-cortical and thalamo-cortical connectivity has been described in rodents (Tucciarone et al. 2009). They concluded that the timing of acquisition post injection is crucial to be able to observe the expected effect. A more elaborate discussion of in vivo tract-tracing experiments in mice, rats, and nonhuman primates can be found in Pautler (2004).

The same technique has been applied to visualize components of the brain circuitry in control of singing behavior in starlings and canaries (for review, see Van der Linden et al. (2004)). Unlike the mammalian brain, the gray matter of the avian forebrain is organized in dense nuclei rather than cortical layers. Using conventional imaging techniques, it is difficult to distinguish between distinct brain nuclei such as those delineating the song control system (Van der Linden et al. 1998). However, after stereotactic injection of $MnCl_2$ in nucleus HVC, a hyperintense signal was found in HVC but also in nucleus RA and Area X, two downstream song control system nuclei to which HVC sends afferent projections (Fig. 29.7). This was one of the first successful in vivo attempts at obtaining anatomical contrast of nucleus RA and Area X. Moreover, by exploiting the activity-dependent tract-tracing characteristics of Mn^{2+}, Van der Linden and colleagues found a functional dimorphism in the pathway connecting HVC and Area X (Van der Linden et al. 2002). Besides the investigation of sexual dimorphisms, songbirds provide a valuable model to study mechanisms underlying seasonal plasticity. Using AIM-MEMRI, a seasonally dependent olfactory sensitivity to a specific biologically relevant odor was found in adult male starlings (De Groof et al. 2010). A similar study has been performed in rats, where peripheral $MnCl_2$ administration, together with mannitol injection and (left) whisker stimulation, leads to the establishment of a statistical map showing all voxels where the signal intensity (Mn^{2+} uptake) differs significantly between the whisker-stimulated and non-stimulated group. The cluster could be colocalized with the right whisker-barrel cortex (Weng et al. 2007). In addition, also higher cognitive functions have been assessed using MEMRI, e.g., fear conditioning in mice (Chen et al. 2007).

Review

- Silva AC, et al. Manganese-enhanced magnetic resonance imaging (MEMRI): methodological and practical considerations. NMR Biomed. 2004;17(8):532–43.
- Massaad C, Pautler R. Manganese-enhanced magnetic resonance imaging (MEMRI). In: Modo M, Bulte JWM, editors. Magnetic resonance neuroimaging. Humana Press; 2011. p. 145–74.
- Inoue T, Majid T, Pautler Robia G. Manganese enhanced MRI (MEMRI): neurophysiological applications. Rev Neurosci. 2011:675.

Iron Oxide Particles

Since the late 1960s after the discovery that neurogenesis persists far into adulthood (Altman and Das 1965), hope was raised that endogenous stem or progenitor cells could be engaged as innate therapy treating various CNS pathologies (Gage et al. 1995; Eriksson et al. 1998; Bazarek and Peterson 2014; Felsenstein et al. 2014). Indeed, several neurodegenerative disorders and injury-induced brain pathologies are characterized by altered neurogenesis and migration patterns of newborn neurons (Villasana et al. 2014; Sierra et al. 2014). Recently, it has been shown that cell death in adult and adolescent rats can be prevented significantly when participating to specific effortful learning tasks, e.g., trace eyeblink associative training (Curlik et al. 2014). In the mammalian brain, adult neurogenesis takes place exclusively in two distinct brain niches, i.e., the subventricular zone near the lateral ventricles and the dentate gyrus of the hippocampus (Oboti and Peretto 2014; Ma et al. 2009; Fuchs et al. 2014).

Shortly after the discovery of adult neurogenesis, efforts were made to track neuronal migration upon neurogenesis longitudinally in vivo using relatively noninvasive imaging tools, e.g., PET (Rueger et al. 2010), bioluminescence, but also several MRI-based methods such as MRI reporter genes, MRS, and an array of different iron oxide particles (for review, see Couillard-Despres et al. (2011)). These in vivo imaging

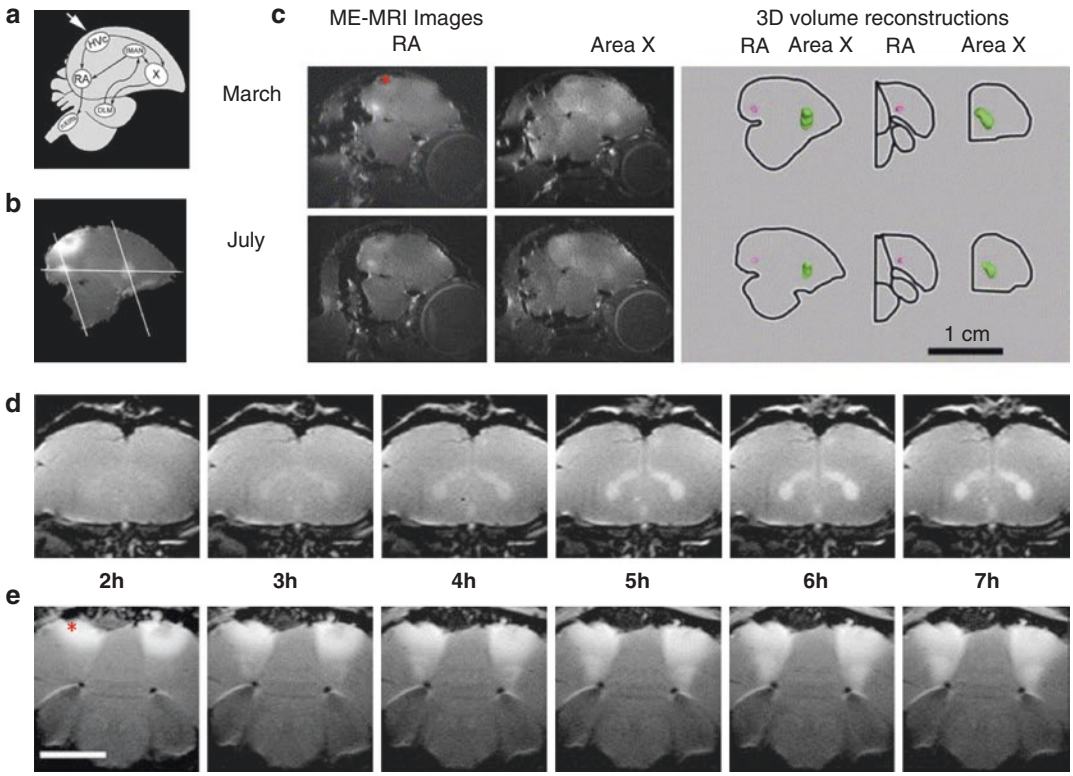

Fig. 29.7 MEMRI to explore song control system nuclei dynamics in a seasonal songbird. (**a**–**b**) Simplified schematic overview of the song control system in songbirds. (**c**) The *left panel* provides sagittal sections in which both the $MnCl_2$ injection site (HVC indicated by *) and the downstream nuclei (RA and Area X) can be found. The *left panels* provide a three-dimensional view of the volume difference picked up by MEMRI when comparing spring to summer. (**d**–**e**) Changes in signal intensity at 2, 3, 4, 5, 6 and 7 h post $MnCl_2$ injection in the brain of a female starling. Over time a hyperintense signal can be colocalized with Area X (*row* **d**) and nucleus RA (*row* **e**) (Reprinted from Van der Linden et al. (2002) and Van Meir et al. (2006) with permission from Elsevier)

tools are most often focused on labeling stem and/or progenitor cells originating from the subventricular zone and following them along the rostral migration stream toward the olfactory bulb. Neurons born in the dentate gyrus migrate to the subgranular zone of the hippocampus which is too close to accurately discriminate with, e.g., MRI or PET, even at high resolution. Indeed, Coquery et al. (2012) implanted rat bone marrow-derived mesenchymal stromal cells labeled with very small superparamagnetic iron oxide particles and used in vivo MRI to visualize the graft 1, 20, and 50 days after transplantation. The graft persisted in the same location. In addition, only a small signal reduction was seen over time which is in contrast to histological findings showing that a vast number of graft cells die during the first days posttransplantation. The authors refer to blooming or oversaturation effects explaining that even a small number of iron oxide particles can cause drastic hypointense signal changes (signal attenuation is dependent on iron content of the particles). Consequently, to quantitatively assess the number of surviving cells upon transplantation, one cannot solely rely on T_2*-weighted MRI (Coquery et al. 2012). Several research groups have been successful at applying iron oxide particles to visualize migration of neuroblast cells in vivo along the rostral migration stream (Vreys et al. 2010; Shapiro et al. 2006; Nieman et al. 2010) (Fig. 29.8). An in-depth study describing interactions between cells and MPIOs over time can be found in Roose et al. (2014).

Unfortunately, there are some disadvantages inherent to this technique. The contrast on the generated MR images only refers to the presence of iron oxide particles (passive contrast agent); it does not inform on the viability or identity of cells carrying the contrast agent. Since more than half of the newly differentiated neurons die before being integrated in their specific neuronal target (Winner et al. 2002), cell debris will be engulfed by cells of the immune system. This lack of specificity might lead to biologically irrelevant, nonspecific observations. In addition, in order for the cells to become labeled with particles, the particles need to be delivered in situ via an intracerebroventricular injection near the niches where neurogenesis takes place, where neural progenitor and/or stem cells will take up the particles via endocytosis, or, alternatively, after in vitro labeling of the progenitor and/or stem cells, the cell graft can be transplanted in situ in the brain.

Review

- Couillard-Despres S, et al. In vivo monitoring of adult neurogenesis in health and disease. Front Neurosci. 2011;5.
- Vande Velde G, et al. In situ labeling and imaging of endogenous neural stem cell proliferation and migration. Wiley Interdiscip Rev Nanomed Nanobiotechnol. 2012;4(6): 663–79.
- Roose D, et al. Multimodal imaging of micron-sized iron oxide particles following in vitro and in vivo uptake by stem cells: down to the nanometer scale. Contrast Media Mol Imaging. 2014: p. n/a-n/a.

29.4.3 Biochemical Basis of Neuroplastic Events

While structural and functional changes can be detected with MRI, MRS provides a wealth of information on various aspects of in vivo neurochemistry, including neuronal health, gliosis, osmoregulation, energy metabolism, neuronal-glial cycling, and molecular synthesis rates in the brain, which may be associated with neuroplasticity in early development, in relation to learning or post injury (Bartha et al. 2008; Choi et al. 2003; Jessen et al. 2001; Krishnan et al. 2003).

29.4.3.1 Basics of the MRS

The interaction of nuclei, such as ^{1}H, with its surrounding molecules induces metabolite-specific alterations in the magnetic field which affect the spin frequency of the atom. Consequently, this change in frequency, otherwise termed as "chemical shift" and expressed in parts per million (ppm, represented on the x-axis in the spectrum), is directly related to the biochemical environment of the nuclei which enables to deduce the metabolic content of the volume of interest (de Graaf (2007b)). MRS can be acquired on a variety of nuclei such as phosphorus (^{31}P), fluorine (^{19}F), carbon (^{13}C), and sodium (^{23}Na); however, most often ^{1}H MRS is used in (pre)clinical research because of its natural abundance and high sensitivity to magnetic manipulations (de Graaf 2007a; Frangou and Williams 1996; Webb et al. 1994). This is the main reason why we will focus on ^{1}H MRS in this chapter.

A detailed description on the practical aspects and theory behind MRS can be found in Sect. 13.4 of this book and in de Graaf (2007a), Bothwell and Griffin (2011), Pagani et al. (2008), Drost et al. (2002), and Poole et al. (2011). In brief, after shimming – to exclude for local inhomogeneities in the magnetic field – and water suppression (only in case of ^{1}H MRS), the spectra are acquired by applying a radio frequency (RF) pulse at a particular resonant frequency to detect the signal of specific nuclei, such as ^{1}H, ^{31}P, etc., in the volume of interest. When the excitation RF pulse is turned off, the spins relax to their equilibrium state by emitting RF waves. These RF waves are collected as the free induction decay (FID) in the time domain (Bothwell and Griffin 2011). The FID is converted to frequency-domain data (i.e., the spectrum) using a technique called Fourier transformation where the data are presented in the form of a one- or two-dimensional spectrum. The spectroscopic data is acquired by using either a localized, i.e., single-voxel or multi-voxel techniques, e.g., chemical shift imaging (CSI) (de Graaf 2007a), or

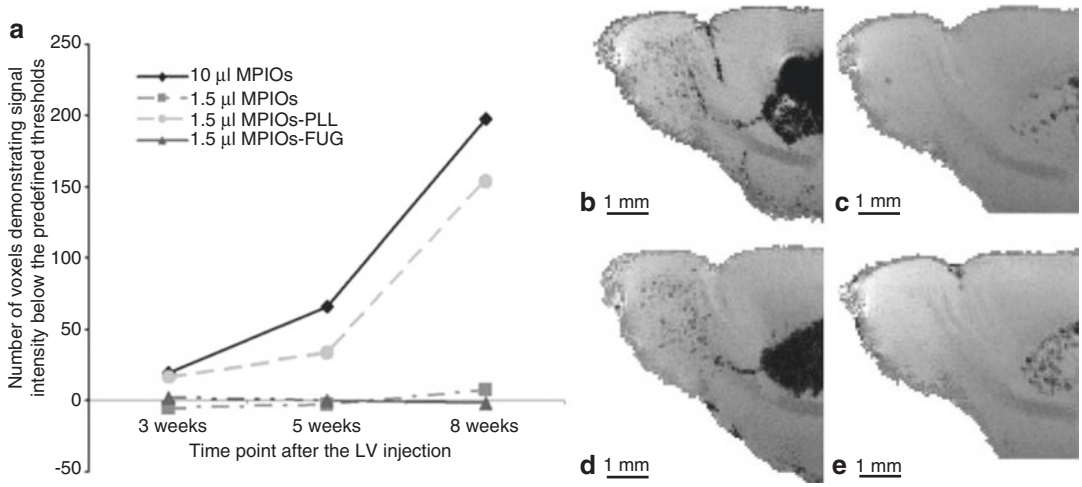

Fig. 29.8 Application of MPIOs to visualize the rostral migration stream noninvasively in rodents. (**a**) Graph indicating an estimation of the number of voxels displaying hypointense spots in the core region of the olfactory bulb ipsilateral to the injection site at 3, 5, and 8 weeks post-particle administration. Four different protocols were applied, i.e., 10.0 µl MPIO's (**b**), 1.5 µl MPIO's (**c**), 1.5 µl MPIO's + poly-L-lysine hydrobromide (PLL, **d**), and 1.5 µl MPIO's + Fugene-6 (FUG, **e**). PLL and FUG are two nonviral transfection agents. (**b**–**e**) Minimum intensity projections (ex vivo MRI) indicating that only two of four methods were successful at visualizing neural progenitor cell migration along the rostral migration stream 8 weeks post-intraventricular injection, similar to what was suggested by panel (**a**). (Reprinted from Vreys et al. (2010) with permission from Elsevier)

whole-brain techniques (Gonen et al. 1998). The most commonly employed single-voxel spectroscopic sequences are point-resolved spectroscopy (PRESS) and stimulated echo acquisition mode (STEAM). A more elaborate discussion on the advantages and disadvantages of single- and multi-voxel MRS techniques along with examples of possible commercial and noncommercial software packages can be found in de Graaf (2007b), Webb et al. (1994), and Drost et al. (2002).

The obtained ^{1}H MRS spectra inform on a variety of metabolic signals such as N-acetylaspartate (NAA), choline (Cho), creatine/phosphocreatine (Cr/PCr), lactate (Lac), glutamine (Gln), glutamate (Glu), γ-aminobutyric acid (GABA), and lipids whose concentrations range between 0.5 and 10 mM. On average, the concentration of the metabolites is estimated using the area under the peak and depends among others on multiple instrumental and biophysical parameters such as relaxation times of metabolites, J-modulation of multiple resonances, and echo time used in the pulse sequence. Quantitative analyses of MRS data can be achieved by expressing metabolites as absolute (millimolar (mM)) or relative concentrations, i.e., proportional to the resonance frequency of an internal standard such as creatine (Cr, metabolite/Cr). Importantly, to allow for relative quantification, the concentration of the internal standard should be stable (de Graaf 2007b; Marino et al. 2011). Since the concentration of metabolites in the brain is often 10^4 lower than the water concentration present in the brain, special MRS sequences are commonly used to suppress the signal from water. Water suppression provides better baseline measurements, which result in a more reliable quantification of metabolite concentrations (de Graaf 2007b).

29.4.3.2 Neurochemical Markers of Neural Plasticity

Based on the relative concentration of metabolites present in the spectra and on preexisting knowledge of the pathways where those compounds are involved, information on the underlying neuroplastic events can be deduced. For example, NAA is generally considered to be a marker of neuroaxonal integrity; creatine/phosphocreatine provides information about energy metabolism; glutamine is a precursor of both

GABA and glutamate; glutamate and GABA are neurotransmitters serving as main excitatory and inhibitory signaling, respectively, in the brain; choline compounds are cell membrane markers; myo-inositol is a glial cell marker and serves as an osmolyte; lactate is a product of anaerobic glycolysis; and lipids are products of brain damage (de Graaf 2007a; Soares and Law 2009; Oz et al. 2014; Albrecht et al. 2010).

^{1}H MRS has been used to detect altered metabolic profiles of brain regions associated with functional and structural reorganization following memory formation (Ferguson et al. 2002), physical exercise (Biedermann et al. 2012), recovery from stroke (Takeuchi and Izumi 2013; Dimyan and Cohen 2011; Munoz Maniega et al. 2008; Sztriha et al. 2012), epilepsy (Hiremath and Najm 2007), and ocular dominance (Chow et al. 2011). For example, a positive correlation between both NAA/total creatine (tCr) and Cho/tCr ratio in the parietal cortex and verbal memory performance of healthy men aged 65–70 years old has been observed suggesting that these metabolites may reflect cognitive performance (Ferguson et al. 2002). Biedermann and colleagues (2012) revealed alterations in control of metabolite levels in the hippocampus of mice after 6–8 weeks of voluntary wheel running, i.e., running mice displayed an increased glutamate peak as compared to sedentary mice (Biedermann et al. 2012). Similar findings have been reported previously in humans, where an increase in Lac/Cr and Glu/Gln was observed in the visual cortex post vigorous exercise (Maddock et al. 2011). The most common inhibitory (i.e., GABA) and excitatory (i.e., Glu) neurotransmitters can be detected via ^{1}H MRS, which has been commonly employed in preclinical epilepsy research (Hiremath and Najm 2007) as well as in motor cortical plasticity (Stagg 2014). However, it should be noted that MRS measurements not only reflect the neurotransmitter pools but also overall brain levels; consequently, extracellular neurotransmitters and intracellular storage pools both participate to the signal.

Besides the establishment of novel functional and structural connections (Takeuchi and Izumi 2013; Dimyan and Cohen 2011; Munoz Maniega et al. 2008; Sztriha et al. 2012), recovery after stroke is characterized by a changing neurochemical profile. Indeed, van der Zijden et al. (van der Zijden et al. 2008) showed a significant decrease in NAA, Cho, and Glu/Gln turnover and increased Glu and Lac immediately after ischemic stroke in rats using ^{1}H/^{13}C MRS imaging (van der Zijden et al. 2008). In addition, early visual deprivation and blindness have both been useful model systems for understanding both developmental and crossmodal plasticity (Wiesel and Hubel 1965a, b). A recent study reported on using ^{1}H MRS to investigate metabolic changes in the visual cortex of macaque monkeys after optic nerve transection, to address questions related to crossmodal plasticity (Wu et al. 2013). They demonstrated a decreased NAA/tCr ratio and increased Ins/tCr and Cho/tCr ratios in the visual cortex compared to those acquired from visual cortex of healthy animals. A relatively similar example relating to cortical reorganization in response to visual deprivation early in life can be found in a study by Chow et al. (Chow et al. 2011). They reported a decrease in taurine and NAA levels in the left visual cortex 3 weeks after right eye monocular enucleation, i.e., surgical removal of one eye (Chow et al. 2011) (Fig. 29.9).

Despite the many studies using MRS to describe plastic changes in response to insults or in neurodegenerative disorders, MRS has only been poorly explored in, e.g., early life plasticity or to characterize biochemical alterations attributable to cognitive training or challenges. Therefore, future studies might find MRS a powerful tool to further disentangle the neurobiochemical basis of plastic events in the brain.

Review

- Bothwell JH, Griffin JL. An introduction to biological nuclear magnetic resonance spectroscopy. Biol Rev Camb Philos Soc. 2011;86(2):493–510.
- de Graaf R. In vivo NMR spectroscopy. 2nd ed. England: Wiley Interscience Chiechester; 2007.
- Pagani E, et al. Basic concepts of advanced MRI techniques. Neurol Sci. 2008;29(Suppl 3):290–5.

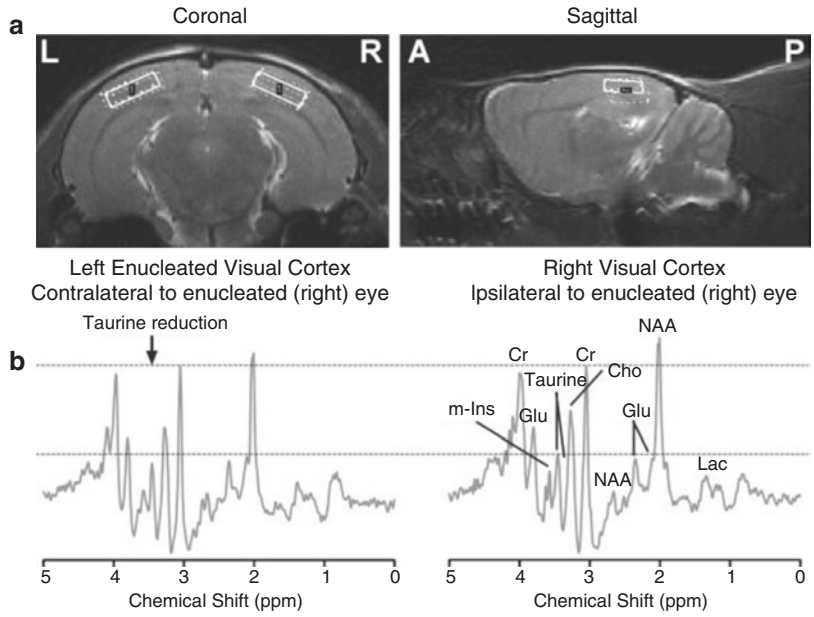

Fig. 29.9 MRS after monocular enucleation to study critical period plasticity of the visual system in rats. (**a**) Visualization of the voxel positioning to acquire ^{1}H MRS spectra in the left and right visual rat cortex. (**b**) ^{1}H MRS spectra of left and right visual cortex 3 weeks after right monocular enucleation (eye removal). A clear reduction in taurine signal is observed in the left visual cortex contralateral to the enucleated eye. The spectrum of the right eye shows great resemblance to intact animals (controls, data not shown). Abbreviations: *L* left, *R* right, *A* anterior, *P* posterior; metabolites can be found in the text (Reprinted from Chow et al. (2011) with permission from Elsevier)

29.5 Concluding Remarks

In vivo MRI represents a unique tool in plasticity and cognitive research given its power to capture functional, structural, and biochemical information from the entire brain on a relatively short time frame. In addition, its noninvasive nature allows repeated measures where the same animal can be followed up along, e.g., the course of development and aging, or over different training sessions. Importantly, this also enables to test for the existence of a causal relationship between the observed neuroplastic events and additional measures such as behavioral assessments or scores of cognitive tests. As compared to other whole-brain imaging methods, MRI does not rely on radiation or radioactive substances, which is of great importance as repeated exposure might provoke deleterious side effects obscuring the actual biologically relevant information. Still, one should not overlook the possible effect of repeated anesthesia – standard for all in vivo imaging methods except after habituation training – on the organisms' physiology or response to treatment.

Despite the three-dimensional abundance of structural, functional, and biochemical information, still relatively little information is given on the underlying biological nature of the observed effects. This lack of specificity can partly be overcome by combining different imaging modalities aimed at a multimodal imaging strategy (Uludağ and Roebroeck 2014), MR fingerprinting (Ma et al. 2013), or by co-registration to ex vivo modalities such as histology, MALDI, and in situ hybridization (cf. Part IV Ex Vivo Validation Methods). In addition, by using quantitative MRI contrasts, "subvoxel" information on the underlying tissue properties such as water content, myelination, etc., can be deduced. Indeed, this was nicely illustrated by Canals et al. (2009) and Sagi et al. 2012, as they both succeeded in detecting experience-dependent changes beyond the typical in vivo sampling rate and voxel size (Sagi

et al. 2012; Canals et al. 2009). So far, most structural and functional MRI contrasts have been widely explored in the field of plasticity and cognitive research. Yet, the versatility of MRS in neuroplasticity research is only beginning to be explored. Given the possibility to detect fluctuations in the balance of metabolites such as GABA and glutamate, MRS will become a valuable tool to address future questions relating to both early and adult plasticity.

Besides a proper methodology, the assessment of neuroplasticity and cognition in preclinical and fundamental research require the appropriate animal models. Natural models of plasticity, such as songbirds, might lead to more fundamental and mechanistic insights, whereas treatment-induced models displaying, e.g., injury-induced plasticity are likely to include effects of, e.g., inflammation which possibly obscure the underlying plasticity, but, on the other hand, are expected to be more translational to the clinic.

Acknowledgments This work is supported by the Belgian Science Policy (Belspo, PLASTOSCINE P7/17), the Research Foundation – Flanders (FWO, G044311N; G.0302.13) – and a grant by the Hercules Foundation (AUHA0012) to AVdL. GDG (postdoc), FK (postdoc), and LVR (PhD) are supported by FWO fellowships.

References

Abe O, et al. Voxel-based analysis of the diffusion tensor. Neuroradiology. 2010;52(8):699–710.

Albrecht J, et al. Roles of glutamine in neurotransmission. Neuron Glia Biol. 2010;6(4):263–76.

Alonso-Ortiz E, Levesque IR, Pike GB. MRI-based myelin water imaging: a technical review. Magn Reson Med. 2015;73:70–81.p. n/a-n/a.

Altman J, Das GD. Autoradiographic and histological evidence of postnatal hippocampal neurogenesis in rats. J Comp Neurol. 1965;124(3):319–35.

Alvarez-Salvado E, et al. Functional MRI of long-term potentiation: imaging network plasticity. Philos Trans R Soc Lond B Biol Sci. 2014;369(1633):20130152.

Amaro Jr E, Barker GJ. Study design in fMRI: basic principles. Brain Cogn. 2006;60(3):220–32.

Anthony H, Karel S. Experience-dependent structural synaptic plasticity in the mammalian brain. Nat Rev Neurosci. 2009;10(9):647–58.

Aschner M. The transport of manganese across the blood–brain barrier. Neurotoxicology. 2006;27(3):311–4.

Ashburner J, Friston KJ. Voxel-based morphometry—the methods. Neuroimage. 2000;11(6):805–21.

Avelino MA, et al. Inherited manganism: the "cock-walk" gait and typical neuroimaging features. J Neurol Sci. 2014;341(1–2):150–2.

Bandettini PA. Twenty years of functional MRI: the science and the stories. Neuroimage. 2012;62(2):575–88.

Barnea A, Nottebohm F. Seasonal recruitment of hippocampal neurons in adult free-ranging black-capped chickadees. Proc Natl Acad Sci. 1994;91(23):11217–21.

Barnea A, Nottebohm F. Recruitment and replacement of hippocampal neurons in young and adult chickadees: an addition to the theory of hippocampal learning. Proc Natl Acad Sci. 1996;93(2):714–8.

Barnes SJ, Finnerty GT. Sensory experience and cortical rewiring. Neuroscientist. 2010;16(2):186–98.

Bartha R, et al. High field (1)H MRS of the hippocampus after donepezil treatment in Alzheimer disease. Prog Neuropsychopharmacol Biol Psychiatry. 2008;32(3):786–93.

Basser PJ, Mattiello J, LeBihan D. MR diffusion tensor spectroscopy and imaging. Biophys J. 1994;66(1):259–67.

Baumans V. Environmental enrichment for laboratory rodents and rabbits: requirements of rodents, rabbits, and research. ILAR J. 2005;46(2):162–70.

Bavelier D, Hirshorn E. I see where you're hearing: how cross-modal plasticity may exploit homologous brain structures. Nat Neurosci. 2010;13(11):1309–11.

Bazarek S, Peterson DA. Prospects for engineering neurons from local neocortical cell populations as cell-mediated therapy for neurological disorders. J Comp Neurol. 2014;522:2857–76: p. n/a-n/a.

Beaulieu C. The basis of anisotropic water diffusion in the nervous system – a technical review. NMR Biomed. 2002;15(7–8):435–55.

Beckmann CF, et al. Investigations into resting-state connectivity using independent component analysis. Philos Trans R Soc Lond B Biol Sci. 2005;360(1457):1001–13.

Berardi N, Pizzorusso T, Maffei L. Critical periods during sensory development. Curr Opin Neurobiol. 2000;10(1):138–45.

Berger JM, Rohn TT, Oxford JT. Autism as the early closure of a neuroplastic critical period normally seen in adolescence. Biol Syst Open Access. 2013;1. http://www.omicsgroup.org/journals/autism-as-the-early-closure-of-a-neuroplastic-critical-period-normally-seen-in-adolescence-2329-6577-1000118.php?aid=43859

Biedermann S, et al. In vivo voxel based morphometry: detection of increased hippocampal volume and decreased glutamate levels in exercising mice. Neuroimage. 2012;61(4):1206–12.

Birn RM, et al. Separating respiratory-variation-related fluctuations from neuronal-activity-related fluctuations in fMRI. Neuroimage. 2006;31(4):1536–48.

Bissig D, Berkowitz BA. Manganese-enhanced MRI of layer-specific activity in the visual cortex from awake and free-moving rats. Neuroimage. 2009;44(3):627–35.

Biswal B, et al. Functional connectivity in the motor cortex of resting human brain using echo-planar MRI. Magn Reson Med. 1995;34(4):537–41.
Bitanihirwe BKY, Woo T-UW. Perineuronal nets and schizophrenia: the importance of neuronal coatings. Neurosci Biobehav Rev. 2014;45:85–99.
Blumenfeld-Katzir T, et al. Diffusion MRI of structural brain plasticity induced by a learning and memory task. PLoS One. 2011;6(6):e20678.
Bothwell JH, Griffin JL. An introduction to biological nuclear magnetic resonance spectroscopy. Biol Rev Camb Philos Soc. 2011;86(2):493–510.
Boumans T, et al. Neural representation of spectral and temporal features of song in the auditory forebrain of zebra finches as revealed by functional MRI. Eur J Neurosci. 2007;26(9):2613–26.
Boumans T, et al. Functional magnetic resonance imaging in zebra finch discerns the neural substrate involved in segregation of conspecific song from background noise. J Neurophysiol. 2008;99(2):931–8.
Boyke J, et al. Training-induced brain structure changes in the elderly. J Neurosci. 2008;28(28):7031–5.
Brainard MS, Doupe AJ. Translating birdsong: songbirds as a model for basic and applied medical research. Annu Rev Neurosci. 2013;36(1):489–517.
Brown J, et al. Enriched environment and physical activity stimulate hippocampal but not olfactory bulb neurogenesis. Eur J Neurosci. 2003;17(10):2042–6.
Bullmore E, Sporns O. Complex brain networks: graph theoretical analysis of structural and functional systems. Nat Rev Neurosci. 2009;10(3):186–98.
Busatto GF, Diniz BS, Zanetti MV. Voxel-based morphometry in Alzheimer's disease. Expert Rev Neurother. 2008;8(11):1691–702.
Butz M, Wörgötter F, van Ooyen A. Activity-dependent structural plasticity. Brain Res Rev. 2009;60(2):287–305.
Cai Y, et al. Use of high resolution 3D Diffusion tensor imaging to study brain white matter development in live neonatal rats. Front Psychiatry. 2011;2:54.
Calhoun VD, et al. A method for making group inferences from functional MRI data using independent component analysis. Hum Brain Mapp. 2001;14(3):140–51.
Campbell BCV, Macrae IM. Translational perspectives on perfusion–diffusion mismatch in ischemic stroke. Int J Stroke. 2015;10:153–62: p. n/a-n/a.
Canals S, et al. Functional MRI evidence for LTP-induced neural network reorganization. Curr Biol. 2009;19(5):398–403.
Carlén M, et al. Functional integration of adult-born neurons. Curr Biol. 2002;12(7):606–8.
Chan KC, et al. In vivo retinotopic mapping of superior colliculus using manganese-enhanced magnetic resonance imaging. Neuroimage. 2011;54(1):389–95.
Chan KC, et al. In vivo evaluation of retinal and callosal projections in early postnatal development and plasticity using manganese-enhanced MRI and diffusion tensor imaging. Neuroimage. 2012;59(3):2274–83.
Chang C, Glover GH. Effects of model-based physiological noise correction on default mode network anti-correlations and correlations. Neuroimage. 2009;47(4):1448–59.
Chen W, Tenney J, Kulkarni P, King JA. Imaging unconditioned fear response with manganese-enhanced MRI (MEMRI). Neuroimage. 2007;37(1):221–9.
Chen C-C, Bajnath A, Brumberg JC. The impact of development and sensory deprivation on dendritic protrusions in the mouse barrel cortex. Cereb Cortex. 2014;25:1638–53.
Choi IY, et al. In vivo NMR studies of neurodegenerative diseases in transgenic and rodent models. Neurochem Res. 2003;28(7):987–1001.
Chow AM, et al. Metabolic changes in visual cortex of neonatal monocular enucleated rat: a proton magnetic resonance spectroscopy study. Int J Dev Neurosci. 2011;29(1):25–30.
Chuang K-H, Belluscio L, Koretsky AP. In vivo detection of individual glomeruli in the rodent olfactory bulb using manganese enhanced MRI. Neuroimage. 2010;49(2):1350–6.
Chung MK, et al. A unified statistical approach to deformation-based morphometry. Neuroimage. 2001;14(3):595–606.
Chung H-W, Chou M-C, Chen C-Y. Principles and limitations of computational algorithms in clinical diffusion tensor MR tractography. Am J Neuroradiol. 2011;32(1):3–13.
Coghlan S, et al. GABA system dysfunction in autism and related disorders: from synapse to symptoms. Neurosci Biobehav Rev. 2012;36(9):2044–55.
Colonnese MT, et al. Development of hemodynamic responses and functional connectivity in rat somatosensory cortex. Nat Neurosci. 2008;11(1):72–9.
Concha L. A macroscopic view of microstructure: using diffusion-weighted images to infer damage, repair, and plasticity of white matter. Neuroscience. 2014;276:14–28.
Coquery N, et al. Intrahippocampal transplantation of mesenchymal stromal cells promotes neuroplasticity. Cytotherapy. 2012;14(9):1041–53.
Couillard-Despres S, et al. In vivo monitoring of adult neurogenesis in health and disease. Front Neurosci. 2011;5:67.
Crawley AP, Henkelman RM. Errors in T2 estimation using multislice multiple-echo imaging. Magn Reson Med. 1987;4(1):34–47.
Curlik DM, DiFeo G, Shors TJ. Preparing for adulthood: thousands upon thousands of new cells are born in the hippocampus during puberty and most survive with effortful learning. Front Neurosci. 2014;8:70.
Damoiseaux JS, et al. Consistent resting-state networks across healthy subjects. Proc Natl Acad Sci U S A. 2006;103(37):13848–53.
de Graaf R. In vivo NMR spectroscopy. 2nd ed. England: John wiley and sons; 2007a.
de Graaf RA. In vivo NMR spectroscopy: principles and techniques. 2nd ed. England: John wiley and sons; 2007b.

De Groof G, Van der Linden A. Love songs, bird brains and diffusion tensor imaging. NMR Biomed. 2010;23(7):873–83.
De Groof G, et al. Seasonal rewiring of the songbird brain: an in vivo MRI study. Eur J Neurosci. 2008;28(12):2475–85.
De Groof G, et al. Structural changes between seasons in the songbird auditory forebrain. J Neurosci. 2009;29(43):13557–65.
De Groof G, et al. Neural correlates of behavioural olfactory sensitivity changes seasonally in European starlings. PLoS One. 2010;5(12):e14337.
De Groof G, et al. Functional changes between seasons in the male songbird auditory forebrain. Front Behav Neurosci. 2013a;7:196.
De Groof G, et al. Functional MRI and functional connectivity of the visual system of awake pigeons. Behav Brain Res. 2013b;239:43–50.
Denk W, Svoboda K. Photon upmanship: why multiphoton imaging is more than a gimmick. Neuron. 1997;18(3):351–7.
Deoni SCL. Quantitative relaxometry of the brain. Top Magn Reson Imaging. 2010;21(2):101–13. doi:10.1097/RMR.0b013e31821e56d8.
Deoni SL. Magnetic resonance relaxation and quantitative measurement in the brain. In: Modo M, Bulte JWM, editors. Magnetic resonance neuroimaging. Humana Press; 2011. p. 65–108.
Desai M, et al. Mapping brain networks in awake mice using combined optical neural control and fMRI. J Neurophysiol. 2011;105(3):1393–405.
Detre JA, Wang J. Technical aspects and utility of fMRI using BOLD and ASL. Clin Neurophysiol. 2002;113(5):621–34.
Di Salle F, et al. Exploring brain function with magnetic resonance imaging. Eur J Radiol. 1999;30(2):84–94.
Dijkhuizen RM, et al. Correlation between brain reorganization, ischemic damage, and neurologic status after transient focal cerebral ischemia in rats: a functional magnetic resonance imaging study. J Neurosci. 2003;23(2):510–7.
Dijkhuizen RM, et al. Functional MRI and diffusion tensor imaging of brain reorganization after experimental stroke. Transl Stroke Res. 2012;3(1):36–43.
Dimyan MA, Cohen LG. Neuroplasticity in the context of motor rehabilitation after stroke. Nat Rev Neurol. 2011;7(2):76–85.
Ding X-Q, et al. Normal brain maturation characterized with age-related T2 relaxation times: an attempt to develop a quantitative imaging measure for clinical use. Invest Radiol. 2004;39(12):740–6.
Dobson AW, Erikson KM, Aschner M. Manganese neurotoxicity. Ann N Y Acad Sci. 2004;1012(1):115–28.
Doupe AJ, Kuhl PK. Birdsong and human speech: common themes and mechanisms. Annu Rev Neurosci. 1999;22(1):567–631.
Drost DJ, et al. Proton magnetic resonance spectroscopy in the brain: report of AAPM MR Task Group #9. Med Phys. 2002;29(9):2177–97.
Dubois J, et al. The early development of brain white matter: a review of imaging studies in fetuses, newborns and infants. Neuroscience. 2014;276:48–71.
Dula AN, Gochberg DF, Does MD. Optimal echo spacing for multi-echo imaging measurements of Bi-exponential T2 relaxation. J Magn Reson. 2009;196(2):149–56.
Einstein A. Investigations on the theory of the brownian movement. Ann der Physik. 1905.
Endo T, et al. Cortical sensory map rearrangement after spinal cord injury: fMRI responses linked to Nogo signalling. Brain. 2007;130(Pt 11):2951–61.
Erikson KM, Aschner M. Manganese neurotoxicity and glutamate-GABA interaction. Neurochem Int. 2003;43(4–5):475–80.
Erikson KM, et al. Interactions between excessive manganese exposures and dietary iron-deficiency in neurodegeneration. Environ Toxicol Pharmacol. 2005;19(3):415–21.
Eriksson PS, Perfilieva E, Bjork-Eriksson T, Alborn A-M, Nordborg C, Peterson DA, Gage FH. Neurogenesis in the adult human hippocampus. Nat Med. 1998;4(11):1313–7.
Erzurumlu RS, Gaspar P. Development and critical period plasticity of the barrel cortex. Eur J Neurosci. 2012;35(10):1540–53.
Fagiolini M, Jensen CL, Champagne FA. Epigenetic influences on brain development and plasticity. Curr Opin Neurobiol. 2009;19(2):207–12.
Feinberg DA, Yacoub E. The rapid development of high speed, resolution and precision in fMRI. Neuroimage. 2012;62(2):720–5.
Felsenstein KM, et al. Regenerative medicine in Alzheimer's disease. Transl Res. 2014;163(4):432–8.
Ferguson KJ, et al. Magnetic resonance spectroscopy and cognitive function in healthy elderly men. Brain. 2002;125(Pt 12):2743–9.
Fernandez F, Garner CC. Over-inhibition: a model for developmental intellectual disability. Trends Neurosci. 2007;30(10):497–503.
Ferris CF, et al. Functional magnetic resonance imaging in conscious animals: a new tool in behavioural neuroscience research. J Neuroendocrinol. 2006;18(5):307–18.
Fledelius HC, et al. Human parallels to experimental myopia? A literature review on visual deprivation. Acta Ophthalmol. 2014;92:724–9: p. n/a-n/a.
Focke NK, et al. Do manual and voxel-based morphometry measure the same? – A proof of concept study. Front Psychiatry. 2014;5:39.
Frangou S, Williams SC. Magnetic resonance spectroscopy in psychiatry: basic principles and applications. Br Med Bull. 1996;52(3):474–85.
Fransson P. Spontaneous low-frequency BOLD signal fluctuations: an fMRI investigation of the resting-state default mode of brain function hypothesis. Hum Brain Mapp. 2005;26(1):15–29.
Frasnelli J, et al. Crossmodal plasticity in sensory loss. Prog Brain Res. 2011;191:233–49.

Freeborough PA, Fox NC. Modeling brain deformations in Alzheimer disease by fluid registration of serial 3D MR images. J Comput Assist Tomogr. 1998;22(5):838–43.
Friston KJ, Harrison L, Penny W. Dynamic causal modelling. Neuroimage. 2003;19(4):1273–302.
Fuchs E, et al. Adult neuroplasticity: more than 40 years of research. Neural Plast. 2014;2014:10.
Gage FH, et al. Survival and differentiation of adult neuronal progenitor cells transplanted to the adult brain. Proc Natl Acad Sci. 1995;92(25):11879–83.
Galinsky VL, Frank LR. Automated segmentation and shape characterization of volumetric data. Neuroimage. 2014;92:156–68.
Gavin CE, Gunter KK, Gunter TE. Manganese and calcium efflux kinetics in brain mitochondria. Relevance to manganese toxicity. Biochem J. 1990;266:329–34.
Gavrilescu M, et al. Functional connectivity estimation in fMRI data: influence of preprocessing and time course selection. Hum Brain Mapp. 2008;29(9):1040–52.
Gervain J, et al. Valproate reopens critical-period learning of absolute pitch. Front Syst Neurosci. 2013;7:102.
Gheusi G, Lledo PM. Chapter 6 – adult neurogenesis in the olfactory system shapes odor memory and perception. In: Edi B, Donald AW, editors. Progress in brain research. Elsevier; 2014. p. 157–75.
Goldman SA, Nottebohm F. Neuronal production, migration, and differentiation in a vocal control nucleus of the adult female canary brain. Proc Natl Acad Sci. 1983;80(8):2390–4.
Golub Y, et al. Reduced hippocampus volume in the mouse model of Posttraumatic Stress Disorder. J Psychiatr Res. 2011;45(5):650–9.
Gonen O, et al. Total brain N-acetylaspartate concentration in normal, age-grouped females: quantitation with non-echo proton NMR spectroscopy. Magn Reson Med. 1998;40(5):684–9.
Gutman D, et al. Mapping of the mouse olfactory system with manganese-enhanced magnetic resonance imaging and diffusion tensor imaging. Brain Struct Funct. 2013;218(2):527–37.
Hannan AJ. Review: environmental enrichment and brain repair: harnessing the therapeutic effects of cognitive stimulation and physical activity to enhance experience-dependent plasticity. Neuropathol Appl Neurobiol. 2014;40(1):13–25.
Hensch TK. Critical period regulation. Annu Rev Neurosci. 2004;27(1):549–79.
Herring A, et al. Environmental enrichment enhances cellular plasticity in transgenic mice with Alzheimer-like pathology. Exp Neurol. 2009;216(1):184–92.
Hiremath GK, Najm IM. Magnetic resonance spectroscopy in animal models of epilepsy. Epilepsia. 2007;48:47–55.
Hofstetter S, et al. Short-term learning induces white matter plasticity in the fornix. J Neurosci. 2013;33(31):12844–50.
Hopkins WD, et al. Gray matter asymmetries in chimpanzees as revealed by voxel-based morphometry. Neuroimage. 2008;42(2):491–7.
Hötting K, Röder B. Beneficial effects of physical exercise on neuroplasticity and cognition. Neurosci Biobehav Rev. 2013;37(9, Part B):2243–57.
Jaime FO, et al. Deafferentation-induced plasticity of visual callosal connections: predicting critical periods and analyzing cortical abnormalities using diffusion tensor imaging. Neural Plast. 2012;2012:250196.
James JS, et al. fMRI paradigm designing and post-processing tools. Indian J Radiol Imaging. 2014;24(1):13–21.
Jessen F, et al. Decrease of N-acetylaspartate in the MTL correlates with cognitive decline of AD patients. Neurology. 2001;57(5):930–2.
Jon JB. Neurodevelopment: unlocking the brain. Nature. 2012;487(7405):24–6.
Jonckers E, et al. Functional connectivity fMRI of the rodent brain: comparison of functional connectivity networks in rat and mouse. PLoS One. 2011;6(4):e18876.
Jonckers E, et al. Different anesthesia regimes modulate the functional connectivity outcome in mice. Magn Reson Med. 2014;72(4):1103–12.
Jones DK. The effect of gradient sampling schemes on measures derived from diffusion tensor MRI: a Monte Carlo study†. Magn Reson Med. 2004;51(4):807–15.
Jones DK. Diffusion MRI: theory, methods, and applications. Oxford: Oxford University Press; 2010.
Jones DK, Basser PJ. "Squashing peanuts and smashing pumpkins": how noise distorts diffusion-weighted MR data. Magn Reson Med. 2004;52(5):979–93.
Jones DK, Knösche TR, Turner R. White matter integrity, fiber count, and other fallacies: the do's and don'ts of diffusion MRI. Neuroimage. 2013;73:239–54.
Kalisch R, et al. Blood pressure changes induced by arterial blood withdrawal influence bold signal in anesthesized rats at 7 Tesla: implications for pharmacologic MRI. Neuroimage. 2001;14(4):891–8.
Kara F, et al. In vivo measurement of transverse relaxation time in the mouse brain at 17.6 T. Magn Reson Med. 2013;70(4):985–93.
Kelly C, et al. Characterizing variation in the functional connectome: promise and pitfalls. Trends Cogn Sci. 2012;16(3):181–8.
Kent K, et al. CA3 NMDA receptors are required for experience-dependent shifts in hippocampal activity. Hippocampus. 2007;17(10):1003–11.
Kharatishvili I, et al. Quantitative T2 mapping as a potential marker for the initial assessment of the severity of damage after traumatic brain injury in rat. Exp Neurol. 2009;217(1):154–64.
Kharatishvili I, et al. MRI changes and complement activation correlate with epileptogenicity in a mouse model of temporal lobe epilepsy. Brain Struct Funct. 2014;219(2):683–706.
Kim SG, et al. Cerebral blood volume MRI with intravascular superparamagnetic iron oxide nanoparticles. NMR Biomed. 2013;26(8):949–62.
King JA, et al. Procedure for minimizing stress for fMRI studies in conscious rats. J Neurosci Methods. 2005;148(2):154–60.

Kral A. Auditory critical periods: a review from system's perspective. Neuroscience. 2013;247:117–33.
Krishnan KR, et al. Randomized, placebo-controlled trial of the effects of donepezil on neuronal markers and hippocampal volumes in Alzheimer's disease. Am J Psychiatry. 2003;160(11):2003–11.
Kwong KK, et al. Dynamic magnetic resonance imaging of human brain activity during primary sensory stimulation. Proc Natl Acad Sci U S A. 1992;89(12):5675–9.
Lahti KM, et al. Imaging brain activity in conscious animals using functional MRI. J Neurosci Methods. 1998;82(1):75–83.
Lamprecht R, LeDoux J. Structural plasticity and memory. Nat Rev Neurosci. 2004;5(1):45.
Lau JC, et al. Longitudinal neuroanatomical changes determined by deformation-based morphometry in a mouse model of Alzheimer's disease. Neuroimage. 2008;42(1):19–27.
Le Bihan D, Delannoy J, Levin RL. Temperature mapping with MR imaging of molecular diffusion: application to hyperthermia. Radiology. 1989;171(3):853–7.
Le Bihan D, et al. Diffusion tensor imaging: concepts and applications. J Magn Reson Imaging. 2001;13(4):534–46.
Lerch JP, et al. Automated deformation analysis in the YAC128 Huntington disease mouse model. Neuroimage. 2008;39(1):32–9.
Lerch JP, et al. Maze training in mice induces MRI-detectable brain shape changes specific to the type of learning. Neuroimage. 2011;54(3):2086–95.
Leuner B, Gould E, Shors TJ. Is there a link between adult neurogenesis and learning? Hippocampus. 2006;16(3):216–24.
Levelt CN, Hübener M. Critical-period plasticity in the visual cortex. Annu Rev Neurosci. 2012;35(1):309–30.
Li J, et al. A meta-analysis of voxel-based morphometry studies of white matter volume alterations in Alzheimer's disease. Neurosci Biobehav Rev. 2012;36(2):757–63.
Li R, et al. Cortical plasticity induced by different degrees of peripheral nerve injuries: a rat functional magnetic resonance imaging study under 9.4 Tesla. J Brachial Plex Peripher Nerve Inj. 2013;8(1):4.
Liang Z, King J, Zhang N. Uncovering intrinsic connectional architecture of functional networks in awake rat brain. J Neurosci. 2011;31(10):3776–83.
Lindquist MA. The statistical analysis of fMRI data. Stat Sci. 2008;23(4):439–64.
Lindquist MA, et al. Modeling the hemodynamic response function in fMRI: efficiency, bias and mis-modeling. Neuroimage. 2009;45(1):S187–98.
Little DM, Foxely S, Lazarov O. A preliminary study targeting neuronal pathways activated following environmental enrichment by resting state functional magnetic resonance imaging. J Alzheimers Dis. 2012;32(1):101–7.
Logothetis NK. What we can do and what we cannot do with fMRI. Nature. 2008;453(7197):869–78.
Logothetis NK, Pfeuffer J. On the nature of the BOLD fMRI contrast mechanism. Magn Reson Imaging. 2004;22(10):1517–31.
Logothetis NK, Wandell BA. Interpreting the BOLD signal. Annu Rev Physiol. 2004;66(1):735–69.
Logothetis N, et al. Neurophysiological investigation of the basis of the fMRI signal. Nature. 2001;412(6843):150–7.
Longwei X. Clinical application of diffusion tensor magnetic resonance imaging in skeletal muscle. Muscles Ligaments Tendons J. 2012;2(1):19–24.
Lövdén M, et al. Structural brain plasticity in adult learning and development. Neurosci Biobehav Rev. 2013;37(9, Part B):2296–310.
Lowe MJ, et al. Correlations in low-frequency BOLD fluctuations reflect cortico-cortical connections. Neuroimage. 2000;12(5):582–7.
Lu H, et al. Rat brains also have a default mode network. Proc Natl Acad Sci U S A. 2012;109(10):3979–84.
Lüscher C. Drug-evoked synaptic plasticity causing addictive behavior. J Neurosci. 2013;33(45):17641–6.
Ma DKB, Michael A, Ming G-l, Song H. Adult neural stem cells in the mammalian central nervous system. Cell Res. 2009;19(6):672–82.
Ma D, et al. Magnetic resonance fingerprinting. Nature. 2013;495(7440):187–92.
MacKay A, et al. In vivo visualization of myelin water in brain by magnetic resonance. Magn Reson Med. 1994;31(6):673–7.
MacKay A, et al. Insights into brain microstructure from the T2 distribution. Magn Reson Imaging. 2006;24(4):515–25.
Maddock RJ, et al. Vigorous exercise increases brain lactate and Glx (glutamate+glutamine): a dynamic 1H-MRS study. Neuroimage. 2011;57(4):1324–30.
Maguire EA, et al. Navigation-related structural change in the hippocampi of taxi drivers. Proc Natl Acad Sci. 2000;97(8):4398–403.
Majewska AK. Imaging visual cortical structure and function in vivo. J Glaucoma. 2013;22:S21–3. doi:10.1097/IJG.0b013e3182934a30.
Malenka RC, Bear MF. LTP and LTD: an embarrassment of riches. Neuron. 2004;44(1):5–21.
Malonek D, et al. Vascular imprints of neuronal activity: relationships between the dynamics of cortical blood flow, oxygenation, and volume changes following sensory stimulation. Proc Natl Acad Sci. 1997;94(26):14826–31.
Mangin JF, et al. Toward global tractography. Neuroimage. 2013;80:290–6.
Margulies DS, et al. Resting developments: a review of fMRI post-processing methodologies for spontaneous brain activity. MAGMA. 2010;23(5–6):289–307.
Marino S, et al. 1H-MR spectroscopy in traumatic brain injury. Neurocrit Care. 2011;14(1):127–33.
Masamoto K, Kanno I. Anesthesia and the quantitative evaluation of neurovascular coupling. J Cereb Blood Flow Metab. 2012;32(7):1233–47.
May A. Experience-dependent structural plasticity in the adult human brain. Trends Cogn Sci. 2011;15(10):475–82.
Mechelli A, et al. Voxel-based morphometry of the human brain: methods and applications. Curr Med Imaging Rev. 2005:1(2);105–13.

Miller MJ, et al. fMRI of the conscious rabbit during unilateral classical eyeblink conditioning reveals bilateral cerebellar activation. J Neurosci. 2003;23(37): 11753–8.

Mori S, Tournier J. Introduction to diffusion tensor imaging 2e: and higher order models. The Boulevard, Langford Lane, Kidlington, Oxford, UK and USA: Elsevier Science & Technology Books; 2013.

Mori S, Zhang J. Principles of diffusion tensor imaging and its applications to basic neuroscience research. Neuron. 2006;51(5):527–39.

Muller D, et al. LTP, memory and structural plasticity. Curr Mol Med. 2002;2:605–11.

Munoz Maniega S, et al. Changes in NAA and lactate following ischemic stroke: a serial MR spectroscopic imaging study. Neurology. 2008;71(24):1993–9.

Nagy C, Turecki G. Sensitive periods in epigenetics: bringing us closer to complex behavioral phenotypes. Epigenomics. 2012;4(4):445–57.

Nahmani M, Turrigiano GG. Adult cortical plasticity following injury: recapitulation of critical period mechanisms? Neuroscience. 2014;283:4–16.

Nairismägi J, et al. Manganese-enhanced magnetic resonance imaging of mossy fiber plasticity in vivo. Neuroimage. 2006;30(1):130–5.

Nieman BJ, et al. In vivo MRI of neural cell migration dynamics in the mouse brain. Neuroimage. 2010;50(2):456–64.

Nottebohm F. Neuronal replacement in adulthood. Ann N Y Acad Sci. 1985;457(1):143–61.

Oboti L, Peretto P. How neurogenesis finds its place in a hardwired sensory system. Front Neurosci. 2014;8:102.

Ogawa S, et al. Intrinsic signal changes accompanying sensory stimulation: functional brain mapping with magnetic resonance imaging. Proc Natl Acad Sci U S A. 1992;89(13):5951–5.

Olson AK, et al. Environmental enrichment and voluntary exercise massively increase neurogenesis in the adult hippocampus via dissociable pathways. Hippocampus. 2006;16(3):250–60.

Overman JJ, Carmichael ST. Plasticity in the injured brain: more than molecules matter. Neuroscientist. 2014;20(1):15–28.

Oz G, et al. Clinical proton MR spectroscopy in central nervous system disorders. Radiology. 2014;270(3):658–79.

Pagani E, et al. Basic concepts of advanced MRI techniques. Neurol Sci. 2008;29 Suppl 3:290–5.

Park CH, et al. Transcranial direct current stimulation increases resting state interhemispheric connectivity. Neurosci Lett. 2013;539:7–10.

Paus T, et al. Maturation of white matter in the human brain: a review of magnetic resonance studies. Brain Res Bull. 2001;54(3):255–66.

Pautler RG. In vivo, trans-synaptic tract-tracing utilizing manganese-enhanced magnetic resonance imaging (MEMRI). NMR Biomed. 2004;17(8):595–601.

Pautler RG, Silva AC, Koretsky AP. In vivo neuronal tract tracing using manganese-enhanced magnetic resonance imaging. Magn Reson Med. 1998;40(5): 740–8.

Pawela CP, et al. Interhemispheric neuroplasticity following limb deafferentation detected by resting-state functional connectivity magnetic resonance imaging (fcMRI) and functional magnetic resonance imaging (fMRI). Neuroimage. 2010;49(3):2467–78.

Pell GS, et al. Voxel-based relaxometry: a new approach for analysis of T2 relaxometry changes in epilepsy. Neuroimage. 2004;21(2):707–13.

Pelled G. MRI of neuronal plasticity in rodent models. Methods Mol Biol. 2011;711:567–78.

Pelled G, Bergman H, Goelman G. Bilateral overactivation of the sensorimotor cortex in the unilateral rodent model of Parkinson's disease – a functional magnetic resonance imaging study. Eur J Neurosci. 2002;15(2):389–94.

Pelled G, et al. Functional MRI detection of bilateral cortical reorganization in the rodent brain following peripheral nerve deafferentation. Neuroimage. 2007;37(1):262–73.

Peltier SJ, et al. Functional connectivity changes with concentration of sevoflurane anesthesia. Neuroreport. 2005;16(3):285–8.

Petersen-Felix S, Curatolo M. Neuroplasticity--an important factor in acute and chronic pain. Swiss Med Wkly. 2002;132:273–8.

Poirier C, et al. Own-song recognition in the songbird auditory pathway: selectivity and lateralization. J Neurosci. 2009;29(7):2252–8.

Poole D, Oitzl M, van der Weerd L. MRI in animal models of psychiatric disorders. In: Schröder L, Faber C, editors. In vivo NMR Imaging. Humana Press; 2011. p. 309–35.

Ptito M, et al. Crossmodal recruitment of the ventral visual stream in congenital blindness. Neural Plast. 2012;2012:304045.

Roebroeck A, Formisano E, Goebel R. Mapping directed influence over the brain using Granger causality and fMRI. Neuroimage. 2005;25(1):230–42.

Roose D, et al. Multimodal imaging of micron-sized iron oxide particles following in vitro and in vivo uptake by stem cells: down to the nanometer scale. Contrast Media Mol Imaging. 2014;9:400–8: p. n/a-n/a.

Roth J, Ponzoni S, Aschner M. Manganese homeostasis and transport. In: Banci L, editor. Metallomics and the cell. The Netherlands: Springer Dordrecht; 2013. p. 169–201.

Rueger MA, et al. Noninvasive imaging of endogenous neural stem cell mobilization in vivo using positron emission tomography. J Neurosci. 2010;30(18): 6454–60.

Sagi Y, et al. Learning in the fast lane: new insights into neuroplasticity. Neuron. 2012;73(6):1195–203.

Sale A, et al. GABAergic inhibition in visual cortical plasticity. Front Cell Neurosci. 2010;4:10.

Sampaio-Baptista C, et al. Gray matter volume is associated with rate of subsequent skill learning after a long term training intervention. Neuroimage. 2014; 96:158–66.

Santamaria AB. Manganese exposure, essentiality & toxicity. Indian J Med Res. 2008;128(4):16.

Särkämö T, et al. Structural changes induced by daily music listening in the recovering brain after middle cerebral artery stroke: a voxel-based morphometry study. Front Hum Neurosci. 2014;8:245.

Sawiak SJ, Picq J-L, Dhenain M. Voxel-based morphometry analyses of in-vivo MRI in the aging mouse lemur primate. Front Aging Neurosci. 2014;6:82.

Schroeter A, et al. Specificity of stimulus-evoked fMRI responses in the mouse: the influence of systemic physiological changes associated with innocuous stimulation under four different anesthetics. Neuroimage. 2014;94:372–84.

Shapiro EM, et al. Magnetic resonance imaging of the migration of neuronal precursors generated in the adult rodent brain. Neuroimage. 2006;32(3):1150–7.

Shrager RI, Weiss GH, Spencer RGS. Optimal time spacings for T2 measurements: monoexponential and biexponential systems. NMR Biomed. 1998; 11(6):297–305.

Sierra A, et al. Surveillance, phagocytosis, and inflammation: how never-resting microglia influence adult hippocampal neurogenesis. Neural Plast. 2014;2014:15.

Silva AC, et al. Detection of cortical laminar architecture using manganese-enhanced MRI. J Neurosci Methods. 2008;167(2):246–57.

Sloot WN, Gramsbergen J-BP. Axonal transport of manganese and its relevance to selective neurotoxicity in the rat basal ganglia. Brain Res. 1994;657(1–2): 124–32.

Small SA, et al. Circuit mechanisms underlying memory encoding and retrieval in the long axis of the hippocampal formation. Nat Neurosci. 2001;4(4):442–9.

Smirnakis SM, et al. Spatial specificity of BOLD versus cerebral blood volume fMRI for mapping cortical organization. J Cereb Blood Flow Metab. 2007;27(6):1248–61.

Soares DP, Law M. Magnetic resonance spectroscopy of the brain: review of metabolites and clinical applications. Clin Radiol. 2009;64(1):12–21.

Soares J, et al. A hitchhiker's guide to diffusion tensor imaging. Front Neurosci. 2013;7:31.

Stagg CJ. Magnetic resonance spectroscopy as a tool to study the role of GABA in motor-cortical plasticity. Neuroimage. 2014;86:19–27.

Stejskal EO, Tanner JE. Spin diffusion measurements: spin echoes in the presence of a time-dependent field gradient. J Chem Phys. 1965;42(1):288–92.

Stepanichev M, et al. Rodent models of depression: neurotrophic and neuroinflammatory biomarkers. Biomed Res Int. 2014;2014:20.

Stuchlik A. Dynamic learning and memory, synaptic plasticity and neurogenesis: an update. Front Behav Neurosci. 2014;8:106.

Sumiyoshi A, et al. Regional gray matter volume increases following 7 days of voluntary wheel running exercise: a longitudinal VBM study in rats. Neuroimage. 2014;98:82–90.

Svirsky MA, Teoh SW, Neuburger H. Development of language and speech perception in congenitally, profoundly deaf children as a function of age at cochlear implantation. Audiol Neurootol. 2004; 9(4):224–33.

Sztriha LK, et al. Monitoring brain repair in stroke using advanced magnetic resonance imaging. Stroke. 2012;43(11):3124–31.

Takeda A, et al. Manganese transport in the neural circuit of rat CNS. Brain Res Bull. 1998;45(2):149–52.

Takesian AE, Hensch TK. Chapter 1 – balancing plasticity/stability across brain development. In: Michael M. Merzenich MN, Thomas MVV, editors. Progress in brain research. Elsevier; 2013. p. 3–34.

Takeuchi N, Izumi S. Rehabilitation with poststroke motor recovery: a review with a focus on neural plasticity. Stroke Res Treat. 2013;2013:128641.

Tapp PD, et al. Application of an automated voxel-based morphometry technique to assess regional gray and white matter brain atrophy in a canine model of aging. Neuroimage. 2006;29(1):234–44.

Tjälve H, et al. Uptake of manganese and cadmium from the nasal mucosa into the central nervous system via olfactory pathways in rats *. Pharmacol Toxicol. 1996;79(6):347–56.

Tramontin AD, Brenowitz EA. Seasonal plasticity in the adult brain. Trends Neurosci. 2000;23(6):251–8.

Tropea D, Van Wart A, Sur M. Molecular mechanisms of experience-dependent plasticity in visual cortex. Philos Trans R Soc B Biol Sci. 2009;364(1515): 341–55.

Tsurugizawa T, et al. Effects of isoflurane and alpha-chloralose anesthesia on BOLD fMRI responses to ingested L-glutamate in rats. Neuroscience. 2010;165(1):244–51.

Tucciarone J, et al. Layer specific tracing of corticocortical and thalamocortical connectivity in the rodent using manganese enhanced MRI. Neuroimage. 2009;44(3):923–31.

Tuch DS. Q-ball imaging. Magn Reson Med. 2004;52(6):1358–72.

Tuch DS, et al. High angular resolution diffusion imaging reveals intravoxel white matter fiber heterogeneity. Magn Reson Med. 2002;48(4):577–82.

Uddin LQ, Supekar K, Menon V. Typical and atypical development of functional human brain networks: insights from resting-state FMRI. Front Syst Neurosci. 2010;4:21.

Uludağ K, Roebroeck A. General overview on the merits of multimodal neuroimaging data fusion. Neuroimage. 2014;102(Pt 1):3–10.

van den Heuvel MP, Hulshoff Pol HE. Exploring the brain network: a review on resting-state fMRI functional connectivity. Eur Neuropsychopharmacol. 2010;20(8): 519–34.

van der Kant A, et al. Representation of early sensory experience in the adult auditory midbrain: implications for vocal learning. PLoS One. 2013;8(4):e61764.

Van der Linden A, et al. Non invasive in vivo anatomical studies of the oscine brain by high resolution MRI microscopy. J Neurosci Methods. 1998;81(1–2):45–52.

Van der Linden A, et al. In vivo manganese-enhanced magnetic resonance imaging reveals connections and

functional properties of the songbird vocal control system. Neuroscience. 2002;112(2):467–74.
Van der Linden A, et al. Applications of manganese-enhanced magnetic resonance imaging (MEMRI) to image brain plasticity in song birds. NMR Biomed. 2004;17(8):602–12.
Van der Linden A, et al. MRI in small brains displaying extensive plasticity. Trends Neurosci. 2009;32(5):257–66.
van der Zijden JP, et al. 1H/13C MR spectroscopic imaging of regionally specific metabolic alterations after experimental stroke. Brain. 2008;131(Pt 8):2209–19.
van Meer MP, et al. Recovery of sensorimotor function after experimental stroke correlates with restoration of resting-state interhemispheric functional connectivity. J Neurosci. 2010;30(11):3964–72.
Van Meir V, et al. In vivo MR imaging of the seasonal volumetric and functional plasticity of song control nuclei in relation to song output in a female songbird. Neuroimage. 2006;31(3):981–92.
Van Ruijssevelt L, et al. Current state-of-the-art of auditory functional MRI (fMRI) on zebra finches: technique and scientific achievements. J Physiol Paris. 2013;107(3):156–69.
Villasana LE, Westbrook GL, Schnell E. Neurologic impairment following closed head injury predicts posttraumatic neurogenesis. Exp Neurol. 2014;261:156–62.
Vivo L, et al. Extracellular matrix inhibits structural and functional plasticity of dendritic spines in the adult visual cortex. Nat Commun. 2013;4:1484.
Voss MW, et al. Bridging animal and human models of exercise-induced brain plasticity. Trends Cogn Sci. 2013;17(10):525–44.
Vreys R, et al. MRI visualization of endogenous neural progenitor cell migration along the RMS in the adult mouse brain: validation of various MPIO labeling strategies. Neuroimage. 2010;49(3):2094–103.
Webb PG, et al. Automated single-voxel proton MRS: technical development and multisite verification. Magn Reson Med. 1994;31(4):365–73.
Weissenbacher A, et al. Correlations and anticorrelations in resting-state functional connectivity MRI: a quantitative comparison of preprocessing strategies. Neuroimage. 2009;47(4):1408–16.
Weng J-C, et al. Functional mapping of rat barrel activation following whisker stimulation using activity-induced manganese-dependent contrast. Neuroimage. 2007;36(4):1179–88.
Whitwell JL. Voxel-based morphometry: an automated technique for assessing structural changes in the brain. J Neurosci. 2009;29(31):9661–4.
Wiesel TN, Hubel DH. Comparison of the effects of unilateral and bilateral eye closure on cortical unit responses in kittens. J Neurophysiol. 1965a;28(6):1029–40.
Wiesel TN, Hubel DH. Extent of recovery from the effects of visual deprivation in kittens. J Neurophysiol. 1965b;28(6):1060–72.
Williams KA, et al. Comparison of alpha-chloralose, medetomidine and isoflurane anesthesia for functional connectivity mapping in the rat. Magn Reson Imaging. 2010;28(7):995–1003.
Winner B, et al. Long-term survival and cell death of newly generated neurons in the adult rat olfactory bulb. Eur J Neurosci. 2002;16(9):1681–9.
Wise RG, et al. Resting fluctuations in arterial carbon dioxide induce significant low frequency variations in BOLD signal. Neuroimage. 2004;21(4):1652–64.
Wu L, et al. Metabolic changes in the visual cortex of binocular blindness macaque monkeys: a proton magnetic resonance spectroscopy study. PLoS One. 2013;8(11):e80073.
Yu X, et al. In vivo auditory brain mapping in mice with Mn-enhanced MRI. Nat Neurosci. 2005;8(7):961–8.
Yu X, et al. 3D mapping of somatotopic reorganization with small animal functional MRI. Neuroimage. 2010;49(2):1667–76.

Imaging in Neurology Research III: Neurodegenerative Diseases

30

Heike Endepols and Bernd Neumaier

Contents

Positron emission tomography (PET) plays an outstanding role among imaging technologies since it enables visualization of physiological and pathophysiological processes at the molecular level in real time. Moreover, it combines low invasiveness with high sensitivity, and numerous biological processes can be measured repeatedly and quantitatively. Therefore, it is ideally suited for translational animal research to investigate different pathologies. Especially neurodegenerative diseases are of particular interest since a plethora of imaging agents exist (Table 30.1), which allow to investigate different molecular targets involved in neurodegenerative processes. Furthermore, various animal models with neurodegenerative diseases are available, facilitating to elucidate dysfunctions associated with the progression of neurodegeneration. Above all, small animal models of Alzheimer's and Parkinson's disease are mainly used in this field since they are the most common pathologies of neurodegenerative diseases.

H. Endepols (✉)
Institute of Radiochemistry and Experimental Molecular Imaging, Department of Nuclear Medicine, University Hospital of Cologne, Kerpener Str. 62, Köln 50937, Germany
e-mail: heike.endepols@uk-koeln.de

B. Neumaier
Institute of Radiochemistry and Experimental Molecular Imaging, University Hospital of Cologne, Kerpener Str. 62, Köln 50937, Germany

Forschungszentrum Jülich GmbH, Institute of Neurosciences and Medicine, INM-5: Nuclear Chemistry, Wilhelm-Johnen-Straße, Jülich 52425, Germany
e-mail: bernd.neumaier@uk-koeln.de

30.1 Alzheimer's Disease

Alzheimer's disease (AD) is the most common form of senile dementia characterized by memory loss and cognitive impairment in the elderly population (Cheng et al. 2015). Its structural hallmarks are two types of insoluble protein aggregates, the extracellular amyloid-ß neuritic plaques and the intracellular tau neurofibrillary tangles. Both proteins form fibers with a cross-ß spine, consisting of two stacked pairs of opposed ß-sheets, a so-called steric zipper (Landau et al. 2011; Sawaya et al. 2007). Each part of the zipper is composed of one protein molecule, either U shaped (amyloid-ß: ß-strand-turn-ß-strand motif (Luhrs et al. 2005)) or straight (tau: one ß-strand motif flanked by two unstructured domains (Wegmann et al. 2013)). It has been hypothesized that small molecule tracers bind near the ß-sheets, parallel to the fibril axis (Wu et al. 2011).

F. Kiessling et al. (eds.), *Small Animal Imaging*, DOI 10.1007/978-3-319-42202-2_30

Table 30.1 PET tracers used in small animal models of neurodegenerative diseases

Abbreviation	Full name	Target protein	Chemical structure
[^{11}C]PiB	Pittsburgh compound B; N-[^{11}C]methyl-2-(4′-methylaminophenyl)-6-hydroxybenzothiazole	Amyloid-β	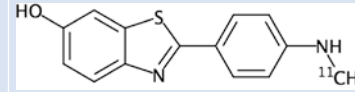
[^{18}F]FDDNP	2-(1-{6-[(2-[^{18}F]Fluoroethyl) (methyl) amino]-2-naphthyl} ethylidene) malononitrile	Amyloid-β	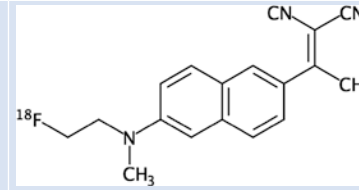
[^{18}F]IBT8	2-(*p*-Methylaminophenyl)-7-(2-[^{18}F]fluoroethoxy) imidazo[2,1-b] benzothiazole	Amyloid-β	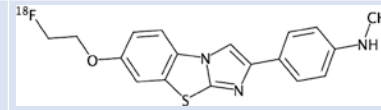
[^{11}C]IBT5	2-(*p*-[^{11}C] Methylaminophenyl)-7-methoxyimidazo[2,1-*b*]benzothiazole	Amyloid-β	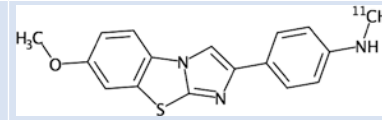
[^{18}F]AV-45 = [^{18}F]florbetaben	(*E*)-2-(2-(2-(2-[^{18}F]Fluoroethoxy) ethoxy) ethoxy)-5-(4-methylaminostyryl)pyridine	Amyloid-β	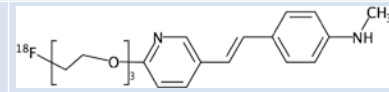
[^{18}F]T807	7-(6-[^{18}F]Fluoropyridin-3-yl)-5H-pyrido[4,3-*b*]indole	Tau	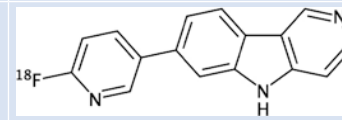
[^{18}F]THK-523	6-(2-[^{18}F]Fluoroethoxy)-2-(4-aminophenyl)quinoline	Tau	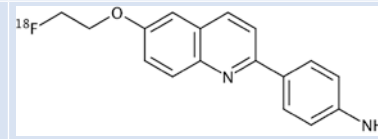
[^{11}C]PBB3	2-((1*E*,3*E*)-4-(6-([^{11}C]Methylamino) pyridin-3-yl)buta-1,3-dienyl)benzo[*d*] thiazol-6-ol	Tau	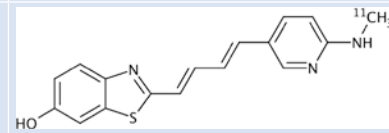
[^{18}F]anle138b	3-(6-[^{18}F]Fluoro-1,3-benzodioxol-5-yl)-5-(3-bromophenyl)-1H-pyrazole	α-synuclein	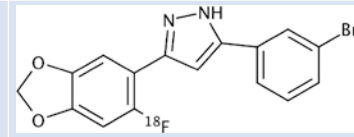
[^{18}F] FE-DAA1106	(N-(5-Fluoro-2-phenoxyphenyl)-N-(2-(2-[^{18}F]fluoroethoxy)-5-methoxybenzyl)acetamide)	TSPO	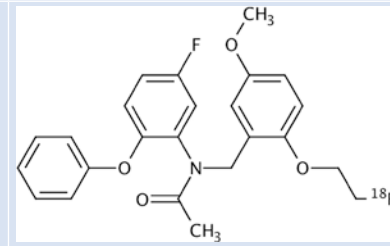

Table 30.1 (continued)

Abbreviation	Full name	Target protein	Chemical structure
[^{11}C]PK11195	1-(2-Chlorophenyl)-N-[^{11}C]methyl-N-(1-methylpropyl)-3-isoquinoline carboxamide	TSPO	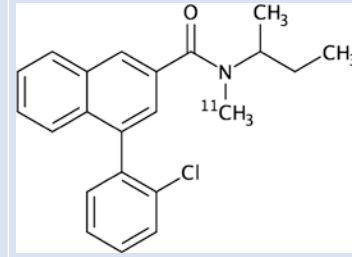
[^{18}F]FDOPA	6-[^{18}F]Fluoro-3,4-dihydroxy-L- phenylalanine	AADC	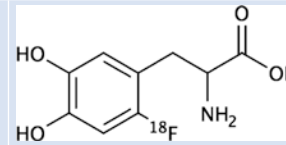
[^{18}F]FP-CIT	N-ω-[^{18}F]Fluoropropyl-2β-carbomethoxy-3β-(4-iodophenyl) nortropane	DAT	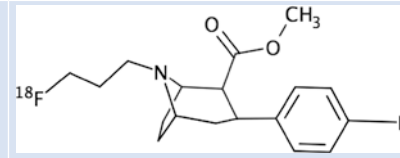
[^{11}C]CFT	[^{11}C]2β-Carbomethoxy-3β-(4-fluorophenyl)tropane	DAT	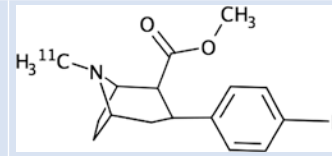
[^{18}F]FECT	2β-carbo-2′-[^{18}F]Fluoroethoxy-3β-(4-chlorophenyl)tropane	DAT	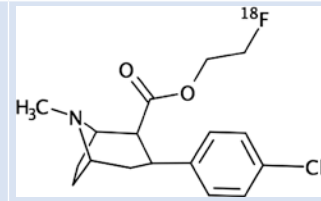
[^{18}F]LBT-999	(E)-N-(4-[^{18}F]Fluorobut-2-enyl)-2β-carbomethoxy-3β-(4′-tolyl)nortropane	DAT	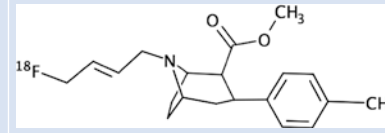
[^{11}C]PE2I	N-(3-Iodopro-2E-enyl)-2β-[^{11}C] carbomethoxy-3β-(4′-methylphenyl) nortropane	DAT	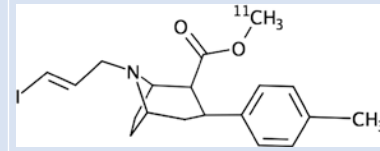
[^{11}C] methylphenidate	[^{11}C]Methyl-2-phenyl-2-(piperidine-2-yl)acetate	DAT	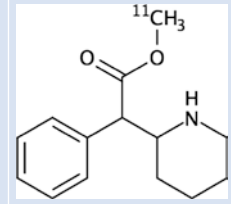

(continued)

Table 30.1 (continued)

Abbreviation	Full name	Target protein	Chemical structure
[^{11}C]DTBZ	[^{11}C](±)Dihydro-tetrabenazine	VMAT2	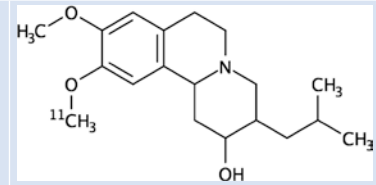
[^{18}F]AV-133	[^{18}F]Fluoropropyl-dihydrotetrabenazine	VMAT2	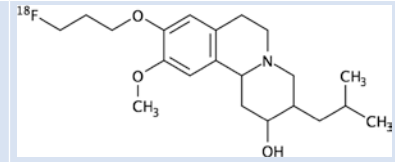
[^{11}C]raclopride	3,5-Dichloro-N-[[(2S)-1-ethylpyrrolidin-2-yl] methyl]-2-hydroxy-6[^{11}C]methoxy-benzamide	D2R	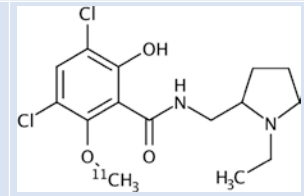
4-[^{18}F]ADAM	(N,N-Dimethyl-2-(2-amino-4-[^{18}F]fluorophenylthio)benzylamine)	SERT	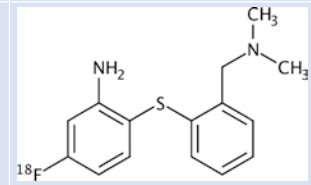

Abbreviations: *AADC* aromatic amino acid decarboxylase, *D2R* dopamine D2 receptor, *DAT* dopamine transporter, *TSPO* translocator protein (18 kDa), *SERT* serotonin transporter, *VMAT2* vesicular monoamine transporter 2

Thioflavin T and its derivatives (e.g., PiB) are thought to interact directly with the ß-sheet backbone, which is accessible in the wide channels created along the filament axis (Wu et al. 2011; Jensen et al. 2011). Other tracers, such as the naphthalene DDNP, may bind in the tubelike cavity within the steric zipper (Landau et al. 2011). Because to date the known radiotracers require stacked ß-sheets for binding, protein monomers and soluble oligomers are invisible in PET. Notably, upcoming innovative strategies use amyloid-ß aggregation inhibitors such as the curcumin derivative CRANAD-58 as probes for fluorescence imaging, detecting both soluble and insoluble amyloid-ß species (Zhang et al. 2013). While this approach still awaits transfer to radiochemistry, the development of PET tracers targeting insoluble amyloid-β species has been very successful.

At the beginning, PET imaging in human Alzheimer's disease focused on the visualization of amyloid-ß deposits. According to the amyloid cascade hypothesis, the central event of the disease is represented by the excessive accumulation of amyloid-β monomers caused by imbalanced amyloid-β clearance. These monomers gradually aggregate into neurotoxic soluble oligomers and finally insoluble fibrils and plaques, which triggers all other pathologic steps such as tau accumulation, cerebral atrophy, and cognitive decline (Karran et al. 2011). Several animal models were developed using known genetic mutations occurring in familial Alzheimer's disease prone to amyloid-ß accumulation (Ribeiro et al. 2013). Plaque formation in these animal models was mainly induced by different combinations of human mutated amyloid precursor protein (APP) and presenilin-1 (PS-1).

The first step in animal research was to reproduce the findings in humans (i.e., reliable visual-

ization of amyloid-ß in the advanced clinical stage and correlation to other disease symptoms) in the available mouse models. Another goal was to develop new ^{18}F-labeled tracers with high affinity, to allow detection of low amyloid-ß loads in preclinical stages (Richards and Sabbagh 2014) and to study the underlying pathophysiological mechanisms. Successful amyloid-ß imaging in mouse models has been realized with the tracers [^{11}C]PiB (Manook et al. 2012; von Reutern et al. 2013; Chen et al. 2015), [^{11}C]IBT5 and [^{18}F]IBT8 (Yousefi et al. 2011a, b), and [^{18}F] AV-45 (=[^{18}F]florbetaben) (Brendel et al. 2015; Poisnel et al. 2012; Rominger et al. 2013). In one study, the therapeutic effect of antibodies directed against amyloid-ß was monitored using the amyloid imaging agents [^{18}F]FDDNP and [^{11}C] PiB. Amyloid removal after antibody application could be clearly demonstrated (Teng et al. 2011). Furthermore, microgliosis was shown by targeting TSPO overexpression with the neuroinflammation marker [^{18}F]FE-DAA1106 (Maeda et al. 2007).

In recent years, the amyloid cascade hypothesis was questioned, because all of the amyloid-ß-centric therapeutic approaches have failed in phase III clinical trials (Karran et al. 2011). Disaggregation of amyloid plaques by active or passive vaccination was not able to reverse cognitive deterioration in AD patients (Lemere 2013). In AD mouse models, anti-amyloid-β antibody treatment was ineffective in repairing neuronal dysfunction while increasing cortical hyperactivity (Busche et al. 2015). Furthermore, it was shown that amyloid plaque deposition measured in postmortem brain tissue hardly correlated with cognitive impairment observed in AD patients (Guerrero-Munoz et al. 2015). A growing body of evidence suggests that soluble amyloid-ß oligomers rather than fully aggregated fibrils are the active neurotoxic species (Bilousova et al. 2016). Soluble amyloid-β, which is released in high quantities from disintegrating plaques (Patton et al. 2006), may be responsible for the failure of immunotherapy in patients (Liu et al. 2015) and also for neuronal hyperactivity found in vaccinated mice (Busche et al. 2012). Unfortunately, there is no radioactive tracer available targeting soluble amyloid-ß oligomers, leaving the key players of amyloid-ß toxicity undetected in patients as well as in animal models.

However, there may be an indirect way to identify the destructive actions of oligomers, because [^{11}C]PiB binds only to a portion of the total aggregated amyloid-ß, which may be associated with those oligomers. There is a low- and high-affinity species of amyloid-ß with a 30-fold difference in affinity (Ni et al. 2013). This explains the puzzling finding in humans as well as in mouse models that the total amounts of insoluble amyloid-ß do not necessarily correlate with [^{11}C]PiB binding (Maeda et al. 2007; Klunk et al. 2005). There is evidence that the subfraction with high affinity to PiB is linked to so-called lipid rafts (Matveev et al. 2014). These structures are detergent-resistant microdomains of the cell membrane enriched in cholesterol and sphingolipids as well as certain proteins (Rushworth and Hooper 2010). They are involved in many cellular functions including synaptic plasticity and maintenance of dendritic spines. Lipid rafts are concentrated in the upper cortical layers in adult rats (Nakadate 2015), overlapping with the localization of high-affinity [^{11}C]PiB binding in humans (Svedberg et al. 2009). It seems that lipid rafts are the physiological site of amyloid-ß production by BACE1 and the gamma-secretase complex, requiring a direct interaction of APP with cholesterol. Furthermore, soluble amyloid-ß oligomers bind to glutamate and prion protein receptors in the same lipid raft, thereby restricting their lateral movement, which leads to the formation of abnormal receptor clusters contributing to synapse loss and cell death (Rushworth and Hooper 2010). It has been suggested that lipid raft components such as cholesterol-associated ganglioside GM1 may serve as a seed for amyloid aggregation and fibril formation (Yanagisawa 2005), inserting and possibly anchoring the first monomers in the lipid raft bilayer (Nicastro et al. 2016). This may lead to oligomers and later to fibrils, which remain attached to the raft. We therefore hypothesize that [^{11}C]PiB imaging is closer to the toxic events of the disease than postmortem histology, which

also stains amorphic amyloid-ß deposits (Ikonomovic et al. 2008).

A comparison of the three transgenic mouse lines APP23, Tg2576, and APP_{swe}-$PS1_{dE9}$ revealed that [^{11}C]PiB with moderate specific activity (100 GBq/µmol) is suitable to visualize amyloid-ß deposits in APP23 mice, but not in the other mouse lines (Snellman et al. 2013). Studies on double transgenic APP/PS1 mice have shown that they are lacking high-affinity [^{11}C]PiB binding sites (Klunk et al. 2005), which may apply to the other PiB-negative mouse models as well. The reasons are so far unclear. Mass spectrometry on human brain samples demonstrated that the high-affinity PiB binding site is associated with the proteins collagen XXVα (CLAC), ubiquitin, tau, and apoE (Matveev et al. 2014). In PiB-negative Tg2576 mice, amyloid-ß aggregates form in lipid rafts and are attached to apoE and tau as well, suggesting similar mechanisms (Kawarabayashi et al. 2004). It is therefore likely that there is another crucial factor for high-affinity PiB binding, which has not yet been discovered.

Because studying solely the actions of amyloid-ß has failed to uncover the key mechanisms of Alzheimer's disease, attention has shifted to tau hyperphosphorylation and accumulation, the latter of which correlates strongly with cognitive status (Nelson et al. 2012). Similar to amyloid tracers, tau tracers bind to the cross-ß-sheet spine of the fibrils, raising the issue of specificity. Tau tracers are designed to detect tau accumulations in the presence of up to 20-fold molar excess of insoluble amyloid-ß (Jensen et al. 2011), to bind an intracellular target and to recognize the different isoforms and posttranslational modifications of the tau protein leading to diverse ultrastructural conformations of neurofibrillary tangles (Villemagne et al. 2015). While tau-specific PET tracers have been successfully applied in human AD patients recently (e.g., [^{18}F]T807 (Chien et al. 2013)), small animal imaging is less far advanced. Transgenic mouse models express human tau with different mutations leading to tau hyperphosphorylation and aggregation (Hochgrafe et al. 2013). Tau deposits in mice have been visualized using the tracers [^{18}F]THK523 (Fodero-Tavoletti et al. 2011) and [^{11}C]PBB3 (Maruyama et al. 2013). However, there is evidence that soluble hyperphosphorylated tau oligomers rather than insoluble neurofibrillary tangles are the neurotoxic species (Guerrero-Munoz et al. 2015). Much like amyloid-ß PET, imaging of tau neurofibrillary tangles therefore shows the final stage of the disease – or even the result of an intervening protective mechanism (Medina and Avila 2014) – but fails to visualize the central pathological process.

In summary, amyloid-ß and tau tracers are invaluable tools for diagnosis in AD patients. But for studying disease pathomechanisms, those tracers are of limited suitability, because they show only late stages in the order of events, which extend over several decades of a human life.

30.2 Parkinson's Disease

Parkinson's disease (PD) is a neurodegenerative disorder with protein aggregates very similar to Alzheimer's disease. The aggregating protein is α-synuclein, which is involved in synaptic functions such as neurotransmitter release and vesicle recycling (Cheng et al. 2011). In Parkinson's disease and other synucleinopathies, the natively unfolded protein forms intracellular protofibrils from pairs of opposing β-sheets composed of 11 residues (Rodriguez et al. 2015), which is the major component of Lewy bodies and Lewy neurites, the hallmark of Parkinson's disease. Because of its affinity to cross-β-sheet structures, the amyloid-ß tracer PiB seemed an ideal candidate to visualize Lewy bodies as well and even showed promising results on α-synuclein filaments generated in vitro (Ye et al. 2008). However, postmortem studies with [^{3}H]PiB in Parkinsonian brain and in vivo studies with [^{11}C]PiB on patients suffering from Parkinson's disease with dementia (PDD) revealed no substantial PiB binding to cerebral α-synuclein deposits (Ye et al. 2008; Maetzler et al. 2008).

A promising approach, which may not only target the mature fibrils but also the toxic oligo-

mers, is provided by aggregation blockers such as diphenyl-pyrazole derivatives, which inhibit the formation of both prion protein and α-synuclein aggregates (Wagner et al. 2013; Levin et al. 2014). The most effective compound anle138b blocks aggregation at the level of small oligomers (Wagner et al. 2013). However, while anle138b binds to α-synuclein fibrils in vitro, no rigid binding to oligomers could be demonstrated (Deeg et al. 2015). 6-[^{18}F]anle138b has been synthesized as a potential PET tracer (Zarrad et al. 2015), but both human and animal imaging studies are lacking so far.

Apart from α-synuclein deposits, PD is characterized by progressive degeneration of the cerebral monoaminergic systems. Loss of dopaminergic neurons in the substantia nigra pars compacta is most striking and accounts for motor impairments like bradykinesia and rigidity. Noradrenergic neurons of the locus coeruleus and serotonergic neurons of the raphe nuclei are affected as well, which may be responsible for resting tremor, attentional problems, impaired executive functions, and depression (Brooks 2007). The reduced number of dopaminergic terminals particularly in the basal ganglia can be compensated by increased dopamine release of the remaining synapses, which is aided by application of levodopa, the dopamine precursor (LeWitt 2015). This dopamine substitution therapy is effective for many years or even decades.

Clinical diagnostic PET imaging monitors the degeneration of the dopaminergic system using a number of approaches: most common is PET imaging with the tracer [^{18}F]FDOPA, i.e. radiolabeled levodopa, which is able to cross the blood-brain barrier (Antonini and DeNotaris 2004). Its uptake expresses the activity of the enzyme DOPA decarboxylase in synaptic terminals of dopaminergic neurons, as well as dopamine storage capacity in synaptic vesicles. With the help of [^{18}F]FDOPA, differential diagnosis of PD versus other diseases of the motor system (e.g., multisystem atrophy) is routinely performed. While in the later stages of PD [^{18}F]FDOPA uptake is related to the density of presynaptic dopaminergic terminals in the striatum, DOPA decarboxylase activity may be upregulated in early stages, leading to underestimation of the degeneration (Antonini and DeNotaris 2004). In patients with minor clinical symptoms, tracers targeting the dopamine transporter (DAT) may be better suited for the estimation of clinical severity (Antonini and DeNotaris 2004). Frequently used is SPECT imaging with the tracer [^{123}I]FP-CIT or [^{123}I]ß-CIT ("DaTscan™"). However, there is evidence that DAT is subject of regulation as well, being downregulated in order to increase extracellular dopamine concentrations (Lee et al. 2000). A third marker for disease progression is the vesicular monoamine transporter (VMAT), which is responsible for dopamine storage in synaptic vesicles. It is not specific for dopaminergic terminals, and tracers therefore show the integrity of the monoaminergic system in general rather than selectively the dopaminergic system (Au et al. 2005). However, since more than 95 % of the monoaminergic nerve terminals in the striatum are dopaminergic, VMAT tracers primarily reflect DA nerve terminal density (Au et al. 2005).

Animal models for PD exist for many decades, the most common being the 6-hydroxydopamine (6-OHDA) neurotoxic model for rodents developed in 1968 (Ungerstedt 1968). Since 6-OHDA does not cross the blood-brain barrier, it has to be injected into the brain, usually into the striatum or the medial forebrain bundle. Typically, 6-OHDA is applied unilaterally, because bilateral lesions affect the animals severely (Blandini and Armentero 2012). With unilateral injections, asymmetrical behavior develops (e.g., rotation) which can be used as a simple behavioral measure of lesion severity (Mokry 1995). For imaging, these "hemiparkinson" models are advantageous as well, because the healthy striatum serves as a convenient baseline control to assess relative tracer binding in the affected striatum. The hemiparkinson model is therefore suitable to develop new tracers detecting Parkinsonian lesions, and numerous rat and mouse studies have described how well the different PET and SPECT tracers reflect lesion severity compared with ex vivo immunohisto-

chemistry. Surprisingly, successful [^{18}F]FDOPA imaging in 6-OHDA rat models was reported only a few years ago (Kyono et al. 2011; Walker et al. 2013; Zlatopolskiy et al. 2015), while previous studies failed to delineate the healthy striatum (mice (Honer et al. 2006); rats (Collantes et al. 2008)). In contrast, DAT imaging is widely performed, using the PET tracers [^{11}C]CFT (Cicchetti et al. 2002), [^{11}C]methylphenidate (Fischer et al. 2012), [^{11}C]PE2I (Inaji et al. 2005), [^{18}F]FECT (Casteels et al. 2010), or [^{18}F]FP-CIT (Choi et al. 2012) and the SPECT tracers [^{123}I]FP-CIT (Booij et al. 2002; Alvarez-Fischer et al. 2007), [^{123}I]ß-CIT (Back et al. 2013), or [^{123}I]altropane (Gleave et al. 2011). All those studies demonstrated that dopaminergic lesions reduce [^{18}F]FDOPA uptake and DAT density in the ipsilesional striatum. VMAT density is reduced as well in the 6-OHDA model, which was measured with the tracers [^{11}C]DTBZ (Sossi et al. 2007; Li et al. 2014; Molinet-Dronda et al. 2015) and [^{18}F]AV-133 (Wang et al. 2010).

Despite the availability of numerous transgenic mouse lines with human mutant α-synuclein, PET imaging in those models has not yet been reported. However, a rat model with unilateral nigral injection of adeno-associated viral vectors (rAAV2/7) encoding human A53T mutant α-synuclein has been thoroughly described with different methods including [^{18}F]FECT-PET. Dopaminergic degeneration reflected by DAT density develops gradually over 30 days after injection and resembles 6-OHDA-induced lesions (Van der Perren et al. 2015).

Small animal PET imaging studies in PD research go far beyond the mere diagnostic level. Neuroprotective therapies were tested on 6-OHDA models using different strategies: one pharmacological approach demonstrated that the COX-2 inhibitor celecoxib is able to suppress neuroinflammation measured with [^{11}C]PK11195 and to prevent degeneration of dopaminergic neurons, measured with the DAT tracer [^{11}C]CFT (Sanchez-Pernaute et al. 2004). The same result was achieved by the nicotinergic α7R agonist PHA 543613 (Serriere et al. 2015), whereby inflammation was assessed with ex vivo autoradiography using [^{3}H]PK11195, and DAT density was measured with [^{18}F]LBT-999.

Gene therapy in PD focuses on enzyme replacement (e.g., of tyrosine hydroxylase and DOPA decarboxylase) and on the addition of neurotrophic factors (Choong et al. 2016). The cerebral dopamine neurotrophic factor (CDNF) was overexpressed in the striatum of a 6-OHDA rat model via adeno-associated virus type 2 (AAV2), which led to functional recovery of dopaminergic neurons, measured with the DAT tracer [^{11}C]CFT (Ren et al. 2013).

A second approach of clinical PET imaging is to assess secondary changes in the basal ganglia, which may lead to medication side effects. Striatal dopamine receptors, particularly the D2 receptors, are often upregulated in PD patients, which can be measured under equilibrium with D2 receptor ligands such as [^{11}C]raclopride (Sioka et al. 2010). Furthermore, in patients prone to levodopa-induced dyskinesias, it has been shown using [^{11}C]raclopride PET that levodopa challenge leads to a strong tracer displacement indicating high and uncontrolled dopamine release in the globus pallidus, possibly via serotonergic terminals (Smith et al. 2015). This may lead to overstimulation of the motor output and most likely contributes to the development of dyskinesias. A potent antidyskinetic drug is (±)3,4-methylenedioxymethamphetamine (MDMA, "ecstasy"), which is a serotonin-, dopamine-, and noradrenaline-releasing agent and reuptake blocker (Meyer 2013). Despite its clear antidyskinetic action in hemiparkinson rats with levodopa-induced abnormal involuntary movements, dopamine release measured with [^{11}C]raclopride was not reduced (Lettfuss et al., 2012). Rather than affecting dopamine release, MDMA seems to act via the serotonergic system (Iravani et al., 2003).

Dyskinesias are not only induced by chronic levodopa treatment but also by dopaminergic cell transplantation, a highly controversial therapeutic approach, which has emerged in the 1980s (Buttery and Barker 2014). Tissue from human fetal ventral mesencephalon was mostly used for grafting, and clinical studies revealed that

although a certain number of patients gained lasting benefits (Ma et al. 2011; Politis and Lindvall 2012), graft-induced dyskinesias were reported as severe side effects (Lane and Winkler 2012). However, the current hope is that modern stem cell-based striatal transplants applied early in the disease process may ameliorate nigrostriatal disease, although the progress of non-motor symptoms will still provide problems (Buttery and Barker 2014). Grafting of fetal mesencephalic cells in 6-OHDA rat models was used to further study the mechanisms of dyskinesias rather than to drive novel cell replacement therapies. It has been shown that dopamine release via serotonergic terminals measured with [^{11}C]raclopride is "buffered" by the presence of grafted dopaminergic neurons (Sahin et al. 2014). Serotoninergic terminal density can be visualized using the serotonin transporter ligand 4-[^{18}F]ADAM (Weng et al. 2013; Chiu et al. 2015).

In summary, PET imaging using small animal PD models is much further advanced than in the field of AD. Research is focused not only on the diagnostic level, but tackles pathomechanisms and therapeutic strategies. An imaging agent targeting α-synuclein deposits is urgently needed for further advances in the field.

References

Alvarez-Fischer D, Blessmann G, Trosowski C, et al. Quantitative [^{123}I]FP-CIT pinhole SPECT imaging predicts striatal dopamine levels, but not number of nigral neurons in different mouse models of Parkinson's disease. Neuroimage. 2007;38:5–12.

Antonini A, DeNotaris R. PET and SPECT functional imaging in Parkinson's disease. Sleep Med. 2004;5:201–6.

Au WL, Adams JR, Troiano AR, Stoessl AJ. Parkinson's disease: in vivo assessment of disease progression using positron emission tomography. Brain Res Mol Brain Res. 2005;134:24–33.

Back S, Raki M, Tuominen RK, et al. High correlation between in vivo [^{123}I]beta-CIT SPECT/CT imaging and post-mortem immunohistochemical findings in the evaluation of lesions induced by 6-OHDA in rats. EJNMMI Res. 2013;3:46.

Bilousova T, Miller CA, Poon WW, et al. Synaptic amyloid-beta oligomers precede p-Tau and differentiate high pathology control cases. Am J Pathol. 2016;186:185–98.

Blandini F, Armentero MT. Animal models of Parkinson's disease. FEBS J. 2012;279:1156–66.

Booij J, de Bruin K, Habraken JB, Voorn P. Imaging of dopamine transporters in rats using high-resolution pinhole single-photon emission tomography. Eur J Nucl Med Mol Imaging. 2002;29:1221–4.

Brendel M, Jaworska A, Griessinger E, et al. Cross-sectional comparison of small animal [^{18}F]-florbetaben amyloid-PET between transgenic AD mouse models. PLoS One. 2015;10:e0116678.

Brooks DJ. Imaging non-dopaminergic function in Parkinson's disease. Mol Imaging Biol. 2007;9:217–22.

Busche MA, Chen X, Henning HA, et al. Critical role of soluble amyloid-beta for early hippocampal hyperactivity in a mouse model of Alzheimer's disease. Proc Natl Acad Sci U S A. 2012;109:8740–5.

Busche MA, Grienberger C, Keskin AD, et al. Decreased amyloid-beta and increased neuronal hyperactivity by immunotherapy in Alzheimer's models. Nat Neurosci. 2015;18:1725–7.

Buttery PC, Barker RA. Treating Parkinson's disease in the 21st century: can stem cell transplantation compete? J Comp Neurol. 2014;522:2802–16.

Casteels C, Lauwers E, Baitar A, et al. In vivo type 1 cannabinoid receptor mapping in the 6-hydroxydopamine lesion rat model of Parkinson's disease. Brain Res. 2010;1316:153–62.

Chen CJ, Bando K, Ashino H, et al. In vivo SPECT imaging of amyloid-beta deposition with radioiodinated imidazo[1,2-a]pyridine derivative DRM106 in a mouse model of Alzheimer's disease. J Nucl Med. 2015;56:120–6.

Cheng F, Vivacqua G, Yu S. The role of alpha-synuclein in neurotransmission and synaptic plasticity. J Chem Neuroanat. 2011;42:242–8.

Cheng X, Zhang L, Lian YJ. Molecular targets in Alzheimer's disease: from pathogenesis to therapeutics. Biomed Res Int. 2015;2015:760758.

Chien DT, Bahri S, Szardenings AK, et al. Early clinical PET imaging results with the novel PHF-tau radioligand [F-18]-T807. J Alzheimers Dis. 2013;34:457–68.

Chiu CH, Li IH, Weng SJ, et al. PET imaging of serotonin transporters with 4-[^{18}F]-ADAM in a Parkinsonian rat model with porcine neural xenografts. Cell Transplant. 2015;25:301–11.

Choi JY, Kim CH, Jeon TJ, et al. Evaluation of dopamine transporters and D2 receptors in hemiparkinsonian rat brains in vivo using consecutive PET scans of [^{18}F]FPCIT and [^{18}F]fallypride. Appl Radiat Isot. 2012;70:2689–94.

Choong CJ, Baba K, Mochizuki H. Gene therapy for neurological disorders. Expert Opin Biol Ther. 2016;16:143–59.

Cicchetti F, Brownell AL, Williams K, et al. Neuroinflammation of the nigrostriatal pathway during progressive 6-OHDA dopamine degeneration in rats monitored by immunohistochemistry and PET imaging. Eur J Neurosci. 2002;15:991–8.

Collantes M, Penuelas I, Alvarez-Erviti L, et al. Use of [11]C-(+)-alpha-dihydrotetrabenazine for the assessment of dopaminergic innervation in animal models of Parkinson's disease. Rev Esp Med Nucl. 2008;27:103–11.

Deeg AA, Reiner AM, Schmidt F, et al. Anle138b and related compounds are aggregation specific fluorescence markers and reveal high affinity binding to alpha-synuclein aggregates. Biochim Biophys Acta. 2015;1850:1884–90.

Fischer K, Sossi V, von Ameln-Mayerhofer A, et al. In vivo quantification of dopamine transporters in mice with unilateral 6-OHDA lesions using [11]C]methylphenidate and PET. Neuroimage. 2012;59:2413–22.

Fodero-Tavoletti MT, Okamura N, Furumoto S, et al. [18]F-THK523: a novel in vivo tau imaging ligand for Alzheimer's disease. Brain. 2011;134:1089–100.

Gleave JA, Farncombe TH, Saab C, Doering LC. Correlative single photon emission computed tomography imaging of [123]I]altropane binding in the rat model of Parkinson's. Nucl Med Biol. 2011;38:741–9.

Guerrero-Munoz MJ, Gerson J, Castillo-Carranza DL. Tau oligomers: the toxic player at synapses in Alzheimer's disease. Front Cell Neurosci. 2015;9:464.

Hochgrafe K, Sydow A, Mandelkow EM. Regulatable transgenic mouse models of Alzheimer disease: onset, reversibility and spreading of Tau pathology. FEBS J. 2013;280:4371–81.

Honer M, Hengerer B, Blagoev M, et al. Comparison of [18]F]FDOPA, [18]F]FMT and [18]F]FECNT for imaging dopaminergic neurotransmission in mice. Nucl Med Biol. 2006;33:607–14.

Ikonomovic MD, Klunk WE, Abrahamson EE, et al. Post-mortem correlates of in vivo PiB-PET amyloid imaging in a typical case of Alzheimer's disease. Brain. 2008;131:1630–45.

Inaji M, Okauchi T, Ando K, et al. Correlation between quantitative imaging and behavior in unilaterally 6-OHDA-lesioned rats. Brain Res. 2005;1064:136–45.

Iravani MM, Jackson MJ, Kuoppamäki M, Smith LA, Jenner P. 3,4-Methylenedioxymethamphetamine (Ecstasy) inhibits dyskinesia expression and normalizes motor activity in 1-methyl-4-phenyl-1,2,3,6-tetrahydropyridine-treated primates. J Neurosci. 2003;23:9107–15.

Jensen JR, Cisek K, Funk KE, et al. Research towards tau imaging. J Alzheimers Dis. 2011;26 Suppl 3:147–57.

Karran E, Mercken M, De Strooper B. The amyloid cascade hypothesis for Alzheimer's disease: an appraisal for the development of therapeutics. Nat Rev Drug Discov. 2011;10:698–712.

Kawarabayashi T, Shoji M, Younkin LH, et al. Dimeric amyloid beta protein rapidly accumulates in lipid rafts followed by apolipoprotein E and phosphorylated tau accumulation in the Tg2576 mouse model of Alzheimer's disease. J Neurosci. 2004;24:3801–9.

Klunk WE, Lopresti BJ, Ikonomovic MD, et al. Binding of the positron emission tomography tracer Pittsburgh compound-B reflects the amount of amyloid-beta in Alzheimer's disease brain but not in transgenic mouse brain. J Neurosci. 2005;25:10598–606.

Kyono K, Takashima T, Katayama Y, et al. Use of [18]F] FDOPA-PET for in vivo evaluation of dopaminergic dysfunction in unilaterally 6-OHDA-lesioned rats. EJNMMI Res. 2011;1:25.

Landau M, Sawaya MR, Faull KF, et al. Towards a pharmacophore for amyloid. PLoS Biol. 2011;9:e1001080.

Lane EL, Winkler C. L-DOPA- and graft-induced dyskinesia following transplantation. Prog Brain Res. 2012;200:143–68.

Lee CS, Samii A, Sossi V, et al. In vivo positron emission tomographic evidence for compensatory changes in presynaptic dopaminergic nerve terminals in Parkinson's disease. Ann Neurol. 2000;47:493–503.

Lemere CA. Immunotherapy for Alzheimer's disease: hoops and hurdles. Mol Neurodegener. 2013;8:36.

Lettfuss NY, Fischer K, Sossi V, Pichler BJ, von Ameln-Mayerhofer A. Imaging DA release in a rat model of L-DOPA-induced dyskinesias: A longitudinal in vivo PET investigation of the antidyskinetic effect of MDMA. Neuroimage 2012;63:423–33.

Levin J, Schmidt F, Boehm C, et al. The oligomer modulator anle138b inhibits disease progression in a Parkinson mouse model even with treatment started after disease onset. Acta Neuropathol. 2014;127:779–80.

LeWitt PA. Levodopa therapy for Parkinson's disease: pharmacokinetics and pharmacodynamics. Mov Disord. 2015;30:64–72.

Li X, Chen Z, Tang J, et al. Synthesis and biological evaluation of 10-[11]C]-dihydrotetrabenazine as a vesicular monoamine transporter 2 radioligand. Arch Pharm (Weinheim). 2014;347:313–9.

Liu YH, Wang YR, Xiang Y, et al. Clearance of amyloid-beta in Alzheimer's disease: shifting the action site from center to periphery. Mol Neurobiol. 2015;51:1–7.

Luhrs T, Ritter C, Adrian M, et al. 3D structure of Alzheimer's amyloid-beta(1–42) fibrils. Proc Natl Acad Sci U S A. 2005;102:17342–7.

Ma Y, Peng S, Dhawan V, Eidelberg D. Dopamine cell transplantation in Parkinson's disease: challenge and perspective. Br Med Bull. 2011;100:173–89.

Maeda J, Ji B, Irie T, et al. Longitudinal, quantitative assessment of amyloid, neuroinflammation, and anti-amyloid treatment in a living mouse model of Alzheimer's disease enabled by positron emission tomography. J Neurosci. 2007;27:10957–68.

Maetzler W, Reimold M, Liepelt I, et al. [11]C]PIB binding in Parkinson's disease dementia. Neuroimage. 2008;39:1027–33.

Manook A, Yousefi BH, Willuweit A, et al. Small-animal PET imaging of amyloid-beta plaques with [11]C] PiB and its multi-modal validation in an APP/PS1 mouse model of Alzheimer's disease. PLoS One. 2012;7:e31310.

Maruyama M, Shimada H, Suhara T, et al. Imaging of tau pathology in a tauopathy mouse model and in Alzheimer patients compared to normal controls. Neuron. 2013;79:1094–108.

Matveev SV, Spielmann HP, Metts BM, et al. A distinct subfraction of Abeta is responsible for the high-affinity Pittsburgh compound B-binding site in Alzheimer's disease brain. J Neurochem. 2014;131:356–68.

Medina M, Avila J. New perspectives on the role of tau in Alzheimer's disease. Implications for therapy. Biochem Pharmacol. 2014;88:540–7.

Meyer JS. 3,4-methylenedioxymethamphetamine (MDMA): current perspectives. Subst Abuse Rehabil. 2013;4:83–99.

Mokry J. Experimental models and behavioural tests used in the study of Parkinson's disease. Physiol Res. 1995;44:143–50.

Molinet-Dronda F, Gago B, Quiroga-Varela A, et al. Monoaminergic PET imaging and histopathological correlation in unilateral and bilateral 6-hydroxydopamine lesioned rat models of Parkinson's disease: a longitudinal in-vivo study. Neurobiol Dis. 2015;77:165–72.

Nakadate K. Developmental changes in the flotillin-1 expression pattern of the rat visual cortex. Neuroscience. 2015;292:101–11.

Nelson PT, Alafuzoff I, Bigio EH, et al. Correlation of Alzheimer disease neuropathologic changes with cognitive status: a review of the literature. J Neuropathol Exp Neurol. 2012;71:362–81.

Ni R, Gillberg PG, Bergfors A, et al. Amyloid tracers detect multiple binding sites in Alzheimer's disease brain tissue. Brain. 2013;136:2217–27.

Nicastro MC, Spigolon D, Librizzi F, et al. Amyloid beta-peptide insertion in liposomes containing GM1-cholesterol domains. Biophys Chem. 2016;208:9–16.

Patton RL, Kalback WM, Esh CL, et al. Amyloid-beta peptide remnants in AN-1792-immunized Alzheimer's disease patients: a biochemical analysis. Am J Pathol. 2006;169:1048–63.

Poisnel G, Dhilly M, Moustie O, et al. PET imaging with [^{18}F]AV-45 in an APP/PS1-21 murine model of amyloid plaque deposition. Neurobiol Aging. 2012;33:2561–71.

Politis M, Lindvall O. Clinical application of stem cell therapy in Parkinson's disease. BMC Med. 2012;10:1.

Ren X, Zhang T, Gong X, et al. AAV2-mediated striatum delivery of human CDNF prevents the deterioration of midbrain dopamine neurons in a 6-hydroxydopamine induced parkinsonian rat model. Exp Neurol. 2013;248:148–56.

Ribeiro FM, Camargos ER, de Souza LC, Teixeira AL. Animal models of neurodegenerative diseases. Rev Bras Psiquiatr. 2013;35 Suppl 2:S82–91.

Richards D, Sabbagh MN. Florbetaben for PET imaging of beta-amyloid plaques in the brain. Neurol Ther. 2014;3:79–88.

Rodriguez JA, Ivanova MI, Sawaya MR, et al. Structure of the toxic core of alpha-synuclein from invisible crystals. Nature. 2015;525:486–90.

Rominger A, Brendel M, Burgold S, et al. Longitudinal assessment of cerebral beta-amyloid deposition in mice overexpressing Swedish mutant beta-amyloid precursor protein using ^{18}F-florbetaben PET. J Nucl Med. 2013;54:1127–34.

Rushworth JV, Hooper NM. Lipid Rafts: Linking Alzheimer's amyloid-beta production, aggregation, and toxicity at neuronal membranes. Int J Alzheimers Dis. 2010;2011:603052.

Sahin G, Thompson LH, Lavisse S, et al. Differential dopamine receptor occupancy underlies L-DOPA-induced dyskinesia in a rat model of Parkinson's disease. PLoS One. 2014;9:e90759.

Sanchez-Pernaute R, Ferree A, Cooper O, et al. Selective COX-2 inhibition prevents progressive dopamine neuron degeneration in a rat model of Parkinson's disease. J Neuroinflammation. 2004;1:6.

Sawaya MR, Sambashivan S, Nelson R, et al. Atomic structures of amyloid cross-beta spines reveal varied steric zippers. Nature. 2007;447:453–7.

Serriere S, Domene A, Vercouillie J, et al. Assessment of the protection of dopaminergic neurons by an alpha7 nicotinic receptor agonist, PHA 543613 using [^{18}F] LBT-999 in a Parkinson's disease rat model. Front Med (Lausanne). 2015;2:61.

Sioka C, Fotopoulos A, Kyritsis AP. Recent advances in PET imaging for evaluation of Parkinson's disease. Eur J Nucl Med Mol Imaging. 2010;37:1594–603.

Smith R, Wu K, Hart T, et al. The role of pallidal serotonergic function in Parkinson's disease dyskinesias: a positron emission tomography study. Neurobiol Aging. 2015;36:1736–42.

Snellman A, Lopez-Picon FR, Rokka J, et al. Longitudinal amyloid imaging in mouse brain with ^{11}C-PIB: comparison of APP23, Tg2576, and APPswe-PS1dE9 mouse models of Alzheimer disease. J Nucl Med. 2013;54:1434–41.

Sossi V, Holden JE, Topping GJ, et al. In vivo measurement of density and affinity of the monoamine vesicular transporter in a unilateral 6-hydroxydopamine rat model of PD. J Cereb Blood Flow Metab. 2007;27:1407–15.

Svedberg MM, Hall H, Hellstrom-Lindahl E, et al. [^{11}C] PIB-amyloid binding and levels of Abeta40 and Abeta42 in postmortem brain tissue from Alzheimer patients. Neurochem Int. 2009;54:347–57.

Teng E, Kepe V, Frautschy SA, et al. [^{18}F]FDDNP microPET imaging correlates with brain Abeta burden in a transgenic rat model of Alzheimer disease: effects of aging, in vivo blockade, and anti-Abeta antibody treatment. Neurobiol Dis. 2011;43:565–75.

Ungerstedt U. 6-Hydroxy-dopamine induced degeneration of central monoamine neurons. Eur J Pharmacol. 1968;5:107–10.

Van der Perren A, Toelen J, Casteels C, et al. Longitudinal follow-up and characterization of a robust rat model for Parkinson's disease based on overexpression of alpha-synuclein with adeno-associated viral vectors. Neurobiol Aging. 2015;36:1543–58.

Villemagne VL, Fodero-Tavoletti MT, Masters CL, Rowe CC. Tau imaging: early progress and future directions. Lancet Neurol. 2015;14:114–24.

von Reutern B, Grunecker B, Yousefi BH, et al. Voxel-based analysis of amyloid-burden measured with [^{11}C]PiB PET in a double transgenic mouse model of Alzheimer's disease. Mol Imaging Biol. 2013;15:576–84.

Wagner J, Ryazanov S, Leonov A, et al. Anle138b: a novel oligomer modulator for disease-modifying therapy of neurodegenerative diseases such as prion and Parkinson's disease. Acta Neuropathol. 2013;125:795–813.

Walker MD, Dinelle K, Kornelsen R, et al. Measuring dopaminergic function in the 6-OHDA-lesioned rat: a comparison of PET and microdialysis. EJNMMI Res. 2013;3:69.

Wang JL, Oya S, Parhi AK, et al. In vivo studies of the SERT-selective [^{18}F]FPBM and VMAT2-selective [^{18}F]AV-133 radiotracers in a rat model of Parkinson's disease. Nucl Med Biol. 2010;37:479–86.

Wegmann S, Medalsy ID, Mandelkow E, Muller DJ. The fuzzy coat of pathological human Tau fibrils is a two-layered polyelectrolyte brush. Proc Natl Acad Sci U S A. 2013;110:E313–21.

Weng SJ, Shiue CY, Huang WS, et al. PET imaging of serotonin transporters with 4-[^{18}F]-ADAM in a Parkinsonian rat model. Cell Transplant. 2013;22:1295–305.

Wu C, Bowers MT, Shea JE. On the origin of the stronger binding of PIB over thioflavin T to protofibrils of the Alzheimer amyloid-beta peptide: a molecular dynamics study. Biophys J. 2011;100:1316–24.

Yanagisawa K. GM1 ganglioside and the seeding of amyloid in Alzheimer's disease: endogenous seed for Alzheimer amyloid. Neuroscientist. 2005;11:250–60.

Ye L, Velasco A, Fraser G, et al. In vitro high affinity alpha-synuclein binding sites for the amyloid imaging agent PIB are not matched by binding to Lewy bodies in post-mortem human brain. J Neurochem. 2008;105:1428–37.

Yousefi BH, Drzezga A, von Reutern B, et al. A novel ^{18}F-labeled imidazo[2,1-b]benzothiazole (IBT) for high-contrast PET imaging of beta-amyloid plaques. ACS Med Chem Lett. 2011a;2:673–7.

Yousefi BH, Manook A, Drzezga A, et al. Synthesis and evaluation of ^{11}C-labeled imidazo[2,1-b]benzothiazoles (IBTs) as PET tracers for imaging beta-amyloid plaques in Alzheimer's disease. J Med Chem. 2011b;54:949–56.

Zarrad F, Zlatopolskiy BD, Neumaier B. Preparation of 6-[^{18}F]Anle138b: a novel PET-tracer potentially suitable for imaging of neurodegenerative and prion diseases. Eur J Nucl Med Mol Imaging. 2015;42:S281-S.

Zhang X, Tian Y, Li Z, et al. Design and synthesis of curcumin analogues for in vivo fluorescence imaging and inhibiting copper-induced cross-linking of amyloid beta species in Alzheimer's disease. J Am Chem Soc. 2013;135:16397–409.

Zlatopolskiy BD, Zischler J, Urusova EA, et al. A practical one-pot synthesis of positron emission tomography (PET) tracers via nickel-mediated radiofluorination. ChemistryOpen. 2015;4:457–62.

When Photons Meet Protons: Optogenetics, Calcium Signal Detection, and fMRI in Small Animals

31

Xin Yu

Contents

31.1 Overview

In the new era of brain research, highlighted by the Human Brain Project and BRAIN Initiative, how to link the cellular, circuit, and system aspects of brain function is one of the key aims of this mission. The multimodal neuroimaging methodology has provided us a promising platform. Among the numerous efforts on brain functional mapping, the combination of optogenetics, calcium signal detection by genetically encoded indictors, and functional magnetic resonance imaging (fMRI) presents a unique perspective to better understand brain function. This chapter will focus on the recent application of optogenetic tools for fMRI studies, as well as a recent development of the fiber optic-mediated simultaneous calcium recording with fMRI. These studies lead to a new concept, the single unit of neurovascular coupling (SUNC) (Fig. 31.1), to better understand the signal propagation through the neuron-glia-vessel network in the brain of rodents.

X. Yu
Translational Neuroimaging and Neural Control Group, High Field Magnetic Resonance Department, Max Planck Institute for Biological Cybernetics, Tuebingen, Germany
e-mail: xin.yu@tuebingen.mpg.de

31.2 Methodological Development

31.2.1 Optogenetics

31.2.1.1 Lighten the Brain with Channelrhodopsin

The optogenetic studies, i.e., channelrhodopsin-mediated optical control of neural activity, can be traced back to the study on the phototactic responses of *Chlamydomonas reinhardtii*, a single-cell green alga (Schmidt and Eckert 1976). Calcium ions were reported to mediate the swimming direction of the alga (Schmidt and Eckert 1976), and the rhodopsin in the eyespot of the alga could regulate calcium current in response to flash of light (Harz and Hegemann

F. Kiessling et al. (eds.), *Small Animal Imaging*, DOI 10.1007/978-3-319-42202-2_31

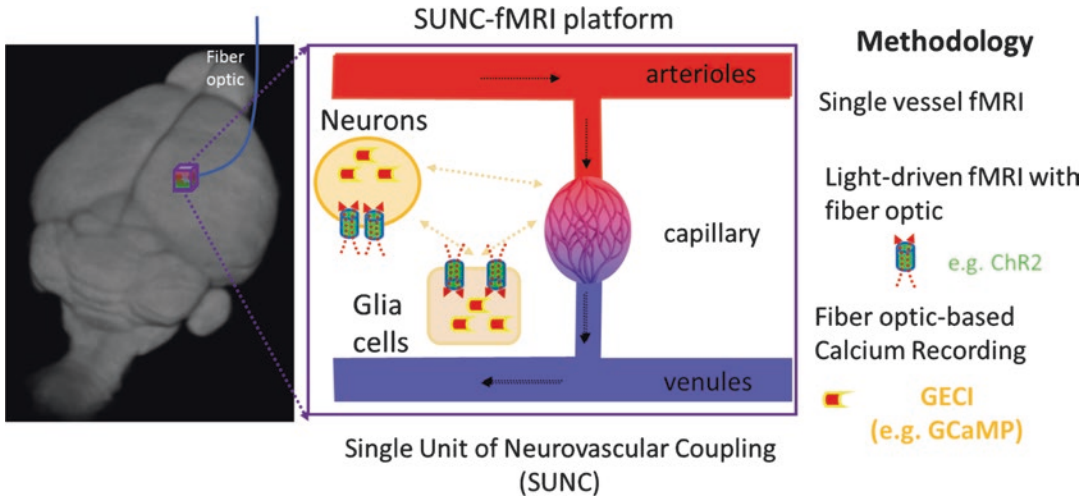

Fig. 31.1 The "single unit" of neurovascular coupling is based on the fiber optic inserting into the targeted brain region of interests. The single-vessel fMRI method was previously developed by Yu et al. to specifically map fMRI signal from individual vessels penetrating the cortex of the rat brain (Yu et al. 2012, 2014). Both light-sensitive proteins (e.g., channelrhodopsin-2, ChR2) (Nagel et al. 2003) and genetically encoded calcium indicators (e.g., GCaMP6) (Akerboom et al. 2013) can be specifically expressed into neurons or glial cells. Upon optical stimulation, the calcium signal from distinct groups of cells can be directly recorded by the fiber optic, and the fMRI signal from individual vessels (arterioles and venules) surrounding the fiber-optic target regions can be mapped simultaneously. The neuron-glia-vessel network can be studied in the single-unit perspective with cellular and vascular specificity. The fiber optic can be inserted to target any brain regions of interests, which is not limited to the superficial cortex as the conventional optical imaging schemes. This SUNC fMRI platform allows the global investigation of the neurovascular coupling in the rat brain

1991) (Fig. 31.2). These studies led to the characterization of the light-sensitive ion channel, called channelrhodopsin-1 (ChR1), from the *C. reinhardtii*. The ChR1 showed light-sensitive conductance for proton (H+) by expressing the ChR1 cDNA in *Xenopus* oocytes (Nagel et al. 2002). In the following year, a second channelrhodopsin (ChR2) was discovered to show cation permeability, including Na^+ and Ca^{2+}, which was tested in both oocytes and mammalian cells. The mammalian brain has sufficient baseline retinal for ChR2 to be photoactivated. The fast kinetics and high cation conductance of the ChR2-mediated photocurrent made it ready to be used to depolarize the membrane potential of neurons. In 2005, Karl Deisseroth's group expressed ChR2 in the rat hippocampal cell cultures through lentiviral vectors, detecting robust light-evoked neural spiking events (Boyden et al. 2005). In contrast to the contemporary genetically encoded photon-stimulation methods, which used synthetized photo-triggering ligand-gated ion channels, such as $P2X_2$ or TRPV1, or engineered K^+ channel (Brake et al. 1994; Valera et al. 1994; Zemelman et al. 2003; Banghart et al. 2004; Lima and Miesenbock 2005), the ChR2-based optogenetic method was quickly adapted for broad neuroscientific applications. Since the ChR2 cDNA can be packaged into the viral vectors with different cell type-specific promoters, one of the key highlights of the optogenetic method is the feasibility to express ChR2 with cellular specificity.

The cell-specific expression of ChR2 in the animal brain has been mainly established in two lines of studies. The first one is to establish a variety of transgenic mouse lines. Using the bacterial artificial chromosome (BAC) transgenic strategy, a few BAC transgenic mouse lines have been established for optogenetic studies (Zhao et al. 2011a) (Table 31.1). In addition, using a Cre reporter mice (Madisen et al. 2010), it is feasible to produce the Cre recombinase – inducible *ChR2* knock-in mouse line with robust ChR2 expression in specific cell types (Madisen et al. 2012). Besides the transgenic mice lines for cell-specific

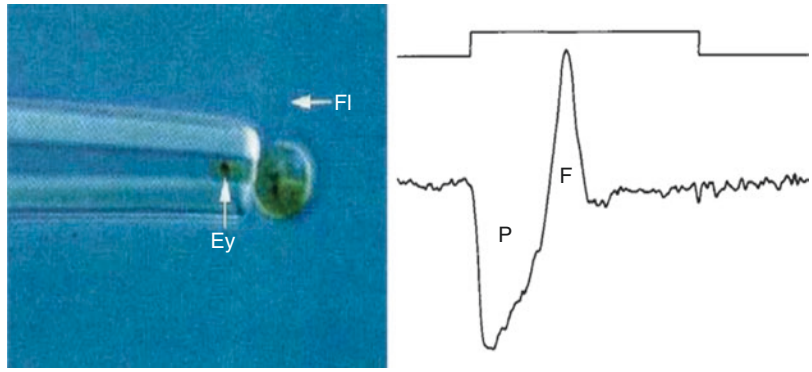

Fig. 31.2 Light-induced photocurrent through eyespot of the alga. The *left panel* is the electrode attached to the eyespot of the *C. reinhardtii*. The *right panel* is the recorded photocurrent from the alga (Harz et al. 1991)

Table 31.1 The ChR2 transgenic mouse line resources from Jackson Laboratory (Zhao et al. 2011a)

Viral vectors	Stock number/mouse lines	Web links
VGAT-ChR2(H134R)-EYFP	014548 B6.Cg-Tg(Slc32a1-COP4*H134R/EYPF)8Gfng/J	http://jaxmice.jax.org/strain/014548.html
ChAT-ChR2(H134R)-EYFP	014546 B6.Cg-Tg(Chat-COP4*H134R/EYPF)6Gfng/J	http://jaxmice.jax.org/strain/014546.html
ChAT-ChR2(H134R)-EYFP	014545 B6.Cg-Tg(Chat-COP4*H134R/EYPF)5Gfng/J	http://jaxmice.jax.org/strain/014545.html
TPH2-ChR2(H134R)-EYFP	014555 B6;SJL-Tg(Tph2-COP4*H134R/EYPF)5Gfng/J	http://jaxmice.jax.org/strain/014555.html
Pvalb-ChR2(H134R)-EYFP	012355 B6; SJL-Tg(Pvalb-COP4*H134R/EYPF)15Gfng/J	http://jaxmice.jax.org/strain/012355.html

ChR2 expression, the direct in vivo injection of viral vectors into targeted brains has been largely implemented to study the light-evoked neural activity in animals (Adamantidis et al. 2007; Alilain et al. 2008; Gradinaru et al. 2009; Sohal et al. 2009; Cruikshank et al. 2010; Johansen et al. 2010; Stuber et al. 2010; Aponte et al. 2011). The optogenetic viral vector sequences can be found from the optogenetic source center[1]. Meanwhile, the customer-made or commercial viral vectors can be directly ordered through the Upenn[2] and UNC vector core[3].

[1]The Optogenetics Resource Center can be accessed online https://www.med.unc.edu/genetherapy/vectorcore.

[2]The Upenn vector core webpage: http://www.med.upenn.edu/gtp/vectorcore/.

[3]The UNC vector core webpage: https://www.med.unc.edu/genetherapy/vectorcore.

31.2.1.2 Optogenetic Tool Development from ChR2

Significant efforts have been made to expand the optogenetic tools. The ChR2 provided a model protein for genetic modification and homologous protein searching from other microbial organisms. Among the numerous opsin candidates, we will discuss ChR2 variants and its homologous proteins from three aspects: kinetics, spectral sensitivity, and ion selectivity. A more detailed analysis of the features of ChR2 variants was reported by Lin et al. (Lin 2011).

The fast kinetics of ChR2 upon light pulse exposure makes it suitable to depolarize the membrane potentials, especially to elicit the millisecond action potential (Fig. 31.3). However, the wide-type ChR2 can lead to extra spikes to a single pulse, long-term plateau depolarization and the lack of sustained spiking at high frequency (40 Hz gamma range) (Gunaydin et al. 2010). The

chimeric combination of the ChR1 and ChR2 with site-specific mutation, i.e., CHEF channel, has faster closure time and can maintain sustainable responses to 20 Hz (Lin et al. 2009). In addition, the ChETA channel with point mutation of ChR2 (Glu123 replaced by Thr) has improved kinetics to allow sustained spike trains up to 200 Hz (Gunaydin et al. 2010). Besides genetic modification to improve the fast kinetic features of ChR2, by replacing the Cys128 of ChR2 by Thr, Ala, or Ser, the membrane potential depolarization can be maintained in long timescale as a step function (Berndt et al. 2009). The genetic modification provided a large pool of variable kinetics of the ChR2-mediated spike events.

The development of ChR variants extends spectral sensitive range from blue to red light. The ChR2 opsin is sensitive to blue light given its peak spectral absorption at 480 nm (Fig. 31.4). In the multicellular green algae, *Volvox carteri*, a novel opsin called *Volvox* channelrhodopsin-1 (VChR1) was discovered with red-shifted absorption spectrum (Zhang et al. 2008). To fuse the N-terminal sequence of the *Chlamydomonas reinhardtii* ChR1 coding sequence (Nagel et al. 2002) with the C-terminal sequence of *Volvox carteri* ChR1 (Zhang et al. 2008), a chimeric C1V1 channel was developed to shift the absorption peak up to 70 nm (Yizhar et al. 2011). To further push the light penetration to the tissue so as to elicit the opsin-mediated neural activity, a red-activable ChR variant (ReaChR) was developed to be sensitive from orange to red light (590–630 nm) (Lin et al. 2013).

Besides the opsin variants permeable to cations, another light-sensitive ion channel, halorhodopsin (NpHR), was discovered from halobacterium *Natronomonas pharaonis* to pump to Cl^- into cells (Bamberg et al. 1993). Neurons

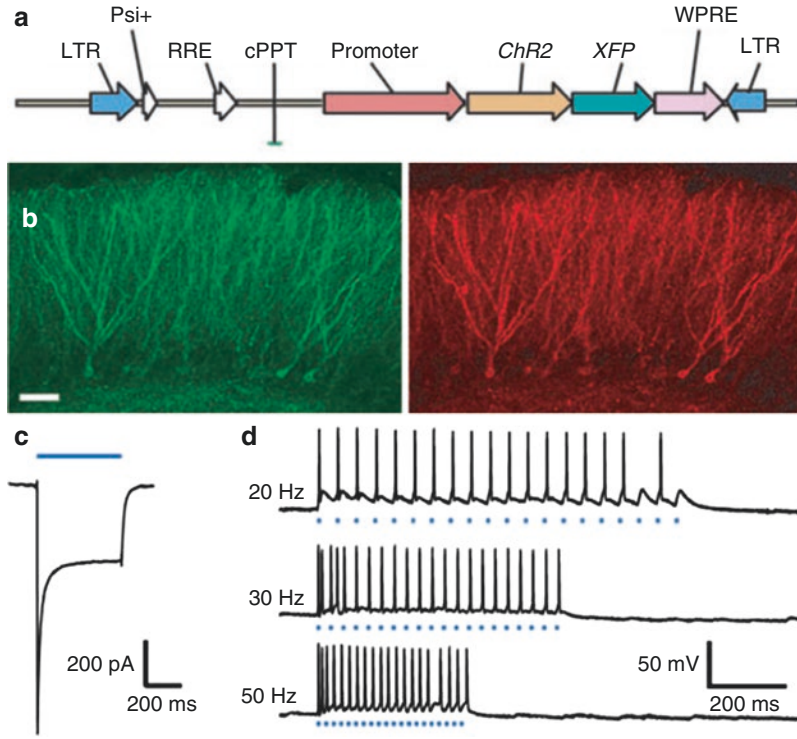

Fig. 31.3 The light-evoked neural activity from the hippocampal slice culture. (**a**) The lentiviral vector map to encode the ChR2 with specific promoter. (**b**) The dentate gyrus granule cells expressing ChR2-EYFP in the adult mouse hippocampus (*left*, EYFP; *right*, rhodamine-conjugated anti-GFP). (**c**) The inward current in a voltage-clamped neuron in an acute slice evoked by 500 ms of 470 nm *blue* light (indicated by *blue bar*). (**d**) Voltage traces showing spikes in a current-clamped hippocampal dentate gyrus hilar interneuron evoked by trains of light pulses (each *blue dash* represents one 10 ms light flash) (Zhang et al. *Nature Methods*, 2006) (Reprinted by permission from Macmillan Publishers Ltd: Nature Methods, Zhang et al., copyright 2006.)

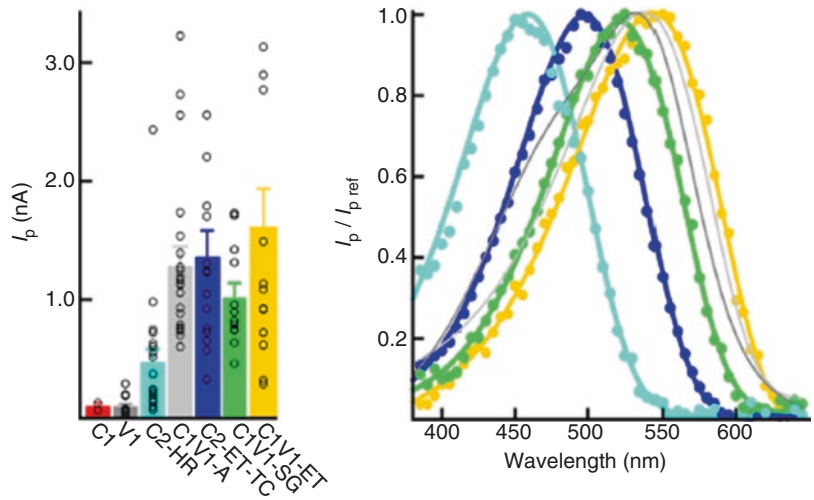

Fig. 31.4 The peak photocurrent from different opsins (ChR1/ChR2 (C1, C2), RChR1, and chimeric variants, C1V1) and their absorption spectra (Preigg et al. *JBC* 2012) Preigg et al. Color-tuned channelrhodopsins for multiwavelength optogenetics. Journal of Biological Chemistry, 2012; 287:31804-12. With permission from American Society for Biochemistry and Molecular Biology.)

expressing NpHR could be hyperpolarized by the orange light up to 580 nm (Zhang et al. 2007). Genetic modification has made the third generation of $NpHR_{3.0}$ to improve the Cl^- conductance and increased the hyperpolarization efficiency (Gradinaru et al. 2008, 2010). In addition, a light-sensitive proton pump, called archaerhodopsin-3, from *Halorubrum sodomense* was discovered to hyperpolarize neurons by yellow light with the similar efficiency to $NpHR_{3.0}$ (Chow et al. 2010).

These studies make it possible to use optogenetic tools to either excite or inhibit neurons in the brain. Besides the cellular specificity of the optical stimulation scheme, the optogenetic method provides a unique advantage to combine with fMRI brain mapping given the lack of electromagnetic inference with radio-frequency (RF) signal.

31.2.2 Genetically Encoded Calcium Indicators (GECIs)

31.2.2.1 Read the Brain Calcium Signal by Genetically Encoded Calcium Indicators (GECIs)

Calcium signal is a key indicator of neuronal activity and the second messenger to mediate crucial intracellular signaling transduction. In contrast to the synthetic molecules/chemicals served as fluorescent calcium indicators, e.g., Calcium Green-1 (Eberhard and Erne 1991), Fluo-3 (Kao et al. 1989), Oregon Green 488 BAPTA (OGB) (Svoboda et al. 1997), Ca2+ crimson (Aad et al. 2012), etc., GECIs have high cellular specificity and reduced toxicity with advantage of cellular specific expression of indictors into the brain (Paredes et al. 2008). One scheme of GECI development is to bind the blue- or cyan-emitting mutant of green fluorescent protein (GFP) and an enhanced GFP, with the endogenous calcium indicators, calmodulin, and calmodulin-binding peptide M13 from myosin light chain kinase (Miyawaki et al. 1997). Ca binding leads to the protein conformational changes and increases the fluorescence resonance energy transfer (FRET) of the two GFP variants. The emitted fluorescent signal can be imaged to estimate the calcium signal changes in cells expressing GECIs. The FRET-based calcium indicators include the cameleon (Miyawaki et al. 1997, 1999) and $FIP\text{-}CB_{SM}$ (Persechini et al. 1997; Romoser et al. 1997). In contrast to the two GFP variants, a single circularly permutated EGFP (cpEGFP, the N and C terminals of GFP are fused) (Baird et al. 1999) was bound to calmodulin and M13, called GCaMP (Fig. 31.5), showing the Ca^{2+}-dependent fluorescent changes (Nakai et al. 2001). GCaMP was first expressed in the smooth muscle of the transgenic

mice to show the feasibility of transient Ca^{2+} signal detection (Ji et al. 2004). The first in vivo mammalian study was performed by using the third generation of the GCaMP (GCaMP3) to measure the calcium signal from the motor cortex of the awake mouse (Tian et al. 2009). The GCaMP3 has better photostability and is more stable to the body temperature than the early generations. The range of the fluorescent signal and calcium affinity of GCaMPs have been subsequently improved by genetic modification. The new generation of GCaMPs has multiple variants with different calcium binding kinetics (GCaMP6f, 6m, 6s) (Chen et al. 2013). The GCaMP6f (fast kinetics) allows the detection of single action potential from the neuronal soma (Fig. 31.6).

Besides the GCaMPs, the calcium indicators were further developed to emit fluorescent signal at a broad spectrum from blue to red light (Fig. 31.7) (Zhao et al. 2011b). The multispectral GECIs allowed the imaging of calcium signal at multiple wavelengths simultaneously. Also, it makes it possible to measure the light-driven calcium signal by optogenetics. By co-expressing RCaMP with ChR2 into cells, it is possible to depolarize cells and record calcium signal from different spectral channels (Akerboom et al. 2013). Thus, the tools using photons to study brain function are ready to be combined with the proton-based imaging methodology.

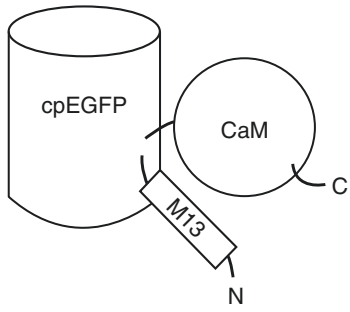

Fig. 31.5 The schematic structure of GCaMP protein (Nakai et al. *Nat. Biotech*. 2001) (Reprinted by permission from Macmillan Publishers Ltd: Nature Biotechnology, Nakai et al., copyright 2001.)

31.2.3 Small Animal fMRI

31.2.3.1 Basics of Functional MRI Methodology

Functional MRI (fMRI) can be considered as a variety of MR imaging schemes to map brain function, because the typical MRI methods are based on the water protons, which are highly enriched in the living tissues up to 70 % of the brain content so as to provide sufficient MR signal to be detected. The basic mechanism of fMRI brain functional mapping is to detect the altered MR properties of the water protons, e.g., relaxation times based on spin-lattice interaction or spin-spin interaction, in a given voxel of the brain area with or without neuronal activation.

The different mapping schemes are based on the biological changes in the local active brain areas. One of the most popular schemes is the neurovascular coupled hemodynamic changes underlying fMRI signal. Ogawa et al. reported that the blood deoxyhemoglobin served as the endogenous contrast in the brain to decrease the T2*-weighted signal in the MRI images due to its paramagnetic property (Ogawa et al. 1990). This work revealed that the physiological changes, such as the oxy-/deoxyhemoglobin ratio changes, in the local brain area can be detected by MRI directly. In contrast to the endogenous hemoglobin as an MRI contrast,

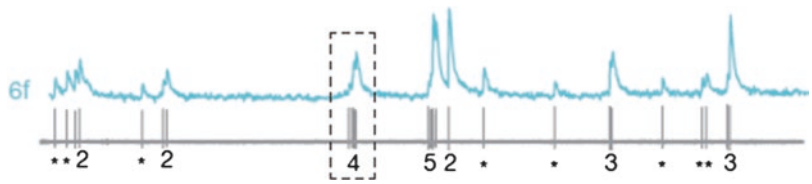

Fig. 31.6 The GCaMP6f-mediated calcium signal was detected from the individual neuron. The light blue line is the recorded calcium transient signal. The *black line* is the recorded action potentials (* means single action potential) (Chen et al. 2013) (Reprinted by permission from Macmillan Publishers Ltd: Nature, Chen et al., copyright 2013.)

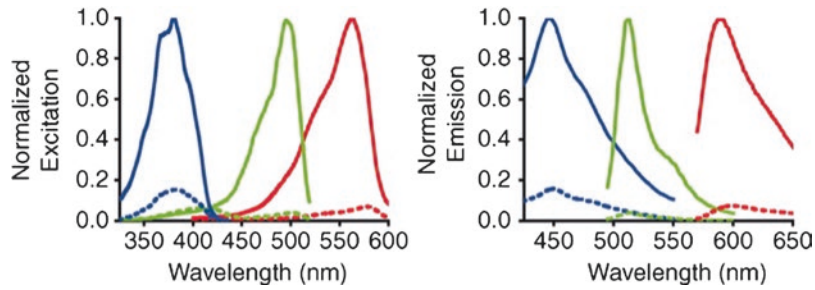

Fig. 31.7 The excitation (*left* panel) and emission spectra of B-GECI (*blue*), G-GECI (*green*), and R-GECI (*red*) with (*solid line*) or without (*dotted line*) calcium (Zhao et al. 2011b (From Zhao et al., Science, 2011b. Reprinted with permission from AAAS.))

Belliveau et al. used a gadolinium (Gd)-based DTPA contrast agent to map the changes of cerebral blood volume (CBV) in the human visual cortex with the dynamic susceptibility contrast (DSC) MRI (Belliveau et al. 1991). This work demonstrated the first example to map the human brain function with MRI. In 1991, three independent groups reported to map the blood-oxygen-level-dependent (BOLD) fMRI signal from the human brain upon neural activation (Bandettini et al. 1992; Kwong et al. 1992; Ogawa et al. 1992). Besides the BOLD contrast, the blood flow changes could also be used to map brain function as an alternative fMRI method (Kwong et al. 1992). The arterial spin labeling (ASL) method was first developed to noninvasively measure the cerebral blood flow (CBF) with MRI in the rat brain (Detre et al. 1992; Williams et al. 1992), which was not only used for brain functional mapping but also for perfusion measurement of brain tumors with labeled endogenous water protons. A flow-sensitive alternating inversion recovery (FAIR) method was later developed to map the local CBF changes for functional mapping (Kim 1995). Meanwhile, the CBV signal changes were characterized by measuring the endogenous blood volume changes with the vascular-space-occupancy (VASO) MRI in the human brain (Lu et al. 2003). The series of methodological development highlighted the closely coupled neural events with vascular responses in the brain and demonstrated the power of MRI to detect the multifaceted features of the hemodynamic signal.

Mapping the hemodynamic signal with MRI is to measure the key relaxation properties of water protons in the activated brain area. To better understand the fMRI signal, let us first review the MR readout from water protons of brain tissue: T2* or T1. T2* indicated how fast the coherence of flipped spins in the transverse plane dephased (cancel each other) due to the inhomogeneous field in the local brain tissue. The T2* changes indicate the fluctuation of the local field homogeneity. The spins dephase slower if the field is more homogenous, i.e., the larger T2* value. If the field becomes less homogenous, the spins dephase faster, and we will detect smaller T2* value from the water protons. Deoxyhemoglobin is highly paramagnetic due to the unpaired electrons in contrast to the oxygen-hemoglobin, which is diamagnetic. Upon neural activation, the vessels (primarily arterioles and capillaries) will be dilated to increase the blood flow. More blood with high concentration of oxyhemoglobin from arteriole side flows through the capillaries to increase the oxy-/deoxyhemoglobin ratio in the venule side. The relative concentration of deoxyhemoglobin in the activated brain area is reduced, which will lead to more homogeneous field, and then increase the T2* values detected by MRI. Thus, we will detect positive BOLD fMRI signal changes in the activated brain.

The cerebral blood volume changes in the activated brain regions can be detected by measuring the T2* values too. The vessel dilation leads to increased partial volume contribution of the blood per given voxel. The paramagnetic contrast agents, such as the gadolinium (Gd)-DTPA or superparamagnetic iron oxide particles (MION), can be injected into the blood to shorten the T2* value of the water protons. The increased partial volume contribution from the dilated vessels will show a reduced T2* signal in the activated brain voxels. Thus, the increased cerebral volume signal can be detected as negative MR signal changes. Besides reducing the T2* value of blood water protons for CBV studies, the VASO fMRI studies used an inversion pulse to

null the signal from blood water protons when acquired at specific inversion time (TI) to match the nulling point for the blood water proton relaxation (T1) (Lu et al. 2003). The VASO method allowed the detection of the CBV-based signal drop in the activated brain area from the T1-weighted MR images. And similarly, the CBF fMRI also directly targeted the blood water protons. In contrast to null the blood signal, the ASL method labeled the water protons of the blood. The labeling means to flip the spin in the transverse plane. It takes a few seconds (T1 time) for the flipped spins (water protons) to relax. The labeled blood has sufficient time to flow into the brain area and is detected in the T1-weighted images. If the blood flow is increased locally in the activated brain area, there will be more labeled water protons, and it will lead to positive T1-weighted signal changes.

Besides measuring the hemodynamic signal, there are other MRI schemes to map brain function. For example, the diffusion fMRI is to detect the water diffusion coefficients due to cell morphology changes upon neural activity, e.g., cell swelling (Le Bihan et al. 2006). Manganese-enhanced MRI (MEMRI) method applied manganese (Mn), as an analog of calcium and a high relaxivity contrast, into the animal brain (Lin and Koretsky 1997). Mn could be accumulated in the activated neurons through the calcium channel. The highly accumulated Mn in the activated brain region shortened the T1 relaxation time of water protons to be detected as brighter signal in the T1-weighted MRI images. Since the mechanisms underlying these methods are not based on the vascular responses but directly interact with the neurons, better specificity could be achieved. However, the hemodynamic signal-based fMRI methods remain the most popular functional mapping method given its high sensitivity and practicability to be used in both animals and human subjects.

31.2.3.2 The Spatiotemporal Limit of Hemodynamic fMRI

A key issue of fMRI studies is to improve the spatial specificity of the MR signal to its neuronal source. Given the increased magnetic field for small animal MRI scanners (up to 21 T), the strengthened gradient set (>1 T/m), and advanced RF coil design, such as cryoprobe, the spatial resolution of fMRI images has been improved to a few hundred micron isotropic. The submillimeter spatial disparity of the neuronal source and coupled vascular signal can be revealed directly by fMRI mapping methods.

Numerous efforts have been made to improve the spatial specificity of the fMRI signal by characterizing the spatiotemporal patterns of the BOLD signal in the activated brain area. In the spatial domain, the draining veins from the cortical surface dominated the fMRI signals and led to mislocalization of the active brain area (Ugurbil et al. 2003; Kim et al. 2004; Lu et al. 2004). To eliminate the contribution of large draining veins, spin-echo sequences were applied to minimize the MRI sensitivity to large vessels (Duong et al. 2003; Zhao et al. 2004; Goense and Logothetis 2006; Uludag et al. 2009). In the temporal domain, the different temporal phases of the fMRI signal were reported to show specific coupling features from distinct vascular components (Silva et al. 2000; Shmuel et al. 2007; Moon et al. 2012). The early fMRI onset signal was considered to be more spatially associated with activated brain region than the fMRI signal of the later phase (Silva and Koretsky 2002; Shmuel et al. 2007). In the rat somatosensory cortex for forepaw/whisker sensation, the early fMRI signal initiated in the deeper layers (Silva and Koretsky 2002; Yu et al. 2012). The early-onset signal elicited before the oxygenated blood reached the venules and then surface draining veins, which indicated that the early-onset signal originated from the microvasculature (arterioles/capillaries) (Silva et al. 2000; Silva and Koretsky 2002; Hutchinson et al. 2006). Besides the BOLD fMRI method, the CBV fMRI, and perfusion fMRI were reported to be more specific to the hemodynamic signal changes from the arteriole and capillaries, which demonstrated better localization of the activated brain regions (Duong et al. 2001; Zhao et al. 2005; Kim and Fukuda 2008). These approaches have not found widespread use as compared to BOLD fMRI due to requirement for contrast

agents or low sensitivity. The abovementioned studies provided sufficient evidence to show that distinct vascular components can contribute to the unique spatiotemporal characteristics of the fMRI signal.

Recently, the echo-planar imaging (EPI) fMRI images were acquired under the high field (11.7 T) with in-plane resolution 150 × 150 μm at every 200 ms. The peak BOLD fMRI signal was primarily located at the penetrating venules in the rat somatosensory cortex (Fig. 31.8) (Yu et al. 2012). This work indicated that the BOLD signal could be detected from individual vessels if sufficient signal-to-noise ratio could be achieved with high spatiotemporal resolution.

Based on a rat fMRI study with reshuffled k-space (Silva and Koretsky 2002), a line-scanning fMRI method was reported to analyze the BOLD fMRI signal from different cortical layers at 50-micron thickness with 20Hz sampling rate (Fig. 31.9) (Yu et al. 2014). The line-scanning method was further developed to map the fMRI signal from individual arterioles and venules in the rat cortex. Both venules and arterioles can be distinguished from the surrounding tissues and from each other using a T1-weighted, multi-echo technique (Yu et al. 2016). The water protons can be saturated in voxels of the brain slice after large flip-angle RF pulsing in multiple short TRs. However, the saturated water protons in vessel voxels are replaced by the unsaturated protons due to the blood flow so as to increase the T1-weighted MRI signal. This phenomenon is called inflow effect. The inflow effect can delineate vessel voxels with brighter signal in MRI images (Wedeen et al. 1985). In contrast, the surrounding tissue signal has been saturated and shows lower intensity (Edelman 1993; Bolan et al. 2006). At the short TE, both arterioles and venules appear as brighter voxels; however, at the longer TE, the deoxygenated blood in venules has faster T2* decay than surrounding tissues or arterioles and leads to darker signal only in venules (Reichenbach et al. 1997). Using inflow to map vessels has been reported previously using a 3D time-of-flight microangiography technique (Bolan et al. 2006).

The single-vessel fMRI signal could be specifically detected from venules as BOLD signal and from arterioles as CBV signal in 10 Hz sampling rate (Yu et al. 2016). This work opened a new avenue to use single-vessel fMRI maps to interpret or represent the unique neurovascular coupling patterns of a given stimulus in the brain.

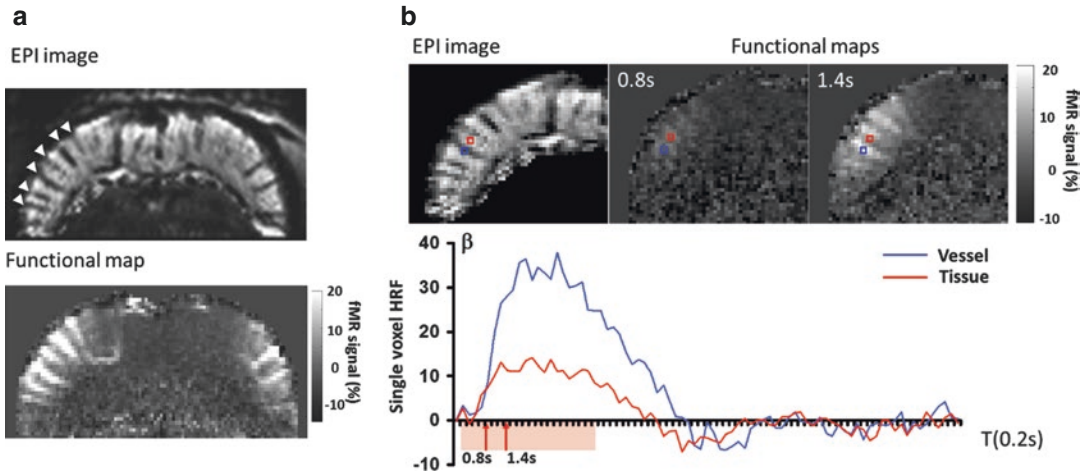

Fig. 31.8 The BOLD fMRI signal detected from the penetrating venules in the rat brain under 11.7 T. (**a**) The raw EPI image was acquired at 200 ms TR showing the penetrating venules as dark stripes. The functional maps demonstrated the most active voxels overlapped with the venules voxels as brighter signal with higher fMRI signal percentage change. (**b**) The functional maps were shown at different time points after the stimulus onset (0.8 and 1.4 s, *upper panel*). The time courses of two voxels (parenchyma voxel, *red* color; venule voxel, *blue* color) showed the early fMRI onset from the parenchyma voxel (Yu et al. 2012)

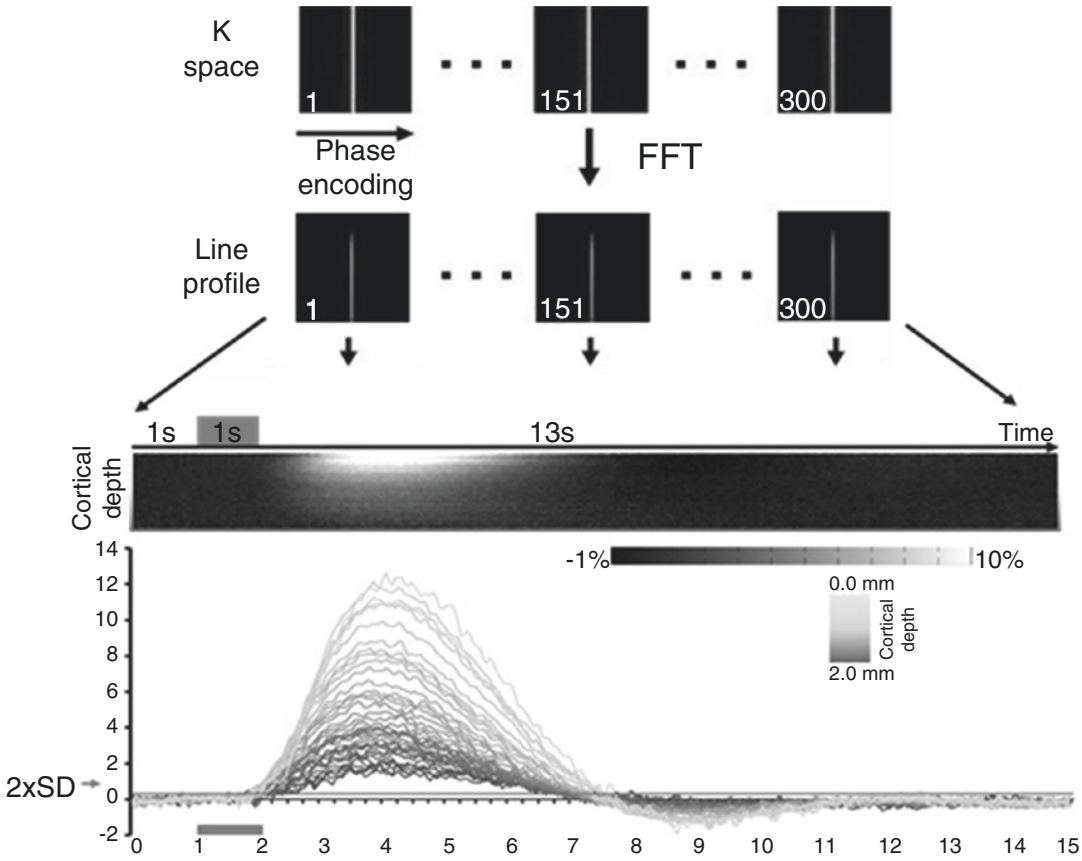

Fig. 31.9 The line-scanning fMRI. The upper panel shows the representative k-space maps in a block design paradigm. The line profile was acquired after fast Fourier transformation (FFT) for each k-space data and was integrated to a map with *x*-axis as time and *y*-axis as the cortical depth. The fMRI signal from 40 trials (50 μm thickness across 2 mm cortical depth) were shown in the *lower* panel (Yu et al. 2014)

31.3 Multimodal Applications

31.3.1 Optogenetic fMRI Studies

In 2010, Lee et al. reported the first work to apply optogenetic tool for small animal fMRI study (Lee et al. 2010). AAV viral vectors were used to express ChR2 in neurons through the CaMKII promoter. Fiber optic was inserted into the rat brain to target the area expressing ChR2, such as the motor cortex. Upon the light exposure, robust fMRI signal was detected in the motor cortex (Fig. 31.10) and the projected thalamic regions. In addition, if the fiber optic targeted the axons expressing ChR2, the fMRI signal was detected not only in projected areas but also at the area where the neuronal soma was located due to back propagation.

There were a few studies to verify the temporal and spatial feature of the light-driven fMRI signal by optogenetics. Kahn et al. analyzed the opto-fMRI signal in the transgenic mice expressing ChR2 in the layer V pyramidal neurons (Kahn et al. 2011). The fiber optic delivered light to the cortical surface of the barrel cortex. The light-driven fMRI signal showed a linear temporal summation in response to a train of light pulses. The spatial pattern of hemodynamic signal changes after optical stimulation was mapped with CCD camera based on the spectroscopic absorption difference of the

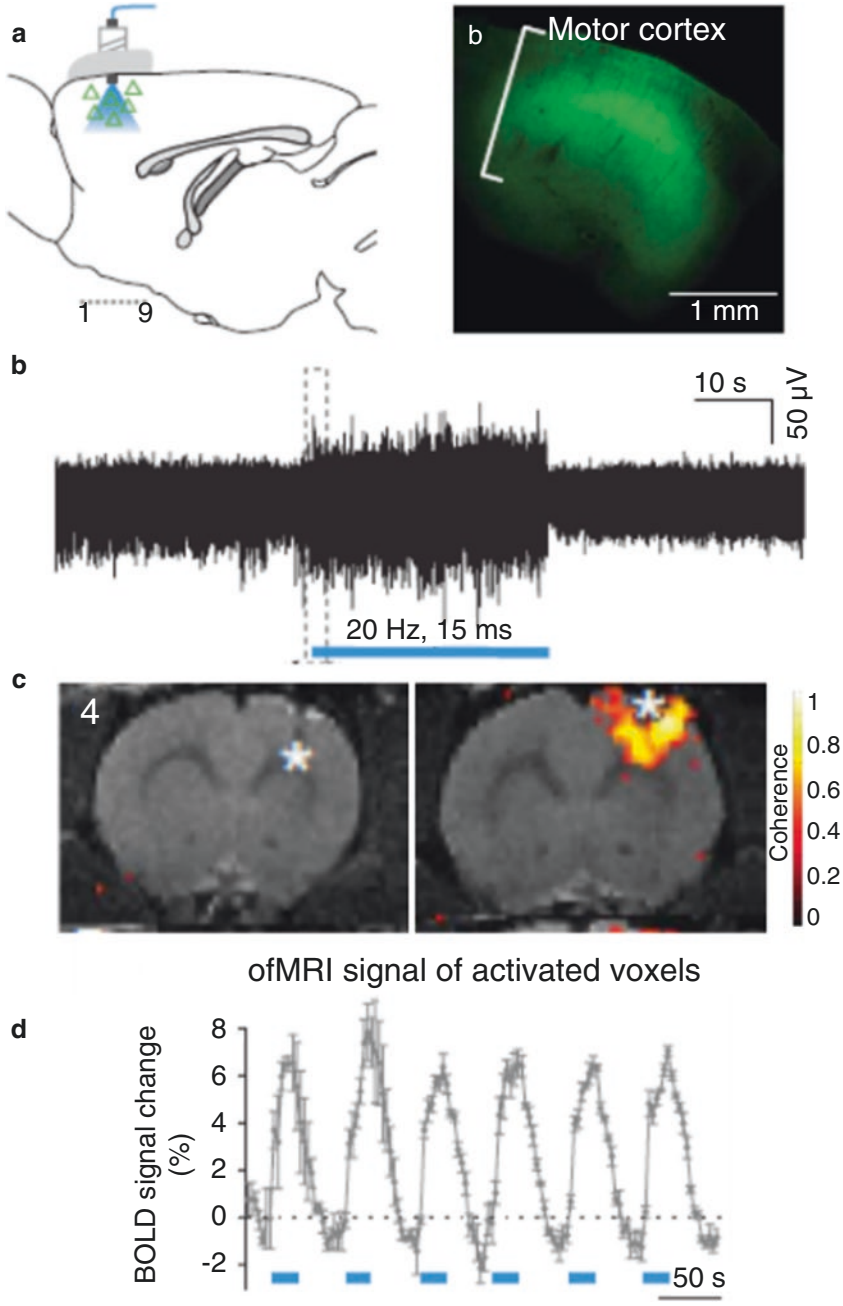

Fig. 31.10 The opto-fMRI in the rat motor cortex. (**a**) The schematic plan of the fiber-optic targeting motor cortex expressing ChR2 (*green* color). (**b**) The light-driven local field potential recorded in the motor cortex. (**c**) The fMRI functional map showed light-driven neural activity in the motor cortex (* indicates the tip of the fiber optic.) (**d**) The averaged time course of the fMRI signal during the optical stimulation block design paradigm (Lee et al. 2010) (Reprinted by permission from Macmillan Publishers Ltd: Nature, Lee et al., copyright 2010.)

oxy- and deoxyhemoglobin in the somatosensory cortex (Vazquez et al. 2014), as well as the BOLD fMRI (Iordanova et al. 2015). The spatial and temporal features of light-driven fMRI signal in the rodent brain were similar to the fMRI signal evoked by sensory stimulation.

Two major advantages of the opto-fMRI techniques are the cell type- and neural circuit-specific targeting schemes. However, it is crucial to better understand the origin of fMRI signal so as to correctly interpret the cellular contribution to the light-driven fMRI signal, as well as the circuit-specific activation of targeted brain regions. In 2001, Logothetis reported the better correlation of the BOLD fMRI signal with the local field potential (LFP) than single-unit and multiunit spikes simultaneously detected in the visual cortex of the monkey brain (Logothetis et al. 2001). This work demonstrated that fMRI detected the hemodynamic signal closely coupled to the integrated neural events of the local neural network. Thus, it is important to know that the fMRI signal detected by optical stimulation represented the integrated neural events, similar to the peripheral stimulation or microelectrode stimulation. The fMRI signal by itself does not bear the cellular specificity based on its underlying mechanism (Logothetis 2010). Another concern of opto-fMRI functional mapping is the heating-related pseudo-BOLD fMRI signal. In the native rats without the ChR2 expression, by increasing the light power and exposure time, the negative BOLD signal can be readily detected from the cortical areas close to the fiber-optic tip (Christie et al. 2013) (Fig. 31.11). However, to carefully control the light power level and the pulse duration, the heat-induced pseudo-fMRI signal can be easily eliminated.

The neural circuit-specific excitation by optogenetics provides a unique angle for small animal fMRI. In the conventional task-related small animal fMRI studies, fMRI responses were usually elicited by an input signal through the sensory system. The task-related mapping paradigms limit the assessable neural circuits only to those relevant to the processing of the input signal. Given the complexity of the signal processing through the neural network, it remains impractical to distinguish the circuit-specific fMRI signal using the conventional mapping methods.

There are a few other fMRI-based methodologies to provide information at the functional connectivity level independent of peripheral input signal. The resting-state fMRI correlated the BOLD signal changes of the individual voxels in

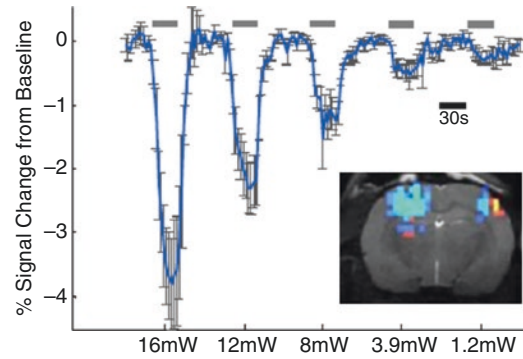

Fig. 31.11 The negative pseudo-BOLD signal was detected at the cortex surrounding the fiber-optic tip. The pseudo-BOLD signal changes are proportional to the power of light delivered to the brain (Christie et al. *NeuroImage*, 2013) (Reprinted from Neuroimage, 66, Christie et al. fMRI response to blue light delivery in the naive brain: implications for combined optogenetic fMRI studies, 634-41, Copyright 2013, with permission from Elsevier.)

the absence of any input signal. The functional connected brain regions may present highly synchronized spontaneous neural activity. The spontaneous neural activity could couple with the vascular responses to initiate hemodynamic fluctuation, which mimics the evoked BOLD signal. By analyzing the correlation of the BOLD dynamic signal, the functional connectivity can be specified from different brain regions (Biswal et al. 1995). The global brain connectivity can be evaluated by the resting-state fMRI, such as the default mode network (Raichle et al. 2001). Another methodology is to use the simultaneously recorded electrophysiological signal from the brain regions, such as hippocampus, as a trigger to correlate with the BOLD dynamic signal in the brain (Logothetis et al. 2012). This method targeted more specific neuronal connection based on the unique spiking pattern recorded by electrophysiology, such as the ripple activity of the hippocampus. However, these studies applied correlation analysis of the BOLD signal dynamics or with the electrophysiological signal to study the neural circuits relevant to the source of the signal detected. It remains challenging to target specific neural circuit for fMRI brain functional mapping. As reported by Lee et al., it is possible to target the axons of the neurons expressing ChR2 by fiber optic directly. Optical stimulation of the axons can lead to neural activity through

the afferent inputs in the projected brain regions. The fMRI signal detected in the local brain area is elicited specifically by the axonal fibers expressing ChR2. This phenomenon set the basis to study neural circuit-specific fMRI brain mapping.

Microstimulation is a conventional way to directly target a brain region to manipulate the neural activity, such as the deep brain stimulation (Kringelbach et al. 2007). However, the stimulation current will flow through the local neural circuit without selectivity. The optical stimulation bears the circuit-specific selectivity only for the axons expressing ChR2. A good example is the optical stimulation of the corpus callosum in the rat brain (Fig. 31.12) (Yu et al. 2013). The ChR2 was expressed in the barrel cortex of rats. The callosal projection neurons expressed the ChR2 along their callosal axonal fibers. Because the AAV vectors are primarily targeting the neuronal soma and express the ChR2 antegradely, only the callosal fibers projected from the ChR2-injected barrel cortex were labeled with ChR2. In contrast to the microstimulation which activated the reciprocal callosal projections, the optical stimulation only activated the callosal fibers projecting to the opposite barrel cortex from the viral vector injection site. This work made is possible to study the callosal fiber-meditated fMRI signal in the rat brain. Thus, the combination of fMRI with optogenetics provides a circuit-specific targeting scheme to map the brain function.

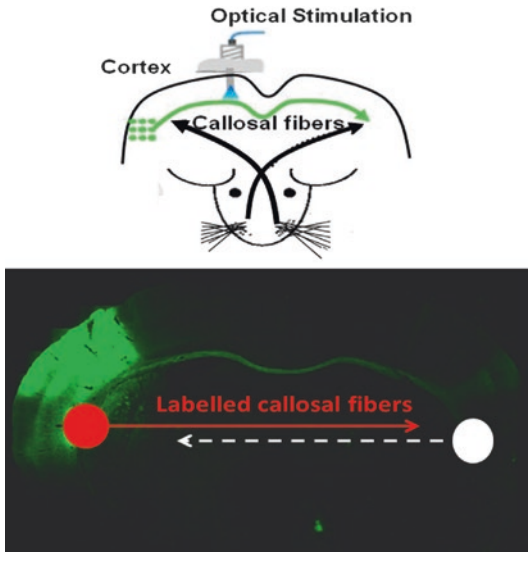

Fig. 31.12 Target the callosal fibers with optogenetics. The *upper* panel is the schematic of the fiber optic-mediated callosal activation. The *lower* panel shows the labeled callosal fibers only from the callosal projection neurons located at the left barrel cortex injected with ChR2 (Yu et al. ISMRM Proceeding, 2013)

31.3.2 Simultaneous fMRI with Calcium Recording

As previously described, the fluorescent calcium-sensitive dyes could be loaded into the brain cells. Under the two-photon microscopy, the cells labeled with the calcium-sensitive dyes, such as the Calcium Green-1 or Fluo-4, could be characterized by their morphology or specific cellular markers, e.g., SR101 for astrocytes (Fig. 31.13) (Stosiek et al. 2003; Oberheim et al. 2006). The calcium imaging and intrinsic hemodynamic signal optical mapping can be performed together in the visual cortex of the ferrets (Schummers et al. 2008). The hemodynamic signal was spatially coupled to the calcium transient signal detected from both neurons and astrocytes, demonstrating similar orientation-selective features for their receptive fields. The astrocytic calcium signal readout is crucial to better understand the contribution of glial cells to the neurovascular coupling underlying the fMRI signal.

By implementing the fiber optic-mediated calcium recording setup in the MRI scanner, Schulz et al. detected the fMRI signal with simultaneous calcium recording based on the calcium-sensitive dyes loaded in the rat brain (Schulz et al. 2012). As shown in the Fig. 31.14, the fiber optic was inserted into the skull of the rat brain just above the dura. The exposed somatosensory cortex (forepaw S1 area) was previously loaded with calcium indicator, OGB-1. The evoked calcium signal changes can be detected as the percentage fluorescent signal emitted by OGB-1 from the rat brain inside the MR scanner through the fiber optic to the photomultiplier. The neurons were primarily loaded with OGB-1 in the forepaw S1 cortex. Upon the forepaw stimulation, the evoked BOLD fMRI and calcium signal in the S1 can be detected simultaneously. In addition, Rhod-2 was able to be loaded specifically in astrocytes. The transient calcium signal can be detected simultaneously with the BOLD fMRI signal during the block design para-

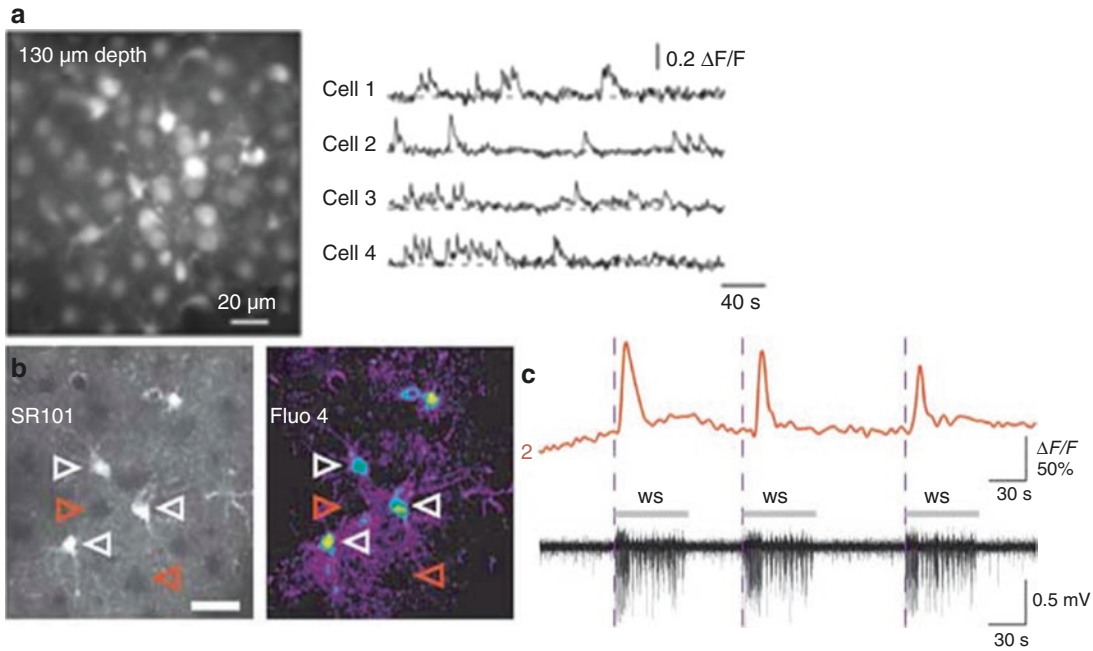

Fig. 31.13 The calcium transient signal was detected in neurons and astrocytes in vivo. (**a**) The neuronal cells were loaded with Calcium Green-1. The spontaneous transient calcium signal from individual neurons was showed in the left panel (Stosiek et al. In vivo two-photon calcium imaging of neuronal networks, Proceedings of the National Academy of Sciences, 2003;100:7319–24, Copyright 2003, National Academy of Sciences). (**b**) The astrocytes were loaded with Fluo-4 (*right*) and specifically labeled with SR101 (*left*) (*white triangles*). Neurons were not loaded by the calcium dyes (*orange triangles*). (**c**) Upon the whisker stimulation (WS, *gray bars*), the evoked astrocytic calcium signal was shown as the *orange* trace. The lower panel showed the local field potential (Wang et al. *Nature Neuroscience*, 2006) (Reprinted by permission from Macmillan Publishers Ltd: Nature Neuroscience, Wang et al., copyright 2006.)

digm. The existence of the astrocytic calcium elevation can elongate the BOLD signal duration to the stimulus, indicating the major contribution of glial cell activity to the later phase of the hemodynamic signal changes.

The fiber optic-mediated calcium recording has two advantages. Firstly, in contrast to the previous calcium imaging work with two-photon microscopy, the majority of studies can only focus on the superficial layers of the cortex. The detected transient calcium signal from different cell types upon stimulation only represented the firing feature of the superficial layers. Although the penetrating depth of the two-photon imaging has been improved (Tian et al. 2010; Mittmann et al. 2011), the signal-to-noise ratio from layer IV/V is much lower than the superficial layers, and the photobleaching is a matter of concern for in vivo studies. The fiber optic can be used to penetrate deep region of the brain. It allowed to measure the calcium transient signal from the subcortical regions. Secondly, the fiber optic-mediated calcium recording setup does not interfere with the fMRI acquisition. The simultaneous fMRI and calcium signal acquisition is less complicated than the simultaneous fMRI and electrophysiological recordings because of the lack of RF interference with the electrical signal (Logothetis et al. 2001). In addition, the cell type-specific calcium signal recording makes it possible to decouple the signaling events from different cellular components of the neuron-glia-vessel network underlying neurovascular coupling.

31.4 Future Studies

To merge optogenetics, GECIs, and fMRI into a multimodal imaging platform can serve as a major direction of small animal imaging. It provides the multidimensional framework to analyze the readout of the signaling events from cellular

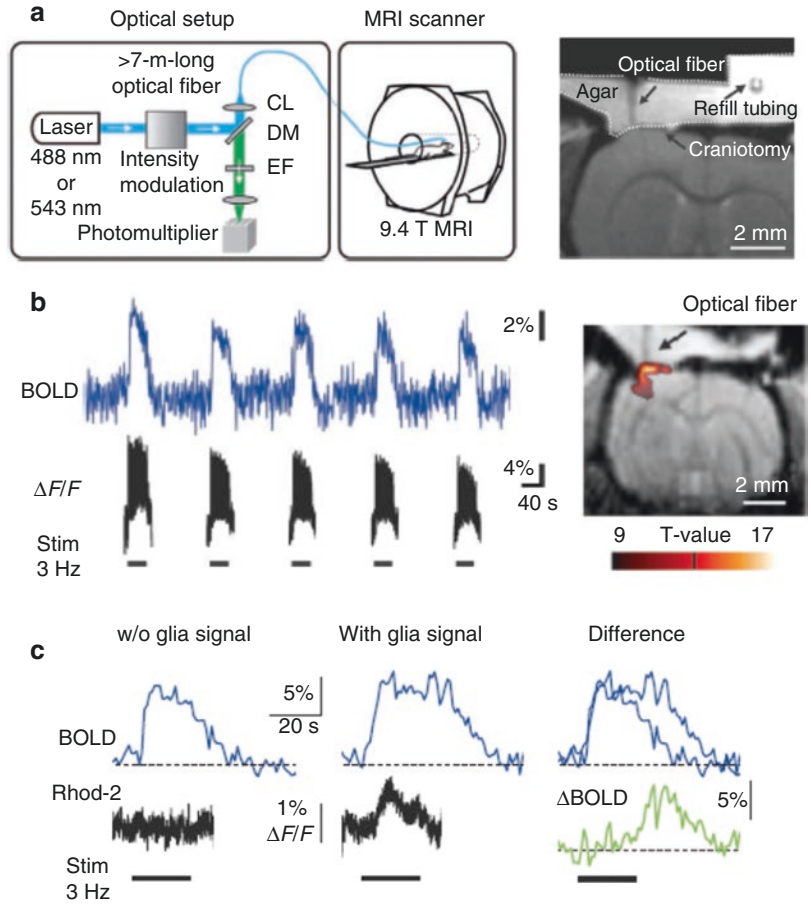

Fig. 31.14 The simultaneous fMRI with fiber optic-mediated calcium recording. (**a**) The basic optic setup for light path and fiber-optic insertion into the rat skull. The coronal brain slice was acquired to show the location of the fiber optic (imbedded in agar) above the cortex. (**b**) The simultaneously acquired BOLD fMRI signal and the fluorescent signal from the somatosensory cortex upon the stimulation. The *right panel* showed the color-coded functional fMRI maps. (**c**) The simultaneously recorded calcium transient signal from glial cells by the calcium dye, Rhod-2. The BOLD signal (*upper blue* curves) was acquired without the existence of astrocytic calcium signal (*black* tracers). The *right panel* showed the temporal difference of the BOLD signal, indicating the elongated BOLD signal may be contributed by the glial activation (Schulz et al. 2012) (Reprinted by permission from Macmillan Publishers Ltd: Nature Methods, Schulz et al., copyright 2012.)

level to neural circuit, to neurovascular network, and to the systems level. The largely expanded opsin variants and multispectral sensitive GECIs with improved kinetics and sensitivity ensure the feasibility to detect the millisecond signaling events in vivo. The advanced functional mapping method, such as the single-vessel fMRI method, makes it possible to detect the vascular signal from individual arterioles and venules in the deep brain regions. More importantly, the fiber-optic targeting scheme readily unites the optical method with MRI method to let the protons and photons work together for us to better understand the brain function.

At last, we summarized a few technical concerns with regard to building up the multimodal imaging platform:

(a) Co-expression of opsin and GECIs *in vivo* for rat fMRI studies

In contrast to the transgenic mouse studies, AAV viral vectors need to be directly injected into the targeted brain regions. When two viral vectors were injected together, the

competition to co-transfection factors and organelles of the targeted cells has to be controlled. The ratio of the two viral vector titers needs to be tested for successful co-expression of the two proteins. The different serotypes of AAV viral vectors showed distinct efficiency of transfection. Although specific promoters determined the expression of the protein of interests, it remains crucial to adjust the titers of the two viral vectors.

(b) Spectral cross talk of opsins and GECIs

Multiple light-sensitive opsins are developed to be activated at different spectra, such as ChR2, 470–480 nm; C1V1, 540–550 nm; and ReaChR, 590–630 nm. Meanwhile, the GECIs also include multiple indicators with different excitation/emission spectra, such as GCaMP6 and RCaMP. To measure the calcium signal fluctuation, a constant light exposure will be delivered at lower power level (5–10 μW/200 μm fiber). The evoked calcium signal from neurons has usually 15–20 ms onset delay. In contrast, the optical stimulation usually delivers a few millisecond light pulse. To select opsin variants and GECIs with light sensitivity at different spectra, such as C1V1-GCaMP6, it is possible to detect the light-driven calcium signal with minimal spectral cross talk.

(c) Fiber selection (Raman scattering), PCF hollow air transmission

The optical signal was mainly delivered through the fiber optic. To choose the appropriate fiber optic is crucial to reduce the background noise. The key noise source from the fiber optic is the Raman scattering, i.e., the low-energy emission after the photons were absorbed by the fiber-optic material. The high-OH fiber optic will cause strong Raman scattering. Thus, the low-OH fiber optic should be chosen for light transmission. Another choice is the photonic-crystal fiber, which confines the light transmission through the hollow core (Russell 2003). The Raman scattering of the air is much less than glass or plastic material of fiber optic. Meanwhile, the PCF hollow cores have very small numerical aperture and will provide high specificity for the targeted brain regions.

(d) MRI image acquisition hardware development

The fiber-optic insertion needs to be secured on the rat skull with dental cement or MRI-compatible glue. To acquire reasonable signal-to-noise ratio (SNR), the surface RF coil needs to be closely attached on the rat head and allows the fiber optic to pass through. The securing material between the coil and brain occupies the most sensitive space for RF signal detection. Different coil design or implanted coil scheme has to be developed to achieve high SNR. In another aspect, a remote MRI-guided device can be developed to target the fiber optic to the brain regions after the rat is positioned inside the MR scanner. An MRI-compatible stereotactic controlling arm can maneuver the fiber-optic position inside the brain based on the real-time acquired MRI images. This MRI-guided stereotactic arm can allow the fiber optic-mediated calcium recording in multiple brain regions with more precise targeting accuracy.

References

Aad G, et al. Search for direct top squark pair production in final states with one isolated lepton, jets, and missing transverse momentum in sqrt[s] = 7 TeV pp collisions using 4.7 fb(-10 of ATLAS data. Phys Rev Lett. 2012;109:211803.

Adamantidis AR, Zhang F, Aravanis AM, Deisseroth K, de Lecea L. Neural substrates of awakening probed with optogenetic control of hypocretin neurons. Nature. 2007;450:420–4.

Akerboom J, et al. Genetically encoded calcium indicators for multi-color neural activity imaging and combination with optogenetics. Front Mol Neurosci. 2013;6:2.

Alilain WJ, Li X, Horn KP, Dhingra R, Dick TE, Herlitze S, Silver J. Light-induced rescue of breathing after spinal cord injury. J Neurosci. 2008;28:11862–70.

Aponte Y, Atasoy D, Sternson SM. AGRP neurons are sufficient to orchestrate feeding behavior rapidly and without training. Nat Neurosci. 2011;14:351–5.

Baird GS, Zacharias DA, Tsien RY. Circular permutation and receptor insertion within green fluorescent proteins. Proc Natl Acad Sci U S A. 1999;96:11241–6.

Bamberg E, Tittor J, Oesterhelt D. Light-driven proton or chloride pumping by halorhodopsin. Proc Natl Acad Sci U S A. 1993;90:639–43.

Bandettini PA, Wong EC, Hinks RS, Tikofsky RS, Hyde JS. Time course EPI of human brain function during task activation. Magn Reson Med. 1992;25:390–7.

Banghart M, Borges K, Isacoff E, Trauner D, Kramer RH. Light-activated ion channels for remote control of neuronal firing. Nat Neurosci. 2004;7:1381–6.

Belliveau JW, Kennedy Jr DN, McKinstry RC, Buchbinder BR, Weisskoff RM, Cohen MS, Vevea JM, Brady TJ, Rosen BR. Functional mapping of the human visual cortex by magnetic resonance imaging. Science. 1991;254:716–9.

Berndt A, Yizhar O, Gunaydin LA, Hegemann P, Deisseroth K. Bi-stable neural state switches. Nat Neurosci. 2009;12:229–34.

Biswal B, Yetkin FZ, Haughton VM, Hyde JS. Functional connectivity in the motor cortex of resting human brain using echo-planar MRI. Magn Reson Med. 1995;34:537–41.

Bolan PJ, Yacoub E, Garwood M, Ugurbil K, Harel N. In vivo micro-MRI of intracortical neurovasculature. Neuroimage. 2006;32:62–9.

Boyden ES, Zhang F, Bamberg E, Nagel G, Deisseroth K. Millisecond-timescale, genetically targeted optical control of neural activity. Nat Neurosci. 2005;8:1263–8.

Brake AJ, Wagenbach MJ, Julius D. New structural motif for ligand-gated ion channels defined by an ionotropic ATP receptor. Nature. 1994;371:519–23.

Chen TW, Wardill TJ, Sun Y, Pulver SR, Renninger SL, Baohan A, Schreiter ER, Kerr RA, Orger MB, Jayaraman V, Looger LL, Svoboda K, Kim DS. Ultrasensitive fluorescent proteins for imaging neuronal activity. Nature. 2013;499:295–300.

Chow BY, Han X, Dobry AS, Qian X, Chuong AS, Li M, Henninger MA, Belfort GM, Lin Y, Monahan PE, Boyden ES. High-performance genetically targetable optical neural silencing by light-driven proton pumps. Nature. 2010;463:98–102.

Christie IN, Wells JA, Southern P, Marina N, Kasparov S, Gourine AV, Lythgoe MF. fMRI response to blue light delivery in the naive brain: implications for combined optogenetic fMRI studies. Neuroimage. 2013;66:634–41.

Cruikshank SJ, Urabe H, Nurmikko AV, Connors BW. Pathway-specific feedforward circuits between thalamus and neocortex revealed by selective optical stimulation of axons. Neuron. 2010;65:230–45.

Detre JA, Leigh JS, Williams DS, Koretsky AP. Perfusion imaging. Magn Reson Med. 1992;23:37–45.

Duong TQ, Kim DS, Ugurbil K, Kim SG. Localized cerebral blood flow response at submillimeter columnar resolution. Proc Natl Acad Sci U S A. 2001;98:10904–9.

Duong TQ, Yacoub E, Adriany G, Hu X, Ugurbil K, Kim SG. Microvascular BOLD contribution at 4 and 7 T in the human brain: gradient-echo and spin-echo fMRI with suppression of blood effects. Magn Reson Med. 2003;49:1019–27.

Eberhard M, Erne P. Calcium binding to fluorescent calcium indicators: calcium green, calcium orange and calcium crimson. Biochem Biophys Res Commun. 1991;180:209–15.

Edelman RR. Magnetic resonance angiography. An overview. Invest Radiol. 1993;28 Suppl 4:S43–6.

Goense JB, Logothetis NK. Laminar specificity in monkey V1 using high-resolution SE-fMRI. Magn Reson Imaging. 2006;24:381–92.

Gradinaru V, Thompson KR, Deisseroth K. eNpHR: a Natronomonas halorhodopsin enhanced for optogenetic applications. Brain Cell Biol. 2008;36:129–39.

Gradinaru V, Mogri M, Thompson KR, Henderson JM, Deisseroth K. Optical deconstruction of parkinsonian neural circuitry. Science. 2009;324:354–9.

Gradinaru V, Zhang F, Ramakrishnan C, Mattis J, Prakash R, Diester I, Goshen I, Thompson KR, Deisseroth K. Molecular and cellular approaches for diversifying and extending optogenetics. Cell. 2010;141:154–65.

Gunaydin LA, Yizhar O, Berndt A, Sohal VS, Deisseroth K, Hegemann P. Ultrafast optogenetic control. Nat Neurosci. 2010;13:387–92.

Harz H, Hegemann P. Rhodopsin-regulated calcium currents in chlamydomonas. Nature. 1991;351:489–91.

Hutchinson EB, Stefanovic B, Koretsky AP, Silva AC. Spatial flow-volume dissociation of the cerebral microcirculatory response to mild hypercapnia. Neuroimage. 2006;32:520–30.

Iordanova B, Vazquez AL, Poplawsky AJ, Fukuda M, Kim SG. Neural and hemodynamic responses to optogenetic and sensory stimulation in the rat somatosensory cortex. J Cereb Blood Flow Metab. 2015;35:922–32.

Ji G, Feldman ME, Deng KY, Greene KS, Wilson J, Lee JC, Johnston RC, Rishniw M, Tallini Y, Zhang J, Wier WG, Blaustein MP, Xin HB, Nakai J, Kotlikoff MI. Ca2+-sensing transgenic mice: postsynaptic signaling in smooth muscle. J Biol Chem. 2004;279:21461–8.

Johansen JP, Hamanaka H, Monfils MH, Behnia R, Deisseroth K, Blair HT, LeDoux JE. Optical activation of lateral amygdala pyramidal cells instructs associative fear learning. Proc Natl Acad Sci U S A. 2010;107:12692–7.

Kahn I, Desai M, Knoblich U, Bernstein J, Henninger M, Graybiel AM, Boyden ES, Buckner RL, Moore CI. Characterization of the functional MRI response temporal linearity via optical control of neocortical pyramidal neurons. J Neurosci. 2011;31:15086–91.

Kao JP, Harootunian AT, Tsien RY. Photochemically generated cytosolic calcium pulses and their detection by fluo-3. J Biol Chem. 1989;264:8179–84.

Kim SG. Quantification of relative cerebral blood flow change by flow-sensitive alternating inversion recovery (FAIR) technique: application to functional mapping. Magn Reson Med. 1995;34:293–301.

Kim SG, Fukuda M. Lessons from fMRI about mapping cortical columns. Neuroscientist. 2008;14:287–99.

Kim DS, Ronen I, Olman C, Kim SG, Ugurbil K, Toth LJ. Spatial relationship between neuronal activity and BOLD functional MRI. Neuroimage. 2004;21:876–85.

Kringelbach ML, Jenkinson N, Owen SL, Aziz TZ. Translational principles of deep brain stimulation. Nat Rev Neurosci. 2007;8:623–35.

Kwong KK, Belliveau JW, Chesler DA, Goldberg IE, Weisskoff RM, Poncelet BP, Kennedy DN, Hoppel BE, Cohen MS, Turner R, et al. Dynamic magnetic

resonance imaging of human brain activity during primary sensory stimulation. Proc Natl Acad Sci U S A. 1992;89:5675–9.

Le Bihan D, Urayama S, Aso T, Hanakawa T, Fukuyama H. Direct and fast detection of neuronal activation in the human brain with diffusion MRI. Proc Natl Acad Sci U S A. 2006;103:8263–8.

Lee JH, Durand R, Gradinaru V, Zhang F, Goshen I, Kim DS, Fenno LE, Ramakrishnan C, Deisseroth K. Global and local fMRI signals driven by neurons defined optogenetically by type and wiring. Nature. 2010;465:788–92.

Lima SQ, Miesenbock G. Remote control of behavior through genetically targeted photostimulation of neurons. Cell. 2005;121:141–52.

Lin JY. A user's guide to channelrhodopsin variants: features, limitations and future developments. Exp Physiol. 2011;96:19–25.

Lin YJ, Koretsky AP. Manganese ion enhances T1-weighted MRI during brain activation: an approach to direct imaging of brain function. Magn Reson Med. 1997;38:378–88.

Lin JY, Lin MZ, Steinbach P, Tsien RY. Characterization of engineered channelrhodopsin variants with improved properties and kinetics. Biophys J. 2009;96:1803–14.

Lin JY, Knutsen PM, Muller A, Kleinfeld D, Tsien RY. ReaChR: a red-shifted variant of channelrhodopsin enables deep transcranial optogenetic excitation. Nat Neurosci. 2013;16:1499–508.

Logothetis NK. Bold claims for optogenetics. Nature. 2010;468:E3–4; discussion E4–5.

Logothetis NK, Pauls J, Augath M, Trinath T, Oeltermann A. Neurophysiological investigation of the basis of the fMRI signal. Nature. 2001;412:150–7.

Logothetis NK, Eschenko O, Murayama Y, Augath M, Steudel T, Evrard HC, Besserve M, Oeltermann A. Hippocampal-cortical interaction during periods of subcortical silence. Nature. 2012;491:547–53.

Lu H, Golay X, Pekar JJ, Van Zijl PC. Functional magnetic resonance imaging based on changes in vascular space occupancy. Magn Reson Med. 2003;50:263–74.

Lu H, Patel S, Luo F, Li SJ, Hillard CJ, Ward BD, Hyde JS. Spatial correlations of laminar BOLD and CBV responses to rat whisker stimulation with neuronal activity localized by Fos expression. Magn Reson Med. 2004;52:1060–8.

Madisen L, Zwingman TA, Sunkin SM, Oh SW, Zariwala HA, Gu H, Ng LL, Palmiter RD, Hawrylycz MJ, Jones AR, Lein ES, Zeng H. A robust and high-throughput Cre reporting and characterization system for the whole mouse brain. Nat Neurosci. 2010;13:133–40.

Madisen L, et al. A toolbox of Cre-dependent optogenetic transgenic mice for light-induced activation and silencing. Nat Neurosci. 2012;15:793–802.

Mittmann W, Wallace DJ, Czubayko U, Herb JT, Schaefer AT, Looger LL, Denk W, Kerr JN. Two-photon calcium imaging of evoked activity from L5 somatosensory neurons in vivo. Nat Neurosci. 2011;14:1089–93.

Miyawaki A, Llopis J, Heim R, McCaffery JM, Adams JA, Ikura M, Tsien RY. Fluorescent indicators for Ca2+ based on green fluorescent proteins and calmodulin. Nature. 1997;388:882–7.

Miyawaki A, Griesbeck O, Heim R, Tsien RY. Dynamic and quantitative Ca2+ measurements using improved cameleons. Proc Natl Acad Sci U S A. 1999;96:2135–40.

Moon CH, Fukuda M, Kim SG. Spatiotemporal characteristics and vascular sources of neural-specific and -nonspecific fMRI signals at submillimeter columnar resolution. Neuroimage. 2012;64C:91–103.

Nagel G, Ollig D, Fuhrmann M, Kateriya S, Musti AM, Bamberg E, Hegemann P. Channelrhodopsin-1: a light-gated proton channel in green algae. Science. 2002;296:2395–8.

Nagel G, Szellas T, Huhn W, Kateriya S, Adeishvili N, Berthold P, Ollig D, Hegemann P, Bamberg E. Channelrhodopsin-2, a directly light-gated cation-selective membrane channel. Proc Natl Acad Sci U S A. 2003;100:13940–5.

Nakai J, Ohkura M, Imoto K. A high signal-to-noise Ca(2+) probe composed of a single green fluorescent protein. Nat Biotechnol. 2001;19:137–41.

Oberheim NA, Wang X, Goldman S, Nedergaard M. Astrocytic complexity distinguishes the human brain. Trends Neurosci. 2006;29:547–53.

Ogawa S, Lee TM, Kay AR, Tank DW. Brain magnetic resonance imaging with contrast dependent on blood oxygenation. Proc Natl Acad Sci U S A. 1990;87:9868–72.

Ogawa S, Tank DW, Menon R, Ellermann JM, Kim SG, Merkle H, Ugurbil K. Intrinsic signal changes accompanying sensory stimulation: functional brain mapping with magnetic resonance imaging. Proc Natl Acad Sci U S A. 1992;89:5951–5.

Paredes RM, Etzler JC, Watts LT, Zheng W, Lechleiter JD. Chemical calcium indicators. Methods. 2008;46:143–51.

Persechini A, Lynch JA, Romoser VA. Novel fluorescent indicator proteins for monitoring free intracellular Ca2+. Cell Calcium. 1997;22:209–16.

Prigge M, Schneider F, Tsunoda SP, Shilyansky C, Wietek J, Deisseroth K, Hegemann P. Color-tuned channelrhodopsins for multiwavelength optogenetics. J Biol Chem. 2012;287:31804–12.

Raichle ME, MacLeod AM, Snyder AZ, Powers WJ, Gusnard DA, Shulman GL. A default mode of brain function. Proc Natl Acad Sci U S A. 2001;98:676–82.

Reichenbach JR, Venkatesan R, Schillinger DJ, Kido DK, Haacke EM. Small vessels in the human brain: MR venography with deoxyhemoglobin as an intrinsic contrast agent. Radiology. 1997;204:272–7.

Romoser VA, Hinkle PM, Persechini A. Detection in living cells of Ca2+-dependent changes in the fluorescence emission of an indicator composed of two green fluorescent protein variants linked by a calmodulin-binding sequence. A new class of fluorescent indicators. J Biol Chem. 1997;272:13270–4.

Russell P. Photonic crystal fibers. Science. 2003;299:358–62.

Schmidt JA, Eckert R. Calcium couples flagellar reversal to photostimulation in chlamydomonas-reinhardtii. Nature. 1976;262:713–5.

Schulz K, Sydekum E, Krueppel R, Engelbrecht CJ, Schlegel F, Schroter A, Rudin M, Helmchen F. Simultaneous BOLD fMRI and fiber-optic calcium recording in rat neocortex. Nat Methods. 2012;9:597–602.

Schummers J, Yu H, Sur M. Tuned responses of astrocytes and their influence on hemodynamic signals in the visual cortex. Science. 2008;320:1638–43.

Shmuel A, Yacoub E, Chaimow D, Logothetis NK, Ugurbil K. Spatio-temporal point-spread function of fMRI signal in human gray matter at 7 Tesla. Neuroimage. 2007;35:539–52.

Silva AC, Koretsky AP. Laminar specificity of functional MRI onset times during somatosensory stimulation in rat. Proc Natl Acad Sci U S A. 2002;99:15182–7.

Silva AC, Lee SP, Iadecola C, Kim SG. Early temporal characteristics of cerebral blood flow and deoxyhemoglobin changes during somatosensory stimulation. J Cereb Blood Flow Metab. 2000;20:201–6.

Sohal VS, Zhang F, Yizhar O, Deisseroth K. Parvalbumin neurons and gamma rhythms enhance cortical circuit performance. Nature. 2009;459:698–702.

Stosiek C, Garaschuk O, Holthoff K, Konnerth A. In vivo two-photon calcium imaging of neuronal networks. Proc Natl Acad Sci U S A. 2003;100:7319–24.

Stuber GD, Hnasko TS, Britt JP, Edwards RH, Bonci A. Dopaminergic terminals in the nucleus accumbens but not the dorsal striatum corelease glutamate. J Neurosci. 2010;30:8229–33.

Svoboda K, Denk W, Kleinfeld D, Tank DW. In vivo dendritic calcium dynamics in neocortical pyramidal neurons. Nature. 1997;385:161–5.

Tian L, Hires SA, Mao T, Huber D, Chiappe ME, Chalasani SH, Petreanu L, Akerboom J, McKinney SA, Schreiter ER, Bargmann CI, Jayaraman V, Svoboda K, Looger LL. Imaging neural activity in worms, flies and mice with improved GCaMP calcium indicators. Nat Methods. 2009;6:875–81.

Tian P, Teng IC, May LD, Kurz R, Lu K, Scadeng M, Hillman EM, De Crespigny AJ, D'Arceuil HE, Mandeville JB, Marota JJ, Rosen BR, Liu TT, Boas DA, Buxton RB, Dale AM, Devor A. Cortical depth-specific microvascular dilation underlies laminar differences in blood oxygenation level-dependent functional MRI signal. Proc Natl Acad Sci U S A. 2010;107:15246–51.

Ugurbil K, Toth L, Kim DS. How accurate is magnetic resonance imaging of brain function? Trends Neurosci. 2003;26:108–14.

Uludag K, Muller-Bierl B, Ugurbil K. An integrative model for neuronal activity-induced signal changes for gradient and spin echo functional imaging. Neuroimage. 2009;48:150–65.

Valera S, Hussy N, Evans RJ, Adami N, North RA, Surprenant A, Buell G. A new class of ligand-gated ion channel defined by P2x receptor for extracellular ATP. Nature. 1994;371:516–9.

Vazquez AL, Fukuda M, Crowley JC, Kim SG. Neural and hemodynamic responses elicited by forelimb- and photo-stimulation in channelrhodopsin-2 mice: insights into the hemodynamic point spread function. Cereb Cortex. 2014;24:2908–19.

Wang XH, Lou NH, Xu QW, Tian GF, Peng WG, Han XN, Kang J, Takano T, Nedergaard M. Astrocytic Ca^{2+} signaling evoked by sensory stimulation in vivo. Nat Neurosci. 2006;9:816–23.

Wedeen VJ, Meuli RA, Edelman RR, Geller SC, Frank LR, Brady TJ, Rosen BR. Projective imaging of pulsatile flow with magnetic resonance. Science. 1985;230:946–8.

Williams DS, Detre JA, Leigh JS, Koretsky AP. Magnetic resonance imaging of perfusion using spin inversion of arterial water. Proc Natl Acad Sci U S A. 1992;89:212–6.

Yizhar O, Fenno LE, Prigge M, Schneider F, Davidson TJ, O'Shea DJ, Sohal VS, Goshen I, Finkelstein J, Paz JT, Stehfest K, Fudim R, Ramakrishnan C, Huguenard JR, Hegemann P, Deisseroth K. Neocortical excitation/inhibition balance in information processing and social dysfunction. Nature. 2011;477:171–8.

Yu X, Dodd S, Koretsky AP. Targeting projection fibers for optogenetics and fMRI. International Magnetic Resonance in Medicine annual meeting proceedings 0758. 2013.

Yu X, Glen D, Wang S, Dodd S, Hirano Y, Saad Z, Reynolds R, Silva AC, Koretsky AP. Direct imaging of macrovascular and microvascular contributions to BOLD fMRI in layers IV-V of the rat whisker-barrel cortex. Neuroimage. 2012;59:1451–60.

Yu X, He Y, Wang M, Merkle H, Dodd SJ, Silva AC, Koretsky AP. Sensory and optogenetically driven single-vessel fMRI. Nat Methods 2016;13:337–40.

Yu X, Qian C, Chen DY, Dodd SJ, Koretsky AP. Deciphering laminar-specific neural inputs with line-scanning fMRI. Nat Methods. 2014;11:55–8.

Zemelman BV, Nesnas N, Lee GA, Miesenbock G. Photochemical gating of heterologous ion channels: remote control over genetically designated populations of neurons. Proc Natl Acad Sci U S A. 2003;100:1352–7.

Zhang F, Wang LP, Boyden ES, Deisseroth K, Channelrhodopsin-2 and optical control of excitable cells. Nat Methods. 2006;3:785–92.

Zhang F, Wang LP, Brauner M, Liewald JF, Kay K, Watzke N, Wood PG, Bamberg E, Nagel G, Gottschalk A, Deisseroth K. Multimodal fast optical interrogation of neural circuitry. Nature. 2007;446:633–9.

Zhang F, Prigge M, Beyriere F, Tsunoda SP, Mattis J, Yizhar O, Hegemann P, Deisseroth K. Red-shifted optogenetic excitation: a tool for fast neural control derived from Volvox carteri. Nat Neurosci. 2008;11:631–3.

Zhao F, Wang P, Kim SG. Cortical depth-dependent gradient-echo and spin-echo BOLD fMRI at 9.4T. Magn Reson Med. 2004;51:518–24.

Zhao F, Wang P, Hendrich K, Kim SG. Spatial specificity of cerebral blood volume-weighted fMRI responses at columnar resolution. Neuroimage. 2005;27:416–24.

Zhao S, Ting JT, Atallah HE, Qiu L, Tan J, Gloss B, Augustine GJ, Deisseroth K, Luo M, Graybiel AM, Feng G. Cell type-specific channelrhodopsin-2 transgenic mice for optogenetic dissection of neural circuitry function. Nat Methods. 2011a;8:745–52.

Zhao Y, Araki S, Wu J, Teramoto T, Chang YF, Nakano M, Abdelfattah AS, Fujiwara M, Ishihara T, Nagai T, Campbell RE. An expanded palette of genetically encoded Ca(2)(+) indicators. Science. 2011b;333:1888–91.

Imaging in Oncology Research

32

Wolfgang A. Weber and Fabian Kiessling

Contents

W.A. Weber (✉)
Molecular Imaging and Therapy Service, Memorial Sloan Kettering Cancer Center,
1275 York Avenue, New York, NY 10065, USA
e-mail: weberw@mskcc.org

F. Kiessling
Department of Experimental Molecular Imaging, RWTH-Aachen, University Clinics, Helmholtz-Institute for Biomedical Engineering,
Pauwelsstr. 20, Aachen 52074, Germany
e-mail: fkiessling@ukaachen.de

32.1 Abstract

Imaging has been extensively used to monitor the development and progression of cancer in laboratory animals. Imaging also plays an increasing role in monitoring tumor response to therapeutic interventions. Using modern imaging technologies, tumor volumes can be measured in subcutaneous and orthotopic models longitudinally. Furthermore, animals can be screened for the development and progression of metastases. Using imaging techniques, it is also feasible to study noninvasively the microenvironment of tumor tissue, such as regional perfusion, vascular permeability, or oxygen tension.

Depending on the specific scientific question, the tumor model, and the location of disease, tumors are best studied by ultrasound, optical imaging, CT, MRI, SPECT, PET, or a combination of these techniques. In this book chapter, we focus on techniques that have been used to study tumor localization and tumor mass, gene and protein expression, tumor microenvironment, tumor cell proliferation, and metabolism and to monitor therapeutic interventions. The aim is to provide the reader an overview of the features of malignant tumors that can be studied on a routine basis in small animal imaging laboratories. Furthermore, practical guidelines for imaging protocols are provided and known "pitfalls" are discussed.

F. Kiessling et al. (eds.), *Small Animal Imaging*, DOI 10.1007/978-3-319-42202-2_32

32.2 Introduction

Imaging has been extensively used to monitor the development and progression of cancer in laboratory animals. Imaging also plays an increasing role in monitoring tumor response to therapeutic interventions. Using modern imaging technologies, tumor volumes can be measured not only in subcutaneous but also in orthotopic models allowing for noninvasive serial studies of the treated animals. Furthermore, animals can be screened for the development and progression of metastases. Using imaging techniques, it is also feasible to study noninvasively the microenvironment of the tumor tissue, such as regional perfusion, vascular permeability, or oxygen tension. In addition to these studies of tumor size, morphology, and functional status, small animal imaging is increasingly used for the development of new diagnostic and therapeutic agents, since imaging studies can greatly reduce the number of animals necessary to study the biodistribution of experimental compounds.

Depending on the specific scientific question, the tumor model, and the location of disease, tumors are best studied by ultrasound, optical imaging, CT, MRI, SPECT, PET, or a combination of these techniques. Given these many applications and different techniques, it would be far beyond the scope of this chapter to provide a comprehensive overview of the literature on small animal imaging in oncology research. Instead we focus on techniques that have been used to study the following key areas: (i) tumor localization and quantification of tumor mass, (ii) imaging gene and protein expression, (iii) characterization of the tumor microenvironment, (iv) studies of tumor cell proliferation and metabolism, and (v) monitoring therapeutic interventions. The use and limitations of imaging in these five areas are discussed for various organ systems. Accordingly we do not intend to provide an overview on developing or cutting-edge imaging technologies, but we focus on techniques that have been thoroughly studied and whose applications and limitations have been critically evaluated. The aim is to provide the reader an overview of the features of malignant tumors that can be studied on a routine basis in small animal imaging laboratories. Furthermore, practical guidelines for imaging protocols are provided and known "pitfalls" are discussed.

32.3 Major Applications of Imaging in Oncology Research

32.3.1 Tumor Detection, Localization, and Quantification of Tumor Mass

In subcutaneous tumors, repeated measurements of tumor diameters continue to play a key role in oncology research. However, the limitations of subcutaneous tumor models are well recognized, and orthotopic (and spontaneous) tumor models are increasingly used in many areas of cancer research. Most orthotopic tumors are not palpable, and their size cannot be measured with calipers or similar techniques. Imaging thus becomes necessary to localize the tumors and determine their growth over time. For many applications of orthotopic tumor models, a large number of animals need to be imaged repeatedly. Thus, imaging technologies need to be fast and robust. Furthermore, imaging should pose only minimal stress to the animals. Ideally, imaging should also be highly sensitive and allow for accurate measurements of small lesions. Currently, no single imaging technology does meet all these needs in all areas of the body. In the following sections, the use and limitations of different imaging technologies are discussed.

32.3.1.1 Tumor Detection and Growth Monitoring with Optical Imaging

Bioluminescence imaging of tumors expressing luciferases allows high-throughput and low-cost studies in mice. A key advantage of bioluminescence imaging is that no signal is produced until the substrate/enzyme interaction of luciferase and luciferin occurs. Consequently, there is a very low background luminescence level in most

animals allowing highly sensitive detection of tumor cells. It has been demonstrated that the intensity of the bioluminescence signal in general correlates with the tumor mass. Furthermore, a signal is only produced by viable cells allowing investigators to differentiate between necrotic and viable tumors. However, sensitivity and spatial resolution quickly degrade for more deep-seated lesions. This is caused by a significant absorption of light as well as due to scatter of the emitted photons. The minimum tumor size that can be detected by optical imaging is therefore not only dependent on the used imaging equipment but also on luciferase expression levels and the location of the tumor. Furthermore, the positioning of the animal in the imaging system can have a significant impact on the measured light signal (Cui et al. 2008). For the same reason, it can also be challenging to compare the degree of tumor involvement in different organs.

Another important parameter is the body temperature of the animal, which has to be kept constant at physiological levels since the enzymatic activity of the luciferase (and thus also the obtained signal) is temperature dependent and strongly decreases if the animal cools down under anesthesia.

There is therefore no general answer to the question "how many tumor cells can be detected by bioluminescence imaging." Using state-of-the art equipment as little as 10–100 superficially located cells with high luciferase expression levels can be detected by a whole-body bioluminescence imaging, but the minimum number of detectable tumors cells may be orders of magnitude higher for deep-seated tumors with lower levels of luciferase expression (Rabinovich et al. 2008). Since lesion detectability depends on multiple factors, it is necessary to validate the correlation between the in vivo light signal and tumor cell numbers by pilot studies with tissue sampling at different time points during tumor development.

Fluorescent reporter genes such as green fluorescent protein (GFP), red fluorescent protein (RFP), and their various mutants have been used extensively to tag tumor cells and to study their migration and metastasis formation. In this context, mutants that show fluorescence emission in or nearby the near-infrared range (such as "tomato," "plum," and "cherry") provide better access to tissues being more deeply localized in the body. Expression of these fluorescent proteins can be imaged at the cellular and subcellular level by advanced microscopy techniques including confocal and multiphoton laser microscopy (MPM) (Denk et al. 1990).

MPM can be used for in vivo imaging with a maximum tissue penetration of about 500 μm. This technique, which depends on the simultaneous absorption of two infrared photons by a fluorophore, resulting in spatially localized fluorescence excitation, is capable of collecting fluorescence images with a spatial resolution of less than 1 μm in living animals (Dunn and Sutton 2008). In addition to providing better penetration and resolution than previous methods of in vivo microscopy, the use of infrared light also makes MPM significantly less toxic for the studied tissues (Andresen et al. 2009). Using fluorescent probes, it is easy to label both tumor cells and the cells that interact with them. MPM systems can acquire 1–2 images per second allowing real-time imaging of cellular motility, invasiveness, and metastasis formation. Subcutaneously implanted tumors are easily accessible for MPM after an incision in the overlying skin and have been most extensively studied. Using a surgical access, tumors have also been imaged in several organs (Kienast et al. 2010).

Whole-body fluorescence imaging has been used to study macroscopic tumors in mice. An advantage of using fluorescent proteins as reporter genes is that no pharmaceutical needs to be injected. Thus, the signal is not dependent on the distribution and delivery of luciferase substrates (Hoffman 2005). Detection of small tumor's fluorescence is, however, in many circumstances limited by autofluorescence of normal tissues or bowel content. In addition, the limited tissue penetration of the green light emitted by GFP makes visualization of deeper lesions challenging. RFP provides better tissue penetration, but is still limited by autofluorescence. In comparative studies, whole-body bioluminescence imaging provided a better signal-to-noise

ratio than fluorescence imaging. Using currently available imaging technologies, GFP imaging is therefore preferable for ex vivo and in vivo microscopy, whereas bioluminescence imaging is more sensitive for whole-body in vivo imaging. Multimodality reporter genes have been generated that allow bioluminescence, fluorescence, and PET imaging (Ray et al. 2007). Using such reporter genes, cell culture and in vivo microscopy studies can be performed using fluorescence imaging, whereas tumor growth and metastasis formation can be monitored in mice by bioluminescence imaging. The PET reporter gene offers the opportunity for studies in larger animals and eventually translational research in patients (Kang and Chung 2008).

32.3.1.2 Tumor Detection and Growth Monitoring with Ultrasound

Ultrasound imaging enables an easy and reliable size determination of subcutaneous tumors. In comparison to caliper measurements, it is of advantage that a third dimension can be assessed. Modern high-frequency ultrasound devices using motor-driven holders of the transducer generate 3D data sets that can be used for semiautomated determination of tumor volumes. This results in a highly accurate determination of tumor volumes.

Also tumors deep inside the animal body like liver tumors or experimental prostate cancers can be localized by ultrasound. However, the access to these areas of the body by ultrasound is much more difficult, and often the tumors cannot be visualized properly. Therefore, ultrasound imaging may be used to check for the existence of orthotopic tumors in deep organs and to estimate their growth, but for the accurate determination of growth kinetics, other imaging modalities like MRI or μCT may be preferred.

32.3.1.3 Tumor Detection and Growth Monitoring with μCT

μCT enables imaging with a very high spatial resolution but usually the tissue contrast is low. This can make visualization of subcutaneous and orthotopic tumors difficult. For orthotopic tumors outside the lungs and bones, contrast agents usually have to be applied to differentiate tumor from normal tissues. However, optimal timing of contrast agent injection and scanning is mandatory, and one has to take into account that circulation and elimination of clinical contrast agents in mice is up to ten times faster than in humans, while high-resolution μCT scans require significantly more time than human CT examinations with modern multislice systems. If timing is considered to be difficult, experimental CT contrast agents with longer blood half-life such as Aurovist (Nanoprobes), Exia (Binitio Biomedical, Inc.), or Fenestra (ART Advanced Research Technologies, Inc.) may be used (see Sect. 12.2). For orthotopic liver tumors, iodinated liposomes or gold nanoparticles are helpful, which are internalized by liver macrophages or hepatocytes and enhance the contrast of the normal liver tissue, thus enabling the delineation of the tumors as darker spot (see Sect. 12.2).

A clear indication for the use of μCT imaging is tumors in the lungs and bones (Li et al. 2006). Nevertheless, the exposure of animals and tumors to x-rays has to be considered carefully in the study planning (see Sect. 12.1). Particularly in longitudinal studies, x-ray exposure can decrease the health status of the animal and affect tumor growth. Please also note that for the imaging of lung and liver tumors, respiratory gating should be applied, which can be done prospectively or retrospectively (Dinkel et al. 2008). Depending on the scanner type and the chosen spatial resolution, the measurement time per animal is in the range of seconds up to more than 30 min.

32.3.1.4 Tumor Detection and Growth Monitoring with MRI

MRI is favorably suited for tumor staging and monitoring in small animals. This holds true for both subcutaneous and orthotopic tumors. The minimal detectable tumor size depends on the field strength of the MR scanner. Please note that for the detection of submillimeter-sized tumors, clinical MR scanners usually will not be sufficient.

For the determination of tumor size, simple protocols with T2-weighted sequences can be used. In this context, the imaging of lung tumors

is more difficult as imaging of tumors in other areas of the body. If liver or lung tumors are in the focus of research, respiratory gating should be applied, which is usually done prospectively. In general, tumor size determination by MRI requires 10–20 min per animal of which 5–15 min is pure scan time (the remaining time is needed for placing the animal in the MR coil, for the adjustment of the MR coil, and for arranging the measurement position).

32.3.1.5 Tumor Detection and Growth Monitoring with Nuclear Imaging Techniques

PET and SPECT imaging can provide high-contrast images of tumors expressing a variety of reporter genes including herpes simplex thymidine kinase (HSV-tk), sodium-iodide symporter (NIS), and norepinephrine transporter (NET) (Kang and Chung 2008). Since gamma radiation is only minimally absorbed in mice, the depth of the tumor has only a negligible influence on detectability. Images are three-dimensional, allowing accurate localization of the tumor, especially when PET or SPECT studies are combined with CT or MRI. Overall, PET and SPECT are less sensitive than bioluminescence imaging. Typically about 100,000–1 million tumor cells can be reliably detected by reporter gene imaging with small animal PET (Johnson et al. 2009). Furthermore, the costs are considerably higher as short-lived radiopharmaceuticals need to be produced for each imaging study.

A key advantage of nuclear imaging techniques is that tumors can also be detected based on the increased expression of endogenous receptors, transporters, or enzymes. Therefore, it is not necessary to genetically modify tumor cells for PET or SPECT imaging studies. This allows, for example, studies of spontaneous tumor development in transgenic animals. In this context PET imaging with the glucose analogon fluorodeoxyglucose (FDG) is of particular interest as this radiopharmaceutical is extensively used clinically for imaging of cancer patients. Thus, FDG is readily available for animal studies at most small animal imaging facilities located at university hospitals.

When using FDG for such studies, several methodological aspects need to be considered. First of all, the PET scanner basically measures activity concentrations within the body of the animal. These can be expressed as counts/voxel or as Bq/ml if the scanner is appropriately calibrated. In order to standardize the results obtained from different experiments, activity concentrations are frequently expressed as the percentage of the injected dose per ml tissue (%ID/ml) or as standardized uptake values (SUVs). All these parameters are not directly related to tumor size or mass, because all of them describe the concentration of FDG within the tumor. In practice, there is a correlation between the PET signal intensity and tumor size, because of partial volume effects. The typical spatial resolution of small animal PET scanners is in the range of 2 mm. Thus, the true activity concentration is significantly underestimated in lesions that have a diameter of less than 4 mm. Accordingly SUVs or other quantitative parameters will increase during tumor growth. However, the relationship between tumor size and PET signal is not linear and depends on the image reconstruction and postprocessing protocols. Furthermore, FDG uptake rates may change during tumor progression. Therefore, increasing FDG uptake over time cannot be interpreted as a direct reflection of tumor growth.

Finally, the normal distribution of FDG needs to be considered. The rapid renal excretion of FDG makes imaging of tumors in the pelvis challenging as the high radioactivity concentration in the bladder causes artifacts in the PET images. Imaging of tumors in the brain is limited by the physiologic FDG uptake of normal gray matter and of the Harderian glands.

32.3.2 Imaging of Cancer-Related Gene and Protein Expression

The expression of genes and proteins has been assessed by genetically encoded reporters and by ligands that specifically bind to the protein of interest. In the reporter gene approach, a reporter gene is put under the control of a

promoter/enhance element that regulates the expression of the gene of interest. Alternatively a fusion gene is generated that consists of the targeted gene and the reporter gene (Kang and Chung 2008). In vivo reporter gene imaging was initially developed for monitoring cancer gene therapy (Tjuvajev et al. 1996). However, subsequent research has demonstrated that this approach is very versatile and allows for a variety of different applications.

The reporter gene approach is fairly general and can in principle be used to study the expression of any gene. In contrast, the number of specific ligands for molecular imaging is still very limited. The development of ligands with the required high affinity and specificity for the targeted protein is a complex and slow process. In addition to binding with high affinity to the target, ligands need to be metabolically stable and demonstrate only low levels of unspecific binding. Furthermore, the clearance and distribution in normal organs need to be optimized. If the clearance is too fast, the amount of ligand bound to the target may be too low for imaging. Conversely, a slow clearance can result in poor contrast between tumors and normal organs. Therefore, ligand development and refinement need to be repeated for each protein of interest.

However, also the reporter gene approach has specific limitations: First of all, cells need to be transfected with the reporter gene which may confound the expression of the target protein. Second, the expression of the target protein can be influenced by posttranslational regulatory mechanisms. These will generally not be captured by reporter gene imaging. Third, the strength of the promoter may be insufficient for in vivo reporter gene imaging. This represents a frequent limitation for reporter gene imaging. Amplification strategies have been developed to overcome these limitations (Iyer et al. 2001), but these require more complex reporter gene constructs and need to be tested for the individual application. Fourth, transfection of cells and coexpression of a reporter gene can change the behavior of cells, e.g., render tumor cells less invasive and metastatic.

32.3.2.1 Assessment of Gene and Protein Expression with Optical Imaging

Optical imaging with genetically encoded reporters has been used by several groups to monitor gene expression in mice. A well-studied example is the use of bioluminescence imaging of hypoxia-inducible factor 1 (HIF-1). In order to image HIF-1 activity, several groups have created a reporter gene based on the fusion between the HIF-1α-oxygen-dependent degradation (ODD) domain and luciferases. The resulting fusion protein (ODD-Luc) is degraded in the presence of oxygen, whereas hypoxia leads to stabilization of the protein. The ODD-Luc signal is therefore responsive to hypoxia and allows for noninvasive imaging of HIF-1 stabilization and degradation in real time (Harada et al. 2005; Moroz et al. 2009). A mouse that ubiquitously expresses an ODD-Luc reporter has been generated (Safran et al. 2006). HIF-1 activity has also been imaged by transcriptional reporters based on the binding of HIF-1 to hypoxia-response elements (HREs) which drive reporter genes (Serganova et al. 2004). Both approaches have been used to monitor HIF-1 levels and the expression of HIF-1-dependent genes during various interventions (Ou et al. 2009).

In recent years a variety of ligands and enzyme substrates have been developed for optical imaging of gene expression. A key enabling technology for this development has been near-infrared range (NIR) fluorochromes with excitation and emission maxima in the NIR between 700 and 900 nm and a high-quantum yield (Kovar et al. 2007). Among the various protease substrates (Montet et al. 2005) that can be used for optical imaging are substrates being activated after cleavage by cathepsins (Kirsch et al. 2007) or matrix metalloproteinases (MMPs) (Bremer et al. 2001). Since a signal is only generated in this activated state, this class of imaging contrast agents is also referred to as "smart probes" or "molecular beacons." These probes are based on a quenching-dequenching mechanism. The probes are optically silent in their native (quenched) state and become highly fluorescent after enzyme-mediated release of fluorochromes

(Mahmood and Weissleder 2003). The most extensively studied groups of enzymes are the cathepsins, a group of enzymes which degrades polypeptides. Several fluorescent imaging agents are commercially available for studies of cathepsin activity. The imaging of cathepsin activity allows for tumor detection without having to genetically engineer the cancer cells.

Quantum dots (QDs) represent another class of imaging probes that are currently extensively studied for imaging of cancer in murine models. QDs facilitate "multiplexed imaging," since quantum dots of different sizes emit a strong fluorescence signal of different wavelengths. Furthermore, excitation of multiple-colored QDs is feasible with a common excitation source (Bentolila et al. 2009; Michalet et al. 2005). Despite these favorable optical properties, when using QDs for imaging, their considerable toxicity has to be considered.

QDs have been coated with a variety of targeting agents including antibodies against prostate-specific membrane antigen (PSMA) (Gao et al. 2004), epidermal growth factor (EGF) for targeting the epidermal growth factor receptor (EGFR) (Diagaradjane et al. 2008), and RGD peptides for targeting the $\alpha_v\beta_3$-integrin (Cai et al. 2007).

Using planar and tomographic devices, pM concentrations of fluorescent QDs can be detected in superficially located tumors (de la Zerda et al. 2009), but the signal intensity rapidly decreases with the depth of the lesion. Similarly, a submillimeter resolution can be achieved for superficial lesions, whereas resolution of planar images degrades to more than 1 cm at a depth of more than 5 mm (de la Zerda et al. 2009). These factors need to be considered when interpreting the results of optical imaging studies in mice and when using the optical signal to quantify the expression of proteins over time.

Fluorescent labeling of proteins, peptides, and biologicals is straightforward in many cases. However, each of these imaging probes needs to be carefully validated, since tumor uptake is not only dependent on the expression of the target but is also influenced by unspecific binding, blood clearance, and metabolism (Kovar et al. 2007). For QDs the fast blood clearance and high liver uptake still represent a significant limitation for in vivo imaging. Furthermore, unspecific uptake of QDs and other nanoparticles due to the enhanced permeability of intratumoral blood vessels needs to be considered (Gao et al. 2004). For example, EGF-coated and EGF-uncoated QDs showed similar tumor uptake at 1 h post injection. Subsequently, however, targeted quantum dots were accumulated by the tumor tissue, whereas untargeted QDs were washed out. At 24 h post injection, the fluorescence signal had returned to baseline value for targeted and untargeted QDs (Diagaradjane et al. 2008). This illustrates that pharmacokinetic analysis may be needed to assess the expression of EGFR in the tumor tissue by nanoparticles.

32.3.2.2 Assessment of Gene and Protein Expression with MRI

Numerous papers have been published about molecularly targeted MRI probes. However, most of these publications only present proof of principle studies, and the methods have not been refined further to be applicable in routine preclinical research. In particular USPIO- and liposome-based diagnostics often have the disadvantage of showing strong unspecific "enhanced permeability and retention (EPR)"-based accumulation in tumors and thus a strong unspecific background. In addition, the lifetime of these probes within tumors is considerably long. Using this kind of MR imaging probes, targets at the endothelium can be reached more easily, and this may be one explanation why many groups prefer to image markers of angiogenesis like the $\alpha_v\beta_3$-integrins. There are only few reports on using molecular MR imaging to track therapy response. For example, Mulder and colleagues showed the proof of principle and demonstrated a reduced accumulation of $\alpha_v\beta_3$-targeted liposomes to tumor xenografts after antiangiogenic therapy (Mulder et al. 2007). Recent promising strategies for intravascular targeting include the use of micrometer-sized iron oxide particles (MPIOs), which remain strictly intravascular and show short circulation times (similarly like molecularly targeted microbubbles for ultrasound imaging; see Sect. 14.2) (Jefferson et al. 2012).

MRI reporter genes are hardly used due to the high complexity of the methods and due to limitations in detection sensitivity. However, some highly experimental methods exist that may gain more importance in the future:

1. Modulation of the relaxivity of lanthanide complexes by enzymatic cleavage of the probe. For example, in *Xenopus* embryos, which were genetically modified to express β-galactosidase, the cleavage of galactose from a gadolinium-containing chelate complex improved the interaction of the lanthanide with the surrounding protons, thus leading to a positive MR signal (Louie et al. 2000).
2. Modification of the cellular iron uptake and storage. By overexpressing the iron storage molecule ferritin, a decrease in T2 and T2* relaxation time can be achieved, which means that a negative contrast of the engineered cells is given (Modo and Bulte 2007). The expression of these genes can be put under control of tetracycline, which allows to switch the contrast on and of depending on the application of the antibiotic drug.
3. Heterologous proteins that act as chemical exchange saturation transfer agents (CEST; see Sect. 13.2). Gilad and co-workers constructed cells that expressed a lysine-rich protein. The magnetization transfer between the bulk water and the macromolecular protons resulted in a detectable CEST effect (Gilad et al. 2007).

32.3.2.3 Assessment of Gene and Protein Expression with Nuclear Imaging Techniques

Radiolabeled reporter probes have been used to study gene expression in a variety of tumor models. Compared to optical imaging approaches, the key advantage of PET and SPECT is the ability to generate three-dimensional quantitative images that are considerably less influenced by the depth of the studied lesion. On the other hand, PET and SPECT imaging is more expensive than optical imaging as short-lived radiolabeled probes need to be synthesized for each experiment.

Using similar techniques as described above for optical imaging, PET with radiolabeled substrates of HSV1-tk has been used to study the expression of HIF1-regulated genes (Serganova et al. 2004). Another example is imaging of genes regulated by the tumor suppressor p53. In these studies the HSV1-tk (Doubrovin et al. 2001) or NIS (Kim et al. 2005) was expressed under the control of an artificial enhancer p53-responsive element (p53RE). Using this reporter gene construct, the upregulation of p53 activity after DNA imaged could be assessed noninvasively in cell cultures and in tumor xenografts (Doubrovin et al. 2001; Kim et al. 2005).

Radiolabeled antisense oligonucleotide probes have been used to directly image endogenous gene expression at the transcription level. This imaging approach is based on short oligonucleotide sequences that bind to complementary segments of target mRNA or DNA. Scintigraphic images of endogenous gene expression using radiolabeled antisense oligonucleotides have been reported (Lendvai et al. 2009; Hnatowich 1999). However, there are formidable biologic barriers for the efficient intracellular delivery of oligonucleotides. Furthermore, the low concentrations of target mRNA or DNA limit the signal. Therefore, antisense imaging still remains experimental (Hnatowich 1999).

There is a variety of radiolabeled ligands for imaging of proteins expressed on the cell surface. These are based on antibodies, antibody fragments, small proteins, and peptides. A thorough discussion of these various ligands is beyond the scope of this chapter. Instead, some examples are discussed for each class of ligands to illustrate the strengths and limitations of the different approaches.

Radiolabeling of antibodies provides a very general approach to image the expression of cell-surface molecules. However, the slow blood clearance of antibodies frequently limits the contrast between tumors and the surrounding normal tissues. Furthermore, antibodies can accumulate unspecifically within tumors due to the leakiness of the intratumoral blood vessels (enhanced permeability and retention (EPR) effect). The specificity of the signal should therefore be

confirmed by unspecific control antibodies. Since imaging needs to be performed several days after injection, radiolabeling with long-lived radioisotopes is generally necessary. This can cause logistic problems, as radioactive waste needs to be stored for longer periods of time. Radioisotopes used for labeling antibodies for PET imaging include iodine-124 (half-life of 4.18 days) and zirconium-89 (half-life of 3.27 days). Antibody fragments of various sizes have also been used for PET imaging. They are cleared faster from the bloodstream, but frequently also show lower tumor uptake. Antibody engineering allows for optimization of pharmacokinetic parameters for imaging (Olafsen et al. 2005). For antibodies with relatively fast binding and excretion, copper-64 (half-life of 0.53 days) or even fluorine-18 (half-life of 110 min) can also be used (Wu and Senter 2005). Targets that have been successfully imaged with radiolabeled antibodies or antibody fragments include, among others, carbonic anhydrase IX (CA-IX) and HER2, carcinoembryonic antigen (CEA), prostate stem cell antigen (PSCA), and prostate-specific membrane antigen (PSMA) (Wu 2009).

Peptide hormone receptors are overexpressed on many malignant tumors. Radiolabeled peptides can be used to image the expression of these receptors (Reubi and Maecke 2008). Well-studied examples include somatostatin (Ginj et al. 2008) and bombesin receptors (Morgat et al. 2014). These imaging probes have also been studied in patients and therefore allow for translational studies. Radiolabeled peptides have also been extensively used to image the expression of alpha-v beta-3 integrins on cancer cells. A variety of ligands based on the arginine-glycine-aspartate (RGD) sequence has been tested (Haubner et al. 2001; Chen 2006). While several integrins bind to the RGD sequence, cyclic pentapeptides with a specific sterical structure allow for specific imaging of $\alpha_v\beta_3$-integrins (Chen 2006; Rylova et al. 2014). These radiolabeled peptides can be used to study the expression of $\alpha_v\beta_3$-integrins and to monitor therapeutic interventions targeting this integrin (Fig. 32.1).

When interpreting these studies, one needs to consider that the relative contribution of integrins on the surface of cancer cells as compared to integrins expressed on activated endothelial cells will depend on the specific model studied. Furthermore, antiangiogenic drugs may affect the delivery of the peptide in a complex way that can confound the correlation between $\alpha_v\beta_3$-integrin expression and uptake of RGD peptides (Rylova et al. 2014). Recently radiolabeled small molecules binding to the enzymatic site of PSMA have been shown to provide high-contrast images

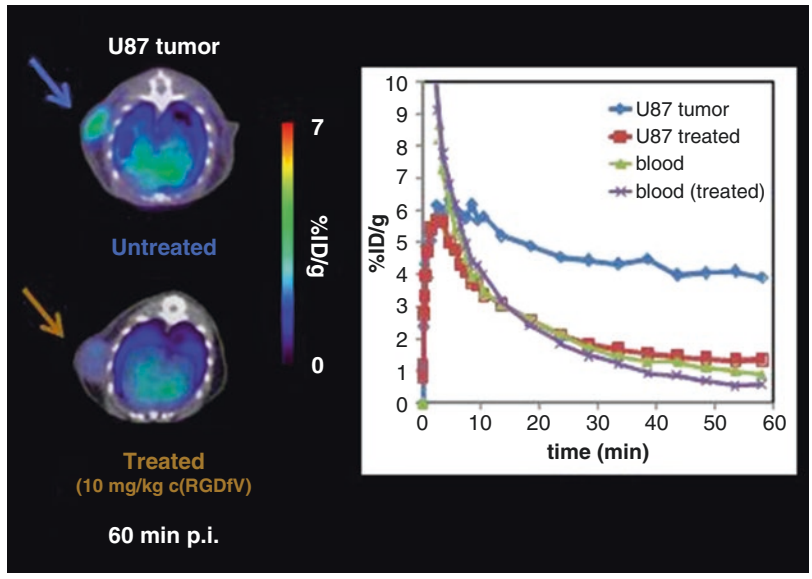

Fig. 32.1 Imaging the expression of alpha-v beta-3 integrins with a Cu-64-labeled RGD peptide. The untreated U87 glioblastoma demonstrates high uptake and retention of the tracer as shown by the PET/CT images and the time activity curves. Treatment with the alpha-v beta-3 ligand c(RGDfV) causes a marked decrease in uptake and rapid washout of the radiolabeled RGD peptide

of PSMA-expressing tumors in animal models and patients. These agents can be used to study prostate cancer in animal models and in the clinic (Mease et al. 2013).

Radiolabeled small molecules allow imaging of intracellular targets with PET or SPECT. Imaging of intracellular targets is more challenging than of extracellular targets, since the image probe needs to cross the plasma membrane in order to reach the target. Then the probe has to be retained in cells expressing the target, whereas it should wash out rapidly from cells not expressing the target. Because of these challenges, considerably less intracellular targets than extracellular targets have been successfully imaged with SPECT or PET. Fluorine-18 fluoroestradiol (FES) binds with affinity to the estrogen receptor-α and allows noninvasive imaging of this target with PET (Sundararajan et al. 2007). Conversely, androgen receptors can be studied with PET and 16β-^{18}F-fluoro-5α-dihydrotestosterone (FDHT) (Larson et al. 2004). However, imaging with these agents in mice can be challenging because high-affinity receptors can easily become saturated which limits its image contrast.

32.3.3 Characterization of the Tumor Microenvironment

The tumor microenvironment has an important influence on the growth rate, invasiveness, and metastatic potential of cancer cells (Gatenby and Gillies 2008). Noninvasive studies to characterize the microenvironment are therefore of great interest. Parameters that can be studied by imaging include perfusion, vascular permeability, oxygen tension, and pH. Noninvasive imaging of these parameters allows monitoring of therapeutic interventions that aim to modulate these factors.

32.3.3.1 Characterization of the Tumor Microenvironment with Optical Imaging

Using intravascular fluorescent dyes, the fractional vascular volume can be estimated by fluorescence tomography (Montet et al. 2007). This parameter can be used to monitor therapeutic interventions targeting intratumoral blood vessels.

Furthermore, fluorescent probes directed toward markers of angiogenesis, stromal activation, and inflammation can be used to investigate remodeling of the microenvironment. Also reporter genes (fluorescent proteins and luciferase) expressed by inflammatory and other stromal cells like fibroblasts and endothelial cells are frequently applied, in particular in combination with multicolor intravital microscopy techniques, such as two-photon microscopy (see Sect. 16.4).

One of the most frequently addressed targets of intratumoral angiogenesis is the $\alpha_v\beta_3$-integrin, which is expressed on the surface of activated endothelial cells. Expression of this integrin can be imaged with fluorescent compounds based on the RGD sequence or non-peptidic ligands (Chen et al. 2004; Kimura et al. 2009), and even commercial probes for its in vivo optical imaging are available (e.g., IntegriSense, PerkinElmer). However, when addressing this target, it is important to consider that $\alpha_v\beta_3$-integrin expression is not specific for endothelial cells. In fact, a variety of cancer cells also express significant amounts of $\alpha_v\beta_3$-integrins. Peptide and other small molecule-based imaging probes cannot be used to differentiate between expression of $\alpha_v\beta_3$ on activated endothelial cells and tumor cells. Imaging with nano- or microparticles may allow specific imaging of integrins expressed on endothelial cells (Cai et al. 2007).

32.3.3.2 Characterization of the Tumor Microenvironment with Ultrasound

Ultrasound imaging is favorably suited to characterize tumor neovascularization (Kiessling et al. 2009). Without the need for contrast agents, Doppler can be used to visualize neovascularization. However, even when using high-frequency ultrasound scanners, the flow-dependent Doppler methods only display larger vessels above 100 μm in diameter. For the visualization of tumor microvascularization ultrasound, contrast agents should be used. Since the larger vessels with higher flow usually are more mature, the

combination of non-enhanced Doppler with contrast-enhanced ultrasound scans can be used to investigate the maturity of the tumor vascularization and to monitor vascular maturation during antiangiogenic treatments (Palmowski et al. 2008a) (Fig. 32.2).

Using ultrasound contrast agents, the relative blood volume (rBV) can easily be determined by performing an automated 3D scan of the tumor and determining the amount of vascularized voxels in relation to all tumor voxels. Nevertheless, it should be noted that this leads to an overestimation of rBV due to partial volume effects. Using contrast-enhanced ultrasound, a reduction of relative blood volume could be visualized after few hours, far before a reduction in tumor volume occurred. Blood flow, blood velocity, and perfusion in tumors can be determined using replenishment kinetics, meaning that during a stable microbubble concentration in the blood, a microbubble-destructive pulse is applied and the replenishment is recorded (Wei et al. 1998). Then, perfusion can be estimated from the initial upslope of the curve. Also using replenishment imaging antiangiogenic therapy, the effects could be determined early and prior to size tumor changes.

The use of molecular ultrasound imaging to characterize tumor angiogenesis is emerging. Among others, the overexpression of VEGFR2, E-selectin, $\alpha_v\beta_3$-integrin, ICAM, and endoglin has been studied using targeted microbubbles in different tumor models (Kiessling et al. 2009). In this context, both phospholipid and hard-shell microbubbles (e.g., polycyanoacrylate based) have been used. In most cases coupling of the biotinylated antibodies and peptides was possible via streptavidin on the microbubble surface. Please note that biotinylated molecular ultrasound contrast agents are commercially available for animal research.

Since microbubbles have a considerably short blood half-life and since they can be destroyed in the tumor with high-energy ultrasound pulses, the sequential investigation of different molecular targets within the same session is feasible. This has been done in a study of Palmowski and colleagues, who longitudinally investigated the expression of VEGFR2 and $\alpha_v\beta_3$-integrin in squamous cell carcinomas treated with a matrix

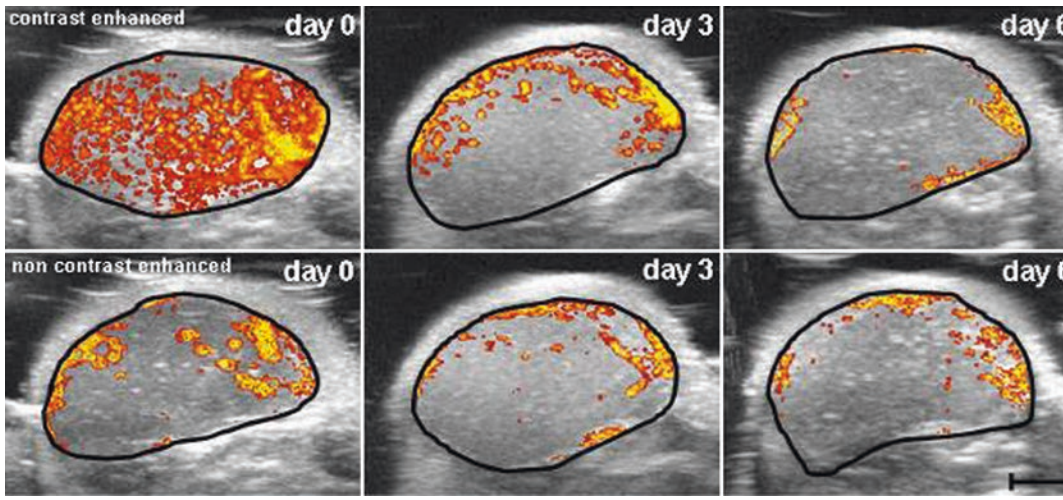

Fig. 32.2 Contrast-enhanced and noncontrast-enhanced multiple image alignments of an A431 tumor xenograft during antiangiogenic treatment. While the tumor appears highly vascularized in the contrast-enhanced scan, noncontrast-enhanced Doppler images (showing blood vessels with higher blood flow) mostly display vessels at the tumor periphery and prominent vascular bundles. Histologically, these vessels are larger and more mature. During therapy a rapid collapse of vascularization in the tumor center can be observed by contrast-enhanced imaging. In contrast, therapy effects on the "more mature vessel fraction" displayed by the noncontrast-enhanced Doppler are less pronounced (bar, 1 mm) (Image taken from Palmowski et al. (2008a))

metalloproteinase inhibitor and the expression of ICAM-1 and $\alpha_v\beta_3$-integrin in prostate cancers treated with a heavy-ion therapy (Palmowski et al. 2008b, 2009). When using molecular ultrasound imaging for therapy monitoring, it is important to measure the relative blood volume as an internal reference and to form ratios between the accumulation of site-specific microbubbles and vascularization. By this, it is possible to distinguish a change in vessel density from a change in the molecular profile of vessels (e.g., during maturation).

Finally, these advanced molecular and functional ultrasound imaging methods may be combined with optoacoustic imaging that enables the assessment of the relative blood volume and even of tumor hypoxia by using hemoglobin as an endogenous contrast agent. In addition, also reporter genes and extracellular targets can be addressed with this technology (please find more information in Sect. 16.5).

32.3.3.3 Characterization of the Tumor Microenvironment with µCT

Dynamic contrast-enhanced CT can be used to determine functional vascular parameters in tumors. Depending on the scan protocol, postprocessing can be performed using the first-pass analysis (e.g., using the Miles model; (Miles 2002)) to determine the relative blood volume and perfusion or using two (or more) compartment models to derive data about relative blood volume, perfusion, and vessel permeability (Brix et al. 1999). However, when intending to perform perfusion CT studies, keep in mind that beam-hardening artifacts coming from the contrast agent bolus within large arteries and veins can significantly disturb the assessment of the concentration time curve in the tumor. Furthermore, the tumor enhancement can be low (usually only 20–60 HU), and a good contrast-to-noise ratio is required to get a reliable curve fit.

An alternative to fast dynamic scans is to assess rBV by static scans using blood-pool contrast agents. By just measuring CT numbers (Hounsfield units (HUs)) before and after contrast agent (CA) injection in the target tissue and a large vessel, rBV can be determined following this simple formula:

$$100 * HU_{tissue}\ \text{after CA} - HU_{tissue}\ \text{before CA} / HU_{blood}\ \text{after CA} - HU_{blood}\ \text{before CA}.$$

Using this approach, Ehling and co-workers showed that even small variations in rBV (less than 10 %) between different tumor models can be reliably monitored and that the obtained data match with the histological correlate (Ehling et al. 2014).

In addition to the functional characterization, µCT can be used for the in vivo and ex vivo visualization of tumor vessels. In particular, in lethal experiments, the casting of vessels with polymerizing suspensions like Microfil (Flow Tech Inc.) enables subsequent high-resolution µCT scans that can provide a detailed view on the tumor vascular network down to capillary level (Fig. 32.3).

Nevertheless, in all of these applications, carefully consider the applied x-ray dose, which is considerably high in dynamic contrast-enhanced µCT scans, increases for scans with higher spatial resolution, and can critically accumulate if subsequent imaging session is performed within a short period of time.

32.3.3.4 Characterization of the Tumor Microenvironment with MRI

MRI offers a broad variety of techniques to characterize the tumor microenvironment, and only the most frequently used ones will be mentioned in this book chapter. DCE MRI is well established to characterize tumor neovascularization. Postprocessing is mostly done by using two-compartment models (mostly the models of Brix and Tofts and modifications thereof) (Kiessling et al. 2007). Semiquantitative descriptors of relative blood volume, perfusion, and vessel permeability can be obtained, and their capability to characterize tumor angiogenesis has been shown frequently. For example, using the permeability-weighted "exchange rate constant," higher vascular maturation in squamous cell carcinomas after PDGF transfection could be demonstrated (Lederle et al. 2010). Also the response of tumors

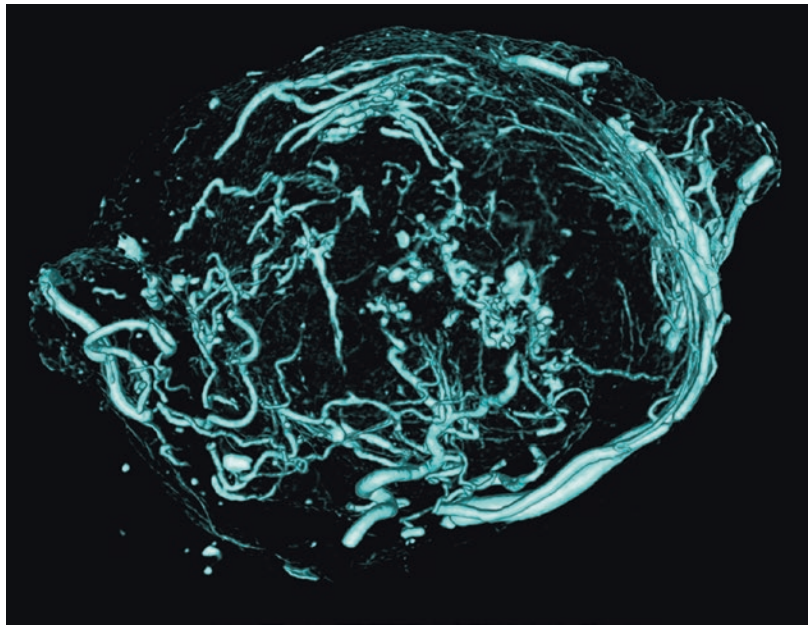

Fig. 32.3 3D reconstruction of high-resolution μCT data of the vasculature of a small Microfil-casted lung cancer xenograft

to different kinds of treatment like radiotherapy, chemotherapy, and antiangiogenic therapy has been demonstrated convincingly (Fig. 32.4).

In line with the findings observed by ultrasound, changes in vascularization often preceded the change of tumor volume. In this context, parameters of relative blood volume and vessel permeability/perfusion (such as k^{trans} and k^{ep}, which derive from two-compartment models) were identified as sensitive markers. Superiority of the one or the other marker seems to highly depend on the tumor model used. Nevertheless, for the accurate quantification of these functional vascular parameters, it is recommended to measure the arterial input function in a large vessel (e.g., the aorta). The use of MR contrast agents of higher molecular weight (e.g., gadolinium-loaded albumin or gadolinium-containing polymers) further facilitates the correct assessment of the signal time course by slowing down the contrast agent exchange with the interstitial space, thus enabling a better separation of perfusion and vessel permeability.

Susceptibility-weighted steady-state MRI is an alternative to determine the relative blood volume. Here long-circulating ultrasmall superparamagnetic iron oxide (USPIO) nanoparticles are injected, and the T2*-relaxation times are recorded before and after contrast agent injection. Bremer and colleagues showed that this method can be used to catch the vascular breakdown following the administration of vascular disruption agents with high congruency to histology (Persigehl et al. 2007). Combining T2 and T2* relaxometry before and after administration of USPIO (or other MR contrast agents) enables the determination of the mean vessel size in tissues by a method called vessel size imaging (Tropres et al. 2001). Using vessel size imaging, changes in the vascular architecture (e.g., maturation) occurring during antiangiogenic therapy can be assessed (Zwick et al. 2009). However, up to now results obtained are controversial and seem to highly depend on the used tumor model. If an MR scanner with sufficiently high-field strength (>4.7 T) is available, vessel maturity and vascular volume fraction can also be investigated with "blood oxygenation level-dependent (BOLD) imaging" (see Sect. 13.1 and Chap. 25), which was proven by the group of Michal

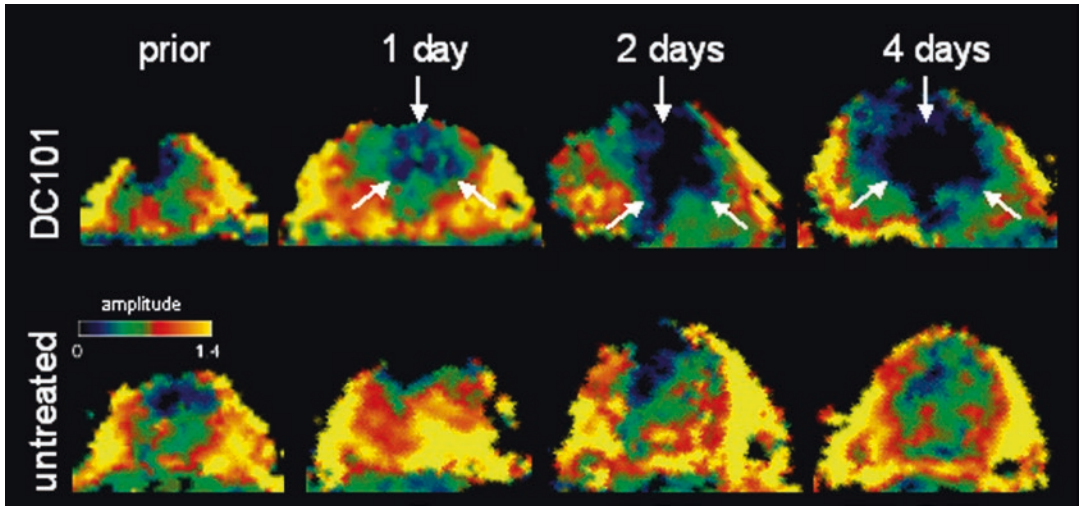

Fig. 32.4 Example for a DCE MRI study to track tumor response to antiangiogenic therapy. Color-coded parameter maps of "amplitude" (a marker correlating with the relative blood volume) of a VEGFR2 antibody(*DC101*)-treated and an untreated tumor are shown before (*0*) and 1, 2, and 4 days after the start of treatment. Two days after the start of antibody treatment, spots occurred in the tumor center, which did not show any contrast enhancement (*arrows*). After 4 days, no central enhancement was found, and thus no amplitudes could be calculated in central tumor areas anymore (*arrows*). During these 4 days of treatment, no significant differences were observed in tumor volume between the treated and the untreated tumors yet (Image taken from Kiessling et al. *Neoplasia* 2004;6:213–223)

Neeman, who used it to investigate vessel responsiveness and maturation in ovarian tumor xenografts (Gilead et al. 2004).

Diffusion-weighted imaging (DWI) is an MRI method to investigate the motion of protons in tissues and it is based on the Brownian motion. The higher the cell density is, the more diffusion barriers exist and the lower the diffusion will be. This leads to high signal intensities in diffusion-weighted images and to low *apparent diffusion coefficient (ADC)* values. Thus, diffusion-weighted imaging is an indirect measure of cellularity. In preclinical studies, DWI can favorably be used to detect and characterize tumors in non-moving organs (e.g., the bones and the brain). There are few reports on the use of DWI to monitor the efficacy of chemo- and antiangiogenic therapy in rodents; however, results obtained were controversial.

Different cell types contribute to the development of a malignant stroma. Among those are macrophages, endothelial progenitor cells, and (myo-)fibroblasts. In order to investigate the migration of these cells to tumors, they can be labeled in vitro by superparamagnetic iron oxide nanoparticles. In this context, since the cellular uptake of dextran-coated commercial *SPIO* and *USPIO* usually is relatively low, transfection agents (e.g., protamine sulfate) should be used to support internalization. Alternatively, cell-penetrating peptides such as HIV tat may be bound to the surface of iron oxide nanoparticles. Imaging usually is performed with T2*-weighted gradient-echo sequences. However, it is recommended to additionally perform T2 or T2* relaxometry. Besides the subjective visual inspection, this enables quantification of the signal changes after injection of the labeled cells. Alternatively to the direct cell-labeling methods, which have the disadvantage that the label becomes weaker over time because cells proliferate or because the label is released from the cells, ferritin can be used as a reporter gene, which offers stable imaging properties of the cells over time (see Sect. 32.2.2.2). In this context, Vandburger and co-workers successfully demonstrated the dynamic recruitment of exogenously adminis-

tered, ferritin-expressing fibroblasts to the vasculature of ovarian cancer xenografts (Vandsburger et al. 2013).

Additionally to the imaging of cells supporting the formation of a malignant stroma, cell tracking can be used to monitor the success of cell-based treatments (e.g., using dendritic cells or T cells). For example, Kircher et al. successfully used MRI to monitor the accumulation of magnetically labeled, activated T cells in melanoma xenografts and to monitor tumor response (Kircher et al. 2003) (Fig. 32.5).

Nevertheless, please note that for most in vivo cell-tracking experiments (except for the case that a very high number of labeled cells accumulate in the tumors) high-field MR scanners (>4.7 T) or additional gradient inserts in clinical MR scanners are required. Please find more information about cell tracking with MRI in Chap. 23.

32.2.3.5 Characterization of the Tumor Microenvironment with Nuclear Imaging Techniques

Several radiolabeled imaging probes have been developed to image *tumor hypoxia* with PET (Serganova et al. 2006). The most extensively studied imaging probe for *hypoxia* imaging is fluorine-18-labeled *fluoromisonidazole (FMISO*). Other imaging probes include *fluorine-18-labeled fluoroazomycinarabinoside (FAZA)* and *copper-64-labeled copper(II)-diacetyl-bis(N(4)-methylthiosemicarbazone) (ATSM)* (O'Donoghue et al. 2005). These probes provide a higher contrast than FMISO, but their ability to image hypoxia has been less thoroughly validated than for FMISO. On a macroscopic level, FMISO uptake has been found to correlate well with other markers of hypoxia, such as oxygen probe measurements, CA-IX expression, and

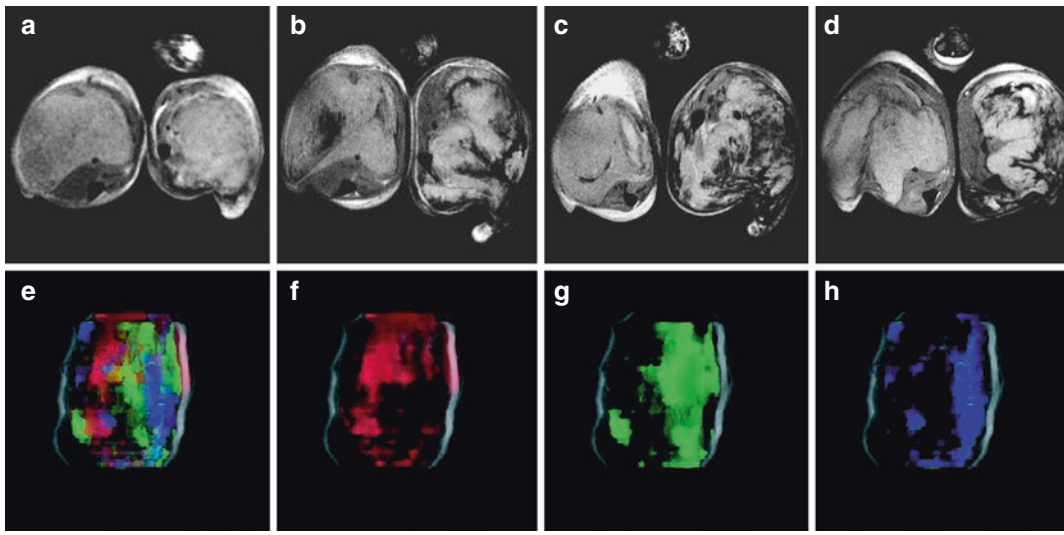

Fig. 32.5 Intratumoral distribution of sequentially administered OT-I CD8+ T cells. Mice were implanted with B16 melanoma (*left*) and OVA-transfected B16 melanoma cells (*right*). Ten days later, 10^7 OT-I CD8+ T cells were labeled with CLIO-HD and adoptively transferred into the recipient (0 h). Sequential adoptive transfers of 10^7 CLIO-HD-labeled OT-I CD8+ T cells were administered to the same mouse at 48 h and 96 h. MR imaging at 8.5 T was performed 12 h after each adoptive transfer of CLIO-HD-labeled OT-I CD8+ T cells; (**a**–**d**) axial slices through the mouse thighs at (**a**) before adoptive transfer; (**b**) 12 h after the first adoptive transfer; (**c**) 12 h after the second adoptive transfer (60 h); and (**d**) 12 h after the third adoptive transfer (108 h), indicating the heterogeneity of OT-I CD8+ T cell recruitment to the B16-OVA tumor with sequential injections. (**e**–**h**) Three-dimensional rendering of the B16-OVA tumor at (**f**) 16 h (*red*, first injection); (**g**) 60 h (*green*, second injection); (**h**) 108 h (*blue*, third injection). (**e**) Color-coded compilation of (**f**–**h**). It can clearly be seen by MRI that the activated OT-I CD8+ T cells selectively home to the OVA-transfected tumor and inhibit its progression (Image taken from Kircher et al. (2003))

pimonidazole binding (Hoffman 2005). FMISO PET cannot, however, resolve regional difference in hypoxia on a microscopic level.

32.3.4 Studies of Tumor Cell Proliferation and Metabolism

Unregulated proliferation is a common characteristic of malignant tumors. Therefore, imaging of *cellular proliferation* is highly interesting for oncology research. Proliferation is closely linked to *metabolism*, since proliferation requires DNA synthesis, which again is dependent on the synthesis of nucleotides. In recent years there has also been renewed interest in the altered tumor glucose metabolism of cancer cells. In normal mammalian cells, glycolysis is inhibited by the presence of oxygen, which allows the mitochondria to oxidize pyruvate to CO_2 and H_2O. This inhibition of glycolysis is termed the "Pasteur effect," after Louis Pasteur, who first demonstrated that glucose flux was reduced by the presence of oxygen. Conversion of glucose to lactic acid in the presence of oxygen is known as aerobic glycolysis and was reported by Otto Warburg at the beginning of the twentieth century as a specific metabolic abnormality of cancer cells (Kroemer and Pouyssegur 2008).

Recent studies have now indicated that several oncogenes involved in the development and progression of common human cancers also play an important role in the regulation of glycolysis. For example, unregulated activity of the serine-threonine kinase Akt has been shown to increase glucose uptake of tumor cells as well as increase resistance to apoptosis. The "glycolytic phenotype" is increasingly considered as necessary for tumor progression, since it provides the necessary building blocks for the synthesis of nucleosides and also allows cancer cells to grow in a hypoxic environment (Kroemer and Pouyssegur 2008; Gatenby and Gillies 2004; Vander Heiden et al. 2009).

In addition to increased glycolytic activity, overexpression of *choline kinase* (ChoK) is frequently observed in many malignant tumors. Experimental studies have indicated that various oncogenic signaling pathways including phosphatidylinositol-3-kinase (PI3K) and *HER2* lead to increased FAS expression (Van de Sande et al. 2002). Several oncogenes such as ras, src, raf, and mos increase choline kinase activity when expressed in mouse fibroblast (Aoyama et al. 2004). Likewise, transfection of human mammary epithelial cells with the erbB2 oncogene has been reported to cause a significant increase in phosphocholine levels (Ramirez de Molina et al. 2004). Choline kinase activity and phosphocholine levels were generally not well correlated with proliferation rates (Bhakoo et al. 1996), suggesting that activation of choline kinase cannot be explained alone by the cell membrane synthesis of proliferating cells.

Another metabolic abnormality of cancer cells is the accelerated rates of *amino acid transport* by the transport systems A and L (McGivan and Pastor-Anglada 1994). Mammalian cells take up amino acids by a set of transport molecules with overlapping substrate specificity. Amino acid transport systems have been functionally characterized by affinity for specific amino acids, sodium dependency, and sensitivity to inhibitors before the actual transporter proteins had been identified. Based on functional characteristics, 13 major amino acid transports system can be differentiated (Aoyama et al. 2004). These include the sodium-dependent systems A, ASC, N, Gly, B^0, B, $B^{0,+}$, X_{AG}^-, and β and the sodium-independent systems L, y^+, $b^{0,+}$, and x_C^- (McGivan and Pastor-Anglada 1994). For imaging purposes system L is particularly interesting, since several imaging probes, such as fluoroethyl tyrosine and fluorodopa, are transported by this system (Verrey 2003). Following transport across the cell membrane amino acids can enter protein synthesis or multiple other anabolic and catabolic processes. However, during the relatively short time interval that can be studied by PET, amino acid transport generally appears to be the dominant factor for the uptake of most clinically used radiolabeled amino acids (Ishiwata et al. 1993).

32.3.4.1 Assessment of Tumor Proliferation and Metabolism with Optical Imaging

There are few fluorescent probes for studies of tumor cell metabolism and proliferation. The chemical properties of small molecules such as nucleosides, glucose, or amino acids are significantly altered by the fluorescent dyes which have a larger molecular weight than the labeled substrates themselves. A fluorescent glucose analog was suggested for in vivo imaging (Kovar et al. 2009). This compound is accumulated in experimental tumors. However, the uptake mechanisms are not well understood. Since the compound is not taken up by the brain, it is not clear whether its uptake actually reflects glucose metabolism (Kovar et al. 2009).

32.3.4.2 Assessment of Tumor Proliferation and Metabolism with MRI

Metabolism and indirect markers of cell proliferation in tumors can be investigated by MR spectroscopy (see Sect. 13.4). In this context, choline is typically upregulated in tumors and can be seen as an indicator of rapid membrane turnover, which is a typical feature for proliferative tissues. In proton MR spectra, choline can be identified even with clinical MR scanners, and in experimental tumors, it has been shown to negatively correlate with therapy response, e.g., under radiotherapy. In this context, creatine often is used as an internal standard, and ratios between choline and creatine are formed. Another prominent peak derives from lipids. Increasing amounts of free lipids have been shown to correlate with tumor aggressiveness in orthotopic liver tumors (Foley et al. 2001) and experimental prostate cancers. Using 31P-MR spectroscopy, the intracellular pH value of tumor tissues can be investigated. However, it is important to note that in tumors the extracellular pH value usually is decreased, but due to upregulation of proton pumps in tumor cells, the intracellular pH value in tumors can be normal or even increased. Using high-field MR scanners, many more interesting metabolites such as N-acetylaspartate, lactate, and taurine can be separated but it would go beyond the scope of this chapter to discuss them all in detail.

In addition to spectroscopy, the pH value can also be obtained using pH-sensitive CEST probes (see Sect. 13.2), which, however, are not commercially available yet and still in the process of evaluation. These will mostly measure the extracellular pH value and thus may be used complementary to phosphor spectroscopy. Recently, CEST imaging was also reported for the use of glucose, and it was shown that ^{18}F-FDG autoradiography correlated with the MRI findings (Walker-Samuel et al. 2013). Indeed, the sensitivity of MRI to probes is several orders of magnitude lower than of PET, which also holds true for CEST applications. However, if injecting unlabeled glucose, toxicological concerns are considerably low, and thus the injected amount of glucose can be increased to a level that almost compensates for the lower sensitivity as compared to PET. However, whether "glucoCEST" can become an acceptable alternative to ^{18}F-FDG-PET imaging still has to be evaluated. This is particularly true since internalized glucose would rapidly be phosphorylated and then not be well detectable by "glucoCEST" anymore.

For the assessment of fast metabolic processes, also hyperpolarized MR imaging is emerging (see Sect. 13.3). This is facilitated by new hyperpolarization methods like dynamic nuclear polarization (DNP) or para-hydrogen-induced polarization (PHIP), which enable hyperpolarization of atoms like 13C and 15 N and thus broaden the range of possible probes. Although the hyperpolarization effect lasts very short in vivo (seconds to few minutes), it has been shown to be fast enough to monitor accumulation and metabolization of pyruvate Nelson et al. (2013). In this context, it is charming that not only the injected compound can be tracked but also its metabolites when using spectroscopic analysis. In principle, many other small molecules can be hyperpolarized including some amino acids like alanine and glutamine. Both mentioned amino acids have already been used successfully in preclinical studies on amino acid transport and metabolism of cancer.

32.3.4.3 Assessment of Tumor Proliferation and Metabolism with Nuclear Imaging Techniques

For imaging of tumor *cell proliferation*, thymidine and thymidine analogs are of special interest, since thymidine is the only nucleoside which is exclusively incorporated into DNA, but not RNA. Radiolabeled thymidine has therefore been used since many years to study cellular proliferation in vitro. However, thymidine is too unstable to be used for routine in vivo imaging of tumor proliferation. By far the most extensively studied probe for imaging of cellular proliferation is therefore the thymidine analog *3′-deoxy-3′-^{18}F-fluorothymidine (FLT)* (Shields et al. 1998). Similar to thymidine FLT is transported across the cell membrane by nucleoside transporters (Krohn et al. 2005). Intracellularly, FLT and thymidine are phosphorylated by thymidine kinase-1 (TK-1). In contrast to thymidine, however, FLT is not incorporated into DNA. Studies have indicated that TK-1 activity is the key factor determining the amount of FLT uptake by cancer cells. In normal cells and most cancer cells, TK-1 activity is strongly upregulated during S phase, while there is only little activity during the other phases of the cell cycle. Studies have shown that FLT flux as measured by dynamic PET studies, as well as FLT uptake at a fixed time post injection, is reasonably well correlated with histopathologic markers of tumor cell proliferations, such as the Ki-67 labeling index (Krohn et al. 2005).

Tumor glucose metabolism can be imaged by PET with the glucose analog *fluorine-18 fluorodeoxyglucose (FDG)*. Following intravenous injection FDG is transported across the cell membrane by sodium-independent, facilitative glucose transporters (Gluts). In malignant tumors Glut-1 is frequently overexpressed, but expression of Glut-3 and more recently Glut-12 has also been reported in some tumor types (Macheda et al. 2005). Unlike glucose, FDG is not a substrate for the sodium-dependent glucose transporters found in the tubulus system of the kidneys. As a consequence FDG is not reabsorbed after glomerular filtration, but excreted with the urine. This contributes to the rapid clearance of FDG from the bloodstream which is important for imaging metabolically active tissues with high contrast. Intracellularly, FDG and glucose are phosphorylated by hexokinase to glucose-6-phosphate and FDG-6-phosphate, respectively. Glucose-6-phosphate is then further metabolized to fructose-1,6-biphosphate and enters glycolysis. Alternatively, glucose-6-phosphate enters the pentose phosphate pathway and is eventually converted to ribose-5-phosphate, which can serve as a building block for DNA and RNA synthesis. In contrast to this complex metabolic fate of glucose-6-phosphate, FDG-6-phosphate cannot be further metabolized in the glycolytic pathway because the fluorine atom at the C2 position prevents FDG-6P from further degradation.

While FDG undergoes only the first two steps of glucose metabolism (transport and phosphorylation by hexokinase), it is important to note that FDG flux nevertheless reflects exogenous glucose utilization of cancer cells, as long as patients are imaged at steady-state conditions. At steady-state conditions, the concentrations of the various metabolites produced during glycolysis are constant, and the net glucose flux across the cell membrane equals total exogenous glucose utilization. Consequently, uptake rates of FDG are not only dependent on the activity of glucose transporters and hexokinase but also on the activity of downstream molecules.

Radiolabeled choline *([^{11}C]choline)* (Hara et al. 1998) and the choline analogs *([^{18}F]choline and [^{18}F]fluoroethyl choline)* (DeGrado et al. 2001; Hara et al. 2002) have been used to study choline metabolism by PET. In patients radiolabeled choline and choline analogs are rapidly and intensely accumulated in a variety of tumors, including prostate cancer, gliomas, non-small cell lung cancer, and esophageal cancer. In mice, however, uptake of choline and choline analogs has been found to be low by many investigators. The reasons for this unexpectedly low uptake are currently not well understood.

Radiolabeled methionine (*L-[^{11}C-methyl]-methionine, MET*), *tyrosine* (*L-[1-^{11}C]tyrosine)*, and various tyrosine analogs including L-[2-^{18}F] fluorotyrosine, O-(2-[^{18}Ffluoroethyl])-L-tyrosine (FET), L-[3-^{18}F]fluoro-α-methyl tyrosine (FMT),

and L-[3-^{123}I]iodo-α-methyl tyrosine (IMT) represent the most commonly used amino acid tracers (Plathow and Weber 2008). A comprehensive review of these various imaging probes is beyond the scope of this review, and only certain common characteristics are addressed here. Cell culture studies indicate that L-type amino acid transport appears to be a common mechanism for tumor uptake of MET, the tyrosine/phenylalanine analogs (Langen et al. 2006). Other amino acid transporters also contribute to a varying but overall lesser degree to the total cellular uptake of these amino acid tracers. Consistent with these in vitro experiments, in vivo studies in tumor-bearing animals and patients with brain tumors have shown a close correlation between the uptake of MET and IMT, MET, and FET (Langen et al. 2006).

The main applications of PET scans with radiolabeled substrates are monitoring of tumor progression (see Sect. 2.1) and evaluating tumor response to therapy (Fig. 32.6). A series of studies has indicated that FLT uptake decreases very rapidly in response to radiotherapy, cytotoxic chemotherapy (Barthel et al. 2003), and various protein kinase inhibitors (Wei et al. 2008a; Ullrich et al. 2008). In some (Barthel et al. 2003; Ullrich et al. 2008), but not all of these studies (Wei et al. 2008a), changes in FLT uptake better reflected the effects of therapy than change in FDG uptake. Some protein kinase inhibitors such as gefitinib and rapamycin cause very rapid changes in FDG uptake, since their targets are involved in regulating tumor glucose use (Wei et al. 2008b).

32.4 Typical Protocols for Imaging Studies

In the following please note that the estimated examination times are based on our experience and highly depend on the imaging device, the chosen spatial resolution, and the protocol.

32.4.1 Optical Imaging

For fluorescence imaging with genetically encoded proteins, no special animal preparation is required. If imaging tumors close to the

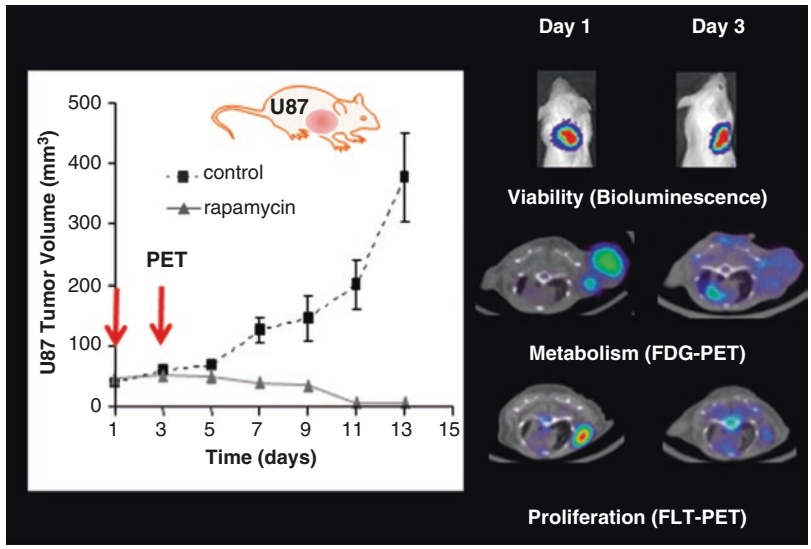

Fig. 32.6 Monitoring tumor response to therapy with PET and bioluminescence imaging. Treatment of U87 human glioblastoma xenograft causes a marked growth inhibition (*left*). After 3 days of rapamycin therapy, there is a marked decrease in tumor proliferation and metabolism as shown by FLT- and FDG-PET studies. However, there is no apparent change the bioluminescence signal indicating that the tumor cells are still viable at the time of PET imaging. Thus, the decrease of the PET signals specifically reflects changes in tumor cell proliferative activity and is not caused by cell death

abdominal cavity, one should consider that chlorophyll, which is often present in animal chow, absorbs at 655 and 411 nm and fluoresces at 673 nm, thus producing a strong signal in the abdominal cavity. For optimal fluorescent imaging performance, purified food formulation that does not contain plant products may be used (Kovar et al. 2007). The nude mouse is an ideal choice for NIR optical imaging, because fur interferes with imaging by blocking, absorbing, and scattering light.

Tumor uptake of fluorescent dyes and image contrast are dependent on the time after injection as well as the route of administration (i.v. or i.p.). Furthermore, the dose of the fluorescent dye can affect the measured signal. High doses may saturate specific target binding, whereas signal-to-noise ratios may be unfavorable for low doses. Pilot studies are frequently necessary to optimize the injected dose and the timing of optical scans in order to ensure sufficient clearance of background activity and maximize specific tumor uptake.

The intensity of the bioluminescence signal is strongly dependent on the time after luciferin injection. For tumors expressing firefly luciferase, the signal typically reaches a peak within 20–30 min after i.p. injection of 100 mg/kg luciferin (Cui et al. 2008) and then decreases gradually. The time to peak is shorter for i.v. injection (Keyaerts et al. 2008). The time to peak light signal varies between different cell lines and is also influenced by the size of the tumor. By mechanisms that are currently not fully understood, anesthesia can markedly influence the intensity signal. In one study the bioluminescence signal was more than three times stronger under anesthesia with ketamine/xylazine than under anesthesia with isoflurane (Cui et al. 2008). Given the large number of potentially confounding factors, it is recommended to perform pilot studies in order to define the time to peak light output and the duration of the peak signal for each tumor model studied.

For planar fluorescence and bioluminescence imaging, one should also consider that the signal is strongly depth dependent. Therefore, imaging animals in the prone and supine position of the animal can be helpful to visualize lesions.

32.4.2 Ultrasound

Tumor size determination can be performed automated in 3D or by the hand in two dimensions and will take about 1 min/animal.

High-frequency Doppler scans of subcutaneous tumors may be used to get a rough orientation on tumor vascularization; however, by this microvessels below 100 μm will hardly be captured (2 min/animal).

Contrast-enhanced scans may be applied subsequently, which can be performed in 2D or 3D. Since catheterization of the animals will be required, the usual examination time increases to about 10–15 min/animal.

The same holds true for molecular ultrasound imaging (approx. 20 min/animal). Here, usually one scan is done before microbubble injection for tumor size determination and orientation. Then, 5–20 min after microbubble injection, a low MI scan is used to assess the amount of microbubbles in the tissue. Subsequently, a microbubble-destructive pulse is applied followed by a second scan after a few seconds, which only captures the nonstationary microbubble fraction. The amount of stationary microbubbles can be obtained by subtracting the signal levels before and after the destructive pulse.

Alternatively, sensitive particle acoustic quantification (SPAQ (Reinhardt et al. 2005)) scans before and after microbubble injection (approximately 10 min/animal) may be used to quantify the amount of stationary microbubbles.

Please note that, when performing repetitive functional and molecular ultrasound scans within short time intervals, pharmacokinetic properties of microbubbles may change. This is due to microbubble uptake by (liver) macrophages and increasing macrophage saturation in subsequent scans. For example, this leads to higher accumulation of molecularly targeted microbubbles in follow-up scans (Rix et al. 2014). The effect can be minimized by using low microbubble doses, by presaturation of the liver macrophages with non-targeted microbubbles, or by keeping the time intervals between repetitive scans long enough.

32.4.3 μCT

For tumor staging it is usually sufficient to image mice with a resolution of 50–100 μm. Using a dedicated animal scanner, this should not take more than 1–10 min. Eventually, respiratory gating has to be performed (e.g., for lung metastases). We recommend retrospective gating (intrinsic or extrinsic) since the animals suffer from intubation (required for prospective gating). Gating can increase the scan time by a factor of 3–5.

32.4.4 MRI

MRI offers a broad variety of scan options but also is time intensive. Imaging protocols have to be adapted to the needed outcome parameters but should be kept as small as possible to minimize the scan time.

32.4.4.1 Tumor Size (~15 Minutes/Animal)

Tumor size determination usually can be performed with a short protocol including T2-weighted sequences, which usually give the best tumor contrast:

Protocol

- Localizer
- Sagittal or coronal T2-weighted (spin-echo or turbo spin-echo) sequence (2D or 3D)
- Transversal T2-weighted (spin-echo or turbo spin-echo) sequence

32.4.4.2 Tumor Size and Morphology (~25 Minutes/Animal; Catheterization Required)

Additional information to tumor size can be obtained without the need to inject contrast agents by including diffusion-weighted imaging and MR spectroscopy. Please note that examination times significantly increase if animals have to be catheterized.

Protocol

- Localizer
- Sagittal or coronal T2-weighted (spin-echo or turbo spin-echo) sequence
- Transversal T2-weighted (spin-echo or turbo spin-echo) sequence
- T1-weighted spin-echo or gradient-echo sequence before and after contrast agent injection
- Eventually diffusion-weighted imaging (5–10 additional minutes)
- Eventually MR spectroscopy (10–15 additional minutes)

32.4.4.3 Tumor Vascularization (30 Minutes/Animal; Catheterization Required)

For the assessment of tumor vascularization, DCE MRI is frequently used. In this context, it is recommended to perform a T1-relaxometry measurement prior to the dynamic scan to enable the conversion of the signal intensity time curve into a concentration time curve. A T1-weighted sequence may be applied at the end to get a well-contrasted high signal-to-noise image of the tumor.

Protocol

- Localizer
- Sagittal or coronal T2-weighted (spin-echo or turbo spin-echo) sequence
- Transversal T2-weighted (spin-echo or turbo spin-echo) sequence
- T1-weighted sequence
- T1 relaxometry (to enable later conversion of signal intensities in concentrations)
- DCE MRI scan (contrast agent injection)
- T1-weighted sequence

32.4.4.4 Molecular Imaging (30–40 Minutes/Animal)

For molecular MR imaging is most important to get quantitative data. For this purpose relaxometric measurements should be performed in combination with high-resolved morphological images at high signal-to-noise levels. If possible, all sequences should be in identical orientation and with identical geometry. Please also take care for suitable controls, e.g., receptor-positive and receptor-negative tumors (in the same mouse), negative control probes (e.g., with a nonbinding peptide or antibody), and competition experiments.

Protocol

- Localizer
- T2-weighted (spin-echo or turbo spin-echo) sequence
- T1, T2 or T2*relaxometry
- Spatially high-resolved T2*- or T1-weighted sequence

32.4.5 Nuclear Imaging

Imaging protocols for PET and SPECT imaging are obviously very dependent on the radiotracer used and the animal model studied. Nevertheless, some general considerations apply to most types of studies. First of all, PET and SPECT can be acquired as "static" or "dynamic" scans. In a static scan, the distribution of radioactivity at one point in time is imaged. Imaging is usually performed when uptake in the tumor has reached a plateau, and activity has sufficiently cleared from the surrounding normal tissues. Furthermore, the radiolabeled probe still needs to emit sufficient signal at the time of imaging. Typically, imaging can be performed during 1–2 physical half-lives of the radiolabel, i.e., 2–4 h for fluorine-18, 1–2 h for gallium-68, and 12–24 h for copper-64. When tumor uptake of the used radiotracer does not reach a plateau during the time frame that is available for imaging, it is very important that all studies are performed at the same time post injection. Otherwise, there may be significant variability in the measured radiotracer uptake values (Fueger et al. 2006).

In a dynamic scan, imaging is started immediately after tracer injection, and a series of images is acquired over a time period of 1–2 h. Using dynamic imaging, one can therefore measure the amount of the radiotracer uptake by the tumor over time. In addition, the clearance of the tracer from the circulation can be determined. Using these data and compartmental modeling or other tracer kinetic approaches, one can calculate tumor uptake rates of the studied radiopharmaceutical. In contrast to uptake values, uptake rates are no longer time dependent. Furthermore, tracer kinetic modeling allows for corrections of differences in the clearance of the tracer from the circulation. Thus, dynamic imaging can reduce the inter- and intra-animal variability of quantitative parameters derived from SPECT or PET studies. In some cases it is even possible to correct for differences in perfusion and vascular permeability by compartmental modeling of dynamic PET studies.

However, dynamic imaging has also limitations. Dynamic imaging takes considerably more time than static imaging. For example, a typical static FDG scan of a mouse can be acquired in 5–10 min, whereas a dynamic study requires 40–60 min. Consequently, only relatively few animals can be imaged in one session. Furthermore, the stress for the animal is higher, especially when repeated PET scans have to be performed for treatment monitoring. Tracer kinetic modeling to correct for the influence of perfusion and vascular permeability is not always feasible. For example, it may be challenging to measure the clearance of the radiotracer from the blood due to the presence of radiolabeled metabolites. Considerable experience and mathematical knowledge are also required in order to obtain reliable corrections.

When using receptor ligands for PET or SPECT imaging, it is important to consider the mass of the tracer injected. Although scintigraphic techniques are extremely sensitive, radiolabeling of the tracer is frequently not highly efficient. Therefore, a considerable amount of unlabeled tracer may be injected into the animal. This unlabeled tracer can partially block binding of the radiolabeled tracer to the receptor. On the one hand, this can limit image contrast and lesion detectability. On the other hand, it may cause errors in quantitative measurements if the amount of unlabeled tracer varies between different studies. The effect of unlabeled tracer on tracer uptake is often called the "mass effect." It is important to know the specific activity (the amount of radioactivity per mol injected tracer) of the injected tracers in order to judge whether the target may be partially blocked. In this context one also needs to consider that for short-lived radioisotopes, the specific activity decreases rapidly over time. For example, if a gallium-68-labeled tracer is injected 3 h after synthesis, its

specific activity will be eight times lower. Consequently, eight times more mass is injected which may reduce the measured signal and image contrast.

For metabolic tracers, such as FDG, anesthesia and animal preparation can have a profound effect on tumor uptake and image contrast. For example, ketamine/xylazine, a commonly used anesthesia for rodents, induces a marked hyperglycemia in mice. Since glucose competes with FDG for uptake and phosphorylation, this can markedly decrease tumor FDG uptake. Isoflurane anesthesia has a less pronounced, but still measurable, impact on glucose levels, which is highly dependent on the studied mouse strain. In some strains isoflurane has been shown to cause mild hyperglycemia, whereas in others hypoglycemia has been observed (Fueger et al. 2006; Flores et al. 2008). When mice are not warmed before and after FDG injection, thermoregulatory brown adipose tissue becomes activated resulting in very intense FDG uptake in the neck and upper thoracic area of mice which can severely affect tumor detection in this area (Fueger et al. 2006).

For a typical FDG-PET study, the mice cages are therefore put on a temperature-controlled heating pad about 30 min prior to the planned FDG injection (Flores et al. 2008). Mice are anesthetized prior to FDG injection, since injection in conscious mice results in high uptake by the skeletal muscles. Fasting may increase tumor FDG uptake, but also results in weight loss, especially when repeated imaging studies are performed.

Most investigators inject FDG in a tail vein, but FDG is rapidly absorbed following i.p. injection. At 1 h post injection, tumor FDG uptake is comparable after i.v. and i.p. injection (Fueger et al. 2006). However, small amounts of FDG may still be present in the abdomen and can interfere with the detection of intra-abdominal lesions. Static PET imaging is performed about 60 min post injection. Using current systems, about 10 MBq FDG is injected per mouse and images are acquired for 5–10 min. Many investigators do not use attenuation correction for the PET scan, since the effect on the measured tracer uptake is small in mice.

Using such a protocol, tumors as small as 2 mm can be visualized by FDG-PET (Woo et al. 2008). However, metabolic activity significantly varies across different tumor models and markedly influences the detection limits. Test-retest reproducibility of FDG-PET scans acquired according to standardized protocol is good with a coefficient of variation of repeated measures in untreated animals of about 15 % (Dandekar et al. 2007).

References

Andresen V, Alexander S, Heupel WM, Hirschberg M, Hoffman RM, Friedl P. Infrared multiphoton microscopy: subcellular-resolved deep tissue imaging. Curr Opin Biotechnol. 2009;20:54–62.

Aoyama C, Liao H, Ishidate K. Structure and function of choline kinase isoforms in mammalian cells. Prog Lipid Res. 2004;43:266–81.

Barthel H, Cleij MC, Collingridge DR, Hutchinson OC, Osman S, He Q, et al. 3′-deoxy-3′-[18F]fluorothymidine as a new marker for monitoring tumor response to antiproliferative therapy in vivo with positron emission tomography. Cancer Res. 2003;63:3791–8.

Bentolila LA, Ebenstein Y, Weiss S. Quantum dots for in vivo small-animal imaging. J Nucl Med. 2009;50:493–6.

Bhakoo KK, Williams SR, Florian CL, Land H, Noble MD. Immortalization and transformation are associated with specific alterations in choline metabolism. Cancer Res. 1996;56:4630–5.

Bremer C, Tung CH, Weissleder R. In vivo molecular target assessment of matrix metalloproteinase inhibition. Nat Med. 2001;7:743–8.

Brix G, Bahner ML, Hoffmann U, Horvath A, Schreiber W. Regional blood flow, capillary permeability, and compartmental volumes: measurement with dynamic CT – initial experience. Radiology. 1999;210:269–76.

Cai W, Chen K, Li ZB, Gambhir SS, Chen X. Dual-function probe for PET and near-infrared fluorescence imaging of tumor vasculature. J Nucl Med. 2007;48:1862–70.

Chen X. Multimodality imaging of tumor integrin alphavbeta3 expression. Mini Rev Med Chem. 2006;6:227–34.

Chen X, Conti PS, Moats RA. In vivo near-infrared fluorescence imaging of integrin alphavbeta3 in brain tumor xenografts. Cancer Res. 2004;64:8009–14.

Cui K, Xu X, Zhao H, Wong ST. A quantitative study of factors affecting in vivo bioluminescence imaging. Luminescence. 2008;23:292–5.

Dandekar M, Tseng JR, Gambhir SS. Reproducibility of 18F-FDG microPET studies in mouse tumor xenografts. J Nucl Med. 2007;48:602–7.

de la Zerda A, Bodapati S, Teed R, Schipper ML, Keren S, Smith BR, et al. A comparison between time domain and spectral imaging systems for imaging quantum dots in small living animals. Mol Imaging Biol. 2009;12:500–8.

DeGrado TR, Coleman RE, Wang S, Baldwin SW, Orr MD, Robertson CN, et al. Synthesis and evaluation of 18F-labeled choline as an oncologic tracer for positron emission tomography: initial findings in prostate cancer. Cancer Res. 2001;61:110–7.

Denk W, Strickler JH, Webb WW. Two-photon laser scanning fluorescence microscopy. Science. 1990; 248:73–6.

Diagaradjane P, Orenstein-Cardona JM, Colon-Casasnovas NE, Deorukhkar A, Shentu S, Kuno N, et al. Imaging epidermal growth factor receptor expression in vivo: pharmacokinetic and biodistribution characterization of a bioconjugated quantum dot nanoprobe. Clin Cancer Res. 2008;14:731–41.

Dinkel J, Bartling SH, Kuntz J, Grasruck M, Kopp-Schneider A, Iwasaki M, et al. Intrinsic gating for small-animal computed tomography: a robust ECG-less paradigm for deriving cardiac phase information and functional imaging. Circ Cardiovasc Imaging. 2008;1:235–43.

Doubrovin M, Ponomarev V, Beresten T, Balatoni J, Bornmann W, Finn R, et al. Imaging transcriptional regulation of p53-dependent genes with positron emission tomography in vivo. Proc Natl Acad Sci U S A. 2001;98:9300–5.

Dunn KW, Sutton TA. Functional studies in living animals using multiphoton microscopy. ILAR J. 2008;49: 66–77.

Ehling J, Theek B, Gremse F, Baetke S, Möckel D, Maynard J, et al. Micro-CT imaging of tumor angiogenesis: quantitative measures describing micromorphology and vascularization. Am J Pathol. 2014;184:431–41.

Flores JE, McFarland LM, Vanderbilt A, Ogasawara AK, Williams SP. The effects of anesthetic agent and carrier gas on blood glucose and tissue uptake in mice undergoing dynamic FDG-PET imaging: sevoflurane and isoflurane compared in air and in oxygen. Mol Imaging Biol. 2008;10:192–200.

Foley LM, Towner RA, Painter DM. In vivo image-guided (1)H-magnetic resonance spectroscopy of the serial development of hepatocarcinogenesis in an experimental animal model. Biochim Biophys Acta. 2001;1526:230–6.

Fueger BJ, Czernin J, Hildebrandt I, Tran C, Halpern BS, Stout D, et al. Impact of animal handling on the results of 18F-FDG PET studies in mice. J Nucl Med. 2006;47:999–1006.

Gao X, Cui Y, Levenson RM, Chung LW, Nie S. In vivo cancer targeting and imaging with semiconductor quantum dots. Nat Biotechnol. 2004;22:969–76.

Gatenby RA, Gillies RJ. Why do cancers have high aerobic glycolysis? Nat Rev Cancer. 2004;4:891–9.

Gatenby RA, Gillies RJ. A microenvironmental model of carcinogenesis. Nat Rev Cancer. 2008;8:56–61.

Gilad AA, McMahon MT, Walczak P, Winnard Jr PT, Raman V, van Laarhoven HW, et al. Artificial reporter gene providing MRI contrast based on proton exchange. Nat Biotechnol. 2007;25:217–9.

Gilead A, Meir G, Neeman M. The role of angiogenesis, vascular maturation, regression and stroma infiltration in dormancy and growth of implanted MLS ovarian carcinoma spheroids. Int J Cancer. 2004;108:524–31.

Ginj M, Zhang H, Eisenwiener KP, Wild D, Schulz S, Rink H, et al. New pansomatostatin ligands and their chelated versions: affinity profile, agonist activity, internalization, and tumor targeting. Clin Cancer Res. 2008;14:2019–27.

Hara T, Kosaka N, Kishi H. PET imaging of prostate cancer using carbon-11-choline. J Nucl Med. 1998; 39:990–5.

Hara T, Kosaka N, Kishi H. Development of (18) F-fluoroethylcholine for cancer imaging with PET: synthesis, biochemistry, and prostate cancer imaging. J Nucl Med. 2002;43:187–99.

Harada H, Kizaka-Kondoh S, Hiraoka M. Optical imaging of tumor hypoxia and evaluation of efficacy of a hypoxia-targeting drug in living animals. Mol Imaging. 2005;4:182–93.

Haubner R, Wester HJ, Weber WA, Mang C, Ziegler SI, Goodman SL, et al. Noninvasive imaging of alpha(v) beta3 integrin expression using 18F-labeled RGD-containing glycopeptide and positron emission tomography. Cancer Res. 2001;61:1781–5.

Hnatowich DJ. Antisense and nuclear medicine. J Nucl Med. 1999;40:693–703.

Hoffman RM. The multiple uses of fluorescent proteins to visualize cancer in vivo. Nat Rev Cancer. 2005;5:796–806.

Ishiwata K, Kubota K, Murakami M, Kubota R, Sasaki T, Ishii S, et al. Re-evaluation of amino acid PET studies: can the protein synthesis rates in brain and tumor tissues be measured in vivo? J Nucl Med. 1993;34: 1936–43.

Iyer M, Wu L, Carey M, Wang Y, Smallwood A, Gambhir SS. Two-step transcriptional amplification as a method for imaging reporter gene expression using weak promoters. Proc Natl Acad Sci U S A. 2001;98: 14595–600.

Jefferson A, Wijesurendra RS, McAteer MA, Choudhury RP. Development and application of endothelium-targeted microparticles for molecular magnetic resonance imaging. Wiley Interdiscip Rev Nanomed Nanobiotechnol. 2012;4:247–56.

Johnson M, Karanikolas BD, Priceman SJ, Powell R, Black ME, Wu HM, et al. Titration of variant HSV1-tk gene expression to determine the sensitivity of 18F-FHBG PET imaging in a prostate tumor. J Nucl Med. 2009;50:757–64.

Kang JH, Chung JK. Molecular-genetic imaging based on reporter gene expression. J Nucl Med. 2008;49 Suppl 2:164S–79.

Keyaerts M, Verschueren J, Bos TJ, Tchouate-Gainkam LO, Peleman C, Breckpot K, et al. Dynamic bioluminescence imaging for quantitative tumour burden

assessment using IV or IP administration of D: –luciferin: effect on intensity, time kinetics and repeatability of photon emission. Eur J Nucl Med Mol Imaging. 2008;35:999–1007.

Kienast Y, von Baumgarten L, Fuhrmann M, Klinkert WE, Goldbrunner R, Herms J, et al. Real-time imaging reveals the single steps of brain metastasis formation. Nat Med. 2010;16:116–22.

Kiessling F, Jugold M, Woenne EC, Brix G. Non-invasive assessment of vessel morphology and function in tumors by magnetic resonance imaging. Eur Radiol. 2007;17:2136–48.

Kiessling F, Huppert J, Palmowski M. Functional and molecular ultrasound imaging: concepts and contrast agents. Curr Med Chem. 2009;16:627–42.

Kim KI, Chung JK, Kang JH, Lee YJ, Shin JH, Oh HJ, et al. Visualization of endogenous p53-mediated transcription in vivo using sodium iodide symporter. Clin Cancer Res. 2005;11:123–8.

Kimura RH, Cheng Z, Gambhir SS, Cochran JR. Engineered knottin peptides: a new class of agents for imaging integrin expression in living subjects. Cancer Res. 2009;69:2435–42.

Kircher MF, Allport JR, Graves EE, Love V, Josephson L, Lichtman AH, et al. In vivo high resolution three-dimensional imaging of antigen-specific cytotoxic T-lymphocyte trafficking to tumors. Cancer Res. 2003;63:6838–46.

Kirsch DG, Dinulescu DM, Miller JB, Grimm J, Santiago PM, Young NP, et al. A spatially and temporally restricted mouse model of soft tissue sarcoma. Nat Med. 2007;13:992–7.

Kovar JL, Simpson MA, Schutz-Geschwender A, Olive DM. A systematic approach to the development of fluorescent contrast agents for optical imaging of mouse cancer models. Anal Biochem. 2007; 367:1–12.

Kovar JL, Volcheck W, Sevick-Muraca E, Simpson MA, Olive DM. Characterization and performance of a near-infrared 2-deoxyglucose optical imaging agent for mouse cancer models. Anal Biochem. 2009;384:254–62.

Kroemer G, Pouyssegur J. Tumor cell metabolism: cancer's Achilles' heel. Cancer Cell. 2008;13:472–82.

Krohn KA, Mankoff DA, Muzi M, Link JM, Spence AM. True tracers: comparing FDG with glucose and FLT with thymidine. Nucl Med Biol. 2005;32: 663–71.

Langen KJ, Hamacher K, Weckesser M, Floeth F, Stoffels G, Bauer D, et al. O-(2-[18F]fluoroethyl)-L-tyrosine: uptake mechanisms and clinical applications. Nucl Med Biol. 2006;33:287–94.

Larson SM, Morris M, Gunther I, Beattie B, Humm JL, Akhurst TA, et al. Tumor localization of 16beta-18F-fluoro-5alpha-dihydrotestosterone versus 18F-FDG in patients with progressive, metastatic prostate cancer. J Nucl Med. 2004;45:366–73.

Lederle W, Linde N, Heusel J, Bzyl J, Woenne EC, Zwick S, et al. Platelet-derived growth factor-B normalizes micromorphology and vessel function in vascular endothelial growth factor-A-induced squamous cell carcinomas. Am J Pathol. 2010;176:981–94.

Lendvai G, Estrada S, Bergstrom M. Radiolabelled oligonucleotides for imaging of gene expression with PET. Curr Med Chem. 2009;16:4445–61.

Li XF, Zanzonico P, Ling CC, O'Donoghue J. Visualization of experimental lung and bone metastases in live nude mice by X-ray micro-computed tomography. Technol Cancer Res Treat. 2006;5:147–55.

Louie AY, Huber MM, Ahrens ET, Rothbacher U, Moats R, Jacobs RE, et al. In vivo visualization of gene expression using magnetic resonance imaging. Nat Biotechnol. 2000;18:321–5.

Macheda ML, Rogers S, Best JD. Molecular and cellular regulation of glucose transporter (GLUT) proteins in cancer. J Cell Physiol. 2005;202:654–62.

Mahmood U, Weissleder R. Near-infrared optical imaging of proteases in cancer. Mol Cancer Ther. 2003;2:489–96.

McGivan JD, Pastor-Anglada M. Regulatory and molecular aspects of mammalian amino acid transport. Biochem J. 1994;299(Pt 2):321–34.

Mease RC, Foss CA, Pomper MG. PET imaging in prostate cancer: focus on prostate-specific membrane antigen. Curr Top Med Chem. 2013;13(8):951–62.

Michalet X, Pinaud FF, Bentolila LA, Tsay JM, Doose S, Li JJ, et al. Quantum dots for live cells, in vivo imaging, and diagnostics. Science. 2005;307:538–44.

Miles KA. Functional computed tomography in oncology. Eur J Cancer. 2002;38:2079–84.

Modo M, Bulte J. Cellular and molecular MR imaging. Boca Raton: CRC Press; 2007. p. 209–10.

Montet X, Ntziachristos V, Grimm J, Weissleder R. Tomographic fluorescence mapping of tumor targets. Cancer Res. 2005;65:6330–6.

Montet X, Figueiredo JL, Alencar H, Ntziachristos V, Mahmood U, Weissleder R. Tomographic fluorescence imaging of tumor vascular volume in mice. Radiology. 2007;242:751–8.

Morgat C, Mishra AK, Varshney R, Allard M, Fernandez P, Hindié E. Targeting neuropeptide receptors for cancer imaging and therapy: perspectives with bombesin, neurotensin, and neuropeptide-Y receptors. J Nucl Med. 2014;55(10):1650–7.

Moroz E, Carlin S, Dyomina K, Burke S, Thaler H, Blasberg R, et al. Real-time imaging of HIF-1a stabilization and degradation. PLoS One. 2009;4:e5077.

Mulder WJ, van der Schaft DW, Hautvast PA, Strijkers GJ, Koning GA, Storm G, et al. Early in vivo assessment of angiostatic therapy efficacy by molecular MRI. FASEB J. 2007;21:378–83.

Nelson SJ, Kurhanewicz J, Vigneron DB, Larson PE, Harzstark AL, Ferrone M, et al. Metabolic imaging of patients with prostate cancer using hyperpolarized [1-^{13}C]pyruvate. Sci Transl Med. 2013;5:198ra108.

O'Donoghue JA, Zanzonico P, Pugachev A, Wen B, Smith-Jones P, Cai S, et al. Assessment of regional tumor hypoxia using 18F-fluoromisonidazole and 64Cu(II)-diacetyl-bis(N4-methylthiosemicarbazone) positron emission tomography: Comparative study

featuring microPET imaging, Po2 probe measurement, autoradiography, and fluorescent microscopy in the R3327-AT and FaDu rat tumor models. Int J Radiat Oncol Biol Phys. 2005;61:1493–502.

Olafsen T, Kenanova VE, Sundaresan G, Anderson AL, Crow D, Yazaki PJ, et al. Optimizing radiolabeled engineered anti-p185HER2 antibody fragments for in vivo imaging. Cancer Res. 2005;65:5907–16.

Ou G, Itasaka S, Zeng L, Shibuya K, Yi J, Harada H, et al. Usefulness of HIF-1 imaging for determining optimal timing of combining bevacizumab and radiotherapy. Int J Radiat Oncol Biol Phys. 2009;75:463–7.

Palmowski M, Huppert J, Hauff P, Reinhardt M, Schreiner K, Socher MA, et al. Vessel fractions in tumor xenografts depicted by flow- or contrast-sensitive three-dimensional high-frequency Doppler ultrasound respond differently to antiangiogenic treatment. Cancer Res. 2008a;68:7042–9.

Palmowski M, Huppert J, Ladewig G, Hauff P, Reinhardt M, Mueller MM, et al. Molecular profiling of angiogenesis with targeted ultrasound imaging: early assessment of antiangiogenic therapy effects. Mol Cancer Ther. 2008b;7:101–9.

Palmowski M, Peschke P, Huppert J, Hauff P, Reinhardt M, Maurer M, et al. Molecular ultrasound imaging of early vascular response in prostate tumors irradiated with carbon ions. Neoplasia. 2009;11:856–63.

Persigehl T, Bieker R, Matuszewski L, Wall A, Kessler T, Kooijman H, et al. Antiangiogenic tumor treatment: early noninvasive monitoring with USPIO-enhanced MR imaging in mice. Radiology. 2007;244:449–56.

Plathow C, Weber WA. Tumor cell metabolism imaging. J Nucl Med. 2008;49 Suppl 2:43S–63.

Rabinovich BA, Ye Y, Etto T, Chen JQ, Levitsky HI, Overwijk WW, et al. Visualizing fewer than 10 mouse T cells with an enhanced firefly luciferase in immunocompetent mouse models of cancer. Proc Natl Acad Sci U S A. 2008;105:14342–6.

Ramirez de Molina A, Banez-Coronel M, Gutierrez R, Rodriguez-Gonzalez A, Olmeda D, Megias D, et al. Choline kinase activation is a critical requirement for the proliferation of primary human mammary epithelial cells and breast tumor progression. Cancer Res. 2004;64:6732–9.

Ray P, Tsien R, Gambhir SS. Construction and validation of improved triple fusion reporter gene vectors for molecular imaging of living subjects. Cancer Res. 2007;67:3085–93.

Reinhardt M, Hauff P, Briel A, Uhlendorf V, Linker RA, Maurer M, et al. Sensitive particle acoustic quantification (SPAQ): a new ultrasound-based approach for the quantification of ultrasound contrast media in high concentrations. Invest Radiol. 2005;40:2–7.

Reubi JC, Maecke HR. Peptide-based probes for cancer imaging. J Nucl Med. 2008;49:1735–8.

Rix A, Palmowski M, Gremse F, Palmowski K, Lederle W, Kiessling F, et al. Influence of repetitive contrast agent injections on functional and molecular ultrasound measurements. Ultrasound Med Biol. 2014;40(10):2468–75.

Rylova SN, Barnucz E, Barnucz E, Fani M, Braun F, Werner M, Lassmann S, Maecke HR, Maecke HR, Weber WA. Does imaging αvβ3 integrin expression with PET detect changes in angiogenesis during bevacizumab therapy? J Nucl Med. 2014;55(11):1878–84.

Safran M, Kim WY, O'Connell F, Flippin L, Gunzler V, Horner JW, et al. Mouse model for noninvasive imaging of HIF prolyl hydroxylase activity: assessment of an oral agent that stimulates erythropoietin production. Proc Natl Acad Sci U S A. 2006;103:105–10.

Serganova I, Doubrovin M, Vider J, Ponomarev V, Soghomonyan S, Beresten T, et al. Molecular imaging of temporal dynamics and spatial heterogeneity of hypoxia-inducible factor-1 signal transduction activity in tumors in living mice. Cancer Res. 2004;64:6101–8.

Serganova I, Humm J, Ling C, Blasberg R. Tumor hypoxia imaging. Clin Cancer Res. 2006;12:5260–4.

Shields AF, Grierson JR, Dohmen BM, Machulla HJ, Stayanoff JC, Lawhorn-Crews JM, et al. Imaging proliferation in vivo with [F-18]FLT and positron emission tomography. Nat Med. 1998;4:1334–6.

Sundararajan L, Linden HM, Link JM, Krohn KA, Mankoff DA. 18F-fluoroestradiol. Semin Nucl Med. 2007;37:470–6.

Tjuvajev JG, Finn R, Watanabe K, Joshi R, Oku T, Kennedy J, et al. Noninvasive imaging of herpes virus thymidine kinase gene transfer and expression: a potential method for monitoring clinical gene therapy. Cancer Res. 1996;56:4087–95.

Tropres I, Grimault S, Vaeth A, Grillon E, Julien C, Payen JF, et al. Vessel size imaging. Magn Reson Med. 2001;45:397–408.

Ullrich RT, Zander T, Neumaier B, Koker M, Shimamura T, Waerzeggers Y, et al. Early detection of erlotinib treatment response in NSCLC by 3′-deoxy-3′-[F]-fluoro-L-thymidine ([F]FLT) positron emission tomography (PET). PLoS One. 2008;3:e3908.

Van de Sande T, De Schrijver E, Heyns W, Verhoeven G, Swinnen JV. Role of the phosphatidylinositol 3′-kinase/PTEN/Akt kinase pathway in the overexpression of fatty acid synthase in LNCaP prostate cancer cells. Cancer Res. 2002;62:642–6.

Vander Heiden MG, Cantley LC, Thompson CB. Understanding the Warburg effect: the metabolic requirements of cell proliferation. Science. 2009;324:1029–33.

Vandsburger MH, Radoul M, Addadi Y, Mpofu S, Cohen B, Eilam R, et al. Ovarian carcinoma: quantitative biexponential MR imaging relaxometry reveals the dynamic recruitment of ferritin-expressing fibroblasts to the angiogenic rim of tumors. Radiology. 2013;268:790–801. 71.

Verrey F. System L: heteromeric exchangers of large, neutral amino acids involved in directional transport. Pflugers Archiv. 2003;445:529–33.

Walker-Samuel S, Ramasawmy R, Torrealdea F, Rega M, Rajkumar V, Johnson SP, et al. In vivo imaging of glucose uptake and metabolism in tumors. Nat Med. 2013;19:1067–72.

Wei K, Jayaweera AR, Firoozan S, Linka A, Skyba DM, Kaul S. Quantification of myocardial blood flow with ultrasound-induced destruction of microbubbles administered as a constant venous infusion. Circulation. 1998;97:473–83.

Wei LH, Su H, Hildebrandt IJ, Phelps ME, Czernin J, Weber WA. Changes in tumor metabolism as readout for Mammalian target of rapamycin kinase inhibition by rapamycin in glioblastoma. Clin Cancer Res. 2008;14:3416–26.

Woo SK, Lee TS, Kim KM, Kim JY, Jung JH, Kang JH, et al. Anesthesia condition for (18)F-FDG imaging of lung metastasis tumors using small animal PET. Nucl Med Biol. 2008;35:143–50.

Wu AM. Antibodies and antimatter: the resurgence of immuno-PET. J Nucl Med. 2009;50:2–5.

Wu AM, Senter PD. Arming antibodies: prospects and challenges for immunoconjugates. Nat Biotechnol. 2005;23:1137–46.

Zwick S, Strecker R, Kiselev V, Gall P, Huppert J, Palmowski M, et al. Assessment of vascular remodeling under antiangiogenic therapy using DCE-MRI and vessel size imaging. J Magn Reson Imaging. 2009;29:1125–33.

PET Imaging in Immunology

33

Melissa N. McCracken and Owen N. Witte

Contents

M.N. McCracken
Department of Molecular and Medical Pharmacology, David Geffen School of Medicine, University of California, 675 Charles E. Young Dr. South, 5-748 MRL, Los Angeles, CA 90095-1662, USA

O.N. Witte (✉)
Department of Molecular and Medical Pharmacology, David Geffen School of Medicine, University of California, 675 Charles E. Young Dr. South, 5-748 MRL, Los Angeles, CA 90095-1662, USA

Eli and Edythe Broad Center of Regenerative Medicine and Stem Cell Research, University of California, Los Angeles, CA 90095, USA

Department of Microbiology, Immunology and Molecular Genetics, University of California, Los Angeles, CA 90095, USA

Jonsson Comprehensive Cancer Center, David Geffen School of Medicine at the University of California, Los Angeles, CA 90095, USA

Molecular Biology Institute, University of California, Los Angeles, CA 90095, USA

Howard Hughes Medical Institute, University of California, Los Angeles, CA 90095, USA
e-mail: OwenWitte@mednet.ucla.edu

33.1 Introduction to PET Imaging in Immunology

The immune system is dynamic and continually adapts to maintain the health of the whole body. Innate immune cells survey tissues for abnormalities and are able to detect and infiltrate infected and/or abnormal tissues. Signals from the initial infiltrating antigen-presenting immune cells lead to activation of the adaptive immune system including: (1) recruitment of adaptive immune cells, (2) activation and rapid expansion of antigen specific adaptive immune cells, (3) differentiation into antigen specific effector cells, and (4) homing to the abnormal tissue if activated in lymphatic organs such as the spleen or lymph nodes (Belardelli and Ferrantini 2002). Once the infected tissue is cleared, there is a rapid decline

F. Kiessling et al. (eds.), *Small Animal Imaging*, DOI 10.1007/978-3-319-42202-2_33

in effector cells and a small number of adaptive immune cells will remain as memory T or B cells that quickly expand upon repeat exposure to the antigen. Defects in proper immune responses can cause complications that include autoimmunity, persistent infection, or malignancies (Cunningham-Rundles and Ponda 2005). Monitoring the response of the immune system can provide insight into proper diagnosis and therapeutic management of these diseases.

Methods used to monitor the immune system can be limited and biased. Most frequently a peripheral blood sample is taken to monitor changes in cell abundance, phenotype, or cytokine levels. On occasion, a tissue biopsy can be obtained for additional analysis of immune cell infiltrates outside of the periphery. Biopsies are invasive, difficult to collect, and suffer from the bias of site specificity. Together these methods provide information on the state of the immune system at a single static time point but are subjective towards the sampled sites and limited in evaluating the state of the immune system across the whole body. This poses a clinical challenge for current immune-based therapies. For example, in order to determine the success of a hematopoietic stem cell transplant requires mature cells to be detected within the periphery, which can take up to 8 weeks. A noninvasive method to detect engraftment and expansion within the marrow and thymus at an earlier time point could reduce transplant complications by earlier detection of marrow failure. Alternatively, cancer immunotherapies that rely on the expansion and infiltration of antitumor cells have limited methods to track cells in vivo. Clinicians are unable to detect the location of on-target/off-tumor cellular cytotoxicity of the infused therapeutic cell product prior to complications and cannot determine the quantity of successful tumor infiltrating cells without biopsy (Park et al. 2011). Noninvasive, whole-body techniques to monitor immune cell function can complement and improve the current clinical and preclinical methods.

Clinical imaging technologies such as X-ray, computed tomography (CT), magnetic resonance imaging (MRI), single-photon emission computed tomography (SPECT), and positron emission tomography (PET) are used as routine diagnostic tools for a wide range of diseases but have had limited immunological applications. Small animal preclinical studies have utilized strategies restricted to small animals such as 2 photon microscopy, fluorescent, and bioluminescent imaging (BLI) or have adapted clinical modalities such as SPECT, PET, CT, and MRI as methods for measuring changes in the immune system (Hildebrandt and Gambhir 2004). Each technology is relevant and in certain instances will be the most appropriate to use, but we have chosen to focus on PET imaging in preclinical studies of immunology due to the diversity of applications. One advantage of PET is that technologies developed preclinically can be applied directly to clinical problems, allowing for imaging agents to go from bench-top to bedside.

33.1.1 The Use of PET Imaging in Immunology

PET allows noninvasive, quantitative, and repetitive in vivo visualization of the biodistribution of positron-emitting probes specific for a wide variety of biological processes (Cherry and Gambhir 2001; Phelps 2000). Released positrons from the radioisotope annihilate with an electron in nearby tissue and emit two antiparallel 511 keV high-energy gamma photons. PET detectors measure the codetection of both events and determine the location, creating a 3-dimensional image (Phelps 2000) (Fig. 33.1a). Preclinical micro-PET has a resolution of 1–2 mm which is sufficient to detect lymph nodes more accurately than BLI. For immunology studies evaluating alterations in lymph nodes, a coregistered PET/CT scan can be most accurate in determining size, location, and probe accumulation, while other imaging modalities are limited due to tissue penetrance and sensitivity. Tissue, including bone, does not scatter the high-energy photons causing no attenuation problems allowing direct scaling from preclinical to clinical studies.

PET scans measure different biological processes based on the probe's design (Massoud and Gambhir 2003). Positron emitting probes include short-lived isotopes (Half-lives: ^{18}F-110 min, ^{11}C-20 min, ^{68}Ga-68 min) that are

commonly engineered into metabolites, or PET reporter probes. A fluorinated glucose analog, 2-deoxy-2-(^{18}F)fluoro-D-glucose ([^{18}F]-FDG), measures glucose consumption and is the most commonly used PET probe (Gambhir 2002). In the clinic, [^{18}F]-FDG is widely used for cancer diagnosis, staging, and response to therapy. Recently, investigators have begun to test whether [^{18}F]-FDG can be used to monitor immune cell function in cases of autoimmunity and blood malignancies (Gambhir 2002). Long-lived positron-emitting nuclides (half-lifes: ^{124}I- 4.1 days, ^{131}I- 8 days, ^{64}Cu- 12.7 h, ^{89}Zr- 3.3 days) are more commonly used in antibody or peptide labeling. Imaging via direct labeling of an antibody can be used for biomarker diagnostics and potentially theranostics (Boswell and Brechbiel 2007; van Dongen et al. 2007).

Preclinical studies using micro-PET for in vivo visualization of immune responses in animal models is expanding. Sections will be divided into the four major subclasses of PET imaging: (1) metabolic-radiolabeling a metabolite to study the utilization of a biochemical compound, (2) labeling-ex vivo labeling of cells with a radioisotope prior to infusion, (3) direct targeting-engineering radiolabeled peptides or antibodies to detect a protein of interest, (4) reporter gene imaging-engineering cells to express a unique protein that can be specifically detected through a cognate probe (Fig. 33.1b).

33.2 Metabolic Probes for Monitoring Changes in the Immune System

The most broadly used PET subclass is metabolic imaging. Metabolite mimetics are designed and radiolabeled to monitor a specific biochemical process in vivo. These probes can mimic sugars, nucleosides, amino acids, hormones, or neurotransmitters (Phelps 2000). The distribution of the probe demonstrates where an

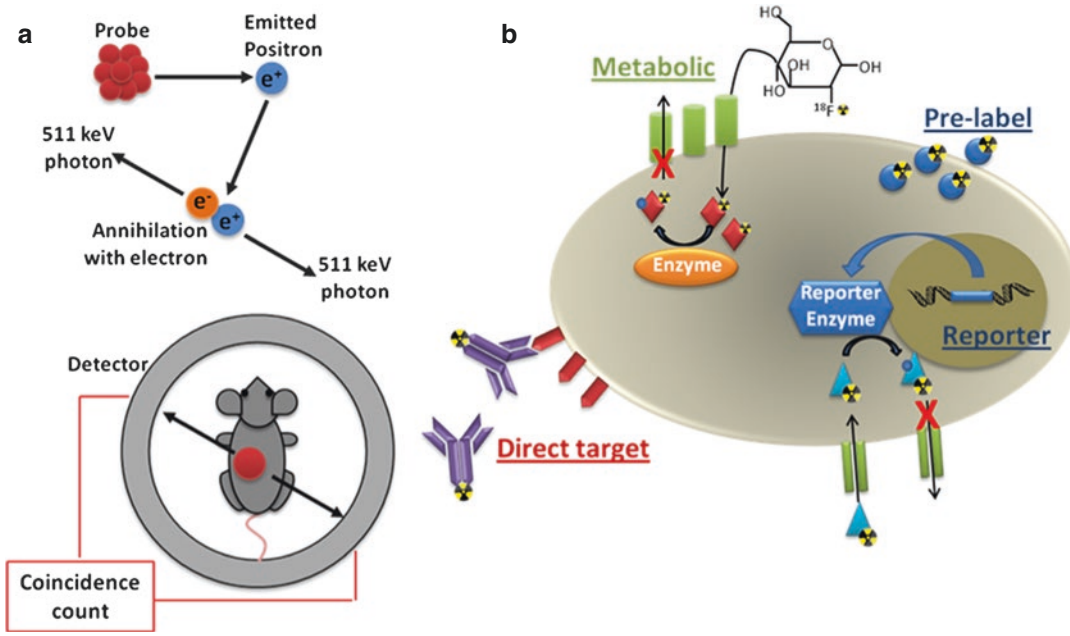

Fig. 33.1 Principles and classes of PET imaging. (**a**) Accumulated probe will emit positrons. Positrons will annihilate with a nearby electron and create two opposing 511 keV gamma rays. The paired 511 keV gamma rays are detected as coincident events in the detector and a 3D image is reconstructed. (**b**) PET images can detect multiple biological processes. Metabolism of a specific substrate can be measured by radiolabeling a mimetic and monitoring the accumulation of the probe. Ex vivo labeling of cells by residualizing isotopes can allow for tracking cells once transplanted in vivo. Antibody or peptides can be used to detect the expression of extracellular proteins. PET reporter genes allow specific detection by exogenous expression of a unique protein that can be targeted with a reporter-specific probe

increased consumption of the metabolite is in comparison with other tissues within the body. Identifying changes in the metabolism of hematopoietic cells in response to an infection, cancer, or autoimmunity can identify key metabolites needed for proper immunity.

During an immune response, innate immunity is the first line of defense followed by an adaptive immune response (Dranoff 2004). Each immune cell lineage has different functional abilities that require certain biochemical substrates. During an immune response, cells will adapt their accumulation and metabolism of certain substrates depending on their activation state or location. Macrophages and granulocytes will increase the expression of glucose transporters and glycolytic enzymes to generate the energy required for phagocytosis and cytokine secretion when located within inflamed tissue (Cramer et al. 2003). PET measurements of differentially regulated metabolic pathways may enable more thorough evaluation of immune cell function in vivo.

Probe design and isotope utilization During the administration of the radiolabeled probe the biodistribution mimics how the body naturally accumulates the metabolite of interest. Metabolites are radiolabeled at a high specific activity and administered at concentrations of pico to femtomole per gram of tissue (Cherry and Gambhir 2001; Phelps 2000). This low concentration allows most probes to function with no biological or pharmacological effect due to the low concentration of the metabolite (Cherry and Gambhir 2001; Massoud and Gambhir 2003). The probe is then excreted with the majority of probes cleared from circulation through renal filtration and hepatic clearance in some instances. The total radiation exposure from metabolic probes is usually highest in the bladder and is the limiting organ for determining the dose based on radiation limits and not on concentrations of the substrate (Gambhir 2002).

The distribution, accumulation, and clearance of most metabolites are short in comparison with peptides or antibodies. For synthesis and radiochemistry, choosing an isotope with a short half-life is best suited for these studies allowing fast detection and decay of the probe in vivo (Cherry and Gambhir 2001). Most PET probes incorporate ^{18}F because of its intermediate half-life (110 min), which is permissive for radiochemical synthesis, transport, application, and imaging, yet undergoes decay rapidly enough to render it harmless within half a day (Serdons et al. 2009). ^{18}F chemistry typically replaces a hydrogen or hydroxyl group with a ^{18}F isotope and allows for a metabolite mimetic. In cases where ^{18}F cannot be used, other positron-emitting radioisotopes such as ^{11}C and rarely ^{15}O and ^{13}N can be used (Cherry and Gambhir 2001; Serdons et al. 2009). ^{11}C has a 20 min half-life. In order to complete a synthesis and purification with enough activity for imaging, the starting ^{11}C activity will be much higher than ^{18}F due to the rapid decay.

To date, thousands of unique PET probes have been made (The Radiosynthesis Database of PET Probes (RaDaP)). We will cover key studies that have applied metabolic probes to address issues in immunology.

Glucose consumption by 2-deoxy-2-(^{18}F)fluoro-D-glucose ([^{18}F]-FDG) [^{18}F]-FDG is the most commonly used PET probe for preclinical and clinical studies (Gambhir 2002). It mimics glucose and can be used as an indication of the glycolytic rate of cells (Fig. 33.2a). Most cancer cells will switch their metabolism towards a highly glycolytic state and the total glucose consumption is increased. [^{18}F]-FDG imaging has exploited this phenotype of cancer by using the accumulation of [^{18}F]-FDG as a method of diagnosis, staging, and response to therapy (Gambhir 2002). Normal tissues with a natural high glucose consumption such as the heart and the brain will also accumulate [^{18}F]-FDG. Most hematopoietic tissues have low glucose accumulation at a basal resting state and because of this [^{18}F]-FDG has only been applied to studies with an activated or abnormal immune system (Hildebrandt and Gambhir 2004).

Cancer Lymphoma and leukemia have higher glucose consumption in comparison with nonmalignant hematopoietic cells. [^{18}F]-FDG accumulation is used as a method for staging and identifying

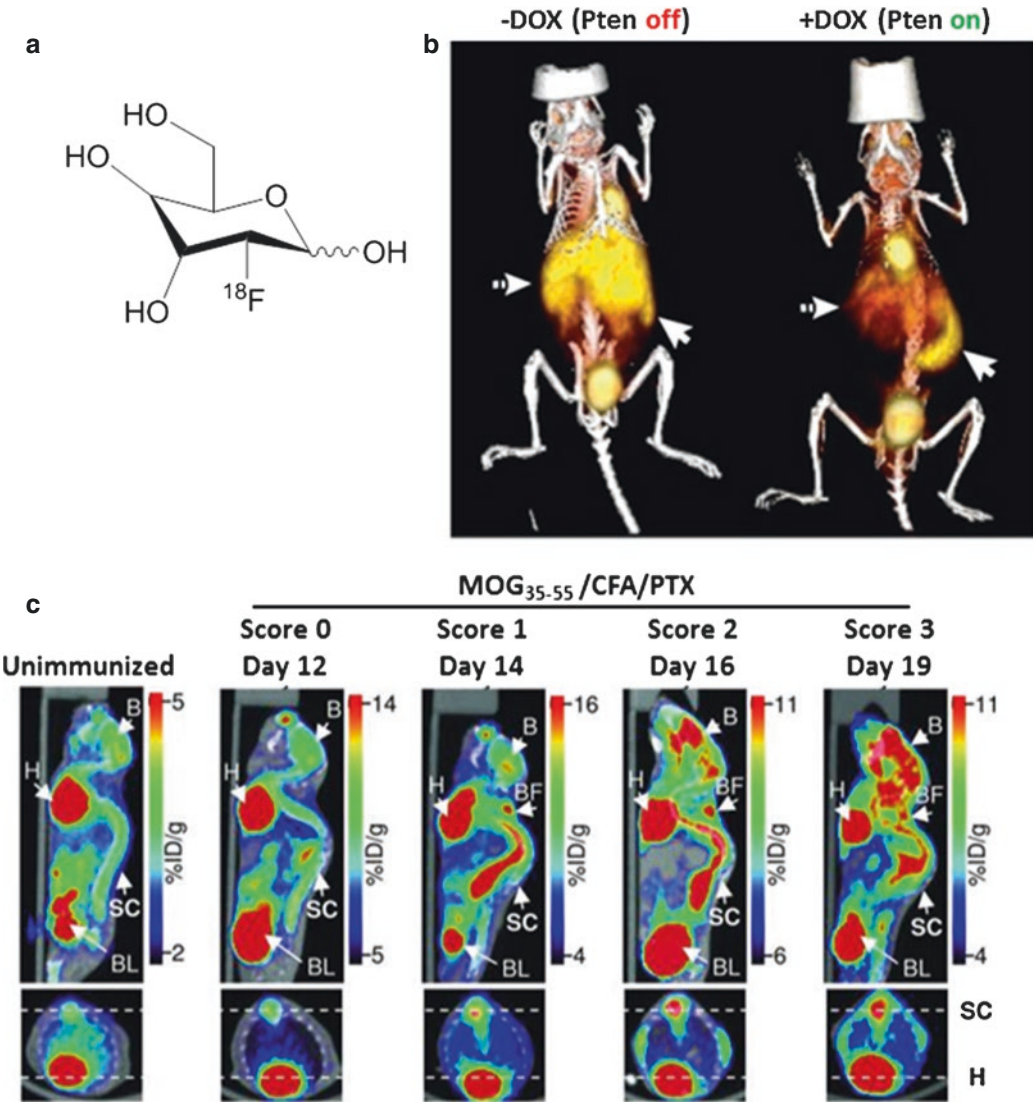

Fig. 33.2 Glucose consumption in immune cells measured by [18F]-FDG. (**a**) Chemical structure of [18F]-FDG. (**b**) T-ALL mice initiated by shRNA Pten silencing. Addition of Dox will turn on Pten and reduce PI3K signaling. [18F]-FDG signal seen in Pten off mice is within the liver and spleen. Pten on reduces total tumor burden and removes majority of the liver signal previously observed (Adapted from Miething et al. 2014) (**c**) [18F]-FDG in EAE mice. In mice with clinical EAE scores, an increase in [18F]-FDG is seen in the spinal column (Adapted from Radu et al. 2007 Copyright (2007) National Academy of Sciences, USA)

cancerous cells in clinical diagnosis (Gambhir 2002). In one study, B cell leukemia cell lines were engineered to express C/EBPα, causing cells to transdifferentiate towards a nonmalignant macrophage phenotype. Total tumor burden after transplantation of parental or transdifferentiated cells was assessed by [18F]-FDG imaging. In animals receiving C/EBPα expressing cells, a decreased tumor burden and reduction in [18F]-FDG imaging was observed (Rapino et al. 2013). This study identified that glucose consumption is correlated with malignancy and that as cells transdifferentiate their metabolic requirements change. Future studies that aim to target cells to transdifferentiate in vivo can apply [18F]-FDG imaging for tracking total disease.

The relative accumulation of [^{18}F]-FDG can also vary depending on the metabolic state of leukemic cells. The activation of the phosphatidylinositol 3-kinase (PI3K) pathway is known to increase glucose consumption and is partially regulated by PTEN. In an experimental mouse model, silencing of PTEN by shRNA led to the development of a T cell acute lymphoblastic leukemia (T-ALL). The shRNA construct was a "Tet-off" system, and addition of doxycycline reactivated PTEN testing whether loss of PTEN is needed for disease maintenance. PTEN activation in T-ALL caused a decrease in the PI3K pathway and as a result the reduced the [^{18}F]-FDG accumulation in specific organs in vivo (Miething et al. 2014) (Fig. 33.2b). Although PTEN was activated systemically in a clonal leukemia, the change in accumulation of [^{18}F]-FDG was heterogeneous, suggesting that the regulation of the PI3K pathway can be affected by different factors within the tissue microenvironment.

Autoimmunity Experimental models of autoimmunity including multiple sclerosis (experimental autoimmune encephalomyelitis, EAE) (Radu et al. 2007) and rheumatoid arthritis (Matsui et al. 2009; Irmler et al. 2010) have been monitored through [^{18}F]-FDG imaging.

The EAE model demonstrated that [^{18}F]-FDG accumulation is not a strong indicator of immune infiltrates prior to disease onset, but as mild clinical symptoms are detectable an increase in glycolysis is seen (Radu et al. 2007) (Fig. 33.2c). The rates of glycolysis as measured by [^{18}F]-FDG signals in the spinal column were not correlated with the severity of the disease; however, when immune cell numbers decreased due to treatment with an immunosuppressive drug, a decrease in [^{18}F]-FDG signal was observed. The limitation with [^{18}F]-FDG was that disease could not be identified prior to clinical manifestation. For autoimmune diseases, [^{18}F]-FDG may not be appropriate for staging of disease but could be useful in monitoring treatment and reduction of immune cells.

Inflammation Inflammation in diseases such as atherosclerosis (Davies et al. 2010), liver damage (Ishimori et al. 2002), or colitis (Brewer et al. 2008) have been measured with [^{18}F]-FDG scans. Mice treated with concanavalin A had a significant increase in [^{18}F]-FDG accumulation within the spleen and liver, while severe combined immunodeficient (SCID) mice had no change between treatment and control (Ishimori et al. 2002). The enhanced [^{18}F]-FDG accumulation was due to the activation of T cells in the spleen and the infiltration of activated immune cells within the liver. SCID mice lack lymphocytes and [^{18}F]-FDG accumulation was unchanged after concanavalin A treatment. Short-term experimental models like this can help identify when [^{18}F]-FDG can be useful in monitoring multiple sites of inflammation.

Cell proliferation by 3′deoxy-3′-[^{18}F]fluorothymidine ([^{18}F]-FLT) accumulation [^{18}F]-FLT is a substrate for thymidine kinase 1 (TK1) which is active in cells during S phase and can be used as a marker for cell proliferation (Barthel et al. 2003; Wagner et al. 2003). Experimental models have looked at [^{18}F]-FLT accumulation in normal tissue and in cancers such as lymphoma. Accumulation of [^{18}F]-FLT is seen within the spleen and bone marrow in healthy animals identifying sites of high cellular proliferation (Wagner et al. 2003). In lymphoma, the accumulation of [^{18}F]-FLT is increased due to a significant increase in the percentage of replicating cells and in their division rate (Wagner et al. 2003). Accumulation of [^{18}F]-FLT can also vary depending on serum and tumor levels of thymidine (Nair-Gill et al. 2010; Zhang et al. 2012). Mouse and rats have high serum thymidine levels and can dilute the accumulation of [^{18}F]-FLT. Human serum has thymidine at concentrations 100 times lower than mice (Nottebrock and Then 1977). The average [^{18}F]-FLT dose in humans is still administered with endogenous thymidine in greater than 150 fold excess potentially explaining the lack of signal in some hyperproliferative cells (Zhang et al. 2012). Deciphering tumor from immune cell infiltrates may be difficult with [^{18}F]-FLT imaging, but in inflammation or infection models, the proliferation of immune cell infiltrates may be detected.

Nucleoside salvage pathway measured by fluorinated nucleoside analogs [^{18}F]-FLT is used as a marker of general cell proliferation and cannot be used to distinguish between the proliferation of immune versus nonimmune cells. Recently, Radu and colleagues have developed nucleoside analog PET probes that target deoxycytidine kinase (dCK) (Radu et al. 2008). dCK is the rate-limiting enzyme in the nucleoside salvage pathway and is known to have high expression in lymphocytes. By targeting a metabolic pathway increased in T cells, the detection of active immune responses can be identified more accurately than with [^{18}F]-FDG or [^{18}F]-FLT alone.

[^{18}F]-FAC (1-(2'-deoxy-2'-[^{18}F]fluoroarabinofuranosyl) cytosine) dCK is the rate-limiting enzyme in the accumulation and phosphorylation of the DNA terminating drug Gemcitabine (dFdC). Accumulation of dFdC was highest in activated T cells, but due to the two fluorine atoms was not amenable for ^{18}F radiochemistry (Radu et al. 2008). [^{18}F]-FAC is a similar compound to dFdC differing only by a hydrogen atom replacing the second fluorine (Fig. 33.3a).

[^{18}F]-FAC had strong retention in the spleen, thymus, and bone marrow of wild-type mice (Radu et al. 2008). A reduction in [^{18}F]-FAC signal was observed when animals were treated with the systemic immunosuppressive drug dexamethasone, which is toxic to lymphocytes (Radu et al. 2008). In a genetic knockout of dCK, a complete loss of [^{18}F]-FAC signal in all lymphoid organs was seen, with a dramatic reduction in the total number of mature T and B cells (Austin et al. 2012; Toy et al. 2010) (Fig. 33.3b). Together these studies demonstrate the specificity of [^{18}F]-FAC for lymphoid tissues and the requirement of dCK for normal lymphopoiesis.

In models of immune cell expansion such as a viral-induced tumor or autoimmunity, an increased [^{18}F]-FAC accumulation was seen in the thymus, lymph nodes, and spleen (Nair-Gill et al. 2010; Radu et al. 2008) (Fig. 33.3c). Analysis of isolated immune cells identified that activated effector CD8 T cells from the draining lymph node had the highest accumulation of [^{18}F]-FAC with other lymphoid cells accumulating [^{18}F]-FAC at lower rates. The authors found that the accumulation of [^{18}F]-FAC was correlated with proliferation, and activated CD8 cells have the highest percentage of cells in S-G_2-M phases (Fig. 33.3d). Tumor infiltrated T cells have lower accumulation, which may be due to a reduction in the proliferation/cell cycling rates (Nair-Gill et al. 2010). [^{18}F]-FAC is more selective for lymphocytes than other metabolic probes but has limited capacity in detecting tumor infiltrating T cells, identifying the need to develop additional T-cell-specific probes.

2′-Deoxy-2′-[^{18}F]fluoro-9-β-D-arabinofuranosylguanine ([^{18}F]F-AraG) In a preliminary study, a radiolabeled AraG was synthesized and incubated with primary, activated, or lymphoblastic T cells (Namavari et al. 2011). Accumulation of [^{18}F]F-AraG was increased in activated T cells and in the leukemic cell line. Although animal studies using [^{18}F]F-AraG are limited, the promising preliminary data suggest that [^{18}F]F-AraG may be useful in detecting T cell malignancies in vivo.

2-[^{18}F]fludarabine Fludarabine is phosphorylatedbydCKintoFludarabinephosphate(2-fluoro-ara-adenosine monophosphate [2-F-ara-AMP]) that is a nucleoside analog resistant to adenosine deaminase. This drug has been used successfully to treat lymphoid malignancies. In wild-type animals, the accumulation of 2-[^{18}F]fludarabine is seen in the spleen, while in SCID animals that signal is lost (Dhilly et al. 2014) (Fig. 33.4a, b). Subcutaneous B cell lymphomas were also detected by 2-[^{18}F]fludarabine demonstrating the selectivity for lymphoid cells in vivo. The lack of thymus signal and high accumulation in B cell lymphomas suggest that 2-[^{18}F]fludarabine may be useful in monitoring B cell locations and malignancies.

Advantages and limitations of metabolic PET The advantage of metabolic PET is that measurements of cell function and metabolism can be obtained in vivo. When cell populations are isolated, their metabolism may change and

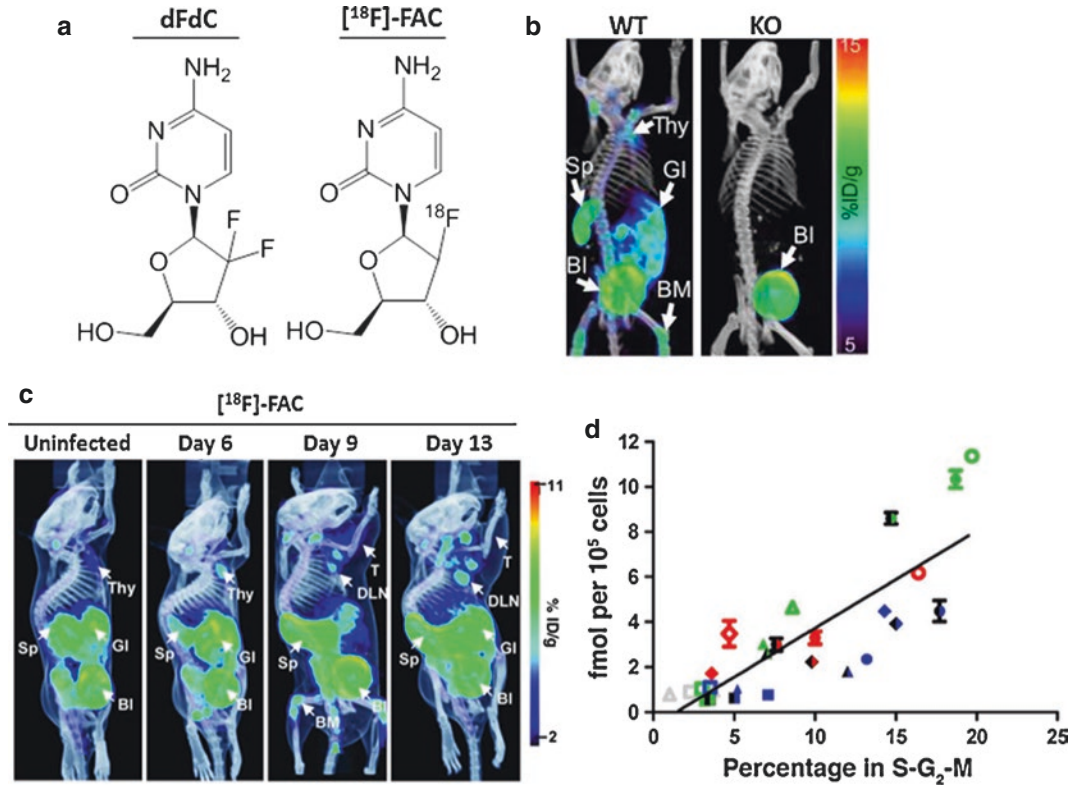

Fig. 33.3 Nucleoside Salvage in PET imaging of immune cells with [^{18}F]-FAC. (**a**) Gemcitabine (dFdC) and [^{18}F]-FAC chemical structure. (**b**) [^{18}F]-FAC imaging of WT and dCK KO mice (Adapted from Toy et al. 2010) (**c**) [^{18}F]-FAC imaging of MSV development in wild-type mice. Signal is observed in the: *Thy* thymus, *Sp* spleen, *GI* gastrointestinal track, *Bl* bladder, *BM* bone marrow, *DLN* draining lymph node, *T* tumor (Adapted from Nair-Gill et al. 2010) (**d**) [^{3}H]-FAC uptake from sorted cells. Cells were fixed and stained with propidium iodide. The percentage in S-G_2-M was plotted against the accumulation of [^{3}H]-FAC. *Open*, *filled*, and *half-filled* symbols represent three experiments. Shapes were assigned according to cell type: *squares* B cells, *triangles* CD4$^+$ T cells, *circles* CD8$^+$ T cells, *diamonds* CD11b^{hi} myeloid cells. Colors were assigned based on the tissues from which a cell population was isolated: *blue* spleen, *green* DLN, *red* tumor, *gray* naive lymph nodes. A positive correlation between [^{3}H]-FAC accumulation and percent in S-G_2-M was observed ($r^2 = 0.68$, $P < 0.0001$) (Adapted from Nair-Gill et al. Republished with permission of *J Clin Invest*, from PET probes for distinct metabolic pathways have different cell specificities during immune responses in mice., Nair-Gill et al. (2010); permission conveyed through Copyright Clearance Center, Inc.)

not represent the true metabolic demands of the cells. For some myeloid derived cells, isolation can be difficult and can cause cell apoptosis prior to analysis. Measuring the accumulation of a radiolabeled metabolite in vivo can provide information of the whole-body metabolic demands of cells.

Probe synthesis can be a limiting step in metabolic PET. Some probes have multiple synthetic steps and low radiochemical yield or require long tedious incubations (Serdons et al. 2009). When scaling from preclinical to clinical studies, this consideration can pose a significant hurdle in obtaining sufficient yield of the chemically pure radiopharmaceutical.

The major disadvantage for imaging immune cell function with metabolic PET is the lack of specificity for immune cells. As seen in [^{18}F]-FDG imaging, other tissues such as the brain and heart will accumulate the metabolic probe. When applying metabolic PET to immunology, it is important to validate that the signal observed is due to changes in immune cell function rather

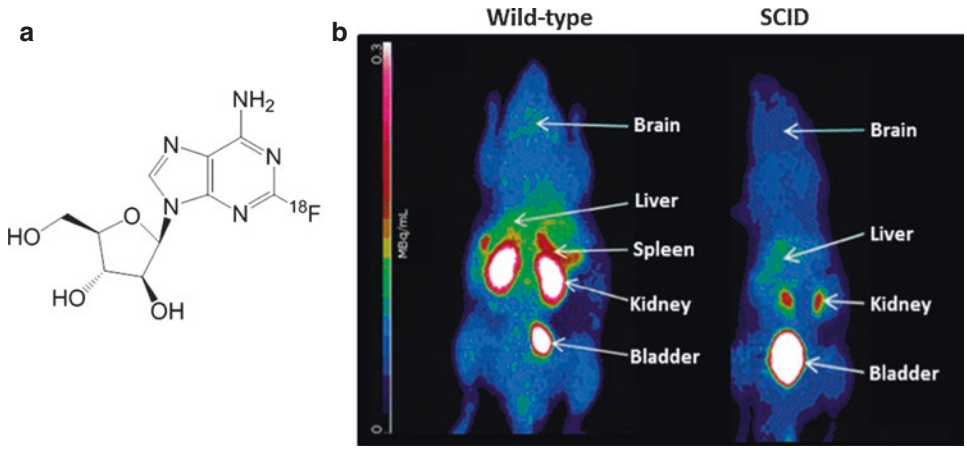

Fig. 33.4 Detection of lymphocytes with 2-[^{18}F]fludarabine PET imaging. (**a**) Chemical structure of 2-[^{18}F]fludarabine. (**b**) Wild-type or SCID mice were scanned with 2-[^{18}F]fludarabine. In wild-type mice, signal was observed within the spleen (Adapted from Dhilly et al. 2014, with kind permission from Springer Science and Business Media)

than an experimental artifact or signal from non-immune cells.

Future applications of metabolic PET Immune cell metabolism is complex and changes based on the activation state and location of cells (Fox et al. 2005). As discussed, probes that measure nucleoside salvage are capable of detecting lymphoid cells, and activated T cells increase their accumulation of [^{18}F]-FAC (Radu et al. 2008). Intratumor T cells have low accumulation of [^{18}F]-FAC probe and may switch their metabolic requirements. New probes that can measure the metabolic requirements of intratumoral T cells are needed as they could have broad applicability to monitor models of cancer immunotherapy.

Identifying unique metabolic states of immune cell subsets will also improve our understanding of the kinetics of an immune response. Probes that distinguish macrophages from dendritic cells or CD4 from CD8 cells could help identify the quantity and location of individual lineages.

Similar to the work of Nair-Gill and colleagues (Nair-Gill et al. 2010), more studies may use a comparison and combination of multiple metabolic PET probes to identify the kinetics of how metabolism changes after a disruption in immune perturbation from drug therapy, infection, or cancer.

33.3 Visualization of Targeted Cell Populations by Prelabeling Ex Vivo

Ex vivo labeling of isolated hematopoietic cells has been utilized to track a range of immune cell subsets. Monocytes (Paik et al. 2002), engineered T cells (Griessinger et al. 2014), bulk lymphocytes, natural killer cells (Melder et al. 1994), and lymphoma cells have all been successfully monitored for their distribution and location by prelabeling cells prior to infusion in SPECT and PET studies (Nair-Gill et al. 2008).

^{64}Cu direct cell labeling technologies Cell-based immunotherapies are currently being developed to treat a broad range of diseases with an emphasis on treating cancer. Some therapies require an ex vivo expansion and culture of these immune cells prior to treatment. This ex vivo expansion can lead to the terminal differentiation of these cells, which are then expected to have a finite life span in vivo. Robust assays to monitor these cells short-term would enable investigators to serially track the location and distribution of transplanted cells. Ex

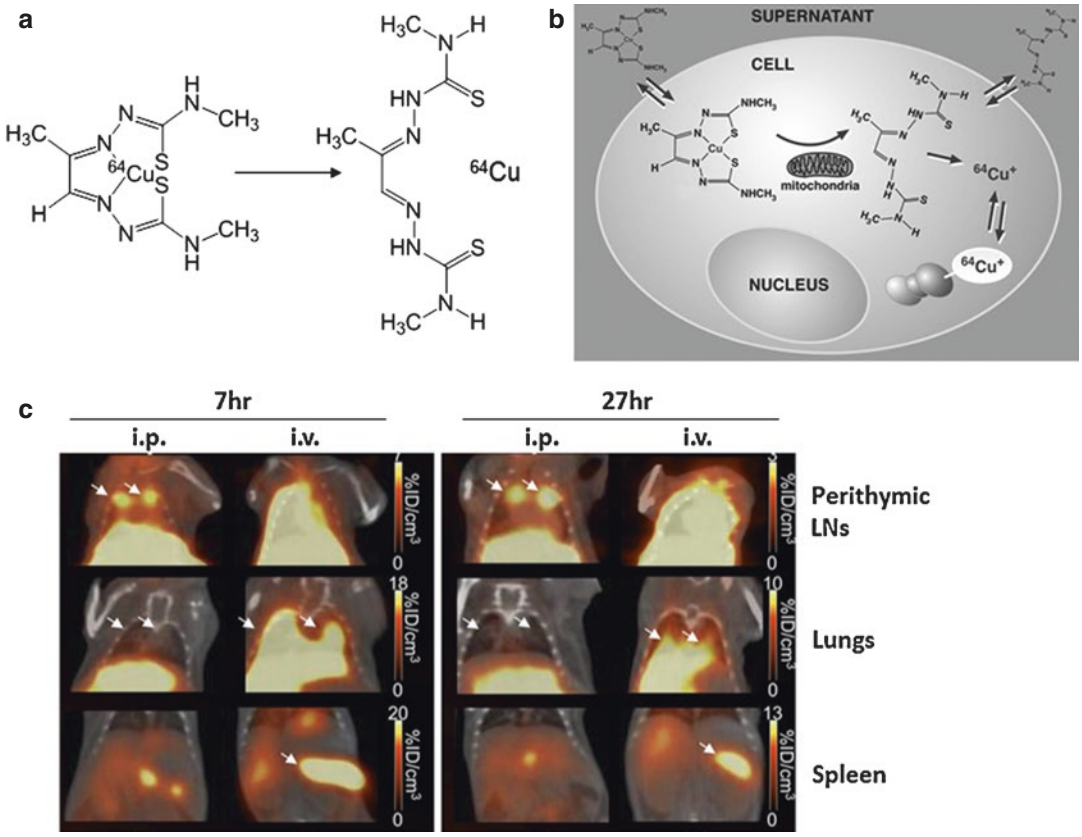

Fig. 33.5 Ex vivo labeling of T cells with [^{64}Cu]-PTSM. (**a**) [^{64}Cu]-PTSM bound and free PTSM. (**b**) Schematic of how [^{64}Cu]-PTSM labels cells ex vivo (Adapted from Adonai et al. 2002 Copyright (2002) National Academy of Sciences, USA.) (**c**) Different administration routes of ^{64}Cu-PTSM–labeled OVA-Th1 cells resulted in distinct homing patterns. Representative PET/CT images at 7 h (*left*) and 27 h (*right*), with focus on perithymic LNs, lung, and spleen (indicated by *arrows*). *i.p.* intraperitoneal, *i.v.* intravenous (Adapted from Griessinger et al. This research was originally published in *JNM*. Christoph M. Griessinger et al. (2014). © by the Society of Nuclear Medicine and Molecular Imaging, Inc.)

vivo incubation of the therapeutic cells with a residualizing probe can provide a simple and consistent method to track cells. The most widely used PET direct cell label is ^{64}Cu-pyruvaldehyde-bis(*N*4-methylthiosemicarbazone) (^{64}Cu-PTSM) (Adonai et al. 2002).

^{64}Cu-PTSM acts as a lipophilic, redox-active transporter of Cu(II) ions that passively diffuses across the cell membrane and delivers copper into the cells. Once inside, the ^{64}Cu and PTSM complex can dissociate, but the ^{64}Cu is retained inside the cell due to the charge, while the neutral PTSM can freely diffuse out of the cell (Fig. 33.5a, b) (Adonai et al. 2002).

The first demonstration of this labeling technique was with total isolated splenocytes labeled for 55 min with ^{64}Cu-PTSM. Cells were injected intravenously and imaged at 10 min and 20 h after infusion. Lymphocytes trafficked from the lungs to the liver and spleen (Adonai et al. 2002).

One concern of prelabeling lymphocytes has been the documented sensitivity and cell death after exposure to radiation. New methods have been developed to minimize the inhibitory effects of ^{64}Cu-PTSM on T cells in mouse models of T cell trafficking (Griessinger et al. 2014). Isolated OVA Th1 were labeled using an optimized method and tested for cell viability, IFN-γ production, proliferation, apoptosis, and DNA double-strand

breaks. Although the optimized parameters were better than previous, defects in total T cell function were still observed. FACS analysis of phosphorylated histones of the H2A.X family (γ-H2A.X) was determined as a marker of radiation-induced DNA double-strand breaks. Three hours after ^{64}Cu-PTSM labeling, the relative γ-H2A.X expression was approximately 9-fold higher than that of unlabeled OVA-Th1 cells. While labeled cells retained similar viability to their unlabeled counterparts, a significant decrease in IFN-gamma production was observed, indicating the probe caused defects in immune cell function.

For imaging purposes, the transplanted cells were tracked for up to 48 h and cell locations were detected even within single lymph nodes. The homing and localization of cells was dependent upon injection route and whether or not the animal was activated by OVA peptide (Fig. 33.5b). Labeled cells retained an equivalent homing capacity in comparison with nonlabeled cells and demonstrated the efficacy in utilizing ^{64}Cu-PTSM for short consecutive scans of T cell homing in vivo.

Limitations in imaging The biggest limitation in PET applications with direct labeling is the potential radiotoxicity from the isotope used (Griessinger et al. 2014). Isotopes with long decay times have continued exposure increasing the damage. Another concern in using radiometals for PET imaging is that only a fraction of the decay is beta emissions that create the 511KeV events detected by PET (Knowles and Wu 2012). The other emissions can be high-energy gamma rays that can cause DNA damage (Weeks et al. 2010; Sundaresan et al. 2003). Additional emissions can cause noise and background within the scans, reducing the image quality (Boswell and Brechbiel 2007; Sundaresan et al. 2003; Tolmachev and Stone-Elander 2010).

33.4 Targeted Imaging by Antibodies and Peptides

Detecting a selective subset of cells can be achieved by multiple PET modalities. Investigators often look for methods that allow for tracking a specific cell population without manipulating the cells via expression of exogenous DNA. These methods can include prelabeling as previously discussed or the use of radiolabeled antibodies and peptides (Massoud and Gambhir 2003; Wu 2009).

To target specific cell populations in vivo with a high specificity antibody and peptides for PET imaging have been used. Preclinical and recent clinical studies have tested these agents for detecting tumor associated cancer antigens or lineage-specific cell surface proteins (Wu 2009). These proteins have high binding affinities allowing for signal accumulation based on binding to the target protein.

Antibody and antibody fragments Immuno-PET uses targeted antibodies for monitoring the expression and distribution of subsets of cells in vivo (van Dongen et al. 2007; Knowles and Wu 2012; Wu 2009). Full-length antibodies are the most commonly used but can be unfavorable for imaging.

An Immunoglobulin G (IgG) antibody is typically 150 kDa and is above the glomerular filtration threshold, which extends the blood half-life. The liver removes circulating antibodies, making this the dose limiting organ in imaging. High retention of circulating antibody within the blood also prevents imaging at early time points. Reducing the antibody size can reduce the half-life, and antibody fragments under 70 kDa can be filtered through the kidney, reducing the radiation dose exposure to the liver.

Antibodies contain their specificity within the Fv portion, while domains of the Fc region contain the components for inducing antibody-dependent cellular cytotoxicity (ADCC), complement-dependent cytotoxicity (CDC), and FcRn salvage receptor binding to keep the antibody in circulation or to activate additional immune cells. Modulating or removing portions of the antibody can alter and remove these biological effects.

Radiolabeling antibodies and peptides can be done by site-specific modification or by modifying exposed lysine residues. For antibodies or

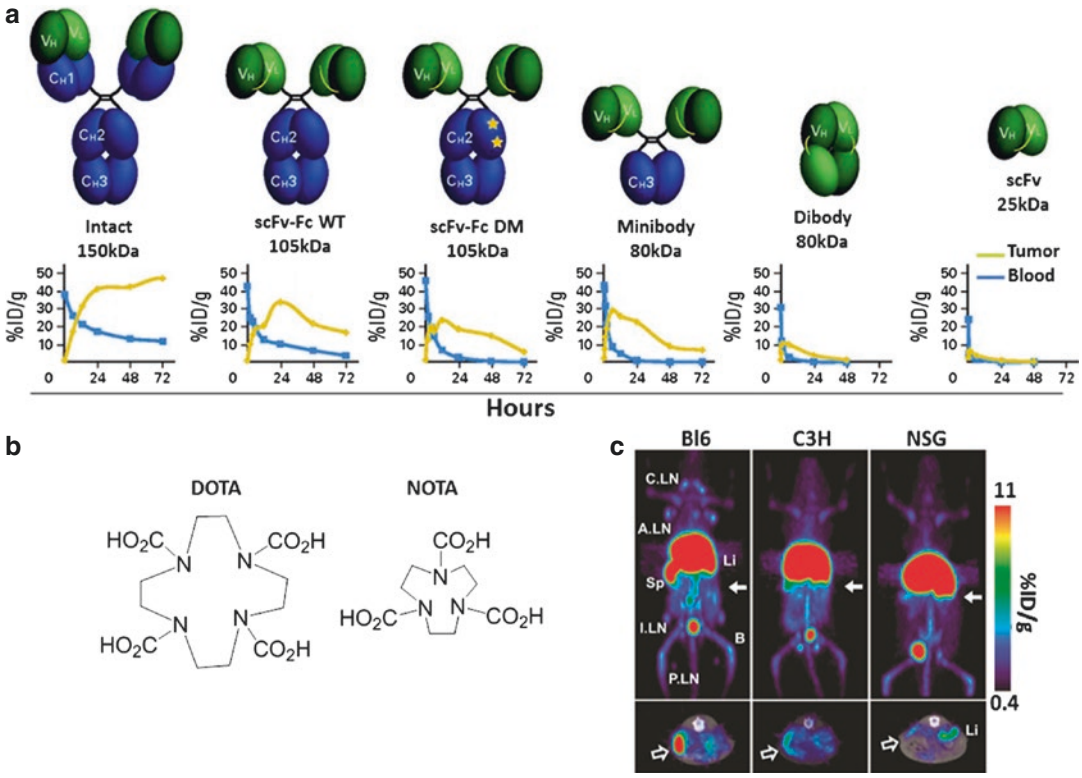

Fig. 33.6 Immuno-PET by antibody engineering and radiolabeling. (**a**) Antibody and antibody fragments. Top-structure and domains of the antibody fragment and size. Bottom-Representative biodistribution (%ID/g) over time of a tumor targeted antibody fragment. Tumor is plotted in *yellow*, blood is plotted in *blue* (Adapted from Knowles and Wu Reprinted with permission. © (2012) American Society of Clinical Oncology. All rights reserved.) (**b**) Chelating agents used for radiolabeling antibodies and peptides. DOTA and NOTA are capable of binding a charged metal isotope within the center ring structure. (**c**) ^{64}Cu-NOTA-2.43 Mb imaging of mice. Bl6 are lyt 2.2 and signal is seen within the spleen and lymph nodes. Spleen and lymph node signal is lost in C3H and NSG. C3H are lyt 2.1 and the 2.43 Mb cannot detect the CD8 cells in vivo. NSG are immunedeficient and contain no endogenous CD8 cells (Adapted from Taváre et al. 2014)

fragments that lose affinity after nonspecific radiolabeling, investigators can engineer free cysteines away from the binding site for site-specific modification (Knowles and Wu 2012; Lewis and Shively 1998; Tinianow et al. 2010).

Antibody fragments from largest to smallest are intact (150 kDa), sc-Fv-Fc (105 kDa), minibody (80 kDa), diabody (50 kDa), and sc-Fv (25 kDa) (Fig. 33.6a). The most commonly used antibody fragments for imaging are minibodies and diabodies. Minibody fragments are covalent dimers of scFv-C_H3 chains. The removal of the C_H2 domain on minibody fragments removes ADCC, CDC, and FcRn salvage receptor binding functions. This also reduces a minibodies half-life in the blood to 5–11 h in comparison with 12 days for intact antibodies. Diabody fragments are dimers of the scFv and retain the high avidity from the bivalency but are under the kidney filtration cutoff allowing a half-life of 3–7 h. Depending on the assay and selected target, an antibody can be engineered for optimal imaging in vivo. For antibody fragments, total overall uptake in target organs is lower, but the ratio of target to background is higher at a much earlier time point postinjection (Fig. 33.6a).

Targeted Peptides Lower molecular weight peptides have also been developed for PET imaging that are smaller than the 25 kDa scFv

antibody fragment. Small peptides such as the Pegylated Arg-Gly-Asp has been used to measure binding to brain tumor integrins (Chen et al. 2004). Cystine knot peptides (knottins) are approximately 3 kDa and nonimmunogenic and can be engineered to bind a protein of interests (Kimura et al. 2009). Affibodies are engineered proteins with 58-amino acid residues that contain a binding surface similar to IgG antibodies (Miao et al. 2010). Nanobodies, which are natural 15 kDa single domain antibodies, are originally isolated from camels (Vaneycken et al. 2011). Lastly, researchers have used the 10th type III domain of human fibronectin (FN3) as a targeted imaging peptide (Natarajan et al. 2013). Current immunology applications have focused on nanobodies and on FN3 domains (Vaneycken et al. 2011; Natarajan et al. 2013).

Nanobodies are a unique antibody format from camels. Nanobodies contain a single variable region of the heavy-chain-only (V_{HH}) and are attractive proteins for therapy and imaging applications due to their small size (15 kDa) and nanomolar affinity (Vaneycken et al. 2011). Due to the fast clearance and high targeting capacity, short-lived isotopes (^{18}F, ^{68}Ga) can be applied, significantly reducing the total radiation exposure. For lymphocytes which are especially sensitive to radiation, reducing the total radiation dose can improve cell viability.

FN3 is a protein that is less than 10 kDa, comprised of a β-sandwich, and has been engineered for high binding affinity to many targets including the B cell marker CD20 (Natarajan et al. 2013). The $FN3_{CD20}$ has high stability and a single lysine for site-specific amine conjugation of radioisotopes. Improvements in tissue perfusion and a short blood half-life make the FN3 proteins attractive for applications in immunology.

Selection of isotopes and methods of radiolabeling The most common radioisotopes applicable for PET that have been used in labeling proteins have been ^{18}F, ^{64}Cu, ^{68}Ga, ^{89}Zr, and ^{124}I. These can be added to the protein of interest through direct conjugation (^{124}I) or by a bifunctional chelate that connects the radioisotope to the protein. For metal groups, a bifunctional chelating agent is typically used as the linker providing a reproducible method to label the protein of interest. Bifunctional chelators can be conjugated to amino acids in proteins such as lysines, tyrosines, or cysteines.

A radioisotope is selected based on the desired imaging time point and half-life of the engineered protein. For larger proteins including antibodies, minibodies, and diabodies, imaging time points are typically 4 h to 4 days after injection and require longer-lived isotopes ^{64}Cu (12.7 h), ^{89}Zr (78.4 h), and ^{124}I (100.2 h) (Tolmachev and Stone-Elander 2010).

A simple and robust labeling method has used direct radioiodination of ^{124}I on antibodies, minibodies and diabodies modifying the exposed tyrosine residues (Tolmachev and Stone-Elander 2010). The limitation is if the target is endocytosed then the ^{124}I will efflux out of the cell and free ^{124}I accumulates within the thyroid and stomach. Residualizing probes should be used instead to allow accumulation of radioactivity such as ^{64}Cu, or ^{89}Zr. These probes remain within the lysosome after the target protein is degraded increasing signal overtime (Knowles and Wu 2012; Tolmachev and Stone-Elander 2010).

Excluding direct radioiodination, a linker is needed to anchor the isotope to the protein. Reactive cysteines are optimal targets and are usually engineered into the peptide or protein for site-specific labeling (Boswell and Brechbiel 2007; van Dongen et al. 2007; Tolmachev and Stone-Elander 2010). By engineering free cysteines, conjugation is consistent with 1–2 conjugates added per protein keeping a relatively consistent specific activity. Without engineering cysteines, exposed lysines can be conjugated with radiometal bound chelates (Tolmachev and Stone-Elander 2010; Vaneycken et al. 2011; Natarajan et al. 2013; Wadas et al. 2010). For small peptides including the nanobodies and FN3 proteins, lysine conjugation is most commonly used. Macrocyclic chelators that bind the radioisotope and target the free amine group are derivatives of (1,4,7,10-tetraazacyclododecane-1,4,7,10-tetraacetic acid) (DOTA) and 2-[4,7-bis (carboxymethyl)-1,4,7-triazonan-1-yl]acetic acid

(NOTA) connected by an activated ester including (N-hydroxysuccinimidyl) ester (NHS) (Fig. 33.6b, 7a). For ^{89}Zr, a common bifunctional chelate used is desferrioxamine (DFO). These chelators are discussed below in the specific examples of peptide imaging in immunology.

Tracking T cell locations with anti-CD8 CD8 is an extracellular marker almost exclusively seen on cytotoxic T cells. CD8 cells can directly target and lyse cells through T cell receptor (TCR)/major histocompatibility (MHC) engagement. Preclinical models of T cell location, development, and function have improved our understanding of how the CD8 cells can clear infections or cancer. Two mouse-specific CD8 minibodies (Mb) were made to target CD8 T cells in vivo (Tavare et al. 2014). The 2.43 Mb reacts with lyt 2.2, an isoform of CD8, in mouse strains such as C57Bl/6, but not in C3H. Radiolabeling of 2.43 by ^{64}Cu-NOTA enabled imaging by micro-PET and detection of endogenous mouse CD8 cells, which were seen predominantly in the spleen and lymph nodes, with minimal signal seen in the bone marrow (Fig. 33.6c). Signal was observed in the liver and is believed to be scavenged ^{64}Cu and protein clearance of the radiolabeled minibody. The high signal seen within the lymph nodes is indicative of the sensitivity of the 2.43 Mb for detecting CD8. It is estimated that a naïve mouse lymph node contains 1 million cells with 7–12 % being CD8. This estimates that between 70,000 and 120,000 CD8 cells can be detected with 2.43 Mb immuno-PET (Tavare et al. 2014). Follow-up studies should investigate the tracking and kinetics of CD8 cells after immunotherapies that stimulate T cell expansion and tumor infiltration in mouse models of cancer.

Tracking B cell locations with anti-CD20 CD20 is a pan B cell marker that has been a successful target in treating lymphomas with antibody therapy. Rituximab, the anti-CD20 antibody has had clinical success and has been extensively studied preclinically. A transgenic mouse was made to express human CD20 enabling investigators to study the human therapy in a mouse models.

A preliminary study demonstrated that ^{64}Cu-DOTA-Rituxumab can target all transgenic CD20 B cells allowing investigators to monitor the location of total B cells in mice (Natarajan et al. 2012). This study demonstrated the efficacy of using intact antibody imaging to identify primary sites of lymphoma. Signal was predominantly seen within the spleen and was blocked when animals were pretreated with cold Rituximab. Biodistribution determined that the highest dose was seen within the spleen and liver. When dose values from the mouse were estimated for human scans, the total exposure was below the safety limits. Together these validated that an intact radiolabeled antibody could be effective in monitoring CD20 expressing lymphoma for staging and response to therapy.

As an alternative to intact antibody imaging, a CD20-specific FN3 protein of less than 10 kDa was developed as an imaging agent. $FN3_{CD20}$ is made and isolated from E. coli and can be lyophilized until needed. The ability to produce and store the $FN3_{CD20}$ is advantageous over antibodies or antibody fragments which can be difficult to produce in large quantities, purify, and store. $FN3_{CD20}$ was labeled the same as ^{64}Cu-DOTA-Rituxumab, by ^{64}Cu bound to the DOTA linker conjugated at a free lysine (Natarajan et al. 2013). Using the transgenic mice expressing human CD20, the ^{64}Cu-DOTA-$FN3_{CD20}$ was able to target the spleen with a faster and 10× higher accumulation measured as target tissue-to-blood ratio. The other organs with residual signal were the liver and kidneys. The liver signal is most likely due to free ^{64}Cu that dissociated from the DOTA label. The kidney signal is due to renal clearance of small peptides. Signals in these organs are lower than the spleen and lower than that seen with ^{64}Cu-DOTA-Rituxumab. In xenograft studies, the ^{64}Cu-DOTA-$FN3_{CD20}$ had the highest tumor:liver ratio compared to the antibody and a minibody. The success with adapting the $FN3_{CD20}$ as an imaging agent will hopefully lead to the development of FN3 imaging agents towards alternate immune markers.

33.4.1 Limitations in Imaging

Protein size and quantity of the protein used can be a limitation in imaging. Proteins too large cannot easily target tumors or tissue with low permeability or perfusion (Vaneycken et al. 2011). Engineering smaller fragments can improve this defect, but smaller proteins may have a faster blood clearance, or lower avidity towards the target (van Dongen et al. 2007; Knowles and Wu 2012; Holliger and Hudson 2005). Nanobodies retain the affinity but can potentially be immunogenic and will need to be tested further (Vaneycken et al. 2011).

Future directions in immuno-PET Improvements in ^{18}F chemistry for labeling can solve current issues with protein imaging such as the radiotoxicity and the long incubation times required prior to scanning. The short half-life and ease in attaining ^{18}F isotope can allow for faster scans with reduced radiotoxicity. As scientists design peptides with optimal blood half-life and biodistribution, ^{18}F radiolabeling can become a more relevant isotope for these studies.

33.5 PET Reporter Genes for Tracking Engineered Cells In Vivo

PET reporter gene overview Reporter genes allow investigators to detect a subset of specific genetically labeled cells in vivo by scanning with the corresponding reporter probe. Applications with PET reporter genes have been used in preclinical PET studies since 1996 with a large portion of studies investigating lymphocyte tracking after immunotherapies (Herschman 2004; Tjuvajev et al. 1996).

Reporter genes are ideal for preclinical studies that need to monitor the fate of transplanted immune cells (Herschman 2004). An exogenous protein is expressed in the selected cells as a PET reporter and is then monitored for location, quantity, and distribution by the corresponding PET probe. Studies have tracked total hematopoietic cells, engineered T cells, dendritic cells, and other phagocytic cells in vivo.

PET reporter genes have utilized three unique subclasses of proteins (Fig. 33.7) (Herschman 2004). Expression of an extracellular protein such as a receptor or transmembrane protein allows for direct targeting by the radiolabeled probe. PET reporters can also be membrane transporters. These allow for detection by active transport and accumulation of their probe intracellular. The most widely used PET reporters are enzymatic kinase reporters, which phosphorylate specific radiolabeled PET probes. Phosphorylated molecules are trapped within cells that express the enzyme reporter. In cells that do not express the reporter, the PET probe can freely efflux from the cell (Herschman 2004). We will cover the applications of PET reporter genes only in immunology, although applications such as stem cell-based therapies have also been tested.

Advantages and disadvantages of PET reporter imaging The advantages of PET reporter gene imaging over metabolic or direct targeting are: (1) the ability to monitor subsets of cells (i.e., only the engineered T cells expressing a CAR); (2) unlike metabolic probes, the ideal

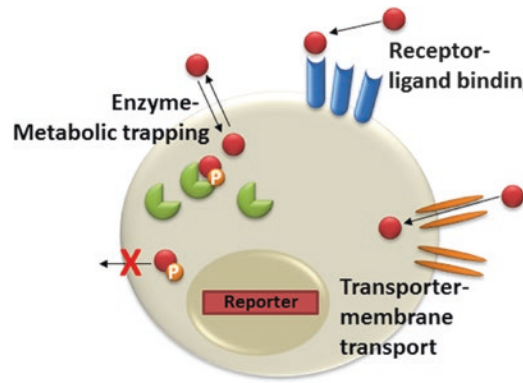

Fig. 33.7 Subclasses of PET reporter genes. PET reporter genes can be one of three subclasses of proteins. Receptor PET reporter genes are a transmembrane protein that allows for reporter imaging by binding a radiolabled ligand or targeted peptide to the protein. Transporter PET reporter genes work by transporting a PET reporter probe intracellular. Enzyme or kinase PET reporter genes work by phosphorylating their cognate probe trapping the probe intracellular

PET reporter probe should have no accumulation in nonmodified cells allowing for whole-body detection of reporter cells; (3) PET reporters expression is stable and should overcome the variability of cellular metabolism and expression/detection can be more consistent regardless of tissue location; and (4) some PET reporter genes have also been demonstrated as effective suicide genes allowing for selective cell elimination if needed.

The major disadvantage of PET reporter gene imaging is the need to manipulate the cell either ex vivo or through targeted vector delivery in vivo. Cells can only express the PET reporter gene after the addition of exogenous DNA. Expression of foreign proteins can be immunogenic, deleterious, or oncogenic to the reporter labeled cells (Kircher et al. 2011). Although this is a potential risk, preclinical studies have tested whether the expression of a PET reporter gene will alter function (McCracken et al. 2013). Expression of a human-based enzymatic reporter did not affect hematopoiesis or T cell function (McCracken et al. 2013; Likar et al. 2010).

Methods for transiently expressing a reporter gene have included transfection, adenoviral infection, or lipid molecule targeting (Herschman 2004; Lam and Dean 2010). These methods are ideal for short-term assays, for cells with limited replication potential so the transient DNA is not diluted, or for cell populations with short finite life spans. Examples of preclinical studies that have used transient expression are dendritic cell vaccine trafficking and in vivo targeting of macrophages (Hildebrandt and Gambhir 2004; Herschman 2004; Kircher et al. 2011).

Viral infection by lenti- or retroviruses allow for lasting expression by genomic integration. Genomic insertion of a PET reporter gene is ideal for tracking hematopoietic stem cell progeny or activated T cells. These cells both have high replication rates and the relative expression of the PET reporter will remain constant with the integrated DNA being passed to daughter cells. The major disadvantage to viral gene delivery is the risk of insertional oncogenesis, vector splicing, or vector silencing (Kircher et al. 2011). Insertional oncogenesis happens when the viral integration is within a tumor suppressor, or there is transactivation or enhancement of an oncogene near the vector integration site (Fischer et al. 2010). In a model of insertional oncogenesis, the dual PET reporter/suicide gene HSV-TK was used (Blumenthal et al. 2007). After treatment of mice with ganciclovir to induce suicide function in HSV-TK cells, escaped leukemic clones due to vector splicing were observed (Blumenthal et al. 2007).

Enzymatic PET reporter genes Kinase PET reporter genes have been the most widely used in immunology studies. One reason for utilizing an enzymatic PET reporter is that even with low enzyme expression, the signal is amplified due to the enzymatic turnover rate of the reporter (Herschman 2004). One limitation of enzymatic PET reporter genes is that the probe must be delivered into cells by endogenous transporters (Tjuvajev et al. 1996; McCracken et al. 2013; Gambhir et al. 2000; Shu et al. 2010). Expression of these transporters is not regulated by the PET reporter gene and may vary depending on cell state or location (Radu et al. 2007; Acton and Zhou 2005; Pastor-Anglada et al. 2001). This may result in inconsistent signal regardless of the expression of the PET reporter gene. Yet one advantage of kinase reporter genes over transporters or some extracellular reporters is that the enzymatic reporters studied to date are relatively small (about 1 kb, hNET is approximately 1.9 kb) (Herschman 2004). In therapeutic vectors with limitations on total vector size, minimizing the PET reporter can help improve viral titer and protein expression.

HSV-TK Herpes simplex virus type 1 thymidine kinase (HSV-TK) was first demonstrated as a suicide gene in vitro with selective elimination of expressing cells by acycloguanosine compounds such as Ganciclovir (GCV) (Tiberghien et al. 1994). In clinical studies, the expression of HSV-TK was immunogenic when expressed in adoptively transferred T cells for graft versus leukemia (Traversari et al. 2007; Berger et al. 2006). Immune responses were from CD8 cells against

the HSV-TK gene and were rapid, most likely due to memory T cell responses. No preclinical studies have reported immunogenicity from HSV-TK in mice. The lack of prior exposure to HSV infection may prevent mice from developing immunogenicity to this PET reporter making it a useful preclinical tool. To validate HSV-TK as a PET reporter, investigators first tested whether SPECT (^{131}I) and PET (^{124}I, ^{18}F) probes of acycloguanosine like compounds could visualize HSV-TK expressing xenografts in mice (Tjuvajev et al. 1996).

In 2002, a mutant form of HSV-TK with improved V_{max}/K_m for GCV (sr39TK, described by (Gambhir et al. 2000)) was used in the first immunology-based application of monitoring tumor burden in Bcr-Abl leukemia (Le et al. 2002). Sequential scans with a radiolabeled penciclovir analog, 9-(4-[^{18}F]-fluoro-3 hydroxymethylbutyl) guanine ([^{18}F]-FHBG), were obtained from animals with BCR-ABL leukemia or BCR-ABL leukemia with G protein-coupled receptor 132 (G2A) knockout. Total tumor burden was visualized within the bone marrow and lymph nodes. Animals with a genetic loss of G2A had significantly elevated signal, which corresponded to increased tumor burden and shorter life expectancy. This study demonstrated the feasibility of PET reporter imaging of HSV-TK as a tool to monitor the location of leukemogenic or normal immune cells in vivo.

HSV-TK was then applied to monitor the location and migration of Epstein Bar Virus (EBV) reactive human T cells (Koehne et al. 2003). Signal was observed in the spleen and in the EBV$^+$ HLA matched tumors 24 h after lymphocyte infusion with peak signal seen at 48 h ([^{124}I]-FIAU probe was administered 4 h prior to scan) (Fig. 33.8). Infused cells could be monitored by PET imaging for up to 15 days postinfusion, while in contrast, when cells were prelabeled with [^{124}I]-FIAU in vitro, signal was only maintained up to 8 days postinfusion. This demonstrates the capacity of being able to prelabel or image cells at distinct time points as needed when cells express the HSV-TK reporter gene.

Additional studies have utilized HSV-TK as a tool to monitor immune responses. The locations and infiltration of tumor reactive T cells have been detected by [^{18}F]-FHBG in mouse and human models of immunotherapy. These have included engineered T cell receptors (TCRs), chimeric antigen receptors (CARs), and tumor reactive T cells from viral-induced sarcomas (Dobrenkov et al. 2008; Dubey et al. 2003;

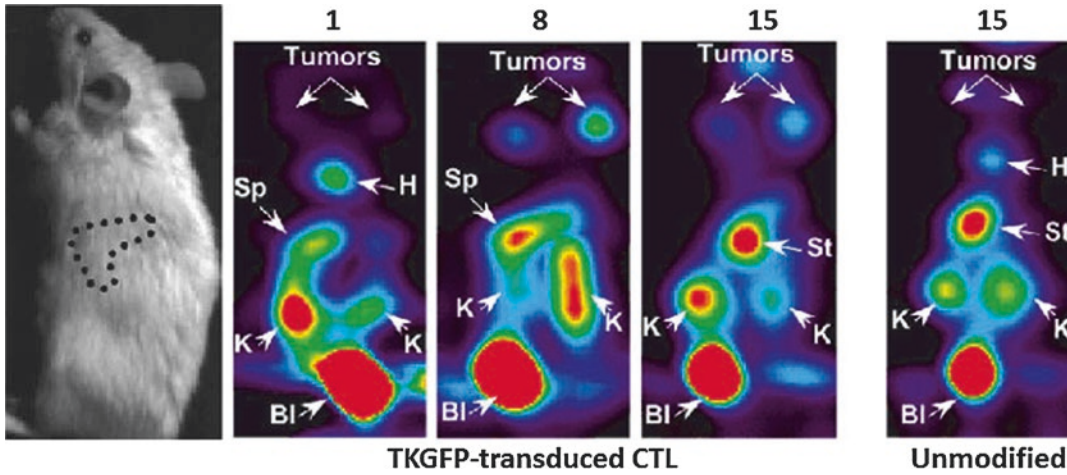

Fig. 33.8 Tracking CTLs with HSV-TK PET reporter imaging. Sequential oblique projections of summed coronal images at a 45° angle to visualize the *Sp* spleen, targeted tumors, *K* kidneys, *St* stomach, *Bl* bladder, *H* heart 4 h after [^{124}I]FIAU injections on days *1*, *8*, and *15* after infusion of CTL-TKGFP. Tumors implanted are autologous and *HLA-A0201*$^+$ EBV$^+$ tumors (Reprinted by permission from Macmillan Publishers Ltd: *Nature Biotechnology* (Koehne et al. 2003), copyright (2003))

Vatakis et al. 2011). Animals that received a bone marrow transplant with cells engineered to express HSV-TK were challenged with a viral-induced sarcoma, and this allowed for the detection of a primary antitumor response in vivo (Shu et al. 2005).

By incorporating HSV-TK, PET reporter gene cells are detected with a 3D image of the location of engineered cells. This has enabled investigators to decipher tumor draining lymph nodes signal from tumor signal because of the improved resolution of PET in comparison with alternate imaging modalities.

Next generation enzymatic PET reporter genes Due to the observed clinical immunogenicity with HSV-TK, alternate enzymatic PET reporters were developed. Homologous to HSV-TK, the human nucleoside kinases were tested in PET reporter applications. Two mutant forms of human deoxycytidine kinase (hdCK) have been successful in monitoring engineered hematopoietic cells (McCracken et al. 2013; Likar et al. 2010).

Expression of hdCKDM (point mutations of R104M and D133A) when probed with 2′-[^{18}F]-fluoro-2′-deoxyarabinofuranosyl-5-ethyluracil ([^{18}F]-FEAU) was able to track tumor infiltrated CAR modified T cells in a model of metastatic prostate cancer (Likar et al. 2010). Human T cells were engineered to express hdCKDM and the Pz-1 CAR that is targeted to prostate-specific membrane antigen (PSMA). T cells were transplanted and imaged 6 h postinfusion with [^{18}F]-FEAU. Signal accumulated in the lung tumors of animals given the hdCKDM expressing T cells. This study demonstrates that hdCKDM could be used in monitoring cellular adoptive immunotherapy to track the location of engineered cells within metastatic tumors.

A separate study evaluated the expression of hdCK3mut (three point mutations within the active site) with [^{18}F]-L-FMAU to monitor long-term hematopoietic stem cell engraftment and expansion (McCracken et al. 2013) (Fig. 33.9a). Expression of hdCK3mut allowed for serial detection of reporter cells up to 32 weeks after a bone marrow transplantation (Fig. 33.9b). Importantly, long-term expression of hdCK3mut was inert in hematopoietic stem cells with the hdCK3mut progeny cells having comparable engraftment, expansion, and longevity to nonreporter labeled cells (Fig. 33.9c).

These studies show that hdCK-based PET reporter genes can be applied to current immunological difficulties in monitoring the location and longevity of transplanted engineered cells. Examples include tracking HSC transplants, engineered T cell therapies, or monitoring experimental GvHD. Expression of a hdCK-based reporter gene is maintained and does not alter the cells function in vivo. To overcome the immunogenicity problem that HSV-TK faces, hdCKDM and hdCK3mut are human enzymes with minimal mutations and should thus not be immunogenic if translated into clinical studies.

Transporter PET reporter In a mouse model of adoptive immunotherapy, the human norepinephrine transporter (hNET) was expressed as a PET reporter gene and detected by ^{124}I-metaiodobenzylguanidine ([^{124}I]-MIBG) (Doubrovin et al. 2007). To test the sensitivity of hNET as a PET reporter, T cells were injected intratumorally and imaging after 4 h detected as little as 10^4 cells. To track tumor infiltration of T cells, EBV reactive CD8 cells were transduced to express hNET and injected intravenous. On day 1, 8, and 28, animals were scanned with [^{124}I]-MIBG which showed a progressive increase in signal from the tumor infiltrating lymphocytes at each time point. Although hNET encodes a human protein with greatly reduced immunogenicity relative to that of HSV-TK in human applications, comparative analysis determined that HSV-TK was more sensitive.

Receptor/ligand PET reporter Although several receptor PET reporter genes have been developed, their applications to immunology have been limited. The recombinant carcinoembryonic antigen (CEA) was tested as a potential PET reporter gene by expression in the T cell leukemia line Jurkat. Anti-CEA minibody imaging detected CEA-positive Jurkats, thereby

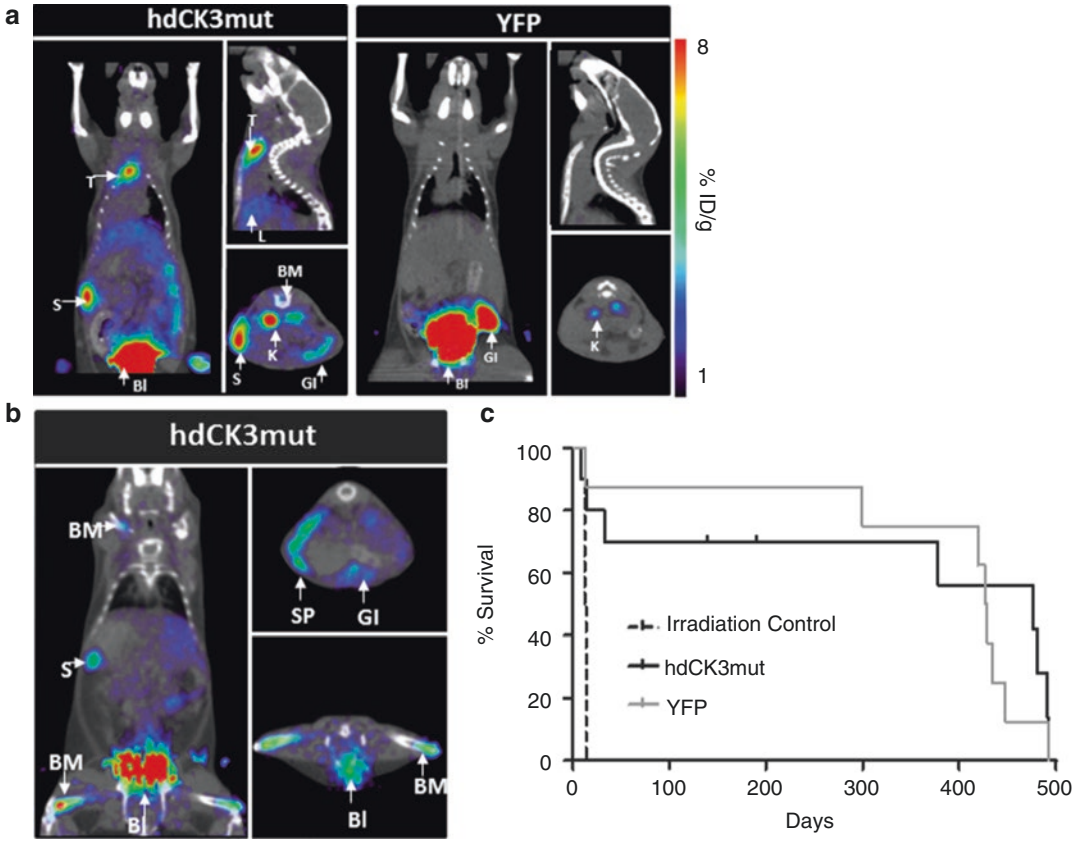

Fig. 33.9 hdCK3mut PET reporter gene imaging of hematopoietic reconstitution. (**a**) Recipient mice received a BMT with either hdCK3mut expressing cells or YFP; scan was obtained 4 weeks after transplant. Signal was observed in the *T* thymus, *S* Spleen, and *BM* bone marrow of hdCK3mut. Clearance of the probe was seen in both recipients in the *GI* gastrointestinal tract, *K* kidney, *Bl* bladder. (**b**) Persistent reporter signal was observed in the BM-bone marrow and Sp-spleen of reporter mice up to 32 weeks post-BMT. (**c**) No defect in longevity or life expectancy was observed between hdCK3mut and YFP recipients (Adapted from McCracken et al. 2013)

demonstrating the potential applications of receptor or extracellular PET reporter genes (Barat et al. 2011; Kenanova et al. 2009).

Future directions of PET reporter genes Only one study has been reported which uses PET reporter imaging for monitoring T cell activation by turning on the expression of HSV-TK (Ponomarev et al. 2001). Although all Jurkat cells were transduced with the inducible HSV-TK construct, the reporter was only activated and detected in those animals treated with anti-CD3 and anti-CD28. Similar inducible reporter systems may also be helpful in addressing the behavior of immune cells after immunotherapies (e.g., anti-PD1, DC vaccine, anti-CTLA4, or engineered T cells with TCRs or CARs) are given. In particular, if signal is weak or absent, one might be able to predict treatment failure or poor response to therapy.

Improvements in lineage-specific reporters could also broaden the use of PET reporter genes. For instance, using lineage-induced reporters would enable tracking of the development/fate of lymphoid lineages post HSC transplant. However, current lineage reporters can be weak, but new methods for amplification of expression will most likely improve these lineage inducible systems (Hildebrandt and Gambhir 2004).

Improvements in the PET reporter gene and probe combination can also allow PET reporter

genes to be used in additional immunology applications. The higher the sensitivity of the reporter and specificity of the probe, the less cells that are then needed for detection in a selected area. For studies that are tracking a small number of cells, this could provide a new method of detection. Applications could include monitoring the location of lymphocytes intratumor or detecting alloreactive cells that cause autoimmune disorders. For enzymatic reporters, improving the enzymatic activity for the probe to lower the K_m and increase the turnover rate will allow for increased probe sequestration. Current PET reporter probes have seen nonspecific clearance in the gallbladder, intestines, liver, kidneys, and bladder (McCracken et al. 2013; Gambhir et al. 2000; Campbell et al. 2012). Metabolism and clearance of ideal PET reporter probes will be through renal filtration, with minimal signal seen in the kidneys and excretion through the bladder.

HSV-TK has been a successful reporter due to its sensitivity, small size, and broad applicability. One key feature of HSV-TK is the dual functionality of being a reporter and suicide gene. When given pharmacological doses of acycloguanosine compounds (e.g., Ganciclovir), the HSV-TK expressing cells are selectively eliminated (Tiberghien et al. 1994). Current literature on novel reporters has discussed the potential of utilizing the human PET reporters as suicide genes (McCracken et al. 2013; Likar et al. 2010) or targeting the receptor reporters with a therapeutic antibody for selective elimination. Development of the suicide gene function will allow investigators to remove reporter cells in case of an adverse event, improving the safety of cell-based therapies.

33.6 Scanner and Quantification Limitations

Resolution limitations The resolution of micro-PET scanners is approximately 1 mm. The resolution of a PET scanner is determined by the size of the scintillator crystals. In some instruments, a continuous sheet of scintillator is used and the resolution is adjusted based on the thickness of the sheet and the size of the photomultiplier tubes reading out (Cherry and Gambhir 2001). It is difficult to improve the resolution of the image due to the reconstruction and scanner sensitivity depending on the isotope used (Cherry and Gambhir 2001). The slight scatter in signal between positron release and annihilation and total sensitivity can be problematic for small areas such as mouse lymph nodes that are at the limit of detection for micro-PET scanners. To date, the maximum predicted resolution is about 0.5 mm for a micro-PET scan (Cherry and Gambhir 2001). A strategy to more accurately detect lymph nodes is to include the coregistration of a CT scan that can provide improved anatomical information at a higher resolution (typically 50–250um) allowing for ROIs drawn on the CT to be applied to the PET scan for quantification.

Scanner Sensitivity The total sensitivity of scanners is actively being investigated to improve current technologies. Micro-PET scanners can detect from 4 to 15 % of total signal (Herrmann et al. 2013). For experimental probes, the total counts or coincidence events needed for an accurate image reconstruction can be limiting when synthesis and production has low yields. For peptide or antibody fragments, the specific activity after radiolabeling can also vary depending on conjugation conditions and concentration of isotope. By utilizing scanners with enhanced sensitivity, less isotope and lower specific activity is needed. Conversely, investigators can choose to conjugate at the same or higher specificity to reduce the total amount of peptide needed per scan. The reduction in radioactivity improves safety and reduces the cost per study. Improved sensitivity also allows sequential scans of the same animal to be extended to longer time points. To increase the sensitivity of the scanner and improve preclinical instrumentation, new technology focuses on utilizing different types of detectors (planar versus cylindrical, material of detector, and range of detectable energy) (Herrmann et al. 2013).

Scanner quantification limitations Partial volume effect can be problematic in immunology studies because it may underestimate the total activity in a small area on the scan (Chatziioannou et al. 1999; Hoffman et al. 1979). In particular, ROIs over areas such as the lymph nodes may be quantified with lower values in comparison to ex vivo biodistribution values. This issue/occurrence can be explained by the imaging software that keeps the minimum size of ROIs during analysis to 1 voxel (approximately 1 mm). Due to partial signal scatter and the actual lymph node size being smaller than 1 mm in some cases, the quantified signal by PET analysis will be lower than actual values creating a partial volume effect. This limitation in accuracy below 1 mM makes quantification not completely accurate for small ROIs due to current image analysis techniques. If possible, biodistribution by gamma counting lymph nodes is the most accurate measurement of total activity per gram.

Low signal in micro-PET imaging Low signal can be missed in organs adjacent to sites of probe metabolism due to the bleed over in signal and difficulty in scaling the scan appropriately (Chatziioannou et al. 1999). For example, with most small molecule probes, clearance occurs in the kidneys and bladder. The prostate, located next to the bladder, can be difficult to detect in both preclinical and clinical scans. Adjusting the imaging protocol to allow a longer conscious uptake including excretion of extra probe through the bladder can help to reduce this issue.

Low cell densities may also dilute the accumulated signal making it hard to register over background in certain studies. Immune cells located intratumor and in other immune organs may not be detected depending on the cell state and the sensitivity of the probe. In a recent study, no signal was observed from PET reporter labeled human cells located within the mouse spleen (McCracken et al. 2013). For this experiment, the human cells comprised less than 5 % of total spleen cells. Potential explanations are due to the low metabolic state of cells or the weak signal to noise ratio.

Intratumor cells have also been difficult to detect in some studies. For metabolic probes, the background tumor metabolism can affect signal. As shown by Radu et al., immune cells can change metabolic states intratumor altering the signal accumulation (Nair-Gill et al. 2010; Radu et al. 2008). Tumors also exhibit the enhanced permeability and retention effect (EPR) causing nonspecific accumulation of some probes (Maeda 2012; Maeda et al. 2000). For preclinical studies, ex vivo analysis and biodistribution studies can complement the PET scan and accurately determine the percent injected dose in each isolated organ.

33.7 Concluding Remarks and Future Directions of PET in Preclinical/Clinical Immunology Applications

PET is a powerful imaging tool for preclinical studies due to the sensitivity, resolution, and wide array of applications and probes. We have covered key PET studies in immunology and emphasized the areas where improvements and future research should be focused. Advancing preclinical PET imaging will not only improve our understanding of disease processes and therapeutics, but also translate into beneficial clinical applications.

Acknowledgments We acknowledge all colleagues who contributed to the work presented here. Melissa N. McCracken was supported by the CIRM training grant (TG2-01169) and the UCLA Graduate Division Dissertation Year Fellowship. Owen N. Witte is an investigator of the Howard Hughes Medical Institute and partially support by the Eli and Edythe Broad Center of Regenerative Medicine and Stem Cell Research.

References

Acton PD, Zhou R. Imaging reporter genes for cell tracking with PET and SPECT. Q J Nucl Med Mol Imaging. 2005;49:349–60.

Adonai N, Nguyen KN, Walsh J, et al. Ex vivo cell labeling with 64Cu-pyruvaldehyde-bis(N4-methylthiosemicarbazone) for imaging cell trafficking in mice

with positron-emission tomography. Proc Natl Acad Sci U S A. 2002;99:3030–5.
Austin WR, Armijo AL, Campbell DO, et al. Nucleoside salvage pathway kinases regulate hematopoiesis by linking nucleotide metabolism with replication stress. J Exp Med. 2012;209:2215–28.
Barat B, Kenanova VE, Olafsen T, Wu AM. Evaluation of two internalizing carcinoembryonic antigen reporter genes for molecular imaging. Mol Imaging Biol. 2011;13:526–35.
Barthel H, Cleij MC, Collingridge DR, et al. 3′-deoxy-3′-[18F]fluorothymidine as a new marker for monitoring tumor response to antiproliferative therapy in vivo with positron emission tomography. Cancer Res. 2003;63:3791–8.
Belardelli F, Ferrantini M. Cytokines as a link between innate and adaptive antitumor immunity. Trends Immunol. 2002;23:201–8.
Berger C, Flowers ME, Warren EH, Riddell SR. Analysis of transgene-specific immune responses that limit the in vivo persistence of adoptively transferred HSV-TK-modified donor T cells after allogeneic hematopoietic cell transplantation. Blood. 2006;107:2294–302.
Blumenthal M, Skelton D, Pepper KA, Jahn T, Methangkool E, Kohn DB. Effective suicide gene therapy for leukemia in a model of insertional oncogenesis in mice. Mol Ther. 2007;15:183–92.
Boswell CA, Brechbiel MW. Development of radioimmunotherapeutic and diagnostic antibodies: an inside-out view. Nucl Med Biol. 2007;34:757–78.
Brewer S, McPherson M, Fujiwara D, et al. Molecular imaging of murine intestinal inflammation with 2-deoxy-2-[18F]fluoro-D-glucose and positron emission tomography. Gastroenterology. 2008;135:744–55.
Campbell DO, Yaghoubi SS, Su Y, et al. Structure-guided engineering of human thymidine kinase 2 as a positron emission tomography reporter gene for enhanced phosphorylation of non-natural thymidine analog reporter probe. J Biol Chem. 2012;287:446–54.
Chatziioannou AF, Cherry SR, Shao Y, et al. Performance evaluation of microPET: a high-resolution lutetium oxyorthosilicate PET scanner for animal imaging. J Nucl Med. 1999;40:1164–75.
Chen X, Hou Y, Tohme M, et al. Pegylated Arg-Gly-Asp peptide: 64Cu labeling and PET imaging of brain tumor alphavbeta3-integrin expression. J Nucl Med. 2004;45:1776–83.
Cherry SR, Gambhir SS. Use of positron emission tomography in animal research. ILAR J/Natl Res Counc Inst Lab Animal Resour. 2001;42:219–32.
Cramer T, Yamanishi Y, Clausen BE, et al. HIF-1alpha is essential for myeloid cell-mediated inflammation. Cell. 2003;112:645–57.
Cunningham-Rundles C, Ponda PP. Molecular defects in T- and B-cell primary immunodeficiency diseases. Nat Rev Immunol. 2005;5:880–92.
Davies JR, Izquierdo-Garcia D, Rudd JH, et al. FDG-PET can distinguish inflamed from non-inflamed plaque in an animal model of atherosclerosis. Int J Cardiovasc Imaging. 2010;26:41–8.
Dhilly M, Guillouet S, Patin D, et al. 2-[18F]fludarabine, a novel positron emission tomography (PET) tracer for imaging lymphoma: a micro-PET study in murine models. Mol Imaging Biol. 2014;16:118–26.
Dobrenkov K, Olszewska M, Likar Y, et al. Monitoring the efficacy of adoptively transferred prostate cancer-targeted human T lymphocytes with PET and bioluminescence imaging. J Nucl Med. 2008;49:1162–70.
Doubrovin MM, Doubrovina ES, Zanzonico P, Sadelain M, Larson SM, O'Reilly RJ. In vivo imaging and quantitation of adoptively transferred human antigen-specific T cells transduced to express a human norepinephrine transporter gene. Cancer Res. 2007;67:11959–69.
Dranoff G. Cytokines in cancer pathogenesis and cancer therapy. Nat Rev Cancer. 2004;4:11–22.
Dubey P, Su H, Adonai N, et al. Quantitative imaging of the T cell antitumor response by positron-emission tomography. Proc Natl Acad Sci U S A. 2003;100:1232–7.
Fischer A, Hacein-Bey-Abina S, Cavazzana-Calvo M. 20 years of gene therapy for SCID. Nat Immunol. 2010;11:457–60.
Fox CJ, Hammerman PS, Thompson CB. Fuel feeds function: energy metabolism and the T-cell response. Nat Rev Immunol. 2005;5:844–52.
Gambhir SS. Molecular imaging of cancer with positron emission tomography. Nat Rev Cancer. 2002;2:683–93.
Gambhir SS, Bauer E, Black ME, et al. A mutant herpes simplex virus type 1 thymidine kinase reporter gene shows improved sensitivity for imaging reporter gene expression with positron emission tomography. Proc Natl Acad Sci U S A. 2000;97:2785–90.
Griessinger CM, Kehlbach R, Bukala D, et al. In vivo tracking of Th1 cells by PET reveals quantitative and temporal distribution and specific homing in lymphatic tissue. J Nucl Med. 2014;55:301–7.
Herrmann K, Dahlbom M, Nathanson D, et al. Evaluation of the Genisys4, a bench-top preclinical PET scanner. J Nucl Med. 2013;54:1162–7.
Herschman HR. PET reporter genes for noninvasive imaging of gene therapy, cell tracking and transgenic analysis. Crit Rev Oncol Hematol. 2004;51:191–204.
Hildebrandt IJ, Gambhir SS. Molecular imaging applications for immunology. Clin Immunol. 2004;111:210–24.
Hoffman EJ, Huang SC, Phelps ME. Quantitation in positron emission computed tomography: 1. Effect of object size. J Comput Assist Tomogr. 1979;3:299–308.
Holliger P, Hudson PJ. Engineered antibody fragments and the rise of single domains. Nat Biotechnol. 2005;23:1126–36.
Irmler IM, Opfermann T, Gebhardt P, et al. In vivo molecular imaging of experimental joint inflammation by combined (18)F-FDG positron emission tomography

and computed tomography. Arthritis Res Ther. 2010;12:R203.
Ishimori T, Saga T, Mamede M, et al. Increased (18) F-FDG uptake in a model of inflammation: concanavalin A-mediated lymphocyte activation. J Nucl Med. 2002;43:658–63.
Kenanova V, Barat B, Olafsen T, et al. Recombinant carcinoembryonic antigen as a reporter gene for molecular imaging. Eur J Nucl Med Mol Imaging. 2009;36:104–14.
Kimura RH, Cheng Z, Gambhir SS, Cochran JR. Engineered knottin peptides: a new class of agents for imaging integrin expression in living subjects. Cancer Res. 2009;69:2435–42.
Kircher MF, Gambhir SS, Grimm J. Noninvasive cell-tracking methods. Nat Rev Clin Oncol. 2011;8: 677–88.
Knowles SM, Wu AM. Advances in immuno-positron emission tomography: antibodies for molecular imaging in oncology. J Clin Oncol. 2012;30:3884–92.
Koehne G, Doubrovin M, Doubrovina E, et al. Serial in vivo imaging of the targeted migration of human HSV-TK-transduced antigen-specific lymphocytes. Nat Biotechnol. 2003;21:405–13.
Lam AP, Dean DA. Progress and prospects: nuclear import of nonviral vectors. Gene Ther. 2010;17: 439–47.
Le LQ, Kabarowski JH, Wong S, Nguyen K, Gambhir SS, Witte ON. Positron emission tomography imaging analysis of G2A as a negative modifier of lymphoid leukemogenesis initiated by the BCR-ABL oncogene. Cancer Cell. 2002;1:381–91.
Lewis MR, Shively JE. Maleimidocysteineamido-DOTA derivatives: new reagents for radiometal chelate conjugation to antibody sulfhydryl groups undergo pH-dependent cleavage reactions. Bioconjug Chem. 1998;9:72–86.
Likar Y, Zurita J, Dobrenkov K, et al. A new pyrimidine-specific reporter gene: a mutated human deoxycytidine kinase suitable for PET during treatment with acycloguanosine-based cytotoxic drugs. J Nucl Med. 2010;51:1395–403.
Maeda H. Vascular permeability in cancer and infection as related to macromolecular drug delivery, with emphasis on the EPR effect for tumor-selective drug targeting. Proc Jpn Acad Ser B Phys Biol Sci. 2012;88:53–71.
Maeda H, Wu J, Sawa T, Matsumura Y, Hori K. Tumor vascular permeability and the EPR effect in macromolecular therapeutics: a review. J Control Release : Off J Control Release Soc. 2000;65:271–84.
Massoud TF, Gambhir SS. Molecular imaging in living subjects: seeing fundamental biological processes in a new light. Genes Dev. 2003;17:545–80.
Matsui T, Nakata N, Nagai S, et al. Inflammatory cytokines and hypoxia contribute to 18F-FDG uptake by cells involved in pannus formation in rheumatoid arthritis. J Nucl Med. 2009;50:920–6.
McCracken MN, Gschweng EH, Nair-Gill E, et al. Long-term in vivo monitoring of mouse and human hematopoietic stem cell engraftment with a human positron emission tomography reporter gene. Proc Natl Acad Sci U S A. 2013;110:1857–62.
Melder RJ, Elmaleh D, Brownell AL, Brownell GL, Jain RK. A method for labeling cells for positron emission tomography (PET) studies. J Immunol Methods. 1994;175:79–87.
Miao Z, Ren G, Liu H, Jiang L, Cheng Z. Small-animal PET imaging of human epidermal growth factor receptor positive tumor with a 64Cu labeled affibody protein. Bioconjug Chem. 2010;21:947–54.
Miething C, Scuoppo C, Bosbach B, et al. PTEN action in leukaemia dictated by the tissue microenvironment. Nature. 2014;510(7505):402–6.
Nair-Gill ED, Shu CJ, Radu CG, Witte ON. Non-invasive imaging of adaptive immunity using positron emission tomography. Immunol Rev. 2008;221:214–28.
Nair-Gill E, Wiltzius SM, Wei XX, et al. PET probes for distinct metabolic pathways have different cell specificities during immune responses in mice. J Clin Invest. 2010;120:2005–15.
Namavari M, Chang YF, Kusler B, Yaghoubi S, Mitchell BS, Gambhir SS. Synthesis of 2′-deoxy-2′-[18F] fluoro-9-beta-D-arabinofuranosylguanine: a novel agent for imaging T-cell activation with PET. Mol Imaging Biol. 2011;13:812–8.
Natarajan A, Gowrishankar G, Nielsen CH, et al. Positron emission tomography of 64Cu-DOTA-Rituximab in a transgenic mouse model expressing human CD20 for clinical translation to image NHL. Mol Imaging Biol. 2012;14:608–16.
Natarajan A, Hackel BJ, Gambhir SS. A novel engineered anti-CD20 tracer enables early time PET imaging in a humanized transgenic mouse model of B-cell non-Hodgkins lymphoma. Clin Cancer Res. 2013;19:6820–9.
Nottebrock H, Then R. Thymidine concentrations in serum and urine of different animal species and man. Biochem Pharmacol. 1977;26:2175–9.
Paik JY, Lee KH, Byun SS, Choe YS, Kim BT. Use of insulin to improve [18 F]fluorodeoxyglucose labelling and retention for in vivo positron emission tomography imaging of monocyte trafficking. Nucl Med Commun. 2002;23:551–7.
Park TS, Rosenberg SA, Morgan RA. Treating cancer with genetically engineered T cells. Trends Biotechnol. 2011;29:550–7.
Pastor-Anglada M, Casado FJ, Valdes R, Mata J, Garcia-Manteiga J, Molina M. Complex regulation of nucleoside transporter expression in epithelial and immune system cells. Mol Membr Biol. 2001;18:81–5.
Phelps ME. Positron emission tomography provides molecular imaging of biological processes. Proc Natl Acad Sci U S A. 2000;97:9226–33.
Ponomarev V, Doubrovin M, Lyddane C, et al. Imaging TCR-dependent NFAT-mediated T-cell activation with positron emission tomography in vivo. Neoplasia. 2001;3:480–8.
Radu CG, Shu CJ, Shelly SM, Phelps ME, Witte ON. Positron emission tomography with computed

tomography imaging of neuroinflammation in experimental autoimmune encephalomyelitis. Proc Natl Acad Sci U S A. 2007;104:1937–42.

Radu CG, Shu CJ, Nair-Gill E, et al. Molecular imaging of lymphoid organs and immune activation by positron emission tomography with a new [18F]-labeled 2'-deoxycytidine analog. Nat Med. 2008;14:783–8.

Rapino F, Robles EF, Richter-Larrea JA, Kallin EM, Martinez-Climent JA, Graf T. C/EBPalpha induces highly efficient macrophage transdifferentiation of B lymphoma and leukemia cell lines and impairs their tumorigenicity. Cell Rep. 2013;3:1153–63.

Serdons K, Verbruggen A, Bormans GM. Developing new molecular imaging probes for PET. Methods. 2009;48:104–11.

Shu CJ, Guo S, Kim YJ, et al. Visualization of a primary anti-tumor immune response by positron emission tomography. Proc Natl Acad Sci U S A. 2005;102:17412–7.

Shu CJ, Campbell DO, Lee JT, et al. Novel PET probes specific for deoxycytidine kinase. J Nucl Med. 2010;51:1092–8.

Sundaresan G, Yazaki PJ, Shively JE, et al. 124I-labeled engineered anti-CEA minibodies and diabodies allow high-contrast, antigen-specific small-animal PET imaging of xenografts in athymic mice. J Nucl Med. 2003;44:1962–9.

Tavare R, McCracken MN, Zettlitz KA, et al. Engineered antibody fragments for immuno-PET imaging of endogenous CD8+ T cells in vivo. Proc Natl Acad Sci U S A. 2014;111:1108–13.

Tiberghien P, Reynolds CW, Keller J, et al. Ganciclovir treatment of herpes simplex thymidine kinase-transduced primary T lymphocytes: an approach for specific in vivo donor T-cell depletion after bone marrow transplantation? Blood. 1994;84:1333–41.

Tinianow JN, Gill HS, Ogasawara A, et al. Site-specifically 89Zr-labeled monoclonal antibodies for ImmunoPET. Nucl Med Biol. 2010;37:289–97.

Tjuvajev JG, Finn R, Watanabe K, et al. Noninvasive imaging of herpes virus thymidine kinase gene transfer and expression: a potential method for monitoring clinical gene therapy. Cancer Res. 1996;56:4087–95.

Tolmachev V, Stone-Elander S. Radiolabelled proteins for positron emission tomography: pros and cons of labelling methods. Biochim Biophys Acta. 2010;1800:487–510.

Toy G, Austin WR, Liao HI, et al. Requirement for deoxycytidine kinase in T and B lymphocyte development. Proc Natl Acad Sci U S A. 2010;107:5551–6.

Traversari C, Marktel S, Magnani Z, et al. The potential immunogenicity of the TK suicide gene does not prevent full clinical benefit associated with the use of TK-transduced donor lymphocytes in HSCT for hematologic malignancies. Blood. 2007;109:4708–15.

van Dongen GA, Visser GW, Lub-de Hooge MN, de Vries EG, Perk LR. Immuno-PET: a navigator in monoclonal antibody development and applications. Oncologist. 2007;12:1379–89.

Vaneycken I, D'Huyvetter M, Hernot S, et al. Immunoimaging using nanobodies. Curr Opin Biotechnol. 2011;22:877–81.

Vatakis DN, Koya RC, Nixon CC, et al. Antitumor activity from antigen-specific CD8 T cells generated in vivo from genetically engineered human hematopoietic stem cells. Proc Natl Acad Sci U S A. 2011;108:E1408–16.

Wadas TJ, Wong EH, Weisman GR, Anderson CJ. Coordinating radiometals of copper, gallium, indium, yttrium, and zirconium for PET and SPECT imaging of disease. Chem Rev. 2010;110:2858–902.

Wagner M, Seitz U, Buck A, et al. 3′-[18F]fluoro-3′-deoxythymidine ([18F]-FLT) as positron emission tomography tracer for imaging proliferation in a murine B-Cell lymphoma model and in the human disease. Cancer Res. 2003;63:2681–7.

Weeks AJ, Paul RL, Marsden PK, Blower PJ, Lloyd DR. Radiobiological effects of hypoxia-dependent uptake of 64Cu-ATSM: enhanced DNA damage and cytotoxicity in hypoxic cells. Eur J Nucl Med Mol Imaging. 2010;37:330–8.

Wu AM. Antibodies and antimatter: the resurgence of immuno-PET. J Nucl Med. 2009;50:2–5.

Zhang CC, Yan Z, Li W, et al. [(18)F]FLT-PET imaging does not always "light up" proliferating tumor cells. Clin Cancer Res. 2012;18:1303–12.

Molecular Imaging of Infectious Diseases

34

Anna-Maria Rolle and Stefan Wiehr

Contents

Despite the success of therapeutics fighting against especially bacteria and fungi, infectious diseases still remain one of the main causes of death worldwide (WHO 2014). Besides effective medication, the early and reliable differential diagnosis of infectious diseases is of utmost importance; here noninvasive imaging can have a huge impact. The host defense against pathogens is dependent on an intact innate and adaptive immune response and effective communication between the immune cells. Dysfunction of one or more of these immune compartments leads to an open gateway for pathogens into the body of humans and animals. Infection is often accompanied with inflammation but both processes differ from each other. Inflammation is basically a nonspecific immune response which can have many reasons but does not necessarily require a microorganism in the inflamed site (Petruzzi et al. 2009). Very well-adapted pathogens have evolved strategies to act immunomodulatory to evade the immune response of the host and to finally enable their survival and transmission (Coombes and Robey 2010).

Traditional, laboratory-based diagnostic modalities such as blood cultures, PCR, antigen tests, and microscopy often result in long turnaround times, making it more difficult when dealing with contaminants thereby compelling clinicians to treat patients empirically with broad-spectrum medication until diagnostic results are available (Bates et al. 1997; Nakamura et al. 2006; Weinstein et al. 2014). Molecular

A.-M. Rolle (✉) • S. Wiehr
Werner Siemens Imaging Center, Department of Preclinical Imaging and Radiopharmacy, Eberhard Karls University Tübingen, Tübingen, Germany
e-mail: Anna-Maria.Rolle@med.uni-tuebingen.de

F. Kiessling et al. (eds.), *Small Animal Imaging*, DOI 10.1007/978-3-319-42202-2_34

imaging has the potential to early and accurately detect infections and monitor treatment efficacies, thereby limiting incorrect or unnecessary treatment and the intrinsic burden of cost, drug resistance, and damage to the patient's health (Stevens et al. 2014; Weinstein et al. 2014). There are several challenging aspects of imaging infectious diseases, not at least the clear and reliable differentiation between fungal, parasitic, bacterial, and viral infection, which is needed for the best treatment option. Furthermore, infection is typically linked to inflammation which makes it mandatory to employ pathogen-specific imaging probes to definitively and rapidly diagnose the causative agent of the infectious disease.

Existing clinically used tracers for PET or SPECT imaging are not able to distinguish between malignancies and sterile or pathogen-induced inflammations or the infectious entities (Bunschoten et al. 2013; Dorward et al. 2012; Signore et al. 2010; Smith et al. 2013). Furthermore, at the late stages of the infection, it is even more challenging to correctly diagnose the cause of illness as the disease can manifest with nonpathogen-induced symptoms resembling malignancies (Glaudemans and Signore 2010). In general, the main problem of identifying the cause of the infectious disease – the pathogen – with the help of imaging methods is to use specific markers for the respective pathogen, which are rarely or not at all available. It has to be noted that most of the used radiopharmaceuticals detect nonspecific inflammation sites but do not accumulate in the pathogen. Because of the lack of a specific marker in nuclear medicine techniques, in most cases invasive puncture or biopsy of tissue or fluids is required to confirm the presence of the infectious pathogens with molecular biology techniques. Those laboratory tests are time-consuming and lack sensitivity and specificity delaying a clear diagnosis and therefore optimal treatment stratification for patients.

Various radiopharmaceuticals were developed and evaluated in both preclinical and clinical studies as potential diagnostic agents to identify the sites of infection (Goldsmith and Vallabhajosula 2009). Arguably, the main limitation to imaging of infectious microorganisms is the availability of pathogen-specific markers. Most of the currently available radiopharmaceuticals detect nonspecific inflammation sites but do not accumulate in microorganisms. Radionuclide imaging with gallium 67 citrate, the most widely used agent for detecting inflammation and infection, is not specific and has the additional disadvantages of long imaging time, low resolution, and high patient radiation dose. The uptake of the radiometal in the liver, the kidneys, and other organs has limited its use for diagnosis of various diseases (Dumarey et al. 2006; Parisi 2011). In vitro radiolabeling of leukocytes with ^{111}In or ^{99m}Tc is considered the gold standard for infection imaging. The radiolabeled leukocytes injected in patients migrate to the sites of infection/inflammation allowing imaging of infectious foci (Parisi 2011). The labeling of leukocytes in vitro requires an expensive and time-consuming procedure with the associated risks of contamination (Petruzzi et al. 2009).

Fluorine-18 fluorodeoxyglucose (^{18}F-FDG), the major clinical PET tracer used for the detection of malignancies, has been used for imaging of infectious diseases or their inflammatory processes (Jamar et al. 2013). However, as a general indicator of metabolic activity of cells, it does not allow the specific identification of pathogens at sites of inflammation (del Rosal et al. 2013).

The PET tracer ^{18}F-FLT, as a surrogate marker for cell proliferation, which is used in the clinics, is primarily used for the detection of cancer cells and has received little attention as a possible tracer for inflammation and infectious disease diagnosis (van Waarde et al. 2004). In the salvage pathway, ^{18}F-FLT is transported across the cell membrane by nucleoside carrier proteins and phosphorylated by the S-phase-specific thymidine kinase 1 (TK-1), which leads to trapping of the tracer in the cytosol as monophosphate without DNA incorporation and subsequent availability as a substrate for cytoplasmic TK-1 (Bading and Shields 2008; Shields et al. 1998). However, ^{18}F-FLT PET does not always correlate with proliferation and, in the preclinical animal setting, is dependent on anesthesia and available serum thymidine, which can compete with ^{18}F-FLT for nucleoside carrier proteins (Cobben et al. 2003;

Fuchs et al. 2013a, b; McKinley et al. 2013, 2014; Nottebrock and Then 1977). So far the proliferation marker ^{18}F-FLT is not suitable to image bacterial, fungal, or parasitic infections.

An increasing number of innovative PET radiopharmaceuticals, employing monoclonal antibodies or their fragments, peptides, and small molecules, have been developed and evaluated for infectious disease imaging (Glaudemans et al. 2012), but compared to cancer research, tracer development for the specific detection of fungi and parasites is in its infancy. Nevertheless, whole-body PET imaging combined with functional magnetic resonance imaging (fMRI) including perfusion imaging, diffusion-weighted imaging (DWI), and magnetic resonance spectroscopy (MRS) has begun to provide valuable insights into host-pathogen interactions (Signore and Glaudemans 2011), permitting real-time in vivo monitoring of pathogen distributions within the infected host, and will lead to better understanding of the biology of the pathogen causing a disease.

Many efforts have already been made to gain further insights in the parasite's or micropathogen's life inside its host (Coombes and Robey 2010). Bioluminescence imaging, two-photon laser scanning microscopy, and intravital imaging techniques are attractive imaging methods because of comparable low costs. Optical imaging can be divided into fluorescence- and bioluminescence-based methods. Intravital imaging can visualize cell-cell or cell-protein interactions, which is not possible with PET or MRI. The drawback of intravital imaging is its invasiveness and the small field of view. The fundamental limitation and disadvantage of optical imaging are the low tissue penetration of light and the lack of absolute quantification of the imaging results.

Various in vitro and in vivo labeling methods are established for labeling cells and are depicted in Fig. 34.1 (Ahrens and Bulte 2013; Kircher et al. 2011). Two major principles for imaging and tracking of cells, direct and indirect labeling, are described by Kirchner et al. (2011). Direct labeling of cells or pathogens is the simplest method, but the label can be diluted by proliferation of the cells and organisms or released during the time. For direct labeling methods in PET, long-lived isotopes are used, such as Cu-64 ($T_{1/2}$ = 12.7) which is generated as ^{64}Cu-PTSM (Griessinger et al. 2014). Genetically engineered cells or organisms are used for indirect labeling methods where reporter genes are introduced into the cell DNA and translated into enzymes, receptors, fluorescence proteins, or bioluminescence luciferase (Coombes et al. 2013; Hasenbach et al. 2012; Kircher et al. 2011). The advantage of stable transfected microorganisms is the possibility of monitoring labeled pathogens or cells over their entire lifetime either with optical imaging methods or with PET/MRI. For the latter, a specific tracer is needed which accumulates within the transfected cell and can be repeatedly injected into the animal after decay of the used radioisotope. The herpes simplex virus thymidine kinase type 1 (HSV-1 TK) is an often used reporter gene for PET imaging because of its restriction to viruses and absence in eukaryotic cells (Hasenbach et al. 2012). PET tracers are, for example, a fluorine-18-labeled acycloguanosine derivative substrate (9-(4-^{18}F-fluoro-3-hydroxymethylbutyl)guanine, ^{18}F-FHBG) for HSV-1 TK and 2′-deoxy-2′-^{18}F-fluoro-5-ethyl-1-β-d-arabinofuranosyluracil (^{18}F-FEAU) where the thymidine kinase phosphorylates the radioactive nucleoside analog substrate, thereby accumulating the tracer into the HSV-1 TK-expressing cell (Kircher et al. 2011). The disadvantage of these tracers is the high unspecific uptake in various organs. Without having the anatomical information of MRI, it is virtually impossible to identify the faint uptake of the tracer in spots where the HSV-1 TK-expressing cells accumulate (Hasenbach et al. 2012).

The rare and chronic zoonotic parasitic disease alveolar echinococcosis (AE) is caused by the larval form (metacestode) of the cestode *Echinococcus multilocularis*, known as the fox tapeworm (Eckert and Deplazes 2004; Tappe et al. 2010). This cancer-mimicking disease is detected in the northern hemisphere including Middle and Eastern Europe, North America, Northern Asia, China, and Japan (Eckert and Deplazes 2004; Knapp et al. 2009). In the advanced stage of the infection, the parasite

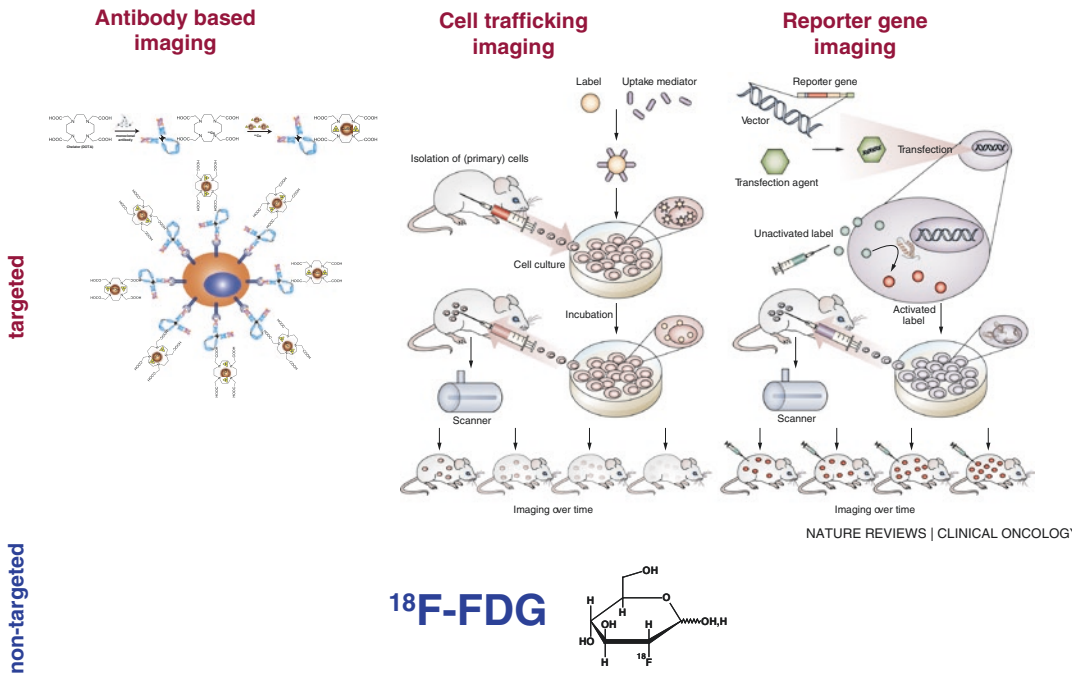

Fig. 34.1 Principles of direct and indirect labeling methods for targeted imaging. For direct labeling of cells, exogenous markers are coupled to a radiolabeled antibody, a transfection agent, or a positively charged peptide and then incubated with cells. Primary cells, such as lymphocytes, are first harvested from a donor, conjugated with a suitable label, and subsequently cells are introduced into the recipient for repeated scanning. Since the label diffuses out of cells and is diluted during cell division, imaging is only feasible over a limited period of time. Indirect cell labeling with reporter genes requires genetic modification of the cells. Cells are transfected with a vector that contains a promoter, which regulates expression of the reporter gene. Such genes can encode receptors, fluorescent proteins, or enzymes, which activate the imaging probe or mediate its accumulation within the cell. Transfected cells are expanded in cell culture before injection. With the exception of fluorescent reporter proteins, each imaging session requires injection of the label, which marks only the transfected cells. In stably transfected cells, the vector is passed on to daughter cells, and cell expansion can be imaged (Adapted from Kircher et al. (2011))

disseminates via the blood or lymphatic vessels to other adjacent organs including the lungs but also to the brain (Tuzun et al. 2002). The proliferation of the metacestode is accompanied by invading immune cells around the multi-chambered cystic structures causing inflammation and necrosis in the periparasitic granuloma (Mejri et al. 2010; Vuitton and Gottstein 2010). The clinical PET tracer ^{18}F-FDG has previously been reported to be useful for the diagnostic and therapy follow-up of AE patients (Reuter et al. 1999; 2008). Nevertheless, small lesions are consistently detected with less reliability, especially in organs with high background activity such as the liver, which possibly leads to false-negative findings. In Fig. 34.2 an *Echinococcus multilocularis*-infected gerbil (*Meriones unguiculatus*) was imaged with PET/MRI using either ^{18}F-FDG or ^{18}F-FLT (Rolle et al. 2015). The disadvantage of the PET tracers ^{18}F-FDG and ^{18}F-FLT is the already mentioned unspecific uptake of glucose and the proliferation marker in the inflamed tissue surrounding the parasite tissue but not by the parasite itself (Rolle et al. 2015).

^{11}C-Choline, another promising tracer that detects membrane synthesis, is first phosphorylated within the cell and then trapped into lecithin of the cell membrane as phosphatidylcholine (Hara 2002). Concentrations of various metabolites in cerebral alveolar echinococcosis lesions were investigated by proton magnetic resonance spectroscopy (^{1}PMRS), and their changes

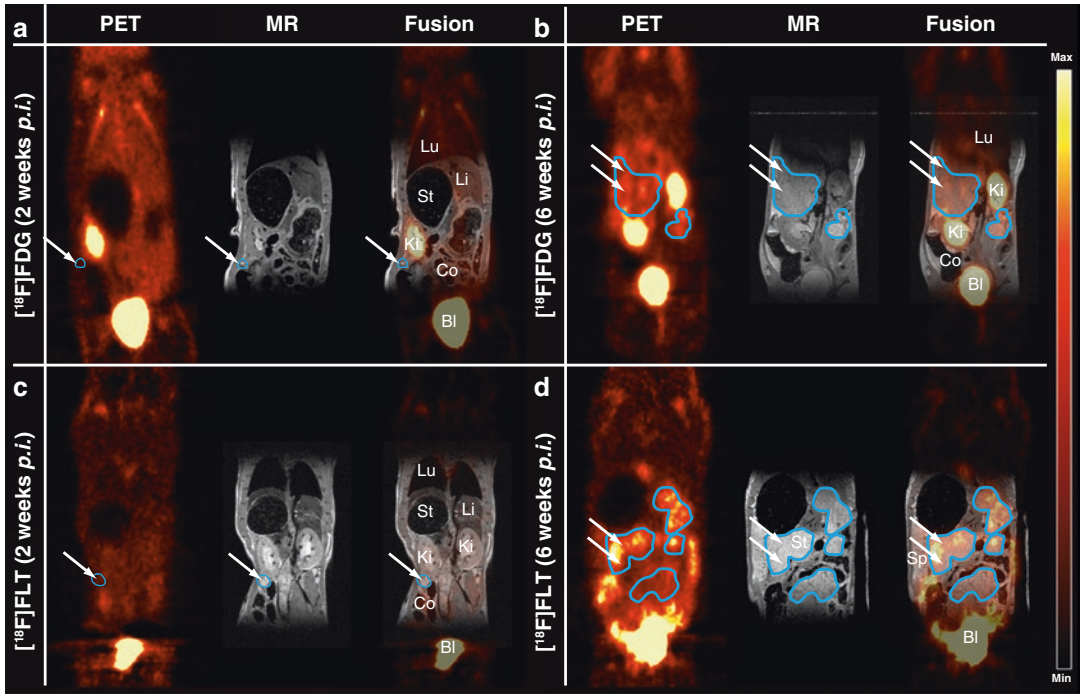

Fig. 34.2 Coronal ^{18}F-FDG or ^{18}F-FLT PET, MR, and fused images from early (*2 weeks p.i.*, **a**, **c**)- and late (*6 weeks p.i.*, **b**, **d**)-stage *E. multilocularis* metacestode-infected gerbils. *Arrows* and *blue lines* indicate the positions of the metacestode tissue (*Bl* bladder, *Co* colon, *Ki* kidney, *Li* liver, *Lu* lung, *Sp* spleen, *St* stomach) (Rolle et al. 2015)

depending on the region of the parasitic mass were recorded. Choline was found to have the highest concentration in the substantial area of the lesions (Wang et al. 2012). A high uptake of ^{11}C-choline in *E. multilocularis* vesicles in cell culture binding assays was observed (Rolle et al. 2015) because choline is quickly integrated as a precursor for the biosynthesis of phospholipids, which are important components of all membranes (Hara 2002). However, the in vivo studies with ^{11}C-choline showed no accumulation in the parasitic lesions in late-stage AE-infected animals (Fig. 34.3a) (Rolle et al. 2015).

Hypoxic regions can be identified using the ^{18}F-fluoro-azomycinarabinofuranoside (^{18}F-FAZA), a 2-nitroimidazole PET tracer. ^{18}F-FAZA is diffusible through cell membranes and undergoes reversible reduction. Therefore, with decreasing intracellular concentration of oxygen, the tracer accumulates within the hypoxic tissue (Marik and Junutula 2011). In preclinical settings and in patients, ^{18}F-FAZA is a widely studied PET tracer for the identification of hypoxic areas within tumors (Beck et al. 2007; Maier et al. 2011; Sorger et al. 2003). Although there have been reports of hypoxia playing an important role in infectious diseases, ^{18}F-FAZA has not been used to date for the detection of infected areas. In vitro binding assays displayed a slightly elevated uptake of ^{18}F-FAZA in *E. multilocularis* vesicles; however, this tracer also revealed to be not applicable for the detection of *E. multilocularis* parasitic lesions at least in the animal model (Fig. 34.3b) (Rolle et al. 2015).

All tested small molecules and clinically used tracers showed elevated uptake pattern in cell culture experiments, which could not be confirmed by the in vivo experiments. A different approach is the use of radiolabeled antibodies specific to the pathogen for PET/MRI. This method is already realized in the preclinical and clinical field of antibody-guided immunoPET (Wiehr et al. 2014) and can be easily transferred to the emerging field of infectious disease

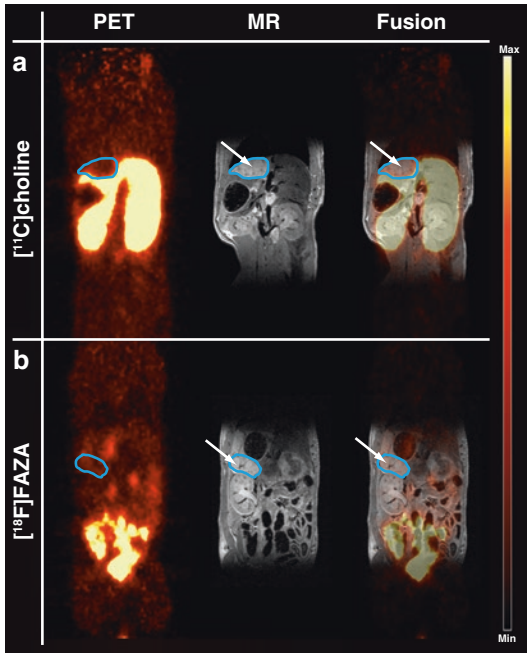

Fig. 34.3 Coronal ^{18}F-FAZA (**a**) and ^{11}C-choline (**b**) PET, MR, and fused images from late (6 weeks *p.i.*)-stage *E. multilocularis* metacestode-infected gerbils. *Arrows* and *blue lines* indicate the positions of the metacestode tissue. Only background uptake of these tracers is observed in the parasite tissue (Rolle et al. 2015)

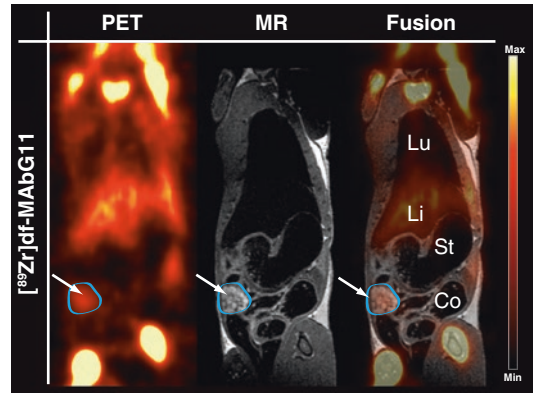

Fig. 34.4 Coronal PET, MR and fused images from early stage *E. multilocularis* metacestode infected gerbils imaged with ^{89}Zr-desferal labeled monoclonal antibody MabG11. *Arrows* and blue lines indicate the localization of the metacestode tissue (*Co* colon, *Ki* kidney, *Li* liver, *Lu* lung, *St* stomach)

imaging. In contrast to the small-molecule (unspecific) PET tracers, a radiolabeled *E. multilocularis*-specific monoclonal antibody binds to the vesicle membrane of the metacestode and clearly depicts the presence of the parasite. In combination with the superior soft tissue contrast of the MRI and the specific marker for PET, PET/MRI can serve as an emerging tool to explicitly identify and diagnose the alveolar echinococcosis disease and exclude it from other cystic liver diseases (Fig. 34.4).

Newly developed disease-specific tracers might be used alongside emerging molecular imaging technologies such as combined PET/MRI to obtain highly accurate spatially and temporally aligned multiparametric molecular, functional, and morphological data of disease progression. Humans with impaired immunity, e.g., those with hematological malignancies or bone marrow transplant recipients, are at a substantially elevated risk of severe, invasive *Aspergillus fumigatus* infection known as invasive pulmonary aspergillosis (IPA) (Brown et al. 2012). Diagnosis of IPA is a major challenge as clinical manifestations of the disease (febrile episodes unresponsive to antibiotics, pulmonary infiltrates, and radiological abnormalities) are nonspecific and methods for the detection of circulating biomarkers such as β-D-glucan or galactomannan (GM) in the bloodstream lack specificity or sensitivity (Freifeld et al. 2011). A convenient, fast, and specific diagnosis of IPA is currently not available, forcing clinicians to implement empiric treatments with costly and toxic antifungal drugs once standard antibiotics have failed to reduce fever in patients with fever of unknown origin (FUO). Consequently, there is the potential to increase the survival rates of aspergillosis patients, if a definitive diagnosis of IPA could be obtained early and its response to treatment monitored and adjusted accordingly.

While it has been reported that ^{18}F-FDG might serve as a useful imaging tool for initial diagnosis and therapy monitoring of IA (Hot et al. 2011), our investigations have shown that increased ^{18}F-FDG uptake in *A. fumigatus*-infected lungs is indistinguishable from the uptake seen during inflammatory reactions due to sterile triggers or other pathogens (Rolle et al. 2016). Attempts have been made to visualize IPA in *A.*

fumigatus-infected animals with microPET/CT using ^{68}Ga radiolabeled siderophores (Haas et al. 2015; Petrik et al. 2010). These small high-affinity chelating compounds are produced by fungi and bacteria to scavenge iron from the host and by gram-negative bacterial pathogens as virulence factors (Holden and Bachman 2015). While rapid uptake of ^{68}Ga by the *A. fumigatus* siderophore TAFC has been shown to occur under conditions of iron depletion, TAFC-mediated ^{68}Ga uptake has also been demonstrated in *Fusarium solani* and *Rhizopus oryzae*, invasive fungal pathogens that cause fusariosis and mucormycosis in immunocompromised patients (Thornton and Wills 2015).

Recently, *A. fumigatus* detection based on single-photon emission computerized tomography (SPECT) with ^{99m}Tc-labeled morpholino oligonucleotides (MORFs) specific for fungal 28S rRNA has been investigated (Wang et al. 2013). While *A. fumigatus* lung infections are clearly discerned using this technique, further investigations in other infectious models are needed to confirm the specificity of this probe.

ImmunoPET has recently been used for tracking simian immunodeficiency virus (SIV) infection in macaques (Santangelo et al. 2015), and another example of the rapid and specific detection of the lethal fungal infection IPA with immunoPET is depicted in Fig. 34.5 (Rolle et al. 2016). *A. fumigatus*-infected, neutropenic mice were imaged with an anti-*Aspergillus* PET marker. The ^{64}Cu-DOTA-labeled anti-*Aspergillus* mAb JF5 was intravenously (*i.v.*) injected, and subsequent PET images were acquired, which show the localization of the tracer in the lungs of infected mice 48 h after the initial pulmonary infection. Due to the long in vivo half-life of the copper-64-radiolabeled mAb specific to *Aspergillus*, the immunoPET approach is able to detect fungal colonization at all stages of mycelial growth and is possibly useful for treatment monitoring. The hyphal-specific nature of our immunoPET tracer may therefore prove useful in monitoring infection in response to antifungal treatment (Rolle et al. 2016).

Several PET tracers for bacterial infections have been developed and tested in preclinical studies using antibiotics, peptides, antibodies, and radiolabeled white blood cells, but have so far had limited clinical impact (Bunschoten et al. 2013; Ning et al. 2014). Radiolabeled antibiotics are active at low concentrations and are therefore not the best candidates for molecular imaging. Clinical studies, for example, with ^{99m}Tc-ciproflaxin, have also shown limited specificity (Langer et al. 2005; Sarda et al. 2003; Vinjamuri et al. 1996; Weinstein et al. 2014).

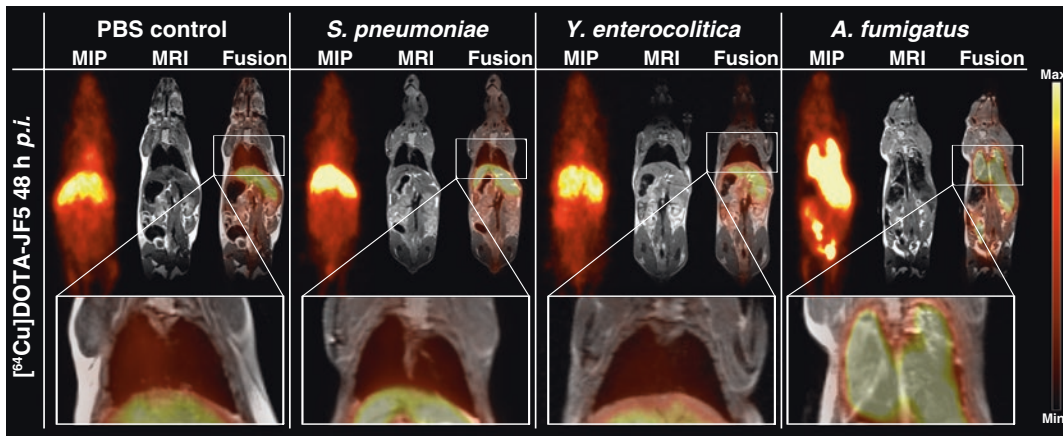

Fig. 34.5 Coronal maximum intensity projection (*MIP*), magnetic resonance imaging (*MRI*), and fused positron emission tomography (PET)/MRI images of PBS-treated and *Streptococcus pneumoniae*-, *Yersinia enterocolitica*-, and *Aspergillus fumigatus*-infected mice injected with ^{64}Cu-DOTA-JF5 (48 h after infection). Images demonstrate highly specific tracer accumulation in *A. fumigatus*-infected lung tissue compared to bacterial-infected or sham-treated animals. Lungs of the respective animals are detailed in the *lower panel* (Rolle et al. 2016)

Recently, bacteria-specific PET tracers have been developed with promising preclinical results. Sugar transporters for sorbitol and maltose or an alternative sugar transporter, the bacterial universal hexose phosphate transporter (UHPT), has been investigated as targets for bacteria-specific imaging using 2-^{18}F-fluorodeoxysorbitol (^{18}F-FDS) (Weinstein et al. 2014), 6-^{18}F-fluoromaltose (MH^{18}F) (Ning et al. 2014), and the analog of glucose ^{18}F-FDG-6-P (Mills et al. 2015). Using these tracers it is possible to distinguish between gram-negative (e.g., *Enterobacteriaceae*) and gram-positive (e.g., *Staphylococcus aureus*) bacteria.

The gram-negative bacterium *Yersinia enterocolitica* belongs to the family of *Enterobacteriaceae* and is an important cause of gastrointestinal infections. Infections are caused by ingestion of contaminated food or drinking water and can cause severe diarrhea and enterocolitis (Schindler et al. 2012). In immunocompromised patients, systemic infection can lead to focal abscesses in the spleen and liver (Bottone 1997). The virulence of *Y. enterocolitica* is associated with *Yersinia* adhesin A (YadA), a trimeric autotransporter expressed on the surface that mediates cell adhesion and is an ideal biomarker candidate for the specific imaging of yersiniosis (Di Genaro et al. 2003). A radiolabeled anti-YadA antibody is able to specifically detect the pathogen in vivo. Furthermore, the antibody uptake occurred in an infection dose-dependent manner in the spleen of low-dose infected animals. In contrast, elevated uptake of the standard PET tracer ^{18}F-FDG was only observed in the spleen of high-dose *Y. enterocolitica*-infected mice, although blood glucose levels were raised in both low- and high-dose infected animals (Fig. 34.6). The most likely explanation for this is the induction of inflammation and ^{18}F-FDG uptake by activated immune cells (del Rosal et al. 2013; Rolle et al. 2015) rather than by the bacteria themselves as there was no correlation with the bacterial load. Consequently, these results argue against the use of ^{18}F-FDG for imaging bacterial infections. This is in agreement with the findings of other groups showing that ^{18}F-FDG is highly unspecific in PET oncology, resulting in high rates of false positives (Chacko et al. 2003; Culverwell et al. 2011; Lukawska et al. 2014; Rosenbaum et al. 2006; Stumpe et al. 2000). Furthermore, it is unable to detect early-stage bacterial infections and in some instances shows increased signal intensities after effective antibiotic treatment (Davis et al. 2009; Jain et al. 2005). Nevertheless, it is currently the principal tracer for imaging infectious diseases in humans (Corstens and van der Meer 1999; Glaudemans and Signore 2010; van Oosten et al. 2013).

Many other diseases might benefit from a rapid specific diagnostic tool with PET/MRI replacing

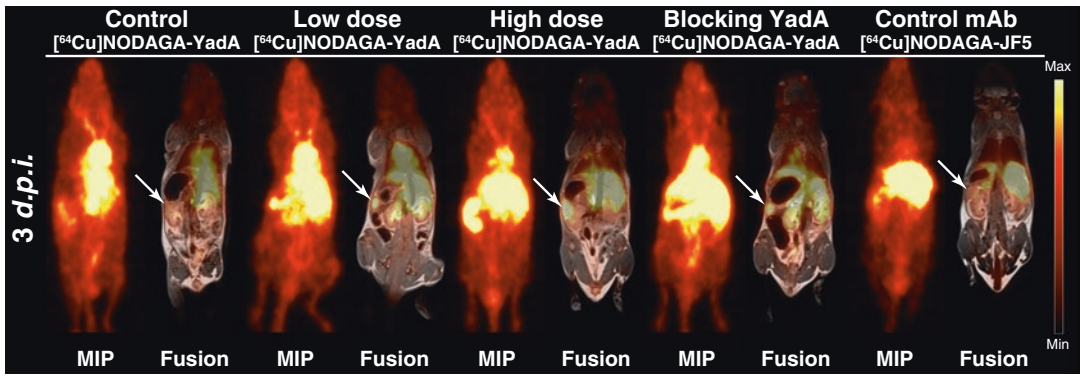

Fig. 34.6 Coronal [^{64}Cu]NODAGA-YadA PET and fused PET and MR images (fusion) from PBS-treated control, low- and high-dose infected mice 3 days *p.i.* Administration of the non-radiolabeled antibody specific to YadA 3 h prior to the injection of the radiolabeled antibody (blocking YadA) or administration of an *A. fumigatus*-specific tracer (control mAb) into high-dose infected mice served as controls. *Arrows* indicate the positions of the spleens, where infectious foci are located, of the mice

cost-intensive, time-consuming, and possible wrong therapeutic decisions. Not at least the non-invasive disease-specific diagnosis with PET/MRI will spare patients from extremely unpleasant and possibly dangerous invasive diagnostic procedures. Using nuclear medicine isotopes with long half-lives for radiolabeling, the biomarker specific for the respective disease, consecutive imaging, and monitoring the success of the therapeutic approach can be achieved with a single application of the diagnostic marker reducing the radiation dose drastically compared to the same number of applied PET/CT measurements. The advantages of simultaneous PET/MRI compared to PET/CT systems are reviewed by Glaudemans et al., pointing out the identical position of the patient in both modalities during acquisition, the functional information of the MRI complementing the molecular information of the PET, the outstanding localization of the PET signal in the soft tissue, and not at least the absence of radiation burden from the MRI system (Glaudemans et al. 2012). The chance to image infectious diseases at an early stage of the disease and at a molecular and cellular level might improve diagnostic potentials and could provide new insights in drug development and so far enigmatic parasite-host interactions. The precise discrimination between infectious disease and inflammation might also solve decisions of the correct therapy.

References

Ahrens ET, Bulte JW. Tracking immune cells in vivo using magnetic resonance imaging. Nat Rev Immunol. 2013;13:755–63.

Bading JR, Shields AF. Imaging of cell proliferation: status and prospects. J Nucl Med. 2008;49 Suppl 2:64S–80.

Bates DW, Sands K, Miller E, Lanken PN, Hibberd PL, Graman PS, Schwartz JS, Kahn K, Snydman DR, Parsonnet J, et al. Predicting bacteremia in patients with sepsis syndrome. Academic Medical Center Consortium Sepsis Project Working Group. J Infect Dis. 1997;176:1538–51.

Beck R, Roper B, Carlsen JM, Huisman MC, Lebschi JA, Andratschke N, Picchio M, Souvatzoglou M, Machulla HJ, Piert M. Pretreatment 18F-FAZA PET predicts success of hypoxia-directed radiochemotherapy using tirapazamine. J Nucl Med. 2007;48:973–80.

Bottone EJ. Yersinia enterocolitica: the charisma continues. Clin Microbiol Rev. 1997;10:257–76.

Brown GD, Denning DW, Gow NA, Levitz SM, Netea MG, White TC. Hidden killers: human fungal infections. Sci Transl Med. 2012;4:165rv113.

Bunschoten A, Welling MM, Termaat MF, Sathekge M, van Leeuwen FW. Development and prospects of dedicated tracers for the molecular imaging of bacterial infections. Bioconjug Chem. 2013;24:1971–89.

Chacko TK, Zhuang H, Nakhoda KZ, Moussavian B, Alavi A. Applications of fluorodeoxyglucose positron emission tomography in the diagnosis of infection. Nucl Med Commun. 2003;24:615–24.

Cobben DC, Elsinga PH, van Waarde A, Jager PL. Correspondence re: H. Barthel et al., 3′-deoxy-3′-[(18)F]fluorothymidine as a new marker for monitoring tumor response to antiproliferative therapy in vivo with positron emission tomography. Cancer Res., 63: 3791–3798, 2003. Cancer Res. 2003;63:8558–9; author reply 8560.

Coombes JL, Robey EA. Dynamic imaging of host-pathogen interactions in vivo. Nat Rev Immunol. 2010;10:353–64.

Coombes JL, Charsar BA, Han SJ, Halkias J, Chan SW, Koshy AA, Striepen B, Robey EA. Motile invaded neutrophils in the small intestine of Toxoplasma gondii-infected mice reveal a potential mechanism for parasite spread. Proc Natl Acad Sci U S A. 2013;110:E1913–22.

Corstens FH, van der Meer JW. Nuclear medicine's role in infection and inflammation. Lancet. 1999;354: 765–70.

Culverwell AD, Scarsbrook AF, Chowdhury FU. False-positive uptake on 2-[(1)(8)F]-fluoro-2-deoxy-D-glucose (FDG) positron-emission tomography/computed tomography (PET/CT) in oncological imaging. Clin Radiol. 2011;66:366–82.

Davis SL, Nuermberger EL, Um PK, Vidal C, Jedynak B, Pomper MG, Bishai WR, Jain SK. Noninvasive pulmonary [18F]-2-fluoro-deoxy-D-glucose positron emission tomography correlates with bactericidal activity of tuberculosis drug treatment. Antimicrob Agents Chemother. 2009;53:4879–84.

del Rosal T, Goycochea WA, Mendez-Echevarria A, Garcia-Fernandez de Villalta M, Baquero-Artigao F, Coronado M, Marin MD, Albajara L. (1)(8)F-FDG PET/CT in the diagnosis of occult bacterial infections in children. Eur J Pediatr. 2013;172:1111–5.

Di Genaro MS, Waidmann M, Kramer U, Hitziger N, Bohn E, Autenrieth IB. Attenuated Yersinia enterocolitica mutant strains exhibit differential virulence in cytokine-deficient mice: implications for the development of novel live carrier vaccines. Infect Immun. 2003;71:1804–12.

Dorward DA, Lucas CD, Rossi AG, Haslett C, Dhaliwal K. Imaging inflammation: molecular strategies to visualize key components of the inflammatory cascade, from initiation to resolution. Pharmacol Ther. 2012;135:182–99.

Dumarey N, Egrise D, Blocklet D, Stallenberg B, Remmelink M, del Marmol V, Van Simaeys G, Jacobs F, Goldman S. Imaging infection with 18F-FDG-labeled leukocyte PET/CT: initial experience in 21 patients. J Nucl Med. 2006;47:625–32.

Eckert J, Deplazes P. Biological, epidemiological, and clinical aspects of echinococcosis, a zoonosis of increasing concern. Clin Microbiol Rev. 2004;17:107–35.

Freifeld AG, Bow EJ, Sepkowitz KA, Boeckh MJ, Ito JI, Mullen CA, Raad II, Rolston KV, Young JA, Wingard JR, et al. Clinical practice guideline for the use of antimicrobial agents in neutropenic patients with cancer: 2010 update by the infectious diseases society of america. Clin Infect Dis. 2011;52:e56–93.

Fuchs K, Kohlhofer U, Quintanilla-Martinez L, Lamparter D, Kotter I, Reischl G, Rocken M, Pichler BJ, Kneilling M. In vivo imaging of cell proliferation enables the detection of the extent of experimental rheumatoid arthritis by 3′-deoxy-3′-18f-fluorothymidine and small-animal PET. J Nucl Med. 2013a;54:151–8.

Fuchs K, Kukuk D, Mahling M, Quintanilla-Martinez L, Reischl G, Reutershan J, Lang F, Rocken M, Pichler BJ, Kneilling M. Impact of anesthetics on 3′-[18F] fluoro-3′-deoxythymidine ([18F]FLT) uptake in animal models of cancer and inflammation. Mol Imaging. 2013b;12:277–87.

Glaudemans AW, Signore A. FDG-PET/CT in infections: the imaging method of choice? Eur J Nucl Med Mol Imaging. 2010;37:1986–91.

Glaudemans AW, Quintero AM, Signore A. PET/MRI in infectious and inflammatory diseases: will it be a useful improvement? Eur J Nucl Med Mol Imaging. 2012;39:745–9.

Goldsmith SJ, Vallabhajosula S. Clinically proven radiopharmaceuticals for infection imaging: mechanisms and applications. Semin Nucl Med. 2009;39:2–10.

Griessinger CM, Kehlbach R, Bukala D, Wiehr S, Bantleon R, Cay F, Schmid A, Braumuller H, Fehrenbacher B, Schaller M, et al. In vivo tracking of Th1 cells by PET reveals quantitative and temporal distribution and specific homing in lymphatic tissue. J Nucl Med. 2014;55:301–7.

Haas H, Petrik M, Decristoforo C. An iron-mimicking, Trojan horse-entering fungi--has the time come for molecular imaging of fungal infections? PLoS Pathog. 2015;11:e1004568.

Hara T. 11C-choline and 2-deoxy-2-[18F]fluoro-D-glucose in tumor imaging with positron emission tomography. Mol Imaging Biol. 2002;4:267–73.

Hasenbach K, Wiehr S, Herrmann C, Mannheim J, Cay F, von Kurthy G, Bolmont T, Grathwohl SA, Weller M, Lengerke C, et al. Monitoring the glioma tropism of bone marrow-derived progenitor cells by 2-photon laser scanning microscopy and positron emission tomography. Neuro Oncol. 2012;14:471–81.

Holden VI, Bachman MA. Diverging roles of bacterial siderophores during infection. Metallomics. 2015;7:986–95.

Hot A, Maunoury C, Poiree S, Lanternier F, Viard JP, Loulergue P, Coignard H, Bougnoux ME, Suarez F, Rubio MT, et al. Diagnostic contribution of positron emission tomography with [18F]fluorodeoxyglucose for invasive fungal infections. Clin Microbiol Infect. 2011;17:409–17.

Jain SK, Kwon P, Moss WJ. Management and outcomes of intracranial tuberculomas developing during antituberculous therapy: case report and review. Clin Pediatr (Phila). 2005;44:443–50.

Jamar F, Buscombe J, Chiti A, Christian PE, Delbeke D, Donohoe KJ, Israel O, Martin-Comin J, Signore A. EANM/SNMMI guideline for 18F-FDG use in inflammation and infection. J Nucl Med. 2013;54:647–58.

Kircher MF, Gambhir SS, Grimm J. Noninvasive cell-tracking methods. Nat Rev Clin Oncol. 2011;8:677–88.

Knapp J, Bart JM, Giraudoux P, Glowatzki ML, Breyer I, Raoul F, Deplazes P, Duscher G, Martinek K, Dubinsky P, et al. Genetic diversity of the cestode Echinococcus multilocularis in red foxes at a continental scale in Europe. PLoS Negl Trop Dis. 2009;3:e452.

Langer O, Brunner M, Zeitlinger M, Ziegler S, Muller U, Dobrozemsky G, Lackner E, Joukhadar C, Mitterhauser M, Wadsak W, et al. In vitro and in vivo evaluation of [18F]ciprofloxacin for the imaging of bacterial infections with PET. Eur J Nucl Med Mol Imaging. 2005;32:143–50.

Lukawska JJ, Livieratos L, Sawyer BM, Lee T, O'Doherty M, Blower PJ, Kofi M, Ballinger JR, Corrigan CJ, Gnanasegaran G, et al. Real-time differential tracking of human neutrophil and eosinophil migration in vivo. J Allergy Clin Immunol. 2014;133(233–239):e231.

Maier FC, Kneilling M, Reischl G, Cay F, Bukala D, Schmid A, Judenhofer MS, Rocken M, Machulla HJ, Pichler BJ. Significant impact of different oxygen breathing conditions on noninvasive in vivo tumor-hypoxia imaging using [(1)(8)F]-fluoro-azomycinarabino-furanoside ([(1)(8)F]FAZA). Radiat Oncol. 2011;6:165.

Marik J, Junutula JR. Emerging role of immunoPET in receptor targeted cancer therapy. Curr Drug Deliv. 2011;8:70–8.

McKinley ET, Ayers GD, Smith RA, Saleh SA, Zhao P, Washington MK, Coffey RJ, Manning HC. Limits of [18F]-FLT PET as a biomarker of proliferation in oncology. PLoS One. 2013;8:e58938.

McKinley ET, Zhao P, Coffey RJ, Washington MK, Manning HC. 3′-Deoxy-3′-[18F]-Fluorothymidine PET imaging reflects PI3K-mTOR-mediated pro-survival response to targeted therapy in colorectal cancer. PLoS One. 2014;9:e108193.

Mejri N, Hemphill A, Gottstein B. Triggering and modulation of the host-parasite interplay by Echinococcus multilocularis: a review. Parasitology. 2010;137:557–68.

Mills B, Awais RO, Luckett J, Turton D, Williams P, Perkins AC, Hill PJ. [(18)F]FDG-6-P as a novel in vivo tool for imaging staphylococcal infections. EJNMMI Res. 2015;5:13.

Nakamura T, Takahashi O, Matsui K, Shimizu S, Setoyama M, Nakagawa M, Fukui T, Morimoto T. Clinical

prediction rules for bacteremia and in-hospital death based on clinical data at the time of blood withdrawal for culture: an evaluation of their development and use. J Eval Clin Pract. 2006;12:692–703.

Ning X, Seo W, Lee S, Takemiya K, Rafi M, Feng X, Weiss D, Wang X, Williams L, Camp VM, et al. PET imaging of bacterial infections with fluorine-18-labeled maltohexaose. Angew Chem Int Ed Engl. 2014;53:14096–101.

Nottebrock H, Then R. Thymidine concentrations in serum and urine of different animal species and man. Biochem Pharmacol. 1977;26:2175–9.

Parisi MT. Functional imaging of infection: conventional nuclear medicine agents and the expanding role of 18-F-FDG PET. Pediatr Radiol. 2011;41:803–10.

Petrik M, Haas H, Dobrozemsky G, Lass-Florl C, Helbok A, Blatzer M, Dietrich H, Decristoforo C. 68Ga-siderophores for PET imaging of invasive pulmonary aspergillosis: proof of principle. J Nucl Med. 2010;51:639–45.

Petruzzi N, Shanthly N, Thakur M. Recent trends in soft-tissue infection imaging. Semin Nucl Med. 2009;39:115–23.

Reuter S, Schirrmeister H, Kratzer W, Dreweck C, Reske SN, Kern P. Pericystic metabolic activity in alveolar echinococcosis: assessment and follow-up by positron emission tomography. Clin Infect Dis. 1999;29:1157–63.

Reuter S, Gruner B, Buck AK, Blumstein N, Kern P, Reske SN. Long-term follow-up of metabolic activity in human alveolar echinococcosis using FDG-PET. Nuklearmedizin. 2008;47:147–52.

Rolle AM, Soboslay PT, Reischl G, Hoffmann WH, Pichler BJ, Wiehr S. Evaluation of the metabolic activity of echinococcus multilocularis in rodents using positron emission tomography tracers. Mol Imaging Biol. 2015;17:512–20.

Rolle AM, Hasenberg M, Thornton CR, Solouk-Saran D, Mann L, Weski J, Maurer A, Fischer E, Spycher PR, Schibli R, et al. ImmunoPET/MR imaging allows specific detection of Aspergillus fumigatus lung infection in vivo. Proc Natl Acad Sci U S A. 2016;113(8):E1026–33.

Rosenbaum SJ, Lind T, Antoch G, Bockisch A. False-positive FDG PET uptake – the role of PET/CT. Eur Radiol. 2006;16:1054–65.

Santangelo PJ, Rogers KA, Zurla C, Blanchard EL, Gumber S, Strait K, Connor-Stroud F, Schuster DM, Amancha PK, Hong JJ, et al. Whole-body immunoPET reveals active SIV dynamics in viremic and antiretroviral therapy-treated macaques. Nat Methods. 2015;12:427–32.

Sarda L, Cremieux AC, Lebellec Y, Meulemans A, Lebtahi R, Hayem G, Genin R, Delahaye N, Huten D, Le Guludec D. Inability of 99mTc-ciprofloxacin scintigraphy to discriminate between septic and sterile osteoarticular diseases. J Nucl Med. 2003;44:920–6.

Schindler MK, Schutz MS, Muhlenkamp MC, Rooijakkers SH, Hallstrom T, Zipfel PF, Autenrieth IB. Yersinia enterocolitica YadA mediates complement evasion by recruitment and inactivation of C3 products. J Immunol. 2012;189:4900–8.

Shields AF, Grierson JR, Dohmen BM, Machulla HJ, Stayanoff JC, Lawhorn-Crews JM, Obradovich JE, Muzik O, Mangner TJ. Imaging proliferation in vivo with [F-18]FLT and positron emission tomography. Nat Med. 1998;4:1334–6.

Signore A, Glaudemans AW. The molecular imaging approach to image infections and inflammation by nuclear medicine techniques. Ann Nucl Med. 2011;25:681–700.

Signore A, Mather SJ, Piaggio G, Malviya G, Dierckx RA. Molecular imaging of inflammation/infection: nuclear medicine and optical imaging agents and methods. Chem Rev. 2010;110:3112–45.

Smith BA, Harmatys KM, Xiao S, Cole EL, Plaunt AJ, Wolter W, Suckow MA, Smith BD. Enhanced cell death imaging using multivalent zinc(II)-bis(dipicolylamine) fluorescent probes. Mol Pharm. 2013;10:3296–303.

Sorger D, Patt M, Kumar P, Wiebe LI, Barthel H, Seese A, Dannenberg C, Tannapfel A, Kluge R, Sabri O. [18F] Fluoroazomycinarabinofuranoside (18FAZA) and [18F]Fluoromisonidazole (18FMISO): a comparative study of their selective uptake in hypoxic cells and PET imaging in experimental rat tumors. Nucl Med Biol. 2003;30:317–26.

Stevens V, Geiger K, Concannon C, Nelson RE, Brown J, Dumyati G. Inpatient costs, mortality and 30-day re-admission in patients with central-line-associated bloodstream infections. Clin Microbiol Infect. 2014;20:O318–24.

Stumpe KD, Dazzi H, Schaffner A, von Schulthess GK. Infection imaging using whole-body FDG-PET. Eur J Nucl Med. 2000;27:822–32.

Tappe D, Kern P, Frosch M. A hundred years of controversy about the taxonomic status of Echinococcus species. Acta Trop. 2010;115:167–74.

Thornton CR, Wills OE. Immunodetection of fungal and oomycete pathogens: established and emerging threats to human health, animal welfare and global food security. Crit Rev Microbiol. 2015;41:27–51.

Tuzun M, Altinors N, Arda IS, Hekimoglu B. Cerebral hydatid disease CT and MR findings. Clin Imaging. 2002;26:353–7.

van Oosten M, Schafer T, Gazendam JA, Ohlsen K, Tsompanidou E, de Goffau MC, Harmsen HJ, Crane LM, Lim E, Francis KP, et al. Real-time in vivo imaging of invasive- and biomaterial-associated bacterial infections using fluorescently labelled vancomycin. Nat Commun. 2013;4:2584.

van Waarde A, Cobben DC, Suurmeijer AJ, Maas B, Vaalburg W, de Vries EF, Jager PL, Hoekstra HJ, Elsinga PH. Selectivity of 18F-FLT and 18F-FDG for differentiating tumor from inflammation in a rodent model. J Nucl Med. 2004;45:695–700.

Vinjamuri S, Hall AV, Solanki KK, Bomanji J, Siraj Q, O'Shaughnessy E, Das SS, Britton KE. Comparison of 99mTc infection imaging with radiolabelled white-cell imaging in the evaluation of bacterial infection. Lancet. 1996;347:233–5.

Vuitton DA, Gottstein B. Echinococcus multilocularis and its intermediate host: a model of parasite-host interplay. J Biomed Biotechnol. 2010;2010:923193.

Wang J, Yao WH, Yi BN, Liu S, Zhang DQ, Jiang CH, Zhang LM, Niu JQ, Jia WX, Wen H. Proton magnetic resonance spectroscopy in the evaluation of infiltration zone of cerebral alveolar echinococcosis. Chin Med J (Engl). 2012;125:2260–4.

Wang Y, Chen L, Liu X, Cheng D, Liu G, Liu Y, Dou S, Hnatowich DJ, Rusckowski M. Detection of Aspergillus fumigatus pulmonary fungal infections in mice with (99m)Tc-labeled MORF oligomers targeting ribosomal RNA. Nucl Med Biol. 2013;40:89–96.

Weinstein EA, Ordonez AA, DeMarco VP, Murawski AM, Pokkali S, MacDonald EM, Klunk M, Mease RC, Pomper MG, Jain SK. Imaging Enterobacteriaceae infection in vivo with 18F-fluorodeoxysorbitol positron emission tomography. Sci Transl Med. 2014;6:259ra146.

Wiehr S, Buhler P, Gierschner D, Wolf P, Rolle AM, Kesenheimer C, Pichler BJ, Elsasser-Beile U. Pharmacokinetics and PET imaging properties of two recombinant anti-PSMA antibody fragments in comparison to their parental antibody. Prostate. 2014;74:743–55.

WHO. World Health Statistics 2014; 2014.

Appendix: Relevant Physiological and Experimental Rodent Parameters

A.1 Relevant Physiological Standard Parameters

	Mouse	Nude mouse	Rat
Body weight (g)	20–35	20–35	250–600
Body temperature (°C)	36–38	37.3	37.5–39
Respiratory frequency (breathing/min)	60–230	84–230	60–170
Heart frequency (beat/min)	300–800	300–800	300–500
Blood pressure (mmHg)	133–160/102–110	133–160/102–110	116/90
Fertility (days)	28–49	56–70	50–72
Urine (ml/animal/day)	1–3	1–3	10–15
Homing temperature (°C)	20–24	24–28	18–24
Homing humidity (%)	50–70	40–65	50–70

The hematologic parameters are highly species and strain specific and can be obtained from the commercial breeders, e.g., Charles River Laboratories, Jackson Laboratories, or Harlan Laboratories.

A.2 Recommendations of the GV-SOLAS

This section contains selected physiological and experimental parameters for selected species from respective recommendation letters of the GV-SOLAS. The selection has been performed with respect to their importance for small-animal imaging and has to be regarded as recommendation as stated by the GV-SOLAS.

A.2.1 Blood Collection

See Tables A.1, A.2, A.3, A.4, A.5, and A.6.

A.2.2 Criteria of Maximum Tumor Burden

The tumor burden should not exceed 5 % of the body weight of animals used for the passage of tumors. Furthermore, the tumor burden should be limited to a maximum of 10 % of the body weight of the animals in therapeutic studies. Animals have to be sacrificed by reaching the mentioned maximum tumor diameter or, in cases that those criteria are met such as tumor ulceration, severe invasiveness resulting in pain and loss of vital functions or loss of body weight at a maximum of 20 % (see Table A.7).

F. Kiessling et al. (eds.), *Small Animal Imaging*, DOI 10.1007/978-3-319-42202-2

Table A.1 Average blood volume

Species	Blood volume[a]			Hematocrit (%)
	ml/animal[b]	ml/kg b.w.	% b. w.	
Mouse (25 g)	1.7	74 (70–80)	6.6	42 (33–50)
Rat (300 g)	19	64 (50–70)	6.4	46 (40–61)
Guinea pig (400 g)	30	75 (65–90)	7.5	44 (37–50)
Golden hamster (100 g)	7.8	78 (65–80)	7.8	51 (39–59)

[a]Differences are possible regarding race, strain, and age; the percentage amount is less in obese animals than in normal weighted
[b]Estimated blood volume at the specified body weight in column 1 of this table

Table A.2 Parameters of blood collection

Species	Examples of total blood volume collection[a]		
	Single[b] (max. 10 %) (ml)	Daily[c] (1 %) (ml)	Final[d] (ml)
Mouse (25 g)	0.17	0.02	0.7–1.0
Rat (300 g)	1.9	0.2	10
Guinea pig (400 g)	3.0	0.3	15
Golden hamster (100 g)	0.7	0.07	3.5

[a]The blood collection parameters are only valid for adult, healthy animals and can be less for freshly manipulated, diseased, old, or stressed animals
[b]A recovery phase for at least 2–3 weeks necessary
[c]After daily blood collection at a maximum of 2 weeks, a recovery phase for at least 2–3 weeks necessary
[d]Only under anesthetic, approx. 50 % of the whole blood volume collectable (determined empirically)

Table A.3 Techniques for blood collection in mice

Blood collection Quantity and frequency	Location	Specific requirements
1. Small amount (0.02–0.04 ml)	(a) Tail vein	
	(b) Amputation of tail tip	(b) Infants only up to the end of the suckling period
	(c) Retrobulbar	(c) Under anesthetic (e.g., isoflurane) by using a glass capillary with an outer diameter of 0.8 mm
	(d) V. facialis	
	(e) V. saphena	
2. Single maximum blood volume (see Table A.2 as well)	(a) Retrobulbar	(a) Identical to (1c)
	(b) Tail vein	(b) 24–26-G needle
	(c) Venous angle	(c) Anesthetic, 23–25-G needle
	(d) V. facialis	
3. Repeated collection (see Table A.2 as well)	(a) Tail vein	Use alternating blood collection locations!
	(b) V. facialis	
	(c) V. saphena	
	(d) Retrobulbar	(d) Anesthetic, only two blood collections per eye in intervals of 2 weeks
4. Final collection (exsanguination)	(a) Cardial	(a), (b), and (c) Anesthetic
	(b) Aorta	
	(c) V. cava	
	(d) Decapitation	(d) Also possible without anesthetic

Table A.4 Techniques for blood collection in rats

Blood collection Quantity and frequency	Location	Specific requirements
1. Small amount (0.04–0.05 ml)	(a) Tail vein (b) Amputation of tail tip (c) V. saphena	(a) 23–26-G needle (b) Infants only up to the end of the suckling period
2. Single maximum blood volume (see Table A.2 as well)	(a) Tail vein (b) Retrobulbar (c) Venous angle	(a) 23–26-G needle (b) Under anesthetic (e.g., isoflurane) by using a glass capillary up to an outer diameter of 0.9 mm (c) Anesthetic; 21–25-G needle
3. Repeated collection (see Table A.2 as well)	(a) Tail vein (b) Permanent catheter in V. jugularis (c) Retrobulbar (d) V. saphena	(b) Anesthetic, polyethylene catheter, outer diameter of 0.61 mm, port system (c) Anesthetic, only two blood collections per eye in intervals of 2 weeks
4. Final collection (exsanguination)	(a) Cardial (b) Aorta (c) V. cava (d) Decapitation	(a), (b), and (c) Anesthetic (a) 20–21-G needle (d) Also possible without anesthetic

Table A.5 Techniques for blood collection in guinea pigs

Blood collection Quantity and frequency	Location	Specific requirements
1. Small amount (0.2 ml)	(a) Ear vein (b) V. saphena	
2. Single maximum blood volume (see Table A.2 as well)	(a) V. jugularis (b) Venous angle	(a) Anesthetic; vessel preparation necessary, 21–22-G needle (b) Anesthetic
3. Repeated collection (see Table A.2 as well)	(a) Permanent catheter in V. jugularis (b) Ear vein (c) V. saphena	(a) Anesthetic, polyethylene catheter or subcutaneous port, outer diameter of 0.6 mm
4. Final collection (exsanguination)	(a) Cardial (b) Aorta (c) V. cava	(a), (b), and (c) Anesthetic

Table A.6 Techniques for blood collection in hamsters

Blood collection Quantity and frequency	Location	Specific requirements
1. Small amount (0.02–0.04 ml)	V. saphena	Anesthetic (e.g., isoflurane)
2. Single maximum blood volume (see Table A.2 as well)	(a) Retrobulbar (b) V. saphena (c) Venous angle	(a), (b), and (c) Anesthetic (a) Glass capillary, outer diameter of 0.8 mm
3. Repeated collection (see Table A.2 as well)	Permanent catheter in V. jugularis	Anesthetic, polyethylene catheter, outer diameter of 0.2 mm
4. Final collection (exsanguination)	(a) Cardial (b) Aorta (c) V. cava	(a), (b), and (c) Anesthetic

A.2.3 Recommended Volumes for Injection

Requirements for injectable solutions are:

- Isotonic solution
- Neutral pH (pH 7.0–7.3)
- Body temperature
- Concentrations, chemical compositions, or physical characteristics which do not induce general damages or local irritations

It has to be taken into account that hyper- or hypotonic solutions or solutions consisting of non-physiologic pH values are able to cause severe pain and tissue damages (e.g., in the case of perivascular injection) or lead to erythrocyte damages (hemolysis) (see Tables A.8 and A.9).

Table A.7 Criteria of maximum tumor burden allowed

Type of tumor	Maximum diameter (cm)	
	Mouse	Rat
Autochthonous tumors		
Single tumor	1.5	3.0
Multiple tumors (sum of all single tumors)	3.0	6.0
Skin tumor	2.0	3.0
Tumors transplanted:		
Subcutaneously[a]	1.5	3.0
Two tumors	Each 1.5	Each 3.0
Intramuscularly	0.5	1.0

[a]Localized in back and flank regions

Table A.8 Volume parameters for local injection of solutions

Species	ml per injection site		µl/animal
	Intradermal	Intramuscular	Intracerebroventricular
Mouse	0.02 (27 G)	0.03 (27 G)	3 (28 G)[a,b]
Rat	0.05 (27 G)	0.10 (23–25 G)	5 (28 G)[a,b]
Guinea pig	0.10 (27 G)	0.25 (25 G)	5 (28 G)[a,b]
Golden hamster	0.02 (27 G)	0.05 (24–25 G)	3 (28 G)[a,b]

[a]A very slow injection speed is required (2–3 min in mouse and rat)
[b]Through a 22-G guidance cannula

Table A.9 Volume parameters for other injection sites

Species	ml/kg b.w.		
	Subcutaneous	Intraperitoneal	Intravenous[a,b]
Mouse	10 (25 G)	10 (25–27 G)	5 (26–28 G)
Rat	10 (25 G)	10 (23–25 G)	5 (25–27 G)
Guinea pig	10 (23–25 G)	10 (23–25 G)	5 (25–27 G)
Golden hamster	10 (23–25 G)	10 (23–25 G)	5 (25–27 G)

[a]i.v. injection time: minimum of 1 min up to 2.5 min
[b]Infusion taking longer than 2 h should not exceed the maximum infusion volume <10 % of the total blood volume

References

Recommended parameters for blood collection in lab animals of the Society for Laboratory Animal Science (GV-SOLAS). http://www.gv-solas.de/fileadmin/user_upload/pdf_publikation/tie_blutentnahme09.pdf.

Recommended criteria for a premature immolation of tumor burden mice and rats of the Society for Laboratory Animal Science (GV-SOLAS). http://www.gv-solas.de/fileadmin/user_upload/pdf_publikation/tie_vorz.toetung2009.pdf.

Recommended maximum injection volumes in lab animals of the Society for Laboratory Animal Science (GV-SOLAS). http://www.gv-solas.de/fileadmin/user_upload/pdf_publikation/Injektionsvol_August_2010.pdf.

Index

F. Kiessling et al. (eds.), *Small Animal Imaging*, DOI 10.1007/978-3-319-42202-2

O